

processes

CFD Based Researches and Applications for Fluid Machinery and Fluid Device

Edited by
Jin-Hyuk Kim, Sung-Min Kim, Minsuk Choi, Lei Tan,
Bin Huang and Ji Pei

Printed Edition of the Special Issue Published in *Processes*

CFD Based Researches and Applications for Fluid Machinery and Fluid Device

CFD Based Researches and Applications for Fluid Machinery and Fluid Device

Editors

Jin-Hyuk Kim

Sung-Min Kim

Minsuk Choi

Lei Tan

Bin Huang

Ji Pei

MDPI • Basel • Beijing • Wuhan • Barcelona • Belgrade • Manchester • Tokyo • Cluj • Tianjin



Editors

Jin-Hyuk Kim Carbon Neutral Technology RnD Department Korea Institute of Industrial Technology Cheonan Korea, South	Sung-Min Kim School of Mechanical Engineering Sungkyunkwan University Suwon Korea, South	Minsuk Choi Department of Mechanical Engineering Myongji University Yongin Korea, South
Lei Tan Department of Energy and Power Engineering Tsinghua University Beijing China	Bin Huang Institute of Ocean Engineering and Technology Zhejiang University Hangzhou China	Ji Pei National Research Center of Pumps Jiangsu University Zhenjiang China

Editorial Office

MDPI
St. Alban-Anlage 66
4052 Basel, Switzerland

This is a reprint of articles from the Special Issue published online in the open access journal *Processes* (ISSN 2227-9717) (available at: www.mdpi.com/journal/processes/special_issues/CFD_Fluid_Device).

For citation purposes, cite each article independently as indicated on the article page online and as indicated below:

LastName, A.A.; LastName, B.B.; LastName, C.C. Article Title. <i>Journal Name</i> Year , <i>Volume Number</i> , Page Range.
--

ISBN 978-3-0365-1816-9 (Hbk)

ISBN 978-3-0365-1815-2 (PDF)

© 2021 by the authors. Articles in this book are Open Access and distributed under the Creative Commons Attribution (CC BY) license, which allows users to download, copy and build upon published articles, as long as the author and publisher are properly credited, which ensures maximum dissemination and a wider impact of our publications.

The book as a whole is distributed by MDPI under the terms and conditions of the Creative Commons license CC BY-NC-ND.

Contents

Preface to "CFD Based Researches and Applications for Fluid Machinery and Fluid Device"	vii
Jin-Hyuk Kim, Sung-Min Kim, Minsuk Choi, Lei Tan, Bin Huang and Ji Pei Special Issue on "CFD Based Researches and Applications for Fluid Machinery and Fluid Device" Reprinted from: <i>Processes</i> 2021 , <i>9</i> , 1137, doi:10.3390/pr9071137	1
Jianjun Ye, Shehab Salem, Juan Wang, Yiwen Wang, Zonggang Du and Wei Wang Effects of Micro-Tab on the Lift Enhancement of Airfoil S-809 with Trailing-Edge Flap Reprinted from: <i>Processes</i> 2021 , <i>9</i> , 547, doi:10.3390/pr9030547	5
Mohamed Murshid Shamsuddeen, Sang-Bum Ma, Sung Kim, Ji-Hoon Yoon, Kwang-Hee Lee, Changjun Jung and Jin-Hyuk Kim Effect of an Inducer-Type Guide Vane on Hydraulic Losses at the Inter-Stage Flow Passage of a Multistage Centrifugal Pump Reprinted from: <i>Processes</i> 2021 , <i>9</i> , 526, doi:10.3390/pr9030526	21
Koldo Portal-Porras, Unai Fernandez-Gamiz, Iñigo Aramendia, Daniel Teso-Fz-Betoño and Ekaitz Zulueta Testing the Accuracy of the Cell-Set Model Applied on Vane-Type Sub-Boundary Layer Vortex Generators Reprinted from: <i>Processes</i> 2021 , <i>9</i> , 503, doi:10.3390/pr9030503	39
Funan Chen, Huili Bi, Soo-Hwang Ahn, Zhongyu Mao, Yongyao Luo and Zhengwei Wang Investigation on Dynamic Stresses of Pump-Turbine Runner during Start Up in Turbine Mode Reprinted from: <i>Processes</i> 2021 , <i>9</i> , 499, doi:10.3390/pr9030499	57
Min-Cheol Park, Sang-Bum Ma and Kwang-Yong Kim Optimization of a Wavy Microchannel Heat Sink with Grooves Reprinted from: <i>Processes</i> 2021 , <i>9</i> , 373, doi:10.3390/pr9020373	77
Xinlong Wang, Honggang Fan and Bing Liu Optimization Control on the Mixed Free-Surface-Pressurized Flow in a Hydropower Station Reprinted from: <i>Processes</i> 2021 , <i>9</i> , 320, doi:10.3390/pr9020320	97
Md Rakibuzzaman, Sang-Ho Suh, Hyoung-Ho Kim, Youngtae Ryu and Kyung Yup Kim Development of a Hydropower Turbine Using Seawater from a Fish Farm Reprinted from: <i>Processes</i> 2021 , <i>9</i> , 266, doi:10.3390/pr9020266	113
Mengcheng Wang, Yanjun Li, Jianping Yuan and Fareed Konadu Osman Matching Optimization of a Mixed Flow Pump Impeller and Diffuser Based on the Inverse Design Method Reprinted from: <i>Processes</i> 2021 , <i>9</i> , 260, doi:10.3390/pr9020260	137
Jacek Stelmach, Czesław Kuncewicz, Szymon Szufa, Tomas Jirout and Frantisek Rieger The Influence of Hydrodynamic Changes in a System with a Pitched Blade Turbine on Mixing Power Reprinted from: <i>Processes</i> 2020 , <i>9</i> , 68, doi:10.3390/pr9010068	153
Miroslav H. Benišek, ore S. Čantrak, Dejan B. Ilić and Novica Z. Janković New Design of the Reversible Jet Fan Reprinted from: <i>Processes</i> 2020 , <i>8</i> , 1671, doi:10.3390/pr8121671	165

Xiaodong Feng, Wentao Su, Yu Ma, Lei Wang and Heping Tan Numerical and Experimental Study on Waviness Mechanical Seal of Reactor Coolant Pump Reprinted from: <i>Processes</i> 2020 , <i>8</i> , 1611, doi:10.3390/pr8121611	177
Xiongfao Gao, Ting Zhao, Weidong Shi, Desheng Zhang, Ya Shi, Ling Zhou and Hao Chang Numerical Investigation of an Open-Design Vortex Pump with Different Blade Wrap Angles of Impeller Reprinted from: <i>Processes</i> 2020 , <i>8</i> , 1601, doi:10.3390/pr8121601	193
Yanjun Li, Yunhao Zheng, Fan Meng and Majeed Koranteng Osman The Effect of Root Clearance on Mechanical Energy Dissipation for Axial Flow Pump Device Based on Entropy Production Reprinted from: <i>Processes</i> 2020 , <i>8</i> , 1506, doi:10.3390/pr8111506	213
Min Seok Hur, Soo In Lee, Seong Won Moon, Tong Seop Kim, Jae Su Kwak, Dong Hyun Kim and Il Young Jung Effect of Clearance and Cavity Geometries on Leakage Performance of a Stepped Labyrinth Seal Reprinted from: <i>Processes</i> 2020 , <i>8</i> , 1496, doi:10.3390/pr8111496	231
Xiaocheng Rui, Limin Lin, Junkui Wang, Xinxue Ye, Haijiang He, Wei Zhang and Zuchao Zhu Experimental and Comparative RANS/URANS Investigations on the Effect of Radius of Volute Tongue on the Aerodynamics and Aeroacoustics of a Sirocco Fan Reprinted from: <i>Processes</i> 2020 , <i>8</i> , 1442, doi:10.3390/pr8111442	249
Seung Il Baek and Joon Ahn Large Eddy Simulation of Film Cooling with Triple Holes: Injectant Behavior and Adiabatic Film-Cooling Effectiveness Reprinted from: <i>Processes</i> 2020 , <i>8</i> , 1443, doi:10.3390/pr8111443	277
Moru Song, Hong Xie, Bo Yang and Shuyi Zhang Influence of Tip Clearance on Flow Characteristics of Axial Compressor Reprinted from: <i>Processes</i> 2020 , <i>8</i> , 1445, doi:10.3390/pr8111445	295
Hongchang Ding, Tao Chang and Fanyun Lin The Influence of the Blade Outlet Angle on the Flow Field and Pressure Pulsation in a Centrifugal Fan Reprinted from: <i>Processes</i> 2020 , <i>8</i> , 1422, doi:10.3390/pr8111422	315
Ujjwal Shrestha and Young-Do Choi A CFD-Based Shape Design Optimization Process of Fixed Flow Passages in a Francis Hydro Turbine Reprinted from: <i>Processes</i> 2020 , <i>8</i> , 1392, doi:10.3390/pr8111392	329
Yao Lei, Yuhui Huang and Hengda Wang Aerodynamic Performance of an Octorotor SUAV with Different Rotor Spacing in Hover Reprinted from: <i>Processes</i> 2020 , <i>8</i> , 1364, doi:10.3390/pr8111364	351
Woo-Yul Kim, Santhosh Senguttuvan and Sung-Min Kim Effect of Rotor Spacing and Duct Diffusion Angle on the Aerodynamic Performances of a Counter-Rotating Ducted Fan in Hover Mode Reprinted from: <i>Processes</i> 2020 , <i>8</i> , 1338, doi:10.3390/pr8111338	363

Seung-Yong Ahn and Kwang-Yong Kim Thermal Performance of T-shaped Obstacles in a Solar Air Heater Reprinted from: <i>Processes</i> 2020 , <i>8</i> , 1305, doi:10.3390/pr8101305	377
Qiao Li, Xiang Ma, Peng Wu, Shuai Yang, Bin Huang and Dazhuan Wu Study on the Transient Characteristics of the Centrifugal Pump during the Startup Period with Assisted Valve Reprinted from: <i>Processes</i> 2020 , <i>8</i> , 1241, doi:10.3390/pr8101241	393
Xiaohui Wang, Kailin Kuang, Zanxiu Wu and Junhu Yang Numerical Simulation of Axial Vortex in a Centrifugal Pump as Turbine with S-Blade Impeller Reprinted from: <i>Processes</i> 2020 , <i>8</i> , 1192, doi:10.3390/pr8091192	411
Sang-Bum Ma, Sung Kim and Jin-Hyuk Kim Optimization Design of a Two-Vane Pump for Wastewater Treatment Using Machine-Learning-Based Surrogate Modeling Reprinted from: <i>Processes</i> 2020 , <i>8</i> , 1170, doi:10.3390/pr8091170	427
Shuyi Zhang, Bo Yang, Hong Xie and Moru Song Applications of an Improved Aerodynamic Optimization Method on a Low Reynolds Number Cascade Reprinted from: <i>Processes</i> 2020 , <i>8</i> , 1150, doi:10.3390/pr8091150	445
Wenjie Wang, Yanpin Li, Majeed Koranteng Osman, Shouqi Yuan, Benying Zhang and Jun Liu Multi-Condition Optimization of Cavitation Performance on a Double-Suction Centrifugal Pump Based on ANN and NSGA-II Reprinted from: <i>Processes</i> 2020 , <i>8</i> , 1124, doi:10.3390/pr8091124	465
Hong Xie, Moru Song and Bo Yang Research on the Application of Partial Similarity for a 1-1/2 Axial Compressor Reprinted from: <i>Processes</i> 2020 , <i>8</i> , 1121, doi:10.3390/pr8091121	485
Lu Yu, Haochen Zhang, Hui Chen, Zhigang Zuo and Shuhong Liu Numerical Study on the Influence of Step Casing on Cavitating Flows and Instabilities in Inducers with Equal and Varying Pitches Reprinted from: <i>Processes</i> 2020 , <i>8</i> , 1103, doi:10.3390/pr8091103	509
Yin Luo, Yakun Fan, Yuejiang Han, Weqi Zhang and Emmanuel Acheaw Research on the Dynamic Characteristics of Mechanical Seal under Different Extrusion Fault Degrees Reprinted from: <i>Processes</i> 2020 , <i>8</i> , 1057, doi:10.3390/pr8091057	523
Xilong Zhang, Yongliang Zhang and Chenggang Lu Flow and Noise Characteristics of Centrifugal Fan in Low Pressure Environment Reprinted from: <i>Processes</i> 2020 , <i>8</i> , 985, doi:10.3390/pr8080985	543

Preface to “CFD Based Researches and Applications for Fluid Machinery and Fluid Device”

The demand for computational fluid dynamics (CFD)-based numerical techniques is increasing rapidly with the development of the computing power system. These advanced CFD techniques are applicable to various issues in the industrial engineering fields and especially contribute to the design of fluid machinery and fluid devices, which have very complicated unsteady flow phenomena and physics. In other words, to aid the rapid development of CFD techniques, the performances of fluid machinery and fluid devices with complicated unsteady flows have been enhanced significantly. In addition, many persistently troublesome problems of fluid machinery and fluid devices such as flow instability, rotor–stator interaction, surging, cavitation, vibration, and noise are solved clearly using advanced CFD techniques.

This Special Issue on “CFD-Based Research and Applications for Fluid Machinery and Fluid Devices” aims to present recent novel research trends based on advanced CFD techniques for fluid machinery and fluid devices. The following topics, among others, are included in this issue:

- CFD techniques and applications in fluid machinery and fluid devices;
- Unsteady and transient phenomena in fluid machinery and fluid devices;
- Pumps, fans, compressors, hydraulic turbines, pump-turbines, valves, etc.

Jin-Hyuk Kim, Sung-Min Kim, Minsuk Choi, Lei Tan, Bin Huang, Ji Pei
Editors

Editorial

Special Issue on “CFD Based Researches and Applications for Fluid Machinery and Fluid Device”

Jin-Hyuk Kim ^{1,2,*} , Sung-Min Kim ³, Minsuk Choi ⁴ , Lei Tan ⁵ , Bin Huang ⁶ and Ji Pei ⁷ 

¹ Clean Energy R&D Department, Korea Institute of Industrial Technology, Cheonan 31056, Korea

² Industrial Technology (Green Process and Energy System Engineering), Korea University of Science and Technology, Daejeon 34113, Korea

³ School of Mechanical Engineering, Sungkyunkwan University, Suwon 16419, Korea; smkim@skku.edu

⁴ Department of Mechanical Engineering, Myongji University, Yongin 17058, Korea; mchoi@mju.ac.kr

⁵ Department of Energy and Power Engineering, Tsinghua University, Beijing 100084, China; tanlei@mail.tsinghua.edu.cn

⁶ Institute of Ocean Engineering and Technology, Ocean College, Zhejiang University, Hangzhou 310058, China; binhuang@zju.edu.cn

⁷ National Research Center of Pumps, Jiangsu University, Zhenjiang 212013, China; jpei@ujs.edu.cn

* Correspondence: jinhyuk@kitech.re.kr

The demand for computational fluid dynamics (CFD)-based numerical techniques is increasing rapidly with the development of the computing power system. These advanced CFD techniques are applicable to various issues in the industrial engineering fields and especially contributing considerably to the design of fluid machinery and fluid devices, which have very complicated unsteady flow phenomena and physics. In other words, with the rapid development of CFD techniques, the performances of fluid machinery and fluid devices with complicated unsteady flows have been enhanced significantly. In addition, many persistently troublesome problems of fluid machinery and fluid devices such as flow instability, rotor–stator interaction, surging, cavitation, vibration, and noise are solved clearly using advanced CFD techniques.

The Special Issue on “CFD-Based Researches and Applications for Fluid Machinery and Fluid Device” in *Processes* deals with topics related to CFD techniques and applications in various fluid machines and devices. Specifically, the 31 papers published in this Special Issue focus on the advancement in the detailed internal flow analyses and methodologies for designing various fluid machines and devices, as the following summaries indicate. The influence of a low-pressure environment on the aerodynamic and noise characteristics of a centrifugal fan was studied numerically and experimentally by Zhang et al. [1]. Luo et al. [2] analyzed systematically the dynamic characteristics of mechanical seals under different fault conditions. Yu et al. [3] numerically studied the influence of step casing on unsteady cavitating flows and instabilities in inducers with equal and varying pitches. A methodology to improve the aerodynamic design with low cost and high accuracy for a 1–1/2 axial compressor was presented by Xie et al. [4]. Wang et al. [5] conducted the multi-condition optimization to enhance the cavitation performance of a double-suction centrifugal pump based on an artificial neural network (ANN) and nondominated sorting genetic algorithm II (NSGA-II). Zhang et al. [6] proposed an improved aerodynamic optimization method for designing effectively a low Reynolds number cascade. The design optimization of a two-vane pump for wastewater treatment using machine-learning-based surrogate modeling was carried out by Ma et al. [7]. Wang et al. [8] analyzed numerically the axial vortex characteristics in a centrifugal pump as a turbine with an S-blade impeller. Li et al. [9] studied numerically and experimentally the transient characteristics of a centrifugal pump during the startup period with assisted valve. The thermal performance with the geometric parametrization of T-shaped obstacles in a solar air heater was performed by Ahn and Kim [10].



Citation: Kim, J.-H.; Kim, S.-M.; Choi, M.; Tan, L.; Huang, B.; Pei, J. Special Issue on “CFD Based Researches and Applications for Fluid Machinery and Fluid Device”. *Processes* **2021**, *9*, 1137. <https://doi.org/10.3390/pr9071137>

Received: 29 June 2021
Accepted: 29 June 2021
Published: 30 June 2021

Publisher’s Note: MDPI stays neutral with regard to jurisdictional claims in published maps and institutional affiliations.



Copyright: © 2021 by the authors. Licensee MDPI, Basel, Switzerland. This article is an open access article distributed under the terms and conditions of the Creative Commons Attribution (CC BY) license (<https://creativecommons.org/licenses/by/4.0/>).

On the other hand, the effect of rotor spacing and duct diffusion angle on the aerodynamic performances of a counter-rotating ducted fan in a hover mode was analyzed numerically by Kim et al. [11]. Lei et al. [12] applied the CFD method to analyze the aerodynamic performance of an octorotor small unmanned aerial vehicle with different rotor spacing in hover. Shrestha and Choi [13] proposed a CFD-based shape design optimization process to improve the flow uniformity in the fixed flow passages of a Francis hydro turbine model. The influence analyses of the blade outlet angle on the flow and pressure pulsation characteristics in a centrifugal fan were carried out by Ding et al. [14]. Rui et al. [15] performed experimental and numerical studies to investigate the effect of the radius of a volute tongue on the aerodynamic and aeroacoustic characteristics of a Sirocco fan. The effect and mechanism of the triple hole on the film-cooling performance based on large eddy simulation (LES) were identified by Baek and Ahn [16]. Song et al. [17] verified the influence of tip clearance on the flow characteristics of an axial compressor through the CFD technique. Hur et al. [18] numerically investigated the effect of clearance and cavity geometries on the leakage performance of a stepped labyrinth seal. The effect of root clearance on the mechanical energy dissipation of an axial flow pump based on entropy production was analyzed by Li et al. [19]. Gao et al. [20] explored the hydraulic performance with different blade wrap angles of an impeller in an open-design vortex pump.

Moreover, the numerical and experimental studies on the waviness mechanical seal of a reactor coolant pump were conducted by Feng et al. [21]. Benišek et al. [22] suggested a new design of the reversible axial jet fan impeller with symmetrical and adjustable blades. Stelmach et al. [23] confirmed the influence of hydrodynamic changes in a system with a pitched blade turbine on mixing power using a particle image velocimetry (PIV) method. Wang et al. [24] optimized the shapes of the impeller and diffuser of a mixed-flow pump using the inverse design method and CFD analysis. Rakibuzzaman et al. [25] designed numerically a new prototype propeller-type tubular turbine utilizing discharge water from a fish farm, and its performance was verified experimentally. The characteristic implicit method based on the upwind differencing and implicit finite difference scheme to solve the mixed free-surface-pressurized flow in a hydropower station was suggested by Wang et al. [26]. Park et al. [27] carried out the multi-objective numerical optimization to simultaneously enhance the heat transfer efficiency and reduce the pressure loss of a wavy microchannel heat sink. Chen et al. [28] investigated numerically the dynamic stresses of the runner during start-up in the turbine mode of a pump turbine. Portal-Porras et al. [29] tested the accuracy of the cell-set model applied on vane-type sub-boundary layer vortex generators by using CFD techniques. Shamsuddeen et al. [30] suggested a new inducer-type guide vane to reduce the hydraulic losses at the inter-stage flow passage of a multistage centrifugal pump. The effect of micro-tab on the lift enhancement of airfoil S-809 with trailing edge flap in wind turbine blades was analyzed numerically by Ye et al. [31].

Finally, as the guest editors of this Special Issue, we would like to especially thank the Section Managing Editor, Ms. Shirley Wang, for organizing and helping the Special Issue of *Processes*. We are also thankful to all the reviewers for their valuable comments for improving the quality of papers published in this Special Issue. In addition, this valuable Special Issue is available at https://www.mdpi.com/journal/processes/special_issues/CFD_Fluid_Device.

Author Contributions: Writing—original draft preparation, J.-H.K.; writing—review and editing, J.-H.K.; S.-M.K.; M.C.; L.T.; B.H., and J.P. All authors have read and agreed to the published version of the manuscript.

Funding: This research received no external funding.

Conflicts of Interest: The authors declare no conflict of interest.

References

1. Zhang, X.; Zhang, Y.; Lu, C. Flow and noise characteristics of centrifugal fan in low pressure environment. *Processes* **2020**, *8*, 985. [[CrossRef](#)]

2. Luo, Y.; Fan, Y.; Han, Y.; Zhang, W.; Acheaw, E. Research on the dynamic characteristics of mechanical seal under different extrusion fault degrees. *Processes* **2020**, *8*, 1057. [[CrossRef](#)]
3. Yu, L.; Zhang, H.; Chen, H.; Zuo, Z.; Liu, S. Numerical study on the influence of step casing on cavitating flows and instabilities in inducers with equal and varying pitches. *Processes* **2020**, *8*, 1103. [[CrossRef](#)]
4. Xie, H.; Song, M.; Yang, B. Research on the application of partial similarity for a 1-1/2 axial compressor. *Processes* **2020**, *8*, 1121. [[CrossRef](#)]
5. Wang, W.; Li, Y.; Osman, M.K.; Yuan, S.; Zhang, B.; Liu, J. Multi-condition optimization of cavitation performance on a double-suction centrifugal pump based on ANN and NSGA-II. *Processes* **2020**, *8*, 1124. [[CrossRef](#)]
6. Zhang, S.; Yang, B.; Xie, H.; Song, M. Applications of an improved aerodynamic optimization method on a low Reynolds number cascade. *Processes* **2020**, *8*, 1150. [[CrossRef](#)]
7. Ma, S.-B.; Kim, S.; Kim, J.-H. Optimization design of a two-vane pump for wastewater treatment using machine-learning-based surrogate modeling. *Processes* **2020**, *8*, 1170. [[CrossRef](#)]
8. Wang, X.; Kuang, K.; Wu, Z.; Yang, J. Numerical simulation of axial vortex in a centrifugal pump as turbine with S-blade impeller. *Processes* **2020**, *8*, 1192. [[CrossRef](#)]
9. Li, Q.; Ma, X.; Wu, P.; Yang, S.; Huang, B.; Wu, D. Study on the transient characteristics of the centrifugal pump during the startup period with assisted valve. *Processes* **2020**, *8*, 1241. [[CrossRef](#)]
10. Ahn, S.-Y.; Kim, K.-Y. Thermal performance of T-shaped obstacles in a solar air heater. *Processes* **2020**, *8*, 1305. [[CrossRef](#)]
11. Kim, W.-Y.; Senguttuvan, S.; Kim, S.-M. Effect of rotor spacing and duct diffusion angle on the aerodynamic performances of a counter-rotating ducted fan in hover mode. *Processes* **2020**, *8*, 1338. [[CrossRef](#)]
12. Lei, Y.; Huang, Y.; Wang, H. Aerodynamic performance of an octorotor SUAV with different rotor spacing in hover. *Processes* **2020**, *8*, 1364. [[CrossRef](#)]
13. Shrestha, U.; Choi, Y.-D. A CFD-based shape design optimization process of fixed flow passages in a Francis hydro turbine. *Processes* **2020**, *8*, 1392. [[CrossRef](#)]
14. Ding, H.; Chang, T.; Lin, F. The influence of the blade outlet angle on the flow field and pressure pulsation in a centrifugal fan. *Processes* **2020**, *8*, 1422. [[CrossRef](#)]
15. Rui, X.; Lin, L.; Wang, J.; Ye, X.; He, H.; Zhang, W.; Zhu, Z. Experimental and comparative RANS/URANS investigations on the effect of radius of volute tongue on the aerodynamics and aeroacoustics of a Sirocco fan. *Processes* **2020**, *8*, 1442. [[CrossRef](#)]
16. Baek, S.I.; Ahn, J. Large eddy simulation of film cooling with triple holes: Injectant behavior and adiabatic film-cooling effectiveness. *Processes* **2020**, *8*, 1443. [[CrossRef](#)]
17. Song, M.; Xie, H.; Yang, B.; Zhang, S. Influence of tip clearance on flow characteristics of axial compressor. *Processes* **2020**, *8*, 1445. [[CrossRef](#)]
18. Hur, M.S.; Lee, S.I.; Moon, S.W.; Kim, T.S.; Kwak, J.S.; Kim, D.H.; Jung, I.Y. Effect of clearance and cavity geometries on leakage performance of a stepped labyrinth seal. *Processes* **2020**, *8*, 1496. [[CrossRef](#)]
19. Li, Y.; Zheng, Y.; Meng, F.; Osman, M.K. The effect of root clearance on mechanical energy dissipation for axial flow pump device based on entropy production. *Processes* **2020**, *8*, 1506. [[CrossRef](#)]
20. Gao, X.; Zhao, T.; Shi, W.; Zhang, D.; Shi, Y.; Zhou, L.; Chang, H. Numerical investigation of an open-design vortex pump with different blade wrap angles of impeller. *Processes* **2020**, *8*, 1601. [[CrossRef](#)]
21. Feng, X.; Su, W.; Ma, Y.; Wang, L.; Tan, H. Numerical and experimental study on waviness mechanical seal of reactor coolant pump. *Processes* **2020**, *8*, 1611. [[CrossRef](#)]
22. Benišek, M.H.; Čantrak, Đ.S.; Ilić, D.B.; Janković, N.Z. New design of the reversible jet fan. *Processes* **2020**, *8*, 1671. [[CrossRef](#)]
23. Stelmach, J.; Kuncewicz, C.; Szufa, S.; Jirout, T.; Rieger, F. The influence of hydrodynamic changes in a system with a pitched blade turbine on mixing power. *Processes* **2021**, *9*, 68. [[CrossRef](#)]
24. Wang, M.; Li, Y.; Yuan, J.; Osman, F.K. Matching optimization of a mixed flow pump impeller and diffuser based on the inverse design method. *Processes* **2021**, *9*, 260. [[CrossRef](#)]
25. Rakibuzzaman, M.; Suh, S.-H.; Kim, H.-H.; Ryu, Y.; Kim, K.Y. Development of a hydropower turbine using seawater from a fish farm. *Processes* **2021**, *9*, 266. [[CrossRef](#)]
26. Wang, X.; Fan, H.; Liu, B. Optimization control on the mixed free-surface-pressurized flow in a hydropower station. *Processes* **2021**, *9*, 320. [[CrossRef](#)]
27. Park, M.-C.; Ma, S.-B.; Kim, K.-Y. Optimization of a wavy microchannel heat sink with grooves. *Processes* **2021**, *9*, 373. [[CrossRef](#)]
28. Chen, F.; Bi, H.; Ahn, S.-H.; Mao, Z.; Luo, Y.; Wang, Z. Investigation on dynamic stresses of pump-turbine runner during start up in turbine mode. *Processes* **2021**, *9*, 499. [[CrossRef](#)]
29. Portal-Porras, K.; Fernandez-Gamiz, U.; Aramendia, I.; Teso-Fz-Betoño, D.; Zulueta, E. Testing the accuracy of the cell-set model applied on vane-type sub-boundary layer vortex generators. *Processes* **2021**, *9*, 503. [[CrossRef](#)]
30. Shamsuddeen, M.M.; Ma, S.-B.; Kim, S.; Yoon, J.-H.; Lee, K.-H.; Jung, C.; Kim, J.-H. Effect of an inducer-type guide vane on hydraulic losses at the inter-stage flow passage of a multistage centrifugal pump. *Processes* **2021**, *9*, 526. [[CrossRef](#)]
31. Ye, J.; Salem, S.; Wang, J.; Wang, Y.; Du, Z.; Wang, W. Effects of micro-tab on the lift enhancement of airfoil S-809 with trailing-edge flap. *Processes* **2021**, *9*, 547. [[CrossRef](#)]

Article

Effects of Micro-Tab on the Lift Enhancement of Airfoil S-809 with Trailing-Edge Flap

Jianjun Ye ^{1,2}, Shehab Salem ¹, Juan Wang ^{3,*}, Yiwen Wang ¹, Zonggang Du ¹ and Wei Wang ¹

¹ School of Energy and Power Engineering, Huazhong University of Science and Technology, Wuhan 430074, China; hustyj@hust.edu.cn (J.Y.); l201821048@hust.edu.cn (S.S.); M201971306@hust.edu.cn (Y.W.); M202071291@hust.edu.cn (Z.D.); M202071328@hust.edu.cn (W.W.)

² Key Laboratory of Low-Grade Energy Utilization Technologies and Systems, Chongqing University, Chongqing 400044, China

³ Xi'an Key Laboratory of Clean Energy, Xi'an University of Architecture and Technology, Xi'an 710055, China

* Correspondence: juanwang@xauat.edu.cn

Abstract: Recently, the Trailing-Edge Flap with Micro-Tab (TEF with Micro-Tab) has been exploited to enhance the performance of wind turbine blades. Moreover, it can also be used to generate more lift and delay the onset of stall. This study focused mostly on the use of TEF with Micro-Tab in wind turbine blades using NREL's S-809 as a model airfoil. In particular, the benefits generated by TEF with Micro-Tab may be of great interest in the design of wind turbine blades. In this paper, an attempt was made to evaluate the influence of TEF with Micro-Tab on the performance of NREL's S-809 airfoils. Firstly, a computational fluid dynamics (CFD) model for the airfoil NREL's S-809 was established, and validated by comparison with previous studies and wind tunnel experimental data. Secondly, the effects of the flap position (H) and deflection angle (α_F) on the flow behaviors were investigated. As a result, the effect of TEF on air-flow behavior was demonstrated by augmenting the pressure coefficient at the lower surface of the airfoil at flap position 80% chord length (C) and $\alpha_F = 7.5^\circ$. Thirdly, the influence of TEF with Micro-Tab on the flow behaviors of the airfoil NREL's S-809 was studied and discussed. Different Micro-Tab positions and constant TEF were examined. Finally, the effects of TEF with Micro-Tab on the aerodynamic characteristics of the S-809 with TEF were compared. The results showed that an increase in the maximum lift coefficient by 25% and a delay in the air-flow stall were accomplished due to opposite sign vortices, which was better than the standard airfoil and S-809 with TEF. Therefore, it was deduced that the benefits of TEF with Micro-Tab were apparent, especially at the lower surface of the airfoil. This particularly suggests that the developed model could be used as a new trend to modify the designs of wind turbine blades.

Keywords: computational fluid dynamics (CFD); trailing edge flap (TEF); trailing edge flap with Micro-Tab; deflection angle of the flap (α_F); aerodynamic performance



Citation: Ye, J.; Salem, S.; Wang, J.; Wang, Y.; Du, Z.; Wang, W. Effects of Micro-Tab on the Lift Enhancement of Airfoil S-809 with Trailing-Edge Flap. *Processes* **2021**, *9*, 547.

<https://doi.org/10.3390/pr9030547>

Academic Editor: Jin-Hyuk Kim

Received: 24 January 2021

Accepted: 1 March 2021

Published: 19 March 2021

Publisher's Note: MDPI stays neutral with regard to jurisdictional claims in published maps and institutional affiliations.



Copyright: © 2021 by the authors. Licensee MDPI, Basel, Switzerland. This article is an open access article distributed under the terms and conditions of the Creative Commons Attribution (CC BY) license (<https://creativecommons.org/licenses/by/4.0/>).

1. Introduction

Wind energy plays a crucial role in tackling global climate issues and shaping tomorrow's energy systems. Recently, the wind turbine industry is becoming one of the best choices for energy production among all renewable energy choices [1]. The wind industry shows extensive financial progress and it is assumed to seriously compete with fossil fuel energy generation in the coming years. This progression attracts most scientists' attention to investigate feasible modifications that can enhance wind turbine performance and sustainability. This is supported by numerous recent studies, in which they claim that the efficiency of a wind turbine depends on many factors, including the rotational speed of the electrical generator [2] and the control of the airfoil aerodynamic shape and forces [3]. It is especially problematic for air-flow separation in the region near the hub. It was reported that the efficiency of wind turbines was diminished due to the drag penalty coming from air-flow separation at large angles of attack around the airfoil [4]. Due to

the increase in the angle of attack (α), the adverse stream-wise pressure counter-gradients increase correspondingly and lead to air-flow separation.

Consequently, it is essential to study air-flow separation control methods to enhance wind turbines' aerodynamic performance. Thus, specialists could use modern methods, such as TEF, Micro-Tabs at the TEF with Tab, and vortex generators, to improve the wind turbine blades' performance. These methods can be applied at a low Reynolds number (Re) number to achieve high aerodynamics efficiency [5]. Hence, this work presents a convenient simulation to modify the airfoil design by using a flap and tabs at the airfoil's trailing edge. By employing a CFD simulation and using shear stress transport SST $k-\omega$ model, the standard airfoil shape is compared to different airfoil shapes with a TEF, and airfoil with TEF with Tab. The latter obtained the highest output power efficiency for the wind turbine blades [6,7].

Compared with the standard shape airfoil, TEF airfoils have been proven useful as wind turbine airfoils since they can be adopted in larger sectional areas, produce more aerodynamic forces (C_L , C_D and C_P), and are insensible to leading-edge roughness [8,9]. Therefore, by using TEF airfoils, further improvement for both the structural strength and the aerodynamic performance of wind turbine blades could be achieved [10,11]. Different angles of installation can be applied in TEF with Micro-Tabs to increase the aerodynamic performance. It was suggested that Micro-Tabs should be maintained below 95% C to maximize the aerodynamic benefits [12]. After conducting a systematic experimental campaign on different shapes of the airfoil, there is compelling evidence that Micro-Tabs enhance the value of C_L of airfoils and decrease the C_D [13,14]. Figure 1 depicts the shape and flow of the streamlines with and without micro tabs

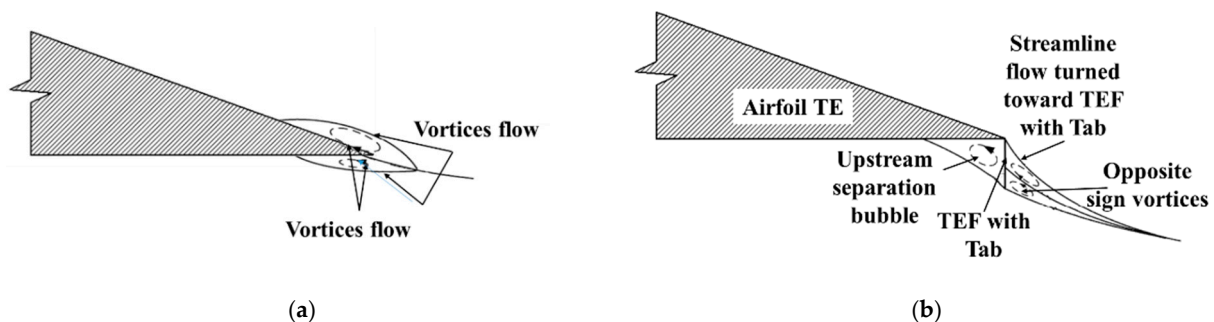


Figure 1. Aerodynamic performance for the streamline over the Micro-Tabs [15]. (a) Streamline over the standard airfoil; (b) streamline over the standard airfoil with a Micro-Tab.

Many researchers and studies later confirmed the presence of a characteristic separation bubble and rotating vortices as a result of installing a Micro-Tab [16,17]. Consequently, this part was fixed to the airfoil surface; it was responsible for an increasing suction on the airfoil upper surface and a pressure on the lower surface of the airfoil.

Interestingly, the aerodynamic impact of Micro-Tabs strongly depends on their design configuration parameters, such as Micro-Tab geometry and their mounting details, whereby the height and angle of installation of the Micro-Tab are indeed one of the most important design parameters. Furthermore, the C_L parameter enhances the aerodynamic performance of any airfoil in different weather conditions. Likewise, for a certain threshold value of the C_D parameter, it is confirmed that its size and angles could nullify the Micro-Tabs advantage. Therefore, many researchers are now looking for the best size and the best angle for an optimal installation of the Micro-Tabs [18,19]. Thus, this could provide the domain with the suite's highest efficiency and obtain a beneficial C_L/C_D .

Micro-Tabs have been confirmed to have interesting inferences in a wide range of flow fields. Wang et al. and Troolin [20,21] provided an extensive overview of Micro-Tab applications, which include different wind speeds [22], aircraft, and wind turbine blade design analysis [23]. In this paper, we focus on the latter application, and many literature

instances suggested Micro-Tabs as a small but useful device for active air-flow control over the airfoil and wind turbine blade's aerodynamic performance increase [24].

Therefore, this study's main purpose is to scrutinize the influences of TEF with Micro-Tab on the performance of the airfoil S-809 with TEF using 2D CFD simulations by using shear stress transport SST $k-\omega$ model [25]. In particular, this study sets some important parameters that selectively tuned the aerodynamic performance by setting different TEF positions of the chord length (C), deflection angle, and angle of incidence TEF. Interestingly, it has been shown that this study is capable of predicting the qualitative effect of TEF with Micro-Tab at different positions on the airfoil surface of the airfoil with TEF, the highest aerodynamic performance, and improves the C_p at a small α . In conclusion, when TEF was deflected, the flow was trapped on the airfoil's lower surface. In turn, a decrease in the flow velocities, an increase in pressure at the airfoil's lower surface, and an adverse pressure gradient may be achieved.

2. Geometric Description of the Trailing Edge Flap with Micro-Tab Airfoil

This section discusses the TEF airfoil geometry parameters with a Micro-Tab at different position by using the airfoil S-809 with TEF. The position of TEF at $H = 80\% C$ and deflection angle α_F of TEF 7.5° are shown in Figure 2a,b when TEF with Micro-Tab are mounted at the trailing edge of the TEF airfoil. Figure 2 and Table 1 show three patterns with different Micro-Tabs positions. The S-809 airfoil has been selected as the standard airfoil that has been identified as the most popular wind turbine on the market [26–29].

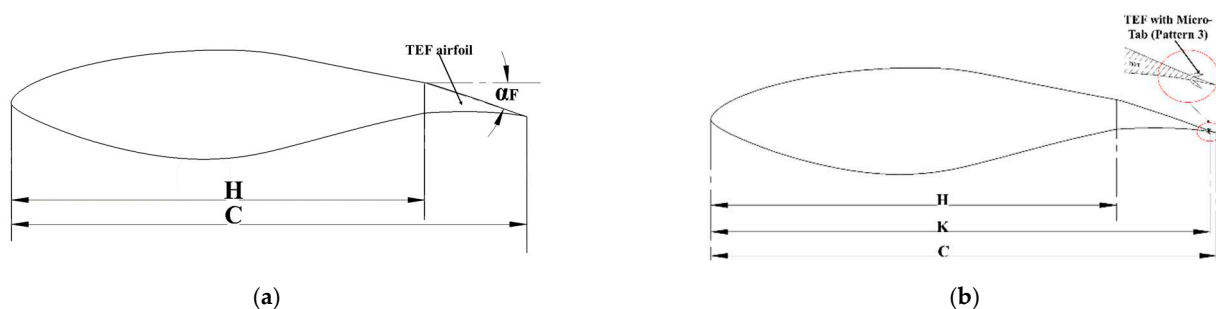


Figure 2. Geometrical parameters (a) of Trailing Edge Flap (TEF), (b) of Trailing-Edge Flap with Micro-Tab (TEF with Micro-Tab).

Table 1. The parameters of the airfoil with TEF with Micro-Tab.

Patterns	H%C	α_F ($^\circ$)	K (%C)	TEF with Micro-Tab
Pattern 1	80%C	7.5°	95%C	Lower
Pattern 2	80%C	7.5°	95%C	Upper
Pattern 3	80%C	7.5°	95%C	Upper/Lower

The TEF was attached at the Trailing-Edge Standard airfoil S-809. For the length of the airfoil chord (C), a suitable length of 0.6 m was chosen. Moreover, the TEF's position and deflection angle were selected to generate the highest dynamic performance (according to the previous article [28]).

Therefore, the current study is based on TEF with a Micro-Tab at three different pattern positions according to the airfoil chord, and they are all further investigated using CFD simulation. Data and illustrations in Table 1 and Figure 3 show the design parameters and the tab position.

All TEF with Micro-Tabs have a height of $2\% C$ with the position $K = 95\% C$, and maximum width is $0.4\% C$, the lower position at $k = 95\% C$, the upper position at $K = 95\% C$, and upper/lower positions at $K = 95\% C$, which are denoted as "Pattern 1", "Pattern 2", and "Pattern 3," respectively, as shown Figure 3a–c.

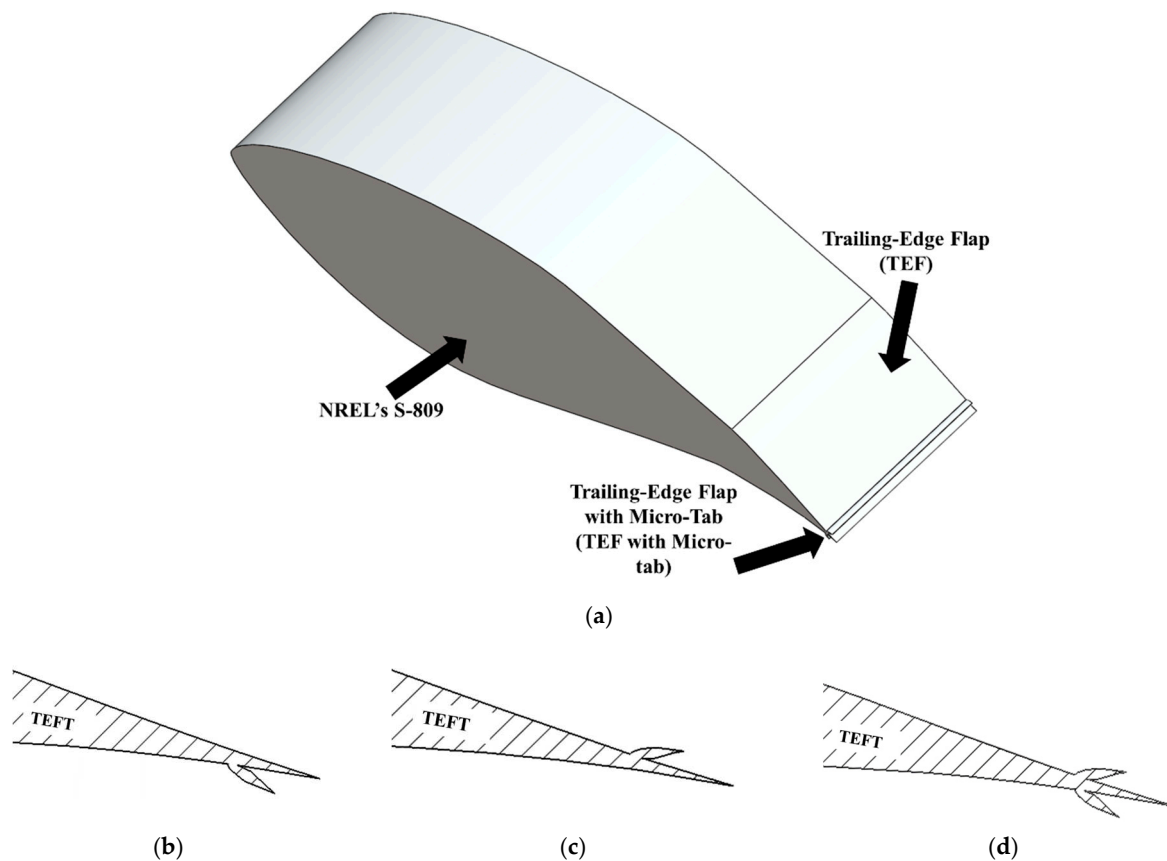


Figure 3. The geometry of TEF with Micro-Tab positions: (a) 3D front view, (b) Pattern 1 with lower Micro-Tab, (c) Pattern 2 with upper Micro-Tab, (d) Pattern 3 with upper and lower Micro-Tabs.

3. Description of the Numerical Method

3.1. The Governing Equations

In this study, ANSYS Fluent was used to generate the 2D CFD model simulation. A finite volume method was applied. The solver was set as a pressure-based viscous, incompressible solver, and the shear stress transport SST $k-\omega$ model [30–32] is used in the steady flow Re-averaged Navier-Stokes (RANS) equations. The spatial RANS equations with second-order accuracy were used and are illustrated as follows:

Mass equation

$$\frac{\partial \rho}{\partial t} + \frac{\partial}{\partial x_i}(\rho U_i) = 0 \quad (1)$$

Momentum equation

$$\rho \left(\frac{\partial U_i}{\partial t} + U_k \frac{\partial U_i}{\partial x_k} \right) = -\frac{\partial P}{\partial x_i} + \frac{\partial}{\partial x_j} \left(\mu \frac{\partial U_i}{\partial x_j} \right) + \frac{\partial}{\partial x_j} \tau_{ij} \quad (2)$$

Here, U_i is the free stream velocity component in the x -direction. P is the pressure, t , μ and ρ are the time, the dynamic viscosity, and air-flow density.

The SIMPLEC algorithm for the treatment of the pressure-velocity coupling was used. Second-order up-wind discretization was adopted for the convection terms and central difference schemes for the diffusion terms.

The SST $k-\omega$ (Shear Stress Transport) turbulence model (previously proposed by Menter [31]) was chosen in this work as it has shown good aerodynamic performance in wind turbines and turbo-machinery experiencing air-flow separation as expected for the blades during rotation [33].

This model's core idea was to utilize the robustness of the $k-\omega$ model to capture the flow within the viscous sub-layer. Moreover, one can use the $k-\epsilon$ model in the mainstream area to ban the disadvantage of the $k-\omega$ turbulence model. Overall, the SST $k-\omega$ model combines the advantages of the standard $k-\omega$ model and the standard $k-\epsilon$ model by mixing functions. Therefore, the SST $k-\omega$ model has higher accuracy and reliability in a wide range of flow fields. Yu et al. and Zhang et al. reported simulation results for the Spalart–Allmaras (S–A) turbulence model [34,35]. There was a good agreement between the simulation and the experimental data.

Additionally, Menter and Rogers et al. detected that for most high-lift problems [36], the S–A and SST $k-\omega$ model estimations were similar. However, it was proposed that the SST $k-\omega$ model is superior in accurately predicting pressure-induced separation. Therefore, the SST $k-\omega$ model was assumed to be more suitable in the present study than the S–A model [34,35] This will be shown in the results and discussions Section 4.1.2.

$$\frac{\partial \rho k}{\partial t} + \frac{\partial}{\partial x_j} (\rho u_j k) = \frac{\partial}{\partial x_j} \left[(\mu + \sigma_k \mu_t) \frac{\partial k}{\partial x_j} \right] + \tau_{ij} S_{ij} - \beta^* \rho \omega k \quad (3)$$

$$\frac{\partial \rho \omega}{\partial t} + \frac{\partial}{\partial x_j} (\rho u_j \omega) = \frac{\partial}{\partial x_j} \left[(\mu + \sigma_\omega \mu_t) \frac{\partial \omega}{\partial x_j} \right] + \frac{C_\omega \rho}{\mu_t} \tau_{ij} S_{ij} - \beta \rho \omega^2 + 2(1 - f_1) \frac{\rho \sigma_{\omega 2}}{\omega} \frac{\partial k}{\partial x_j} \frac{\partial \omega}{\partial x_j} \quad (4)$$

where U_j is the velocity component in the x -direction. β , C_ω , σ_k , and σ_ω are coefficients of the SST turbulence model that can be obtained by blending the coefficients of the $k-\omega$ model.

3.2. CFD Grid Model

This research adopts the chord length $C = 0.6$ m and the free stream velocity $V \simeq 51$ m/s, and the Reynolds number $Re = 2 \times 10^6$. The C-type mesh provided by the elliptical method in ICEM CFD was used because of its high accuracy, as verified by Ma et al. [37]. The computational grid, shown in Figure 4, constituted 9×10^5 grid elements on the airfoil surface. The respective distance of the inlet and outlet boundaries away from the leading edge was $20 C$ and $30 C$, respectively. The top and bottom boundaries were $15 C$ away from the chord. In particular, to capture the boundary layer, the grid should have a y^+ value of less than one ($y^+ < 1$). The y^+ is a non-dimensional distance that indicates the degree of grid fineness in the near-wall region. In the current simulation, the first grid node above the surface was 1.5×10^{-5} times of chord length, in turn, $y^+ = 0.02$. The mesh quality and the mesh at the edge of the airfoil for the TEF with Micro-Tab are depicted in Figure 4b. Figure 4b shows several details of the computational grid used for the airfoil's CFD simulations analysis, with a specific focus on the improvement zones used to properly discretize the airfoil LE and TE, such as the Pattern 3 configuration. The whole count of elements demonstrated that there is a very fine meshing in the sections inside the airfoil and a relatively rough meshing outside. However, the number of elements inside the airfoil was about 11×10^5 . To capture the boundary layer for Pattern 3, the grid should have a y^+ value of $y^+ < 1$. A mesh independency test was achieved to emphasize that the difference in the number of elements did not affect the solution, as shown in the results and discussions Section 4.1.1.

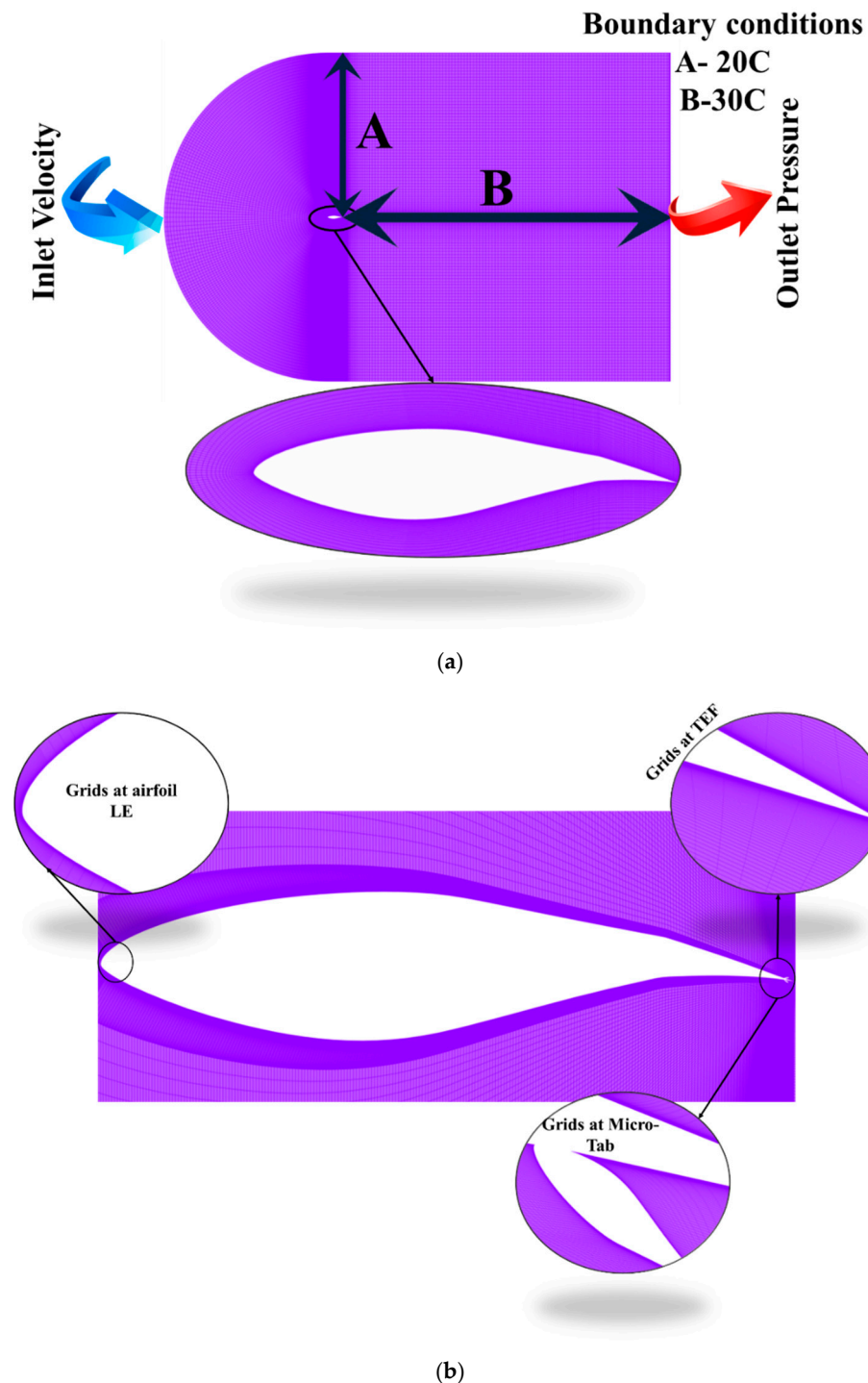


Figure 4. Detail of the grid structure of the airfoil: (a) boundary conditions and mesh domain on the airfoil S-809 with TEF; (b) mesh domain of TEF with Micro-Tab pattern 3.

4. Results and Discussion

4.1. Validation of Accuracy S-809 and S-809 with TEF Airfoil

4.1.1. Grid Independence Validation

To ensure grid independence in the CFD simulation predictions, calculations have been made for a typical TEF airfoil shape and air-flow configuration, using different grid accuracies. The verification of the predicted C_L with the total number of the grid elements for the considered TEF airfoil and Pattern 3 is displayed in Figure 5a,b. The achievement of sufficient grid independence for grids with elements larger than 8×10^5 is observed

in Figure 5a. Thereby, the grids created by the ICEM program and using the same grid strategy possessed an even finer resolution corresponding to the number of elements 9×10^5 and according to the grid independence curve.

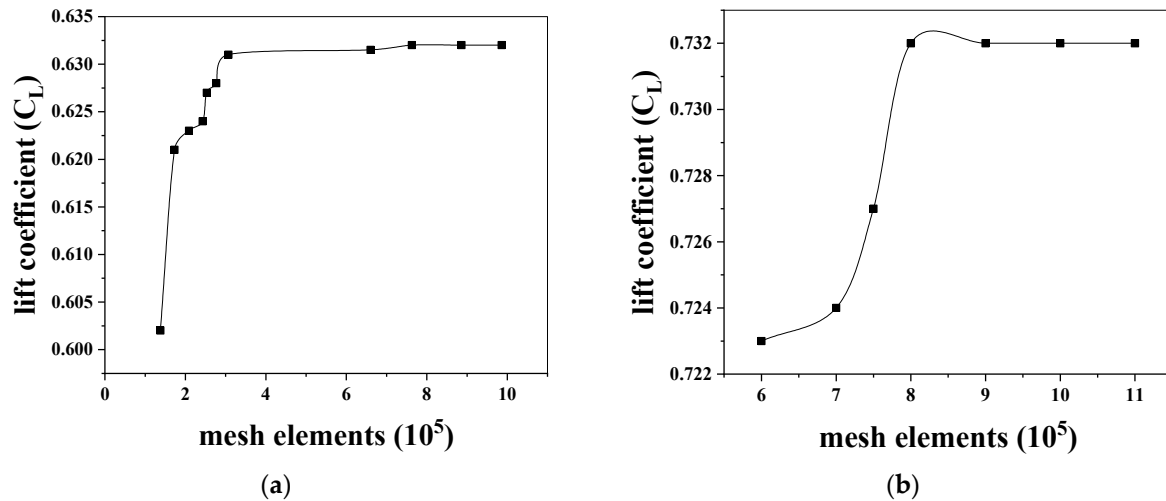


Figure 5. Mesh verification: (a) mesh independence for TEF airfoil S-809; (b) mesh independence for TEF with Micro-Tab (pattern 3).

The illustrations in Figure 5b verify the grid independence around the airfoil for Pattern 3 (Micro-Tab position at the upper and lower on the TEF surface), where the flow-field model of grid elements ranged from 6×10^5 to 11×10^5 . From these findings, it was observed that the convergence was determined with high accuracy and the aerodynamic performance reached a stable value when the number of grid elements reached a value of more than 9×10^5 . Therefore, a model with a grid element number of 11×10^5 was further selected for the next modelling assessments.

4.1.2. Comparison between CFD and Experimental Data for TEF Airfoil S-809

To validate the CFD simulation, the experimental data of the S-809 airfoil with TEF provided by the Ohio State University were compared with the numerical results [38,39]. The Mach number ($Ma \simeq 0.15$) and the $Re = 2 \times 10^6$ in the numerical simulation are the same as those of the wind tunnel test. The chord of the S-809 airfoil with TEF was $C = 0.6$ m. The simulation results are compared with the experimental data in Figure 6. The findings illustrate that the C_L coincides with the measurement for the range of angles of attack from -2° to 13° , as shown in Figure 6a. After the flow separation took place, the C_L was a little overestimated but within an acceptable range. Moreover, the variation trend was well observed. The C_D was obviously overestimated, as shown in Figure 6b. The possible reason was that the S-809 with TEF was a laminar airfoil, and there probably existed a transition flow on the airfoil surface during the experiment. Table 2 shows a comparison of the CFD results and experimental data for the TEF airfoil. For example, for the angle $= 4^\circ$, the CFD simulation lift coefficient is now equal to the experimental value. Table 2 presents the results obtained from the preliminary CFD analysis (SST- $k\omega$ and S-A). The C_L compared with the experimental data has a 2% error and the error in the calculated drag has been reduced to 9%. The errors in the coefficients at 0° and 1° have also been significantly reduced. These angles of attack were rerun using the same grid as for all cases. In summary, the numerical results concur with the experimental data. This indicated the accuracy of the numerical method in this study. Besides, Ramsay carried out a similar validation strategy to validate their numerical results [40]. Therefore, the present study's subsequent research used the full turbulence model to carry out the numerical simulations.

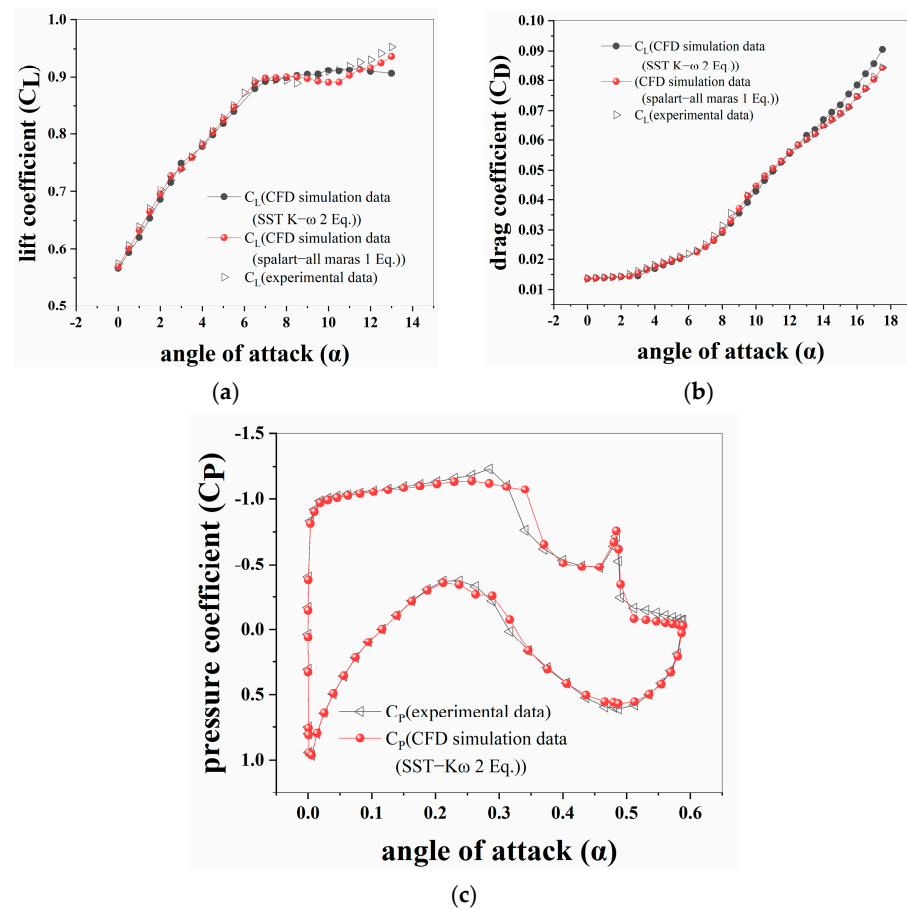


Figure 6. Comparisons between the computational fluid dynamics (CFD) calculated and experimentally determined pressure distributions for TEF airfoil with angles of attack of 0°: (a) C_L distribution; (b) C_D distribution; (c) C_p distribution.

Table 2. Comparisons between CFD results and experimental data for the TEF airfoil.

α°	$C_{L_SST_K\omega}$ (2 Eq.)			$C_{L_Spalart-All\ Maras}$ (1 Eq.)			$C_{D_SST_K\omega}$		
	CFD Calc.	Exper. Data	Error %	CFD Calc.	Exper. Data	Error %	CFD Calc.	Exper. Data	Error %
0	0.56625	0.57418	2.48639	0.5600	0.57418	2.53214	0.01300	0.01368	5.23077
4	0.77832	0.760	2.35379	0.78078	0.76087	2.46757	0.01655	0.01809	9.30514
8	0.89883	0.89423	2.07158	0.90033	1.0054	11.0573	0.02900	0.03145	8.44828

Figure 6c shows the comparison between the CFD calculated and experimental surface pressure coefficient distributions for an angle of attack of 0° [40]. The C_p comparisons for 0° are in a reasonably good agreement over the entire S-809 airfoil with TEF surface except in the regions of the laminar separation bubbles. The experimental pressure distributions show the laminar separation bubbles just near the chord on both the upper and lower surfaces. They are indicated in the experimental data that become more-or-less constant with respect to X/C , followed by an abrupt increase in pressure as the flow undergoes turbulent reattachment. Since the calculations assume a fully turbulent flow, no separation is indicated in the numerical results.

4.2. Effect of the Trailing Edge Flap with Micro-Tab (TEF with Micro-Tab) on the Air-Flow Behaviour

This section presents the results of our investigation on the aerodynamic performance of TEF with Micro-Tab attachment. The aerodynamic performance results presented

include stall angles of attack α , C_L , C_D , and C_L/C_D distribution. In order to articulate the results, the 2D air-flow streamlines distribution and vortices in the wake area have been analyzed. Different TEF's aerodynamic performance with Micro-Tab at different positions have been analyzed to control the proposed TEF's control aerodynamic performance with Micro-Tab. The angles of attack ranging from 0° to 25° to simulate the S-809 airfoil by using TEF with Micro-Tab were chosen. The position of the TEF ($H = 80\% C$) and deflection angle ($\alpha_F = 7.5^\circ$) was chosen based on airfoil S-809 with TEF results (the TEF result in Section 4.1.2); as it showed the highest aerodynamic performance. Subsequently, the TEF with Micro-Tab attachments was readjusted to S-809 with TEF ($H = 80\%$ and deflection angle $\alpha_F = 7.5^\circ$).

Figure 7a shows a comparison of the different settings for the aerodynamic performance effect. As seen in the figure, the C_L curves depict a gradual upward shift due to the TEF airfoil with Micro-Tab for the proposed α values and for the TEF. When $\alpha = 13^\circ$, C_L was enhanced by 15% and 28.6% for Pattern 2 and Pattern 3, respectively. Figure 7b shows the variation of C_D with varying α at different TEF airfoil with Micro-Tab configurations. Thus, when the TEF with Micro-Tab was positioned at both directions (up and lower flap surface), as seen in Pattern 3, the F_L showed the highest values compared with the other configurations.

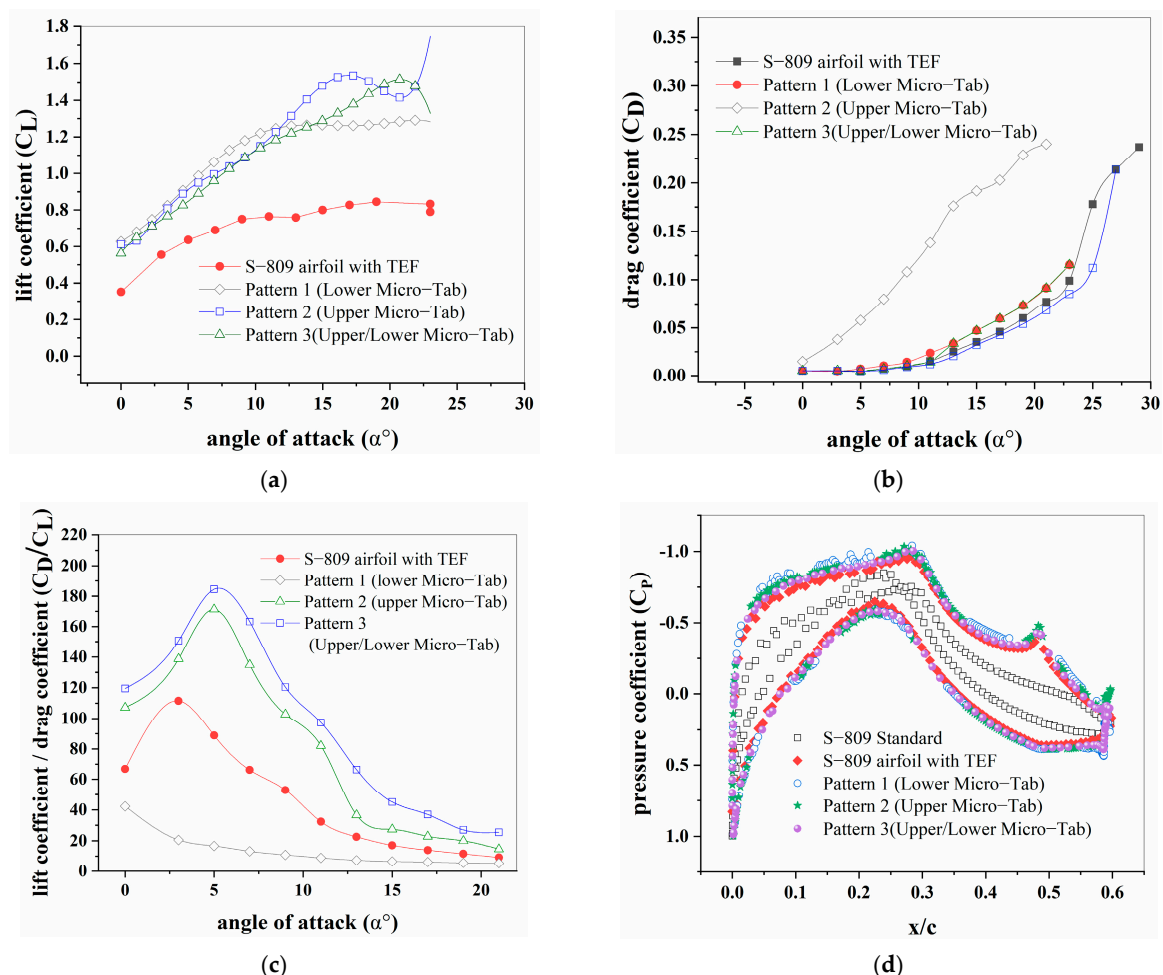


Figure 7. The aerodynamic performance effect of TEF with Micro-Tab: (a) comparison of C_L ; (b) comparison of C_D , (c) comparison of C_L/C_D ; (d) comparison of C_p distribution at $\alpha = 0^\circ$.

The analysis of the F_L and F_D curves described before is not comprehensive enough to design blades. Thus, a comprehensive understanding of blades' design needs the estimation of the C_L/C_D ratio for the design of the wind turbine blades. The C_L/C_D

ratio is important in determining the most appropriate angle and TEF with Micro-Tab configurations for the proposed blade design. The estimate of C_L/C_D based on parameters in Figure 7a,b is shown in Figure 7c. The results reaffirm that value of C_L was increasing due to the TEF airfoil with Micro-Tab attachment. A possible explanation for the increase in the C_L/C_D ratio of an airfoil is due to TEF with Micro-Tab attachment. The C_L ranged between 0.9 (Pattern 1) and 1.6 (Pattern 3) at $\alpha = 15^\circ$, and the value of C_D decreased from 0.03536 to 0.03219 when the TEF airfoil with Micro-Tab was attached.

The α was readjusted between 5° to 15° to obtain the optimal effect on the C_L/C_D ratio, as seen in Pattern 3 in Figure 7c. Comparing the airfoil with TEF to the other patterns, no air-flow separation on the airfoil was observed at an angle less than 23° . Pattern 3 depicts the highest lifting force compared to other patterns.

A possible explanation for this might be the opposite sign vortices caused by fitting the TEF with upper/lower Micro-Tabs.

Upon closer inspection of Pattern 3, as seen in both C_D (Figure 7b) and C_L/C_D (Figure 7c), one observes a higher aerodynamic performance ($C_L/C_D > 35\%$) in comparison to the standard airfoil and other patterns. A higher aerodynamic performance results from the opposite sign vortices and, at the same time, the contribution of the low C_D decreases. Another important finding is that Pattern 3 is an optimal choice when α is between 15° to 23° and for an airfoil with TEF with Micro-Tab. The high efficacy experienced for Pattern 3 is assumed to be due to the C_L/C_D ratio that increases by over 35% and due to the low C_D contribution.

Figure 7d illustrates the C_P distribution on the standard airfoil, airfoil with TEF, and TEF with Micro-Tab patterns. The C_P factor of the Trailing-Edge changed when deploying TEF with Micro-Tab.

The C_P factor of the Trailing-Edge changed from -1200 Pa at the TEF airfoil to 1000 Pa when TEF airfoil with Micro-Tab was attached. Correspondingly, an enhancement in the suction of the upper surface for the airfoil and an increase in the pressure at the lower surface was observed and the performance of the airfoil was increased. Finally, the configuration of Pattern 3 did not show the air-flow separation compared with the TEF airfoil. This was probably due to the separation bubble and opposite sign vortices. Therefore, the air flowed smoothly along the upper surface of the airfoil without separation.

The next section gives a detailed discussion of the pressure distribution at the small and large angles of attack for each pattern.

4.3. Discussion of the Surface Pressure Distribution of the TEF Airfoil with/without Micro-Tab

In order to investigate the effects of different Micro-Tab positions on the pressure distribution, contours of C_P are used, as shown in Figure 8. Each subplot in Figure 8 represents the C_P values as a function of airfoil chord location in the x-axis direction and the Micro-Tab positions.

The upper-pressure distribution represents the airfoil's suction side, whereas the lower C_P distribution represents the pressure side of the airfoil. The Micro-Tab position at 98% C Pattern 1 at the lower surface for the TEF airfoil, for the Pattern 2 the Micro-Tab position 98% C and the upper surface for the TEF airfoil, for the Pattern 3 the MicroTab at 98% C at the lower and upper surface for the TEF airfoil, and the TEF airfoil when there is no Micro-Tab on the airfoil S-809.

To better explain the C_P displayed in this analysis at $\alpha = 0^\circ$ – 13° , the traditional C_P polar for the TEF airfoil upper and lower sides is presented for the three patterns of the TEF airfoil with Micro-Tab that are specified by the solid and dashed lines on the color contour plots. Figure 8 displays an overview of the C_P distribution corresponding to $\alpha = 0$ to 13° with standard airfoil, TEF airfoil, Pattern 1, Pattern 2, and Pattern 3. These pressure distributions over the airfoil were then integrated to determine the lift (C_L) and drag (C_D) coefficients.

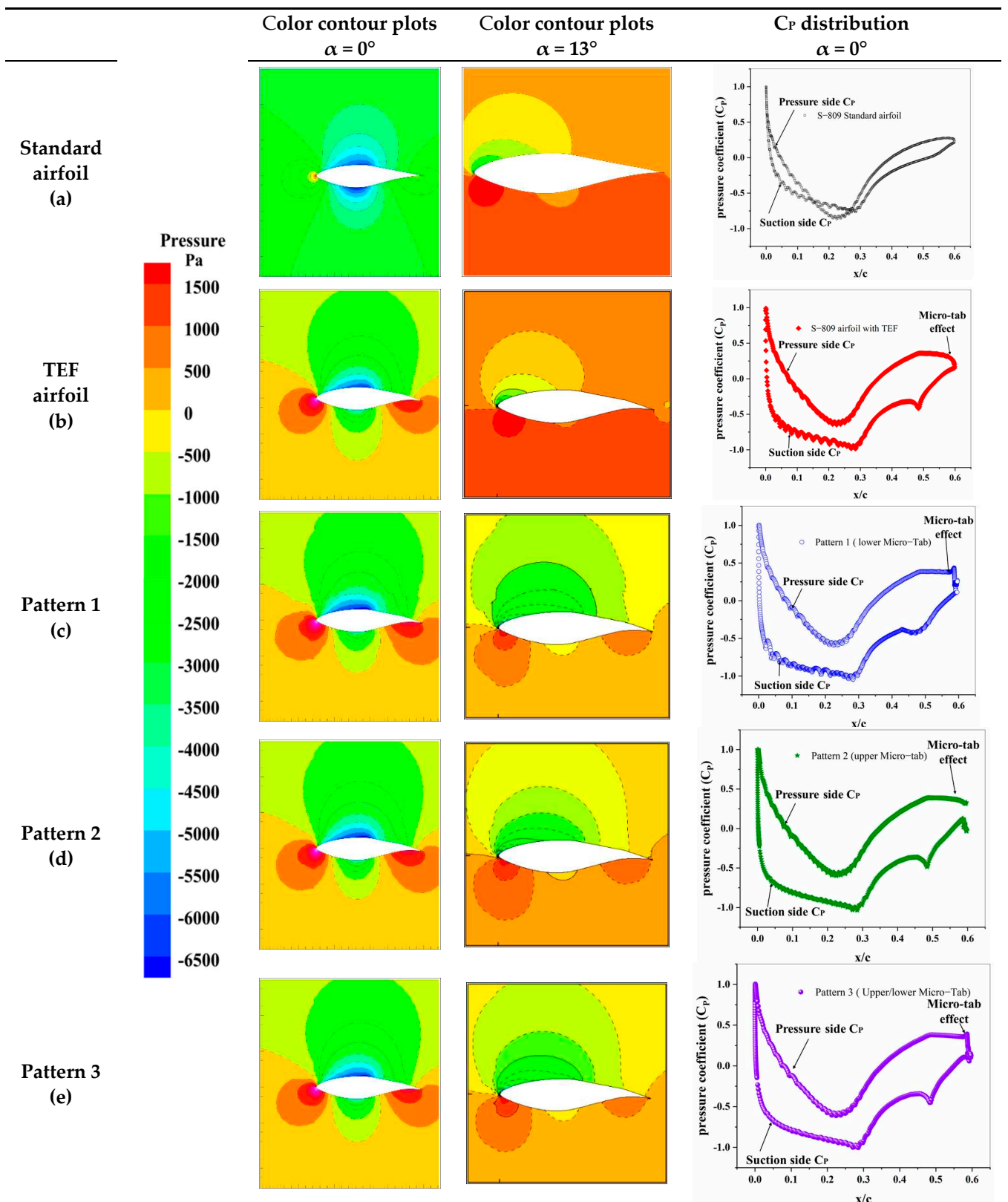


Figure 8. Pressure distribution and color contour plots at the $\alpha = 0^\circ$ – 13° , (a) S–809 airfoil, (b) TEF airfoil, (c) Pattern 1, (d) Pattern 2, (e) Pattern 3.

Two C_p distributions are presented for two different α , which represent low and high α , respectively. Unsurprisingly, for both angles, Pattern 1 increases the pressure on the

pressure side of the airfoil, Pattern 2 decreases the suction on the suction side, and Pattern 3 increases the pressure on the pressure side and the suction side of the airfoil compared to TEF airfoil and standard airfoil. A case-study approach was used to evaluate TEF airfoil's effectiveness with Micro-Tab on pressure distributions and lift force. This effectiveness clearly comes from the increased adverse pressure gradient, opposite sign vortices, and separation bubbles generated in front of the Micro-Tab on the side on which it has been attached. On the other hand, it is important to indicate that the TEF airfoil with Micro-Tab has also changed the effective aerodynamic performance, angle of attack, and the effective airfoil camber, both of which can considerably impact the pressure distribution over both surface sides of the TEF airfoil. The Micro-Tab effect on the suction side of the airfoil is also noticeable; this appears in Pattern 1 and Pattern 3, as shown in Figure 8c,e.

Pattern 1 has improved the suction on the TEF airfoil's top surface, even though, at the lowest α , the effect is not high, and, as the angle of attack increases, this effect becomes enhanced. Pattern 2 also affects the pressure the side of the airfoil. As observed for lower angles of attack, Pattern 2 has significantly reduced the pressure on the bottom side of the TEF airfoil, and, for the highest angles, this effect is not high. As for Pattern 3, it combined each of the features of Pattern 1 and Pattern 2. This is because both of these enhance the lower pressure of the wing and increase the lift force, as shown in Figure 8e. It is also fairly apparent that, for average angles, Pattern 1, Pattern 2, and Pattern 3 show comparable effectiveness of the aerodynamic performance on both sides of the TEF airfoil. This investigation of the pressure measurements clearly shows that the Micro-Tab's effectiveness is not only Micro-Tab dependent but also depends considerably on the airfoil angle of attack and the TEF of the airfoil. The velocity profiles and the streamline distribution data from the CFD simulation can better clarify this dependency.

4.4. Discussion of the Streamline Distribution and the Velocity Profiles of the TEF Airfoil with/without Micro-Tab

This study identified the dependency of the angle of attack (α) of the TEF airfoil with Micro-Tab performance on the TEF airfoil. CFD results near the airfoil trailing edge are shown for different patterns in Figure 9. Each column in Figure 9 shows three different TEF configurations for the same angle of attack (α). The deflection of the airfoil trailing-edge flow when the TEF with Micro-Tab is deployed is clear for each attack angle. When Pattern 1 is attached, the findings show that the down-wash flow is more apparent, as shown in Figure 9c. This would imply that the lift is greater in these cases. On the other side, Pattern 2 decreases the down-wash flow, which insinuates a smaller lift at the small angle of attack, as shown in Figure 9d. At $\alpha = 0^\circ$ Pattern 2 has induced an up-wash that implies a negative lift in this configuration. These deflections in the airfoil down-wash imply that the effective camber and angle of attack have changed. These changes significantly affect the pressure distribution and, as a result, the lift and moment behavior of the airfoil change.

Following the previous discussion that suggested the dependency of the TEF airfoil with Micro-Tab effectiveness on the angle of attack, it can be clearly observed that, at lower angles, Pattern 2 is more exposed to the flow. Concurrently, Pattern 1 is more exposed to the flow at higher angles of attack. The CFD results clearly show this dependency and support the observations in the pressure distributions. Physically, it can be inferred that, for the Pattern 1 cases at lower angles of attack, the pressure gradient on the airfoil's pressure side is so high that the increment produced by the flap is no longer significant. As a result of configuring the opposite sign vortices at the Micro-Tab, as shown in Figure 9c. For a higher angle of attack, when the Micro-Tab is exposed to the suction side of the airfoil, the pressure gradient on the suction side of the airfoil is so high that the Micro-Tab cannot affect the flow in a manner as significant as at smaller angles of attack; as a result, the pressure gradients are much weaker. Finally, Pattern 3 has an overall advantage because it combines Pattern 1 and Pattern 2 to the same TEF airfoil. Pattern 3 can work at both small and large angles of attack as a result of high aerodynamic performance.

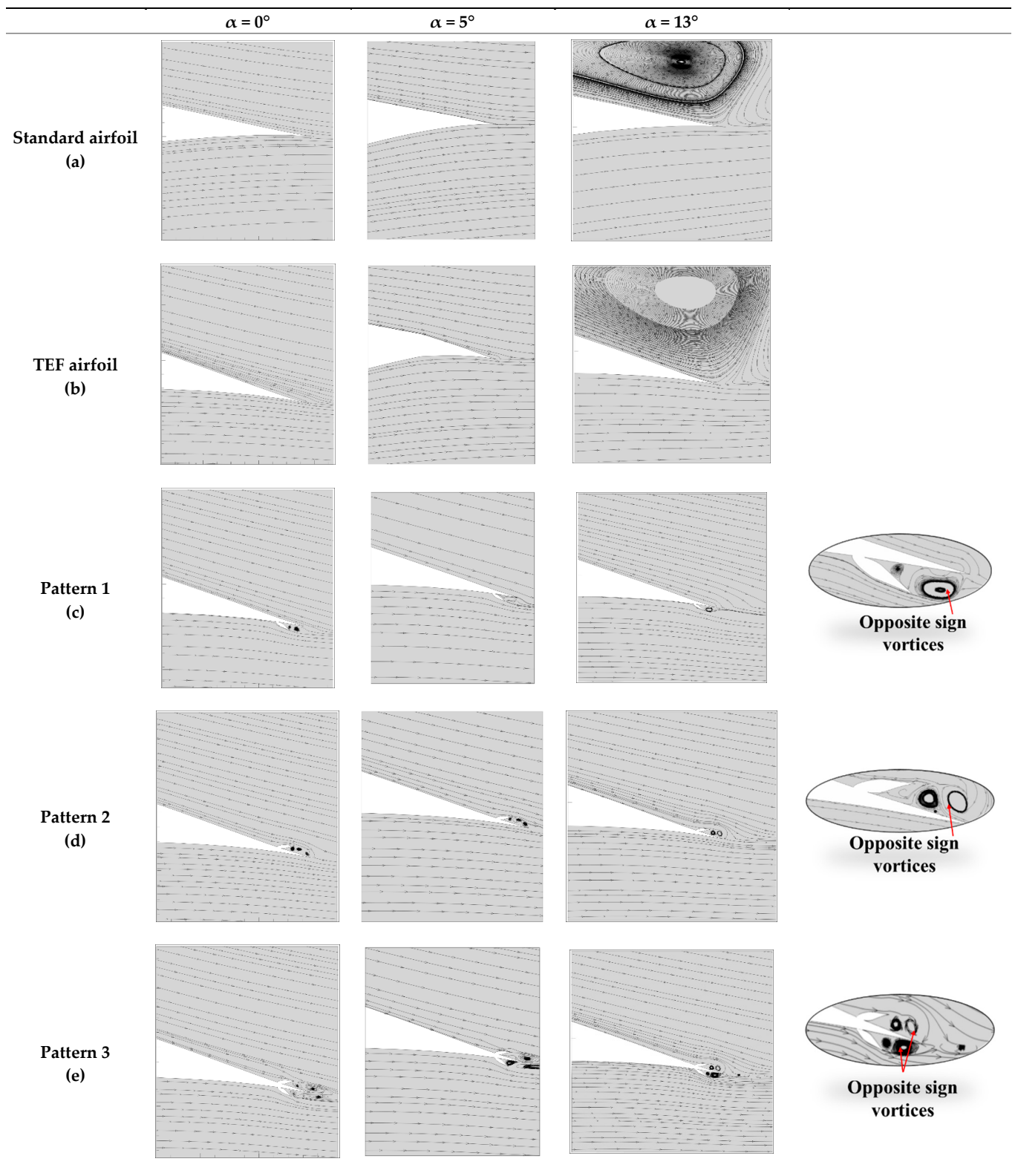


Figure 9. Comparison of streamline distribution of the TEF airfoil with/without Micro-Tab at three different positions, (a) Standard airfoil, (b) TEF airfoil, (c) Pattern 1, (d) Pattern 2, (e) Pattern 3.

5. Conclusions

This paper describes a methodology for computing the effect of TEF with Micro-Tab on airfoil sections by using CFD. A grid generation method was developed to allow an easy way for repositioning the TEF in the chord-wise direction on the S-809 airfoil. This study was able to predict the qualitative effect of TEF with Micro-Tab, and it was possible to obtain the highest aerodynamic performance at a high C_p value. The findings indicated that the best pattern with the highest aerodynamic performance was provided by three patterns of TEF with Micro-Tab. Based on the above, the following may be concluded:

- For the TEF study, the TEF has been deflected, and the flow has been trapped on the lower surface of the airfoil. In return, the flow velocities decreased, and there was an increase in the pressure at the lower surfaces of the airfoil. However, the increase of the adverse pressure gradient with TEF and different deflection angles α_F , may yield an inverse vortex flow behind the TEF and increase the pressure at the lower surface of the airfoil and TEF. Moreover, the highest aerodynamic performance has been produced at $\alpha_F = 7.5^\circ$ at $H = 80\% C$.
- Concerning the TEF with Micro-Tab study, the numerical simulation has shown that the TEF with Micro-Tabs can significantly improve the C_L of the low Reynolds number airfoil adopted in this investigation. The more obvious the TEF with the Micro-Tabs position, the larger the effect of lift-enhancement will be. Interestingly, Micro-Tabs can delay the air-flow stall at a small $\alpha \leq 2^\circ$. At a different angle of attack α , C_p and C_L increased due to the bubble separation and the opposite sign vortices. Moreover, the increase of the C_L has also been detected while holding a constant position of TEF at 80% C and changing the position of TEF with Micro-Tab. Therefore, the utilization of the TEF with Micro-Tab at aerodynamics $H = 80\%$, deflection angle $\alpha_F = 7.5^\circ$, and $K = 95\%$; the C_L and C_p was increased, and the highest aerodynamic performance was achieved for Pattern 3.

Author Contributions: Conceptualization, J.Y. and S.S.; methodology, S.S.; software, S.S. and Y.W.; validation, J.Y., J.W. and S.S.; formal analysis, W.W.; investigation, S.S. and Z.D.; resources, J.Y.; data curation, Z.D.; writing "original draft preparation, S.S.; writing "review and editing, J.Y.; visualization, J.Y.; supervision, J.Y. and J.W.; project administration, J.Y.; funding acquisition, Y.W. All authors have read and agreed to the published version of the manuscript.

Funding: National Natural Science Foundation of China, Grant/Award Number: 51976067, the Open Foundation of the Key Laboratory of Low-grade Energy Utilization Technologies and Systems, Grant/Award Number: LLEUTS-201905, the Open Foundation of the State Key Laboratory of Fluid Power and Mechatronic Systems, Grant/Award Number: GZKF-201811.

Data Availability Statement: The data used to support the findings of this study are available from the corresponding author upon request.

Conflicts of Interest: The authors declare no conflict of interest.

Abbreviations

C	Airfoil chord length (m)
C_D	Drag coefficient (dimensionless)
C_L	Lift coefficient (dimensionless)
C_L/C_D	Lift coefficient/ Drag coefficient ratio (dimensionless)
$C_{L,max}$	Maximum lift coefficient (dimensionless)
Re	Reynolds number (dimensionless)
P	Pressure
C_p	Pressure coefficient (dimensionless)
H	TEF position
K	TEF with Micro-Tab position
α_F	Deflect angle of flap ($^\circ$)

α	Angle of attack (°)
CFD	Computational fluid dynamics
TEF	Trailing-Edge Flap
TEF with Tab	Trailing-Edge Flap Micro-Tab

References

- MacPhee, D.W.; Beyene, A. Performance analysis of a small wind turbine equipped with flexible blades. *Renew. Energy* **2019**, *132*, 497–508. [[CrossRef](#)]
- Ram, K.R.; Lal, S.P.; Ahmed, M.R. Design and optimization of airfoils and a 20 kW wind turbine using multi-objective genetic algorithm and HARP_Opt code. *Renew. Energy* **2019**, *144*, 56–67. [[CrossRef](#)]
- Rocha, P.C.; de Araujo, J.C.; Lima, R.P.; da Silva, M.V.; Albiero, D.; de Andrade, C.; Carneiro, F. The effects of blade pitch angle on the performance of small-scale wind turbine in urban environments. *Energy* **2018**, *148*, 169–178. [[CrossRef](#)]
- Chamorro, L.P.; Arndt, R.; Sotiropoulos, F. Drag reduction of large wind turbine blades through riblets: Evaluation of riblet geometry and application strategies. *Renew. Energy* **2013**, *50*, 1095–1105. [[CrossRef](#)]
- Aramendia, I.; Saenz-Aguirre, A.; Fernandez-Gamiz, U.; Zulueta, E.; Lopez-Guede, J.M.; Boyano, A.; Sancho, J. *Gurney Flap Implementation on a DU91W250 Airfoil*; Multidisciplinary Digital Publishing Institute Proceedings: Basel, Switzerland, 2018; p. 1448.
- Anaya-Lara, O.; Jenkins, N.; Ekanayake, J.B.; Cartwright, P.; Hughes, M. *Wind Energy Generation: Modelling and Control*; John Wiley & Sons: Hoboken, NJ, USA, 2011.
- Manwell, J.F.; McGowan, J.G.; Rogers, A.L. *Wind Energy Explained: Theory, Design and Application*; John Wiley & Sons: Hoboken, NJ, USA, 2010.
- Berry, D.; Lockard, S.; Jackson, K.; Zuteck, M.; van Dam, C. Innovative design approaches for large wind turbine blades final report. In *SAND2004-0074*; Sandia National Laboratories: Albuquerque, NM, USA, 2004.
- Jackson, K.; Zuteck, M.V.; Van Dam, C.; Standish, K.; Berry, D. Innovative design approaches for large wind turbine blades. *Wind Energy Annu. Int. J. Prog. Appl. Wind Power Convers. Technol.* **2005**, *8*, 141–171. [[CrossRef](#)]
- Simic, Z.; Havelka, J.G.; Vrhovcak, M.B. Small wind turbines—A unique segment of the wind power market. *Renew. Energy* **2013**, *50*, 1027–1036. [[CrossRef](#)]
- Barlas, T.K.; van Kuik, G.A. Review of state of the art in smart rotor control research for wind turbines. *Prog. Aerosp. Sci.* **2010**, *46*, 1–27. [[CrossRef](#)]
- Giguere, P.; Lemay, J.; Dumas, G. Gurney flap effects and scaling for low-speed airfoils. In Proceedings of the 13th Applied Aerodynamics Conference, San Diego, CA, USA, 19–22 June 1995; p. 1881.
- Fernandez-Gamiz, U.; Zulueta, E.; Boyano, A.; Fernandez-Gauna, B. Parametric study of a microtab on a DU airfoil. *WSEAS Trans. Fluid Mech.* **2016**, *11*, 121–126.
- Fernandez-Gamiz, U.; Zulueta, E.; Boyano, A.; Ramos-Hernanz, J.A.; Lopez-Guede, J.M. Microtab design and implementation on a 5 MW wind turbine. *Appl. Sci.* **2017**, *7*, 536. [[CrossRef](#)]
- Battisti, L.; Ricci, M. *Wind Energy Exploitation in Urban Environment*; Springer: Berlin, Germany, 2018.
- Li, Y.; Wang, J.; Zhang, P. Influences of mounting angles and locations on the effects of Gurney flaps. *J. Aircr.* **2003**, *40*, 494–498. [[CrossRef](#)]
- Jeffrey, D.; Zhang, X.; Hurst, D.W. Aerodynamics of Gurney flaps on a single-element high-lift wing. *J. Aircr.* **2000**, *37*, 295–301. [[CrossRef](#)]
- Li, Y.; Wang, J.; Zhang, P. Effects of Gurney flaps on a NACA0012 airfoil. *Flow Turbul. Combust.* **2002**, *68*, 27. [[CrossRef](#)]
- Xie, Y.; Jiang, W.; Lu, K.; Zhang, D. Numerical investigation into energy extraction of flapping airfoil with Gurney flaps. *Energy* **2016**, *109*, 694–702. [[CrossRef](#)]
- Wang, J.; Li, Y.; Choi, K.-S. Gurney flap—Lift enhancement, mechanisms and applications. *Progr. Aerosp. Sci.* **2008**, *44*, 22–47. [[CrossRef](#)]
- Troolin, D.R. A Quantitative Study of the Lift-Enhancing Flow Field Generated by an Airfoil with a Gurney Flap. Ph.D. Thesis, University of Minnesota, Minneapolis, MN, USA, December 2009.
- Bae, E.; Gandhi, F. Upstream active Gurney flap for rotorcraft vibration reduction. In Proceedings of the American Helicopter Society 68th Annual Forum, Fort Worth, TX, USA, 1–3 May 2012; pp. 1354–1362.
- Chen, H.; Qin, N. Trailing-edge flow control for wind turbine performance and load control. *Renew. Energy* **2017**, *105*, 419–435. [[CrossRef](#)]
- Frunzulica, F.; Dumitrescu, H.; Dumitrache, A. Numerical investigations of dynamic stall control. *Incas Bull.* **2014**, *6*, 67.
- Uddin, M.A.; Hasan, A.T. A CFD Analysis on the Effects of Geometry of Gurney Flap on Aerodynamics of NACA0012 Airfoil. In Proceedings of the International Conference on Mechanical Engineering (ICME2011), Dhaka, Bangladesh, 18–20 December 2011; pp. 18–20.
- Ashwill, T.D.; Gershin, S. *CFD Calculations of S809 Aerodynamic Characteristics*; Sandia National Lab (SNL-NM): Albuquerque, NM, USA, 2011.
- Wolfe, W.; Ochs, S.; Wolfe, W.; Ochs, S. CFD calculations of S809 aerodynamic characteristics. In Proceedings of the 35th Aerospace Sciences Meeting and Exhibit, Reno, NV, USA, 6–10 January 1997; p. 973.

28. Bofeng, X.; Junheng, F.; Qing, L.; Chang, X.; Zhenzhou, Z.; Yue, Y. Aerodynamic performance analysis of a trailing-edge flap for wind turbines. *J. Phys. Conf. Ser.* **2018**, *1037*, 022020. [[CrossRef](#)]
29. Timmer, W.; Van Rooij, R. Summary of the Delft University wind turbine dedicated airfoils. *J. Sol. Energy Eng.* **2003**, *125*, 488–496. [[CrossRef](#)]
30. Menter, F. Two-equation eddy-viscosity turbulence models for engineering applications. *AIAA J.* **2002**, *40*, 254–266. [[CrossRef](#)]
31. Menter, F.R. Two-equation eddy-viscosity turbulence models for engineering applications. *AIAA J.* **1994**, *32*, 1598–1605. [[CrossRef](#)]
32. Mishra, P.; Aharwal, K. A review on selection of turbulence model for CFD analysis of air flow within a cold storage. *IOP Conf. Ser. Mater. Sci. Eng.* **2018**, *402*, 012145. [[CrossRef](#)]
33. Menter, F. Zonal two equation kw turbulence models for aerodynamic flows. In Proceedings of the 23rd Fluid Dynamics, Plasmadynamics, and Lasers Conference, Orlando, FL, USA, 6–9 July 1993; p. 2906. [[CrossRef](#)]
34. Rogers, S.; Menter, F.; Durbin, P.; Mansour, N. A comparison of turbulence models in computing multi-element airfoil flows. In Proceedings of the 32nd Aerospace Sciences Meeting and Exhibit, Reno, NV, USA, 10–13 January 1994; p. 291. [[CrossRef](#)]
35. Yu, T.; Wang, J.; Zhang, P. Numerical simulation of Gurney flap on RAE-2822 supercritical airfoil. *J. Aircr.* **2011**, *48*, 1565–1575. [[CrossRef](#)]
36. Zhang, P.; Liu, A.; Wang, J. Aerodynamic modification of NACA 0012 airfoil by trailing-edge plasma gurney flap. *AIAA J.* **2009**, *47*, 2467–2474. [[CrossRef](#)]
37. Ma, D.; Zhao, Y.; Qiao, Y.; Li, G. Effects of relative thickness on aerodynamic characteristics of airfoil at a low Reynolds number. *Chin. J. Aeronaut.* **2015**, *28*, 1003–1015. [[CrossRef](#)]
38. Ramsay, R.; Janiszewska, J.; Gregorek, G. *Wind Tunnel Testing of Three S809 Aileron Configurations for Use on Horizontal Axis Wind Turbines*; Airfoil Performance Report NREL/TP-442-7817; National Renewable Energy Laboratory: Golden, CO, USA, July 1996.
39. Ramsay, R.; Hoffman, M.; Gregorek, G. *Effects of Grit Roughness and Pitch Oscillations on the S809 Airfoil*; Airfoil Performance Report DE-AC36-83CH10093; National Renewable Energy Laboratory: Golden, CO, USA, December 1995.
40. Ramsay, R.; Janiszewska, J.; Gregorek, G. Wind tunnel testing of an S809 spoiler flap model. In Proceedings of the 35th Aerospace Sciences Meeting and Exhibit, Reno, NV, USA, 6–10 January 1997; p. 976. [[CrossRef](#)]

Article

Effect of an Inducer-Type Guide Vane on Hydraulic Losses at the Inter-Stage Flow Passage of a Multistage Centrifugal Pump

Mohamed Murshid Shamsuddeen ^{1,2} , Sang-Bum Ma ², Sung Kim ², Ji-Hoon Yoon ³, Kwang-Hee Lee ⁴, Changjun Jung ⁴ and Jin-Hyuk Kim ^{1,2,*} 

¹ Industrial Technology (Green Process and Energy System Engineering), Korea University of Science & Technology, Daejeon 34113, Korea; murshishams@kitech.re.kr

² Clean Energy R&D Department, Korea Institute of Industrial Technology, Cheonan-si 31056, Korea; sbma@kitech.re.kr (S.-B.M.); ks2928@kitech.re.kr (S.K.)

³ Dongyang Chemical Pump Company, Paju 10832, Korea; isimi@dycp.co.kr

⁴ GS Caltex Corporation, Seoul 06141, Korea; kayhlee@gscaltex.com (K.-H.L.); cjjung@gscaltex.com (C.J.)

* Correspondence: jinhyuk@kitech.re.kr; Tel.: +82-41-5898447

Abstract: A multistage centrifugal pump was developed for high head and high flow rate applications. A double-suction impeller and a twin-volute were installed at the first stage followed by an impeller, diffuser and return vanes for the next four stages. An initial design feasibility study was conducted using three-dimensional computational fluid dynamics tools to study the performance and the hydraulic losses associated with the design. Substantial losses in head and efficiency were observed at the interface between the first stage volute and the second stage impeller. An inducer-type guide vane (ITGV) was installed at this location to mitigate the losses by reducing the circumferential velocity of the fluid exiting the volute. The ITGV regulated the pre-swirl of the fluid entering the second stage impeller. The pump with and without ITGV is compared at the design flow rate. The pump with ITGV increased the stage head by 63.28% and stage efficiency by 47.17% at the second stage. As a result, the overall performance of the pump increased by 5.78% and 3.94% in head and efficiency, respectively, at the design point. The ITGV has a significant impact on decreasing losses at both design and off-design conditions. An in-depth flow dynamic analysis at the inducer-impeller interface is also presented.

Keywords: multistage centrifugal pump; double-suction impeller; twin-volute; computational fluid dynamics; inducer-type guide vane



Citation: Shamsuddeen, M.M.; Ma, S.-B.; Kim, S.; Yoon, J.-H.; Lee, K.-H.; Jung, C.; Kim, J.-H. Effect of an Inducer-Type Guide Vane on Hydraulic Losses at the Inter-Stage Flow Passage of a Multistage Centrifugal Pump. *Processes* **2021**, *9*, 526. <https://doi.org/10.3390/pr9030526>

Academic Editor:
Krzysztof Rogowski

Received: 15 February 2021

Accepted: 12 March 2021

Published: 15 March 2021

Publisher's Note: MDPI stays neutral with regard to jurisdictional claims in published maps and institutional affiliations.



Copyright: © 2021 by the authors. Licensee MDPI, Basel, Switzerland. This article is an open access article distributed under the terms and conditions of the Creative Commons Attribution (CC BY) license (<https://creativecommons.org/licenses/by/4.0/>).

1. Introduction

According to statistics, electric motors consume 46 percent of the world's electricity and account for nearly 70% of the net consumption of industrial energy [1]. Power consumption by pump systems alone accounts for about 22% of the world's energy out of which centrifugal pumps consume 16% [2]. Centrifugal pumps have tremendous energy consumption and substantial potential for energy savings. Therefore, researching the possibilities of increasing the efficiency of pump units are need of the hour.

Multistage centrifugal pumps are capable of increasing liquid pressure and pump fluids to a large distance and are widely used in field irrigation, urban afforestation, groundwater supply, and chemical and petroleum industries. Among them, the double-suction centrifugal pumps can achieve twice the flow rate of a single-suction pump with the same diameter and have better cavitation performance [3]. A double-suction multistage centrifugal pump requires a great deal of energy for the year-round operation and achieving an energy-efficient design can save cost and improve the overall pump performance.

A double-suction multistage centrifugal pump was designed for specific applications in the petrochemical processing plants. The design feasibility study of the pump showed effectiveness in handling multiple fluids without performance degradation [4]. In our

previous study [5], the hydraulic loss analysis of the pump revealed vast potentiality in stage-wise performance recovery specifically at the second stage. The losses were mostly associated with large radial forces in the fluid passing from Stage 1 to 2 through a twin volute. The high circumferential velocity of the fluid at the interface between Stages 1 and 2 caused excessive pre-swirl at the second stage impeller inlet. The fluid pre-swirl induced losses at the second stage impeller thereby decreasing the pump efficiency. Certain design recommendations were provided to control the pre-swirl and enhance the pump characteristics. The recommendation to use a guide vane between the first and second stages is presented in this paper.

Inlet guide vane installation is a common technique to control the fluid circulation and pressure ratio at the inlet of a turbomachine. This method was initially carried out in compressors and fans and was recently applied to centrifugal pumps to regulate fluid pre-swirl at the inlet [6]. Tan et al. [7] studied the effect of an adjustable inlet guide vane for the pre-swirl regulation of a single-stage centrifugal pump and obtained a higher efficiency and head at the design point at an angle of 24° . Yuchuan et al. [8] studied the same IGV for angles $\pm 36^\circ$ and $\pm 60^\circ$ to find the influence of guide vanes on unsteady flow. Qu et al. [9] studied the clocking effect of the same IGV and found little influence on pump performance. Liu et al. [10] compared the performance between a 2D IGV and a 3D IGV with a similar design and obtained a higher efficiency with a minimum impact velocity moment for the 3D IGV model. Further investigation by Liu et al. [11] succeeded in suppressing the losses associated with high pressure near the impeller inlet and facilitated a uniform distribution of pressure in the impeller channels at the rotational frequency. Liu et al. [12] studied the influence of the IGV angle and axial distance range between IGV and impeller. The IGV angle had a significant impact in reducing the pressure fluctuation at the blade leading edge while the axial distance had only a slight impact on the pump performance. Lin et al. [13] used an adjustable two plate inlet guide vane at the suction pipe of a single-stage centrifugal pump to reduce the negative pressure at the impeller leading edge. The pump performance was improved at a vane angle of 25° , weakening the vortex flow at the pump inlet. Hou et al. [14] studied the effect of the number of IGV vanes on the hydraulic characteristics and suggested a six-vane design for a higher head and better efficiency. It is evident from the literature that an IGV is capable of regulating the pre-swirl at the impeller inlet. However, all these IGV configurations were applied to regulate the pre-swirl in single-stage pumps with an option to control the IGV angle. This is not the case with multistage centrifugal pumps. The usage of pre-swirl regulation of IGV is extremely rare for multistage pumps simply due to the physical constraint to control the IGV angle using gears or levers during operation. Typically, radial diffusers and return guide vanes of fixed angles are used in multistage pumps to transfer fluid from one stage to another. However, a radial diffuser-return vane combination cannot be used to regulate the axial flow exiting the twin volute of the proposed pump. An axial diffuser or a guide vane with a fixed angle is the technically feasible unit that can be installed to regulate this flow.

In order to govern the pre-swirl of the flow between the volute and the second stage impeller, the stationary guide vane design must be meticulously configured since the vane angle is not adjustable. An inducer type, a screw-type, or a helico-axial design is selected for this purpose since the twisted vane design can convert the rotational inertia of the fluid to axial momentum without the need to adjust the angle. Several inducer type pump designs can be found in the literature. Li et al. [15] studied the flow through a three-blade inducer on an axial flow pump and found that the maximum pressure is generated when the inducer angle is aligned with the impeller such that the wake from the inducer impinges the impeller blade minimizing hydraulic losses. Campos-Amezcuca et al. [16] studied a two-blade inducer design in a turbo-pump with and without clearance and observed that a uniform axial velocity profile is obtained for an inducer without clearance. Yang et al. [17] studied the clocking effect between the inducer and impeller in a high-speed centrifugal pump and obtained the best performance when the relative

angle between the inducer trailing edge and impeller leading edge was 0° . Several pump designers used inducers at the upstream of the impeller to reduce pump cavitation [18–22]. Although inducers were used in centrifugal pumps for decades, they are not commonly found in multistage centrifugal pumps. Sedlár et al. [23] installed a three-bladed inducer in a two-stage centrifugal pump between the inlet guide vane and the first stage impeller. The pump with an inducer showed better cavitation reduction than the pump without an inducer. From these works of literature, it can be said that the application of inducers in centrifugal pumps showed great potential in improving the performance and decreasing the cavitation phenomena. However, all the inducers mentioned are rotating devices with the same speed as the impeller. Since a stationary guide vane is the requirement of the proposed pump, the number of vanes and other design configurations of the inducer shape is influenced by the literature to create an inducer-type guide vane. The ITGV design specifications are provided in the next section.

A multistage centrifugal pump design with an ITGV device to minimize the hydraulic losses occurring at the inter-stage flow passage between the twin volute and second-stage impeller is presented in this paper. The effect of the ITGV design on the overall performance of the pump and the dynamics of the fluid passing through the ITGV is explained in detail.

2. Design Configurations

The centrifugal pump is designed to pump fluids used in petrochemical refineries satisfying high-head and high-flow rate requirements. The number of stages, the impeller dimensions and other design parameters are determined by API BB5 centrifugal pump standards [24]. The initial pump model is obtained from a dynamically similar scaled-down pump model used for low flow rate operations. The multistage centrifugal pump consists of an inlet passage, a double-suction impeller and a twin-volute in the first stage. Stages 2–4 have a single-suction impeller, a stationary diffuser and return guide vanes. The fifth stage consists of the impeller, diffuser, and outlet volute. Figure 1 shows the exploded view of the pump components.

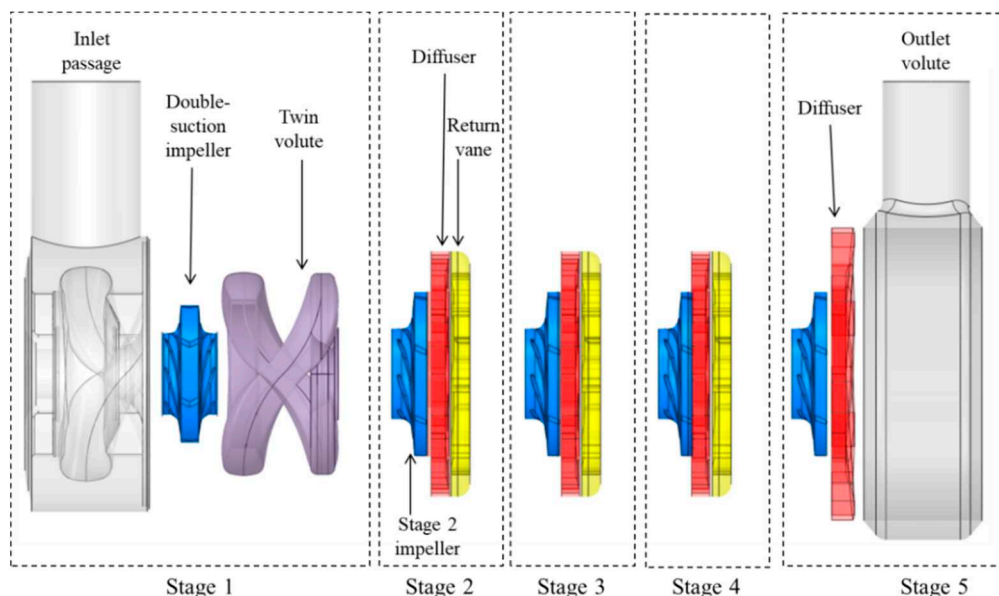


Figure 1. Exploded view of the multistage centrifugal pump and its components.

The theoretical performance curve of the pump is obtained from the pump affinity laws as shown below:

$$\frac{Q_1}{Q_2} = \left(\frac{n_1}{n_2}\right); \frac{H_1}{H_2} = \left(\frac{n_1}{n_2}\right)^2; \frac{P_1}{P_2} = \left(\frac{n_1}{n_2}\right)^3 \quad (1)$$

where Q , H , P , and n represents the flow rate, head, input power and rotational velocity, respectively. The subscripts 1 and 2 correspond to the model and the prototype.

Water is chosen as the working fluid for the simulations as the pump affinity laws apply only for water or pure liquids with kinematic viscosity less than 10 cS [25]. The five-stage centrifugal pump has a flow coefficient of $\phi = 0.01$ and head coefficient $\psi = 0.67$. The impellers at stages 2–5 have a diameter 20% larger than the first stage impeller. The fifth stage diffuser is 16% larger in diameter than the diffusers in stages 2–4. The twin-volute is staggered at 180° to each other to balance out the radial forces. The impellers contain seven blades while the diffuser and return vane consist of eight vanes.

The flow coefficient, the head coefficient and efficiency are calculated using the following equations:

$$\psi = \frac{gH}{n^2 D^2} \quad (2)$$

$$\phi = \frac{Q}{nD^3} \quad (3)$$

$$\eta = \frac{\rho Q g H}{P} \quad (4)$$

where D , g , η , and ρ corresponds to the diameter of the impeller, acceleration due to gravity, the efficiency and the density of the fluid, respectively.

A stationary inducer-type guide vane is installed between the first and the second stage with a length of $0.27D$. The ITGV consists of three blades shrouded to the casing without clearance. The preliminary design is inspired by a helico-axial impeller designed and optimized in our laboratory [26–28]. The design thus obtained is modified to suit the pump dimensions. The ITGV inlet is designed symmetrically with the fluid which exits the volute being with perfect hydraulic symmetry at all flow conditions. The exit blade angle is matched with the second stage impeller inlet blade angle. The shroud diameter of the ITGV is chosen to be the same as the second stage impeller diameter while the hub diameter is equal to the diameter of the pump shaft. The thickness is maintained equally throughout the blade length. Figure 2 shows the 3D ITGV CAD model and the overall pump design with ITGV.

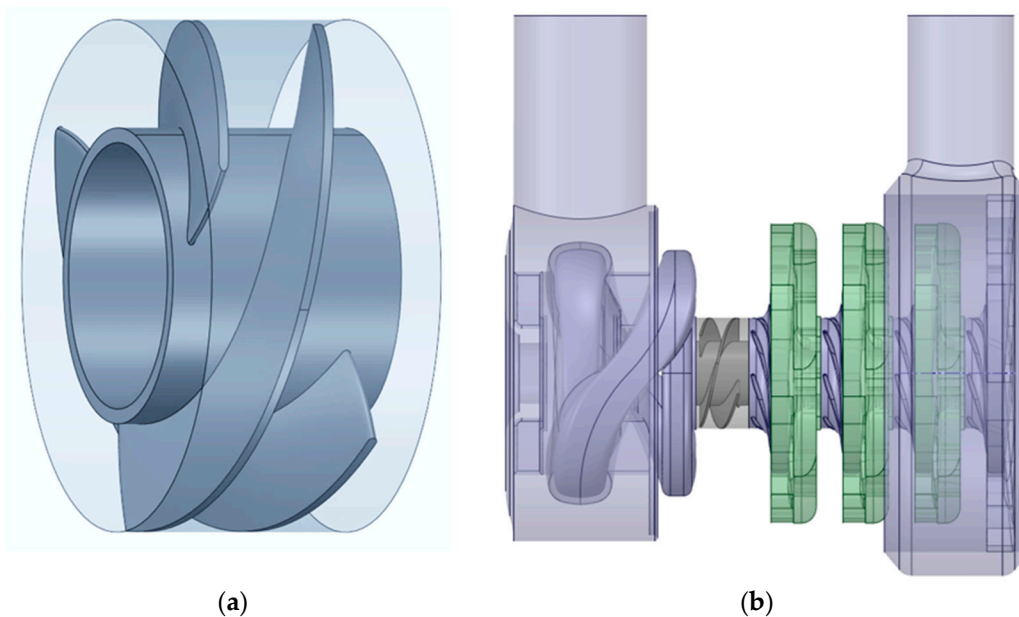


Figure 2. (a) The ITGV CAD model and, (b) the entire pump with ITGV.

3. Numerical Model

Three-dimensional mass and momentum equations are solved in a commercial CFD solver to study the flow behavior inside the pump. The fluid transportation equations are based on the steady incompressible Reynolds-averaged Navier–Stokes (RANS) equations solved using an iterative approach in ANSYS CFX 19.1®software (ANSYS, Inc., Pennsylvania, PA, USA). These equations are very well documented in numerous literature [29–31]. The turbulence model, k – ω based shear stress transport (SST) is used to predict the turbulence occurring inside the pump. The SST model uses an integrated feature to shift from a high Reynold’s number form of the k – ϵ model away from the boundary layer and the k – ω model near the wall region [32]. A blending function is used to ensure a smooth transition between the models. Similar studies by the authors using the SST model are well proved to predict the turbulent behavior in a three-stage centrifugal pump [33,34].

The 3D design of the impeller blades, ITGV blades, diffuser and return channel vanes are generated using ANSYS Bladegen®tools (ANSYS, Inc. Pennsylvania, PA, USA) while the inlet passage, the twin-volute and the outlet volute are designed using CAD software. The fluid domains are extracted using ANSYS SpaceClaim®module (ANSYS, Inc. Pennsylvania, PA, USA)while ANSYS meshing tool is used for the grid generation. The impeller domain grids are created using ANSYS TurboGrid®software (ANSYS, Inc. Pennsylvania, PA, USA)which provides an exceptional level of mesh quality with preferred boundary layer resolution. The CFD model including the boundary conditions for the numerical analysis was prepared using CFX-Pre. The governing equations were solved in CFX-Solver and the post-processing was done in CFX-Post. Figure 3a shows the CFD domain used for the pump without the ITGV component. Due to the periodic nature of the geometry; the impellers, diffuser, and return channel domains are chosen as a single passage to save computational resources without compromising on the accuracy of the results. The impeller domains are rotating along the rotational axis while all other domains remain stationary. The outlet pipe is extended to avoid any unlikely backflow occurring at the outlet. The working fluid is water. Atmospheric pressure condition and mass flow rate is defined at the inlet and outlet, respectively. Since the pitch ratio is high at the interface between the stationary domains and rotating domains, the mixing-plane (stage) interface model is applied for the steady-state simulations. General Grid Interface (GGI) mesh connection is provided at all the interfaces to connect the non-conformal elements between the domains. The GGI determines the connectivity between the grids on either side of the interface using an intersection algorithm [35]. The convergence criterion for the RMS residual target was set at 1×10^6 . Due to the complexity of the multistage pump geometry, the convergence was ensured by monitoring important variables such as the flow rate at the pump outlet, the torque at the impeller blades and the head generated by the pressure gradient at all timesteps. A reasonable convergence was obtained for all the simulations.

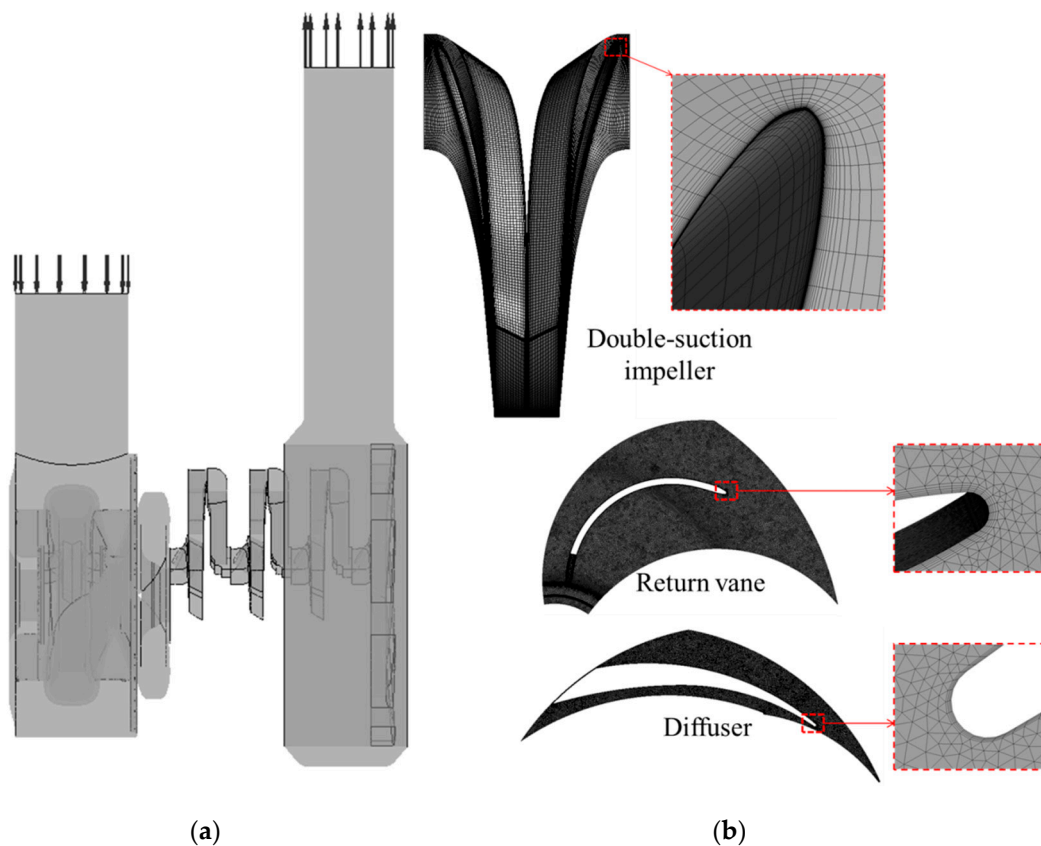


Figure 3. (a) Computational domain of entire pump. (b) Generated grids.

Overview of Grid Generation

The simulation-based study requires a grid independency test to ensure that the results obtained do not vary with grid size. Due to the complexity of the multistage centrifugal pump, the grid study was carried out separately for stages 1 and 2. The optimum grids thus obtained would satisfy the entire pump model since the other stages are a replication of the second stage. The grid number for the outlet volute in the fifth stage is generated analogously to the first stage inlet passage. Since the simulations for the grid independency tests are carried out in two stages, the boundary domains of the individual stages are extended to avoid possible backflow in the simulations. The generated grids are shown in Figure 3b. To resolve the boundary layers, multiple layers of hexahedral meshes are stationed along the blade suction and pressure side surfaces for the impeller, diffuser, and return vanes. The y^+ values at these boundaries are kept below 30 while they are maintained below 100 at other locations.

The grid convergence index (GCI), derived based on the Richardson extrapolation method, is the most reliable method for a grid convergence study [36]. An approximate relative error (e_a) and fine grid convergence index (GCI_{fine}) is calculated for a key variable obtained from three different sets of grids with significant resolutions. The efficiency of the centrifugal pump is taken as the key variables in this study. The grid convergence index can be calculated from:

$$GCI_{fine} = \frac{1.25 e_a}{r - 1} \quad (5)$$

where r is the grid refinement factor.

The GCI_{fine} for stage 1 and stage 2 were obtained as 0.6% and 0.91%, respectively. Since the efficiency obtained for the fine grid has GCI value of less than 1%, it can be said that the generated grids are optimum and further grid refinement is not necessary. The number of nodes for the optimum grid was 1.75 and 1.35 million for stages 1 and 2,

respectively. The total number of nodes generated to create the entire pump domain was 6.25 million. Based on the optimum grid, the grid for the ITGV domain was generated with almost the same number of nodes as the impeller blades. Therefore, further grid study with the ITGV pump is unnecessary.

4. Pump Performance

The performance of the pump design obtained from the affinity laws are firstly calculated theoretically and then numerically using CFD tools. The overall pump performance curve obtained by the theoretical calculation is compared with the CFD results in Figure 4. The head coefficient, flow coefficient and efficiency are normalized by their corresponding design point values. The predicted trend of the head and efficiency curves along the change of flow has concurred with the theoretical prediction. The curves obtained from the CFD simulations are in reasonable agreement with the theoretical calculations with an error percentage of less than 8%. The calculation accuracy has a certain influence because of the limitations of the steady-state simulation, the simplified geometrical model and overlooking of losses in the CFD simulation. Since this is a preliminary design feasibility study prior to experimental analysis without considering the unaccounted mechanical losses, the obtained CFD results are acceptable for further analysis.

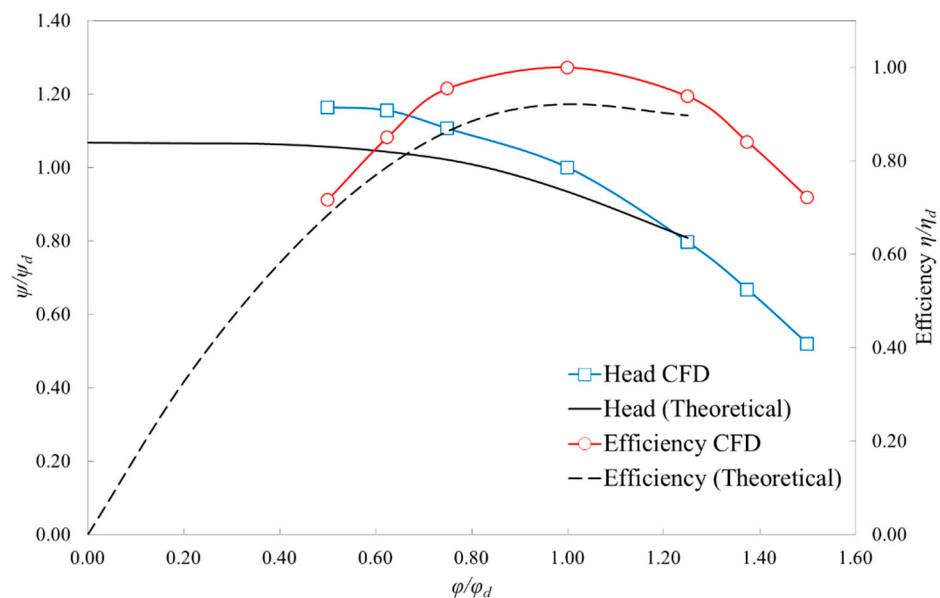


Figure 4. Pump performance comparison of theoretical calculation and numerical simulations.

The overall performance of the pump with and without ITGV is compared in Figure 5. The efficiency of the pump remains unaffected in the low flow rate condition while the head increases slightly due to a minor increase in pressure gradient at the ITGV. At the best efficiency point (BEP), the efficiency has increased by 3.94% while the head increased by 5.78%. The overall performance of the pump has increased by a great margin with the installation of ITGV. The improvement in the pump performance, however, comes at a cost of increased power consumption. The power consumption increased by 1.78% at the BEP and by 8.85% at the maximum flow rate condition with the installation of ITGV. The increase in power consumption is not high at the BEP point at which the pump would be operated normally, and it is high at the maximum flow rate, which is seldom operated. Even with the rise in power consumption at the maximum flow rate condition, the increase in efficiency and head is large enough to offset the difference.

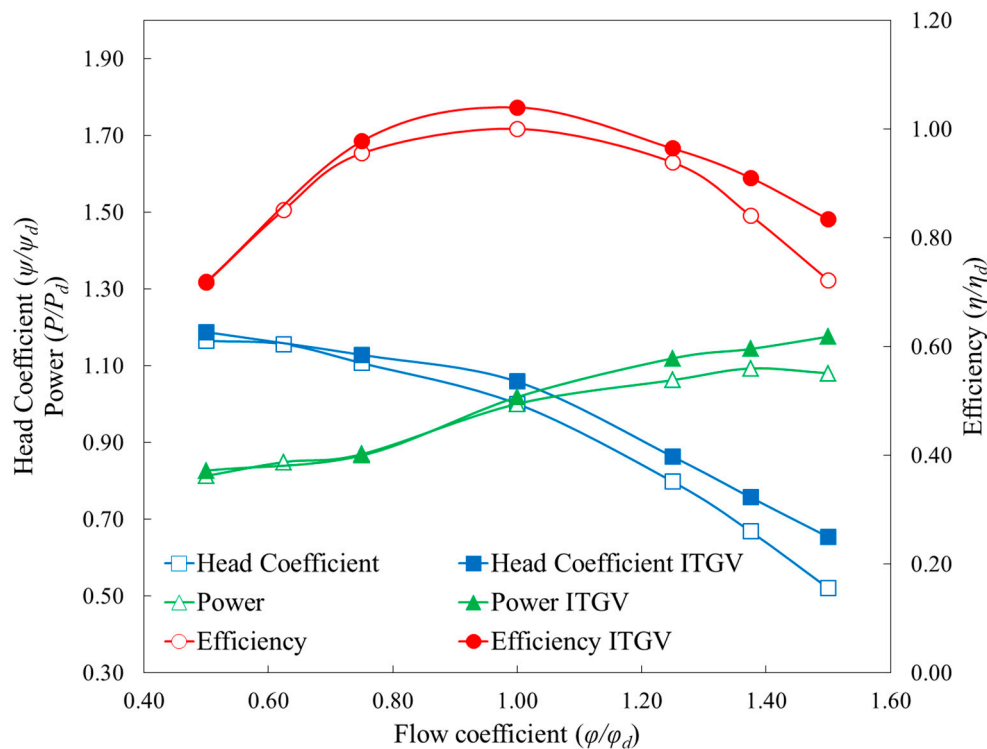


Figure 5. Performance comparison of the pump with and without ITGV.

The performance study of the individual stages is as important as the overall performance in a multistage centrifugal pump. The stage-wise efficiency and head coefficient curves of the two pumps are presented in Figure 6. The efficiency at the low flow rate is almost the same at all stages for the pump with and without ITGV. As the flow rate increases, the hydraulic efficiency improves for all stages except for stage 2. The efficiency at stage 2 descends at high rates beyond BEP for the reference pump. Similarly, the head coefficient drops near 0.1 at the maximum flow rate. The large drop in efficiency and head of the reference pump indicates a very large loss at the second stage. The pump with ITGV has improved the efficiency by 47.17% and head by 63.28% at the design point of stage 2. A similar increase is also observed at the maximum flow rate condition of stage 2. The small improvement in the parameters can be found in other stages as well. Installing the ITGV has thus not only improved the performance of stage 2 by a great margin but also improved the performance at all stages. This increase in efficiency and head at all stages reflects the overall improvement in the pump performance as found in Figure 5.

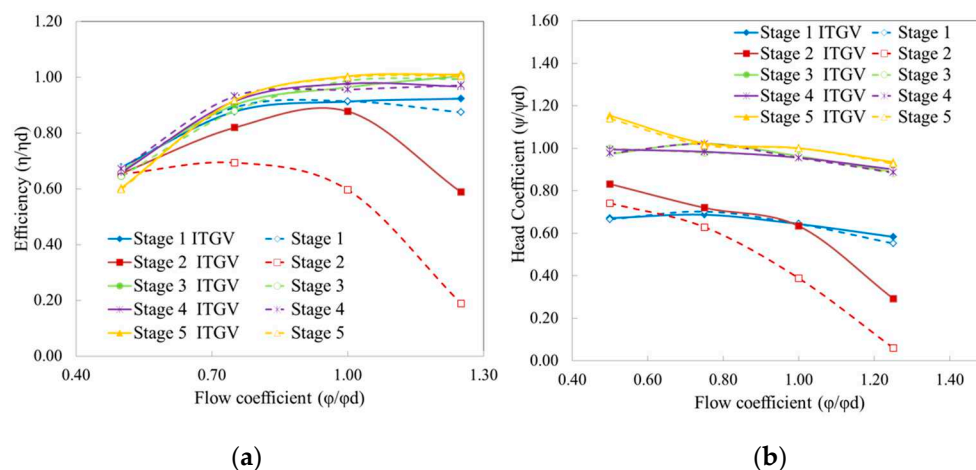


Figure 6. Stage performance comparison: (a) Efficiency; (b) head coefficient.

A detailed analysis of the losses observed at stage 2 and the influence of the ITGV in mitigating these losses must be studied in-depth to understand the flow physics at the ITGV-Impeller interface. The pump is operated at the design point more often than others and as a reason; the pump operating at the design point is chosen for the in-depth analysis. The second stage consists of the impeller, diffuser and return vanes. The losses are mostly observed at the inlet of the impeller and, thus, the loss analysis is focused on the flow through the ITGV and second stage impeller only. Henceforth, the term ‘impeller’ refers to the second stage impeller unless stated otherwise.

The blade loading at the mid-span of the impeller along the streamwise direction of the pump with and without ITGV is shown in Figure 7. The pressure is normalized by its maximum value. A large drop in pressure at the leading edge is observed in the reference pump indicating the location of the maximum loss. Such sharp pressure drops may cause the formation of cavitation bubbles and can easily lead to pump failure. The installation of the ITGV device at the upstream of the impeller has decreased the pressure drop by 66.13% at the leading edge of the impeller. The overall blade loading has improved significantly by a weighted average of 35.6% with the installation of the ITGV. The weighted average is calculated to accurately represent the average of the percentage change in quantity. The ITGV not only has an impact on the stage 2 impeller but also on the downstream impellers. The blade loading of impellers at stages 3, 4, and 5 (not shown here) was also improved by a weighted average of 17.96%, 10.32%, and 7.09%, respectively.

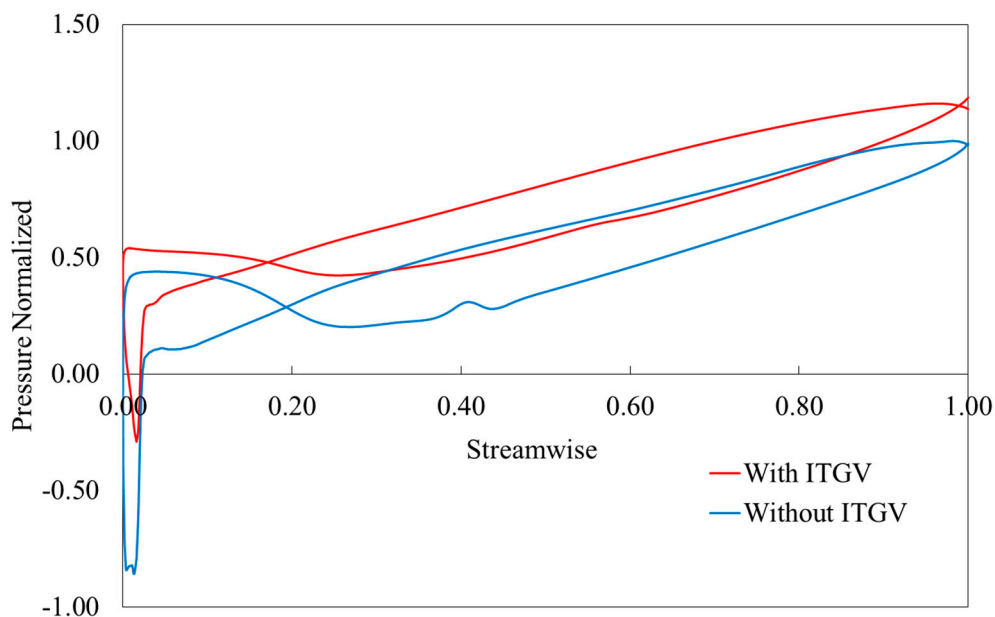


Figure 7. Blade loading comparison of the second stage impeller at mid-span.

The significance of improvement in the blade loading is explained by its effect on individual stages. The head and efficiency trend graph along the mid-span of the impellers for stages 2–5 at the design point is plotted in Figure 8. The parameters are normalized by the corresponding maximum values of the reference pump. Since the ITGV does not affect the upstream flow, the trend line is not plotted for stage 1. A head drop is observed at the second stage of the reference pump at about 20% of the streamwise direction. This corresponds to the pressure drop observed in Figure 7 at 0.2 streamwise. The head rises again towards the trailing edge of the impeller. The head increases at each stage and finally achieves the maximum head at the end of the 5th stage. The ITGV has prevented the drop in pressure gradient at the 2nd stage, which resulted in an increase of head at this stage and an overall increase in the consecutive stages. The overall head trend graph increased by a weighted average of 17.87% with ITGV compared to the reference pump.

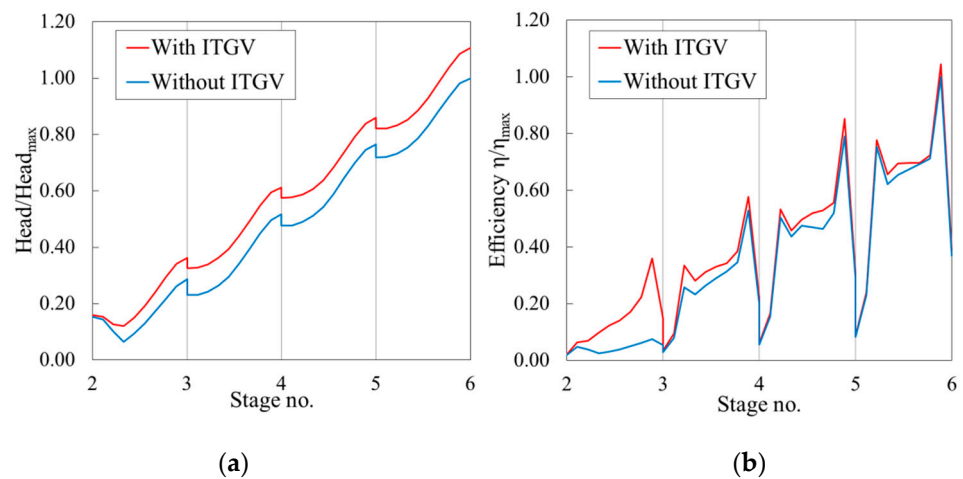


Figure 8. Head (a), and efficiency (b) trend graphs plotted at the mid-span of the impellers at the design point.

The efficiency trend graph shows the rise in efficiency at each stage. At the beginning of each stage, the dip in the efficiency curve is due to the abrupt change in the pressure gradient as the fluid travels from one stage to another. While the efficiency dips at each impeller's leading-edge, it immediately climbs back up and rises sharply at the trailing edge. However, the efficiency remains the lowest at the second stage of the reference pump due to the losses mentioned earlier. The introduction of ITGV has aided in reducing the losses and improving the efficiency at the second stage as well as an overall increase in the consecutive stages. The weighted average increase in the overall efficiency trend graph is 14.48% compared to the pump without ITGV. The potential of the ITGV is remarkable in improving the pump characteristics. However, how the ITGV design affects the fluid flow behavior and the reason for losses and the effects of ITGV are studied qualitatively in the next section.

5. Flow Field Analysis

The fluid flowing through the volute, ITGV and the second stage impeller is analyzed in detail to determine the causes for the losses and the correction by the ITGV at the design point. From the first stage impeller, the fluid entering the volute splits into the two arms of the 180° staggered twin-volute, flows along the surfaces of the volute and joins back towards the exit of the volute. The fluid is found to have a greater radial force than the axial force at the volute exit and, as a result, produces a pre-swirl at the inlet of the second stage impeller. This high-intensity swirl flow causes deviation between the fluid incidence angle and blade angle at the impeller leading edge. The flow through the volute and the impeller is shown in Figure 9a. The 3D velocity streamlines show a shift in the flow direction due to the fluid moving from a stationary domain to a rotating domain. However, the flow direction entering the impeller flows away from the blade incidence angle due to the high swirl intensity. The absolute velocity increases at the impeller inlet due to the large circumferential velocity at the volute exit. This causes flow separation at the leading edge and gives rise to recirculation regions at the inlet and the pressure side of the impeller, leading to the formation of vortices in the flow. The vortex core region formed at the impeller is shown in Figure 9b. The vortices thus formed cause blockage to the incoming flow thereby decreasing the pressure at this region. The pressure drop directly affects the stage performance and result in losses at the second stage impeller.

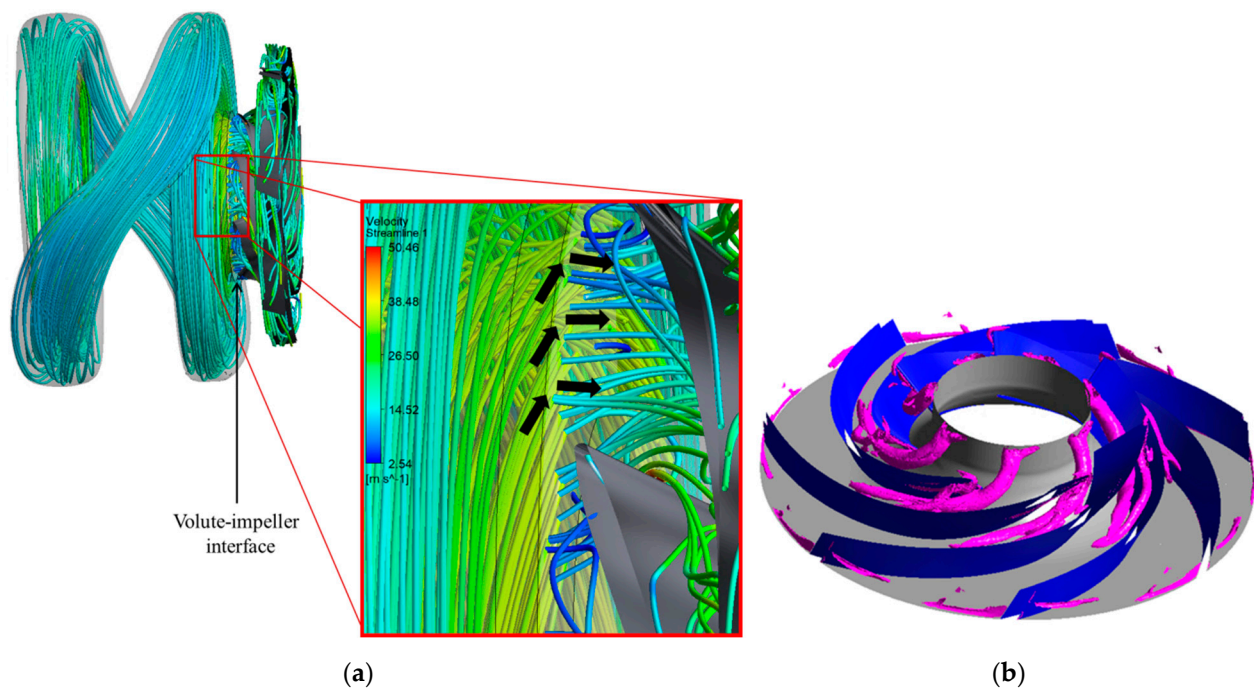


Figure 9. (a) Three-dimensional velocity streamlines of the fluid flowing through the volute and impeller, (b) Vortex core region inside the second stage impeller (velocity swirling strength = 1500 s^{-1}).

The installation of the ITGV does not prevent the formation of the high-intensity swirl flow observed at the exit of the twin-volute; it rather continues the flow along the ITGV blades without changing its direction. The magnitude of the velocity decreases as the fluid flows through the stationary blades of the ITGV as shown in Figure 10a. The average velocity of the fluid decreased from 33.86 m/s at the volute exit to 22.65 m/s at the ITGV exit. The decrease in circumferential velocity at the exit of the ITGV allows the fluid to flow towards the incidence angle of the blade leading edge. This is because the ITGV exit blade angle is configured to match the impeller inlet blade angle. As a result, the flow separation at the impeller leading edge is moderated and thereby decrease the intensity of the vortices formed at the impeller. Figure 10b shows the decrease in vortex core in the second stage impeller. The blockage in the flow is removed with the installation of ITGV and hence the pressure losses are diminished.

The flow angles are explained in detail by plotting the velocity diagram at the leading edge of the impeller in Figure 11. The vectors U and C_U represent the blade velocity and the tangential velocity, respectively. In Figure 11a, the relative flow angle is $\beta = 128.5^\circ$ while the absolute flow angle is $\alpha = 11.86^\circ$ at the inlet of the impeller for pump without ITGV. The large relative flow angle force the fluid to flow virtually perpendicular to the blade. The relative flow angle decreases sharply to $\beta = 56.4^\circ$ and the absolute flow angle rises to $\alpha = 17.6^\circ$ for the pump with ITGV as shown in Figure 11b. The magnitude of the relative velocity (W) remains essentially the same while the direction changes towards the blade angle similar to the observation in Figure 10a. The magnitude of the absolute velocity (C) decreases by 22.46%. The velocity triangles of the rest of the stages are approximately the same for both pumps.

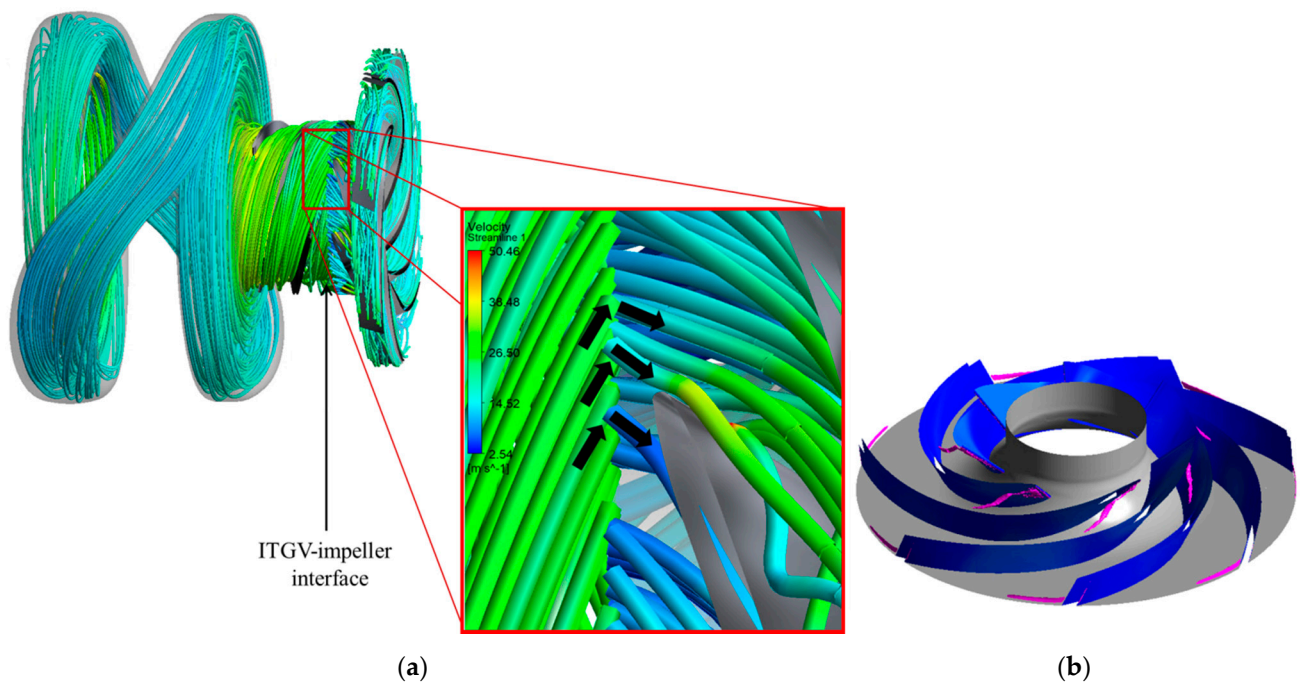


Figure 10. (a) Three-dimensional velocity streamlines of the fluid flowing through the volute, ITGV, and impeller. (b) Vortex core region inside the second stage impeller (velocity swirling strength = 1500 s^{-1}).

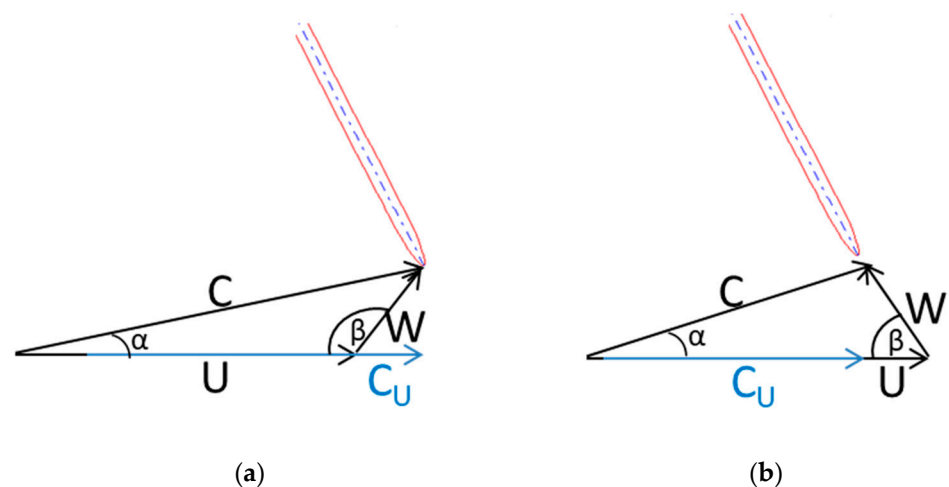


Figure 11. Velocity triangles at the leading edge of the impeller (a) pump without ITGV, and (b) pump with ITGV.

The relative flow angle correction achieved by the ITGV has a significant impact on the fluid inside the impeller. The velocity streamlines at the mid-span of the impeller is compared in Figure 12a,b. There is an adverse pressure gradient between the blades leading to the formation of the vortex and a non-uniform flow is observed at the reference pump. The flow through the impellers appears to be smooth and uniform with the disappearance of vortices in the pump with ITGV. The total pressure in stationary frame contour is shown in Figure 12c,d. The low-pressure region at the pressure-side of the blades is eliminated to obtain a smooth transition of fluid pressure from the inlet to the outlet of the ITGV pump impeller. The increasing pressure increases the head developed at this stage as observed earlier.

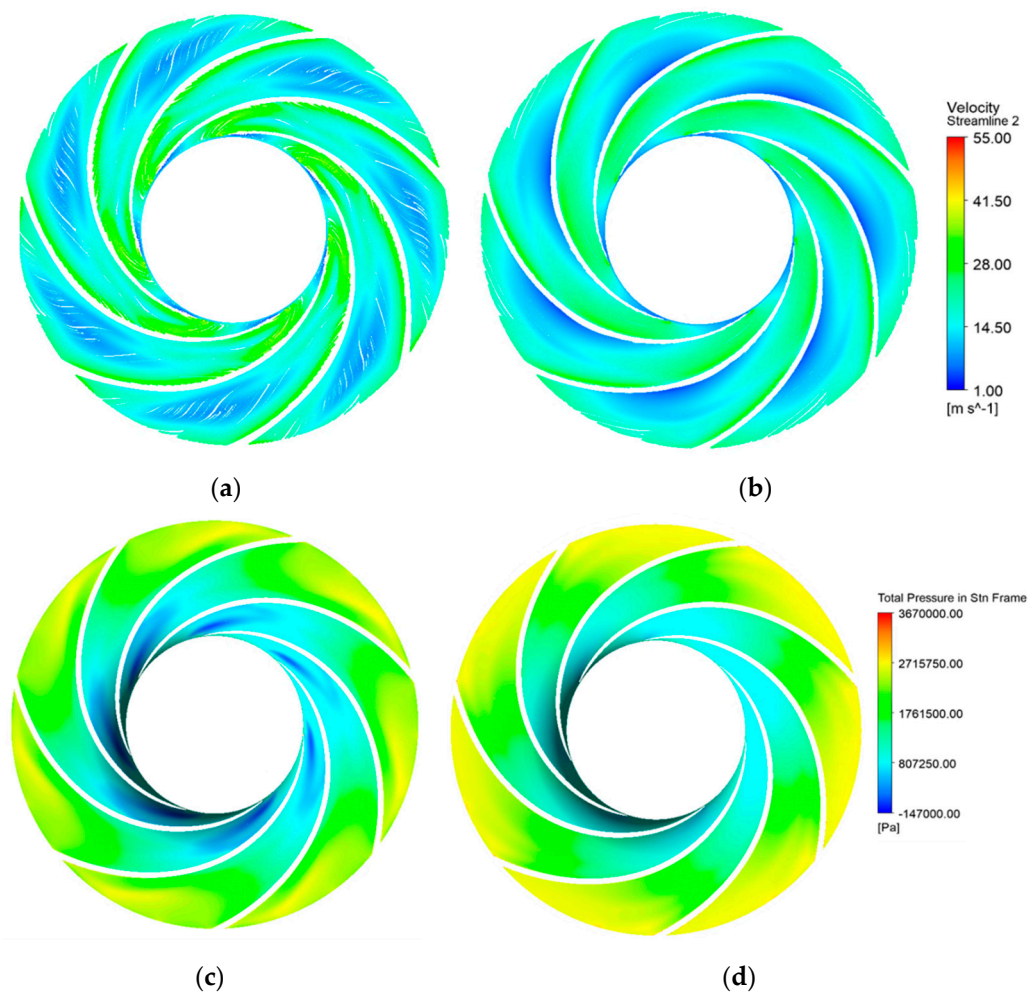


Figure 12. Velocity streamlines at the mid-plane of the impeller for (a) a pump without ITGV, (b) a pump with ITGV, and the total pressure contour in a stationary frame at the mid-plane of the impeller for (c) a pump without ITGV and (d) a pump with ITGV.

6. Performance Analysis at Off-Design Conditions

The centrifugal pump is generally operated at its design point (Q_d) at which the efficiency curve reaches its maximum. However, the pump may be operated at off-design points at times by force of circumstances to deliver fluid either below or above the capacity at BEP. An adverse pressure gradient, flow separation, and flow recirculation at the inlet and exit always occurs under off-design points. The flow phenomenon is more complex than the design point, especially at the high flow rate conditions. Therefore, it is necessary to study the pump performance at these conditions too. Two off-design conditions are tested at 25% below and excess flow capacity of the design point. The head trend line is compared for low flow rate and high flow rate for both the pumps in Figure 13a,b. There is a minor increase in the head trend line of the pump with ITGV at $0.75Q_d$ and a significant increase at the $1.25Q_d$ flow condition. The head increases by a weighted average of 3.58% at the low flow rate and gains a weighted average of 20.48% at the high flow rate condition for the ITGV pump. A similar increase of weighted average head by 17.87% was observed previously at the design point, too. The losses inside the pump escalate as the flow rate rises but the ITGV is capable of executing head loss correction at all flow rates.

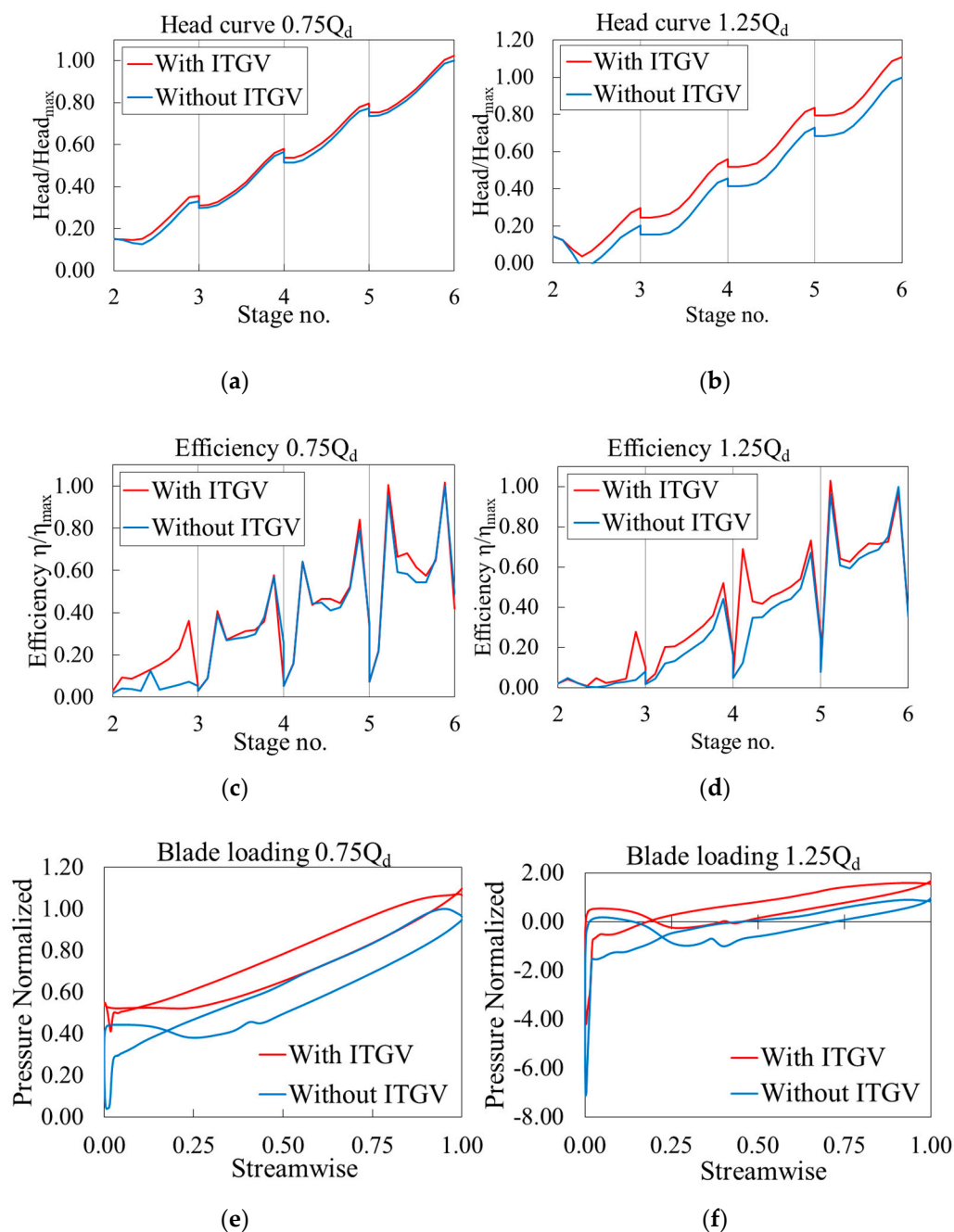


Figure 13. Head and efficiency trend graphs (a–d) and second stage blade loading chart (e,f) comparison at the mid-span of the impellers at off-design conditions for the pump with and without ITGV.

The efficiency trend graph measured at the mid-span of the impellers at both flow rates is compared for the two pumps in Figure 13c,d. A notable improvement in efficiency is found at the second stage of $0.75Q_d$ for the ITGV pump while there is only a slight improvement at other stages. Meanwhile, there is no significant improvement in efficiency at the leading edge of the second stage impeller at $1.25Q_d$ for the pump with ITGV, but it rises near the trailing edge. The rise in efficiency continues for stages 3–5. The ITGV installation improved the overall efficiency of the stages by a weighted average of 13.7% and 18.45% at $0.75Q_d$ and $1.25Q_d$, respectively. This also proves that correcting the losses at the second stage improves the performance at other downstream stages too. This can be analyzed by plotting the blade loading curve at the mid-span of the second stage impeller along the streamwise direction as shown in Figure 13e,f. The blade loading distribution was improved by a weighted average of 24.9% and 37.6% at $0.75Q_d$ and $1.25Q_d$, respectively,

for the pump with ITGV. Even though the pressure-drop at the leading edge of the impeller decreased by 41% at the high flow rate of the ITGV pump, the pressure is still low enough to cause cavitation damage in the long run. A detailed cavitation analysis may be necessary to find the cavitation zones in the off-design points.

The vortex core region formed near the second stage impeller has practically disappeared with the installation of ITGV at the $0.75Q_d$ flow condition as shown in Figure 14a,b. Several large and small vortices are observed at the high flow rate condition near the impeller inlet (Figure 14c). The large vortices are formed due to huge flow separation at the leading edge which increases with the flow rate. The ITGV pump has diminished the large vortices formed at the blade suction side and decreased the intensity of the vortices formed at the pressure side of the impeller (Figure 14d). Further suppression of the vortices may be achieved after a design optimization strategy applied to optimize the ITGV and impeller shapes with an objective function to minimize leakage vortices and improve the pump performance at this particular flow condition.

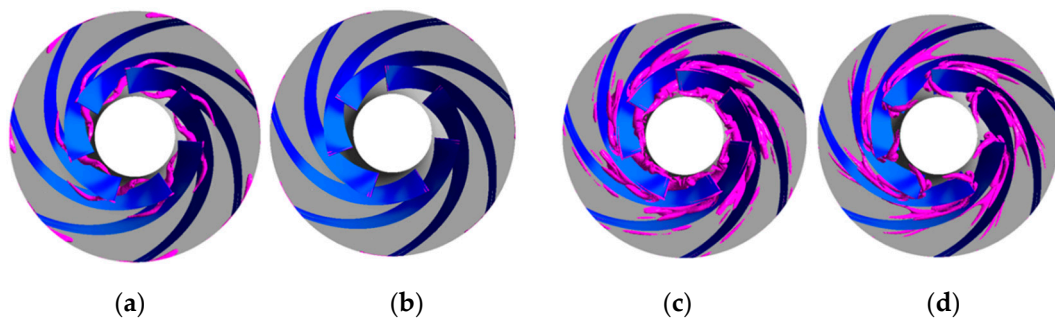


Figure 14. Vortex core region inside the second stage impeller (velocity swirling strength = 1500 s^{-1}) calculated at (a) $0.75Q_d$ without ITGV (b) $0.75Q_d$ with ITGV (c) $1.25Q_d$ without ITGV, and (d) $1.25Q_d$ with ITGV

The installation of ITGV has aided in improving the pump efficiency and head at various flow rates. The losses associated with the twin-volute and the second stage blades have been successfully diminished by placing the ITGV between them. However, the ITGV installation comes with certain restrictions. Firstly, the ITGV installation expanded the pump size by $0.27D$. This may come as a drawback at locations with size restrictions for a multistage centrifugal pump. Secondly, manufacturing the ITGV unit requires precision machining tools and skilled operators which may induce additional cost to the pump manufacturer. This is determined in the economic analysis and feasibility study of the pump in the manufacturing stage.

7. Conclusions

Installation of an inducer-type guide vane at the inter-stage flow passage of a multistage centrifugal pump is studied for its loss mitigating capability and performance enhancement. The CFD model consisted of an inlet passage that contains a double-suction impeller and a twin volute in the first stage. Series of impeller, diffuser, and return vanes were installed for the rest of the stages with an outlet volute at the end of the fifth stage. The grids generated are tested for grid independency and they satisfy the GCI criteria. The pump performance was analyzed analytically and compared with the CFD results for initial validation. The design was tested for loss analysis at individual stages. Very large losses were observed at the inlet of the second stage impeller due to the large circumferential velocity of the fluid exiting the twin volute. A stationary ITGV was installed between the twin volute and the second stage impeller to regulate the pre-swirl and correct the incoming flow angle at the blade inlet. The beta angle at the ITGV trailing edge was designed to match the beta angle at the leading edge of the impeller such that the relative flow angle is tangential to the blade incidence angle. The effects of the ITGV compared to the initial pump model are:

1. The overall efficiency of the ITGV pump was improved by 3.94% while the head rose by 5.78% at the design point. The pump power consumption was 1.78% higher than the reference pump but the overall increase in performance has offset the rise in power.
2. The stage efficiency at the second stage increased by a huge margin of 47.17% while the stage head developed by 63.28% at the design point. Similar growth was observed at other flow rates as well.
3. The pressure loss at the second stage impeller was identified by plotting the blade loading diagram along the mid-span of the impeller. The pressure drop declined sharply at the leading edge by 66.13% with an overall weighted average increase of pressure by 35.6%. The effect on the second stage also reflected in the subsequent stages, too.
4. Plotting the efficiency and head trend graph along the mid-span of the impellers provided a clear picture of the ITGV effect on individual stages. The overall weighted average increase of the head trend graph was 17.87% while that of the efficiency trend graph was 14.48%.
5. A detailed flow field analysis at the volute-impeller interface aided in understanding the change in flow phenomenon with the ITGV installation. The circumferential velocity reduced by 21.65% while the absolute flow velocity decreased by 22.46%. Thus, the blade velocity triangle was corrected to meet the expectation.
6. The pump performance improvement at the off-design points also proved to be effective with the ITGV pump. The head and efficiency improved by 3.58% and 13.7% at the low flow rate while it was improved by 17.87% and 18.45% at the high flow rate condition. The head development resulted in an overall increase of the impeller blade loading by 24.9% and 27.6% at the $0.75Q_d$ and $1.25 Q_d$, respectively.

The ITGV was successful not only in decreasing the circumferential velocity of the fluid but also improved the overall performance of the pump by diminishing the losses occurring at the second stage. The ITGV pump would be tested experimentally to validate the CFD results and is ongoing research. The effect of ITGV on pump cavitation and the optimization of the ITGV blade design is the future work of this study. The optimized design would be tested again in the laboratory before commercialization.

Author Contributions: Conceptualization: J.-H.K., S.-B.M. and M.M.S.; methodology: S.-B.M. and M.M.S.; software: M.M.S.; validation: J.-H.Y. and M.M.S.; formal analysis: M.M.S.; investigation: S.K., S.-B.M. and M.M.S.; resources: J.-H.Y., K.-H.L. and C.J.; data curation: M.M.S. and S.-B.M.; writing—original draft preparation: M.M.S.; writing—review and editing: S.-B.M. and M.M.S.; visualization: M.M.S.; supervision: J.-H.K.; project administration: K.-H.L.; funding acquisition: J.-H.K. and K.-H.L. All authors have read and agreed to the published version of the manuscript.

Funding: This research was supported by grants (no. EE200001) and (no. JB210001) of the Korea Institute of Industrial Technology (KITECH).

Institutional Review Board Statement: Not Applicable.

Informed Consent Statement: Not Applicable.

Conflicts of Interest: The authors declare no conflict of interest.

References





1. Goman, V.; Oshurbekov, S.; Kazakbaev, V.; Prakht, V.; Dmitrievskii, V. Energy Efficiency Analysis of Fixed-Speed Pump Drives with Various Types of Motors. *Appl. Sci.* **2019**, *9*, 5295. [[CrossRef](#)]
2. Shankar, A.; Kalaiselvan, V.; Umashankar, S.; Paramasivam, S.; Hanigovszki, N. A comprehensive review on energy efficiency enhancement initiatives in centrifugal pumping system. *Appl. Energy* **2016**, *181*, 495–513. [[CrossRef](#)]
3. Osman, K.M.; Wang, W.; Yuan, J.; Zhao, J.; Wang, Y.; Liu, J. Flow loss analysis of a two-stage axially split centrifugal pump with double inlet under different channel designs. *Proc. Inst. Mech. Eng. Part C* **2019**, *233*, 5316–5328. [[CrossRef](#)]
4. Shamsuddeen, M.M.; Ma, S.-B.; Kim, S.; Yoon, J.-H.; Kim, T.-H.; Lee, K.-H.; Jung, C.; Kim, J.-H. Design Feasibility Study of a Multistage Centrifugal Pump for Chemical Processing Application. In Proceedings of the Korea Society for Fluid Machinery Winter Conference, Venezia Hotel, Yeosu, Korea, 25–27 November 2020; p. 7475.

5. Shamsuddeen, M.M.; Ma, S.-B.; Kim, S.; Yoon, J.-H.; Lee, K.-H.; Jung, C.; Kim, J.-H. Flow Field Analysis and Feasibility Study of a Multistage Centrifugal Pump Designed for Low-Viscous Fluids. *Appl. Sci.* **2021**, *11*, 1314. [[CrossRef](#)]
6. Liu, M.; Tan, L.; Cao, S. A review of prewhirl regulation by inlet guide vanes for compressor and pump. *Proc. Inst. Mech. Eng. Part A J. Power Energy* **2019**, *233*, 803–817. [[CrossRef](#)]
7. Tan, L.; Zhu, B.; Cao, S.; Wang, Y.; Wang, B. Influence of Prewirl Regulation by Inlet Guide Vanes on Cavitation Performance of a Centrifugal Pump. *Energies* **2014**, *7*, 1050–1065. [[CrossRef](#)]
8. Yuchuan, W.; Lei, T.; Baoshan, Z.; ShuLiang, C.; Binbin, W. Numerical investigation of influence of inlet guide vanes on unsteady flow in a centrifugal pump. *Proc. Inst. Mech. Eng. Part C J. Mech. Eng. Sci.* **2015**, *229*, 3405–3416. [[CrossRef](#)]
9. Qu, W.; Tan, L.; Cao, S.; Wang, Y.; Xu, Y. Numerical investigation of clogging effect on a centrifugal pump with inlet guide vanes. *Eng. Comput.* **2016**, *33*, 465–481. [[CrossRef](#)]
10. Liu, M.; Tan, L.; Liu, Y.; Xu, Y.; Cao, S. Controllable velocity moment and prediction model for inlet guide vanes of a centrifugal pump. *Eng. Comput.* **2018**, *35*, 1364–1382. [[CrossRef](#)]
11. Liu, M.; Tan, L.; Cao, S. Influence of Geometry of Inlet Guide Vanes on Pressure Fluctuations of a Centrifugal Pump. *J. Fluids Eng.* **2018**, *140*, 091204. [[CrossRef](#)]
12. Liu, Y.; Tan, L.; Liu, M.; Hao, Y.; Xu, Y. Influence of Prewirl Angle and Axial Distance on Energy Performance and Pressure Fluctuation for a Centrifugal Pump with Inlet Guide Vanes. *Energies* **2017**, *10*, 695. [[CrossRef](#)]
13. Lin, P.; Li, Y.; Xu, W.; Chen, H.; Zhu, Z. Numerical Study on the Influence of Inlet Guide Vanes on the Internal Flow Characteristics of Centrifugal Pump. *Processes* **2020**, *8*, 122. [[CrossRef](#)]
14. Zhang, Y.; Hou, H.; Li, Z.; Zhang, Y. A CFD study of IGV vane number on hydraulic characteristics and pressure pulsation of a centrifugal pump. *J. Vibroengineering* **2017**, *19*, 563–576. [[CrossRef](#)]
15. Li, Y.-J.; Wang, F.-J. Numerical Investigation of Performance of an Axial-Flow Pump with Inducer. *J. Hydrodyn.* **2007**, *19*, 705–711. [[CrossRef](#)]
16. Campos-Amezcuca, R.; Khelladi, S.; Mazur-Czerwiec, Z.; Bakir, F.; Campos-Amezcuca, A.; Rey, R. Numerical and experimental study of cavitating flow through an axial inducer considering tip clearance. *Proc. Inst. Mech. Eng. Part A J. Power Energy* **2013**, *227*, 858–868. [[CrossRef](#)]
17. Yang, B.; Li, B.; Chen, H.; Liu, Z. Entropy production analysis for the clogging effect between inducer and impeller in a high-speed centrifugal pump. *Proc. Inst. Mech. Eng. Part C J. Mech. Eng. Sci.* **2019**, *233*, 5302–5315. [[CrossRef](#)]
18. Guo, X.-M.; Zhu, Z.-C.; Shi, G.-P.; Huang, Y. Effects of rotational speeds on the performance of a centrifugal pump with a variable-pitch inducer. *J. Hydrodyn.* **2017**, *29*, 854–862. [[CrossRef](#)]
19. Karakas, E.S.; Watanabe, H.; Aureli, M.; Evrensel, C.A. Cavitation Performance of Constant and Variable Pitch Helical Inducers for Centrifugal Pumps: Effect of Inducer Tip Clearance. *J. Fluids Eng.* **2019**, *142*, 021211. [[CrossRef](#)]
20. Cheng, X.; Zhang, A. Effect of axial matching between inducer and centrifugal pump suction chamber on cavitation performance. *Proc. Inst. Mech. Eng. Part A J. Power Energy* **2019**, *234*, 947–956. [[CrossRef](#)]
21. Dong, W.; Zhang, H.; Chen, D. Numerical analysis of the flow mechanism and axial force characteristics of the cavity in a centrifugal pump with a front inducer. *J. Vibroengineering* **2020**, *22*, 1210–1227. [[CrossRef](#)]
22. Jiang, J.; Li, Y.-H.; Pei, C.-Y.; Li, L.-L.; Fu, Y.; Cheng, H.-G.; Sun, Q.-Q. Cavitation performance of high-speed centrifugal pump with annular jet and inducer at different temperatures and void fractions. *J. Hydrodyn.* **2019**, *31*, 93–101. [[CrossRef](#)]
23. Sedlár, M.; Zima, P.; Bajorek, M.; Krátký, T. CFD analysis of unsteady cavitation phenomena in multistage pump with inducer. In Proceedings of the IOP Conference Series: Earth and Environmental Science, 15(PART 6), 26th IAHR Symposium on Hydraulic Machinery and Systems, Beijing, China, 19–23 August 2012. [[CrossRef](#)]
24. *API 610-Centrifugal Pumps for Petroleum, Heavy Duty Chemical, and Gas. Industry Services*, 8th ed.; American Petroleum Institute: Washington, DC, USA, 2003.
25. Nourbakhsh, A.; Jaumotte, A.; Hirsch, C.; Parizi, H.B. Affinity laws. In *Turbopumps and Pumping Systems*; Springer: Berlin/Heidelberg, Germany, 2008; p. 35. [[CrossRef](#)]
26. Suh, J.-W.; Kim, J.-W.; Choi, Y.-S.; Kim, J.-H.; Joo, W.-G.; Lee, K.-Y. Multi objective optimization of the hydrodynamic performance of the second stage of a multi-phase pump. *Energies* **2017**, *10*, 1334. [[CrossRef](#)]
27. Suh, J.-W.; Kim, J.-W.; Choi, Y.-S.; Kim, J.-H.; Joo, W.-G.; Lee, K.-Y. Development of numerical Eulerian-Eulerian models for simulating multiphase pumps. *J. Pet. Sci. Eng.* **2018**, *162*, 588–601. [[CrossRef](#)]
28. Suh, J.-W.; Kim, J.-H.; Choi, Y.-S.; Joo, W.-G.; Lee, K.-Y. A study on numerical optimization and performance verification of multiphase pump for offshore plant. *Proc. Inst. Mech. Eng. Part A J. Power Energy* **2017**, *231*, 382–397. [[CrossRef](#)]
29. ANSYS. *ANSYS TurboSystem User's Guide, ANSYS BladeModeler; Software Handbook*; ANSYS: Fort Cannon, PA, USA, 2013.
30. Siddique, M.H.; Bellary, S.A.I.; Samad, A.; Kim, J.-H.; Choi, Y.-S. Experimental and Numerical Investigation of the Performance of a Centrifugal Pump When Pumping Water and Light Crude Oil. *Arab. J. Sci. Eng.* **2017**, *42*, 4605–4615. [[CrossRef](#)]
31. Shamsuddeen, M.M.; Cha, D.-A.; Kim, S.-C.; Kim, J.-H. Effects of decompression condition and temperature on drying rate in a hybrid heat pump decompression type dryer used for seafood drying. *Dry. Technol.* **2020**, 1–15. [[CrossRef](#)]
32. Wilcox, D.C. *Turbulence Modeling for CFD*, 2nd ed.; DCW Industries Inc., Palm Drive: La Canada, CA, USA, 1994.
33. Kim, J.-H.; Cho, B.-M.; Kim, S.; Lee, Y.-K.; Choi, Y.-S. Steady and unsteady flow characteristics of a multi-stage centrifugal pump under design and off-design conditions. *Int. J. Fluid Mach. Syst.* **2019**, *12*, 64–70. [[CrossRef](#)]

34. Kim, J.-H.; Cho, B.-M.; Kim, S.; Lee, Y.-K.; Choi, Y.-S. Detailed flow characteristic analysis of a three-stage centrifugal pump at design and off-design conditions. In *IOP Conference Series: Earth and Environmental Science, Proceedings of the 29th IAHR Symposium on Hydraulic Machinery and Systems, Kyoto, Japan, 16–21 September 2018*; IPO Publishing: Bristol, UK, 2019; Volume 240. [[CrossRef](#)]
35. ANSYS. Domain Interfaces. In *ANSYS CFX-Pre User's Guide*; Release 14.0; ANSYS, Inc.: Pennsylvania, PA, USA, 2011; pp. 146–147.
36. Celik, I.B.; Ghia, U.; Roache, P.J.; Freitas, C.J.; Coleman, H.; Raad, P.E. Procedure for Estimation and Reporting of Uncertainty Due to Discretization in CFD Applications. *J. Fluids Eng.* **2008**, *130*, 078001. [[CrossRef](#)]

Article

Testing the Accuracy of the Cell-Set Model Applied on Vane-Type Sub-Boundary Layer Vortex Generators

Koldo Portal-Porras ¹, Unai Fernandez-Gamiz ^{1,*}, Iñigo Aramendia ¹, Daniel Teso-Fz-Betoño ²
and Ekaitz Zulueta ²

- ¹ Nuclear Engineering and Fluid Mechanics Department, University of the Basque Country, Nieves Cano 12, Vitoria-Gasteiz, 01006 Araba, Spain; koldo.portal@ehu.eus (K.P.-P.); inigo.aramendia@ehu.eus (I.A.)
² Automatic Control and System Engineering Department, University of the Basque Country, Nieves Cano 12, Vitoria-Gasteiz, 01006 Araba, Spain; daniel.teso@ehu.eus (D.T.-F.-B.); ekaitz.zulueta@ehu.eus (E.Z.)
* Correspondence: unai.fernandez@ehu.eus; Tel.: +34-945-014-066

Abstract: Vortex Generators (VGs) are applied before the expected region of separation of the boundary layer in order to delay or remove the flow separation. Although their height is usually similar to that of the boundary layer, in some applications, lower VGs are used, Sub-Boundary Layer Vortex Generators (SBVGs), since this reduces the drag coefficient. Numerical simulations of sub-boundary layer vane-type vortex generators on a flat plate in a negligible pressure gradient flow were conducted using the fully resolved mesh model and the cell-set model, with the aim on assessing the accuracy of the cell-set model with Reynolds-Averaged Navier-Stokes (RANS) and Large Eddy Simulation (LES) turbulence modelling techniques. The implementation of the cell-set model has supposed savings of the 40% in terms of computational time. The vortexes generated on the wake behind the VG; vortical structure of the primary vortex; and its path, size, strength, and produced wall shear stress have been studied. The results show good agreements between meshing models in the higher VGs, but slight discrepancies on the lower ones. These disparities are more pronounced with LES. Further study of the cell-set model is proposed, since its implementation entails great computational time and resources savings.

Keywords: vortex generator (VG); computational fluid dynamics (CFD); cell-set model; RANS; LES



Citation: Portal-Porras, K.; Fernandez-Gamiz, U.; Aramendia, I.; Teso-Fz-Betoño, D.; Zulueta, E. Testing the Accuracy of the Cell-Set Model Applied on Vane-Type Sub-Boundary Layer Vortex Generators. *Processes* **2021**, *9*, 503. <https://doi.org/10.3390/pr9030503>

Academic Editor: Jin-Hyuk Kim

Received: 15 February 2021

Accepted: 9 March 2021

Published: 11 March 2021

Publisher's Note: MDPI stays neutral with regard to jurisdictional claims in published maps and institutional affiliations.



Copyright: © 2021 by the authors. Licensee MDPI, Basel, Switzerland. This article is an open access article distributed under the terms and conditions of the Creative Commons Attribution (CC BY) license (<https://creativecommons.org/licenses/by/4.0/>).

1. Introduction

Vortex Generators (VGs) are passive flow control devices, whose objective is to delay or remove the flow separation, transferring the energy generated from the outer region to the boundary layer region. They are small vanes placed before the expected region of separation of the boundary layer. They are usually mounted in pairs, with an incident angle with the oncoming flow. Regarding their shape, VGs can be of various geometries, but they are mainly triangular or rectangular. Their height is typically similar to the boundary layer thickness where the VG is applied, in order to ensure a good interaction between the boundary layer and the vortex generated in the VG. However, since tall VGs lead to high drag forces, VGs with smaller heights than the local boundary thickness, i.e., Sub-Boundary-Layer Vortex Generators (SBVGs), are used in many applications, see Ashill et al. [1,2]. Aramendia et al. [3,4] comprehensively reviewed the available flow control devices, including VGs, and Lin [5] conducted an in-depth review of the control of flow separation in the boundary layer using SBVGs.

Since their introduction by Taylor [6] in the late 1940s, VGs have been used in a wide range of industries for numerous applications. Among these industries, aerodynamics and thermodynamics are the most remarkable. Øye [7] and Miller [8] implemented VGs on 1 MW and 2.5 MW wind turbines, respectively. Heyes and Smith [9] added VGs of numerous shapes on the wing tip of an aircraft, and Tai [10] studied the effect of Micro-

Vortex Generators (MVGs) on V-22 aircraft. All of them showed a significant aerodynamic performance improvement when implementing VGs.

Another sector in which VGs are widely used is thermodynamics. Currently, major efforts are being made in the thermodynamics field to increase heat and mass transfer, see Agnew et al. [11]. For this reason, numerous authors have implemented in different thermodynamic systems. For example, Joardar and Jacobi [12] studied the heat transfer and pressure drop of a heat exchanger before and after the addition of VGs, showing an increase of the heat transfer coefficient between 16.5% and 44% with a single VG pair and between 30% and 68.8% with 3 VG pairs.

Although many studies use experimental techniques, the use of Computational Fluid Dynamics (CFD) tools for performing numerical studies is becoming a very popular choice for studying VGs. CFD studies of VGs are currently focused on two main goals. The first goal is to optimize the position and distribution of VGs, see the studies of Subbiah et al. [13] and Yu et al. [14]. The second goal is to analyze the swirling vortexes generated on the wake behind the VG, see the studies of Carapau and Janela [15] and Sheng et al. [16] about this phenomenon.

Many authors have studied SBVGs using CFD. Ibarra-Udaeta et al. [17] and Martinez-Filgueira et al. [18] analyzed the vortices generated by rectangular vane-type SBVGs on a flat plate under negligible pressure gradient flow conditions. They analyzed VGs with heights equal to 0.2, 0.4, 0.6, 0.8, 1, and 1.2 δ and incident angles equal to 10°, 15°, 18°, and 20°. Fernandez-Gamiz et al. [19] studied three different SBVGs with heights of 0.21, 0.25, and 0.31 δ and an incident angle equal to 18°. Gutierrez-Amo et al. [20] analyzed a rectangular, a triangular, and a symmetrical NACA0012 SBVG. Fully resolved mesh modelling technique was used in all the mentioned studies, and all of them showed good agreements with experimental data.

The main disadvantage of the fully resolved mesh model is the fine mesh that requires to accurately capture the physical phenomena, especially in the near-VG region and in the wake behind the VG. For that reason, numerous authors [21–23] have implemented alternative models. The majority of these models are based on the BAY model developed by Bender et al. [24], which models the force produced by a VG. Errasti et al. [25] implemented the jBAY source-term model developed by Jirasek [26] in vane-type SBVGs under adverse pressure flow conditions and showed accurate results in terms of vortex path, vortex decay, and vortex size.

The cell-set model is another alternative model, which consists of leveraging the previously generated mesh to build the desired geometry. Besides the advantages that the cell-set model provides over the fully resolved mesh model, there are not many studies in which this model has been applied. Ballesteros-Coll et al. [21,27] used the cell-set model to generate Gurney flaps and microtabs on DU91W250 airfoils, and Ibarra-Udaeta et al. [28] modelled conventional vane-type VGs with this model.

The goal of the present paper is to evaluate the accuracy of the cell-set model applied on SBVGs with heights of 0.2, 0.4, 0.6, 0.8, and 1 δ . For that purpose, CFD simulations of SBVGs on a flat plate in a negligible streamwise pressure gradient flow conditions are conducted using the fully resolved mesh model and the cell-set model, and the results obtained with the fully resolved mesh model are taken as benchmark. With the purpose of testing the cell-set model with RANS and LES, both models are used to conduct the simulations.

The remainder of the manuscript is structured as follows: Section 2 provides a general description of the used numerical domain and meshing models. Section 3 explains the results obtained in the present work. Finally, Section 4 summarizes the main conclusions reached from the results and future directions.

2. Numerical Setup

CFD simulations of sub-boundary layer vane-type VGs on a flat plate in a negligible streamwise pressure gradient flow were conducted with the intention of investigating the

accuracy cell-set model. Star CCM+v14.02.012 [29] CFD commercial code was used to conduct all the simulations.

2.1. Computational Domain and Physic Models

The computational domain consists of a block with a rectangular VG situated on its lower surface. The flow goes from the upstream part of the block to its downstream part; hence, they are set as inlet and outlet, respectively. The bottom surface of the block and the faces of the VG are set as no-slip walls, and symmetry plane conditions are assigned to the rest of the surfaces, ensuring that the flow is not affected by their presence. The computational domain has been designed to ensure that the boundary layer thickness (δ) at the location of the VG is equal to 0.25 m.

Regarding the fluid, an incompressible turbulent flow is considered, in a steady-state with RANS and in an unsteady-state with LES. According to expression (1), the Reynolds number (Re) of this flow is around 27,000.

$$Re = \frac{U_{\infty} \cdot \delta}{\nu}, \quad (1)$$

where ν refers to the kinematic viscosity and U_{∞} to the free stream velocity of the flow, which is set at 20 m/s for this study.

As the objective of this paper is to analyze the cell-set model on SBVGs, 10 different SBVGs are considered. Five different VG heights (H), 0.2, 0.4, 0.6, 0.8, and 1 δ , and two different incident (α) angles, 18° and 25°, are considered. The length (L) of the VG is equal to 2 δ for every case. More information about the VGs and the computational domain is shown in Table 1 and Figure 1.

Table 1. Vortex Generator (VG) dimensions.

VG Height (H)	Vane Height to Boundary Layer Thickness (H/ δ)	VG Length (L)	Aspect Ratio
0.05 m	0.2	0.50 m	10
0.10 m	0.4	0.50 m	5
0.15 m	0.6	0.50 m	3.33
0.20 m	0.8	0.50 m	2.5
0.25 m	1	0.50 m	2

For the simulations in which α is equal to 18°, Menter's k- ω SST (Shear Stress Transport) [30]. RANS-based turbulence model is selected. This model has been selected since, as demonstrated by Allan et al. [31], SST models provide more accurate vortex trajectory and streamwise peak vorticity predictions than other RANS models. In contrast, Urkiola et al. [32] showed that when working with high incident angles, RANS-based models are not able to capture flow characteristics as accurately as when working with low incident angles. Hence, for the simulations in which the incident angle is equal to 25°, LES Smagorinsky SGS (sub-grid-scale) [33] model is selected. Furthermore, this selection of turbulence models allows the cell-set model to be analyzed using both RANS and LES.

For data extraction, 12 spanwise planes normal to the streamwise direction located on the wake behind the VG are considered. These planes are located from 3 to 25 δ from the LE (Leading Edge), separated 2 δ between each other.

2.2. Fully Resolved Mesh Model

Five different structured meshes of around 11.5 million hexahedral cells were generated, one for each VG height. In all the cases, the normalized height of the closest cell to the wall ($\Delta z/\delta$) was set at 1.5×10^{-6} . For the generation of these meshes, the procedure described by Urkiola et al. [32] was followed. In order to obtain more accurate results in the near-VG region, these meshes are refined in this zone. The meshes were rotated to obtain the desired incident angles ($\alpha = 18^\circ$ and $\alpha = 25^\circ$). Figure 2 shows the mesh refinement around the VG for the case $H = 1 \delta$.

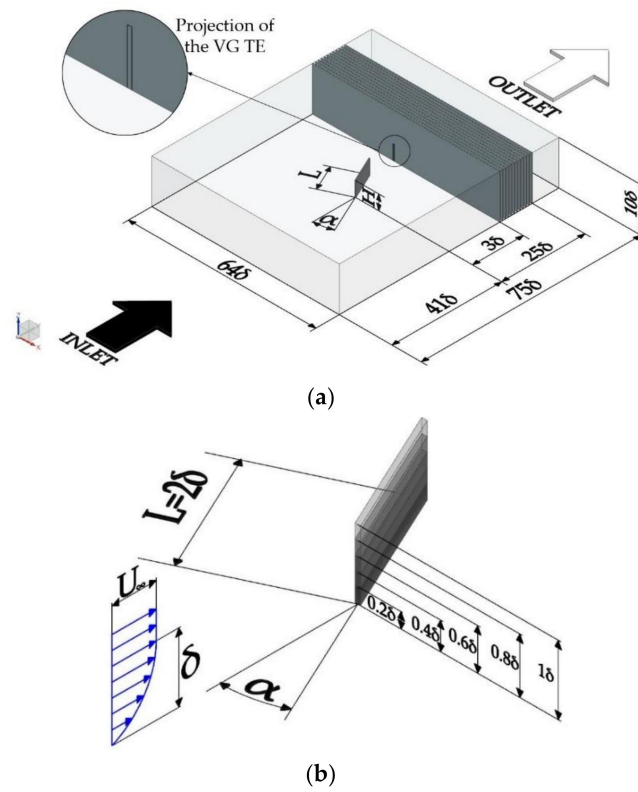


Figure 1. (a) Numerical domain (not to scale). (b) Vortex Generator (VG) parameters.

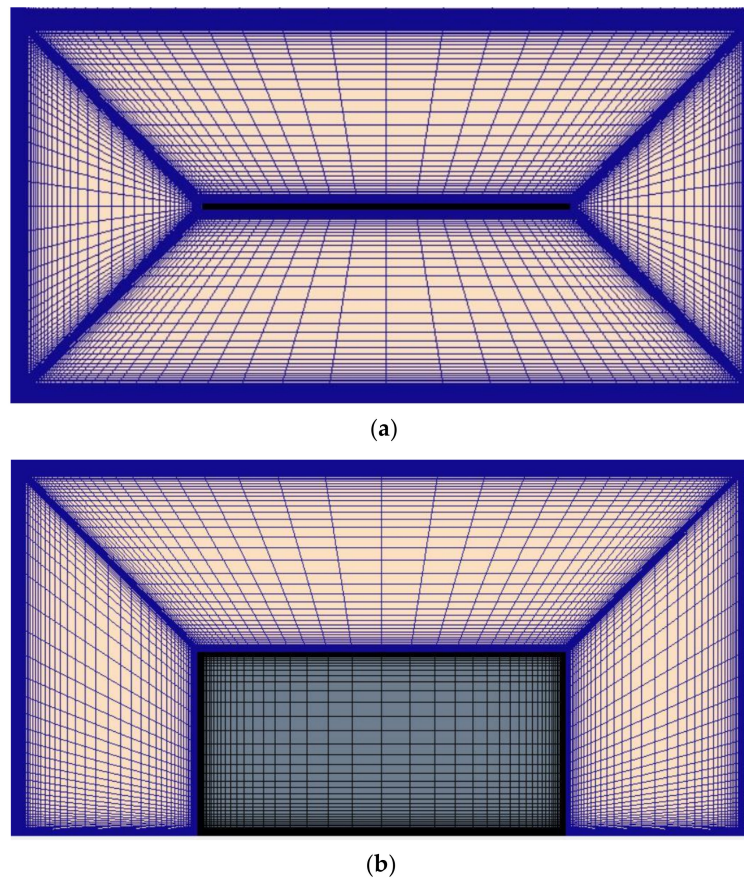


Figure 2. Refined mesh around the VG for $H = 1 \delta$. (a) Top view and (b) side view.

The skewness angle, volume change, and face validity cell quality parameters have been selected to assess the quality of the tested meshes. The skewness angle is the angle between a face normal vector of a cell and the vector connecting the centroids of this cell and the neighbor cells. The volume change is the ratio of the volume of a cell to that of its largest neighbor. The face validity is a measure of the correctness of the face normal relative to its attached cell centroid.

According to [29], the skewness angle should be as low as possible, and cells with a skewness angle greater than 85° could result in solver convergence issues, so they are considered low-quality cells. These problems appear since the diffusion term for transported scalar variables contains in its denominator the dot product between the face normal vector and the vector connecting the centroids, and therefore, skewness angles close to 90° imply very high values of this term. The volume change ratio should be close to 1, since large jump in volume from one cell to its neighbor can cause inaccuracies and instability in the solvers. Therefore, cells with volume changes below 0.01 are considered inadequate. The face validity must be equal to 1, since different values mean that the face normals do not point away from the cell centroid correctly, and values below 0.5 signify a negative volume cell. As Table 2 shows, all the meshes fulfill these criteria.

Table 2. Cell quality parameters of the used meshes with the fully resolved mesh model.

VG Height	Maximum Skewness Angle	Minimum Volume Change	Minimum Face Validity
0.2 δ	81.1°	0.029	1
0.4 δ	75.1°	0.029	1
0.6 δ	66.7°	0.029	1
0.8 δ	64.8°	0.03	1
1 δ	65.3°	0.03	1

To verify sufficient mesh resolution, two different procedures were followed, one for each turbulence model. Both mesh resolution studies were applied for the case $H = 1 \delta$. For RANS, the General Richardson Extrapolation method [34] was performed, applied to lift and drag forces of the VG. This method consists of estimating the value of the analyzed parameter when the cell quantity tends to infinite from a minimum of three meshes. For this study, a coarse mesh (0.2 million cells), a medium mesh (1.4 million cells), and a fine mesh (the previously explained mesh, 11.5 million cells) were considered. As summarized in Table 3, the convergence condition, which should be between 0 and 1 to ensure a monotonic convergence, is fulfilled, and the estimated values (RE) of the evaluated parameters are close to the ones obtained with the fine mesh. Therefore, the mesh is suitable for RANS simulations.

Table 3. Mesh verification for Reynolds-Averaged Navier-Stokes (RANS).

Variable	Mesh Resolution			Richardson Extrapolation		
	Coarse (N)	Medium (N)	Fine (N)	RE (N)	P	R
Drag force	98.0699	89.8929	87.199	85.875	1.6018	0.329
Lift force	261.605	247.715	241.39	236.1	1.135	0.455

In LES, Taylor length-scale (λ) was examined to verify sufficient mesh resolution. According to Kuczaj et al. [35], the mesh resolution ($\Delta = \sqrt[3]{V_{cell}}$) should at least be in order of λ to completely solve the Taylor length-scale. As explained in [35], Taylor length-scale calculation procedure consists of obtaining the autocorrelation function from the Taylor expansion coefficient, then, calculating the Taylor time-scale, and finally, estimating λ from the Taylor hypothesis [36]. This method has been applied on the wake behind the VG, at $y/\delta = 1$, since this area is expected to be the area where the effects of the turbulence are most noticeable, and therefore, the area where the best resolution is required. As Figure 3

shows that the criteria proposed by Kuczaj et al. [35] is fulfilled along the whole wake behind the VG, which means that the mesh is suitable for LES simulations.

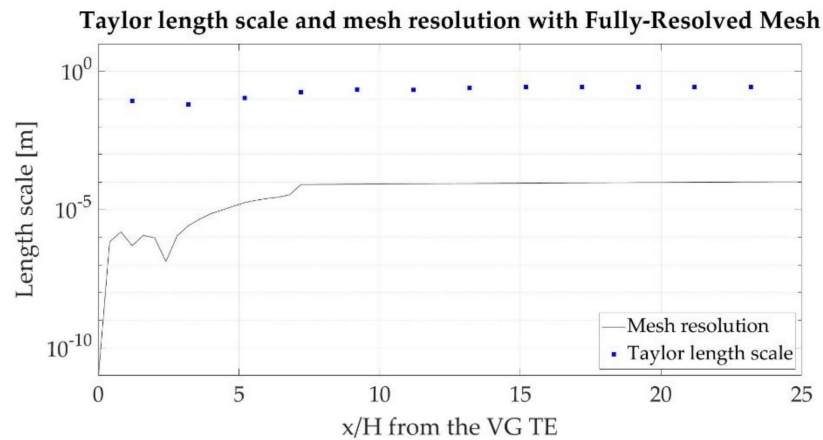


Figure 3. Mesh resolution and Taylor length scale on the wake behind the VG at $y/\delta = 1$ for the case $H = 1 \delta$ with the fully resolved mesh model.

2.3. Cell-Set Model

In the present work, the accuracy of the cell-set model applied on sub-boundary layer VGs is evaluated. This model consists of generating the desired geometry in a mesh that initially does not contain such geometry. To apply the cell-set model, the place where the geometry should be located in the mesh is indicated, as displayed in Figure 4a. Later, the cells that correspond to this geometry are selected by means of their cell ID. Finally, with the selected cells a new cell-set region is created, as shown in Figure 4b, and wall conditions are assigned to this new region.

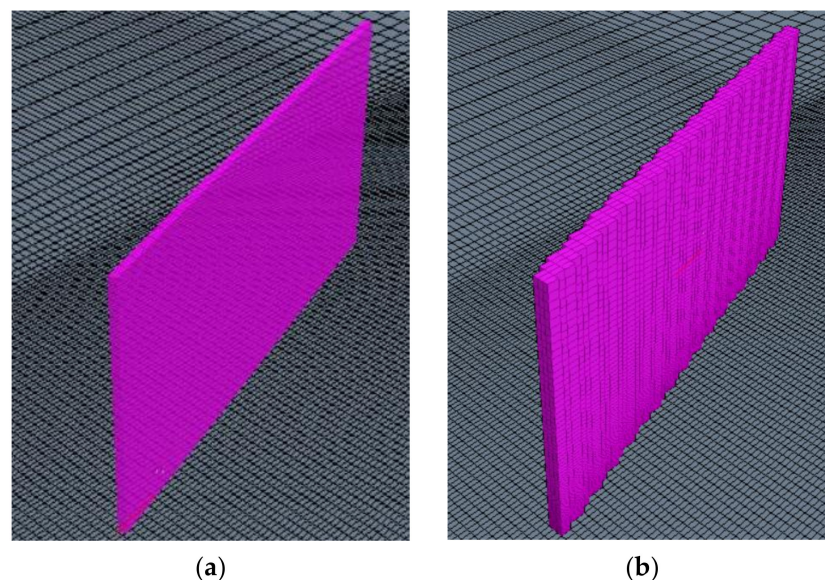


Figure 4. Sketch of the selected cells when using the cell-set model. (a) Geometry of the VG and (b) cell-set representation.

With the cell-set model, meshes of around 7.2 million cells have been generated. Thus, the meshes are coarser with this model than with the fully resolved mesh model. In addition, the mesh design and generation processes are faster with the cell-set model. As in the fully resolved mesh, $\Delta z/\delta$ is equal to 1.5×10^{-6} . Figure 5 shows the top and side views of the VG generated with the cell-set model for $H = 1 \delta$ and $\alpha = 18^\circ$.

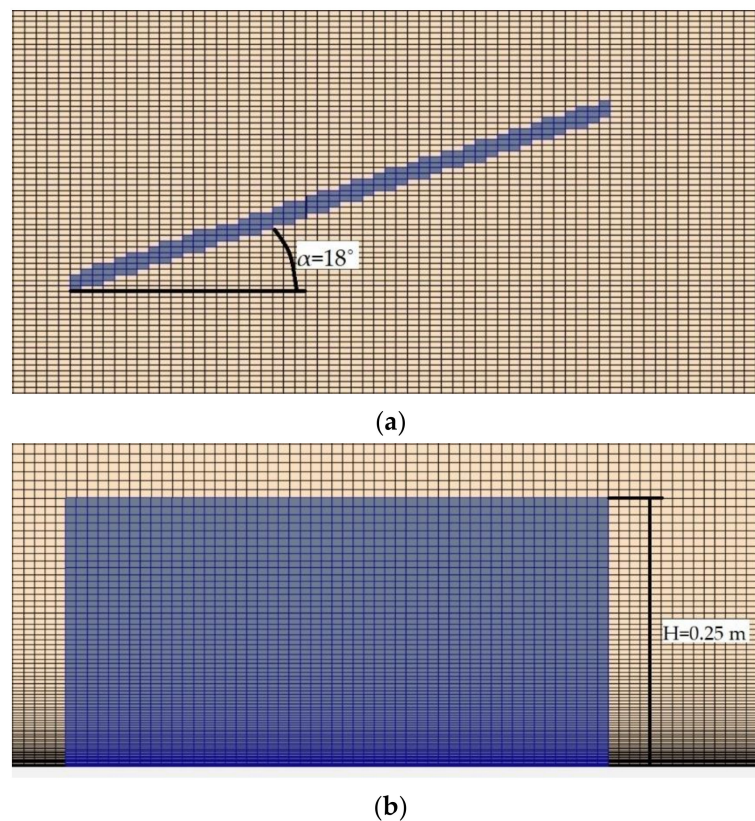


Figure 5. Cell-set construction of the VG with the cell-set model for $\alpha = 18^\circ$ and $H = 1 \delta$. (a) Top view and (b) side view.

As with the fully resolved mesh model, the quality of the meshes generated with the cell-set model has been evaluated with skewness angle, volume change and face validity parameters. As shown in Table 4, and according to the previously explained criteria, the cell quality of the meshes generated with the cell-set model is adequate.

Table 4. Cell quality parameters of the used meshes with the cell-set model.

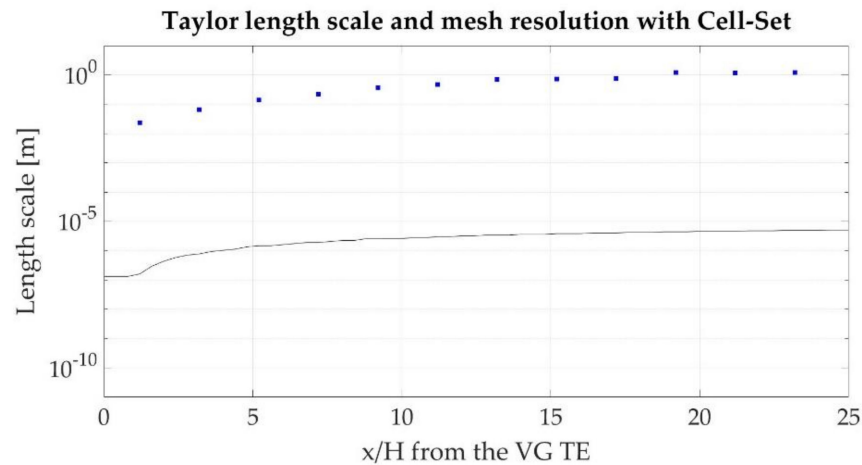
VG Height	Maximum Skewness Angle	Minimum Volume Change	Minimum Face Validity
0.2 δ	83.8°	0.365	1
0.4 δ	83.8°	0.365	1
0.6 δ	87.2°	0.359	1
0.8 δ	81.5°	0.355	1
1 δ	80.6°	0.352	1

To verify sufficient mesh resolution, as with the fully resolved mesh model, two different procedures have been followed, one for each turbulence model. In both cases, the mesh verification has been performed with the $H = 1 \delta$ case. For RANS, the General Richardson Extrapolation method has been applied. However, in this case, the three meshes are made of 7.2 million cells (fine mesh), 3.6 million cells (medium mesh), and 1.8 million cells (coarse mesh). As Table 5 shows, the results fulfill the convergence condition. Thus, the mesh generated using the cell-set model is adequate for RANS simulations.

For LES simulations, Taylor length-scale (λ) is examined to verify sufficient mesh resolution. As shown in Figure 6, the mesh satisfies the criteria proposed by Kuczaj et al. [35] on the whole wake behind the VG, and therefore, it is suitable for LES simulations.

Table 5. Mesh verification for RANS.

Variable	Mesh Resolution			Richardson Extrapolation		
	Coarse (N)	Medium (N)	Fine (N)	RE (N)	P	R
Drag force	101.632	98.1029	96.3945	94.5856	1.0466	0.484
Lift force	259.1973	252.912	248.5026	237.7241	0.0495	0.7015

**Figure 6.** Mesh resolution and Taylor length scale on the wake behind the VG at $y/\delta = 1$ for the case $H = 1 \delta$ with the cell-set model.

3. Results and Discussion

In this study, the vortices generated in the wake behind the VGs have been analyzed. Moreover, an exhaustive analysis of the primary vortex has been performed, studying its path, size, and strength and the wall shear stress behind it.

For the interpretation of RANS results, the last obtained values have been considered, whereas for the results of LES simulations, the average values of 2 s of simulation have been considered, after the flow is completely developed.

Parallel computing with 56 Intel Xeon 5420 cores and 45 GB of RAM were used to carry out all the simulations. Simulations performed with fully resolved mesh modelling were run for about 47 h using the RANS turbulence model and for around 184 h using the LES model. In contrast, simulations in which cell-set modelling was applied were run for approximately 28 h for RANS and 111 h for LES.

3.1. Vortex Structure Regimes in the Wake

As measured by Velte [37], two basic vortex mechanism appear in the wake behind the VG. The main vortex system is composed of a primary vortex (P), which is formed on the wing tip, and a horseshoe vortex, which is generated from the rollup vortex around the LE of the VG. This horseshoe vortex is divided in two sides, the pressure side (Hp) and the suction side (Hs). As the primary vortex is stronger than these sides, the primary vortex pulls the suction side. As the primary vortex and the pressure side have the same sign, the pressure side remains undisturbed.

The secondary vortex structure is created by the local separation of the boundary layer in the lateral direction between the primary vortex and the wall. Due to the dragging of the suction side by the primary vortex, the primary vortex becomes stronger, the boundary layer region grows, and finally detaches, forming a discrete vortex (D). Figure 7 shows a representation of the primary and secondary vortices.

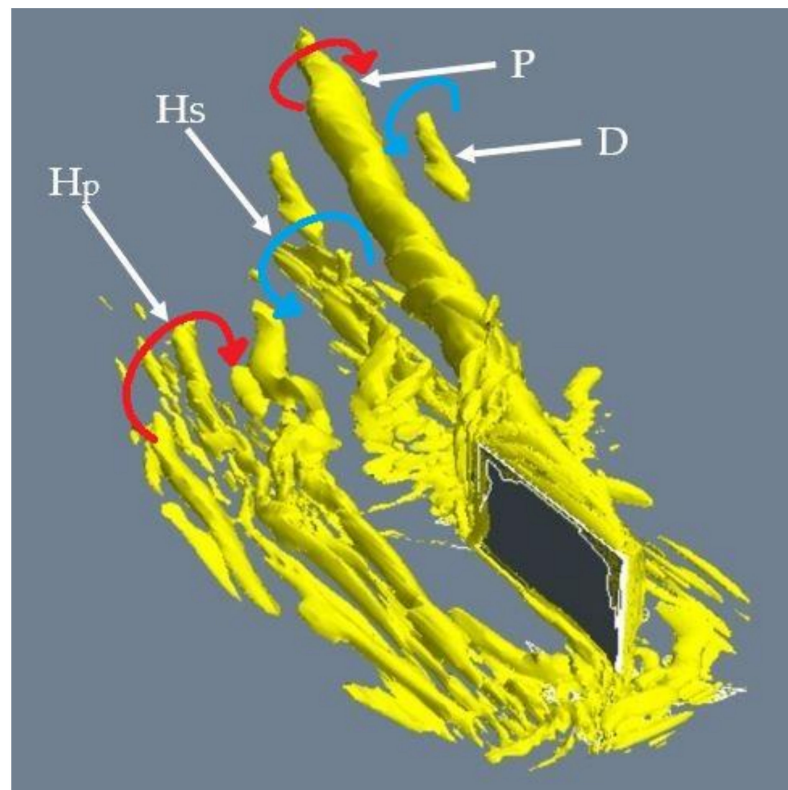


Figure 7. Vortex mechanisms in the wake behind a VG.

Nevertheless, Velte [37] showed that these structures can vary, depending on the incident angle and the height of the VG. Figure 8 displays a comparison of the vortical structures predicted by the numerical simulations with both studied models at a distance of 5δ from the VG Trailing Edge (TE), and the vortical structures measured by Velte [37].

Regarding the main vortex structure, the results show that both RANS and LES are able to accurately predict the primary vortex with the fully resolved mesh model and the cell-set model. In LES simulations, the horseshoe vortex, which is expected to appear in VGs with heights above 0.4δ , is predicted for all the heights, including 0.2δ . In contrast, RANS is not able to capture the pressure side of this horseshoe vortex for heights below 0.8δ .

The largest discrepancies between the simulations and the experimental results appear in the secondary vortex structure. This vortex structure is expected to appear in VGs whose heights are below 0.4δ . In LES, this vortex is only visible for $H = 0.2 \delta$ with the fully resolved mesh model. This vortex is not predicted in RANS for neither height.

Despite showing different values, the fully resolved mesh model and the cell-set model predict very similar vortices in terms of vortex shape and direction.

3.2. Vortical Structure of the Primary Vortex

The Q-criterion [38] method has been used to compare qualitatively the primary vortex generated by each VG in terms of shape and size. This method visualizes structures of the flow, and its value is defined by $Q = \frac{1}{2} (\|\Omega\|^2 - \|S\|^2)$, where Ω is the spin tensor and S the strain-rate tensor. As the value of Q is set at $Q = 2500 \text{ s}^{-2}$, the vortical structures are displayed. Figure 9 shows the representation of the primary vortex at 5δ from the VG TE by means of the Q-criterion.

The results show that for $\alpha = 18^\circ$, the taller the VG, the larger the vortex. However, for $\alpha = 25^\circ$, although this also occurs, the differences between heights are smaller, with the size of the vortices being more similar than when $\alpha = 18^\circ$.

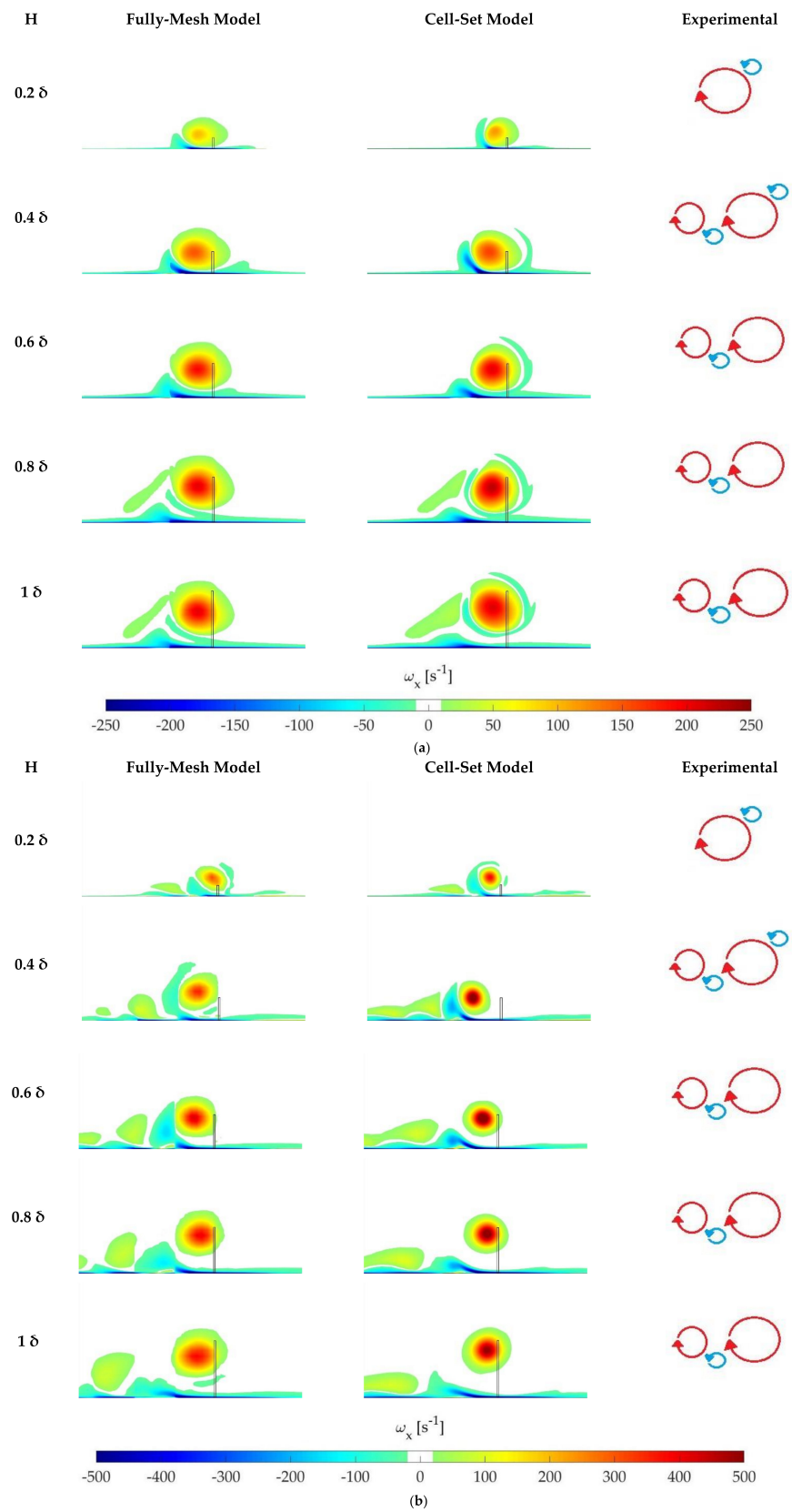


Figure 8. Vortical structures predicted on the wake behind the VG. (a) Reynolds-Averaged Navier-Stokes (RANS) ($\alpha = 18^\circ$) and (b) Large Eddy Simulation (LES) ($\alpha = 25^\circ$).

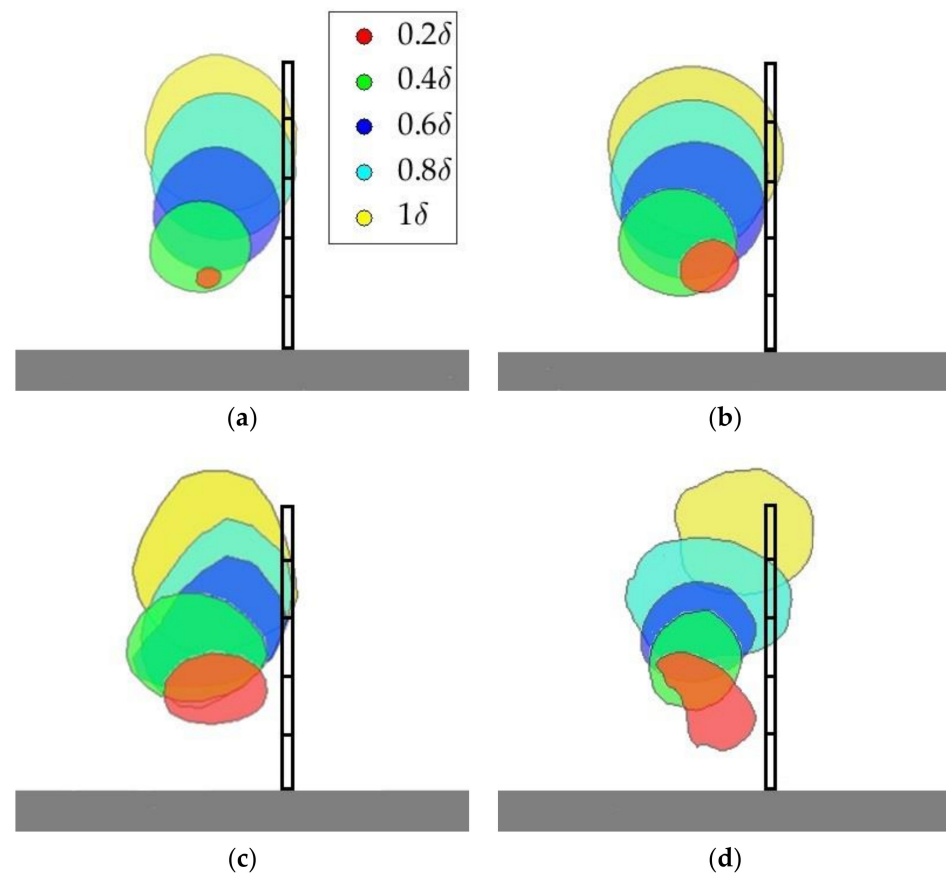


Figure 9. Primary vortex represented by the Q-criterion with a value of $Q = 2500 \text{ s}^{-2}$. The black squares are the projections of the VG Trailing Edges: (a) RANS Fully Resolved Mesh model ($\alpha = 18^\circ$), (b) RANS cell-set model ($\alpha = 18^\circ$), (c) LES fully resolved mesh model ($\alpha = 25^\circ$), and (d) LES cell-set model ($\alpha = 25^\circ$).

With RANS, even if they have the same circular shape, the vortices predicted by the cell-set model are larger than the ones predicted by the fully resolved mesh model. With LES, generally, the vortices predicted by the cell-set model are smaller than those predicted by the fully resolved mesh model. In this case, slight disparities between models are visible in terms of vortex shape, which are attributed to the unsteadiness of the flow.

3.3. Vortex Path

In order to analyze the vortex path of the primary vortex, the location of the center of this vortex is studied. According to Yao et al. [39], the vortex center is the point in where the peak vorticity appears. Figure 10 shows the vertical and lateral path of the primary vortex normalized with the height of each VG. The lateral path obtained in the present study for $\alpha = 18^\circ$ is compared to the one obtained experimentally by Bray [40].

The lateral path shows that in all the cases, the vortex tends to follow the flow direction, showing a linear trend. With both turbulence models, the lower the height of the VG, the greater the horizontal displacement. Good agreements are obtained with the experimental data reported by Bray [40]. Near the VG, the lateral displacements are nearly equal, except with $H = 0.2 \delta$ and $\alpha = 18^\circ$, but as the flow distances from the VG, the differences between cases increase, most notably with $\alpha = 25^\circ$.

Corresponding the vertical path, the results show that the vortices tend to collapse near $y/H = 1$, except for the case $H = 0.2 \delta$, in which the vortex continues its upward climb as it distances from the VG, this is more noticeable with $\alpha = 18^\circ$ than with $\alpha = 25^\circ$.

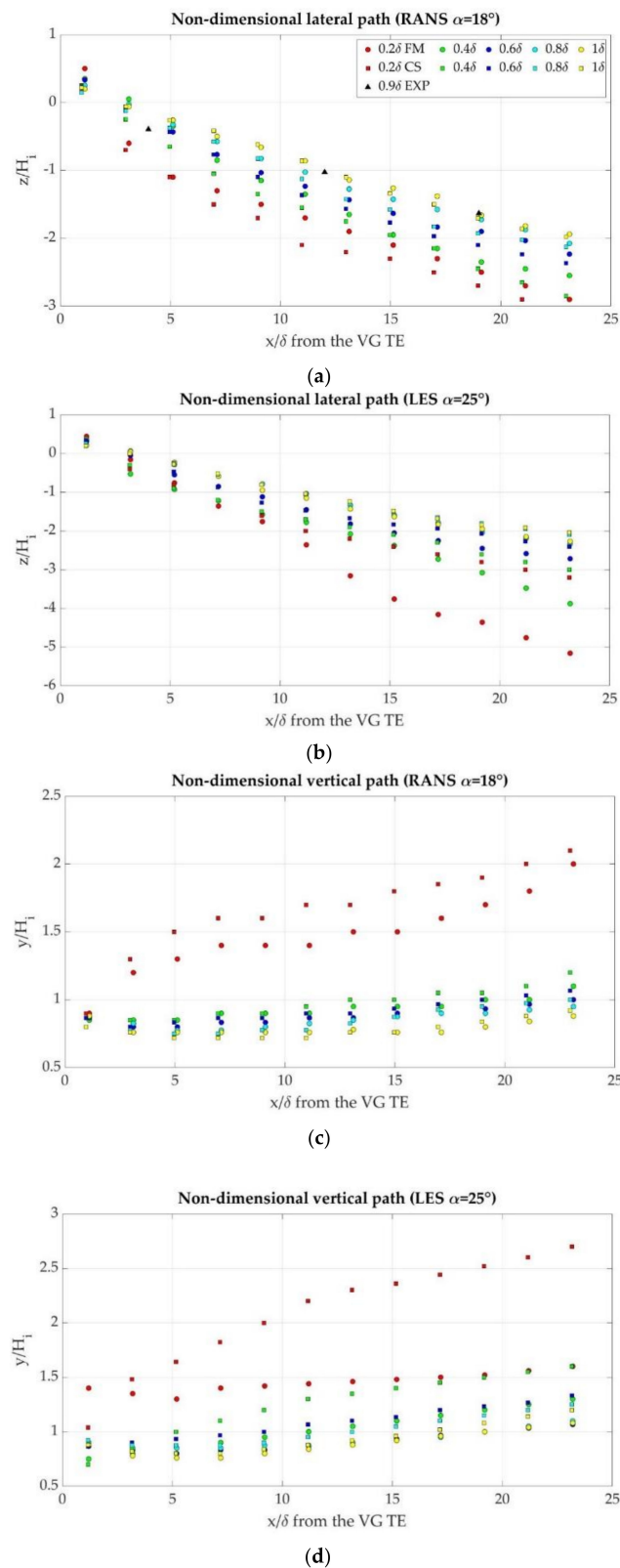


Figure 10. Non-dimensional path of the primary vortex obtained with the fully resolved mesh model (FM), the cell-set model (CS), and experimentally (EXP). (a) Non-dimensional lateral path with RANS, (b) non-dimensional lateral path with LES, (c) non-dimensional vertical path with RANS, and (d) non-dimensional vertical path with LES.

The comparison between the fully resolved mesh model and the cell-set model shows that in both cases, the same trend is followed with both models. With RANS, larger lateral displacements are obtained with the cell-set model, while with LES, the larger lateral displacements are obtained with the fully resolved mesh model. The cell-set model predicts larger vertical displacements with RANS and LES. For the highest VGs, the results are very similar with both models, but as the VG height decreases, the differences between models increase, especially with LES.

3.4. Vortex Size

The vortex size is analyzed by the Half-Life Radius (R_{05}) parameter developed by Bray [40]. This parameter determines the distance between the vortex center and the point where the local vorticity is equal to $\frac{\omega_{peak}}{2}$. As shown in Figure 9, the vortex shape is not always circular, therefore, R_{05} has been estimated by averaging the values in vertical and lateral directions. Figure 11 shows the R_{05} values normalized with δ on the wake behind the VG for the tested cases.

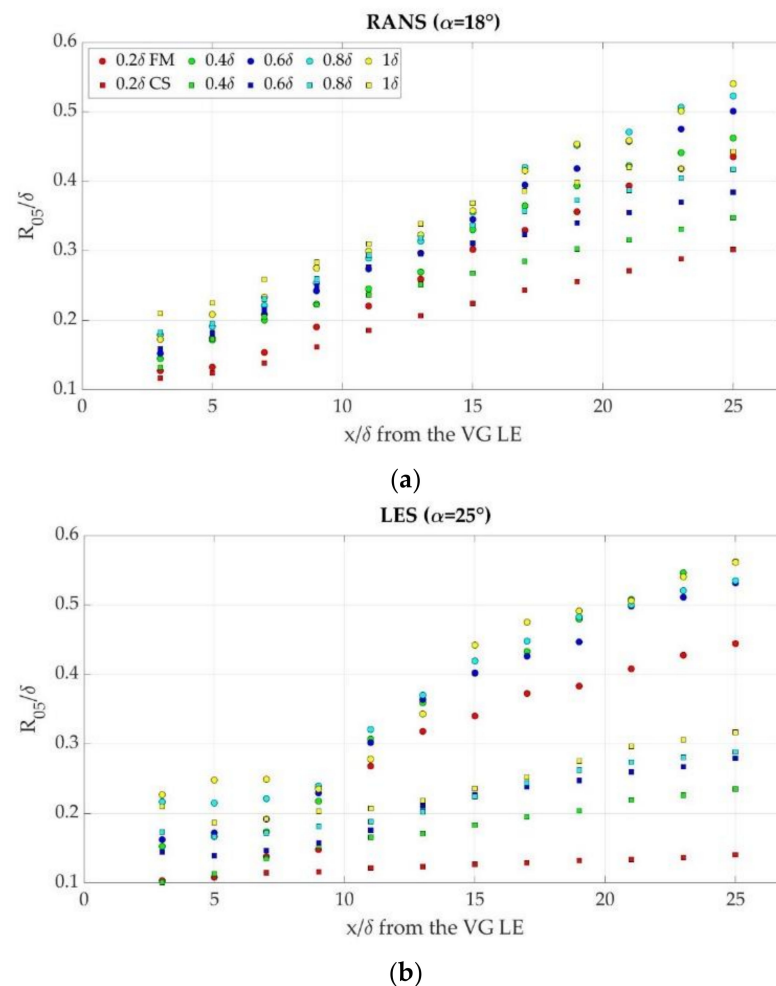


Figure 11. R_{05} normalized with δ . (a) RANS and (b) LES.

The results show that the greatest vortices appear in the taller VGs. In RANS, the R_{05} increases linearly from the near-VG region, but in LES, R_{05} remains almost constant near the VG, and it starts increasing at 10δ from the VG LE.

Despite showing the same trend, in all the cases, the cell-set model predicts smaller vortices than the fully resolved mesh model, these differences are more notable with LES. The largest discrepancies between models are visible in the lower VGs, most notably with LES.

3.5. Vortex Strength

To quantify the vortex strength, vortex circulation (Γ) is considered. This parameter determines the capacity of the vortex to mix the outer flow with the boundary layer [2]. According to Yao et al. [39], the vortex circulation can be estimated by expression (2). Figure 12 shows the vortex circulation normalized with the VG height and the flow streamwise velocity.

$$\Gamma = \frac{\omega_{peak} \times \pi \times R_{05}^2}{0.693}. \quad (2)$$

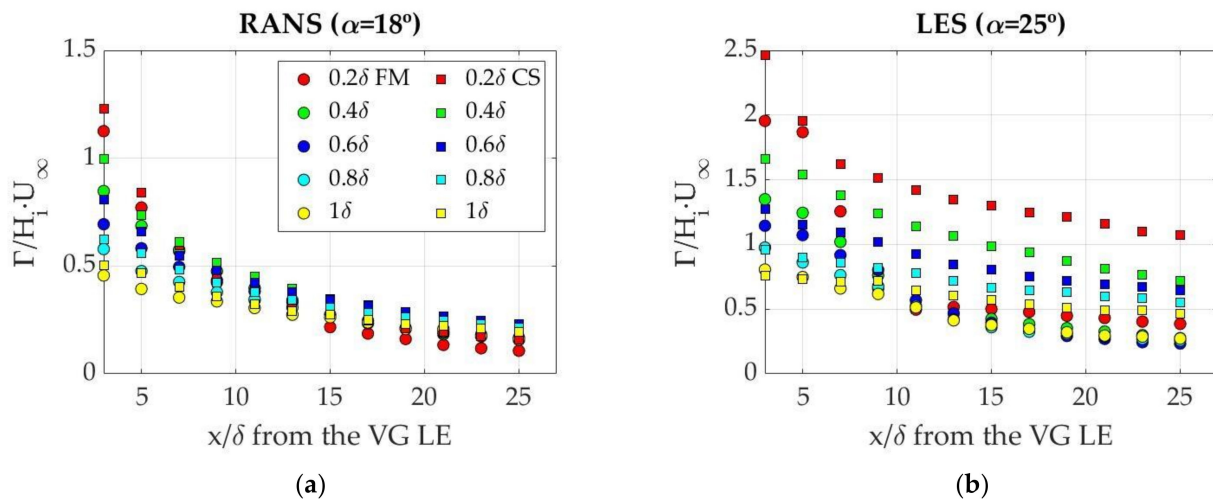


Figure 12. Vortex circulation normalized with the VG height and the flow streamwise velocity. (a) RANS and (b) LES.

As expected, the vortex loses its strength as it distances from the VG. Close to the VG, the stronger vortices appear in the lower VGs. With RANS, as the distance between the VG and the flow increases, the results tend to collide with both models. In contrast, with LES, this trend is only visible with fully resolved mesh modelling, since with the cell-set model, despite following a falling tendency, the collision of the results is not achieved. With this turbulence model, the normalized circulations are considerably higher with the cell-set model than with the fully resolved mesh model for the lower VGs, but for the higher ones, the differences decrease.

Although, as mentioned before, the R_{05} values predicted with the fully resolved mesh model are higher, vortex circulation values are very similar with the RANS model. This is attributed to the consideration of the vorticity in the expression of the circulation. With LES, despite showing less differences in Γ than in R_{05} , differences are significant for low VG cases.

3.6. Wall Shear Stress

Wall shear stress is a major parameter to quantify the capacity of the VG to delay the flow separation. Figure 13 shows the values of the wall shear stress on the wake behind the VG for all the tested cases.

In the tested cases, the wall shear stress goes from a low value to a maximum value, which appears between $x/\delta = 3$ and $x/\delta = 6$, depending on the case. The lower the VG, the closer to the VG the maximum appears. Then, as expected, wall shear stress slightly decreases as it distances from the VG.

According to Godard and Stanislas [41], the optimum angle for the maximum wall shear stress is around 18° , and the wall shear stress is not very sensitive to the aspect ratio. The obtained results are in accordance to these statements, since the values obtained with $\alpha = 18^\circ$ are greater than the ones obtained with $\alpha = 25^\circ$, and in the majority of the cases, very similar values are obtained, specially far away from the VG.

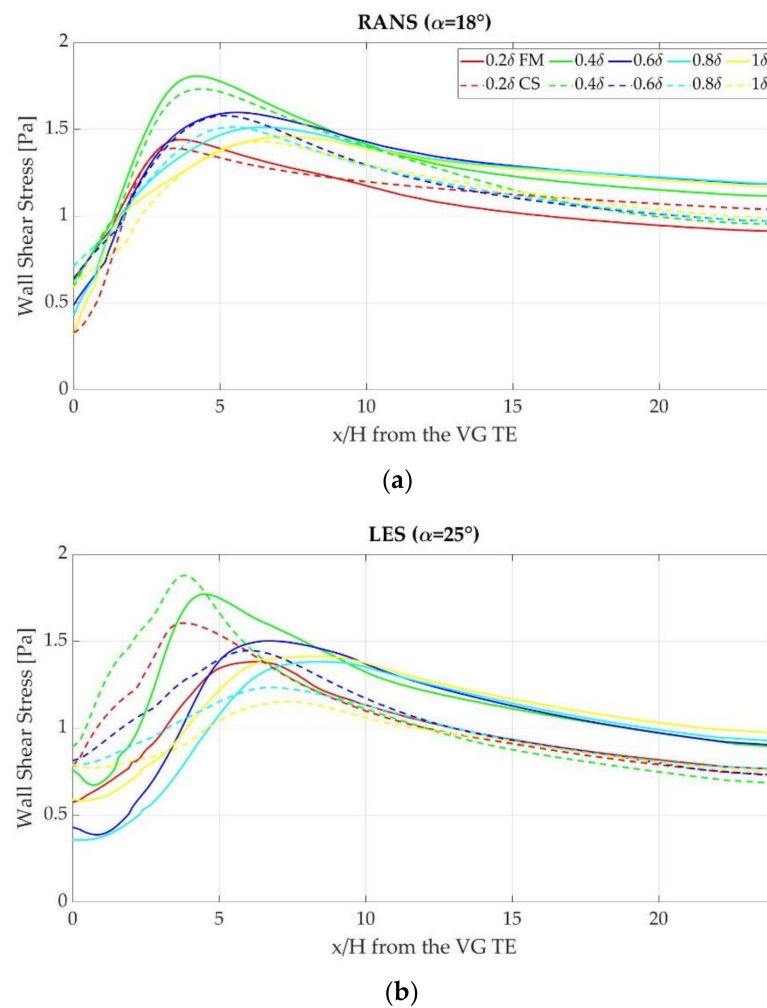


Figure 13. Wall shear stress on the wake behind the Trailing Edge (TE) of the VG. (a) RANS and (b) LES.

With RANS, nearly equal locations of the maximums are obtained with both models. Considering the values, very similar values are obtained with both models, but the biggest deviations between models appear when $H = 0.2 \delta$ and $H = 0.4 \delta$. With LES, larger discrepancies between models are visible regarding the locations of the maximums, since the cell-set predicts the maximum closer to the VG. The values of the maximums show that the cell-set underpredicts these values for the taller VGs ($H = 0.8 \delta$ and $H = 1 \delta$) and overpredicts the values for the lower VGs ($H = 0.2 \delta$ and $H = 0.4 \delta$). Far away from the VG, the cell-set model underpredicts the wall shear stress value for all the cases, except for $H = 0.2 \delta$.

The differences visible on the lower VGs for the LES case are attributed to the fact that these VGs are located on the buffer layer region, where the viscous effects are dominant and the flow is strongly turbulent. In this region, the cell-set seems not to be able to provide accurate predictions of both the viscous and turbulent shear stresses.

4. Conclusions

Numerical simulations of 10 different SBVGs on a flat plate in a negligible streamwise pressure gradient flow conditions were conducted using the fully resolved mesh model and the cell-set model with RANS and LES turbulence models, with the objective of analyzing the accuracy of the cell-set model.

The meshes generated with the fully mesh model are made of around 11.5 million cells, while the meshes generated with the cell-set model are composed of around 7.2 million cells. This fact has resulted in savings of around the 40% in terms of computational time.

This study is mainly focused on analyzing the vortices generated on the wake behind the VG. Therefore, the vortex structure regimes on the wake behind the VG; the path, size, and strength of the primary vortex; and the wall shear stress behind it have been studied. The results demonstrate that the cell-set model is able to predict the vortices generated on the wake behind the VG. Regarding the primary vortex, nearly equal values of its path and fairly accurate predictions of its size have been obtained. The vortex size and strength show that the cell-set models overpredict the vorticity of the core of the primary vortex, but underpredicts its size, especially with LES. This is reflected in the large differences that appear in the R_{05} , but close values obtained in Γ and wall shear stress.

The major agreements between models appear in the higher VGs, and the biggest disparities appear in the lower ones. This is attributed to the location of the VGs on the boundary layer, since the lower VGs ($H = 0.2 \delta$) are located on the buffer layer and the higher ones ($H = 0.8 \delta$ and $H = 1 \delta$) on the outer region. These discrepancies are more notable in LES.

In conclusion, it has been demonstrated that the cell-set model is suitable for RANS turbulence modelling with all the tested SBVGs. With LES, it is adequate for VGs whose height is around the boundary layer, but for lower VGs, the differences with the fully resolved mesh model are significant. Hence, the cell-set model presented in the current work seems to be not very accurate for vane heights within the buffer layer.

Since the cell-set model represents a great advantage in terms of computational and meshing time savings, additional research is proposed, applying the studied meshing model on VGs with different conditions and geometries, or using it for generating other devices. Furthermore, more investigations should be done in order to improve the accuracy of the cell-set modelled geometries with heights within the buffer layer.

Author Contributions: K.P.-P., U.F.-G. and I.A. wrote the paper. K.P.-P. and U.F.-G. prepared the numerical simulations and D.T.-F.-B. validated them. E.Z. provided effectual guidelines to prepare the manuscript. All authors have read and agreed to the published version of the manuscript.

Funding: The authors are thankful to the government of the Basque Country and the University of the Basque Country UPV/EHU for the ELKARTEK20/78 and EHU12/26 research programs, respectively.

Institutional Review Board Statement: Not applicable.

Informed Consent Statement: Informed consent was obtained from all subjects involved in the study.

Data Availability Statement: The data presented in this study are available on request from the corresponding author.

Acknowledgments: The authors thank for technical and human support provided by SGIker (UPV/EHU/ERDF, EU). This research has been developed under the framework of the Joint Research Laboratory on Offshore Renewable Energy (JRL-ORE).

Conflicts of Interest: The authors declare no conflict of interest.

Nomenclature

	Definition
CFD	Computational Fluid Dynamics
CS	Cell-Set model
D	Discrete vortex
FM	Fully resolved Mesh model
H	Height of the VG
H_s	Suction side of the horseshoe vortex
H_p	Pressure side of the horseshoe vortex
L	Length of the VG
LE	Leading Edge
LES	Large Eddy Simulation

MVG	Micro-Vortex Generator
P	Primary vortex
RANS	Reynolds-Averaged Navier-Stokes
SBVG	Sub-Boundary Layer Vortex Generator
SGS	Sub-Grid-Scale
SST	Shear Stress Transport
TE	Trailing Edge
VG	Vortex Generator
x/δ	Normalized axial distance
y/δ	Normalized vertical distance
z/δ	Normalized lateral distance
α	Incident angle ($^{\circ}$)
Δ	Mesh resolution (m)
δ	Boundary layer thickness (m)
λ	Taylor length-scale (m)
Γ	Circulation ($\text{m}^2 \cdot \text{s}^{-1}$)
Re	Reynolds number
R_{05}	Half-Life Radius (m)
U_{∞}	Free stream velocity (m/s)
ν	Kinematic viscosity (m^2/s)
ω	Vorticity (s^{-1})


References

1. Ashill, P.; Fulker, J.; Hackett, K. Research at DERA on Sub Boundary Layer Vortex Generators (SBVGs). In Proceedings of the 39th Aerospace Sciences Meeting and Exhibit, Reno, NV, USA, 8–11 January 2001; American Institute of Aeronautics and Astronautics: Reston, VA, USA, 2001.
2. Ashill, P.; Fulker, J.; Hackett, K. Studies of Flows Induced by Sub Boundary Layer Vortex Generators (SBVGs). In Proceedings of the 40th AIAA Aerospace Sciences Meeting & Exhibit, Reno, NV, USA, 14–17 January 2002; American Institute of Aeronautics and Astronautics: Reston, VA, USA, 2002.
3. Aramendia-Iradi, I.; Fernandez-Gamiz, U.; Sancho-Saiz, J.; Zulueta-Guerrero, E. State of the Art of Active and Passive Flow Control Devices for Wind Turbines. *DYNA* **2016**, *91*, 512–516. [[CrossRef](#)]
4. Aramendia, I.; Fernandez-Gamiz, U.; Ramos-Hernanz, J.A.; Sancho, J.; Lopez-Guede, J.M.; Zulueta, E. Flow Control Devices for Wind Turbines. In *Energy Harvesting and Energy Efficiency*; Bizon, N., Mahdavi Tabatabaei, N., Blaabjerg, F., Kurt, E., Eds.; Lecture Notes in Energy; Springer: Cham, Switzerland, 2017; Volume 37, pp. 629–655, ISBN 978-3-319-49874-4.
5. Lin, J.C. Review of Research on Low-Profile Vortex Generators to Control Boundary-Layer Separation. *Prog. Aerosp. Sci.* **2002**, *38*, 389–420. [[CrossRef](#)]
6. Taylor, H.D. *Summary Report on Vortex Generators*; Research Department Report No. R-05280-9; Research Department, United Aircraft Corporation: Moscow, Russia, 1947.
7. Øye, S. The Effect of Vortex Generators on the Performance of the ELKRAFT 1000 KW Turbine. In Proceedings of the 9. Symposium on Aerodynamics of Wind Turbines, Stockholm, Sweden, 11–12 December 1995.
8. Miller, G. *Comparative Performance Tests on the Mod-2, 2.5-MW Wind Turbine with and without Vortex Generators*; NASA TM: Cleveland, OH, USA, 1984.
9. Heyes, A.L.; Smith, D.A.R. Modification of a Wing Tip Vortex by Vortex Generators. *Aerosp. Sci. Technol.* **2005**, *9*, 469–475. [[CrossRef](#)]
10. Tai, T. Effect of Micro-Vortex Generators on V-22 Aircraft Forward-Flight Aerodynamics. In Proceedings of the 40th AIAA Aerospace Sciences Meeting Exhibit, Reno, NV, USA, 14–17 January 2002; American Institute of Aeronautics and Astronautics: Reston, VA, USA, 2002.
11. Agnew, B.; Tam, I.C.; Shi, X. Optimization of Heat and Mass Exchange. *Processes* **2020**, *8*, 314. [[CrossRef](#)]
12. Joardar, A.; Jacobi, A.M. Heat Transfer Enhancement by Winglet-Type Vortex Generator Arrays in Compact Plain-Fin-and-Tube Heat Exchangers. *Int. J. Refrig.* **2008**, *31*, 87–97. [[CrossRef](#)]
13. Subbiah, G.; Allaudeen, A.S.; Janarthanam, H.; Mani, P.; Gnanamani, S.; Raja, K.S.S.; Raja, T.A. Computational Investigation and Design Optimization of Vortex Generator for a Sport Utility Vehicle Using CFD. *AIP Conf. Proc.* **2020**, *2311*, 090001. [[CrossRef](#)]
14. Yu, C.; Zhang, H.; Zeng, M.; Wang, R.; Gao, B. Numerical Study on Turbulent Heat Transfer Performance of a New Compound Parallel Flow Shell and Tube Heat Exchanger with Longitudinal Vortex Generator. *Appl. Therm. Eng.* **2020**, *164*, 114449. [[CrossRef](#)]
15. Carapau, F.; Janela, J. A One-Dimensional Model for Unsteady Axisymmetric Swirling Motion of a Viscous Fluid in a Variable Radius Straight Circular Tube. *Int. J. Eng. Sci.* **2013**, *72*, 107–116. [[CrossRef](#)]

16. Sheng, T.C.; Sulaiman, S.A.; Kumar, V. One-Dimensional Modeling of Hydrodynamics in a Swirling Fluidized Bed. *IJMME* **2012**, *12*, 13–22.
17. Ibarra-Udaeta, I.; Errasti, I.; Fernandez-Gamiz, U.; Zulueta, E.; Sancho, J. Computational Characterization of a Rectangular Vortex Generator on a Flat Plate for Different Vane Heights and Angles. *Appl. Sci.* **2019**, *9*, 995. [[CrossRef](#)]
18. Martínez-Filgueira, P.; Fernandez-Gamiz, U.; Zulueta, E.; Errasti, I.; Fernandez-Gauna, B. Parametric Study of Low-Profile Vortex Generators. *Int. J. Hydrogen Energy* **2017**, *42*, 17700–17712. [[CrossRef](#)]
19. Fernandez-Gamiz, U.; Errasti, I.; Gutierrez-Amo, R.; Boyano, A.; Barambones, O. Computational Modelling of Rectangular Sub-Boundary Layer Vortex Generators. *Appl. Sci.* **2018**, *8*, 138. [[CrossRef](#)]
20. Gutierrez-Amo, R.; Fernandez-Gamiz, U.; Errasti, I.; Zulueta, E. Computational Modelling of Three Different Sub-Boundary Layer Vortex Generators on a Flat Plate. *Energies* **2018**, *11*, 3107. [[CrossRef](#)]
21. Ballesteros-Coll, A.; Fernandez-Gamiz, U.; Aramendia, I.; Zulueta, E.; Lopez-Guede, J.M. Computational Methods for Modelling and Optimization of Flow Control Devices. *Energies* **2020**, *13*, 3710. [[CrossRef](#)]
22. Chillón, S.; Uriarte-Uriarte, A.; Aramendia, I.; Martínez-Filgueira, P.; Fernandez-Gamiz, U.; Ibarra-Udaeta, I. JBAY Modeling of Vane-Type Vortex Generators and Study on Airfoil Aerodynamic Performance. *Energies* **2020**, *13*, 2423. [[CrossRef](#)]
23. Fernandez-Gamiz, U.; Réthoré, P.-E.; Sørensen, N.N.; Velte, C.M.; Frederik, Z.; Egusquiza, E. *Comparison of Four Different Models of Vortex Generators*; European Wind Energy Association (EWEA): Copenhagen, Denmark, 2012.
24. Bender, E.E.; Anderson, B.H.; Yagle, P.J. Vortex Generator Modelling for Navier–Stokes Codes. In Proceedings of the 3rd ASME-JSME Joint Fluids Engineering Conference: FEDSM '99, San Francisco, CA, USA, 18–23 July 1999. ASME Paper FEDSM99-6919.
25. Errasti, I.; Fernández-Gamiz, U.; Martínez-Filgueira, P.; Blanco, J.M. Source Term Modelling of Vane-Type Vortex Generators under Adverse Pressure Gradient in OpenFOAM. *Energies* **2019**, *12*, 605. [[CrossRef](#)]
26. Jirasek, A. Vortex-Generator Model and Its Application to Flow Control. *J. Aircr.* **2005**, *42*, 1486–1491. [[CrossRef](#)]
27. Ballesteros-Coll, A.; Fernandez-Gamiz, U.; Aramendia, I.; Zulueta, E.; Ramos-Hernanz, J.A. Cell-Set Modelling for a Microtab Implementation on a DU91W(2)250 Airfoil. *Energies* **2020**, *13*, 6723. [[CrossRef](#)]
28. Ibarra-Udaeta, I.; Portal-Porras, K.; Ballesteros-Coll, A.; Fernandez-Gamiz, U.; Sancho, J. Accuracy of the Cell-Set Model on a Single Vane-Type Vortex Generator in Negligible Streamwise Pressure Gradient Flow with RANS and LES. *J. Mar. Sci. Eng.* **2020**, *8*, 982. [[CrossRef](#)]
29. STAR-CCM+ V2019.1. Available online: <https://www.plm.automation.siemens.com/> (accessed on 2 June 2020).
30. Menter, F. Zonal Two Equation K- ω Turbulence Models for Aerodynamic Flows. In Proceedings of the 23rd Fluid Dynamics, Plasmadynamics, and Lasers Conference, Orlando, FL, USA, 6–9 July 1993; American Institute of Aeronautics and Astronautics: Reston, VA, USA, 1993.
31. Allan, B.; Yao, C.-S.; Lin, J. Numerical Simulations of Vortex Generator Vanes and Jets on a Flat Plate. In Proceedings of the 1st Flow Control Conference, St. Louis, MO, USA, 24–26 June 2002; American Institute of Aeronautics and Astronautics: Reston, VA, USA, 2002.
32. Urkiola, A.; Fernandez-Gamiz, U.; Errasti, I.; Zulueta, E. Computational Characterization of the Vortex Generated by a Vortex Generator on a Flat Plate for Different Vane Angles. *Aerosp. Sci. Technol.* **2017**, *65*, 18–25. [[CrossRef](#)]
33. Smagorinsky, J. General Circulation Experiments with the Primitive Equations. *Mon. Weather Rev.* **1963**, *91*, 99–164. [[CrossRef](#)]
34. Richardson, L.F.; Gaunt, J.A. The Deferred Approach to the Limit. *Philos. Trans. R. Soc. Lond. Ser. A Contain. Pap. A Math. Phys. Character* **1927**, *226*, 299–361. [[CrossRef](#)]
35. Kuczaj, A.K.; Komen, E.M.J.; Loginov, M.S. Large-Eddy Simulation Study of Turbulent Mixing in a T-Junction. *Nucl. Eng. Des.* **2010**, *240*, 2116–2122. [[CrossRef](#)]
36. Tennekes, H.; Lumley, J.L. *A First Course in Turbulence*; MIT Press: Cambridge, MA, USA, 1972; ISBN 978-0-262-20019-6.
37. Velte, C.M.; Hansen, M.O.L.; Okulov, V.L. Multiple Vortex Structures in the Wake of a Rectangular Winglet in Ground Effect. *Exp. Therm. Fluid Sci.* **2016**, *72*, 31–39. [[CrossRef](#)]
38. Hunt, J.C.R.; Wray, A.A.; Moin, P. *Eddies, Stream, and Convergence Zones in Turbulent Flows*; Center for Turbulence Research Report CTR-S88; Center for Turbulence Research: Stanford, CA, USA, 1988; pp. 193–208.
39. Yao, C.; Lin, J.; Allen, B. Flowfield Measurement of Device-Induced Embedded Streamwise Vortex on a Flat Plate. In Proceedings of the 1st Flow Control Conference, St. Louis, MO, USA, 24–26 June 2002; American Institute of Aeronautics and Astronautics: Reston, VA, USA, 2002.
40. Bray, T.P. A Parametric Study of Vane and Air-Jet Vortex Generators. Ph.D. Thesis, Cranfield University, College of Aeronautics, Bedford, UK, 1998.
41. Godard, G.; Stanislas, M. Control of a Decelerating Boundary Layer. Part 1: Optimization of Passive Vortex Generators. *Aerosp. Sci. Technol.* **2006**, *10*, 181–191. [[CrossRef](#)]

Article

Investigation on Dynamic Stresses of Pump-Turbine Runner during Start Up in Turbine Mode

Funan Chen, Huili Bi, Soo-Hwang Ahn , Zhongyu Mao, Yongyao Luo and Zhengwei Wang *

State Key Laboratory of Hydrosience and Engineering & Department of Energy and Power Engineering, Tsinghua University, Beijing 100084, China; cfn18@mails.tsinghua.edu.cn (F.C.); bihuili2014@mail.tsinghua.edu.cn (H.B.); shahn@mail.tsinghua.edu.cn (S.-H.A.); maozy14@mails.tsinghua.edu.cn (Z.M.); luoyy@tsinghua.edu.cn (Y.L.)

* Correspondence: wzw@mail.tsinghua.edu.cn

Abstract: The startup process occurs frequently for pumped storage units. During this process, the rotating rate that changes rapidly and unsteady flow in runner cause the complex dynamic response of runner, sometimes even resonance. The sharp rise of stress and the large-amplitude dynamic stresses of runner will greatly shorten the fatigue life. Thus, the study of start-up process in turbine mode is critical to the safety operation. This paper introduced a method of coupling one dimensional (1D) pipeline calculation and three-dimensional computational dynamics (3D CFD) simulation to analyze transient unsteady flow in units and to obtain more accurate and reliable dynamic stresses results during start up process. According to the results, stress of the ring near fixed support increased quickly as rotating rate rose and became larger than at fillets of leading edge and band in the later stages of start-up. In addition, it was found that dynamic response can be caused by rotor stator interaction (RSI), but also could even be generated by the severe pressure fluctuation in clearance, which can also be a leading factor of dynamic stresses. This study will facilitate further estimation of dynamic stresses in complex flow and changing rotating rate cases, as well as fatigue analysis of runner during transient operation.

Keywords: pump-turbine; dynamic stress; start-up process; pressure fluctuation; clearance



Citation: Chen, F.; Bi, H.; Ahn, S.-H.; Mao, Z.; Luo, Y.; Wang, Z. Investigation on Dynamic Stresses of Pump-Turbine Runner during Start Up in Turbine Mode. *Processes* **2021**, *9*, 499. <https://doi.org/10.3390/pr9030499>

Academic Editors:
Krzysztof Rogowski and
Jin-Hyuk Kim

Received: 14 January 2021
Accepted: 8 March 2021
Published: 10 March 2021

Publisher's Note: MDPI stays neutral with regard to jurisdictional claims in published maps and institutional affiliations.



Copyright: © 2021 by the authors. Licensee MDPI, Basel, Switzerland. This article is an open access article distributed under the terms and conditions of the Creative Commons Attribution (CC BY) license (<https://creativecommons.org/licenses/by/4.0/>).

1. Introduction

Pumped storage units have great significance to the power grid. Recent years have witnessed the development of new renewable energy sources such as wind and solar. However, both wind and solar are not stable and continuous, causing large oscillation for the load of electrical power grid. Therefore, pumped storage units are required to absorb extra electric energy generated by wind or sun, maintaining the safety and stability of power grid. In addition, pumped storage units can also help solving the problem of frequency modulation, phase modulation as well as peak regulation for their effective storage and flexible switch between turbine mode and pump mode [1]. As the critical component of pumped storage unit, the pump turbine runner may suffer from dynamic stresses, and sometimes cracks at the location of stress concentration. Damages have been reported by many researchers [2–4] and may cause a great loss to power station.

The complex and unstable internal flow is one of the main causes of dynamic stresses. Rotor-stator interaction (RSI) is one of the most common phenomena in hydraulic units and has been studied for many years [1,5,6]. For a runner with low specific speed, it is the main reason of dynamic stresses at full load conditions [7]. When working at part load, the vortex rope in draft tube also affects the dynamic stresses of runner. The rate of damage caused by dynamic stresses becomes larger as the load decreases, and at part load it can be 100 times higher than at best efficiency point (BEP) [8]. At some working conditions, the Von-Karman vortex shedding induces the vibration of blades [9]. The S-shaped region of pump turbine has been studied widely and deep understanding is still needed because

the flow structure is very complicated. When runner is working in the S-shaped region, the greater static stress and dynamic stress amplitudes can result in earlier occurrence of cracks and fatigue failures. Moreover, the stochastic hydraulic loads tend appear in the S-shaped region, especially at no-load condition [10]. C Mende et al. [11] and JF Morissette et al. [12] suggested that Large Eddy Simulation (LES) turbulence model is a better choice to predict the stochastic pressure fluctuations, and low-frequency events can be captured by one-way fluid structure interaction (FSI) simulation method.

Dynamic stresses in transient processes can lead to more damage to runner than normal working conditions because the hydraulic loads and performance characteristics change rapidly. Many researches focused on the operating mechanism of pump turbine and studied the unstable behavior during transient processes. Rotating stall has been studied both in turbine mode [13,14] and in pump mode [15]. Rotating stall was observed in a reduced scale model at runaway and became more obvious when discharge decreased [16]. The flow separations in several neighboring runner channels caused a stall cell, and back-flow and vortices were induced. Several studies [17–21] indicated the vortex appearing in runner and vaneless space is the main reason of dynamic instability in transient process. The vortex varies with time, enhances the pressure fluctuations, and causes some low-frequency components in pressure fluctuations. In addition, Li et al. [22] observed a ring-shaped flow enlaced the vaneless space and blocked the flow during start up in turbine mode. Zuo et al. [23] summarized the stability criteria of the overall system which can evaluate the unstable characteristics of pump-turbine. These unstable behaviors affect the dynamic stresses of runner. The measurements on runner [24] suggested that the static stress and the amplitude of dynamic stress during start-stop are both greater than at normal operating conditions and can cause severe damage to runner.

As described above, the research on dynamic stresses and its influencing factors mainly focused on the normal working conditions. Various studies have discussed the hydraulic excitation and its unsteady and complex characteristics in transient process. However, only a few papers have dealt with its influence on dynamic stresses of runner, especially in the transient process. Furthermore, other factors such as rotating rate and flow in clearance were rarely mentioned.

In this paper, the dynamic stresses of a pump-turbine runner during start up are analyzed using FSI method. The hydraulic loads during start up are obtained from computational fluid dynamics (CFD) simulation, with one dimensional (1D) pipeline calculation providing the boundary conditions. The paper initially discusses the effects of rotating rate, torque of runner, and the axial force. Then, the dynamic stresses are analyzed not only from viewpoint of the RSI but also under angle of the severe pressure fluctuation in clearance. This study can provide a better understanding to the dynamic response of runner under complex external excitation.

2. Numerical Method

2.1. Structural Governing Equations

The dynamic response of structure can be solved using finite element method (FEM). The matrix formulation of the governing equations can be expressed as

$$[M]\{\ddot{u}\} + [C]\{\dot{u}\} + [K]\{u\} = \{F_s\} \quad (1)$$

where $[M]$, $[C]$, and $[K]$ represent for structure mass matrix, damping matrix and stiffness matrix, respectively, $\{F_s\}$ is the load vector and $\{u\}$ is the displacement vector.

Normally, the Von-Mises equivalent stress σ_{equ} is used to evaluate the stress characteristics of runner. It can be expressed as

$$\sigma_{equ} = \sqrt{\frac{1}{2}[(\sigma_1 - \sigma_2)^2 + (\sigma_2 - \sigma_3)^2 + (\sigma_3 - \sigma_1)^2]} \quad (2)$$

where σ_1 , σ_2 , and σ_3 represent for first, second and third principal stress, respectively.

2.2. 1D Pipeline Governing Equations

The flow in pipeline can be simplified into one dimensional flow and solved by method of characteristics (MOC). The continuity equation and momentum equation are

$$V \frac{\partial H}{\partial x} + \frac{\partial H}{\partial t} - V \sin \alpha + \frac{a^2}{g} \frac{\partial V}{\partial x} = 0 \quad (3)$$

$$g \frac{\partial H}{\partial x} + V \frac{\partial V}{\partial x} + \frac{\partial V}{\partial t} + \frac{fV|V|}{2D} = 0 \quad (4)$$

where V is the average velocity at cross section, H is piezometric head, α is the angle between center line of pipe and horizontal line. a is wave speed, g is gravity acceleration, f is Darcy–Weisbach friction factor, D is the pipe diameter.

Other components in hydraulic system such as surge tank and pipe with branches can also be simplified and solved.

2.3. CFD Governing Equations and Turbulence Model

The flow in the unit is assumed as three-dimensional incompressible unsteady flow. According to the Reynolds averaged theory, the governing equations are described as follows:

$$\frac{\partial \bar{u}_i}{\partial x_i} = 0 \quad (5)$$

$$\frac{\partial \bar{u}_i}{\partial t} + \bar{u}_j \frac{\partial \bar{u}_i}{\partial x_j} = F_i - \frac{1}{\rho} \frac{\partial \bar{p}}{\partial x_i} + \nu \frac{\partial^2 \bar{u}_i}{\partial x_j \partial x_j} - \frac{\partial}{\partial x_j} (\overline{u_i' u_j'}) \quad (6)$$

where u is velocity, p is pressure, F is body force, ρ is density, and ν is kinematic viscosity. Turbulence model is needed to close the equations above. In this paper, the Shear-Stress Transport (SST) k - ω model is used to calculate the turbulence in pump-turbine.

3. Calculation Model and Boundary Conditions

3.1. The Pump-Turbine Runner

3.1.1. The Finite Element Model

The runner has 5 main blades and 5 splitter blades with the inlet diameter of 4.3 m and outlet diameter of 2.125 m. The runner is made of stainless steel. The Young's modulus is 2.1×10^{11} Pa, Poisson's ratio is 0.3 and density is 7850 kg/m^3 .

The finite element model of runner is shown in Figure 1. Most of the meshes are hexahedral and in regions of low stress gradients, some wedges are used. Refinements are made at the stress contribution regions, as shown in Figure 1.

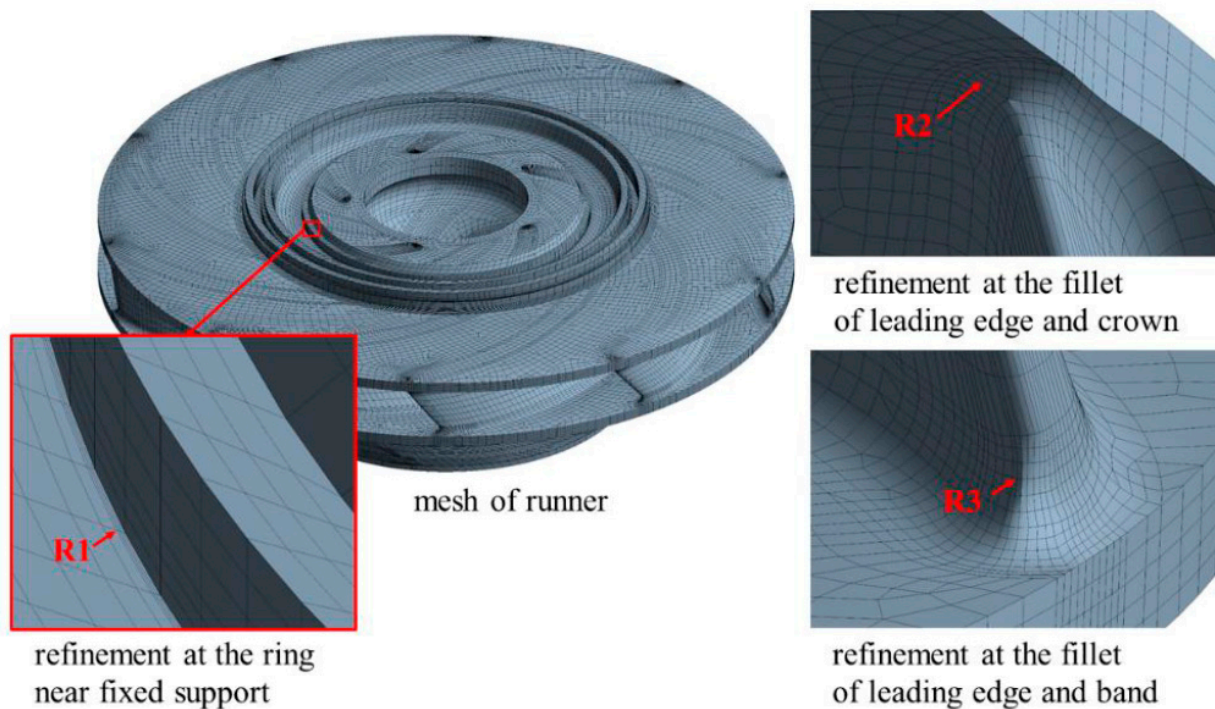


Figure 1. Finite element model of runner (R1 is the node at the ring near fixed support; R2 is the node at the fillet of leading edge and crown; R3 is the node at the fillet of leading edge and band).

3.1.2. Mesh Independency Check

The calculation grids were checked with gravity and centrifugal force acting on the runner. The results shown in Figure 2 indicate that the grid with 305,505 nodes is enough for this calculation. This mesh was used in the following analysis.

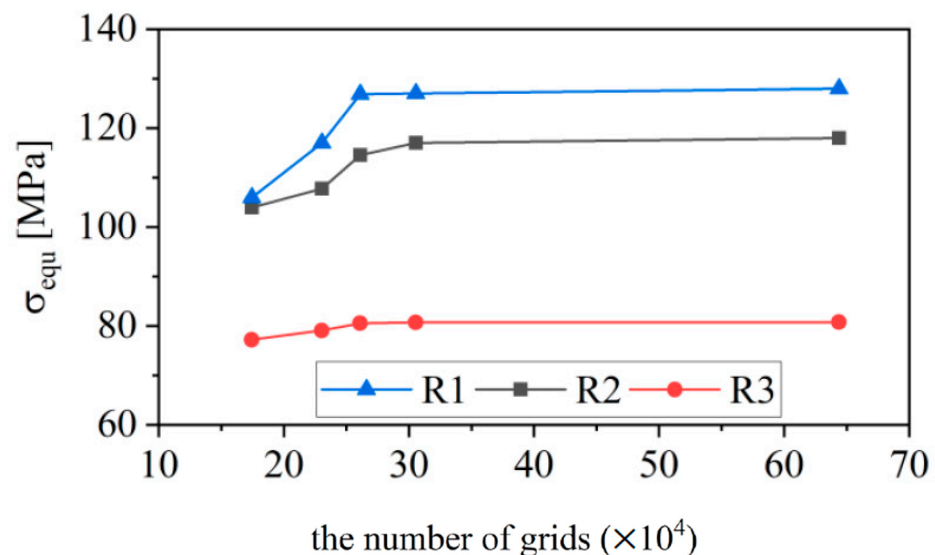


Figure 2. Mesh independency analysis.

It is worth noting that besides the fillets of leading edge, a ring near fixed support is also the stress concentration area and suffers from higher stress than other parts. On one hand, the centrifugal force of whole runner results in a bending moment acting on the ring. On the other hand, the geometry changes suddenly at the corner of ring without any fillets for transition and, thus, concentrates the stress sharply. Stress singularity appears at the nodes closest to the corner. Fillets with 5–20 mm radius can help reduce the stress

singularity but cannot eliminate it. Thus, the results of nodes closest to the corner were ignored. Node with the convergence stress (node R1 in Figure 1) was chosen in mesh independency check and in the following analysis.

3.1.3. Boundary Conditions

Fixed support is defined at area where bolts connect the shaft and runner. The loads of runner include gravity acceleration, centrifugal force and hydraulic loads. The rotating rate is changed over time during start-up process. Therefore, the centrifugal force is different at different time. The hydraulic loads on both inner surface and outer surface can be obtained from CFD simulation, as shown in Figure 3. In traditional FSI simulation, only loads on inner surface are considered. However, the loads on outer surface also have a great influence on the stress-state of runner [25] and were considered in this paper.

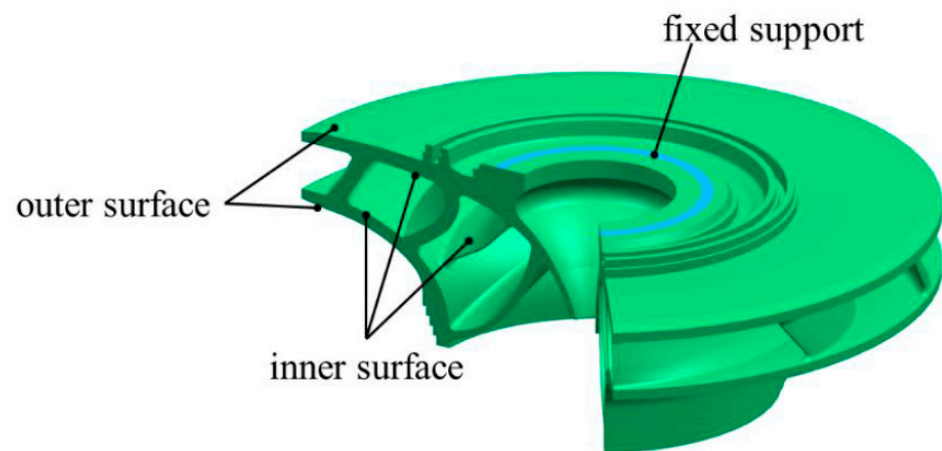


Figure 3. The fluid structure interaction (FSI) interface.

3.2. The Hydraulic System of Pump Storage Station

The considered hydraulic system consists of reservoirs, surge tanks, tunnels, pipelines, pump turbine units, and valves. The diagram of the hydraulic system is shown in Figure 4. The layout of three units with one diversion tunnel is adopted. The total length of the pipeline is more than 3.6 km. Surge tanks are placed at the upstream and downstream to reduce the rapid change of pressure caused by water hammer.

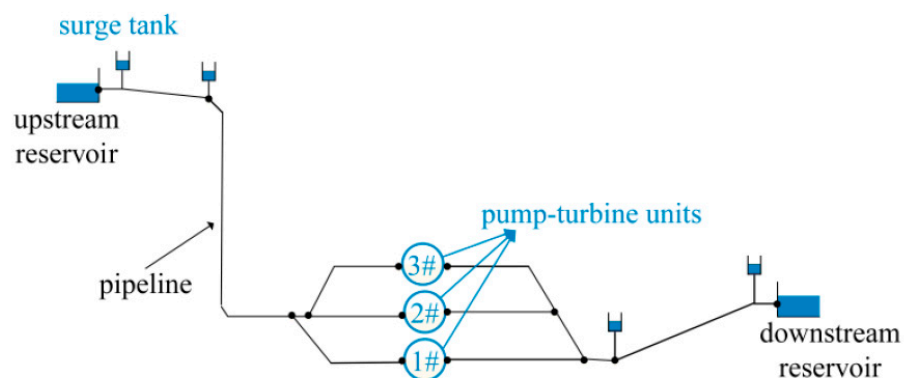


Figure 4. The diagram of the hydraulic system.

In this paper, the start-up process of 1# unit is the major concern. The other 2 units operate at normal condition and suffer small fluctuations induced by the start-up of 1# unit. The water level is 762.1 m at upstream reservoir and 98.0 m at downstream reservoir and assumed to remain constant during start up process. The guide vane opens with the rate of

0.48 degrees per second until the rotating rate reaches rated value, then speed controller begins to work and controls the guide vane opening angle.

3.3. Pump-Turbine Unit

The internal flow of casing, stay vane, guide vane, runner, and draft tube can be simulated as three-dimensional (3D) turbulent flow. The unit is shown in Figure 5. In order to provide complete hydraulic loads of runner, the labyrinth seals and clearances around runner are also considered. The rated head of the unit is 653 m. There are 16 guide vanes and the maximum opening degree is 24°.

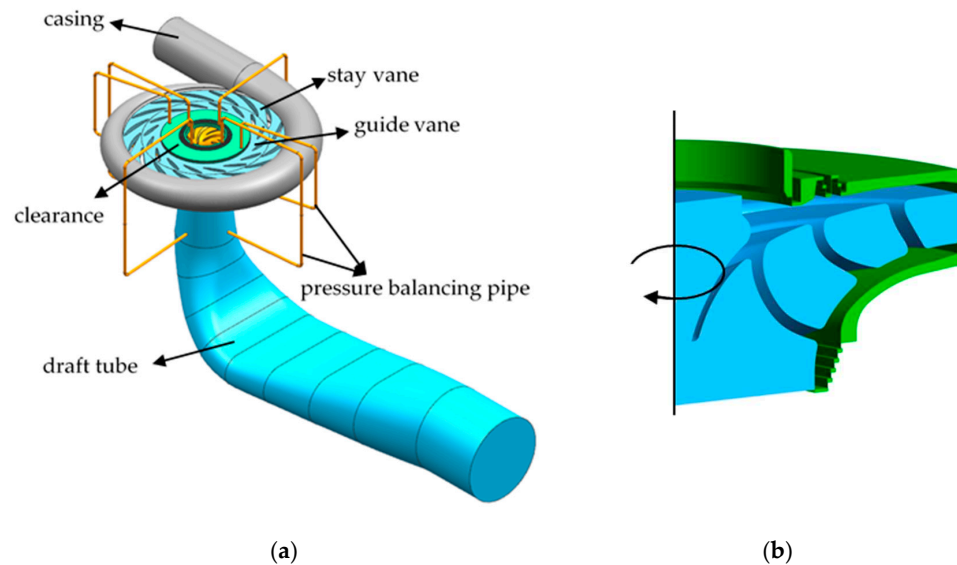


Figure 5. The pump-turbine unit (a) pump-turbine unit; (b) runner (blue) and clearances (green).

The flow domain was discretized by tetrahedral mesh and hexahedral mesh. The total number of nodes is 4,643,402 and the number of elements is 9,737,666. The domain of runner has 1,171,402 nodes and the clearance has 1,771,714 nodes. In the region of high stress gradient, the size of mesh cells in CFD analysis is similar to that in FEM analysis. The mesh is shown in Figure 6.

The internal flow of the pump-turbine unit at typical time points was calculated, as shown in Table 1. Figure 7 shows the boundary conditions of CFD method. In this paper, the relative pressure coefficient C_p is defined as

$$C_p = \frac{p - P_{ref}}{\rho g H} \quad (7)$$

where p is pressure, P_{ref} is the pressure at the end of downstream pipeline, H is the rated head. In Figure 7, P_{in} is total pressure coefficient at casing inlet, and P_{out} is static pressure coefficient at draft tube. These are calculated through 1D MOC and used as inlet and outlet boundary conditions of 3D CFD. All walls are set as no-slip walls. The domain of runner and clearances are rotating domains. The model of interface between rotating domain and stationary domain is set as transient rotor-stator to simulate the RSI phenomenon. The unsteady calculation is conducted with steady simulation result as initial guess. The number of timesteps is 300 in each revolution. In addition, the pressure-based solver is used in this study. Second-order accuracy is used for the pressure equation and second-order upwind discretization for other convection-diffusion equations.

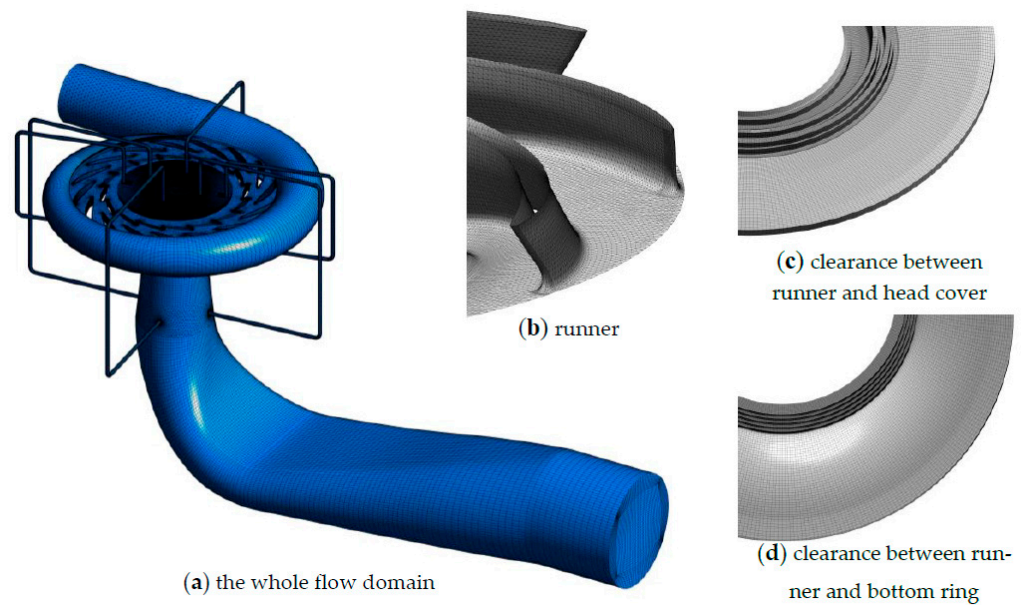


Figure 6. Mesh of the flow domain (a) the whole flow domain; (b) runner; (c) clearance between runner and head cover; (d) clearance between runner and bottom ring.

Table 1. Time points.

Time Point Number	Time [s]
TP1	3
TP2	6
TP3	9
TP4	12
TP5	15
TP6	18
TP7	21
TP8	24
TP9	27

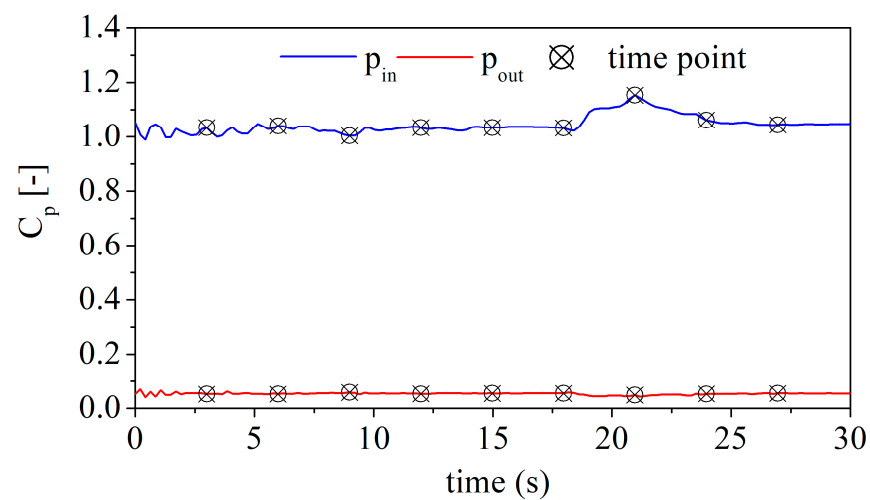


Figure 7. The inlet and outlet boundary conditions.

3.4. The Structure-Fluid Coupling Model

In this study, the influence of 3D flow on the dynamic response of runner is analyzed by one-way FSI simulation method, which is calculated using a coupling of Fluent and ANSYS Mechanical. The coupling process is as follows.

First, the Fluent simulation is conducted. The hydraulic loads at each step are obtained.

Second, the data transfer is performed manually. Pressure from the cell zones of Fluent simulation can be mapped onto locations associated with the ANSYS Mechanical mesh by using an interpolation method provided by ANSYS (ANSYS, Inc., Pittsburgh, PA, USA). Many FSI simulations require strict match at the interface of CFD grid and structural grid, which increases the complexity of meshing, and may cause a too fine mesh in modeling the dynamic stresses of runner. The interpolation method effectively avoids this problem.

Third, the ANSYS Mechanical simulation is performed, and the timestep is the same with CFD calculation.

4. Results and Discussion

4.1. The Variation of Performance Characteristics

The energy characteristics such as discharge and power change rapidly during start-up process. Meanwhile, the pressure wave as a result of the operating condition change of unit travels through pipeline, and this travel in turn affects the operating condition change of unit. Through 1D MOC, this complex process can be simulated. However, in this paper, the pressure wave is not the key point and is not discussed here.

3D simulation was conducted based on the result of 1D MOC at typical time points. Total pressure and static pressure are set as inlet and outlet boundary condition respectively, so head is a given quantity. Discharge and torque on blades of 1# unit are calculated by 3D simulation and the verification is shown in Figure 8. The guide vane opening is also plotted here. The discharge, torque and guide vane opening are expressed as relative values: Q/Q_n , T/T_n and A/A_{max} , where Q_n and T_n are rated discharge and torque, A_{max} is the maximum guide vane opening. The calculation of 1D MOC are based on model test, therefore the consistency of 3D CFD results and 1D MOC results in Figure 8 indicates that the accuracy of 3D CFD is enough for this study.

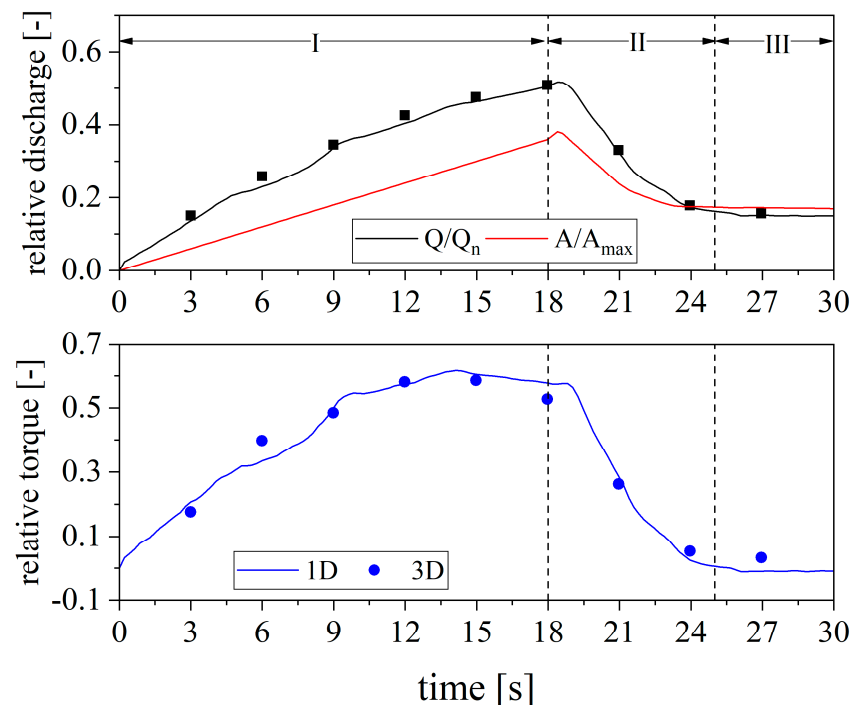


Figure 8. The variation of torque and discharge during start-up process.

The relative rotating rate is plotted in Figure 9, where N is the rated rotating rate. The start-up process in turbine mode can be divided into three stages. In the first stage, guide vane opens at preset speed. As a consequence of increasing water flow, torque on the blades increases. The increasing torque accelerates the rotation of runner, raising the

rotating rate. At 18 s, rotating rate nearly reaches the rated value. Then the unit goes through the second stage. Torque on blades is reduced by closing the guide vanes while the rotating rate is maintained at rated value. At 25 s, the torque almost drops to zero. In third stage, the unit reaches speed-no-load condition and stabilizes in this condition.

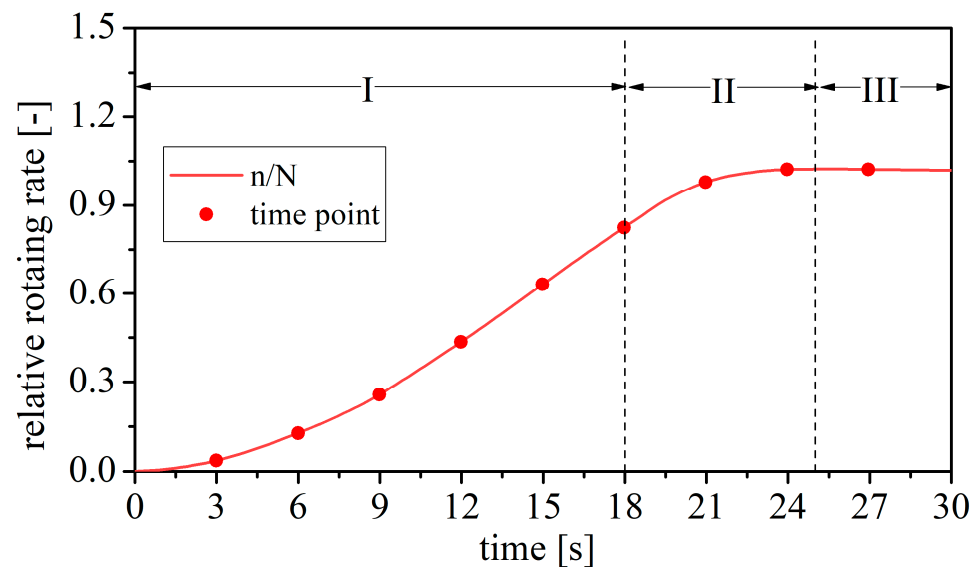


Figure 9. The variation of rotating rate (n/N).

In steady state CFD calculation, the flow in runner is modelled with Moving Reference Frame (MRF), and the phenomenon of RSI cannot be considered. Therefore, the static stress calculation at each point is not enough to reflect the true stress of runner. In this paper, unsteady simulation was conducted to model the flow in a whole rotation cycle. The dynamic stresses of runner were calculated using FSI method, which encounter for their temporal changes as the relative position of runner and guide vanes changing. Then the mean value is defined to describe the stress at each time point. It can be called as mean stress and expressed as

$$\bar{\sigma}_{equ} = \frac{1}{T} \int_{t=0}^T \sigma_{equ} dt \quad (8)$$

where T is the time for a whole rotation cycle of each time point.

4.2. Mean Stresses of Runner

The stress characteristics of pump-turbine runner were obtained by FEM simulation. Two different types of stress distribution can be observed, as shown in Figure 10. In the first stage of start-up process, the fillets of leading edge and band suffered the maximum stress, as shown Figure 10a. There was no stress concentration appearing in other parts of runner. Among time points 1–6, the maximum stress at the concentration region was 245.7 MPa at TP3, the stress of other parts was less than 78 MPa. In the last two stages of start-up process, the ring near fixed support was the region of maximum stress, as shown in Figure 10b. The fillets of leading edge and band suffered low stress less than 55 MPa.

Further observation indicates that in the last two stages of start-up process, stress concentration also appeared at the fillets of leading edge and crown. For further explanation of the stress characteristics during start-up process, five nodes were selected in the high stress regions and marked as S1–S5, as shown in Figure 11. S2 and S3 locate at splitter blade while S4 and S5 locate at the main blade.

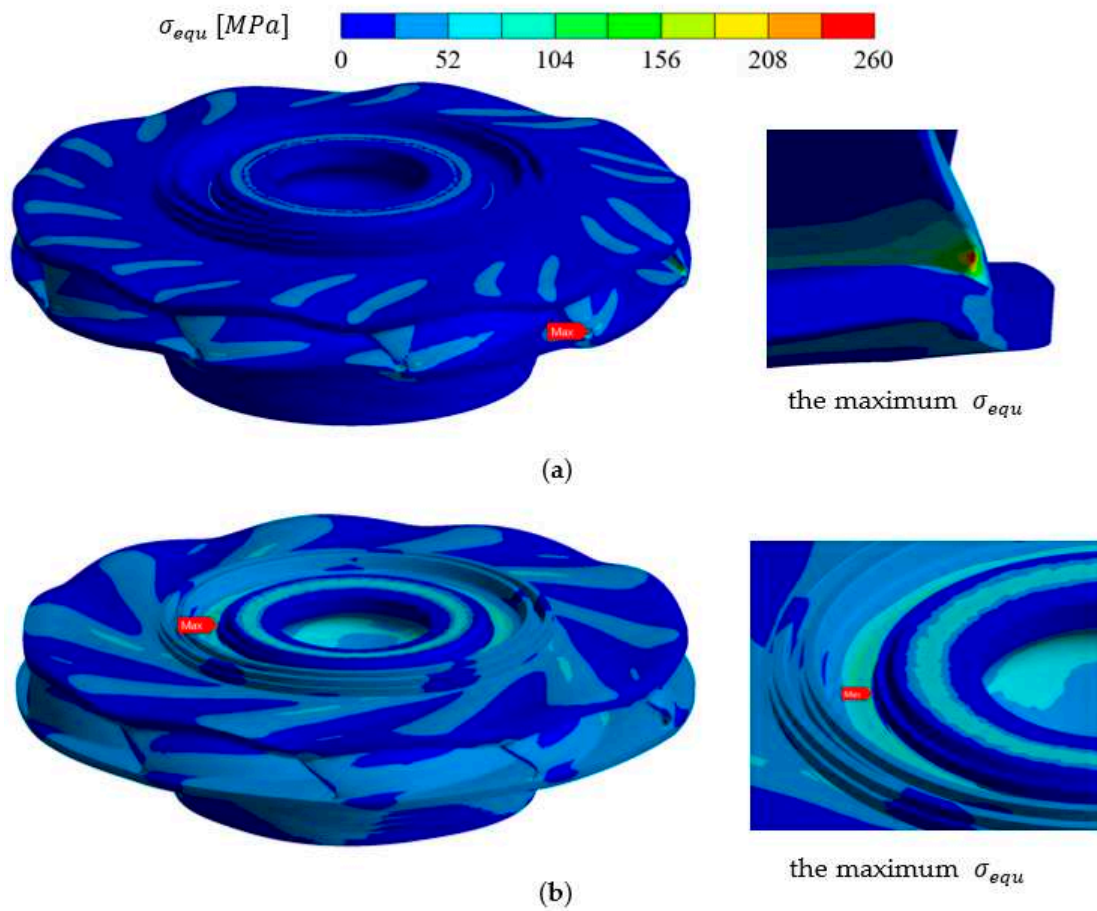


Figure 10. Stress distribution at start-up process (a) TP3; (b) TP9.

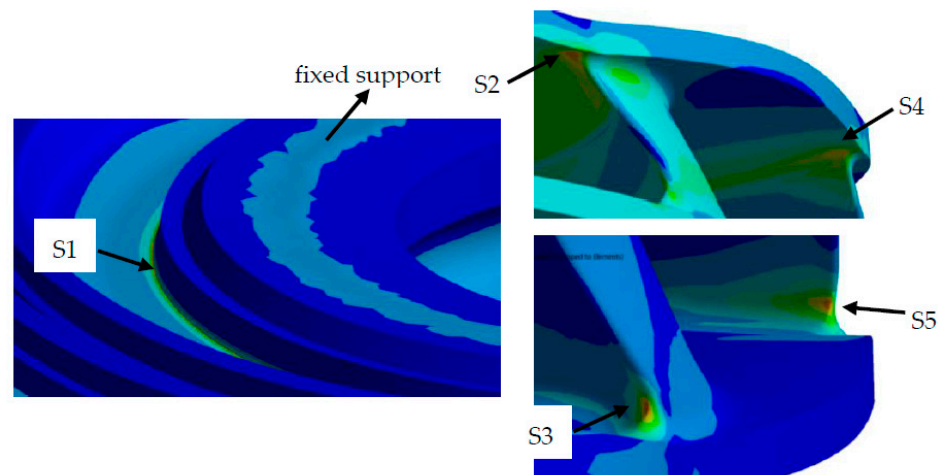


Figure 11. Selected nodes in high stress regions.

The mean stress of S1–S5 during start-up process is plotted in Figure 12. In order to make the influence of hydraulic loads explicit, the FEM analysis considering only hydraulic loads was performed and the mean stress is also shown in Figure 12. The stress at rated working condition was calculated, and marked as grey dotted lines.

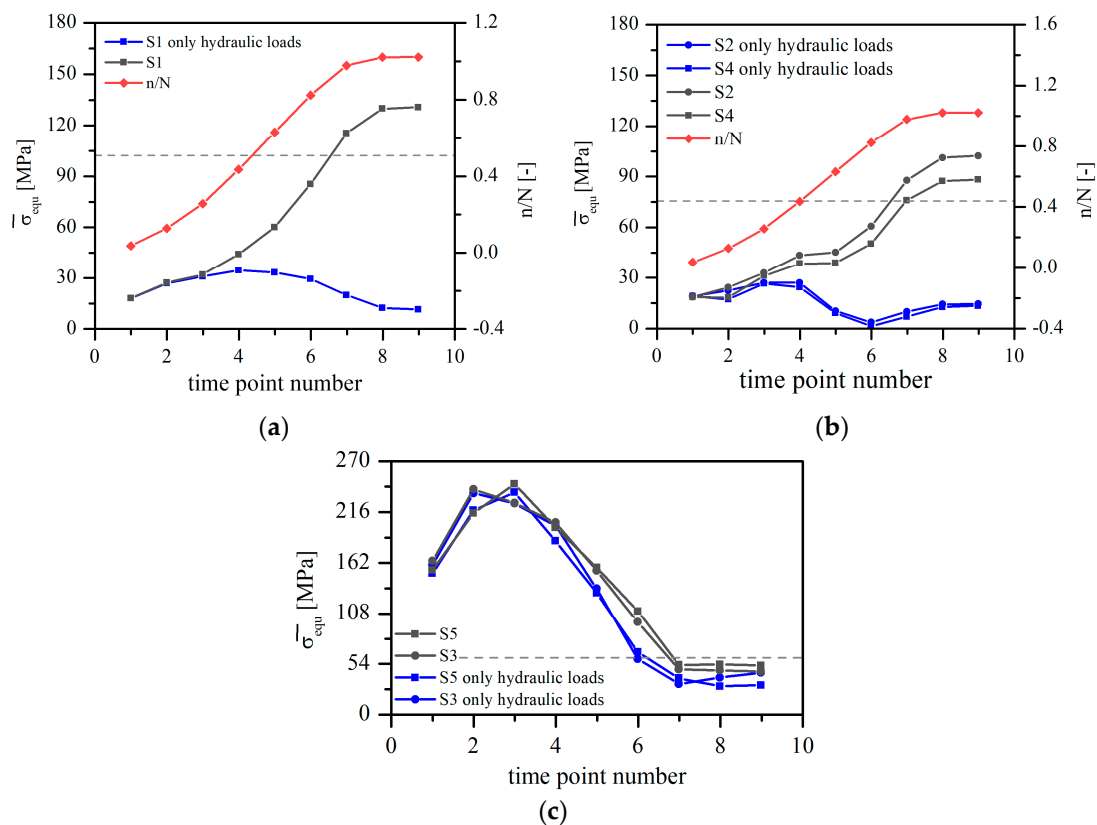


Figure 12. The change of mean stresses in start-up process (a) S1; (b) S2 and S4; (c) S3 and S5.

As indicated in Figure 12, for S1, S2, and S4, the high stress in the last two stages of start-up process was mainly caused by centrifugal force. The stress is slightly higher than the value under rated working condition. Meanwhile, the hydraulic loads lead to the high stress of S3 and S5 in the first stage. The maximum stress of S5 at TP3 can be 3.56 times of rated working condition.

During start-up process, the rotating rate rises quickly in the first stage, and later the growth rate is under control, the value is near the rated value. Thus, centrifugal force contributes to a rapid rise of stress in first stage and the stable high stress in the last two stages. In addition to large centrifugal force, high rotating rate also leads to flow instabilities [26,27], which is another factor causing the high stress. There is circumferential velocity gradient between upper wall and lower wall of clearance, as shown in Figure 13. As rotating rate rises, velocity gradient increases; thus, the shear stress becomes larger, leading to the high stress of runner.

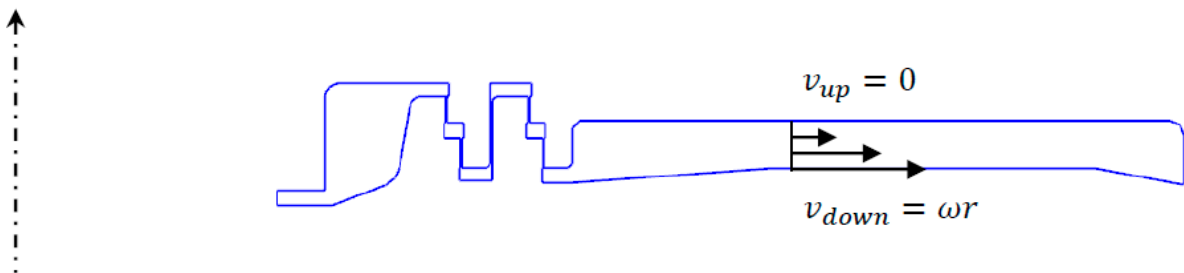


Figure 13. The velocity gradient in clearance.

Due to the shape of the runner, the regions with sudden change of geometry such as S1–S5 can be easily influenced by centrifugal force. In addition, the fillets of trailing edge and crown\band are also high stress regions though these regions are not discussed in

detail in this paper. Other parts of runner, for instance, the middle parts of blades, suffer low stress in the whole process and are hardly affected by centrifugal force.

From Figure 12b, more information can be found that the mean stress of S2 was larger than S4. Considering the fact that the size of elements near S2 is similar to that near S4, a reasonable explanation is the geometry difference of main blade and splitter blade caused the difference of mean stress. The leading edges of the two blades are almost the same. However, the splitter blade is more curved than main blade, as shown in Figure 14. The centrifugal force of blade causes the bending moment on the fillet of blade and crown, which is one of the reasons for the stress of S2 and S4. The more curved blade leads to the larger moment and larger mean stress.

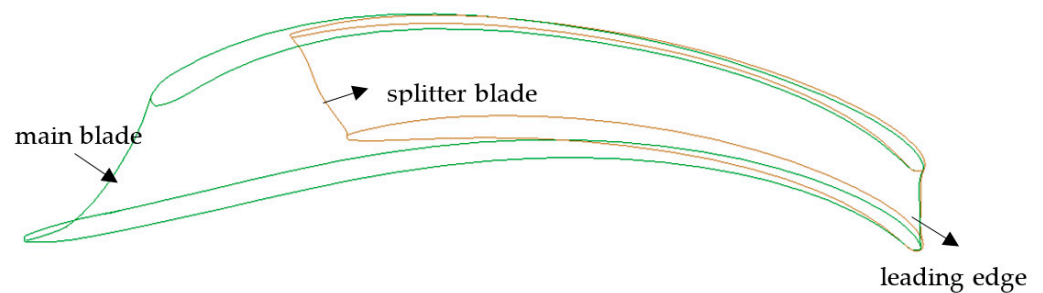


Figure 14. The comparison of geometry between main blade and splitter blade.

For all the five nodes, the mean stress caused by hydraulic loads followed a similar law: increase and reach the maximal value in the first stage and then decrease. In this paper, the hydraulic loads on runner can be simplified as two axial forces (F_{crown} and F_{band}) and a torque on blades (T). It is the superposition of axial hydraulic forces and hydraulic torque on the blade that leads to this law.

Figure 15 provides the relative value of F_{crown} and F_{band} , which are defined as

$$F_{crown}^* = \frac{F_{crown}}{m_r g} \quad (9)$$

$$F_{band}^* = \frac{F_{band}}{m_r g} \quad (10)$$

where m_r is the mass of all the rotating components. According to the regulations, the downward axial force is defined as positive. At TP1–6, F_{crown} and F_{band} drag crown and band away from each other. At TP7, F_{crown} and F_{band} both drop to near zero. At TP8 and TP9, F_{crown} and F_{band} change direction and begin to push crown and band to each other. The stress of runner decreases to the minimum value at TP7 and then increases under the influence of axial forces.

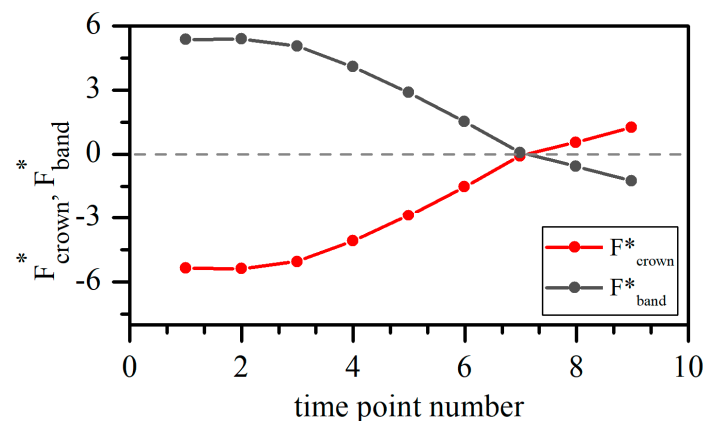


Figure 15. Axial forces of runner.

The variation of T can be found in Figure 8 as relative value T/T_n . At TP3–6, the value of T is higher than other time points, making the stress of runner higher. At TP7–9, T is close to 0, and the stress of runner also decreases.

The axial force and the torque both have great influence on the mean stress of runner. They are loaded together on the runner, causing the higher stress at TP3–4 and the lower stress at TP7–9.

However, compared to centrifugal force, the hydraulic loads effected only S3 and S5, as shown in Figure 12. The maximum stress caused by hydraulic loads of S1, S2, and S4 was less than 35 MPa, while that of S3 and S5 was as high as 236 MPa. First, the discharge is quite small in start-up process, so the flow direction is different from blade angle. When the water flows into runner, it impacts on the pressure side of blade, causing a high-pressure region at the impact point, as shown in Figure 16. The pressure distribution shows the pressure difference mainly affects the inlet area of blade. Therefore, S3 and S5 are easier to suffer large stress. Second, the angle between leading edge and axis is 32.9 degree for main blade and 32.6 degree for splitter blade. Compared with other pump-turbine runner shown in Figure 17, the runner in this paper has a more leaning leading edge. As shown in the sketch map, this leaning leading edge contributes to the gentle transition to crown and the steep transition to band. When hydraulic loads act on the runner, S3 concentrates stress more quickly than S2, as do S5 and S4.

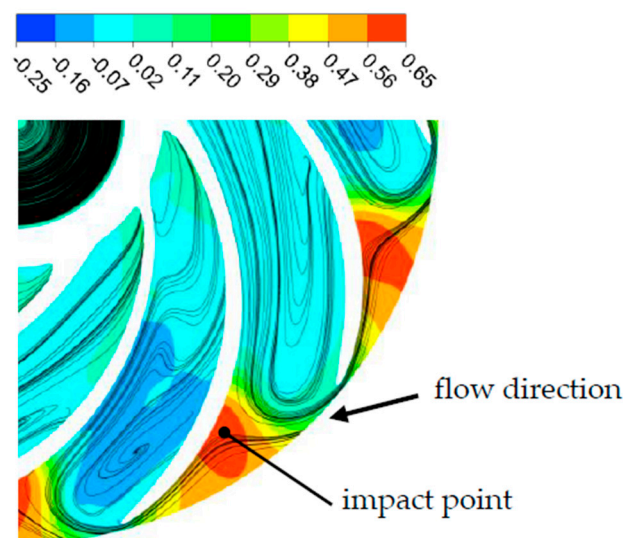


Figure 16. Pressure distribution and streamlines in the middle section of runner (Cp).

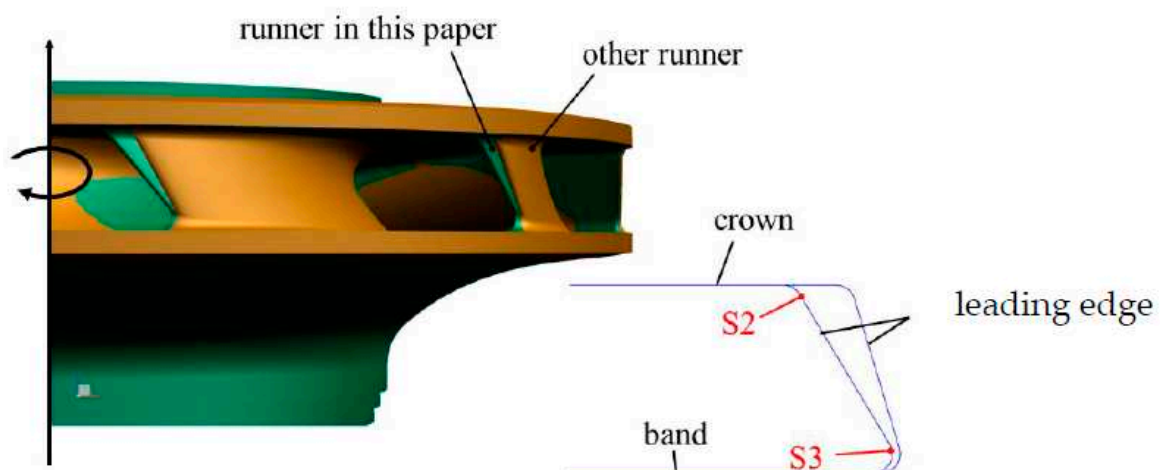


Figure 17. The leaning leading edge of runner studied in this paper.

At most time points, there was little difference between the pressure distributions in each passage of runner. Therefore, the mean stresses of S3 and S5 were almost the same. At TP3, the pressure distributions of two neighboring passages were different from each other, which can be seen in Figure 16. That is the reason why the mean stress of S5 was larger than of S3 at TP3.

4.3. The Amplitudes and Frequency Components of Dynamic Stresses

At each time point, the stress of runner will change as the relative position of runner and guide vanes changes, also known as RSI. The pressure fluctuations induced by RSI are the main reason of dynamic stresses of runner. In this section, the variation of amplitudes and frequencies of dynamic stresses during start-up process will be discussed.

Figure 18 is the frequency domain diagram of dynamic stresses at TP6. The variable of horizontal axis is the ratio of frequency and rotating frequency f_n . As can be seen from Figure 18, the amplitudes of S3 and S5 were far larger than that of S1, S2, and S4. This is consistent with the previous analysis that stress of S3 and S5 were mainly affected by hydraulic loads while S1, S2, and S4 were by centrifugal force.

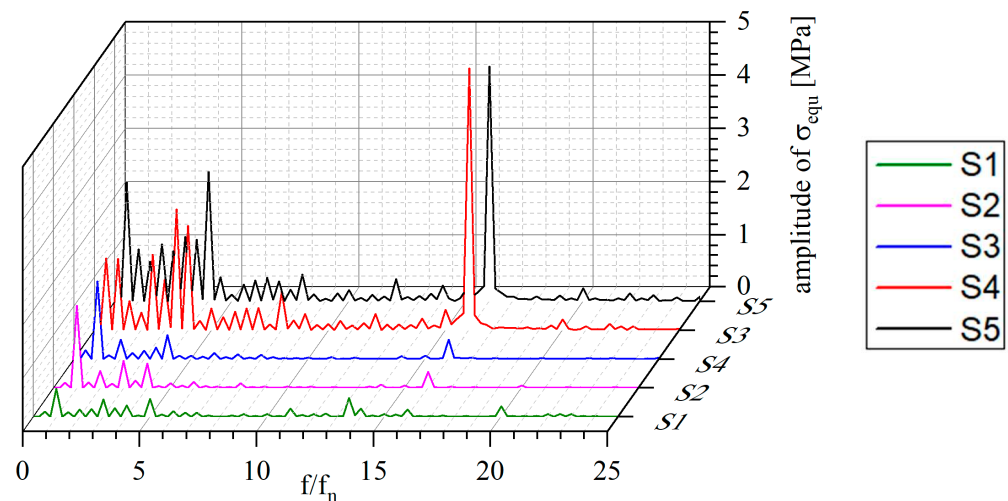


Figure 18. Frequency domain diagram of dynamic stresses at TP6.

Two points in flow domain were selected to reflect the pressure fluctuation. The point in runner was named P1 and the point in clearance was P2, as shown in Figure 19. Figure 20 is the frequency domain diagram of relative pressure coefficient at TP6. The main frequency was $16f_n$, usually called as vane passing frequency (VPF). The pressure fluctuations also included low frequency components ($1-4f_n$), which were induced by the irregular flow in runner with small discharge. Under the effect of pressure fluctuation, the main frequency of dynamic stresses was also VPF. The low frequency components also existed in dynamic stresses, as shown in Figure 18.

The dynamic stresses at other time points were also investigated. The peak-to-peak value during start-up process is shown in Figure 21. In first stage, though the discharge and rotating rate were increasing, the peak-to-peak value did not show a significant growth trend and stabilized about 20 MPa. At TP7, the value increased and reached 50 MPa. Later on, it dropped back to about 20 MPa. Compared with the normal condition, peak-to-peak value in start-up process was far larger and may cause fatigue crack after a few times.

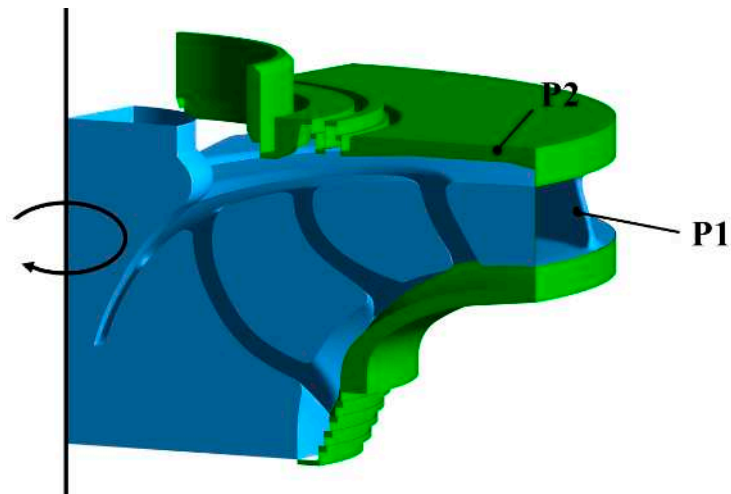


Figure 19. The pressure fluctuation measure points (P1 is the pressure fluctuation recording point in runner; P2 is the pressure fluctuation recording point in clearance).

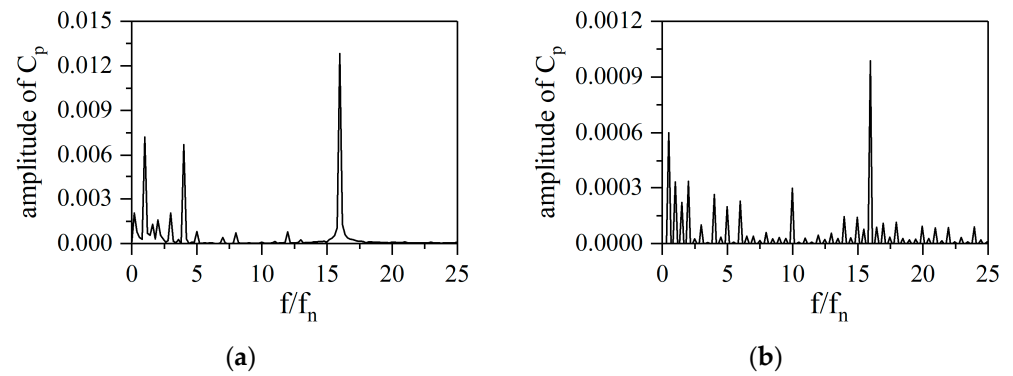


Figure 20. Frequency domain diagram of pressure coefficient at TP6. (a) P1; (b) P2.

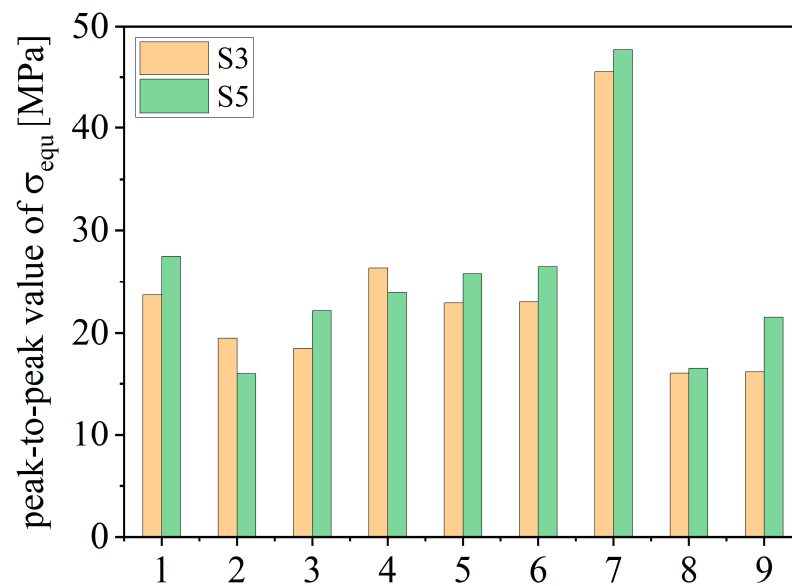


Figure 21. The peak-to-peak value of dynamic stress.

Figure 22 shows the amplitudes of 1/4 VPF and VPF in start-up process. At TP1, the pressure fluctuation in runner was mainly caused by RSI, thus VPF was the main

frequency of dynamic stress while the amplitude of 1/4 VPF was almost zero. Later as the discharge and torque of runner increased, the amplitude of VPF rose slightly. The irregular flow in runner also became violent and led to an amplitude growth of 1/4 VPF. In second and third stage, the torque and discharge began to drop, but the influence of RSI continued, so the amplitude of VPF did not decrease. Moreover, there was a sudden rise of 1/4 VPF at TP7, and the amplitude fell rapidly at TP8. That was the reason for the maximum peak-to-peak value at TP7 in Figure 21.

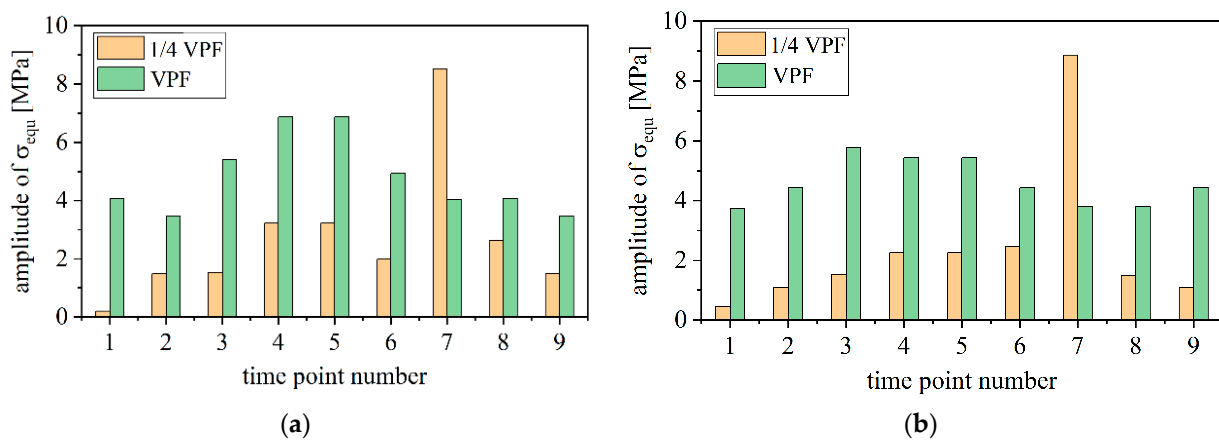


Figure 22. The dynamic stress amplitude of 1/4 VPF and VPF. (a) S3; (b) S5.

The modal analysis was performed to tell whether the sudden rise of 1/4 VPF was caused by resonance. The natural frequency of first mode is 95.95 Hz and the mode shape is shown in Figure 23. There is a nodal diameter in this mode shape, so it is usually marked as 1ND [28]. This is a common mode shape for most runners and other structure similar with the disc [29,30]. The rotating rate at TP7 is 489.24 rpm, and the value of 1/4 VPF is 32.62 Hz, far from 95.95 Hz. Therefore, the steeply increase of dynamic stress at TP7 is not the contribution of resonance.

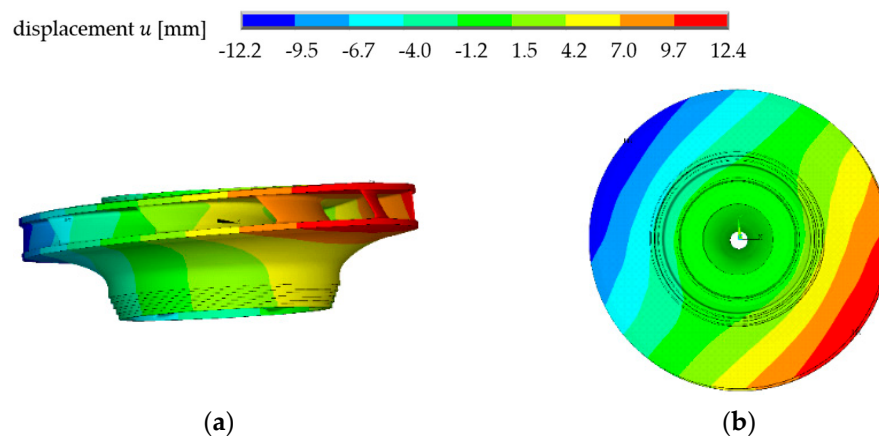


Figure 23. The mode shape of runner. (a) front view; (b) top view.

Then the effect of pressure fluctuation is taken into consideration. The amplitudes of two specific frequencies, 1/4 VPF and VPF at all time points were obtained and shown in Figure 24. For P1, VPF was the main frequency at most time points, as shown in Figure 24a. The pressure fluctuation induced by RSI and the vortex flow were violent in guide vane and runner. When it spread to clearances, the amplitude decreased. Thus, in most cases, the amplitude of P2 was far smaller than P1, as shown in Figure 24b. However, at TP7, the amplitude of 1/4 VPF was much greater than other time points. Considering the high-speed rotating flow in clearances and the approximately axial symmetry of clearances,

the amplitude of pressure fluctuation is similar in the circumferential direction. When the strength of pressure fluctuation in clearances is enough, it can have a great influence on the dynamic stress of runner. At other time points, the strength of pressure fluctuation in clearance is low, the dynamic stress is mainly affected by the pressure fluctuation in runner.

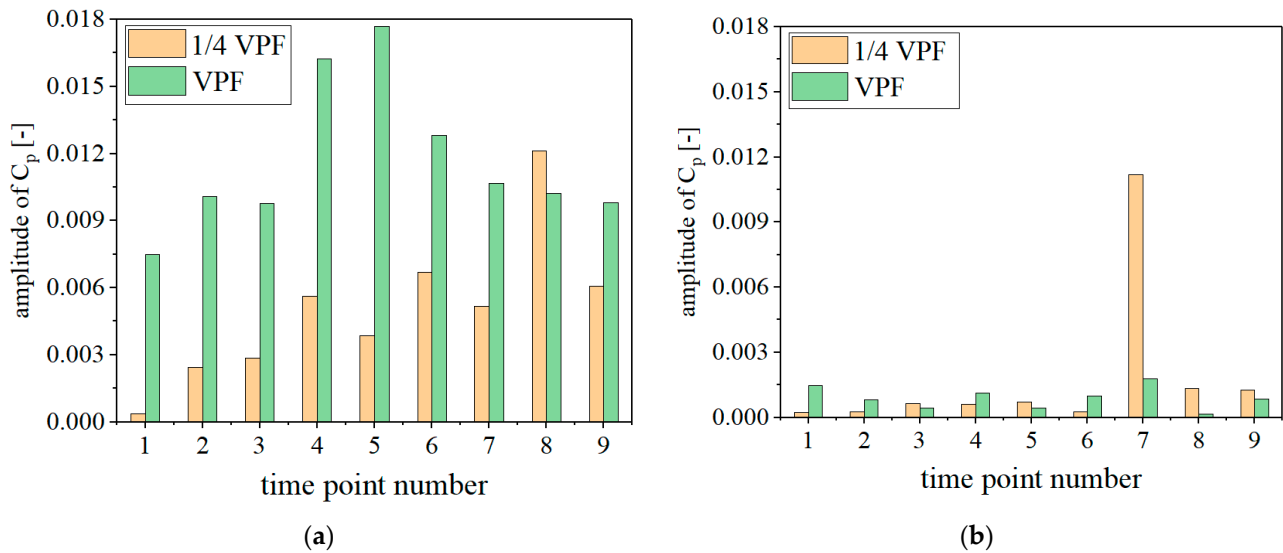


Figure 24. The pressure fluctuation amplitude at 1/4 VPF and VPF. (a) P1; (b) P2.

The low frequency component such as 1/4 VPF in clearance may come from the vortex generation and shedding process or the stochastic events as mentioned in Ref. [12]. The reasons of the sudden increase of 1/4 VPF pressure fluctuation will be discussed in further work.

5. Conclusions

The dynamic stresses of pump-turbine runner during start-up process in turbine mode were calculated in this paper. The coupling of 1D pipeline and 3D pump-turbine unit was conducted to obtain the performance characteristics and internal flow characteristics of the unit during the transient process. The dynamic stresses of runner were simulated using one-way FSI method. The influence of both inner surface and outer surface was taken into consideration in the interaction of fluid and structure. The conclusions are as follows:

(1) The start-up process was divided into three stages in this paper. In the first stage the discharge and hydraulic torque rise up, the runner is accelerated. In the second stage, rotating rate reaches the rated value, the guide vane begins to close, and the hydraulic torque of blades decreases gradually to zero. Finally, in the third stage, the unit stabilizes in speed-no-load condition.

(2) In the first stage of start-up, the maximum stress could be generated at the fillets of leading edge and band, and can reach 3.56 times of rated working condition. It was mainly induced by the increasing torque on blades and the large axial forces of crown and band. Moreover, as rotating rate rise, the centrifugal force and fluid shear stress in clearance increases. As a result, stress of the ring near fixed support quickly increased in first stage and was finally maximized in contrast with other parts of runner in the second and third stage.

(3) The amplitude of dynamic stresses could be maximized at the fillets of leading edge and band. In most of time during start-up, the dynamic stress was mainly characterized by VPF due to the RSI, which was the determining factor causing pressure fluctuation. However, the severe pressure fluctuation in clearance was found in the second stage with the main frequency of 1/4 VPF. It can also be a leading factor of dynamic stresses in a short

time. Therefore, the pressure fluctuation in clearance should be taken into consideration in the stage of runner design.

In this paper, the added mass and transient integral effect were not taken into consideration. Their influence on the dynamic stresses in start-up process will be studied in further work.

Author Contributions: Methodology, Z.W.; investigation, F.C.; validation, H.B. writing—original draft preparation, F.C.; writing—review and editing, S.-H.A., Z.M., and Y.L.; funding acquisition, Z.W. All authors have read and agreed to the published version of the manuscript.

Funding: This research was funded by National Key R&D Program of China, grant number 2016YFC0401905 and National Natural Science Foundation of China, grant number 51909131.

Institutional Review Board Statement: Not applicable.

Informed Consent Statement: Not applicable.

Data Availability Statement: Not applicable.

Acknowledgments: Special thanks are due to the Construction and Management Branch of CSG Power Generation Co. Ltd.

Conflicts of Interest: The authors declare no conflict of interest.

References

- Li, D.Y.; Gong, R.Z.; Wang, H.J.; Wei, X.Z.; Liu, Z.S.; Qin, D.Q. Analysis of Rotor-Stator Interaction in Turbine Mode of a Pump-Turbine Model. *J. Appl. Fluid Mech.* **2016**, *9*, 2559–2568. [[CrossRef](#)]
- Frunzăverde, D.; Muntean, S.; Mărginean, G.; Campian, V.; Marsavina, L.; Terzi, R. Failure analysis of a Francis turbine runner. *IOP Conf. Ser. Earth Environ. Sci.* **2010**, *12*, 012115. [[CrossRef](#)]
- Egusquiza, E.; Valero, C.; Huang, X.; Jou, E.; Guardo, A.; Rodriguez, C. Failure investigation of a large pump-turbine runner. *Eng. Fail. Anal.* **2012**, *23*, 27–34. [[CrossRef](#)]
- Egusquiza, M.; Egusquiza, E.; Valentin, D.; Valero, C.; Presas, A. Failure investigation of a Pelton turbine runner. *Eng. Fail. Anal.* **2017**, *81*, 234–244. [[CrossRef](#)]
- Wang, H.; Tsukamoto, H. Fundamental Analysis on Rotor-Stator Interaction in a Diffuser Pump by Vortex Method. *ASME J. Fluids Eng.* **2001**, *123*, 737–747. [[CrossRef](#)]
- Kubota, Y.; Suzuki, T.; Tomita, H.; Nagafugi, T.; Okamura, C. Vibration of rotating bladed disc excited by stationary distributed forces. *Bull. JSME* **1983**, *26*, 1952–1957. [[CrossRef](#)]
- Seidel, U.; Hübner, B.; Löfflad, J.; Faigle, P. Evaluation of RSI-induced stresses in Francis runners. *IOP Conf. Ser. Earth Environ. Sci.* **2012**, *15*, 5. [[CrossRef](#)]
- Bouajila, S.; De Colombel, T.; Lowys, P.Y.; Maitre, T. Hydraulic Phenomena Frequency Signature of Francis Turbines Operating in Part Load Conditions. *IOP Conf. Ser. Earth Environ. Sci.* **2016**, *48*, 082001. [[CrossRef](#)]
- Ausoni, P.; Farhat, M.; Escaler, X.; Egusquiza, E.; Avellan, F. Cavitation Influence on von Kármán Vortex Shedding and Induced Hydrofoil Vibrations. *ASME J. Fluids Eng.* **2007**, *129*, 966–973. [[CrossRef](#)]
- Nennemann, B.; Morissette, J.F.; Chamberland-Lauzon, J.; Monette, C.; Braun, O.; Melot, M. Challenges in Dynamic Pressure and Stress Predictions at No-Load Operation in Hydraulic Turbines. *IOP Conf. Ser. Earth Environ. Sci.* **2014**, *22*, 032055. [[CrossRef](#)]
- Mende, C.; Weber, W.; Seidel, U. Progress in load prediction for speed-no-load operation in Francis turbines. *IOP Conf. Ser. Earth Environ. Sci.* **2016**, *49*, 062017. [[CrossRef](#)]
- Morissette, J.F.; Chamberland-Lauzon, J.; Nennemann, B.; Monette, C.; Giroux, A.M.; Coutu, A. Stress predictions in a Francis turbine at no-load operating regime. *IOP Conf. Ser. Earth Environ. Sci.* **2016**, *49*, 072016. [[CrossRef](#)]
- Botero, F.; Hasmatuchi, V.; Roth, S.; Farhat, M. Non-intrusive detection of rotating stall in pump-turbines. *Mech. Syst. Signal Process.* **2014**, *48*, 162–173. [[CrossRef](#)]
- Nicolle, J.; Giroux, A.M.; Morissette, J.F. CFD configurations for hydraulic turbine startup. *IOP Conf. Ser. Earth Environ. Sci.* **2014**, *22*, 032021. [[CrossRef](#)]
- Pacot, O.; Kato, C.; Guo, Y.; Yamade, Y.; Avellan, F. Large Eddy Simulation of the Rotating Stall in a Pump-Turbine Operated in Pumping Mode at a Part-Load Condition. *J. Fluids Eng.* **2016**, *138*, 111102. [[CrossRef](#)]
- Hasmatuchi, V.; Farhat, M.; Roth, S.; Botero, F.; Avellan, F. Experimental Evidence of Rotating Stall in a Pump-Turbine at Off-Design Conditions in Generating Mode. *J. Fluids Eng.* **2011**, *133*, 5. [[CrossRef](#)]
- Li, D.; Gong, R.; Wang, H.; Wei, X.; Liu, Z.; Qin, D. Numerical investigation on transient flow of a high head low specific speed pump-turbine in pump mode. *J. Renew. Sustain. Energy* **2015**, *7*, 063111. [[CrossRef](#)]
- Fu, X.; Li, D.; Wang, H.; Zhang, G.; Li, Z.; Wei, X. Influence of the clearance flow on the load rejection process in a pump-turbine. *Renew. Energy* **2018**, *127*, 310–321. [[CrossRef](#)]

19. Fu, X.; Li, D.; Wang, H.; Zhang, G.; Li, Z.; Wei, X. Analysis of transient flow in a pump-turbine during the load rejection process. *J. Mech. Sci. Technol.* **2018**, *32*, 2069–2078. [[CrossRef](#)]
20. Li, D.; Wang, H.; Li, Z.; Nielsen, T.K.; Goyal, R.; Wei, X. Transient characteristics during the closure of guide vanes in a pump turbine in pump mode. *Renew. Energy* **2018**, *118*, 973–983. [[CrossRef](#)]
21. Jintao, L.; Shuhong, L.; Yuekun, S.; Yulin, W.; Leqin, W. Three dimensional flow simulation of load rejection of a prototype pump-turbine. *Eng. Comput.* **2012**, *29*, 417–426. [[CrossRef](#)]
22. Li, Z.; Bi, H.; Wang, Z.; Yao, Z. Three-dimensional simulation of unsteady flows in a pump-turbine during start-up transient up to speed no-load condition in generating mode. *Proc. Inst. Mech. Eng. Part A J. Power Energy* **2016**, *230*, 570–585. [[CrossRef](#)]
23. Zuo, Z.; Fan, H.; Liu, S.; Wu, Y. S-shaped characteristics on the performance curves of pump-turbines in turbine mode—A review. *Renew. Sustain. Energy Rev.* **2016**, *60*, 836–851. [[CrossRef](#)]
24. Huang, X.; Chamberland-Lauzon, J.; Oram, C.; Klopfer, A.; Ruchonnet, N. Fatigue analyses of the prototype Francis runners based on site measurements and simulations. *IOP Conf. Ser. Earth Environ. Sci.* **2014**, *22*, 012014. [[CrossRef](#)]
25. He, L.; Zhou, L.; Ahn, S.-H.; Wang, Z.; Nakahara, Y.; Kurosawa, S. Evaluation of gap influence on the dynamic response behavior of pump-turbine runner. *ENG Comput.* **2019**, *36*, 491–508. [[CrossRef](#)]
26. Shafieian, M.; Zavar, M.; Rahmadian, M. Simulation and Control of Surge Phenomenon in Centrifugal Compressors. *Traitement Signal* **2019**, *36*, 259–264. [[CrossRef](#)]
27. Jin, Y.; Fu, Y.; Qian, Y.; Zhang, Y. A Moore-Greitzer Model for Ducted Fans in Ground Effect. *J. Appl. Fluid Mech.* **2020**, *13*, 693–701. [[CrossRef](#)]
28. Egusquiza, E.; Valero, C.; Liang, Q.; Coussirat, M.; Seidel, U. Fluid Added Mass Effect in the Modal Response of a Pump-Turbine Impeller. In Proceedings of the ASME 2009 International Design Engineering Technical Conferences and Computers and Information in Engineering Conference (IDETC/CIE2009), San Diego, IL, USA, 30 August–2 September 2009; Volume 1, pp. 715–724.
29. Valentín, D.; Presas, A.; Egusquiza, E.; Valero, C. Experimental study on the added mass and damping of a disk submerged in a partially fluid-filled tank with small radial confinement. *J. Fluids Struct.* **2014**, *50*, 1–17. [[CrossRef](#)]
30. Valentín, D.; Presas, A.; Egusquiza, E.; Valero, C.; Egusquiza, M. Experimental Study of a Vibrating Disk Submerged in a Fluid-Filled Tank and Confined with a Nonrigid Cover. *J. Vib. Acoust.* **2017**, *139*, 436. [[CrossRef](#)]

Article

Optimization of a Wavy Microchannel Heat Sink with Grooves

Min-Cheol Park, Sang-Bum Ma and Kwang-Yong Kim * 

Department of Mechanical Engineering, Inha University, Incheon 22212, Korea; pjch0825@naver.com (M.-C.P.); sbma@kitech.re.kr (S.-B.M.)

* Correspondence: kykim@inha.ac.kr; Tel.: +82-32-860-7317

Abstract: In this study, a wavy microchannel heat sink with grooves using water as the working fluid is proposed for application to cooling microprocessors. The geometry of the heat sink was optimized to improve heat transfer and pressure loss simultaneously. To achieve optimization goals, the average friction factor and thermal resistance were used as the objective functions. Three dimensionless parameters were selected as design variables: the distance between staggered grooves, groove width, and groove depth. A modified Latin hypercube sampling (LHS) method that combines the advantages of conventional LHS and a three-level full factorial method is also proposed. Response surface approximation was used to construct surrogate models, and Pareto-optimal solutions were obtained with a multi-objective genetic algorithm. The modified LHS was proven to have better performance than the conventional LHS and full factorial methods in the present optimization problem. A representative optimal design showed that both the thermal resistance and friction factor improved by 1.55% and 3.00%, compared to a reference design, respectively.

Keywords: microchannel heat sink; wavy microchannel; groove; heat transfer performance; laminar flow; multi-objective optimization; LHS; full factorial methods



Citation: Park, M.-C.; Ma, S.-B.; Kim, K.-Y. Optimization of a Wavy Microchannel Heat Sink with Grooves. *Processes* **2021**, *9*, 373. <https://doi.org/10.3390/pr9020373>

Academic Editor: Fabrizio Scala

Received: 16 January 2021

Accepted: 15 February 2021

Published: 18 February 2021

Publisher's Note: MDPI stays neutral with regard to jurisdictional claims in published maps and institutional affiliations.



Copyright: © 2021 by the authors. Licensee MDPI, Basel, Switzerland. This article is an open access article distributed under the terms and conditions of the Creative Commons Attribution (CC BY) license (<https://creativecommons.org/licenses/by/4.0/>).

1. Introduction

Microprocessors generate high heat flux and thermally interact with their surroundings. Because they are composed of many integrated components, their efficiency and performance are significantly influenced by temperature. The temperature must be kept between 363 K and 383 K to maintain the best performance [1]. Therefore, it is essential to develop an effective cooling system to maintain a proper temperature even with high heat generation.

Cooling systems are being made less noisy and smaller, and it is estimated that heat sinks capable of cooling at more than 1000 W/cm² will be required in the near future [2]. Both air and water can be used for cooling systems, but as the heat generation increases with the development of microprocessors, air cooling systems have a limitation in maintaining effective cooling performance [1]. In addition, to increase air-cooling performance, the fan speed must be increased, which increases noise.

Water-cooling microchannel heat sinks have been widely used to reduce noise and meet increased requirements for cooling. Numerical and experimental studies on these heat sinks have been actively conducted. Tuckerman and Pease [3] experimented with a microchannel heat sink consisting of straight channels with heat flux of 790 W/cm² using water as a coolant. They confirmed that the water had great heat transfer characteristics. Wang et al. [4] carried out experiments and numerical analyses on a microchannel heat sink consisting of straight channels with ribs and grooves. They found that secondary flows occurring behind the ribs and grooves prevented the formation of the thermal boundary layer and promoted fluid mixing and heat transfer.

Ansari et al. [5] and Farhanieh et al. [6] investigated the cooling performance of straight microchannels with grooves. They found that the interfacial area of heat transfer is increased by the grooves, thereby increasing the cooling performance. Ansari et al. [5]

suggested that high local Nusselt numbers are obtained near the upstream and downstream regions of the groove structures. Farhanieh et al. [6] confirmed that although the heat transfer performance was low due to recirculating flow in the grooved area, the groove structure prevented the formation of the thermal boundary layer, enhancing the overall heat transfer performance.

Greiner et al. [7] evaluated the friction coefficient and cooling performance of flow paths with triangular grooves through experimental and numerical analyses. In the case of laminar flow, the friction coefficient decreased as the hydraulic diameter was increased by the grooves. As the Reynolds number increased, the flow over the triangular grooves became more complex. Consequently the heat transfer performance improved. Xie et al. [8] confirmed that in the case of grooved channels, the heat transfer performance improved in the area, where the fluid velocity increased due to the narrowed channel.

Recently, some studies were performed on curved microchannel heat sinks [9,10]. Gong et al. [9] proposed wavy microchannels for a heat sink and studied its cooling performance. They found that the wavy microchannel heat sink caused a vortex at the trough and crest sections in each cycle, resulting in a significant improvement in cooling performance compared to a straight-microchannel heat sink. The pressure losses did not increase significantly. Sui et al. [10] investigated a wavy microchannel heat sink for various flow conditions and amplitudes. They compared three-dimensional numerical analyses and experiments in all cases. The numerical results of the cooling performance and friction coefficient were reliable, and vortices were developed at the trough and crest sections in each cycle.

With the rapid development of computing power, optimization designs that can handle a huge amount of data have become practical [11–13]. In particular, optimization based on a surrogate model has been widely used to reduce the computing time [14–16]. A surrogate model is constructed using sample data at several selected points in the design space. Design of experiments (DOE) is used to extract the sample data. The prediction accuracy of surrogate models is affected by the sample data, so DOE should be carried out carefully [17]. DOE can typically be classified into two categories according to the extraction method: factorial design [18] based on orthogonal extraction and Latin hypercube sampling (LHS) [19], which uses random extraction.

Factorial designs are experiments that combine all levels of each factor with all levels of all other factors in an experiment [18]. This method is very intuitive, and the number of sample data is determined by the number of design variables. Therefore, it is easy to use because it can be applied without considering the distribution and number of sample data. However, the features within the design space are considered less because the sample data are focused on the boundaries of the design space.

LHS uses a random extraction method for sample points within the design space. This method is widely used because the space-filling quality of the sampling points is good. In addition, it can create any allotted number of sampling points [19]. However, since LHS extracts sample data inside the design space, the boundary values of each design variable are not considered. Therefore, a surrogate model based on LHS often makes predictions that are too high at the bounds of design variables.

In the present work, a modified LHS that uses the advantages of orthogonal and random extraction methods is proposed. The modified LHS extracts sample data by applying LHS inside the design space and prevents excessive prediction of the surrogate model by applying the three-level full factorial method to the boundaries of the design space. A wavy microchannel heat sink improves the heat transfer efficiency compared with straight microchannels. In this study, a wavy microchannel heat sink with grooves attached to the channel walls is proposed. A numerical analysis of the laminar flow and heat transfer in the microchannels was performed using three-dimensional Navier-Stokes equations.

Multi-objective optimization of the wavy microchannels was also performed to simultaneously enhance the heat transfer efficiency and reduce the pressure loss. The proposed modified LHS was compared with conventional DOE methods to determine the effec-

tiveness of the proposed sampling method in constructing surrogate models. For the optimization, response surface approximation (RSA) [20] and a genetic algorithm [21] were used as a surrogate model and searching algorithm, respectively.

2. Numerical Analysis

The computational domain and design variables are shown in Figure 1. The heat sink consists of 62 wavy microchannels, and the computational domain includes one of them, which is composed of 10 cycles. Two grooves are attached to each channel wall in one cycle of the channel, as shown in Figure 1. The amplitude of the wavy channel is $138\ \mu\text{m}$, and the total length ($20P$) is $25,000\ \mu\text{m}$. The thickness of the side wall ($2t$) is $193\ \mu\text{m}$, the channel width (W) is $207\ \mu\text{m}$, and the height of the flow path (h) is $406\ \mu\text{m}$.

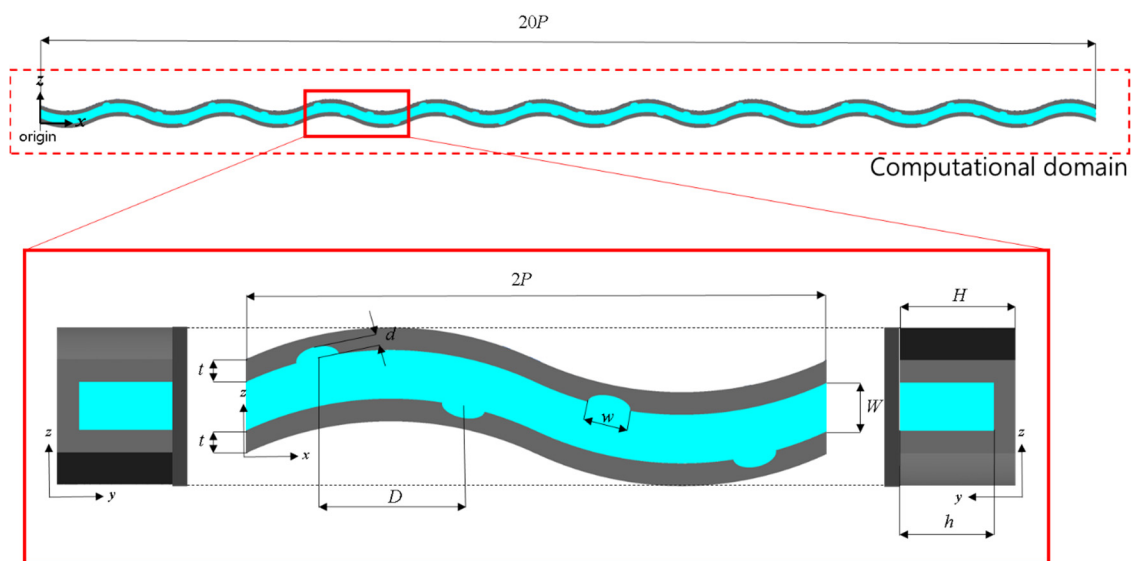


Figure 1. Geometry of the wavy microchannel with grooves and computational domain comprising 10 cycles of wavy channel.

The information for the reference channel is shown in Table 1. In the reference channel, the horizontal locations of grooves on both the walls are the same ($D = 0$). Grooves are attached to crests and troughs when $D = 0$. As D increases, grooves on the left wall (located at $z = 406\ \mu\text{m}$ in Figure 1) move in the $-x$ direction, and grooves on the right wall (located at $z = 0$ in Figure 1) move in the $+x$ direction from a crest (or a trough).

Table 1. Dimensions of the reference wavy channel with grooves.

Parameter	Value (μm)
Width of channel, W	207
Wall thickness of channel, $2t$	193
Length of channel	25,000
Half of wave length, P	1250
Depth of groove, d	48.5
Width of groove, w	187.5
Distance between staggered grooves, D	0.0
Amplitude of channels	138
Height of flow path, h	406
Height of microchannel, H	502.5

Conjugate heat transfer analysis was carried out on the flow channel and solid domain for laminar flow in steady state using three-dimensional Navier-Stokes equations. The commercial computational fluid dynamics code ANSYS CFX 15.0[®] (Version 15.0, ANSYS Inc., Canonsburg, PA, USA, 2013) [22] was used for the analysis. The boundary conditions are shown in Figure 2. The boundary conditions were used in the same way as in a previous study [10]. The working fluid was water at 300 K, and the material of the solid wall was copper.

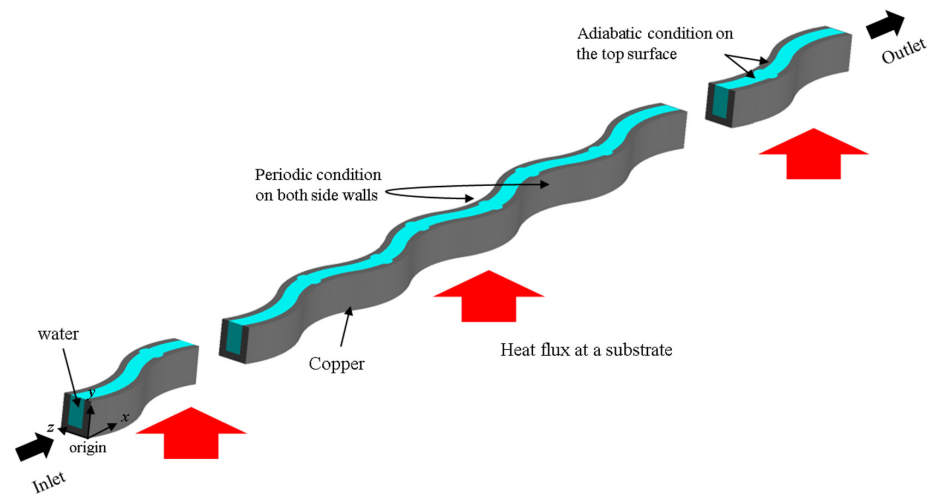


Figure 2. Boundary conditions.

The inlet Reynolds number ($Re = \rho U D_h / \mu$) was 700, and the corresponding flow rate was assigned at the inlet. The average velocity of water at the inlet is 1.992 m/s. The static pressure was used as an exit boundary condition. Periodic conditions for temperature were applied to both side boundaries (i.e., wavy surfaces) considering the neighboring microchannels. Uniform heat flux conditions (50 W/cm^2) were applied to the bottom boundary (substrate), and the upper boundary was assumed to be adiabatic.

The fluid and solid computational domains consist of hexahedral and unstructured tetrahedral meshes, respectively. Since the flow velocity changes near the groove, dense meshes are placed there. Near the solid wall, dense meshes were also placed in anticipation of large temperature and velocity gradients due to the boundary layer. Figure 3 shows an example of the grid system. Convergence conditions were set so that the root-mean-squared residual values of all parameters fell to 1.00×10^{-6} . Each computation took about 5–6 h on a computer with an Intel Core i7–4790K 4GHz CPU.

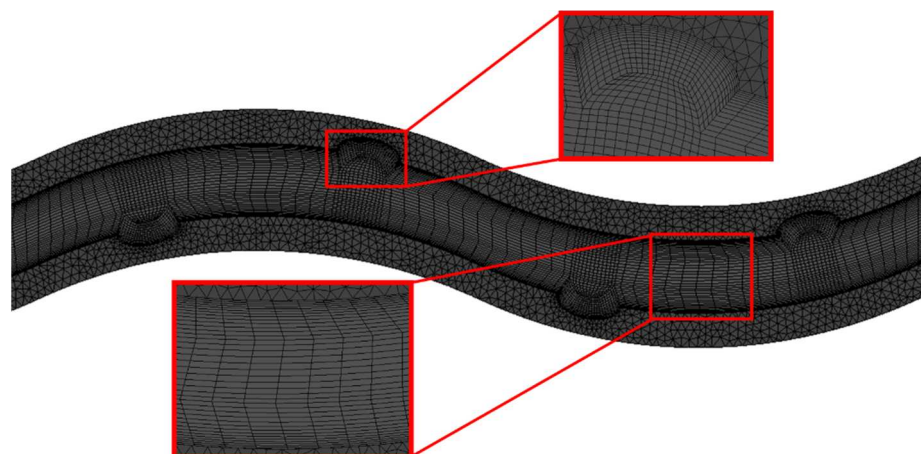


Figure 3. Example of a computational grid system on one cycle of wavy channel.

3. Optimization Procedure

The multi-objective optimization problem was formulated as follows:

Minimize: $\mathbf{F}(\mathbf{x}) = [F_1(\mathbf{x}), F_2(\mathbf{x})]$

Design variable bound: $\mathbf{LB} \leq \mathbf{x} \leq \mathbf{UB}, \mathbf{x} \in \mathbf{R}$,

where $\mathbf{F}(\mathbf{x})$ is the vector of real-valued objective functions, \mathbf{x} is a vector of the design variables, and \mathbf{LB} and \mathbf{UB} indicate the vectors of the lower and upper bounds, respectively [23]. Figure 4 shows a flowchart for the multi-objective genetic algorithm (MOGA) optimization process using a surrogate model. Firstly, the objective functions and constraints are defined according to the design goals. Secondly, the design variables and their ranges are selected.

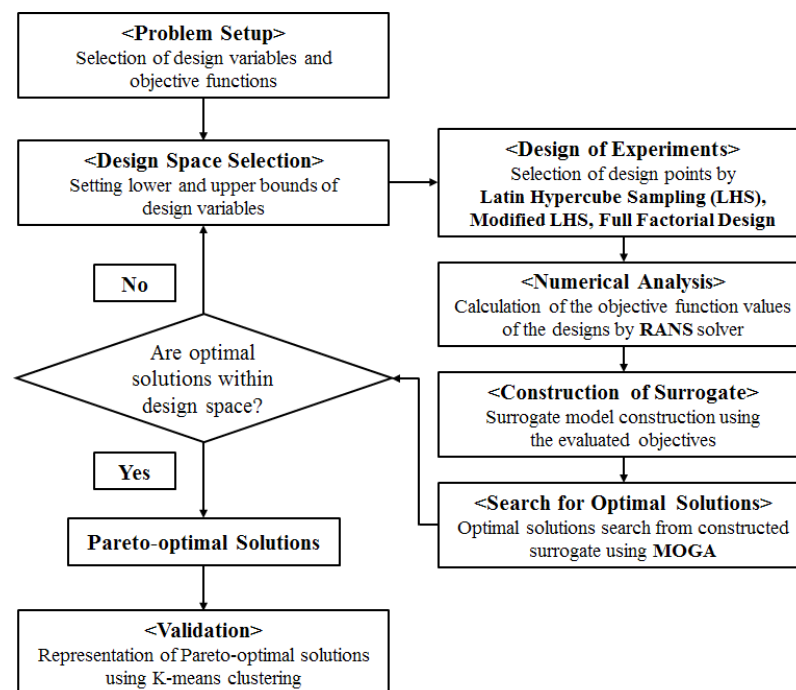


Figure 4. Multi-objective optimization procedure.

The full factorial method, LHS, and modified LHS were used in DOE to select design points (i.e., sample designs). Values of the objective functions were evaluated by numerical analysis at these design points. Next, to approximate the objective functions, surrogate models were constructed using these objective function values. A genetic algorithm (GA) was used to find the global optima. Finally, Pareto-optimal solutions (a collection of non-dominated solutions) were derived using MATLAB (Release 14, the Math Work Inc., Natick, MA, USA, 2004) [24].

3.1. Design Variables and Objective Functions

For optimization, three geometric parameters were selected as the design variables through a preliminary parametric study: the ratio of the groove depth to half of the side wall thickness (d/t), the ratio of the groove width to half of the cycle length (w/P), and the distance between staggered grooves on the opposite walls to half of the cycle length (D/P). The depth and width of the grooves were expected to affect the vortices occurring around the grooves and thus have sensitive effects on the heat transfer. The distance between staggered grooves affects the disturbance of the main flow.

The average Nusselt number \overline{Nu} is defined as follows [10]:

$$\overline{Nu} = \frac{\overline{h}D_h}{k_w} \quad (1)$$

where D_h is the hydraulic diameter of the microchannel, and k_w is the thermal conductivity of water. \bar{h} is the average convective heat transfer coefficient, which is defined as follows:

$$\bar{h} = \frac{q}{(A_b + 2A_s)(T_w - T_m)} \quad (2)$$

where q is the heat flux, A_b and A_c are the bottom area and the side area of the flow channel, and T_w and T_m are the average temperature at the solid wall and the average of the inlet and outlet temperatures, respectively.

The friction factor f is defined as follows [10]:

$$f = \frac{(dp/dx)D_h}{0.5\rho U^2} \quad (3)$$

where dp , ρ , and U are the pressure difference between the inlet and outlet, the density of water, and the average velocity at the inlet, respectively. The thermal resistance R_{th} is defined as follows [5]:

$$R_{th} = \frac{T_{s,max} - T_{f,inlet}}{qA} \quad (4)$$

where $T_{s,max}$ and $T_{f,inlet}$ are the highest temperature at the bottom substrate and the average temperature of the cooling fluid at the inlet, respectively, and A is the area of the microchannel substrate. The local Nusselt number (Nu_x) is defined as follows:

$$Nu_x = \frac{q_l D_h}{(T_{w,l} - T_{f,inlet})k_w} \quad (5)$$

where q_l and $T_{w,l}$ are the local heat flux and local temperature at the surface of the solid wall, respectively.

R_{th} and f were selected as objective functions for the multi-objective optimization: $F_{Rth} = R_{th}$ and $F_f = f$. The thermal resistance R_{th} is related to the highest local temperature, which affects the performance of micro devices. The friction factor f was used to reduce the pressure drop through the microchannel. A parametric study was carried out for the performance functions using three design variables: D/P , w/P , and d/t . Based on the parametric study, the ranges of the three design variables were selected, as shown in Table 2.

Table 2. Ranges of design variables.

	d/t	w/P	D/P
Lower bound	0.1	0.05	−1.0
Reference	0.5	0.15	0
Upper bound	0.9	0.25	1.0

3.2. Modified LHS

Factorial design [18,25] is a classical DOE method that explores the design space. 2-level and 3-level full factorial designs are widely used to estimate interactions between design variables. Figure 5 shows examples of 2- and 3-level full factorial designs for two design variables. In the 2-level full factorial design, the sample points are located at the ends of each boundary, as shown in Figure 5a. In the 3-level full factorial design, the sample points are located at the ends and middle of each boundary, as shown in Figure 5b. In these full factorial designs, the distribution and number of the sample points are determined according to the number of design variables when the level is determined.

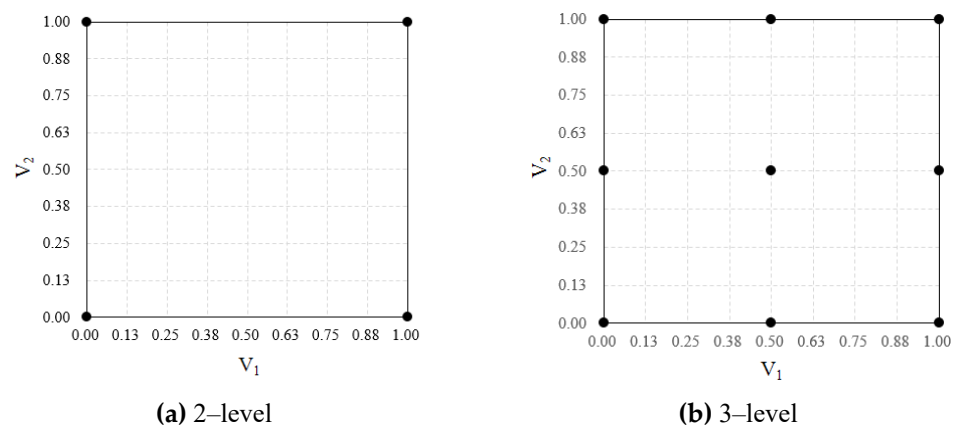


Figure 5. Examples of the full factorial designs.

LHS [19] is one of the most popular DOE methods for random sample distributions. To allocate p samples using LHS, the range of each parameter is separated into p bins, which yields a total number of p^n bins for n design variables in the design space. The samples are randomly chosen in the design space, each sample is randomly arranged inside a bin, and for all one-dimensional projections of the p samples and bins, there is exactly one sample in each bin, as shown in Figure 6. Therefore, LHS is relatively incapable of handling samples at the boundaries of the design space compared to the full factorial designs.

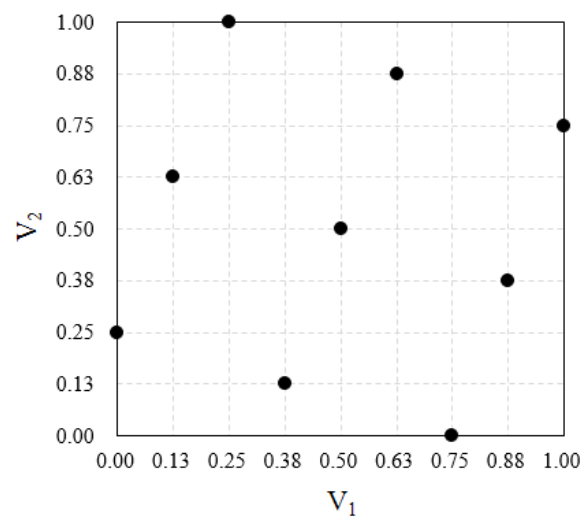


Figure 6. Example of conventional LHS.

Since the surrogate model is built using the data at the sample points, the distribution of the sample points has a very significant influence on the prediction accuracy of the surrogate model. Therefore, when using LHS with sample points concentrated inside the design space, it is possible to predict the interaction well inside the design space, but predictions that are too high may occur at the boundaries where there are no data. On the other hand, in the full factorial design, the sample points are focused on the boundaries of the design space, so it is possible to make a relatively accurate prediction at the boundaries, but there is a problem in the prediction inside the design space.

To solve this problem, a modified LHS is proposed. In the modified LHS, sample points are extracted using the 2-level full factorial method at the boundaries of the design space, and the LHS method is used to select sample points inside the design space. An example of the modified LHS for two design variables is shown in Figure 7. In this method, the surrogate model does not show high predictions at the boundaries of the design space. Furthermore, by selecting the sample points inside the design space, the shortcomings of

the full factorial design can be overcome. MATLAB [24] was used to extract the sample points. Three-level full factorial design, LHS, and the modified LHS were tested for the same optimization problem. Twenty-seven sample points were extracted for all these DOE methods.

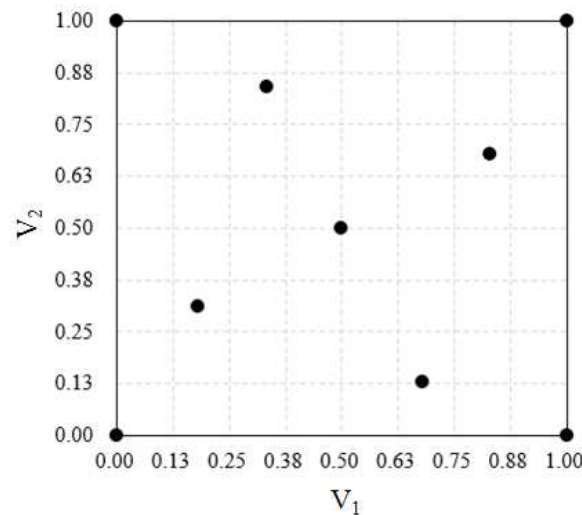


Figure 7. Example of the modified LHS.

3.3. Surrogate Model and Searching Algorithm

The surrogate model was configured based on the sample points obtained using DOE methods. Response surface approximation (RSA) [20] was used as the surrogate model. MOGA coupled with the RSA model was used to obtain Pareto-optimal solutions [24].

The RSA model is multivariate polynomial model, and a continuous response $y(x)$ is usually modeled as follows [20]:

$$y(x) = \sum_{j=1}^N \beta_j f_j(x) + \varepsilon, \quad E(\varepsilon) = 0, \quad V(\varepsilon) = \sigma^2 \quad (6)$$

where x is a vector of design variables, $f_j(x)$ ($j = 1, \dots, N$) are the terms of the model, β_j ($j = 1, \dots, N$) are the coefficients, and the error ε is assumed to be uncorrelated and distributed with a mean of 0 and constant variance [20]. A second-order polynomial is used for the RSA model, and the model can be expressed as follows:

$$y(x) = \beta_0 + \sum_{i=1}^N \beta_i x_i + \sum_{i=1}^N \beta_{ii} x_i^2 + \sum_{i < j}^N \beta_{ij} x_i x_j \quad (7)$$

The model involves an intercept, linear terms, quadratic interaction terms, and squared terms (from left to right). R^2 and R_{adj}^2 are used to decide the goodness of the fit and should be close to 1 for a good fit [20].

GA is a random global search technique that solves problems based on natural evolution. An initial population of individuals is defined to represent a part of the solution to a problem [21]. Before starting the search, a set of chromosomes is randomly selected from the design space to obtain the initial population. Through subsequent computations, the individuals adapt in a competitive way. The initially selected set of chromosomes is called the parental generation, and the subsequent selected set of chromosomes is called the child generation. In this process, genetic search operators (selection, mutation, and crossover) are used to obtain chromosomes that are superior to the previous generation [21]. MATLAB [24] was used to invoke the GA for multi-objective optimization.

4. Results and Discussion

4.1. Grid Dependency Test and Validation of Numerical Results

A grid dependency test was carried out for the reference shape based on Richardson's extrapolation method and grid convergence index (GCI), which represents numerical uncertainty by estimating the discretization error according to the procedure presented by Roache [26] and Celik and Karatekin [27].

Table 3 shows the results of calculating the discretization error for \overline{Nu} . The number of grid nodes was adjusted by setting the grid segmentation index to 1.3, and three different grid systems were analyzed. When N_2 was used, the extrapolation error (e_{ext}^{21}) was about 0.3%, and GCI_{fine}^{21} was about 0.4%, which indicate small numerical uncertainty. Therefore, N_2 was selected as the optimal grid system.

Table 3. Analysis of grid convergence index.

Parameter		Value
Number of cells	N_1	2.58×10^6
	N_2	2.37×10^6
	N_3	2.22×10^6
Grid refinement factor	r	1.3
Computed efficiency (\overline{Nu}) corresponding to N_1, N_2, N_3	\overline{Nu}_1	20.09
	\overline{Nu}_2	20.02
	\overline{Nu}_3	19.88
Apparent order	P	2.90
Extrapolated values	φ_{ext}^{21}	20.15
Approximate relative error	e_{α}^{21}	$3.35 \times 10^{-1}\%$
Extrapolated relative error	e_{ext}^{21}	$2.93 \times 10^{-1}\%$
Grid convergence index	GCI_{fine}^{21}	$3.68 \times 10^{-1}\%$

To verify the numerical results, they were compared with experimental data obtained by Sui et al. [10] for the Nusselt number and friction factor in a wavy microchannel under the same boundary conditions, as shown in Figure 8. As shown in Figure 8, the numerical results for the friction factor show good agreement with the experimental data, except at the lowest Reynolds number. The numerical results for the Nusselt number deviate slightly from the experimental data over the whole Re range but show the same qualitative tendency. At $Re = 300$, the errors are relatively large because the pressure drop and the flow rate are relatively small, as discussed by Sui et al. [10].

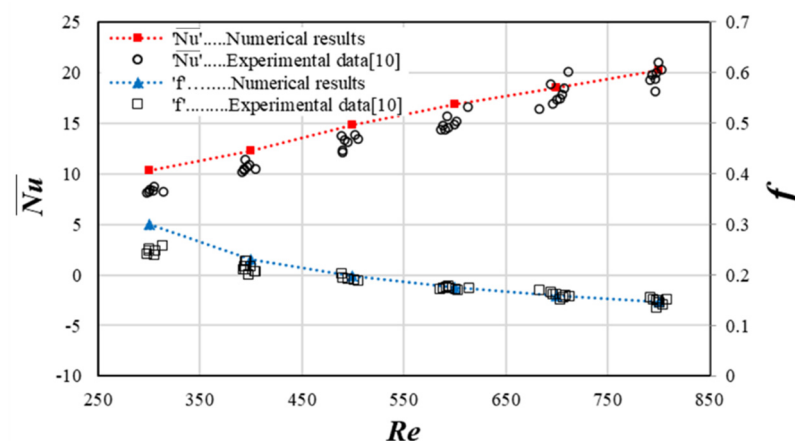


Figure 8. Validation of numerical results compared with experimental data [10].

4.2. Heat Transfer Performance Enhancement by Grooves

Table 4 shows the comparison of the performance parameters between the smooth and reference wavy microchannels. In the wavy channel with grooves, \overline{Nu} increased by about 8.34%, and R_{th} decreased by about 2%, but the friction factor f also increased by about 1.25% in comparison with the smooth wavy channel. This means that the grooves largely enhance the heat transfer but with less increase in the friction. This improvement in the heat sink performance with grooves is expected to be further increased by optimization.

Table 4. Performance comparison between reference and smooth wavy microchannels.

	Performance Function		
	\overline{Nu}	R_{th} (K/W)	f
Reference microchannel	20.02	4.58	1.61×10^{-1}
Smooth microchannel	18.48	4.67	1.59×10^{-1}

The temperature distributions on the wavy wall on the right side of the reference and smooth microchannels are shown in Figure 9. In the case of the reference design, it can be seen that the temperature increase in the flow direction is smaller than that of the smooth microchannel, resulting in lower maximum temperature. This shows improved heat transfer performance on the sidewalls and confirms the results shown in Table 4.

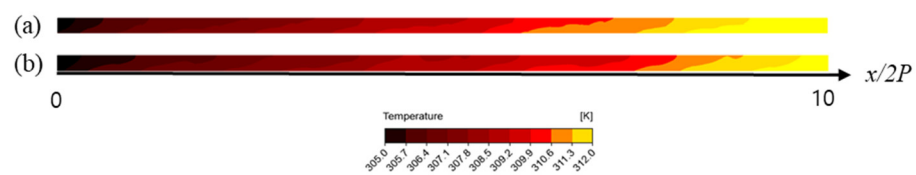


Figure 9. Temperature distributions on a right side wall: (a) smooth microchannel and (b) reference design.

The local Nusselt number (Nu_x) distributions on the wavy side walls are shown in Figure 10. High Nu_x regions are found between the crest and the trough (e.g., $x/2P = 5.75$ – 6.25) on the left wall, but they are found between a trough and crest (e.g., $x/2P = 6.25$ – 6.75) on the right wall. In addition, most of the high Nu_x regions are distributed near the top and bottom of the flow path. In the case of the smooth microchannel, a low Nu_x region is found near the middle height of the flow path immediately after each crest (e.g., $x/2P = 5.75$). In the reference design, the high Nu_x regions are found just downstream of the grooves, and the total area of the high Nu_x regions is larger than that of the smooth channel. This results in high \overline{Nu} in the grooved microchannel, as shown in Table 4.

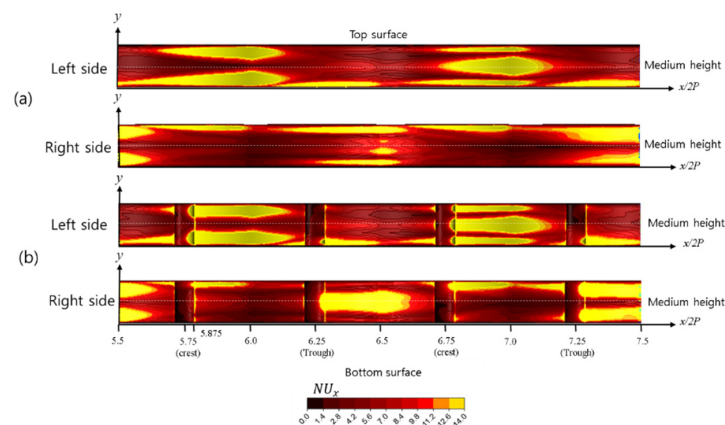


Figure 10. Local Nusselt number distributions on wavy walls: (a) smooth microchannel and (b) reference design.

Figure 11 shows the flow fields of the reference design and the smooth wavy microchannel. Figure 11a shows that the velocity gradients near the left wall are larger than those near the right wall between a crest and trough ($x/2P = 5.75-6.25$), but vice versa between the trough and crest ($x/2P = 6.25-6.75$). This phenomenon occurs due to the fluid inertia. The regions with high velocity gradients and those with high Nu_x shown in Figure 10 are nearly the same. Thus, it can be inferred that the high velocity gradient near the wall promotes the heat transfer and enhances Nu_x .

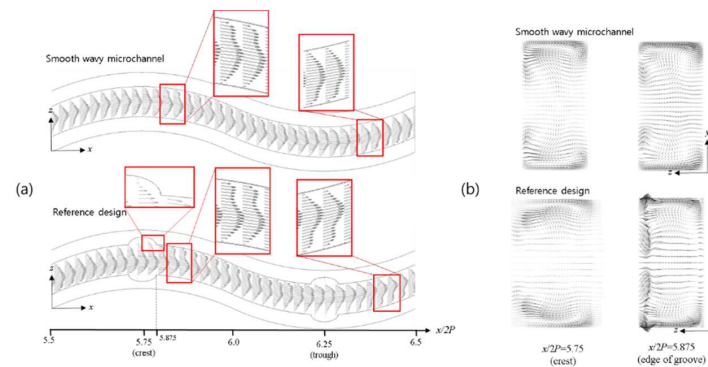


Figure 11. Velocity vectors on $x-z$ plane and $y-z$ plane (a) velocity vectors on the $x-z$ plane ($y/H = 0.6$) (b) velocity vectors on the $y-z$ plane.

Figure 11b shows the velocity vectors in the $y-z$ plane. Vortices are found near the top and bottom of the flow channel in the crest. In the case of the reference design with grooves, a complicated flow structure is found near the left wavy wall at the edge of a groove ($x/2P = 5.875$) due to the upward flow escaping from the groove, which promotes mixing of the fluid (and thereby heat transfer) in these regions. This is due to sudden contraction of the flow area just downstream of a groove and provides a reason for the high Nu_x regions downstream of the grooves shown in Figure 10b. Even though the grooves are at the same locations on both the wavy walls, the flow fields shown in Figure 11b are not symmetric in the z direction because the main flow upstream of the groove proceeds in the $+z$ direction.

Figure 12 shows the temperature distributions in the $y-z$ plane at the inflection point of the wavy channel ($x/2P = 6$). The temperature gradient is relatively small near the upper and lower sides of the flow path in common. This is thought to be due to the strong vortices shown in Figure 11b. These low temperature gradients also contribute to the distribution of high Nu_x in these regions (Figure 10). Figure 12 shows that the temperature on the left side in the reference design is still low, even at the medium height, unlike in the smooth wavy microchannel. This is due to the fluid mixing caused by the strong secondary flow downstream of the grooves.

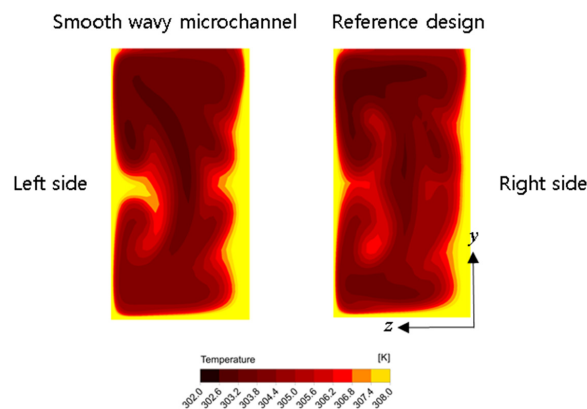


Figure 12. Temperature distributions at inflection point ($x/2P = 6$) in the $y-z$ plane.

4.3. Parametric Study

Figure 13 shows the results of the parametric study for \overline{Nu} , R_{th} , and f . When one parameter was changed, the other parameters were fixed at the reference values shown in Table 2. With the change of parameters, the friction factor f shows small variations of less than 2.5%. At $d/t = 0.5$, the maximum \overline{Nu} and f and minimum R_{th} are found, which indicates that there is an optimum groove depth for heat transfer enhancement.

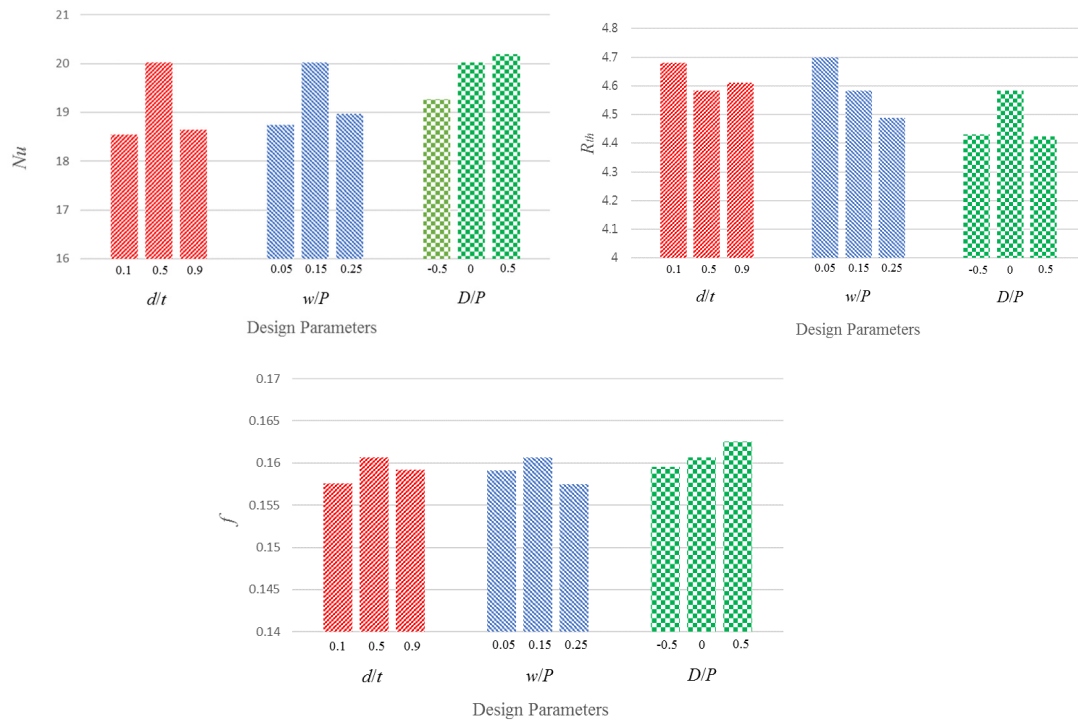


Figure 13. Results of the parametric study.

R_{th} and \overline{Nu} are inversely correlated with the variation of d/t . \overline{Nu} and f have maximum values at $w/P = 0.15$, but R_{th} has a minimum value at $w/P = 0.25$. R_{th} decreases as w/P increases in the tested range. This means that wide grooves are effective in reducing thermal resistance. In the case of D/P , \overline{Nu} and f increase as D/P increases, but R_{th} shows a maximum at $D/P = 0$ (non-staggered grooves). This indicates that if the absolute value of D is fixed, the relative locations of grooves between the two wavy walls do not affect R_{th} unlike \overline{Nu} and f .

At $D/P = 0.5$, \overline{Nu} shows the maximum value of 20.2. This is the value improved by 23.2% from the value ($\overline{Nu} = 16.4$) of the wavy microchannel heat sink without grooves predicted by Sui et al. [10] under the same geometric and Reynolds number conditions.

4.4. Optimization Results with Different DOEs

Figure 14 shows the distribution of sample points of three different DOEs. In Figure 14a, the 3-level full factorial design shows that the sample points are located on only the boundaries of the design space. In the case of the conventional LHS, the sample points are distributed in only the design space, as shown in Figure 14b. However, in the modified LHS, the sample points are located on the boundaries and inside of the design space, as shown in Figure 14c. The RSA models for the objective functions, F_f and $F_{R_{th}}$, were formulated in terms of the design variables normalized between 0 and 1 for three different DOEs as follows:

$$\begin{aligned}
F_{f_fullfactorial} &= 0.1591 + 0.0092\left(\frac{d}{s_w}\right) - 0.0120\left(\frac{D}{P}\right) - 0.0018\left(\frac{w}{P}\right) - 0.0025\left(\frac{d}{s_w}\right)\left(\frac{D}{P}\right) \\
&+ 0.0084\left(\frac{d}{s_w}\right)\left(\frac{w}{P}\right) - 0.0008\left(\frac{D}{P}\right)\left(\frac{w}{P}\right) - 0.0049\left(\frac{d}{s_w}\right)^2 + 0.0139\left(\frac{D}{P}\right)^2 \\
&- 0.0031\left(\frac{w}{P}\right)^2
\end{aligned} \quad (8)$$

$$\begin{aligned}
F_{R_{th_fullfactorial}} &= 4.6438 - 0.0086\left(\frac{d}{s_w}\right) + 0.2094\left(\frac{D}{P}\right) + 0.1187\left(\frac{w}{P}\right) \\
&+ 0.0703\left(\frac{d}{s_w}\right)\left(\frac{D}{P}\right) - 0.2730\left(\frac{d}{s_w}\right)\left(\frac{w}{P}\right) - 0.0409\left(\frac{D}{P}\right)\left(\frac{w}{P}\right) \\
&- 0.0403\left(\frac{d}{s_w}\right)^2 - 0.3249\left(\frac{D}{P}\right)^2 - 0.0534\left(\frac{w}{P}\right)^2
\end{aligned} \quad (9)$$

$$\begin{aligned}
F_{f_conventionalLHS} &= 0.1589 + 0.0099\left(\frac{d}{s_w}\right) - 0.0095\left(\frac{D}{P}\right) - 0.0050\left(\frac{w}{P}\right) \\
&- 0.0110\left(\frac{d}{s_w}\right)\left(\frac{D}{P}\right) + 0.0092\left(\frac{d}{s_w}\right)\left(\frac{w}{P}\right) + 0.0041\left(\frac{D}{P}\right)\left(\frac{w}{P}\right) \\
&- 0.0060\left(\frac{d}{s_w}\right)^2 + 0.0150\left(\frac{D}{P}\right)^2 + 0.0005\left(\frac{w}{P}\right)^2
\end{aligned} \quad (10)$$

$$\begin{aligned}
F_{R_{th_conventionalLHS}} &= 4.9136 - 1.0222\left(\frac{d}{s_w}\right) - 0.2633\left(\frac{D}{P}\right) - 0.4524\left(\frac{w}{P}\right) \\
&+ 0.9502\left(\frac{d}{s_w}\right)\left(\frac{D}{P}\right) - 0.4268\left(\frac{d}{s_w}\right)\left(\frac{w}{P}\right) - 0.2243\left(\frac{D}{P}\right)\left(\frac{w}{P}\right) \\
&+ 0.7657\left(\frac{d}{s_w}\right)^2 - 0.0067\left(\frac{D}{P}\right)^2 + 0.4980\left(\frac{w}{P}\right)^2
\end{aligned} \quad (11)$$

$$\begin{aligned}
F_{f_modifiedLHS} &= 0.1588 - 0.0082\left(\frac{d}{s_w}\right) - 0.0038\left(\frac{D}{P}\right) + 0.0074\left(\frac{w}{P}\right) \\
&- 0.0025\left(\frac{d}{s_w}\right)\left(\frac{D}{P}\right) + 0.0085\left(\frac{d}{s_w}\right)\left(\frac{w}{P}\right) - 0.0002\left(\frac{D}{P}\right)\left(\frac{w}{P}\right) \\
&+ 0.0137\left(\frac{d}{s_w}\right)^2 + 0.0048\left(\frac{D}{P}\right)^2 - 0.0118\left(\frac{w}{P}\right)^2
\end{aligned} \quad (12)$$

$$\begin{aligned}
F_{R_{th_modifiedLHS}} &= 4.6170 - 0.2504\left(\frac{d}{s_w}\right) + 0.5430\left(\frac{D}{P}\right) - 0.2220\left(\frac{w}{P}\right) \\
&- 0.0329\left(\frac{d}{s_w}\right)\left(\frac{D}{P}\right) - 0.2677\left(\frac{d}{s_w}\right)\left(\frac{w}{P}\right) - 0.0816\left(\frac{D}{P}\right)\left(\frac{w}{P}\right) \\
&+ 0.2165\left(\frac{d}{s_w}\right)^2 - 0.5965\left(\frac{D}{P}\right)^2 + 0.3226\left(\frac{w}{P}\right)^2
\end{aligned} \quad (13)$$

Figure 15 shows the Pareto-optimal solutions using three different DOEs. The Pareto-optimal solutions are the best solutions that can be achieved for one objective without disadvantaging another objective and are sensitive to the constructed surrogate model [28]. Pareto-optimal fronts obtained using the conventional and modified LHS methods have similar smooth curves, as shown in Figure 15. However, the full factorial design shows a curve that has two inflection points, unlike the other curves. The Pareto-optimal front from modified LHS predicts the lowest optimum values of the two objective functions among the tested DOEs in most of the range. The Pareto-optimal fronts of the two LHS methods cover wider ranges than that of the full factorial design.

To compare the optimization results, three Pareto-optimal designs (PODs) were extracted from each Pareto-optimal front using K-means clustering [29], as presented in Figure 15. The predicted objective function values at the PODs and numerical calculations at the same PODs are compared in Table 5. In case of the full factorial design, the PODs are close to the boundaries of one or two design variables. However, the PODs of conventional LHS are found inside the design space. In this case, a POD close to a boundary ($D/P = -0.8802$ in POD A) yields a larger relative error between the predicted and calculated objective function values than the other PODs. As mentioned earlier, the surrogate model obtained using conventional LHS over-predicts the values at the boundary of the design space, and the error increases near the boundary.

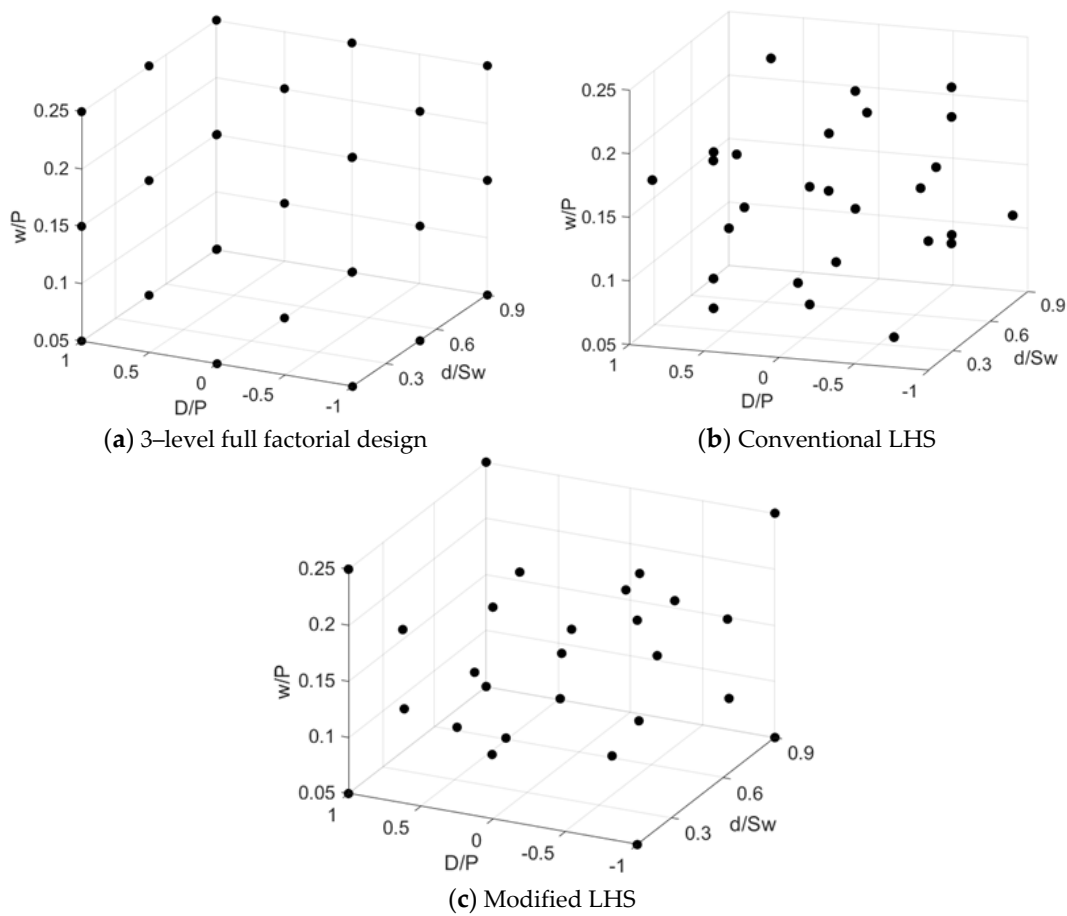


Figure 14. Distributions of sample points for three different DOEs.

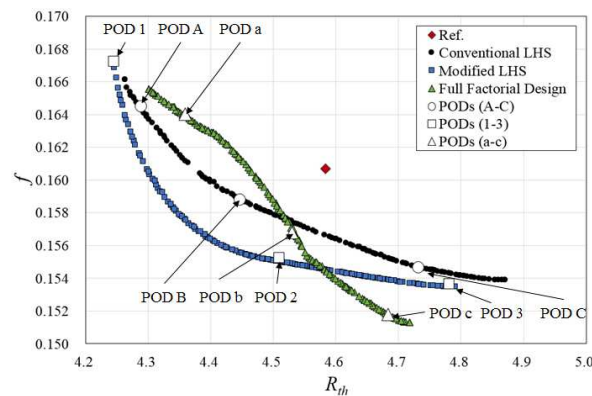


Figure 15. Pareto-optimal solutions for three different DOEs.

In the case of the modified LHS, even the POD located close to the boundary shows good prediction with maximum relative error less than 1.5%. Thus, the modified LHS shows the best prediction accuracy among the tested DOEs. The full factorial design and conventional LHS generally over-predict the objective function values with positive relative errors at the three PODs, but the modified LHS generally under-predicts the values. Therefore, there is not much difference in the calculated objective function values at the PODs among the tested DOEs.

Table 5. Results of optimizations with three different DOEs. (a) Full factorial design; (b) Conventional LHS; (c) Modified LHS.

(a)									
Full Factorial Design	Design Variables			Predicted Values		Numerical Solutions		Relative Errors (%)	
	d/t	D/P	w/P	F_{Rth} (K/W)	F_f	F_{Rth} (K/W)	F_f	F_{Rth} (K/W)	F_f
POD a	0.7862	0.9300	0.2462	4.360	0.1640	4.328	0.1679	0.7301	−2.365
POD b	0.2226	0.8809	0.2472	4.530	0.1568	4.512	0.1549	0.3890	1.216
POD c	0.1095	0.2327	0.2473	4.683	0.1518	4.519	0.1573	3.496	−3.630
(b)									
Conventional LHS	Design Variables			Predicted Values		Numerical Solutions		Relative Errors (%)	
	d/t	D/P	w/P	F_{Rth} (K/W)	F_f	F_{Rth} (K/W)	F_f	F_{Rth} (K/W)	F_f
POD A	0.7218	−0.8802	0.2083	4.288	0.1645	4.534	0.1608	−5.731	2.278
POD B	0.4156	−0.3492	0.2026	4.446	0.1588	4.593	0.1580	−3.287	0.5225
POD C	0.1580	−0.4159	0.2198	4.731	0.1547	4.701	0.1536	0.6289	0.6969
(c)									
Modified LHS	Design Variables			Predicted Values		Numerical Solutions		Relative Errors (%)	
	d/t	D/P	w/P	F_{Rth} (K/W)	F_f	F_{Rth} (K/W)	F_f	F_{Rth} (K/W)	F_f
POD 1	0.8879	1.0000	0.2163	4.246	0.1672	4.309	0.1675	−1.496	−0.1857
POD 2	0.2942	0.8214	0.2491	4.510	0.1552	4.512	0.1556	−0.0465	−0.2670
POD 3	0.1452	−0.1498	0.2211	4.781	0.1536	4.843	0.1558	−1.295	−1.412

The R^2 and adjusted R^2 values of the RSA models constructed using three different DOEs are listed in Table 6. As mentioned earlier, values closer to 1 indicate a better surrogate model. In this respect, the modified LHS shows the best results in Table 6. This is consistent with the results shown in Table 5. In addition, the RSA model with the full factorial design has the worst performance. Applying a DOE method that properly locates the sample points on the boundaries and inside of the design space makes it possible to construct a more accurate surrogate model and obtain superior optimization results.

Table 6. Statistical analysis of the RSA models. (a) Full factorial design; (b) Conventional LHS; (c) Modified LHS.

(a)		
	R^2	Adjusted R^2
F_{Rth}	0.7905	0.6454
f	0.8451	0.7379
(b)		
	R^2	Adjusted R^2
F_{Rth}	0.8751	0.8039
f	0.8579	0.7964
(c)		
	R^2	Adjusted R^2
F_{Rth}	0.9339	0.9005
f	0.9175	0.8927

4.5. Analysis of the Optimized Design

POD 2 obtained with the modified LHS was selected for further analysis because the values of both the objective functions were improved compared to the reference design. In POD 2, R_{th} and f are reduced by 1.55% and 3.00%, respectively, compared with those of the reference design. The Nu_x distributions on the wavy walls are shown in Figure 16, which compares the heat transfer performance between POD 2 and the reference design. In the

case of the reference design, there are high Nu_x regions on the left wall between the grooves in the crest and the trough ($x/2P = 5.75\text{--}6.25$). In the case of POD 2, high Nu_x regions are shown on the left side wall between the inflection point where the groove is located and the trough ($x/2P = 5.50\text{--}6.25$). The right wall between $x/2P = 7.00$ and 7.50 shows the same Nu_x distribution as the left wall between $x/2P = 5.50$ and 6.25 . Unlike the reference design, the high Nu_x distribution for POD 2 from the inflection point to the crest ($x/2P = 5.50\text{--}5.75$) seems to be one of the important factors in reducing R_{th} compared to the reference design.

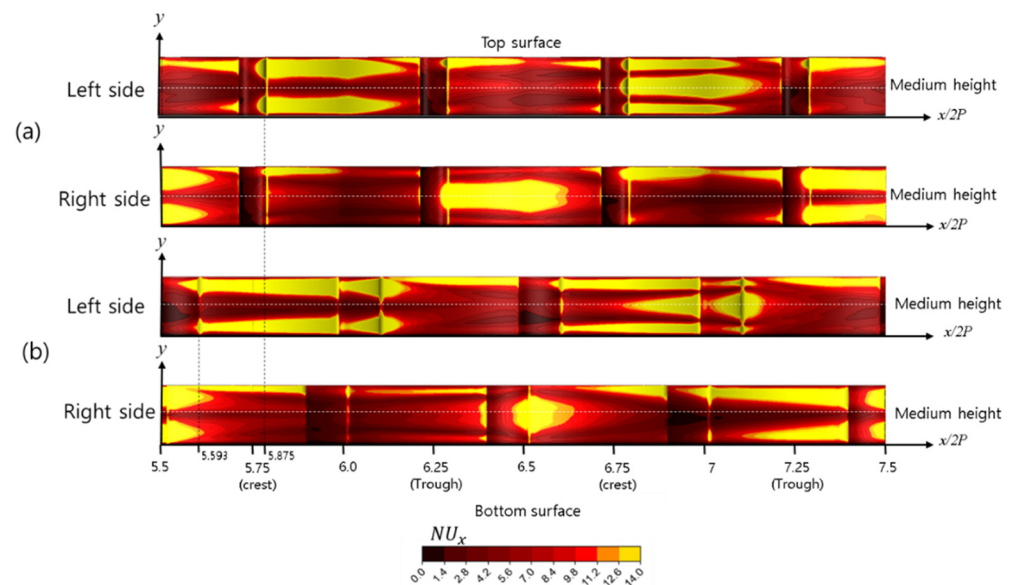


Figure 16. Local Nusselt number distributions on wavy walls: (a) reference design, and (b) optimal design (POD2).

Figure 17 shows the streamlines and velocity vectors. Figure 17a shows that the recirculating flow develops in the grooves in the reference design. These recirculating flow regions correspond to the low Nu_x regions in the grooves in Figure 16. This occurs because the flow recirculation hinders the heat transfer on the wall. Figure 17b shows the velocity vectors at the cross sections perpendicular to the flow direction. As mentioned earlier, in the reference design, a strong interaction between the vortical flow in the channel and upward flow from the groove is found near the left wall at the edge of the groove ($x/2P = 5.875$). In the case of POD 2, this phenomenon is also found near the left wavy wall at the edge of the groove ($x/2P = 5.593$) but is weaker than in the reference design. This seems to be affected by the location of the groove (which is the crest in the reference design but an inflection point in POD 2) and the fact that the two grooves on both the walls are attached at the same location in the reference design.

However, in POD 2, the vortices in the channel become stronger at a location downstream ($x/2P = 5.875$). This is consistent with the Nu_x distributions shown in Figure 16. In the reference design, the high Nu_x region persists from the groove edge ($x/2P = 5.875$) to a location far downstream but disappears before the next groove. However, in POD 2, the high Nu_x region is relatively narrow at the edge of the groove ($x/2P = 5.593$) but grows downstream and becomes widest at the upstream edge of the next groove. Thus, the total area of the high Nu_x regions is larger in POD 2 than that in the reference design.

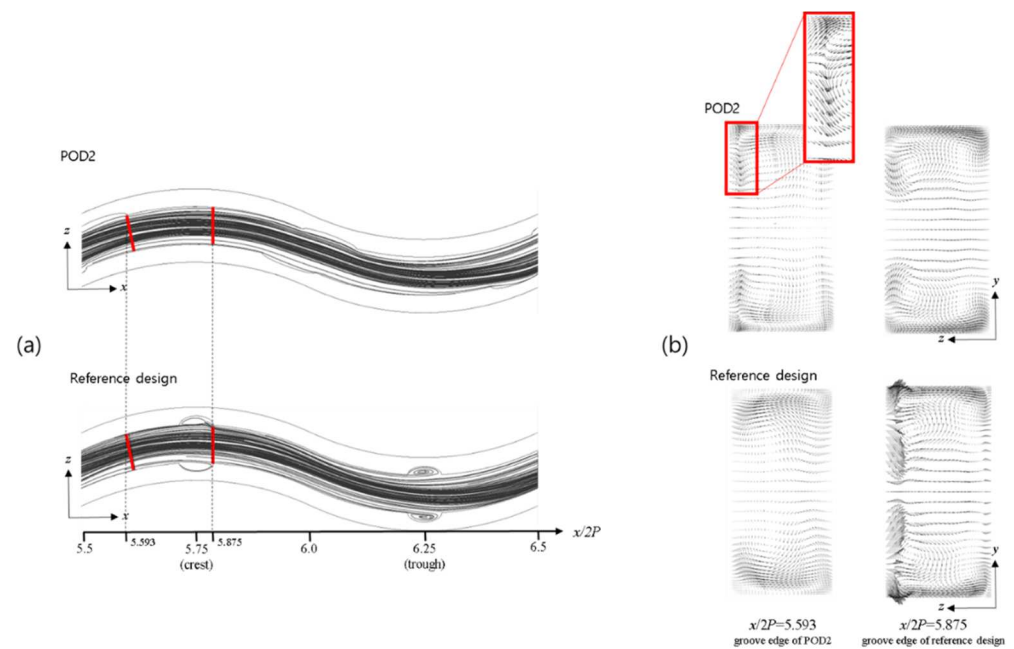


Figure 17. Streamlines and velocity vectors: (a) streamline distributions on the x - z plane ($y/H = 0.6$) (b) velocity vector in cross-section perpendicular to flow direction.

5. Conclusions

A wavy microchannel heat sink with grooves was optimized using RANS analysis of the flow and conjugate heat transfer. In the reference wavy channel with grooves, \overline{Nu} increased by about 8.34%, and R_{th} decreased by about 2%, but the friction factor f also increased by about 1.25% compared to the smooth wavy channel. Thus, using grooves, the enhancement of the heat transfer surpasses the increase in the friction.

For optimization, the distance between staggered grooves on opposite wavy walls, the groove depth, and the groove width were selected as design variables. The thermal resistance (R_{th}) and friction factor (f) were used as objective functions. A modified LHS that uses the advantages of conventional LHS and the three-level full factorial method was also proposed. The optimization performance of three DOE methods was estimated. Surrogate models of the objective functions were constructed by RSA with each DOE method. The corresponding Pareto optimal solutions were derived, and three representative optimal solutions were selected to compare the predictions of the DOE methods.

The results showed that the optimal solutions using modified LHS methods have the best predictions with less than 1.5% error compared to the numerical calculations. They also had the largest R^2 and adjusted R^2 values, which indicate the best statistical accuracy of the RSA models. For one of the representative optimal solutions, POD2, R_{th} and f decreased by 1.55% and 3.00%, respectively, compared to the reference design, indicating that both the objective functions were improved. Therefore, the multi-objective optimization with modified LHS could effectively improve the performance of the wavy microchannel heat sink with grooves.

Author Contributions: M.-C.P. presented the main idea of the wavy microchannel heat sink with groove; M.-C.P. and S.-B.M. contributed to the overall composition and writing of the manuscript; M.-C.P. analyzed the proposed wavy microchannel with grooves and performed the numerical analysis; S.-B.M. analyzed the data; K.-Y.K. revised and finalized the manuscript. All authors have read and agreed to the published version of the manuscript.

Funding: This work was supported by the National Research Foundation of Korea (NRF) grant funded by the Korean government (MSIT) (No. 2019R1A2C1007657).

Institutional Review Board Statement: Not applicable.

Informed Consent Statement: Not applicable.

Data Availability Statement: Data is contained within the article.

Conflicts of Interest: The authors declare no conflict of interest.

Abbreviations

A_b	The bottom area of the flow channel (m^2)
A_s	Side area of the flow channel (m^2)
d	Groove depth (μm)
D	Distance between staggered grooves (μm)
D_h	Hydraulic diameter (m)
F	Friction factor
h	Height of flow path (μm)
H	Height of microchannel (μm)
k_w	Thermal conductivity (W/K)
Nu	Nusselt number
Nu_x	Local Nusselt number
U	Average velocity at the inlet (m/s)
p	Pressure (N/m^2)
P	Half of wave length of channel wall (μm)
q	Heat flux (W/cm^2)
Re	Reynolds number
R_{th}	Thermal resistance (K/W)
t	Side wall thickness of channel (μm)
T_w	Average temperature at the solid wall (K)
T_m	Average temperature of the inlet and outlet (K)
$T_{s,max}$	Highest temperature at the bottom substrate (K)
$T_{f,inlet}$	Average temperature of the cooling fluid at the inlet (K)
w	Groove width (μm)
W	Width of channel (μm)
x, y, z	Rectangular coordinates
ρ	Density (kg/m^3)

References

1. Sauciu, L.; Chrysler, G.; Mahajan, R.; Szleper, M. Air-cooling Extension-Performance Limits for Processor cooling applications. In Proceedings of the 19th Annual IEEE Semiconductor Thermal Measurement and Management Symposium, San Jose, CA, USA, 11–13 March 2003; pp. 74–81.
2. Krishnan, S.; Garimella, S.V.; Chrysler, G.M.; Mahajan, R.V. Towards a Thermal Moore's Law. *IEEE Trans. Adv. Packag.* **2007**, *30*, 462–474. [[CrossRef](#)]
3. Tuckerman, D.F.; Pease, R.F.W. High-Performance heat sinking for VLSI. *IEEE Electron Device Lett.* **1981**, *2*, 126–129. [[CrossRef](#)]
4. Wang, G.-L.; Yang, D.-W.; Wang, Y.; Niu, D.; Zhao, X.-L.; Ding, G.-F. Heat Transfer and Friction Characteristics of the Microfluidic Heat Sink with Various-Shaped Ribs for Chip Cooling. *Sensors* **2015**, *15*, 9547–9562. [[CrossRef](#)] [[PubMed](#)]
5. Ansari, D.; Husain, A.; Kim, K.-Y. Multiobjective Optimization of a Grooved Micro-Channel Heat Sink. *IEEE Trans. Components Packag. Technol.* **2010**, *33*, 767–776. [[CrossRef](#)]
6. Farhanieh, B.; Herman, C.; Sundén, B. Numerical and experimental analysis of laminar fluid flow and forced convection heat transfer in a grooved duct. *Int. J. Heat Mass Transf.* **1993**, *36*, 1609–1617. [[CrossRef](#)]
7. Greiner, M.; Spencer, G.J.; Fischer, P.F. Direct Numerical Simulation of Three-Dimensional Flow and Augmented Heat Transfer in a Grooved Channel. *J. Heat Transf.* **1998**, *120*, 717–723. [[CrossRef](#)]
8. Xie, Y.; Shen, Z.; Zhang, D.; Lan, J. Thermal Performance of a Water-Cooled Microchannel Heat Sink With Grooves and Obstacles. *J. Electron. Packag.* **2014**, *136*, 021001. [[CrossRef](#)]
9. Gong, L.; Kota, K.; Tao, W.; Joshi, Y. Parametric Numerical Study of Flow and Heat Transfer in Microchannels with Wavy Walls. *ASME J. Heat Transf.* **2011**, *133*, 1356–1373. [[CrossRef](#)]
10. Sui, Y.; Lee, P.; Teo, C. An experimental study of flow friction and heat transfer in wavy microchannels with rectangular cross section. *Int. J. Therm. Sci.* **2011**, *50*, 2473–2482. [[CrossRef](#)]
11. Qun, A.K.; Huang, V.L.; Suganthan, P.N. Differential Evolution Algorithm with Strategy Adaption for Global Numerical Optimization. *IEEE Trans. Evol. Comput.* **2008**, *13*, 398–417. [[CrossRef](#)]

12. Leung, Y.W.; Wang, Y. An orthogonal genetic algorithm with quantization for global numerical optimization. *IEEE Trans. Evol. Comput.* **2001**, *5*, 41–53. [[CrossRef](#)]
13. Tu, Z.; Lu, Y. A robust stochastic genetic algorithm (StGA) for global numerical optimization. *IEEE Trans. Evol. Comput.* **2004**, *8*, 456–470. [[CrossRef](#)]
14. Kim, J.-H.; Ovgor, B.; Cha, K.-H.; Kim, J.-H.; Lee, S.; Kim, K.-Y. Optimization of the Aerodynamic and Aeroacoustic Performance of an Axial-Flow Fan. *AIAA J.* **2014**, *52*, 2032–2044. [[CrossRef](#)]
15. Kim, K.-Y.; Samad, A.; Benini, E. *Design Optimization of Fluid Machinery*; John Wiley & Sons. Ltd.: Hoboken, NJ, USA, 2019; ISBN 978-1-119-18829-2.
16. Robinson, T.D.; Eldred, M.S.; Willcox, K.E.; Haimes, R. Surrogate-Based Optimization Using Multifidelity Models with Variable Parameterization and Corrected Space Mapping. *AIAA J.* **2008**, *46*, 2814–2822. [[CrossRef](#)]
17. Regis, R.G. Trust regions in Kriging-based optimization with expected improvement. *Eng. Optim.* **2016**, *48*, 1037–1059. [[CrossRef](#)]
18. Buragohain, M.; Mahanta, C. A novel approach for ANFIS modelling based on full factorial design. *Appl. Soft Comput.* **2008**, *8*, 609–625. [[CrossRef](#)]
19. Pholdee, N.; Bureerat, S. An efficient optimum Latin hypercube sampling technique based on sequencing optimization using simulated annealing. *Int. J. Syst. Sci.* **2013**, *46*, 1780–1789. [[CrossRef](#)]
20. Goel, T.; Haftka, R.T.; Shyy, W.; Queipo, N.V. Ensemble of surrogates. *Struct. Multidiscip. Optim.* **2006**, *33*, 199–216. [[CrossRef](#)]
21. Deb, K.; Agrawal, S.; Pratap, A.; Meyarivan, T. A Fast Elitist Non-Dominated Sorting Genetic Algorithm for Multi-Objective Optimization: NSGA-II. In *Parallel Problem Solving from Nature PPSN VI*; Springer: Berlin/Heidelberg, Germany, 2000; pp. 849–858.
22. *ANSYSCFX 15.0 Solver Theory Guide*; ANSYS Inc.: Canonsburg, PA, USA, 2013.
23. Afzal, A.; Kim, K.-Y. Optimization of pulsatile flow and geometry of a convergent–divergent micromixer. *Chem. Eng. J.* **2015**, *281*, 134–143. [[CrossRef](#)]
24. MATLAB. *The Language of Technical Computing*; Release 14; the Math Work Inc.: Natick, MA, USA, 2004.
25. Koziel, S.; Yang, X.-S. Surrogate-Based Methods. In *Computational Optimization, Methods and Algorithms*; Springer: Berlin/Heidelberg, Germany, 2011; Volume 356, pp. 33–59.
26. Roache, P.J. Verification of Codes and Calculations. *AIAA J.* **1998**, *36*, 696–702. [[CrossRef](#)]
27. Celik, I.; Karatekin, O. Numerical Experiments on Application of Richardson Extrapolation with Nonuniform Grids. *J. Fluids Eng.* **1997**, *119*, 584–590. [[CrossRef](#)]
28. Baumgartner, U.; Magele, C.; Renhart, W. Pareto Optimality and Particle Swarm Optimization. *IEEE Trans. Magn.* **2004**, *40*, 1172–1175. [[CrossRef](#)]
29. Afzal, A.; Kim, K.-Y. Three-objective optimization of a staggered herringbone micromixer. *Sens. Actuators B Chem.* **2014**, *192*, 350–360. [[CrossRef](#)]

Article

Optimization Control on the Mixed Free-Surface-Pressurized Flow in a Hydropower Station

Xinlong Wang ¹, Honggang Fan ^{1,*} and Bing Liu ^{2,*}

¹ State Key Laboratory of Hydrosience and Engineering, Department of Energy and Power Engineering, Tsinghua University, Beijing 100084, China; xinlongwang1995@163.com

² College of Mechanical and Electronic Engineering, Shandong University of Science and Technology, Qingdao 266000, China

* Correspondence: fanhonggang@tsinghua.org.cn (H.F.); metrc@sdust.edu.cn (B.L.); Tel.: +86-10-6279-4297 (H.F.)

Abstract: The mixed free-surface-pressurized flow in the tailrace tunnel of a hydropower station has a great impact on the pressure, velocity, and operation stability of the power station. In the present work, a characteristic implicit method based on the upwind differencing and implicit finite difference scheme is used to solve the mixed free-surface-pressurized flow. The results of the characteristic implicit method agree well with the experimental results, which validates the accuracy of the method. Four factors that influence the amplitude of pressure fluctuation are analyzed and optimized, and the results show that the relative roughness can influence the maximum pressure in the tailrace tunnel. Additionally, the maximum pressure decreases with the increase of the tunnel's relative roughness. When the surface relative roughness increases from 0.010 to 0.018, the maximum pressure can decrease by 4.33%. The maximum pressure in the tailrace tunnel can be effectively restrained by setting vent holes in the flat-topped tunnel section (tunnel (4)) and a vent hole at 81.25%L (L is the length of tunnel (4)), which can reduce the maximum pressure by 56.72%. Increasing the vent hole number can also reduce the maximum pressure of the mixed free-surface-pressurized flow in the tailrace tunnel. An optimal set of two ventilation holes 10 m in diameter at 93.75%L and 56.25%L is proposed, which can reduce the maximum pressure by 15.30% in comparison with the single vent case.

Keywords: the mixed free-surface-pressurized flow; characteristic implicit method; relative roughness; vent holes; optimization control



Citation: Wang, X.; Fan, H.; Liu, B. Optimization Control on the Mixed Free-Surface-Pressurized Flow in a Hydropower Station. *Processes* **2021**, *9*, 320. <https://doi.org/10.3390/pr9020320>

Academic Editors: Hussein

A. Mohammed and Jin-Hyuk Kim

Received: 15 December 2020

Accepted: 2 February 2021

Published: 9 February 2021

Publisher's Note: MDPI stays neutral with regard to jurisdictional claims in published maps and institutional affiliations.



Copyright: © 2021 by the authors. Licensee MDPI, Basel, Switzerland. This article is an open access article distributed under the terms and conditions of the Creative Commons Attribution (CC BY) license (<https://creativecommons.org/licenses/by/4.0/>).

1. Introduction

Energy is one of the most important basic elements of economic and social development, and the utilization of energy can greatly improve the living quality of humans. After hundreds of years of exploitation and utilization, traditional fossil energy is decreasing day by day. As a consequence, the development of renewable energy has become an important development direction for global energy. Every country takes the development of renewable energy, such as hydropower, wind energy, and solar energy, as an important means to meet the challenges of energy security and climate change [1–4]. Among them, hydropower, with its low power generation cost and high power generation efficiency, has become a great alternative in recent years [5–10].

With the development of the national economy and hydropower, many large-scale water conservancy and hydropower projects have been built in China, such as the Three Gorges power station, Baise Underground power station, Xiangjiaba power station, and Xiluodu power station. To ensure the safe operation of hydropower stations, sufficient hydraulic analysis and hydraulic calculation must be carried out for the hydraulic transition process. The purpose of the transition process calculation is to reveal the dynamic

hydro-mechanical characteristics of the water transmission and power generation system of a hydropower station in various transitional processes. To improve the reliability, stability, flexibility, and overall economy of hydropower station operation, reasonable control methods and technical measures are necessary. The hydraulic transition process of the hydropower station is complex and involves many theoretical and computational problems. In the tailrace tunnel of the hydropower station, the free surface flow and the pressurized flow may appear alternately in the transition process, which is called the mixed free-surface-pressurized flow. When the mixed free-surface-pressurized flow occurs, the wave velocity and pressure at the interface will change rapidly.

This complicated flow phenomenon will have an important impact on the stability of the whole system's operation and will cause great pressure fluctuation in the transition process, especially for the tailwater systems of hydropower stations. Therefore, it is necessary to establish a reasonable, feasible, and identical model for calculation. At present, the main calculation methods are the virtual slit method [11–13], the shock wave fitting method [14,15], and the rigid water body method [16]. The virtual slit method was proposed by Preissmann [17], which assumes that there is a very narrow gap at the top of the closed tunnel and the gap does not increase the cross-section of the pressure water pipe and the hydraulic radius. When the pipeline is full of water, it can be regarded as an open channel with a very small water surface, and then the unified St. Venant equation can be used to solve free surface flow and pressurized flow. This model has been successfully used by Chaudhry and Kao [18] to analyze the mixed free-surface-pressurized flow in the tailwater system of the Shrum hydropower station in Canada. Ji [13] also used this model to calculate the mixed free-surface-pressurized flow in a rainwater drainage pipe. Trajkovic et al. [19] used the Maccormack scheme to simulate the mixed free-surface-pressurized flow in a circular cross-section pipeline, and the numerical results were in good agreement with the experimental results. Ferreri et al. [20] analyzed the steady pressurized flow in a sewer by using the virtual slit method. Maranzoni et al. [21] applied the virtual slit method to the two-dimensional transient mixed flow.

However, the setting of the virtual slit method is not consistent with actual situations under some conditions. Firstly, the criterion to determine the open channel flow and the pressurized flow is that the water pressure is lower or higher than the pipe's top. If there is a large bubble, even if the pressure is higher than the pipe's top, the open channel flow will not become the pressurized flow. Secondly, the equation of unsteady flow in an open channel is only applicable to the gradual change flow. Guo and Song [22] found that when the sudden change flow was formed and the surge wavefront was steep, the calculation of the virtual slit method would be unstable or not convergent when they studied the mixed free-surface-pressurized flow in the joint underground drainage system in Chicago.

When bubbles and negative pressure appear in the mixed free-surface-pressurized flow, the shock wave fitting method is proposed, which regards the free surface flow and pressurized flow as two flow states and calculates the velocity and position of the moving interface. Wiggert [23] introduced a moving interface between the free surface flow and pressurized flow to modify the Preissmann slit method, and the free surface flow was solved by the characteristic line method. Miyashiro and Yoda [15] used the characteristic line method to solve the Venant equation for free surface flow in a study of the mixed free-surface-pressurized flow in the underground drainage system. Song [24] used a shock wave moving equation and interface characteristic line equation to calculate the free surface flow and pressurized flow for the transition process of the pipeline.

However, some calculation results showed that the shock wave fitting method was not stable enough. When the surge wavefront is steep, it will lead to numerical divergence. Because the wave velocities of the free surface flow and the pressurized flow are quite different, special mesh generation technology should be adopted to meet the requirements of calculation accuracy and stability. When the moving interface passes through boundary conditions such as bifurcation pipes and surge chambers, it will become very difficult to deal with the shock wave. In particular, the shock wave fitting method considers

that the interface of the mixed free-surface-pressurized flow and positive surge wave is consistent, which is not suitable for some cases, such as a positive surge wave in a tailrace tunnel with a variable top height. Hamam and McCorquodale [25,26] proposed the rigid water body method to solve the mixed free-surface-pressurized flow, which assumes that water is incompressible and the flow velocity is uniform. Rigid water body theory is adopted for the liquid phase, and compressible flow theory is adopted for the gas phase. Li and Alex [16] developed the rigid water body method to calculate the bubble motion. However, the algorithm of the rigid water body method is complex, and there are many discrepancies with physical reality. Therefore, this method is rarely used to simulate the mixed free-surface-pressurized flow.

The existing work outlined above shows that the three calculation methods to solve the mixed free-surface-pressurized flow have their limits. Therefore, it is vital to propose a stable calculation format for the mixed free-surface-pressurized flow which can smoothly calculate and obtain results consistent with the actual situation, even when the water surface fluctuates greatly and the pressure fluctuates violently.

The basic structure of the present work is as follows. Firstly, the characteristic implicit scheme method [27] is used to solve the mixed free-surface-pressurized flow, and the experimental validation is carried out. Then, the influence of the relative roughness of the tailrace tunnel on the maximum pressure in the tunnel is analyzed. The restraining effect of setting single vent holes at different positions in the flat-topped tunnel section on the maximum pressure in the tunnel is discussed. The influence of ventilation holes with different diameters on the maximum pressure in the tunnel is calculated. The influence of setting multiple vent holes in the flat-topped tunnel section on suppressing the pressure fluctuation in the tunnel is also studied.

2. Research Object and Mathematical Model

2.1. Research Object

Figure 1 shows the layout of the water conveyance system of a hydropower station. The downstream is a tailwater tunnel that starts at the altitude of 548.70 m and ends at the altitude of 577.00 m. As shown in Tables 1 and 2, the total length of tunnels (1), (2), (3), and (4) is 1541.10 m, where the mixed free-surface-pressurized flow may occur. The shape of tunnel (4) is rectangular with an arch crown; its width is 18 m, and its height is 20 m. The operating conditions are 825 m at the upstream and 597 m at the downstream, respectively, which means that the downstream water level is equal to the top of tunnel (4).

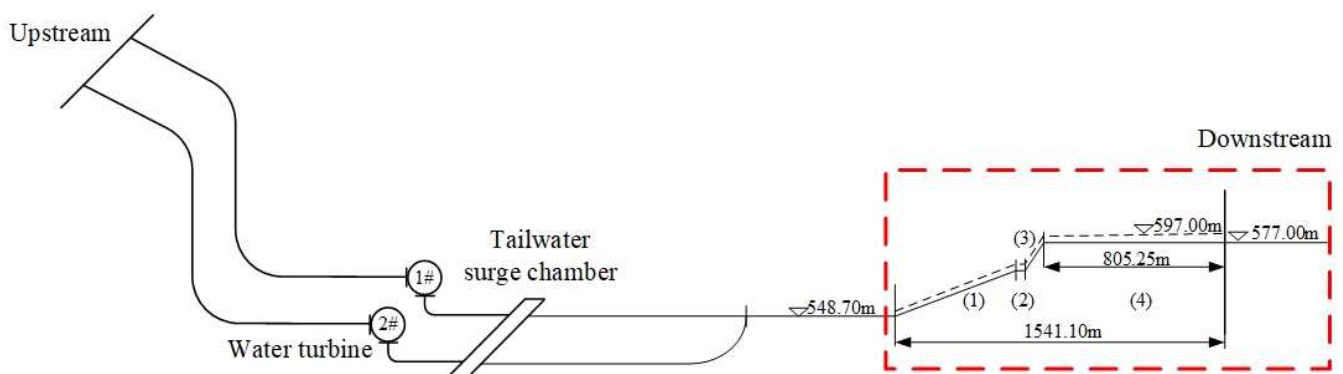


Figure 1. The layout of the water conveyance system of a hydropower station.

Table 1. Tunnel parameters.

Tunnel Number	Tunnel Shape Number	Length (m)	Roughness	Starting Elevation (m)	Ending Elevation (m)
(1)	1	614.73	0.014	548.70	562.00
(2)	2	20.00	0.014	562.00	562.00
(3)	3	101.12	0.014	562.00	577.00
(4)	4	805.25	0.014	577.00	577.00

Table 2. Description of the tunnel shape.

Tunnel Shape Number	Description of the Tunnel Shape
1	Arch-like. The bottom width changes linearly from 18 m to 15 m, the tunnel height changes linearly from 21 m to 25 m, and the radius of the circular arc at the top of the tunnel changes linearly from 9 m to 7.5 m.
2	Arch-like. The bottom width is 16 m, the tunnel height is 17 m, and the tunnel top arc radius is 10.5 m.
3	Arch-like. The bottom width changes linearly from 16 m to 18 m, the tunnel height changes linearly from 17 m to 20 m, and the radius of the circular arc at the top of the tunnel changes linearly from 10.5 m to 11.25 m.
4	Arch-like. The bottom width is 18 m, the tunnel height is 20 m, and the circular radius of the top of the tunnel is 11.25 m.

2.2. Mathematical Model

In recent work, the virtual slit method was mainly used to calculate the alternating full flow. According to the Preissmann model [17], a virtual slot on the top of the pipe or tunnel is assumed, and the slot will slightly influence the tunnel cross-section area A . The wave velocity of the free surface flow c is determined by $c = \sqrt{gA/B}$, where B is the surface width and g is gravity. Then, the wave velocity of the pressurized flow a can be chosen as $a = c$. This is a way to simulate the pressurized flow by modifying the free surface wave velocity. Then, the free surface flow and the pressurized flow can be described by the same partial equations [28] as follows:

$$g \frac{\partial h}{\partial x} + v \frac{\partial v}{\partial x} + \frac{\partial v}{\partial t} = g(i - J_f) \quad (1)$$

$$v \frac{\partial h}{\partial x} + \frac{\partial h}{\partial t} + \frac{a^2}{g} \frac{\partial v}{\partial x} = 0 \quad (2)$$

where h is the flow depth, v is the flow velocity, i is the tunnel slope, and J_f is the slope of the energy grade line.

2.3. Characteristic Implicit Method

With the rapid increase of the wave velocity c , the numerical calculation would be difficult to converge when the interface of the free surface flow and the pressurized flow passes the computational nodes. In the present work, the characteristic implicit method provides a differencing scheme with good stability and high accuracy to solve the mixed free-surface-pressurized flow. Since the system made up of the continuity and momentum equations is a hyperbolic system, upwind differencing can avoid nonphysical oscillations, and the implicit scheme is used for stability and accuracy.

To transform Equations (1) and (2) into the norm forms of the hyperbolic system and to replace v with Q/A , where Q is the volume flow, Equations (3) and (4) are derived as follows:

$$Bc^- \left(\frac{\partial h}{\partial t} + c^+ \frac{\partial h}{\partial x} \right) - \left(\frac{\partial Q}{\partial t} + c^+ \frac{\partial Q}{\partial x} \right) = f \quad (3)$$

$$Bc^+ \left(\frac{\partial h}{\partial t} + c^- \frac{\partial h}{\partial x} \right) - \left(\frac{\partial Q}{\partial t} + c^- \frac{\partial Q}{\partial x} \right) = f \quad (4)$$

where $c^\pm = \frac{Q}{A} \pm \sqrt{gA/B}$, $f = -gA(i - J_f)$, $J_f = \frac{n^2 Q^2}{A^2 R^{4/3}}$, and R is the hydraulic diameter. Equations (3) and (4) are differenced at the point of (m, n) by using the differencing scheme as follows. The forward differencing in time is found by

$$\begin{aligned} \frac{\partial Q}{\partial t} &= \frac{Q_m^{n+1} - Q_m^n}{\Delta t} \\ \frac{\partial h}{\partial t} &= \frac{h_m^{n+1} - h_m^n}{\Delta t} \end{aligned} \quad (5)$$

For the upwind differencing in space, Equation (3) is differenced along the c^+ line:

$$\frac{\partial Q}{\partial x} = \frac{Q_m^{n+1} - Q_{m-1}^{n+1}}{\Delta x} \quad \frac{\partial h}{\partial x} = \frac{h_m^{n+1} - h_{m-1}^{n+1}}{\Delta x} \quad (6)$$

Equation (4) is differenced along the c^- line:

$$\frac{\partial Q}{\partial x} = \frac{Q_{m+1}^{n+1} - Q_m^{n+1}}{\Delta x} \quad \frac{\partial h}{\partial x} = \frac{h_{m+1}^{n+1} - h_m^{n+1}}{\Delta x} \quad (7)$$

The substitution of Equations (5) and (6) into Equation (3), as well as the substitution of Equations (5) and (7) into Equation (4), lead to the system in Equation (8):

$$\begin{cases} a_1 h_{m-1}^{n+1} + b_1 Q_{m-1}^{n+1} + c_1 h_m^{n+1} + d_1 Q_m^{n+1} = e_1 \\ a_2 h_m^{n+1} + b_2 Q_m^{n+1} + c_2 h_{m+1}^{n+1} + d_2 Q_{m+1}^{n+1} = e_2 \end{cases} \quad (8)$$

where $a_1 = -\frac{B_m^n c^- \Delta t}{\Delta x}$, $b_1 = \frac{c^+ \Delta t}{\Delta x}$, $c_1 = B_m^n c^- - a_1$, and $d_1 = -(1 + b_1)$. Additionally,

$$\begin{aligned} e_1 &= B_m^n c^- h_m^n - Q_m^n + \Delta t f, & a_2 &= B_m^n c^+ + a_1, \\ b_2 &= -(1 - \frac{c^- \Delta t}{\Delta x}), & c_2 &= -a_1, \\ d_2 &= -(1 + b_2), & e_2 &= B_m^n c^+ h_m^n - Q_m^n + \Delta t f, \\ c^\pm &= \frac{Q_m^n}{A_m^n} \pm \sqrt{\frac{g A_m^n}{B_m^n}}, \\ f &= -g A_m^{n+1} \left(i_m^{n+1} - \frac{n^2 Q |Q|}{A^2 R^{4/3}} \Big|_m^{n+1} \right) \end{aligned}$$

Equation (8) is constituted by a set of two nonlinear algebraic equations with six independent unknowns, two of which are the same in any two neighboring nodes, and a similar pair of equations are written for each of the $M-2$ internal points in the tunnel. Thus, there are two $M-2$ equations in $2M$ unknowns. Equation (8) can provide one equation for each boundary point. The boundary condition at the end of the tunnel can provide two additional equations, so a unique solution can be obtained. In this paper, the new method is named the characteristic implicit method with first-order accuracy. By using the friction term and gravity term of the $n + 1$ time step, the computation precision and stability can be improved.

2.4. Experimental Validation

The purpose of this experiment was to verify the correctness of the characteristic implicit method for solving the mixed free-surface-pressurized flow. In this experimental model, the diversion system and tailwater system adopted the diversion mode that one tunnel distributed one machine. The tailrace adopted the four-in-one arrangement scheme, in which four branch tunnels converged to one main tunnel. Figure 2 shows the diagram and experimental rig of the tailrace tunnel.

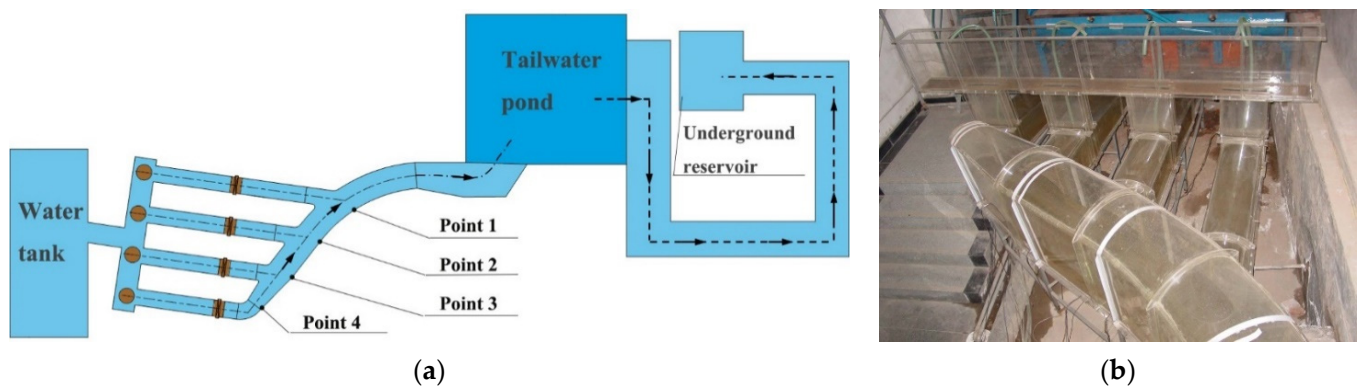


Figure 2. The diagram (a) and experimental rig (b) of the tailrace tunnel.

The experimental tunnel was a model with a proportion scale $\lambda_L = 30$, according to the gravity similarity principle [29]. The prototype of the tailrace runner was the concrete surface, and its relative roughness was 0.014. According to the scale of relative roughness, the relative roughness of the model material was 0.0079, while the relative roughness of the plexiglass pipe was also 0.0079, so the tailrace channel model was made of plexiglass could meet the requirement.

The model structure and schematic diagram of the monitoring points on the main tailrace tunnel are shown in Figure 2a, in which the tailrace of the power station was connected with a large tailwater pond. The reason for this was that the tailrace of the prototype power station flowed into the natural river channel, and the tailrace water level of the power station was determined by the discharge flow of the discharge structure and the discharge flow of the power station. The discharge flow of the power station was relatively low, and the tailrace water level of the power station was relatively stable in the transient process. In the present experiment, the discharge flow was only from the power station, so it was necessary to manually adjust the actual tailrace level. In the unsteady experiment, a relatively stable boundary condition of downstream tailrace could be obtained by connecting a large pool with the model tailrace and adopting a wide weir at the pool end.

In the present experiment, the flow rate was measured by the rectangular, thin-walled weir, and the zero reading of the thin-walled weir was calibrated before the experiment. The water depth at each point of the main tunnel was measured by the pulsating pressure sensor. The pulsating pressure sensor was connected with the computer through a DJ800 multifunctional monitor to form a data acquisition and processing system. The system was used to measure the fluctuation of the water depth at various points in the tailrace system. To observe the obvious mixed free-surface-pressurized flow in the main tailrace tunnel, the downstream water level was set to 0.807 m. Under this condition, the first half of the tailrace was the pressurized flow, and the second half of the tailrace was the free surface flow. The discharge was calculated to be $0.066279 \text{ m}^3/\text{s}$, according to the Rehbock weir formula [30]. When the butterfly valves at the inlets of four branch tunnels were suddenly closed, the phenomenon of mixed free-surface-pressurized flow in the main tailrace tunnel could be observed.

The flow rate condition was given at the upstream, and the flow rate of the four adits was assumed to be the same at $0.016570 \text{ m}^3/\text{s}$. When the butterfly valve quickly closed, the flow rate became zero in a short time, and the variation of the flow rate was recorded. Although the downstream was a large pool, there were still small fluctuations in the water level, which were recorded and input into the calculation. Figure 3a–h shows the comparison curves of the water depth in the experiment and calculations. The results show that the water levels of the time domain agreed well between the experiment and calculations. The frequency results of the experiment and calculations also coincided well, and the dominant frequencies were both 0.1 Hz. It can be seen that the calculation results and the experimental results were consistent, and the change period of the water depth

was nearly the same. The water level at point 1 exceeded the tunnel's top, so the flow in the transient process was pressurized. The water level at point 4 was below the tunnel top, so the flow in the transient process was a free surface flow. In the transient process, the water level at the second and third points would be below or exceed the tunnel's top, so the mixed free-surface-pressurized flow would occur. This is consistent with the experimental results that the separation interface between pressurized flow and free surface flow appeared near point 3 under the initial water level of 0.807 m.

Figure 3e shows that when the water surface reached the tunnel's top at point 3, the free surface flow became the pressurized flow. The curve of the experimental results shows a large pressure fluctuation at this time, which agrees well with the calculated results. Due to the pressure fluctuation at measuring point 3, the pressure fluctuation also appeared at points 1 and 2. Therefore, the calculation model could accurately predict the interface of the free surface flow and the pressurized flow.

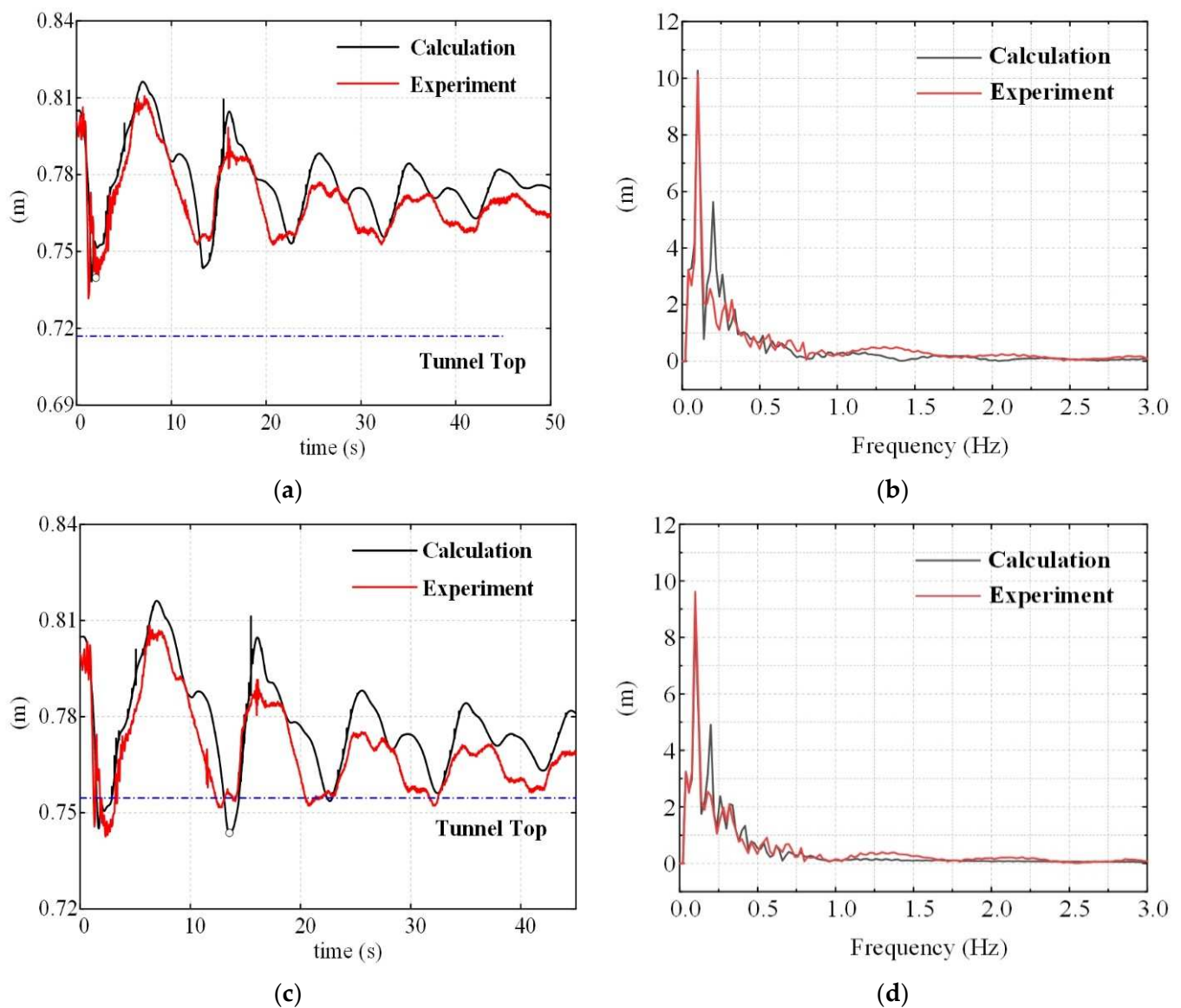


Figure 3. Cont.

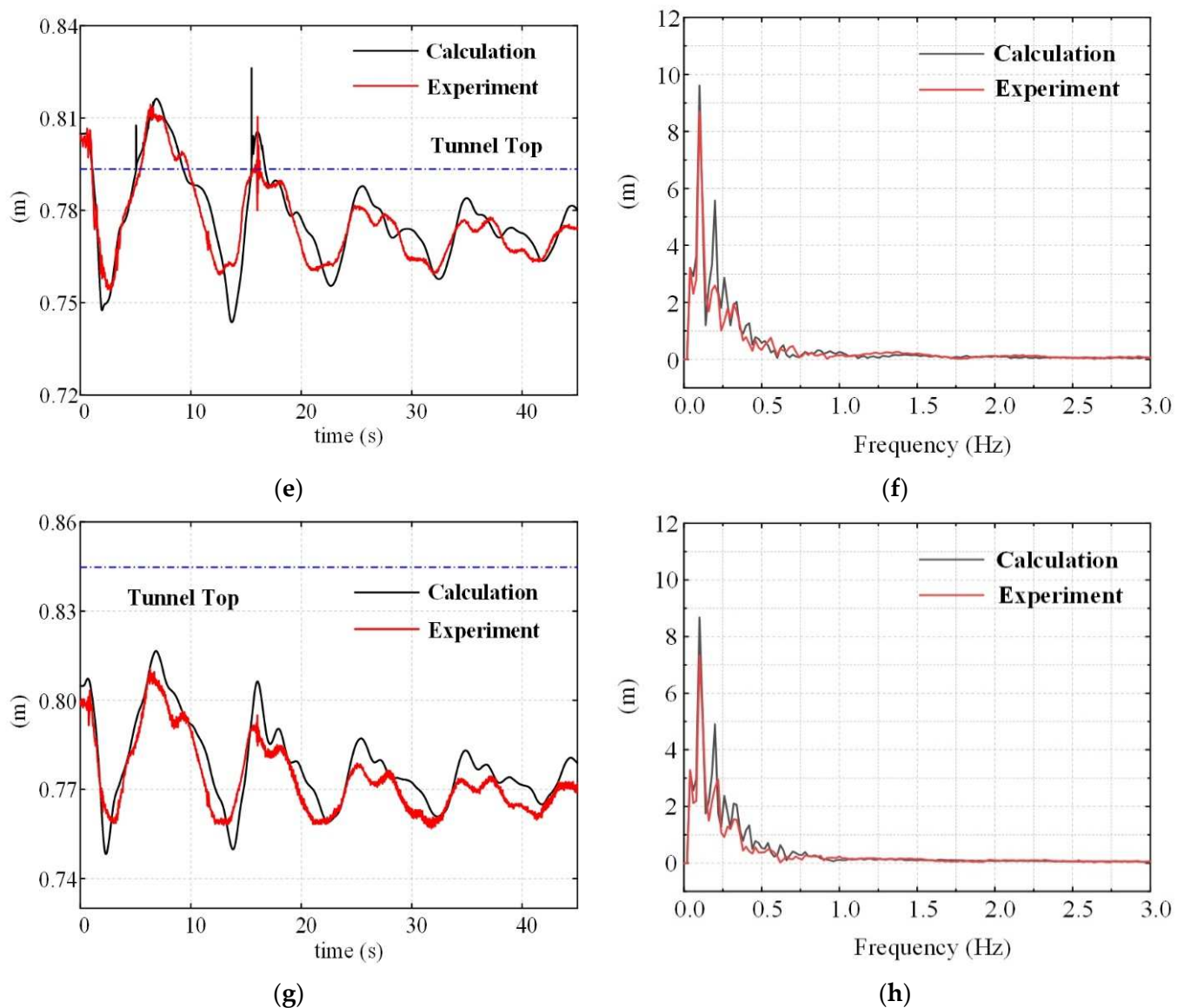


Figure 3. The curve of the stage (pressure) in the tailrace tunnel, shown for (a) the time domain of point 1, (b) frequency domain of point 1, (c) time domain of point 2, (d) frequency domain of point 2, (e) time domain of point 3, (f) frequency domain of point 3, (g) time domain of point 4, and (h) frequency domain of point 4.

3. Analysis of Influencing Factors for the Mixed Free-Surface-Pressurized Flow

Many factors can affect the occurrence and development of mixed free-surface-pressurized flow, which are important for the construction design of hydraulic engineering and the operation of hydraulic machinery.

3.1. Influence of the Tunnel Relative Roughness

When the mixed free-surface-pressurized flow occurs in the tailrace tunnel, the wave velocity at the interface between the free surface flow and the pressurized flow will change suddenly and cause great pressure fluctuation. According to Equations (3) and (4), the surface relative roughness of the tunnel wall will affect the amplitude of the pressure fluctuation.

Tunnels with the relative roughness of 0.010/0.012/0.014/0.016/0.018 were selected to calculate the influence of the tunnel surface relative roughness on the mixed free-surface-pressurized flow. The maximum pressure in the tunnel with different relative roughnesses was calculated and shown in Table 3, and the results show that the maximum pressure

in the tunnel decreased with the increase of the tunnel's relative roughness. This means that increasing the relative roughness of the tunnel surface could suppress the maximum pressure in the tunnel. The reason for this is that the increasing relative roughness will increase the hydraulic loss, which makes the maximum pressure lower. When the surface relative roughness increased from 0.010 to 0.018, the maximum pressure of the tunnel could decrease by 4.33%. However, increasing the relative roughness of the tunnel surface would reduce the power generation efficiency of the hydropower station. Therefore, a relative roughness of 0.014 is recommended upon consideration of the balance of economy and construction.

Table 3. Maximum pressure in the tailrace tunnel with different relative roughnesses.

Tunnel Relative Roughness	Maximum Pressure (mH ₂ O)
0.010	155.904
0.012	154.322
0.014	152.785
0.016	151.185
0.018	149.146

3.2. Influence of Vent Position

The vent can greatly discharge pressure when the mixed free-surface-pressurized flow appears. To study the effect of vent holes at different positions on the maximum pressure in the tunnel, the water level of the tailrace tunnel under the mixed free-surface-pressurized flow was calculated, as is shown in Figure 4. The diameter of the vent hole was set as $D = 10$ m in the calculation. In Figure 4, the red line represents the water level in the tunnel when the mixed free-surface-pressurized flow occurred, the blue line represents the tunnel's top, and the black line represents the tunnel's bottom.

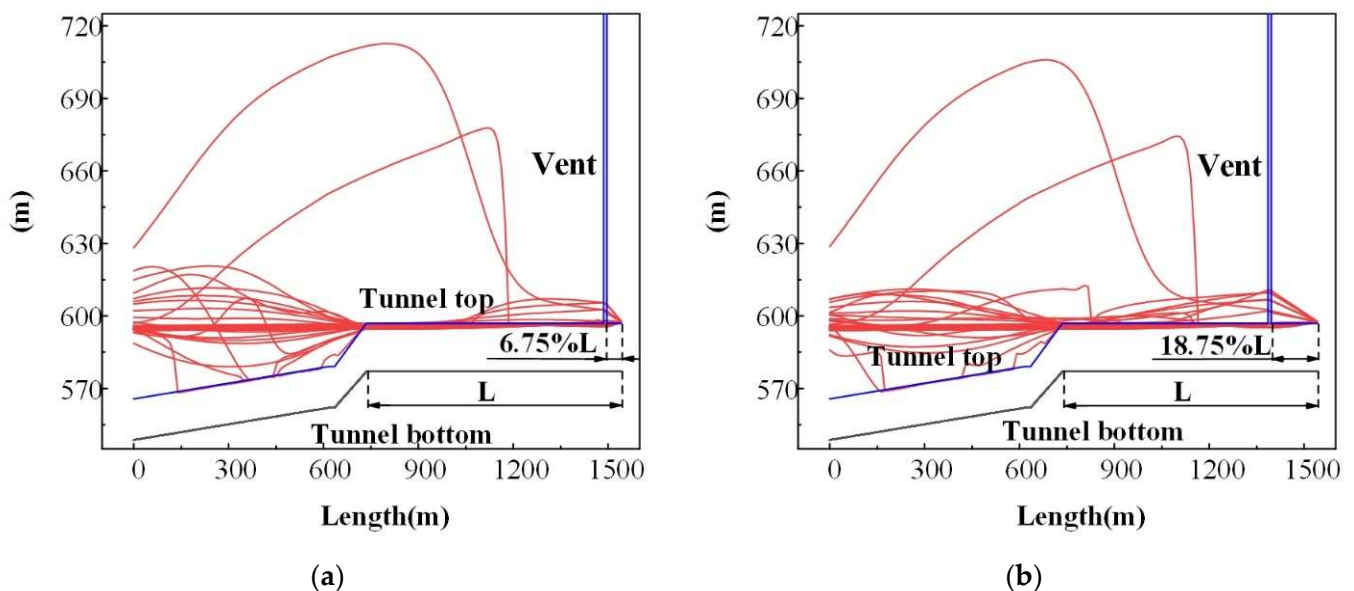


Figure 4. Cont.

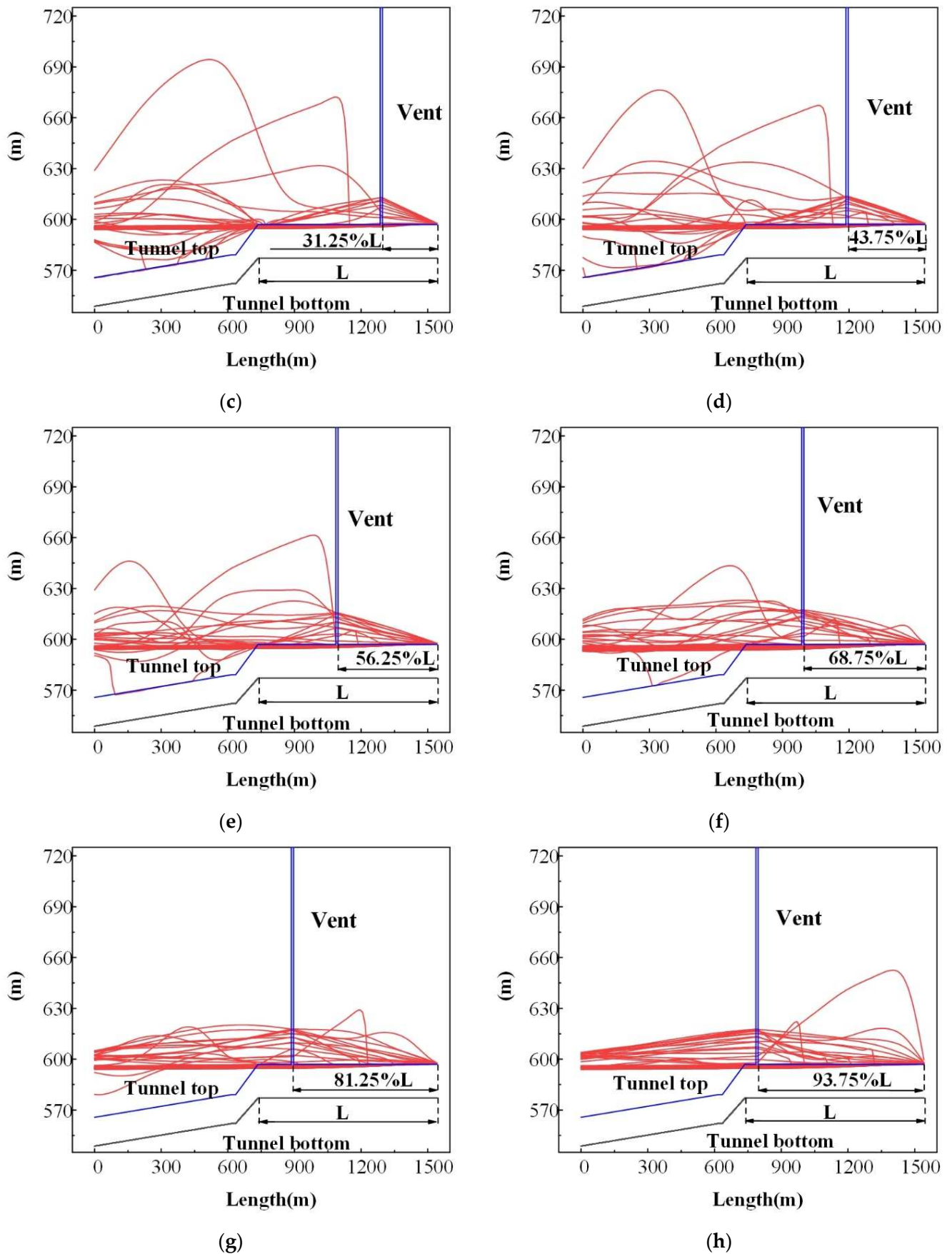


Figure 4. Cont.

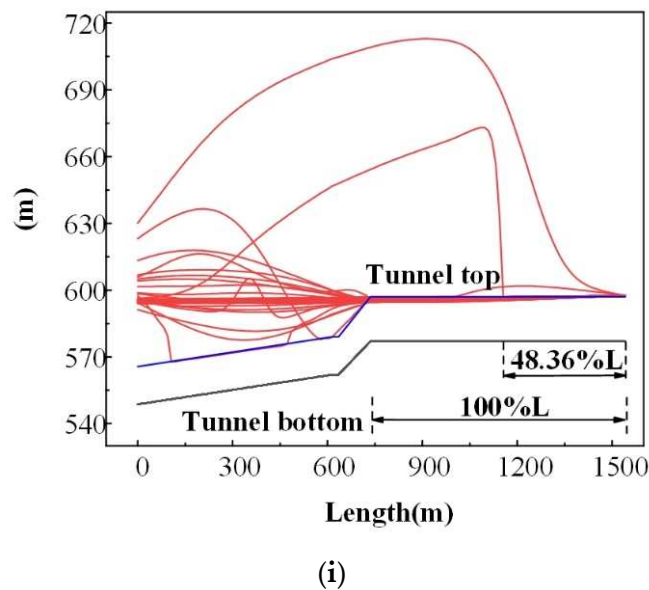


Figure 4. Water level with a vent at different positions: (a) 6.25%L, (b) 18.75%L, (c) 31.25%L, (d) 43.75%L, (e) 56.25%L, (f) 68.75%L, (g) 81.25%L, (h) 93.75%L, and (i) no vent.

For the no vent scenario, the maximum value of the pressure in the tunnel was 152.785 mH₂O. For the different vent positions of 6.25%L, 18.75%L, 31.25%L, 43.75%L, 56.25%L, 68.75%L, 81.25%L, and 93.75%L, the maximum values of the pressure in tunnel were 151.493 mH₂O, 144.734 mH₂O, 134.734 mH₂O, 120.974 mH₂O, 104.851 mH₂O, 86.844 mH₂O, 66.124 mH₂O, and 77.665 mH₂O, respectively. It can be seen that the vent at 81.25%L had the best suppression effect on the maximum pressure in the tunnel, and the corresponding maximum pressure was 66.124 mH₂O with a decrease of 56.72%. When the free surface flow turned into the pressurized flow, the wave velocity increased instantaneously, which caused a rapid increase of the pressure fluctuation in the tunnel. On the one hand, according to the design manual of the hydropower station, the wave velocity of the tailwater tunnel of the prototype power station was 1160 m/s under the pressurized flow. On the other hand, the vents in the tunnel could be thought of as small open channels, and the wave velocity in the vent could be calculated to be about 19 m/s by the wave velocity formula. Therefore, the maximum values of the pressure in tunnel 4 could be greatly reduced by setting proper vent positions. This method can be an alternative with the surge shafts to guarantee the stable operation of the hydropower station.

3.3. Influence of the Vent Diameter

According to the formula of the wave velocity for the open channel, the wave velocity decreased with the increase of the vent diameter. It can be inferred that the diameter of the ventilation holes affected the maximum pressure inside the tunnel. Vent holes with different diameters were set at 81.25%L, and the maximum pressure when the mixed free-surface-pressurized flow occurred in the tunnel was calculated, as is shown in Figure 5.

Three vent diameters of 5 m, 10 m, and 15 m were set to investigate the influence of the vent diameter on the suppression effect on the maximum pressure in the tunnel. The results show that the maximum pressure in the tunnel decreased with the increase of the vent diameter. When the diameter of the vent hole increased from 5 m to 10 m and 15 m, the maximum values of the pressure in the tunnel were 68.541 mH₂O, 66.124 mH₂O, and 66.026 mH₂O, with a decrease of 3.53% and 3.67%, respectively. Therefore, further increasing the diameter had a slight effect on the maximum pressure suppression.

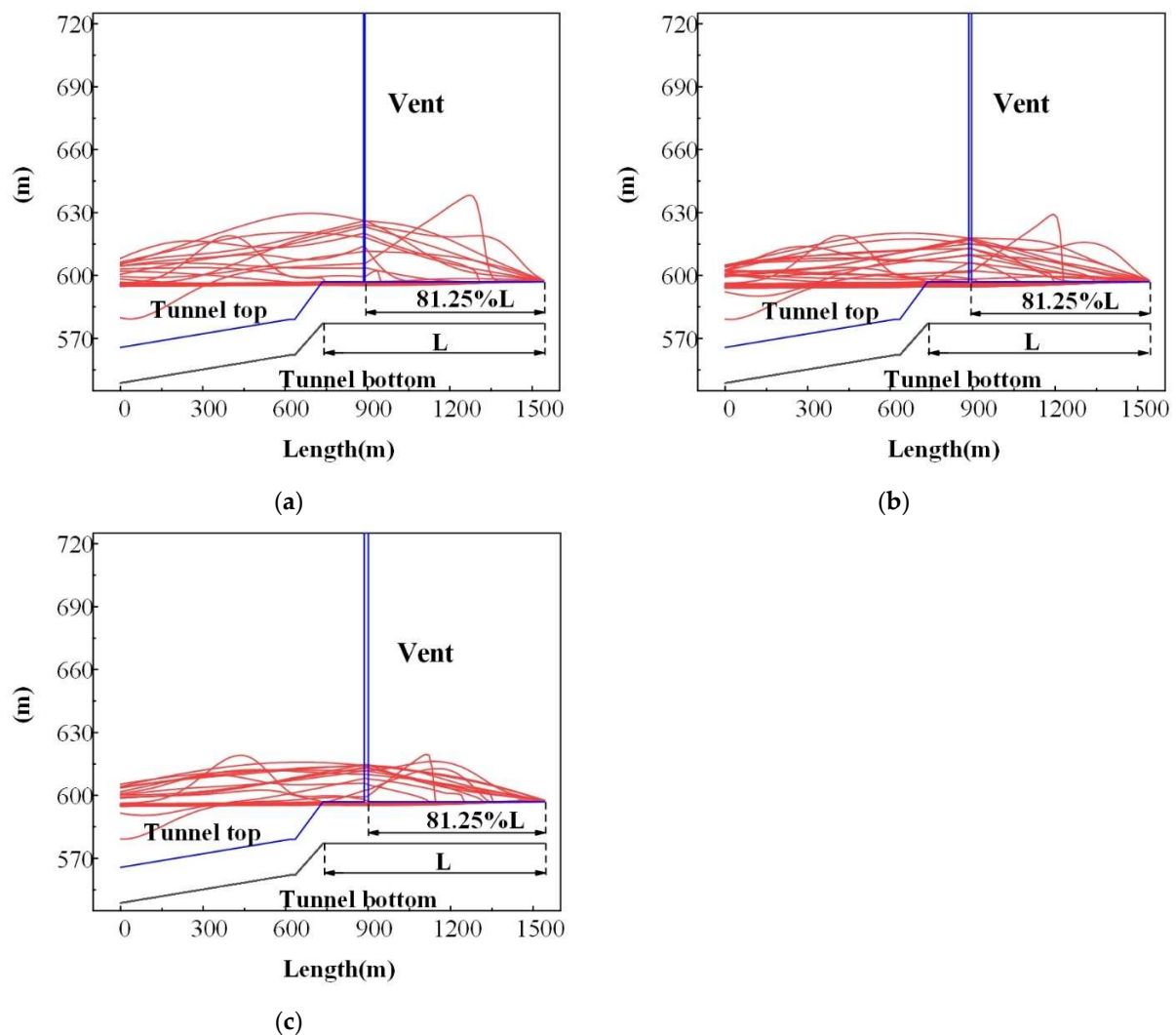


Figure 5. Water level with different vent diameters: (a) vent diameter of 5 m, (b) vent diameter of 10 m, and (c) vent diameter of 15 m.

3.4. Influence of the Vent Number

A vent can effectively reduce the maximum pressure in the tunnel, so the influence of the vent number should be further investigated. Because the vent position at 93.75%L could effectively suppress the maximum pressure at the upstream of the tunnel, the first vent position was set at 93.75%L. Then, the second or third vent was set at different positions, and five cases with different vent numbers and corresponding positions were determined, as is shown in Table 4.

Table 4. Maximum pressure in the tailrace tunnel with different numbers of vents.

Items	Number of Vents	Vent Positions	Maximum Pressure (mH ₂ O)
Case 1	2	93.75%L 43.75%L	62.517
Case 2	2	93.75%L 56.25%L	56.006
Case 3	2	93.75%L 68.75%L	56.345
Case 4	2	93.75%L 81.25%L	61.087
Case 5	3	93.75%L 68.75%L 43.75%L	55.398

Figure 6 shows the maximum pressure of the mixed free-surface-pressurized flow in the tunnel with vents. The results show that the maximum pressure in the tunnel was

56.006 mH₂O for vent positions at 93.75%L and 56.25%L, which was reduced by 15.30% in comparison with the single-vent case. For the three vent positions at 93.75%L, 68.75%L, and 43.75%L, the maximum pressure in the tunnel was 55.398 mH₂O, which was reduced by 16.22% in comparison with the single-vent case. It can be concluded that increasing the vent number can strengthen the suppression effect on the maximum pressure; however, more vents may influence the safety of the tunnel structure.

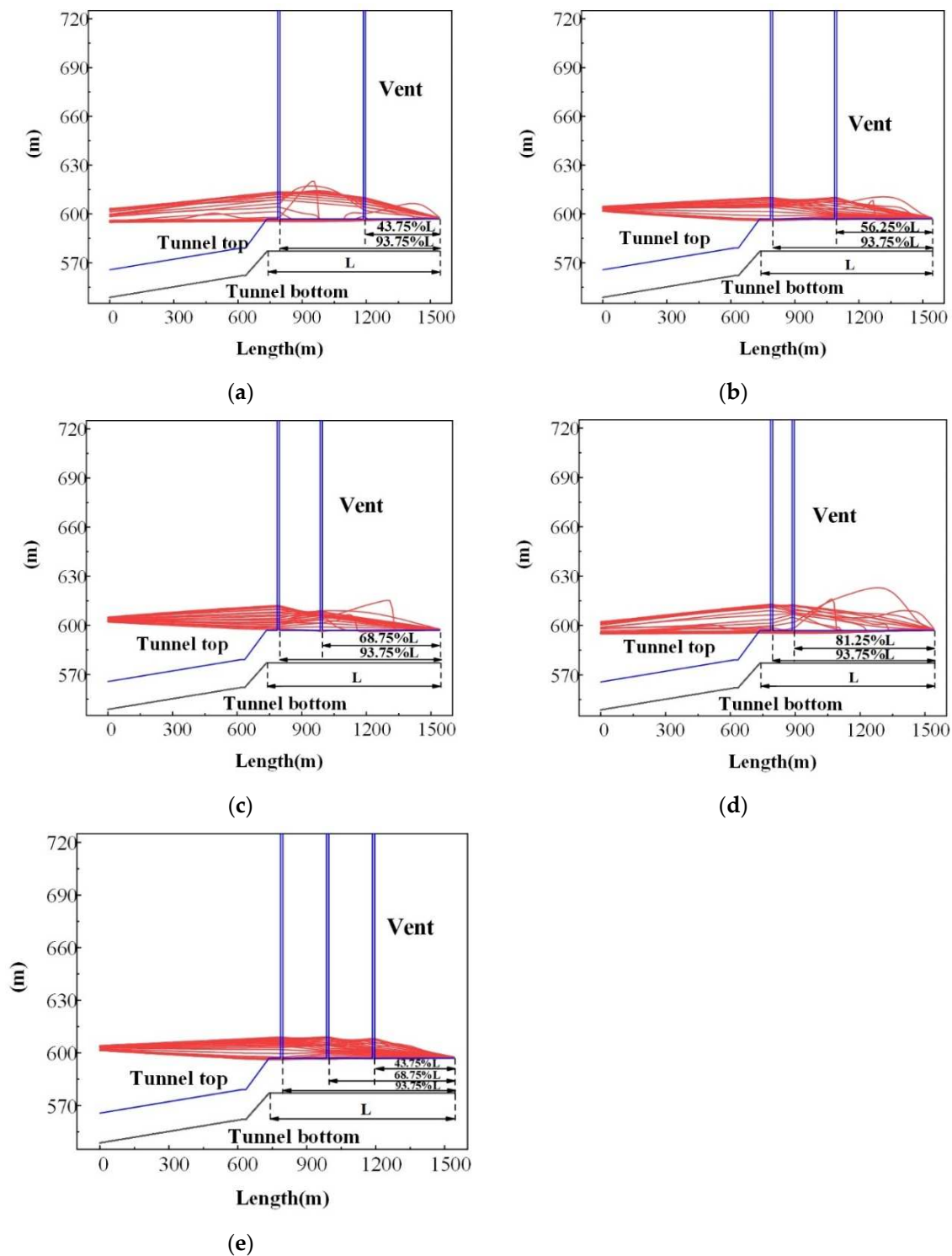


Figure 6. Water level with different numbers of vents: (a) 93.75%L/43.75%L, (b) 93.75%L/56.25%L, (c) 93.75%L/68.75%L, (d) 93.75%L/81.25%L, and (e) 93.75%L/68.75%L/43.75%L.

4. Conclusions

In the present work, the characteristic implicit method was used to investigate the mixed free-surface-pressurized flow in the tailrace tunnels of a hydropower station, and the main conclusions are as follows:

1. Based on the upwind differencing and implicit finite difference scheme, the characteristic implicit method can detect and simulate the mixed free-surface-pressurized flow, which has good calculation stability. The experiment agreed well with the calculated results and validated the accuracy of the characteristic implicit method;
2. The relative roughness of the tailrace tunnel influences the maximum pressure in the tailrace tunnel, and the maximum pressure decreases with the increase of the tunnel's relative roughness when the mixed free-surface-pressurized flow occurs;
3. Setting vent holes in the flat-topped tunnel section can restrain the maximum pressure caused by the mixed free-surface-pressurized flow in the tunnel, and a vent hole at 81.25%L can reduce the maximum pressure by 56.72%;
4. When the diameter of the vent hole is in the range of 5~15 m, the maximum pressure in the tunnel decreases with the increase of the ventilation hole diameter;
5. By increasing the number of ventilation holes in the flat-topped tunnel section, the maximum pressure in the tunnel can be reduced when the mixed free-surface-pressurized flow occurs. An optimal set of two ventilation holes at 93.75%L and 56.25%L was proposed, which could reduce the maximum pressure by 15.30%. Meanwhile, when considering the suppression effect and tunnel safety, an optimal hole diameter of 10 m is recommended.

Author Contributions: Conceptualization, H.F., B.L.; methodology, H.F., B.L.; software, X.W.; validation, H.F. and X.W.; formal analysis, H.F. and X.W.; investigation, B.L.; resources, B.L.; data curation, X.W.; writing—original draft preparation, X.W.; writing—review and editing, H.F. and B.L.; visualization, B.L.; supervision, H.F.; project administration, H.F.; funding acquisition, H.F. All authors have read and agreed to the published version of the manuscript.

Funding: This work has been funded by the National Key R&D Program of China, grant number [2016YFC0401905], the National Natural Science Foundation of China, grant number [51879140], the Tsinghua-Foshan Innovation Special Fund, grant number (TFISF)[2020THFS0107], and the Creative Seed Fund of the Shanxi Research Institute for Clean Energy.

Acknowledgments: This work has been supported by the National Key R&D Program of China [2016YFC0401905], the National Natural Science Foundation of China [51879140], the Tsinghua-Foshan Innovation Special Fund (TFISF) [2020THFS0107], and the Creative Seed Fund of the Shanxi Research Institute for Clean Energy.

Conflicts of Interest: The authors declare no conflict of interest.


References

1. Zhang, D.; Wang, J.; Lin, Y.; Si, Y.; Huang, C.; Yang, J.; Huang, B.; Li, W. Present situation and future prospect of renewable energy in China. *Renew. Sustain. Energy Rev.* **2017**, *76*, 865–871. [[CrossRef](#)]
2. Zhang, N.; Lior, N.; Jin, H. The energy situation and its sustainable development strategy in China. *Energy* **2011**, *36*, 3639–3649. [[CrossRef](#)]
3. Liu, W.; Lund, H.; Mathiesen, B.V.; Zhang, X. Potential of renewable energy systems in China. *Appl. Energy* **2011**, *88*, 518–525. [[CrossRef](#)]
4. Chai, Q.; Zhang, X. Technologies and policies for the transition to a sustainable energy system in China. *Energy* **2010**, *35*, 3995–4002. [[CrossRef](#)]
5. Mathiesen, B.V.; Lund, H.; Karlsson, K. 100% renewable energy systems, climate mitigation and economic growth. *Appl. Energy* **2011**, *88*, 488–501. [[CrossRef](#)]
6. Huang, H.; Yan, Z. Present situation and future prospect of hydropower in China. *Renew. Sustain. Energy Rev.* **2009**, *13*, 1652–1656. [[CrossRef](#)]
7. Chang, X.; Liu, X.; Zhou, W. Hydropower in China at present and its further development. *Energy* **2010**, *35*, 4400–4406. [[CrossRef](#)]
8. Lu, Y.-m. The exploitation and sustainable development of hydropower in China. *Water Resour. Hydropower Eng.* **2004**, *36*, 1–4.
9. Kong, Y.; Wang, J.; Kong, Z.; Song, F.; Liu, Z.; Wei, C. Small hydropower in China: The survey and sustainable future. *Renew. Sustain. Energy Rev.* **2015**, *48*, 425–433. [[CrossRef](#)]

10. Liu, J.; Zhao, D.; Gerbens-Leenes, P.W.; Guan, D. China's rising hydropower demand challenges water sector. *Sci. Rep.* **2015**, *5*, 11446. [[CrossRef](#)]
11. Chaudhry, M.H. *Applied Hydraulic Transients*, 3rd ed.; Springer: Berlin, Germany, 2014.
12. De Almeida, A.B.; Koelle, E. *Fluid Transients in Pipe Networks*; Computational Mechanics Publications: Southampton, UK; Elsevier Applied Science: London, UK, 1992.
13. Ji, Z. General hydrodynamic model for sewer/channel network systems. *J. Hydraul. Eng.* **1998**, *124*, 307–315. [[CrossRef](#)]
14. Guo, Q.; Song, C.C. Surging in urban storm drainage systems. *J. Hydraul. Eng.* **1990**, *116*, 1523–1537. [[CrossRef](#)]
15. Miyashiro, H.; Yoda, H. *An Analysis of Hydraulic Transients in Tunnels with Concurrent Open-Channel and Pressurized Flow*; ASME, Fluids Engineering Division: New York, NY, USA, 1983.
16. Li, J.; McCorquodale, A. Modeling mixed flow in storm sewers. *J. Hydraul. Eng.* **1999**, *125*, 1170–1180. [[CrossRef](#)]
17. Priessmann, A.; Cunge, J.A. Calcul des intumescences sur machines électronique. In Proceedings of the 9th Congress of International Association for Hydraulic Research, Belgrade, Yugoslavia, 3–7 September 1961.
18. Chaudhry, M.H.; Kao, K.H. *Shrum Generating Station: Tailrace Surges and Operating Guidelines During High Tailwater Levels*; British Columbia Hydro and Power Authority: Vancouver, BC, Canada, 1976.
19. Trajkovic, B.; Ivetic, M.; Calomino, F.; D'Ippolito, A. Investigation of transition from free surface to pressurized flow in a circular pipe. *Water Sci. Technol.* **1999**, *39*, 105–112. [[CrossRef](#)]
20. Ferreri, G.B.; Freni, G.; Tomaselli, P. Ability of Preissmann slot scheme to simulate smooth pressurisation transient in sewers. *Water Sci. Technol.* **2010**, *62*, 1848–1858. [[CrossRef](#)]
21. Maranzoni, A.; Dazzi, S.; Aureli, F.; Mignosa, P. Extension and application of the Preissmann slot model to 2D transient mixed flows. *Adv. Water Resour.* **2015**, *82*, 70–82. [[CrossRef](#)]
22. Guo, Q.; Song, C.C. Dropshaft hydrodynamics under transient conditions. *J. Hydraul. Eng.* **1991**, *117*, 1042–1055. [[CrossRef](#)]
23. Wiggert, D.C. Transient flow in free-surface, pressurized systems. *J. Hydraul. Div.* **1972**, *98*, 11–27. [[CrossRef](#)]
24. Song, C.C.; Cardie, J.A.; Leung, K.S. Transient mixed-flow models for storm sewers. *J. Hydraul. Eng.* **1983**, *109*, 1487–1504. [[CrossRef](#)]
25. Hamam, M.A.; McCorquodale, J.A. Transient conditions in the transition from gravity to surcharged sewer flow. *Can. J. Civ. Eng.* **1982**, *9*, 189–196. [[CrossRef](#)]
26. McCorquodale, J.A.; Hamam, M.A. Modeling surcharged flow in sewers. In Proceedings of the International Symposium on Urban Hydrology, Hydraulics and Sediment Control, University of Kentucky, Lexington, KY, USA, 25–28 July 1983.
27. Afshar, M.H.; Rohani, M. Water hammer simulation by implicit method of characteristic. *Int. J. Press. Vessel. Pip.* **2008**, *85*, 851–859. [[CrossRef](#)]
28. Chunge, J.A. Numerical integration of Barre de Saint-Venant's flow equations by means of an implicit scheme of finite differences. *La Houille Blanche* **1964**, *1*, 33–39.
29. Liu, M.; Li, G.; Guala, M.; Sun, D. Experimental research on hydraulics of flood discharge tunnel and improving schemes for choking. *La Houille Blanche* **2017**, *1*, 24–32. [[CrossRef](#)]
30. Aydin, I.; Altan-Sakarya, A.B.; Sisman, C. Discharge formula for rectangular sharp-crested weirs. *Flow Meas. Instrum.* **2011**, *22*, 144–151. [[CrossRef](#)]

Article

Development of a Hydropower Turbine Using Seawater from a Fish Farm

Md Rakibuzzaman ¹, Sang-Ho Suh ^{2,*}, Hyoung-Ho Kim ^{3,*} , Youngtae Ryu ⁴ and Kyung Yup Kim ⁵

¹ Department of Mechanical Engineering, International University of Business Agriculture and Technology, Dhaka 1230, Bangladesh; rakibuzzaman@iubat.edu

² School of Mechanical Engineering, Soongsil University, Seoul 06978, Korea

³ School of Mechanical Engineering, GNTech, Seoul 52725, Korea

⁴ Namhae Energy Co., Ltd., Seoul 51395, Korea; ytryu@nhenergy.co.kr

⁵ Department of Mechanical Engineering, Korea Polytechnic University, Seoul 15073, Korea; kykim@kpu.ac.kr

* Correspondence: suhsh@ssu.ac.kr; khh106@gntech.ac.kr; Tel.: +82-031-387-4877

Abstract: Discharge water from fish farms is a clean, renewable, and abundant energy source that has been used to obtain renewable energy via small hydropower plants. Small hydropower plants may be installed at offshore fish farms where suitable water is obtained throughout the year. It is necessary to meet the challenges of developing small hydropower systems, including sustainability and turbine efficiency. The main objective of this study was to investigate the possibility of constructing a small hydropower plant and develop 100 kW class propeller-type turbines in a fish farm with a permanent magnet synchronous generator (PMSG). The turbine was optimized using a computer simulation, and an experiment was conducted to obtain performance data. Simulation results were then validated with experimental results. Results revealed that streamlining the designed shape of the guide vane reduced the flow separation and improved the efficiency of the turbine. Optimizing the shape of the runner vane decreased the flow rate, reducing the water power and increasing the efficiency by about 5.57%. Also, results revealed that tubular or cross-flow turbines could be suitable for use in fish farm power plants, and the generator used should be waterproofed to avoid exposure to seawater.

Keywords: small hydropower; tubular turbine; fish farm; computational fluid dynamics; performance test; design factors; optimum model



Citation: Rakibuzzaman, M.; Suh, S.-H.; Kim, H.-H.; Ryu, Y.; Kim, K.Y. Development of a Hydropower Turbine Using Seawater from a Fish Farm. *Processes* **2021**, *9*, 266. <https://doi.org/10.3390/pr9020266>

Academic Editor: Jin-Hyuk Kim

Received: 31 December 2020

Accepted: 26 January 2021

Published: 30 January 2021

Publisher's Note: MDPI stays neutral with regard to jurisdictional claims in published maps and institutional affiliations.



Copyright: © 2021 by the authors. Licensee MDPI, Basel, Switzerland. This article is an open access article distributed under the terms and conditions of the Creative Commons Attribution (CC BY) license (<https://creativecommons.org/licenses/by/4.0/>).

1. Introduction

Hydropower is expected to remain the world's largest source of renewable electricity and to play a critical role in decarbonizing the power system and improving system flexibility. In 2016, world hydropower installed capacity was 1064 GW, and annual power generation was 3940 TWh [1]. Hydropower generation has been declining in Southeast Asia and the Americas due to continued drought caused by climate change. However, demand for hydroelectric power generation is increasing to cope with the increasing proportion of renewable energy and to adapt to increasing power demands from industrialization and the climate change crisis [2]. The hydropower industry is improving its efficiency, output, and system resilience through modernization, improving old facilities and renovating and expanding existing facilities [3,4]. Small scale hydropower development is being studied worldwide to improve technology to make it more reliable and economically efficient, which is necessary due to climate change, high oil prices, and environmental problems [2]. In addition, domestic small hydroelectric power generation technologies are being localized due to new and renewable energy certificates (RECs) and the sale of electric power in domestic institutions and corporations; a continuous decrease in the development unit price has also been affected by small and medium enterprises [3,5,6]. Therefore, particular attention should be paid to small scale hydropower plants operating in low head conditions [7,8], the significant possibility of which is still not fully identified.

Small hydropower (SHP) has been used to produce renewable, clean, and abundant energy [9]. In a study of SHP, Ma et al. conducted a study on runners to develop general purpose 2.5 kW micro-water vehicles [10]. Borkowski et al. validated computational fluid dynamics (CFD) on SHP with electrical generator integrated with experiments, and the main results were the mechanical power losses in the hydro-set gap and selection of suitable turbulence model [11]. Huidong et al. conducted a study on the possibility of replacing composite runner blades and mechanical stainless steel runner blades as a way to increase the economics of SHP in stream sites [12]. Wen-Quan et al. investigated the development of water turbines available in rivers through computational fluid dynamics [13]. Punys et al. [14], reviewed small scale hydropower resource assessment for the development of small hydropower plants using sophisticated software tools.

However, it represents only around 1.5% of the world's total installed electricity capacity, 4.5% of its total renewable energy capacity, and 7.5% (<10 MW) of its total hydropower capacity [15,16]. Currently, there are few possibilities to develop and construct small hydropower plants [17].

In Korea, fish farms operate approximately 600 units from the southern area, which is at 350 units, and Jeju Island, which is at 250 units. Fish farms are environmentally friendly, pollution-free, low cost, and guarantee the income of fishing villages. A small hydropower plant that produces from 20–500 kW can utilize surplus recirculated water from fish farms [18–20]. Propeller-type tubular turbines could be suitable for use in fish farm hydropower plants [21]. Propeller turbines have a simple structure and a fixed blade, the cost is relatively lower than that of the Kaplan turbine, and they have a high likelihood of successful use in small hydropower plants [22–25]. Li et al. [26], analyzed hydraulic performance according to the operating conditions of turbines through numerical analysis and studied the effects of the opening angle of the guide vanes.

CFD has been applied to the design of hydro turbines and can be used in numerical simulation to obtain hydraulic performance. Vu et al. [27] studied a Pico propeller hydro turbine using the old runner model and improved the performance of the turbine using CFD. Park et al. [28] studied the flow analysis of 30 kW gate turbines using a permanent magnetic generator as well as the dynamic behavior of the flow stability of operating conditions. Nasir, B. A. [29] was focused on the selection of suitable micro-scale hydropower plant components. In [30], the authors focused on preliminary studies of economic feasibility, the design of civil works, and the selection of electro mechanical components, and developed a 15 kW micro-scale hydropower plant for rural electrification. In [31], the authors investigated four different propeller turbine models with head ranges of 4–9 m and generated an efficiency of 68%. The efficiency of small hydropower plants is generally in the range of 60–80% [27]. In [32], the authors studied the fish passage experience and passage facilities, especially how fish friendly they were, at a small scale hydropower plant. However, the study did not show design and performance improvements in a micro-scale hydropower plant using seawater from a fish farm.

Therefore, this study has especially focused on the applicability of a 100 kW class small propeller-type turbine (with an annular permanent magnetic generator). It is intended to serve as a reference for researchers who want to approach this field in the future by conducting prior research on the development of SHP available in Korea's marine characteristics, such as fish farms, through computational fluid dynamics and certificated field tests. In addition, we intend to provide basic data on the possibility of hydrodynamic characteristic changes due to simple feature changes in draft tubes, guide vanes, and runner vanes, which are important components of SHP.

2. Hydropower Turbine Design

2.1. Fish Farm Facilities

In fish farm facilities, seawater is supplied through the water supply system by a pipeline 20–30 m above sea level. The water is recirculated for use in the fish farm and finally discharged through the discharge channel into the sea. Fish farm facilities are shown

in Figure 1. The plan was to install the hydropower plant on a shared water surface along the coast. Therefore, data regarding sea level and tide observations was important for the development of the fish farm. Figure 2 illustrates the monthly average tide levels in the southern sea off the coast of Korea [33].



Figure 1. Fish farm facilities: (a) water supply system; (b) discharge water system; (c) fish farm.

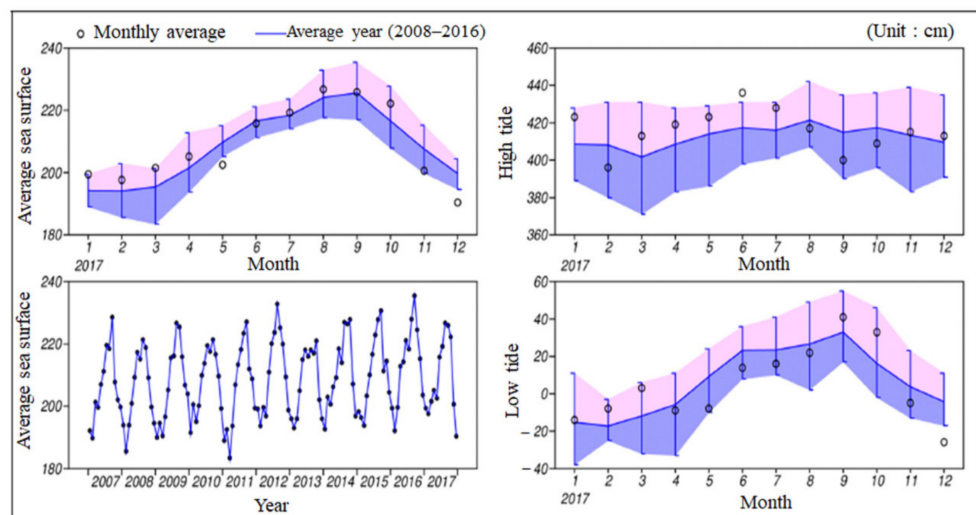


Figure 2. Monthly average tidal status, Southern sea, Korea.

2.2. Hydroturbine Design

A horizontal propeller type tubular turbine was designed with nine fixed guide vanes, which were attached via a guide vane casing. Runner blades were directly attached to the end of the permanent magnet synchronous generator (PMSG) [34], and an s-shaped draft tube, which was chosen to ensure maximum recovery with minimum loss. The generator was designed to be installed on a shared seawater surface. The fish farm hydropower plant layout was chosen for its low head and flow rate, compact and simple mechanism, low maintenance needs, and environmental friendliness. Table 1 shows the major design parameters of the tubular turbine. When the one dimensional (1-D) design of the turbine was considered, specific speed (N_S) was a meaningful parameter for identical geometric proportions if the sizes and speeds were different. The specific speed was expressed as follows:

$$N_S = N \frac{\sqrt{P}}{H^{5/4}} \quad (1)$$

where N is the turbine rotational speed in rpm, H is the net head in m, and P is the turbine power in kW. The choice of the blade rotational speed depends on the generator and the type of the drive used [35–37].

Table 1. Design specifications of the tubular turbine.

Description	Dimension
Theoretical head (m)	15.00
Flow rate (m ³ /s)	1.13
Max. power (kW)	100
Rotational speed (rpm)	850
Runner blade	4
Guide vane	9

We considered two rotational speeds in this study, 600 rpm and 900 rpm. The turbine selection was referenced from the H – N_S chart [37]. The chart shows that at 600 and 900 rpm, the specific speeds were 230 and 345 respectively. The diameter of the turbine is calculated as follows:

$$D = \frac{60k_u \sqrt{2gH}}{\pi N} \quad (2)$$

where, k_u is the non-dimensional blade velocity, and the value is 1.5~2 [35]. The main specifications of the turbine runner blade are shown in Table 2. The hub ratio was 0.5. The block diagram of the design process for the new propeller turbine model has been shown in Figure 3. The turbine design process used a trial and error-based algorithm with several times numerical analyses for optimum geometry [35].

Table 2. Main design parameters of the turbine blade.

Description	Dimension
Runner blade diameter (m)	0.50
Runner blade	4
Hub diameter (m)	0.25
Hub ratio	0.50

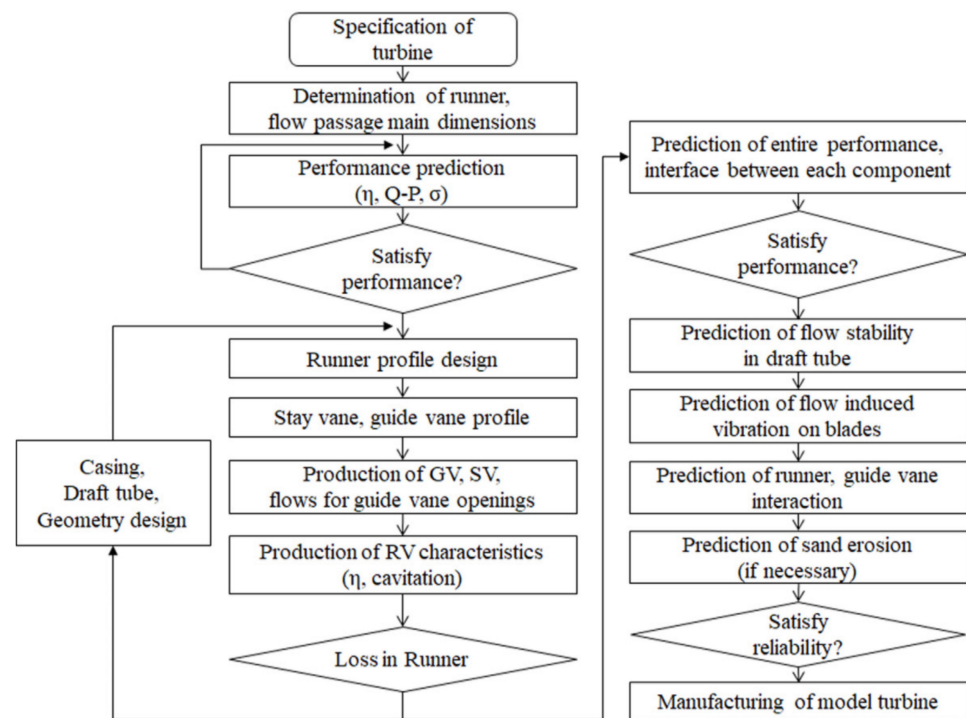


Figure 3. Block diagram of the design process for the hydraulic turbine.

3. Methodology

The installation location of the small hydropower plant was the southern area of Korea. This fish farm was equipped with a water pump supply system. Seawater is recirculated into the fish farm and discharged through the discharge water channel. The installation facilities were designed to be installed in a shared water surface without a building, that is, they were environmentally friendly. A schematic installation diagram of the marine small hydropower plant has been shown in Figure 4.

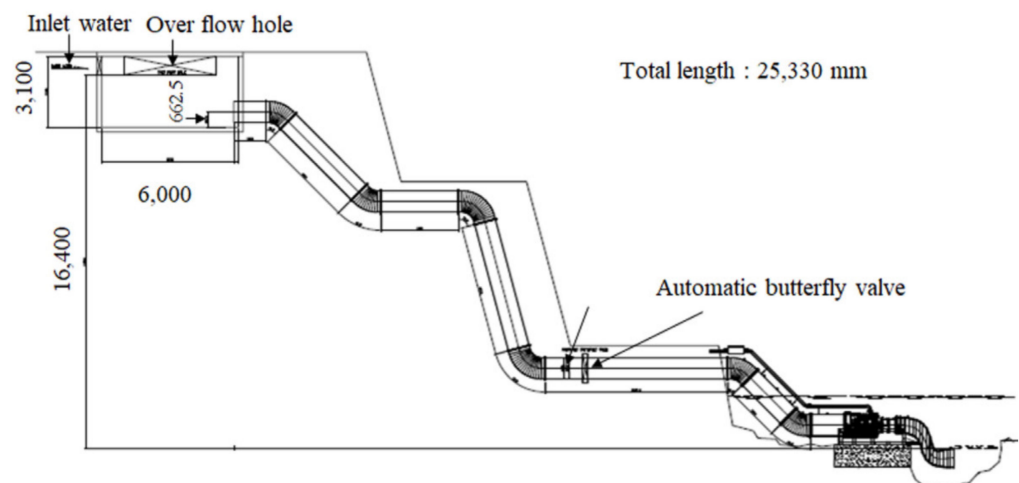


Figure 4. Schematic installation diagram of an offshore small hydropower plant.

3.1. Numerical Method

3.1.1. Geometrical Model and Meshing

The three dimensional (3D) geometry of the horizontal prototype propeller type tubular turbine was selected to analyze the flow characteristics as shown in Figure 5. The 3D turbine model was meshed by ANSYS ICEM-CFX (16.2) software (16.2, ANSYS Inc.,

Canonsburg, PA, USA, 2016) The flexibility of the complex design of the hydraulic turbine allowed the unstructured prism tetrahedral grid system to be employed to make the grid. Overall, meshing grids comprised 1,192,047 nodes and 4,302,575 elements. Unstructured tetra-prism meshing grids have been shown in Figure 6. To precisely simulate the flow in a whole turbine channel, further grid refinement is required. However, the grid cannot be too large, which is needed for a comparatively fine grid, as numerical simulations lead to a considerable amount of computational data. To reduce the influence of grid number on computational results, a grid dependency study at the rated head (15 m) operating condition (GV 60° and RV 24°) was conducted. This showed that the efficiency deviation was less than 1% [38,39], as shown in Figure 7. The grid independency test was carried out based on the grid convergence index (GCI) method [40–42]. With this, the approximate and extrapolated relative errors can be written as:

$$\varepsilon_a = \left| \frac{\varepsilon_{new} - \varepsilon_{old}}{\varepsilon_{new}} \right| \times 100\% \quad (3)$$

The grid convergence index can be calculated as

$$GCI = \frac{1.25 \times \varepsilon_a}{r^2 - 1} \quad (4)$$

where ε_a is the relative error and r is the mesh ratio.

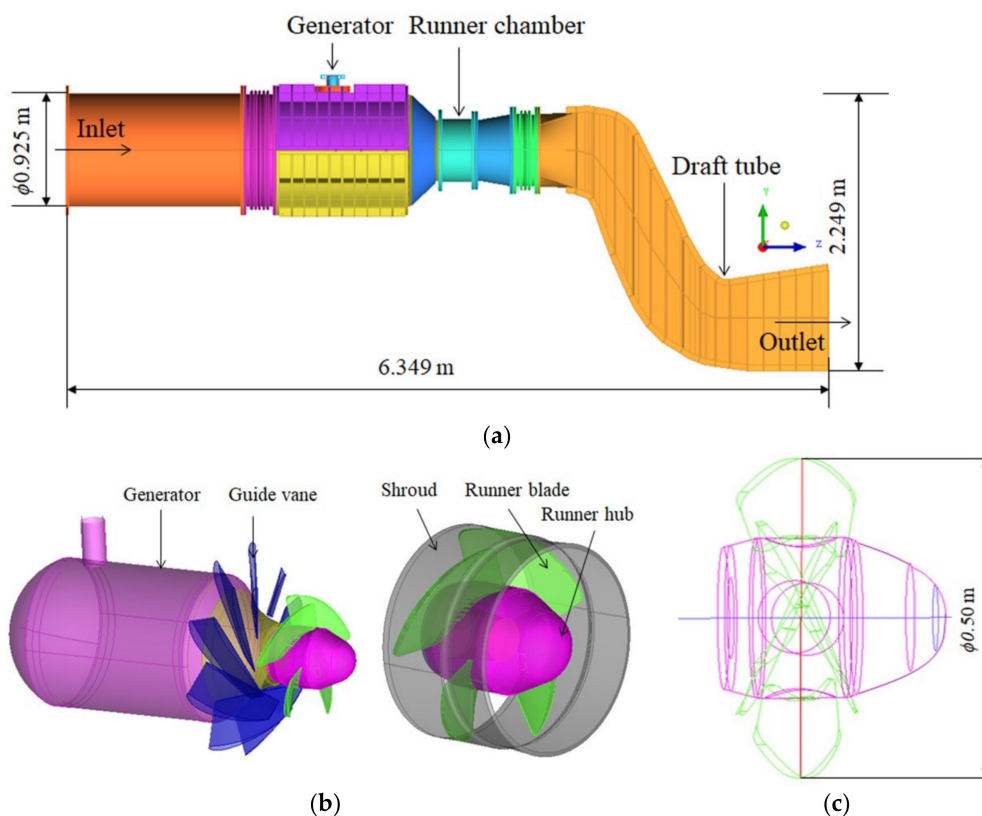


Figure 5. Three dimensional (3D) geometry of a propeller type turbine: (a) turbine; (b) generator, runner, and guide vane; (c) dimension of runner.

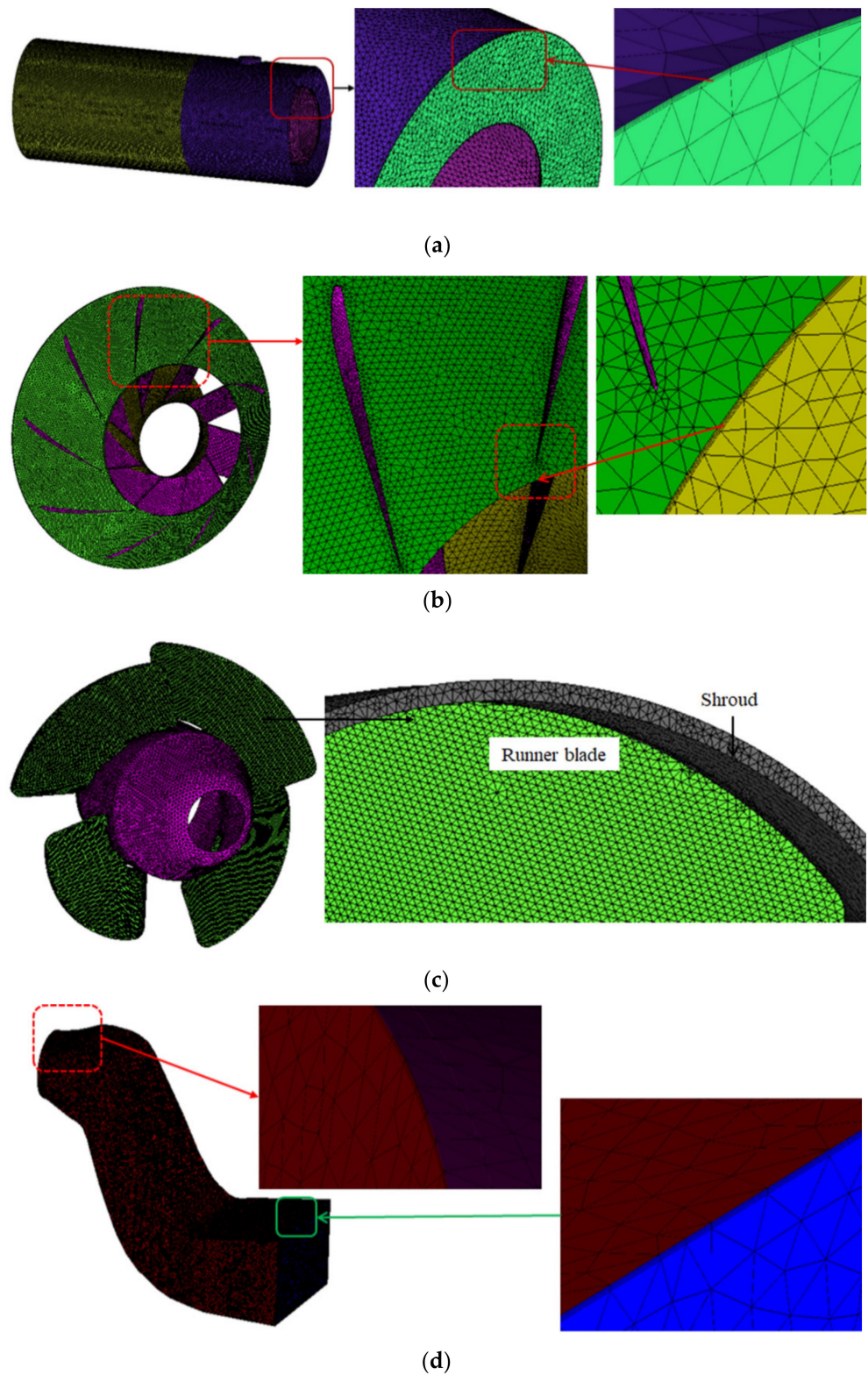


Figure 6. Unstructured prism grids: (a) inlet pipe and generator; (b) guide vane; (c) runner; (d) draft tube.

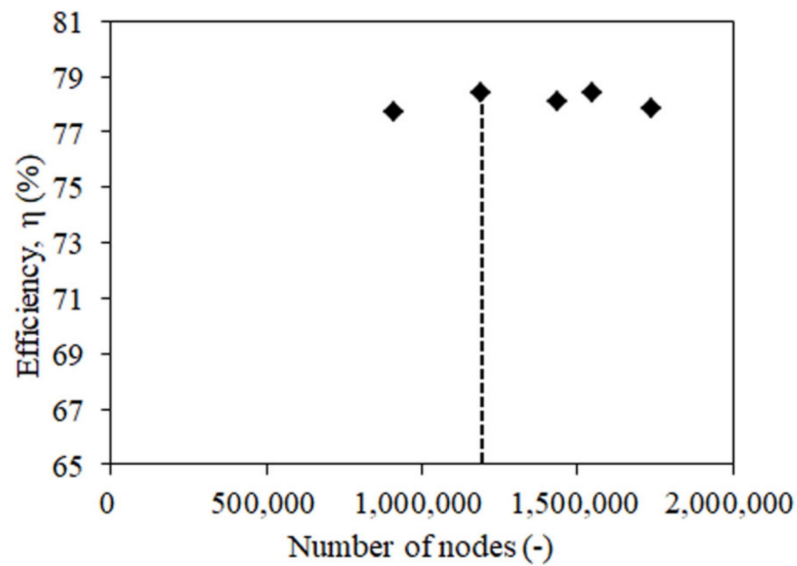


Figure 7. Grid independency test of the tubular turbine (vertical dotted line represents the used grid).

The cells' finite volume approaches near the wall boundary are irregular, potentially requiring a special procedure. First, prisms create a layer near the wall of regular prisms and then mesh the remaining volume with tetrahedrons [39,43]. This grid approach improves the near walls and provides better solutions and convergence of computational methods [43].

The mesh quality of the tubular turbine is shown in Table 3. The estimated numerical uncertainties in the hydraulic turbine are shown in the Table 4. From the table, the 1,192,047 grid density showed higher efficiency with lower uncertainties compared to the other grid density. Therefore, 1,192,047 grid densities were selected as the final grid scheme for numerical computation. The Y^+ contour of the runner and hub has been shown in Figure 8.

Table 3. Grid quality of the tubular turbine.

Description	Elements	Nodes	Min. Y^+	Max. Y^+
Inlet pipe	1,089,171	299,348	2.60	64.85
Guide vane	562,824	152,061	1.41	360.67
Runner	1,583,989	453,384	1.25	343.16
Draft tube	1,066,591	287,254	1.33	85.19
Total	4,302,575	1,192,047		

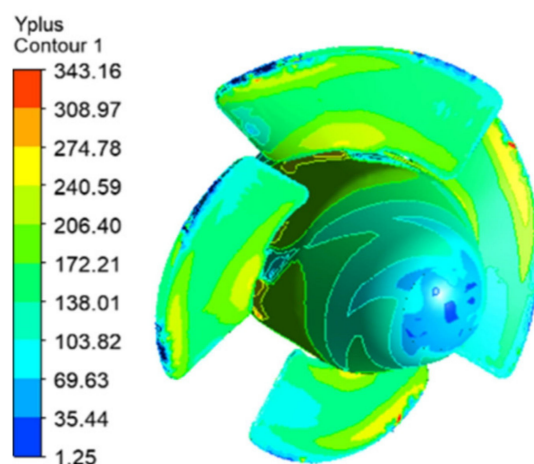


Figure 8. Y^+ contour of the runner.

Table 4. Grid convergence uncertainties in the numerical solutions.

No.	Nodes	Grid Ratio, r	Efficiency (%)	Error, ϵ_a	GCI
1	912097	1.31	77.74	0.90043	1.5896
2	1192047	1.21	78.44	0.42070	1.1502
3	1438976	1.07	78.11	0.38407	3.0851
4	1546893	1.13	78.41	0.71419	3.3582
5	1740401	0.90	77.85	0.15414	1.0281

3.1.2. Governing Equations

Numerical analysis of the fluid flow was based on continuity and momentum equations [44,45], which are expressed as:

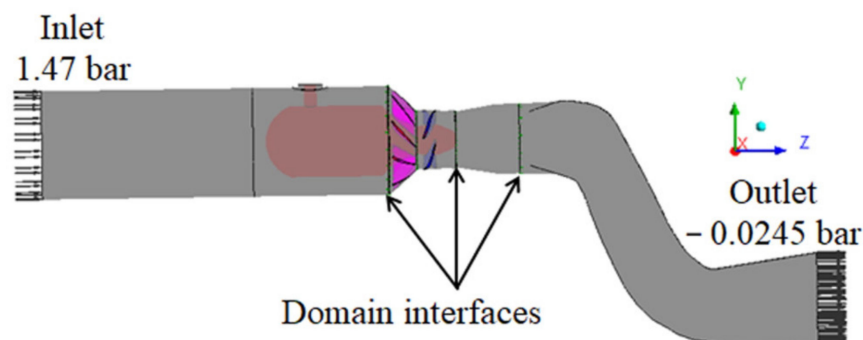
$$\frac{\partial u_i}{\partial x_i} = 0 \quad (5)$$

$$\rho \left(\frac{\partial u_i}{\partial t} + u_j \frac{\partial u_i}{\partial x_j} \right) = -\frac{\partial p}{\partial x_i} + \frac{\partial}{\partial x_j} \left(\mu \frac{\partial u_i}{\partial x_j} - \overline{\rho u'_i u'_j} \right) \quad (6)$$

where ρ and μ are density and dynamic viscosity respectively, p is the pressure scalar, and $-\overline{\rho u'_i u'_j}$ is the apparent turbulent stress tensor.

For numerical simulation, the tubular turbine domain was considered a steady-state, incompressible flow. The flow through the tubular turbine was simulated with the commercial code ANSYS-CFX (16.2) based on finite volume methods (FVM) [44]. The runner domain was rotating on the z -axis at a given rotating speed of 850 rpm, and the inlet pipe, generator, guide vane, and draft tube were a stationary domain.

Figure 9 shows the tubular turbine domain for the computer simulation. All boundary conditions were assumed as smooth walls with no-slip, and automatic wall functions were considered in the near wall region. Moreover, regular smooth wall functions were used, so that at a non-dimensional distance from the walls Y^+ the first grids were placed. Near a no-slip wall, there are negative gradients in dependent variables, according to conventional theory. Also, the viscous effects on transport processes are relatively high; these measurements are spread across the wall-adjacent viscosity-affected sublayer. Computer performances and ability demands are greater than those of the wall function, and a certain strong computational resolution in the near-wall area can be taken care of to understand the rapid difference in variables [44]. An automated wall treatment mechanism has been developed by ANSYS-CFX to minimize the resolution requirements, allowing a gradual switch between wall functions and low-Reynolds number grids, without loss of precision [44]. The well-accepted way to account for wall effects is through wall functions. In CFX, an automatic near-wall treatment feature was reported in the near-wall region for k - ω -based models (including the SST model) [44,45].

**Figure 9.** Prototype turbine domain for computational analysis.

The static pressure boundary conditions were imposed on the inlet and outlet of 1.47 bar and -0.0245 bar. A frozen rotor was applied to couple the rotation and stationary domain. Menter's shear stress transport (SST) $k-\omega$ turbulence model [46,47] was used to solve the turbulence phenomena of the fluid. Also, the SST model accounts give highly accurate predictions of the onset and the amount of flow separation under adverse pressure gradients [46]. Advection term dealt with high-resolution discretization scheme, and the first-order upwind difference was used to solve the turbulence numeric. The residual value was 1×10^{-5} controlled by convergence criteria.

3.2. Experimental Method

The performance of the manufactured water turbine was measured in the field. Experimental measurements and calibrations were taken using the IEC-60193 procedure and guidelines [48]. The inlet pipe diameter was 925 mm. A pressure gauge at a range of 0~1 MPa was installed and located at the turbine upstream. Flow rates were measured by the differential pressure sensors located near the generator. The flow rate was measured based on the pressure differential chart provided by Korea Testing Certification (KTC). The experiment was carried out three times at 30 min intervals. The combined standard uncertainty in the hydraulic turbine is the effect of the standard uncertainty of the independent variable on the uncertainty of the flow rate. Unfortunately, only three measurement data for the degree of freedom (DoF) could not illustrate the 95% confidence limit and error propagation from the result (Table 5) [39]. Figure 10 illustrates the experimental layout and devices of the small hydropower plant at the fish farm.

Table 5. Comparison of experimental and simulation test results of the tubular turbine.

Description	Rotational Speed (rpm)	Head (m)	Flow Rate (m ³ /s)	Power (kW)	Efficiency (%)
Experimental	496	13.00	0.95	98.70	79.90
Simulation	500	12.97	0.97	91.45	73.43
Error (%)	0.806	0.231	2.105	7.345	8.097

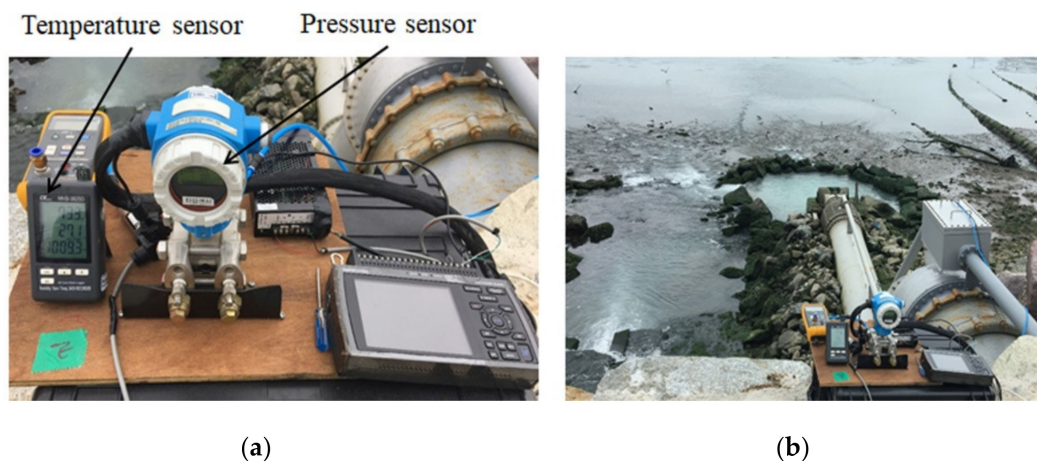


Figure 10. Experimental layout and devices: (a) pressure and temperature sensor; (b) offshore small hydro power plant.

4. Results and Discussion

4.1. Validation of Numerical Results

Numerical simulations were validated with experimental data. Table 5 illustrates CFD performance and experimental results for the tubular turbine. As shown in Table 6, the average deviation of the head was 0.231%, and the flow rate deviation was only 2.105% at a rotational speed of 496 rpm [39,49]. The power output and efficiency of the turbine were different due to the different runner vane openings in the experiment and simulation. The power and efficiency of the measuring procedure were different due to the different runner

vane angles in the experiment and simulation. Also, in simulation, we did not take into account the bearing and generator loss. In a hydraulic system, the three kinds of losses are hydraulic loss, shaft loss, and generator or bearing loss. However, in the simulation, we only considered the hydraulic part, as shown in Figure 11, that included hydraulic and shaft losses. Also, different runner vane openings were used in the simulation because when it created the exact opening angle, the runner blades were crossed the interface between the guide vane outlet and runner vane inlet. If it could happen in the computer-aided design (CAD) model, the simulation would not run by the ANSYS-CFX solver. Therefore, we solved this issue as much by opening the runner vane angle which was closed to the experimental vane opening. When the runner vane opening angle was 24° , and the guide vane opening angle was 60° , the power output was 97.13 kW. As the opening angle of the runner vane decreased, efficiency increased, but flow rate and power decreased. When the opening angle of the guide vane angle was 40° , and the opening angle of the runner vane was 19° ; maximum power output (128.78 kW) was possible under a flow condition of $1.13 \text{ m}^3/\text{s}$. Further review of this part is needed. With an efficiency of 79.90% in close proximity, the runner vane angle was between 26° and 28° . However, power and flow decreased. A field performance test was conducted under the environmental conditions of $1024 \text{ kg}/\text{m}^3$, a working dry temperature of 26°C , a relative humidity of 74%, and an atmospheric pressure of 101 kPa. Turbine output obtained from the field performance test was 98.7 kW, and the overall efficiency of the hydraulic turbine was 79.90%, which was 3.9% higher than the guaranteed efficiency of 76%. The turbine efficiency curve is shown in Figure 12 as a comparison between the expected efficiency of the computer simulation and the efficiency obtained from the field performance test.

Table 6. Performance according to guide vane shape ($H = 14.84 \text{ m}$).

Description	Runner Vane Angle ($^\circ$)	Guide Vane Angle ($^\circ$)	Flow Rate (m^3/s)	Power (kW)	Efficiency (%)
Short chord	19	40	1.127	126.84	77.13
Long chord	19	40	1.091	123.47	77.69

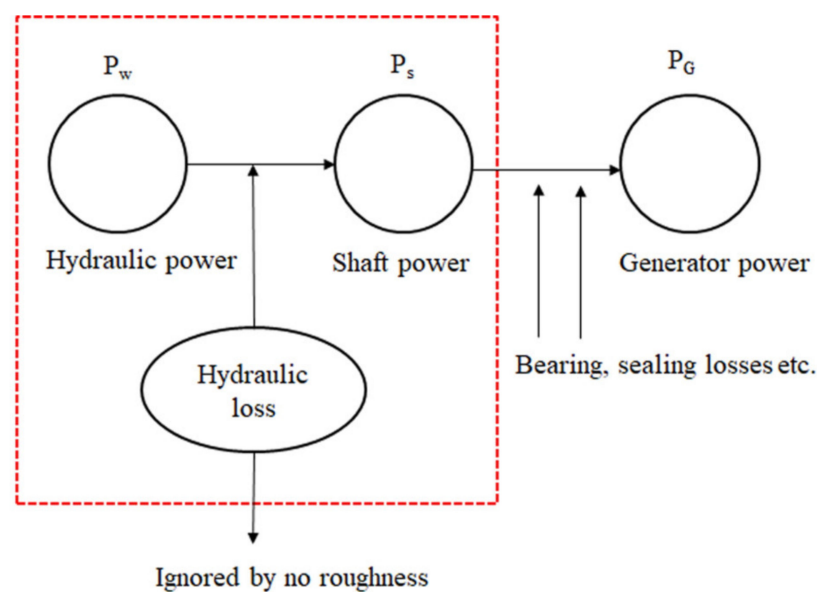


Figure 11. Different losses in the hydraulic turbine (P_w = hydraulic power, P_s = shaft power, and P_G = generator power).

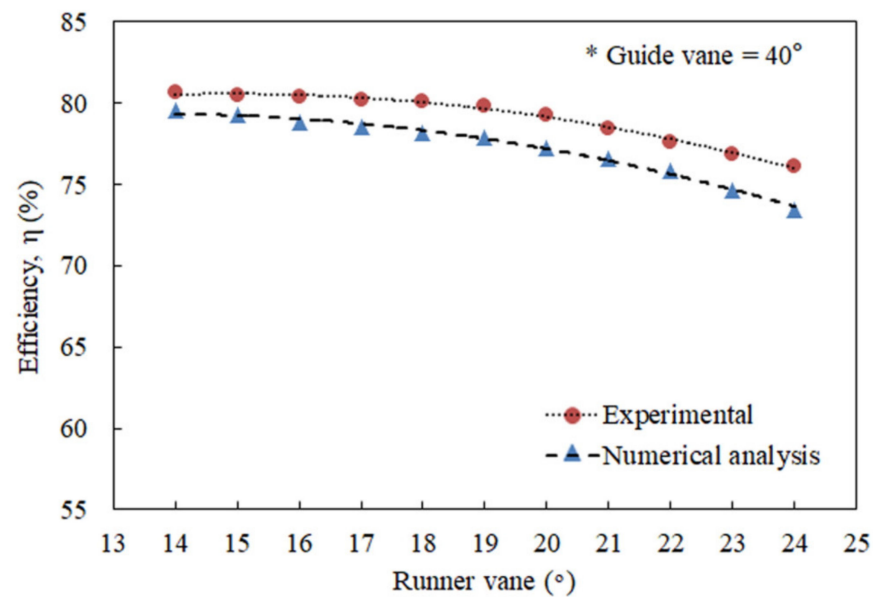


Figure 12. Comparison of turbine efficiency across various runner vane opening angles.

4.2. Performance Characteristics

Computer simulations were conducted at different flow rates by changing the guide vane and runner vane opening angles of the tubular turbine. Guide vane opening angles varied from 40° – 60° , and runner vane opening angles varied from 14° – 24° . Figures 13 and 14 show the efficiency, flow rate, and power performance characteristics of the tubular turbine with different runner vane and guide vane opening angles. In the graph, maximum efficiency was 81.67%, and power output was 101.54 kW at a flow rate of $0.854 \text{ m}^3/\text{s}$. In this case, the runner vane opening angle was 14° , and the guide vane opening angle was 50° . As the runner vane angle increased, the flow rate increased linearly, and the power increased sharply as shown in Figure 14. Also, when runner vane and guide vane angles varied to maximum (fully open, Figures 13 and 14), efficiency was low (67.13%), and power was 97.13 kW at a flow rate of $0.994 \text{ m}^3/\text{s}$.

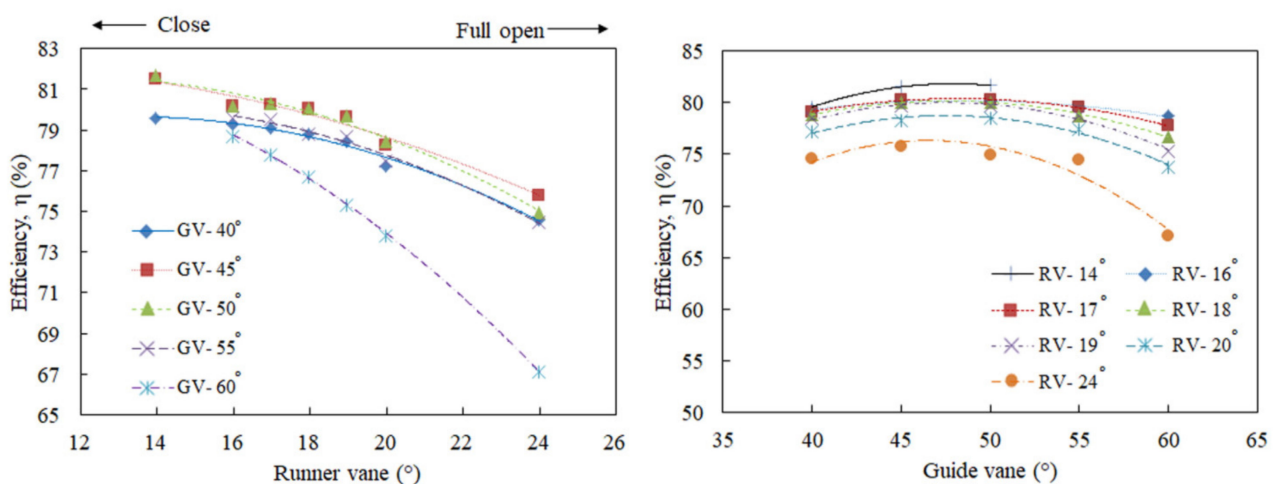


Figure 13. Efficiency changes according to runner vane and guide vane opening angles.

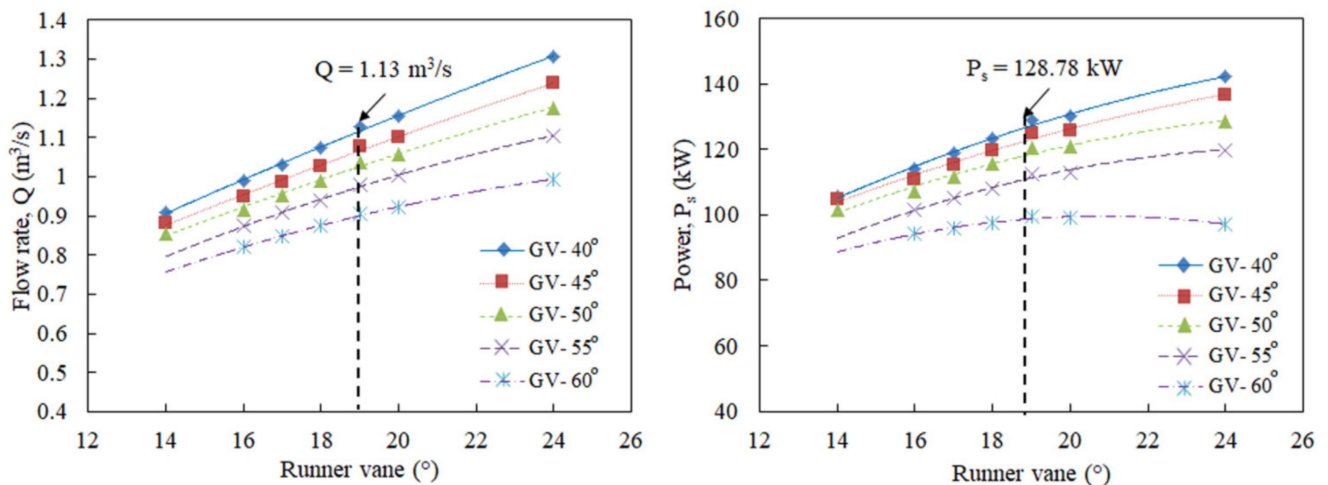


Figure 14. Flow rates, power versus runner vane, and guide vane opening angles.

The rated flow rate was found when the runner vane opening angle was 19° , and the guide vane opening angle was 40° . In this case, efficiency was found to be 78.44%, and power output was 128.78 kW at a flow rate of $1.13 \text{ m}^3/\text{s}$. Figure 15 shows the blade-to-blade pressure and velocity (magnitude) distributions at a 0.5 span (non-dimensional blade height = 0.5). In this figure, the dotted circle represents the leading edge and trailing edge of the runner blade. The pressure was maximum, and the velocity was minimum at the leading edge of the pressure side. Velocity was not distributed uniformly from the leading edge to the trailing edge of the runner vane. Velocity decreased at the trailing edge of the runner vane, and a small vortex formed in this region.

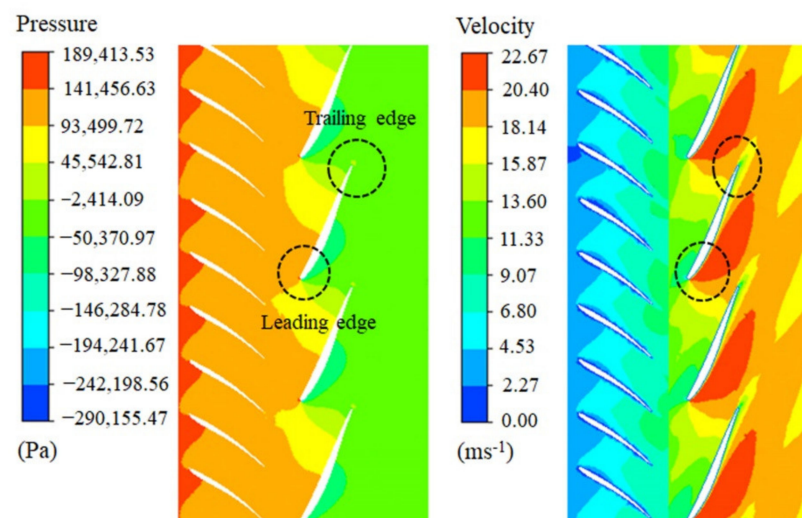


Figure 15. Blade-to-blade pressure and velocity contours (span = 0.5).

Figure 16 shows the velocity vector and streamlines of the blade-to-blade guide and runner vane. The figure shows that the guide vane makes the flow pattern non-uniform through the runner vane, and this phenomenon could not reach the desired value. A vortex was also formed near the front of the guide vane and a recirculating flow occurred. Large recirculation flow occurred near the hub of the runner outlet [49].

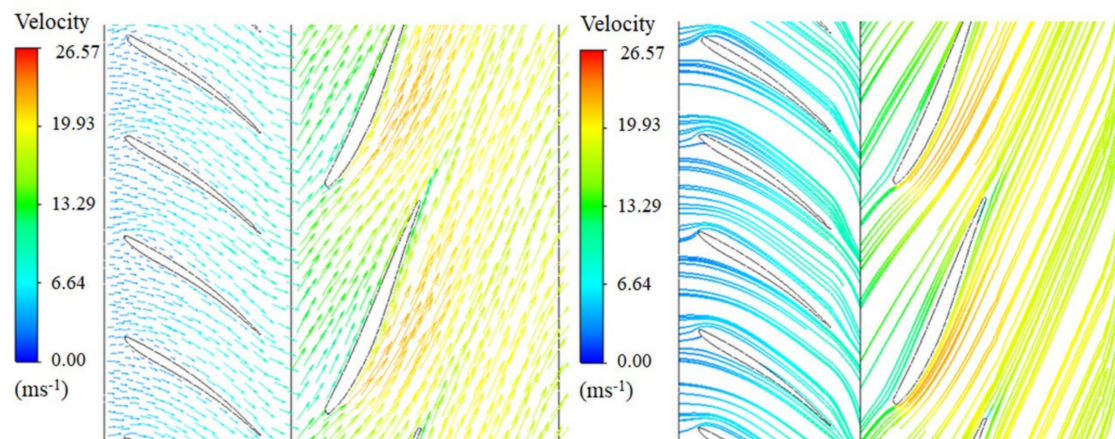


Figure 16. Blade-to-blade velocity vector and velocity streamlines (span = 0.5).

4.3. Design Modification for Performance Improvement of Turbine

4.3.1. Shape of Guide Vanes

The performance of guide vanes with short and long chords was compared. Figure 17 shows the cross-section before and after the shape of the guide vane was changed. The vane-to-vane streamlines distribution of guide vanes and runner vanes are shown in Figure 18. In Figure 18, a vortex occurred at the leading edge of the guide vane in both the short and long blade chords. When the blade chord was long, the pressure difference between the leading edge and the trailing edge of the guide vane was large, but the size of the recirculation area was slightly reduced. Additionally, velocity decreased slightly in the leading edge of the guide vane.

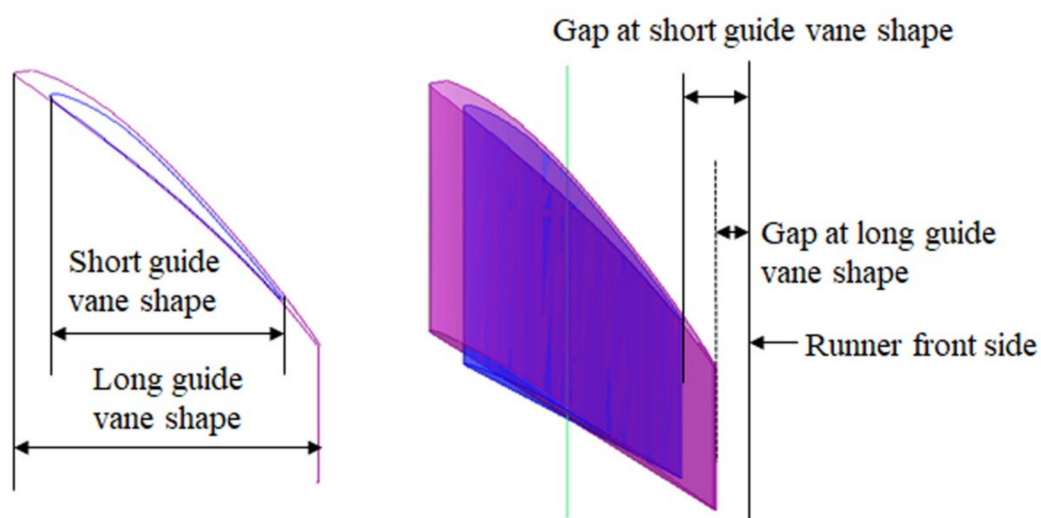


Figure 17. Shapes of short and long guide vanes.

Table 6 shows performance characteristics according to guide vane shape. As the size of the blade chord of the guide vane increased, flow rate decreased, as a result of reducing the water power and shaft power and increasing the efficiency by 0.56%. Compared to guide vanes with short chords, guide vanes with long blade chords had lower flow rates due to the change in pressure distribution, even though the recirculation area was slightly reduced. Figure 19 shows the turbine loss analysis. From a loss analysis point of view, efficiency changed generally around 1–2% according to changes in the length of the guide vane. Additionally, it was more important to change the shape of the runner vane than the shape of the guide vane.

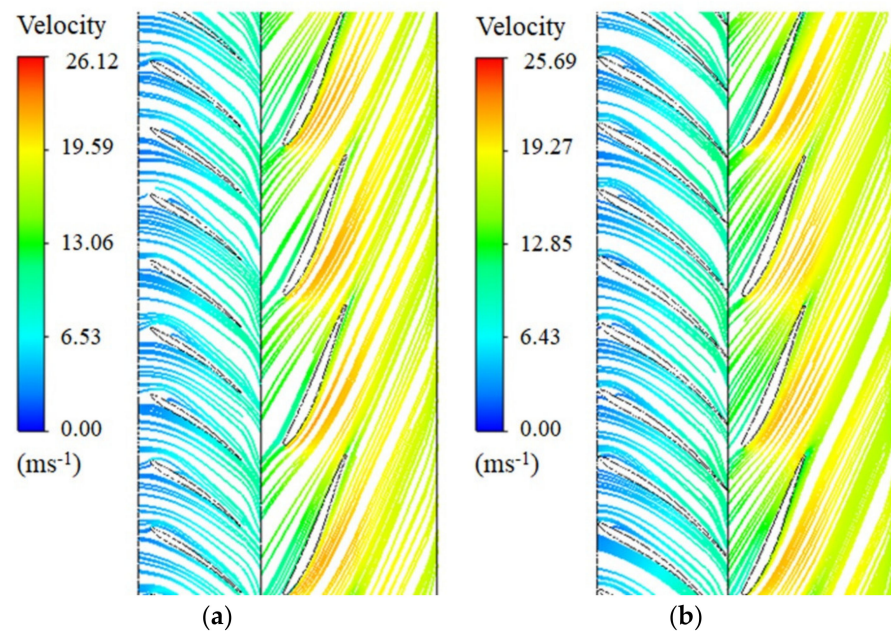


Figure 18. Vane-to-vane velocity streamline distribution of guide vanes and runner vanes: (a) at short chord; (b) at long chord.

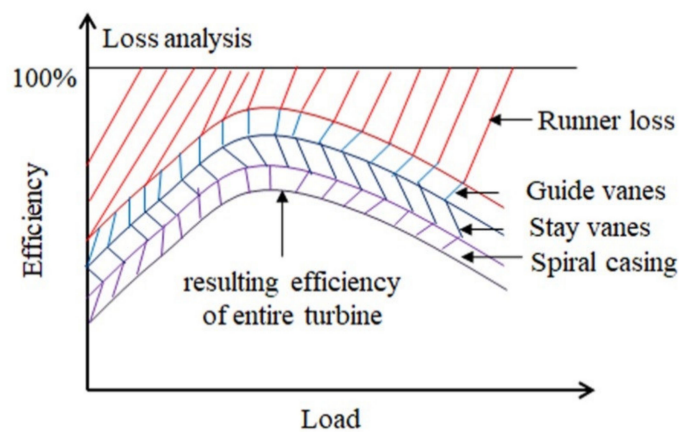


Figure 19. Turbine loss analysis.

The optimum total efficiency depends on the design and operating conditions of turbine, it is especially important to reduce the main losses which are divided the losses into frictional and kinetic parts. Loss analysis states that loss due to runner is a mainly large part of the number of losses and determines hydraulic overall efficiency [37,50]. Therefore, it is necessary to first look at the efficiency changes caused by the change in runner shape and analyze the effects of the closely related guide vane shape changes. From a loss analysis point of view, efficiency changed generally around 1–2% according to changes in the length of the guide vane. The flow rate into the runner is controlled by the shape of the guide vanes. As a result, the velocity triangles in the runner will vary from section to section. Thus, it was more important to change the shape of the runner vane than the shape of the guide vane.

4.3.2. Guide Vanes Attached to the Generator Side

Figure 20 shows that the guide vane is attached to the generator side when the chord is short. Figure 21 shows the vane-to-vane pressure and streamline distribution of the guide vane and runner vane. Table 7 shows performance characteristics of the guide vane attached to the generator side. Results showed that efficiency increased by 1.33% when

guide vanes were attached to the generator side. However, a vortex flow occurred at the front of the guide vane, and a large pressure drop appeared.

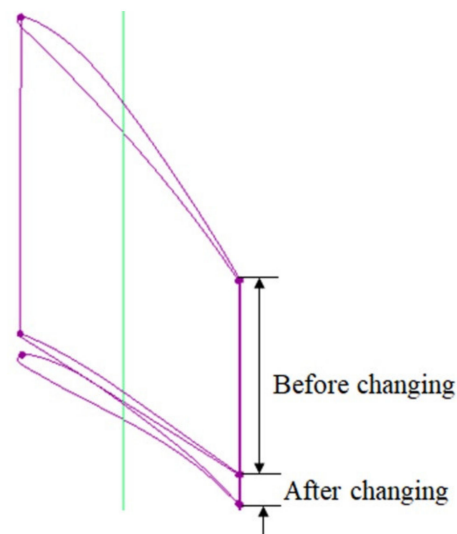


Figure 20. Guide vane attached to the generator side (short chord).

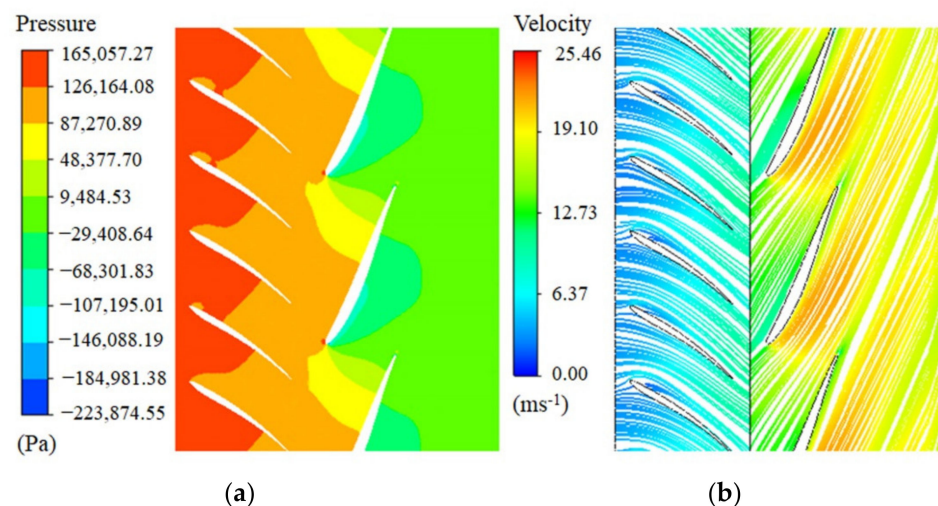


Figure 21. Vane-to-vane pressure and streamline distribution of guide vanes and runner vanes: (a) pressure contours; (b) streamline contours.

Table 7. Performance of guide vane attached to the generator side (short chord, $H = 14.84$ m).

Description	Runner Vane Angle (°)	Guide Vane Angle (°)	Flow Rate (m ³ /s)	Power (kW)	Efficiency (%)
Before attachment	19	40	1.127	126.84	77.13
After attachment	19	40	1.113	127.23	78.46

4.3.3. Streamlining the Shape of the Guide Vane

(1) In the case of a short cord

In this investigation, the shape of the guide vane was changed to a streamlined shape. Figure 22 illustrates a cross-sectional view of the guide vane's streamlined shape. Figure 23 shows the vane-to-vane streamline distributions of guide vanes and runner vanes. Changing the streamline shape of the guide vane improved its pressure distribution. As shown in the streamline diagram (Figure 23), flow separation was also reduced due to the streamlined shape around the front of the guide vane, improving the efficiency of the

turbine. Table 8 shows performance characteristics of guide vanes with a streamlined shape when the wing string was short. After guide vanes were streamlined, efficiency decreased, and the rated flow rate was not reached. Changing the opening degrees of guide vanes and runner vanes to bring out the rated flow increased efficiency by 0.21%. It was believed that efficiency did not increase much, because the shape of the leading edge of the runner vane was designed incorrectly.

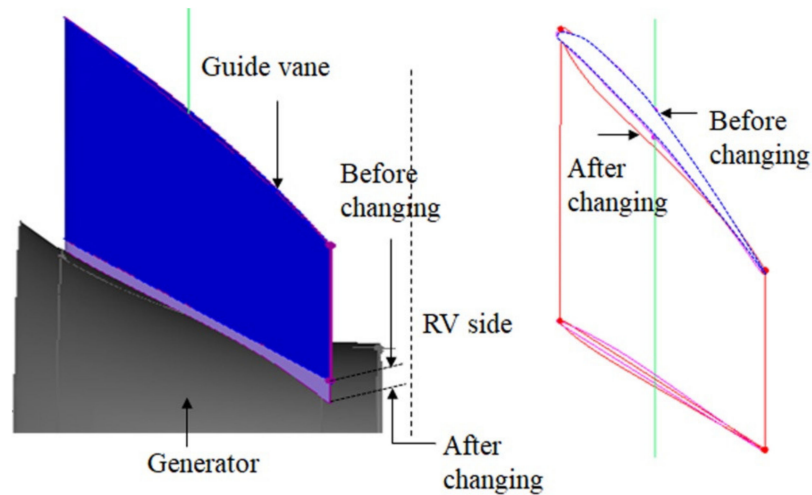


Figure 22. Changing the shape of guide vanes with short chords to make them streamlined.

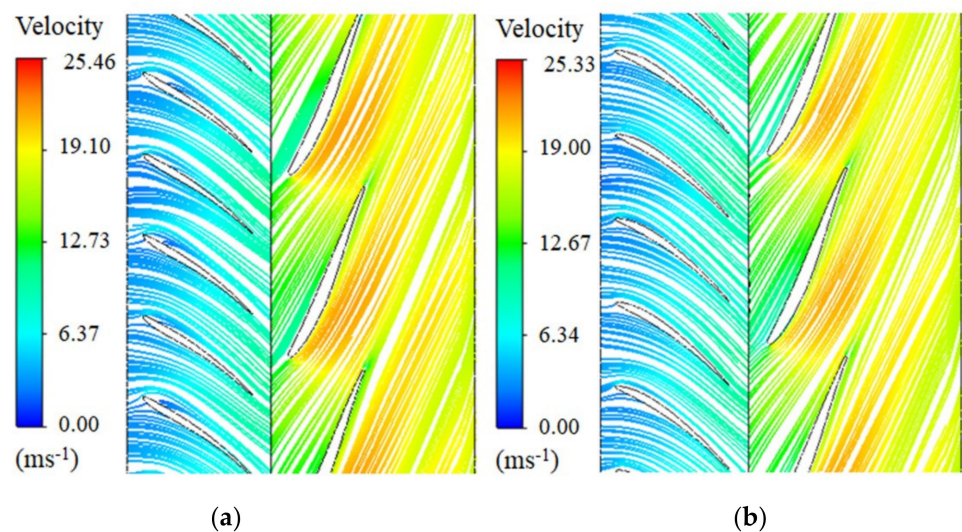


Figure 23. Vane-to-vane streamline distribution of guide vanes and runner vanes: (a) streamline distribution before shape change; (b) streamline distribution after shape change.

Table 8. Performance characteristics according to guide vane shape (short chord, $H = 14.84$ m).

Description	Runner Vane Angle (°)	Guide Vane Angle (°)	Flow Rate (m ³ /s)	Power (kW)	Efficiency (%)
Before change	19	40	1.113	127.23	78.46
	19	40	1.086	123.91	78.35
	19	42	1.067	121.06	77.95
After change	19	38	1.110	126.69	78.67
	19	45	1.016	115.16	77.83
	20	40	1.118	126.52	77.71

(2) In the case of long chords

In this investigation, the long chord shape of the guide vane was chosen. Figure 24 shows the vane-to-vane pressure and streamlines distributions of guide vanes and runner vanes. The flow separation was disappeared from the guide vane. Table 9 illustrates the performance characteristics of streamlined guide vanes when the wing string was long. In Table 9, efficiency changes were insignificant in the case of short and long chords.

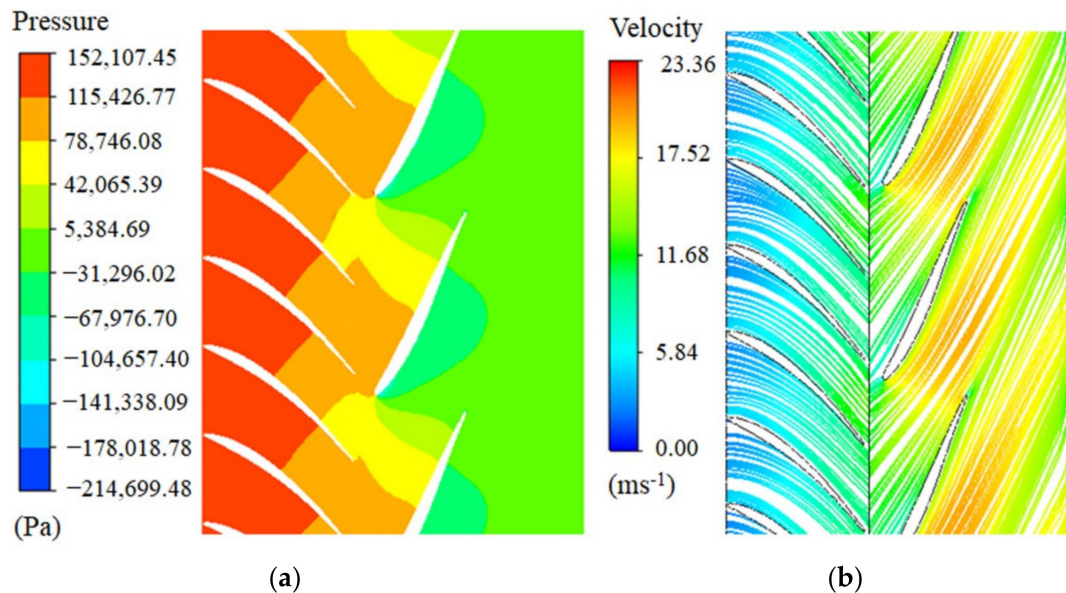


Figure 24. Vane-to-vane pressure and streamline distribution of guide vanes and runner vanes when chords were long: (a) pressure distribution; (b) streamline distribution.

Table 9. Performance characteristics according to guide vane shape (long chord, $H = 14.84$ m).

Description	Runner Vane Angle (°)	Guide Vane Angle (°)	Flow Rate (m ³ /s)	Power (kW)	Efficiency (%)
Attached short chord	19	38	1.110	126.69	78.67
	19	40	1.011	114.57	77.84
	19	38	1.043	118.80	78.24
Attached long chord	20	40	1.040	117.78	77.58
	20	45	0.966	107.44	76.38
	22	40	1.104	124.22	77.78

4.3.4. Runner Vane Shape

The shape of the runner vane was changed as shown in Figure 25. Table 10 shows the performance characteristics of different runner vane shapes. Flow rate decreased according runner vane shape, reducing the water power and increasing the efficiency by about 5.57%.

Table 10. Performance characteristics according to runner vane shape ($H = 14.84$ m).

Description	Runner Vane Angle (°)	Guide Vane Angle (°)	Flow Rate (m ³ /s)	Water Power (kW)	Power (kW)	Efficiency (%)
Compact shape	19	40	1.011	147.20	114.57	77.84
	19	40	0.966	140.55	116.53	82.91
Expanded shape	24	40	1.101	159.96	133.43	83.41
	24	38	1.131	164.50	135.37	82.31

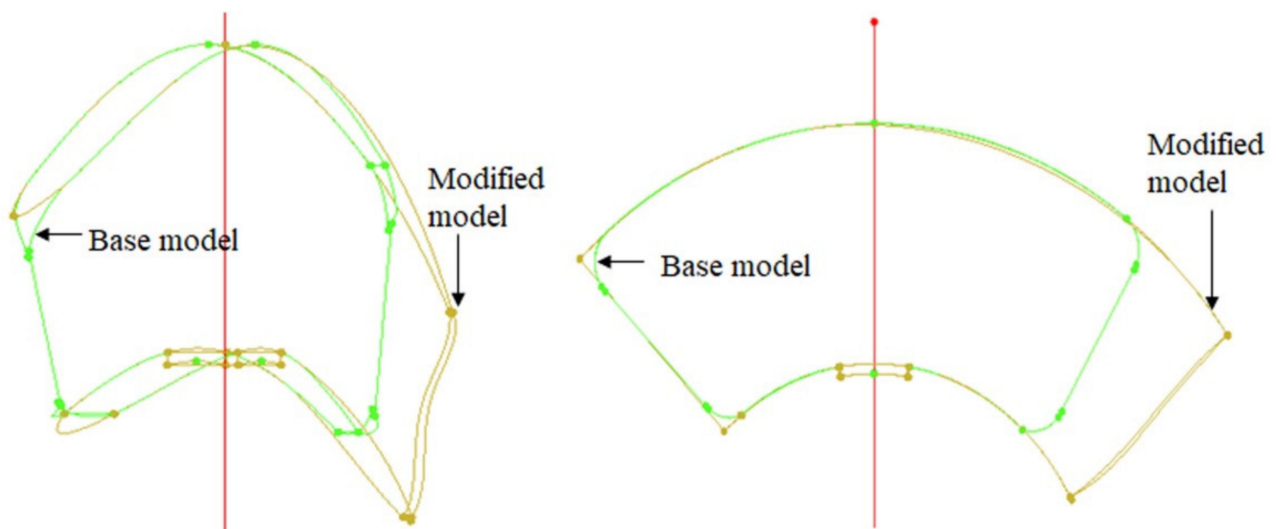


Figure 25. Changing the shape of the runner vane.

When the opening angle of the guide vane and runner vane was changed to reach the rated flow rate ($1.131 \text{ m}^3/\text{s}$), efficiency increased by 4.47%. Figure 26 shows the vane-to-vane pressure and streamline distribution of guide vanes and runner vanes. In the figure, flow separation disappeared after changing the shape of the runner vane. Also, performance characteristics of turbines with different shapes were compared. Figure 27 shows the efficiency and flow performance characteristics of guide vanes with different opening degrees ($\text{GV-}38^\circ$ and $\text{GV-}40^\circ$). Results showed that efficiency was lower in short guide vanes than in long guide vanes.

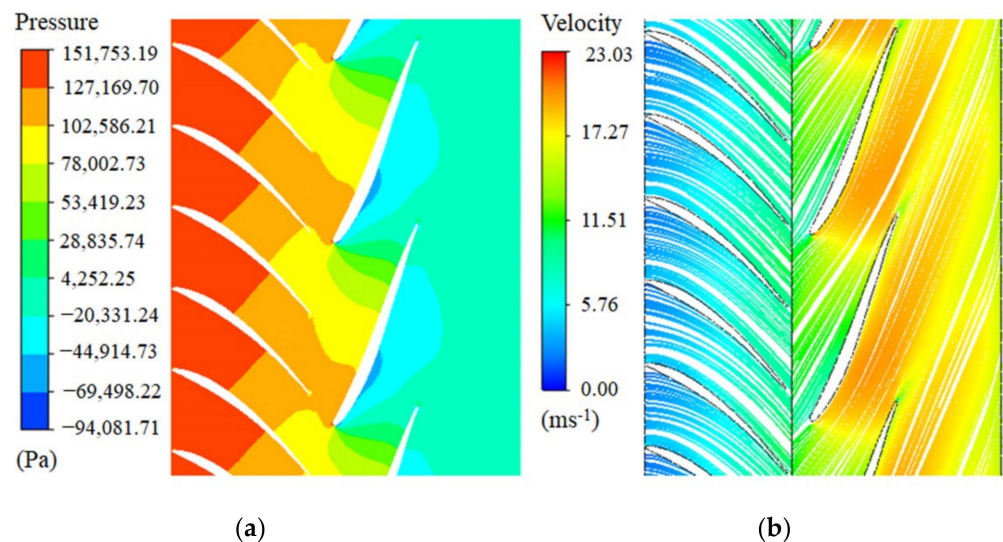


Figure 26. Pressure and streamline distribution between guide vanes and runner vanes: (a) pressure contour after shape change; (b) streamline contour after shape change.

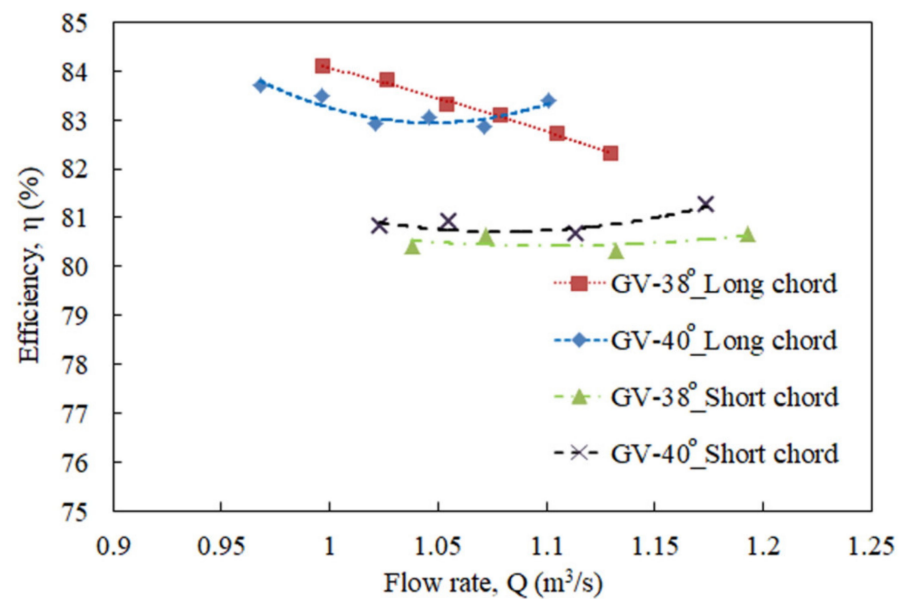


Figure 27. Comparison of efficiency and flow rate according to guide vane opening (RV-19~24°).

4.3.5. Rotational Speed

The performance characteristics of generators with different rotational speeds were investigated. When the generator ran at 850 rpm, the tubular turbine would not operate functionally, and an increase in vibration could stop the hydroelectric power plant. Therefore, a reduced rotational speed was considered to stabilize the turbine operation. Table 11 shows the performance of runner vanes with different rotation speeds. In the table, efficiency gradually decreased as rotational speed decreased. The flow rate and output also decreased sharply. There was no major change in efficiency (only 0.86% difference) when the rotation speed was 650 rpm.

Table 11. Performance characteristics according to runner vane rotation speed (H = 14.84 m, GV-40°).

Rotational Speed (rpm)	Runner Vane Angle (°)	Flow Rate (m³/s)	Power (kW)	Efficiency (%)
850	24	1.101	133.43	83.41
750	24	1.046	124.46	81.77
700	24	1.019	119.29	80.37
650	24	0.994	114.03	78.75
650	23	0.975	113.08	79.61
650	27	1.076	123.84	79.02

The effect of tidal level on the turbine was investigated. Figure 28 shows changes in performance characteristics according to the rotational speed and tidal level (high and low tide). At higher tides, the efficiency and flow rate of the turbine was slightly higher than at low tides for different rotational speeds. There was a remarkable power output difference between high and low tides (Figure 28c).

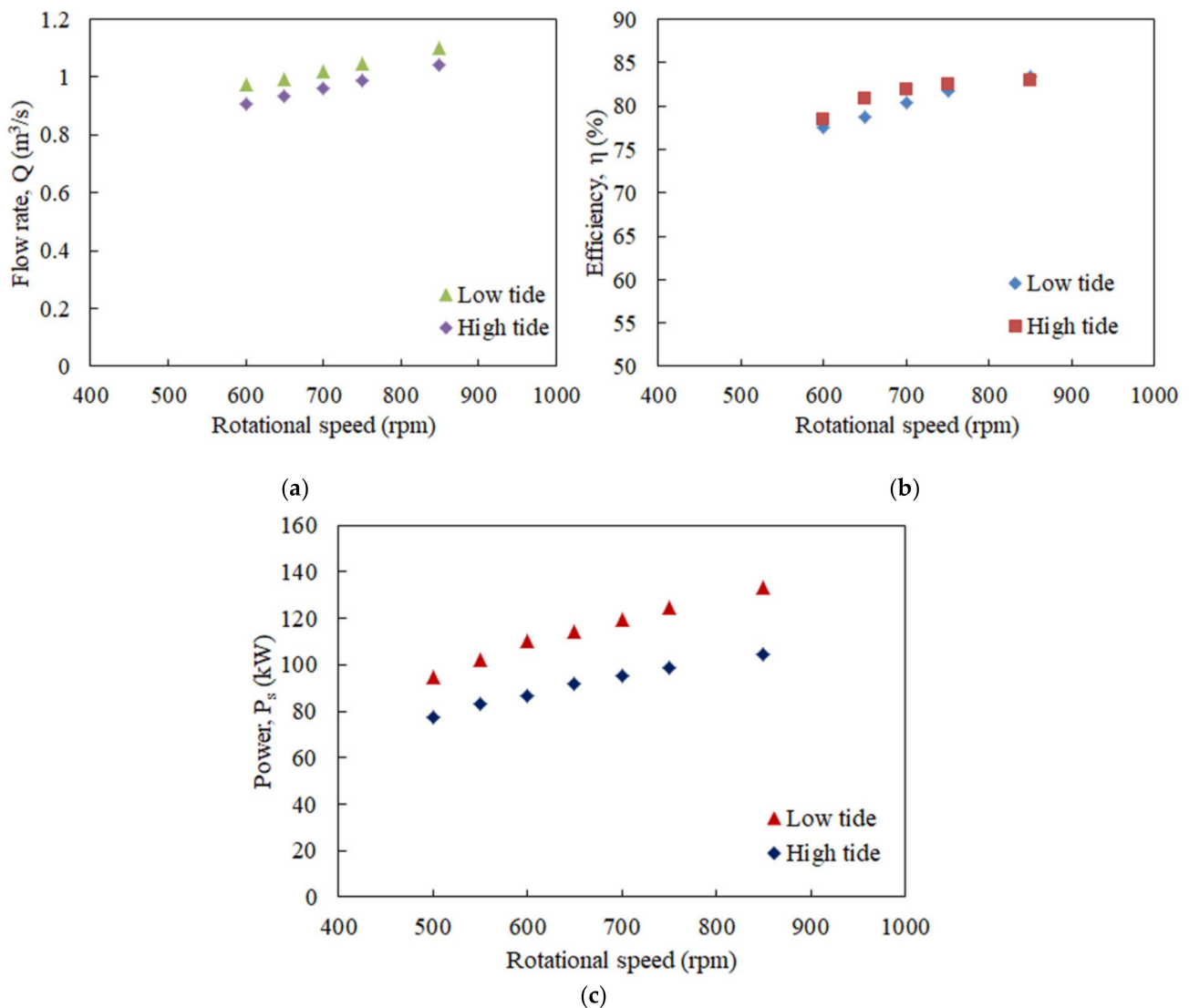


Figure 28. Performance changes according to rotational speed and tidal level: (a) rotational speed versus flow rate; (b) rotational speed versus efficiency; (c) rotational speed versus power.

4.3.6. Optimum Model

After changing the shape of the turbine draft tube, performance characteristics were reviewed. Efficiency after the shape modification of the draft tube was 77.67%, which was 0.98% less than efficiency before modification. The influence of the shape of the draft tube on efficiency was insignificant. Performance changes when the guide vane was changed to short and long blade strings were examined. Vortex flow occurred at the leading edge of the guide vane for both short and long blade strings. As flow rate decreased, the difference in efficiency in the case of power was within the error range. Efficiency increased by 1.33% when guide vanes were attached to the generator side. Streamlining the shape of the guide vane improved the pressure distribution around it. Streamlining the shape around the front side of the guide vane reduced flow separation and improved efficiency. Changing the shape of the guide vane made the recirculation zone and flow separation disappear when blade chords were both long and short. However, it was more important to change the shape of the runner vane than the shape of the guide vane. Changing the runner vane shape increased efficiency by 4.47%, and the rated flow rate emerged at a runner vane opening angle of 24° . When comparing the performance characteristics of runner vanes with long and short chorded guide vanes, the efficiency of short guide vanes was lower than that of long guide vanes.

The optimized runner vane and guide vane angles were RV-24° and GV-40°, respectively. Design specifications were considered for the manufacture and development of the fish farm power plant. At a rotational speed of 850 rpm, the flow rate was 1.101 m³/s, output was 133.43 kW, and efficiency was 83.41%. At a rotation speed of 650 rpm, stable performance was obtained. In this case, the flow rate was 0.994 m³/s, output was 114.03 kW, and efficiency reached 78.75%.

5. Conclusions

This study investigated the applicability of using fish farm recirculating discharge water. A new prototype propeller type tubular turbine was designed, and a CFD analysis was carried out to analyze its performance. Numerical simulations were validated with experiments using the IEC-60193 procedure. Various design parameters were investigated to determine the rated flow rate at the best efficiency. When runner vane and guide vane angles varied to the maximum (fully open), efficiency was low (67.13%), and power was 97.13 kW at a flow rate of 0.994 m³/s. With smaller runner vane opening angles, efficiency increased, but flow rate and output decreased. The maximum output (133.43 kW) was reached at a flow rate of 1.13 m³/s when the opening angle of the guide vane angle was 40°, and the runner vane opening angle was 19°. In this case, turbine efficiency was 78.44%. Recirculation formed near the front of the guide vane and rear of the hub. Velocity streamline distributions of the turbine were distributed non-uniformly. The tubular turbine was optimized using computer simulation to modify the shapes of runner and guide vanes, opening angles, and so on. From a loss analysis point of view, the runner component was the main part of the loss, more than the guide vane component. Thus, total efficiency sharply increased when the shape of the runner vane changed. Optimized runner vane and guide vane angles were RV-24° and GV-40°, respectively. The guide vane should be fixed, and the runner vane should be adjustable, so the vane angle can be adjusted according to the installation location. Turbine performance was optimized satisfactorily. Tubular or cross-flow type turbines are suitable for use in fish farm power plants, and generators should be waterproofed to prevent exposure to seawater. Using renewable energy from the circulated water of fish farms could meet the challenges faced during the development of hydroelectric power plants.

Author Contributions: M.R. conceived and designed the study, analyzed the results, wrote the paper, and edited the draft; S.-H.S. contributed to project administration, conceptualization and supervised the work; H.-H.K. managed resources and edited the draft; Y.R. contributed to fund acquisitions and resources the work; and K.Y.K. managed resources, fund acquisition, and advised on project work. All authors have read and agreed to the published version of the manuscript.

Funding: This research was funded by the Korea Technology and Information Promotion Agency for SMEs (TIPA), grant number S8025391, and the article processing charge (APC) was funded by grant number S8025391.

Data Availability Statement: The data that support the findings of this study are available from the corresponding author, upon reasonable request.

Acknowledgments: This research was supported by TIPA. The grant number was S8025391 for the promotion of science. Authors also extend their gratitude to Hyung-Woon Roh for his assistance during the project work.

Conflicts of Interest: The authors declare no conflict of interest.

Abbreviations

CFD	Computational fluid dynamics
GCI	Grid convergence index
PMSG	Permanent magnet synchronous generator
DoF	Degree of Freedom

D	Turbine diameter, m
g	Acceleration due to gravity, m/s^2
H	Head, m
k_u	Non-dimensional velocity
P	Power, kW
Q	Flow rate, m^3/s
u_i	Velocity vector, m/s
Greek Symbols	
ρ	Density, kg/m^3
η	Turbine efficiency, %
μ	Viscosity, Pa·s
Subscript	
i, j	Tensor indices

References

- Girling, B.; Lane, T. *World Energy Resources Hydropower 2016*; World Energy Council: London, UK, 2016.
- Koch, F.; Prasch, M.; Bach, H.; Mauser, W.; Appel, F.; Weber, M. How Will Hydroelectric Power Generation Develop under Climate Change Scenarios? A Case Study in the Upper Danube Basin. *Energies* **2011**, *4*, 1508–1541. [CrossRef]
- Kim, H.-G. *Korea Institute of Energy Research, New and Renewable Energy Resource Mapping and Utilization System Construction Project*; Korea Institute of Energy Research: Daejeon, Korea, 2013.
- Park, N. *Development of Hydraulic Gate Turbine and Its Evaluation of Hydraulic and Dynamic Performances*; Soongsil University: Seoul, Korea, 2018.
- Byun, J.-R. *Korea Energy Agency, 2014 Annual Report*; Korea Energy Agency Global Strategy Division: Gyeonggi-Do, Korea, 2015.
- Liu, H.; Maser, D.; Esser, L. *World Small Hydropower Development Report 2013*, Korea ed; United Nations Industrial Development Organization, International Center on Small Hydro Power: Hangzhou, China, 2013.
- Balkhair, K.S.; Ur Rahman, K. Sustainable and economical small-scale and low-head hydropower generation: A promising alternative potential solution for energy generation at local and regional scale. *Appl. Energy* **2017**, *188*, 378–391. [CrossRef]
- Zhou, D.; Deng, Z.D. Ultra-low-head hydroelectric technology: A review. *Renew. Sustain. Energy Rev.* **2017**, *78*, 23–30. [CrossRef]
- Hwang, Y.-H.; Lee, Y.-H.; Choi, Y.-D. Performance Measurement of a Tubular Type Turbine System for Small Hydropower by Field Test. *KSFJ J. Fluid Mach.* **2011**, *14*, 5–10. [CrossRef]
- Ma, S.B.; Kim, S.; Choi, Y.S.; Cha, D.A.; Kim, J.H. Development of 2.5 kW class propeller type micro hydraulic turbine. *Trans. Korean Hydrog. New Energy Soc.* **2020**, *31*, 314–321.
- Borkowski, D.; Wegiel, M.; Ocloń, P.; Wegiel, T. CFD model and experimental verification of water turbine integrated with electrical generator. *Energy* **2019**, *185*, 875–883. [CrossRef]
- Li, H.; Zhou, D.; Martinez, J.J.; Deng, Z.D.; Johnson, K.I.; Westman, M.P. Design and performance of composite runner blades for ultra low head turbines. *Renew. Energy* **2019**, *132*, 1280–1289. [CrossRef]
- Wang, W.Q.; Yin, R.; Yan, Y. Design and prediction hydrodynamic performance of horizontal axis micro-hydrokinetic river turbine. *Renew. Energy* **2019**, *133*, 91–102. [CrossRef]
- Punys, P.; Dumbrasukas, A.; Kvaraciejus, A.; Vyciene, G. Tools for Small Hydropower Plant Resource Planning and Development: A Review of Technology and Applications. *Energies* **2011**, *4*, 1258–1277.
- Liu, D.; Liu, H.; Wang, X.; Kremere, E. *World Small Hydropower Development Report 2019*, Korea ed; United Nations Industrial Development Organization, International Center on Small Hydro Power: Hangzhou, China, 2019.
- Korea Energy Management Corporation. *New & Renewable Energy 2010*; KEA Global Strategy Division: Gyeonggi-Do, Korea, 2010.
- Rheinhafen-Dampfkraftwerk Block 8 Achieved A 47.5% Net Thermal Efficiency to World-Class Level, World Energy. 2019. Available online: <https://www.world-energy.org/article/1198.html> (accessed on 6 August 2019).
- Ullah, I.; Kim, D.H. An Optimization Scheme for Water Pump Control in Smart Fish Farm with Efficient Energy Consumption. *Processes* **2018**, *6*, 65. [CrossRef]
- Jeong, H.G.; So, J.Y.; Chung, D.H.; Ahn, K.S.; Cho, C.H.; Kim, D.K. Development of 10 kW Permanent Magnet Synchronous Generator for Small Hydropower Generation. *J. Korean Inst. Illum. Electr. Install. Eng.* **2013**, *27*, 44–52.
- Kim, B.-K. Development of a Submerged Propeller Turbine for Micro Hydro Power. *KSFJ J. Fluid Mach.* **2015**, *18*, 45–56. [CrossRef]
- Gatte, M.T.; Kadhim, R.A. Hydro power. *Energy Conserv.* **2012**, *9*, 95–124.
- Hwang, Y.-C.; Choi, Y.-D. Construction of Marine Small Hydro Power Plant using Discharge Water of Fish Farm. *KSFJ J. Fluid Mach.* **2013**, *16*, 11–17.
- Kim, D.Y.; Kim, Y.T. Design and performance analysis of a 115kW class bulb-type hydro-turbine. *J. Korean Soc. Mar. Eng.* **2018**, *42*, 304–311.
- Kim, B.-K. Performance Characteristics of Micro Propeller Turbine. *KSFJ J. Fluid Mach.* **2014**, *17*, 25–32. [CrossRef]
- Park, J.H.; Kim, Y.T.; Cho, Y.; Kim, B.K.; Lee, Y.H. Performance Analysis of 10 kW Class Propeller Hydro Turbine by the Change of Flow Rates and the Number of Runner Vane Using CFD. *KSFJ J. Fluid Mach.* **2014**, *17*, 5–11.

26. Li, K.M.; Kwon, W.; Lee, Y.W. Numerical study on effects of guide vane opening of a bulb turbine. *J. Korean Soc. Mar. Eng.* **2019**, *43*, 528–534.
27. Vu, L.V.; Chen, Z.; Choi, Y.-D. Design and Performance of a Pico Propeller Hydro Turbine Model. *KSFJ. Fluid Mach.* **2018**, *21*, 44–51. [[CrossRef](#)]
28. Park, N.; Rakibuzzaman, M.; Suh, S.-H. Flow Analysis of 30 kW Gate Turbine using Permanent Magnetic Generator. *Heat Transf. Eng.* **2019**, *40*, 1511–1522. [[CrossRef](#)]
29. Nasir, B.A. Suitable Selection of Components for the Micro-Hydro-Electric Power Plant. *Adv. Energy Power* **2014**, *2*, 7–12.
30. Michael, P.A.; Jawahar, C.P. Design of 15 kW Micro Hydro Power Plant for Rural Electrification at Valara. *Energy Procedia* **2017**, *117*, 163–171. [[CrossRef](#)]
31. Alexander, K.V.; Giddens, E.P.; Fuller, A.M. Axial-Flow Turbines for Low Head Micro Hydro Systems. *Renew. Energy* **2009**, *34*, 35–47. [[CrossRef](#)]
32. Larinier, M. Fish Passage Experience at Small-Scale Hydro-Electric Power Plants in France. *Hydrobiologia* **2008**, *609*, 97–108. [[CrossRef](#)]
33. Korea Hydrographic and Oceanographic Agency, Busan, South Korea in 2017. Available online: http://www.khoa.go.kr/oceangrid/koofs/kor/observation/obs_real_detail.do?tsType=0&tsId=44 (accessed on 7 October 2018).
34. Madani, N.; Cosic, A.; Sadarangani, C. A Permanent Magnet Synchronous Generator for a Small Scale Vertical Axis Wind Turbine. In Proceedings of the IEEE International Electric Machines & Drives Conference (IEMDC), Coeur d’Alene, ID, USA, 10–13 May 2015; pp. 48–52. [[CrossRef](#)]
35. Suh, S.H.; Kim, K.Y.; Kim, B.H.; Kim, Y.T.; Kim, T.G.; Roh, H.W.; Yoo, Y.I.; Park, N.H.; Park, J.M.; Shin, C.S.; et al. *Theory and Applications of Hydraulic Turbines*, 1st ed.; Dong Myeong Publishers: Seoul, Korea, 2014.
36. Fox, R.W.; McDonald, A.T.; Pritchard, P.J.; Leylegain, J.C. *Fluid Mechanics*, 8th ed.; John Wiley and Sons, Inc.: Hoboken, NJ, USA, 2012.
37. Drtina, P.; Sallaberger, M. Hydraulic Turbines—Basic Principles and State-of-the-Art Computational Fluid Dynamics Applications. *Proc. Inst. Mech. Engrs: Part C* **1999**, *213*, 85–102. [[CrossRef](#)]
38. Kim, H.-H.; Rakibuzzaman, M.; Kim, K.; Suh, S.-H. Flow and Fast Fourier Transform Analyses for Tip Clearance Effect in an Operating Kaplan Turbine. *Energies* **2019**, *12*, 264. [[CrossRef](#)]
39. Rakibuzzaman, M.; Kim, H.-H.; Kim, K.; Suh, S.-H.; Kim, K.Y. Numerical Study of Sediment Erosion Analysis in Francis Turbine. *Sustainability* **2019**, *11*, 1423.
40. Trivedi, C.; Cervantes, M.J.; Gandhi, B.K.; Dahlhaug, O.G. Experimental and Numerical Studies for a High Head Francis Turbine at Several Operating Points. *J. Fluids Eng.* **2013**, *135*. [[CrossRef](#)]
41. Celik, I.B.; Ghia, U.; Roache, P.J.; Freitas, C.J.; Coleman, H.; Raad, P.E. Procedure for Estimation and Reporting of Uncertainty due to Discretization in CFD Applications. *ASME J. Fluids Eng.* **2008**, *130*, 078001.
42. Taylor, J.R. *An Introduction to Error Analysis*, 2nd ed.; University Science Books: Mill Valley, CA, USA, 1982.
43. Friziger, J.H.; Peric, M. *Computational Methods for Fluid Dynamics*, 3rd ed.; Springer: New York, NY, USA, 2002.
44. Ansys Inc. ANSYS-CFX (CFX Introduction, CFX Reference guide, CFX Tutorials, CFX-Pre User’s Guide, CFX-Solver Manager User’s Guide, Theory Guide), Release 16.00, USA. 2016. Available online: <https://www.ansys.com/products/fluids/ansys-cfx>.
45. Georgiadis, N.J.; Yoder, D.A.; Engblorn, W.B. Evaluation of Modified Two-Equation Turbulence Models for Jet Flow Predictions. *Aiaa J.* **2006**, *44*, 3107–3114. [[CrossRef](#)]
46. Wilcox, D.C. *Turbulence Modeling for CFD*, 1st ed.; DCW Industries, Inc.: La Cañada Flintridge, CA, USA, 1994.
47. Menter, F.R. Two-Equation Eddy-Viscosity Turbulence Models for Engineering Applications. *AIAA J.* **1994**, *32*, 1598–1605. [[CrossRef](#)]
48. CEI/IEC-60193, *Hydraulic Turbines, Storage Pumps and Pump-Turbines-Model Acceptance Tests*; International Standard; International Electrotechnical Commission: Geneva, Switzerland, 1999.
49. Rakibuzzaman, M.; Suh, S.-H.; Ryu, Y.T.; Kim, K.Y. Utilization of Hydraulic Energy in a Fish Farm. In Proceedings of the 12th International Conference on Computational Heat and Mass Transfer, Rome, Italy, 3–6 September 2019.
50. Liu, X.; Luo, Y.; Karney, B.W.; Wang, W. A selected literature review of efficiency improvements in hydraulic turbines. *Renew. Sustain. Energy Rev.* **2015**, *51*, 18–28. [[CrossRef](#)]

Article

Matching Optimization of a Mixed Flow Pump Impeller and Diffuser Based on the Inverse Design Method

Mengcheng Wang , Yanjun Li ^{*}, Jianping Yuan and Fareed Konadu Osman 

National Research Center of Pumps, Jiangsu University, Zhenjiang 212013, China; jdwmc2018@163.com (M.W.); yh@ujs.edu.cn (J.Y.); 5102190340@stmail.ujs.edu.cn (F.K.O.)

^{*} Correspondence: lyj782900@ujs.edu.cn; Tel.: +86-150-0610-9630

Abstract: When considering the interaction between the impeller and diffuser, it is necessary to provide logical and systematic guidance for their matching optimization. In this study, the goal was to develop a comprehensive matching optimization strategy to optimize the impeller and diffuser of a mixed flow pump. Some useful tools and methods, such as the inverse design method, computational fluid dynamics (CFD), design of experiment, surrogate model, and optimization algorithm, were used. The matching optimization process was divided into two steps. In the first step, only the impeller was optimized. Thereafter, CFD analysis was performed on the optimized impeller to get the circulation and flow field distribution at the outlet of the impeller. In the second step of optimization, the flow field and circulation distribution at the inlet of the diffuser were set to be the same as the optimized impeller outlet. The results show that the matching optimization strategy proposed in this study is effective and can overcome the shortcomings of single-component optimization, thereby further improving the overall optimization effect. Compared with the baseline model, the pump efficiency of the optimized model at $1.2Q_{des}$, $1.0Q_{des}$, and $0.8Q_{des}$ is increased by 6.47%, 3.68%, and 0.82%, respectively.



Citation: Wang, M.; Li, Y.; Yuan, J.; Osman, F.K. Matching Optimization of a Mixed Flow Pump Impeller and Diffuser Based on the Inverse Design Method. *Processes* **2021**, *9*, 260. <https://doi.org/10.3390/pr9020260>

Academic Editor: Jin-Hyuk Kim
Received: 27 December 2020
Accepted: 26 January 2021
Published: 29 January 2021

Publisher's Note: MDPI stays neutral with regard to jurisdictional claims in published maps and institutional affiliations.



Copyright: © 2021 by the authors. Licensee MDPI, Basel, Switzerland. This article is an open access article distributed under the terms and conditions of the Creative Commons Attribution (CC BY) license (<https://creativecommons.org/licenses/by/4.0/>).

Keywords: inverse design method; matching optimization; diffuser; impeller; flow field

1. Introduction

As one of the most important machines in modern civilization, the performance of rotating machinery will have a great influence on the development of wider society. Published data in the Annual Work Report of the Chinese Government in 2019 revealed that more than 98% of the country's electric power conversion is done by rotating machinery. Consequently, a marginal increase in the efficiency of rotating machinery will produce unimaginable economic benefits. For instance, in China, for every 1% increase in rotating machinery efficiency, about 70 billion kilowatts of electricity can be saved annually. As a kind of rotating machinery, mixed flow pumps play an important role in industrial production, agricultural irrigation, and urban drainage due to their moderate head, wide high efficiency range, and good anti-cavitation performance. Thus, it is of great significance to study the optimization design of mixed flow pumps.

In the field of rotating machinery optimization, computational fluid dynamics (CFD) prediction is a better method than experimental investigation, because the former is more convenient and cheaper [1]. More importantly, CFD prediction can provide flow details inside the rotating machinery, which can help designers better understand the reasons for performance changes and make targeted optimization [2]. However, CFD prediction cannot directly provide the optimal solution for the optimization of rotating machinery. Like most complex optimization problems, the optimization of rotating machinery usually entails multiple indicators, and each target affects the other. Therefore, considering the multi-objectivity of the rotating machinery optimization is inevitable [3]. Several attempts have been made to solve the above problem. Eventually, the method of combined optimization strategy consisting of CFD, design of experiment (DOE), surrogate models, and

optimization algorithms came to the fore and achieved satisfactory results. Meng et al. [4] combined CFD, Latin hypercube sampling (LHS), a two-layer artificial neural network (ANN), and a non-dominated sorting genetic algorithm (NSGA) to successfully improve the reverse operation performance of the axial flow pump without reducing the forward flow performance. Shi et al. [5] applied LHS, the response surface method (RSM), and an adaptive mutation probability genetic algorithm (AMGA) to the multi-disciplinary optimization of the axial flow pump. This effectively reduced the weight of the blade and enhanced its hydraulic efficiency on the premise of meeting the requirements of blade strength. Pei et al. [6] and Wang et al. [7] used LHS, ANN and modified particle swarm optimization (MPSO) to optimize the impeller and diffuser of a centrifugal pump, and widen the high efficiency area. Shim et al. [8] optimized the efficiency, cavitation, and stability of a centrifugal pump by combined usage of LHS, kriging model, and NSGA. Kim et al. [9] studied the influence of hub ratio on the performance of the mixed flow pump at the same specific speed through the combined optimization strategy. Suh et al. [10] combined central composite design (CCD), RSM, and sequence quadratic program (SQP) to improve the efficiency and cavitation performance of mixed flow pumps at the design point.

In the above optimization, the parameterization of the impeller is completed by geometric parameters. With the development of computational fluid dynamics, the use of hydrodynamic parameters to parameterize the impeller has shown great potential. This technique is also known as the inverse design method (IDM). In IDM, the blade shape is controlled by blade loading, circulation, and stacking condition. Compared with the former, the latter requires fewer design parameters and has a closer relationship between design parameters and hydraulic performance [11]. Goto et al. [12] and Zangeneh et al. [13] ascertained the efficacy of IDM in mixed flow pump design by simulation and experiment. Huang et al. [14] improved the head and efficiency of the mixed flow pump at design point by using IDM, LHS, radial basis neural network (RBNN), and NSGA. Yiu et al. [15] increased the mixed flow pump efficiency and suction performance by combined usage of IDM and a genetic algorithm (GA). Zhu et al. [16] optimized the pressure distribution of the compressor through IDM, GA, and adjoint method, thus expanding its high efficiency area. The efficiency, stability, and cavitation performance of pump as turbine were improved by combining the use of IDM, DOE, RSM/RBNN, and NSGA [17–20].

There is a common point in the above studies, which is only the impeller or diffuser was optimized in each study, and the interaction between the two was ignored. Only a few kinds of research have studied the matching optimization of impeller and diffuser. Bonaiuti et al. [21] studied the simultaneous optimization of compressor impeller and diffuser through five loading parameters. Subsequently, in another work [22], by optimizing the diffuser first and then the impeller, the matching optimization of a waterjet pump diffuser and impeller was studied by the trial-and-error method. Yang et al. [23] investigated the influence of blade loading on the impeller and diffuser of the submersible axial-flow pump. However, due to the particularity of IDM, there are still some defects in these matching optimization studies. In IDM, the flow field and circulation distribution at the diffuser inlet are two important input parameters. To reduce the hydraulic losses, the flow field and circulation distribution at the diffuser inlet should be set to be the same as the impeller outlet [24]. Therefore, in the matching optimization of impeller and diffuser, the impeller should be optimized before the diffuser was optimized.

This study aims to provide systematic guidance for the matching optimization of a mixed flow pump impeller and diffuser based on IDM. Firstly, the mixed flow pump design specification and matching optimization strategy were introduced, and the accuracy of the CFD analysis was verified. Then, the strategy was applied to the matching optimization of the impeller and diffuser, and the key points of matching optimization were introduced. Finally, the optimization mechanism was clarified by a comparative analysis of the internal flow field of the two models.

2. Mixed Flow Pump Model

The mixed flow pump as shown in Figure 1 was selected as the baseline model, which consists of an outlet elbow, a seven-blade diffuser, a four-blade impeller and a straight inlet pipe. The design flow rate Q_{des} is $0.4207 \text{ m}^3/\text{s}$, the design head H_{des} is 12.66 m, the rotational speed N of the impeller is 1450 r/min, and the specific speed n_s can be calculated by Equation (1):

$$n_s = \frac{3.65N\sqrt{Q_{des}}}{H^{0.75}} \quad (1)$$

The performance of the baseline model was tested by Tianjin experimental bench, China. On the test bench, an intelligent differential pressure transmitter and intelligent torque speed sensor are used to measure head and torque, respectively. These devices yielded measurement errors of $<\pm 0.1\%$. Also, an intelligent electromagnetic flowmeter is used to measure flow rate, and the measurement errors is $<\pm 0.2\%$. The random uncertainty and overall uncertainty of this test bench are less than 0.1% and 0.3%, respectively. The test results shown in Figure 2 show that the efficiency of the baseline model at the design point is 86.3%. In this figure, $Q^* = Q/Q_{des}$ is the normalized flow rate, and $H^* = H/H_{des}$ is the normalized head. (The same dimensionless method was used in other parts of this paper.)

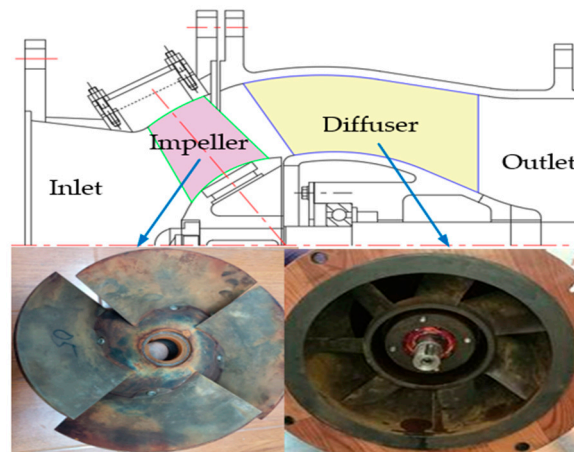


Figure 1. Baseline model.

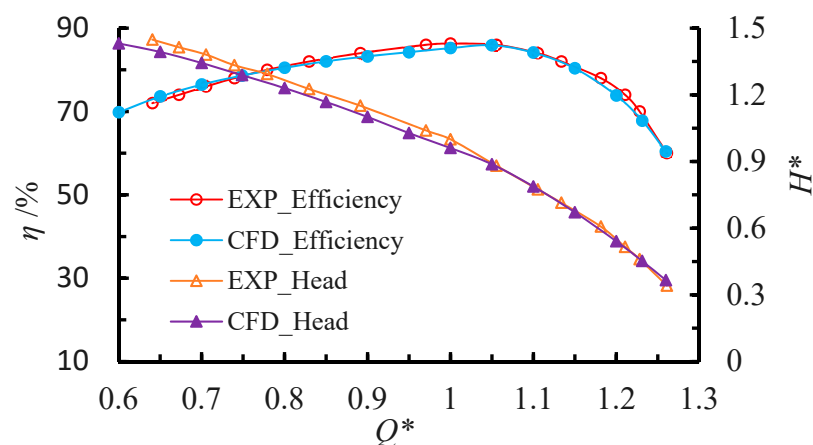


Figure 2. Performance curves for the baseline model.

3. Optimization Strategy

As shown in Figure 3, the optimization system was built by combining the IDM, CFD, optimal Latin hypercube sampling (OLHS), RSM, Multi-island genetic algorithm (MIGA) and NSGA-II. The entire optimization process was divided into two steps. In the first step

of optimization, only the impeller was optimized, and the objective function was set as the impeller weighted efficiency at $1.2Q_{des}$, $1.0Q_{des}$ and $0.8Q_{des}$. Thereafter, CFD analysis was performed on the optimized impeller to get the circulation and flow field distribution at the outlet of the optimized impeller. In the second step of optimization, the diffuser was optimized, and the objective functions were the levels of pump efficiency at $1.2Q_{des}$, $1.0Q_{des}$ and $0.8Q_{des}$. To improve the optimization effect of this step, the flow field and circulation distribution at the inlet of the diffuser were set to be the same as the optimized impeller outlet.

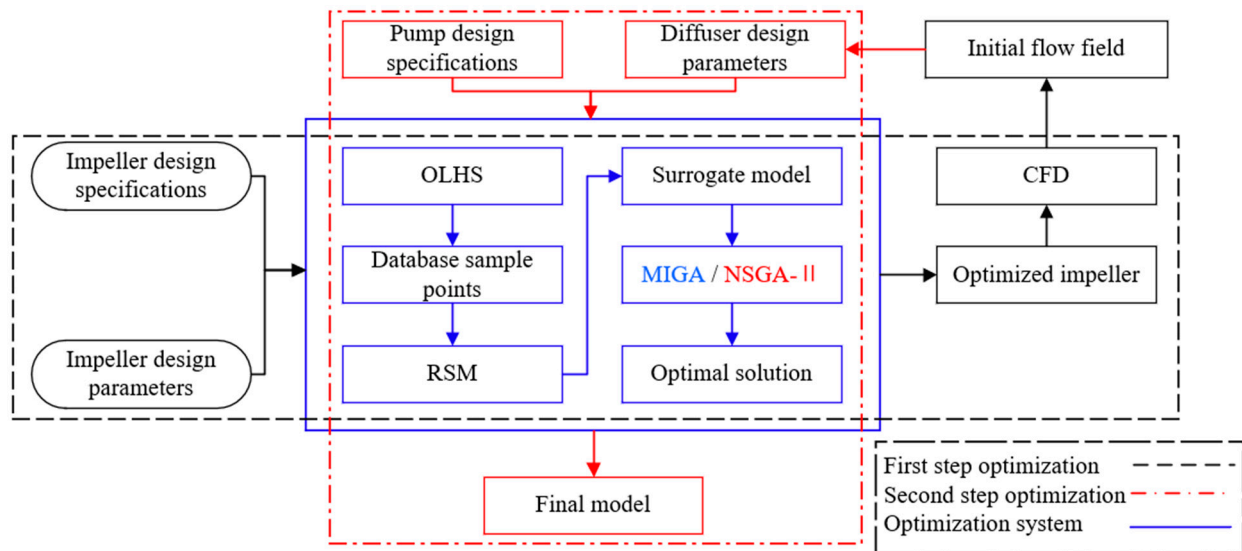


Figure 3. Flowchart of optimization strategy.

3.1. 3D Inverse Design Method

The parameterization of the impeller is done by the inverse design software TURBODESIGN 6.4 developed by Advanced Design Technology. In this procedure, we assume that the fluid is steady, inviscid and uniform, so that the only vorticity is the bound vorticity on the blades, and its strength was determined by a specified distribution of circumferentially averaged swirl velocity $r\bar{V}_\theta$ (directly related to the bound circulation $2\pi r\bar{V}_\theta$) [11,25]:

$$r\bar{V}_\theta = \frac{B}{2\pi} \int_0^{2\pi} rV_\theta d\theta \quad (2)$$

Here, $r\bar{V}_\theta$, B , and r are the circumferentially averaged velocity, blade numbers, and radius, respectively.

When the meridional shape and the distribution of $r\bar{V}_\theta$ are given, the pressure field in the blade passage can be calculated by the meridional derivation of circulation $\partial(r\bar{V}_\theta)/\partial m$:

$$p^+ - p^- = \frac{2\pi}{B} \rho \bar{W}_m \frac{\partial r\bar{V}_\theta}{\partial m} \quad (3)$$

Here, $p^+ - p^-$, ρ , m , and \bar{W}_m are pressure difference across the blade, fluid density, normalized streamline on the meridional shape, and pitch-wise averaged relative velocity, respectively.

The blade shape can be calculated by the following equation:

$$(\bar{V}_z + v_{zbl}) \frac{\partial f}{\partial z} + (\bar{V}_r + v_{rbl}) \frac{\partial f}{\partial r} = \frac{r\bar{V}_\theta}{r^2} + \frac{v_{\theta bl}}{r} - \omega \quad (4)$$

Here, v and \bar{V} are the periodic velocity and circumferential average velocity, respectively, and subscripts r and z represent the radial and axial components of velocity, respectively. f is the blade wrap angle that is θ value at the blade between the leading edge and trailing edge.

3.2. CFD Analyses and Validation

In this study, CFD analyses have the following three functions: one is to calculate the objective functions, the other is to analyze the flow field distribution of the optimized impeller and provide inlet flow field information for diffuser optimization, and the third is to verify the final optimization results. Therefore, the accuracy of CFD analyses is critical to the reliability of this work.

Thus, 3D steady incompressible Reynolds-Averaged Navier–Stokes (RANS) equation was used in the full-passage simulation of the mixed flow pump. The RANS equation was solved by the shear stress transport $k - \omega$ turbulence model, because this model has the advantage of accurately calculating the internal flow pattern of the mixed flow pump [26]. A high-resolution scheme was selected to discretize the convective-diffusion terms [27]. The mass flow rate was set at the inlet, and the static pressure was set at the outlet. The frozen rotor frame of reference was adopted at the interface between the stationary and rotating domains. The convergence criteria were set to 5×10^{-5} .

The discretization of the computational domain is the basis of CFD analysis. In this study, the discretization of the computational domain is completed by structured grids, which have the advantages of controllable quality and quantity compared to unstructured grids. Mesh refinement was performed to all walls to ensure a small Y^+ near the wall, O-type grids were used near the blade surface, and H/C-type grids were used near the blade edge. The meshing of the entire computational domain was completed by hexahedral grids as shown in Figure 4. Table 1 shows the results of the mesh independence analysis by using the same boundary conditions and governing equations. When the total number of grids is greater than 4.71 million, the head and efficiency reveal a small difference with the increase in grid numbers. Meanwhile, the maximum Y^+ on the blades is no more than 65.

To verify the accuracy of the CFD analysis, the baseline model was numerically calculated using the above grid division and calculation setting, and the results are shown in Figure 2. The maximum head difference does not exceed 4% and the maximum efficiency difference does not exceed 2.5%. Therefore, the numerical simulation method adopted in this study is reliable.

Table 1. Mesh independence analysis.

Inlet Pipe ($\times 10^5$)	Impeller ($\times 10^5$)	Diffuser ($\times 10^5$)	Outlet Pipe ($\times 10^5$)	Total Number ($\times 10^5$)	Head (m)	Efficiency (%)
43	63	70	58	234	12.13	84.52
83	121	130	95	429	12.11	84.92
83	141	152	95	471	12.10	85.21
118	172	187	133	610	12.12	85.19
167	241	269	172	849	12.11	85.23

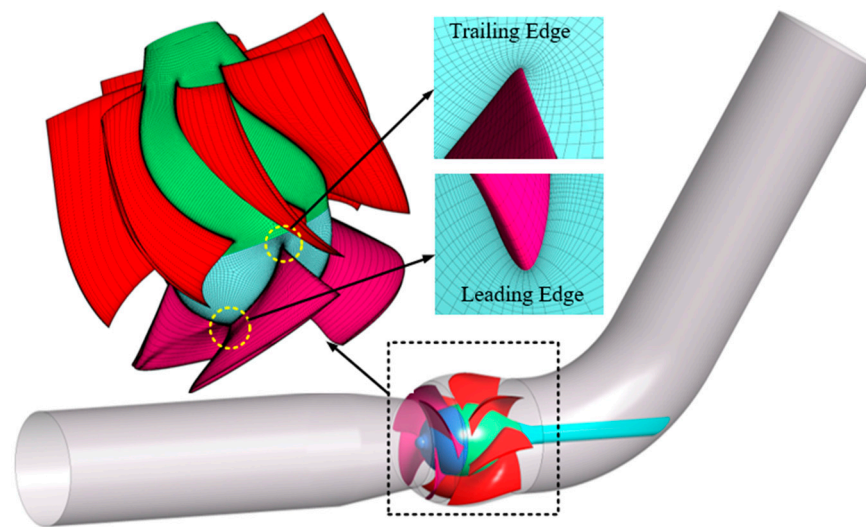


Figure 4. Mesh of computational domains.

3.3. Optimization Process

The optimization process can be accelerated by constructing the approximate model between optimization objectives and design parameters. In this study, the second-order RSM was used to construct the approximate model:

$$y = \alpha_0 + \sum_{i=1}^N \alpha_i x_i + \sum_{i=1}^N \alpha_{ii} x_i^2 + \sum_{i \neq j}^N \alpha_{ij} x_i x_j \quad (5)$$

Here, α_0 , α_i , α_{ii} and α_{ij} are the undetermined coefficients and can be obtained by the least square method from the optimization objectives and design parameters.

In DOE, the optimal Latin hypercube sampling (OLHS) method was employed to generate the random, equiprobable, and orthogonally distributed sample points [28]. The structure of the sample space is consistent with the design space, which helps to reduce the number of calculation times.

A genetic algorithm (GA) was used for global optimization in the entire design space. In GA, crossover and mutation were adopted to ensure that the final result is the global optimal solution. Generally, the two main strategies for solving multi-objective optimization problems are the aggregation approach [29] and Pareto front [30]. Compared with the Pareto front, the aggregation approach has lower complexity because it converts the multi-objective optimization problem into a single-objective optimization problem through the weighted average method. However, in Pareto front, the nature of the trade-offs between optimization objectives can be more intuitively reflected.

The optimization process starts from the selection of the optimization objectives and design parameters. After determining the range of the design parameters, OLHS was used to generate different combinations of design parameters. Thereafter, IDM was used to perform 3D modeling for each parameter combination, and CFD analysis was used to calculate the model optimization objectives. Then, RSM was used to construct the approximate model between optimization objectives and design parameters. Finally, GA was used to determine the global optimal solution.

4. Redesign Setting

4.1. Design Parameters

In this study, no changes have been made to the meridional shape of the mixed flow pump; thus, the mixed flow pump can be parameterized by the parameterization of the blade. As described in Section 3.1, circulation, blade loading, and stacking have the

greatest effect on blade shape in IDM. As a result, these parameters were selected as design parameters.

Generally, we assume that the circumferential distribution of the circulation is uniform. Therefore, the three-dimensional distribution of the circulation can be simplified to a two-dimensional distribution along the spanwise. Wang et al. [31,32] and Chang et al. [33] pointed out that the non-linear circulation distribution has more advantages than the linear circulation distribution in the mixed flow pump optimization design. Therefore, the curve shown in Figure 5 was used to control the circulation distribution with controlled parameters of rV_h and rV_s . In this figure, $r\tilde{V}_\theta = r\bar{V}_\theta/\omega^2 r_{\text{shroud}}$ is the normalized circulation, and $\tilde{r} = (r - r_{\text{hub}})/(r_{\text{shroud}} - r_{\text{hub}})$ is the normalized spanwise distance.

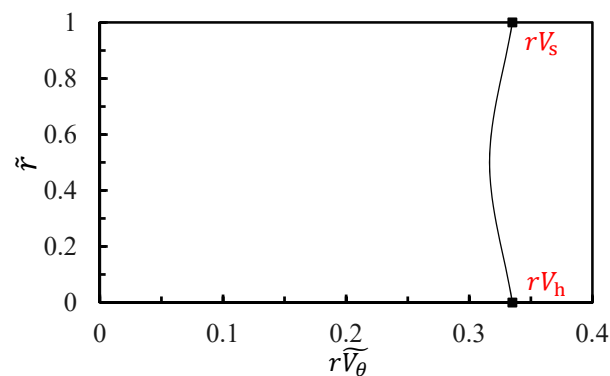


Figure 5. Circulation distribution at the impeller outlet and diffuser inlet.

The blade loading distribution is usually controlled by two parabolas and a connecting straight line as shown in Figure 6, where $\tilde{m} = m/m_{\text{total}}$ is the normalized meridional distance. The control parameters are the loading $DRVT$ at the leading edge, the locations NC and ND of the connection point, and the slope K of the middle straight line.

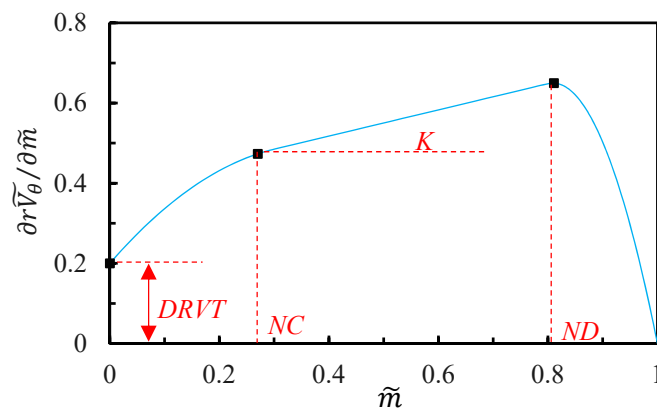


Figure 6. Blade loading distribution along the streamline.

The stacking condition α shown in Figure 7 is usually imposed linearly along the blade trailing edge. Zangeneh [13] pointed out that it plays an important role in suppressing the flow separation in mixed flow pump. Zhu [34] also reported that it has a greater influence on the pressure pulsation in the impeller.

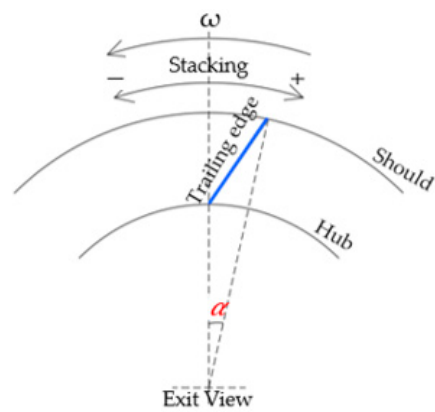


Figure 7. Stacking condition.

4.2. Optimization Setting

To determine the undetermined coefficients in Equation (5), the minimum number of sample points required is $S_{\min} = (N + 1) \times (N + 2)/2$, where N is the number of design parameters. However, to improve the accuracy of the approximate model, the number of sample points used in this study is $2S_{\min}$. As shown in Figure 3, the impeller and diffuser of the mixed flow pump were optimized by the two-step optimization method. In Table 2, the design parameters (subscripts h for hub and s for shroud), constraints, and optimization objectives during the two-step optimization process were given.

Table 2. Design parameters, constraints and optimization objectives.

	First Step of Optimization			Second Step of Optimization		
	Type	Parameters	Range	Type	Parameters	Range
Design parameters	Circulation	RV_h	0.29~0.34	Blade loading	$DRVT_h$	-0.2~0.2
		RV_s	0.29~0.34		NC_h	0.1~0.5
	Blade loading	$DRVT_h$	-0.2~0.2		ND_h	0.5~0.9
		NC_h	0.1~0.5		K_h	-1.0~1.0
		ND_h	0.5~0.9		$DRVT_s$	-0.2~0.2
		K_h	-2.0~2.0		NC_s	0.1~0.5
		$DRVT_s$	-0.2~0.2		ND_s	0.5~0.9
		NC_s	0.1~0.4		K_s	-1.0~1.0
		ND_s	0.4~0.9		Stacking	α
	K_s	-2.0~2.0				
	Stacking	α	-20.0~20.0			
Constraints	Impeller head at design point			Pump head at design point		
Optimization objectives	Weighted efficiency of the impeller at $0.8Q_{des}$, $1.0Q_{des}$ and $1.2Q_{des}$			Pump efficiency at $0.8Q_{des}$, $1.0Q_{des}$ and $1.2Q_{des}$		

In the first step of optimization, only the impeller was optimized. The design parameters are the two circulation distribution control parameters, eight blade loading distribution control parameters and stacking condition. The range of these eleven parameters is shown in Table 2. To achieve the two purposes of maximizing overall efficiency and reducing the complexity of multi-objective optimization at the same time, the aggregation approach was used in this step. The weighted efficiency of the impeller at $1.2Q_{des}$, $1.0Q_{des}$ and $0.8Q_{des}$ was set as the optimization objective, with weights of 0.25, 0.5, and 0.25, respectively. To make the head difference between the optimized impeller and the baseline impeller fall within an acceptable range, the impeller head change at the design point of less than

3% was taken as the constraint condition. The impeller head (H) and efficiency (η) are calculated by Equations (6) and (7), respectively.

$$H = \frac{p_{\text{out}} - p_{\text{in}}}{\rho g} \quad (6)$$

$$\eta = \frac{(p_{\text{out}} - p_{\text{in}})Q}{T\omega} \quad (7)$$

where p_{out} , p_{in} , ρ , g , ω , and T are the impeller outlet total pressure, impeller inlet total pressure, fluid density, acceleration due to gravity, rotational angular velocity of the impeller, and the torque of the impeller, respectively.

After the first step of optimization, the impeller with the best performance was selected. CFD analysis was performed on the optimized impeller to extract the axial and circumferential velocity distribution at the outlet. Due to the non-uniformity of velocity distribution at the impeller outlet, directly using it as the inlet condition of the diffuser will result in the divergence of the IDM calculation, and thus the shape of the diffuser cannot be obtained. Therefore, the optimized impeller outlet velocity distribution needs to be smoothed, and the smoothed velocity will be taken as the initial condition for the second step of optimization.

In the second step of optimization, the diffuser was optimized. To reduce the hydraulic loss at the inlet of the diffuser, the circulation and flow field distribution at the diffuser inlet was set to be consistent with the optimized impeller outlet. Therefore, only the blade loading and stacking were selected as design parameters in this step. To comprehend the nature of the trade-offs made in choosing the final solution, Pareto front was used in this step, and the pump efficiencies at $1.2Q_{\text{des}}$, $1.0Q_{\text{des}}$, and $0.8Q_{\text{des}}$ were selected as the optimization objectives. To reduce the head change of the optimized mixed flow pump at the design point, the pump head change at the design point was restricted to less than 3%.

Therefore, in this study, to improve the accuracy of the RSM in the optimization process, the number of sample points used in the first and second steps is 156 and 110, respectively. The parameter settings for MIGA and NSGA-II are shown in Table 3, and the number of impellers and diffusers with different configurations generated in the first and second steps are both 12,000.

Table 3. Parameters setting for MIGA and NSGA-II.

MIGA		NSGA-II	
Setting	Value	Setting	Value
Population size	30	Population size	100
Number of generations	40	Number of generations	120
Number of islands	10	Crossover probability	0.9
Crossover probability	0.9	Cross distribution index	10
Mutation probability	0.05	Mutation distribution index	20
Migration probability	0.05	Initialization mode	Random

4.3. Optimization Result

The iteration history of the first step optimization is shown in Figure 8, and the best impeller A is obtained after 12,000 steps of calculation. The performance predicted by RSM and CFD of optimized impeller A is shown in Table 4, which indicates a good consistency between the two. The weighted efficiency of the optimized impeller A is 94.29%, which is 1.63% higher than the baseline impeller. In detail, the maximum improvement of the impeller efficiency occurred at $1.2Q_{\text{des}}$, which is 5.5%. At $1.0Q_{\text{des}}$, the efficiency of the optimized impeller is improved by 0.79%. However, at $0.8Q_{\text{des}}$, the efficiency of the optimized impeller is reduced by 0.56%. Moreover, the best efficiency point in the optimized impeller A is consistent with the design point, while in the baseline impeller, the best efficiency point appears at small flow conditions.

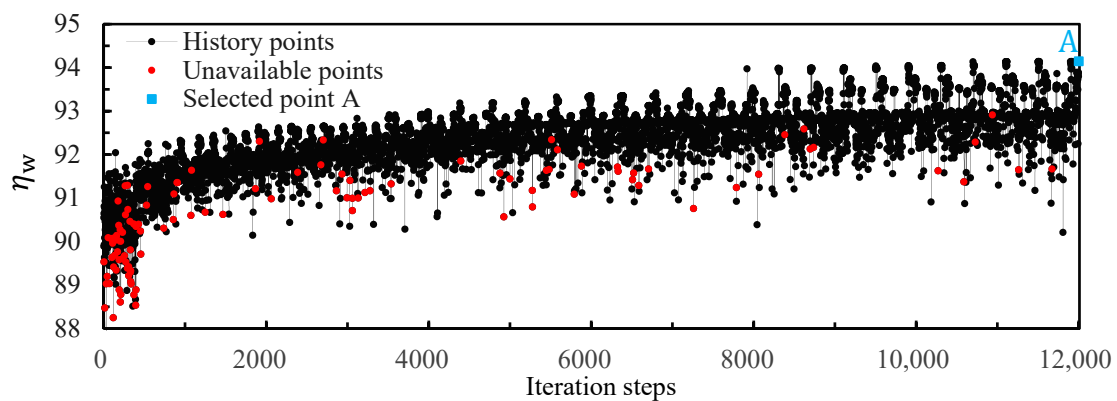


Figure 8. Optimization results of the first step.

Table 4. Performance comparison between computational fluid dynamics (CFD) calculation and response surface method (RSM) prediction.

	Impeller Efficiency			Pump Efficiency		
	Baseline Impeller	First Step Optimization RSM	CFD	Baseline Pump	Second Step Optimization RSM	CFD
$\eta_{0.8}$	95.66		95.10	80.48	81.48	81.30
$\eta_{1.0}$	95.05		95.84	85.21	88.55	88.89
$\eta_{1.2}$	84.86		90.36	73.84	80.05	80.31
η_w	92.66	94.14	94.29			
H	13.51	13.58	13.26	12.10	12.32	12.06

Figure 9 shows the axial and circumferential velocity distribution at the outlet of the impeller A, these values were extracted at $0.15\tilde{r} \sim 0.85\tilde{r}$ after considering the influence of the wall on the flow field. As described in Section 4.2, the velocity distribution needs to be smoothed. In this study, the widely used linear distribution assumption was used, and the results of the smoothing treatment are shown in Figure 9.

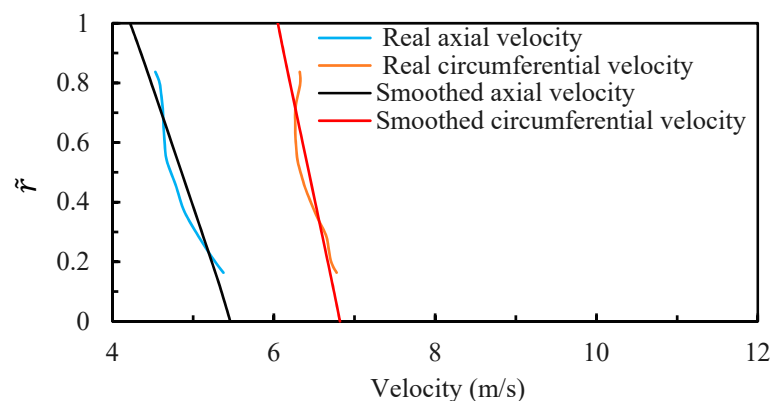


Figure 9. Velocity distribution at the impeller outlet and diffuser inlet.

The optimization result of the second step is shown in Figure 10. In this step, the Pareto front seems separated, which means there is a trade-off relationship between the pump efficiency at $0.8Q_{des}$ ($\eta_{0.8}$), $1.0Q_{des}$ ($\eta_{1.0}$) and $1.2Q_{des}$ ($\eta_{1.2}$). Figure 10a shows that $\eta_{0.8}$ and $\eta_{1.2}$ have a strong competitive relationship, while Figure 10b shows an interesting fact that $\eta_{1.0}$ and $\eta_{1.2}$ are positively correlated to some extent. After carefully considering the relationship between $\eta_{0.8}$, $\eta_{1.0}$ and $\eta_{1.2}$, the optimized diffuser B was selected for further study. The performance predicted by RSM and CFD of the optimized mixed flow pump is shown in Table 4. It is observed that the RSM prediction results corroborate with the CFD

calculation results with the maximum error not exceeding 1%. The pump efficiency of the optimized mixed flow pump at $1.2Q_{des}$, $1.0Q_{des}$ is $0.8Q_{des}$ is 80.31%, 88.89% and 81.30%, respectively, which is 6.47%, 3.68% and 0.82% higher than the baseline model.

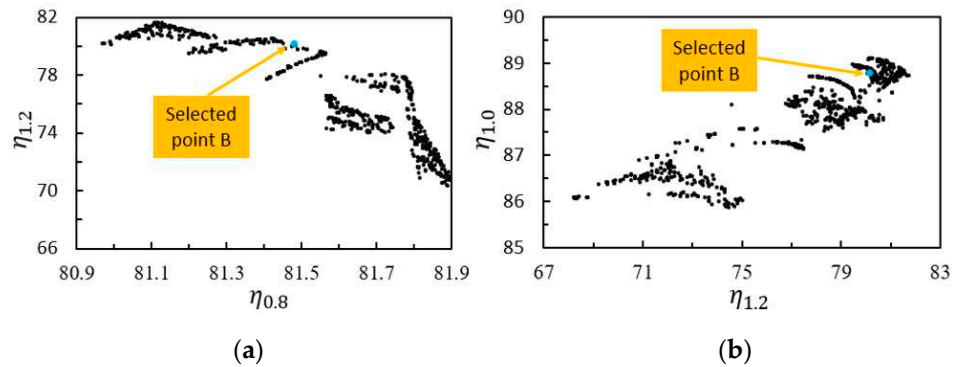


Figure 10. Optimization results of second step. (a) $\eta_{0.8}$ vs. $\eta_{1.2}$; (b) $\eta_{1.0}$ vs. $\eta_{1.2}$.

Figure 11 shows the blade loading and circulation distribution of the optimized impeller and diffuser. It can be seen that the blade loading distribution at the hub and shroud of the optimized impeller A is fore-loaded and mid-loaded, respectively, while the blade loading distribution at the hub and shroud of the optimized diffuser B is fore-loaded and aft-loaded, respectively. The circulation distribution at the optimized impeller A outlet and the optimized diffuser B inlet is a second-order parabola, and the value of the circulation at the mid-span is the smallest.

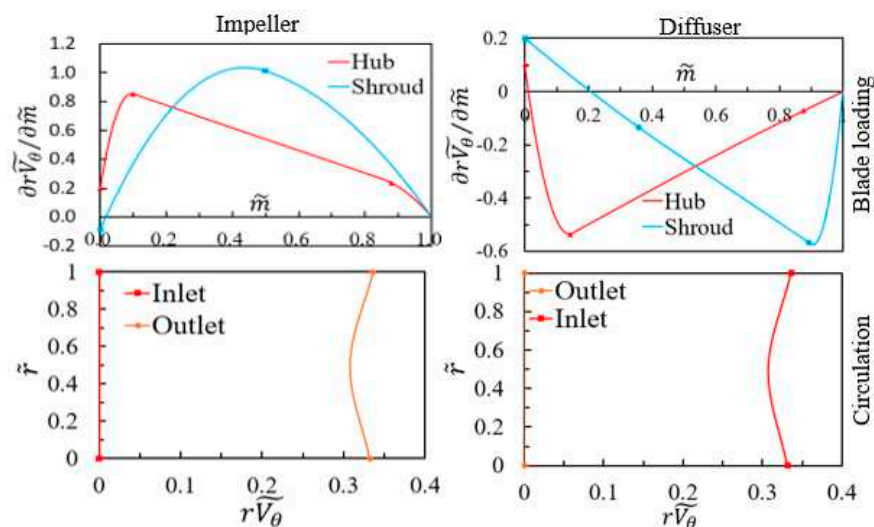


Figure 11. Blade loading distribution and circulation distribution of optimized impeller and diffuser.

5. Performance Comparison and Analysis

Figure 12 shows the performance comparison of the optimized mixed flow pump with the baseline model. When the flow rate is greater than $0.75Q_{des}$, the pump efficiency of the optimized model is higher than the baseline model, and the location of the best efficiency point does not change. The head of the optimized model presented an interesting change compared to the baseline model. Under the design condition, the pump head of the optimized model is almost the same as the baseline model, which means that the matching optimization results meet the constraints. However, under small flow conditions, the pump head of the optimized model is lower than the baseline model, and the lower the flow rate, the greater the head difference. The decreased head and increased efficiency under

small flow conditions represented the reduction of shaft power and energy-saving when the pump is operating in this area.

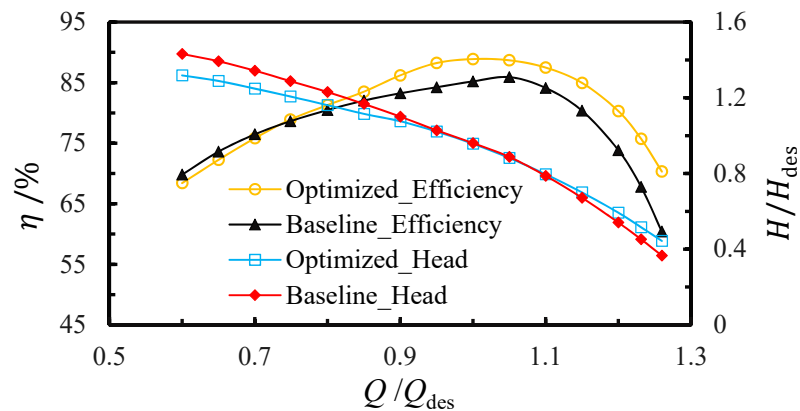


Figure 12. Performance comparison between optimized model and baseline model.

Table 5 shows the comparison of hydraulic losses of each flow passage component between the optimized model and baseline model under different flow rates. Compared with the baseline model, the hydraulic loss of the optimized impeller under large flow conditions is effectively suppressed, and the hydraulic loss of the optimized diffuser under the design condition is significantly reduced. Moreover, the hydraulic loss of the inlet pipe is positively related to the flow rate and independent of the impeller. However, the hydraulic loss of the outlet pipe is related to both the diffuser and flow rate. Compared with the baseline model, the hydraulic loss of the optimized model outlet pipe is reduced under all flow conditions.

Table 5. Analysis of hydraulic loss.

	Baseline Model				Optimized Model			
	Inlet	Impeller	Diffuser	Outlet	Inlet	Impeller	Diffuser	Outlet
$0.8Q_{des}$	0.09%	4.34%	9.72%	4.45%	0.09%	4.90%	9.18%	3.62%
$0.9Q_{des}$	0.13%	4.16%	7.56%	4.01%	0.13%	3.78%	6.33%	2.73%
$1.0Q_{des}$	0.18%	4.95%	5.32%	3.40%	0.18%	4.16%	3.85%	2.03%
$1.1Q_{des}$	0.25%	8.14%	3.52%	2.99%	0.25%	5.65%	3.33%	2.16%
$1.2Q_{des}$	0.37%	15.14%	5.13%	3.92%	0.36%	9.64%	5.04%	3.08%

To clarify the reasons for the change of hydraulic loss in detail, the internal flow field of the optimized model and the baseline model were analyzed and compared. The streamline contours and total pressure on the mid-span of the baseline model and optimized model are shown in Figure 13. At $0.8Q_{des}$ and $1.0Q_{des}$, a large-scale flow separation occurs at the diffuser outlet of the baseline model, which not only increased the hydraulic losses at the diffuser but also at the outlet pipe. At $1.2Q_{des}$, an obvious low-pressure region appeared on the working surface near the impeller inlet of the baseline model. Zhang [35] pointed out that this region has a great influence on the blade vibrations and pressure fluctuation. After the matching optimization, the flow separation in the optimized diffuser was effectively suppressed, especially at $1.0Q_{des}$, and the low-pressure region at the impeller inlet at $1.2Q_{des}$ was also weakened. As Zangeneh [12,13,36] mentioned, in the optimization design of mixed flow pump, the flow separation can be effectively suppressed by fore-loading at the hub and aft-loading at the shroud. This paper verifies this point of view again.

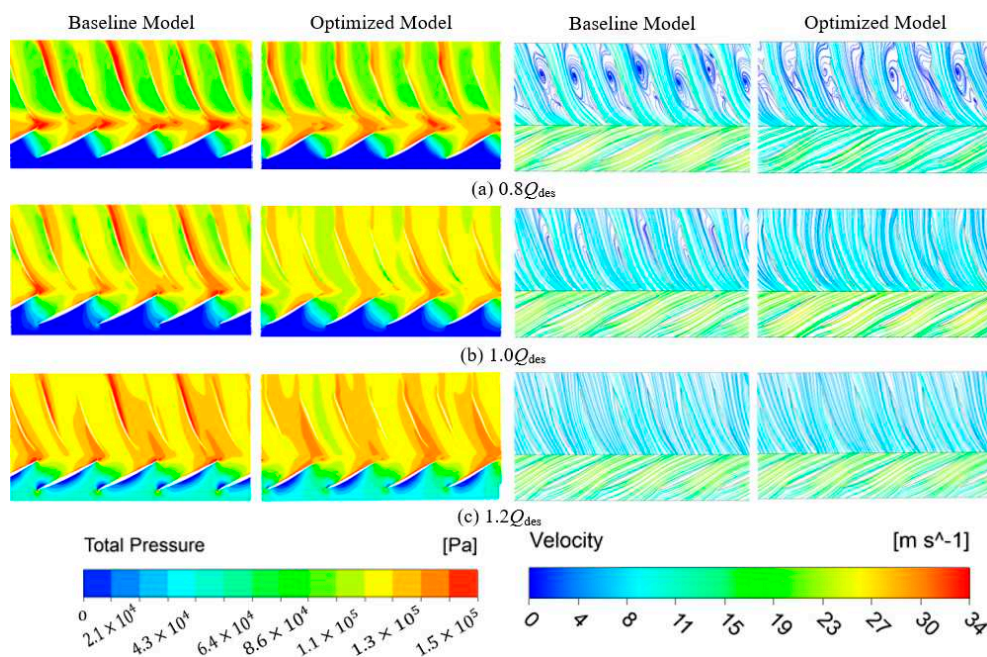


Figure 13. Comparison of the internal flow field between the optimized model and baseline model.

The comparison of the total pressure distribution along the streamline between the baseline model and the optimized model is shown in Figure 14. The horizontal axis is the standardized streamline distance \tilde{S} , $\tilde{S} = 0$ means at the impeller inlet and $\tilde{S} = 2$ means at the diffuser outlet. It can be seen that the total pressure rises rapidly between $0.2\tilde{S} \sim 0.8\tilde{S}$ due to the work done by the impeller to the fluid. However, the total pressure drops rapidly between $0.8\tilde{S} \sim 1.2\tilde{S}$, because the fluid in this interval has just left the blade zone of the impeller and has not yet entered the blade zone of the diffuser. Compared with the baseline model, the hydraulic loss of the optimized model in this interval was significantly reduced, which may be related to the setting of the diffuser inlet conditions during the matching optimization. The total pressure decreases slowly between $1.2\tilde{S} \sim 2\tilde{S}$ due to the rectification effect of the diffuser.

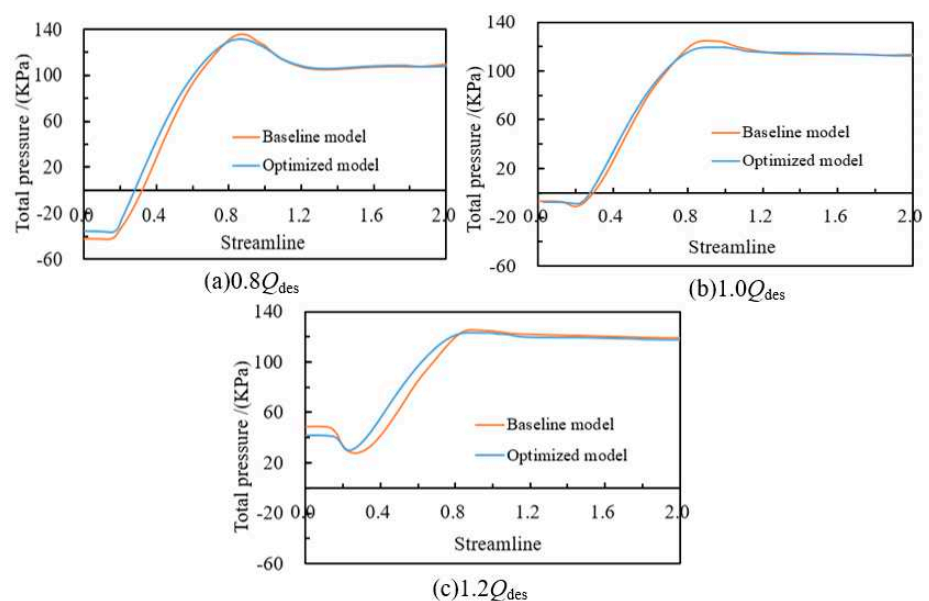


Figure 14. Total pressure distribution along the streamline.

6. Conclusions

To further improve the optimization effect of the mixed flow pump, a matching optimization strategy of impeller and diffuser was proposed in this study. The matching optimization process was divided into two steps. In the first step of optimization, only the impeller was optimized. In the second step of optimization, the diffuser was optimized. Some important conclusions are as follows:

1. After the first step of optimization, the weighted efficiency of the optimized impeller A is 1.63% higher than the baseline impeller. In detail, the impeller efficiency of the optimized impeller A at $1.2Q_{des}$ and $1.0Q_{des}$ is 5.5% and 0.79% higher than the baseline impeller, respectively, but 0.56% lower at $0.8Q_{des}$. Besides, the best efficiency point in the optimized impeller A is consistent with the design point, while in the baseline impeller, the best efficiency point appears at small flow conditions.
2. In the matching optimization, the circulation and flow field distribution at the diffuser inlet in IDM was set to be consistent with the optimized impeller outlet, which helps to reduce the hydraulic loss at the diffuser inlet. Compared with the baseline diffuser, the hydraulic loss of the optimized diffuser B at $1.2Q_{des}$, $1.0Q_{des}$, and $0.8Q_{des}$ reduced by 0.09%, 1.47%, and 0.54%, respectively.
3. The diffuser has a great impact on the hydraulic loss of downstream components. The hydraulic loss of the optimized model outlet pipe at $1.2Q_{des}$, $1.0Q_{des}$, and $0.8Q_{des}$ is 0.84%, 1.37%, and 0.83% lower than the baseline diffuser outlet pipe, respectively.
4. In total, the pump efficiency of the optimized model at $1.2Q_{des}$, $1.0Q_{des}$, and $0.8Q_{des}$ is 80.31%, 88.89% and 81.30%, respectively. These efficiencies correspond to 6.47%, 3.68%, and 0.82% improvement over the baseline model.

In summary, the matching optimization strategy proposed in this study is effective and can overcome the shortcomings of single-component optimization and thereby further improve the overall hydraulic performance of the mixed flow pump. The results of this study can also provide guidance for the optimization of other rotating machinery.

Author Contributions: Conceptualization, Methodology, Software, Writing—original draft and Writing—review and editing, M.W.; Data curation, Project administration and Validation, Y.L. and J.Y.; Writing—review and editing and Validation F.K.O. All authors have read and agreed to the published version of the manuscript.

Funding: This study supported by Science and Technology Plan of Wuhan (Grant No.2018060403011350), National Key Research and Development Plan (Grant No. 2018YFB0606103).

Institutional Review Board Statement: Not applicable.

Informed Consent Statement: Not applicable.

Data Availability Statement: All the data is already in the article.

Acknowledgments: The author sincerely thanks the ADT for its support, and reviewers for their constructive comments, and editors for their enthusiastic work.

Conflicts of Interest: The authors declare no conflict of interest.

Nomenclature

n_s	Specific speed
Q	Volume flow rate
H	Pump head
\overline{W}_m	Relative velocity
\overline{V}_θ	Tangential velocity
r	Radius
v	Periodic velocity

N	Rotational speed
B	Blade number
p	Static pressure at blade surface
m	Streamline
\bar{V}	Circumferential average absolute velocity
η	Pump efficiency
p	Total pressure
T	Torque
ω	Angular velocity
ρ	Density of the fluid
f	Wrap angle
ω	Angular velocity
Superscripts	
+	Work surface
-	Suction surface
~	Normalization
Subscripts	
h	Hub
s	Shroud

References

- Wu, J.; Shimmei, K.; Tani, K.; Niikura, K.; Sato, J. CFD-Based Design Optimization for Hydro Turbines. *J. Fluids Eng.* **2007**, *129*, 159–168. [[CrossRef](#)]
- Ma, Z.; Zhu, B.S.; Rao, C.; Shangguan, Y.H. Comprehensive Hydraulic Improvement and Parametric Analysis of a Francis Turbine Runner. *Energies* **2019**, *12*, 307. [[CrossRef](#)]
- Chikh, M.A.A.; Belaidi, I.; Khelladi, S.; Hamrani, A.; Bakir, F. Coupling of Inverse Method and Cuckoo Search Algorithm for Multiobjective Optimization Design of an Axial Flow Pump. *Proc. Inst. Mech. Eng. Part A J. Power Energy* **2019**, *233*, 988–1006. [[CrossRef](#)]
- Meng, F.; Li, Y.; Yuan, S.; Wang, W.; Zheng, Y.; Osman, M.K. Multiobjective Combination Optimization of an Impeller and Diffuser in a Reversible Axial-Flow Pump Based on a Two-Layer Artificial Neural Network. *Processes* **2020**, *8*, 309. [[CrossRef](#)]
- Shi, L.; Zhu, J.; Tang, F.; Wang, C. Multi-Disciplinary Optimization Design of Axial-Flow Pump Impellers Based on the Approximation Model. *Energies* **2020**, *13*, 779. [[CrossRef](#)]
- Pei, J.; Gan, X.; Wang, W.; Yuan, S.; Tang, Y. Multi-objective Shape Optimization on the Inlet Pipe of a Vertical Inline Pump. *J. Fluids Eng.* **2019**, *141*, 061108. [[CrossRef](#)]
- Wang, W.J.; Yuan, S.Q.; Pei, J.; Zhang, J.F. Optimization of the Diffuser in a Centrifugal Pump by Combining Response Surface Method with Multi-island Genetic Algorithm. *Proc. Inst. Mech. Eng. Part E J. Process. Mech. Eng.* **2017**, *231*, 191–201. [[CrossRef](#)]
- Shim, H.S.; Afzal, A.; Kim, K.Y.; Jeong, H.S. Three-objective Optimization of a Centrifugal Pump with Double Volute to Minimize Radial Thrust at Off-design Conditions. *Proc. Inst. Mech. Eng. Part A J. Power Energy* **2016**, *230*, 598–615. [[CrossRef](#)]
- Kim, S.; Jeong, U.-B.; Lee, K.-Y.; Kim, J.-H.; Yoon, J.-Y.; Choi, Y.-S. Multi-objective Optimization for Mixed-flow Pump with Blade Angle of Impeller Exit and Diffuser Inlet. *J. Mech. Sci. Technol.* **2017**, *31*, 5099–5106.
- Suh, J.-W.; Yang, H.-M.; Kim, Y.-I.; Lee, K.-Y.; Kim, J.-H.; Joo, W.-G.; Choi, Y.-S. Multi-objective Optimization of a High Efficiency and Suction Performance for Mixed-flow Pump Impeller. *Eng. Appl. Comput. Fluid Mech.* **2019**, *13*, 744–762. [[CrossRef](#)]
- Zangeneh, M. A Compressible 3D Design Method for Radial and Mixed Flow Turbomachinery Blades. *Int. J. Numer. Methods Fluids* **1991**, *13*, 599–624. [[CrossRef](#)]
- Goto, A.; Takemura, T.; Zangeneh, M. Suppression of Secondary Flows in a Mixed-Flow Pump Impeller by Application of Three-Dimensional Inverse Design Method: Part 2—Experimental Validation. *J. Turbomach.* **1996**, *118*, 544–551. [[CrossRef](#)]
- Zangeneh, M.; Goto, A.; Takemura, T. Suppression of Secondary Flows in a Mixed-Flow Pump Impeller by Application of Three-Dimensional Inverse Design Method: Part 1—Design and Numerical Validation. *J. Turbomach.* **1996**, *118*, 536–543. [[CrossRef](#)]
- Huang, R.F.; Luo, X.W.; Ji, B.; Wang, P.; Yu, A.; Zhai, Z.H.; Zhou, J.J. Multi-objective Optimization of a Mixed-Flow Pump Impeller Using Modified NSGA-II Algorithm. *Sci. China Technol. Sci.* **2015**, *58*, 2111–2130. [[CrossRef](#)]
- Yiu, K.F.C.; Zangeneh, M. Three-Dimensional Automatic Optimization Method for Turbomachinery Blade Design. *J. Propuls. Power* **2000**, *16*, 1174–1181. [[CrossRef](#)]
- Zhu, Y.J.; Ju, Y.P.; Zhang, C.H. An Experience-independent Inverse Design Optimization Method of Compressor Cascade Airfoil. *J. Power Energy* **2018**, *233*, 431–442. [[CrossRef](#)]
- Zhu, B.; Wang, X.; Tan, L.; Zhou, D.; Zhao, Y.; Cao, S. Optimization Design of a Reversible Pump–Turbine Runner with High Efficiency and Stability. *Renew. Energy* **2015**, *81*, 366–376. [[CrossRef](#)]
- Yang, W.; Xiao, R.F. Multiobjective Optimization Design of a Pump–turbine Impeller Based on an Inverse Design using a Combination Optimization Strategy. *J. Fluid. Eng.* **2014**, *136*, 249–256. [[CrossRef](#)]

19. Zangeneh, M.; Daneshkhah, K. A Fast 3D Inverse Design Based Multi-Objective Optimization Strategy for Design of Pumps. In Proceedings of the ASME 2009 Fluids Engineering Division Summer Meeting, Vail, CO, USA, 2–6 August 2009.
20. Wang, P.; Vera-Morales, M.; Vollmer, M.; Zangeneh, M.; Zhu, B.S.; Ma, Z. Optimization of a Pump-as-turbine Runner Using a 3D Inverse Design Methodology. In Proceedings of the 29th IAHR Symposium on Hydraulic Machinery and Systems, Kyoto, Japan, 16–21 September 2018; Volume 240.
21. Bonaiuti, D.; Zangeneh, M. On the Coupling of Inverse Design and Optimization Techniques for the Multiobjective, Multipoint Design of Turbomachinery Blades. *J. Turbomach.* **2009**, *131*, 134–149.
22. Bonaiuti, D.; Zangeneh, M.; Aartojarvi, R.; Eriksson, J. Parametrical Design of a Waterjet Pump by Means of Inverse Design, CFD Calculations and Experimental Analyses. *J. Fluid. Eng.* **2010**, *132*, 201–215. [[CrossRef](#)]
23. Yang, W.; Lei, X.; Zhang, Z.; Li, H.; Wang, F. Hydraulic Design of Submersible Axial-flow Pump Based on Blade Loading Distributions. *Trans. Chin. Soc. Agric. Mach.* **2017**, *48*, 179–187. (In Chinese)
24. Yin, J.; Wang, D. Review on Applications of 3D Inverse Design Method for Pump. *Chin. J. Mech. Eng.* **2014**, *27*, 520–527. [[CrossRef](#)]
25. Hawthorne, W.R.; Wang, C.; Tan, C.S.; McCune, J.E. Theory of blade design for large deflections: Part I—Two dimensional cascades. *Trans. ASME J. Eng. Gas Turb. Power* **1984**, *106*, 346353. [[CrossRef](#)]
26. Hellsten, A.; Laine, S. Extension of the k-omega-SST Turbulence Model for Flows over Rough Surfaces. In Proceedings of the 22nd Atmospheric Flight Mechanics Conference, New Orleans, LA, USA, 11–13 August 1997.
27. Menter, F.R.; Galpin, P.F.; Esch, T.; Kuntz, M.; Berner, C. CFD Simulations of Aerodynamic Flows with a Pressure-based Method. In Proceedings of the 24th International congress of the aeronautical sciences, Yokohama, Japan, 29 August–3 September 2004.
28. Pebesma, E.J.; Heuvelink, G.B. Latin Hypercube Sampling of Gaussian Random Fields. *Technometrics* **1999**, *41*, 303–312. [[CrossRef](#)]
29. Coello, C.A.C. A Comprehensive Survey of Evolutionary-Based Multiobjective Optimization Techniques. *Knowl. Inf. Syst.* **1999**, *1*, 269–308. [[CrossRef](#)]
30. Srinivas, N.; Deb, K. Multiobjective Optimization Using Nondominated Sorting in Genetic Algorithms. *Evolut. Comput.* **1994**, *2*, 221–248. [[CrossRef](#)]
31. Wang, M.C.; Li, Y.J.; Yuan, J.P.; Meng, F.; Appiah, D.; Chen, J.Q. Comprehensive Improvement of Mixed-flow Pump Impeller Based on Multi-objective Optimization. *Processes* **2020**, *8*, 905. [[CrossRef](#)]
32. Wang, M.C.; Li, Y.J.; Yuan, J.P.; Chen, J.Q.; Zheng, Y.H.; Yang, P.H. Performance of Mixed Flow Pump under Condition of Non-linear Distribution of Impeller Exit Circulation. *Chin. Soc. Agric. Mach.* **2020**, *51*, 204–211. (In Chinese)
33. Chang, S.P.; Shi, Y.F.; Zhou, C.; Ding, J. Effect of Exit Circulation Distribution on Performances of Mixed-flow Pump. *Trans. Chin. Soc. Agric. Mach.* **2014**, *45*, 89–93. (In Chinese)
34. Zhu, B.S.; Tan, L.; Wang, X.H.; Ma, Z. Investigation on Flow Characteristics of Pump-Turbine Runners with Large Blade Lean. *J. Fluids Eng.* **2017**, *140*. [[CrossRef](#)]
35. Zhang, P.Y.; Zhu, B.S.; Zhang, L.F. Numerical Investigation on Pressure Fluctuations Induced by Interblade Vortices in a Runner of Francis Turbine. *Large Electron. Mach. Hydraul. Turbine* **2009**, *35*, 35–38. (In Chinese)
36. Zangeneh, M.; Goto, A.; Harada, H. On the Design Criteria for Suppression of Secondary Flows in Centrifugal and Mixed Flow Impellers. *J. Turbomach.* **1998**, *120*, 723. [[CrossRef](#)]

Article

The Influence of Hydrodynamic Changes in a System with a Pitched Blade Turbine on Mixing Power

Jacek Stelmach ¹, Czesław Kuncewicz ¹, Szymon Szufa ^{1,*} , Tomas Jirout ² and Frantisek Rieger ²

¹ Faculty of Process and Environmental Engineering, Lodz University of Technology, Wolczanska 213, 90-924 Lodz, Poland; jacek.stelmach@p.lodz.pl (J.S.); czeslaw.kuncewicz@p.lodz.pl (C.K.)

² Faculty of Mechanical Engineering, Czech Technical University in Prague, Technicka 4, 166 04 Praha 6, Czech Republic; tomas.jirout@fs.cvut.cz (T.J.); frantisek.rieger@fs.cvut.cz (F.R.)

* Correspondence: szymon.szufa@p.lodz.pl; Tel.: +48-606-134-239

Abstract: This paper presents an analysis of hydrodynamics in a tank with a 45° and 60° pitched blade turbine impeller operating while emptying the mixer and with an axial agitator working during axial pumping-down of water at different water levels above the impeller. Measurements made with the PIV method confirmed the change in direction of pumping liquid after the level dropped below the critical value, with an almost unchanged liquid stream flowing through the mixer. It was found that an increase in the value of the tangential velocity in the area of the impeller took place and the quantity of this increase depended on the angle of the blade pitch and the rotational frequency of the impeller. Change in this velocity component increased the mixing power.

Keywords: mixing; power consumption; pitched blade turbine; impeller



Citation: Stelmach, J.; Kuncewicz, C.; Szufa, S.; Jirout, T.; Rieger, F. The Influence of Hydrodynamic Changes in a System with a Pitched Blade Turbine on Mixing Power. *Processes* **2021**, *9*, 68. <https://doi.org/10.3390/pr9010068>

Received: 14 December 2020

Accepted: 28 December 2020

Published: 30 December 2020

Publisher's Note: MDPI stays neutral with regard to jurisdictional claims in published maps and institutional affiliations.



Copyright: © 2020 by the authors. Licensee MDPI, Basel, Switzerland. This article is an open access article distributed under the terms and conditions of the Creative Commons Attribution (CC BY) license (<https://creativecommons.org/licenses/by/4.0/>).

1. Introduction

Batch production of suspensions in mechanically stirred tanks is often used in industrial practice [1,2]. The impeller is left running inside to prevent the solids from falling when emptying the tank. During tests on the suspension production process in a tank with a capacity of 300 m³, an increase in the need for mixing power was observed when emptying the tank shortly before the emergence of the impeller from the mixed liquid [3]. The observed increase in power is significant and can lead to engine overload and even damage. This phenomenon has not been described so far in classic monographs on mixing processes [4–6]. Only in the work of Paul et al. [7] is there mention of a significant increase in the forces acting on the agitator as the liquid surface passes through it. However, this has not been fully explained so far.

Detailed studies [8] only provide information on the possible increase in mixing power after activating the impeller while stirring the suspension, when the solid particles lifted from the bottom reach the stirrer level. This effect is most likely due to changes in the density of the slurry near the impeller.

In the course of our research on the phenomenon of an increase in mixing power when emptying the tank with a working pitched blade turbine (PBT) set to pump liquid downwards, it was established [9,10] that for a given geometric system, the higher the rotational frequency of the impeller, the lower the increase in mixing power as the liquid surface passes through the impeller. In the case of turbine-blade impellers, the influence of the blade inclination angle on the observed increase in mixing power was also noted. In this case, the greater the angle of inclination, the smaller the increase in power, and for the flat blade turbine (FBT) mixers no increase in power was observed at all. Thus, this phenomenon must be related to the hydrodynamics of the liquid in the mixer. Based on visual observations when emptying the mixer, changes were found in the liquid circulation in the tank. At the crucial moment—corresponding to a power surge—the PBT impeller stopped pumping liquid downwards. At the same time, it was found that the phenomenon

of an abrupt increase in the mixing power does not occur when filling the tank. If the impeller rotates at a constant angular velocity, then the torque applied to it is transferred by blades to the liquid stream pumped by the stirrer and increases the momentum (angular momentum) of the liquid.

2. Materials and Methods

Theoretical Background

This can be described by the equation [11]:

$$M = \rho \cdot V_p \cdot R_m \cdot C_u \quad (1)$$

where: M —torque (Nm), ρ —liquid density (kg/m^3), V_p —liquid stream flowing (m^3/s), $R_m = D/2$ —impeller radius (m), D —impeller diameter (m), $C_u = k \cdot U$ —tangential velocity component at the exit of the impeller (m/s), k —coefficient, $U = \pi \cdot N \cdot D$ —tangential speed of the end of the stirrer blade (m/s). The above formula is true assuming that the liquid entering the agitator has no circumferential (tangential) component (i.e., it does not make a circular motion like at the inlet of a centrifugal pump [12,13]). This means that the momentum for this component can be neglected. The mixing power is determined based on the known relationship

$$P = M \cdot \omega = 2 \cdot \pi \cdot N \cdot M \quad (2)$$

where: ω —angular velocity (rad/s), N —rotational frequency of the impeller (s^{-1}). It is worth noting that the relationship (2) is universal and is applicable in the description and analysis of other unit processes, e.g., mixing of granular materials and granulation [14–16].

The liquid stream flowing through the impeller with blades inclined in relation to the plane $z = \text{const}$ at the angle $\alpha = \text{const}$ (the angle does not vary along the radius r) can be estimated based on theoretical considerations. Figure 1 shows the components of the velocity vector in the radial and axial directions (b —the width of the shoulder blade, α —the angle of inclination of the blade relative to the plane of movement, $U = \omega \cdot r$ —tangential speed of the blade).

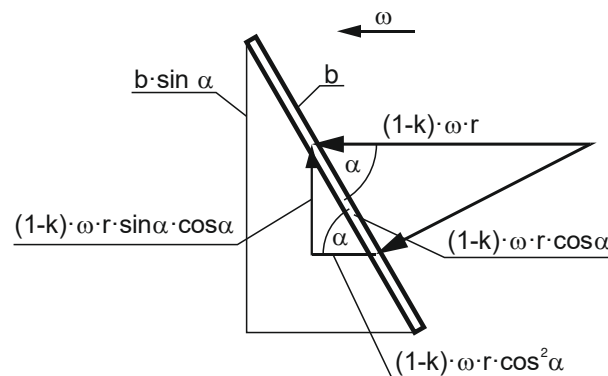


Figure 1. Distribution of velocity vectors for an inclined blade.

The starting point for calculating the velocity components is the difference between the tangential speed of the blade and the tangential velocity of the liquid $(\omega - \omega_c) \cdot r = (1 - k) \cdot \omega \cdot r$, k , which acts as the tangential velocity on the paddle in the plane of stirrer motion $z = \text{const}$. This speed can be broken down into its components: radial $(1 - k) \cdot \omega \cdot r \cdot \cos^2 \alpha$ and axial $(1 - k) \cdot \omega \cdot r \cdot \sin \alpha \cdot \cos \alpha$. Therefore, the radial flux for a cylindrical surface $\pi \cdot b \cdot D$ for the condition $\omega \cdot r = \pi \cdot D \cdot N$ is calculated as follows.

$$V_{pr} = \pi^2 \cdot (1 - k) \cdot b \cdot N \cdot D^2 \cdot \cos^2 \alpha \quad (3)$$

Axial flux for the cross-section $\pi \cdot D^2 / 4$ is calculated by integration, taking the elementary section $2 \cdot \pi \cdot r \cdot dr$ and lifting speed $\omega = 2 \cdot \pi \cdot N \cdot r$ for specific radius. Hence:

$$V_{pz} = (1 - k) \cdot 2 \cdot \pi \cdot N \cdot \sin \alpha \cdot \cos \alpha \cdot 2 \cdot \pi \cdot \int_0^{D/2} r^2 \cdot dr \quad (4)$$

After integration you receive:

$$V_{pz} = \pi^2 \cdot (1 - k) \cdot N \cdot \sin \alpha \cdot \cos \alpha \cdot \frac{D^3}{6} \quad (5)$$

The relationships describing the pumping of liquids through axial impellers can also be found in other papers [17,18].

For normal operation of turbine mixers with inclined blades ($H = D$ or $H \gg h_m$) it can be assumed that axial flow only occurs through the liquid and the radial flow is negligible ($V_p \approx V_{pz}$, $V_{pr} \approx 0$). However, it should be noted that Equation (5) also shows the dependence of the liquid stream flowing through the stirrer on the component of the peripheral velocity. Therefore, a dependence of the mixing power on this component in the area of the agitator should be expected. It is justified because the resistance force of the blades during their rotation in the liquid comes mainly from this component. This force can be calculated from these dependencies [19]:

$$F_i = \frac{P \cdot B_i \cdot \sin \alpha}{z \cdot \omega \cdot A} \quad (6)$$

where: P —power used for mixing (W), ω —angular velocity of the impeller (rad/s), z —number of impeller blades, α —the angle of inclination of the blade relative to the horizontal, $B_i = \frac{h_i}{3} (R_i^3 - r_i^3)$ —for the rectangular i -th impeller element, $A_i = \sum_{i=0}^n \frac{h_i}{4} (R_i^4 - r_i^4)$ —for all rectangular elements of the impeller blade. The aim of the work is to determine the effect of changes in the liquid flow in the mixer on the mixing power during emptying with the mixer working.

The tests were carried out in a flat-bottomed glass tank with a diameter of $T = 292$ mm, equipped with four baffles with a width of $B = 0.1 \cdot T$. A six-blade pitched blade turbine with diameter $D = 100$ mm and blade width $b = 20$ mm was placed at height $h_m = 100$ mm ($h_m \approx T/3$) above the bottom of the tank. Impellers with a blade inclination angle were used, at 45° (PBT45—Figure 2a) and 60° (PBT6—Figure 2b). This type of axial impeller provides the shortest mixing times compared to other axial mixers, but with the highest mixing power [20–23]. The tank was filled with distilled water ($t = 20^\circ \text{C}$) up to $H = 300$ mm ($H \approx D$). Medium diameter glass tracer particles of $10 \mu\text{m}$ were added to the water. In order to reduce optical distortions, the cylindrical tank was placed in a rectangular tank, and the space between the walls of the tanks was filled with water. Based on the analysis of the data on the mixing power, the speed measurements were limited to only two rotational frequencies of the impeller $N = 90 \text{ min}^{-1}$ (corresponding to the value of the number Froude $Fr = N^2 \cdot D / g = 0.023i$ and Reynolds number $Re = N \cdot D^2 \cdot \rho / \eta = 15,000$) and $N = 240 \text{ min}^{-1}$ ($Fr = 0.163$, $Re = 40,000$). The direction of rotation of the impeller was such that the axial flow of liquid generated by the impeller was directed to the bottom of the tank, as is usual when mixing suspensions.

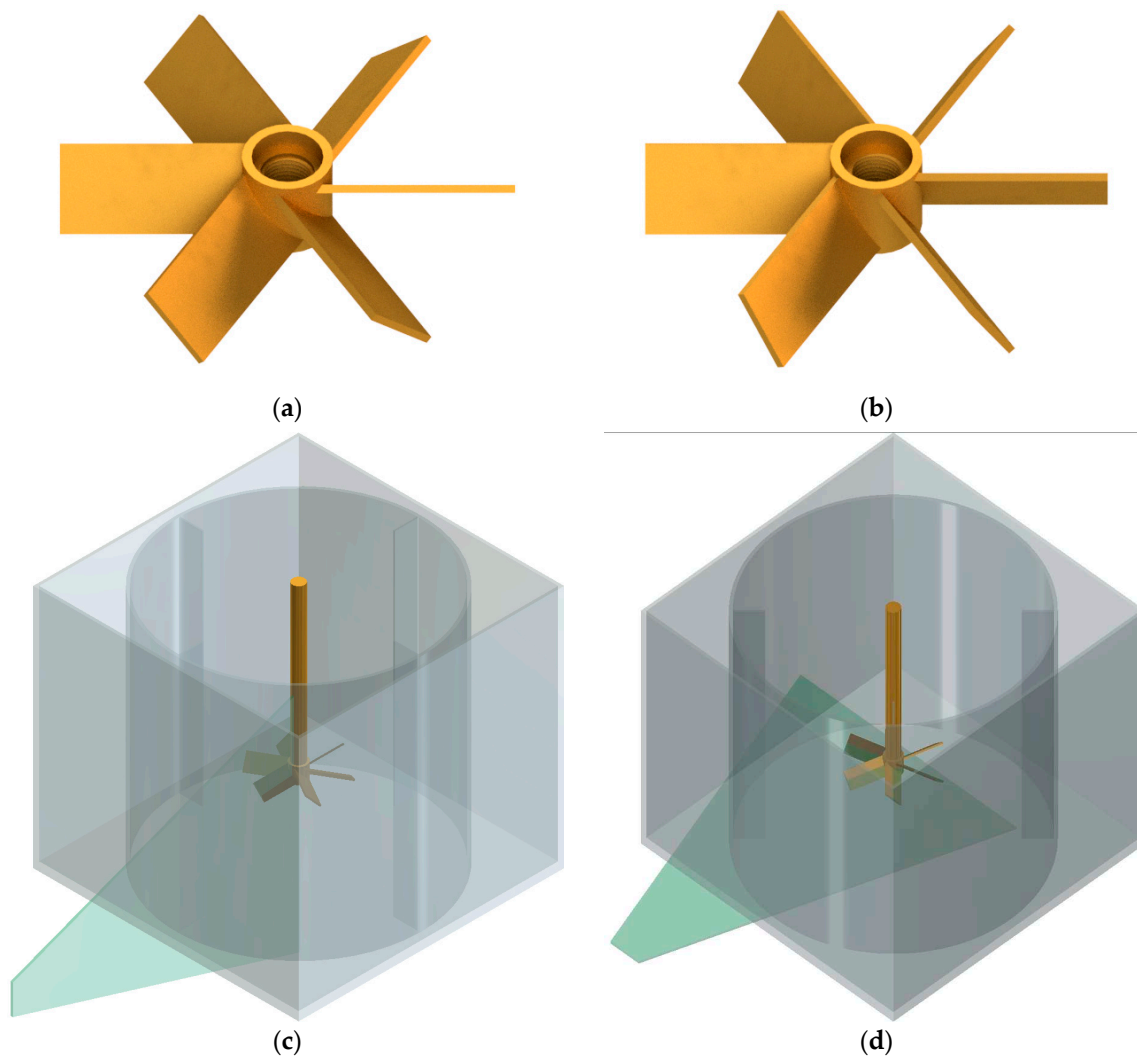


Figure 2. Tested impellers (a) PBT45, (b) PBT60 and the position of the light knife during the measurements, (c) vertical: measurement of radial and axial components, (d) horizontal: measurement of tangential and radial components.

The measurements were performed using the LaVision PIV Particle Image Velocimetry measurement system [24–27] with a two-pulse laser with a maximum power of 135 mW and an ImagePro camera with a resolution of 2048 px × 2048 px with a Nikkor 1.8/50 lens. The lens aperture was stopped down to the value ensuring the maximum resolving power (i.e., the aperture value was 5.6 [28]).

In order to determine the tangential and radial velocities, a 1 mm thick light knife was placed at the height of the stirrer. In the measurements of radial and axial velocities, the plane of the light knife was located about 2° in front of the baffle. A diagram showing the positions of the light knife is shown in Figure 2c,d. The measurement field was approximately 180 mm × 180 mm in the first case and approximately 190 mm × 190 mm in the second case. The laser frequency (pulses) was 2.7 Hz. Thus, for both configurations, the images were recorded for different positions of the blades with respect to the plane of symmetry between the baffles, although in the PIV method it is possible to synchronize the laser flashes with a specific position of the stirrer blade by using an external trigger [29] or selecting the frequency of the flashes [30].

Measurements were made for the height of the liquid in the tank equal to $h_w = 140$ mm, 135 mm, 130 mm, 125 mm, 120 mm, 115 mm, 110 mm, and 105 mm. For each combination of rotational frequency and liquid height, 100 duplicates were taken to average the results. The proprietary DaVis 7.2 program was used for data processing. Two-pass data processing

was used with the final size of the analyzed field $32 \text{ px} \times 32 \text{ px}$ (i.e., approximately $2.8 \text{ mm} \times 2.8 \text{ mm}$) without overlapping.

In order to facilitate comparisons, dimensionless velocities were used in the further part of the work, i.e., the velocity of the liquid was divided by the peripheral velocity of the end of the impeller blade: $U = \pi \cdot D \cdot N$.

3. Results

3.1. Changes in Fluid Circulation during Changes in the Height of the Liquid in the Tank

The liquid circulation method for PBT impellers is shown in Figure 3. At higher levels of liquid in the vessel, it is pumped down towards the bottom of the tank. After leaving the rotor, the liquid flows obliquely, so that centrally under the impeller there is a conical space in which the liquid flows upwards at a slow speed, with the apex angle of the cone being greater for a larger blade inclination angle (Figure 3a,b). The flow patterns obtained for large heights of liquid in the tank are consistent with the literature information [31–36]. After exceeding the critical height, the flow direction changes, the liquid under the impeller flows upwards and is radially directed over the impeller towards the tank wall, and the rising cone disappears (Figure 3c,d). From a height of $h = 50 \text{ mm}$, the liquid flows practically in the axial direction, but with a uniform radial distribution. At the same time, the circulation core moves up to the level of the lower edge of the blades.

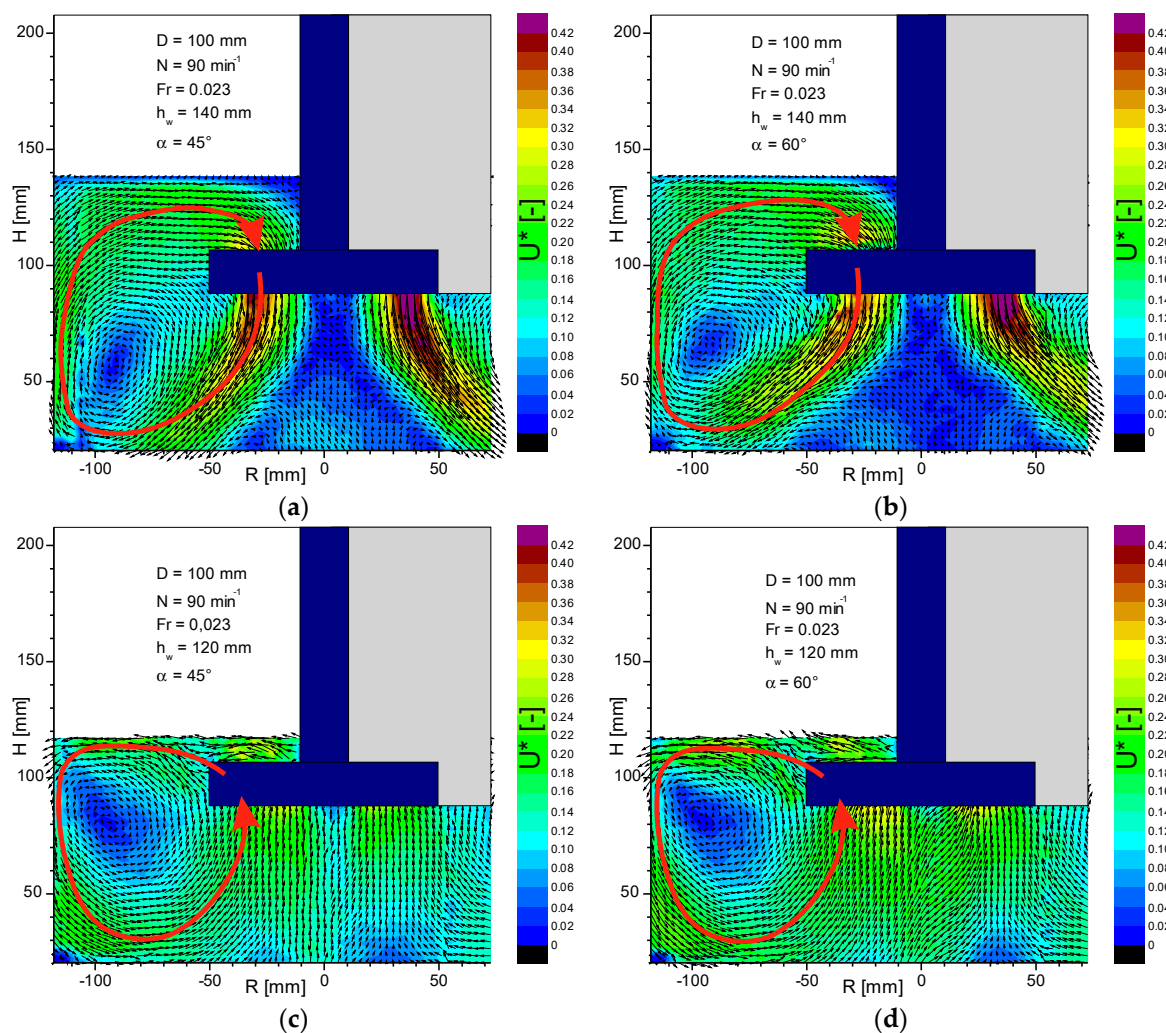


Figure 3. Liquid flow before the partition for the PBT45 and PBT60 impellers: (a) $h_w = 140 \text{ mm}$, $\alpha = 45^\circ$; (b) $h_w = 140 \text{ mm}$, $\alpha = 60^\circ$; (c) $h_w = 120 \text{ mm}$, $\alpha = 45^\circ$; (d) $h_w = 120 \text{ mm}$, $\alpha = 60^\circ$.

Analysis of Figure 3 shows that pumping of the liquid through the impeller only takes place in the axial direction, i.e., $V_p = V_{pz}$ and, as assumed in the introduction, there is no radial discharge at the height of the stirrer. As Equation (1) shows, changes in mixing power should be correlated with changes in pumping efficiency. To specify numeric values V_p and V_{pz} , appropriate measurements of the distribution of axial and radial velocities were performed using the PIV system. After decomposing the velocity into the axial and radial components, the velocity profiles can be determined by interpolation in the program Origin, as shown in Figure 4. The obtained profiles agree with the literature information [37,38].

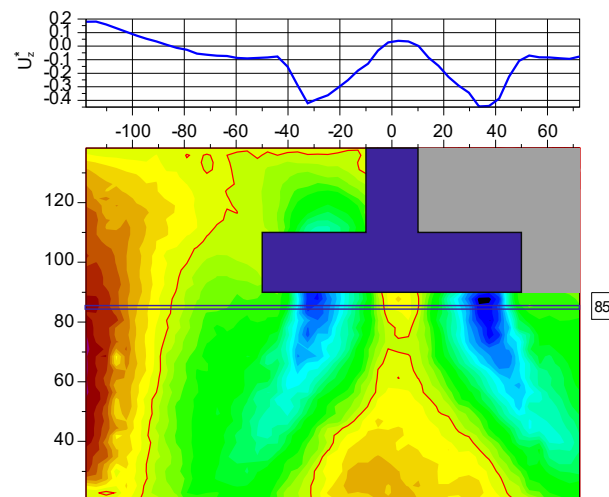


Figure 4. Map and profile of axial velocity at a height of $h = 85$ mm above the bottom for $h_w = 140$ mm and $N = 90 \text{ min}^{-1}$ (PBT45 impeller).

On the basis of the velocity profiles obtained, the pumping capacity was determined in MathCAD $V_p = \sum_i V_{z_i} \cdot \pi \cdot d_i \cdot c$ below the stirrer ($h = 85$ mm, $d_i = 1, 3 \dots 99$ mm, $c = 2$ mm) assuming the invariability of individual velocity components in the circumferential direction. The results obtained in the form of dimensionless pumping numbers $K_p = V_p / (N \cdot D^3)$ are shown in Figure 5 and depend on the dimensionless parameter $(h_w - h_d) / T$, in which h_w —liquid level, $h_d = h_m - 0.5 \cdot b \cdot \sin \alpha$ —distance of the bottom edge of the agitator from the bottom.

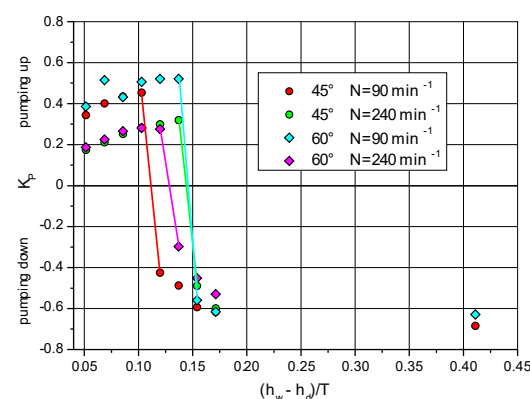


Figure 5. Pumping capacity depending on the height of the liquid in the tank.

Lines (sections) connect the points between which the direction of the liquid flow through the impeller changes. After changing the pumping direction, no significant differences in the absolute values of the pumping numbers are observed. Moreover, when pumping upwards, in some cases the pumping capacity is even slightly reduced. This means that the mixing power should remain constant or it should decrease minimally when

changing the pumping direction. Therefore, the source of the increase in mixing power should be sought in the behavior of the peripheral velocity component. The theoretical value of the pumping number can be determined by transforming the Equation (5).

$$K_p = \frac{V_p}{N \cdot D^3} = \frac{\pi^2}{6} \cdot (1 - k) \cdot \sin \alpha \cdot \cos \alpha \quad (7)$$

For $k = 0$ i $\alpha = 45^\circ$ we obtain $K_p = 0.822$, and for $\alpha = 60^\circ$ $K_p = 0.712$ and similar values can be found in the literature [39]. The values obtained are greater than those measured, because in fact the peripheral velocity of the liquid is lower than the speed of the blade, i.e., $k > 0$. Even more value $K_p = 1.167$ dla $h/T = 0.33$ is obtained from the correlation given by Fořt [40] for mixers with a blade inclination angle $\alpha = 45^\circ$

$$K_p = 0.947 \cdot \left(\frac{h}{T} \right)^{-0.19} \quad (8)$$

3.2. Tangential Velocity Profiles

Based on the data obtained from the PIV system, the tangential velocity profiles were determined in the program Origin at the height of the impeller in the plane of symmetry between the baffles. The results in the form of dimensionless velocities U_t^* are shown in Figure 6.

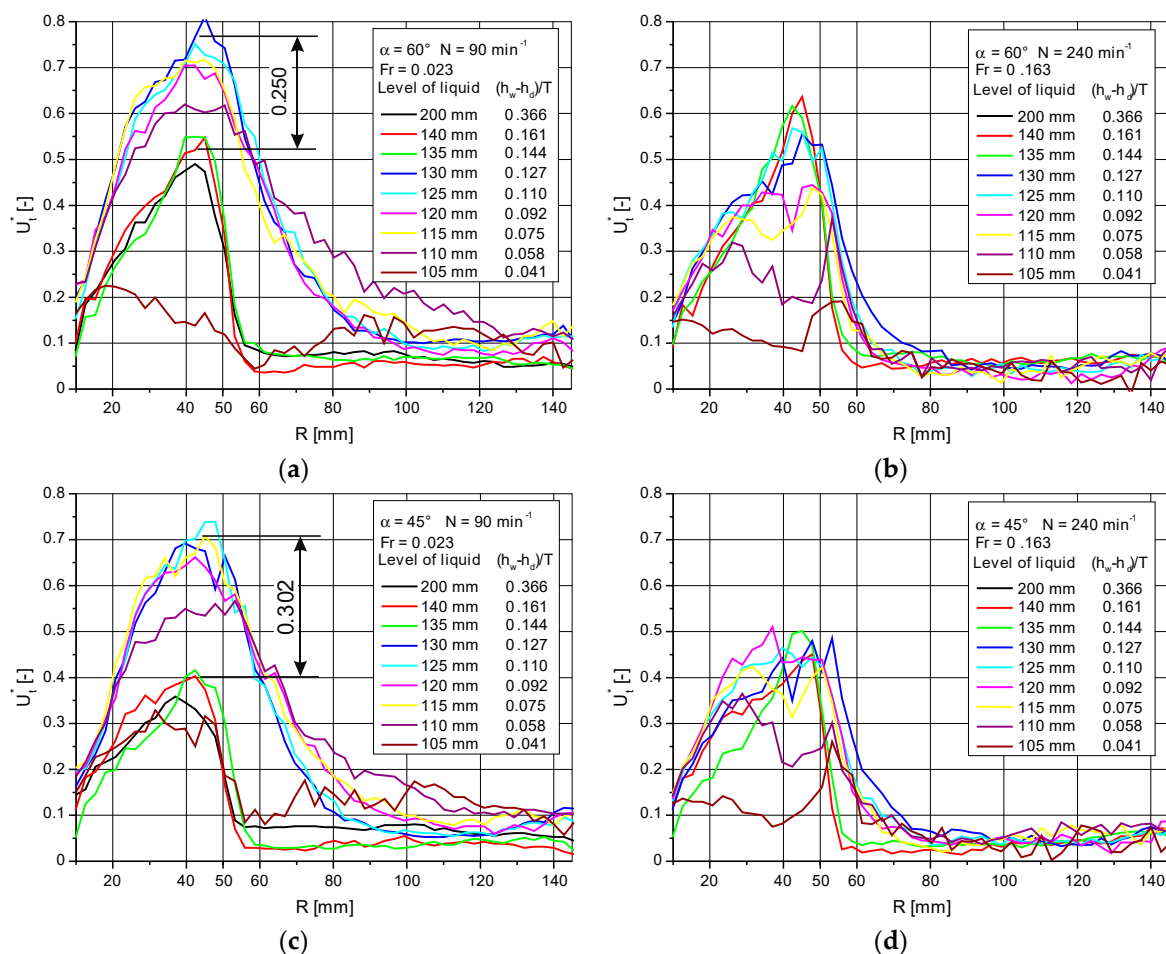


Figure 6. Tangential velocity profiles at the height of the impeller h_m . (a) $N = 90 \text{ min}^{-1}$, $\alpha = 60^\circ$; (b) $N = 240 \text{ min}^{-1}$, $\alpha = 60^\circ$; (c) $N = 90 \text{ min}^{-1}$, $\alpha = 45^\circ$; (d) $N = 240 \text{ min}^{-1}$, $\alpha = 45^\circ$.

For the smallest of the analyzed rotational frequencies $N = 90 \text{ min}^{-1}$, an increase in velocity in the area of the impeller at the moment of changing the pumping direction is visible (marked in the figure). The greater difference occurs in the case of a smaller blade inclination angle $\alpha = 45^\circ$. Increasing the rotational frequency results in smaller speed variations when the fluid flow direction is changed.

The ratio of the maximum velocity values before and after the change of the circulation method is approximately 1.75 for the inclination angle $\alpha = 45^\circ$ and 1.46 for $\alpha = 60^\circ$. These values are close to the multiplicity of the mixing power increase, 2 and 1.5 respectively. Thus, it can be assumed that the increase in mixing power is caused by the change in the peripheral speed of the liquid in the area of the impeller.

3.3. Estimating the Mixing Power

The relationship (1) presented at the beginning is less accurate than the direct measurement of the torque due to the need to experimentally determine the velocity of the liquid in the area of the impeller. Moreover, in the PIV method it is very difficult to estimate the measurement error, and the importance of this is evidenced by the information about new algorithms appearing in the literature [40–42]. Nevertheless, it should reflect the behavior of the system during hydrodynamic changes taking place in it. The results of calculating the power number using Equation (1) are shown in Figure 7, where the mixing power number is placed on the ordinate axis: $Eu = Po = P / (N^3 \cdot D^5 \cdot \rho)$.

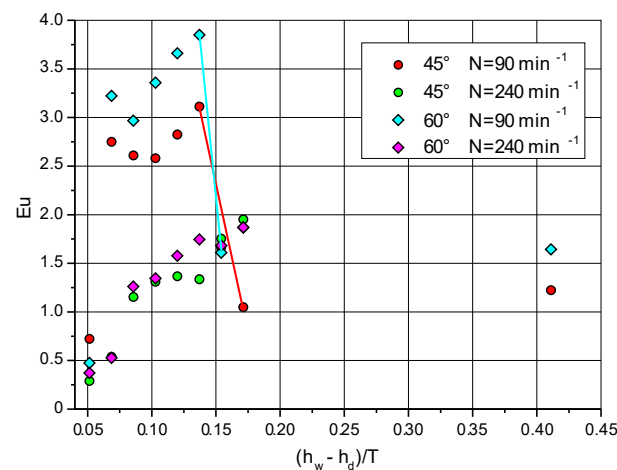


Figure 7. The power number calculated using Equation (1).

For pumping the liquid down (towards the bottom) at high liquid heights in the tank, low values of the mixing power were obtained. For the PBT45 impeller, direct measurements gave $Eu = 1.53$, and for the PBT60 impeller, $Eu = 2.18$. These results are consistent with the data in the literature [43,44]. The tangential velocity of the liquid at the outlet of the agitator has a great influence on the results obtained. For example, for the PBT45 impeller under the conditions of $N = 90 \text{ min}^{-1}$, $h_w = 140 \text{ mm}$, the measurements obtained the value of $Eu = 1.05$ for $C_u = 0.09 \text{ m/s}$, but at a distance of $R = 48.4 \text{ mm}$ from the impeller axis the tangential velocity of the liquid is 0.132 m/s and the calculated power number value is $Eu = 1.535$. Unfortunately, it is practically impossible to determine the measurement error in the PIV method [45]. In addition, in asynchronous measurement, when the position of the blades in relation to the velocity profile determination line (plane) changes, the initial position of the blade may affect the results obtained. This is illustrated in Figure 8 showing the results of five consecutive measurements made to test this thesis. The differences in the values of the tangential velocity of the liquid for the radius of the stirrer $R_m = 50 \text{ mm}$ may reach about 0.05 of the velocity of the end of the stirrer blade. For the profiles from Figure 8, the values of the power numbers are obtained from $Eu = 1.195$ to $Eu = 1.445$ for $N = 90 \text{ min}^{-1}$ and from $Eu = 1.888$ to $Eu = 2.145$ for $N = 240 \text{ min}^{-1}$.

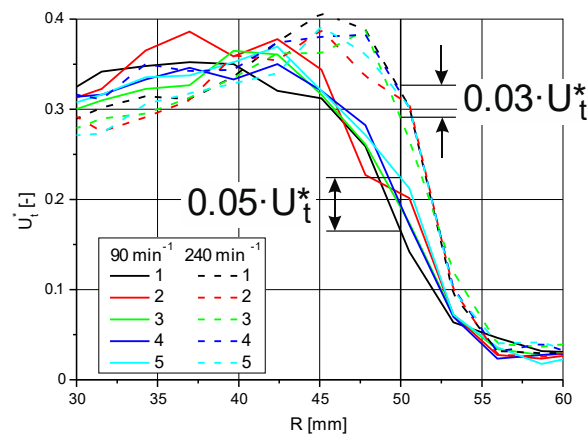


Figure 8. Profiles for five consecutive measurements (PBT45, $h_w = 140$ mm).

The multiplicity of the increase in mixing power is greater than the values obtained in direct measurements. Figure 7 shows that for blades set at an angle of 45° there should be a threefold increase, and for a 60° angle, a two-fold increase in power. In the measurements of torque for PBT45, a two-fold increase in power was achieved; for PBT60 this increase was 1.5 times, which can be read from Figure 9 presenting the results of previous studies [10]. These differences may result from incomplete fulfillment of the condition (assumption) that the liquid influencing the agitator impeller does not rotate.

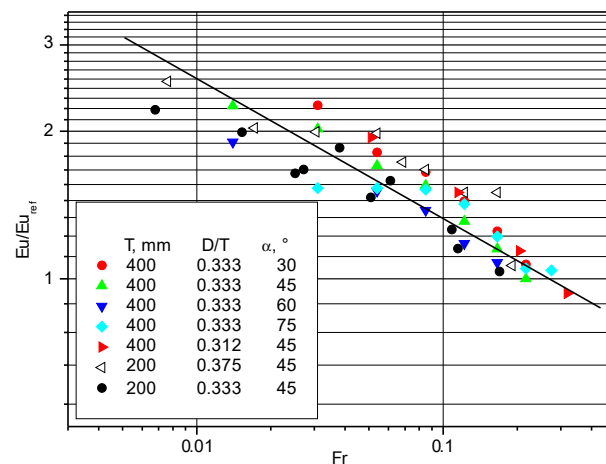


Figure 9. Increase in mixing power when emptying the tank for various sizes of impellers.

4. Discussion

The results of the experiments presented in the paper allow for a preliminary hypothesis concerning the mechanism of increasing mixing power when emptying the mixers during the operation of the axial impeller while pumping the liquid down the tank [46]. The critical moment of the mechanism analyzed is undoubtedly the moment of changing the direction of the liquid flow through the impeller area, despite the unchanging parameters of the impeller itself. According to results from the analysis of the velocity distributions shown in Figure 3 for the liquid height in the tank $h_w = 140$ mm, the liquid flows in the direction of liquid pumping through the rotating impeller (Figure 3a,b), and for $h_w = 120$ mm the liquid flows through the area of the impeller in the opposite direction, i.e., to the bottom of the tank. This occurs when the liquid height above the upper edge of the impeller is approximately 10–15 mm. With high probability, it can be assumed that at this point the liquid layer above the impeller is so small that there is no possibility for secondary circulation lines, i.e., axial-radial circulation, to close within it. The rotating impeller starts to work like a radial-circumferential agitator (Figure 6). The impeller accumulates the

liquid in front of the paddle, which increases the resistance to motion and increases the tangential velocity. At the same time, the stream of liquid ejected from the area of the impeller at a relatively high speed (Figure 9) begins to flow towards the bottom of the tank at the wall, thus changing the direction of circulation, which is shown in Figure 3c,d. It should be emphasized that this is a working hypothesis and a more extensive cycle of tests should be performed to confirm it. Figure 10 Radial represent the velocity maps: (a) $h_w = 140$ mm; (b) $h_w = 120$ mm.

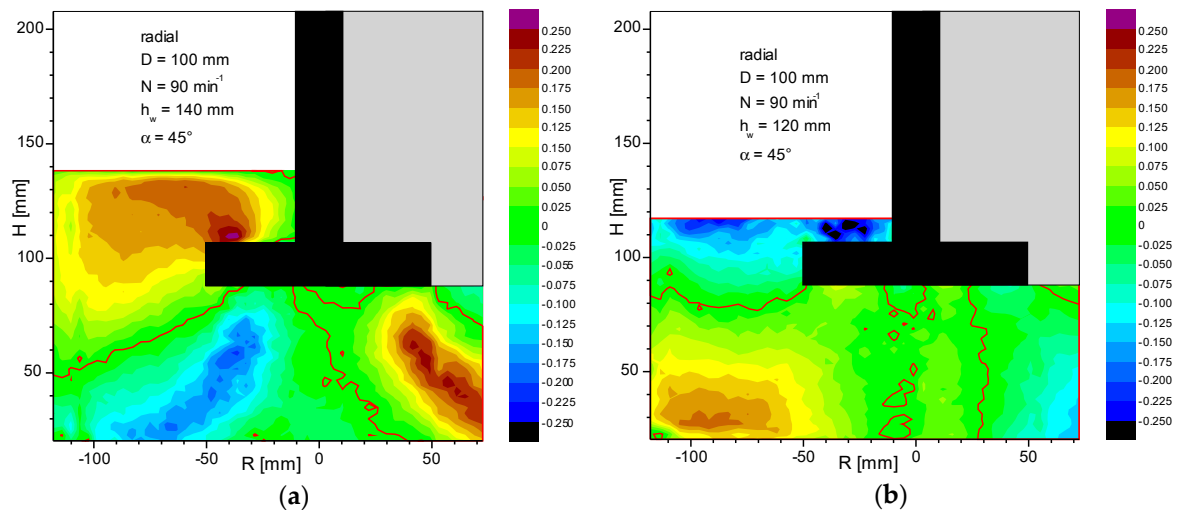


Figure 10. Radial velocity maps: (a) $h_w = 140$ mm; (b) $h_w = 120$ mm.

5. Conclusions

Due to the incomplete fulfillment of the conditions, relationship (1) can be used to determine energy changes (mixing power) in a system with a mechanical impeller and a six-blade pitched blade turbine during hydrodynamic changes of the centrifugation of the liquid flowing into the impeller. Furthermore, this allows achievable accuracy of velocity measurements in the area of the impeller taking place when emptying the tank.

The increase in the mixing power when emptying the tank with the impeller working is determined by the abrupt increase in the tangential velocity component in the area of the impeller after changing the direction of liquid circulation. The increase in the value of the tangential velocity depends on the angle of the blades' inclination and the rotational frequency of the impeller and is correlated with the changes in the mixing power when emptying the tank. As in the case of mixing power, smaller increments are observed for larger blade angles. Furthermore, increasing the rotational frequency (at the same angle of inclination) results in smaller increases in tangential velocity. In the paper, it is stated that it is practically impossible to determine the measurement error in the PIV method. According to Lehr and Boelcs [47] the standard measurement uncertainty of PIV velocity measurements for the mean velocity field is less than 4%, and in the regions of strong velocity gradients it is smaller than 5% when the test-section is quasi-two-dimensional and the out-of-plane components of the vectors cause only minor errors.

Author Contributions: Conceptualization, J.S. and C.K.; methodology, J.S., C.K., S.S., T.J., and F.R.; validation, J.S., C.K., S.S., T.J., and F.R.; formal analysis, J.S., C.K., S.S., T.J., and F.R.; investigation, J.S., C.K., S.S., T.J., and F.R.; resources, J.S., C.K., S.S., T.J., and F.R.; data curation, J.S., C.K., S.S., T.J., and F.R.; writing—original draft, J.S., C.K., S.S., T.J., and F.R.; writing—review and editing, J.S., C.K., S.S.; visualization, J.S., C.K., S.S., T.J., and F.R.; supervision, J.S., C.K., S.S., T.J., and F.R.; project administration, J.S., C.K., S.S., T.J., and F.R.; funding acquisition, J.S., C.K., S.S., T.J., and F.R. All authors have read and agreed to the published version of the manuscript.

Funding: This research was funded by Ministry of Education, Youth and Sports of the Czech Republic: OP RDE CZ.02.1.01/0.0/0.0/16_019/ 0000753.

Institutional Review Board Statement: Not applicable.

Informed Consent Statement: Not applicable.

Data Availability Statement: Not applicable.

Acknowledgments: The work was created as part of the statutory activity of the Department of Chemical Engineering of Lodz University of Technology and the grant OP RDE CZ.02.1.01/0.0/0.0/16_019/0000753 financed by the Ministry of Education, Youth and Sports of the Czech Republic.

Conflicts of Interest: The authors declare no conflict of interest.

References

- Rieger, F.; Jirout, T.; Rzycki, E. Mixing of suspensions. Selection of the mixer and tank. *Inż. Ap. Chem.* **2002**, *41*, 111–112. (In Polish)
- Grenville, R.K.; Mak, A.T.C.; Brown, D.A.R. Suspension of solid particles in vessels agitated by axial flow impellers. *Chem. Eng. Res. Des.* **2015**, *100*, 282–291. [[CrossRef](#)]
- Mazoch, J.; Rieger, F.; Jirout, T. *Report TH 01020879*; TECHMIX: Brno, Czech Republic, 2016. (In Czech)
- Uhl, V.W.; Gray, J.B. *Mixing. Theory and Practice*; Academic Press: London, UK, 1973; pp. 112–176.
- Nagata, S. *Mixing: Principles and Applications*; John Wiley & Sons: New York, NY, USA, 1975; pp. 62–65.
- Zlokarnik, M. *Stirring. Theory and Practice*; Wiley-VCH: Weinheim, Germany, 2001; pp. 76–96.
- Paul, E.L.; Atiemo-Obeng, V.A.; Kresta, S.M. *Handbook of Industrial Mixing*; John Wiley & Sons: Hoboken, NJ, USA, 2004; pp. 543–584.
- Mak, A.T.C. Solid-Liquid Mixing in Mechanically Agitated Vessels. Ph.D. Thesis, University College, London, UK, 1992.
- Rieger, F.; Jirout, T.; Moravec, J.; Stelmach, J.; Kuncewicz, C.Z. The phenomenon of increased mixing power consumption during tank emptying. *Przemysł Chemiczny* **2019**, *98*, 962–966. (In Polish)
- Stelmach, J.; Kuncewicz, C.Z.; Rieger, F.; Moravec, J.; Jirout, T. Increase of mixing power during emptying of tanks with turbine-blade impellers. *Przemysł Chemiczny* **2020**, *99*, 239–243. (In Polish)
- C, ϕ . *Па Ааа аа*; Leningrad, Russia, 1975; pp. 111–117. (In Russian)
- Perry, R.H. Section 10 Transport and storage of fluids, 10–24 Centrifugal pump. In *Perry's Chemical Engineers Handbook*, 7th ed.; McGraw-Hill: New York, NY, USA, 1997.
- Introduction to Hydraulic Pumps. Available online: <https://www.engineeringclicks.com/hydraulic-pumps/> (accessed on 12 December 2020).
- Heim, A.; Gluba, T.; Obraniak, A. The effect of the wetting droplets size on power consumption during drum granulation. *Granul. Matter* **2004**, *6*, 137–143. [[CrossRef](#)]
- Heim, A.; Kaźmierczak, R.; Obraniak, A. Model of granular bed dynamics in the disk granulator: Model dynamiki złoża ziarnistego w granulatorze talerzowym. *Chem. Proc. Eng.* **2004**, *25*, 993–998. (In Polish)
- Obraniak, A.; Gluba, T. Model of energy consumption in the range of nucleation and granule growth in drum granulation bentonite. *Physicochem. Probl. Miner. Process.* **2012**, *48*, 121–128.
- Fort, I.; Seichter, P.; Pes, L. Axial thrust of axial flow impellers. *Chem. Eng. Res. Des.* **2013**, *91*, 789–794. [[CrossRef](#)]
- Chapple, D.; Kresta, S.M.; Wall, A.; Afacan, A. The effect of impeller and tank geometry on power number for a pitched blade turbine. *Trans. IChemE* **2002**, *80*, 364–372. [[CrossRef](#)]
- Kozulin, N.A.; Sokołow, W.N.; Szapiro, A.J. *Maszyny Przemysłu Chemicznego. Przykłady i Zadania*; WNT: Warszawa, Poland, 1976; pp. 32–38. (In Polish)
- Fořt, I.; Jirout, T. A study on blending characteristics of axial flow impellers. *Chem. Proc. Eng.* **2011**, *32*, 311–319. [[CrossRef](#)]
- Jirout, T.; Rieger, F. Impeller design for mixing of suspensions. *Chem. Eng. Res. Des.* **2011**, *89*, 1144–1151. [[CrossRef](#)]
- Amira, B.B.; Driss, Z.; Karray, S.; Abid, M.S. PIV Study of the Down-Pitched Blade Turbine Hydrodynamic Structure. In Proceedings of the Fifth International Conference on Design and Modeling of Mechanical Systems, Djerba, Tunisia, 25–27 March 2013; pp. 237–244.
- Amira, B.B.; Driss, Z.; Abid, M.S. Experimental Study of the 60° PBT6 Pitching Blade Effect with a PIV Application. In Proceedings of the Multiphysics Modelling and Simulation for Systems Design Conference, Sousse, Tunisia, 17–19 December 2014; pp. 91–100.
- Raffel, M.; Willert, C.; Wersley, S.; Kompenhans, J. *Particle Image Velocimetry*, 2nd ed.; Springer: Berlin/Heidelberg, Germany, 2007; pp. 15–122.
- Brossard, C.; Monnier, J.C.; Barricau, P.; Vandernoot, F.X.; Le Sant, Y.; Champagnat, F.; Le Besnerais, G. Principles and Applications of Particle Image Velocimetry. Available online: <https://hal.archives-ouvertes.fr/hal-01180587/document> (accessed on 12 December 2020).
- Bastiaans, R.J.M. Cross-correlation PIV.; Theory, Implementation and Accuracy. Available online: https://www.researchgate.net/publication/241849539_Cross-correlation_PIV_theory_implementation_and_accuracy (accessed on 12 December 2020).
- 2D & Stereo PIV. Available online: <https://www.lavision.de/en/applications/fluid-mechanics/2d-stereo-piv/index.php> (accessed on 12 December 2020).

28. Available online: https://www.optyczne.pl/66.4-Test_obiektu-Nikon_Nikkor_AF_50_mm_f_1.8D_Rozdzielczo%C5%9B%C4%87_obrazu.html (accessed on 2 July 2020).
29. Ranade, V.V.; Perrard, M.; Le sauze, N.; Xuereb, C.; Bertrand, J. Trailing vortices of Rushton turbine: PIV Measurements and CFD Simulations with snapshot approach. *Trans. IChemE* **2001**, *79*, 3–12. [[CrossRef](#)]
30. Heim, A.; Stelmach, J. The comparison of velocities at the self-aspirating disk impeller level. *Przemysł Chem.* **2011**, *90*, 1642–1646. (In Polish)
31. Khopkar, A.R.; Mavros, P.; Ranade, V.V.; Bertrand, J. Simulation of flow generated by an axial-flow impeller. Batch and Continuous Operation. *Chem. Eng. Res. Des.* **2004**, *82*, 737–751. [[CrossRef](#)]
32. Aubin, J.; Mavros, P.; Fletcher, D.F.; Bertrand, J.; Xuereb, C. Effect of axial agitator configuration (up-pumping, down-pumping, reverse rotation) on flow patterns generated in stirred vessels. *Trans. IChemE* **2001**, *79*, 845–856. [[CrossRef](#)]
33. Jaworski, Z.; Dyster, K.N.; Nienow, A.W. The effect of size, location and pumping direction of pitched blade turbine impellers on flow patterns: LDA Measurements and CFD Predictions. *Trans. IChemE* **2001**, *79*, 887–894. [[CrossRef](#)]
34. Mavros, P.; Xuereb, C.; Fořt, I.; Bertrand, J. Investigation by laser Doppler velocimetry of the effects of liquid (flow rates and feed positions) on the flow patterns induced in a stirred tank by an axial-flow impeller. *Chem. Eng. Sci.* **2002**, *57*, 3939–3952. [[CrossRef](#)]
35. Ge, C.-Y.; Wang, J.-J.; Gu, X.-P.; Feng, L.-F. CFD simulation and PIV measurement of the flow field generated by modified pitched blade turbine impellers. *Chem. Eng. Res. Des.* **2014**, *92*, 1027–1036. [[CrossRef](#)]
36. Schafer, M.; Yianneskis, M.; Wachter, P.; Durst, F. Trailing Vortices around a 45° Pitched-Blade Impeller. *AIChE J.* **1998**, *44*, 1233–1246. [[CrossRef](#)]
37. Sahu, A.K.; Kumar, P.; Joshi, J.B. Simulation of flow in stirred vessel with axial flow impeller: Zonal modeling and optimization of parameters. *Ind. Eng. Chem. Res.* **1998**, *37*, 2116–2130. [[CrossRef](#)]
38. Ozcan-Taskin, G.; Wei, H. The effect of impeller-to-tank diameter ratio on draw down of solids. *Chem. Eng. Sci.* **2003**, *58*, 2011–2022. [[CrossRef](#)]
39. Tsui, Y.-Y.; Chou, J.-R.; Hu, Y.-C. Blade angle effects on the flow in a tank agitated by the pitched-blade turbine. *J. Fluids Eng.* **2006**, *128*, 774–782. [[CrossRef](#)]
40. Fořt, I.; Sedláková, V. Pumping effect of high-speed rotary mixers. *Collect. Czechoslov. Chem. Commun.* **1967**, *33*, 836–849. [[CrossRef](#)]
41. Lecordier, B.; Trinite, M. Advanced PIV Algorithms with Image Distortion Validation and Comparison Using Synthetic Images of Turbulent Flow. Available online: https://www.researchgate.net/publication/228862071_Advanced_PIV_algorithms_with_Image_Distortion_Validation_and_Comparison_using_Synthetic_Images_of_Turbulent_Flow (accessed on 12 December 2020).
42. Stanislas, M.; Okamoto, K.; Kahler, C.J.; Westerweel, J. Main results of the Second International PIV Challenge. *Exp. Fluids* **2005**, *39*, 170–191. [[CrossRef](#)]
43. Major-Godlewska, M.; Karcz, J. Power consumption for an agitated vessel equipped with pitched blade turbine and short baffles. *Chem. Pap.* **2018**, *72*, 1081. [[CrossRef](#)] [[PubMed](#)]
44. Pietranski, J.F. Mechanical Agitator Power Requirements for Liquid Batches. Available online: https://www.google.pl/url?sa=t&rct=j&q=&esrc=s&source=web&cd=&cad=rja&uact=8&ved=2ahUKEwiA6e_ys8PtAhUPxosKHTPsA0sQFjAAegQIBRAC&url=https%3A%2F%2Fwww.researchgate.net%2Fprofile%2FPrem_Baboo%2Fpost%2FWhat_is_the_required_power_of_submerged_mixer_in_equalization_tank_before_ABR%2Fattachment%2F59d626b379197b8077984f89%2FAS%253A322848827084802%25401453984566839%2Fdownload%2Fk103content.pdf&usq=AOvVaw2oZkJL_36DSIXTg0wsemod (accessed on 12 December 2020).
45. Adrian, Ł.; Piersa, P.; Szufa, S.; Romanowska-Duda, Z.; Grzesik, M.; Cebula, A.; Kowalczyk, S.; Ratajczyk-Szufa, J. Experimental research and thermographic analysis of heat transfer processes in a heat pipe heat exchanger utilizing as a working fluid R134A. In *Renewable Energy Sources: Engineering, Technology, Innovation*; Springer Proceedings in Energy ICORES 2017; Mudryk, K., Werle, S., Eds.; Springer: Berlin/Heidelberg, Germany, 2018; pp. 413–421. ISBN 978-3-319-72370-9. [[CrossRef](#)]
46. Dzikuć, M.; Kuryło, P.; Dudziak, R.; Szufa, S.; Dzikuć, M.; Godzisz, K. Selected Aspects of Combustion Optimization of Coal in Power Plants. *Energies* **2020**, *13*, 2208. [[CrossRef](#)]
47. Lehr, A.; Bölcs, A. Application of a particle image velocimetry system to the investigation of unsteady transonic flows in turbomachinery. In *Proceedings of the 9th International Symposium on Unsteady Aerodynamics, Aeroacoustics and Aeroelasticity of Turbomachines*, Lyon, France, 4–8 September 2000; Ferrand, P., Aubert, S., Eds.; Springer: Berlin/Heidelberg, Germany, 2000.

Article

New Design of the Reversible Jet Fan

Miroslav H. Benišek, Đorđe S. Čantrak *, Dejan B. Ilić  and Novica Z. Janković

Faculty of Mechanical Engineering, University of Belgrade, Kraljice Marije 16, 11120 Belgrade 35, Serbia; mbenisek@mas.bg.ac.rs (M.H.B.); dilic@mas.bg.ac.rs (D.B.I.); njankovic@mas.bg.ac.rs (N.Z.J.)

* Correspondence: djcantrak@mas.bg.ac.rs

Received: 18 November 2020; Accepted: 15 December 2020; Published: 17 December 2020



Abstract: This paper presents two designs of the axial reversible jet fan, with the special focus on the impeller. The intention was to develop a reversible axial jet fan which operates in the same way in both rotating directions while generating thrust as high as possible. The jet fan model with the outer diameter 499.2 ± 0.1 mm and ten adjustable blades is the same, while it is in-built in two different casings. The first construction is a cylindrical casing, while the second one is profiled as a nozzle. Thrust, volume flow rate, consumed power and ambient conditions were measured after the international standard ISO 13350. Results for both constructions are presented for three impeller blade angles: 28° , 31° and 35° , and rotation speed in the interval $n = 400$ to 2600 rpm. The smallest differences in thrust, depending on the fan rotation direction, as well as the highest thrust are achieved for the first design with the cylindrical casing and blade angle at the outer diameter of 35° . Therefore, it was shown that fan casing significantly influences jet fan characteristics. In addition, the maximum thrust value and its independence of the flow direction is experimentally obtained for the angle of 39° in the cylindrical casing.

Keywords: axial fan; reversible; jet; design; thrust; energy characteristics

1. Introduction

Reversible jet fans are present in road tunnels ventilation and garages, underground car parks, fire protection, good air quality systems, etc. They are designed to operate efficiently in both directions and produce adequate jets. Tunnel jet fans are, in fact, a substantial, i.e., core part of the tunnel ventilation, as well in smoke extraction systems. They should combine the highest technical requirements like efficiency and performance, as well as noise emission. Numerous CFD calculations have been performed in order to study the road tunnel ventilation and firefighting systems [1–8]. One of the choices for impulse ventilation of the tunnels is jet fan. “Impulse ventilation of tunnels involves the application of one or more jets of air into a tunnel, to drive the airflow in a desired direction. In essence, the kinetic energy of a high-velocity jet is transferred, with various degrees of efficiency, into the kinetic energy of slower-moving tunnel air” [4]. Therefore, the role of the jet fans is to provide an impulse to the air flow. “The average jet velocity is in the range of 30 to 40 ms^{-1} ” [4].

Experimental determination of tunnel ventilation axial ducted fan performance using a two-sensor hot wire X-probe with added pair of near-wall positioning pins is presented in [9]. Experimental results, obtained in the laboratory in the 1:19 scale tunnel, are used for ventilation performance of CFD test in a uni-directional traffic road tunnel [3,9,10]. Proposal for the improvement of CFD models of the tunnel fire development based on experimental data are also reported [7]. Improvement of the aerodynamic performance of a tunnel ventilation jet fan is performed by the application of multiobjective optimization technique [11].

Contemporary CFD tools include aerodynamic optimization of axial fan impeller with its blade geometry, guide vanes if they exist, casing and nozzle shapes, etc. Fan energy

characteristics, i.e., the aerodynamic fan curves, prior to experiments, could be estimated numerically. Experimental validation could be done according to the international standard ISO 13350 [12].

Three high pressure reversible fan concepts, like a two-stage counter rotating fan, a single-stage high speed fan and a two-stage fan with a single motor and impeller on each end of the motor shaft are presented in paper [13].

Paper [14] presents the designed reversible jet fan, obtained experimental data and CFD results. Reversible aerodynamic design, in fact, limits the maximum fan pressure side [13]. Paper [15] presents a numerical optimization procedure for performance improvement of a jet fan. Authors in [16] point out that aerodynamically desirable axial fan rotor blades, which would have identical aerodynamic performances in both flow directions, are still insufficiently developed. They present a method to profile these blades.

This paper presents a design of the reversible jet fan, geometries of two versions of the casings and experimentally obtained data. The axial fan impeller is the same in both cases, while casings are different. Experimentally determined thrust, after ISO 13350 [12], power and volume flow rates for various fan rotation speeds in both rotating directions are presented in this paper. The intention was to design the impeller with good characteristics in both rotating directions, so the automatic fan speed control system could adopt the rotation direction depending on draft direction in the car tunnel. This should result in better maintenance of environmental conditions in car tunnels.

2. Reversible Jet Axial Fan Designs

The design is developed in cooperation of the Hydraulic Machinery and Energy Systems Department (HMESD) University of Belgrade Faculty of Mechanical Engineering (UB FME) and company Rudnap Group Minel Kotlogradnja from Belgrade, Serbia, where it was also manufactured. The demand from industry was to develop jet fan prototype with the following characteristics: volume flow rate— $Q_p = 17 \text{ m}^3\text{s}^{-1}$, impeller outer diameter— $D_{a,p} = 0.71 \text{ m}$, fan rotation speed $n_p = 2950 \text{ rpm}$, fan motor power— $P_p = 39 \text{ kW}$ and axial force, i.e., thrust— $F_{z,p} = 938 \text{ N}$. Here, index “p” denotes “prototype”. Axial thrust is calculated using the Equation (4). According to the reference [4]: “The average jet velocity is in the range of 30 to 40 m/s.” This is, also, fulfilled for this prototype. These conventional jet fans are aligned parallel to the tunnel axis. The maximal achievable thrust ($F_{z,p,max}$) is calculated using Equation (6) in [4]. This relation could be simplified for the axial fan impeller in a free stream in the following way:

$$F_{z,p,max} = \rho A_j c_{z,j} (c_{z,j} - c_{z,fs}), \quad (1)$$

where ρ is air density, A_j is the jet fan outlet cross section, $c_{z,j}$ is the jet axial average velocity and $c_{z,fs}$ is the free stream velocity, i.e., air velocity in the tunnel in the region without jet fan influence. Of course, the effective thrust is lower and calculated as follows:

$$F_{z,p} = \rho A_j c_{z,j} (c_{z,j} - c_{z,fs}) \eta_p \eta_{p,inst}, \quad (2)$$

where η_p is the jet fan efficiency, and $\eta_{p,inst}$ is the jet fan installation efficiency. In some cases, it could be assumed that $\eta_p = 1$ [4]. Installation efficiency depends on the jet fan position in the tunnel. It could be assumed that $\eta_{p,inst} = 1$, if the jet fan is positioned in the middle of the tunnel, without the influence of other fans, other obstacles, as well as tunnel surfaces [4]. However, influence of the wall on the propulsion jet is studied in [16]. Therefore, the installation efficiency ($\eta_{p,inst}$) could be estimated on the basis of Equation (9) in [4], which is derived using the experimental data presented in [17]. In the case of the presented constructions, the guide vanes and slanted silencers do not exist, so the regulation could be performed only by the fan speed rotation number. For the flow direction purpose, the flow straighteners in the “cross” shape are in-built in both silencers. The flow straighteners need to eliminate or, at least, minimize the turbulent swirling flow, which occurs behind the axial fan impellers [18], and maximize the axial velocity component which generates thrust. The sound power level according to the A-weighting was not experimentally determined.

Jet fan head, i.e., pressure rise, could be determined in the following way:

$$\Delta p_{t,p} = P_p \eta_p / Q_p = 39 \cdot 10^3 \cdot 0.55 / 17 \approx 1262 \text{ Pa}, \quad (3)$$

where the jet fan efficiency could be estimated as $\eta_p = 55\%$. Besides Equation (2), thrust could be also determined as follows:

$$F_{z,p} = \rho Q_p c_{z,p} = \rho Q_p^2 / A = 938 \text{ N}, \quad (4)$$

where $c_{z,p}$ is average axial velocity calculated as $c_{z,p} = Q_p / A$ and surface of the cross-section.

The jet fan model parameters are determined on the basis of the similarity law and equality of coefficients such as flow (φ), head (ψ), power (λ) and efficiency (η). Reversible jet fan model is developed using the following parameters: $D_a = 0.5 \text{ m}$ (punctually $499.2 \text{ mm} \pm 0.1$) and fan power $P = 3 \text{ kW}$. By introducing power coefficient (λ) as follows:

$$\lambda_p = P_p / (D_{a,p}^2 u_p^3), \quad (5)$$

where u_p is circumferential velocity on diameter $D_{a,p}$. Equality of these coefficients for the prototype and model lead to the equation:

$$n = n_p (P/P_p (D_a/D_{a,p})^5)^{1/3} = 2251 \text{ rpm}. \quad (6)$$

Flow coefficient is derived, on the basis of kinematic similarity, as follows:

$$\varphi = 4Q / [u_a (D_a^2 - D_i^2) \pi], \quad (7)$$

where D_i is hub diameter.

Flow coefficients for the model and prototype are equal:

$$\varphi = \varphi_p \quad (8)$$

It is assumed that non-dimensional diameter (ν), defined as $\nu = D_i/D_a$, is equal for the model and prototype:

$$\nu = \nu_p \quad (9)$$

Volume flow rate of the jet fan model could be determined on the basis of Equations (7)–(9) as follows:

$$Q = Q_p \cdot \left(\frac{D_a}{D_{a,p}} \right)^3 \cdot \frac{n}{n_p} = 17 \cdot \left(\frac{500}{710} \right)^3 \cdot \frac{2251}{2950} = 4.53 \frac{\text{m}^3}{\text{s}}. \quad (10)$$

Head coefficient (ψ) is defined after the dynamic similarity as follows:

$$\psi = 2Y / u_a^2, \quad (11)$$

where Y is fan head defined in the following way:

$$Y = \Delta p_t / \rho, \quad (12)$$

where Δp_t is difference of total pressures after and before the fan, i.e., total pressure rise in the jet fan.

Applying Equations (11) and (12), as well as introducing the equality of model and prototype head coefficients lead to the following expression:

$$\Delta p_t = \Delta p_{t,p} \cdot \left(\frac{D_a}{D_{a,p}} \right)^2 \cdot \left(\frac{n}{n_p} \right)^2 = 1262 \cdot \left(\frac{500}{710} \right)^2 \cdot \left(\frac{2251}{2950} \right)^2 = 364.41 \text{ Pa}. \quad (13)$$

Using Equations (4) and (7), the following expression is derived:

$$\frac{F_z}{D_a^4 \cdot n^2} = \pi^3 \cdot \varphi^2 \cdot \rho \cdot \frac{(1 - v^2)^2}{120^2}. \quad (14)$$

Right hand side of the Equation (14), by assuming that air density is equal, depends only on flow coefficient and dimensionless radius, which are identical for the model and prototype, so the following equation for thrust could be derived:

$$F_z = \left(\frac{D_a}{D_{a,p}} \right)^4 \left(\frac{n}{n_p} \right)^2 F_{z,p} = \left(\frac{500}{710} \right)^4 \left(\frac{2251}{2950} \right)^2 \cdot 938 = 134.32 \text{ N}. \quad (15)$$

In this way, all necessary data for jet fan model design are determined.

The greatest challenge was to develop axial fan impeller geometry to provide the same energy characteristics in both directions. It is even more important for the reversible axial fan functionality in traffic tunnels where pressure could vary in regions close to the inlet, i.e., exit. In this case, due to the fact that the complete fan construction cannot be rotated, or simpler geometries where blade angles cannot be adjusted, it is clear that axial fan impeller geometry must be symmetrical. This would result in the axial fan impeller with symmetrical blades. They should be designed in the way to use symmetrical airfoil and to be symmetrical to the axis normal to the chord, i.e., in this case, also camber line, which divides it in two halves. The fan is designed after the law of constant head in the radial direction, i.e., constant circulation in order to achieve higher energy efficient fans, i.e., equal energy distribution along the radius. The result is the twisted blade presented in Figure 1a. Threaded connection M20 is used for blade positioning in the axial fan hub. Six symmetrical profiles and their geometry are shown in Figure 1a. Geometry parameters for the first and sixth one are presented in Table 1, where r —radius measured from the axial fan rotation axis, $R1$ —radius at the blade leading/trailing edge, $R2$ —radius of the profile pressure/suction side, β —profile angle measured from the fan rotation axis and y_{max} —maximum thickness. Profile maximum thickness is positioned in the center of the straight camber line, which has constant length along the blade $L = 106$ mm.

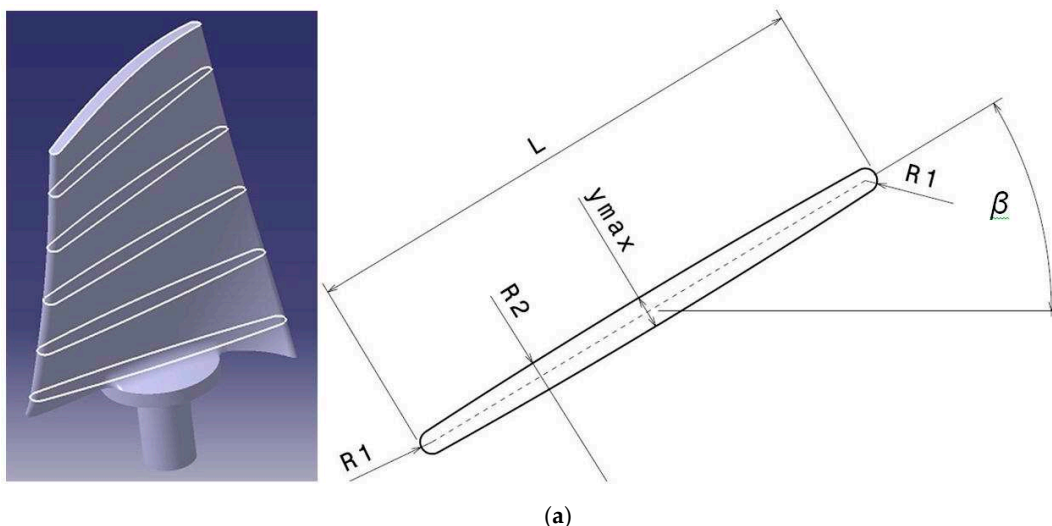


Figure 1. Cont.

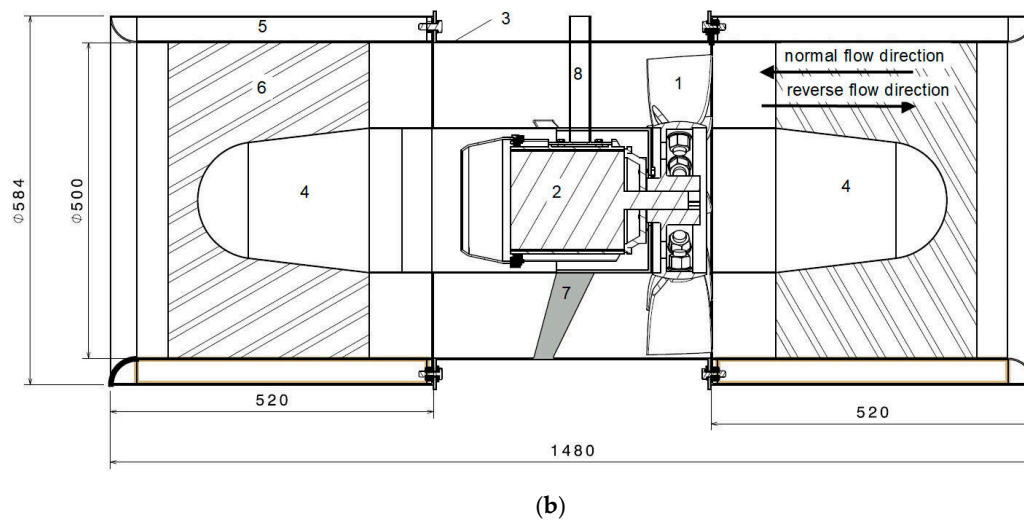


Figure 1. (a) Geometry of the impeller symmetrical blade and (b) Reversible jet axial fan with specified normal and reverse flow directions.

Table 1. Table of the geometry parameters of the symmetrical blade profiles (No. 1 and 6).

r [mm]	R1 [mm]	R2 [mm]	β [°]	y _{max} [mm]
125	3.5	690	0	10.6
250	2.1	1653	35	5.6

Geometry of the whole construction of the reversible jet axial fan, with specified normal and reversible flow directions, is presented in Figure 1b, where: 1—impeller, 2—AC motor, 3—impeller casing, 4—profiled impeller hub cap, 5—silencer (sound suppressor), 6—flow straighteners, 7—AC motor support and 8—AC motor cable casing (pipe form). Flow straighteners are not specially profiled, due to the intention to obtain similar flow characteristics in both directions. They are only sheet metal parts which form the “cross” geometry.

Asynchronous electric motor with two poles is placed in the casing in the way not to disturb fluid flow. Axial fan casing with a hub and carrier is designed in the way to stabilize operation and connection with the electromotor.

The jet fan has profiled bell-mouth inlet, and casings have inner diameter of 500 mm, while outer is 584 mm (Figure 1b). Casing consists of perforated plate, mineral wool and steel plate envelope, which minimize noise. Flow straighteners (Figure 1b, position 6) decrease generated turbulent swirling flow jet and direct the flow. Namely, the main role is to improve generated jet strength, i.e., maximize thrust and fan efficiency.

The jet fan model is designed for the following parameters determined above: fan rotation speed— $n = 2251$ rpm, volume flow rate— $Q = 4.53 \text{ m}^3\text{s}^{-1}$, impeller outer diameter— $D_a = 0.5$ m and axial force— $F_z = 130$ N. It has ten adjustable blades and dimensionless ratio $\nu = D_i/D_a = 0.5$. The manufactured jet fan model is presented in Figure 2.

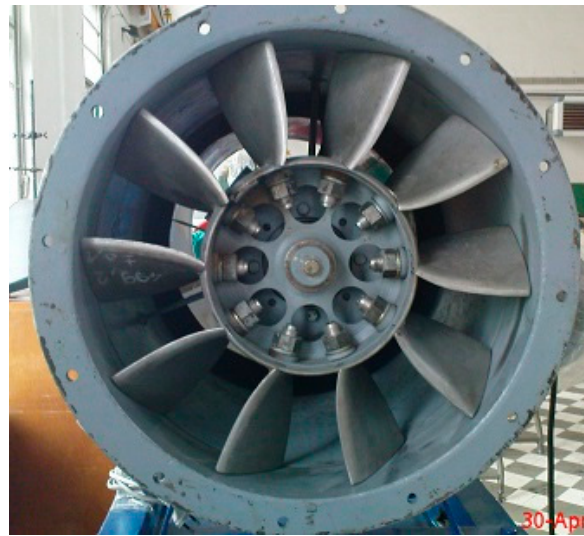


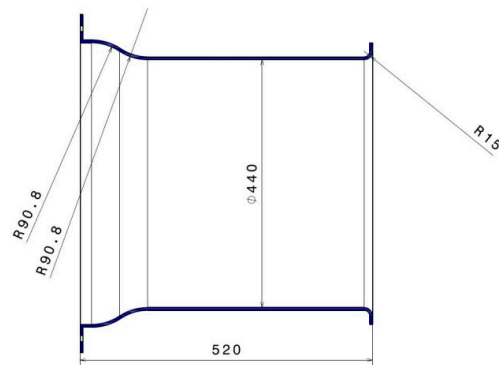
Figure 2. Developed axial fan impeller with its casing and AC electric motor.

The reversible jet fan 3D model was developed in academic software package CATIA V5R18 (64 bit) for the flow analysis. This model had certain level of “intelligence” based on the CATIA Knowledge tools, which provided blade angle easy variation and blade shape variation according to its angle position. In this way, clearances are minimized.

The second construction is with nozzles and flow straighteners as shown in Figure 3. It has nozzles with inner diameter 440 mm (Figure 3b).



(a)



(b)

Figure 3. The second construction of the casing: (a) at the thrust measurement table and (b) nozzle geometry.

3. Experimental Test Rig

Experimental investigation of the designed jet fan was conducted on the designed and manufactured thrust measurement table in the Laboratory of the Hydraulic Machinery and Energy Systems Department at the Faculty of Mechanical Engineering University of Belgrade (Figure 4).

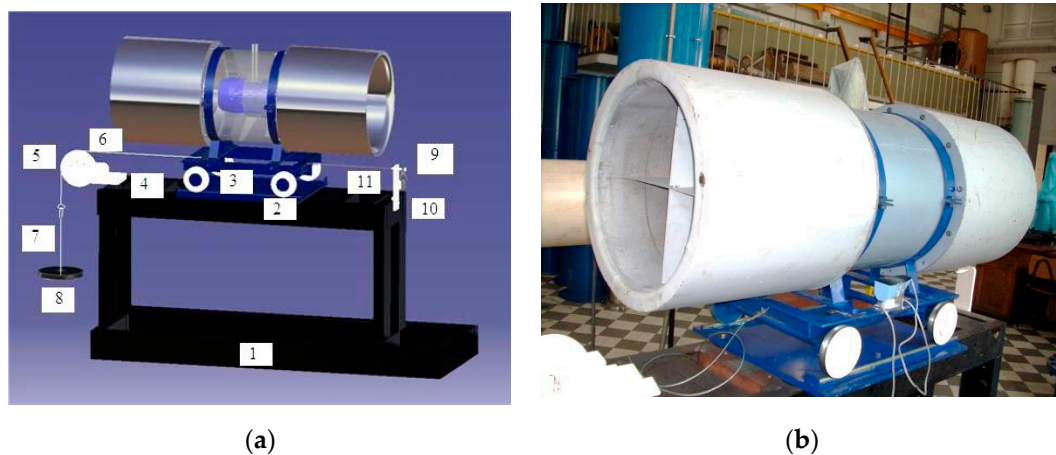


Figure 4. Thrust measurement table in the laboratory: (a) 3D model for calibration and (b) real model.

The test rig (Figure 4), i.e., the thrust measurement table, is composed of numerous elements. The fundament of the test rig construction is manufactured with massive steel U-shaped profiles (Figure 4a, position 1). It is heavy and provides operating stability important for obtaining precise measuring results. Rails are assembled with the steel plate to the fundament (Figure 4a, position 2) so that axial fan with wheel chair could safely move along the rails and enable axial force, i.e., thrust measurements (Figure 4a, position 3). On the measurement table, a wheel fundament is attached, also made of steel. This wheel (pos. 5) is positioned on the wheel fundament (pos. 4) by the axle. Wheel rotation is possible by the use of radial rolling one-row bearing. Steel chrome polished cable with 3 mm in diameter (pos. 6) moves over it and connects weights carrier (pos. 7) with calibrated weights (pos. 8) and wheel chair. Weight carrier has two parts, of which the lower one is used for holding calibrated weights and the upper one is a hook for hanging on the steel rope. It is also calibrated and made of steel. Wheel chair is, on the other side, connected via measuring tape, with a force transducer (pos. 9). This is a construction for force transducer calibration. Calibration preceded each measurement. During measurements the steel cable is dismantled. However, the force transducer is always connected via measuring tape (pos. 11) with the wheelchair, and it is mounted on the steel carrier (pos. 10), which provides appropriate axial force measurements. The Vishay force transducer model 355, type C3, hermetically sealed, was used (Figure 5, pos. 1). Specified total error is $\pm 0.02\%$ of rated output, which is here for C3, 50 kg, i.e., ± 10 g.

A force transducer was carefully calibrated at the thrust measurement table by first loading up to 45 kg and afterwards unloading due to hysteresis determination. A linear characteristic is obtained. A measuring tape transfers axial force from the axial fan to the force transducer. It provides stable work and precise measurements. A signal conditioner is used for the axial force transducer signal conditioning and acquisition. A frequency regulator is used to control the axial fan rotation speed. A digital frequency regulator DS2000, company MOOG, Serbia, was used. It has a three-phase regulator which works over the voltage interval from 65 V till 506 V and frequencies from 50 till 60 Hz. Working temperature interval is 0 till 40 °C. A multifunctional measuring device Testo 450 with appropriate probes was used in these experiments for measuring air temperature and humidity, as well as for velocity measurements with attached vane anemometer probe. On the basis of the velocity measurements, in positions specified by ISO 5801 [19], the volume flow rate was determined. It is compared with the ones calculated on the basis of the measured axial velocity in the following way: $Q = D_a (F_z \pi / \rho)^{0.5} / 2$, where ρ is air density. A mercury barometer measured atmospheric pressure before each test. Fan rotation speed was determined by a stroboscope DRELLOSCOP 3009.

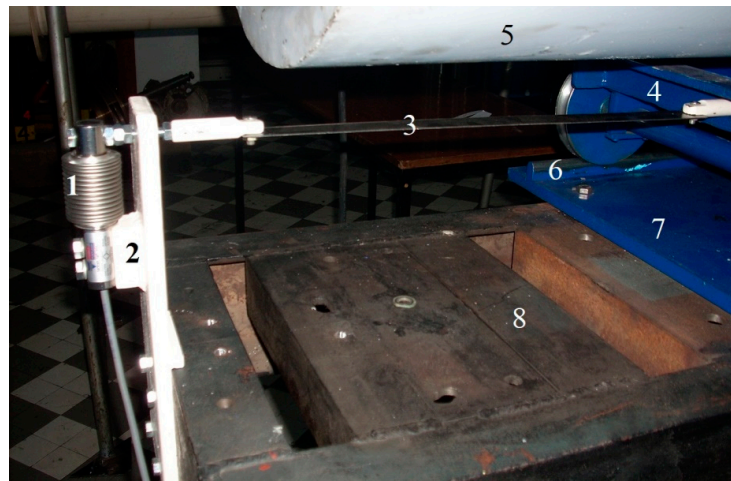


Figure 5. Connection of the force transducer with wheel chair: 1—force transducer, 2—force transmitter, 3—measuring tape, 4—wheel chair, 5—axial fan, 6—rails, 7—steel plate for connection of rails with wheel chair loaded with reversible jet fan and 8—fundament.

4. Experimental Results and Discussion

In the conducted experiments, the following physical values have been measured: axial force, i.e., thrust, velocity field at the fan inlet and outlet, fan rotation speed, electromotor power, air temperature, humidity and atmospheric pressure. Measurements were performed for various angle positions of both blade impeller sets, controlled at the outer diameter D_a : $\beta_{Ra} = 28^\circ, 31^\circ, 33^\circ, 35^\circ, 39^\circ$ and 45° as well as for various fan rotation speeds $n = 400, 800, 1200, 1600, 2080, 2200, 2500$ and 2565 rpm. Measurements have also been performed for both fan rotating, i.e., flow directions and are presented in Figure 6.

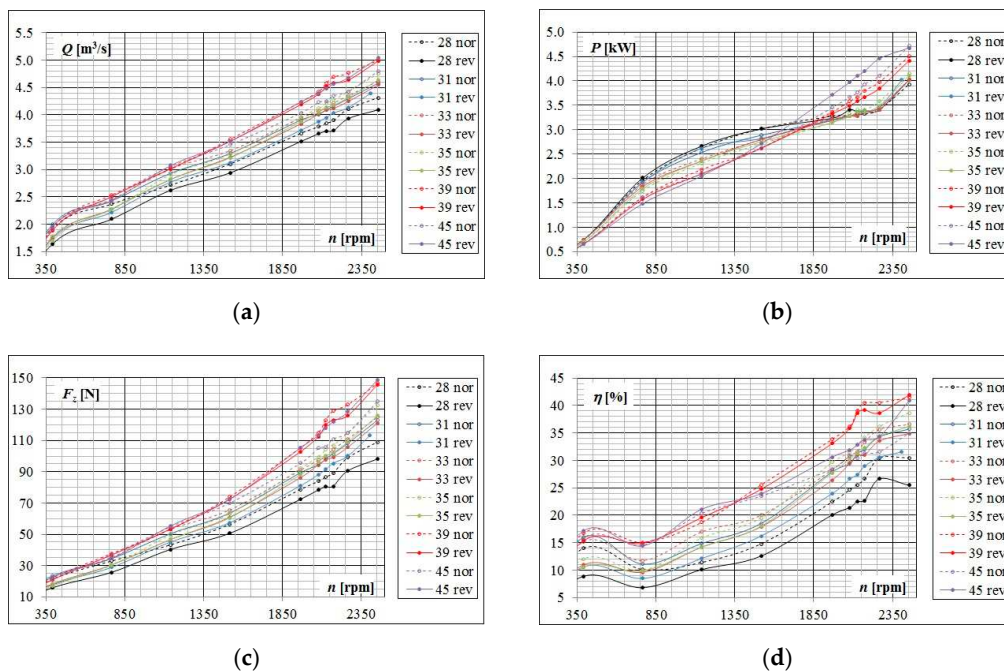


Figure 6. Reversible jet fan characteristics in the function of the fan rotation speed and angle β_{Ra} for both flow directions: (a) volume flow rate, (b) internal consumed power, (c) thrust and (d) efficiency.

The fan efficiency is calculated, only after the contribution of the kinetic energy at the fan outlet, i.e., in the jet, as follows:

$$\eta = Q\rho c^2/2P, \quad (16)$$

where c is velocity at the fan outlet and ρ air density. It is assumed that the inlet velocity is zero. It is calculated on the basis of the approximated internal power, presented in Figure 6b.

All fan characteristics, normally, increase with the fan rotation speed. Hierarchy of increasing the volume flow rate and thrust with increasing the blade angle, up to the angle 39° , is obvious. Fan characteristics depend on flow direction for all angles, but the smallest difference is obtained for angle 39° .

The best angle position (β_{Ra}) of the blade impeller blades is determined on the basis of a large amount of experimental data (Figure 6). Measuring results for the angle position at the outer diameter $\beta_{Ra} = 39^\circ$ are presented in the following charts (Figure 7).

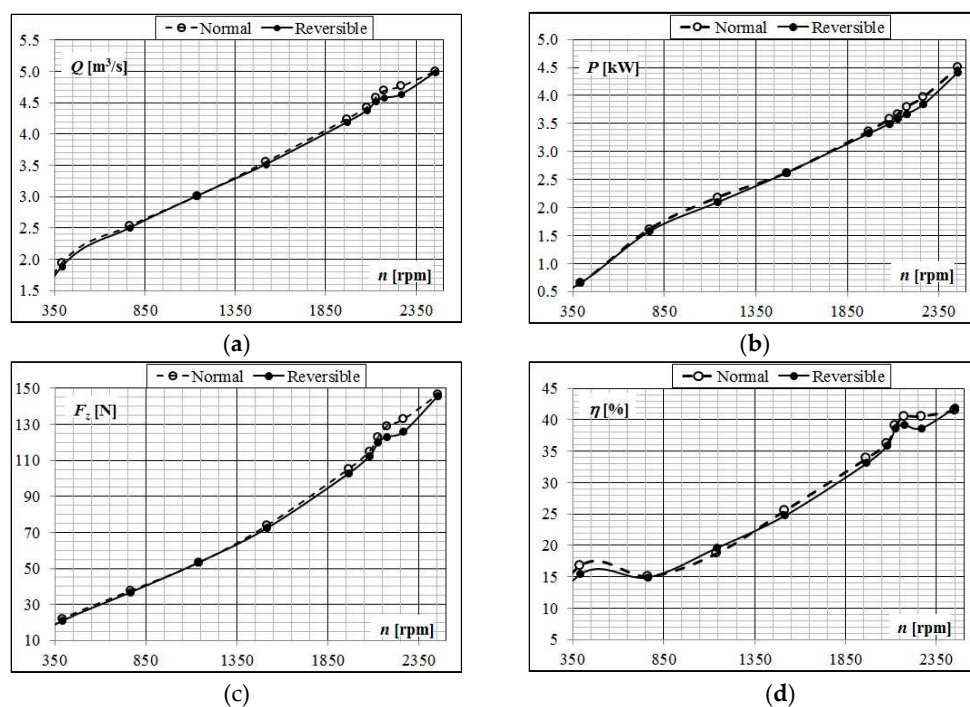


Figure 7. Reversible jet fan characteristics in the function of the fan rotation speed for both flow directions and angle $\beta_{Ra} = 39^\circ$: (a) volume flow rate, (b) internal consumed power, (c) thrust and (d) efficiency.

Small differences of thrust are obtained for angle $\beta_{Ra} = 39^\circ$ depending on the flow direction in fan (Figure 7c). It is almost independent of the flow direction. This was the aim of this design. In this case, the maximum thrust is achieved in both directions (Figures 6c and 7c). The fan was also tested for $\beta_{Ra} = 45^\circ$, but thrust started to decrease, i.e., is significantly lower for normal flow direction. In addition, the highest fan efficiency, calculated after fan contribution to the jet kinetic energy, is reached for angle 39° (Figures 6d and 7d), and it is almost the same for both flow directions $\eta_{I,max} = 41.45\%$ and $\eta_{II,max} = 41.94\%$.

Obtained experimental results could be scaled-up to the prototype on the basis of the procedure presented in [14]. This procedure involves equality of the turbomachinery coefficients for flow, head and power. It is shown here that designed thrust of 134.32 N for rotation speed 2251 rpm after Equation (15) is achieved for angle 39° . Obtained values are $F_z = 133$ N for $n = 2266.8$ rpm.

In addition, axial fan impeller was tested in two casing constructions. The first construction is a cylindrical casing, while the second one is profiled as a nozzle. Results for both models are presented and compared in Figure 8. This design was tested for $\beta_{Ra} = 28^\circ, 31^\circ$ and 35° .

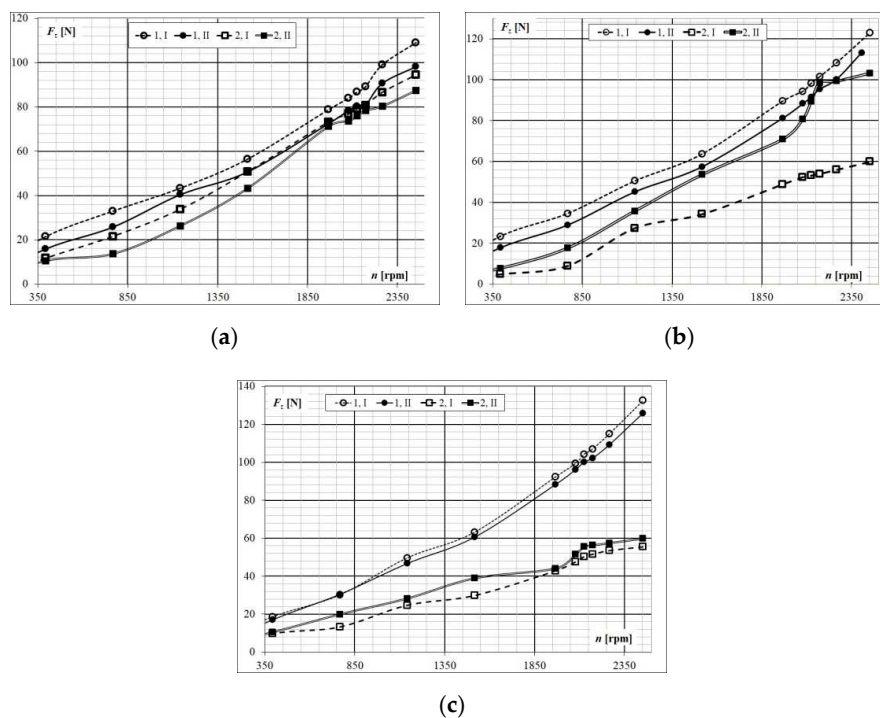


Figure 8. Comparison of the fan thrust in cylindrical (1) and nozzle (2) profiled casings for various angles β_{Ra} and rotational directions (I-normal and II-reversible flow directions) in the function of the fan rotation speed: (a) 28° , (b) 31° and (c) 35° .

Angle β_{Ra} variation leads to good thrust in normal, while to worse ones in reversible flow direction (Figure 8). In all cases, the highest thrust values are reached for the highest fan rotation speed, what was expected. The smallest differences in thrust are achieved for $\beta_{Ra} = 35^\circ$ and presented in Figure 8c. This is obvious for the model 1 with cylindrical casing. The highest values of thrust are also achieved for this angle $\beta_{Ra} = 35^\circ$.

Influence of the flow direction in the reversible axial jet fan is more obvious for the second model with profiled nozzle. For this case significantly lower values of thrust are achieved for all angles β_{Ra} . This is obvious for the highest presented angle $\beta_{Ra} = 35^\circ$ (Figure 8c). It could be concluded that this nozzle casing was not properly designed for the tested fan. Construction of model 2 resulted in a lower flow rate and thrust.

Analysis of sources of error and of uncertainty evaluation for the thrust measurement is provided for the one measurement point ($n = 2266.8$ rpm) which is close to the designed fan rotation speed ($n = 2251$ rpm). Calibration uncertainty of axial force (thrust) calibration, i.e., weights used for calibration, is ± 0.54 g. Systematic uncertainty combines the uncertainty of transducer and calibration by the root-sum-square method and is $\pm 0.075\%$. Random uncertainty of thrust measurements at 95% confidence level is 1.689 %, and total uncertainty of thrust measurement is 1.7%. This is in accordance with the used standard ISO 13350.

5. Conclusions

This paper presents the design of the axial jet fan impeller with symmetrical and adjustable blades and experimental results of the testing on the test rig following ISO 13350. Two designs of fan casings are presented too. Axial fan was tested for various angles and rotation speeds in both cases. These fans work in pairs for the case of bigger tunnels, and the distance between two pairs of fans is, among other things, defined by the experimentally determined thrust. It could be concluded the following:

- Herein, the procedure is presented for determination of the jet fan model parameters on the basis of the parameters demanded for the prototype. This procedure is based on the geometry, kinematic

and dynamic similarity law. Anyhow, this approach does not result in the same Reynolds number (Re), so ΔRe is incorporated in the equation of recalculation/conversion, i.e., efficiency scale-up from a model to the prototype which is treated in IEC 60193. This is not discussed in the used standard here ISO 13350 [12].

- The test rig, i.e., thrust measurement table, for experimental investigations was designed and manufactured after the international standard ISO 13350. A force transducer was carefully installed and calibrated, and measure of uncertainty was determined.
- The main idea for this research was to design the axial fan with good thrust independent of the fan rotation direction.
- It was experimentally shown that differences for all fan characteristics depend on the flow direction in the axial fan, and this was noticed for almost all fan regimes and both casing designs. Hierarchical distribution of fan characteristics is present for almost all angles and rotation speeds up to the angle 39° . Thrust starts decreasing for the angle 45° for normal flow direction (Figure 6c). Therefore, this could be considered as a stalling effect which could occur for higher blade angles. Clearance is small in our design, but it increases with the blade impeller angle increment, and it has the highest value for 45° . Therefore, this loss of aerodynamic performance could be the consequence of the tip leakage vortex, i.e., flow from the blade tip with a strong vortex.
- Anyhow, the maximum thrust, and its almost independence of the flow direction is experimentally obtained for the angle at the fan outer diameter $\beta_{Ra} = 39^\circ$ (Figures 6c and 7c). Flow rate and power are also independent of the flow direction in this case and reach the highest values for the maximum fan rotation speed (Figure 7a,b). The highest efficiency, calculated after Equation (16), is also achieved for this blade angle position (Figure 7d).
- In addition, it is shown that designed value for the thrust $F_z = 134.32$ N for rotation speed $n = 2251$ rpm (Equation (15)) is achieved for angle 39° . Obtained thrust value is 133 N for $n = 2266.8$ rpm. Therefore, the complete design is proved here.
- It is shown that fan casing significantly influences jet fan characteristics. It has a convergent–divergent geometry (Figure 3b). This was an attempt to produce a fan with better characteristics. Some concepts are still under consideration.
- Experimentally determined thrust for the second design is presented and compared with the first one only for the angles $\beta_{Ra} = 28^\circ, 31^\circ$ and 35° (Figure 8). The smallest differences in thrust depending on the fan rotation direction are achieved for the first design with cylindrical casing and angle at the outer diameter $\beta_{Ra} = 35^\circ$ (Figure 8c). In this case, a significantly higher thrust is achieved than for the second design.
- It is shown that jet fan has a small reaction factor, and that in the best case, with the highest thrust, impeller specific energy is almost completely transformed into the kinetic energy achieving high velocities, high flow rates and thrust. This is why the efficiency rate is calculated and presented using Equation (16).
- Experimental results of the axial reversible jet fans testing are very rarely presented in the literature, so the adequate comparison of the obtained data was not possible. Obtained experimental results data basis is at disposal for CFD calculations for interested researchers.

Author Contributions: Conceptualization and methodology, all authors; validation, Đ.S.Č., N.Z.J. and D.B.I.; formal analysis, investigation and writing, all authors; All authors have read and agreed to the published version of the manuscript.

Funding: This research was funded by the Ministry of Education, Science and Technological Development, Republic of Serbia (MESTD RS), contract number 451-03-68/2020-14/200105 (subproject TR 35046) and by the Bilateral project “Joint Research on the Development Technology of Low-head Run-of-the-river Hydropower”, between MESTD RS and Ministry of Water Resources in China and Renewable Energy and Rural Electrification Zhejiang International Science Center, contract number 401-00-00588/2018-09, which authors hereby gratefully acknowledge.

Acknowledgments: This article is partially based on a paper presented at the 40th International HVAC congress, 2009, “Fan for Ecological Condition Sustain in Tunnels” held on 18–19 September 2009 in Belgrade, Serbia,

so authors are thankful for technical support to M. Pajnić and M. Begović from Rudnap Group; Minela Kotlogradnja, Belgrade, Serbia.

Conflicts of Interest: The authors declare no conflict of interest.

References

1. Weisenpacher, P.; Valasek, L. Computer simulation of airflows generated by jet fans in real road tunnel by parallel version of FDS 6. *Int. J. Vent.* **2019**. [[CrossRef](#)]
2. Brzezińska, D. Practical aspects of jet fan ventilation systems modelling in fire dynamics simulator code. *Int. J. Vent.* **2018**, *17*, 225–239. [[CrossRef](#)]
3. Šekularac, M.B.; Janković, N.Z.; Vukoslavčević, P.V. Ventilation performance and pollutant flow in a unidirectional-traffic road tunnel. *Therm. Sci.* **2017**, *21* (Suppl. S3), S783–S794. [[CrossRef](#)]
4. Tarada, F.; Brandt, R. Impulse Ventilation for Tunnels—A State of the Art Review. In Proceedings of the 13th International Symposium on Aerodynamics and Ventilation of Vehicle Tunnels, New Brunswick, NJ, USA, 13–15 May 2009.
5. Rudelgass, H.; Barbeta, C. An Improved Jet Fan. *Tunn. Tunn. Int.* **2012**, *7*, 58–60.
6. Vidaković, B.M.; Banjac, M.J. Improvement of CFD models of tunnel fire development based on experimental data. *Therm. Sci.* **2017**, *21* (Suppl. S3), S705–S716. [[CrossRef](#)]
7. Banjac, M.; Nikolić, B. Numerical Study of Smoke Flow Control in Tunnel Fires Using Ventilation Systems. *FME Trans.* **2008**, *36*, 145–150.
8. Viegas, C.J. The use of impulse ventilation to control pollution in underground car parks. *Int. J. Vent.* **2016**, *8*, 57–74. [[CrossRef](#)]
9. Šekularac, M.B. Experimental determination of tunnel ventilation axial ducted fan performance. *Therm. Sci.* **2016**, *20*, 209–221. [[CrossRef](#)]
10. Šekularac, M.B.; Janković, N.Z. Experimental and numerical analysis of flow field and ventilation performance in a traffic tunnel ventilated by axial fans. *Theor. Appl. Mech.* **2018**, *45*, 151–165. [[CrossRef](#)]
11. Kim, J.-H.; Kim, J.-H.; Yoon, J.-Y.; Choi, Y.-S.; Yang, S.-H. Application of multi-objective optimization technique to improve the aerodynamic performance of a tunnel ventilation jet fan. *J. Mech. Eng. Sci.* **2015**, *229*, 91–105. [[CrossRef](#)]
12. ISO. *Standard ISO 13350:2015 Fans—Performance Testing of Jet Fans*; ISO: Geneva, Switzerland, 2015.
13. Sheard, A.G.; Daneshkhah, K. The conceptual design of high pressure reversible axial tunnel ventilation fans. *Adv. Acoust. Vib.* **2012**, *2012*. [[CrossRef](#)]
14. Benišek, M.; Ilić, D.; Čantrak, Đ.; Božić, I.; Pajnić, M.; Begović, M.; Janković, N. Fan for Ecological Condition Sustain in Tunnels. In Proceedings of the 40th International HVAC Congress, Belgrade, Serbia, 2–4 December 2009; pp. 320–331. (In Serbian)
15. Kim, J.-H.; Kim, J.H.; Kim, J.-Y.; Yang, S.-H.; Choi, Y.-S. High-efficiency design of a tunnel ventilation jet fan through numerical optimization techniques. *J. Mech. Sci. Technol.* **2012**, *26*, 1793–1800. [[CrossRef](#)]
16. Nishi, M.; Liu, S.; Yoshida, K.; Okamoto, M.; Nakayama, H. A new blade profile for bidirectional flow properly applicable to a two-stage jet fan. *Int. J. Fluid Mach. Syst.* **2009**, *2*, 449–455. [[CrossRef](#)]
17. Kempf, J. Einfluss der Wandeffekte auf die Treibstrahlwirkung eines Strahlgebläses. *Schweiz. Bauztg.* **1965**, *83*, 47–52.
18. Benišek, M.H.; Lečić, M.R.; Čantrak, Đ.S.; Ilić, D.B. The school of the turbulent swirling flow at the Faculty of Mechanical Engineering University of Belgrade. *Therm. Sci.* **2017**, *21* (Suppl. S3), S899–S911. [[CrossRef](#)]
19. ISO. *Standard ISO 5801:2017 Fans—Performance Testing Using Standardized Airways*; ISO: Geneva, Switzerland, 2017.

Publisher’s Note: MDPI stays neutral with regard to jurisdictional claims in published maps and institutional affiliations.



© 2020 by the authors. Licensee MDPI, Basel, Switzerland. This article is an open access article distributed under the terms and conditions of the Creative Commons Attribution (CC BY) license (<http://creativecommons.org/licenses/by/4.0/>).

Article

Numerical and Experimental Study on Waviness Mechanical Seal of Reactor Coolant Pump

Xiaodong Feng ^{1,2,*}, Wentao Su ¹, Yu Ma ³, Lei Wang ² and Heping Tan ¹

¹ School of Energy Science and Engineering, Harbin Institute of Technology, Harbin 150001, China; suwentao@hit.edu.cn (W.S.); tanheping@hit.edu.cn (H.T.)

² Harbin Electric Power Equipment Co. Ltd., Harbin 150066, China; hpc_wanglei@harbin-electric.com

³ Sino-French Institute of Nuclear Engineering and Technology, Sun Yat-Sen University, Zhuhai 519082, China; mayu9@mail.sysu.edu.cn

* Correspondence: 17B902055@stu.hit.edu.cn

Received: 10 October 2020; Accepted: 4 December 2020; Published: 7 December 2020



Abstract: Based on the fluid hydrodynamic lubrication theory, a mathematical model of liquid film lubrication was established for the waviness hydrodynamic mechanical seal of a reactor coolant pump. The influences of the waviness amplitude and pressure on the sealing performance were investigated by the numerical simulation. The numerical results showed that the leakage rate increases linearly as the pressure and waviness amplitude increase under the force balance condition. The minimum liquid film thickness decreases first and then increase as the pressure increases. Stationary slide rings with three different waviness amplitudes were processed using the pre-deformation method and tested at different pressure and temperature. The experiments showed that all the three kinds of seal have good stability under different pressure conditions. The experimental results showed that the leakage rate is influenced by the pressure, waviness amplitude, and temperature, and the leakage rate increases as the pressure increases. The comparison between experimental and numerical results showed that both the temperature and pressure affect the seal performance, and tends to a smaller leakage rate, which is quite different from the numerical values. Therefore, the multi-physics coupling effect should be considered in the numerical analysis of seal performance, and this will be studied in the further works.

Keywords: reactor coolant pump (RCP); waviness; mechanical seal; leakage rate; liquid film

1. Introduction

The reactor coolant pump (RCP) is one of the most critical pieces of primary equipment in a nuclear power plant, and the only rotating equipment in the nuclear island which suffers both high temperature and pressure [1]. The RCP's shaft seal consists of three stages identical hydrodynamic mechanical seals in series to prevent the leakage of primary medium from the outside of the RCP. The mechanical seal is designed to operate normally under 17.3 MPa for 10 h. Compared with the ordinary mechanical seals, the hydrodynamic mechanical seal realizes the non-contact between the sealing surfaces by using the closing force caused by the hydrodynamic effect between the sealing end faces, with a variety of grooves on the sealing surface. This characteristic greatly reduces the wear of the sealing surface and improves the reliability and lifespan [2,3]. Two types of mechanical seal are always used in the shaft-sealed RCP, including the waviness end face [4–6] mechanical seal and ordinary mechanical seal [7,8], where the former has a longer lifespan due to its hydrodynamic characteristics. Due to its excellent hydrodynamic effect and good controlled leakage ability, the waviness end face has been widely applied in the field of the RCP. By utilizing the hydrodynamic effect, the waviness mechanical seal can form a micro-scale thin layer of fluid film between the end faces, which avoids the direct contact between the seal pairs, reduces

the wear and prolongs the life [9]. Because of these outstanding advantages, many studies on the waviness end face mechanical seal have been made [10–14]. The wavy tilt dam (WTD) as one type of the waviness surface was studied by many researchers. The concept of WTD was first proposed by Lebeck and Young [15] who suggest that the hydrostatic and hydrodynamic effects are produced by the radial taper and the circumferential waviness of the end face, respectively, which leads to sufficient opening force and liquid film stiffness, and is suitable for high-parameter conditions. The stability researches of WTD mechanical seal are mainly focus on several aspects. Etsion et al. [13] established a closed analytical solution for the mechanical seal model to study the lubricating film pressure and the axial separating force, whereby the face geometry is combined with waviness and coning. To improve the leakage rate control, Salant et al. [16] simulated the hydraulically controlled RCP's seal under different deformations and geometries of the end face by changing the pressure in the cavity of non-rotating seal ring. In addition to the independent hydrodynamic research, some coupling simulations were also applied to analyze the coupled thermo-hydrodynamic characteristics. To study the 3D detailed behavior of the WTD mechanical seal, based on the Reynolds equation [17,18], Liu et al. [14,19–21] simulated and analyzed the WTD seal based on the three-dimensional thermal elastic hydrodynamic model, and the results showed that the sealing mechanism was the combined effect of hydrodynamic and hydrostatic. The film cavitation occurs at the high velocity region, and the hydrostatic effect prevailed at the high-pressure region. Djamaï et al. [22] established a numerical model of thermo-hydrodynamic mechanical face seals based on the coupling Reynolds equation and energy equation to analyze the influence of operating and design parameters. Brunetière et al. [23] analyzed the influence of the design and operating parameters on the thermo-hydrodynamic behavior of the mechanical end face seals in steady and dynamic tracking modes. To research the influence factors of cavitation starting and evolution, Li et al. [24] analyzed the effects of different waviness amplitudes, numbers and tapers on the cavitation characteristics. The results indicated that the start and evolution of the cavitation were affected by both the waviness and radial taper, and the change of the cavitation region along the circumferential direction was influenced by the waviness, while that along the radial direction depended on the taper.

As for the manufacture of the waviness groove on the sealing end face, the normal processing methods used mainly include the milling, electric spark processing, grinding and etc. Huo et al. [25–27] proposed a three-axis, ultra-precision grinding method using line contact kinematics for machining the WTD seal rings, which can achieve high form accuracy and low surface roughness of the waviness end faces. Han [28] researched the super precision milling process for the waviness end face of the tungsten carbide seal ring. The surface roughness could reach about 7 nm. Wang [29] used the electric spark processing method to pre-machine the waviness end face of the static ring. However, this work should be improved. On one hand, this method has suffers from a long processing time and serious carbon deposits, and on the other hand, the surface roughness cannot meet the requirements of less than 0.4 μm . Recently, Feng et al. [30] proposed a new grinding method through extrusion deformation of the seal ring. The extrusion deformation tooling and metal gaskets were used to deform the sealing ring into a waviness shape. After grinding, the required waviness shape was formed. The experimental results showed that the seal completely satisfies the requirements of nuclear power plant, while it can obtain high accuracy surface roughness and high reliability. In short, as for the field of waviness end face mechanical seal research, the main focus is on the predicting sealing performance by using theoretical models and cavitation characteristics, which are relatively rare in experimental research. The forming of the waviness end face limited to the equipment conditions and process methods is only focused on the research method of the contractible scale model. The leakage of reference work for the research of the prototype leads to a disconnection between the theoretical research and the experimental results.

In view of the above problems, this work, based on the Reynolds equation of liquid film lubrication, combined with the actual processing waviness end face, establishes a liquid film lubrication mathematical model of the mechanical seal which can represent waviness groove. The influences of

waviness amplitude, temperature and pressure on the leakage rate of the mechanical seal systematically were studied by comparing the numerical results with experimental results. Moreover, it obtains the difference between theoretical analysis and experimental research, which provides a reference for the parameter optimization design of the seal end face and the coupling study of multiple physical fields.

2. Numerical Analysis

The mechanical seal of RCP mainly consists of stationary base ring (SBR), rotating slide ring (RSR), stationary slide ring (SSR) and rotating base ring (RBR), as shown in Figure 1a. The structure of SSR is as in Figure 1b.

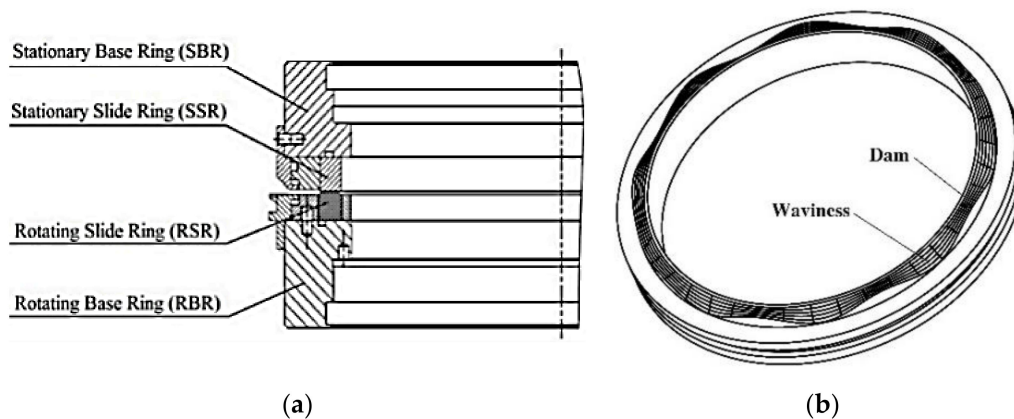


Figure 1. Schematic of the mechanical seal, including (a) mechanical seal configuration and (b) stationary slide ring (SSR).

2.1. Geometric Model

The geometric model is composed of rotating slide ring (RSR) and stationary slide ring (SSR), as shown in Figure 2. The lubrication film lies between rotating slide ring and stationary slide ring. Rotating slide ring has an ideal plane on the sealing end face. A uniform circumferential waviness lies on the end face of the stationary slide ring, and a flat dam lies at the inner diameter. The thickness of the liquid film at any position can be expressed as follows:

$$h(r, \hat{\theta}) = \begin{cases} h_i & , R_i \leq r \leq R_d \\ h_i + \frac{r-R_d}{R_o-R_d} h_a (1 - \cos(z \times \hat{\theta})) & , R_d \leq r \leq R_o \end{cases} \quad (1)$$

where the inner and outer radius of the sealing end face are R_i and R_o , respectively, the dam radius of the sealing end face is R_d , the minimum distance between rotating slide ring and stationary slide ring is h_i , and the waviness amplitude is h_a . $\hat{\theta}$ is the coordinates of the rotating direction.

2.2. Mathematical Model

In order to establish the mathematical model, the following basic assumptions are listed:

1. The lubrication film between is the Newtonian fluid, and the flow is laminar flow. Since the working fluid of the mechanical seal is always the water, the assumption of Newtonian fluid is reasonable, and since the velocity of working fluid is small enough, the assumption of laminar flow also is reasonable.
2. The heat generation of the viscous shear is ignored, and the liquid film viscosity is considered to be constant. Since the heat generation of the viscous shear is very low and the temperature of the liquid film is basically constant, this assumption is reasonable.

3. The pressure variation along the direction of the film thickness is not considered. This is the basic assumption of Reynolds equation.

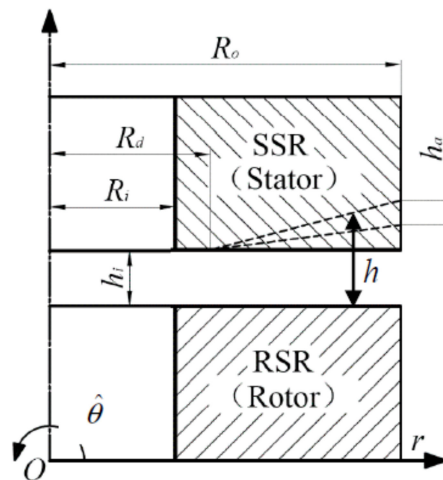


Figure 2. Model of the sealing gap.

The governing equation of the lubrication film in rectangular coordinates can be expressed by the steady-state Reynolds equation considering cavitation of the liquid film, and the expression is expressed as follows:

$$\frac{\partial}{\partial x} \left(\frac{h^3}{12\mu} \frac{\partial p}{\partial x} \right) + \frac{\partial}{\partial y} \left(\frac{h^3}{12\mu} \frac{\partial p}{\partial y} \right) = \frac{1}{2} U_x \frac{\partial(\theta h)}{\partial x} + \frac{1}{2} U_y \frac{\partial(\theta h)}{\partial y} \quad (2)$$

where μ is the dynamic viscosity, which is defined as:

$$\mu = \mu_0 e^{-\beta(T-T_0)} \quad (3)$$

where μ_0 is the dynamic viscosity under the reference temperature T_0 ; T is the local temperature of the fluid film and β is the viscosity-temperature coefficient; p is the pressure; U_x and U_y are the shear velocity in the x and y directions; θ is the ratio of the density of the liquid film during cavitation to that in the liquid state, and when the flow is in full liquid film, $\theta = 1$. When $0 < \theta < 1$, the flow is in cavitation state.

In order to solve Equation (2), two kinds of boundary conditions need to be added, among which the JFO cavitation boundary conditions for liquid film cavitation is defined as follows:

$$\begin{cases} p = p_c, 0 < \theta < 1 & \text{in non-cavitation zone} \\ p > p_c, \theta = 1 & \text{in cavitation zone} \end{cases} \quad (4)$$

The pressure boundary condition is defined as follows:

$$\begin{cases} p = p_i, r = R_i \\ p = p_o, r = R_o \end{cases} \quad (5)$$

In Equations (4) and (5), p_c is the cavitation pressure of the liquid film and is set to 0 MPa in this work because of the large sealing pressure. Pressure p_i and p_o are respectively the medium pressure at the inner and outer radius of the sealing end face.

The governing equation is calculated using the finite element method (FEM) due to its complication. The convection-diffusion Equation (2) will be convective dominant when the speed of the sealing ring is large, which will lead to numerical oscillation of Galerkin FEM. Therefore, the streamline

upwind/Petrov–Galerkin (SUPG) technology described in reference [31] is used to solve the lubrication Equation (2), and the relevant sealing performance parameters could be calculated after obtaining the liquid film pressure. In order to obtain the sealing performance in the force balance state of the stationary slide ring, the axial force balance equation is solved by using dichotomy method to obtain the minimum film thickness. The axial force balance equation is written as:

$$F_o = G + F_s \quad (6)$$

where F_o is the axial opening force, G is the gravity of static ring, and F_s is the downward spring force.

The triangular mesh configuration is used in this simulation, and a perturbation term is added to the weight function in the streamline direction, which can suppress the diffusion perpendicular to the flow direction in advance and overcome the false diffusion problem of the upwind discretization. The weak integral form of lubrication control Equation (2) can be written as:

$$\int_{\Omega} \left[\frac{h^3}{6\mu} \left(\frac{\partial w}{\partial x} \frac{\partial p}{\partial x} + \frac{\partial w}{\partial y} \frac{\partial p}{\partial y} \right) \right] d\Omega - \int_{\Omega} \left[w \left(U \frac{\partial(\theta h)}{\partial x} + V \frac{\partial(\theta h)}{\partial y} \right) + \frac{1}{2} \tau^{\text{SUPG}} \left(U \frac{\partial w}{\partial x} + V \frac{\partial w}{\partial y} \right) \left(U \frac{\partial(\theta h)}{\partial x} + V \frac{\partial(\theta h)}{\partial y} \right) \right] d\Omega = 0 \quad (7)$$

where w is the weight function and Ω is the calculation domain and τ^{SUPG} is the coefficient of stability. By defining the FEM variables as: $w = w_i N_i$, $p = p_i N_i$, $\theta = \theta_i N_i$ with N being the interpolation function of element, the Equation (7) can be rewritten as:

$$K_{ij}^p p_j - K_{ij}^{\theta} \theta_j = 0 \quad (8)$$

$$\begin{cases} K_{ij}^p = \int_{\Omega} \frac{h^3}{6\mu} \left(\frac{\partial N_i}{\partial x} \frac{\partial N_j}{\partial x} + \frac{\partial N_i}{\partial y} \frac{\partial N_j}{\partial y} \right) d\Omega \\ K_{ij}^{\theta} = \int_{\Omega} h N_i \left(U \frac{\partial N_j}{\partial x} + V \frac{\partial N_j}{\partial y} \right) d\Omega - \int_{\Omega} \frac{1}{2} \tau^{\text{SUPG}} h \left(U \frac{\partial N_i}{\partial x} + V \frac{\partial N_i}{\partial y} \right) \left(U \frac{\partial(h N_j)}{\partial x} + V \frac{\partial(h N_j)}{\partial y} \right) d\Omega \end{cases} \quad (9)$$

To solve Equation (8), the switch function F is introduced, and the unknown variable p and θ can be expressed using the general variable Φ as:

$$\Phi = Fp + (1 - F)\theta \quad (10)$$

For the liquid film intact area, $F = 1$ and $\Phi = p$, while for the cavitation area, $F = 0$ and $\Phi = \theta$. Substituting Equation (9) into Equation (7), one obtains:

$$A_{ij} \Phi_j = K_{ij}^{\theta} F_j \quad (11)$$

where

$$A_{ij} = K_{ij}^p C_{ij} - K_{ij}^{\theta} (I_{ij} - C_{ij}) \quad (12)$$

with I being the unit matrix; C is a matrix whose other areas are 0 except for the same value as F on the diagonal. After obtaining the film pressure p , the sealing performance parameters such as liquid film bearing capacity, leakage rate and friction coefficient can be calculated.

Since the static seal ring is in floating state, the thickness of the lubricating oil film is determined by the balance between the bearing capacity of the lubricating liquid film and the gravity of the static seal ring, spring force and the static pressure of the sealing medium. Therefore, the balance film thickness of the liquid film needs to be obtained by solving the force balance equation of the static seal ring as:

$$\int p d\Omega - F_c = 0 \quad (13)$$

where F_c is the closing force of the static ring, which is the summation of the gravity G of the static ring, the spring force F_s , and the hydrostatic pressure in the sealed cavity.

2.3. Calculating Results and Analysis

Table 1 shows the geometric and operating parameters used in this work and the materials of the friction pair are carbon and tungsten carbide (WC). Except for special instructions, all the parameters taken in this work are shown in Table 1. The listed waviness amplitude is the actual measured value of the end face of the stationary slide ring manufactured, and is corresponds to Section 2. The simulating parameters are the same as the experimental parameters.

Table 1. Geometric and operating parameters.

Item	Value
Outer radius R_o (mm)	152
Inner radius R_i (mm)	138.55
Dam radius R_d (mm)	141.5
Numbers of waviness z	9
Waviness amplitude h_a (μm)	5.0; 6.3; 6.9
Balance ratio	0.745
Outer pressure p_o (MPa)	2.0; 5.3; 10.6; 15.9
Inner pressure p_i (MPa)	0
Pressure difference $\Delta p = p_o - p_i$ (MPa)	2.0; 5.3; 10.6; 15.9
Rotor speed n (rpm)	1485
Medium	Water
Density ρ (kg/m^3)	998.2
Viscosity μ ($\text{kg}/(\text{m}\cdot\text{s})$)	1.003×10^{-3} (20 °C)

In Figure 3, it shows the variation law of the minimum liquid film thickness h_i and the leakage rate Q with the pressure in balance state. As can be seen from Figure 3a, the minimum liquid thickness decreases first and then increases with the increase of pressure, which is consistent with the research results in literature [5], which is due to the cavitation of the lubrication film under the small film thickness that leads to the enhancement of the hydrodynamic effect of the liquid film. Under the same pressure, the larger waviness amplitude leads to higher minimum liquid film thickness. The hydrostatic effect of the liquid film increases with the waviness amplitude increases. As can be seen from Figure 3b, the leakage rate increases approximately linearly with the increase of the pressure, and the larger waviness amplitude leads to larger leakage rate. Moreover, the upward trend of the leakage rate curve is more obvious.

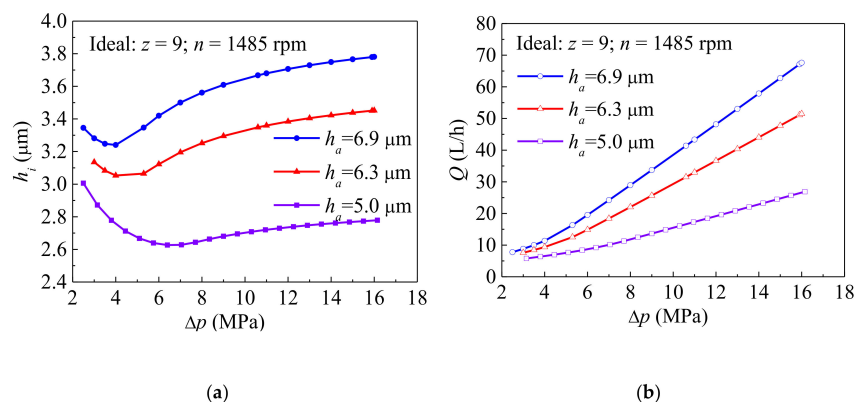


Figure 3. Comparison of minimum fluid film thickness h_i (a) and leakage rate Q (b), including waviness amplitude h_a . The viscosity is taken as 1.003×10^{-3} $\text{kg}/(\text{m}\cdot\text{s})$.

3. Experimental Research

3.1. Manufacture and Experiment of the Sealing Rings

According to the method and process described in literature [17], three kinds of the morphologies with different waviness amplitude on seal end face of the stationary slide rings are ground by using the metal gaskets with different thickness ($\delta = 0.12$ mm, 0.15 mm and 0.20 mm). In order to make the surface roughness of the sealing end face satisfy the requirement, the grinding powder F1200 named boron carbide (B4C) is used for grinding. Its particle size is 1–7 μm and Vickers hardness is 31 GPa. The final roughness of the sealing end face of the stationary slide ring is about 0.0572 μm . The three stationary slide rings are shown in Figure 4.

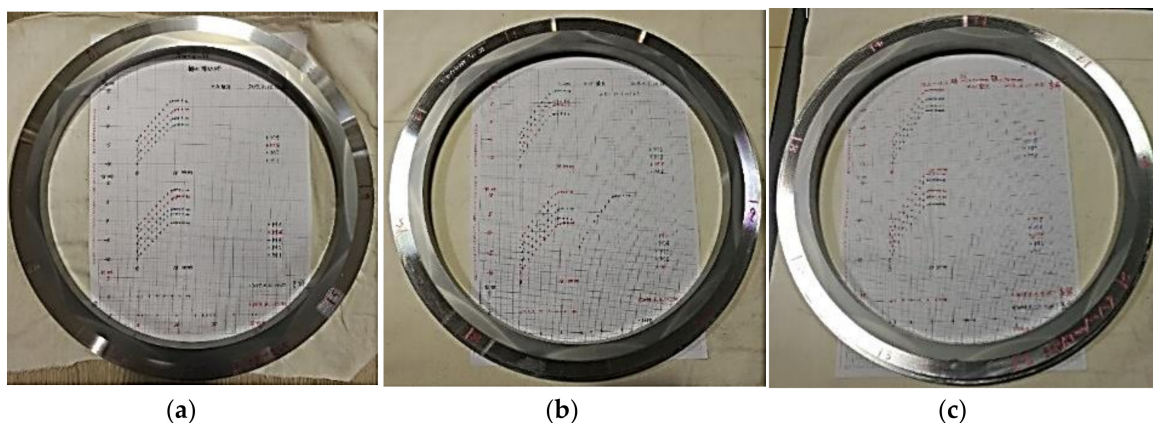


Figure 4. Manufacture status of the stationary slide rings, including (a) $\delta = 0.12$ mm, (b) $\delta = 0.15$ mm, (c) $\delta = 0.20$ mm.

Each wave groove of the static ring is divided equally in the radial direction, and the detection is recorded by moving slowly from the outer circle of the static ring along the inner circle. The nine waves are measured in nine groups, namely: M1–M9. The 9 waves of each static ring are made of the same metal gasket by compression deformation, which can ensure the same wave amplitude, and the single wave is also the same. The central section of each waviness is used as the measurement section of the waviness amplitude. The height of the waviness is measured and recorded by sliding from the outside to the inside of the sealing end face of the stationary slide ring to obtain the waviness amplitude h_a . It can be seen from the Figure 5 that the processed waviness has good variation consistency. According to Equation (1), the waviness amplitude h_a of the corresponding metal gasket thickness of 0.12 mm, 0.15 mm, and 0.20 mm is about 5.0 μm , 6.3 μm , and 6.9 μm , respectively.

3.2. Performance Test

Figure 6 shows the test rig, which consists of the testing device, motor, oil supply unit, charge pump, water reservoir, water deionization system, cooling water cycle, PLC cabinet, DAQ cabinet, cooling water basin, and other components. The test medium is purified tap water (6–8 pH, conductivity ≤ 20 $\mu\text{S/cm}$) which supplied by the water deionization system and stored in the water reservoir. The high-pressure charge pump supplies the testing device with pressurized barrier water, which is necessary for test rig operation, and is fed directly from the water reservoir. The process water returns from the testing device to the water reservoir via multiple leakage water pipes. The oil supply unit ensures the necessary lubrication of the upper roller bearing of the testing device, and the lower bearing of the testing device is a medium lubricated hydrodynamic bearing. A cooling water basin supplies the water for the cooling pump and should be situated outside of the test bench room. The constant temperature of the water from the cooling water basin ensures the thermal stability of the testing device. The operation and control of the test rig are regulated and controlled by the PLC unit in the

PLC cabinet. The DAQ switching cabinet contains components necessary to collect, record and display data during a test run. The measurement point data collected by the measuring instrument (see Table 2) are fed back to the DAQ unit.

As for the above three kinds of waviness sealing end faces, the measurement of the leakage rate under different temperature and pressure are performed. During the test, the speed of the shaft is 1485 rpm, the pressure is gradually increased to the highest and then decreased (the pressures are 2.0 MPa, 5.3 MPa, 10.6 MPa, and 15.9 MPa respectively). The medium temperature in the sealing chamber and leakage rate of the low-pressure side are recorded in per second. In order to consider the different working pressure, the pressure increase and decrease is applied via three steps. Beginning with about 2.0 MPa, the pressure is increased to 5.3 MPa rapidly (representing normal operation of a 3-stage application). After about 10 min, the pressure goes up to 10.6 MPa (representing normal operation of a 2-stage application), and after 20 min, it goes up to 15.9 MPa (representing accidental load on one stage). Finally, the reduction of the pressure is realized via the same steps within 15 min. The system pressure is changed slowly by adjusting the opening of the ball valve during the whole process to ensure not damaging the test loop and mechanical seal.

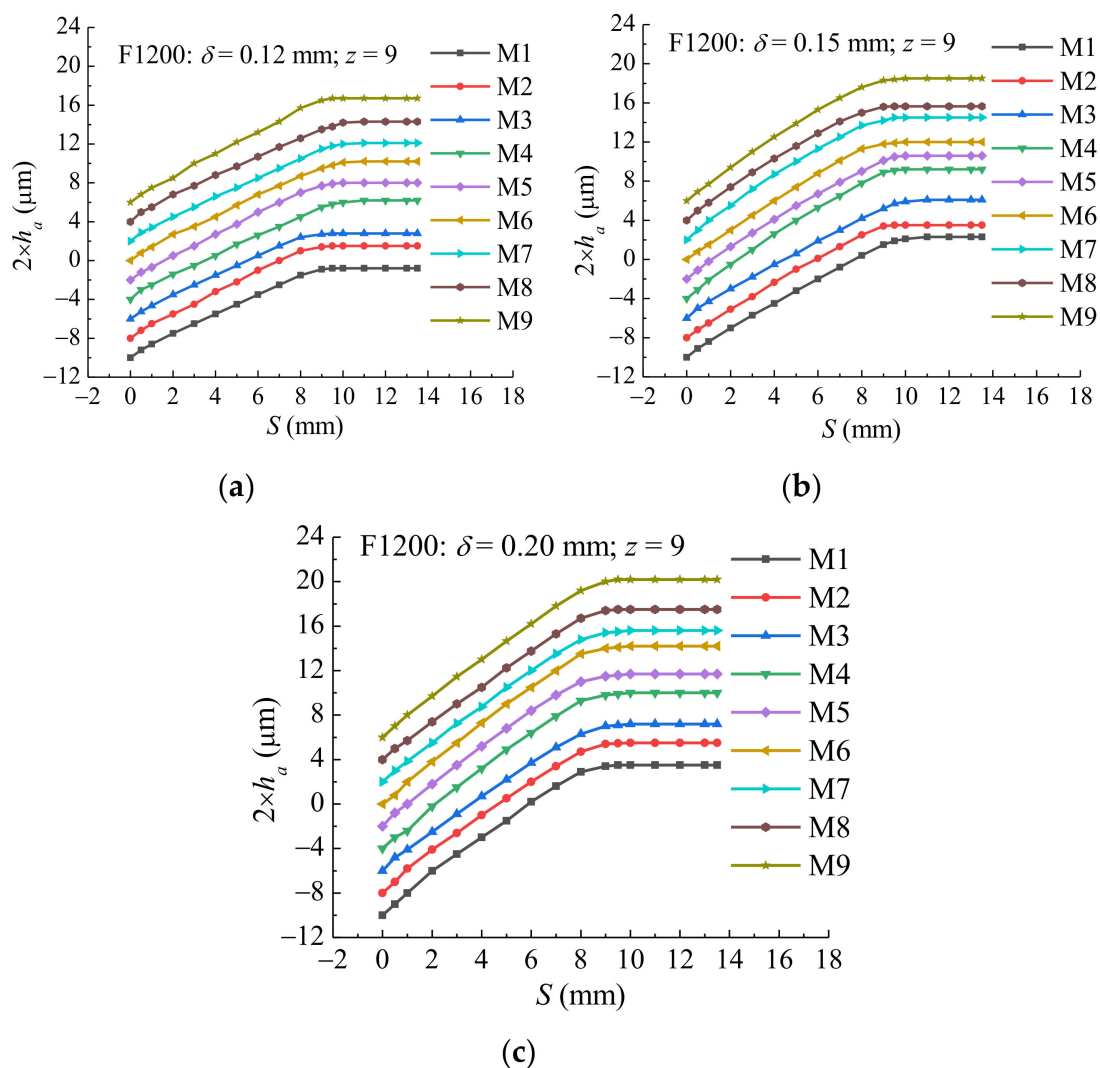


Figure 5. Measurement of the waviness amplitude, including (a) $\delta = 0.12$ mm, (b) $\delta = 0.15$ mm, (c) $\delta = 0.20$ mm.

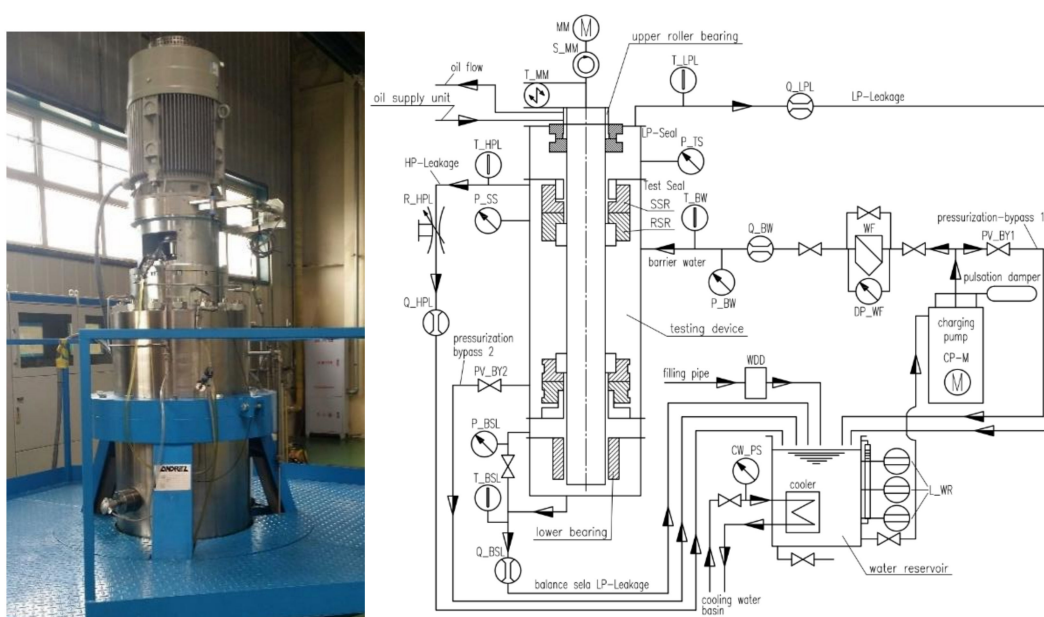


Figure 6. Test rig.

Figure 7 shows the leakage rate with different waviness amplitudes. The sealing end faces with waviness amplitude $5.0\ \mu\text{m}$ have similar law with the other two (the waviness amplitude is $6.3\ \mu\text{m}$ and $6.9\ \mu\text{m}$ respectively), which will not be repeated here. From these figures, it can be seen that the leakage rate of the seal increases with the increase of the pressure. The leakage rate increases slowly at the beginning of each stage (the slope of leakage rate plot is very small) due to the leakage hysteresis on seal faces, and then increases rapidly in about 200 s (the slope of leakage rate plot is very large). After that, it remained at a stable value. At 2700 s, the pressure instantly dropped from 15.9 MPa to below 10.6 MPa, and the leakage rate did not change suddenly with the instantaneous rapid pressure drop, but slowly decreased. It can be predicted that, if the pressure maintenance time is enough during the pressure relief, the leakage rate can also be at a stable value. Due to the occasional air bubbles in the medium during the test, the measured value will suddenly change after passing through the low-pressure leakage measuring instrument, but then it returns to a stable value. The experimental results show that the waviness end face seal has excellent stability under the constant working conditions. In comparison, the temperature in the seal chamber gradually increases as the test progresses under a lower medium temperature as shown in Figure 7a,b. Although the pressure increases step by step and then decreases during the test, the temperature presents an obvious step change. As shown in Figure 7c, the measured temperature does not increase significantly under a higher medium temperature, which may be caused by the heat generation of the sealing end face that is in equilibrium with the heat dissipation of the test system. Moreover, the high capacity of the tank may also suppress the increase of measured temperature.

Table 2. Measuring instruments.

Measurement	Identification	Output Signal	Accuracy	Range
Medium pressure	P_BW	4–20 mA	$\pm 1\%$	0–25 MPa
Low-pressure leakage rate	Q_LPL	4–20 mA	$\pm 0.5\%$	0–100 L/h
Medium temperature	T_BW	4–20 mA	Grade B	0–100 °C
Rotating speed	S_MM	4–20 mA	0.01%	0–2000 rpm

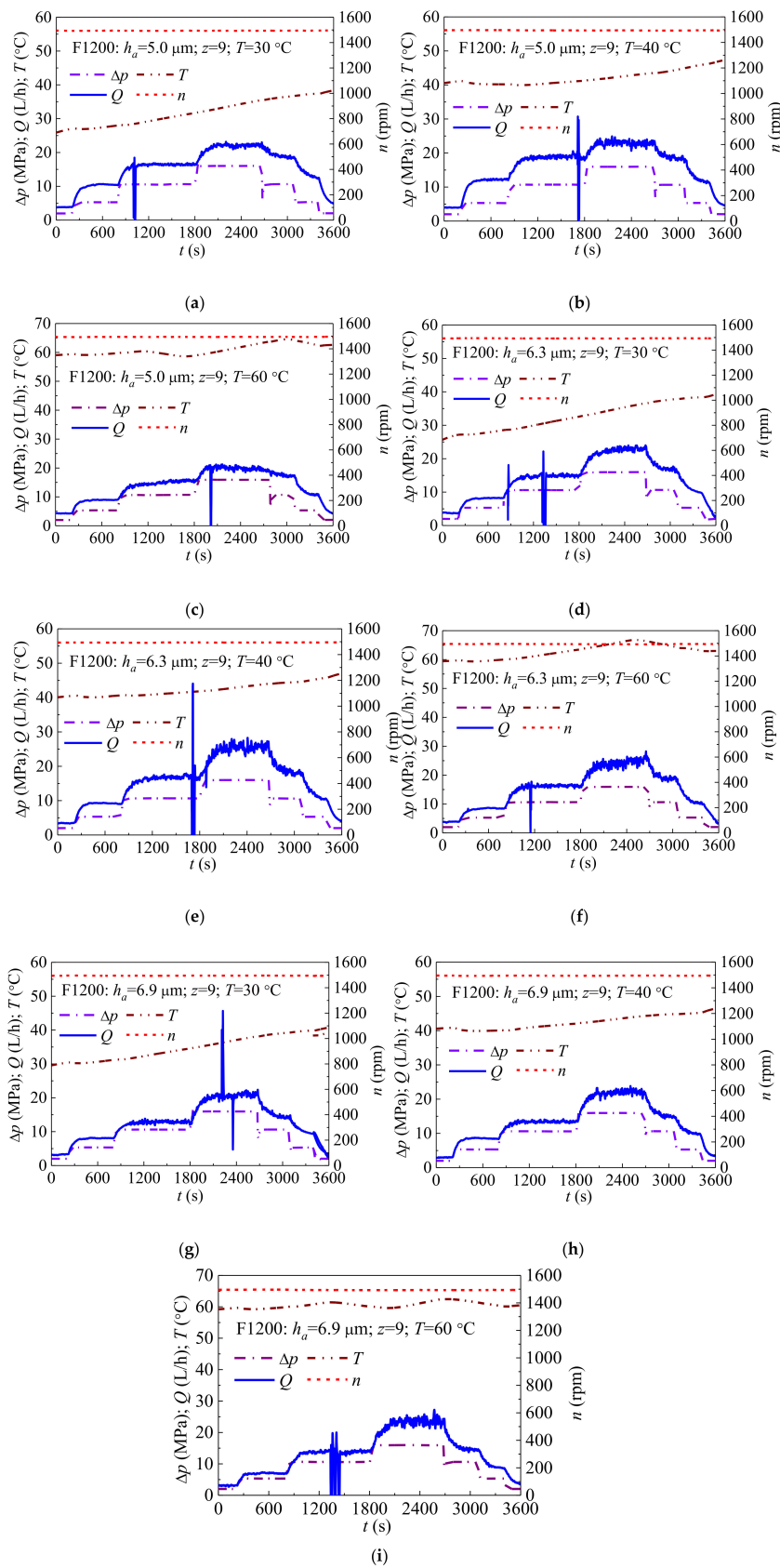


Figure 7. The leakage rate with different waviness amplitudes, including (a) $h_a = 5.0 \mu\text{m}$, $T = 30 \text{ }^\circ\text{C}$, (b) $h_a = 5.0 \mu\text{m}$, $T = 40 \text{ }^\circ\text{C}$, (c) $h_a = 5.0 \mu\text{m}$, $T = 60 \text{ }^\circ\text{C}$, (d) $h_a = 6.3 \mu\text{m}$, $T = 30 \text{ }^\circ\text{C}$, (e) $h_a = 6.3 \mu\text{m}$, $T = 40 \text{ }^\circ\text{C}$, (f) $h_a = 6.3 \mu\text{m}$, $T = 60 \text{ }^\circ\text{C}$, (g) $h_a = 6.9 \mu\text{m}$, $T = 30 \text{ }^\circ\text{C}$, (h) $h_a = 6.9 \mu\text{m}$, $T = 40 \text{ }^\circ\text{C}$, (i) $h_a = 6.9 \mu\text{m}$, $T = 60 \text{ }^\circ\text{C}$.

3.3. Test Comparative Analysis

Figure 8 shows the variation trend of measured leakage rate under different waviness amplitudes, pressures and temperatures, which are mean values for all 9 cases. Since the temperature gradually increases with the work of the motor and the seal, it is difficult to maintain a constant during the test period of one minute. The temperature corresponding to the test is an approximate value. Figure 8a shows that, under the same pressure, the leakage rate reaches the maximum and minimum values at 40 °C and 60 °C, respectively. As shown in Figure 8b, when $h_a = 6.3 \mu\text{m}$, under the same pressure, the leakage rate reaches the maximum and minimum values at 40 °C and 30 °C, respectively. Figure 8c shows that when $h_a = 6.9 \mu\text{m}$, determining the pressure difference Δp at 10.6 MPa or 15.9 MPa, the leakage rate reaches the maximum and minimum values at 60 °C and 30 °C, respectively. When $\Delta p = 5.3 \text{ MPa}$, the leakage rate is the largest at $T = 40 \text{ }^\circ\text{C}$, and is the smallest at $T = 60 \text{ }^\circ\text{C}$. According to these conditions, for these three kinds of waviness end face seals, their leakage rates all increase along the increases of pressure. Although the temperature also has a large effect on leakage rate, the change of temperature shows a non-obvious influence on these three waviness end faces, which may be caused by the unstable state of temperature distribution and the large influence of thermal effect on deformation of the end faces of the rotating and stationary slide ring for the mechanical seals. Generally, the increase of temperature will lead to the decrease of viscosity of the lubricating liquid film, and enhances the leakage ability of the liquid film. However, the effect of the temperature on the deformation of the seal end face is not obvious, which affects the actual distribution of the liquid film thickness. Therefore, the influence of temperature on leakage rate still needs to be further analyzed based on thermal elasto-hydrodynamic theory.

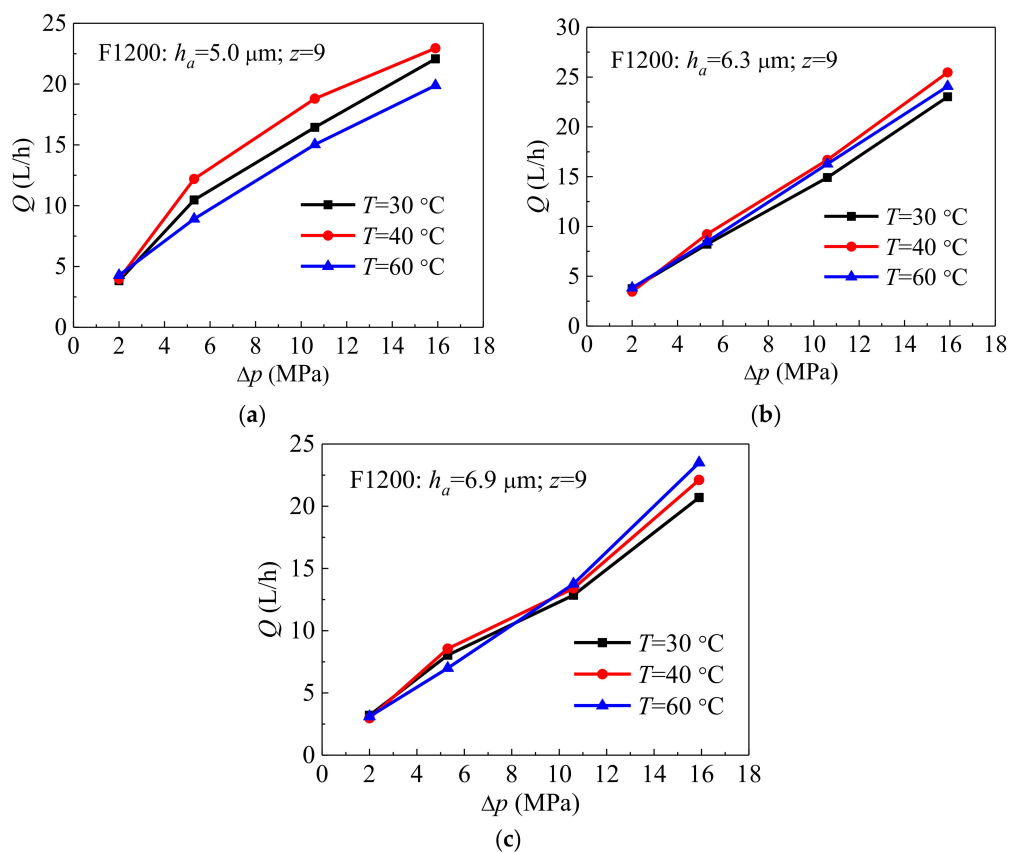


Figure 8. The comparison of the leakage rate at different temperature, including (a) $h_a = 5.0 \mu\text{m}$, (b) $h_a = 6.3 \mu\text{m}$, (c) $h_a = 6.9 \mu\text{m}$.

Figure 9 shows the effect of the waviness amplitude h_a on the leakage rate Q at the same temperature. When the temperature T is 30 °C and 40 °C and $\Delta p \leq 10.6$ MPa, the smaller waviness amplitude leads to the larger leakage rate. When $\Delta p = 10.6$ MPa, the leakage rate of the waviness amplitude $h_a = 6.3$ μm suddenly increases, which indicates that the pressure effect on the deformation is obvious under this waviness amplitude state. When the temperature $T = 60$ °C, the deformation of the seal rings with different waviness amplitudes varies greatly due to the combined effects of the temperature and pressure.

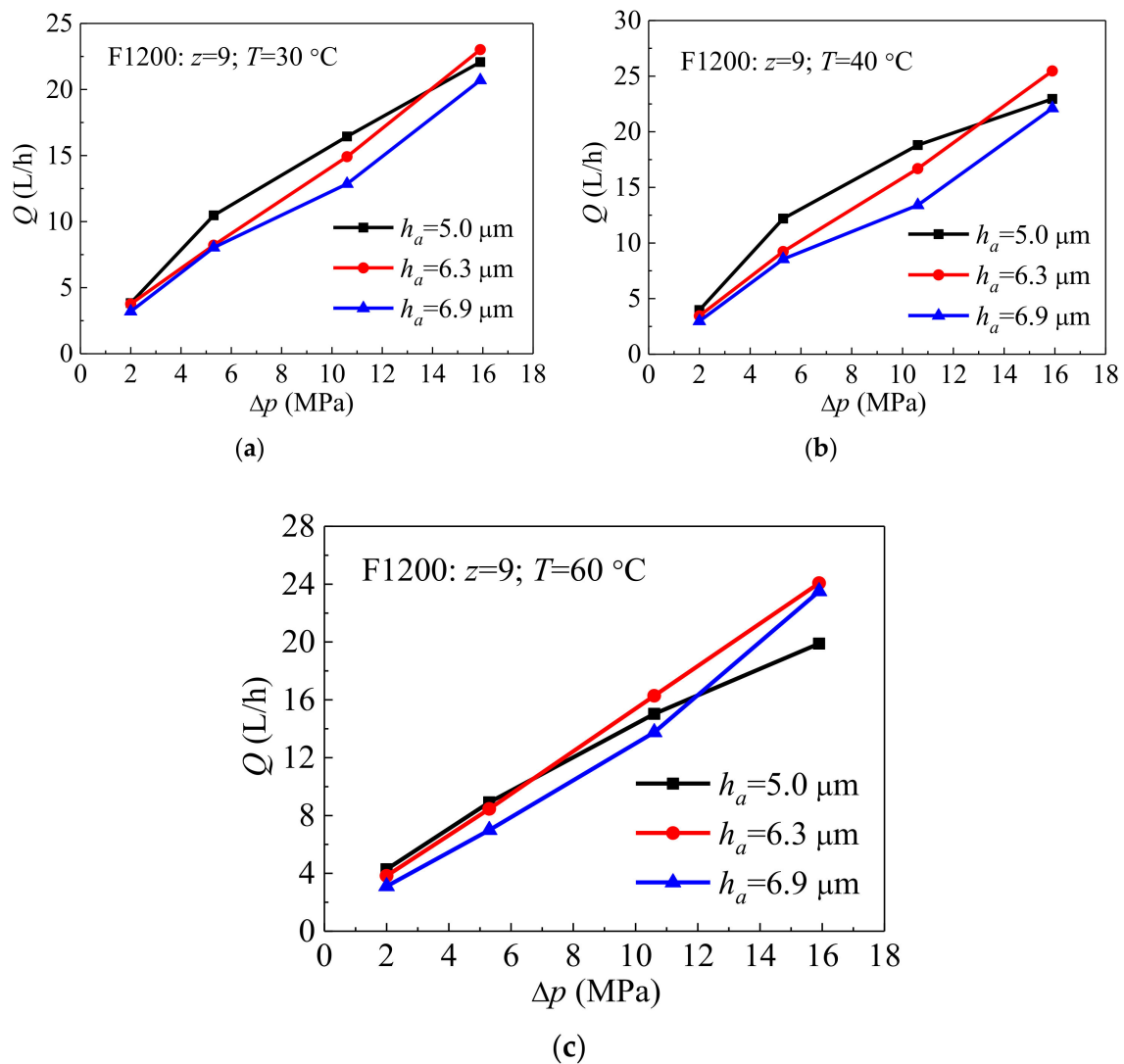


Figure 9. The comparison of the leakage rate at different waviness amplitude, including (a) $T = 30$ °C, (b) $T = 40$ °C, (c) $T = 60$ °C.

4. Comparisons of Test and Simulation Results

Table 3 shows the comparisons of the test measured and calculated leakage rates under different pressures. It can be seen that the test value is in good agreement with the calculated value for the seal end face with a waviness amplitude $h_a = 5$ μm , and the calculated values are significantly greater than the test values for the seal face with the larger waviness amplitudes $h_a = 6.3$ μm and $h_a = 6.9$ μm .

Table 3. Calculation and test results comparison at the different pressures.

$h_a/\mu\text{m}$	Pressure/MPa	Test Value/L·h ⁻¹	Calculated Value/L·h ⁻¹
5.0	5.3	10.65	5.02
	10.6	16.44	15.76
	15.9	22.08	25.55
6.3	5.3	8.22	12.52
	10.6	14.91	31.52
	15.9	23.02	51.11
6.9	5.3	8.04	16.31
	10.6	12.85	41.40
	15.9	23.02	51.11

The higher sealing pressure leads to the greater deviation between the test and the calculation, since the thermal deformation of the rotating and stationary slide rings for the mechanical seals is not considered in the theoretical model. In addition, under the high sealing pressure and the large waviness amplitude conditions, the seal end face is more likely to generate a non-uniform circumferential liquid film pressure distribution. The pressure distribution causes the ignored axial deformation, which affects the thickness of the lubricant liquid film. Therefore, in order to accurately predict the leakage rate under the high-pressure conditions, it is necessary to consider the thermo-mechanics coupling effect of the entire system, including the sealing rotating slide ring, stationary slide ring, lubricant liquid film, and base rings, and to establish a multi-field coupling model of mechanical seal for analysis.

5. Conclusions

In the paper, a mathematical model of the waviness mechanical seal for RCP is established to simulate the leakage rate and minimum liquid film thickness. The SUPG finite element method is applied to solve the lubrication equation considering the mass-conservation with JFO cavitation boundary. The predicted leakage rate was taken under different conditions (such as waviness amplitude, pressure, temperature). Three waviness seals were manufactured and tested. Through the comparison of the results between calculation and test, the following conclusions are obtained.

1. The calculated results show that when the waviness amplitude is constant, the leakage rate increases linearly with the increase of the pressure. The minimum liquid film thickness decreases first and then increases with the decrease of the pressure. There is a minimum limit value due to the phenomenon of liquid film cavitation. The larger waviness amplitude led to the smaller thickness of the liquid film and the larger leakage rate under the same pressure.
2. The test results show that the leakage rate is basically stable under the steady-state conditions and increases with pressure. The sealing performance is superior during the step-up and step-down processes of the pressure, and the seal ring does not lock up, which indicates the operation stability of the waviness end face seal.
3. The test pressure, temperature and waviness amplitude have important effects on the leakage rate of the mechanical seal. The effect of the sealing pressure is the largest, and the influence of the temperature and waviness amplitude is not obvious, which is caused by the complex thermo-mechanics coupling effect of the mosaic for the rotating and stationary slide ring, and the inconsistency of the temperature control during the test.
4. The calculated value of the leakage rate is greater than the measured value, which indicates that the thermo-mechanics coupling effect of the rotating and stationary slide rings for the mechanical seal cannot be ignored. The accurate calculation of the thermal deformation of the seal waviness end face is very important for the prediction of the leakage rate. The waviness mechanical seal needs to be further developed by multi-physics coupling modelling analysis.

Author Contributions: X.F.: conceptualization, methodology, software, validation, formal analysis, data curation, visualization, writing—original draft, writing—review & editing; W.S.: supervision, formal analysis, investigation, resources, project administration, funding acquisition; Y.M.: conceptualization, validation, formal analysis, investigation, resources, data curation, writing—review & editing, project administration, funding acquisition; L.W.: software, validation, formal analysis, data curation; H.T.: formal analysis, investigation, writing—review & editing. All authors have read and agreed to the published version of the manuscript.

Funding: This research was funded by Natural Science Foundation of Heilongjiang Province of China, Grant number E2018018; National Natural Science Foundation of China, Grant number 51976043 and National Natural Science Foundation of China, Grant number 11875330.

Conflicts of Interest: The authors declare no conflict of interest.

References

1. Allaire, P.E. Noncontacting Face Seals for Nuclear Applications—A Literature Review. *Lubr. Eng.* **1984**, *40*, 344–351.
2. Hu, S.T.; Huang, W.F.; Liu, X.F.; Wang, Y.M. Influence Analysis of Secondary O-ring Seals in Dynamic Behavior of Spiral Groove Gas Face Seals. *Chin. J. Mech. Eng.* **2016**, *29*, 507–514.
3. Wang, Y.; Sun, J.J.; Tao, K.; Ma, C.B.; Tu, Q.A. Numerical Analysis of T-groove Dry Gas Seal and Groove Optimization. *Tribology* **2014**, *34*, 420–427.
4. Iny, E.H. A Theory of Sealing with Radial Face Seals. *Wear* **1971**, *18*, 51–69.
5. Cochain, J. Numerical and Experimental Study of Misaligned and Wavy Mechanical Face Seals Operating under Pressure Pulses and Pressure Inversions. Ph.D. Thesis, Université de Poitiers, Poitiers, France, 2018.
6. Cochain, J.; Brunetière, N.; Parry, A.; Denoix, H.; Maoui, A. Experimental and Numerical Study of Wavy Mechanical Face Seals Operating under Pressure Inversions. *Proc. Inst. Mech. Eng. Part J J. Eng. Tribol.* **2020**, *234*, 247–260.
7. Shen, M.X.; Peng, X.D.; Meng, X.K.; Zheng, J.P.; Zhu, M.H. Fretting Wear Behavior of Acrylonitrile-butadiene Rubber (nbr) for Mechanical Seal Applications. *Tribol. Int.* **2016**, *93*, 419–428.
8. Varney, P.; Green, I. Impact Phenomena in a Noncontacting Mechanical Face Seal. *J. Tribol.* **2017**, *139*, 022201.
9. Lebeck, A.O. *Principles and Design of Mechanical Face Seals*; Wiley: Hoboken, NJ, USA, 1991.
10. Lebeck, A.O. Mechanical Loading—A Primary Source of Waviness in Mechanical Face Seals. *ASLE Trans.* **1977**, *20*, 195–208.
11. Lebeck, A.O. A Test Apparatus for Measuring the Effects of Waviness in Mechanical Face Seals. *ASLE Trans.* **1981**, *24*, 371–378.
12. Lebeck, A.O. Hydrodynamic Lubrication in Wavy Contacting Face Seals—A Two Dimensional Model. *J. Tribol.* **1981**, *103*, 578.
13. Etsion, I. The Effect of Combined Coning and Waviness on the Separating Force in Mechanical Face Seals. *J. Mech. Eng. Sci.* **2006**, *22*, 5964.
14. Liu, Y.; Liu, W.; Li, Y.; Liu, X.; Wang, Y. Mechanism of a Wavy-tilt-dam Mechanical Seal under Different Working Conditions. *Tribol. Int.* **2015**, *90*, 43–54.
15. Lebeck, A.O.; Young, L.A. Wavy-tilt-dam Seal Ring and Apparatus for Shaping Seal Rings. U.S. Patent No. 4,887,395, 1989.
16. Salant, R.F.; Payne, J.W.; Johnson, W.R.; Boles, G. Simulation of a Hydraulically Controllable Reactor Coolant Pump Seal. *Tribol. Int.* **2018**, *122*, 163–168.
17. Gustafsson, T.; Hakula, H.; Leinonen, M. Stochastic Galerkin Approximation of the Reynolds Equation with Irregular Film Thickness. *Comput. Math. Appl.* **2017**, *74*, 1590–1606.
18. Chandramoorthy, N.; Hadjiconstantinou, N. A Reynolds Lubrication Equation for Dense Fluids Valid Beyond Navier-Stokes. In Proceedings of the 69th Annual Meeting of the APS Division of Fluid Dynamics, Portland, Oregon, 20–22 November 2016.
19. Liu, W.; Liu, Y.; Huang, W.F.; Suo, S.F.; Wang, Y.M. Effect of Disturbances on the Dynamic Performance of a Wavy-tilt-dam Mechanical Seal. *Tribol. Int.* **2013**, *64*, 63–68.
20. Liu, W.; Liu, Y.; Wang, Y.; Peng, X. Parametric Study on a Wavy-tilt-dam Mechanical Face Seal in Reactor Coolant Pumps. *Tribol. Trans.* **2011**, *54*, 878–886.
21. Liu, W.; Liu, Y.; Zhai, J.; Huang, W.; Wang, Y. Three-dimensional Flow-heat Coupling Model of a Wavy-tilt-dam Mechanical Seal. *Tribol. Trans.* **2013**, *56*, 1146–1155.

22. Djamai, A.; Brunetière, N.; Tournerie, B. Numerical Modeling of Thermohydrodynamic Mechanical Face Seals. *Tribol. Trans.* **2010**, *53*, 414–425.
23. Brunetière, N.L.; Tournerie, B.; Jean Frêne, J. Tehd lubrication of Mechanical Face Seals in Stable Tracking Mode: Part 2—Parametric Study. *J. Tribol.* **2003**, *125*, 617–627.
24. Li, Z.D.; Hao, M.; Yang, W.; Han, J.; Ren, B. Effects of Waviness and Taper on Cavitation Characteristics of Liquid Lubricated Mechanical Seals. *CIESC J.* **2016**, *67*, 2005–2014.
25. Huo, F.W. Ultra-precision Grinding of the Complex Surfaces of Hydrodynamic Seal Rings Used in Reactor Coolant Pumps. *J. Mech. Eng.* **2012**, *48*, 184.
26. Huo, F.W. Ultra-precision Grinding of the Wavy-tilt-dam Seal Rings Used in Reactor Coolant Pumps. *J. Mech. Eng.* **2013**, *49*, 154.
27. Feng, G.; Guo, D.M.; Huo, F.W.; Jin, Z.J.; Kang, R.K. Implementation Strategies for High Accuracy Grinding of Hydrodynamic Seal Ring with Wavy Face for Reactor Coolant Pumps. *Sci. China Technol. Sci.* **2013**, *56*, 2403–2412.
28. Han, C. *Study on Process of Wolfram Carbide Sealing Ring with Waviness Surface by Accurate Grinding*; National University of Defense Technology: Changsha, China, 2011.
29. Wang, X.X. *Mechanism Analysis and Experimental Study on Combined Coning and Waviness Mechanical Face Seal for Nuclear Reactor Coolant Pump*; Tsinghua University: Beijing, China, 2011.
30. Feng, X.D.; Ma, Y.; Song, K.L.; Tan, H.P.; Li, M.Q.; Lyu, Y.G. Engineering Development and Application of Hydrodynamic Mechanical Seal of Reactor Coolant Pump. *Nucl. Power Eng.* **2019**, *40*, 142–145.
31. Meng, X.K.; Bai, S.X.; Peng, X.D. An Efficient Adaptive Finite Element Method Algorithm with Mass Conservation for Analysis of Liquid Face Seals. *J. Zhejiang Univ. Sci. A* **2014**, *15*, 172–184.

Publisher’s Note: MDPI stays neutral with regard to jurisdictional claims in published maps and institutional affiliations.



© 2020 by the authors. Licensee MDPI, Basel, Switzerland. This article is an open access article distributed under the terms and conditions of the Creative Commons Attribution (CC BY) license (<http://creativecommons.org/licenses/by/4.0/>).

Article

Numerical Investigation of an Open-Design Vortex Pump with Different Blade Wrap Angles of Impeller

Xiongfao Gao ^{1,*}, Ting Zhao ¹, Weidong Shi ^{1,2,*}, Desheng Zhang ¹, Ya Shi ¹, Ling Zhou ¹ and Hao Chang ¹

¹ National Research Center of Pumps, Jiangsu University, Zhenjiang 212013, China; zt060527@gmail.com (T.Z.); zds@ujs.edu.cn (D.Z.); shiya0109@gmail.com (Y.S.); lingzhou@ujs.edu.cn (L.Z.); changhao@ujs.edu.cn (H.C.)

² School of Mechanical Engineering, Nantong University, Nantong 226000, China

* Correspondence: gxfyq@ujs.edu.cn (X.G.); wdshi@ntu.edu.cn (W.S.)

Received: 29 October 2020; Accepted: 1 December 2020; Published: 4 December 2020



Abstract: The blade wrap angle of impeller is an important structural parameter in the hydraulic design of open-design vortex pump. In this paper, taking a vortex pump with a cylindrical blade structure as the research object, two kinds of different blade wrap angle of vortex pump impellers are designed. The experiment and numerical simulation research is carried out, and the results of external characteristics and internal flow field are obtained under different flow rate. The results show that when ensuring that other main structural parameters remain unchanged, the efficiency and head of open-design vortex pump increase with the blade wrap angle decreases. In the case of blade wrap angle increasing, the length of rotating reflux back from lateral cavity to inlet is longer. For the same type of vortex pump, the length of rotating reflux to inlet decreases with the increase of flow rate. At the inlet area of impeller front face, there is an area where liquid flows back to the lateral cavity. The volute section shows that after passing through the impeller and lateral cavity, the liquid is discharged to the pump outlet with strong spiral strength. It is found that the blade wrap angle decreases and the shaft power increases, while the pump efficiency increases. The impeller blade wrap angle of vortex pump can be considered to select a smaller value.

Keywords: numerical simulation; vortex pump; lateral cavity; open-design; spiral flow

1. Introduction

Vortex pump is widely used in sewage treatment, slurries, and large particle transportation along with continuous development of industrial and agricultural production. The impeller is installed on one side of the pump cavity, and it has a wide lateral cavity, there are flow of through flow and circulation flow in the pump cavity simultaneously under the rotation of the impeller. This type of pump anti-clogging performance is better. However, this equipment exhibits disadvantages, which include low efficiency and high energy consumption [1]. At present, detailed information is still unavailable for flow fields in vortex pumps. Schivley [2] put forward a flow model to investigate internal flow of vortex pumps and pointed out that fluids can be sucked into pumps under effects of atmospheric pressure when static pressure is negative at central region of the vortex. There is a lateral cavity in the vortex pump, and the impeller has no front cover. Hence, the vortex pump anti-clogging performance is better than that of general centrifugal pumps. However, the pump efficiency is relatively low [3–5].

Numerical simulations of different end clearance conditions were carried out while ensuring that other design parameters remain unchanged.

The influence of pump structure on its performance was experimentally studied by Zheng [6]. A new method was developed in which the volumetric ratio of the lateral cavity to the impeller was used to design vortex pumps. According to the statistics of a number of experimental data,

the authors believe that the pump can get a good performance in the ratio between 3 and 5. Sha et al. [7] combined theory and experiment to derive a unified experience coefficient for use of hydraulic design method on vortex pump, further analyzed the hydraulic model, and inferred experience coefficient for least-square equation of centrifugal slurry and vortex pumps. Liu et al. [8] obtained the influence of the special volute structure of the vortex self-priming pump on its self-priming performance through 2D PIV and numerical calculation. The results show that the combination of the guide wall and the impeller outlet promotes the gas-water mixing and the formation of bubble flow, and improves the self-priming performance. To understand flow conditions in vortex pumps, Alexander Steinmann carried out numerical and experimental investigations [9], with further objective of investigating URANS-CFD (Unsteady Reynolds-Averaged Navier–Stokes –Computational Fluid Dynamics) method using cavitation model for numerical stability and accuracy.

The experiments on changing the axial location of impeller by Sha et al. [10,11], and measurement of flow field in lateral cavity with five-hole probe were conducted on a self-built vortex pump. Based on the experiments, the characteristic performance curves and the absolute velocity, the circumferential velocity, the radial velocity, the axial velocity, and the flow static pressure were obtained. The experimental results proved that the cavitation characteristic curve showed opposite tendency in the operating conditions of small charge compared with centrifugal pump and anti-cavitation were improved with the increase of the scale that impeller was inserted into lateral cavity. In order to study the influence of end clearance of impeller on the performance of a multi-stage pump, a change end clearance of impeller method was studied through CFD by Zhou et al. [12] to analyze performances of pump. The results show that the existence of end clearance, which leads to the flow aggravation separation in the diffuser passage, and further reduces the performance of the pump. The wear characteristics of slurry pump are studied based on particle model under low flow conditions by Peng et al. [13]. The results showed that there was serious local wear in the interface between the sheath and the rotor near the tongue under small flow condition. By removing the front and rear back blades, the wear degree at the junction can be effectively reduced, but the wear of the inner side of the front guard board will be intensified. The author established the apparatus first for measuring the velocity distribution on the axial vertical profile in vortex pump impeller and pressure distribution on blade surface [14]. The measuring methods are explained in more detail and the measured results are presented. An exploratory study on numerical calculation of solid–liquid two-phase flow by Gao et al. [15], the numerical calculation of vortex pump base on CFD-DEM (Discrete Element Model) coupling calculation method, and numerical simulation was carried out under different particle sizes and concentrations, then the rapeseed was used for solid particles to the experiment, and obtained that the values of inlet rotating reflux length under different flow rate conditions. The slurry pump was used to investigate into influences of blade camber profile on pump hydraulic performance and impeller wear characteristic in terms of limestone-water slurry as transported medium [16]. The relationships of both hydraulic performance and wear characteristic with blade camber profile were analyzed numerically in Fluent 16.0 by using discrete phase model (DPM) model. The results show that the cylindrical blade designed by the logarithmic spiral method with variable angle can improve hydraulic efficiency, but will lead to a slight reduction in the head. Wear characteristics in centrifugal pump simulation method are based on DPM model and semi empirical wear model by Zhao et al. [17]. The main wear positions of the centrifugal pump structure components are obtained.

At present, the research on this kind of vortex pump with special structure is scarce. Especially in the open-design vortex pump, if the improper blade wrap angle of impeller was chosen, impeller passage partial blockage and wear will occur, causing performance reduction. Even the pump passage will be blocked and operation is stopped. Therefore, the appropriate blade wrap angle of impeller is crucial for the performance and operation of the vortex pump. This article took a typical open-design vortex pump as the research object, and designed two different type of blade wrap angle of impeller. Numerical simulations of different blade wrap angle of impeller conditions were carried out. The test

validated the effect of impeller blade wrap angle on vortex pump performance and also provided a reference for impeller design and engineering application.

2. Calculation Model

2.1. Physical Model

An open-design vortex pump with a specific speed of 166 was selected as the research object. The design flow rate was $Q_{des} = 400$ L/min; rated speed $n = 1485$ r/min. The main impellers structural parameters are shown in Table 1. Figure 1 shows the vortex pump two-dimensional assembly. The blade wrap angle of impeller as shown in Figure 2. In order to facilitate comparative analysis, numerical simulations of different impeller blade wrap angle conditions were carried out with the main impeller parameters unchanged.

Table 1. Parameters of impellers.

Parameters	Model Pump 1	Model Pump 2
Blade wrap angle of impeller (ψ)	35°	65°
Inlet setting angle of impeller (β_1)	60°	40°
Outlet setting angle of impeller (β_2)	50°	35°
Impeller inlet diameter (D_1)	50 mm	
Impeller outlet diameter (D_2)	128 mm	
Blade number of impeller (z)	10	

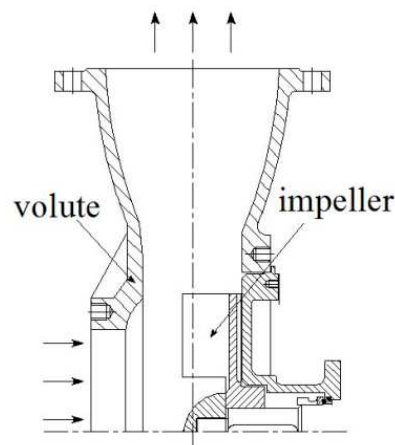


Figure 1. Simple diagram of pump section model.

2.2. Grid Independence Verification

The computational domains were formed in Unigraphics NX 10.0 software by 2d hydraulic design drawing, as shown in Figure 3, The entire mesh generation was carried out in ICEM 19.0 software, as shown in Figure 4. In theory, with increase in grid element number, errors caused by grid will reduce gradually until they disappear. However, the number of grid elements cannot be too large for the reason of considering computer performance and computer time [18–21].

In this paper, model pump 1 is used for grid independence verification. The structured mesh of computational domains was built based on ANSYS-ICEM 19.0 software (Customer Number: 1079741, NASDAQ:ANSS, Cannonsburg, PA, USA). Four calculation schemes were created with different grid numbers in this paper. The efficiency and head of the pump were taken as grid independence indicators, as shown in Table 2. The values of efficiency and head of Scheme 1 and Scheme 2 are lower than that of other schemes. The efficiency and head value of Scheme 3 are close to that of Scheme 4 as the grid increased, which means that Scheme 3 had achieved the requirement of numerical precision. Hence, considering the calculation performance and calculation time of the computer, Scheme 3 was selected

as the final grid scheme for numerical computation. Meanwhile, the entire computational domain $30 < y+ < 100$ was ensured to meet the requirement of standard wall functions [22,23], and the $y+$ contour of the impeller as shown in Figure 5, and the mesh quality as Table 3. The mesh quality is shown in Table 3, when the value of mesh quality is >0.4 , the percentage of the mesh is $>99.9\%$, while the value of mesh quality is >0.67 , the percentage of the mesh is $>90\%$.

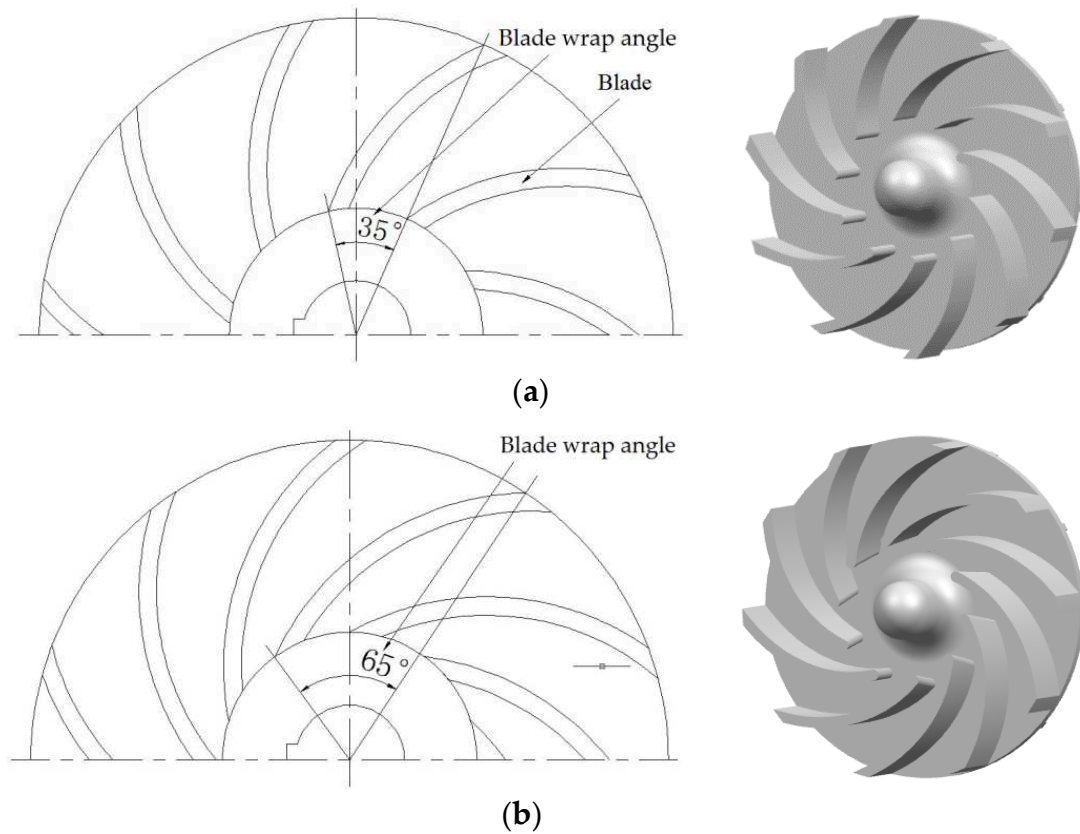


Figure 2. Blade wrap angle of impeller. (a) Impeller 1, (b) impeller 2.

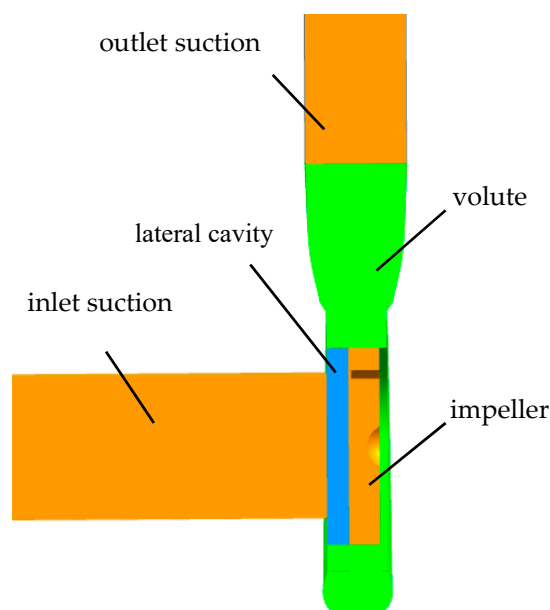


Figure 3. Calculation domains.

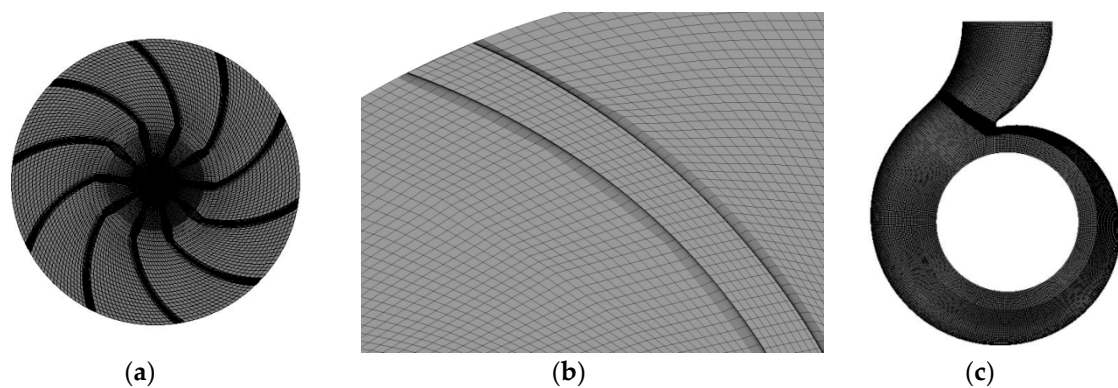


Figure 4. Sketch of the structured mesh: (a) impeller; (b) close-up view of near the trailing edge; (c) volute.

Table 2. Grid independence analysis.

Scheme No.	Grid Number	Efficiency (%)	Head (m)
Scheme 1	833662	49.83	3.78
Scheme 2	1096575	50.58	3.95
Scheme 3	1483790	50.95	4.03
Scheme 4	1756421	50.91	4.04

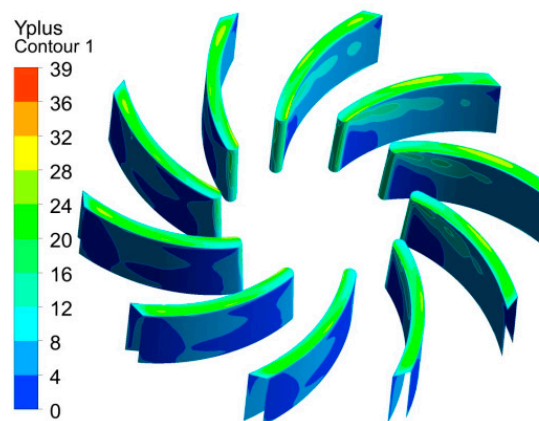


Figure 5. y^+ contour of the impeller.

Table 3. Mesh quality.

Mesh quality	>0.4	>0.5	>0.67
Percentage of grids (%)	>99.9%	>99%	>90%

2.3. Numerical Algorithm

The calculation domain of pump is divided into two types of subdomains in CFD numerical simulation, which includes a total of five subdomains as shown in Figure 3, namely inlet section, lateral cavity, impeller, volute, and outlet section, and the interfaces are formed between different subdomains. The first type of subdomain includes the inlet section, the lateral cavity, the volute, and the outlet section. The equations for this type of region are solved in a stationary framework. The second type of subdomain is the impeller, which is attached to the rotating frame and solved in a rotating framework via the multiple reference frame (MRF), and the rotational speed was set as 1485 r/min [23].

The flow through the model pump was simulated with the commercial code ANSYS-Fluent 19.0, which uses the finite volume method to solve the Reynolds averaged Navier-Stokes equations for 3D incompressible steady flow. Second order upwind discretization was used for the convective

and the diffusive terms. The time dependent term scheme was second order implicit [24]. The pressure–velocity coupling was calculated by means of the SIMPLE algorithm, and the convergence precision was set to 10^{-5} .

The mass-flow rate was specified at the inlet of the CFD domain, and the outlet boundary was assumed to be outflow. At the exit, there is an unavoidable effect on the final flow solution as a result of the boundary conditions. A reasonable length was added to the real machine geometry to avoid this effect as much as possible. At the outlet, which is roughly four impeller-diameters, the gradients of the velocity components are assumed to be zero, and all physical surfaces of the pump were set as the no-slip wall.

The maximum number of iterations is set to 20, and the convergence precision is set to 10^{-5} . In the process of iteration, if the convergence accuracy is reached, the next iteration will be carried out. If the convergence accuracy is not reached after 20 iterations, it is also considered to have reached the convergence accuracy and automatically jumps to the next step.

2.4. Turbulence Model

Predicting the performance of fluid machinery based on CFD, different turbulence models were used to calculate the fluid machinery, and the predicted results were different. There is no universally valid turbulence model which will yield optimum results for all applications [25–27]. It needs to select a turbulence model most suitable for vortex pump to be calculated, and comparing the numerical results with the experimental results for validate. Five turbulence models were selected to calculate in the design condition, namely, the standard $k-\varepsilon$ model, RNG (Re-normalization group) $k-\varepsilon$ model, realizable $k-\varepsilon$ model, standard $k-\omega$ model, and SST (Shear stress transfer) $k-\omega$ model.

In Table 4, the test results and the numerical results with different turbulence models were compared. Generally speaking, the RNG $k-\varepsilon$ and SST $k-\omega$ models predict the highest pump efficiency and head, and the standard $k-\varepsilon$ model has the lowest and most close predicted value. Thus, the standard $k-\varepsilon$ model is chosen for the following numerical calculation. It is should be noted that the standard $k-\omega$ model also has good predicted accuracy and the lowest computational time. There is around a 10% error with the test data, the reason for the increase in calculation results was probably the neglect of mechanical and leakage losses. The calculated losses in numerical simulation are considered less than the actual losses. The difference may be that in the numerical simulation in this paper, the fluid flow in the gap of rear cover plate is simplified, neglecting the volume losses caused by gap flow.

Table 4. Numerical results with different turbulence models at Q_{des} .

Turbulence Model	Standard $k-\varepsilon$	RNG $k-\varepsilon$	Realizable $k-\varepsilon$	Standard $k-\omega$	SST $k-\omega$	Test Data
Efficiency η (%)	50.95	52.74	52.13	51.13	53.18	46.66
H (m)	4.03	4.28	4.18	4.11	4.32	3.62

3. Results and Discussion

3.1. Pump Performance Test

In this paper, two impellers with different blade wrap angles are processed by polymethyl methacrylate, as shown in Figure 6. In order to continue the research later, the inlet pipeline is also processed into transparent polymethyl methacrylate. Test rig comprises two parts, namely, data acquisition system and water circulation system [28]. The open test bench is shown in Figure 7, which has the identification from the technology department in Jiangsu province of China. Test facilities and measurement methods abide by measurement requirements described [29]. It includes flow control device, data acquisition device, and data processing device. During the experiment, the flow and pressure were measured by LBBE-50S-M2X102-25 electromagnetic flowmeter (Wuxi Dihua Automation Equipment Co. Ltd., Wuxi, China) and WT2000 pressure sensor (Shanghai Welltech

Automation Co., Ltd., Shanghai, China), and the shaft power was measured by JN338-20A shaft power tester (Wuxi Antok Automation Technology Co. Ltd., Wuxi, China). The range of LBBE-50S-M2X102-25 electromagnetic flowmeter is 30 L/min–850 L/min, the range of JN338-20A shaft power tester is 0–20 N m, the range of inlet pressure transmitter is –100 kpa–100 kpa; the range of outlet pressure transmitter is 0–100 kpa. Then, under the valve opening adjustment, we measure the inlet and outlet pressure and shaft power at different flow rates, and input all the signals into the computer software for calculation.

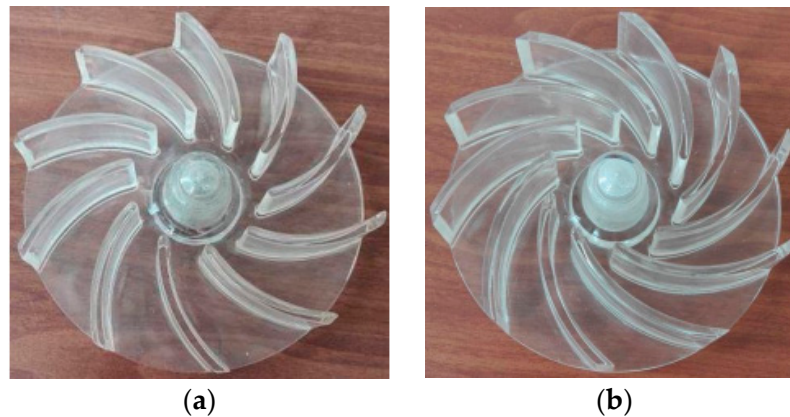


Figure 6. Impeller of open-design vortex pump. (a) Impeller 1; (b) Impeller 2.

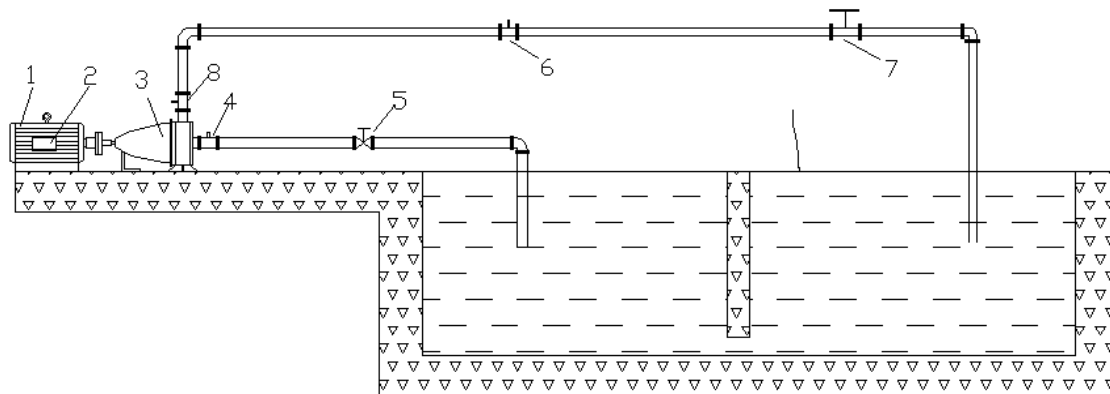


Figure 7. Testing system. 1. Motor; 2. rotational speed meter; 3. test pump; 4. inlet pressure sensor; 5. inlet valve; 6. turbine flowmeter; 7. outlet valve; 8. outlet pressure sensor.

In the pump performance test, pump efficiency is defined as follows [30]:

$$\eta = \frac{\rho g Q H}{P_s} \times 100\%, \quad (1)$$

where η is pump efficiency, Q is flow rate (m^3/s), H is pump head (m), and P_s is output power of motor (W).

$$H = \frac{p_{out} - p_{in}}{\rho g}, \quad (2)$$

where p_{in} is inlet total pressure, and p_{out} is outlet total pressure (p_{in} and p_{out} unit is Pa).

In this paper, experimental and numerical uncertainty analysis was performed [26,31,32]. The experimental total uncertainty is the combination of random uncertainty and systematic uncertainty, while the numerical uncertainty is caused by discretization in CFD applications. The numerical results compared to experimental results are shown in Figure 8. The performance tests under the wrap angle of the two types of impeller blades show that the efficiency and head of the impeller 1 are higher than that of the impeller 2. The numerical calculation results are in good agreement with the experimental

results, and the experimental results are lower than the numerical calculation results, but the error is less than 5%. The change trend is the same under different flow. Therefore, this research method is credible. The reason for the decrease in the calculation result may be that in the numerical simulation in this paper, the fluid flow in the gap of the rear cover plate is simplified, neglecting the volume losses caused by gap flow. According to the references below, the experimental uncertainty in this study was estimated as 2.8%, the numerical uncertainty in this study was estimated as 2.1%.

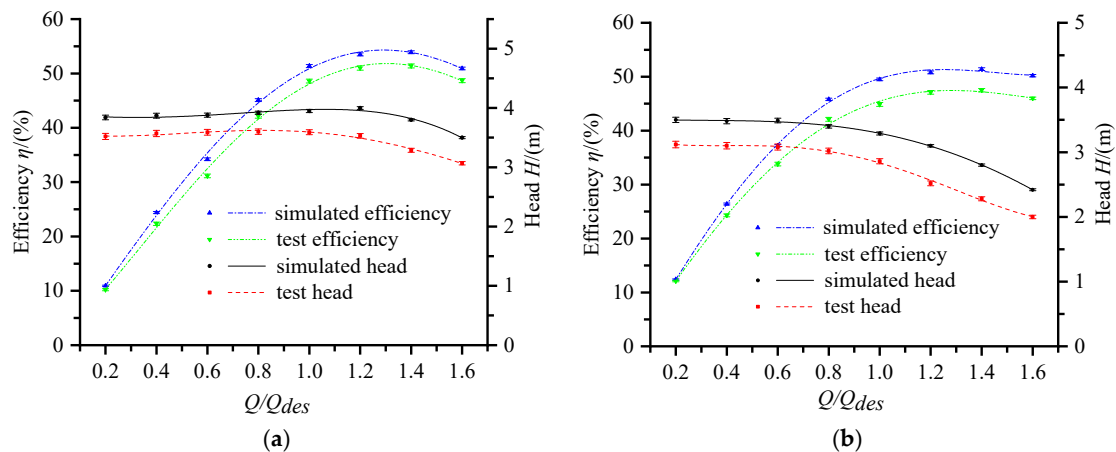


Figure 8. Comparison of pump performance between numerical and experimental results. (a) Model pump 1; (b) model pump 2.

3.2. Flow Field Analysis

3.2.1. The Influence of Blade Wrap Angle on Inlet Backflow

At present, there are many studies on the covered design vortex pump. From the existing research conclusions, the vortex pump has both circulating flow and through flow inside. The structure of the open-design vortex pump is different from the impeller design of the covered design vortex pump. The impeller of the open-design vortex pump does not retract to the rear pump cavity, but is on one side of the pump cavity, and its internal flow mode shows different flow characteristics. In this paper, two types of vortex pump models with different impeller blade wrap angles are analyzed by numerical simulation of the full flow field.

Figures 9–11 shows the flow field in inlet region of two model pumps at the flow rates of $0.6Q$, $1.0Q$, and $1.4Q$. It can be seen from the figure that part of the medium flows backwards from the pump cavity to the inlet section along the inlet wall. The direction of rotation of the backflow is consistent with the direction of rotation of the impeller, and it enters the inlet section in a spiral form adjacent to the wall of the inlet pipe, and is constantly mixed with the incoming flow of the inlet, causing the return flow energy to gradually weaken, and finally the return flow and the incoming flow reach equilibrium and stop at a certain position. After analysis, it is found that this backflow into the inlet pipe is caused by the unique structure of the vortex pump. The unique lateral cavity of the vortex pump, and the inlet diameter of the vortex pump is larger than that of the ordinary centrifugal pump, driven by the rotation of the impeller, the lateral cavity produces a circulating flow, driven by the strength of the circulating flow, part of the backflow flows into the pump inlet segment. This part of the backflow causes a large energy loss in the vortex pump.

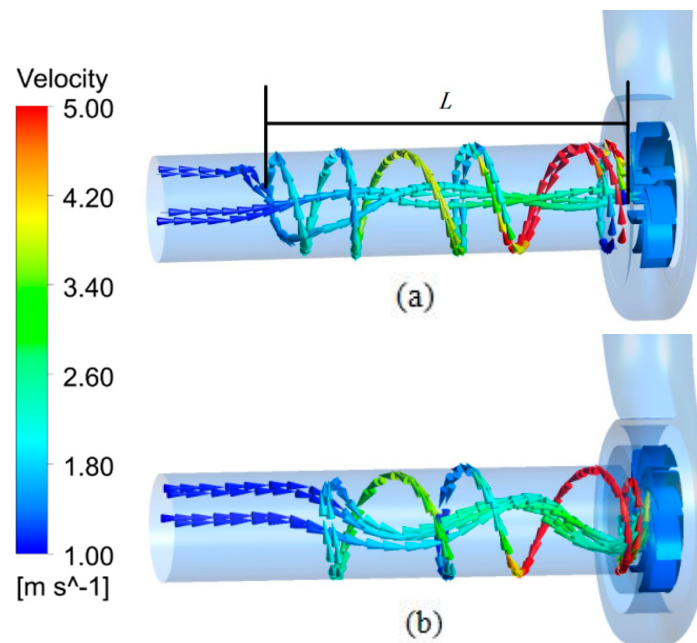


Figure 9. $0.6Q_{des}$ condition. (a) Impeller 1; (b) Impeller 2.

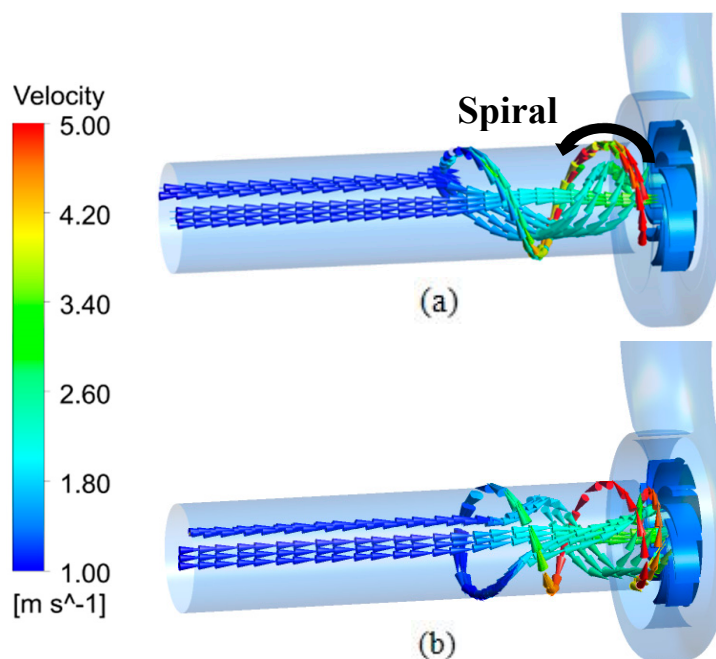


Figure 10. $1.0Q_{des}$ condition. (a) Impeller 1; (b) Impeller 2.

The values of inlet rotating reflux length under different flow rate conditions are shown in Figure 12. Through the comparison of 3 different working conditions, it can be clearly seen that the stop position of the spiral reflux moves toward the pump cavity under the large flow working condition, which is mainly caused by the increase of the flow speed and the increase of kinetic energy under the large flow working condition. At the same time, the interference degree of the flow characteristic in the middle area of the inlet pipe also decreases as the flow rate increases. Under the same flow condition, when the blade wrap angle is 35° , the value of L is longer than that of the value of blade wrap angle is 65° . Under large flow, the change of the wrap angle of the impeller blade has no obvious effect on the stop position of the inlet spiral reflux.

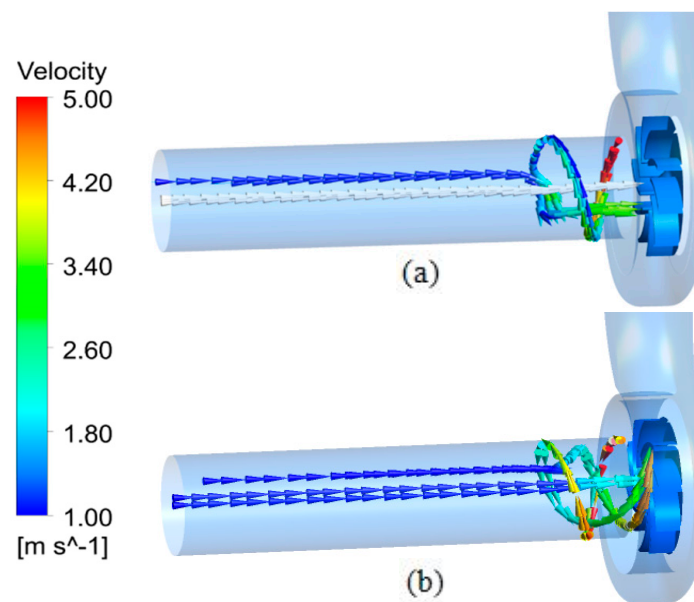


Figure 11. $1.4Q_{des}$ condition. (a) Impeller 1; (b) Impeller 2.

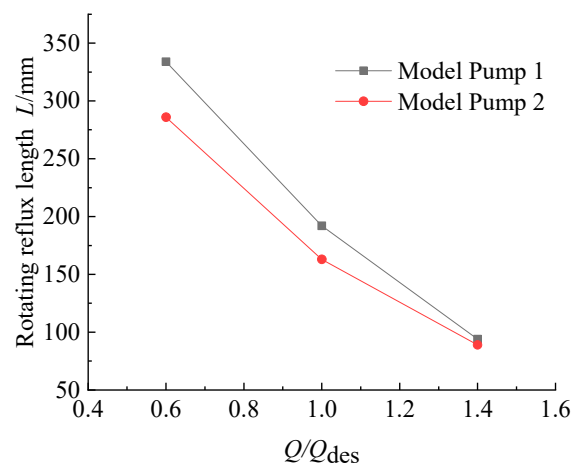


Figure 12. The values of inlet rotating reflux length under different flow rate conditions.

3.2.2. The Influence of the Blade Wrap Angle on the Flow Characteristic of the Impeller Front Face

In order to further explore the development process of the circulating flow in the pump cavity, focusing on the flow characteristics of the lateral cavity and the impeller, the axial velocity distribution at the impeller front face is analyzed under the two impeller blade wrap angles. The blade number is defined in Figure 13. Take the intersection line of the front face of the blade with the pressure side and the suction side respectively, and name them from blade 1 to blade 10 in turn according to the rotation direction of the impeller, and the blade 1 is located at the first section under the tongue. In Figures 14–16, ps represents the intersection line of pressure side and the front face, ss represents the intersection line of the suction side and the front face. Since the positive direction of the Z-axis is set to be opposite to the inlet flow velocity during modeling, a negative axial velocity means fluid flows into the impeller, and a positive axial velocity means fluid flows from the impeller into the pump cavity. The ratio of the position of a point on the intersection line to the radius of the impeller are treated as dimensionless to indicate the relative position of the data point, that is the length–diameter ratio r/R (r represents the vertical distance from a point in the pump to the axis, R represents the radius of the impeller). The relative velocity of a point on the intersection line can be obtained by numerical simulation as shown in Figures 14–16.

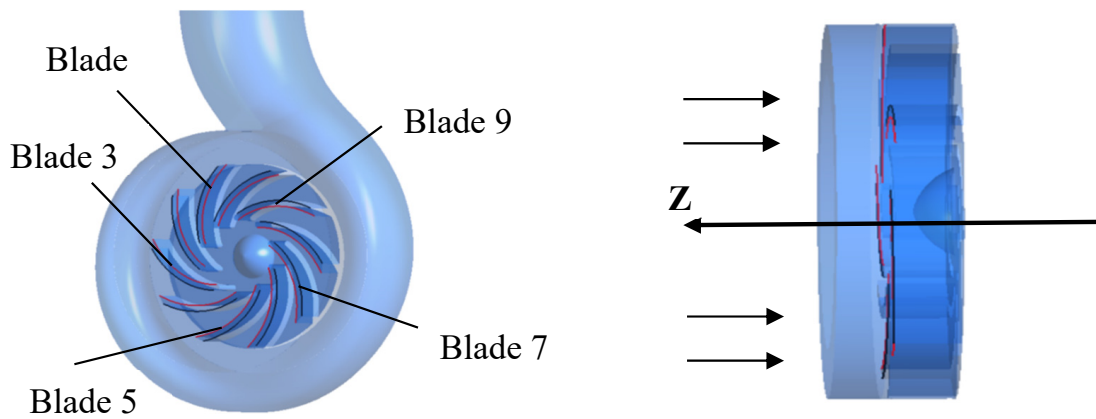


Figure 13. Schematic of blade number.

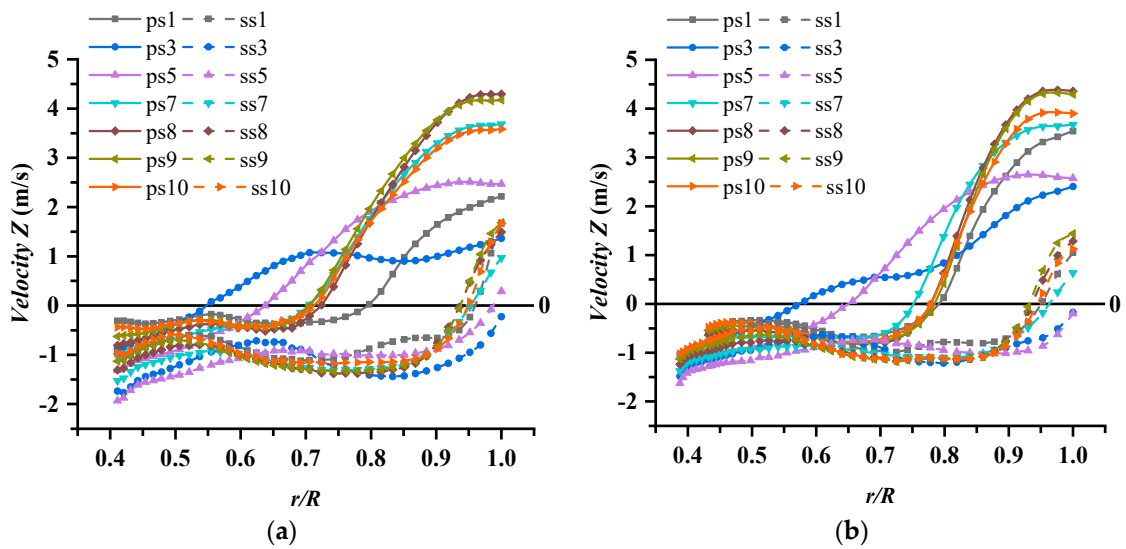


Figure 14. $0.6Q_{des}$ condition. (a) Model pump 1; (b) model pump 2.

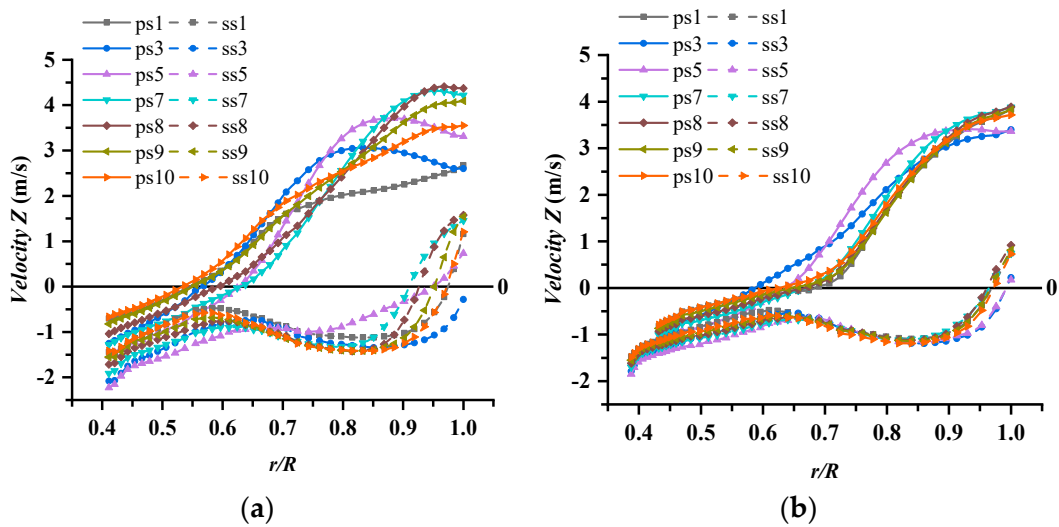


Figure 15. $1.0Q_{des}$ condition. (a) Model pump 1; (b) model pump 2.

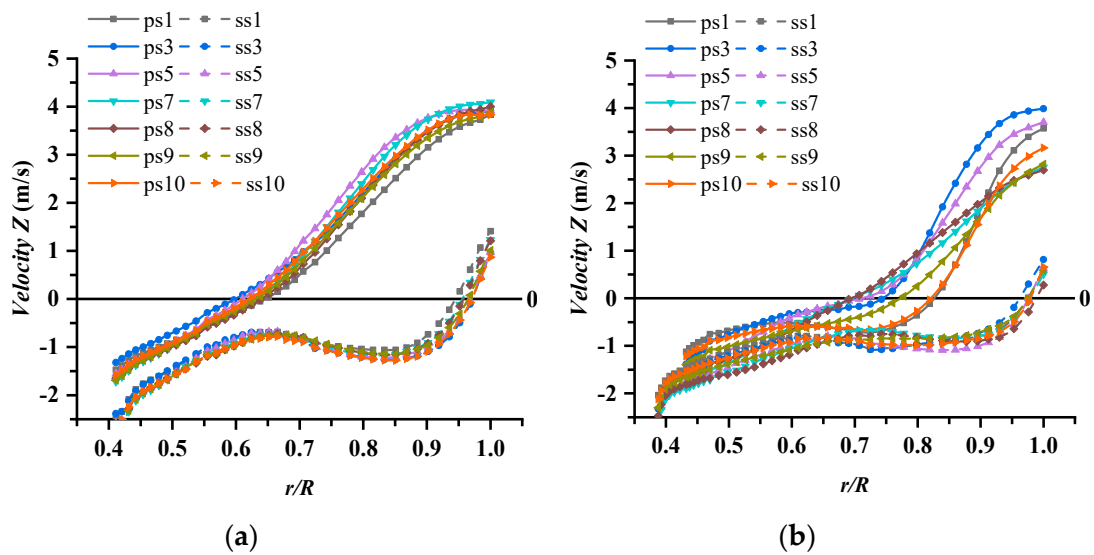


Figure 16. $1.4Q_{des}$ condition. (a) Model pump 1; (b) model pump 2.

Due to the existence of lateral cavity, the flow characteristic in the pump cavity is more complicated than that of ordinary centrifugal pumps. The main reason is that the impeller is semi-open and has no front cover. The front face of the impeller is connected with the lateral cavity. This special structure makes the impeller area and the lateral cavity have fluid exchange flow, and the internal flow characteristic is very complicated.

A part of the fluid in the impeller passage enters the lateral cavity directly from the impeller front face. This part of the fluid contains large circumferential kinetic energy due to the rotation of the impeller, which can further drive the fluid in the pump cavity to do circumferential movement, and also affects the flow of the inlet section of pump.

It can be clearly seen from Figures 14–16 that under $0.6Q_{des}$, $1.0Q_{des}$, and $1.4Q_{des}$ flow rate conditions, the axial velocity of the fluid at the pressure side of the impeller front face changes from negative to positive, which indicates that the fluid in the latter half of the blade begins to flow out into the lateral cavity. The flow characteristics are mainly concentrated in the middle and rear sections of the blade pressure side. Due to the large inlet pipe diameter of this type of vortex pump, the ratio of pump inlet radius to impeller radius r/R is 0.74, and the inlet flow has a greater impact on the front end of the impeller. Therefore, the value of r/R of the impeller front face is about 0.74, where the area becomes a boundary area for liquid in and out. For the suction side, except for the area after value of r/R 0.95, the values of axial velocity are negative, indicating that the liquid flow from the lateral cavity into the impeller at the entire suction side area. The axial velocity of the suction side of the blade tail turned from a negative value to a positive value, there is liquid entering the lateral cavity in this area. This phenomenon may be caused by the rotation of the impeller and the existence of circulating flow in the lateral cavity.

From the two model pumps, under small flow conditions, in the transition area between the impeller front face and the lateral cavity, the axial velocity values of the blade pressure sides show large differences, such as intersection lines of ps1, ps3 and ps5, indicating that in this area, axial velocity is disordered, while the axial velocity value of the intersection lines of suction side is relatively stable. With the increase of the flow rate, the circumferential velocity trends of the pressure side and suction side of each intersection line in the impeller front face are basically the same.

At $0.6Q_{des}$ condition, the r/R value of model pump 1 and model pump 2 is about 0.55, the liquid starts to flow out from the impeller pressure side to the lateral cavity. For model pump 2, when the value of r/R is about 0.6, the liquid starts to flow out of the impeller pressure side into lateral cavity. When the flow rate increases to $1.4Q_{des}$, the r/R value of the model pump 1 and model pump 2 are 0.6

and 0.7, respectively, the liquid from the pressure side flow out to the lateral cavity. Thus, with the flow rate increases the r/R value, where liquid from the pressure side flow into the lateral cavity increases.

3.2.3. The Influence of Blade Wrap Angle on the Flow Characteristic inside the Volute

The vortex pump has lateral cavity and the volute is asymmetric, so it is very important to analyze the flow characteristic in the volute. In this paper, four sections of the volute were selected as shown in Figure 17, namely sections I, III, V, and VII, and analyzed for streamline velocity.

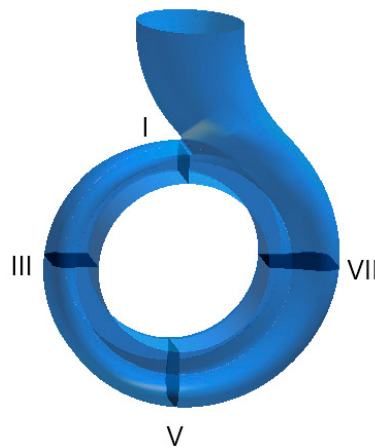


Figure 17. Volute sections.

The velocity streamline contours of the four sections in volute are shown in Figures 18–20. The relative velocity in the volute chamber presents non axisymmetric distribution, and the velocity in the volute decreases gradually from the first section of the volute to the outlet of the volute, which shows that the dynamic energy is gradually transformed into the pressure energy. From the first section of the volute to the outlet, the liquid entering from the impeller and the lateral cavity is discharged out of the volute outlet in a spiral flow state. Section I is at the volute tongue. Due to the blocking effect of the tongue, there is no spiral flow in the section, the spiral flow is gradually formed from the section I to the outlet of the volute. For the model pump 1, under small flow and rated flow conditions, it is found from the streamline velocity contour of section III that two spiral vortices of different sizes occur, the spiral vortex on the left is in a counterclockwise direction, the spiral vortex on the right flows in a clockwise direction. With the sectional area of the volute increases, these two spiral vortices increase. When the sectional position of the volute increases to VII, the spiral vortex on the left disappears, and the strength of the spiral vortex on the right increases to occupy the entire volute. Under the large flow rate condition, only the right side (The corresponding side of the impeller) of the volute forms a spiral vortex.

Under the same flow rate condition, the model pump 2 streamline velocity contour compares to model pump 1, it is found that at $0.6Q_{des}$ condition, there is a small spiral vortex near the wall in the left side of the III, V section, and the spiral vortex is smaller than that of model pump 1. Under the conditions of $1.0Q_{des}$ and $1.4Q_{des}$, there is only a large spiral vortex generated on the right side of the volute. The spiral vortex on the right moves to the middle area of the volute with the increase of the volute section. When the volute section is larger than the seventh section, the spiral vortex occupies the whole volute space, and the liquid is flow to the pump outlet in a spiral shape.

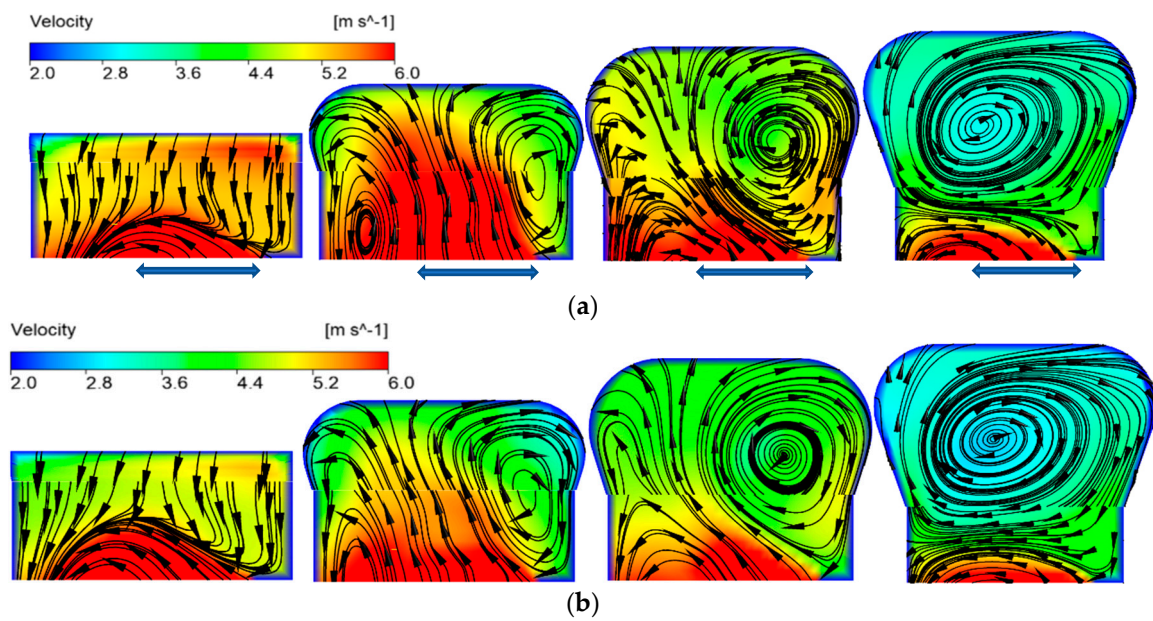


Figure 18. $0.6Q_{des}$ streamline diagram of volute section. (a) Model pump 1; (b) model pump 2.

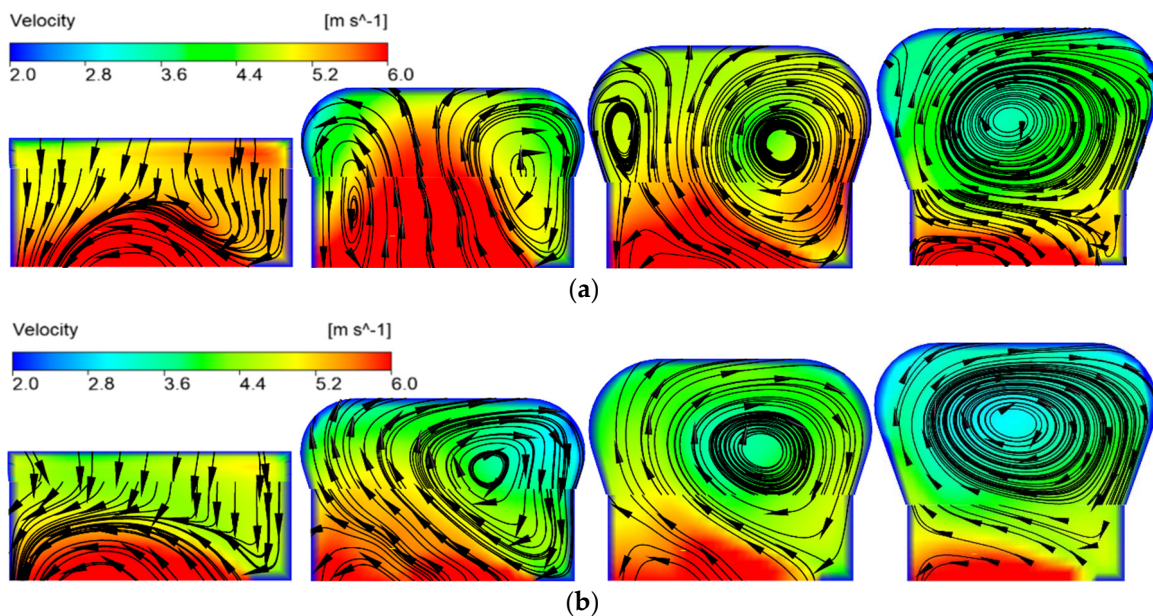


Figure 19. $1.0Q_{des}$ streamline diagram of volute section. (a) Model pump 1; (b) model pump 2.

Generally speaking, there is a large vortex area in the volute, which mainly occurs in the corresponding side of the impeller. Under the same flow rate condition, the velocity of the volute in model pump 2 is lower than that of model pump 1, this is consistent with the result that the head of model pump 1 is higher than that of model pump 2, which is consistent with the previous comparison and analysis of external characteristics, the previous performance curve also shows this.

As the blade wrap angle increases, the flow passage of impeller becomes narrower, and the binding force of the blade to the liquid in the passage increases, while the pump efficiency decreases. The reduced blade wrap angle can widen the flow passage and weaken the blade's binding force to the liquid in the flow passage. It will also increase circulating flow in the lateral cavity and improve the efficiency. It is suggested that a smaller blade wrap angle should be considered.

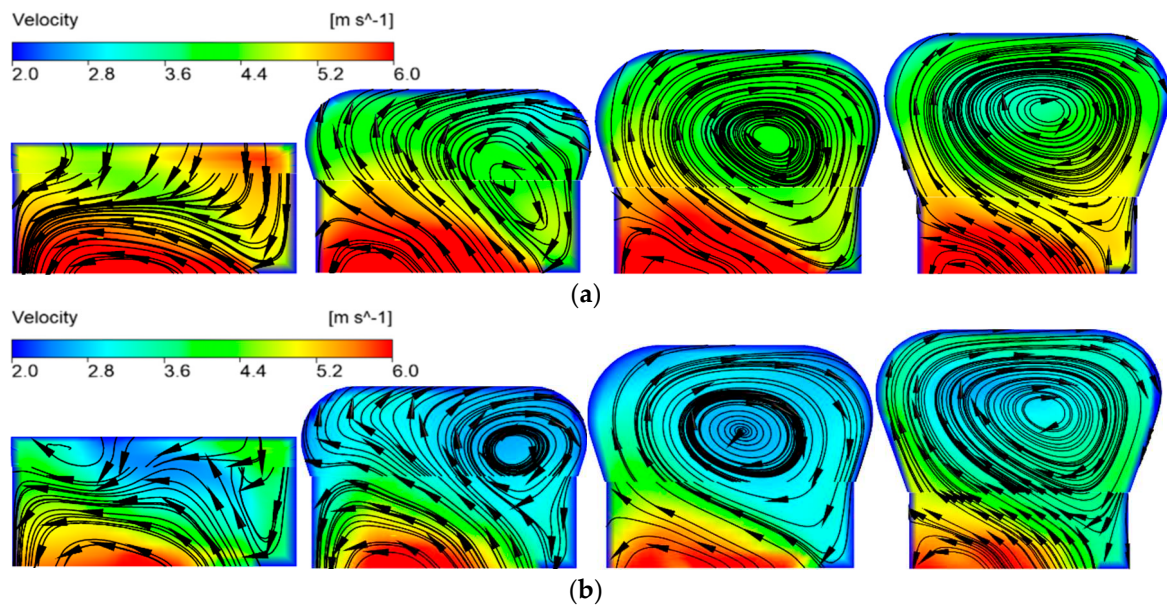


Figure 20. $1.4Q_{des}$ Streamline diagram of volute section. (a) Model pump 1; (b) model pump 2.

3.2.4. Vorticity Analysis in the Volute

In this paper, the regularized helicity H_n is used to determine the vortex core [33]. This method mainly captures the position of the vortex core according to the angle between the velocity vector and the vorticity. It is defined as the modeling of the point product of the velocity and the vorticity, which is used to judge the rotation direction of the vortex core. The value is $[-1, 1]$, the vortex turns counterclockwise with positive H_n , while it turns clockwise with negative H_n [33].

$$H_n = \frac{w \cdot \Omega}{|w| |\Omega|} \quad (3)$$

where w is relative velocity, Ω is absolute vorticity.

$$S_{ij} = \frac{1}{2} \left(\frac{\partial u_i}{\partial x_j} - \frac{\partial u_j}{\partial x_i} \right) \quad (4)$$

$$\Omega_{ij} = \frac{1}{2} \left(\frac{\partial u_i}{\partial x_j} + \frac{\partial u_j}{\partial x_i} \right) \quad (5)$$

$$Q = \frac{1}{2} (\|\Omega^2\| - \|S^2\|) \quad (6)$$

where S is the strain rate tensor.

The Q criterion is selected to identify the vortex in this paper. The imaging vortex structure in the pump cavity is shown in Figure 21a,b. When $Q = 54,288 \text{ s}^{-2}$, the strong vortex structure is observed in the areas of the impeller outlet volute tongue. The vortex structure of the impeller rim area is symmetrical, and there are obvious vortices in the lateral cavity near the pump inlet area. With the Q value increases to 5301 s^{-2} , strong vortices appear inside the volute, especially on the Sections I to V of the volute. The vortices are widely distributed in the lateral cavity, and the vortex strength is greater near the pump inlet. The reason of the strong vortices occurring in the lateral cavity is mainly attributed to the rotation of the main flow in the cavity driven by the spinning impeller. There is a strong and wide vortex area in the entire pump cavity, mainly because the vortex pump has lateral cavity and there is circulating flow in the lateral cavity. The asymmetry of volute leads to the wide and complex vortex area in the whole pump cavity. In addition, a strong vortex appears in the tongue area and it flows to the exit of the volute due to the through flow.

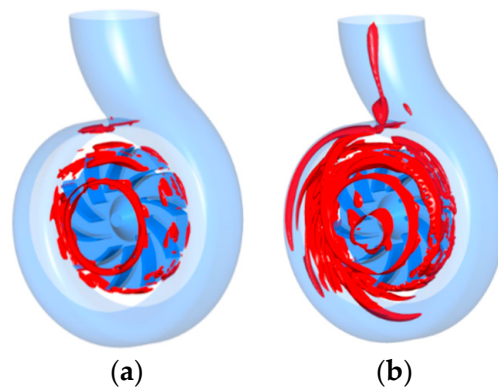


Figure 21. Vortex structures of pump cavity: (a) $Q = 54,288 \text{ s}^{-2}$; (b) $Q = 5301 \text{ s}^{-2}$.

Figure 22a show the vortex distribution in the volute diffuser region with $Q = 5301 \text{ s}^{-2}$. Five section faces are made at an average interval of 22 mm in the volute diffuser region. It is found that there is a strong vortex flow in the diffusion region. The vortex flow occurs in the front of the volute diffuser region and moves vertically to the outlet of the volute. The formation of vortex flow may be caused by the existence of a tongue and lateral cavity. The H_n of the volute diffuser region is shown in Figure 22b, and the vortex core distribution in the volute diffuser region is relatively disordered. In particular, the vortex cores in the tongue region, and both clockwise and counterclockwise rotating vortices occurred, especially the counterclockwise rotating vortices were produced in larger area of volute diffuser region. The clockwise rotating vortices occurred in the front wall of the volute diffuser region, and the vortex cores move from the front side of the tongue to the middle side of the outlet. It was found that the liquid is discharged to the volute outlet in the form of a spiral by analyzing Figure 22.

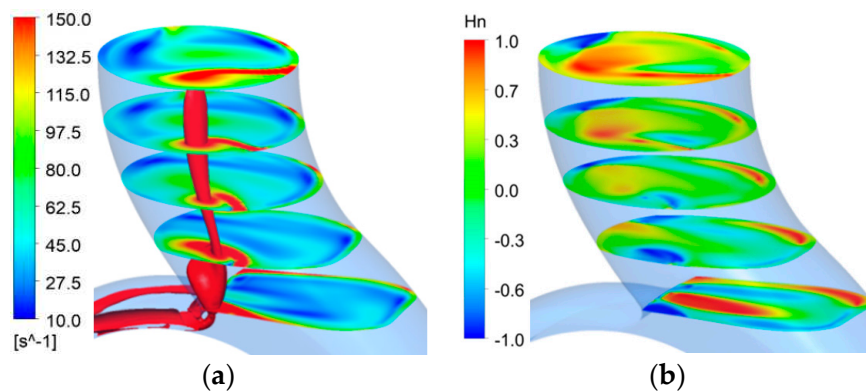


Figure 22. Vortex structure of volute diffusion section: (a) Module distribution of vorticity; (b) H_n .

4. Summary

In this paper, two types of vortex pumps with different impeller blade wrap angles have been numerically simulated and experimentally studied under different flow conditions. Through numerical simulation and experiments, performance curves and internal flow field results have been obtained. The conclusions include the following aspects.

- (1) Under small flow conditions, the rotating backflow at the inlet of the open-design vortex pump is more serious. With other structural parameters unchanged, when the blade wrap angle decreases, the stop position of the inlet spiral reflux increases from the pump cavity, and the hydraulic loss increases, but the efficiency and head of the vortex pump increase. The performance of the smaller impeller blade wrap angle is better than impeller performance with larger wrap angle.
- (2) In the area between the front end of the impeller and the lateral cavity of the pump, in the pressure side, the fluid flows into the impeller from the lateral cavity in the front half of impeller, and then

flows out from the back half of impeller into the lateral cavity. In the suction side, the fluid in the lateral cavity flows back to the impeller. It shows that fluid flows in and out of the front face of the impeller, which leads to a decrease in hydraulic performance.

- (3) Since the impeller is installed on one side of the pump cavity, as the blade wrap angle increases, the flow passage of impeller becomes narrower, and the binding force of the blade to the liquid in the passage increases, while the pump efficiency decreases. The reduced blade wrap angle can widen the flow passage and weaken the blade's binding force to the liquid in the flow passage. It will also increase circulating flow in the lateral cavity and improve the efficiency. It is suggested that a smaller blade wrap angle should be considered.

Author Contributions: Conceptualization, X.G. and W.S.; methodology, X.G. and W.S.; software, Y.S.; validation, H.C. and W.S.; formal analysis, X.G.; investigation, D.Z.; resources, X.G.; data curation, T.Z.; writing—original draft preparation, X.G.; writing—review and editing, W.S. and H.C.; visualization, L.Z.; supervision, W.S.; project administration, W.S.; funding acquisition, X.G. All authors have read and agreed to the published version of the manuscript.

Funding: This research was funded by the National Natural Science Foundation of China (Grant No. 51909108), National Natural Science Foundation of China (Grant No. 51979138).

Conflicts of Interest: The authors declare no conflict of interest.

Nomenclature

Q_{des}	design flow rate
Q	flow rate
D_2	impeller outer diameter
D_1	impeller inlet diameter
z	number of blade
ψ	blade wrap angle of impeller
β_1	impeller inlet blade angle
β_2	impeller outlet blade angle
H	head
η	pump efficiency
n	rated speed
n_s	specific speed
ρ	liquid density
g	gravity acceleration
P_s	output power of motor
p_{out}	total pressure at impeller outlet
p_{in}	total pressure at impeller inlet
L	rotating reflux length
r	value of the vertical distance from a point in the pump to the axis
R	impeller radius
H_n	regularize helicity
w	relative velocity
Ω	absolute vorticity
S	the strain rate tensor

References

- OHBA, H.; NAKASHIMA, Y.; SHIRAMOTO, K. A study on internal flow and performance of a vortex pump: Part 1, theoretical analysis. *Trans. J. Soc. Mech. Eng. Ser. B* **1983**, *26*, 999–1006. [[CrossRef](#)]
- SCHIVLEY, G.P.; DUSSOURD, J.L. An analytical and experimental study of a vortex pump. *J. Basic Eng. Ser. D* **1970**, *92*, 889–900. [[CrossRef](#)]
- SHA, Y.; HOU, Y. Effect of impeller position on performance and measurement of vaneless cavity flow field. *J. Agric. Mach.* **2010**, *11*, 57–62.

4. Gerlach, A.; Thamsen, P.U.; Wulff, S.; Jacobsen, C.B. Design parameters of vortex pumps: A meta-analysis of experimental studies. *Energies* **2017**, *1*, 58. [[CrossRef](#)]
5. Gao, X.; Shi, W.; Zhang, D.; Zhang, Q.; Fang, B. Optimum design and test of cyclone pump based on CFD orthogonal test. *J. Agric. Mach.* **2014**, *5*, 101–106.
6. Zheng, M.; Yuan, S.; Chen, C. Influence of structural parameter of a vortex pump on its performance. *Trans. Chin. Soc. Agric. Eng.* **2000**, *31*, 46–49.
7. Sha, Y.; Yang, M.; Kang, C.; Wang, J.; Chen, H. Design method and characteristic analysis of vortex pump. *Trans. Chin. Soc. Agric. Eng.* **2004**, *36*, 124–127.
8. Liu, K.; Wang, C.; Feng, Y.; Hu, B. PIV measurements and CFD computations of internal flow characteristics of rotational flow self-priming pump. *J. Drain. Irrig. Mach. Eng.* **2019**, *37*, 1025–1030.
9. Alexander, S.; Hendrik, W.; Alfred, O. Numerical and experimental investigations of the unsteady cavitating flow in a vortex pump. *J. Hydrodyn.* **2010**, *22*, 324–329.
10. Sha, Y.; Hou, Y. Effect of Impeller Location and Flow Measurement in Volute of a vortex pump. *Trans. Chin. Soc. Agric. Eng.* **2010**, *41*, 57–62.
11. Sha, Y. Experiments on performance and internal flow of a vortex pump. *Trans. Chin. Soc. Agric. Eng.* **2011**, *27*, 141–146.
12. Zhou, L.; Wang, W.; Hang, J.; Shi, W.; Yan, H.; Zhu, Y. Numerical Investigation of a High-Speed Electrical Submersible Pump with Different End Clearances. *Water* **2020**, *12*, 1116. [[CrossRef](#)]
13. Peng, G.; Zhou, G.; Hu, Z.; Zhou, H. Influence of back blade on wear of heavy slurry pump under low flow condition. *J. Drain. Irrig. Mach. Eng.* **2020**, *38*, 332–338.
14. Chen, H. Measurement of rotating flow field with in the impeller of vortex pump. *Trans. Chin. Soc. Agric. Eng.* **1996**, *27*, 49–54.
15. Gao, X.; Shi, W.; Shi, Y.; Chang, H.; Zhao, T. DEM-CFD Simulation and Experiment on Flow Characteristics of Particles in Vortex Pump. *Water* **2020**, *12*, 2444. [[CrossRef](#)]
16. Li, J.; Zhang, R.; Guo, R.; Li, R. Influence of blade camber profile on hydraulic performance of slurry pump and impeller wear characteristic. *J. Drain. Irrig. Mach. Eng.* **2020**, *38*, 21–27.
17. Zhao, W.; Zheng, Y.; Liu, Y.; Han, X. The numerical analysis of the influence of sand volume fraction on the wear characteristics of centrifugal pumps. *J. Drain. Irrig. Mach. Eng.* **2018**, *2*, 98–103.
18. Gopalakrishnan, S. Pump Research and Development: Past, Present, and Future—An American Perspective. *J. Fluids Eng.* **1999**, *121*, 237–247. [[CrossRef](#)]
19. Hergt, P.H. Pump Research and Development: Past, Present, and Future. *J. Fluids Eng.* **1999**, *121*, 248–253. [[CrossRef](#)]
20. Shi, W.; Hou, Y.; Zhou, L.; Li, Y.; Xue, S. Numerical simulation and test of performance of deep-well centrifugal pumps with different stages. *J. Drain. Irrig. Mach. Eng.* **2019**, *37*, 562–567.
21. Zhou, L.; Shi, W.; Lu, W.; Hu, B.; Wu, S. Numerical Investigations and Performance Experiments of a Deep-Well Centrifugal Pump with Different Diffusers. *J. Fluids Eng.* **2012**, *134*, 071102. [[CrossRef](#)]
22. *Fluent User's Guide*; Fluent Inc.: New York, NY, USA, 2003.
23. Wang, F. Application of Boundary Conditions. In *Computational Fluid Dynamics Analysis-CFD Principles and Application*; Ying, Q., Sang, R., Eds.; Tsinghua University Press: Beijing, China, 2004; pp. 144–158.
24. Gonzalez, J.; Parrondo, J.; Stantolaria, C.; Blanco, E. Steady and Unsteady Radial Forces for a Centrifugal Pump with Impeller to Tongue Gap Variation. *J. Fluids Eng.* **2006**, *128*, 454–462. [[CrossRef](#)]
25. Gulich, J.F. Numerical Flow Calculations. In *Centrifugal Pumps*; Springer: New York, NY, USA, 2007; pp. 439–506.
26. Celik, I.B.; Ghia, U.; Roache, P.J.; Freitas, C.J.; Coleman, H.; Raad, P.E. Procedure for Estimation and Reporting of Uncertainty Due to Discretization in CFD Applications. *J. Fluids Eng.* **2008**, *130*, 078001.
27. Lewis, F.; Richardson, F.R.S.; Gaunt, J.A. VIII. The deferred approach to the limit. *Philos. Trans. R. Soc. Lond.* **1927**, *226*, 299–361.
28. Benigni, H.; Jaberg, H.; Yeung, H.; Salisbury, T.; Berry, O.; Collins, T. Numerical simulation of low specific speed American petroleum institute pumps in part-load operation and comparison with test rig results. *J. Fluids Eng.* **2012**, *134*, 024501. [[CrossRef](#)]
29. *ISO 9906 Rotodynamic Pump-Hydraulic Performance Acceptance Tests-Grades 1 and 2*; International Standardization Organization: Geneva, Switzerland, 1999.

30. Guan, X. Design of Vortex Pump. In *Modern Pumps Theory and Design*; China Astronautic Publishing House: Beijing, China, 2010; pp. 412–420.
31. ASME. *Test Uncertainty, Standard No. PTC 19.1*; The American Society of Mechanical Engineers: New York, NY, USA, 2005.
32. Coleman, H.W.; Steele, W.G. *Experimentation and Uncertainty Analysis for Engineers*; Wiley: New York, NY, USA, 1989.
33. Furukawa, M.; Inoue, M.; Saiki, K.; Yamada, K. The role of tip leakage vortex breakdown in compressor rotor aerodynamics. *J. Turbomach.* **1999**, *3*, 469–480. [[CrossRef](#)]


Publisher’s Note: MDPI stays neutral with regard to jurisdictional claims in published maps and institutional affiliations.



© 2020 by the authors. Licensee MDPI, Basel, Switzerland. This article is an open access article distributed under the terms and conditions of the Creative Commons Attribution (CC BY) license (<http://creativecommons.org/licenses/by/4.0/>).

Article

The Effect of Root Clearance on Mechanical Energy Dissipation for Axial Flow Pump Device Based on Entropy Production

Yanjun Li ¹, Yunhao Zheng ¹, Fan Meng ^{1,*} and Majeed Koranteng Osman ^{1,2} 

¹ Research Center of Fluid Machinery Engineering and Technology, Jiangsu University, Zhenjiang 212013, China; lyj782900@ujs.edu.cn (Y.L.); js_yunhao@yeah.net (Y.Z.); mjk@ujs.edu.cn (M.K.O.)

² Mechanical Engineering Department, Wa Technical University, Wa, XW-0547-6186 Upper West, Ghana

* Correspondence: mf@ujs.edu.cn

Received: 8 October 2020; Accepted: 17 November 2020; Published: 20 November 2020



Abstract: The axial flow pump is a low head, high discharge pump usually applicable in drainage and irrigation facilities. A certain gap should be reserved between the impeller blade root and the impeller hub to ensure the blade adjustability to broaden the high-efficiency area. The pressure difference between its blade surface induces leakage flow in the root clearance region, which decreases hydraulic performance and operational stability. Therefore, this study was carried out to investigate the effect of root clearance on mechanical energy dissipation using numerical simulation and entropy production methods. The numerical model was validated with an external characteristics test, and unsteady flow simulations were conducted on the axial flow pump under four different root clearance radii. The maximum reductions of 15.5% and 6.8% for head and hydraulic efficiency are obtained for the largest root clearance of 8 mm, respectively. The dissipation based on entropy theory consists of indirect dissipation and neglectable direct dissipation. The leakage flow in the root clearance led to the distortion of the impeller's flow pattern, and the indirect dissipation rate and overall dissipation of the impeller increased with increasing root clearance radius. The inflow pattern in the diffuser was also distorted by leakage flow. The diffuser's overall dissipation, indirect dissipation rate on the blade surface, and indirect dissipation rate near inlet increased with increasing root clearance radius. The research could serve as a theoretical reference for the axial flow pump's root clearance design for performance improvement and operational stability.

Keywords: axial-flow pump; root clearance radius; computational fluid dynamics; entropy production; energy dissipation

1. Introduction

The axial flow pump is a high flow rate pump with a low head, usually applied in drainage and irrigation engineering [1,2]. In this pump, the fluid approaches the impeller axially and leaves but with a swirling motion resulting from the impeller rotation. To effectively improve on its performance characteristics, an adjustable blade angle has been proven to widen the operating range of the axial flow pump, with an impeller tip clearance (radial clearance between impeller rim and impeller housing) [3–5] and root clearance (radial clearance between impeller hub and impeller root) [6]. However, the pressure difference between the suction side and the blade's pressure side induces leakage flow in the tip clearance [7,8] and root clearance regions. This can generate flow blockage within the impeller passage [9,10], resulting in decreased hydraulic performance and operational stability [11–13]. In comparison, the tip clearance region is more susceptible to cavitation and clearance leakage vortices due to the large internal velocity circulation compared to the root clearance.

Laborde et al. [14] studied the effect of clearance geometry, clearance height, and the operating condition on tip vortex cavitation in an axial flow pump by visual experiment. Farrell et al. [15] built a correlation of variables to predict the vortex minimum pressure. This was validated by experimental tests and other existing data from the literature. Zhang et al. [16] analyzed tip leakage flow structure and the evolution of tip vortex based on a modified filter-based turbulence model. Wu et al. [17,18] performed the particle image velocimetry test to study the tip leakage flow structure and the formation process of tip leakage vortex in the water-jet pump. Although circumferential velocity was low, and the flow was relatively stable in the axial flow pump's root clearance, excessive root clearance would also significantly impact the hydraulic performance. If the blade root clearance were rather too small, the blade's adjustability would be affected, resulting in a reduction of the high-efficiency operation range. Considering the state of the art, the root clearance of the axial flow pump has not been extensively researched, and therefore there is the need to investigate further the flow losses and loss mechanisms in the blade root clearance of the axial flow pump.

In identifying and evaluating hydraulic loss distributions in pumps, entropy production analysis has become very popular since it can help the pump designer improve hydraulic performance. In the past, local entropy production based on empirical correlations was applicable to laminar flow problems only [19,20]. However, in 2003, Kock et al. [21,22] proposed a calculation model of local entropy production suitable for turbulent shear flows by Reynolds-averaging the entropy generation equation. The local entropy could be estimated from calculation results from Computational Fluid Dynamics (CFD) using a proposed calculation model without solving the transport equation. This method has been widely used to obtain the spatial distribution of hydraulic losses in pumps [23–25].

In this paper, the root clearance radius on energy dissipation in the axial flow pump was studied. The axial flow pump's external characteristic test was first performed at two root clearance radii (0 mm and 2.7 mm) to validate the numerical model. The theory of entropy production was then applied to the unsteady calculation results with 4 root clearance radii (0 mm, 2.7 mm, 5 mm, and 8 mm) to identify the effect of the flow rate and root clearance radius on energy losses for each hydraulic component. Finally, the loss distribution and mechanism resulting from indirect dissipation within the impeller and diffuser were analyzed, and a reference was established for root clearance design in the axial flow pump.

2. Numerical Simulation

2.1. Computational Domain

Figure 1 shows that the axial flow pump model consists of an elbow inflow runner, an axial flow impeller, a diffuser, and an outflow runner. In this paper, the pump performance, and four kinds of root clearance radius (0 mm, 2.7 mm, 5 mm, 8 mm) of impeller were designed. The main design and geometry parameters of the pump model are shown in Table 1, and the specific speed was calculated based on Equation (1) [26]:

$$n_s = \frac{3.65nQ_{des}^{0.5}}{H_{des}^{0.75}} \quad (1)$$

where n_s and n stand for the specific speed and shaft rotational speed, respectively, Q_{des} presents the design volume flow rate, and H_{des} is the design pump head.

In order to precisely analyze the detailed flow loss distributions within the gap position, ANSYS ICEM was used to generate high-quality structural hexahedral grids for the inflow runner, impeller, and outflow runner. Turbogrid was used to generate grids of the diffuser automatically. Figure 2 presents the mesh of the calculation domain. The average Y^+ of impeller and diffuser were 10.1 and 10.9, respectively. For the inflow runner and outflow runner, the average Y^+ values were 5.0 and 15.4, respectively. In ensuring the simulation's speed and accuracy, a grid independence analysis of the pump was conducted in Figure 3. When the total number of grid nodes of pump exceeded 5.6 million, the calculation results were seen to be stable, and the relative error of the efficiency was

within 0.15%. Therefore, to ensure the calculation accuracy and save calculation resources, the number of grid nodes of inflow runner, impeller, guide vane, and outflow runner was finally controlled at 1.8 million, 1.2 million, 1.5 million, and 1.5 million, respectively.

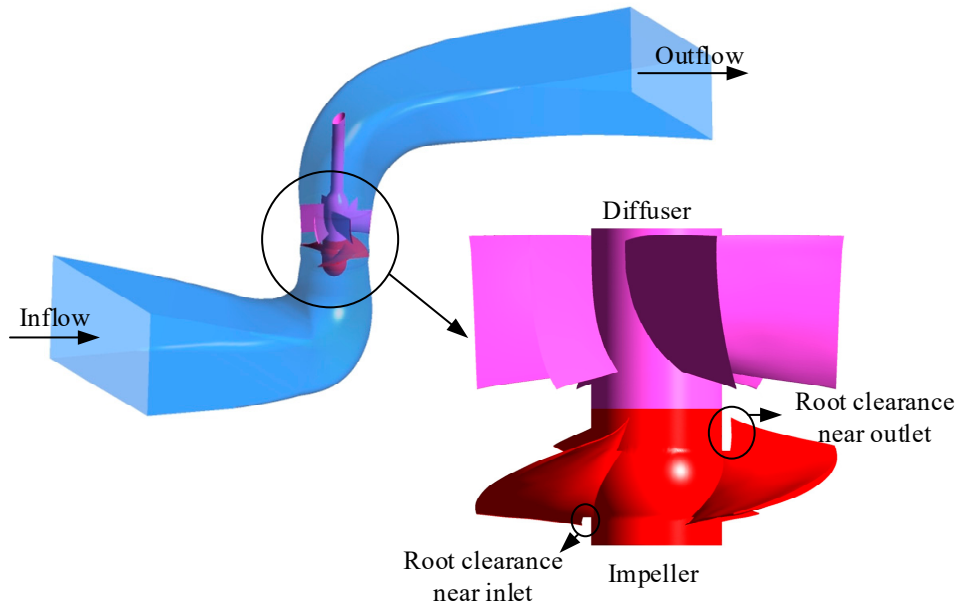
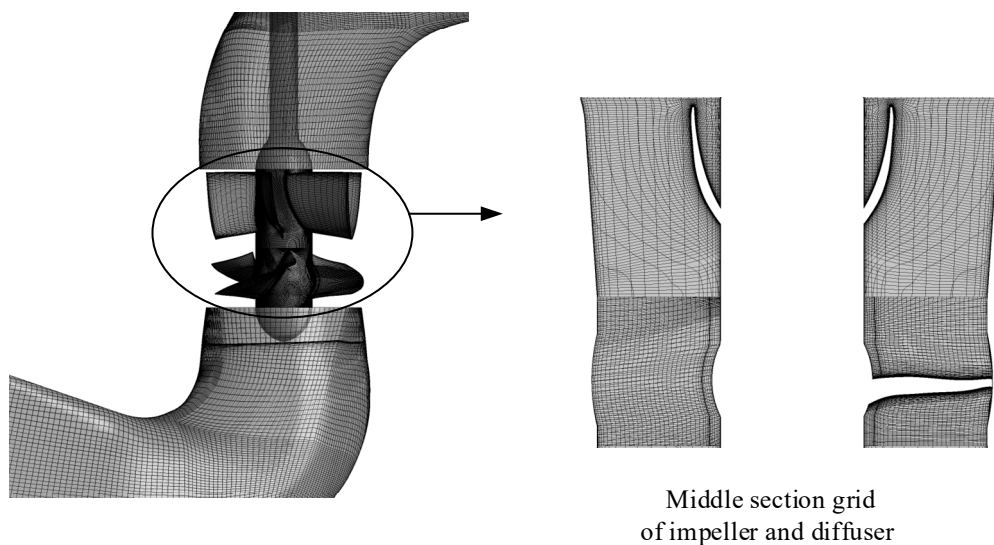


Figure 1. 3D model of the axial flow pump device.

Table 1. Main parameters of the axial flow pump device.

Design Parameters (CFD Results Under R_t of 0 mm)			
design flow rate (m^3/s)	0.308	Rotational speed (r/min)	1340
Design head (m)	4.44	Specific speed	887.4
Geometry Parameters			
Impeller blade number	3	Diffuser blade number	6
Impeller diameter (mm)	300	Outlet diameter of diffuser (mm)	312.8
Tip clearance (mm)	0.3	Root clearance radius (mm)	0/2.7/5/8



Middle section grid of impeller and diffuser

Figure 2. Mesh of axial flow pump device.

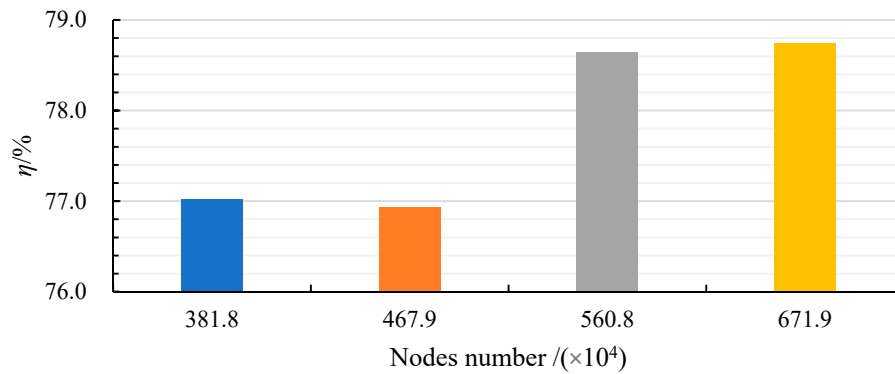


Figure 3. Grid independence of pump device without root clearance.

2.2. Boundary Condition

In this study, 25 °C was chosen as the temperature of the working fluid. The governing equation was Reynolds Averaged Navier–Stokes (RANS) equation, which is defined as follows:

$$\frac{\partial \bar{v}_j}{\partial x_j} = 0 \quad (2)$$

$$\frac{\partial(\rho \bar{v}_i)}{\partial t} + \frac{\partial(\rho \bar{v}_i \bar{v}_j)}{\partial x_j} = -\frac{\partial \bar{p}}{\partial x_i} + \frac{\partial}{\partial x_j} \left(\mu \frac{\partial \bar{v}_i}{\partial x_j} - \overline{\rho v'_i v'_j} \right) + \rho f_i \quad (3)$$

where i and j stand for cartesian direction; $\frac{\partial \bar{v}_j}{\partial x_j} = 0$ and \bar{p} present the time-average speed and time-average pressure, respectively; ρ and μ stand for the fluid density and the dynamic viscosity. $\overline{\rho v'_i v'_j}$ is the Reynolds stress and ρf_i is the source item.

The SST k - ω turbulence model [27,28] was used to enclose the Equation. It was a Baseline (BSL) k - ω model with a limiter to the formulation of eddy-viscosity. The Baseline (BSL) k - ω model can be described as follows:

$$\frac{\partial(\rho k)}{\partial t} + \frac{\partial(\rho v_j k)}{\partial x_j} = \frac{\partial}{\partial x_j} \left[\left(\mu + \frac{\mu_t}{\sigma_{k3}} \right) \frac{\partial k}{\partial x_j} \right] + P_k - \beta' \rho k \omega + P_{kb} \quad (4)$$

$$\frac{\partial(\rho \omega)}{\partial t} + \frac{\partial(\rho v_j \omega)}{\partial x_j} = \frac{\partial}{\partial x_j} \left[\left(\mu + \frac{\mu_t}{\sigma_{\omega 3}} \right) \frac{\partial \omega}{\partial x_j} \right] + 2\rho(1 - F_1) \frac{1}{\sigma_{\omega 2} \omega} \frac{\partial k}{\partial x_j} \frac{\partial \omega}{\partial x_j} + \alpha_3 \frac{\omega}{k} P_k - \beta_3 \rho \omega^2 + P_{\omega b} \quad (5)$$

The coefficient σ_{k3} is a linear combination of σ_{k1} and σ_{k2} ; $\sigma_{\omega 3}$ is a linear combination of $\sigma_{\omega 1}$ and $\sigma_{\omega 2}$; α_3 is a linear combination of α_1 and α_2 ; β_3 is a linear combination of β_1 and β_2 . P_{kb} and $P_{\omega b}$ are buoyancy production terms; μ_t is turbulence viscosity.

The calculation method of linear combination is as follows:

$$\Phi_3 = F_1 \Phi_1 + (1 - F_1) \Phi_2 \quad (6)$$

where $\sigma_{k1} = 1.176$, $\sigma_{\omega 1} = 2$, $\beta_1 = 0.075$, $\alpha_1 = 5/9$, $\beta_1 = 0.09$, $\sigma_{k2} = 1$, $\sigma_{\omega 2} = 1/0.856$, $\alpha_2 = 0.44$, $\beta_2 = 0.0828$. The F_1 is a blending function of the wall distance, the value of which is 1 near the wall and decreases to 0 outside the boundary layer.

In order to improve the prediction accuracy of k - ω model for 3D flows, the shear stress transfer model (SST) should be applied to limit the formulation of eddy-viscosity.

$$v_t = \frac{\alpha_1 k}{\max(\alpha_1 \omega, SF_2)} \quad (7)$$

$$v_t = \frac{\mu t}{\rho} \quad (8)$$

where F_2 is a blending function similar to F_1 .

Inlet and outlet boundary conditions were set as “Mass flow rate” and “Opening”, respectively. The reference pressure was 1 atm, and the outlet relative pressure was 0 atm. The no-slip wall and automatic wall function [29] was adopted as the wall condition for each hydraulic component. In addition, the roughness of the impeller and diffuser was set as 0.0125 mm, and that of the inflow runner and outflow runner was set as 0.05 mm.

Five flow conditions, $0.8 Q_{des}$, $0.9 Q_{des}$, $1.0 Q_{des}$, $1.1 Q_{des}$ and $1.2 Q_{des}$ were analyzed based on unsteady calculation. The time step and total time were set as 0.000373134s and 0.447761s, respectively. The interface condition between rotor and stator was set as “Transient rotor stator” [30], and the interface condition between stators was set as “None”. In each time step, when the residual value of convergence was less than 5×10^{-5} or the number of iteration steps reached 10, the calculation would stop. In addition, the advection scheme and transient scheme were set as “Upwind” and “second order Backward Euler.”

2.3. Entropy Production Theory

The entropy production model’s derivation was based on the entropy transport equation (Equation (9)), which was applied to the single-phase incompressible fluid [27].

$$\rho \left(\frac{\partial s}{\partial t} + v_1 \frac{\partial s}{\partial x} + v_2 \frac{\partial s}{\partial y} + v_3 \frac{\partial s}{\partial z} \right) = \text{div} \left(\frac{\vec{q}}{T} \right) + \frac{\phi}{T} + \frac{\phi_\theta}{T^2} \quad (9)$$

where s is the specific entropy; v_1, v_2, v_3 are the velocity components in Cartesian direction: x, y, z ; T is the temperature. $\text{div} \left(\frac{\vec{q}}{T} \right)$ stands for reversible heat transfer term. $\frac{\phi_\theta}{T^2}$ and $\frac{\phi}{T}$ present the entropy production by heat transfer and the entropy production by dissipation.

An isothermal heat transfer rate was set to render the system into a thermal equilibrium state. Hence, $\frac{\phi_\theta}{T^2}$ and $\text{div} \left(\frac{\vec{q}}{T} \right)$ were neglected.

Because all calculated results were based on RANS equation. $\frac{\phi}{T}$ should be time-averaged. $\overline{\left(\frac{\phi}{T} \right)}$ can be divided into the entropy production by direct dissipation $\frac{\phi_D}{T}$ and entropy production by indirect dissipation $\frac{\phi_I}{T}$. $\frac{\phi_D}{T}$ and $\frac{\phi_I}{T}$ are defined as follows.

$$\overline{\left(\frac{\phi_D}{T} \right)} = \frac{\mu}{T} \cdot \left[2 \left\{ \left(\frac{\partial \bar{v}_1}{\partial x} \right)^2 + \left(\frac{\partial \bar{v}_2}{\partial y} \right)^2 + \left(\frac{\partial \bar{v}_3}{\partial z} \right)^2 \right\} + \left(\frac{\partial \bar{v}_1}{\partial y} + \frac{\partial \bar{v}_2}{\partial x} \right)^2 + \left(\frac{\partial \bar{v}_3}{\partial x} + \frac{\partial \bar{v}_1}{\partial z} \right)^2 + \left(\frac{\partial \bar{v}_2}{\partial z} + \frac{\partial \bar{v}_3}{\partial y} \right)^2 \right] \quad (10)$$

$$\overline{\left(\frac{\phi_I}{T} \right)} = \frac{\mu}{T} \cdot \left[2 \left\{ \overline{\left(\frac{\partial v'_1}{\partial x} \right)^2} + \overline{\left(\frac{\partial v'_2}{\partial y} \right)^2} + \overline{\left(\frac{\partial v'_3}{\partial z} \right)^2} \right\} + \overline{\left(\frac{\partial v'_1}{\partial y} + \frac{\partial v'_2}{\partial x} \right)^2} + \overline{\left(\frac{\partial v'_3}{\partial x} + \frac{\partial v'_1}{\partial z} \right)^2} + \overline{\left(\frac{\partial v'_2}{\partial z} + \frac{\partial v'_3}{\partial y} \right)^2} \right] \quad (11)$$

where $\bar{v}_1, \bar{v}_2, \bar{v}_3$ are time-average velocity; v'_1, v'_2, v'_3 are instantaneous velocity fluctuation.

Because the v'_1, v'_2, v'_3 cannot be obtained when solving the RANS equation, Kock et al. [22] proposes another method and the $\frac{\phi_I}{T}$ can be calculated as follows:

$$\frac{\phi_I}{T} = \frac{\rho \varepsilon}{T} \quad (12)$$

The overall dissipation of each hydraulic component can be obtained by integrating the dissipation rate over the whole fluid-producing domain as follows:

$$P_D = \int_V \phi_D dV \quad (13)$$

$$P_I = \int_V \phi_I dV \quad (14)$$

where P_D represents direct power loss, and P_I represents indirect power loss.

3. Test Measurement

3.1. Test Equipment

The closed test bench adopted a double-floor vertical structure, as shown in Figure 4. The flow meter was located on the -2.6 m floor, and the pressure transducers and torque meter were located on the 4.2 m floor. The basic parameters of test equipment are shown in Table 2. In addition, the flowmeter was arranged horizontally, and the length of straight pipes was greater than five times the pipe diameter. The test measuring point of the head was located on the inlet and outlet water tank.

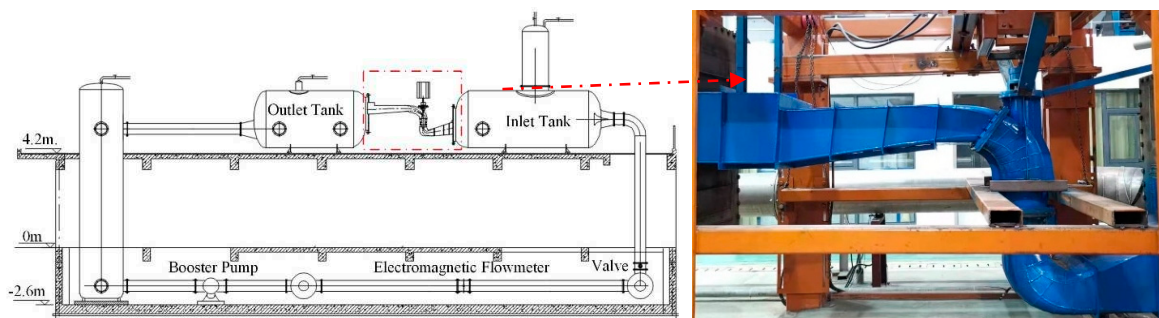


Figure 4. Photo of the axial flow pump device.

Table 2. Basic parameters of test equipment.

Equipment name	Instrument Model	Measuring Range	Measurement Uncertainty
Intelligent electromagnetic flowmeter	OPTIFLUX2000F	0 ~ 1800 m ³ /h	≤±0.2%
Smart differential pressure transmitter	EJA	0 ~ 10 m	≤±0.1%
Intelligent torque speed sensor	JCL1	0 ~ 200 N·m	≤±0.1%

3.2. Test Validation

Figure 5 shows the external characteristic test results of an axial flow pump with two different root clearance radii (0 mm and 2.7 mm). The hydraulic efficiency and head were defined as follows:

$$\eta = \frac{(P_{out} - P_{in})Q}{P_m} \quad (15)$$

$$H = \frac{P_{out} - P_{in}}{\rho g} \quad (16)$$

where P_{out} and P_{in} present the total pressure at the outlet of outflow runner and inlet of inflow runner, respectively. P_m stand for the motor input power, ρ and g are the fluid density and gravitational acceleration.

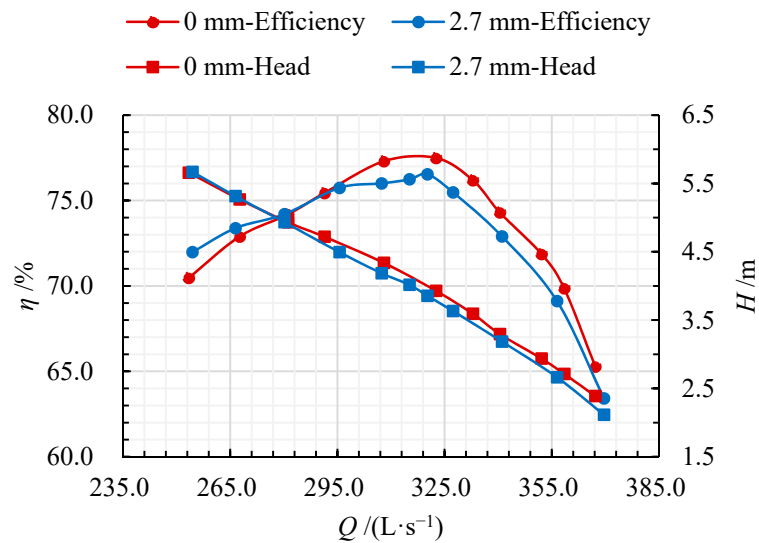


Figure 5. Comparison of simulated pump performance under different root clearance radii.

For the pump with a root clearance of 2.7 mm, the pump head was lower than that without root clearance under all flow rates, and the drop of performance parameters caused by root clearance increased with increasing flow rate. Under the part-load condition, the pump efficiency with 2.7 mm root clearance was slightly higher than that without root clearance, but the pump efficiency with 2.7 mm root clearance was significantly lower than that without root clearance under design condition and over-load condition. The experimental (EXP) results proved that the root clearance radius has a significant influence on hydraulic pump performance.

In order to verify the accuracy of numerical simulation, the experiment data with a root clearance of 0 mm was compared with calculated results in Figure 6. Under part-load flow rates, the simulated head and efficiency were lower than test data, but the simulated head and efficiency were higher than experiment data under design and over-load flow conditions. In addition, the maximum relative deviation between the measured results and the calculated data was less than 3% under the design flow rate. This shows that the numerical simulation results could accurately predict the pump's internal flow characteristics, and the numerical simulation results are reliable.

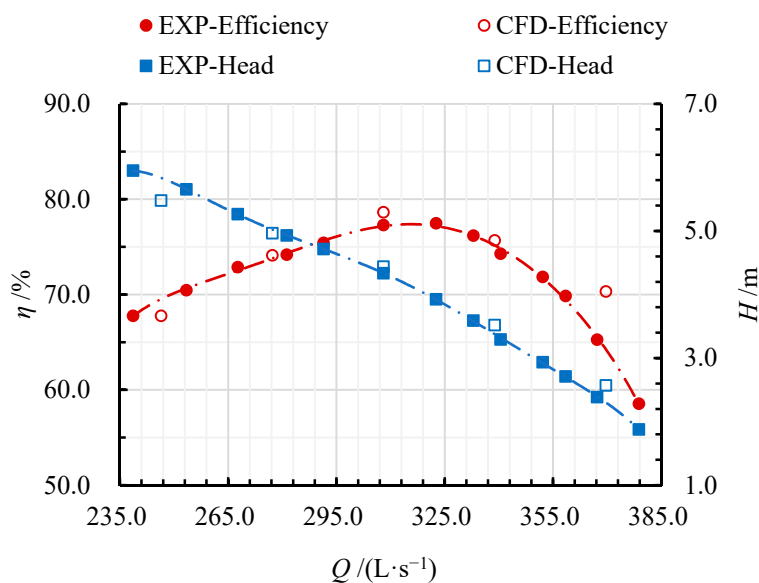


Figure 6. Comparison of pump performance between simulated data and test results ($R_t = 0$ mm).

4. Analysis of Calculation Results

4.1. Comparison of Pump Performance

Figure 7 shows the hydraulic performance of the pump under different root clearance radii. As shown in Figure 7a, the hydraulic efficiency under $0.8 Q_{des}$ did not fluctuate obviously with the increase of root clearance radius. However, the hydraulic efficiency under $1.0 Q_{des}$ and $1.2 Q_{des}$ decreased with increasing root clearance radius, and the maximum drop in efficiency was 2.5% and 6.8% at $1.0 Q_{des}$ and $1.2 Q_{des}$, respectively. In Figure 7b, the pump head decreased with increasing root clearance radius under all flow conditions, while a head drop of 2.6%, 5.6%, and 15.5% occurred at $0.8 Q_{des}$, $1.0 Q_{des}$, and $1.2 Q_{des}$, respectively. In conclusion, under $0.8 Q_{des}$, the root clearance radius had no significant effect on the hydraulic performance of the axial flow pump device, but under $1.0 Q_{des}$ and $1.2 Q_{des}$, the hydraulic performance decreased significantly as the root clearance radius increased. This was consistent with the test results above.

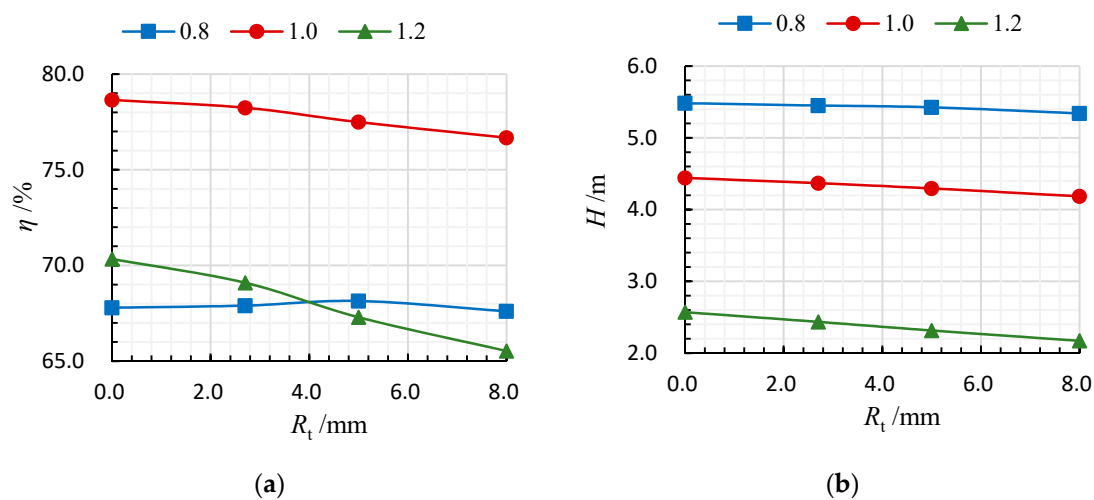


Figure 7. Comparison of simulated (a) hydraulic efficiency and (b) head under different root clearance radii.

To illustrate why the hydraulic performance decreased with increasing root clearance radius, the entropy production theory was applied to the unsteady calculated results to analyze the additional energy losses caused by leakage flow in root clearance. Firstly, each hydraulic component's overall dissipation without root clearance under different flow rates was shown in Figure 8. Figure 8a shows the distribution of overall indirect dissipation P_I . Due to the small rotational kinetic energy inside the inflow runner, the P_I of this component was much lower than that of other hydraulic components. In addition, the P_I of impeller and outflow runner was minimal near the design condition, and that of diffuser decreased with flow rate was increasing. Figure 8b shows the distribution of overall direct dissipation P_D . As shown in the figure, the P_D of the impeller was significantly higher than that of other hydraulic components, the effect of the flow rate had little influence on the P_D . Compared with P_I , the P_D was so small that could be ignored, so the following section only analyzed the distribution of P_I in axial flow pump.

Figure 9 shows the P_I of four hydraulic components with four root clearance radii at $1.0 Q_{des}$. As shown in the figure, the P_I of each hydraulic component from high to low is as follows: impeller, outflow runner, diffuser, and inflow runner. The effect of root clearance radius on P_I in inflow runner was not obvious, and that of other hydraulic components increased with root clearance radius increasing, which explained why the hydraulic performance decreased with increasing root clearance radius. In addition, the maximum increases in P_I in the impeller, diffuser, and outflow runner caused by the increase of root clearance radius were 3%, 5%, and 8%, respectively.

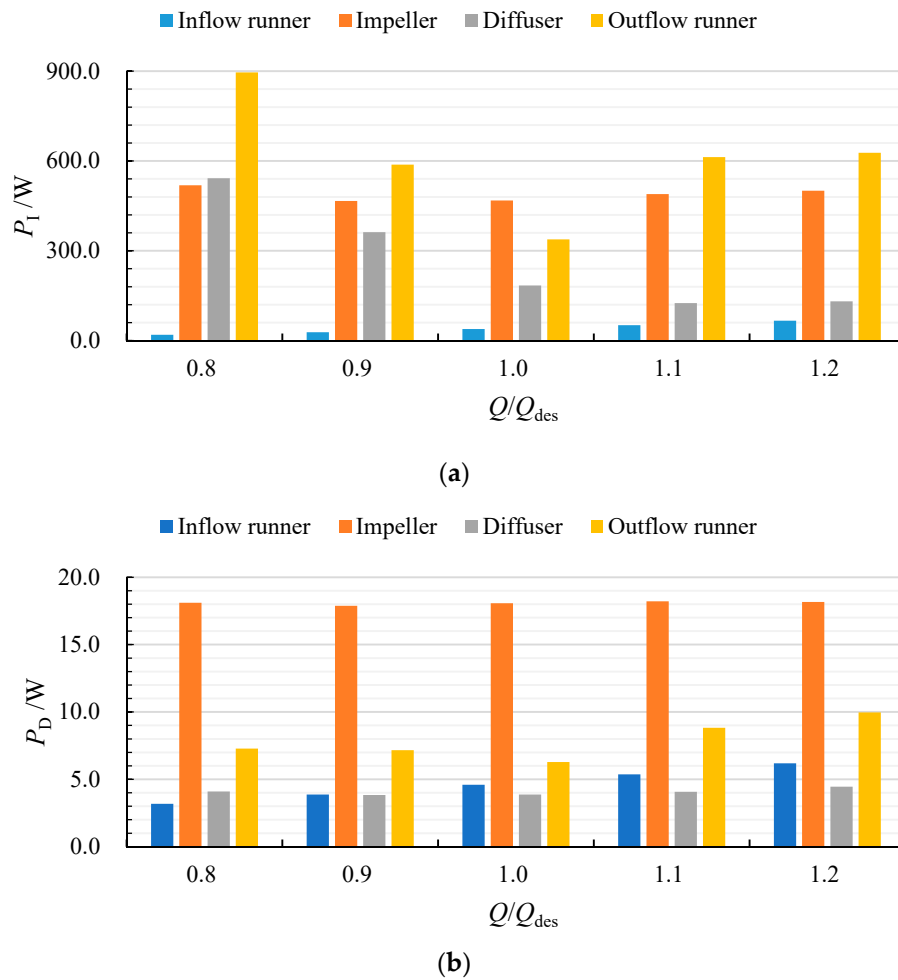


Figure 8. Distribution of (a) power loss due to indirect dissipation and (b) power loss due to direct dissipation of different hydraulic components without root clearance under five flow rates.

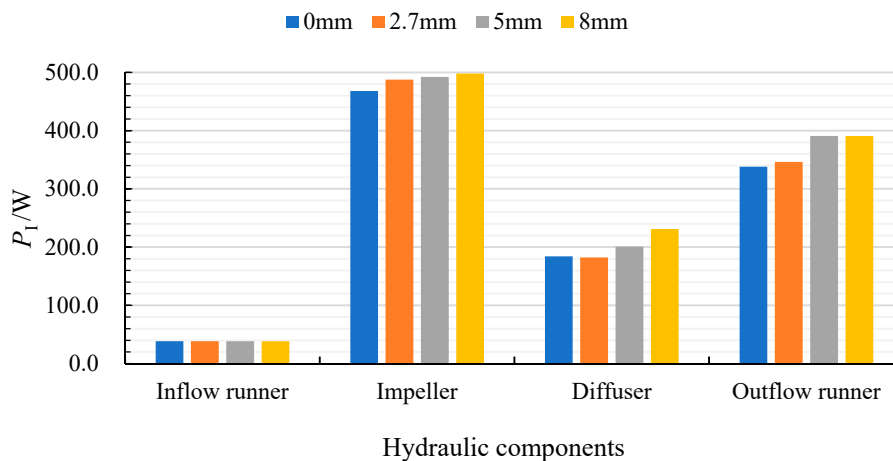


Figure 9. Distribution of power loss due to indirect dissipation at $1.0 Q_{des}$ for varying root clearances ($R_t = 0$ mm, 2.7 mm, 5 mm, 8 mm).

4.2. Analysis of Inner Flow Dissipation

To understand the reason for the rise in overall dissipation with increasing root clearance radius, the internal velocity distribution and indirect dissipation rate within the impeller passage and diffuser

passage were analyzed under different root clearance radii. Figure 10 shows the cylindrical cross-section for the impeller and diffuser at a specific blade height position *Span*, which is defined as follow:

$$\text{Span} = (r - r_h) / (r_t - r_h) \quad (17)$$

where, *r* is the calculated ring radius, *r_h* and *r_t* are the the hub radius and radius of the impeller rim.

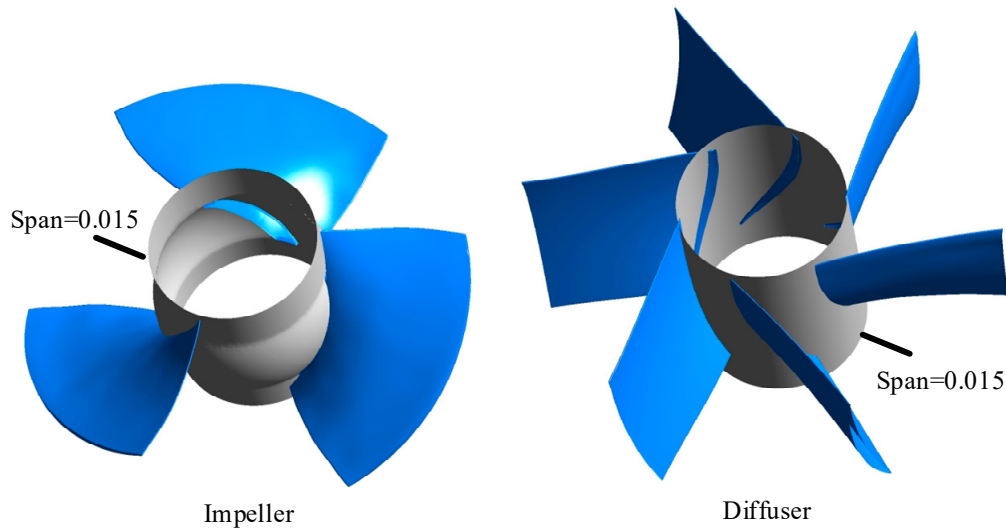


Figure 10. The cylindrical cross-section for impeller and diffuser.

Figure 11 shows the distribution of the relative velocity vector within the cross-section of the impeller passage with *Span* = 0.015 at 1.0 *Q_{des}*. In the impeller passage without root clearance, the inlet angle matched the inlet edge of the blade better, and the fluid moved closer to the blade profile. There was only a small range of backflow at the trailing edge of the blade. The pressure difference between the pressure side and the blade's suction side causes the leakage flow to appear in the blade root clearance. In addition, the collision between the root leakage flow and the main flow leads to the deviation of the flow direction near the impeller inlet and outlet to the circumferential direction. The degree of deviation for the flow direction increased with the increasing root clearance radius.

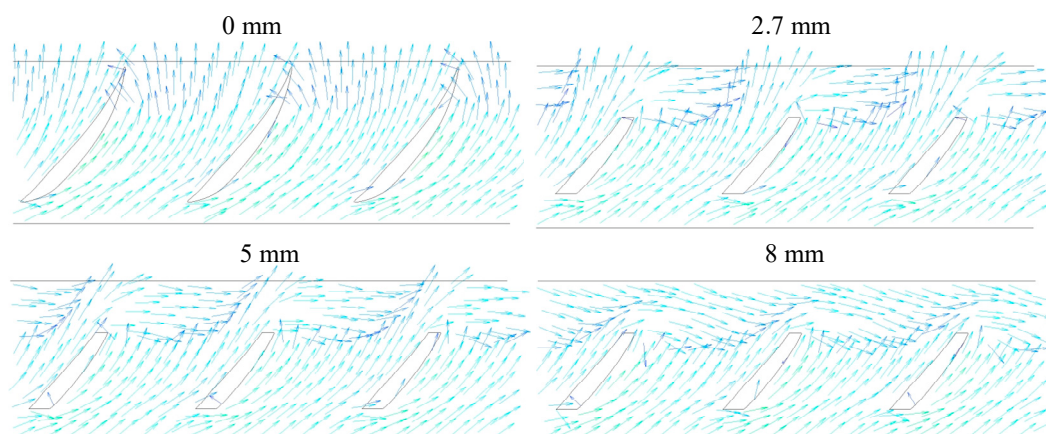


Figure 11. Distribution of velocity vector at *Span* = 0.015 in impeller passage with varying root clearances (*R_t* = 0 mm, 2.7 mm, 5 mm 8 mm; *Q* = 1.0 *Q_{des}*).

Figure 12 shows the relative velocity distribution in the cross-section of the impeller passage at *Span* = 0.015 under 1.0 *Q_{des}*. In the impeller passage without root clearance, the low velocity caused by the wake vortex can be found near the trailing edge of the suction side, and the high velocity was

obtained near the leading edge of the blade suction side. In the passage with root clearance, the low velocity near the trailing edge of the suction side was offset horizontally, causing leakage flow, thereby reducing the high-velocity area near the trailing edge of the suction side.

Figure 13 shows the distribution of indirect dissipation rate in the cross-section of impeller passage at Span = 0.015 under $1.0 Q_{des}$. In impeller passage without root clearance, the dissipation rate near the blade's trailing edge was higher due to the wake vortex, but there was no obvious high dissipation region. When the blade root clearance appeared in the impeller passage, a high dissipation region appeared near the trailing edge of the blade due to the impact of the leakage flow and the mainstream flow. The larger the clearance radius is, the greater the leakage velocity, resulting in a more obvious flow instability. Therefore, the area of the high dissipation region near the trailing edge of the blade increases with increasing root clearance radius.

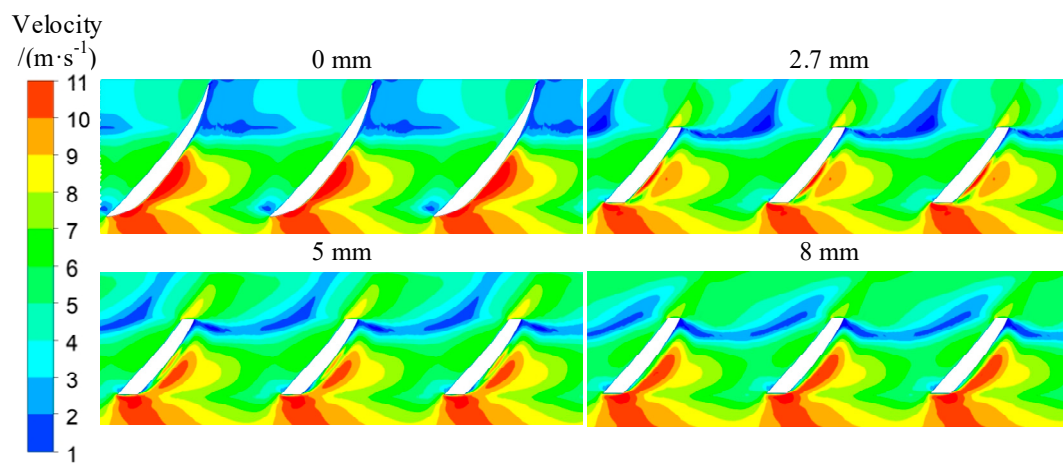


Figure 12. Velocity contour at Span = 0.015 in impeller passage with varying root clearances ($R_t = 0$ mm, 2.7 mm, 5 mm 8 mm; $Q = 1.0 Q_{des}$).

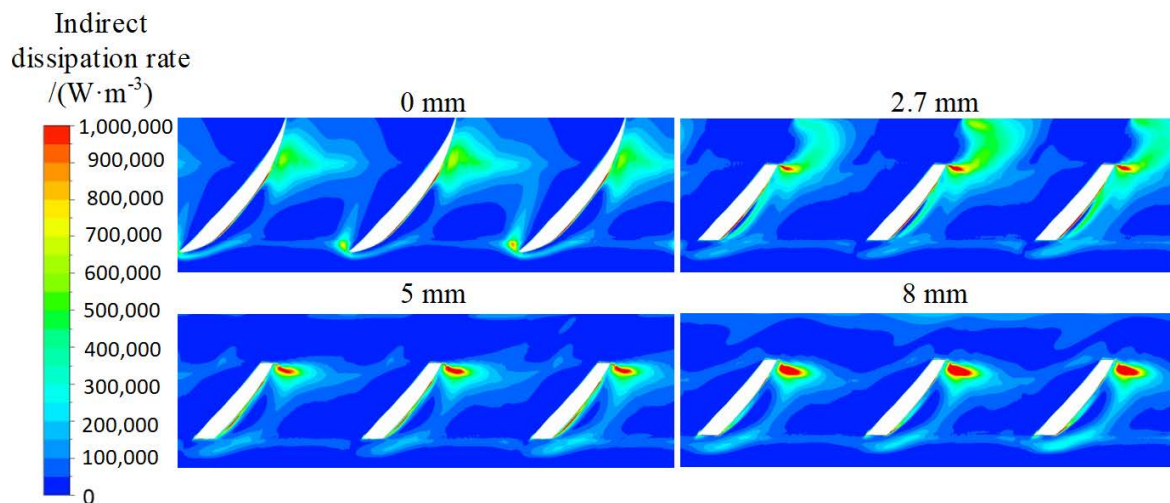


Figure 13. Distribution of the indirect dissipation rate at Span = 0.015 in the impeller passage with varying root clearances ($R_t = 0$ mm, 2.7 mm, 5 mm 8 mm; $Q = 1.0 Q_{des}$).

The standard deviation of relative velocity represents the fluctuation and stability of velocity in the last period. It was defined as:

$$\bar{V} = \frac{1}{N} \sum_{i=1}^N V_i \quad (18)$$

$$V_{sd} = \sqrt{\frac{\sum_{i=1}^N (V_i - \bar{V})^2}{N}} \quad (19)$$

where V_i is the velocity at every time step; \bar{V} is the average velocity in a single rotation cycle; V_{sd} is the standard deviation velocity in a single rotation cycle; N represents the sampling times of velocity data in a single rotation cycle.

Figure 14 shows the standard deviation of the velocity distribution within the impeller passage with four root clearance radii at $\text{Span} = 0.015$. In the impeller passage without root clearance, the internal flow field was relatively stable, and there was no high fluctuation intensity of velocity. In the impeller passage with 2.7 mm root clearance, the velocity fluctuation near the impeller outlet became stronger due to the influence of leakage flow in root clearance. When the root clearance continued to increase, the velocity fluctuation intensity in the blade passage decreased gradually, while the velocity fluctuation intensity at the impeller outlet increased. This result shows that the leakage flow in root clearance leads to the enhancement of rotor-stator interaction between the impeller and diffuser and worsens the diffuser's inflow condition.

Figure 15 shows the distribution of the velocity vectors in the guide vane passage with four root clearance radii. After passing through the impeller, the fluid generated a large amount of rotational kinetic energy, which caused some flow separation near the leading edge of the guide vane since the inlet angle of the guide vane was large. Furthermore, the inflow direction was obviously affected by the clearance radius of the blade root. The guide vane's inlet angle gradually deviated to the horizontal direction with increasing blade root clearance radius, which could affect the flow of the fluid between the guide vanes. The flow pattern inside the guide vane was expected to deteriorate with the increase of the root clearance radius, particularly at 5 and 8 mm, where an obvious backflow phenomenon at the inlet of the guide vane occurs.

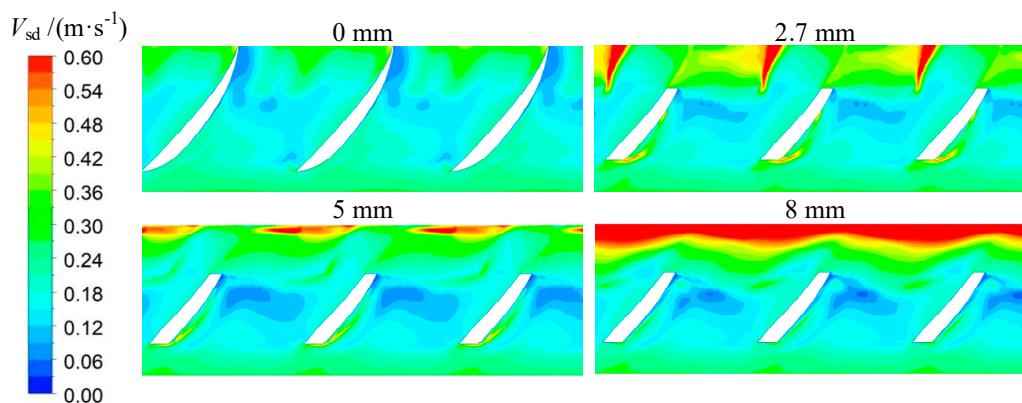


Figure 14. Standard deviation of the velocity distribution at $\text{Span} = 0.015$ in the impeller passage with varying root clearances ($R_t = 0 \text{ mm}, 2.7 \text{ mm}, 5 \text{ mm}, 8 \text{ mm}; Q = 1.0 Q_{des}$).

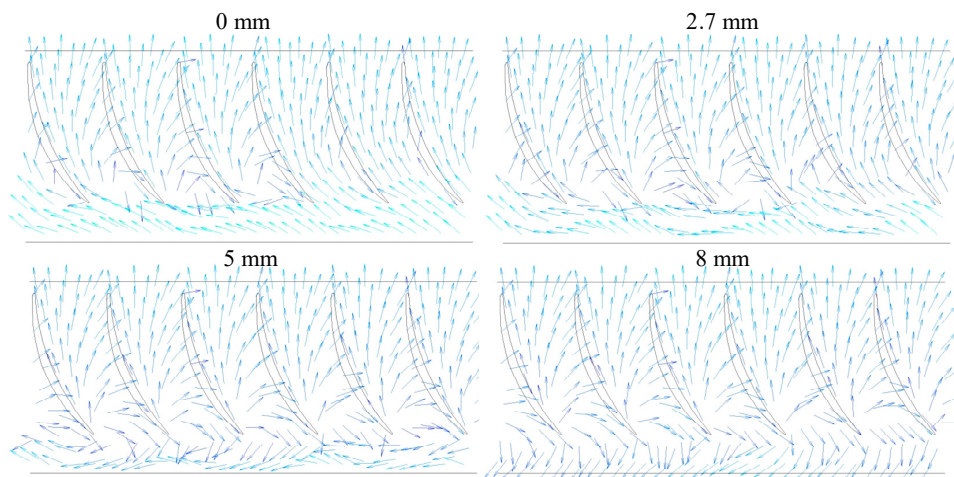


Figure 15. Velocity vectors at Span = 0.015 in guide vane passage with varying root clearances ($R_t = 0$ mm, 2.7 mm, 5 mm 8 mm; $Q = 1.0 Q_{des}$).

Figure 16 shows the distribution of indirect dissipation rate at Span = 0.015 in the diffuser passage at $1.0 Q_{des}$. When there is no root clearance in the diffuser passage, a high indirect dissipation rate occurred at the leading edge of the suction side as a result of flow separation. The backflow near the diffuser inlet could hinder the inlet flow of the guide vane into the blade passage, and the recirculation area near the diffuser inlet gradually increases with increasing root clearance. So, the indirect dissipation rate near the leading edge of the suction side and diffuser inlet decreased and increased with root clearance increasing, respectively.

Figure 17 shows the distribution of indirect dissipation rate on the surface of the diffuser blades at $1.0 Q_{des}$. At the diffuser inlet, the blade surface's indirect dissipation rate gradually decreased from the leading edge of the blade towards the trailing edge, as shown in Figure 17a. Particularly near the hub, the indirect dissipation rate of the blade surface was very high. Since the leakage flow in the blade root clearance would worsen the inflow condition of the guide vane, thereby affecting the stability of the flow field in the guide vane channel, the area of the high dissipation zone near the hub is increased with increasing blade root clearance radius. For the diffuser outlet, the blade surface's overall indirect dissipation rate was low, and the indirect dissipation rate gradually decreased from the leading edge to the trailing edge, as shown in Figure 17b. In addition, the indirect dissipation rate near the guide vane hub was also low, and only a small area of high dissipation rate existed near the leading edge.

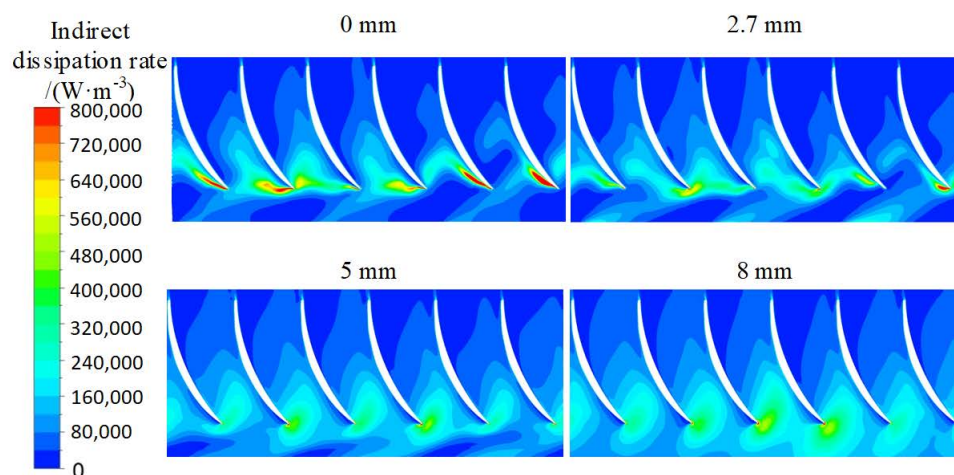


Figure 16. Indirect dissipation rate at Span = 0.015 in guide vane passage with varying root clearances ($R_t = 0$ mm, 2.7 mm, 5 mm 8 mm; $Q = 1.0 Q_{des}$).

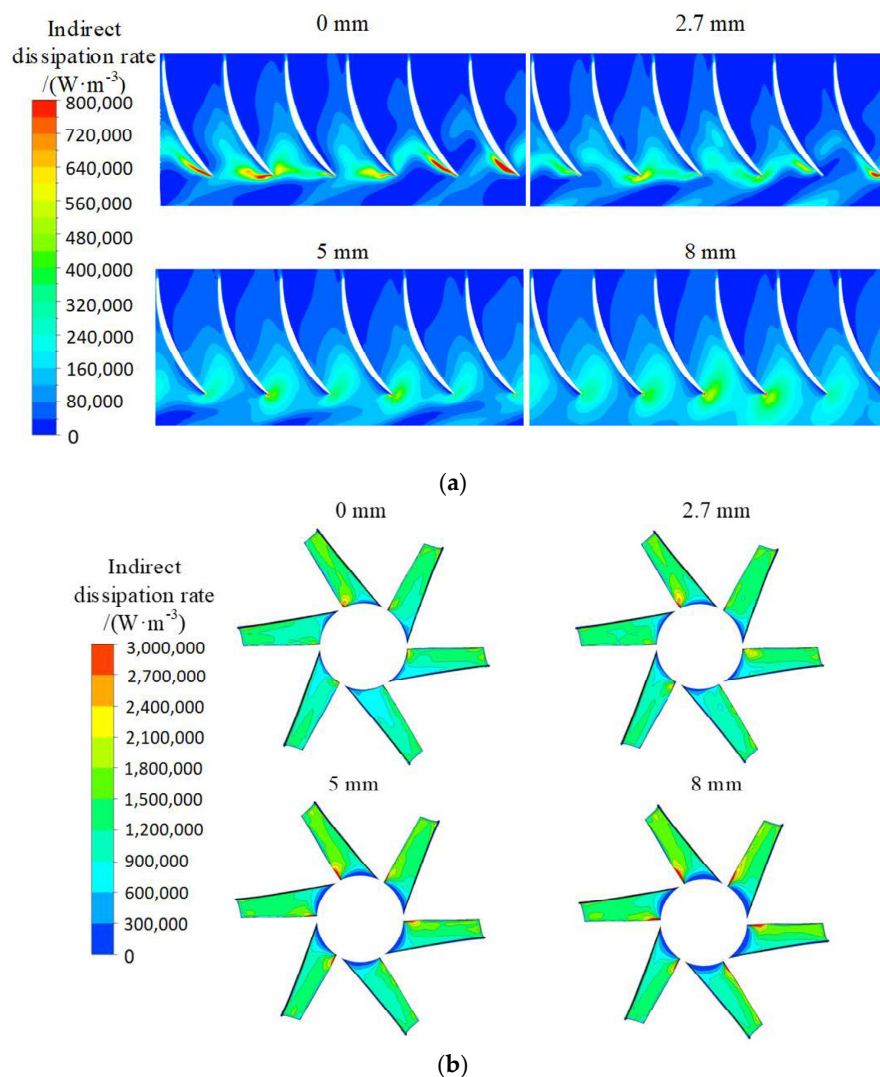


Figure 17. Distribution of indirect dissipation rate (a) from diffuser inlet and (b) from diffuser outlet on the surface of diffuser blades with varying root clearances ($R_t = 0 \text{ mm}, 2.7 \text{ mm}, 5 \text{ mm}, 8 \text{ mm}; Q = 1.0 Q_{des}$).

5. Conclusions

In this paper, the unsteady internal flow state of the axial flow pump under four root clearance radii (0 mm, 2.7 mm, 5 mm, 8 mm) was calculated to establish the influence of root clearance radius on hydraulic performance. The external characteristics test of an axial flow pump with root clearance radii 0 mm and 2.7 mm was completed to verify the numerical simulation method's reliability. In addition, the entropy production theory was adopted to determine the turbulence dissipation distribution within the flow domain in the axial flow pump. These conclusions were drawn to provide a reference for mixed flow pumps with similar specific speed:

In the axial flow pump, both the hydraulic efficiency and head decreased with root clearance radius increasing, and the decline magnitude rose with increasing flow rate. At $0.8 Q_{des}$, the effect of root clearance on hydraulic efficiency and the head was not obvious. With an increase in flow rate, the effect of root clearance became obvious. The maximum reductions in the head and hydraulic efficiency were 15.5% and 6.8%, with the root clearance of 8 mm at $1.2 Q_{des}$, respectively.

- (1) The overall direct dissipation P_D of each hydraulic component was negligible, compared with overall indirect dissipation P_I . In addition, the P_I of the inflow runner was much lower than that of the impeller, outflow runner, and diffuser. The P_I of outflow runner decreased with

decreasing flow rate, whereas that of impeller and diffuser reach a minimum value at $0.9 Q_{des}$ and $1.1 Q_{des}$, respectively.

- (2) Driven by the pressure difference on the blade surface, the leakage flow in the root clearance led to the distortion of the flow pattern in the impeller, and the impeller-diffuser interaction became stronger. The indirect dissipation rate near the trailing edge of the blade and the P_1 of the impeller increased with increasing root clearance.
- (3) The flow pattern inside the diffuser was unsteady due to deterioration of inflow conditions caused by leakage flow from the root clearance. Therefore, both the indirect dissipation rate at the leading edge of the blade and near inlet and P_1 of the diffuser increased with increasing root clearance radius.
- (4) The hydraulic losses increased with increasing root clearance. However, if the root clearance is too small, the range of blade adjustment will be reduced, thereby narrowing the high-efficiency region range. The research results can reference the axial flow pump's root clearance design and help designers find a balance point between the range of blade adjustment and hydraulic performance.

Author Contributions: Conceptualization, Y.L., and F.M.; data curation, Y.L., and Y.Z.; methodology, Y.L., and Y.Z.; project administration, Y.L., and F.M.; supervision, Y.L.; validation, F.M.; Writing—original draft, Y.L.; Writing—review & editing, Y.Z., and M.K.O. All authors have read and agreed to the published version of the manuscript.

Funding: This research was supported by the Science and Technology Plan of Wuhan (Grant No.2018060403011350).

Acknowledgments: The authors sincerely thank the Science and Technology Plan of Wuhan.

Conflicts of Interest: The authors declare no conflict of interest.

Nomenclature

Q . (m ³ /s)	Flow rate
Q_{des} . (m ³ /s)	Design flow rate
H . (m)	Head of axial flow pump device
H_{des} . (m ³ /s)	Design head of axial flow pump device
η . (%)	Efficiency of axial flow pump device
η_{des} . (%)	Design efficiency of axial flow pump device
n . (r/min)	Rotating speed
n_s (°)	Specific speed of axial flow pump device
V_{sd} (m/s)	Standard deviation of relative velocity
T (K)	Temperature
P_m (W)	Motor input power
ρ (kg/m ³)	Water density
ε	Dissipation rate of turbulence energy
\bar{v}_1 (m/s)	Average velocity component in x direction
\bar{v}_2 (m/s)	Average velocity component in y direction
\bar{v}_3 (m/s)	Average velocity component in z direction
v'_1 (m/s)	Velocity fluctuation component in x direction
v'_2 (m/s)	Velocity fluctuation component in y direction
v'_3 (m/s)	Velocity fluctuation component in z direction
S [J/(K·kg)]	Specific entropy
P_D (W)	Direct power loss
P_1 (W)	Indirect power loss
R_t (mm)	Root clearance radius
\bar{V} (m/s)	Average velocity of the node in a single rotation cycle
r_h (mm)	Hub radius
r_t (mm)	Impeller rim radius
3D	Three-Dimensional
RANS	Reynolds Averaged Navier–Stokes
CFD	Computational Fluid Dynamics
EXP	Experiment

References

1. Yang, F.; Chen, S.; Liu, C.; Wang, M.; Zhou, J. Influence of division pier on pressure fluctuation and internal flow pattern in outlet conduit of axial-flow pumping system. *Trans. Chin. Soc. Agric. Mach.* **2018**, *49*, 212–217. (In Chinese)
2. Song, X.; Liu, C.; Luo, C. Influence of inlet vortex on pressure pulsation in axial flow pump unit. *Trans. Chin. Soc. Agric. Mach.* **2018**, *49*, 212–217. (In Chinese)
3. Li, C.; Ke, T.; Zhang, J.; Zhang, H.; Huang, W. Experimental and Numerical Investigation of the Unsteady Tip Leakage Flow in Axial Compressor Cascade. *J. Therm. Sci.* **2013**, *22*, 103–110. [[CrossRef](#)]
4. Storer, J.A.; Cumpsty, N.A. Tip leakage flow in axial compressors. *J. Turbomach.* **1991**, *113*, 252–259. [[CrossRef](#)]
5. Xu, B.; Shen, X.; Zhang, D.; Zhang, W. Experimental and Numerical Investigation on the Tip Leakage Vortex Cavitation in an Axial Flow Pump with Different Tip Clearances. *J. Fluids Eng.* **2019**, *7*, 935. [[CrossRef](#)]
6. Meng, F.; Li, Y.; Yuan, S. Effect of Hub Clearance on Hydraulic Performance in Bidirectional Axial-flow Pump. *Trans. Chin. Soc. Agric. Mach.* **2020**, *51*, 131–138. (In Chinese)
7. Liu, Y.; Han, Y.; Tan, L.; Wang, Y. Blade rotation angle on energy performance and tip leakage vortex in a mixed flow pump as turbine at pump mode. *Energy* **2020**, *206*, 118084. [[CrossRef](#)]
8. Liu, Y.; Tan, L. Theoretical Prediction Model of Tip Leakage Vortex in a Mixed Flow Pump with Tip Clearance. *J. Fluids Eng.* **2020**, *142*, 021203. [[CrossRef](#)]
9. Zhang, D.; Shi, W.; Van Esch, B.B.; Shi, L.; Dubuisson, M. Numerical and experimental investigation of tip leakage vortex trajectory and dynamics in an axial flow pump. *Comput. Fluids* **2013**, *112*, 61–71. [[CrossRef](#)]
10. Murayama, M.; Yoshida, Y.; Tsujimoto, Y. Unsteady Tip Leakage Vortex Cavitation Originating From the Tip Clearance of an Oscillating Hydrofoil. *J. Fluids Eng.* **2006**, *128*, 421–429. [[CrossRef](#)]
11. Mailach, R.; Lehmann, I.; Vogeler, K. Rotating Instabilities in an Axial Compressor Originating From the Fluctuating Blade Tip Vortex. *J. Turbomach.* **2001**, *123*, 453–460. [[CrossRef](#)]
12. Khalid, S.A.; Khalsa, A.S.; Waitz, I.A.; Tan, C.S.; Greitzer, E.M.; Cumpsty, N.A.; Adamczyk, J.J.; Marble, F.E. Endwall Blockage in Axial Compressors. *J. Turbomach.* **1999**, *121*, 499. [[CrossRef](#)]
13. Hsiao, C.T.; Chahine, G.L. Scaling of Tip Vortex Cavitation Inception Noise With a Bubble Dynamics Model Accounting for Nuclei Size Distribution. *J. Fluids Eng.* **2005**, *127*, 55–65. [[CrossRef](#)]
14. Laborde, R.; Chantrel, P.; Mory, M. Tip Clearance and Tip Vortex Cavitation in an Axial Flow Pump. *J. Fluids Eng.* **1997**, *119*, 680–685. [[CrossRef](#)]
15. Farrell, K.J.; Billet, M.L. A Correlation of Leakage Vortex Cavitation in Axial-Flow Pumps. *J. Fluids Eng.* **1994**, *116*, 551–557. [[CrossRef](#)]
16. Zhang, D.; Shi, L.; Zhao, R.; Shi, W.; Pan, Q.; van Esch, B.B. Study on unsteady tip leakage vortex cavitation in an axial-flow pump using an improved filter-based model. *J. Mech. Technol.* **2017**, *31*, 659–667. [[CrossRef](#)]
17. Wu, H.; Miorini, R.L.; Katz, J. Measurements of the tip leakage vortex structures and turbulence in the meridional plane of an axial water-jet pump. *Exp. Fluids* **2011**, *50*, 989–1003. [[CrossRef](#)]
18. Wu, H.; Tan, D.; Miorini, R.L.; Katz, J. Three-dimensional flow structures and associated turbulence in the tip region of a waterjet pump rotor blade. *Exp. Fluids* **2011**, *51*, 1721–1737. [[CrossRef](#)]
19. Shuja, S.Z.; Yilbas, B.S.; Budair, M.O. Entropy analysis of a flow past a heat-generated bluff body. *Int. J. Energy Res.* **2015**, *23*, 1133–1142. [[CrossRef](#)]
20. Abu-Hijleh BA, K.; Heilen, W.N. Entropy generation due to laminar natural convection over a heated rotating cylinder. *Int. J. Heat Mass Transf.* **1999**, *42*, 4225–4233. [[CrossRef](#)]
21. Kock, F.; Herwig, H. Local entropy production in turbulent shear flows: A high-Reynolds number model with wall functions. *Int. J. Heat Mass Transf.* **2004**, *47*, 2205–2215. [[CrossRef](#)]
22. Kock, F.; Herwig, H. Entropy production calculation for turbulent shear flows and their implementation in cfd codes. *Int. J. Heat Fluid Flow* **2005**, *26*, 672–680. [[CrossRef](#)]
23. Li, D.; Wang, H.; Qin, Y.; Han, L.; Wei, X.; Qin, D. Entropy production analysis of hysteresis characteristic of a pump-turbine model. *Energy Convers. Manag.* **2017**, *149*, 175–191. [[CrossRef](#)]
24. Shen, S.; Qian, Z.; Ji, B. Numerical Analysis of Mechanical Energy Dissipation for an Axial-Flow Pump Based on Entropy Generation Theory. *Energies* **2019**, *12*, 4162. [[CrossRef](#)]
25. Behzadmehr, A.; Mercadier, Y. Numerical study of flow parameters and entropy generation on a centrifugal fan. *Int. J. Exergy* **2009**, *6*, 80–92. [[CrossRef](#)]

26. Wang, M.; Li, Y.; Yuan, J.; Meng, F.; Appiah, D.; Chen, J. Comprehensive Improvement of Mixed-Flow Pump Impeller Based on Multi-Objective Optimization. *Processes* **2020**, *8*, 905. [[CrossRef](#)]
27. Zhang, F.; Appiah, D.; Hong, F.; Zhang, J.; Yuan, S.; Adu-Poku, K.A.; Wei, X. Energy loss evaluation in a side channel pump under different wrapping angles using entropy production method. *Int. Commun. Heat Mass Transf.* **2020**, *113*, 104526. [[CrossRef](#)]
28. Menter, F.R. Two-equation eddy-viscosity turbulence models for engineering applications. *Aiaa J.* **1994**, *32*, 1598–1605. [[CrossRef](#)]
29. Mentor, F.; Ferreira, J.C.; Esch, T.; Konno, B. The SST turbulence model with improved wall treatment for heat transfer predictions in gas turbines. In Proceedings of the International Gas Turbine Congress, Tokyo, Japan, 2–7 November 2003.
30. Pei, J.; Yuan, S.; Benra, F.K.; Dohmen, H.J. Numerical prediction of unsteady pressure field within the whole flow passage of a radial single-blade pump. *J. Fluids Eng.* **2012**, *134*, 101103. [[CrossRef](#)]

Publisher’s Note: MDPI stays neutral with regard to jurisdictional claims in published maps and institutional affiliations.



© 2020 by the authors. Licensee MDPI, Basel, Switzerland. This article is an open access article distributed under the terms and conditions of the Creative Commons Attribution (CC BY) license (<http://creativecommons.org/licenses/by/4.0/>).

Article

Effect of Clearance and Cavity Geometries on Leakage Performance of a Stepped Labyrinth Seal

Min Seok Hur ¹, Soo In Lee ², Seong Won Moon ¹, Tong Seop Kim ^{1,*}, Jae Su Kwak ²,
Dong Hyun Kim ³ and Il Young Jung ³ 

¹ Department of Mechanical Engineering, Inha University, 100 Inha-ro, Michuhol-Gu, Incheon 22212, Korea; 22191280@inha.edu (M.S.H.); 22161642@inha.edu (S.W.M.)

² School of Aerospace and Mechanical Engineering, Korea Aerospace University, 76 Hanggongdaehak-ro, Deogyang-gu, Goyang 10540, Korea; sooin0510@kau.kr (S.I.L.); jskwak@kau.ac.kr (J.S.K.)

³ Hanwha Aerospace Co. Ltd., 1204 Changwon-daero, Seongsans-Gu, Changwon 51542, Korea; donghyu1.kim@hanwha.com (D.H.K.); iyjung@hanwha.com (I.Y.J.)

* Correspondence: kts@inha.ac.kr

Received: 11 October 2020; Accepted: 17 November 2020; Published: 19 November 2020



Abstract: This study evaluated the leakage characteristics of a stepped labyrinth seal. Experiments and computational fluid dynamics (CFD) analysis were conducted for a wide range of pressure ratios and clearance sizes, and the effect of the clearance on the leakage characteristics was analyzed by determining the performance of the seal using a dimensionless parameter. It was observed from the analysis that the performance parameter of the seal decreases as the clearance size increases, but it tends to increase when the clearance size exceeds a certain value. In other words, it was revealed that there exists a specific clearance size (S_{\min}) which minimizes the performance parameter of the seal. To identify the cause of this tendency change, a flow analysis was conducted using CFD. It was confirmed that the leakage characteristics of the stepped seal are affected by the size of the cavity, which is the space between the teeth. Therefore, a parametric study was conducted on the design parameters related to the cavity size (tooth height and pitch). The results show that the performance parameter decreases as the tooth height and pitch decreases. Moreover, S_{\min} increases as the tooth height increases and the pitch decreases.

Keywords: clearance; flow function; gas turbine; leakage; pressure ratio; stepped labyrinth seal

1. Introduction

The power and efficiency of gas turbines are being improved to meet the demands of users, leading to increased operating pressures and temperatures. However, the increased operating pressure and temperature increases the leakage flow at the blade tip, which disturbs the main flow and decreases turbine efficiency. Labyrinth seals are devices used to prevent such leakages and have benefits such as relatively simple structures and durability at high temperatures. Among the various geometric parameters of labyrinth seals, the parameter having the most dominant impact on the seal performance is the clearance size. The clearance size varies depending on the operating conditions (rotational speed and degree of thermal expansion of the blades) of the gas turbine. If the clearance is too large, the stage efficiency of the turbine decreases, and flow instability increases. In contrast, if it is too small, mechanical losses, such as wear, occur, thereby affecting the blade life [1]. Therefore, accurate predictions of the leakage characteristics of labyrinth seals according to the clearance are required.

Labyrinth seals are manufactured in various shapes by varying the arrangement of teeth to increase pressure loss and thereby reduce leakage. The commonly used geometries include straight seals with

teeth arranged in a straight line on one side, stepped seals with teeth arranged in the form of steps, and staggered seals with teeth arranged in a staggered manner. Many studies involving experimental and numerical analyses have been conducted to understand the complex flow phenomenon inside labyrinth seals. The most basic research was conducted by Vermes [2]. He performed experiments using a labyrinth seal with the most basic configuration and developed an analytical model based on the experimental data. Stocker et al. [3,4] conducted an experimental study on various seal geometries. They also investigated the sealing characteristics of several seals, including honeycomb seals considering the design parameters. Witting et al. [5–7] conducted experimental studies on the leakage characteristics of the flow and on heat transfer, and they analyzed the influence of the scale of the experiment and the rotation effect on the results. Tipton et al. [8] summarized previous studies on leakage prediction and analyzed the effects of the main design parameters of seals on leakage. Research on the characteristics of labyrinth seals has been performed steadily with the development of experimental methods and performance prediction software programs based on existing data [9,10].

During the past couple of decades, studies comprehensively evaluating the flow characteristics inside labyrinth seals have increased owing to advancements in experimental techniques and numerical methods. Zimmermann et al. [11] analyzed the effects of various design parameters of straight/stepped seals on leakage and examined the changes in the leakage characteristics of the seals due to the wear of the tooth tip. Rhode et al. [12] researched labyrinth seals with added grooves and observed changes in the flow field inside the seals using the flow visualization technique. Schramm et al. [13,14] optimized the geometry of labyrinth seals and compared the leakage characteristics of honeycomb and solid land seals using computational fluid dynamics (CFD). Willenborg et al. [15] performed experiments in a wide range of Reynolds numbers and confirmed that the discharge coefficient depended only on the pressure ratio at high Reynolds numbers. Doğu et al. [16] analyzed the leakage characteristics of mushroom-shaped labyrinth seals using CFD and confirmed that more leakage occurred due to shape changes, caused by rubbing. Yan et al. [17,18] conducted experiments and CFD analysis considering not only mushroom-shaped wear, but also deformation of teeth by bending. In addition, they conducted research on the hole-patterned labyrinth seal that arranged the holes regularly in the casing instead of honeycomb cells.

In recent years, experimental and numerical studies have focused on stepped labyrinth seals, which are the most common types of seals used to prevent leakage at the turbine blade tip. Kim et al. [19–21] conducted an experimental study on the pressure ratio and clearance size for straight/stepped seals and analyzed the leakage characteristics using CFD. Kang et al. [22] conducted experimental and numerical studies on stepped labyrinth seals according to the number of teeth and clearance size. They also compared the leakage characteristics of solid and honeycomb seals and confirmed that solid seals exhibited better sealing performance. Zhang et al. [23] performed experiments using clearance sizes applied to actual engine blades to exclude the influence of the scale of the experiments on the results. They also numerically analyzed the influence of various design parameters of stepped labyrinth seals, such as the clearance size, step height, and the number of teeth.

According to several previous studies, the performance parameters of stepped labyrinth seals tend to decrease as the clearance size increases [19–24]. However, some studies have reported that this is not always true, and the performance parameters tend to increase again as the clearance size exceeds a certain value [25]. Nevertheless, these studies did not present comprehensive cause-and-effect analyses. Therefore, it is necessary to conduct basic research on the performance parameter according to the clearance size. In this regard, we conducted experiments and CFD analysis in this study to analyze the leakage characteristics of a stepped labyrinth seal, and the effect of the clearance size on leakage performance was analyzed thoroughly. The stepped seal geometry used at the tips of rotating blades in gas turbines was selected as the target and a diverging flow path in which the diameter increases in the flow direction was considered the leakage flow path as in real applications in the tip section of turbine blades. The minimum performance parameter was determined by observing the leakage characteristics according to the clearance

size. To explain the cause for tendency change in the performance parameter, the effects of several design parameters (tooth height and pitch) on leakage were analyzed.

2. Labyrinth Seal and Experiment

2.1. Test Rig

Labyrinth seals used in actual gas turbines are ring-shaped, and there is an empty space (i.e., clearance or gap) between the rotating and stationary parts. However, it has been widely accepted that the rotation effect on the leakage flow rate is important only when the rotational speed is very high [7] and thus a stationary two-dimensional (2D) rig provides almost the same results as those obtained using an axisymmetric three-dimensional (3D) rig [4]. Therefore, numerous studies including those surveyed in the introduction have used 2D test rigs and 2D CFD simulations to obtain fundamental flow physics and accumulate vast amounts of information. Accordingly, a 2D test rig was also used in our study.

Figure 1 shows the overall configuration of the test rig and Figure 2 illustrates the geometry of the labyrinth seal used in the test. To minimize the 3D flow effect due to the wall, the width of the test section, which is the depth of the test section into the page of Figure 2, was set to be sufficiently large (approximately 67 times the smallest clearance size) compared to the clearance size. The components of the test rig included the air tank, valve, mass flow meter, honeycomb panel, and the test section. The pressure of the air inside the tank was as high as 8.5 bar and the pressure ratio was adjusted from 1.1 to 3.0 using the control valve between the tank and the test section. The pressure ratio (PR) was defined as the ratio of total pressure at the inlet to static pressure at the outlet of the test section. The inlet pressure was measured using a pressure transducer (PX409-050GI, OMEGA, Norwalk, CT, USA). The flow rate at each PR was measured using a thermal electronic mass flow meter (KMSG-8040MT, KOMETER, Incheon, Republic of Korea), and the inlet temperature was measured using a thermocouple (T-type SCPSS-040E-6, OMEGA, Norwalk, CT, USA). In addition, a honeycomb panel was installed at the inlet of the test section for ensuring straight and uniform flow, and the test section was scaled up to the actual geometry to improve the accuracy of the test results.

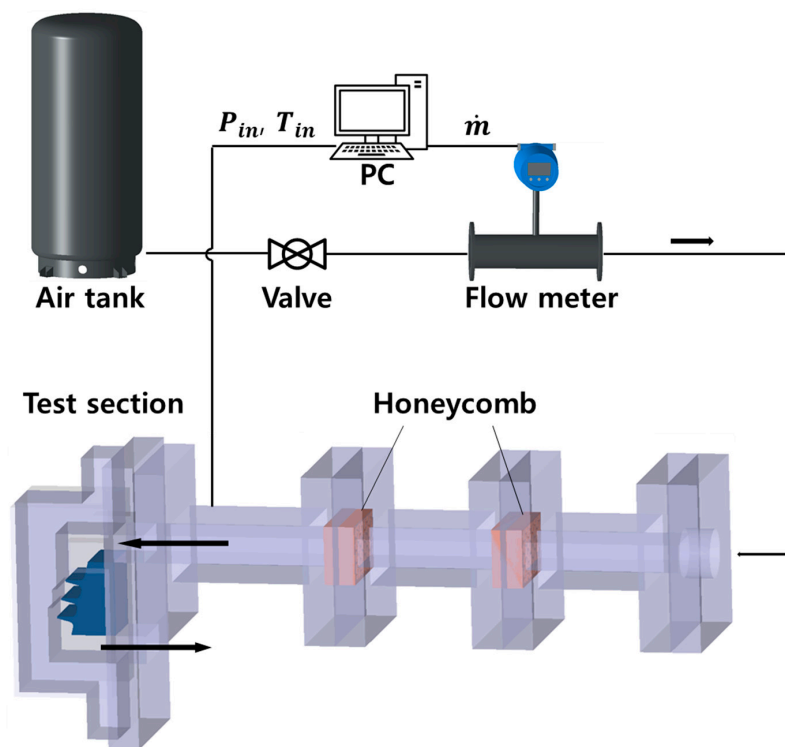


Figure 1. Schematic diagram of the test facility.

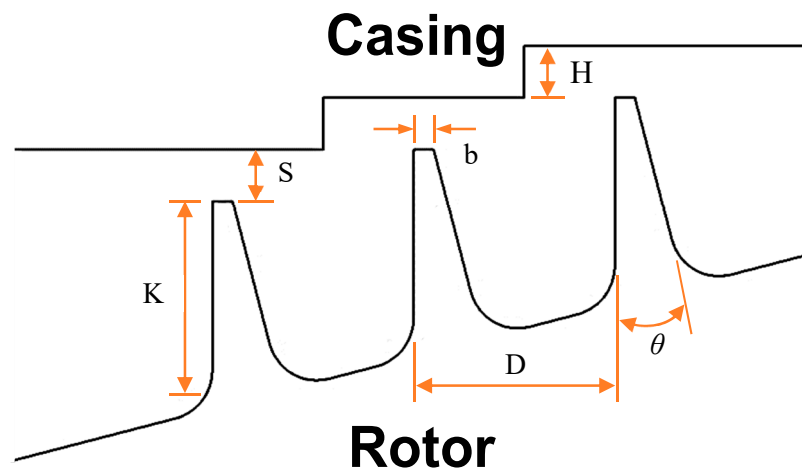


Figure 2. Seal geometry and parameters.

Table 1 summarizes the symbols and names of each design parameter and the non-dimensionalized expressions of the parameters of the labyrinth seal geometry. The test section was divided into an upper part and a lower part, which represent the stationary and rotating parts, respectively, in an actual turbine. The air comes into the test section from the left-hand side of Figure 2 and exits at the right-hand side, simulating a diverging flow path in actual turbine tip sections. The main geometric parameters of the stepped labyrinth seal include the clearance size (S), tooth thickness (b), tooth height (K), pitch (D), step height (H), and tooth angle (θ). In this study, numerical analysis and experiments were conducted by setting the range of the non-dimensionalized clearance size (step height ratio, S/H) from 0.2 to 1.2.

Table 1. Design parameters of the stepped labyrinth seal.

Parameter	Description	Value
S/H	Clearance/Step height	0.2~1.2
D/H	Pitch/Step height	4
K/H	Tooth height/Step height	4
θ	Tooth angle	15°
N	Number of teeth	3

2.2. Seal Performance

The performance of the labyrinth seal was determined using the relationship between the PR and a performance parameter. The most commonly used performance parameter is the flow function, which is defined in Equation (1).

$$\phi = \frac{\dot{m} \sqrt{T_{o,in}}}{A_c P_{o,in}} \quad (1)$$

where \dot{m} is the flow rate, A_c is the throat area, $P_{o,in}$ is the inlet total pressure, $T_{o,in}$ is the inlet total temperature. The flow function is the semi-dimensionless number which facilitates real leakage flow rate prediction for any arbitrary operating condition. The smaller the flow function is, the better the performance of the labyrinth seal becomes.

2.3. Measurement Uncertainty

The method proposed by Kline [26] was used to check the measurement uncertainty. The equation used for calculating the uncertainty of the flow function is given below.

$$\Delta\phi = \sqrt{\left(\frac{\partial\phi}{\partial\dot{m}}\Delta\dot{m}\right)^2 + \left(\frac{\partial\phi}{\partial T_0}\Delta T_0\right)^2 + \left(\frac{\partial\phi}{\partial S}\Delta S\right)^2 + \left(\frac{\partial\phi}{\partial d}\Delta d\right)^2 + \left(\frac{\partial\phi}{\partial P_0}\Delta P_0\right)^2} \quad (2)$$

$$u = \frac{\Delta\phi}{\phi} \quad (3)$$

We used 0.3% of the measured flow rate as the uncertainty of the mass flow rate measurement ($\Delta\dot{m}$) and 0.5 °C as that of the temperature (ΔT_0) according to the manufacturer's manual. The uncertainty of the tip clearance measurement (ΔS) was set at 0.01 mm according to the least count of the gap gauge, and the uncertainty of the section width measurement (Δd) was set at 0.005 mm according to the least count of the Vernier calipers. The sum of 0.01% of the maximum measurable limit and 0.008% of the measured value was used as the value for the uncertainty of the pressure measurement (ΔP_0) according to the manufacturer's manual. Therefore, the uncertainty of the flow function (u) was calculated to be 3.4%.

3. Analysis

3.1. Numerical Approach

ANSYS CFX (ver. 19.0, ANSYS Inc., Canonsburg, PA, USA, 2018) [27], a commercial software program, was used for CFD analysis. Figure 3 shows examples of the analysis domain and grid structure. As the 2D flow was secured in the experiment, the 2D calculations were also sufficient for CFD. However, as ANSYS CFX is based on 3D calculations, the 3D domain was set as shown in Figure 1; nevertheless, we ensured that the 3D was practically close to the 2D domain by setting the smallest width as far as we could and applied symmetry conditions to lateral faces. This method is recommended for 2D calculations according to the CFX manual [28]. ANSYS ICEM (ver. 19.0, ANSYS Inc., Canonsburg, PA, USA, 2018) was used for mesh generation. The grids of the overall leakage flow path were composed of unstructured meshes and only the wall portion was composed of prism layers so that y^+ could be ≤ 2 . Figure 3 shows an example of generated meshes. It is clearly shown that dense meshes were generated around the tip clearance. Grid dependence tests were performed to select appropriate numbers of meshes. Figure 4 illustrates an example for the case when the clearance to step height ratio (S/H) is 0.4. The results confirmed that the flow function, which was the target function, became almost constant when the number of meshes was 120,000 or more. Accordingly, 130,000 meshes were adopted in a specific case. Of course, the number of meshes generally increased as the clearance increased. It ranged from 130,000 to 150,000 when the S/H ratio increased from 0.2 to 1.2.

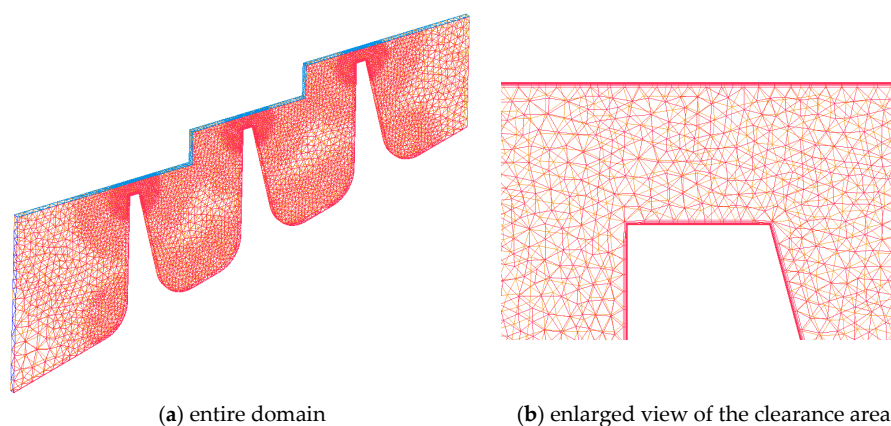


Figure 3. Example of the computational domain and meshes ($S/H = 0.4$).

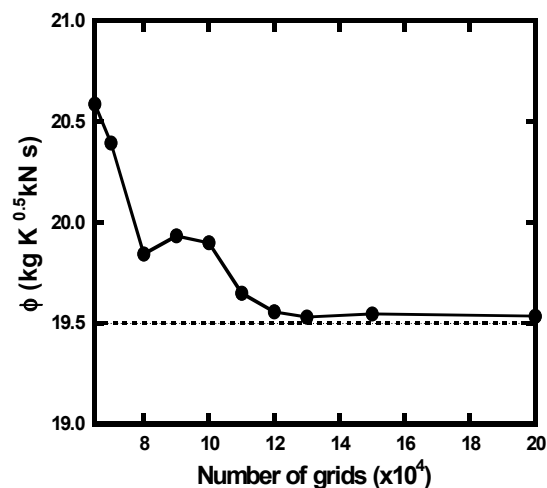


Figure 4. Example of grid dependence of the computational fluid dynamics (CFD) result ($S/H = 0.4$).

3.2. Boundary Conditions and Validation

Inlet total pressure and temperature and outlet static pressure were used as boundary conditions to simulate the operating conditions of the test. Adiabatic and no-slip conditions were used for the solid surfaces, and the symmetry condition was used at the two side boundary surfaces (lateral faces). The high-resolution advection scheme was used, which adequately uses the first and second order scheme depending on the situation, satisfying both the numerical stability and accuracy of the analysis. In addition, the first-order turbulence numerics was selected. The residual value (RMS) of the flow parameter was set to less than 1.0×10^{-4} as the convergence condition for the analyses. Table 2 summarizes the numerical analysis method and boundary conditions. A turbulence model that accurately captures the flow characteristics inside the seal cavity is required because of a strong vortex flow which is one of the major causes of the pressure loss in the seal. Therefore, the SST turbulence model, which is known to predict the vortex size and separation point accurately [29,30], was adopted. Figure 5 compares the sample test run results obtained using the SST model with those obtained using other turbulence models ($k-\omega$, $k-\epsilon$ and RNG $k-\epsilon$ models). Although there were no significant differences in the calculation results obtained using the various turbulence models, the SST model produced results closest to the experimental values with errors less than 3%. In addition, a comparison between the experimental and CFD results shown in Figure 6 confirms that CFD has sufficient accuracy for evaluating the leakage performance of the labyrinth seal.

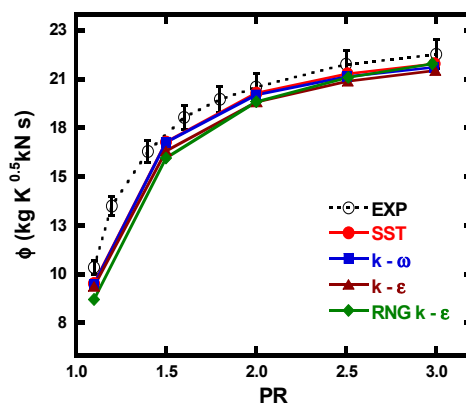


Figure 5. Comparison of turbulence models ($S/H = 1.0$, $K/H = 4$, $D/H = 4$).

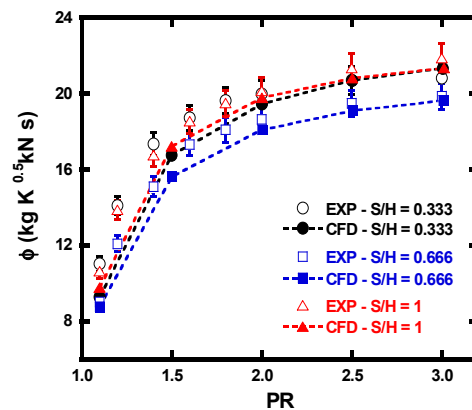


Figure 6. Comparison between the CFD and experimental results ($K/H = 4$, $D/H = 4$).

Table 2. Numerical methods and boundary conditions.

Software	ANSYS CFX 19.0
Turbulence model	Shear Stress Transport (SST)
Advection scheme	High resolution
Fluid	Air (ideal gas)
Pressure ratio	1.1~3.0
Inlet total temperature	295 K
Outlet static pressure	101.325 kPa
Wall	Adiabatic, no slip
Lateral faces	Symmetry

4. Results and Discussion

4.1. Leakage Characteristics According to Clearance Size

Figure 7 shows the flow function obtained using CFD at different PR and S/H values. For all S/H values, the flow function increases as the PR increases and exhibited choking after a certain PR. For example, the choking pressure ratio is around 2.5 when S/H is 0.2. As well known, the fact that the flow becomes choked does not necessarily mean that the actual flow rate is constant. It varies with the inlet total pressure and temperature. In our cases, the actual mass flow rate increases in proportion to the inlet total pressure because a higher pressure ratio means a higher inlet total pressure: remember that the inlet total temperature and the outlet static pressure were fixed.

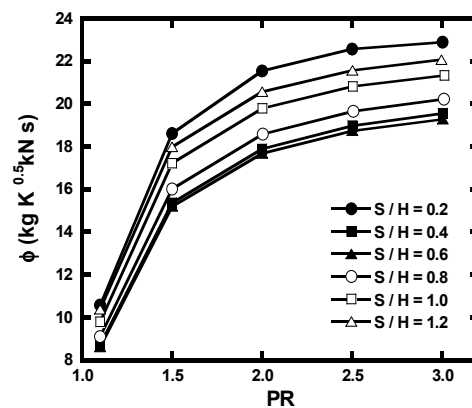


Figure 7. Variations in flow function with pressure ratio (PR) and S/H ($K/H = 4$, $D/H = 4$).

An important observation was that change in flow parameter due to the increase in the clearance size clearly differs below and above $S/H = 0.6$. To intensively examine changes in the flow function according to the clearance, the flow function at the PR of 2.5 was plotted in Figure 8 and compared with the experimental values under the same conditions. As the clearance increases, the flow function decreases and then tends to increase again at a certain clearance size, as observed commonly in the CFD and experimental results. This result confirmed that the stepped labyrinth seal has a specific clearance size (S_{\min}) that minimizes the flow function. It should be noted that the flow function does not represent the actual leakage flow rate but indicate relative leakage performance. Therefore, a lower flow function does not necessarily mean a lower flow rate but represents a better relative seal performance. The actual leakage flow rate increases as the clearance size increases in all the test cases in our study.

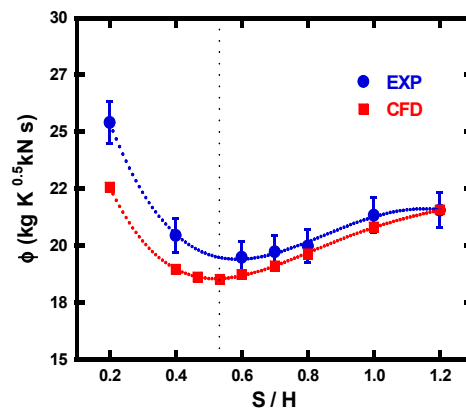


Figure 8. Variation in flow function with S/H (PR = 2.5, $K/H = 4$, $D/H = 4$).

To identify the cause of such changes in the flow function due to the increase in the clearance size, the flow inside the seal was analyzed using the details of the flow phenomena obtained by CFD. Figures 9 and 10 show the contours of the total pressure and static pressure, respectively, for various S/H ratios at the PR of 2.5. As S/H increases, the flow through the clearance develops a type of high-speed flow layer (see Figure 9). Figure 10 shows that the flow layer passing the clearance collides with the next tooth, resulting in a local increase in static pressure, which means that the kinetic energy of the leakage flow significantly dissipates. The collision point moves toward the tooth tip gradually as the S/H increases, and after $S/H = 1.0$, it is located at the tip of the tooth. In other words, in the specific S/H range in which the flow function decreased (S/H from 0.2 to 0.533), the flow rate gradually increases and the pressure loss due to collision with the tooth increases, improving the sealing performance. However, when the clearance continues to increase over the critical value of 0.533, most of the leakage flow through the previous clearance directs to the next clearance space without hitting the tooth, as shown in Figure 9. Accordingly, the kinetic energy loss caused by the collision reduced, resulting in a decrease in the sealing performance. In addition, it is seen from Figure 9 that the total pressure inside the cavity slightly increases as S/H increases from 0.2 to 0.533. This indicates that the leakage performance improves (i.e., the flow function decreases) as the flow trapped inside the cavity is increased by the flow layer moving at a high speed. However, after $S/H = 0.533$, the total pressure inside the cavity tends to decrease which means the flow trapped inside the cavity decreases. Figure 11 clarifies the change of the pressure inside the cavity with respect to S/H . It shows the variation in the averaged total pressure inside the cavity according to S/H , which clearly shows that total pressure decreases after the maximum point.

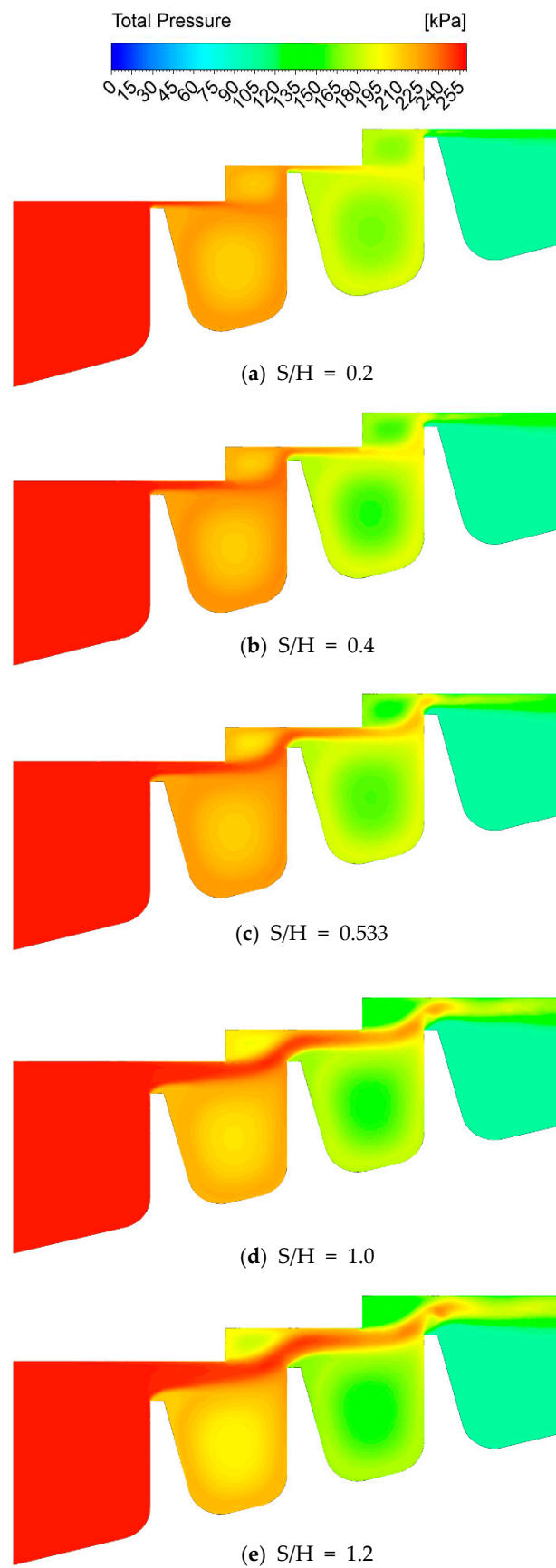


Figure 9. Total pressure contour plots for various S/H ratios (PR = 2.5, K/H = 4, D/H = 4).

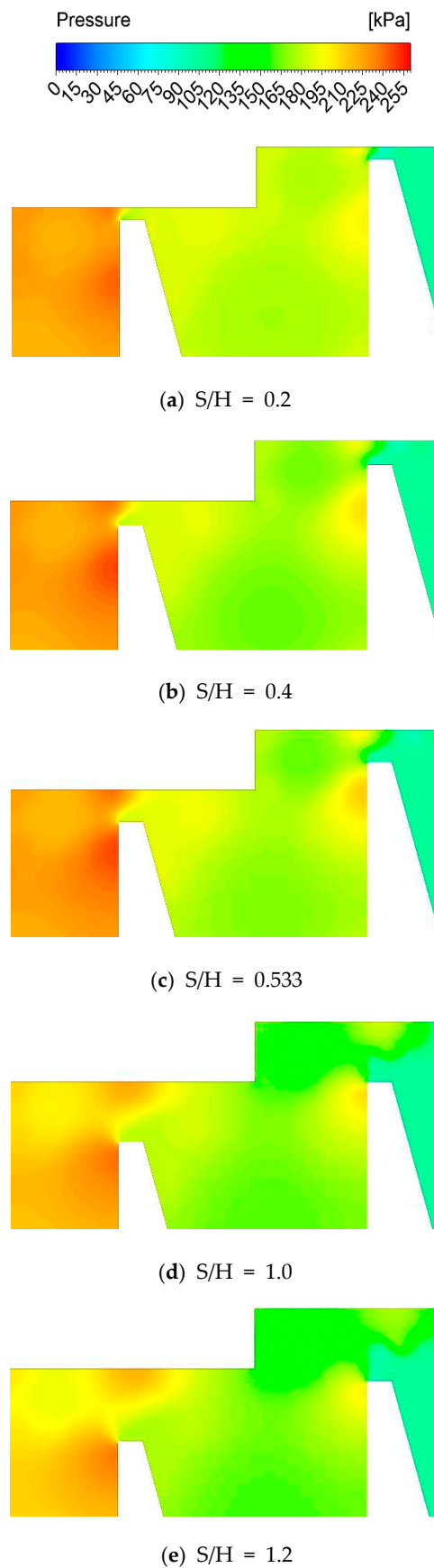


Figure 10. Static pressure contour plots for various S/H ratios ($PR = 2.5$, $K/H = 4$, $D/H = 4$).

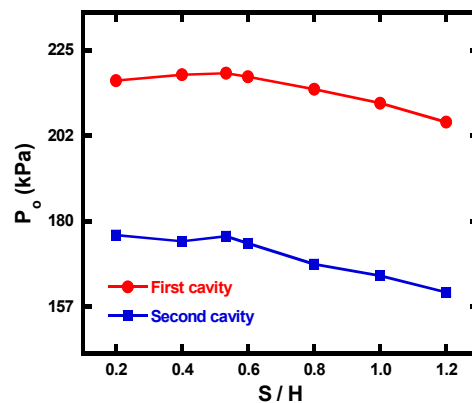


Figure 11. Variation in the averaged total pressure inside the cavity with S/H ($PR = 2.5$, $K/H = 4$, $D/H = 4$).

In summary, the tendency of the variations in flow function with clearance change at $S/H = 0.533$. In other words, when the clearance size is approximately half the step height, the maximum resistance to leakage flow occurs, leading to decreases in the flow function. As the clearance size further increases, the resistance to leakage flow decreases, leading to increases in the flow function.

4.2. Parametric Study on the Impact of Cavity Size

4.2.1. Outline

Through the flow analysis, we identified two main reasons for the reduced flow function (i.e., enhanced leakage performance) of the stepped labyrinth seal. The first is the significant dissipation of the kinetic energy during the leakage flow that occurs as the fluid passing through the clearance collides with the next tooth. The second is the formation of a strong flow layer owing to the high-speed flow passing through the clearance and the subsequent confinement of the rotating flow inside the cavity. The identification indicates that the leakage characteristics of the stepped labyrinth seal are affected not only by the clearance size but also by the value of S/H relative to the cavity size. Based on this observation, a parametric study on the tooth height and pitch, which are geometrical parameters affecting the cavity size, was conducted using the CFD. Table 3 gives the analysis range set for each parameter.

Table 3. Variation range of the non-dimensional parameters.

Parameter	Description	Value	Variation Range
D/H	Pitch/Step height	4	2~6
K/H	Tooth height/Step height	4	3~5

4.2.2. Tooth Height

Figure 12 shows the change in the flow function according to the values of S/H and K/H at the PR of 2.5. As the value of K/H decreases, the flow function decreases. The minimum value of the flow function is 8.4% lower at $K/H = 2$ and 5.9% higher at $K/H = 6$ compared to the reference value at $K/H = 4$. Figure 13 shows the velocity vector according to the K/H value at constant S/H and PR values. As the value of K/H decreases, the cavity size decreases, thereby increasing the velocity of the rotating flow in the cavity. Accordingly, a high-velocity flow layer is formed at the point where the flow in the axial direction (i.e., the throughflow) and the rotating flow inside the cavity joined. Following this, the joined flow collides with the tooth, increasing the local pressure, as shown in Figure 14. This indicates significant dissipation of the kinetic energy is induced by the leakage flow. In addition, as the velocity of the flow layer is higher, a larger separation occurs at the tooth tip, as shown in the velocity contour of Figure 15. This reduces the flow function because the effective area in which the flow can actually move is reduced. In addition, as the tooth height decreases, S_{\min} slowly decreases owing to the reduced flow rate inside the cavity.

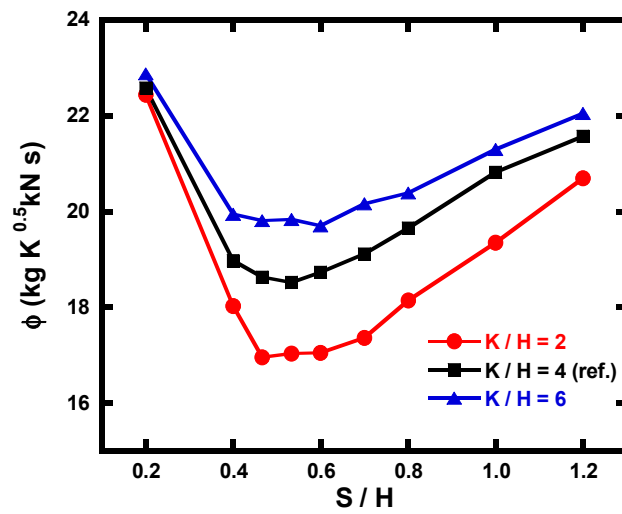


Figure 12. Variation in the flow function with S/H and K/H (PR = 2.5, D/H = 4).

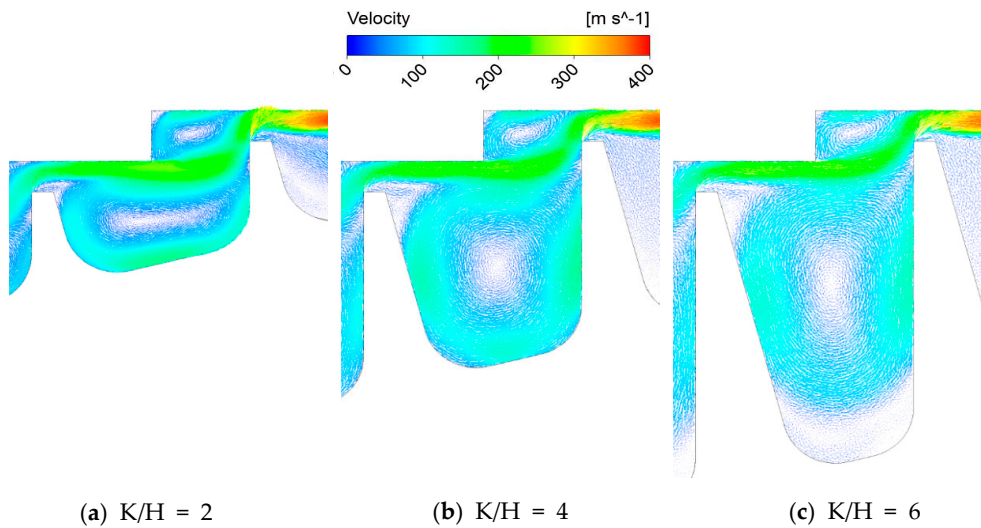


Figure 13. Velocity vectors for various K/H ratios (PR = 2.5, S/H = 0.6, D/H = 4).

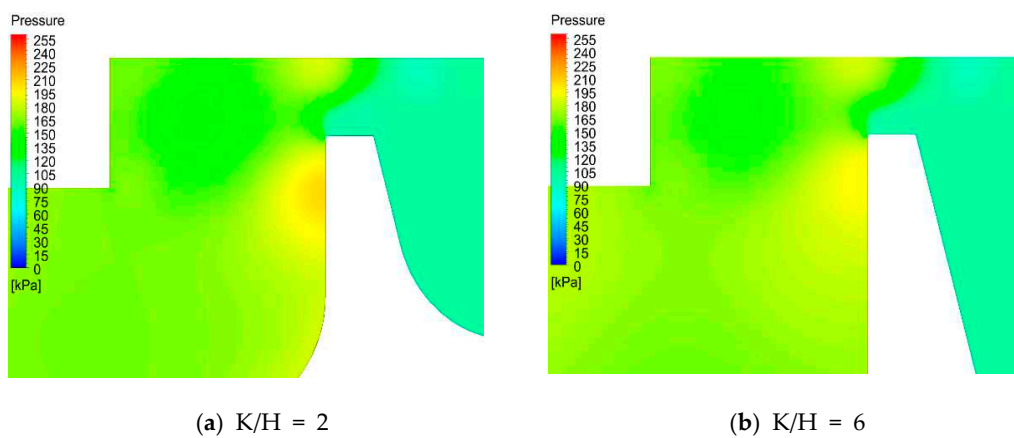


Figure 14. Static pressure contour plots for the smallest and largest K/H ratios (PR = 2.5, S/H = 0.6, D/H = 4).

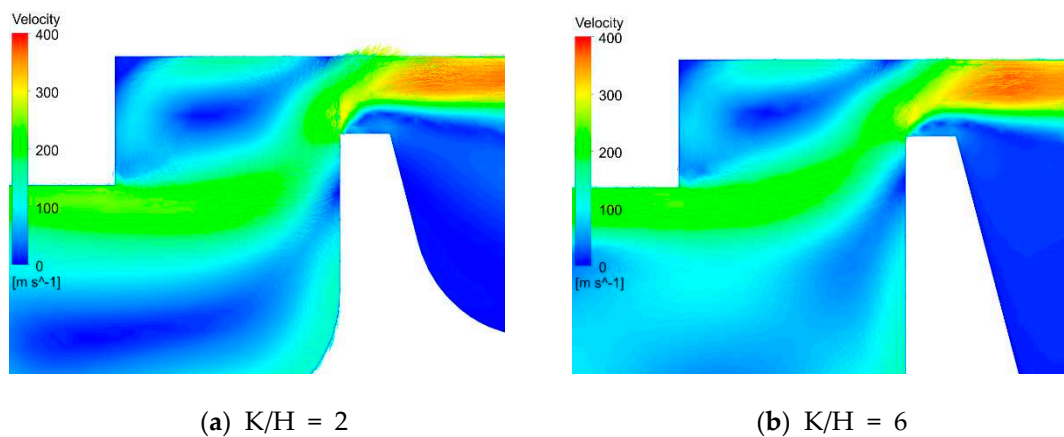


Figure 15. Velocity contour plots for the smallest and largest K/H ratios ($PR = 2.5$, $S/H = 0.6$, $D/H = 4$).

The impact of S/H is summarized as follows. At $S/H = 0.2$ which is the smallest value in our study, the change in tooth height did not affect the flow function (see Figure 12) because the clearance is too small for the flow separation to be an important factor. As S/H increases, the influence of K/H increases, which means the favorable impact of a lower K/H increases. However, as S/H increases above the minimum flow function point, the influence of K/H increases again.

4.2.3. Pitch

Figure 16 shows the flow function according to the S/H and D/H values at the PR of 2.5. As the value of D/H decreases, the flow function decreases. The minimum value of the flow function is 5.4 % lower at $D/H = 3$ and 0.7% higher at $D/H = 5$ compared to the reference value at $D/H = 4$. Figure 17 shows the streamlines when D/H is the highest and lowest at constant S/H and PR values. As D/H decreases, the velocity of the flow layer increases because the travel distance of the flow in the axial direction decreases. In addition, larger separation occurs because of the rapid movement of the flow in the radial direction. This reduces the effective area, thereby further increasing the leakage reduction effect (see Figure 18). In addition, as the pitch decreases, S_{\min} tends to increase. This is because flow into the cavity continuously occurs despite the increase in cavity size owing to the reduction in the travel distance in the axial direction.

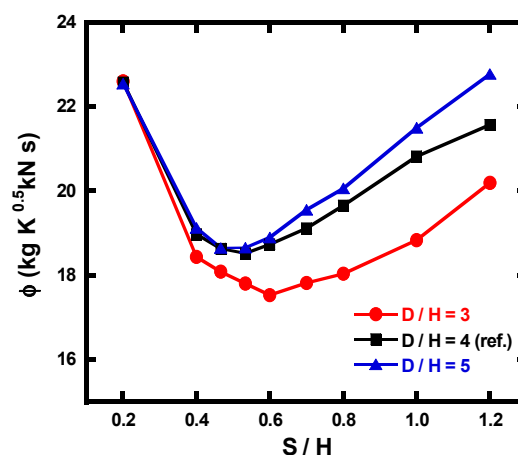


Figure 16. Variation in the flow function with S/H and D/H ($PR = 2.5$, $K/H = 4$).

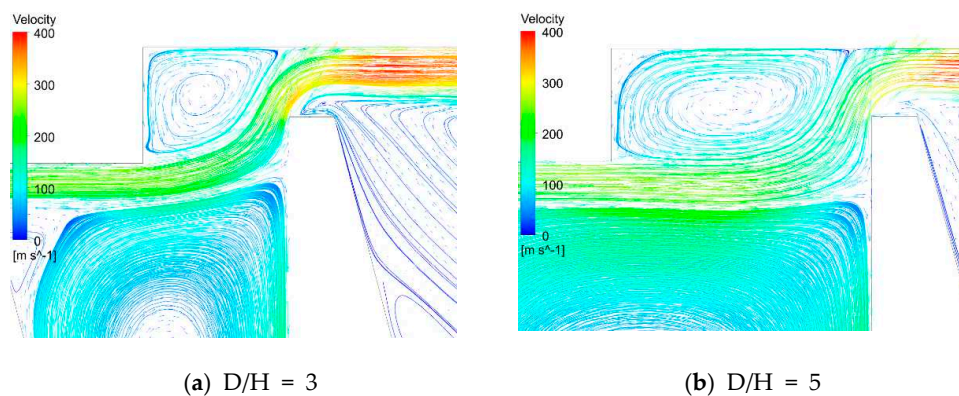


Figure 17. Velocity streamline plots for the smallest and largest D/H ratios ($PR = 2.5$, $S/H = 0.6$, $K/H = 4$).

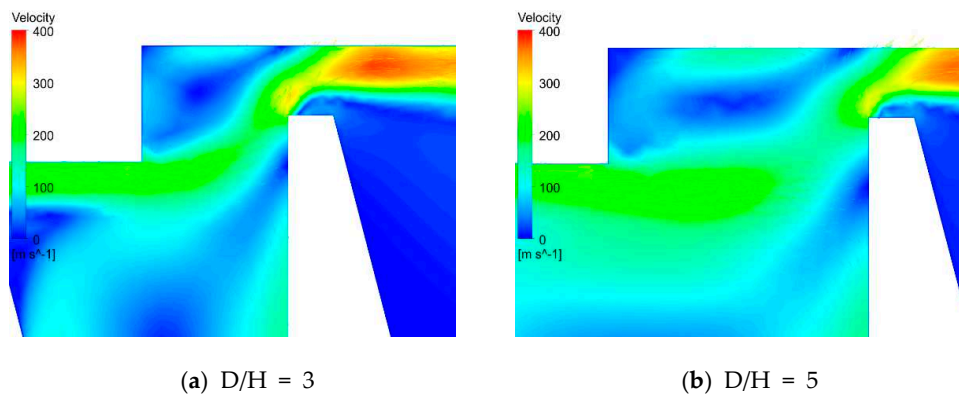


Figure 18. Velocity contour plots for the smallest and largest D/H ratios ($PR = 2.5$, $S/H = 0.6$, $K/H = 4$).

As with the case of the tooth height, when $S/H = 0.2$, the change in pitch does not affect the flow function because the clearance is too small for the flow separation to be an important factor. Despite the increase in the clearance size, changes in the flow function due to the pitch were hardly observed before S_{\min} . Although the relative flow velocity decreases owing to the increase in the travel distance in the axial direction, there is almost no difference in the overall leakage performance because the flow rate into the cavity increases. However, as the clearance continues to increase, the flow rate inside the cavity sharply decreases, causing differences in the flow function owing to the difference in the velocity of the flow layer.

4.2.4. Summary of the Parametric Study

The results obtained from analyzing the effects of the tooth height and pitch on leakage performance can be summarized as follows. Overall, changes in the tooth height cause more significant changes in leakage characteristics than changes in the pitch. The influence of the clearance change is also stronger according to the tooth height variation. In addition, when the clearance is considerably small, changes in the two design parameters have little influence on the flow function. However, as the clearance gradually increases, the flow function shows different tendencies owing to changes in the two design parameters before and after S_{\min} . As the values of both the parameters decrease, the leakage performance improves (i.e., the flow function decreases), but S_{\min} decreases as K/H decreases and D/H increases. As the tooth height decreases, S_{\min} decreases owing to the reduction in the flow rate into the cavity. In contrast, as the pitch decreases, the flow rate into the cavity decreases, but S_{\min} increases because the flow into the cavity continuously occurs despite the increase in the clearance size due to the relatively reduced travel distance in the axial direction.

5. Conclusions

In this study, the leakage characteristics of a stepped labyrinth seal, which is mainly used for sealing at the blade tips of gas turbines, were analyzed through experiments and CFD simulations for a wide range of PRs and clearance sizes. We focused on determining the clearance size at which the tendency of the flow function changed owing to changes in the design parameters. The main results and conclusions of this study are summarized as follows:

1. As the clearance size increases, the flow function of the seal decreases initially, but it tends to increase at a certain clearance size. In other words, the stepped labyrinth seal has a clearance size that minimizes the flow function and this specific clearance size is approximately half the step height ($S/H = 0.533$). This change in the tendency of the flow function was examined through flow analysis. The analysis results showed that the leakage characteristics of the stepped labyrinth seal are affected by the value of S/H relative to the cavity size.
2. The flow function of the stepped labyrinth seal is affected by the tooth height and pitch, and the leakage reduction effect increases as both these geometric parameters decrease (the minimum value of the flow function is 8.4% lower at $K/H = 2$ in comparison to the reference value at $K/H = 4$ and 5.4% lower at $D/H = 3$ in comparison to the reference value at $D/H = 4$). In addition, as the tooth height and pitch decrease, the changes in flow function due to the increase in clearance increase. When the clearance is considerably small, changes in the tooth height and pitch hardly affect the flow function.
3. The most important conclusion obtained in this study is that the stepped labyrinth seal has a specific clearance size (S_{\min}) at which the flow function is minimized. The finding that S_{\min} varies depending on the tooth height and pitch is also important. Another important finding is that S_{\min} decreases as the tooth height increases and the pitch decreases. This study is significant in that it provides basic data required for optimizing the geometry of stepped labyrinth seals to improve their leakage performance through determining the clearance size and geometric parameters that minimize the flow function.

Author Contributions: Conceptualization, M.S.H., T.S.K., methodology, M.S.H., S.I.L., S.W.M., software, M.S.H., S.W.M., validation, M.S.H., S.I.L., formal analysis, M.S.H., investigation, M.S.H., S.I.L., resources, T.S.K., J.S.K., data curation, M.S.H., writing—original draft, M.S.H., S.I.L., writing—review and editing, T.S.K., M.S.H., supervision, T.S.K., J.S.K., project administration, I.Y.J., D.H.K., and funding acquisition, T.S.K., J.S.K., I.Y.J., D.H.K. All authors have read and agreed to the published version of the manuscript.

Funding: This study was conducted with the support of the Korea Evaluation Institute of Industrial Technology (KEIT) at the Ministry of Industry, Commerce and Energy in 2020 (No. 20002700). The authors gratefully acknowledge this support.

Conflicts of Interest: The authors declare no conflict of interest.

Nomenclature

A_c	Throat area [m ²]
b	Tooth width [mm]
D	Pitch [mm]
d	Test section width [mm]
H	Step height [mm]
K	Tooth height [mm]
k	Specific heat ratio
\dot{m}	Mass flow rate [kg/s]
N	Number of teeth
P_o	Total pressure [kPa]
P	Static pressure [kPa]
PR	Pressure ratio
R	Gas constant [kJ/kg · K]
S	Clearance [mm]
S_{\min}	Clearance for a minimal flow function [mm]
T_o	Total temperature [K]
u	Uncertainty
ϕ	Flow function [kgK ^{0.5} /kNs]
θ	Tooth angle [°]

Subscripts

c	Contraction
in	Inlet
min	Minimum
out	Outlet

References

1. Lattime, S.B.; Steinetz, B.M. *Turbine Clearance Control Systems: Current Practices and Future Directions*; TM-2002-211794; NASA: Washington, DC, USA, 2002.
2. Vermes, G. A fluid mechanics approach to the labyrinth seal leakage problem. *J. Eng. Power* **1961**, *83*, 161–169. [[CrossRef](#)]
3. Stocker, H.L.; Cox, D.M.; Holle, G.F. *Aerodynamic Performance of Conventional and Advanced Design Labyrinth Seals with Solid-Smooth, Abradable, and Honeycomb Lands*; CR-135307; NASA: Washington, DC, USA, 1977.
4. Stocker, H.L. Determining and improving labyrinth seal performance in current and advanced high performance gas turbines. *AGARD Conf. Proc.* **1978**, *237*, 13.1–13.22.
5. Wittig, S.; Dorr, L.; Kim, S. Scaling effects on leakage losses in labyrinth seals. *J. Eng. Power* **1983**, *105*, 305–309. [[CrossRef](#)]
6. Wittig, S.; Schelling, U.; Jacobsen, K.; Kim, S. Numerical Predictions and Measurements of Discharge Coefficients in Labyrinth Seals. In Proceedings of the ASME 1987 International Gas Turbine Conference and Exhibition, Anaheim, CA, USA, 31 May–4 June 1987. ASME Paper 87-GT-188.
7. Waschka, W.; Wittig, S.; Kim, S. Influence of high rotational speeds on the heat transfer and discharge coefficients in labyrinth seals. *J. Turbomach.* **1992**, *114*, 462–468. [[CrossRef](#)]
8. Tipton, D.L.; Scott, T.E.; Vogel, R.E. *Labyrinth Seal Analysis*; ASME: New York, NY, USA, 1986; Volume III: Analytical and experimental development of a design model for labyrinth seals, AFWAL-TR-85-2103.
9. Chupp, R.E.; Holle, G.; Scott, T.E. *Labyrinth Seal Analysis*; ASME: New York, NY, USA, 1986; Volume IV: User's manual for the labyrinth seal design model, AFWAL-TR-85-2103.
10. Zimmermann, H.; Wolff, K.H. Air System Correlations, Part 1: Labyrinth Seals. In Proceedings of the ASME 1998 International Gas Turbine and Aeroengine Congress and Exhibition, Stockholm, Sweden, 2–5 June 1998. ASME Paper 98-GT-206.
11. Zimmermann, H.; Kammerer, A.; Wolff, K.H. Performance of Worn Labyrinth Seals. In Proceedings of the ASME 1994 International Gas Turbine and Aeroengine Congress and Exposition, The Hague, The Netherlands, 13–16 June 1994. Paper 94-GT-131.
12. Rhode, D.L.; Johnson, J.W.; Broussard, D.H. Flow Visualization and Leakage Measurements of Stepped Labyrinth Seal: Part 1—Annular Groove. In Proceedings of the ASME 1996 International Gas Turbine and Aeroengine Congress and Exposition, Birmingham, UK, 10–13 June 1996. ASME Paper 96-GT-136.
13. Schramm, V.; Willenborg, K.; Kim, S.; Wittig, S. Influence of a honeycomb facing on the flow through a stepped labyrinth seal. *J. Eng. Gas Turbines Power* **2000**, *124*, 140–146. [[CrossRef](#)]
14. Schramm, V.; Denecke, J.; Kim, S.; Wittig, S. Shape optimization of a labyrinth seal applying the simulated annealing method. *Int. J. Rotating Mach.* **2004**, *10*, 365–371. [[CrossRef](#)]
15. Willenborg, K.; Kim, S.; Wittig, S. Effects of Reynolds Number and Pressure Ratio on Leakage Loss and Heat Transfer in a Stepped Labyrinth Seal. In Proceedings of the ASME Turbo Expo 2001: Power for Land, Sea, and Air, New Orleans, LA, USA, 4–7 June 2001. ASME Paper 2001-GT-0123.
16. Doğu, Y.; Sertçakan, M.C.; Bahar, A.S.; Pişkin, A.; Arıcan, E.; Kocagül, M. CFD Investigation of Labyrinth Seal Leakage Performance Depending on Mushroom Shaped Tooth Wear. In Proceedings of the ASME Turbo Expo 2015: Power for Land, Sea, and Air, Montreal, QC, Canada, 15–19 June 2015. ASME Paper GT2015-43607.
17. Yan, X.; Dai, X.; Zhang, K.; Li, J.; He, K. Effect of teeth bending and mushrooming damages on leakage performance of a labyrinth seal. *J. Mech. Sci. Technol.* **2018**, *32*, 4697–4709. [[CrossRef](#)]
18. Yan, X.; Dai, X.; Zhang, K.; Li, J.; He, K. Influence of Hole-Pattern Stator on Leakage Performance of Labyrinth Seals. In Proceedings of the ASME Turbo Expo 2018: Power for Land, Sea, and Air, Oslo, Norway, 11–15 June 2018. ASME Paper GT2018-75349.
19. Kim, T.S.; Kang, Y.; Moon, H.K. Aerodynamic performance of double-sided labyrinth seals. In *Fluid Machinery and Fluid Mechanics*; Springer: Berlin/Heidelberg, Germany, 2009; pp. 377–382.
20. Kim, T.S.; Cha, K.S. Comparative analysis of the influence of labyrinth seal configuration on leakage behavior. *J. Mech. Sci. Technol.* **2009**, *23*, 2830–2838. [[CrossRef](#)]
21. Kim, T.S.; Kang, S.Y. Investigation of leakage characteristics of straight and stepped labyrinth seals. *Int. J. Fluid Mach. Syst.* **2010**, *3*, 253–259. [[CrossRef](#)]

22. Kang, Y.; Kim, T.S.; Kang, S.Y.; Moon, H.K. Aerodynamic Performance of Stepped Labyrinth Seal for Gas Turbine Applications. In Proceedings of the ASME Turbo Expo 2010: Power for Land, Sea, and Air, Glasgow, UK, 14–18 June 2010. ASME Paper GT2010-23256.
23. Zhang, L.; Zhu, H.R.; Liu, C.L.; Tong, F. Experimental and Numerical Investigation on Leakage Characteristic of Stepped Labyrinth Seal. In Proceedings of the ASME Turbo Expo 2016: Power for Land, Sea, and Air, Seoul, Korea, 13–17 June 2016. Paper GT2016-56743.
24. Vakili, A.D.; Meganathan, A.J.; Michaud, M.; Radhakrishnan, S. An Experimental and Numerical Study of Labyrinth Seal Flow. In Proceedings of the ASME Turbo Expo 2005: Power for Land, Sea, and Air, Reno, NV, USA, 6–9 June 2005. ASME Paper GT2005-68224.
25. Braun, E.; Dullenkopf, K.; Bauer, H.J. Optimization of Labyrinth seal Performance Combining Experimental, Numerical and Data Mining Methods. In Proceedings of the ASME Turbo Expo 2012: Power for Land, Sea, and Air, Copenhagen, Denmark, 11–15 June 2012. ASME Paper GT2012-68077.
26. Kline, S.J. The purposes of uncertainty analysis. *J. Fluids Eng. Trans.* **1985**, *107*, 153–160. [[CrossRef](#)]
27. ANSYS Inc. *ANSYS CFX 19.0*; ANSYS Inc.: Canonsburg, PA, USA, 2018.
28. ANSYS Inc. *ANSYS CFX-Solver Modeling Guide*; ANSYS Inc.: Canonsburg, PA, USA, 2011.
29. Menter, F.R. Two-equation eddy-viscosity turbulence models for engineering applications. *AIAA J.* **1994**, *32*, 1598–1605. [[CrossRef](#)]
30. Coughtrie, A.R.; Borman, D.J.; Sleigh, P.A. Effects of turbulence modelling on prediction of flow characteristics in a bench-scale anaerobic gas-lift digester. *Bioresour. Technol.* **2013**, *138*, 297–306. [[CrossRef](#)] [[PubMed](#)]


Publisher’s Note: MDPI stays neutral with regard to jurisdictional claims in published maps and institutional affiliations.



© 2020 by the authors. Licensee MDPI, Basel, Switzerland. This article is an open access article distributed under the terms and conditions of the Creative Commons Attribution (CC BY) license (<http://creativecommons.org/licenses/by/4.0/>).

Article

Experimental and Comparative RANS/URANS Investigations on the Effect of Radius of Volute Tongue on the Aerodynamics and Aeroacoustics of a Sirocco Fan

Xiaocheng Rui ¹, Limin Lin ², Junkui Wang ³, Xinxue Ye ², Haijiang He ², Wei Zhang ^{1,*}  and Zuchao Zhu ¹

¹ National-Provincial Joint Engineering Laboratory for Fluid Transmission System Technology, Zhejiang Sci-Tech University, Hangzhou 310018, Zhejiang, China; rxc_swiss@126.com (X.R.); zhuzuchao@zstu.edu.cn (Z.Z.)

² Zhejiang Yilida Ventilator Co., Ltd., Taizhou 318056, Zhejiang, China; linlimin@yilida.com (L.L.); yexinxue@yilida.com (X.Y.); hehj.tz@yilida.com (H.H.)

³ Beijing Aerospace Control Center, Beijing 100076, China; junkui34@163.com

* Correspondence: zhangwei@zstu.edu.cn

Received: 19 October 2020; Accepted: 9 November 2020; Published: 11 November 2020



Abstract: The geometry of volute tongue is crucial in the design of Sirocco fans. The size of the volute tongue determines its relative position and distance from the impeller which affects the local flow characteristics and thus the aerodynamic and aeroacoustic performances of the fan. In this work, we performed experimental and numerical investigations on the effect of volute tongue radius on the aerodynamic and aeroacoustic characteristics of a Sirocco fan. The internal flow characteristics are analyzed and discussed in terms of the spatial distribution and temporal variation of pressure and streamlines, the pulsating behaviors of pressure both in the impeller and on the volute surface with emphasis in the volute tongue region, the variation of passage flow with the rotation of impeller and the aeroacoustic features of the fan. We conducted numerical simulations using both steady Reynolds-Averaged Navier-Stokes (RANS) and unsteady Reynolds-Averaged Navier-Stokes (URANS) approaches with realizable $k-\varepsilon$ turbulence model with rotation effect correction and the results are compared against the experimental data to assess the prediction capability and accuracy in qualitative and quantitative manners. Experimental and numerical results show that as the volute tongue radius increases, the static pressure rises as well as the far-field noise of the fan and pronounced fluctuation of flow is observed within the whole impeller and volute; the reversed flow in the passage of the impeller is reduced and the high-pressure region is found to be moving towards the outlet of the volute. The decreasing radius also enlarges the size of the adverse pressure gradient (APG) region on the volute tongue which contributes to the formation of recirculating flow. The comparative RANS and URANS simulations reveal that both approaches produce generally consistent results regarding the time-averaged flow although the URANS data are much closer to those of the experimental ones. However, the fluctuating flow which is not capable to be modeled by RANS still dominates for the present configuration and thus URANS is necessary for the accurate prediction of the flow details.

Keywords: Sirocco fan; URANS; volute tongue radius; internal flow; noise

1. Introduction

Sirocco fans, also named as multi-blade centrifugal fans, are widely used in industrial and civil applications due to its small size, large flow coefficient and high pressure coefficient, while the

disadvantages of low static pressure and low efficiency have always restricted the development of the Sirocco fans. The analysis and research of the internal flow of the Sirocco fans by means of reasonable and applicable approaches play a meaningful guiding role in further improving and optimizing the performance of the fans.

The volute is one of the main components of the Sirocco fans which plays an important role in guiding the flow outside of the impeller and converting kinetic energy into pressure energy and has received wide extensive attention from many researchers. Rafael et al. applied a numerical model to compute the pressure fluctuation on the volute wall of the fan and obtained an important peak of pressure fluctuation near the volute tongue [1]. By controlling the volute tongue which determines the recirculation flow, Dilin et al. obtained the velocity and pressure distribution under a wide range of azimuth angles [2]. Because the design of the recirculation channel and the volute tongue have a greater impact on the performance and flow stability of the centrifugal fans, Okauchi et al. used four alternative volute designs and accurately measured the flow near the volute outlet and volute tongue and studied the effect of the volute structure on the performance of the fan. The results show that the optimized volute improves the performance of the fan but the flow is unstable when the flow rate increases [3]. Whitfield and Johnson took the compressor as the research object and studied the influence of the volute design on its performance. It was found that while improving the performance of the whole machine, the design method of reducing the flow area under the condition of large flow rate does not have a better effect [4]. Xiao et al. used the energy gradient theory to study the flow instability of the centrifugal fan and finally showed that the impeller outlet and the volute tongue area are prone to produce flow instability and the flow near the hub was more stable than that near the shroud [5]. Pan et al. extended the initial conceptual design of the centrifugal fan and compressor volute and the detailed internal flow data under design and off-design conditions obtained by numerical simulations showed that without changing the ratio of the volute outlet area, the flow area of the volute adjacent to the volute region is increased and the flow distribution is improved [6]. Lun et al. studied the effect of inclined volute on the internal flow and performance of centrifugal fans and found an optimal incline angle to obtain better performance improvement [7]. Sandra et al. conducted an experimental study on the two radial outlet positions of a certain forward curved blade centrifugal fan by hot wire techniques and found a strong flow asymmetry, especially in the circumferential position near the volute tongue and other ones and there is a big difference between the locations [8]. Sina and Javad studied the effect of the volute spread angle on the efficiency and internal flow pattern of Sirocco fans by experimental and numerical methods. The results showed that in a finite space, a fan with a spread angle of 5° has the highest head and efficiency [9]. Zhou and Li studied the characteristics of the centrifugal fan volute based on the method of dynamic torque correction to design a better volute profile. It was found that the radial velocity component at the outlet of the volute increases sharply while the noise is reduced without affecting the performance of the fan [10]. Sunil et al. focused on the effect of volute tongue gap on the performance of backward curved blade centrifugal blowers. The comparison of the four sets of data showed that the volute tongue gap has a significant impact on its performance and the total pressure and efficiency of the blower increased with the decrease of the clearance [11].

The impeller is the main component of the Sirocco fans and its geometry, size, number of blades and so forth have a crucial influence on the performance of the fan. Taking a widely used centrifugal fan as the research object, Zhang et al. analyzed the influence of the optimized combination of impeller geometrical parameters, such as the number of blades and the impeller outlet width, on the performance and noise of the fan. Under the design conditions, the combination of parameters after optimization makes the total pressure significantly increasing by 6.91% [12]. Lee et al. proposed a method of redesigning the centrifugal impeller and its intake passage. The resulting effect not only satisfies the pressure requirements but also reduces the power of the fan by 8.8% compared with the baseline model [13]. Wang et al. proposed an inverse design method for calculating the meridional surface of the centrifugal impeller. The final computation results show that the performance of the fan inlet is improved and the velocity distribution is more uniform [14]. Kim et al. conducted a

parameter optimization study on the impeller geometry of the forward curved blade centrifugal fan. The height of the annular plate separating the impeller and the angle between the upper and lower impellers were chosen as geometric parameters. The influence of these parameters on the efficiency of the fan was analyzed. The results show that reasonable parameters are conducive to improving the aerodynamic performance of the fan [15]. Ni et al. changed the straight blades of the baseline Sirocco fan impeller into inclined blades with a certain angle, obtained an optimal value of the inclination angle and improved the aerodynamic performance of the fan [16]. Kim and Seo successfully applied the response surface optimization method of three-dimensional N-S analysis to the aerodynamic design of forward curved blade centrifugal fans and obtained the maximum static pressure efficiency [17].

The influential factors, such as the interaction or positional relationship between the impeller and the volute or other components, have a significant effect on the internal flow of the fans. Tarek and Seung conducted a numerical simulation analysis of the interactions among the impeller, diffuser and volute. It was found that the vortex flow area in the volute is gradually attenuated from the part near the volute tongue to the fan outlet [18]. Koen and Rene proposed a numerical method for predicting the interaction between impeller and volute in a single-stage centrifugal compressor and analyzed the influence of the interaction between impeller and volute on the circumferential distortion of static pressure [19]. Karanth and Sharma considered the complex flow between the impeller outlet and the diffuser, studied and predicted the flow characteristics caused by the radial clearance by numerical simulation analysis and the results showed that there is an optimal radial clearance which made better energy conversion of the impeller [20]. Lee conducted a study and analysis of the gap effect between the inlet duct and the rotating impeller of the centrifugal fan. The results showed that improper gap determination would reduce the overall performance of the fan by 2–5% [21]. Jose et al. studied the interaction between the impeller and the volute and numerically analyzed the secondary flow in the volute through the helicity magnitude. The results showed that there is a strong secondary flow in the radial position near the outlet of the impeller [22]. Daniel et al. considered the influence of the relative position of the impeller and the volute on the performance of the centrifugal pump. Through the research, it was found that the efficiency of circular volute and spiral volute increases by 5% and 3.5%, respectively, as the impeller is in the optimal position compared with the central position [23]. Younsi et al. studied the interaction and unsteady characteristics of the rotating blades relative to the movement of the volute. Analysis of the pressure fluctuations on the volute surface showed that the main source of flow disturbance and instability in the centrifugal fan is the volute region [24].

Bechara et al. devised a stochastic noise generation and radiation (SNGR) model for noise generation and radiation from the turbulent flow field [25]. Billson et al. used a SNGR method to capture the sound field of a high Reynolds number, high Mach number subsonic jet. The directivity of the far-field sound is well predicted but the amplitude and spectral information differ from the measurements [26]. Ewert studied the application of a low-cost computational aeroacoustics (CAA) approach to a slat noise problem. Slat noise simulations are carried out for a high-lift airfoil and the Mach number scaling law of the broadband slat noise component is evaluated based on three different free-stream velocities ($M = 0.088, 0.118, 0.165$) [27]. In the following work, the simulated 1/3-octave spectrum exhibits the main features of an empirical slat-noise mode [28]. Bailly et al. introduced an application of direct calculation of aerodynamic noise in subsonic and supersonic jet noise, cavity noise and self-excited internal flows [29]. Sandberg conducted direct numerical simulations (DNS) to airfoil self-noise. It is found that the contribution of trailing edge noise dominates at low frequencies while for the high frequencies the radiated noise is mainly due to flow events in the reattachment region on the suction side [30]. Dawi and Akkermans studied spurious noise generated in direct noise computation using finite volume methods. Different sources of spurious noise are examined as well as the mechanism of their generation [31]. In another work, they used direct noise computation and Ffowcs Williams-Hawkings equation to calculate far-field spectral. The peaks of vortex shedding frequency were well predicted, however, the amplitude of the spectra at these frequencies is smaller than the ones in the wind tunnel [32]. Deuse and Sandberg studied the self-noise of an isolated

controlled-diffusion aerofoil using direct noise computation. Two main noise sources were observed, one at the trailing edge and one in the transition/reattachment region. For the cases investigated, the latter is even more important than the trailing edge noise component [33]. Dawi and Akkermans demonstrated the applicability of a finite volume method for the direct noise computation of road vehicles, the results of the DNC showed good agreement with wind tunnel measurements within a certain frequency range. However, at higher frequencies, simulated acceleration spectra showed lower spectral levels than the measured ones [34]. Dierke et al. investigated the effect of installation on propeller sound. It is found that the installation effect due to the presence of the high-lift wing increases the sound pressure levels by 5–10 dB in most directions [35]. The research by Dobrzynski et al. on airframe noise prediction and reduction methods pointed out that the noise level of gears installed under the wings is reduced by about 4 decibels relative to gears installed on the fuselage. The aerodynamic optimum design of current slotted slats causes maximum gap-flow velocities and thus high slat noise levels [36]. Ewert et al. analyzed the changes of acoustic level due to a change of slat position and found that by changing the slat gap, the acoustic level of some frequency segments also changed correspondingly [37].

It can be concluded from the above literature review that the geometry of the volute, especially the volute tongue radius, the distance to the impeller outlet and the axial change of the volute surface determine the flow in the vicinity of the impeller outlet and volute tongue and affect the interaction between the fluid within the impeller and the volute, with a vital influence on the performance of the Sirocco fan. Considering that the radius of the volute tongue determines the distance between the local volute wall and the impeller, in this work we performed experimental and numerical investigation on the internal flow of a Sirocco fan with various volute tongue radii to identify its effect on the aerodynamic and aeroacoustic characteristics of the fan. Only the radius of the volute tongue is varied but the distance to the outlet of the impeller keeps unchanged and the internal flow is analyzed in terms of the spatial distribution and temporal variation of pressure and streamlines, the pulsating behaviors of pressure both in the impeller and on the volute surface with emphasis in the volute tongue region, the variation of passage flow with the rotation of impeller and the aeroacoustic features of the fan. Another objective of the present work is to explore the capability, reliability and accuracy of RANS and URANS approaches in modeling flow in similar fan configurations both in qualitative and quantitative manners and provide meaning conclusions in further simulations.

The paper is organized as follows—Section 2 is a general description of the fan configuration, the employed numerical methods, the experiment details and the validation. Section 3 presents and discusses the numerical and experimental results for the effect of radius of volute tongue. Some conclusions are drawn in Section 4.

2. Numerical Methods

2.1. Fan Configuration

The fan in this investigation is a double-suction, forward-curved multi-blades Sirocco fan which is shown in Figure 1. The blades are staggered on both sides of the impeller's central disk with 41 blades on each side. The air enters the volute and impeller from the inlet domain on both sides of the fan and moves out from the outlet domain. Table 1 lists the specifications of the baseline model. The radius of volute tongue of the baseline model is 11 mm and the location is denoted in the figure. In this work, we investigate the effect of volute tongue radius at four values, that is, $r = 4$ mm, 9 mm, 11 mm and 13 mm, on the aerodynamic and aeroacoustic characteristics of the fan at the designed flow rate 365 m³/h.

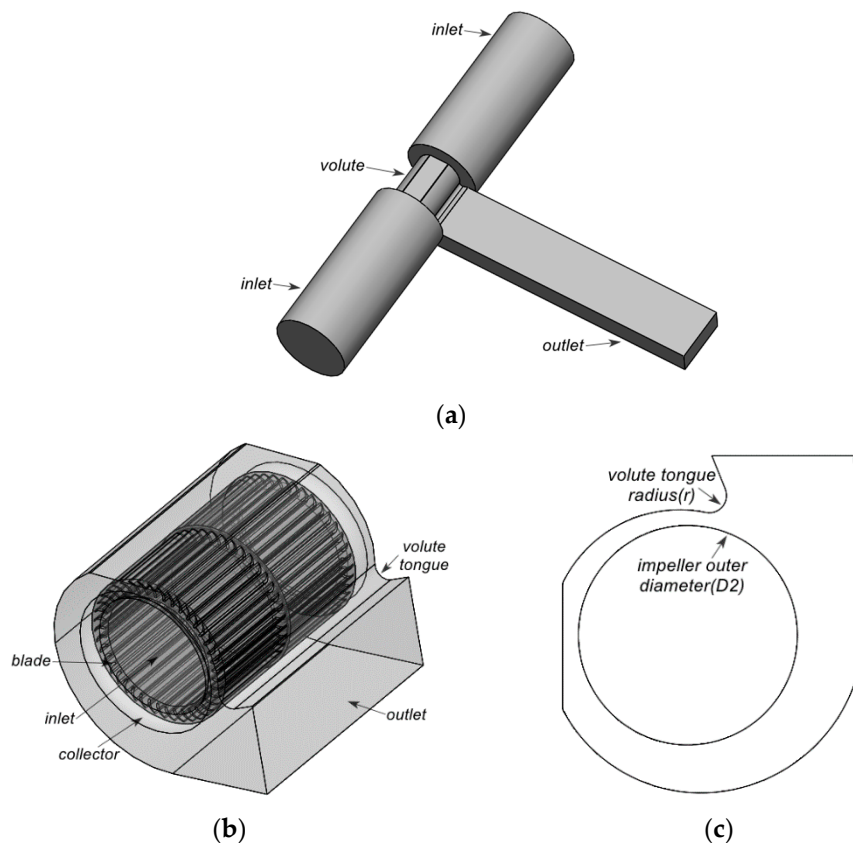


Figure 1. Baseline model. (a) fan model; (b) impeller and volute; (c) definition of radius of volute tongue.

Table 1. Specifications for the baseline Sirocco fan.

Specification	Value
Flow rate, Q_n (m^3/h)	365
Rotation speed of impeller (rpm)	1200
Impeller outer diameter, D_2 (mm)	140
Impeller inner diameter, D_1 (mm)	55
Volute width, B (mm)	228
Impeller width, b (mm)	190
Number of blades, Z	41
Volute tongue radius, r (mm)	11

2.2. Numerical Simulation Method

The internal flow of the Sirocco fan is governed by the conservation of mass and momentum equations:

$$\frac{\partial u_i}{\partial x_i} = 0 \quad (1)$$

$$\frac{\partial u_i}{\partial t} + u_j \frac{\partial (u_i)}{\partial x_j} = f_i - \frac{1}{\rho} \frac{\partial P^*}{\partial x_i} + \nu \frac{\partial^2 u_i}{\partial x_j \partial x_j}, \quad (2)$$

where ρ represents the density of the air; x_i is the direction component of the Cartesian coordinate system; u_i is the velocity component; P^* is the pressure considering the conversion of turbulent kinetic energy and centrifugal force; f_i is the component of the volume force. ν is the kinematic viscosity coefficient:

$$\nu = \frac{1}{\rho} (\mu + \mu_t) = \frac{\mu}{\rho} + C_\mu \frac{k^2}{\varepsilon}, \quad (3)$$

where μ is the molecular viscosity coefficient and μ_t is the vortex viscosity coefficient. In the numerical simulation, we use the realizable k - ε turbulence model with rotation effect correction in which C_μ is calculated by the following formula:

$$C_\mu = \frac{1}{A_0 + A_S \frac{kU^*}{\varepsilon}}, \quad (4)$$

in which $A_0 = 4.04$, $A_S = \sqrt{6} \cos \phi$, $\phi = \frac{1}{3} \cos^{-1}(\sqrt{6}W)$, $W = \frac{S_{ij}S_{jk}S_{ki}}{\bar{S}}$, $\bar{S} = \sqrt{S_{ij}S_{ij}}$, $S_{ij} = \frac{1}{2}\left(\frac{\partial u_j}{\partial x_i} + \frac{\partial u_i}{\partial x_j}\right)$, $U^* \equiv \sqrt{S_{ij}S_{ij} + \bar{\Omega}_{ij}\bar{\Omega}_{ij}}$, $\bar{\Omega}_{ij} = \Omega_{ij} - 2\varepsilon_{ijk}\omega_k$, $\Omega_{ij} = \bar{\Omega}_{ij} - \varepsilon_{ijk}\omega_k$. $\bar{\Omega}_{ij}$ is the laminar curl with angular velocity.

The transport equations for the turbulent kinetic energy k and turbulent dissipation rate ε in realizable k - ε turbulence models are as follows:

$$\frac{\partial}{\partial t}(k) + \frac{\partial}{\partial x_i}(ku_j) = \frac{1}{\rho} \frac{\partial}{\partial x_i} \left[\left(\mu + \frac{\mu_t}{\sigma_k} \right) \frac{\partial k}{\partial x_j} \right] + G_k + G_b - \rho\varepsilon - Y_M + S_k \quad (5)$$

$$\frac{\partial}{\partial t}(\varepsilon) + \frac{\partial}{\partial x_j}(\varepsilon u_j) = \frac{1}{\rho} \frac{\partial}{\partial x_j} \left[\left(\mu + \frac{\mu_t}{\sigma_\varepsilon} \right) \frac{\partial \varepsilon}{\partial x_j} \right] + C_{1\varepsilon} \frac{\varepsilon}{k} G_b + S_\varepsilon - C_2 \frac{\varepsilon^2}{k + \sqrt{\nu\varepsilon}} + C_{1\varepsilon} \frac{\varepsilon}{k} C_{3\varepsilon} G_b + S_\varepsilon. \quad (6)$$

In the equation, G_k and G_b represent the turbulent kinetic energy terms generated by laminar velocity gradient and buoyancy, respectively. Y_M represents the contribution to the dissipation rate of the expansion of turbulent pulsation to the global flow in compressible flows. $C_{1\varepsilon}$ and C_2 are constants. σ_k and σ_ε are the Prandtl numbers. S_k and S_ε are user-defined turbulent kinetic energy and turbulent dissipation source terms. For the incompressible air as the working medium, $G_b = 0$ and $Y_M = 0$.

In this work, we performed both RANS and URANS simulations using ANSYS-Fluent 17.0 (Version, ANSYS, Inc., Canonsburg, PA, USA, 2016) for the same models and flow parameters. In the simulations, second-order upwind scheme is used for the spatial discretization of all derivative terms; the SIMPLE method is used for the coupling of velocity and pressure and the moving reference frame (MRF) method is used to treat the rotation of the impeller. The boundary conditions are the same for both simulation approaches. Constant mass flow rate is prescribed at the two inlet sections and zero gauge pressure at the outlet section. No-slip boundary condition is set for velocity on all solid walls. We first perform the RANS simulation until the converged result with relative residual less than 10^{-3} is obtained for the equations of mass, momentum, turbulent kinetic energy and turbulent dissipation rate. The result is then used as initial condition to start the URANS simulation and the simulation continues as the impeller rotates for ten revolutions before the data are collected. The physical time step size is fixed as the impeller rotates for one degree, thus 360 steps are required for one revolution of the impeller.

2.3. Grid Independence Study

The computational domains of the fan include two inflow domains on both sides, an outflow domain, a volute domain, an impeller domain and the intermediate flow channel domain of the impeller. The impeller and intermediate flow channel of the impeller constitute the rotational domain, while the other domains are set stationary. The impeller, inflow and outflow domains are discretized by block-structured grid, while the volute domain is discretized by unstructured grids considering its complex geometry and subsequent geometrical modifications. Figure 2 shows the grid distributions adjacent to the impeller and volute and the grids number is shown in Table 2.

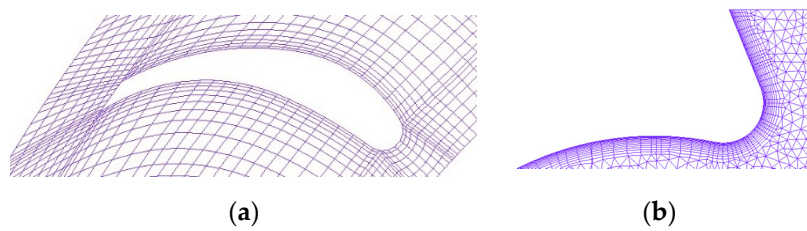


Figure 2. (a): The grids around the blade, (b): The grids around the volute tongue.

Table 2. Number of grids of the computational domain.

Component	Number of Grids (10^3)
Impeller	5685
Inlet	904
Outlet	204
Volute	1513
Total	8306

In this paper, the static pressure rise, computed as the difference between the static pressure at the outflow and inflow sections of the fan, is used as the indicator for the grid independence study under design flow rate of $365 \text{ m}^3/\text{h}$. The grid number is changed mainly for the impeller domain. Three sets of impeller grids with the number of about 4.6 million, 5.7 million and 6.7 million are used, respectively. The variation of static pressure rise with grid number is shown in Figure 3. As the number of grids increases from 4.6 million to 5.7 million, the variation of static pressure is 1.07 Pa; as the grid number continues to change to 6.7 million, the variation of static pressure rise is only 0.08 Pa, which is only 0.1% higher than the static pressure at 5.7 million. Therefore, we consider that the influence of a higher grid number on the computational results can be negligible, so the impeller domain with a grid number about 5.7 million is chosen for subsequent work.

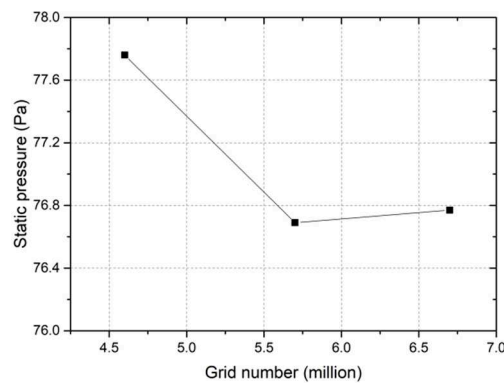


Figure 3. Variation of static pressure rise with grid number of impeller domain.

2.4. Experiment Details

The various volute models of the Sirocco fan are made by 3D printing and are experimentally tested in the aerodynamic-aeroacoustic laboratory of Zhejiang Yilida Ventilator Co., Ltd. (Taizhou, China). The experimental device is designed according to National Standard of China GB/T1236-2017 and conforms to the International Standard ISO5801-2007. The semi-anechoic noise test is designed according to ISO3745-2003. The noise monitoring can be carried out synchronously when the aerodynamic performance of the fan is tested. The volute models and the impeller are comparably shown in Figure 4. The schematic diagram and photo of the experimental facility are shown in Figure 5. The size of the east and west semi-anechoic room is $5200 \text{ mm} \times 4800 \text{ mm} \times 7000 \text{ mm}$ and $5200 \text{ mm} \times 5600 \text{ mm} \times 7000 \text{ mm}$, respectively and the air compartment size is $3000 \text{ mm} \times 3000 \text{ mm} \times 9000$

mm. The semi-anechoic room and the air compartment are connected by a circular pipe and the overall loop is a closed-chamber circulation structure. The measurement system mainly includes fan, motor, photoelectric infrared speed sensor, microphone and so forth, as shown in Figure 6. The test facility could measure and record the pressure and temperature of the inlet and outlet flows and the aerodynamic noise in a synchronous way.



Figure 4. Impeller and volute with tongue radius $r = 4$ mm, 9 mm, 11 mm and 13 mm.

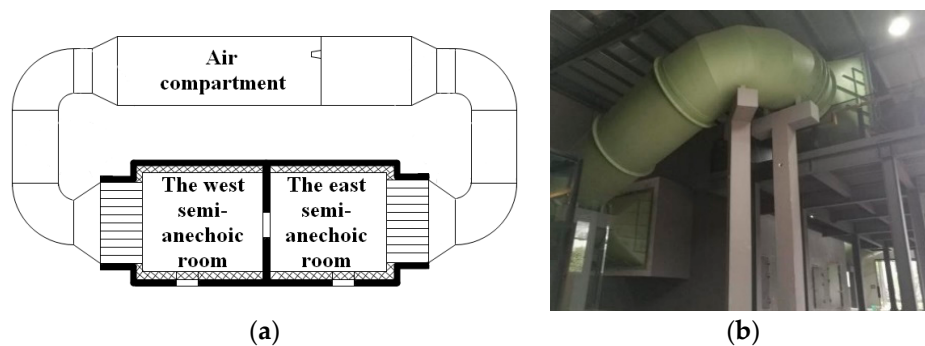


Figure 5. (a) The schematic diagram, (b) photo of the facility.

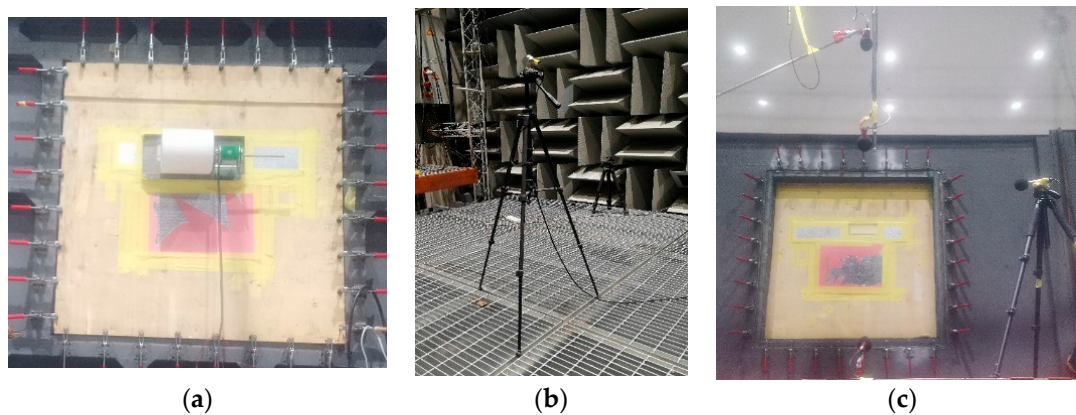


Figure 6. Test equipment: (a) fan and motor; (b) photoelectric infrared speed sensor; (c) microphone.

3. Results and Discussion

3.1. Aerodynamic Performances

The static pressure rise and static pressure efficiency are the key parameters reflecting the aerodynamic performances of the Sirocco fan and is experimentally measured as well as simulated in this work. Figure 7 gives the time history and time-averaged value of the static pressure rise of the fan obtained by URANS and compared with those obtained by RANS simulation and experiment. Tables 3 and 4 list the static pressure rise and efficiency predicted by experiment, RANS and URANS in time-averaged sense.

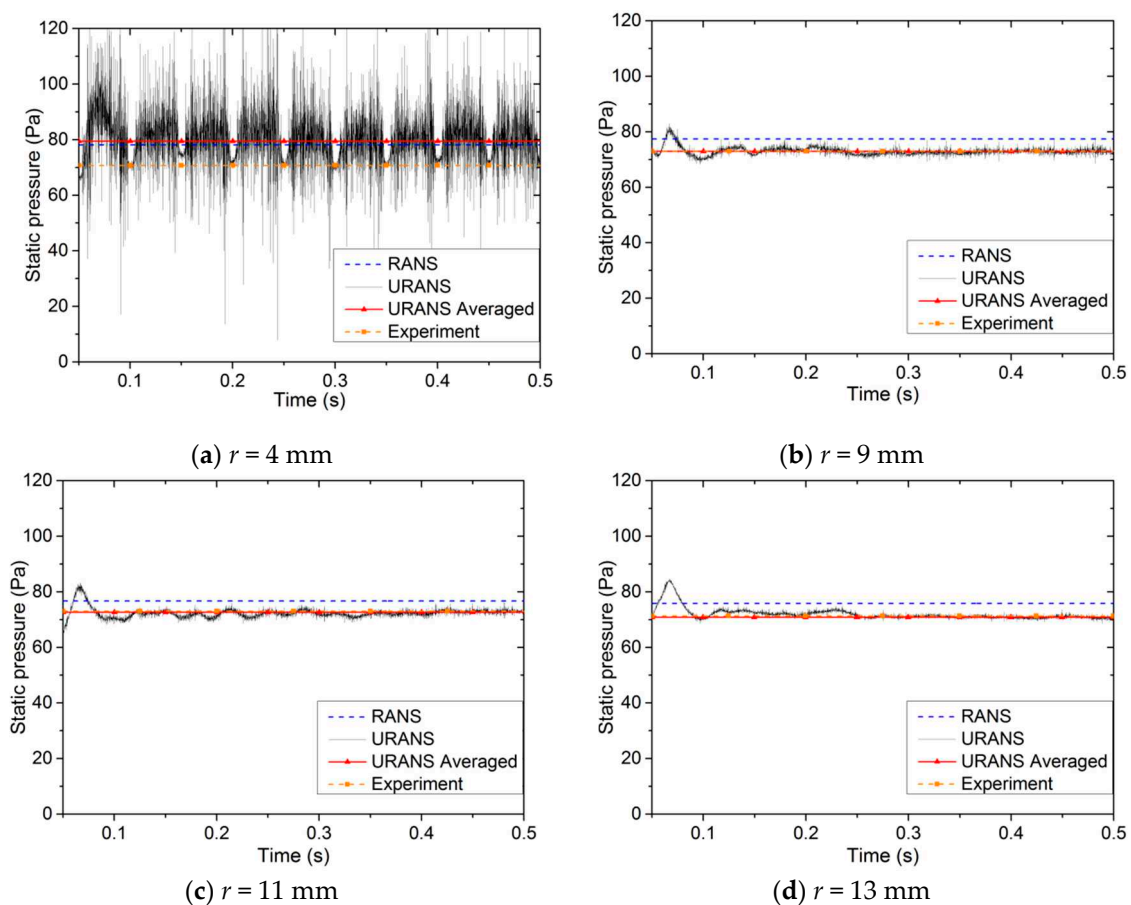


Figure 7. Time history of static pressure and its averaged value computed by unsteady Reynolds-Averaged Navier-Stokes (URANS) in comparison with those of Reynolds-Averaged Navier-Stokes (RANS) and experiment.

Table 3. Experimental and numerical results of static pressure.

Method	$r = 4 \text{ mm}$	$r = 9 \text{ mm}$	$r = 11 \text{ mm}$	$r = 13 \text{ mm}$
Experiment	70.68	72.98	73.04	71.33
RANS	78.37	77.38	76.69	75.83
URANS averaged	79.43	72.91	72.65	70.84

Table 4. Experimental and numerical results of static pressure efficiency.

Method	$r = 4 \text{ mm}$	$r = 9 \text{ mm}$	$r = 11 \text{ mm}$	$r = 13 \text{ mm}$
Experiment	30.66%	32.01%	31.22%	30.53%
RANS	31.00%	30.17%	29.86%	29.00%
URANS averaged	37.18%	33.27%	33.75%	32.33%

It is seen from the figure and tables that for models with $r = 9 \text{ mm}$, 11 mm and 13 mm , the relative difference between the results of RANS and experiment is 6.3% at maximum which is of engineering significance. However, the URANS produce much better consistent data with respect to the experimental one; the maximum relative difference between the time-averaged static pressure rise and experimental data is only 0.7%. This reflects that the URANS simulation is more consistent with the realistic operation of the fan and is capable to simulate the flow inside the fan more accurately. For the model with $r = 4 \text{ mm}$, the sharper volute tongue strongly destabilize the local flow around the outlet of the volute, thus the pressure rise substantially fluctuates with a large amplitude and the periodicity due to impeller rotation is clearly observed. Both the results produced by RANS and

URANS in time-averaged sense notably deviate from the experimental data with relative difference about 10%. Therefore, we believe that the accuracy of simulation is greatly affected by the pulsating flow and the simulation is less capable in accurately predicting the internal flow of the fan.

Comparing the models with different volute tongue radius, it can be found that the pressure fluctuation in URANS from the 5th to the 10th revolution of the impeller presents the smallest amplitude for the $r = 13$ mm volute, which almost perfectly coincides with the time-average value. For the $r = 9$ mm and 11 mm models, the amplitude slightly increases but is still small compared with the magnitude of pressure rise. The amplitude is the highest for the $r = 4$ mm model. It is also noted that as the radius decreases, the time-averaged pressure monotonically increases from $r = 13$ mm to $r = 9$ mm, while the increasing generally stops for $r = 4$ mm. This indicates that smaller radius will generate stronger pressure pulsation and increases the pressure rise to different degrees. For the $r = 4$ mm model, notable quasi-periodic pressure fluctuation is observed in which one cycle approximately corresponds to 0.05 s as the revolution of the impeller; this is an indication that the sharper volute tongue could generate strong pulsating flow compared with other models.

3.2. General Characteristics of Internal Flow

The transient flow in the impeller and volute is analyzed for the 10th revolution of the impeller at four moments, that is, T1, T2, T3 and T4, with time interval between neighboring two moments as the impeller rotates for 90° . Figures 8–11 show the distribution of static pressure on axial cross-section $Z = 4$ mm which is close to the central disc of the impeller.

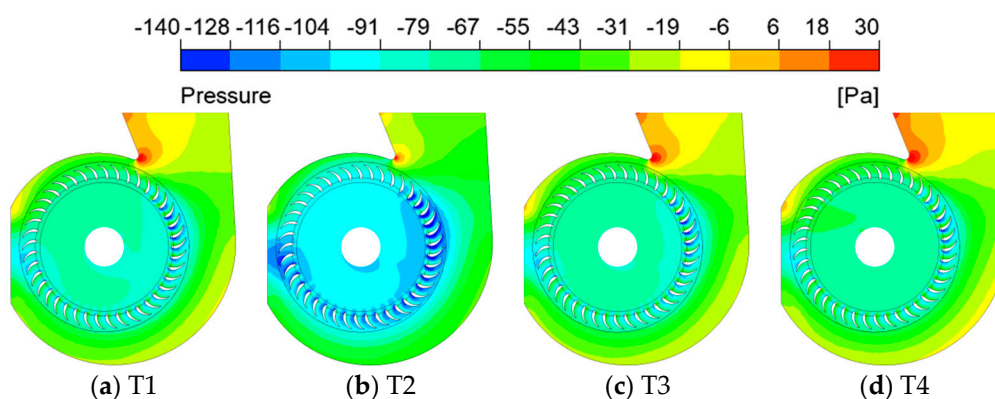


Figure 8. Distribution of static pressure on $Z = 4$ mm cross-section for the $r = 4$ mm model.

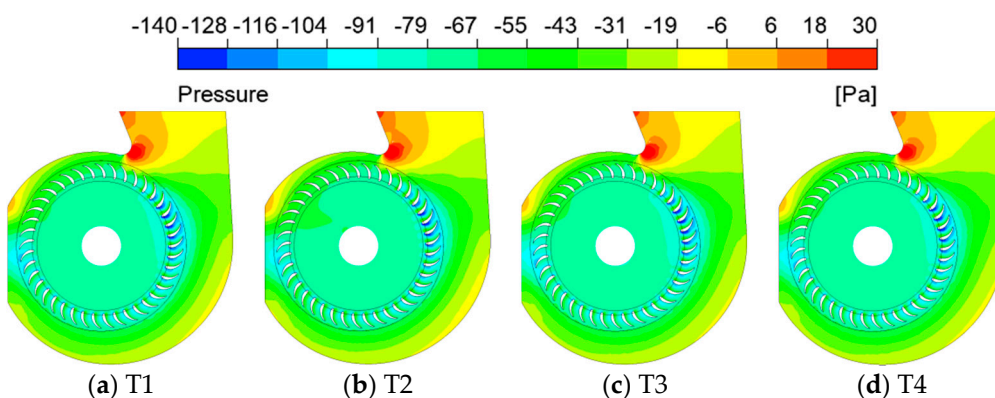


Figure 9. Distribution of static pressure on $Z = 4$ mm cross-section for the $r = 9$ mm model.

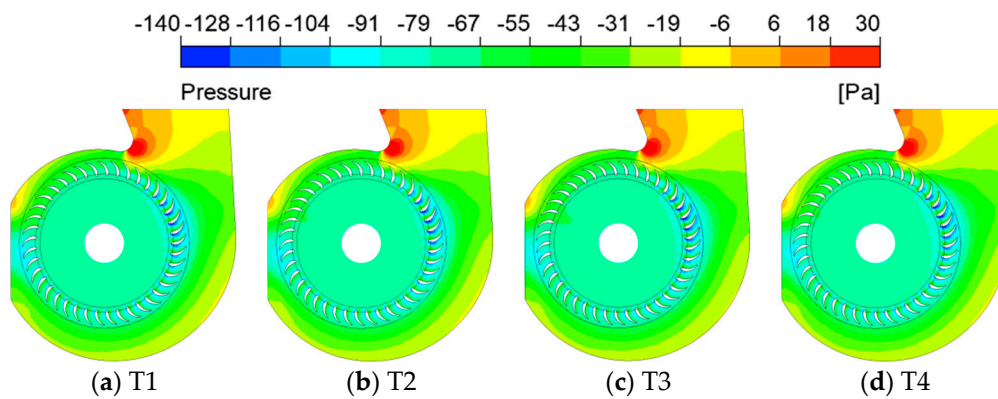


Figure 10. Distribution of static pressure on $Z = 4$ mm cross-section for the $r = 11$ mm model.

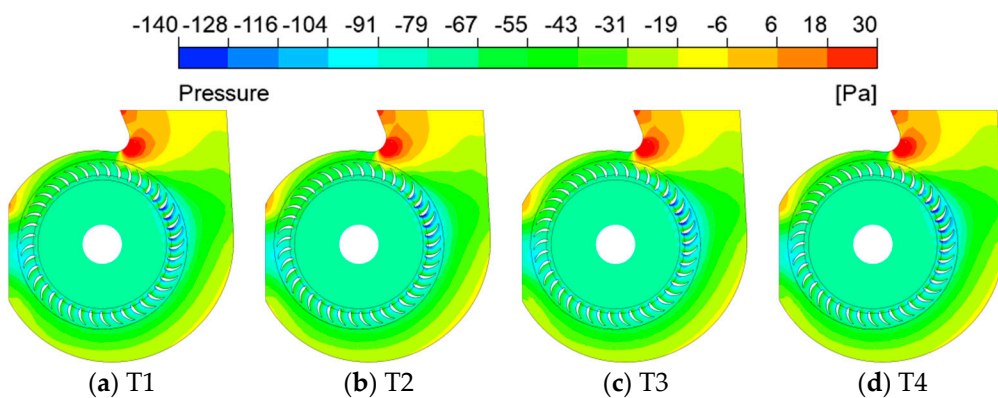


Figure 11. Distribution of static pressure on $Z = 4$ mm cross-section for the $r = 13$ mm model.

It is clearly seen that for models with $r = 9$ mm, 11 mm and 13 mm, the pressure distribution is quite similar at different moments in both the impeller and volute which is consistent with the conclusion obtained in Figure 7. The pressure has a minor fluctuation not only exhibited by its global behavior as the static pressure rise of the fan but also in a local manner. For the $r = 4$ mm model, noticeable temporal variations of pressure field are observed especially in the region between the volute tongue and outlet of the impeller. At time T2, the high-pressure area near the volute tongue is substantially smaller than that at the moment T1, while it increases in size at T3 and continues increasing to a certain extent at T4. Meanwhile, the low-pressure region that covers most of the impeller at time T2 has a wider distribution and a lower pressure magnitude. The above phenomenon indicates that the velocity of passage flow in the impeller is higher at T2 and the flow moves smoothly around the volute tongue. However, the flow is greatly affected by the sharp volute tongue and experiences pronounced changes.

Comparing the pressure distribution of different models, it can be found that for the $r = 9$ mm, 11 mm and 13 mm models, the high-pressure region in the vicinity of the volute tongue slightly expands in area, while it is notably smaller for the $r = 4$ mm model. As the flow velocity is in a state of change, at T2, part of the impeller passage exhibits a certain range of low pressure areas due to the higher flow velocity. This indicates that the volute tongue radius not only affects the flow near the volute tongue but also indirectly affects the flow in other region away from it.

3.3. Reversed Flow in Impeller Near the Volute Tongue

3.3.1. Reversed Flow Predicted by RANS

It is seen in Figures 8–11 that there is great pressure fluctuation in the passages of the impeller near the volute tongue, thus reversed flow, that is, in the direction from the outlet to inlet of the impeller,

may form during part of the revolution cycle. In order to explore the influence of volute tongue radius on reversed flow, in this section we present and analyze the flow in the impeller passages near the volute tongue. Figure 12 gives the schematic of the eight selected impeller passages. The angular cross-section at the 50% spanwise height is chosen as a representation covering the passages around the volute tongue and is expanded as on the X-Z plane in the figure. The distribution of v -velocity of flow in the selected passages is plotted in Figure 13. Since the selected blade passages are basically located in the region between 30° and 100° , the positive and negative v -velocity could generally indicate the forward passage flow which moves from the inlet to outlet of the blade passage and the reversed flow moving from the outlet to the inlet of the impeller.

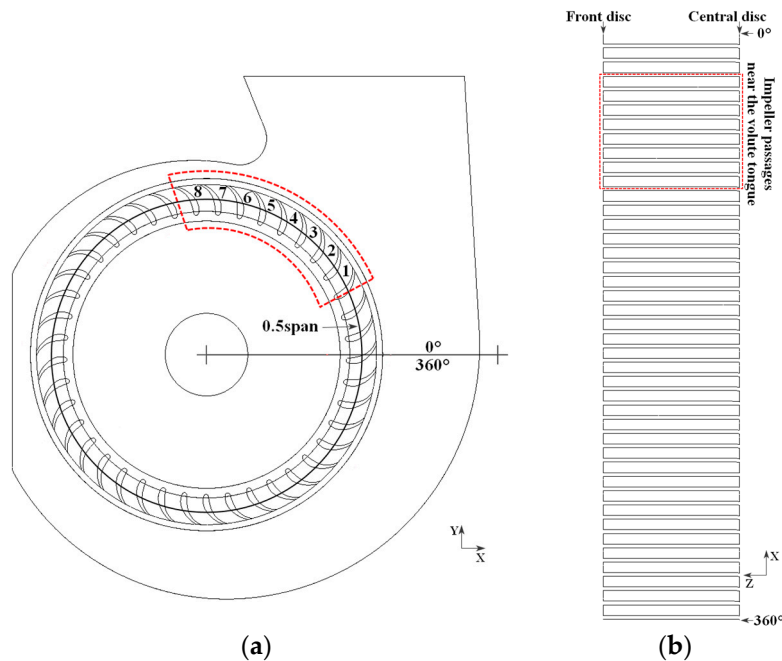


Figure 12. (a) Selected blade passages near the volute tongue, (b) the expanded view of the passages.

It is seen in Figure 13 that there is almost no reversed flow in passage-7 and passage-8 as predicted by the steady-state RANS simulation, while reversed flow of different scales and intensity form in passages 1–6. There is a large region with strong reversed flow close to the suction surface of the impeller and the central disc of the impeller, while forward flow is mainly observed near the pressure surface of the blade. Reversed flow starts to form in passage-6; the reversed flow with small magnitude occupies only a small region for the $r = 4$ mm mode but gradually expands in size and intensified as the radius increases. The same variation pattern of the reversed flow is also observed in passage-5. This variation pattern is attributed to the fact that the volute surface covers almost the whole passage-5 and passage-6 for the $r = 4$ mm model that the passage flow is not affected by the volute tongue, while for the models of $r = 9$ – 13 mm the volute tongue locates right beside the two passages, thus the flow is influenced by the local flow in the volute and presents reversed flow. For flow in passage 1–4, it is found that as the radius increases, there is more forward flow in the corner region of the pressure surface of the blade and the front disc of the impeller and the reversed flow still exists especially for passage-3 and passage-4. In general, the results of steady-state RANS simulation could reflect the primary characteristics of flow direction in the blade passages near the volute tongue.

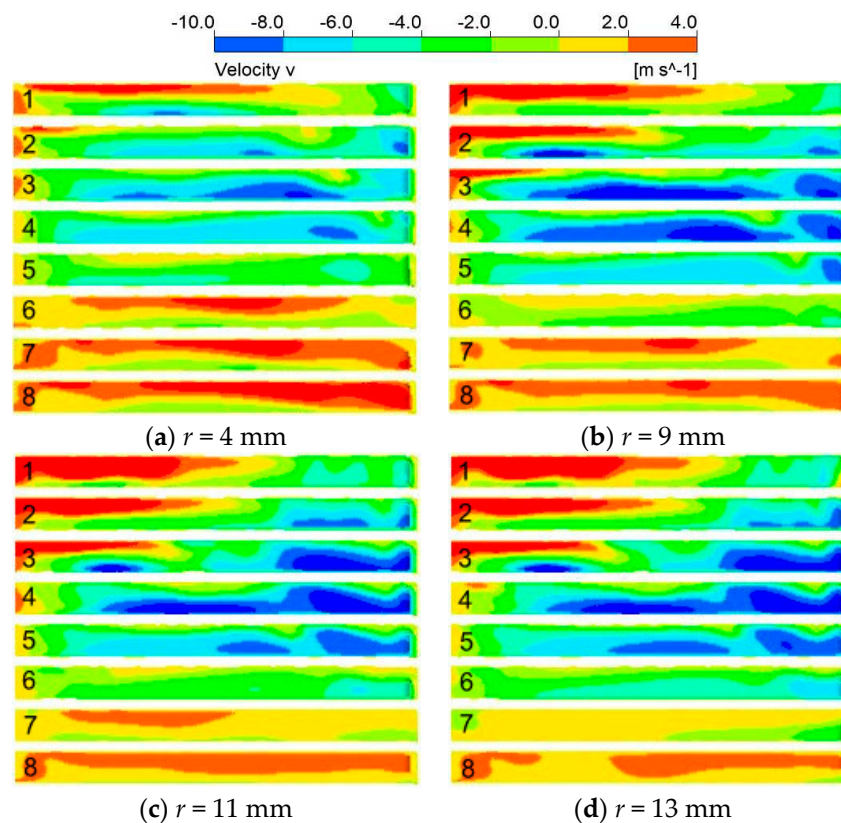


Figure 13. Distribution of v -velocity in the blade passages near the volute tongue.

3.3.2. Reversed Flow Predicted by URANS

In this section, the temporal variation of passage flow in the impeller is analyzed based on the transient results obtained by URANS simulation. We choose three fixed points in passage-1 at the middle between the pressure and suction side of the blade and on the $Z = 4$ mm, 45 mm and 90 mm axial cross-sections as the monitoring points and record the temporal variation of radial (r -) velocity as the passage moves to a series of circumferential positions with the rotation of impeller, as shown in Figure 14a, thus the variation of velocity reflect the temporal variation of the passage flow. The radial velocity is computed by vector manipulation based on u -velocity and v -velocity and forward and backward flows are identified as the radial velocity is positive and negative, respectively. To focus on the effect of volute tongue on the passage flow in the impeller, more circumferential positions are selected in the region near the volute tongue, while fewer monitoring points are positioned in the rest part of the circumference. Moreover, to facilitate the direct comparison with the steady-state RANS result, we also computed the radial velocity based on the result of RANS simulation at several circumferential positions which are identical with those for the URANS result, as shown in Figure 14b. Since the impeller is axisymmetric about the center of the geometry, the RANS result presents the variation of radial velocity under the Euler framework, while the URANS result is obtained under the Lagrange framework. The difference between the RANS and URANS results reveal the different capabilities of the two approaches.

Figure 15 presents the circumferential distribution of radial velocity for monitoring points on the $Z = 4$ mm, 45 mm and 90 mm axial cross-sections. For the $Z = 4$ mm cross-section close to the central disc of the double-suction impeller, the transient results show that there are primarily three regions for all four models categorized by the radial velocity, that is, the forward flow region roughly lower than 30° , the reversed flow region in the range between 30° and 130° and forward flow region after 130° . For the $r = 4$ mm model, the reversed flow is observed to occupy only a small region and the magnitude of radial velocity is lower compared with other three models and the flow turns to be forward around

70°. As the volute tongue radius increases to $r = 13$ mm, stronger reversed flow generates within this region. Referring Figure 14a, it can be concluded that as the blade passage approaching to the circumferential position $\Phi 1$, the magnitude of radial velocity of the reversed flow first increases and then decreases and then exhibits a local maximum near $\Phi 2$. The reduction of the volute tongue radius could reduce the range and velocity magnitude of reversed flow. In the range 0–30°, the radial velocity gradually decreases until it reaches zero and gradually increases in the range 130–360°. Comparing the RANS and URANS results, we can notice that there is great difference between the curves for both forward and reversed flows and for almost the entire circumference of the impeller which may be attributed to the existence of the central disc. For the $Z = 45$ mm cross-section, the transient result show that reversed flow also exists in quite small regions around the circumferential positions 30° and 120°, that is, close to $\Phi 1$ and $\Phi 2$ as shown in Figure 14a. The variation pattern of radial velocity in the circumferential direction is similar with that of the $Z = 4$ mm cross-section. A comparison of RANS and URANS results demonstrate that significant differences in the range 320–400° (40°) and 80–180°; in particular, the flow can be falsely predicted as reversed flow by RANS and the magnitude of velocity also deviate a lot compared with the URANS data. For the $Z = 90$ mm cross-section close to the front disc of the impeller, the transient result shows that reversed flow appear in the regions 0–40°, 110–130° and 200–270° although the magnitude of radial velocity is minor. The influence of volute tongue radius on the radial velocity is comparably smaller than those on the $Z = 4$ mm and 45 mm cross-sections. Pronounced difference is still observed between the RANS and URANS results.

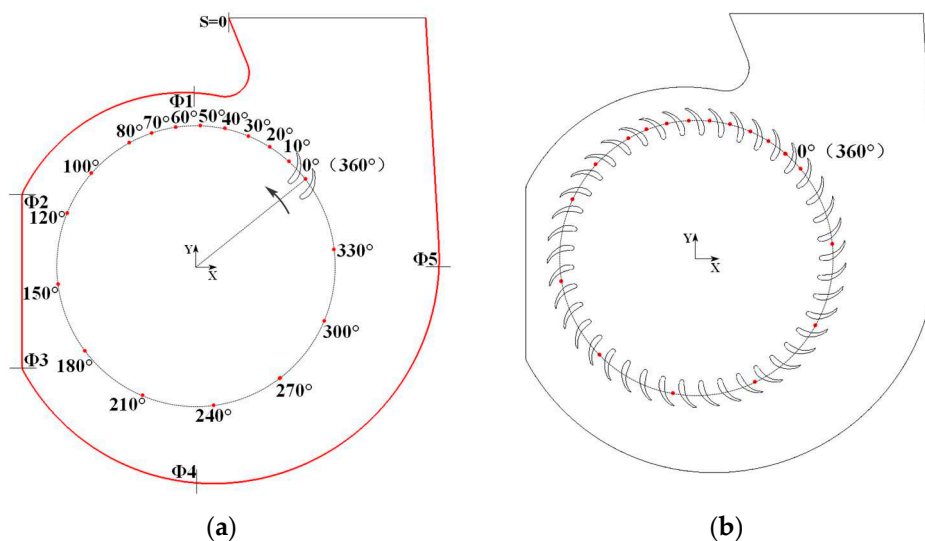


Figure 14. (a) Positions for the transient motion of the fixed point where pressure is recorded in URANS simulation; (b) positions where pressure is recorded in RANS simulation.

Since the flow enters the impeller from the front disc, the velocity direction changes from axial to radial as it gradually approaches the central disc. Therefore, near the front disc of the impeller, the radial velocity of the flow is relatively small and the degree of velocity change is small, which can be observed by comparing the distribution of the radial velocity on the three sections. The reversed flow roughly in the region 30–130° has the smallest and largest range on the $Z = 45$ mm and $Z = 90$ mm cross-sections in RANS and URANS results, respectively, which reflects that the flow near the central disc is less affected by the rotation of impeller. The comparison of RANS and URANS results show that the circumferential variation of velocity magnitude is much larger for the RANS simulation particularly on the $Z = 4$ mm cross-section where the RANS result is also greatly affected by the volute tongue radius.

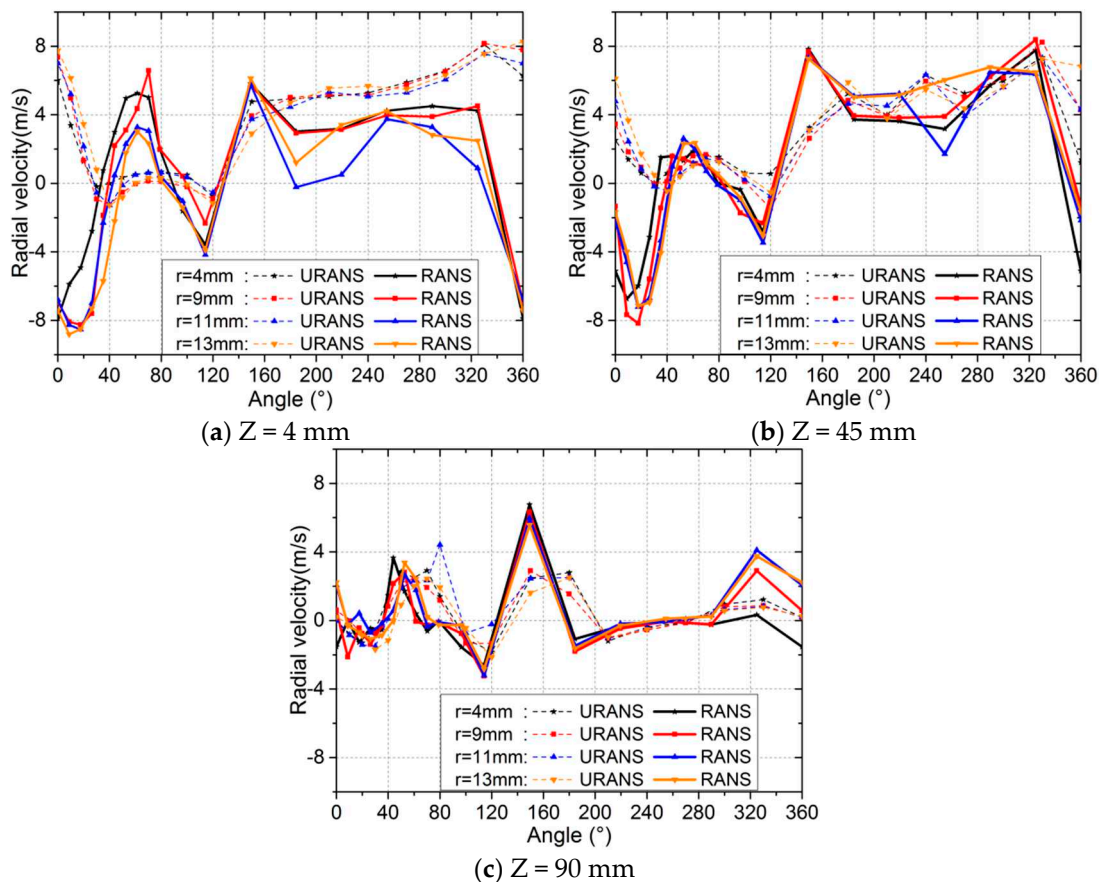


Figure 15. Variation of radial velocity within the blade passages.

3.4. Near-Wall Flow of the Volute Surface

For the Sirocco fan investigated in this work, the geometry of the volute is modified only for its tongue, while the rest majority part of the volute surface keeps unchanged. In this section, we analyze the near-wall flow of the volute surface to explore how the modification on the volute tongue affects the flow around the whole circumference of the volute. The near-wall flow is studied on the $Z = 4$ mm axial cross-section close to the central disc at four moments T1, T2, T3 and T4 same as those shown in Figures 8–11 and the steady-state RANS result is also provided for comparison. The distributions of pressure coefficient and skin friction coefficient will be given on a local coordinate S along the surface of the volute with the origin chosen at the exit of the volute, as shown in Figure 14a.

3.4.1. Distribution of Skin Friction Coefficient on the Volute Surface

Figure 16 shows the distribution of skin friction coefficient (C_f) around the whole surface of the volute (left subfigure) and the enlarge view for the curves around the volute tongue (right subfigure). For the $r = 4$ mm model, the magnitude of C_f drastically increases in the volute tongue region and the local near-wall flow is almost steady-state from $S = 0$ to $S = \Phi_1$, as reflected by the overlapping curves of various moments; this indicates that although the flow in the impeller is highly fluctuating (as seen in Figure 8), it hardly impose obvious fluctuation for the near-wall flow of the volute. we have observed two peaks of C_f and one valley in the region around the volute tongue and the magnitude of C_f changes dramatically, This is because it is not only close to the outlet of the volute but also has significant changes in wall structure, so the flow state here is the most complex and diverse. The temporal fluctuation of C_f in the rest part of the volute surface is relatively significant. In the region from Φ_1 to Φ_2 , the magnitude of C_f gradually decreases which indicates the decelerated flow. From Φ_2 to Φ_3 , the magnitude of C_f increases first and then decreases. Since Φ_2 and Φ_3 are located at

the two corners of the bottom of the volute, it suggests that the abrupt change of volute geometry will affect the local near-wall flow. From $\Phi 3$ to $\Phi 5$, the magnitude of C_f first increases rapidly and then slowly decreases to varying degrees. This variation pattern may be caused by the varied geometry of volute surface from a flat one to a curved one and then gradually varies as an arc and it is also related to the variation of spacing between the impeller and volute surface. In general, in the majority part from $\Phi 3$ to $\Phi 5$, the variation of C_f is mild as well as the near-wall flow. For the surface at the outlet section of the volute beyond $\Phi 5$, the distance between the volute and the impeller is large that the local flow is decelerated, thus the magnitude of C_f also reduces.

For other models of $r = 9$ mm, 11 mm and 13 mm, the curves of C_f shows a certain degree of temporal fluctuations and the variation pattern is basically consistent with that of $r = 4$ mm. Comparing the several models, it can be observed that in the range between $S = 0$ and $S = \Phi 1$, there are always two local peaks. The difference is that with decreasing radius, the slope of C_f curve before and after the valley point is higher and the variation is more intense, which indicates that the decreasing radius generates a smaller low-velocity region where the flow is less affected and thus is beneficial to the aerodynamic performance of the fan. Moreover, the magnitude of second peak reduces with increasing radius from about 5.7 at $r = 4$ mm to 4.7 at $r = 13$ mm; it means small radius is more likely to produce a high-velocity flow at the initial position of the recirculating flow at the tongue. In the region beyond $\Phi 1$, the unsteadiness of near-wall flow is observed to be quite different on the volute surface; substantial fluctuation is found beyond $\Phi 1$, $\Phi 3$, $\Phi 2$ and $\Phi 1$ for the four models but the fluctuation is generally the strongest for the $r = 4$ mm model. The RANS and URANS simulations have generally consistent predictions on the variation of C_f around the volute surface especially in the region beyond $\Phi 1$. There is a significant gap between the results of two approaches in the region from $S = 0$ to $S = \Phi 1$ and the RANS approach fails to capture the two peaks, which demonstrates that although RANS could only depict the general variation of near-wall flow but not capable for the details in the region with great geometrical variation.

3.4.2. Distribution of Pressure Coefficient on the Volute Surface

The near-wall flow of the volute surface is greatly affected by the pressure gradient field. Figure 17 shows the distribution of pressure coefficient (C_p) around the whole surface of the volute (left subfigure) and the enlarge view for the curves around the volute tongue (right subfigure). For the $r = 4$ mm model, the distribution of C_p varies generally as a whole in time, that is, the magnitude of C_p at different position synchronously increases or decreases, which indicates that the pressure on the volute surface has obvious unsteady characteristics during the whole cycle of the revolution of impeller. In the region from $S = 0$ to $S = \Phi 1$, there is noticeable fluctuation of C_p compared with the quasi-steady C_f , while the pressure gradient field, as measured by the slope of the curve, does not vary a lot during the whole cycle, thus the velocity of near-wall flow does not show remarkable temporal variation. From the peak value at $S = 0$, favorable pressure gradient (FPG) with a sharp decrease and then a relatively slow decrease of pressure deteriorates the movement of flow towards the outlet of volute. The APG field from the valley to $\Phi 1$ will accelerates the near-wall flow. At the volute tongue, the sharp increase and decrease of C_p clearly show the pressure variation characteristics under the impact of the flow. There is an adverse pressure gradient field ($dp/ds > 0$) from $\Phi 1$ to $\Phi 2$ which is detrimental to the movement of the near-wall flow and may even cause flow separation. From $\Phi 2$ to $\Phi 3$, the pressure coefficient first decreases and then increases, indicating that the flow velocity may be accelerated and then decelerated in this region. In the region from $\Phi 3$ to $\Phi 5$, the magnitude of C_p varies relatively smoothly with only minor increase. It is found that the distance between the volute surface and the impeller gradually expands within this region, the geometry of the volute surface abruptly changes from a flat surface to a curved surface and then slowly changes to an arc, which makes the flow smooth in this region. In the region after $\Phi 5$, the magnitude of C_p decreases and then increases again until the outlet of the volute because the distance between the impeller and the volute surface increases rapidly which reduces the pressure. For other three models, the variation of C_p is similar to that of the $r = 4$ mm model.

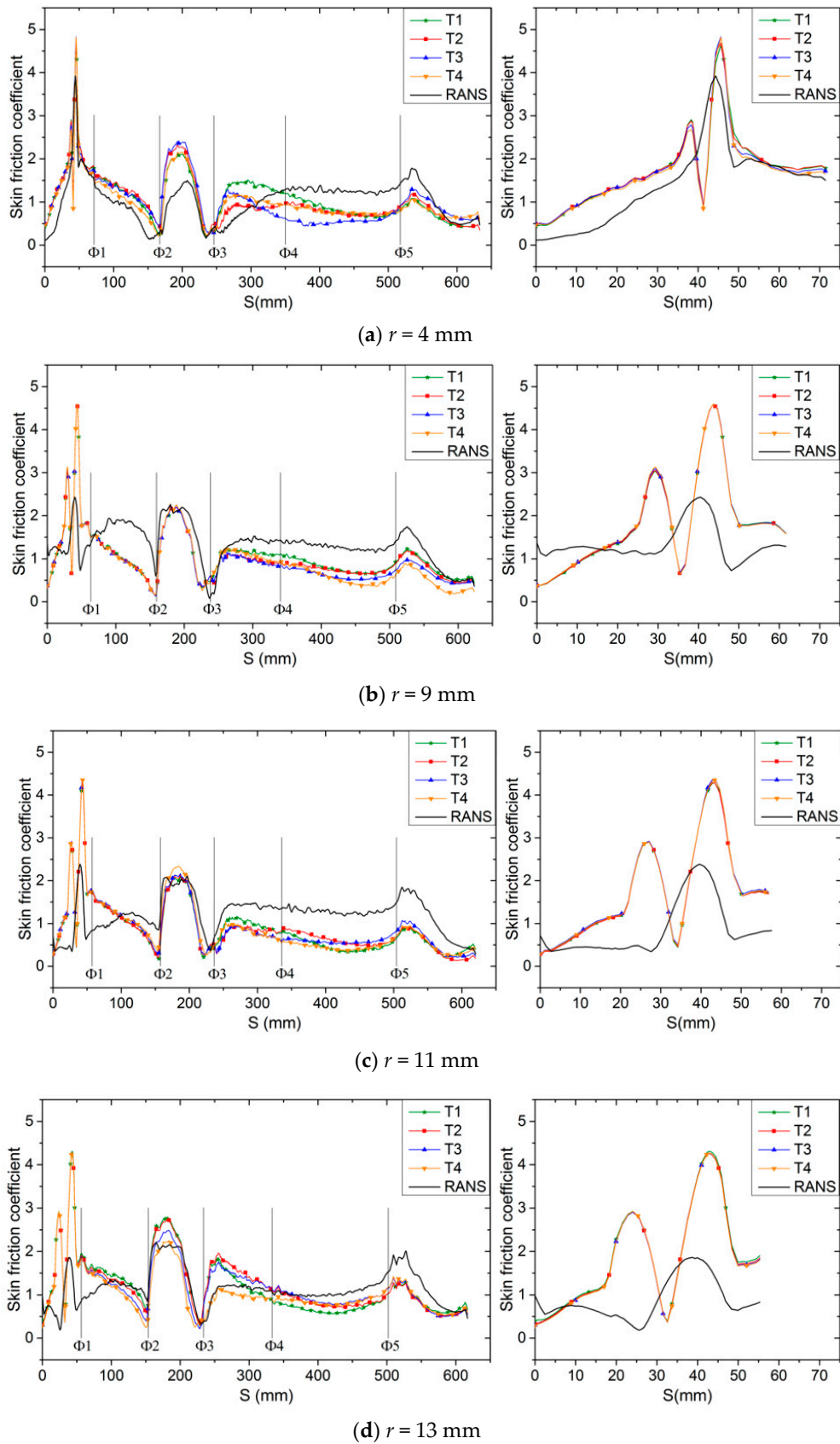
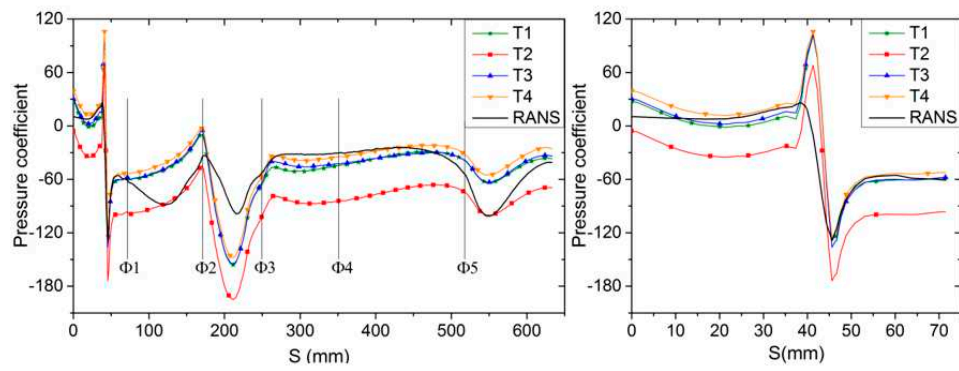
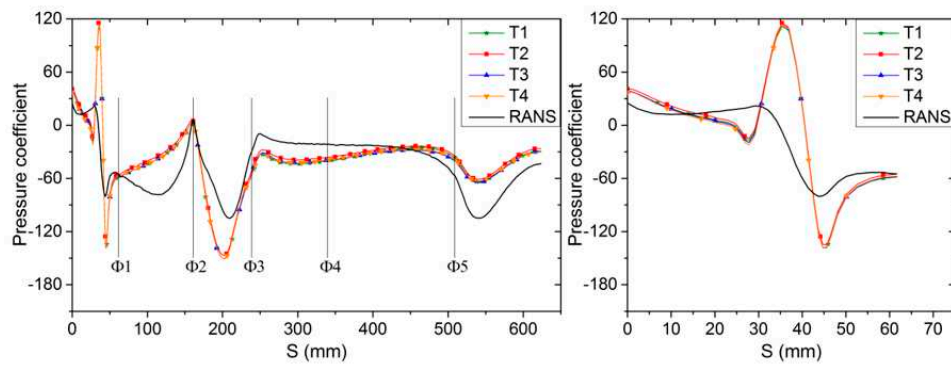


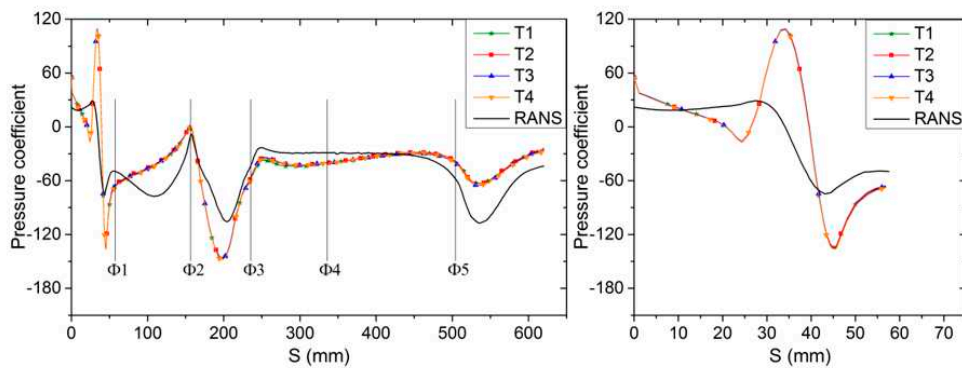
Figure 16. Distribution of skin friction coefficient around the volute surface (left column) and the enlarged view around the volute tongue (right column) on the $Z = 4$ mm cross-section.



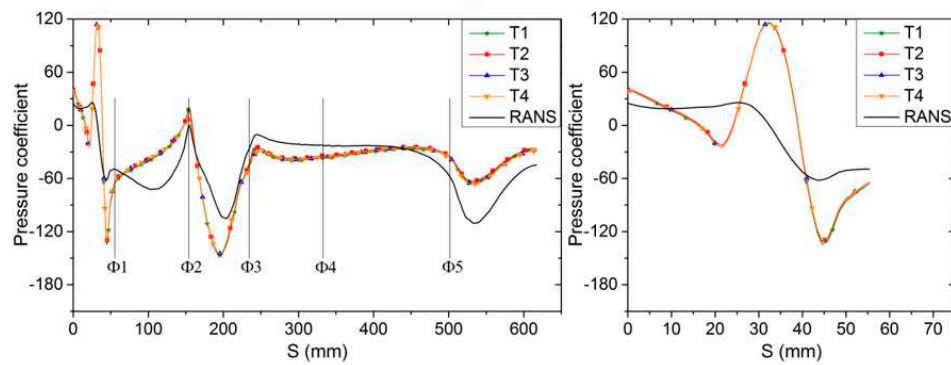
(a) $r = 4$ mm



(b) $r = 9$ mm



(c) $r = 11$ mm



(d) $r = 13$ mm

Figure 17. Distribution of pressure coefficient around the volute surface (left column) and the enlarged view around the volute tongue (right column) on the $Z = 4$ mm cross-section.

Comparing the C_p distribution of four models, it can be seen that the variation is quite similar for the $r = 9\text{--}13$ mm models where the temporal variation is negligible, while the highly fluctuating flow induce noticeable pressure fluctuation for the $r = 4$ mm model which is consistent with the observations in Figure 8. Around the volute tongue, the C_p curve has the steepest increasing and decreasing trend, while the variation is less pronounced for other three models.

The variation of C_p has similar pattern as predicted by RANS and URANS approaches although the magnitude deviates to some degree; the steady-state RANS result could generally reflect the variation but the magnitude is still not accurately predicted even for the $r = 9\text{--}13$ mm models where the flow is quasi-steady.

3.5. Static Pressure Fluctuation and Its Propagation

From the discussions above, we can conclude that the fluctuation of flow is dependent on the volute tongue radius and is different in the impeller or in the volute. To further analyze the static pressure fluctuation, a series of static pressure monitoring points are set on the $Z = 4$ mm axial cross-section near the central disc where the time history of pressure are recorded during the 8th to 10th revolution in the URANS simulation, as shown in Figure 18. The monitoring points are located in the region where the temporal variation of local flow is significant and can be compared to reveal the propagation of the fluctuation. Monitors A/B/C1/D1 are set along the circumference of impeller with a radius of 70.5 mm (the outer diameter of the impeller is 70 mm) to analyze the circumferential variation of pressure. Monitors C1/C2/C3 and D1/D2/D3 are respectively set in the 270° and 360° directions of the coordinate system. The distance between C1, C2 and C3 is 14.8 mm and the distance between D1, D2 and D3 is 20.8 mm. These monitors are chosen to analyze the time history of static pressure in radial direction between impeller and volute. In order to analyze the influence of volute tongue radius on the surrounding flow, monitors F and E are set at the exit of the impeller close to the volute tongue and the pressure fluctuation data at monitor A is also used for analysis. On the surface of the volute tongue, the apex H and two points G and I where the curved section connects with the straight sections tangentially are selected to analyze the pressure fluctuation of the volute tongue region.

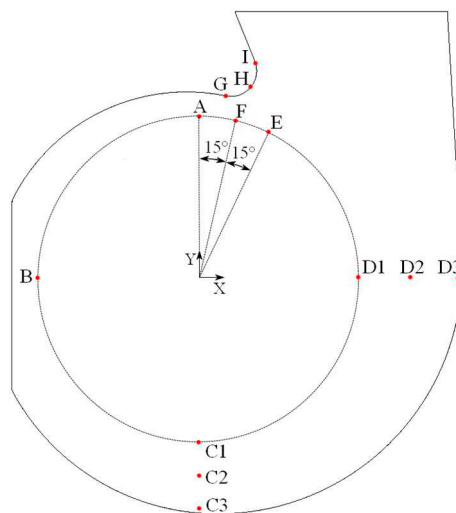


Figure 18. Positions for the static pressure monitors within the volute.

3.5.1. Static Pressure Fluctuation along the Circumference of the Impeller Outlet

Figure 19 shows the time history of pressure at monitors A/B/C1/D1 along the circumference of the outlet of the impeller. It is seen that for the $r = 4$ mm model, the pressure exhibits a remarkable fluctuating mode at all four monitors; three periods with large amplitudes are observed corresponding to the three revolutions of the impeller. The remarkable fluctuation shows different patterns at the

various monitors. However, for the $r = 9$ mm, 11 mm and 13 mm models, the fluctuating amplitude is greatly reduced for all monitors; the pressure actually fluctuates in a quasi-periodic mode with the number of period during one revolution of impeller equals to the number of blades. The fluctuation at the four monitors shows obvious differences; the amplitude is the maximum for monitor-A and minimum for monitor-B and is mild for monitor-C and monitor-D. This indicates that the unsteadiness of pressure is greatly weakened as the monitor is away from the volute tongue, while the weakening is not proportional to the distance from the monitor to volute tongue but also depends on the interaction of impeller and volute.

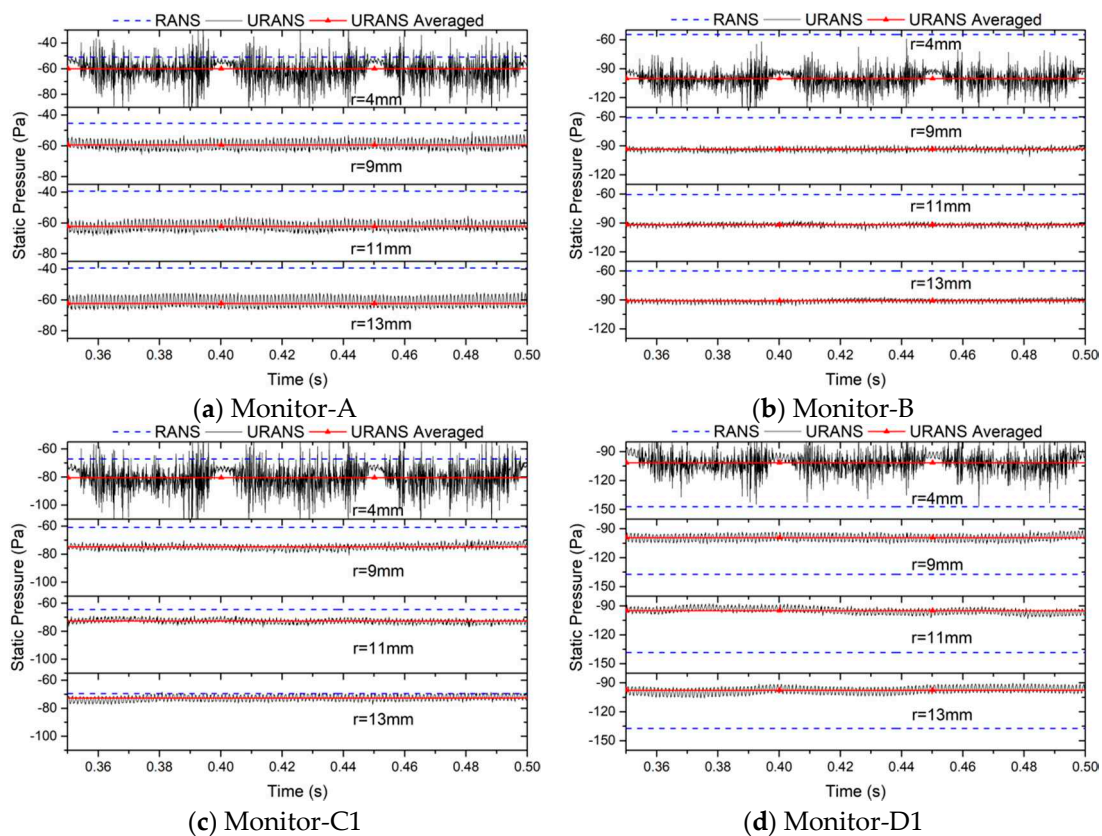


Figure 19. Static pressure fluctuation at monitors A/B/C1/D1.

The time-averaged value of pressure is also affected the volute tongue radius. For monitor-A, the time-averaged pressure is relatively higher for the $r = 4$ mm and 9 mm models and lower for other two but the difference is minor. The time-averaged value for the $r = 4$ mm model is always the lowest for other three monitors. Although the volute is modified only around the tongue, it does have influence on the flow in the volute far away from the tongue through an indirect way; as the volute tongue radius decreases, the time-averaged pressure at the outlet of the impeller close to the volute tongue is increased, while decreased to a certain extent at other three monitors away from the volute tongue.

Considering the volute geometry exemplified in Figure 18 and the URANS data of radial velocity in Figure 15, it can be found that the radial velocity is near zero in the blade passages corresponding to monitor-A (around 52°), while it increases to around 3 m/s at monitor-B (around 140°) which results in the decreasing pressure from monitor-A to monitor-B. However, the magnitude of radial velocity in the blade passages further increases to 4.5 m/s at monitor-C1 (around 230°) and the pressure is also increased; this may be caused by the significant increase in the distance between impeller and volute. From point C1 to point D1 (around 325°), although the distance is increased to a certain extent than

that at point C1, the radial velocity in the blade passages changes from 4.5 m/s to 8 m/s, so the pressure at point D1 may be more affected by the radial velocity which reduces the local pressure.

For the pressure at the present monitors, the pressure obtained by RANS is normally far deviated from the time-averaged URANS result. The pressure computed by RANS is normally over-predicted for monitor-A, -B and -C1 but is under-predicted by monitor-D and the relative difference can be up to about 30%. For the volute with small tongue radius such as $r = 4$ mm, the minimum relative difference is found at the monitor near the volute tongue, while for other models well consistency is found at monitor-C1 which is the furthest away from the volute tongue.

3.5.2. Static Pressure Fluctuation along the Radial Direction in the Volute

The comparison of pressure fluctuation monitored at C1/C2/C3 reflects the influence of volute tongue radius on flow far away from it, as given in Figure 20. It is seen that generally, the pressure presents strong fluctuation at all three monitors for the $r = 4$ mm model and quasi-periodic fluctuation is clearly seen corresponding to the three revolutions of the impeller. The fluctuation reduces significantly for monitors of other three models. This indicates that although only the volute tongue is modified, it induces the variation of local flow which would further affect the flow in the whole volute in an indirect way.

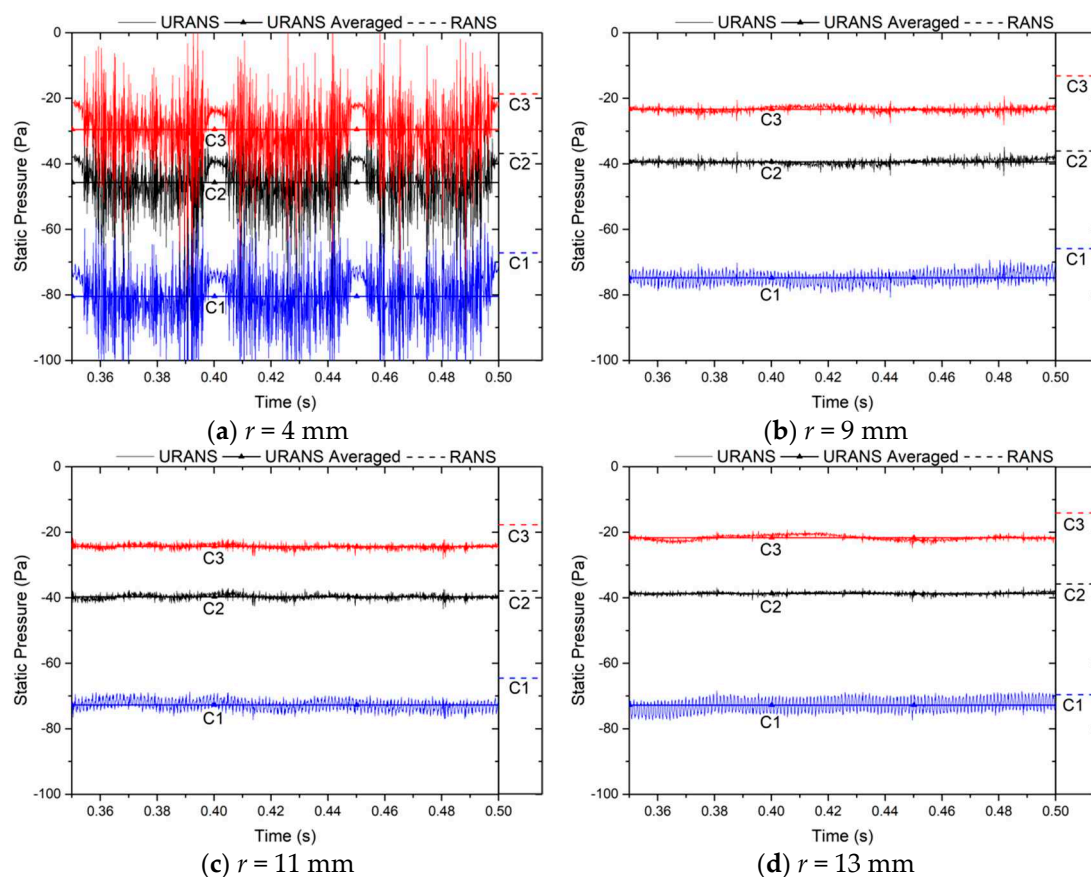


Figure 20. Static pressure fluctuation at monitors C1/C2/C3.

The time-averaged pressure does not vary a lot for different models but is greatly dependent on the radial position of the monitor. For each model, the time-averaged pressure is the lowest for monitor-C1 which locates near the volute outlet and increases as the flow moves outwards toward the volute where the pressure is recovered from the kinetic energy of fluid. For the $r = 9$ mm, 11 mm and 13 mm models, the amplitudes of pressure fluctuation of monitor-C2 and -C3 are similar and are

much smaller than that of monitor-C1, which reveals that the fluctuation of near-wall of the volute surface is greatly damped via viscous mechanism by the wall.

By comparing the results obtained by RANS and URANS, it is found that the RANS simulation normally over-predicts the pressure at all monitors. The degree of over-prediction is larger for the model with smaller tongue radius as the flow has stronger unsteadiness and is relatively larger for monitor-C1 since the jet-wake structure for the outflow of impeller is inherently unsteady and could not be revealed by RANS.

The time-history of pressure for flow towards the outlet of the volute is represented by monitors D1/D2/D3 as shown in Figure 21. It is seen that substantial fluctuation of pressure appear for the $r = 4$ mm model, while the fluctuation is greatly attenuated for other models. For each model, the pressure is the highest for the monitor close to the volute surface and lowest close to the impeller, the same variation tendency as the monitors C1/C2/C3. The amplitude of fluctuation is also the largest for monitor-D1 where the unsteady flow out of the impeller dominates. As the volute tongue radius increases, the fluctuating amplitude does not vary much at all in monitors for the $r = 9$ mm, 11 mm and 13 mm models. For the data obtained by monitors D1/D2/D3, it is different from those of C1/C2/C3 that the steady-state RANS simulations always under-predict the time-averaged pressure especially for monitor-D1 which is the closest to the outlet of impeller.

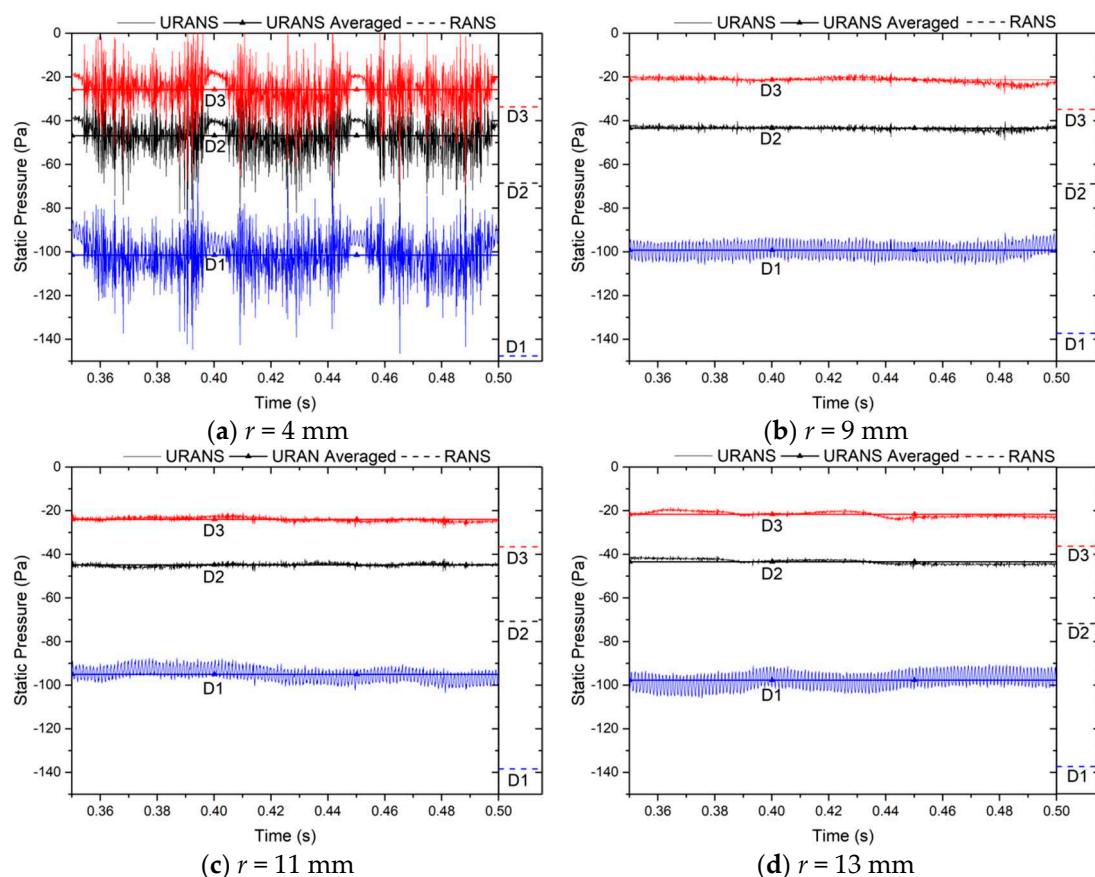


Figure 21. Static pressure fluctuation at monitors D1/D2/D3.

3.5.3. Static Pressure Fluctuation Near the Volute Tongue

Since the flow moving out of the impeller will directly impinge on the volute tongue in the region around monitor-A, here we present and discuss the pressure fluctuation at monitors A/F/E in Figure 22 which are located at the outlet of the impeller and around the volute tongue. The time-averaged pressure is the lowest at monitor-A and highest at monitor-E for the $r = 4$ mm model, while for other

models the value can be higher for monitor-E or -F depending on the volute radius and the difference is relatively smaller. This is partially attributed to the modification of volute tongue geometry that as its radius decreases, the flow patterns at monitor-E approach to that of monitor-F since monitor-E is also blocked by the volute tongue. Consequently, the position of the highest pressure at the outlet of the impeller near the volute tongue also changes accordingly, that is, distance between the circumferential position at the outlet of impeller with highest pressure and the volute tongue is almost fixed. Although there is a certain degree of difference between RANS and URANS results, we find RANS usually over-predict the pressure at monitor-A and -F and the magnitude of over-prediction gets remarkable as the volute tongue radius increases. For the flow at monitor-E, the predicted pressure of RANS is higher than that of the time-averaged URANS data for the $r = 4$ mm model and lower for $r = 11$ mm and 13 mm models.

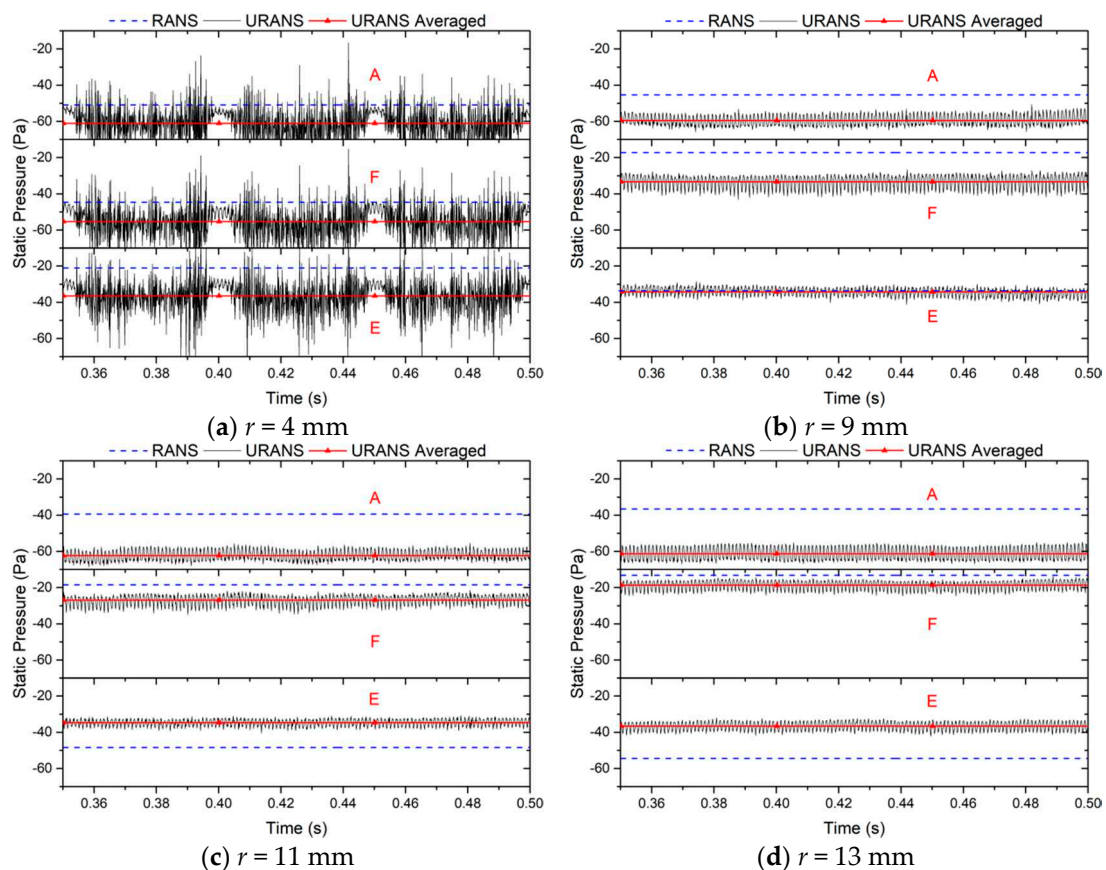


Figure 22. Static pressure fluctuation at monitors A/E/F.

3.5.4. Characteristics of Static Pressure Pulsation at the Volute Tongue

The monitors G/H/I are positioned right at the surface of volute tongue in which monitor-G and monitor-H are closer to the impeller that the flow may impinge on them, while monitor-I is at the outlet section of the volute and is free of flow impingement. Figure 23 shows the time history of pressure at the three monitors. The pressure fluctuation is still notable for the $r = 4$ mm model, while the amplitude is negligible for the other three models compared with data obtained at other monitors. The time-average pressure for monitor-H at the curved section of the volute tongue has the largest value and is lowest for monitor-G inside of the volute tongue. This indicates that the outflow of the impeller generally impinges on the position of monitor-H but moves partially in a tangential way over the volute surface at monitor-G in the form of recirculating flow. The time-averaged pressure at a certain monitor varies with the volute tongue radius. For all monitors G/H/I, the pressure is the lowest for the $r = 4$ mm model and highest for the $r = 13$ mm model, indicating that the increasing of volute

tongue radius will increase the local pressure at the center of the tongue region; however, the pressure in the volute tongue region close to the volute exit will be reduced to a certain extent.

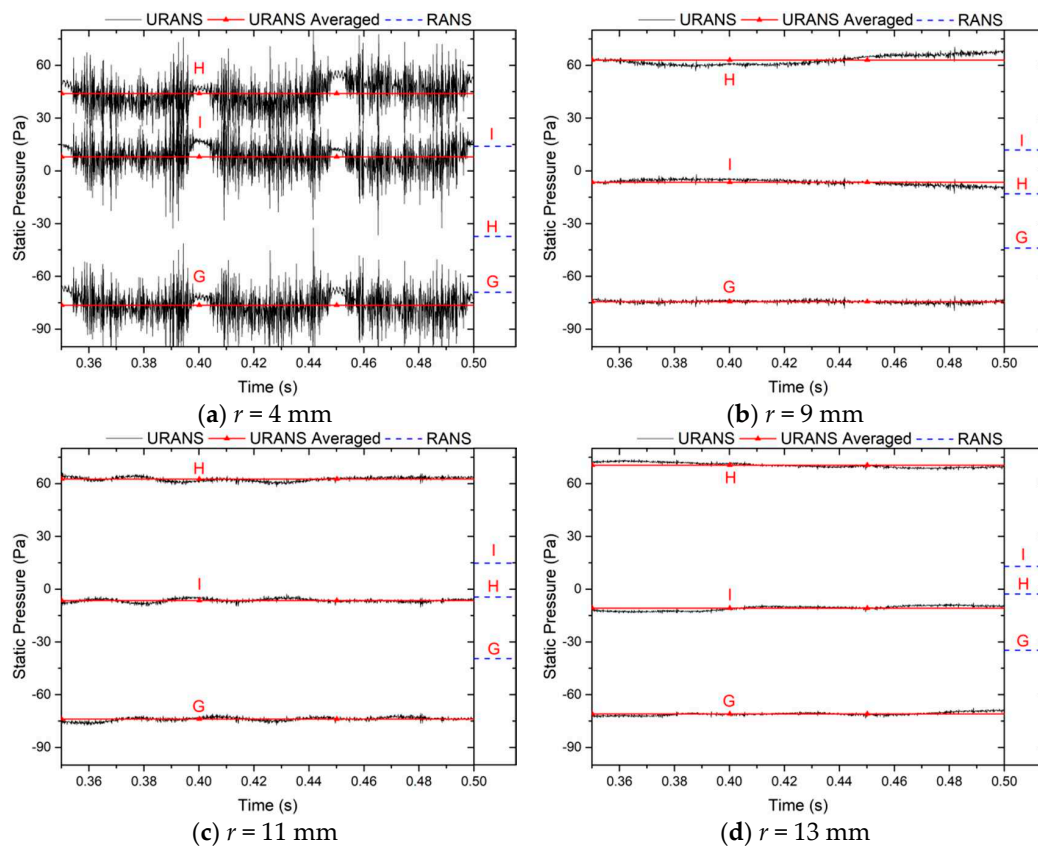


Figure 23. Static pressure fluctuation at monitors G/H/I.

The steady-state RANS simulation gives the worst prediction of pressure especially for monitor-H in the curved section probably due to the inaccurate solution of local flow velocity. It shows that for the pressure distribution at the volute tongue, the high-pressure concentration area predicted by RANS is more biased toward the exit of the volute. For the same model, the RANS results at the monitor-I do not show a pressure variation trend as the URANS results, while it is the same for monitor-G and monitor-H.

3.6. Aeroacoustic Characteristics

In this work, the internal flow of the Sirocco fans is numerically investigated using the RANS and URANS approaches considering the efficiency and feasibility of computational resources. The results reflect the general characteristics of the temporal variation and spatial distributions of certain quantities but is insufficient in capturing the subtle pressure fluctuation, thus the aeroacoustic characteristics cannot be numerically computed. In this section, we present the experimental results regarding the aeroacoustic characteristics of the various models.

The influence of volute tongue radius of the far-field noise characteristics are analyzed in this section. The schematic of the arrangements of microphones is shown in Figure 24; four microphones A/B/C/D are positioned at the inlet of the fan and one microphone-E is positioned at the outlet of the fan. The sound pressure level (SPL) measured at each microphone is listed in Table 5 for the various volute models. For the microphones A/B/C/D at the outlet of the fan, it is seen in the table that the SPL measured at microphones A/B/C/D increases significantly as the volute tongue radius decreases especially for the $r = 4$ mm model. The SPL of the $r = 9$ mm, 11 mm and 13 mm models is of the same level with maximum relative difference less than 2%. The SPL measured at microphone-E at the

inlet of the fan exhibits smaller difference for the several models. By comparing the SPL at the several microphones, it can be found that the SPL measured by microphone B/C is relatively higher than that of A/D because the flow at the outlet of the volute has a larger velocity in the direction of B/C which will produce a stronger SPL.

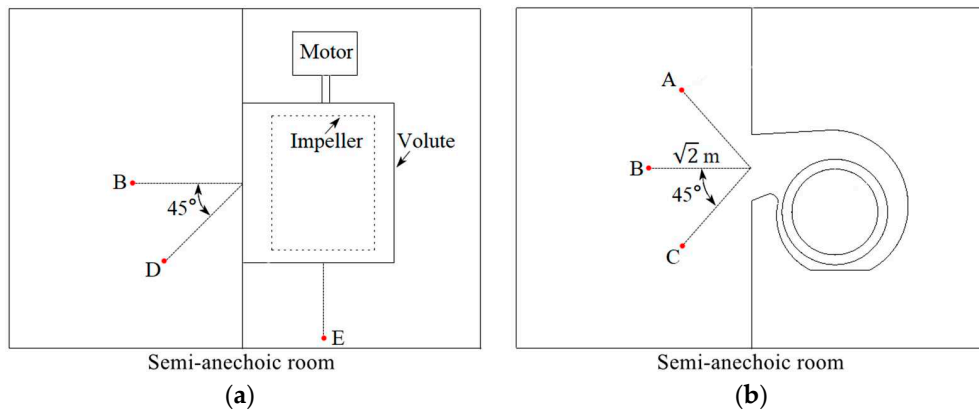


Figure 24. Positions of microphones in the aeroacoustic test. (a) Top view of the positions of the probes; (b) side view of the positions of the probes.

Table 5. The sound pressure level monitored by different microphones (dB).

Model	A	B	C	D	E
$r = 4$ mm	44.41	46.99	46.39	45.43	43.03
$r = 9$ mm	41.68	41.77	41.89	41.17	42.76
$r = 11$ mm	41.04	41.06	41.12	40.27	42.47
$r = 13$ mm	40.97	40.97	41.66	40.61	42.93

Figure 25 shows the spectrum of 1/3 octave band of noise obtained at monitor-B at the outlet of volute and monitor-E at the inlet of volute. Considering that the blade passage frequency (BPF) of the impeller is 820 Hz, it is seen in the figure that the maximum SPL of the two monitors is around the frequency of BPF for all models, thus it contributes the most to the overall SPL of the fan. The volute model with smaller radius has a higher magnitude of SPL roughly for the low frequency regime, while in the high frequency regime the volute with larger radius has a higher SPL. The SPL increases significantly in most of the low frequency regime for volutes with small tongue radius, while the reduction in the high frequency regime is relatively small. As the volute tongue radius varies within a certain range, such as $r = 9$ mm to $r = 13$ mm, the SPL in most frequency regimes is relatively less affected by the tongue radius.

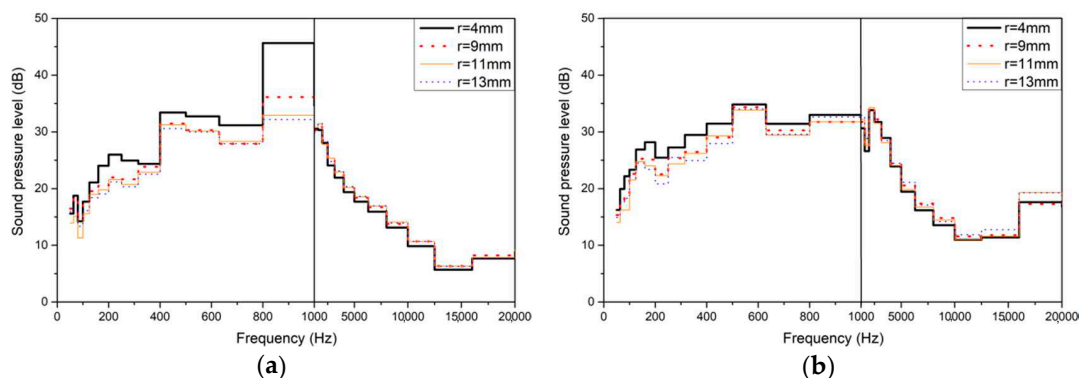


Figure 25. Noise spectrum: (a) Spectrum of 1/3 octave band of microphone-B; (b) Spectrum of 1/3 octave band of microphone-E.

4. Conclusions

This work presents an experimental and numerical investigation on the influence of volute tongue radius on the aerodynamic and aeroacoustic characteristics of a Sirocco fan. The simulations are performed by both RANS and URANS approaches to comparably explore their capability, accuracy and reliability for such configurations. The characteristics of internal flow under the effect of different volute tongue radius are presented in terms of the aerodynamic quantities, the flow within the impeller and near-wall flow on the volute surface, the pressure fluctuation within the volute and the aeroacoustic characteristics. The experimental and numerical results have the following conclusions:

1. The volute with small tongue radius could improve the static pressure and static pressure efficiency of the fan until $r = 9$ mm by affecting the flow patterns in the tongue region as well as far away from the volute tongue. The steady-state RANS simulation fails to accurately predict the static pressure for all models, while the URANS results are highly consistent with the experimental data.
2. Reversed flow forms within the impeller passages close to the volute tongue, as captured by both RANS and URANS simulations by monitoring the passage flow at a fixed point for the whole revolution of the impeller. The volute tongue with small radius could reduce the size and velocity magnitude of reversed flow; the variation amplitude of velocity of passage flow is small near the front disc, while is larger for that near the central disc.
3. The near-wall flow of the volute surface is affected by the volute tongue radius in the vicinity of the volute tongue as well as far away from it, as revealed by the distribution of pressure coefficient and skin friction coefficient. The reduction of volute tongue radius produces FPG and APG field in the tongue region and thus affects the local near-wall flow. For models with small volute tongue radius, the pressure coefficient and skin friction coefficient on the volute surface exhibit notable unsteady pulsations depending on the circumferential position.
4. The pressure fluctuation is monitored by URANS at the outlet of the impeller, in the volute and around the volute tongue. The fluctuating amplitude is substantially large for the $r = 4$ mm model which shows time-periodicity regarding the passing of single blade as well as the revolution of whole impeller, while the pressure fluctuation for all monitors of the other models is comparably minor. It is also found that the steady-state RANS simulation could over-predict or under-predict the pressure depending on the position of the monitor and the volute model and the discrepancy could up to more than 30%.
5. The comparison between RANS and URANS results shows that generally, the RANS approach could reasonably reveal the flow patterns within the fan. However, the quantitative analysis on the local flow shows discrepancy compared with the time-average value obtained from URANS simulation and the difference can be large for certain quantities. The RANS approach may not be a suitable choice even if results of engineering accuracy are required.
6. The experimental results show the noise of the fan generally decreases with the volute tongue radius and the sound pressure level is the most pronounced for the $r = 4$ mm model because of the highly fluctuating flow. The noise measured at the inlet of the fan is less affected by the volute tongue radius.

It should be emphasized here that the findings concluded in this work is considered only suitable for fan models of similar geometry, especially the small-size Sirocco fans and centrifugal fans under certain flow conditions. The effect of volute tongue radius on other types of fans or fluid machines needs to be investigated in the following works. The comparison of RANS and URANS approaches is also limited to the $k-\varepsilon$ turbulence model and the conclusions may be different both in variation trend and magnitude as other turbulence models are employed.

Author Contributions: Conceptualization, X.R. and W.Z.; data curation, X.R.; formal analysis, X.R.; funding acquisition, W.Z. and Z.Z.; investigation, X.R. and W.Z.; methodology, X.R.; project administration, W.Z. and Z.Z.; resources, J.W., X.Y., H.H. and W.Z.; software, X.R.; validation, X.R., L.L., J.W., X.Y., H.H. and W.Z.; writing—original draft, X.R.; writing—review and editing, W.Z. and Z.Z. All authors have read and agreed to the published version of the manuscript.

Funding: This work was supported by National Natural Science Foundation of China (51706205), Zhejiang Public Welfare Project (LGG20E060001) and Zhejiang Province Science and Technology Plan Project (2020C04011).

Conflicts of Interest: The authors declare no conflict of interest.

References

- Rafael, B.T.; Sandra, V.S.; Juan, P.H.C.; Carlos, S.M. Numerical calculation of pressure fluctuations in the volute of a centrifugal fan. *J. Fluids Eng.* **2006**, *128*, 359–369. [[CrossRef](#)]
- Dilin, P.; Sakai, T.; Wilson, M.; Whitfield, A. Computational and experimental evaluation of the performance of a centrifugal fan volute. *Proc. Inst. Mech. Eng. Part A J. Power Energy* **1998**, *212*, 235–246. [[CrossRef](#)]
- Okauchi, H.; Suzuka, T.; Sakai, T.; Whitfield, A. The effect of volute tongue and passage configuration on the performance of centrifugal fan. In Proceedings of the International Compressor Engineering Conference, West Lafayette, IN, USA, 16–19 July 2002.
- Whitfield, A.; Johnson, M.A. The effect of volute design on the performance of a turbocharger compressor. International. In Proceedings of the Compressor Engineering Conference, West Lafayette, IN, USA, 16–19 July 2002.
- Xiao, M.N.; Xiao, Q.; Dou, H.S.; Ma, X.Y.; Chen, Y.N.; He, H.J.; Ye, X.X. Study of flow instability in a centrifugal fan based on energy gradient theory. *J. Mech. Sci. Technol.* **2016**, *30*, 507–517. [[CrossRef](#)]
- Pan, D.; Whitfield, A.; Wilson, M. Design considerations for the volutes of centrifugal fans and compressors. *Proc. Inst. Mech. Eng. Part C J. Mech. Eng. Sci.* **1999**, *213*, 401–410. [[CrossRef](#)]
- Lun, Y.X.; Lin, L.L.; He, H.J.; Ye, X.X.; Zhu, Z.C.; Wei, Y.K. Effects of vortex structure on performance characteristics of a multiblade fan with inclined tongue. *Proc. Inst. Mech. Eng. Part A J. Power Energy* **2019**, *233*, 1–15. [[CrossRef](#)]
- Sandra, V.S.; Rafael, B.T.; Carlos, S.M.; Jose, G.P. Unsteady flow pattern characteristics downstream of a forward-curved blades centrifugal fan. *J. Fluids Eng.* **2001**, *123*, 265–270. [[CrossRef](#)]
- Sina, S.; Javad, A. Experimental and numerical analysis of eight different volutes with the same impeller in a squirrel-cage fan. In Proceedings of the 13th WSEAS International Conference on Automatic Control, Modelling & Simulation, Lanzarote, Spain, 27–29 May 2011; pp. 198–203.
- Zhou, S.Q.; Li, Y.B. Volute characteristics of centrifugal fan based on dynamic moment correction method. *Proc. Inst. Mech. Eng. Part A J. Power Energy* **2019**, *233*, 176–185. [[CrossRef](#)]
- Sunil, R.P.; Sandip, T.C.; Nitin, S.J.; Shivaraj, S.V. Effect of volute tongue clearance variation on performance of centrifugal blower by numerical and experimental analysis. *Mater. Today-Proc.* **2018**, *5*, 3883–3894. [[CrossRef](#)]
- Zhang, L.; Wang, S.L.; Hu, C.X.; Zhang, Q. Multi-objective optimization design and experimental investigation of centrifugal fan performance. *Chin. J. Mech. Eng.* **2013**, *26*, 1267–1276. [[CrossRef](#)]
- Lee, Y.T.; Vineet, A.; Ashvin, H.; Michael, E.S.; Lawrence, P.M.; Roger, B.; Roderick, M.C. Impeller design of a centrifugal fan with blade optimization. *Int. J. Rotating Mach.* **2011**, *2011*, 537824. [[CrossRef](#)]
- Wang, Y.; Dong, Q.L.; Zhang, Y.L. Meridional shape design and the internal flow investigation of centrifugal impeller. *Proc. Inst. Mech. Eng. Part C J. Mech. Eng. Sci.* **2017**, *231*, 4319–4330. [[CrossRef](#)]
- Kim, J.H.; Cha, K.H.; Kim, K.Y. Parametric study on a forward-curved blades centrifugal fan with an impeller separated by annular plate. *J. Mech. Sci. Technol.* **2013**, *27*, 1589–1595. [[CrossRef](#)]
- Ni, S.S.; Cao, W.B.; Xu, J.; Wang, Y.D.; Zhang, W. Effects of an inclined blade on the performance of a sirocco fan. *Appl. Sci.* **2019**, *9*, 3154. [[CrossRef](#)]
- Kim, K.Y.; Seo, S.J. Shape optimization of forward-curved-blade centrifugal fan with Navier-Stokes analysis. *J. Fluids Eng.* **2004**, *126*, 735–742. [[CrossRef](#)]
- Tarek, M.; Seung, O.P. A study of impeller-diffuser-volute interaction in a centrifugal fan. *J. Turbomach.* **2005**, *127*, 84–90. [[CrossRef](#)]
- Koen, H.; Rene, A.V.D.B. Numerical simulation of impeller-volute interaction in centrifugal compressors. *J. Turbomach* **1999**, *121*, 603–608. [[CrossRef](#)]

20. Karanth, K.V.; Sharma, N.Y. CFD analysis on the effect of radial gap on impeller-diffuser flow interaction as well as on the flow characteristics of a centrifugal fan. *Int. J. Rotating Mach.* **2009**, *2009*, 293508. [[CrossRef](#)]
21. Lee, Y.T. Impact of fan gap flow on the centrifugal impeller aerodynamics. *J. Fluids Eng.* **2010**, *132*, 091103. [[CrossRef](#)]
22. Jose, G.; Joaquin, F.; Eduardo, B.; Carlos, S. Numerical simulation of the dynamic effects due to impeller-volute interaction in a centrifugal pump. *J. Fluids Eng.* **2002**, *124*, 348–355. [[CrossRef](#)]
23. Daniel, O.B.; Lutz, K.; Ronald, D.F. Effect of relative impeller-to-volute position on hydraulic efficiency and static radial force distribution in a circular volute centrifugal pump. *J. Fluids Eng.* **2000**, *122*, 598–605. [[CrossRef](#)]
24. Younsi, M.; Bakir, F.; Kouidri, S.; Rey, R. Numerical and experimental study of unsteady flow in a centrifugal fan. *Proc. Inst. Mech. Eng. Part A J. Power Energy* **2007**, *221*, 1025–1036. [[CrossRef](#)]
25. Bechara, W.; Bailly, C.; Lafon, P.; Candel, S.M. Stochastic approach to noise modeling for free turbulent flows. *AIAA J.* **1994**, *32*, 455–463. [[CrossRef](#)]
26. Billson, M.; Eriksson, L.E.; Davidson, L. Jet noise prediction using stochastic turbulence modeling. In Proceedings of the 9th AIAA/CEAS Aeroacoustics Conference and Exhibit, Hilton Head, SC, USA, 12–14 May 2003. [[CrossRef](#)]
27. Ewert, R. Slat Noise Trend Predictions using CAA with Stochastic Sound Sources from a Random Particle Mesh method (RPM). In Proceedings of the 12th AIAA/CEAS Aeroacoustics Conference (27th AIAA Aeroacoustics Conference), Cambridge, MA, USA, 8–10 May 2006. [[CrossRef](#)]
28. Ewert, R. Broadband slat noise prediction based on CAA and stochastic sound sources from a fast random particle-mesh (RPM) method. *Comput. Fluids* **2008**, *37*, 369–387. [[CrossRef](#)]
29. Bailly, C.; Bogey, C.; Marsden, O. Progress in direct noise computation. *J. Aeroacoust.* **2010**, *9*, 123–143. [[CrossRef](#)]
30. Sandberg, D.; Jones, L.E. Direct numerical simulations of airfoil self-noise. *Procedia Eng.* **2010**, *6*, 274–282. [[CrossRef](#)]
31. Dawi, A.H.; Akkermans, R.A.D. Spurious noise in direct noise computation with a finite volume method for automotive applications. *Int. J. Heat Fluid Flow* **2018**, *72*, 243–256. [[CrossRef](#)]
32. Dawi, A.H.; Akkermans, R.A.D. Direct and integral noise computation of two square cylinders in tandem arrangement. *J. Sound Vib.* **2018**. [[CrossRef](#)]
33. Deuse, M.; Sandberg, R.D. Parametric study of multiple aerofoil self-noise sources using direct noise computation. In Proceedings of the 25th AIAA/CEAS Aeroacoustics Conference, Melbourne, Australia, 20–23 May 2019. [[CrossRef](#)]
34. Dawi, A.H.; Akkermans, R.A.D. Direct noise computation of a generic vehicle model using a finite volume method. *Comput. Fluids* **2019**, *191*, 104243. [[CrossRef](#)]
35. Dierke, J.; Akkermans, R.A.D.; Delfs, J.W.; Ewert, R. Installation Effects of a Propeller Mounted on a Wing with Coanda Flap. Part II: Numerical Investigation and Experimental Validation. In Proceedings of the 20th AIAA/CEAS Aeroacoustics Conference, Atlanta, GA, USA, 16–20 June 2014. [[CrossRef](#)]
36. Dobrzynski, W.; Ewert, R.; Pott-Pollenske, M.; Herr, M.; Delfs, J. Research at DLR towards airframe noise prediction and reduction. *Aerosp. Sci. Technol.* **2008**, *12*, 80–90. [[CrossRef](#)]
37. Ewert, R.; Dierke, J.; Siebert, J.; Neifeld, A.; Appel, C.; Siefert, M.; Kornow, O. CAA broadband noise prediction for aeroacoustic design. *J. Sound Vib.* **2011**, *330*, 4139–4160. [[CrossRef](#)]


Publisher’s Note: MDPI stays neutral with regard to jurisdictional claims in published maps and institutional affiliations.



© 2020 by the authors. Licensee MDPI, Basel, Switzerland. This article is an open access article distributed under the terms and conditions of the Creative Commons Attribution (CC BY) license (<http://creativecommons.org/licenses/by/4.0/>).

Article

Large Eddy Simulation of Film Cooling with Triple Holes: Injectant Behavior and Adiabatic Film-Cooling Effectiveness

Seung Il Baek and Joon Ahn * 

School of Mechanical Engineering, Kookmin University, 77 Jeongneung-ro, Seongbuk-gu, Seoul 02707, Korea; greenjet50@gmail.com

* Correspondence: jahn@kookmin.ac.kr

Received: 19 October 2020; Accepted: 9 November 2020; Published: 11 November 2020



Abstract: This study investigated the effect of adding two sister holes placed downstream the main hole on film cooling by employing large eddy simulation. Here, film-cooling flow fields from a triple-hole system inclined by 35° to a flat plate at blowing ratios of $M = 0.5$ and unity were simulated. Each sister hole supplies a cooling fluid at a flow rate that is a quarter of that for the main hole. The simulations were conducted using the Smagorinsky–Lilly model as the subgrid-scale model, and the results were compared with those for a single-hole system for the same amount of total cooling air and same cross-sectional area of the holes. Relative to the single-hole system, the spanwise-averaged film-cooling effectiveness in the triple-hole configuration at $M = 1.0$ increased by as much as 345%. The subsequent proper orthogonal decomposition analysis showed that the kinetic energy of a counter-rotating vortex pair in the triple-hole system dropped by 30–40% relative to that of the single-hole system. This indicates that the additional sister holes promoted the suppression of the mixing of the coolant jet with the mainstream flow, thus keeping the temperature of the latter low. Cross-sectional views of the root-mean-square temperature contours were also analyzed; with the results confirming that the effect of the sister holes on the jet trajectory greatly contributes in promoting film-cooling effectiveness as compared to the effect of the reduced mixing.

Keywords: film cooling; large eddy simulation; triple holes; blowing ratio; adiabatic film-cooling effectiveness; proper orthogonal decomposition

1. Introduction

The principle of idealized Brayton cycle states that gas turbine efficiency can be improved by increasing the inlet temperature of the turbine [1]. Here, to avoid the excessive thermal stress build-up on the turbine blades, the surface temperature of the blades must remain below a tolerable limit. Various cooling methods can be employed, among which the film-cooling technique has been widely used. In this technique, the cooling air which is bled from the compressor is injected through holes on the turbine blade surface—this reduces the surface temperature and protects the surface from the main flow. For the holes, a cylindrical shape is often appropriate because of its simplicity and ease of manufacture.

However, substantial investigations of the physics of film cooling in such a cylindrical hole system have revealed that a single cylindrical hole can be relatively vulnerable to the generation of the jet liftoff [2] and that a specific hole arrangement could produce film cooling that provides better thermal protection than single cylindrical holes do. Practically, specific hole arrangements make the intended vortex interactions between film cooling jets to increase film-cooling effectiveness.

Film cooling in turbine engines can be effectively studied at a reasonable cost using computational fluid dynamics (CFD). High turbulence is generated in the film-cooling flow field, after which a model is

constructed for the turbulence. Another option is the well-known large eddy simulation (LES), which can predict the mixing between the main flow and coolant jet better than Reynolds-averaged Navier–Stokes Simulation (RANS) [3–5], although such requires much higher computational costs. Comparatively speaking, RANS cannot accurately predict the complex flow structures induced in film-cooling flow fields as all of the turbulent fluctuations are ensemble-averaged, whereas LES resolves large-scale eddies directly in the turbulent flow, resulting in more accurate predictions of the complex flow [6,7].

Heidmann et al. [8] showed in a numerical investigation that relative to a one-hole system, three holes (consisting of the main hole and two side holes) can increase film-cooling effectiveness, as well as decrease the heat transfer coefficients at a blowing ratio of unity, using RANS. They also reported that the fabrication of cylindrical triple holes is economically more viable than that of other shapes. Meanwhile, Javadi et al. [9] constructed square sister holes to control vortex interactions between the jet and crossflow at $M = 0.5$ by employing RANS. They found that two sister holes with a square cross-section reduce the mixing between the coolant and crossflow, thus improving film-cooling effectiveness. Ely et al. [10] also used RANS to investigate an increase in film-cooling effectiveness with two cylindrical sister holes. Using blowing ratios of 0.2, 0.5, 1.0, and 1.5, they demonstrated that definite improvements in film-cooling effectiveness occur at high blowing ratios.

Furthermore, Wu et al. [11] conducted both experimental and numerical studies of film cooling given three sister-hole configurations and confirmed an improvement in the performance as above. Here, they compared the experimental and numerical data only in terms of spatially averaged film-cooling effectiveness, which showed a difference of more than 30% under blowing ratios of unity and 1.5.

Farhadi-Azar et al. [12] introduced LES to study the effects of the triple jets on film cooling. On the basis of their demonstration, triple jets from the main hole along with two small sister holes increased film-cooling effectiveness because of weaker counter-rotating vortex pairs in the jet from the main hole, which led to less mixing between the coolant jets and main flow. However, several limitations could be found in their study. For instance, they employed an injection angle (α) of 90° on their hole, which is very uncommon for a gas turbine design because of the strong jet liftoff. Aside from this, the plenum was not included in the simulation, and a flow with a uniform velocity was applied to the hole inlet, which is unrealistic in gas turbine scenarios.

Considering the above, this paper aims to investigate the effect of a triple-hole system on film-cooling performance on a flat plate at blowing ratios of 0.5 and 1.0. The simulation was conducted using LES under a more realistic flow condition and at an injection angle (α) of 35° for the hole. The plenum is included, and the velocity in the hole is nonuniform with both the high-momentum region generated by the jetting effect and low-momentum region.

The LES results are used to understand the effect of the flow generated in the triple hole on the trajectory of the film-cooling jet and mixing with the mainstream flow. Vortex structures that affect the mixing are identified through time-averaged velocity fields and instantaneous flow fields, whereas the contribution of these vortices is determined through a proper orthogonal decomposition (POD) analysis. The film-cooling performance, degree of mixing with the main flow, and trajectory of the film-cooling jet are also observed through the time-averaged temperature fields. On the basis of the analysis results, the effect and mechanism of the triple hole on the film-cooling performance are identified.

2. Geometry and Boundary Conditions

The geometry of the single-hole system in the test case was taken from Seo et al. [13], whose experimental apparatus consisted of a row of five cooling holes. Herein, a single-hole configuration was adopted to simplify the computational domain, and a periodic boundary condition was applied on the mesh sides to reduce the computational cost. The computational domains of the single- and triple-hole systems are delineated by the orange dashed lines in Figure 1, whereas a schematic of the cooling holes in each case is shown in Figure 2. In the single-hole geometry (Figure 2a), the hole diameter D was 25 mm. The triple holes comprised two sister holes which are placed slightly downstream of the primary hole (Figure 2b) as

described in Ely et al. [10]. In the triple-hole geometry, the hole diameters were calculated to match their total cross-sectional areas to the cross-sectional area of the single-hole. Thus, the primary hole diameter D' was 20.4124 mm, and the diameter of each sister hole was $D'/2 = 10.2062$ mm. The hole length-to-diameter ratio (L/D), injection angle (α), and pitch-to-hole diameter (P/D) were set to 1.6, 35° , and 3.0, respectively. In addition, the holes were cylindrical, with no compound angles.

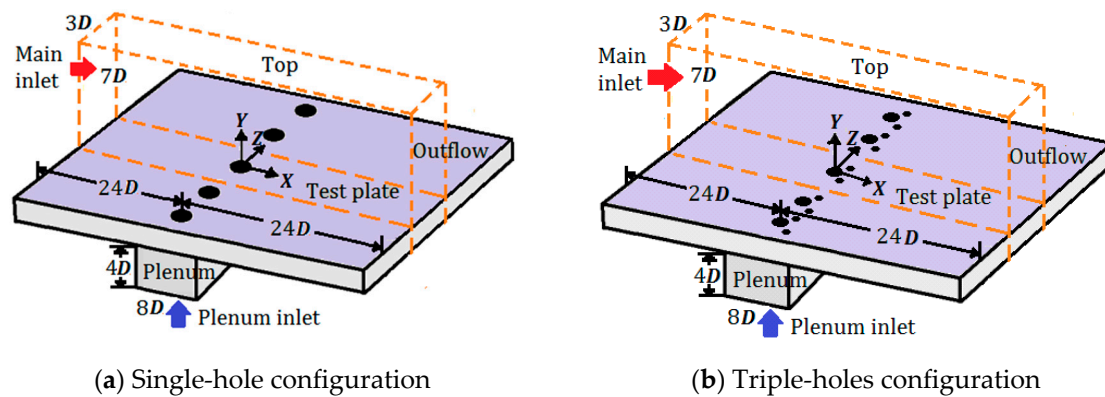


Figure 1. Computational domains of the single- and triple-hole configurations (orange dashed lines).

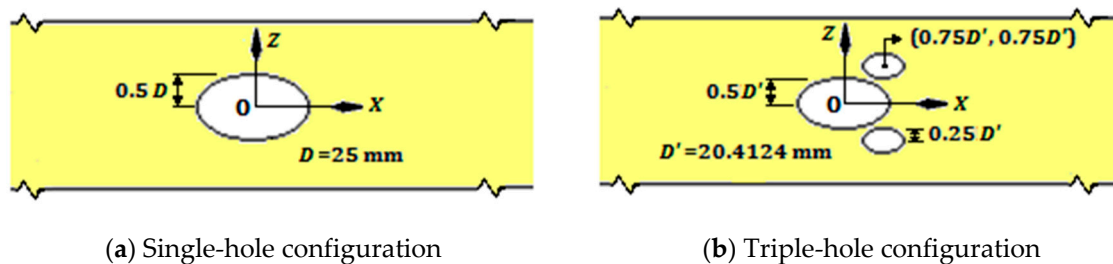


Figure 2. Schematics of the single hole and triple holes cooling hole configurations.

The boundary conditions in each computational domain are specified in Table 1. The turbulence intensity of the mainstream flow was 0.2% at the main inlet (as reported experimentally [13]), and the main flow velocity was 10 m/s. The temperatures of the main flow and coolant at the inlets were 313 and 293 K, respectively. Moreover, the boundary layer thickness at the cooling hole center is about D .

Table 1. Boundary conditions of the computational fluid dynamics (CFD) domain.

Surface	Boundary Condition
Main inlet	Velocity inlet
Plenum inlet	Velocity inlet
Top	Symmetry
Test plate	Adiabatic wall
Outflow	Pressure outlet
Main sides	Periodic
Sides of plenum	Wall
Tube wall	Wall

As is well-known, injecting the film-cooling jet induces a counter-rotating vortex pair (CRVP) in the system (see Figure 3a). This vortex pair is sourced from the vortices generated in the boundary layer of the coolant tube wall and around the leading edge of the hole [12,14,15]. Interactions between the jet and main flow cause the injected coolant to split into two directions, whereas the vortices generated in the coolant are stretched and turned. As the CRVP vortices draw closer together, their mutual induction increases, promoting coolant jet liftoff. The consequent strong entrainment of the hot main flow under the jet increases the adiabatic temperature on the test plate and decreases film-cooling effectiveness. Moreover,

when two sister holes are placed slightly downstream of the primary hole (Figure 2b), their jets generate an anti-CRVP, as illustrated in Figure 3b. Therefore, film-cooling effectiveness is increased by establishing vortex interactions between the jets and by reducing the intensity of the main CRVP [9–12].

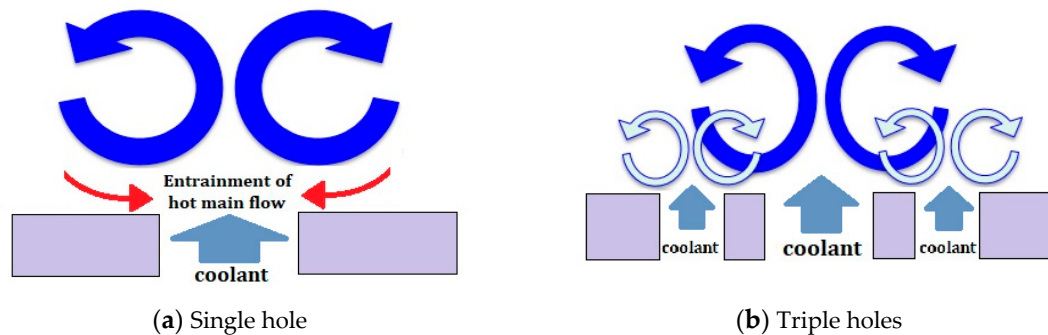


Figure 3. Cross-sectional schematic of a counter rotating vortex pair generated in the single- and triple-hole configurations.

3. Validation of Numerical Methods

The CFD calculations were performed in ANSYS Fluent v.19.1 [16], and the meshes were generated in Pointwise v.18.1 [17]. The numerical simulations were executed in the LES using the Smagorinsky–Lilly model as the subgrid-scale model. The time step was set to 6.25×10^{-6} s. Assuming the mainstream convected the hole diameter after 400 time steps, the simulations were carried out with the computational time step $\Delta t = 0.0025D/U_\infty$ [18,19]. Once the system had reached a statistical steady state, the statistics of the solution was collected in multiples of the period. In each time step, approximately 10 subiterations were executed to obtain well-resolved data [20]. The LES runtime using 18 cores of an Intel Xeon Gold 6148 processor was 1–2 months in each case.

The fluid was assumed as Newtonian and incompressible and had temperature-dependent variable properties. The compressibility effect was negligible because the main flow velocity was 10 m/s (Mach 0.029) and the jet injection velocities were 5 and 10 m/s at $M = 0.5$ and $M = 1.0$, respectively; that is, both velocities were far below Mach 0.3 [21]. The governing equations of the CFD simulations are the continuity and momentum equations. The filtered Navier–Stokes equations in the LES approach are given by [22]

$$\frac{\partial \rho}{\partial t} + \frac{\partial}{\partial x_i}(\rho \bar{u}_i) = 0 \quad (1)$$

and

$$\frac{\partial(\rho \bar{u})}{\partial t} + \frac{\partial}{\partial x_j}(\rho \bar{u}_i \bar{u}_j) = \frac{\partial}{\partial x_j} \left[\mu \left(\frac{\partial \bar{u}_i}{\partial x_j} + \frac{\partial \bar{u}_j}{\partial x_i} \right) - \frac{2}{3} \mu \frac{\partial \bar{u}_l}{\partial x_l} \delta_{ij} \right] - \frac{d\bar{p}}{dx} + \frac{\partial \tau_{ij}}{\partial x_j} \quad (2)$$

where τ_{ij} , the subgrid-scale turbulent stress, needs modeling using the Boussinesq hypothesis like RANS models as

$$\tau_{ij} - \frac{1}{3} \tau_{kk} \delta_{ij} = -\mu_t \left(\frac{\partial \bar{u}_i}{\partial x_j} + \frac{\partial \bar{u}_j}{\partial x_i} \right) \quad (3)$$

where μ_t is the turbulent viscosity on the subgrid scale. In the Smagorinsky–Lilly model, the turbulent viscosity is modeled as [18]

$$\mu_t = \rho L_s^2 \sqrt{\frac{1}{2} \left(\frac{\partial \bar{u}_i}{\partial x_j} + \frac{\partial \bar{u}_j}{\partial x_i} \right) \left(\frac{\partial \bar{u}_i}{\partial x_j} + \frac{\partial \bar{u}_j}{\partial x_i} \right)} \quad (4)$$

Figures 4 and 5 show the meshes of the single- and triple-hole systems in the xy and yz planes, respectively. The computational domains of the systems were composed of 2.04 (single-hole) and 2.69

(triple-hole) million hexahedron cells. Figure 6 shows a close-up of the mesh near the hole, where P2 and P1 are the static pressures at the inlet and outlet of the hole, respectively, as mentioned earlier.

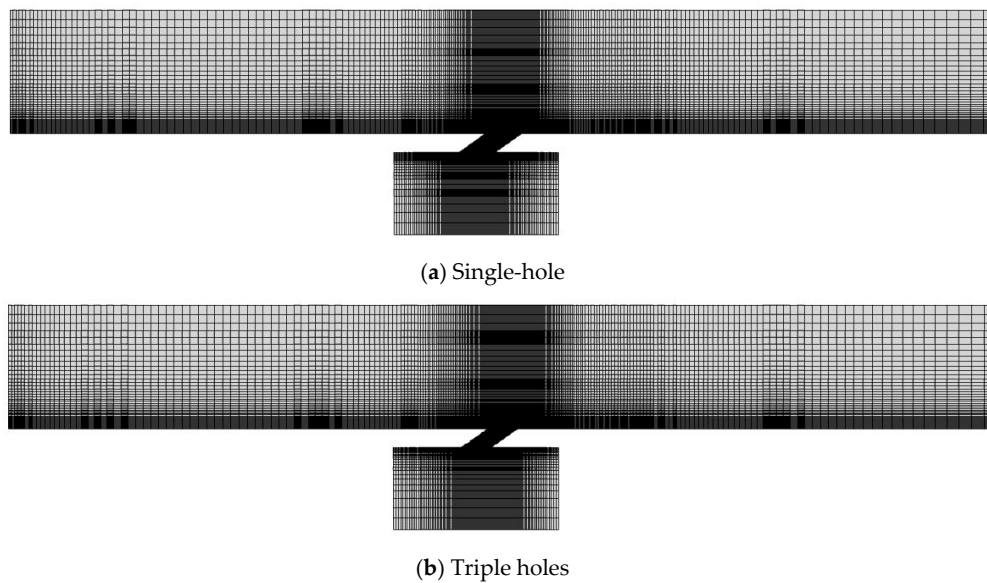


Figure 4. CFD meshes of the single- and triple-hole systems in the xy plane.

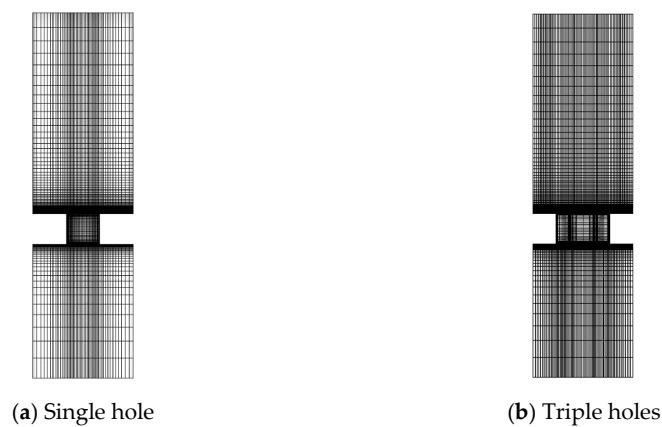


Figure 5. CFD meshes in the yz plane.

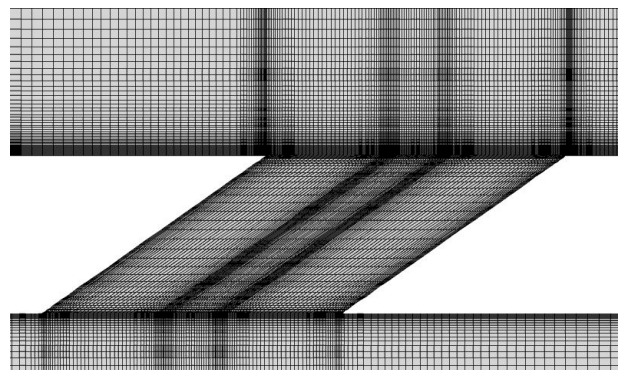


Figure 6. Close-up of the mesh near the hole.

Figures 7 and 8 show the results of the grid sensitivity tests in each system at a blowing ratio of 0.5, with the grid descriptions given in Tables 2 and 3. The results were obtained using the Smagorinsky–Lilly model in LES, and the tests were performed on five different grids. In the single-hole system, the

effectiveness value along the centerline ($z = 0, y = 0$) on the third grid almost matched those of the finer fourth and fifth grids.

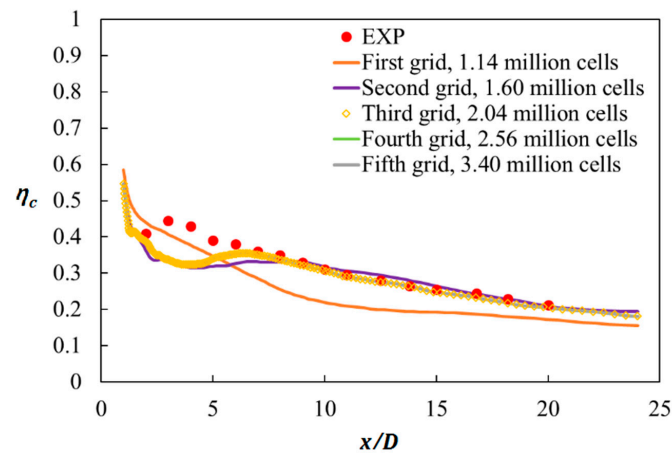


Figure 7. Grid sensitivity test of the large eddy simulation (LES) calculation in the single-hole system.

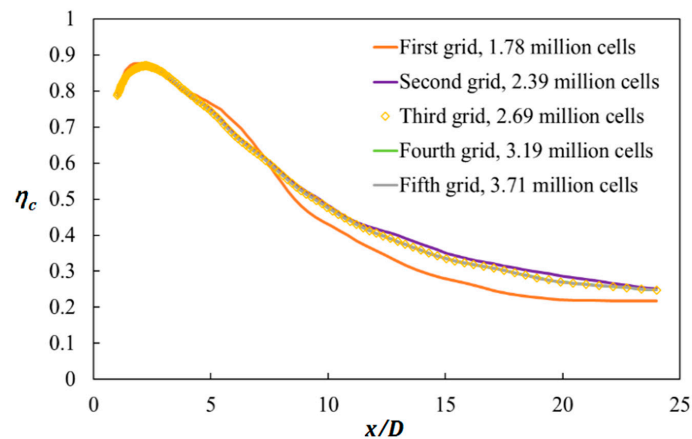


Figure 8. Grid sensitivity test of the LES calculation in the triple-hole system.

Table 2. Specifications of mesh arrangements in the grid sensitivity test of the single-hole system.

Grid	Number of Cells in the x Direction	Number of Cells in the y Direction	Number of Cells in the z Direction	Number of Cells in Cross Flow Block (million)	Total Cells Number (million)
First	320	50	32	0.52	1.14
Second	334	60	48	0.98	1.60
Third	352	80	50	1.42	2.04
Fourth	364	94	56	1.94	2.56
Fifth	390	110	64	2.78	3.4

Table 3. Specifications of mesh arrangements in the grid sensitivity test of the triple-hole system.

Grid	Number of Cells in the x Direction	Number of Cells in the y Direction	Number of Cells in the z Direction	Number of Cells in Crossflow Block (million)	Total Cells Number (million)
First	300	46	65	1.01	1.78
Second	330	60	75	1.62	2.39
Third	350	70	80	1.92	2.69
Fourth	370	80	85	2.41	3.19
Fifth	390	90	90	2.94	3.71

Therefore, the adiabatic film-cooling effectiveness in the single-hole system was evaluated on the 2.04 million-cell grid. In the triple-hole system, the third grid with 2.69 million cells again showed

almost the same centerline effectiveness as the fourth and fifth grids. Therefore, the 2.69 million-cell grid was selected for modeling the film-cooling effectiveness in the triple-hole system.

4. Results and Discussion

4.1. Centerline and Spanwise-Averaged Film Cooling Effectiveness

Figure 9 shows the centerline and spanwise-averaged effectiveness values in the single- and triple-hole systems at $M = 0.5$ and 1.0 . The centerline effectiveness decreased as the main flow traveled downstream. This degradation is attributable to the turbulence generation and rapid mixing between the main flow and jet, which increases the test plate temperature. For the same total cross-sectional hole area and same amount of total cooling air, the triple holes improved the centerline and spanwise-averaged effectiveness values, respectively, by approximately 36% and 45% over the single-hole configuration at $M = 0.5$ and approximately 250% and 345% at $M = 1.0$. In Figure 9a–d, the LES-predicted centerline film-cooling effectiveness in the single-hole system showed a good match to the experimental data by Seo et al. [13], whereas the LES model under-predicted the triple-hole, spanwise-averaged effectiveness experimental data by Cao et al. [22] because the data were measured for $L/D = 10$. Thus, compared to lower L/D cases, higher L/D values of the hole increase the adiabatic film-cooling effectiveness under the same operating condition as the coolant velocity at the hole exit becomes more uniform [13].

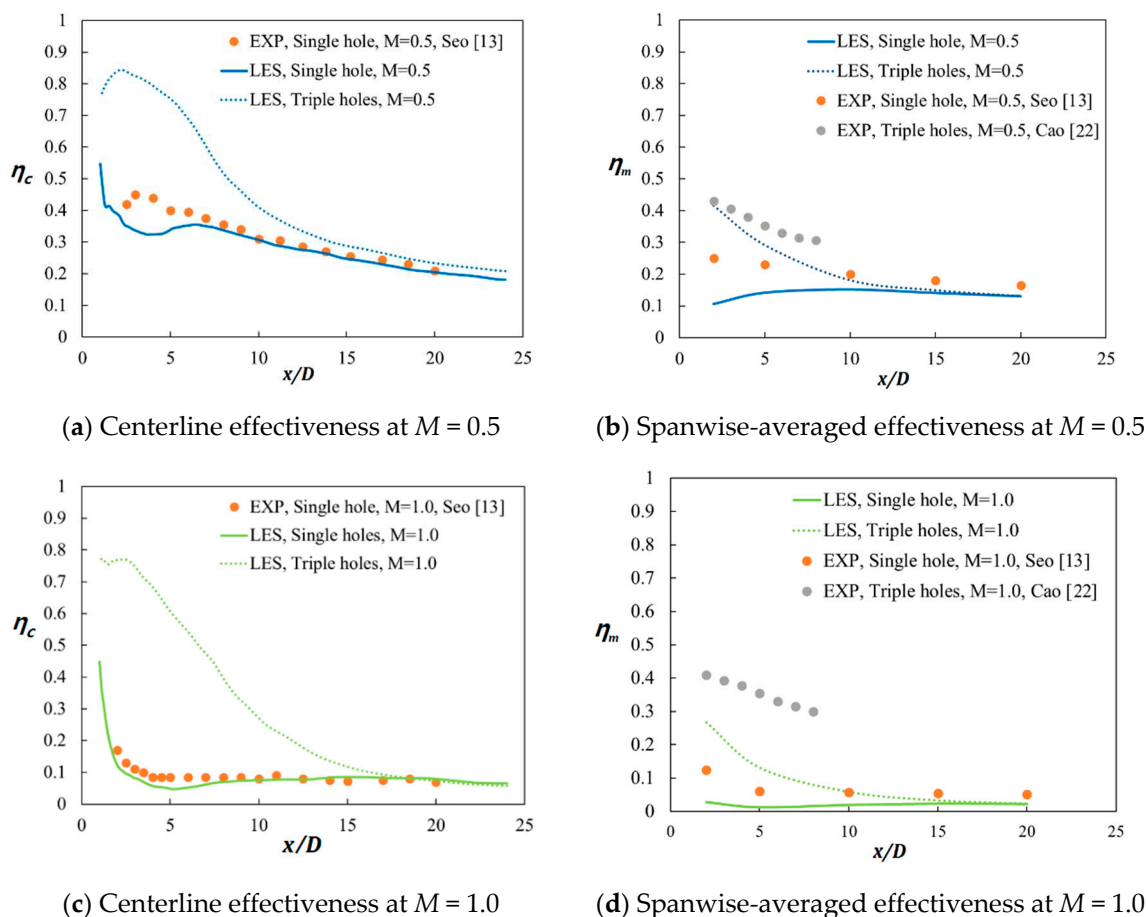


Figure 9. Film cooling effectiveness values of the single- and triple-hole systems.

The ratios of the spanwise-averaged effectiveness values in the triple-hole system to those in the single-hole system as functions of x/D for $M = 0.5$ and 1.0 are plotted in Figure 10. Note that increasing the blowing ratio improves the ratio of the spanwise-averaged effectiveness. This indicates

that under high blowing ratios, configuring the main hole and two sister holes is more effective for film cooling than using an ordinary single hole mainly because the jet trajectory in the single-hole system is mostly governed by the jet liftoff at a high blowing ratio of $M = 1.0$. The result is very low adiabatic film-cooling effectiveness, as indicated in Figure 9c,d, and very high ratios of the spanwise-averaged effectiveness values, as shown in Figure 10. The maximum value of the ratio at $M = 1.0$ is observed around at $x/D = 4$ since the minimum value of the spanwise-averaged effectiveness in the single-hole system is shown around at $x/D = 4$ due to the jet lift off, as shown in Figure 9d.

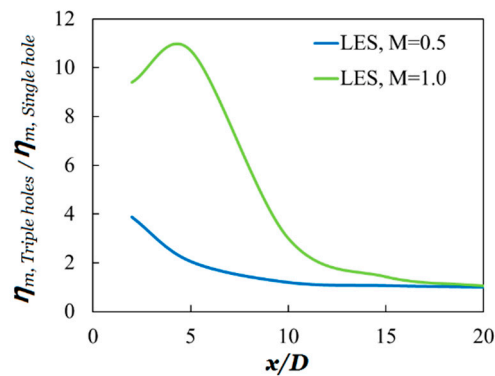


Figure 10. Ratios of spanwise-averaged effectiveness in the triple hole system to those in the single-hole system.

4.2. Contours of Film Cooling Effectiveness and Dimensionless Temperature

Figure 11 presents top views of the time-averaged film-cooling effectiveness contours on the test plate in each hole system. The additional sister holes largely increased the amount of coolant in contact with the test plate, which boosts film-cooling effectiveness. Moreover, the spread of the coolant in the spanwise direction in the triple-hole system was much larger than that in the single-hole configuration as the main CRVP weakens. Furthermore, lower film-cooling effectiveness was predicted at M of unity than at $M = 0.5$ because of strong jet liftoff.

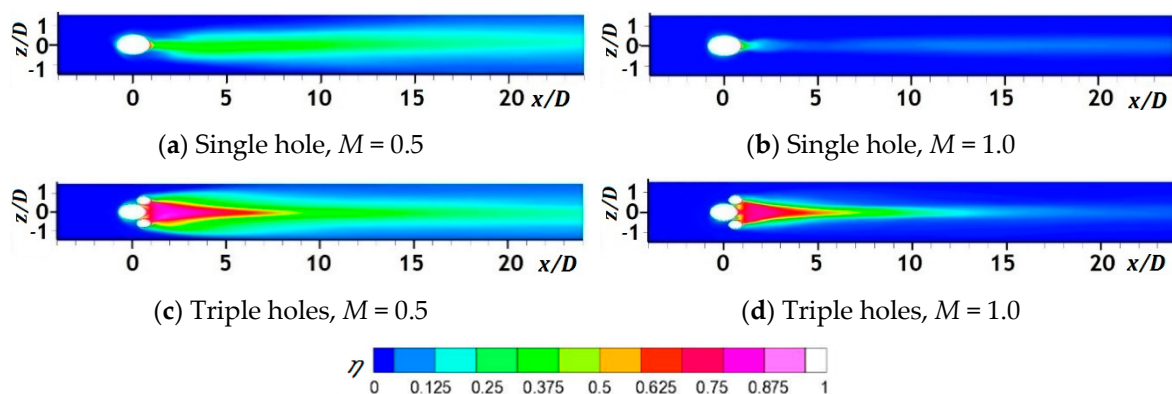


Figure 11. Time averaged film cooling effectiveness on the test plate.

The cross-sectional views of the dimensionless mean temperature contours at $x/D = 2, 5, 10, 15,$ and 20 in the two systems are illustrated in Figure 12. Initially, the dimensionless temperature near the test plate was higher in the triple-hole system than in the single-hole configuration, which increased film-cooling effectiveness on the test plate. As the main flow went downstream, the dimensionless temperatures near the test plate in the triple-hole system became similar to those in the single-hole system, leading to almost identical film-cooling effectiveness in the range of $x/D > 15$ (Figures 8 and 9) because of intensive mixing between the mainstream flow and coolant jet.

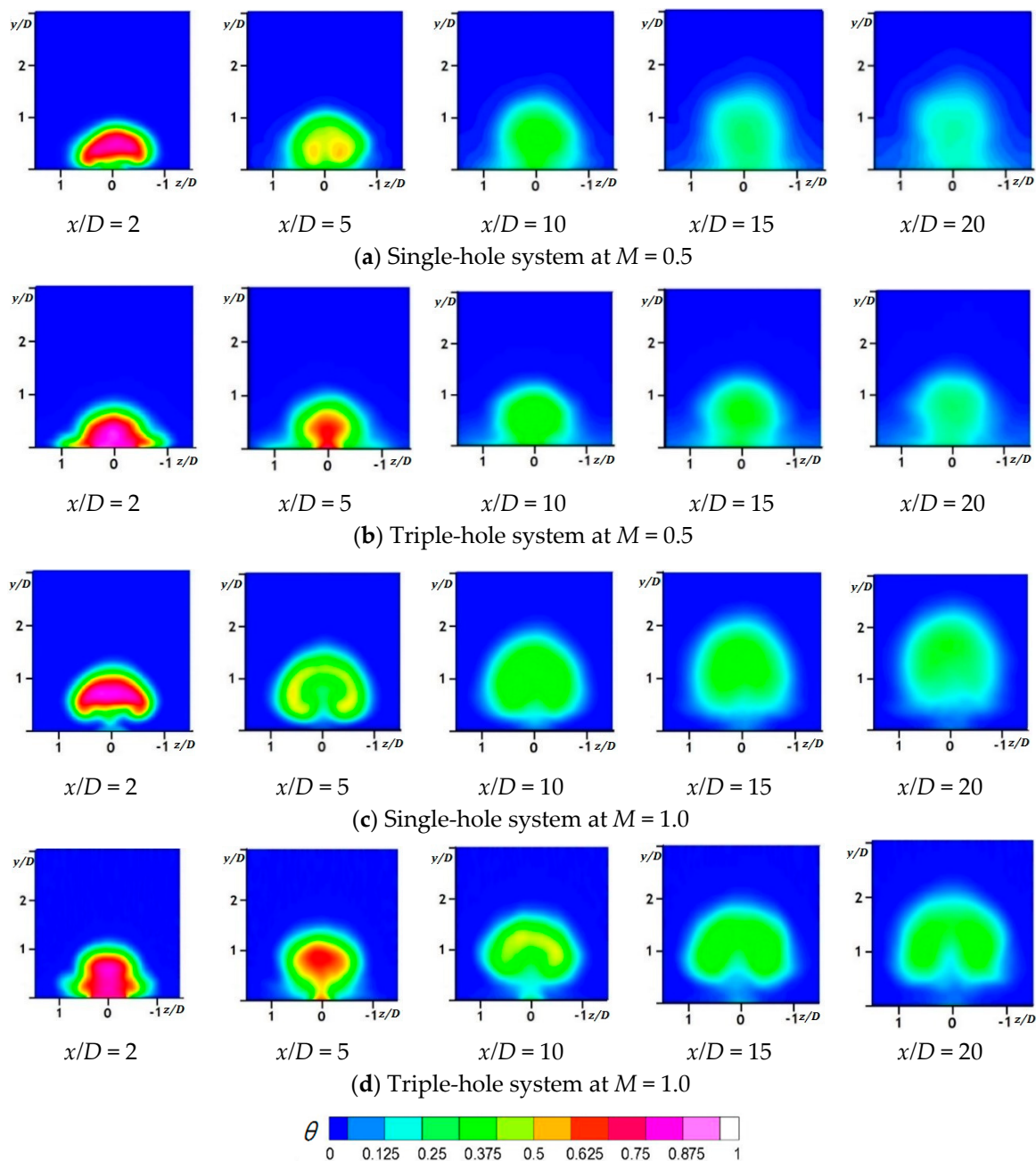


Figure 12. Cross-sectional contours of the dimensionless mean temperatures.

Figure 13 shows the central cross-sectional contours of the dimensionless mean temperatures in the $z = 0$ plane for both hole systems. The entrainment of the main flow under the cooling jet in the triple-hole system was noticeably weaker than that in the single-hole system. Many researchers have argued that the jet lifted off because of the high momentum of the coolant and reattached downstream to the plate at a high blowing ratio [2,22,23]. However, as illustrated in Figure 13b, the dispersion of the coolant jet increases without reattachment with the test plate as the flow goes downstream after the jet liftoff, followed by the entrainment of the main flow under the jet. In addition, the dimensionless temperature near the test plate in the near-hole region in the triple-hole system was much higher than that in the single-hole configuration as vortex interactions between the jets were established, thereby reducing the intensity of the main CRVP at $M = 0.5$ and 1.0 and increasing film-cooling effectiveness on the test plate.

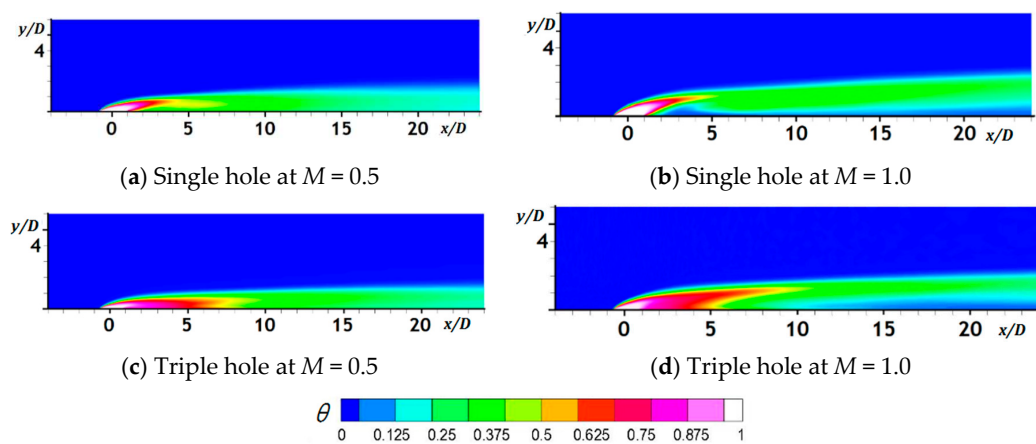


Figure 13. Central cross-sectional contours of the dimensionless mean temperatures in the $z = 0$ plane.

Figure 14 illustrates the streamlines of cooling jets to a cross-sectional plane at $x/D = 5$ and film-cooling effectiveness on the test plate in the single- and triple-hole systems at $M = 0.5$ and unity. Unlike in a single hole, more streamlines of the coolant head to the region near the test plate in the $x/D = 5$ plane appeared in the triple-hole system, with these streamlines more dispersed, which resulted in higher adiabatic film-cooling effectiveness on the plate given that most streamlines from the sister holes have converged to the centerline. At $M = 1.0$, the strong jet liftoff caused the streamlines to cover smaller regions laterally in the $x/D = 5$ plane even in the triple-hole system.

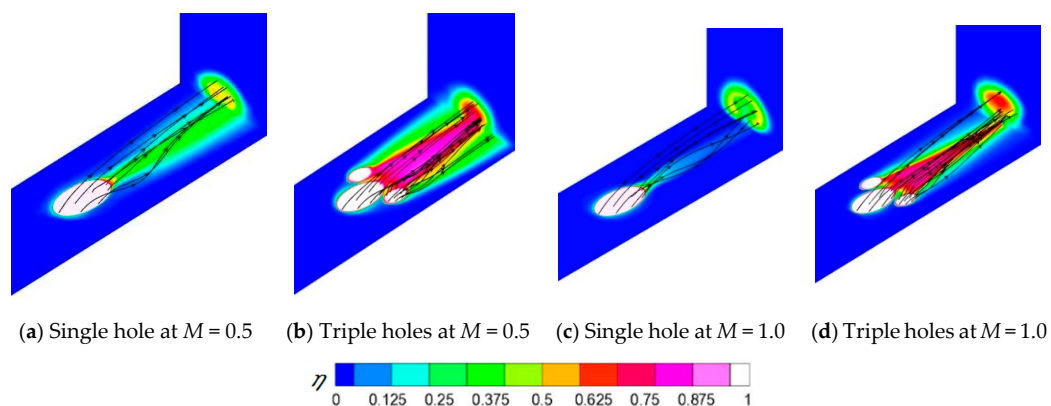


Figure 14. The streamlines of cooling jets to cross-sectional plane at $x/D = 5$.

4.3. Contours of x -Vorticity and Mean Velocity Vectors

Figure 15 shows the cross-sectional contours of the mean x -vorticity at the $x/D = 2$ and $x/D = 5$ planes in the single- and triple-hole systems at $M = 0.5$ and unity. The mean velocity vectors are superimposed on the contours. As shown in Figure 15b,d of the triple-hole system, distinct anti-CRVPs were found from the sister holes around the $x/D = \pm 0.5$ and $y/D = 0.2$ regions in the $x/D = 2$ plane. The anti-CRVPs weakened the main CRVP and reduced the main jet liftoff, thereby reducing the entrainment of the hot mainstream gas under the coolant and increasing the dimensionless mean temperature and film-cooling effectiveness, as illustrated in Figures 11 and 13. However, the intensity of the anti-CRVPs became very small in the $x/D = 5$ plane because the anti-CRVP from the sister holes was not as strong as the main CRVP. In the triple-hole system, the upward velocity vectors around the line of $z/D = 0$ were less concentrated than those in the single-hole system. Thus, coolant liftoff was weakened by the generated anti-CRVPs. At $M = 1.0$, the positions of the core for the CRVPs were higher than those at $M = 0.5$ because of the strong jet liftoff generated.

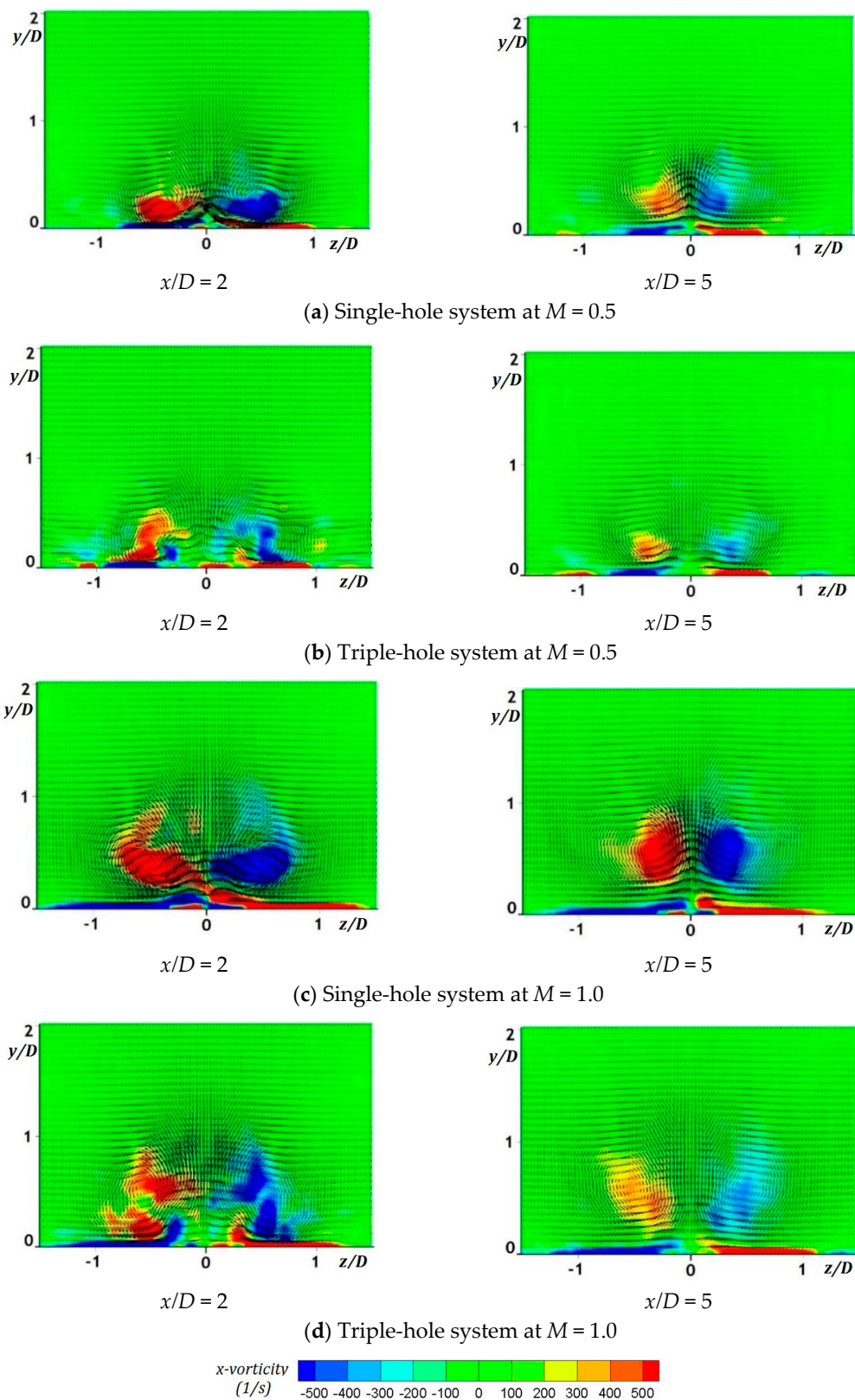


Figure 15. Cross-sectional contours of the x -vorticity and velocity vectors.

Figure 16 shows the cross-sectional velocity vectors of POD Mode 1 at $x/D = 2$ in the two-hole systems at $M = 0.5$ and unity. The POD was introduced by Dr. John Lumley in 1967 in order to decompose a random velocity vector field of turbulence into a set of portions of the total kinetic

energy [24,25]. On the basis of the figure, CRVP was most distinct in the velocity vector field at $x/D = 2$. Figure 17 illustrates the portion of the total kinetic energy at $x/D = 2$ for Modes 1, 2, 3, and 4 in the single- and triple-hole systems at $M = 0.5$ and $M = 1.0$, which showed Mode 1 as the most dominant. At $M = 0.5$, POD Mode 1 contributed to about 60% and 36% of the total kinetic energy in the single- and triple-hole systems, respectively, which means that CRVP was dominant for both, although relative to the former, the portion of the kinetic energy in the latter system was largely decreased by about 40% because of a weakened main CRVP by anti-CRVPs from the two sister holes. Similarly, at $M = 1.0$, POD Mode 1 contributed to about 71% and 49% of the total kinetic energy in the single- and triple-hole systems, respectively, indicating that the portion of the kinetic energy was decreased by nearly 30%. Indeed, it could be inferred that compared to that in the single-hole system, the kinetic energy of the CRVP in the triple-hole system was reduced by about 30–40%.

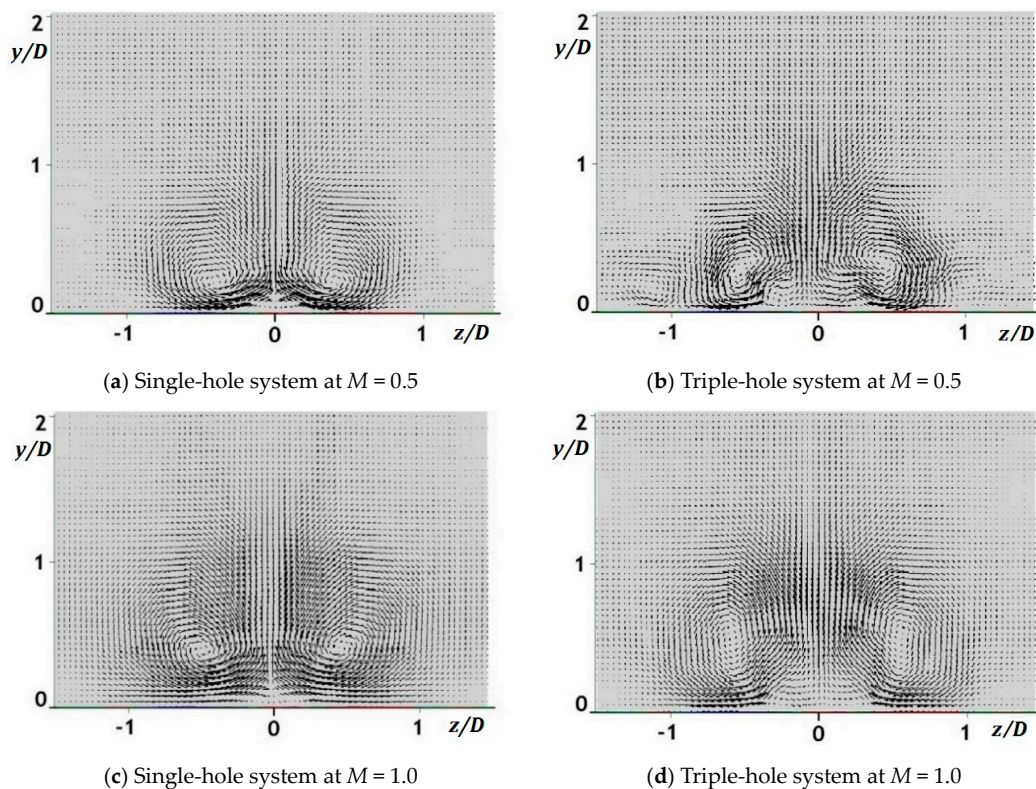


Figure 16. Cross-sectional velocity vectors at $x/D = 2$ for POD Mode 1.

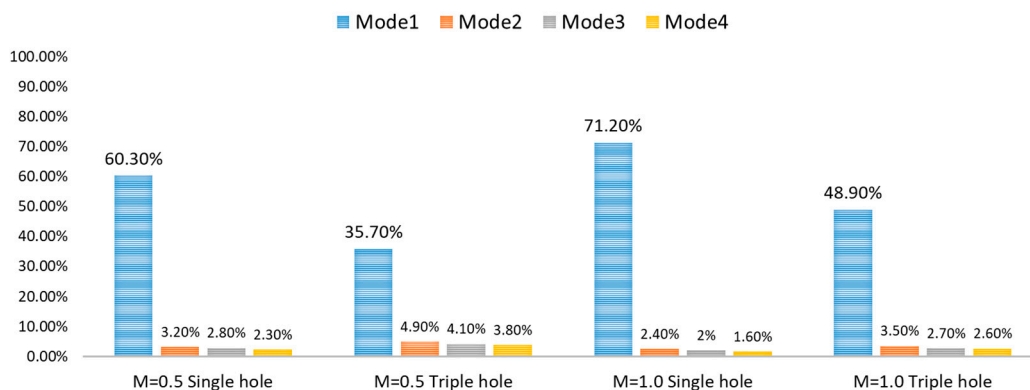


Figure 17. Portions of the total kinetic energy for Mode 1, 2, 3, and 4 in the plane of $x/D = 2$.

4.4. Root-Mean-Square Temperature Contours

Figure 18 illustrates the cross-sectional views of the root-mean-square (RMS) temperature contours at $x/D = 2, 5, 10, 15,$ and 20 for the mixing region between the mainstream flow and coolant in the single- and triple-hole systems. The mixing area was more expanded in the triple-hole system in the spanwise direction, especially in the near-hole region as $x/D = 2$, because the weakened main CRVP allowed wider spreading and closer contact of the coolant jet with the test plate. Although no significant difference in the mixing intensity was observed in both hole systems, the T_{rms} in the $x/D = 2$ plane reached maximum values of 6.25, 6.24, 6.08, and 5.19, as shown in Figure 18a–d, respectively, which indicates a similar but slightly decreased mixing intensity in the triple-hole system relative to the single-hole system. This reduced mixing intensity is beneficial to film cooling because increased mixing between the coolant and mainstream flow consequently decreases film-cooling effectiveness [22]. Nevertheless, it could be stated that in the triple-hole system, the effect of the sister holes on the jet trajectory contributes greatly to improve film-cooling effectiveness as compared to the effect of less mixing between the main flow and coolant.

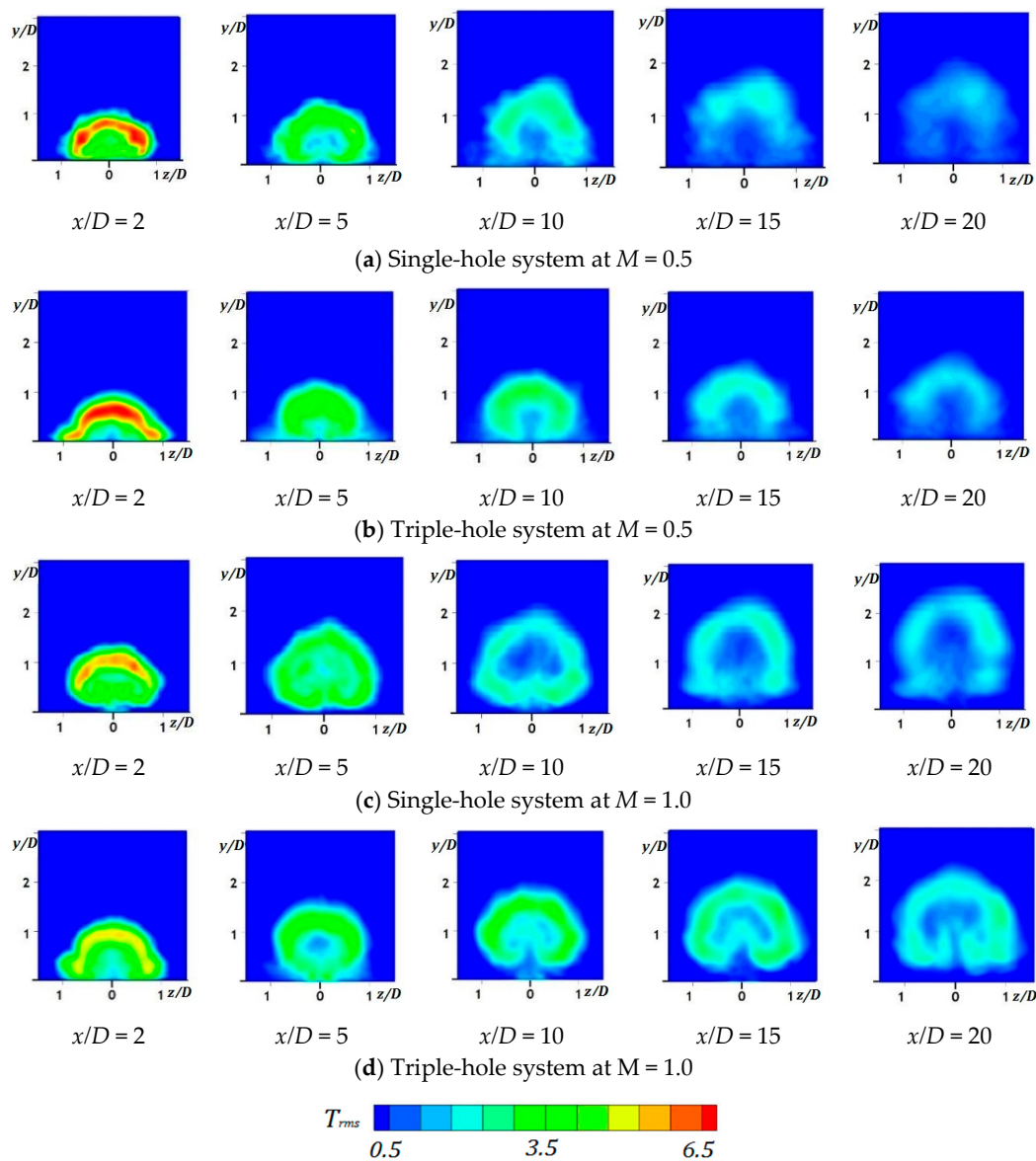


Figure 18. Cross-sectional contours of the T_{rms} .

4.5. Q-Criterion Iso-Surfaces

In the Q-criterion, Q is defined as the difference between the magnitudes of the rotation rate and strain rate, representing the dominance of the former over the latter [26–28]. The instantaneous contours of a Q-criterion with iso-surfaces of level 80,000 at $M = 0.5$ and unity are displayed in Figure 19. Q-criterion contours in the single-hole system clearly showed various vortex structures, such as the CRVP, hairpin and jet shear layer vortices, and horseshoe vortex, whereas those in the triple-hole configuration had smaller hairpin and jet shear layer vortices and were not very distinguishable. These smaller and indistinct hairpin vortices represent the weakened CRVP as the hairpin vortex is closely related to the generation of the CRVP [22]. A weakened CRVP positively affects the cooling performance on the plate because it increases film-cooling effectiveness on the test plate.

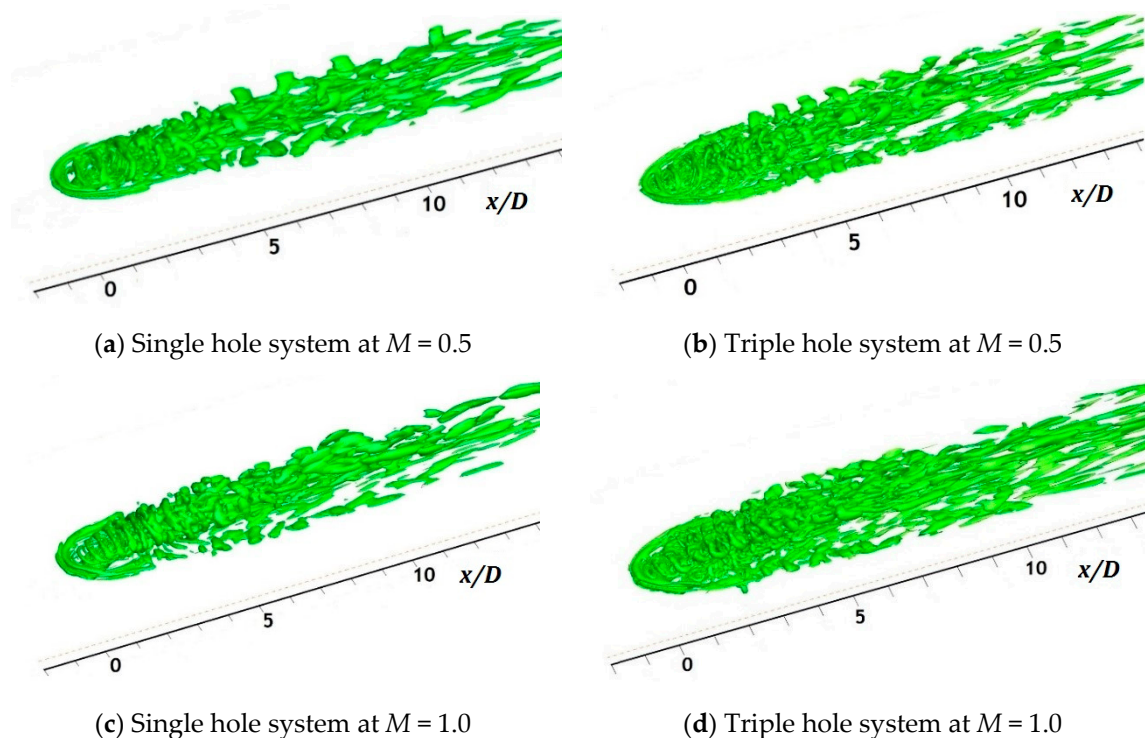


Figure 19. Q-criterion contours with iso-surfaces of level 80,000.

4.6. Cross-Sectional Contours of the Mean Velocity Magnitude in the Hole

Figure 20 shows the cross-sectional contours of the mean velocity magnitude in the hole measured around the hole exit ($y/D = -0.2$). As mentioned earlier, the ratio of the delivery tube length to the hole diameter in the single-hole system was 1.6, whereas it was 1.8 and 3.6 for the main hole and sister holes in the triple-hole system, respectively, because the triple holes had the same total cross-sectional hole area as the single hole. Therefore, the mean velocity magnitude in the main hole is not uniform but has high- and low-momentum regions, whereas that in the sister holes shows more developed coolant flow. The cooling jet having a uniform velocity profile is advantageous to film-cooling performance because of less jet liftoff. Thus, it could be stated that relative to the single-hole system, the sister holes improve film-cooling effectiveness by the generation of the anti-CRVP, as well as higher L/D ratios.

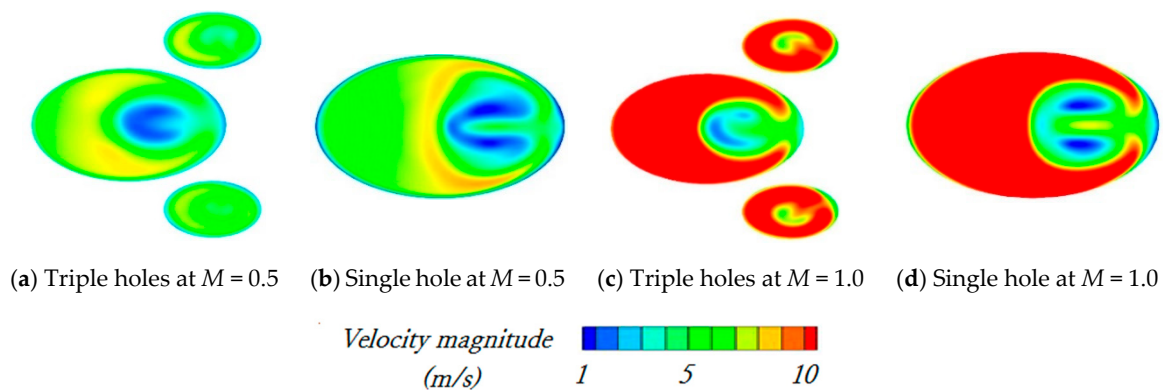


Figure 20. Cross-sectional contours of the mean velocity magnitude in the hole at $y/D = -0.2$.

5. Conclusions

Film-cooling simulations of the single- and triple-hole systems on a flat plate were carried out in this paper at blowing ratios of $M = 0.5$ and unity by employing LES. On the basis of these simulations, when two sister holes which were placed slightly downstream the main hole, the coolant jets from the former generated an anti-CRVP, which increased film-cooling effectiveness. Thus, for the same total cross-sectional hole area and same amount of total cooling air, the triple-hole system increased the centerline and spanwise-averaged effectiveness values by approximately 36% and 45% at $M = 0.5$ and by approximately 250% and 345% at $M = 1.0$ as compared to that done by the single-hole configuration. Moreover, the ratios of the spanwise-averaged effectiveness values in the triple-hole system indicate that it is the more effective system for film cooling under a high blowing ratio.

Meanwhile, the time-averaged film-cooling effectiveness contours on the test plate and the cross-sectional views of the dimensionless mean temperature contours in the two hole systems showed that additional sister holes can increase the amount of coolant contacting with the test plate and boost film-cooling effectiveness. Specifically, the mean dimensionless temperature contours in the $z/D = 0$ plane showed that in the single-hole system at M of unity, as the cooling jet goes downstream, the jet gets dispersed without reattachment with the test plate, and the entrainment of the main flow under the jet is generated.

Furthermore, the cross-sectional mean x -vorticity contours in the triple-hole system showed that the generated anti-CRVPs weaken the main CRVP. The results of the POD analysis confirmed that the kinetic energy of the CRVP in the triple-hole system was reduced by about 30–40% relative to that in the single-hole system. Streamlines of the cooling jets to the cross-sectional plane at $x/D = 5$ also showed that most streamlines from the sister holes converge to the centerline. As with the Q -criterion contours in the triple-hole system, the hairpin and jet shear layer vortices were smaller and indistinguishable, unlike in the single-hole system.

Lastly, on the basis of the cross-sectional views of the RMS temperature contours, the effect of the sister holes on the cooling jet trajectory contributes significantly to the increase in film-cooling effectiveness, as compared to the effect of less mixing. Accordingly, the sister holes improve film-cooling effectiveness using higher L/D ratios.

Author Contributions: S.I.B. carried out the simulations, analyzed the CFD data and wrote the paper. J.A. supervised the research, analyzed the CFD data and wrote the paper. All authors have read and agreed to the published version of the manuscript.

Funding: This research received no external funding.

Conflicts of Interest: The authors declared no conflict of interest.

Nomenclature

C_s	Smagorinsky constant
D	hole diameter for a single hole [mm]
D'	diameter of primary hole for triple holes [mm]
E_{ij}	rate of deformation
L	delivery tube length [mm]
L_s	mixing length of sub-grid scales = $\min(\kappa d, C_s \Delta)$
M	blowing ratio = $(\rho_C U_C) / (\rho_G U_G)$
P	pitch between holes [mm]
T	temperature [K]
t	time [s]
U	flow velocity [m/s]
V_{mi}	main flow velocity at the main inlet [m/s]
V_{pi}	coolant velocity at the plenum inlet [m/s]
x	streamwise coordinate
y	wall-normal coordinate
z	spanwise coordinate

Greek symbols

κ	von Karman's universal constant = 0.41
η	adiabatic film cooling effectiveness = $\frac{(T_G - T_{aw})}{T_G - T_C}$
η_C	centerline film cooling effectiveness
η_m	spanwise-averaged film cooling effectiveness
ρ	density [kg/m ³]
τ_{ij}	sub-grid scale turbulent stress = $\overline{\rho u_i u_j} - \rho \overline{u_i} \overline{u_j}$
μ_t	sub-grid scale turbulent viscosity [kg/(m·s)]
ν	local kinematic viscosity [m ² /s]
Δ	local grid scale
Θ	dimensionless temperature = $\frac{(T_G - T)}{T_G - T_C}$

Subscripts

aw	adiabatic wall
c	centerline
C	coolant
G	mainstream gas
m	spanwise averaged
μ	local dynamic viscosity [m ² /s]

References

- Moran, M.; Shapiro, H.; Boettner, D.; Bailey, M. *Fundamentals of Engineering Thermodynamics*, 8th ed.; Wiley: Hoboken, NJ, USA, 2014; p. 532.
- Bogard, D. Airfoil Film Cooling. In *The Gas Turbine Handbook*; National Energy Technology Laboratory: Albany, NY, USA, 2006.
- Leedom, D.H.; Acharya, S. Large Eddy Simulations of Film Cooling Flow Fields From Cylindrical And Shaped Holes. In Proceedings of the ASME Turbo Expo 2008, Berlin, Germany, 9–13 June 2008; GT2008-51009. pp. 865–877.
- Acharya, S.; Leedom, D.H. Large Eddy Simulations of Discrete Hole Film Cooling With Plenum Inflow Orientation Effects. *J. Heat Transf.* **2013**, *135*, 011010. [[CrossRef](#)]
- Tyagi, M.; Acharya, S. Large Eddy Simulation of Film Cooling Flow From an Inclined Cylindrical Jet. *J. Turbomach.* **2003**, *125*, 734–742. [[CrossRef](#)]
- Fujimoto, S. Large Eddy Simulation of Film Cooling Flows Using Octree Hexahedral Meshes. In Proceedings of the ASME Turbo Expo 2012, Copenhagen, Denmark, 11–15 June 2012. GT-2012-7009.
- Rozati, A.; Tafti, D. Large-eddy simulations of leading edge film cooling: Analysis of flow structures, effectiveness, and heat transfer coefficient. *Int. J. Heat Fluid Flow* **2008**, *29*, 1–17. [[CrossRef](#)]

8. Heidmann, J.; Ekkad, S. A Novel Anti-Vortex Turbine Film Cooling Hole Concept. In Proceedings of the ASME Turbo Expo 2007, GT2007-27528, Montreal, QC, Canada, 14–17 May 2007. [CrossRef]
9. Javadi, K.; Taeibi-Rahni, M.; Darbandi, M.; Javadi, K. Jet-into-Crossflow Boundary Layer Control: Innovation in Gas Turbine Blade Cooling. *AIAA J.* **2007**, *45*, 2910–2925. [CrossRef]
10. Ely, M.J.; Jubran, B.A. A Numerical Evaluation on the Effect of Sister Holes on Film Cooling Effectiveness and the Surrounding Flow Field. *Heat Mass Transf.* **2009**, *45*, 1435–1446. [CrossRef]
11. Wu, H.; Cheng, H.; Li, Y.; Rong, C.; Ding, S. Effects of Side Hole Position and Blowing Ratio on Sister Hole Film Cooling Performance in a Flat Plate. *Appl. Therm. Eng.* **2016**, *93*, 718–730. [CrossRef]
12. Farhadi-Azar, R.; Ramezanzadeh, M.; Taeibi-Rahni, M.; Salimi, M. Compound Triple Jets Film Cooling Improvements via Velocity and Density Ratios: Large Eddy Simulation. *J. Fluids Eng.* **2011**, *133*, 031202. [CrossRef]
13. Seo, H.; Leea, J.; Ligrani, P. The Effect of Injection Hole Length on Film Cooling with Bulk Flow Pulsations. *Int. J. Heat Mass Transf.* **1998**, *41*, 3515–3528. [CrossRef]
14. Fric, T.F.; Roshko, A. Vortical structure in the wake of a transverse jet. *J. Fluid Mech.* **1994**, *279*, 1–47. [CrossRef]
15. Haven, B.A.; Kurosaka, M. Kidney and anti-kidney vortices in crossflow jets. *J. Fluid Mech.* **1997**, *352*, 27–64. [CrossRef]
16. ANSYS Fluent Theory Guide version 19. Available online: <https://www.ansys.com/products/fluids/ansys-fluent> (accessed on 7 October 2020).
17. Pointwise version 18. Available online: <http://www.pointwise.com/> (accessed on 7 October 2020).
18. Renze, P.; Schröder, W.; Meinke, M. Large-eddy Simulation of Film Cooling Flows with Variable Density Jets. *Flow Turbul. Combust.* **2008**, *80*, 119–132. [CrossRef]
19. Peet, Y.; Lele, S. Near field of film cooling jet issued into a flat plate boundary layer: LES STUDY. In Proceedings of the ASME Turbo Expo 2008, GT2008-50420, Berlin, Germany, 9–13 June 2008.
20. Yao, Y.; Zhang, J.; Yang, Y. Numerical study on film cooling mechanism and characteristics of cylindrical holes with branched jet injections. *Propuls. Power Res.* **2013**, *2*, 30–37. [CrossRef]
21. Cao, N.; Li, X.; Wu, Z.; Luo, X. Effect of film hole geometry and blowing ratio on film cooling performance. *Appl. Therm. Eng.* **2020**, *165*, 114578. [CrossRef]
22. White, F. *Fluid Mechanics*, 4th ed.; McGraw-Hill: New York, NY, USA, 1999.
23. Bacci, T.; Picchi, A.; Facchini, B. Flat plate and turbine vane film cooling performance with laid-back fan shaped holes. *Int. J. Turbomach. Propuls. Power* **2019**, *4*, 14. [CrossRef]
24. Lumley, J. The structure of inhomogeneous turbulent flows. In *Atmospheric Turbulence and Radio Wave Propagation, Proceedings of the International Colloquium, Moscow, Russia, 15–22 June 1965*; Publishing House Nauka: Moscow, Russia, 1967; Available online: <https://www.amazon.com/Atmospheric-Turbulence-Radio-Wave-Propagation/dp/B007V5IG6W> (accessed on 7 October 2020).
25. Weiss, J. A tutorial on the proper orthogonal decomposition. In Proceedings of the AIAA Aviation Forum, Dallas, TX, USA, 17–21 June 2019.
26. Kolar, V. Vortex identification: New requirements and limitations. *Int. J. Heat Fluid Flow* **2007**, *28*, 638–652. [CrossRef]
27. Schroder, A.; Willert, C. *Particle Image Velocimetry: New Developments and Recent Applications*; Springer: New York, NY, USA, 2008; p. 382.
28. Haydt, S.; Lynch, S. Flowfield of a shaped film cooling hole over a range of compound angles. In Proceedings of the ASME Turbo Expo proceeding, GT2018-75728, Lillestrom, Norway, 11–15 June 2018.

Publisher’s Note: MDPI stays neutral with regard to jurisdictional claims in published maps and institutional affiliations.



© 2020 by the authors. Licensee MDPI, Basel, Switzerland. This article is an open access article distributed under the terms and conditions of the Creative Commons Attribution (CC BY) license (<http://creativecommons.org/licenses/by/4.0/>).

Article

Influence of Tip Clearance on Flow Characteristics of Axial Compressor

Moru Song , Hong Xie, Bo Yang * and Shuyi Zhang

School of Mechanical Engineering, Shanghai Jiao Tong University, Shanghai 200240, China; samuel0624@sjtu.edu.cn (M.S.); xiehong1211@sjtu.edu.cn (H.X.); shuyizhang@sjtu.edu.cn (S.Z.)

* Correspondence: byang0626@sjtu.edu.cn; Tel.: +86-21-3420-6871

Received: 9 September 2020; Accepted: 10 November 2020; Published: 11 November 2020



Abstract: This paper studies the influence of tip clearance on the flow characteristics related to the performance. Based on full-passage numerical simulation with experimental validation, several clearance models are established and the performance curves are obtained. It is found that there exists an optimum clearance for the stable working range. By analyzing the flow field in tip region, the role of the tip leakage flow is illustrated. In the zero-clearance model, the separation and blockage along the suction side is the main reason for rotating stall. As the tip clearance is increased to the optimum value, the separation is suppressed by the tip leakage flow. However, with the continuing increasing of the tip clearance, the scale and strength of the tip clearance vortex is increased correspondingly. When the tip clearance is larger than the optimum value, the tip clearance vortex gradually dominates the flow field in the tip region, which can increase the unsteadiness in the tip region and trigger forward spillage in stall onset.

Keywords: axial compressor; tip clearance; flow field; numerical simulation

1. Introduction

It is the tip region of a rotor that is one of the most unstable regions in an axial compressor. For example, for the tip-critical rotors, the rotating stall was first observed in the tip region. In the tip region, there exists the maximum rotating linear velocity, tip leakage flow, and boundary layer flow, etc. Among these flows, the tip leakage flow, induced by the pressure difference between blade sides, plays the most important role on the flow behavior. The tip leakage flow is closely related to the tip clearance, which is one of the key parameters for the design and manufacture of an axial compressor. As the tip clearance is changed, not only is the strength of the leakage flow changed, but also other flow structure and distribution are influenced greatly, especially under a near-stall condition. Therefore, the performance and stable working range is varied with the tip clearance.

In the last century, many researches focused on the influence of tip clearance in an overall manner. Combined experiment data with potential-vortex model, Lakshminarayana [1] proposed a formula, firstly, to evaluate the stage efficiency in different tip clearance. Based on this formula, the pressure ratio and efficiency can be improved by the reduction of the tip clearance. Inoue et al. [2,3] obtained and described the roll-up tip clearance vortex (TCV) by hotwire. From the vortex model, the flows in the tip region could be divided into the main flow region and tip leakage flow region. Day [4] also proposed the influence of the tip clearance on off-design conditions in axial compressors.

As the experiment method and computational fluid dynamic method have been both highly improved, the flow structures and special phenomenon in the tip region were studied in detail, which included double leakage, vortex breakdown, self-induced flow, and active control technology, etc. For double leakage, it was first noticed by Khalsa et al. [5] in the experiment and simulation results. They pointed out that the relative stagnation pressure is decreased by double leakage; therefore, the loss

and blockage were increased. Double leakage flow was much influenced by clearance size, working condition, and unsteady interaction from the stator, which was illustrated by Mailach et al. [6,7], Sirakov et al. [8], and Du et al. [9]. By the means of Large-eddy simulation (LES) approach, Hah [10] studied the double leakage flow under the large tip clearance model. As double leakage flow occurred in all working conditions with large tip clearance, vortex rope is generated near leading edge, which results in the high mixing loss and non-synchronous vibration.

For the breakdown of tip clearance vortex, Lotzerich [11] and Furukawa et al. [12] both noticed this phenomenon at almost the same time. Later, Furukawa et al. [13,14] summarized the characteristics by the means of experiment and computational fluid dynamics (CFD). When the vortex breakdown occurs, the disappearance of vortex core and the roll-up structure causes the large low-velocity cells. The vortex breakdown always occurred in near-stall condition, because the adverse pressure gradient and the unsteadiness reached the maximum values in the tip region. Yamada et al. [15] presented the unsteady flowing field near the tip region by the CFD method with a single passage grid. It is shown that the TCV is broken down by the effect of the shock wave, and the type of vortex breakdown in near-peak point was different with its in near-stall condition.

From the research above, it is understood that, under near-stall condition, the tip clearance vortex will be highly unsteady and unstable. Therefore, the stall inception was always detected in the tip region. Using a hotwire arranged around the rotor tip of the axial compressor, circumferentially, McDougall et al. [16,17] captured the large propagating wave with small amplitude in near-stall condition, which is called a modal type rotating stall. Later, Day et al. [4,18] captured the short propagating wave with large amplitude, which was a spike type rotating stall. Hoying et al. [19] studied the relation between the rotating stall and tip clearance vortex in the E3 compressor. By using Reynolds averaged Navier-Stokes simulation (RANS) method, it was found that the tip clearance vortex will move forward to rotor inlet in near-stall condition. Hah et al. [20] and Vo et al. [21] proposed the criterion for the spike initiated rotating stall, which had leading edge spillage and trailing edge backflow. This criterion was already accepted by many researchers. However, many people misunderstood this criterion and considered the tip clearance vortex as the origin of the rotating stall.

By means of unsteady multi-passage simulation, Pullan et al. [22] illustrated two different stall mechanisms. It was pointed out that the stall originated from high incidence of the rotor inlet. Although tip clearance was not necessary for the rotating stall, it does influence the stall characteristics a lot. Later, Smith et al. [23] illustrated the influence of tip clearance on the rotating stall. There existed an optimum tip clearance for stall margin, which can balance the effect from the different stall mechanisms.

However, in their works, the stall was triggered by several re-staggered blades. It was more appropriate to use the non-re-staggered blade model. Although they studied the relationship between stall and tip clearance, they focused on the stall mechanism in the zero clearance model, the evolution of stall mechanism and the effect of the tip clearance vortex in different clearances were not analyzed enough. In addition, the benefit of leakage flow was not mentioned.

This paper studies the influence of tip clearance on flow characteristics related to performance. Based on the full-passages model, steady and unsteady results are obtained by the RANS method. The relationship between the stability of the compressor and the tip clearance is discussed. Then, the flowfield characteristics under different tip clearances are compared, and the effects of the separation and the tip leakage flow on the efficiency and stability are discussed.

2. Experiment and Numerical Setup

2.1. Description of the Test Rig and the Measurement

The test was conducted in the 1–1/2 stage axial subsonic compressor in Shanghai Jiao Tong University. The blade number of inlet guide vane (IGV) is 32, and 29 and 37 for rotor and stator, respectively. The hub-tip ratio is 0.76. The design rotating speed is 17,000 rpm. Since this research is

focused on the subsonic conditions, the rotational speed is adopted as 12,000 rpm, so that the tip Mach number is less than 0.9. The design tip clearance is 98.7% of span.

Compressor performance is obtained by the adjusting of the throttle area behind the stator. A flowmeter is equipped at the upstream of IGV to obtain flow rate. Total pressure is measured by two five-hole total pressure probes mounted at upstream and downstream of the compressor, respectively. Temperature probes are also used at both upstream and downstream to estimate isentropic efficiency.

The overall performance parameters are defined by the following equations.

$$\eta = \frac{H_{i,out} - H_{in}}{H_{out} - H_{in}} \quad (1)$$

$$\pi = \frac{p_{t,out}}{p_{t,in}} \quad (2)$$

$$\xi = \frac{\dot{m}_{in} / \pi}{\dot{m}_{in,DP} / \pi_{DP}} \quad (3)$$

where η is isentropic efficiency, $H_{i,out}$ isentropic outlet enthalpy, H_{in} inlet enthalpy, H_{out} outlet enthalpy, π total pressure ratio, $p_{t,out}$ isentropic outlet total pressure, $p_{t,in}$ inlet total pressure, ξ flow rate coefficient, \dot{m}_{in} mass flow rate, $\dot{m}_{in,DP}$ mass flow rate at design point, and π_{DP} total pressure ratio at design point.

2.2. Numerical Model

The numerical simulation is accomplished by using a commercial CFD code, NUMECA. It is a popular solver for the flowfield simulation of turbomachinery. With the features of structured-grid supported, the finite-volume method and the suitable numerical treatments, the three-dimensional (3D) steady and unsteady flowfield can be obtained for the axial compressor.

The calculation area is between Section A and Section B in Figure 1. The upstream channel and downstream channel are extended as much as two IGV blade chord lengths and three stator blade chord lengths, respectively. Five cases with different tip clearance sizes from 0% to 2% of chord length are established and marked as 0%, 0.5%, 1%, 1.5%, and 2% of the chord length of blade tip τ , respectively.

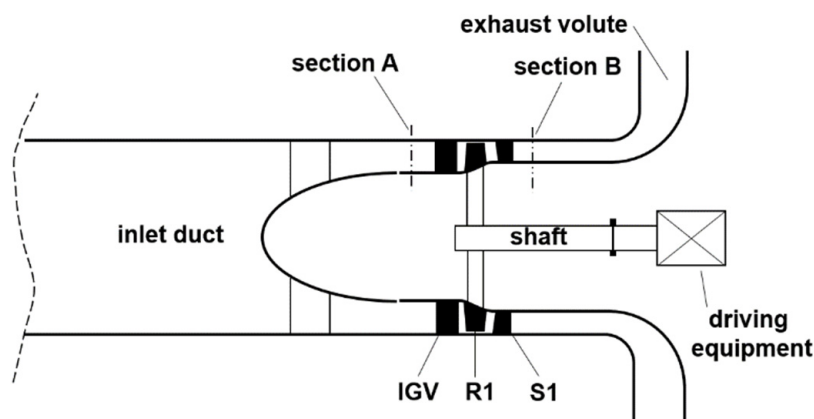


Figure 1. Sketch of the test rig.

Real air model is adopted as working fluid. The two-order central difference spatial scheme of Jameson is adopted in this study. Spalart–Allmaras (SA) model by Spalart et al. [24], which is widely applied in industry and academia, is also used in this study. For the inlet condition, total pressure, total temperature, and the velocity direction are specified, and refer to the experiment data. For the outlet condition, the static pressure is applied with the radial equilibrium. The rotating speed is applied on the rotor passage, while the other passages keep station. When processing the steady simulation, the mixing plane method is used to transfer the flowfield information between rotating

region and station region. Multigrid and local time stepping treatment are also applied to accelerate the calculation. The steady simulation is considered as converged when the mass flow is balanced and all of the residual lines are stable or fluctuate periodically. With the increasing of the outlet pressure, the last converged steady simulation is considered as near-stall (NS) condition. The unsteady method for this model had been discussed by Song et al. [25], including using the dual time step method of Jameson [26] and the sliding mesh method [27]. The 20 timesteps are set in every rotor passing period, and the number of the inner iteration step is set to 50. When the periodic fluctuation of the mass flow and the static pressure on the numerical probes is continued for ten passing times, it is considered as converged for the unsteady simulation.

2.3. Grid Generation and Independent Test

O4H-type topology is adopted in every row. The y^+ is less than 5 to ensure capturing the blade loading more accurately. Mesh in tip clearance is refined to 17 layers in radial direction. Three sets of grids are generated to validate the grid independence. The grid number of every passage is shown in Table 1. From validation results shown in Figure 2, grid2 is appropriate for the calculation. A three level multi-grid is adopted to accelerate the calculation. The chosen grid is shown in Figure 3. In order to transfer the flow information between stational region and rotational region, the mixing plane method is used in this simulation.

Table 1. Grid number of three sets of grids ($\times 10^6$).

Mesh	Inlet Guide Vane (IGV)	Rotor	Stator	Full-Passages
Grid1	0.34	0.31	0.38	33.55
Grid2	0.53	0.64	0.58	56.40
Grid3	0.64	0.79	0.71	68.95

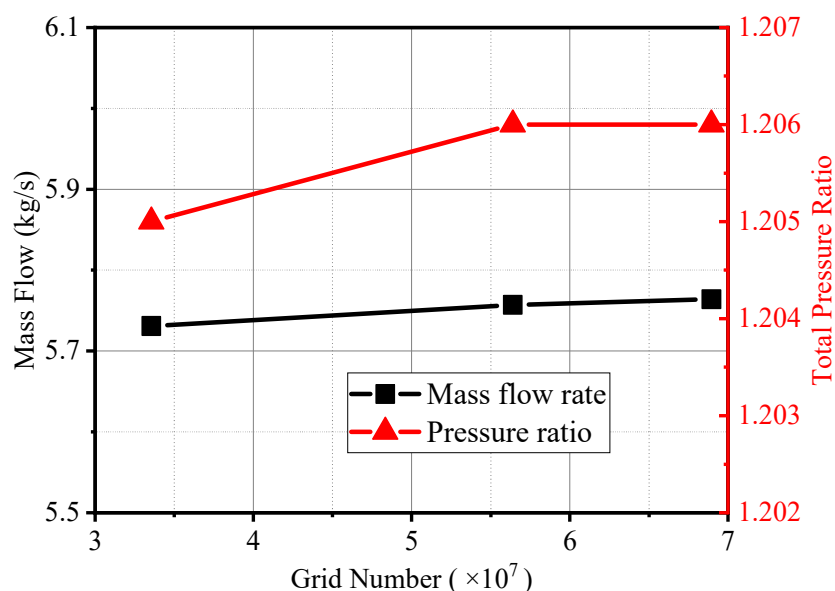


Figure 2. Validation for grid independence.

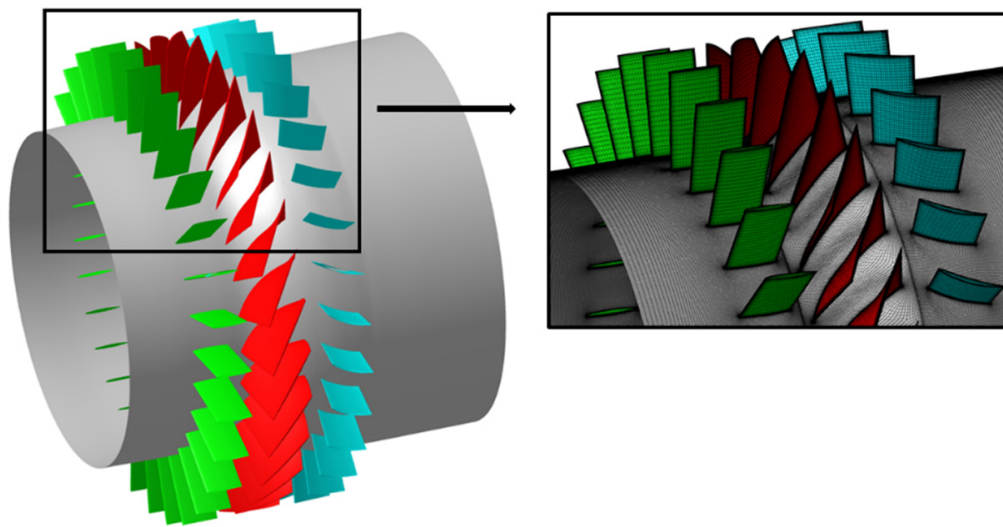


Figure 3. One passage of grid for simulation.

2.4. Model Validation

Based on the chosen grid, the performance curve is obtained by the numerical simulation. From Figure 4, by using the full-wheel simulation, the simulated mass flow range is enlarged and the numerical result is closer to the experiment data. It is found that the numerical results are always larger than experiment data; this might be the result of the neglect of the blade hub fillet in the numerical model. Even so, the numerical results match well with the experiment data on most mass flow conditions.

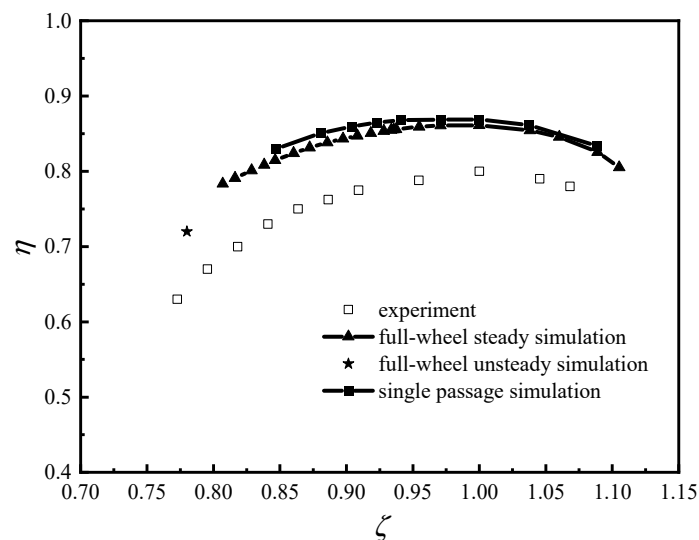


Figure 4. Performance comparison between experimental and numerical results.

3. Results

In this section, the influence of tip clearance on the performance is studied. The trend of performance change is discussed with the clearance increased from zero ($0\%\tau$) to large ($2\%\tau$), and the characteristics under peak efficiency (PE) working point and near stall (NS) working point are compared and discussed.

3.1. Overall Performance

Performance curves of every clearance model are shown in Figure 5. In a mass, the efficiency and pressure ratio are decreased as clearance size is increased, which is coherent with conclusions from predecessors' work. However, there is a certain tip clearance size, so that the stable working range can reaches to the maximum, which can be observed from stall margin change (Figure 6). The maximum surge margin is found in the design clearance model. When the tip clearance is larger or less than the design clearance model, the stall margin is decreased, obviously. In other words, with the tip leakage flow, the stability of the compressor might be enhanced. So, it is meaningful to find out the mechanism of leakage flow that turns the negative influence to positive influence on stall margin.

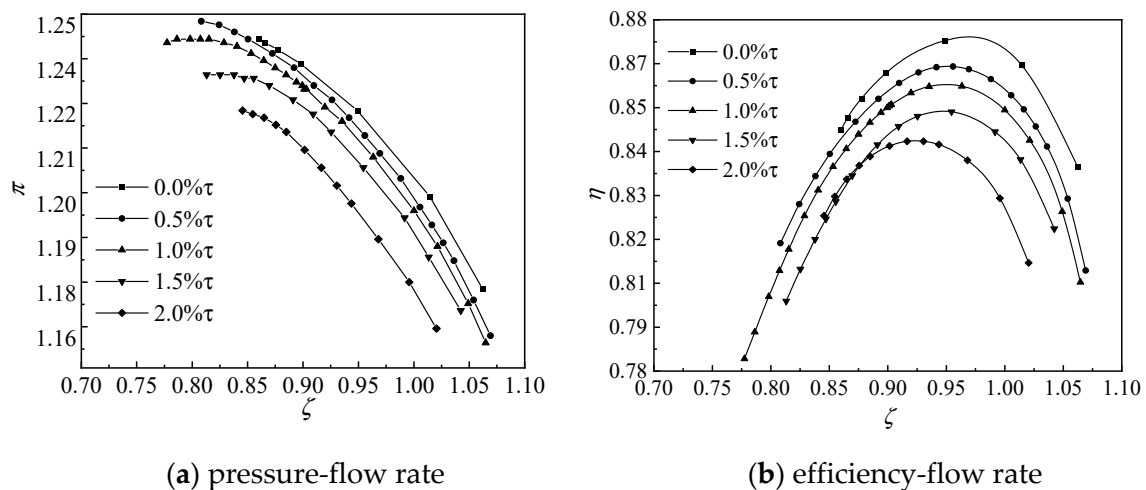


Figure 5. Performance curves of different tip clearance models. (a) pressure-flow rate; (b) efficiency-flow rate.

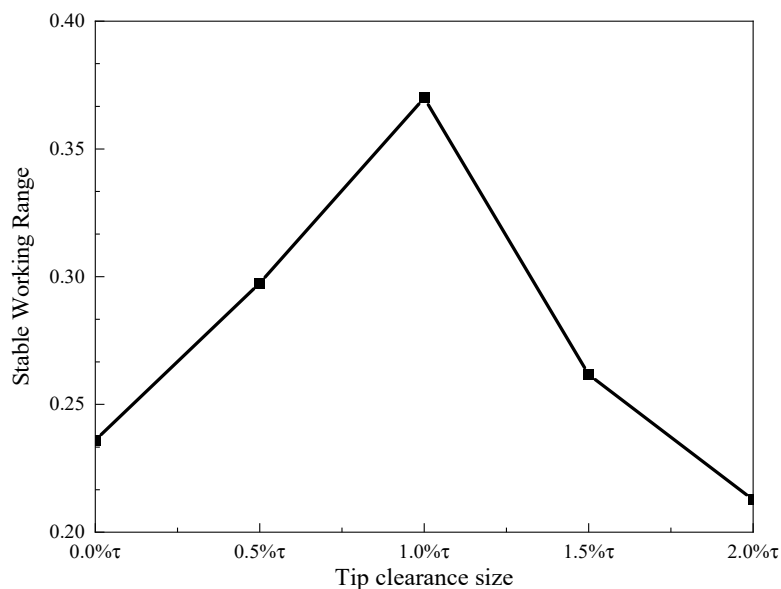


Figure 6. Stable working range under different clearance models.

The rotor loss factors along span is shown in Figure 7. The dimensionless rotor loss factor is defined in Equation (4).

$$F_r = \frac{P_{i,t,r} - P_{o,t,r}}{P_{i,d,r} - P_{o,d,r}} \tag{4}$$

where P is the pressure, subscript i, o, t, d , and r represent the rotor inlet, outlet, total, dynamic quantities and relative quantities, respectively. Along the span, the loss in tip region is the maximum. With the increasing of tip clearance, the loss in tip region is increased correspondingly. In addition, in tip region, loss factor is increased rapidly from $0\% \tau$ to $1\% \tau$, which illustrates the negative impact of tip leakage on efficiency. When the tip clearance is over $1\% \tau$, loss in tip region is stable with the increasing of tip clearance.

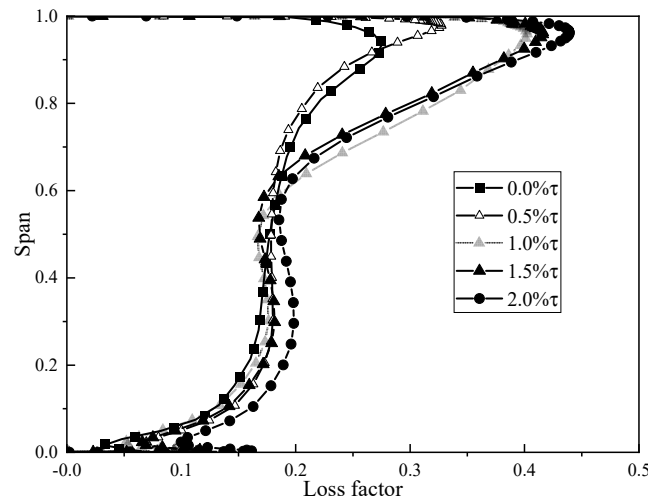


Figure 7. Loss factor distribution under different clearance models.

Figure 8 shows the blade loading at 98% of span. Pressure coefficient is defined in Equation (5):

$$CP = \frac{P_{s,o} - P_{s,i}}{P_{s,i}} \tag{5}$$

where subscript s represents the static quantities. The blade loading of zero-clearance model is over two times larger than that of design-clearance. As the tip clearance is increased, the blade loading is decreased, which is benefit for the safety of the blade. This can be explained that the tip leakage flow can balance the pressure difference between the pressure side (PS) and the suction side (SS).

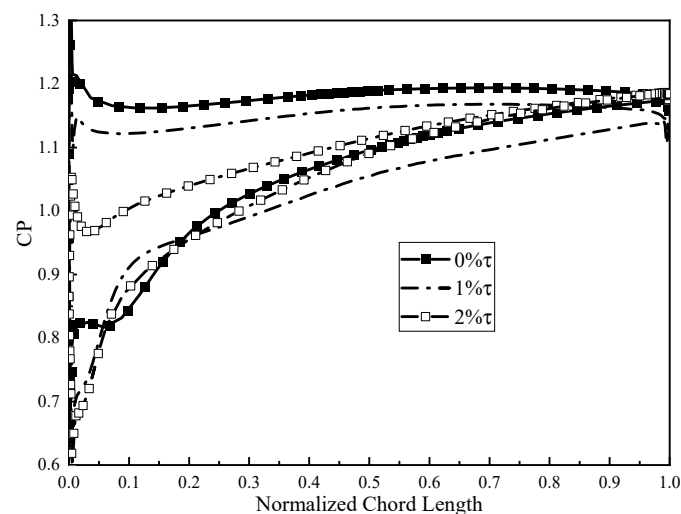


Figure 8. Pressure coefficient distribution at blade tip under different clearance models.

3.2. Detail Results of Zero Clearance Model

In this model, there is no tip leakage flow or tip clearance vortex at all. At 96% of span, relative Mach number contours with streamline of relative velocity are presented in Figure 9a. Under PE condition, there is seldom low-Mach region, except the boundary layer on the blade surface. From the streamline, since the incidence angle matches with the stagger angle, the flowfield is well without any vortex or separation. Under NS condition, there is a large area of the blockage region from the LE to the neighboring LE, and from the SS to PS. Since the mass flow is decreased, the incidence angle is far from the blade stagger angle, so a vortex is generated near the PS close to LE, and enrolls the surrounding fluid, with which the leading-edge spillage is occurred.

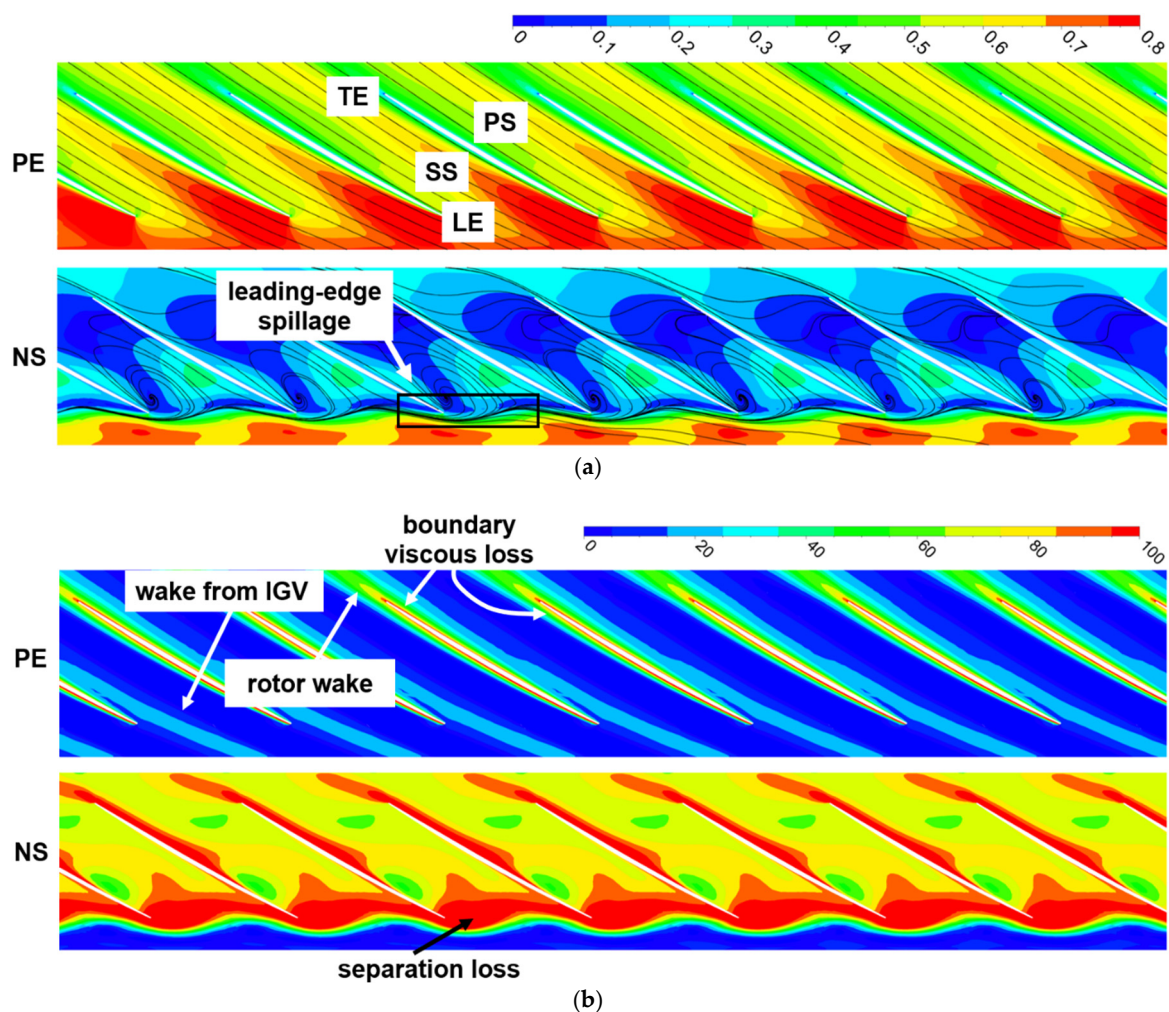


Figure 9. Time-averaged results at 96% of span. (a): Relative Mach contours with streamline of relative velocity. (b): Entropy contours (J/(kg K)).

Static entropy contour is often used to illustrate the loss distribution. Moreover, it is often used at tip span to locate the boundary of the tip leakage flow and the separation flow, because high loss will be induced when circumferential tip leakage flow/separation flow and main flow are interacted, in which the vortex would be generated and developed, and by which the entropy gradient is largest among tip-span contour. Static entropy contours are shown in Figure 9b. Under PE condition, the loss in the tip region consists of the wake loss from IGV, the boundary viscous loss and the wake from the rotor blade. The loss area and the amplitude are both low. Under the NS condition, it is found that the high-gradient interface is shifted forwardly to the front of the LE, which is coherent with the LE spillage from Figure 9a. Compared with the figure of PE, the loss region and the amplitude are

highly increased. The separation loss occupies the whole passage inlet, by which the loss on the whole passage, especially on the pressure, is highly increased.

In order to observe 3D distribution of separation and blockage, streamlines in the tip region are drawn in Figure 10 with velocity flux contours at passage cutting planes. The blockage area is attached to the casing-suction corner and reduced with the decreasing of radial distance. Along the suction side surface, streamline flows toward the tip region. When the flow arrives to casing, it turns to the middle passage along the casing side, and finally flows to the downstream due to the mixing process with the main flow. From the 3D streamline in Figure 10a, and limiting streamline in Figure 10b, the separation and blockage along the suction side is caused by leading-edge separation and the corner separation.

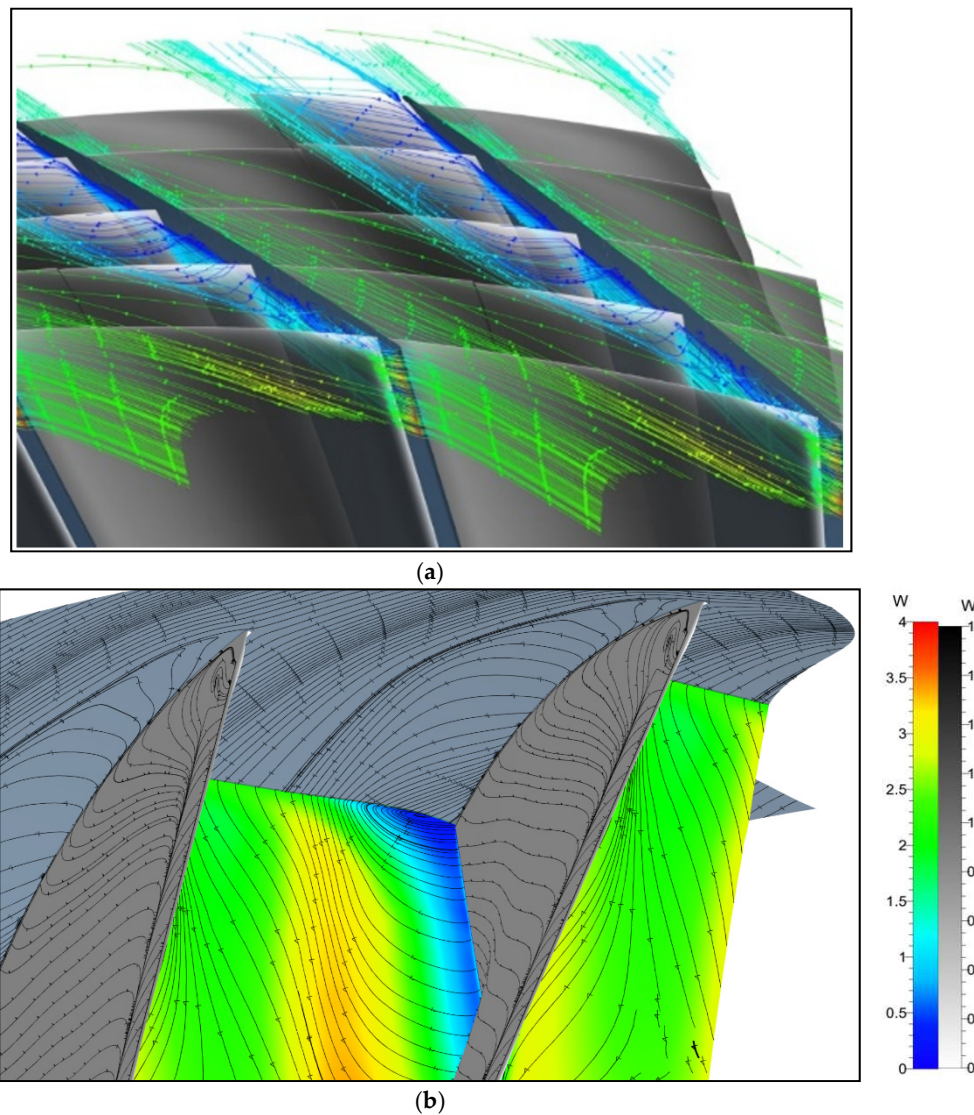


Figure 10. The three-dimensional (3D) figures for the passage flowfield. (a): streamlines in tip region with velocity flux contours at passage cutting planes. (b): streamlines in tip region with velocity flux contours at passage cutting planes.

For PE and NS conditions, here are the iso-surfaces of vorticity at $v = 0.25$ in Figure 11. v is defined as follows.

$$v = \frac{\Omega^2 + S^2}{\omega^2} \quad (6)$$

where Ω , S , ω are the symmetric and antisymmetric parts of the gradient velocity tensor. Since the flow is very steady, only the steady result is shown for the PE condition.

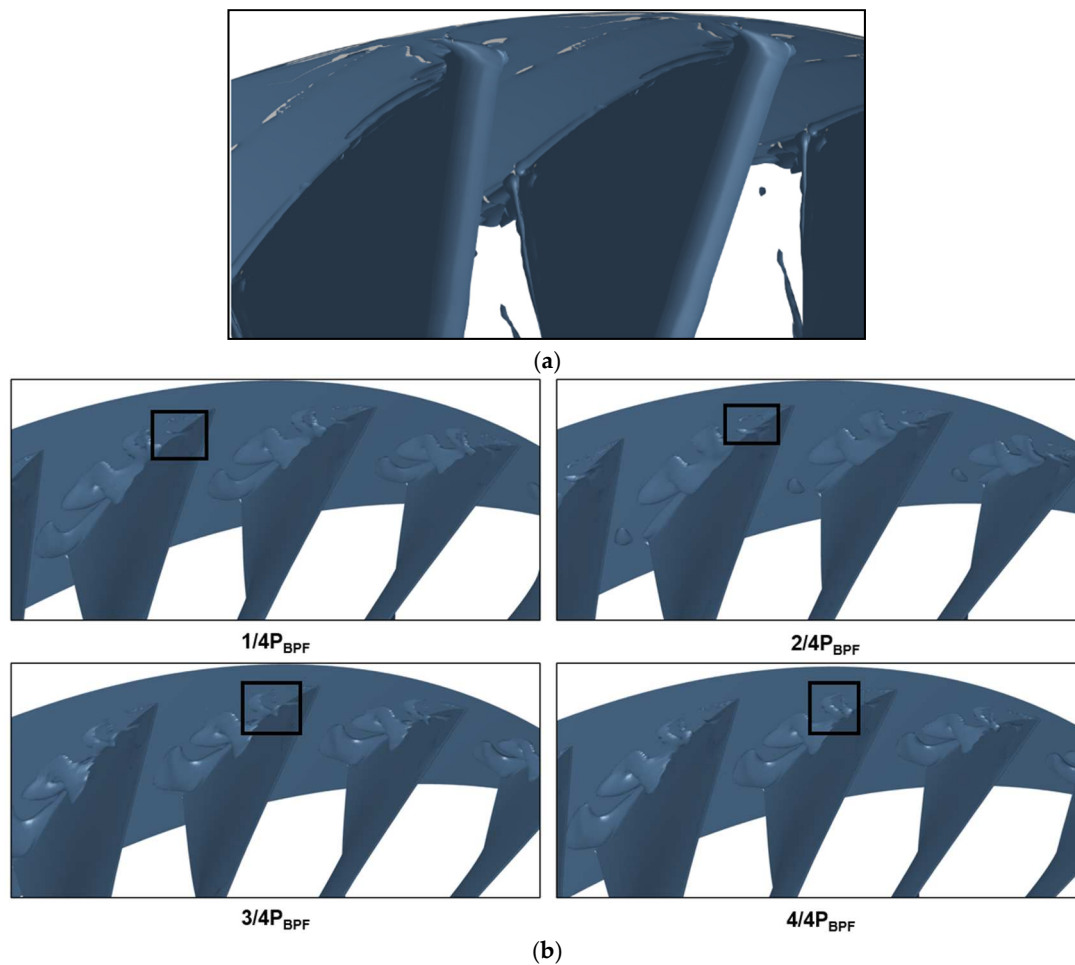


Figure 11. Iso-surfaces of instantaneous vorticity at $\lambda = 0.25$. (a): Peak efficiency (PE), steady results. (b): Near-stall (NS), transient result, P_{BPF} is the period of the blade passing.

It is different between the vortex distribution in PE and NS condition. For PE condition, there is no large vorticity cell in flow passage. However, there are two parts that are worthy to pay attention to. In the front and rear part of suction side, some little vorticity cells attach to the corner, from which the effect of corner separation is illustrated. In addition, vorticity cells in front of LE develop in a circumferential direction, which is the result of the effect of LE separation and casing separation. When the condition reaches to NS, from the black box in Figure 11b, these vorticity cells grow up to large cells, and shed with the period of blade passing. Flow incidence in front of the rotor passage will be increased because of the blockage, which will cause larger separation and corresponding larger blockage in the next passage. When the flow incidence increases to extent, leading edge spillage will occur, as shown in Figure 9a.

In Figure 12, the axial component of the velocity is shown in order to illustrate the unsteadiness of the velocity under NS condition. Although there is the vortex generation and moving by the leading-edge separation and corner flow, the unsteadiness is still very low. From the $\frac{1}{4}$ of the period of the blade passing (P_{BPF}) to $\frac{4}{4} P_{BPF}$, there is seldom unsteadiness that can be observed. This is because the blockage decreases the amplitude of the unsteadiness. In order to qualify the unsteadiness in NS condition, we set static pressure probes in front of LE, and the spectrum result is shown in Figure 13.

The spectrum is dominated by character frequency related to rotation, including rotation frequency and blade passage frequency.

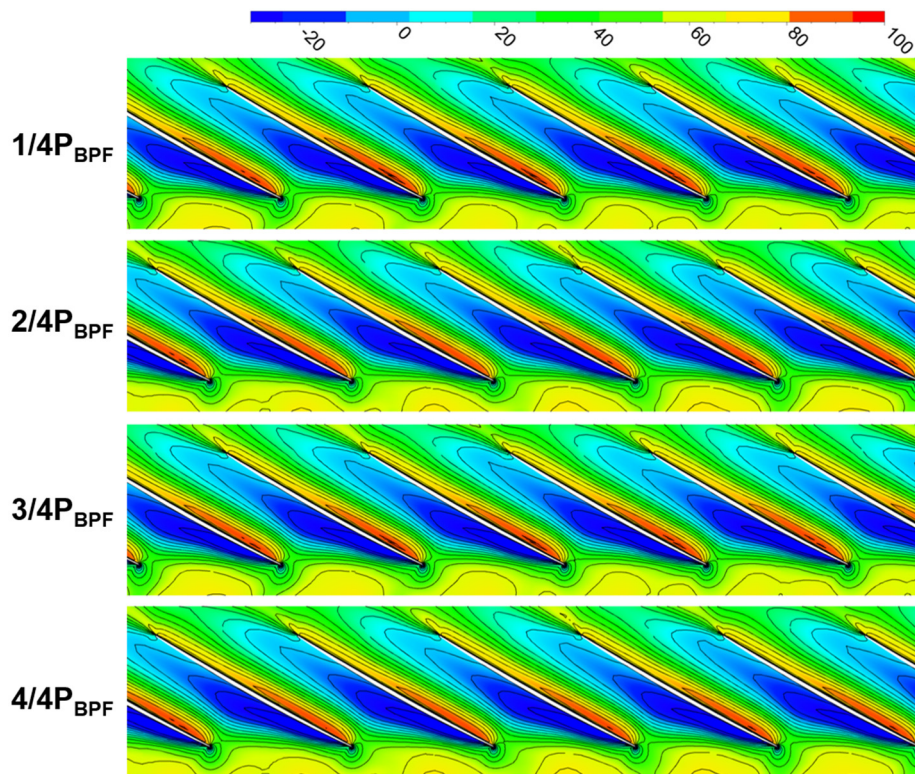


Figure 12. Axial component of velocity under NS condition, 99.35% of span, P_{BPF} is the period of the blade passing.

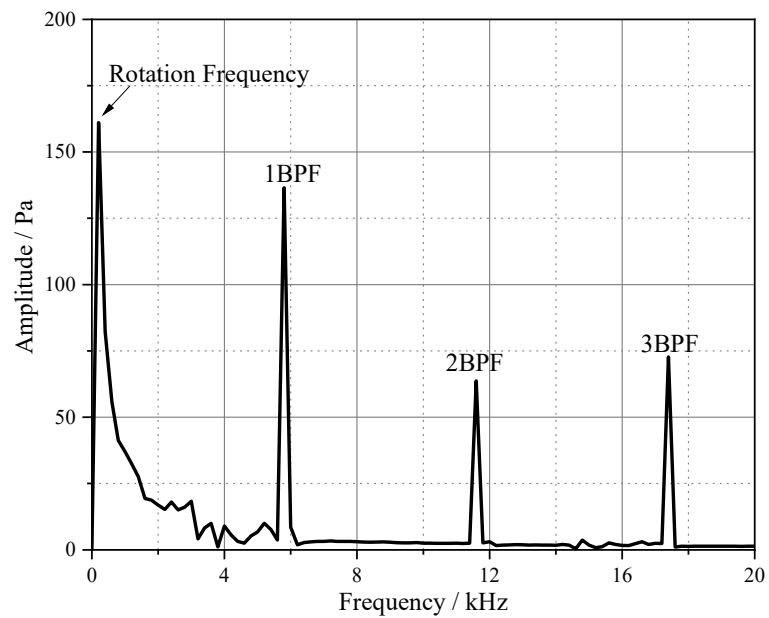


Figure 13. Pressure spectrum in front of LE under zero clearance model.

3.3. Detail Results of Design Clearance Model

Figure 14 delineates distribution of the time-averaged axial momentum of tip leakage flow. MD represents the condition at which the flow rate is intermediate between PE and NS. μ is defined as follows:

$$\mu = \int_{r_{\text{tip}}}^{r_{\text{casing}}} \frac{\rho V_n V_t}{\dot{m}_{\text{in}} V_z / c_x} dr \quad (7)$$

where \dot{m}_{in} is mass flow rate at rotor passage inlet, c_x is chord length of blade, subscript n is normal direction, t is tangent direction, z is axial direction.

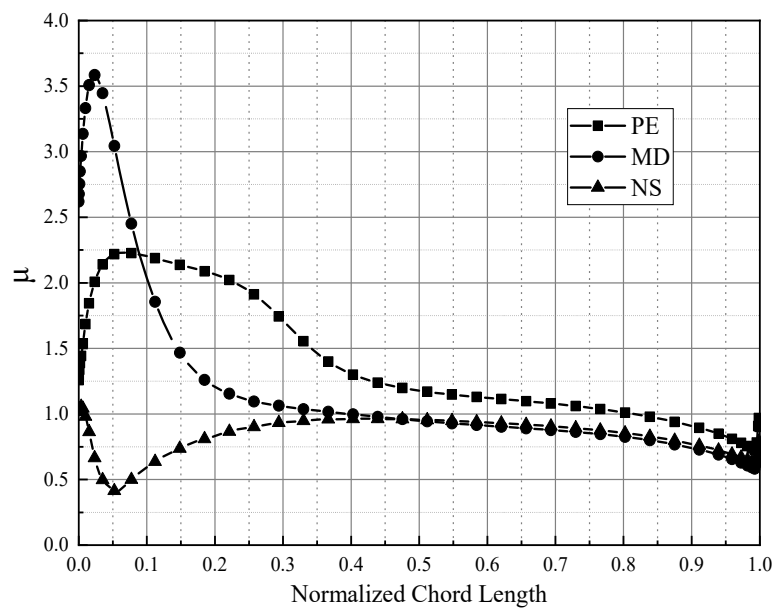


Figure 14. Momentum distribution of tip clearance flow along chord.

From this distribution, the axial momentum is concentrated at the front part of the chord. As the flow rate decreases, the centroid of μ moves to the leading edge, hence, the leakage flow in the rear of the clearance is smaller. The effect of the existence and the distribution of leakage flow will be discussed in following paragraphs.

Figure 15 shows contours of the Mach number and entropy at 99.35% of span. In general, with the influence of the tip leakage flow, flow field in the tip region is much different with the zero-clearance model. From Mach contours, in both PE and NS conditions, flow separation and serious blockage are suppressed at the suction side, which is the result in mixing with circumferential leakage flow. However, in the NS condition, there is a block of a low speed region along the pressure side, which is due to the tip clearance vortex. The leading-edge spillage also occurred, but the reason is not the leading-edge separation, but the TCV. From entropy contours, the high-gradient interface has moved to the rotor inlet. Hence, the main flow could not flow pass the passage, which caused the low speed region. However, with the circumferential flow from the tip clearance, the low speed region will not develop to a large blockage. When it is at a rear part of the passage, the low speed region could cross the passage and expend to the suction side. This is because the tip leakage flow in the rear part of the clearance is too small to supply enough momentum for a low speed region. As the flow in the tip region is dominated by the tip clearance vortex and tip leakage flow, from the streamlines at the passage outlet in Figure 16, in the rear part of clearance, there is the vortex generated by the sheared tip leakage flow.

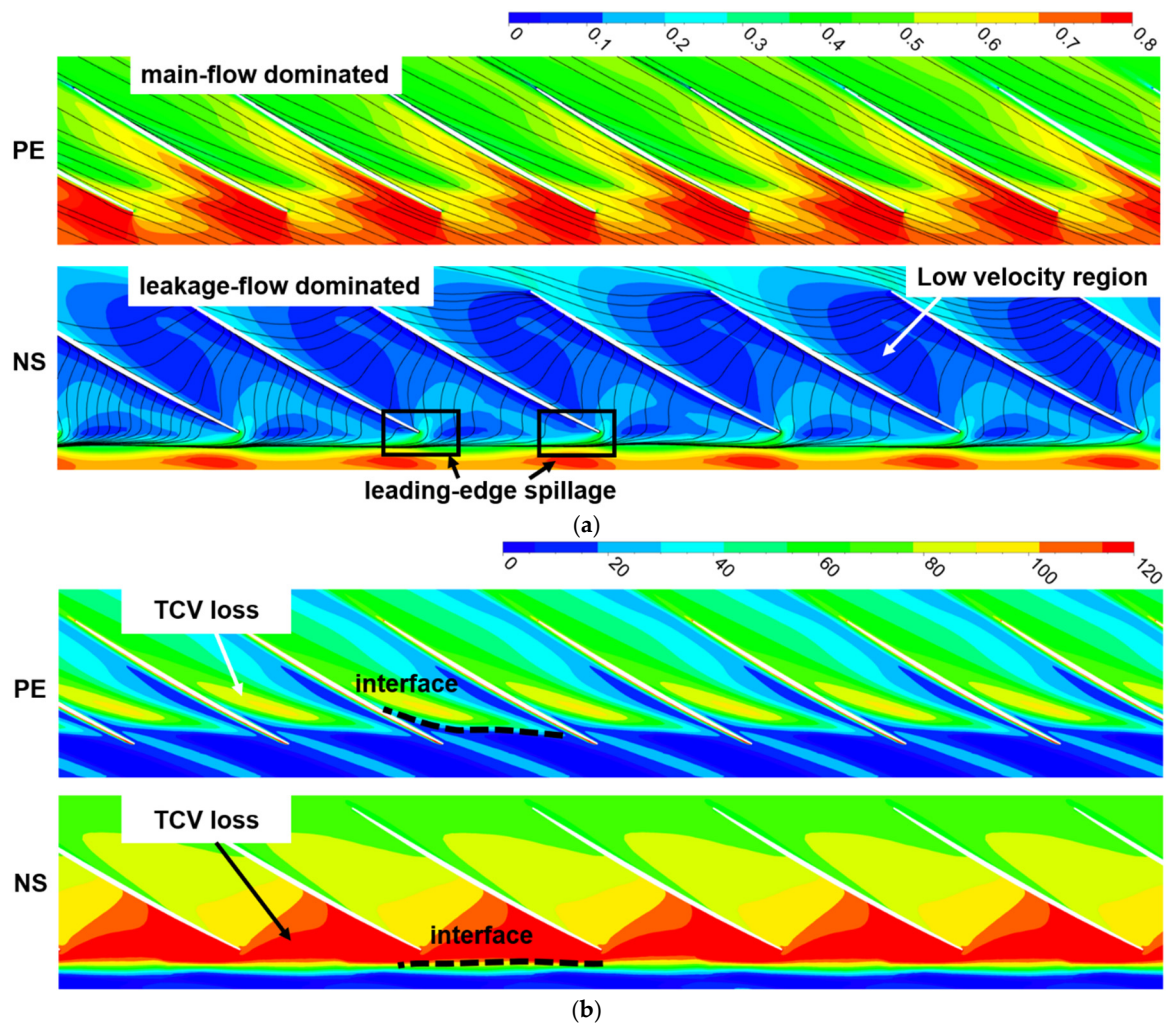


Figure 15. Time-averaged results at 96% of span. (a): Relative Mach contours with streamline of relative velocity. (b): Entropy contours (J/(kg K)).

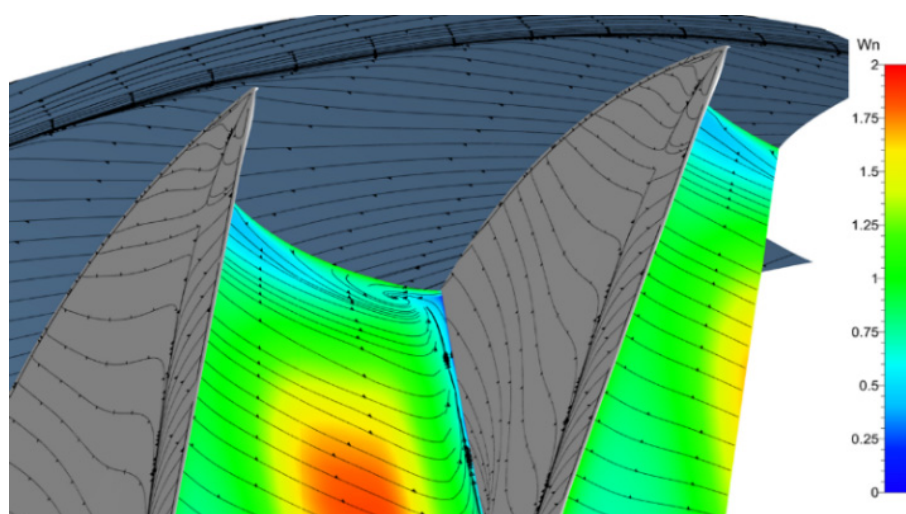


Figure 16. Streamline on suction side, casing, and passage outlet.

Figure 17 shows the axial component of the velocity, which can represent the location of the clearance vortex. P_{TCV} is a period of the shedding of the tip clearance vortex, which corresponds to about 0.5 Blade passing frequency (BPF). The tip clearance vortex results in the leading-edge spillage and mixing process between the main flow and tip leakage flow. Tip clearance vortex is formed near the leading edge, developed along the rotor passage inlet, interacted with the leading edge of the other side, and reduced along the pressure side. Streamlines from the tip clearance are shown in Figure 18, which can show the detail of the tip clearance vortex. Streamlines from the tip clearance roll up to a vortex, which is the result in the mixing process, with main flow near the leading edge. As the axial momentum ratio between the leakage flow and main flow increases, the vortex trajectory moves to the rotor inlet. When the streamlines reach the next leading edge, they are diverged. Some streamlines cross in front of the leading edge to the next passage, which is called leading-edge spillage. Streamline in the core of the vortex is developed and finally stagnated. Then the vortex breakdown occurs (as yellow blank locates), because the flow is a counter-pressure along the vortex trajectory. It can trigger several low speed cells (as the red dot line shows); some of them will be developed to become larger at the mid-passage. The streamlines near the large low-velocity cell begin to diverge by the blockage effect of low-velocity cells, which is called secondary vortex as black arrow shows. Moreover, when the larger low-velocity cell is developed near the next leading edge, the spillage streamlines will be increased by the blockage effect.

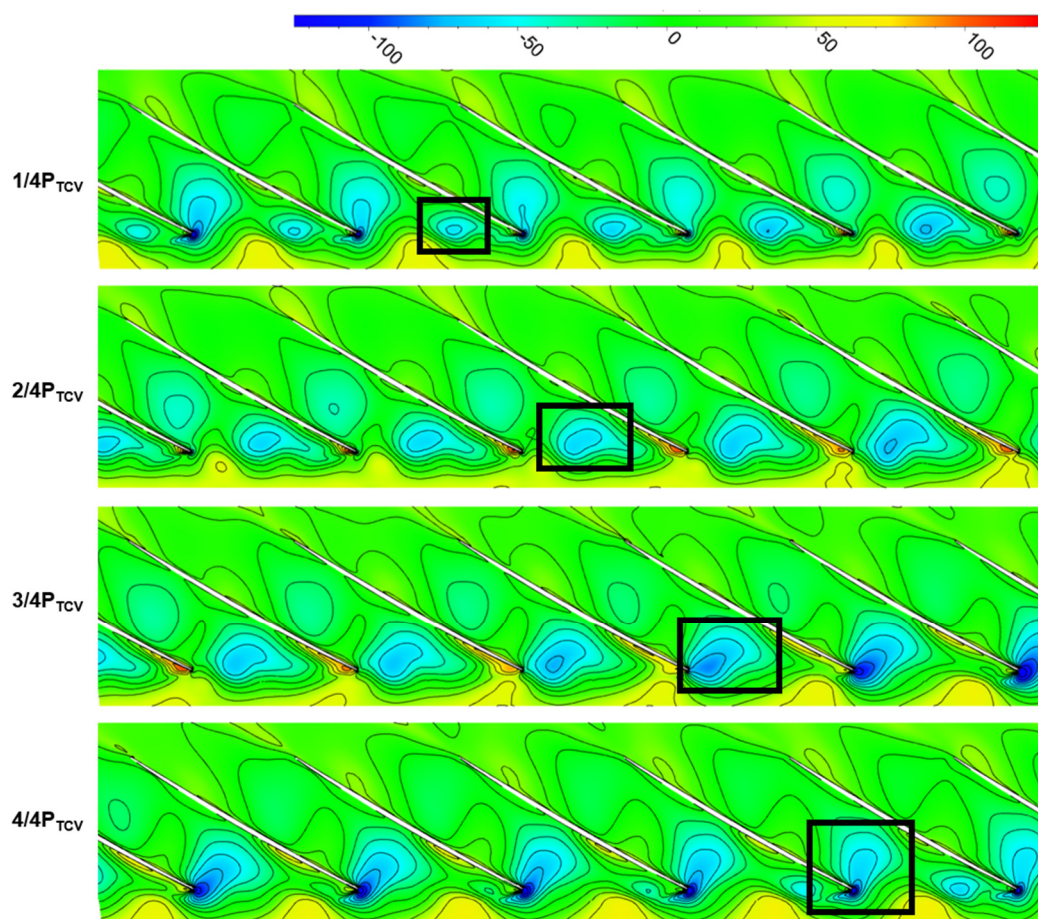


Figure 17. Unsteady contours of axial component of velocity. (P_{TCV} is the period of the TCV (tip clearance vortex) shedding).

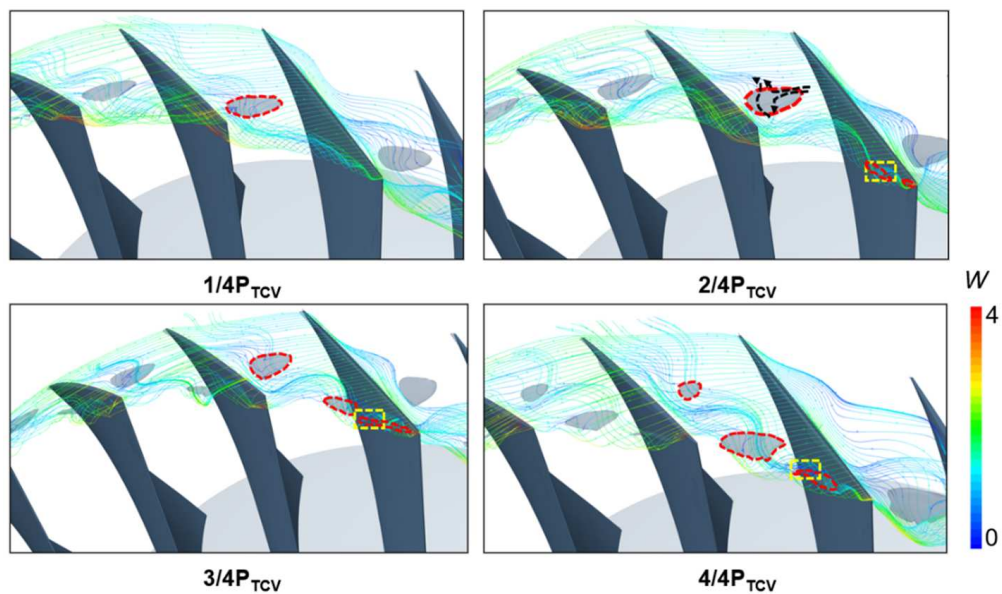


Figure 18. Unsteady streamlines from tip clearance with the iso-surface of $Ma_r = 0.2$, P_{TCV} is the period of the TCV (tip clearance vortex) shedding.

In addition, the unsteadiness in the tip region is enhanced (a lot) by vortex breakdown and secondary vortex, which is illustrated in Figure 19. Compared with the spectrum in PE and NS condition, the amplitude increasement at BPFs are limited. However, the amplitudes at the frequencies related to the tip clearance vortex and rotation are increased from nearly zero. Compared with the spectrum of zero-clearance model in the NS condition, amplitude at BPFs are increased, while amplitudes at rotation frequencies are about the same.

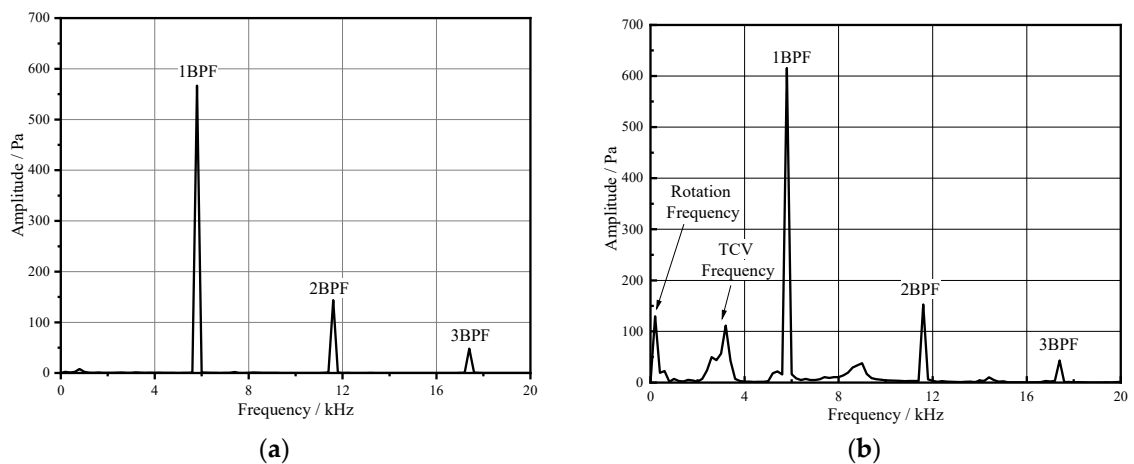


Figure 19. Pressure spectrum in front of LE under design clearance model. (a): under PE condition. (b): under NS condition.

To sum up, under design clearance model, the influence of tip clearance dominates flow field in the tip region. The separation at leading edge and casing-suction can be eliminated by the tip leakage flow. However, the low-velocity region can be triggered by the tip clearance vortex in NS condition. Moreover, the unsteadiness in the tip region is enhanced by the evolution of the tip vortex.

3.4. Detailed Results of Large Clearance Model

As the clearance is increased, the total leakage flow is increased correspondingly. From the Mach number in Figure 20a, the separation in the tip region is inhibited furtherly. However, as the tip leakage flow is increased in scale and value, flow structure in the tip region will be influenced, and the loss is increased with the tip clearance in Figure 20b. On the one hand, the radial scale of leakage flow is increased, which will enlarge the scale of the tip clearance vortex. On the other hand, the axial momentum ratio between leakage flow and main flow is increased, which is the reason for the forward-moving of the tip clearance vortex. Therefore, compared with design clearance, the forward spillage occurred in a larger flow rate. In addition, the low-velocity cell can only be developed to the front-middle passage, then its velocity will increase by the increased circumferential leakage flow. The unsteadiness in the tip region is also enhanced by the increasing of the tip clearance, which is illustrated by the moving of the low-velocity cell in Figure 21. As the spectrum shows in Figure 22, compared with that from the zero-clearance and design-clearance models, the amplitude at BPFs increased a lot.

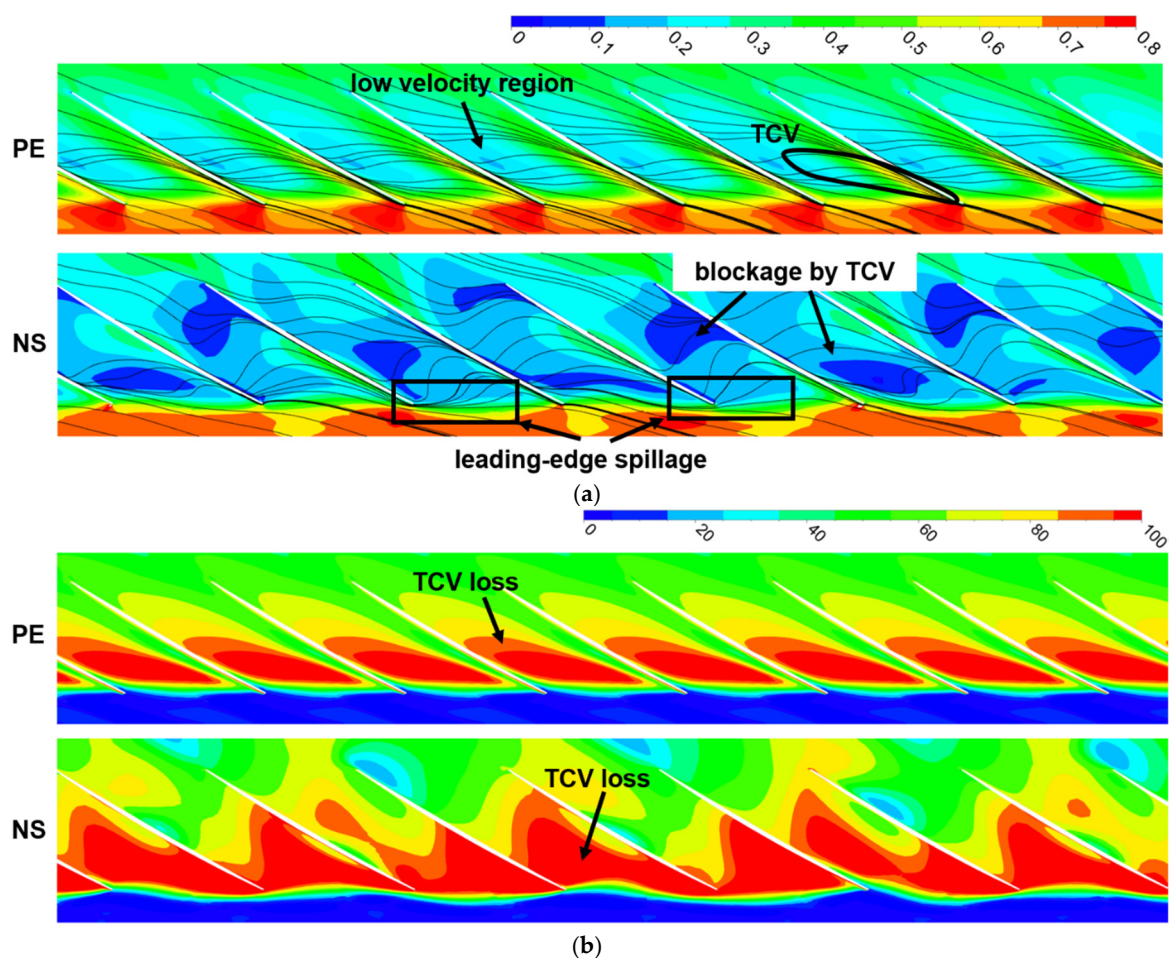


Figure 20. Time-averaged results at 96% of span. (a): Relative Mach contours with streamline of relative velocity. (b): Entropy contours (J/(kg K)).

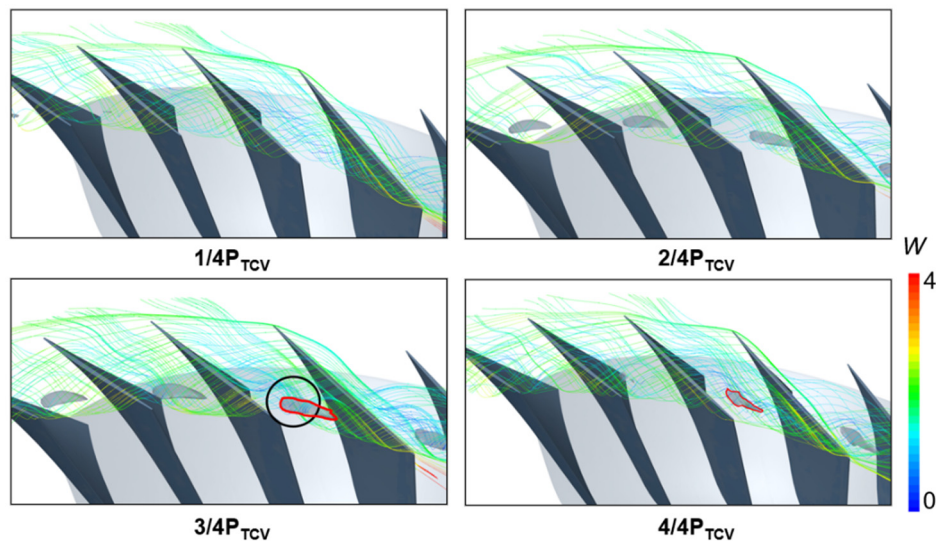


Figure 21. Unsteady streamlines from tip clearance with the iso-surface of $Ma_r = 0.2$, P_{TCV} is the period of the TCV (tip clearance vortex) shedding.

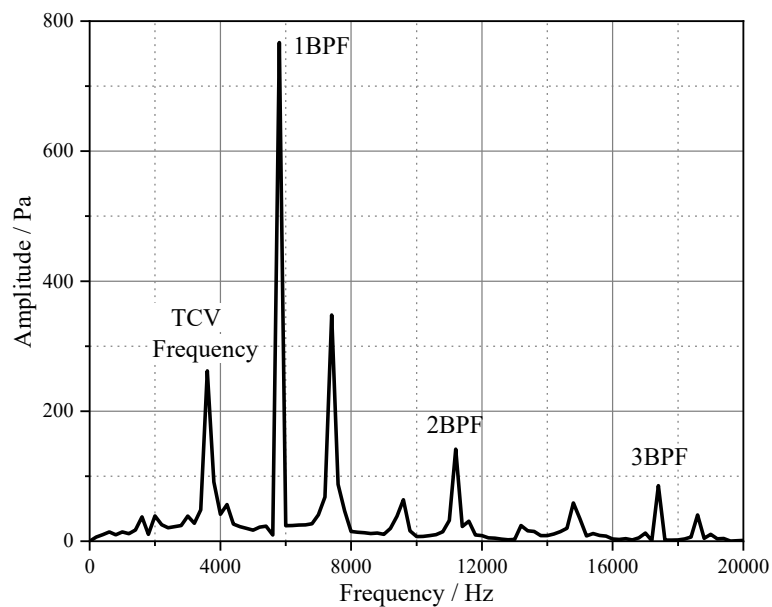


Figure 22. Pressure spectrum in front of LE under large clearance model.

4. Conclusions

This paper studies the influence of tip clearance on flow characteristics related to performance. Based on full-passage grids, the validated results are obtained by the means of the RANS method. A series of performance curves are obtained in different clearance models, from which it is found there exists an optimum clearance for a stable working range. It is found that the tip leakage flow can benefit the stable working range if the tip clearance is small enough, while it turns out to be harmful to the stability if the tip clearance is too large.

Under the zero clearance model, it is the separation at the casing-suction corner that dominates the flow field in the tip region. Under this blockage, incidence of upstream is increased, which will trigger larger separation in the next passage. Finally, some passages are fully blocked and stall occurs. As the tip clearance is increased from zero to the optimum value, the separation and blockage along the suction side are suppressed by tip leakage flow.

Under the design clearance model, the influence of the tip clearance dominates flow field in the tip region. The existence of the tip leakage flow can benefit to the reduction of separation at the leading edge and casing-suction. However, the low-velocity region can be triggered by the tip clearance vortex in NS condition. Moreover, the unsteadiness in the tip region is enhanced by the evolution of the tip vortex.

When the tip clearance increases to extent the tip leakage flow increases in scale and value. Therefore, the scale and unsteadiness of the tip clearance vortex increases correspondingly, which can trigger the forward spillage earlier.

Author Contributions: Conceptualization, M.S. and B.Y.; methodology, M.S.; software, M.S.; validation, M.S.; formal analysis, M.S.; investigation, M.S.; resources, B.Y.; data curation, M.S.; writing—original draft preparation, M.S.; writing—review and editing, H.X., B.Y.; and S.Z.; visualization, M.S.; supervision, B.Y.; project administration, B.Y.; funding acquisition, B.Y. All authors have read and agreed to the published version of the manuscript.

Funding: This research was funded by the National Science and Technology Major Project (2017-II-0006-0019).

Conflicts of Interest: The authors declare no conflict of interest.

Nomenclature

c	chord length at rotor tip
m	mass flow rate
p	pressure
v	velocity
w	relative velocity
T	Time
U	tangential velocity
V	absolute velocity projection to the span
W	relative velocity projection to the span

Greek Symbols

ρ	density
φ	normalized mass flow
π	total pressure ratio
τ	radial length of the tip clearance
ξ	isentropic efficiency

Abbreviations

BPF	blade passing frequency
CFD	computational fluid dynamics
IGV	inlet guide vane
DP	design condition
LE	leading edge
Ma	Mach number
NS	near stall condition
PE	peak efficiency condition
PS	pressure side
R1	rotor
S1	stator
SS	suction side
TCV	tip clearance vortex
TE	trailing edge
TLF	tip leakage flow

Subscript

i	inlet
o	outlet
r	relative
s	static variable
t	total variable
BPF	quantity related to the period of blade passing
TCV	quantity related to the period of the generation of tip clearance vortex

References

1. Lakshminarayana, B. Methods of predicting the tip clearance effects in axial flow turbomachinery. *J. Basic Eng.* **1970**, *92*, 467–480. [[CrossRef](#)]
2. Inoue, M.; Kuroumaru, M.; Fukuhara, M. Behavior of tip leakage flow behind an axial compressor rotor. *J. Eng. Gas Turbines Power* **1986**, *108*, 7–14. [[CrossRef](#)]
3. Inoue, M.M.; Kuroumaru, M.M. Structure of tip clearance flow in an isolated axial compressor rotor. *J. Turbomach.* **1989**, *111*, 250–256. [[CrossRef](#)]
4. Day, I.J. Stall inception in axial flow compressors. *J. Turbomach.* **1991**, *115*, 1–9. [[CrossRef](#)]
5. Khalid, S.A.; Khalsa, A.S.; Waitz, I.A.; Tan, C.S.; Greitzer, E.M.; Cumpsty, N.A.; Adamczyk, J.; Marble, F.E. Endwall blockage in axial compressors. *J. Turbomach.* **1999**, *121*, 499–509. [[CrossRef](#)]
6. Mailach, R.; Lehmann, I.; Vogeler, K. Rotating instabilities in an axial compressor originating from the fluctuating blade tip vortex. *J. Turbomach.* **2001**, *123*, 453–460. [[CrossRef](#)]
7. Mailach, R.; Sauer, H.; Vogeler, K. The periodical interaction of the tip clearance flow in the blade rows of axial compressors. In *ASME Turbo Expo 2001: Power for Land, Sea, and Air*; American Society of Mechanical Engineers: New York, NY, USA, 2001; p. V001T03A004. [[CrossRef](#)]
8. Sirakov, B.T.; Tan, C.S. Effect of unsteady stator wake—Rotor double-leakage tip clearance flow interaction on time-average compressor performance. *J. Turbomach.* **2003**, *125*, 465–474. [[CrossRef](#)]
9. Du, H.; Yu, X.; Liu, B. Modeling of the double leakage and leakage spillage flows in axial flow compressors. *J. Therm. Sci.* **2014**, *23*, 103–113. [[CrossRef](#)]
10. Hah, C. Effects of double-leakage tip clearance flow on the performance of a compressor stage with a large rotor tip gap. *J. Turbomach.* **2017**, *139*, 061006. [[CrossRef](#)]
11. Schlechtriem, S.; Lötzerich, M. Breakdown of tip leakage vortices in compressors at flow conditions close to stall. In *ASME 1997 International Gas Turbine and Aeroengine Congress and Exhibition*; American Society of Mechanical Engineers: New York, NY, USA, 1997; p. V001T03A004. [[CrossRef](#)]
12. Furukawa, M.; Saiki, K.; Nagayoshi, K.; Kuroumaru, M.; Inoue, M. Effects of stream surface inclination on tip leakage flow fields in compressor rotors. *J. Turbomach.* **1998**, *120*, 683–692. [[CrossRef](#)]
13. Furukawa, M.; Inoue, M.; Saiki, K.; Yamada, K. The role of tip leakage vortex breakdown in compressor rotor aerodynamics. In *ASME 1998 International Gas Turbine and Aeroengine Congress and Exhibition*; American Society of Mechanical Engineers: New York, NY, USA, 1998; p. V001T01A054. [[CrossRef](#)]
14. Furukawa, M.; Saiki, K.; Yamada, K.; Inoue, M. Unsteady flow behavior due to breakdown of tip leakage vortex in an axial compressor rotor at near-stall condition. In *ASME Turbo Expo 2000: Power for Land, Sea, and Air*; American Society of Mechanical Engineers: New York, NY, USA, 2000; p. V001T03A112. [[CrossRef](#)]
15. Yamada, K.; Funazaki, K.; Furukawa, M. The behavior of tip clearance flow at near-stall condition in a transonic axial compressor rotor. In *ASME Turbo Expo 2007: Power for Land, Sea, and Air*; American Society of Mechanical Engineers: New York, NY, USA, 2007; pp. 295–306. [[CrossRef](#)]
16. McDougall, N.M.; Cumpsty, N.A.; Hynes, T.P. Stall inception in axial compressors. *J. Turbomach.* **1990**, *112*, 116–123. [[CrossRef](#)]
17. McDougall, N.M. A comparison between the design point and near stall performance of an axial compressor. In *ASME 1989 International Gas Turbine and Aeroengine Congress and Exposition*; American Society of Mechanical Engineers: New York, NY, USA, 1989; p. V001T01A040. [[CrossRef](#)]
18. Camp, T.R.; Day, I.J. A Study of Spike and Modal Stall Phenomena in a Low-Speed Axial Compressor. *J. Turbomach.* **1998**, *120*, 393–401. [[CrossRef](#)]
19. Hoying, D.A.; Tan, C.S.; Vo, H.D.; Greitzer, E.M. Role of blade passage flow structures in axial compressor rotating stall inception. In *ASME 1998 International Gas Turbine and Aeroengine Congress and Exhibition*; American Society of Mechanical Engineers: New York, NY, USA, 1998; p. V001T01A138. [[CrossRef](#)]
20. Hah, C.; Bergner, J.; Schiffer, H.P. Short length-scale rotating stall inception in a transonic axial compressor: Criteria and mechanisms. In *ASME Turbo Expo 2006: Power for Land, Sea, and Air*; American Society of Mechanical Engineers: New York, NY, USA, 2006; pp. 61–70. [[CrossRef](#)]
21. Vo, H.D.; Tan, C.S.; Greitzer, E.M. Criteria for spike initiated rotating stall. *J. Turbomach.* **2008**, *130*, 011023. [[CrossRef](#)]
22. Pullan, G.; Young, A.M.; Day, I.J.; Greitzer, E.M.; Spakovszky, Z.S. Origins and structure of spike-type rotating stall. *J. Turbomach.* **2015**, *137*, 051007. [[CrossRef](#)]

23. Hewkin-Smith, M.; Pullan, G.; Grimshaw, S.D.; Greitzer, E.M.; Spakovszky, Z.S. The Role of Tip Leakage Flow in Spike-Type Rotating Stall Inception. In *ASME Turbo Expo 2017: Turbomachinery Technical Conference and Exposition*; American Society of Mechanical Engineers: New York, NY, USA, 2017; p. V02DT46A009. [[CrossRef](#)]
24. Spalart, P.; Allmaras, S. A one-equation turbulence model for aerodynamic flows. In Proceedings of the 30th Aerospace Sciences Meeting and Exhibit, Reno, NV, USA, 6–9 January 1992; p. 439.
25. Song, M.R.; Yang, B.; Dong, G.M.; Liu, X.L.; Wang, J.Q.; Xie, H.; Lu, Z.H. Research on Accuracy of Flowing Field Based on Numerical Simulation for Tonal Noise Prediction in Axial Compressor. In *ASME Turbo Expo 2018: Turbomachinery Technical Conference and Exposition*; American Society of Mechanical Engineers: New York, NY, USA, 2018; p. V02BT43A006.
26. Jameson, A. Time dependent calculations using multigrid, with applications to unsteady flows past airfoils and wings. In Proceedings of the 10th Computational Fluid Dynamics Conference, Honolulu, HI, USA, 24–26 June 1991; p. 1596.
27. Rai, M.M. Three-dimensional Navier-Stokes simulations of turbine rotor-stator interaction. Part I-Methodology. *J. Propuls. Power* **1989**, *5*, 305–311. [[CrossRef](#)]

Publisher's Note: MDPI stays neutral with regard to jurisdictional claims in published maps and institutional affiliations.



© 2020 by the authors. Licensee MDPI, Basel, Switzerland. This article is an open access article distributed under the terms and conditions of the Creative Commons Attribution (CC BY) license (<http://creativecommons.org/licenses/by/4.0/>).

Article

The Influence of the Blade Outlet Angle on the Flow Field and Pressure Pulsation in a Centrifugal Fan

Hongchang Ding *, Tao Chang and Fanyun Lin

College of Mechanical and Electronic Engineering, Shandong University of Science and Technology, Qingdao 266590, China; 17863935466@163.com (T.C.); 15662728726@163.com (F.L.)

* Correspondence: dhchang@sdust.edu.cn; Tel.: +86-178-5272-8669

Received: 29 September 2020; Accepted: 5 November 2020; Published: 8 November 2020



Abstract: This paper takes centrifugal fan as the research object and establishes five impeller models with different blade outlet angles. By means of computational fluid dynamics (CFD), the external characteristics of the centrifugal fan and the internal characteristics, including the velocity, pressure, and turbulent energy distribution, at the middle span plane of the impeller or fan were obtained and compared. In addition, the pressure fluctuations surrounding the impeller outlet were also analyzed. The results showed that the change of the blade outlet angle of the centrifugal fan had a great influence on the performance; the total pressure and efficiency of the fan were the highest when the outlet angle of the blade was increased to 29.5° under the design flow rate; and the influence of the outlet angle on the fan performance was different in off-design conditions. On the other hand, at different flow rates, the change of the internal flow field with the increase of the outlet angle was different. For the pressure fluctuation of the fan, by increasing the blade outlet angle properly under high flow conditions, the fluctuation amplitude of the fan at the blade frequency and its frequency multiplication could be reduced, which is conducive to decreasing the impeller noise. The research results have good guiding significance regarding the design of the pneumatic performance and noise reduction performance of centrifugal fans.

Keywords: centrifugal fan; blade outlet angle; aerodynamic performance; numerical simulation

1. Introduction

Fans belong to the category of general machinery and are widely used in various industries of national economy. They are indispensable equipment for industrial and agricultural production. According to statistics, the power consumption of wind turbines accounts for 8–10% of the total power generation in China (Chen [1]). At present, centrifugal fans occupy a large proportion in China's energy system. Therefore, it is of great significance to research and improve the pneumatic performance of fans for energy saving. However, in the process of optimizing the performance of fans, the traditional experimental methods have long cycles and high cost, and it is difficult to visually display the gas distribution inside a fan. Therefore, a CFD (Computational Fluid Dynamics) numerical simulation technology that can effectively reduce the sample size of experimental design and capture the details of flow inside the fan more specifically, has increasingly caught the interest of scholars. Many scholars have used numerical simulation technology to study centrifugal fans (Zhang et al. [2]; Zhou et al. [3]; Lin et al. [4]; Yu et al. [5]; Kishokanna et al. [6]).

The impeller is the main moving part of a centrifugal fan, and the structural parameters of the impeller include the blade shape, blade profile, outlet width, number of blades, inlet and outlet diameter, etc. An excellent impeller design is helpful to improve the aerodynamic performance of the fan. At present, many scholars have studied the influence of certain impeller parameters on the aerodynamic performance of fans.

Li et al. [7] studied the influence of blade shapes on the performance of high specific speed centrifugal fans, and found that the blockage phenomenon at the blade outlet of impeller with plate blade and the turbulent kinetic energy inside the volute were weakened under the condition of a large flow rate, so that the performance of the fan with plate blade was better than that of the airfoil blade.

Wu et al. [8] compared the performance of a centrifugal fan with different blade profiles, and found that the centrifugal fan with a double-arc blade was higher in the efficiency and total pressure under the design condition, but the axial power consumed by equal deceleration blade was smaller. However, under the condition that other parameters of the fan remain unchanged, the internal flow of the fan with an equal deceleration blade was more uniform under the condition of low flow.

Jian et al. [9] found that when the blade outlet width changed, various losses of the fan increased, and the efficiency decreased. With the decrease of the blade outlet width, the flow-pressure curve of the fan shifted to the lower left and the pressure decreased with the increase of the flow rate. This provides a reference for the design of the outlet width of the impeller and the reconstruction of the impeller. Liu et al. [10] found that the aerodynamic performance of the fan can be improved by increasing the number of blades and the diameter of the blade outlet. The optimized fan with a 12-blade number and increased blade outlet diameter was better than the prototype fan in terms of the total pressure and efficiency.

In addition, some scholars studied the interaction among several structural parameters of the impeller. For example, Esra et al. [11] used a neural network method to determine the optimal family of the impeller inlet and outlet radius and inlet and outlet angle to reduce the noise level in the early stage of fan design. Meng et al. [12] studied the influence of three blade structure parameters on the performance of a centrifugal fan, which were inlet angle, outlet angle, and blade number, and obtained that the best combination of the three blade structure parameters using the response surface model (RSM) optimization method. The maximum efficiency was 93.7%.

Shi et al. [13] optimized the combination of the impeller and guide vane by studying the internal flow law of fans and combining this with numerical calculation results. They found that the streamline in the optimized guide vane was uniform and that the vorticity was reduced compared with the original guide vane. HEO et al. [14] analyzed the aerodynamic characteristics of a centrifugal fan with additional splitter blades in the impeller by using three-dimensional Reynolds-averaged Navier–Stokes (RANS). The global Pareto optimal frontier for centrifugal fan design was obtained by using a hybrid multi-objective evolutionary algorithm and response surface approximation model.

As the main parameter of impeller, the blade outlet angle of centrifugal fans has also been studied by scholars. Wang et al. [15] optimized the fan design based on an orthogonal experimental design method and CFD numerical simulation and obtained the relative optimal combination model of the impeller geometric parameters and speed. Through the range analysis of the calculation results, they found that the blade outlet angle had the greatest impact on the fan efficiency.

Recently, Swe et al. [16] discussed the flow characteristics of centrifugal fans with different blade outlet angles using the CFD numerical simulation method. The results showed that when the blade outlet angle was 25°, the steady flow and unsteady flow were more uniform, and the flow distribution in the circumferential direction had little change. Yu et al. [17] also studied the effect of the blade outlet angle on the performance of a multi-blade centrifugal fan, and found that the wind pressure and efficiency of the fan increased in the flow range of 420–725 m³/h with the increase of the blade exit angle, and properly increasing the blade outlet angle can reduce the pulsation amplitude of the fan at the blade frequency and its multiplier frequency.

Although many scholars have studied the blade outlet angle on the centrifugal fan, few have studied the effect of the blade outlet angle on the internal flow field and pressure fluctuation of the straight blade fan. In this paper, a type of straight plate blade fan was selected as the research model. Then, on the basis of the original blade outlet angle, five outlet angles (26.5°, 28°, 29.5°, 31°, and 32.5°) were obtained, and the geometric model was established using SolidWorks software. ANSYS CFX software was used for the numerical simulation, and the feasibility of the calculation results was

verified by experiments. Through the software post-processing, the influence of different blade outlet angles on the internal flow field and performance of the centrifugal fan was studied. The amplitudes of fan blades with different outlet angles were obtained and analyzed using fast Fourier transform. The research results can provide certain reference values for the efficient, safe, and stable operation of a centrifugal fan.

2. Research Model and Simulation Method

2.1. Research Model

This paper took a certain type of centrifugal fan as the research model, and the main design parameters of the fan are shown in Table 1.

Table 1. Main design parameters of the centrifugal fan.

Parameters	Values
Rated air flow	6200 m ³ /h
Rated total pressure	2700 Pa
Rated power	30 kW
Rated speed	1490 r/min

The strategy of this paper was to change the blade outlet angle of the original fan model, and its specific impeller parameters are shown in Table 2. The overall geometric model was established in SolidWorks as shown in Figure 1.

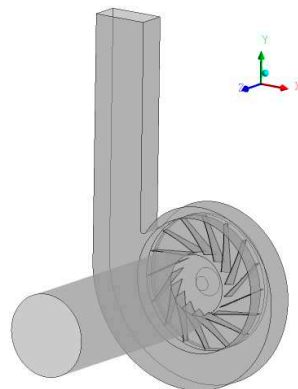


Figure 1. Geometric model of the original fan.

Table 2. Specific parameters of model fan impeller.

Parameters/Marks	Value
Impeller outer diameter D_2	810 mm
Number of blades Z	16
Impeller inner diameter D_1	368 mm
Blade outlet width b_2	43 mm
Blade outlet angle β_2	29.5°
Blade thickness δ	3 mm

2.2. Mesh and Check of Grid Independence

In this paper, SolidWorks was used for the three-dimensional modeling of the centrifugal fan. In the process of modeling, the geometric model of the original fan was simplified, and some unimportant chamfers, fillets, and gaps were ignored. Based on this, the flow-path model of the centrifugal fan was established. The flow-path model was divided into three parts: air inlet flow-path, impeller flow-path

and volute flow-path, and they were combined to form the centrifugal fan model. To ensure the real working condition of the air flow, the inlet and outlet flow-path model were extended properly.

After completing the establishment of the fan model, the mesh generation of the model began. Due to the simplicity of the axisymmetric model of the fan inlet section, the hexahedron structure was used for mesh generation. However, the impeller and volute were meshed with the tetrahedron structure due to the complexity of their flow passages, and the meshing of impeller and volute is shown in Figure 2. To make the numerical simulation as close to the actual situation as possible, all boundary layer grids were refined to meet the requirements of the wall function method. The minimum orthogonal angle of the mesh was greater than 27° , and the maximum extension ratio was less than 2.1, which will ensure high mesh quality.

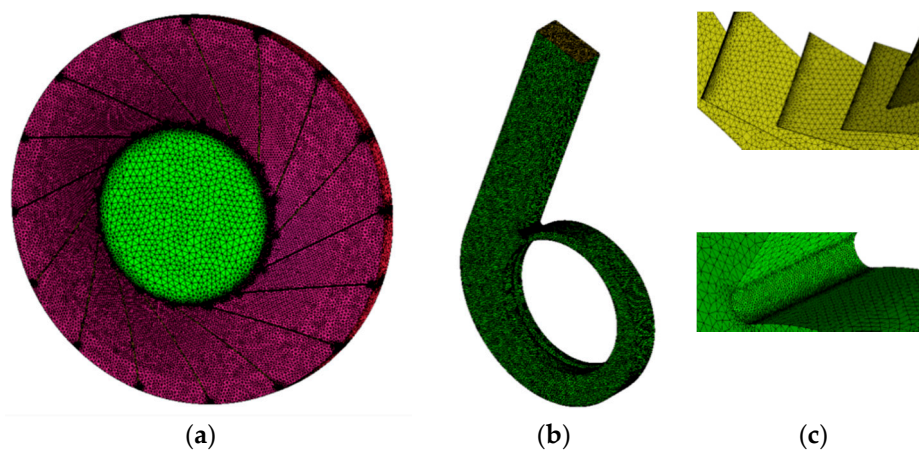


Figure 2. Mesh generation of the impeller and volute. (a) Impeller. (b) Volute. (c) Local refinements.

Table 3 shows the grid independence verification results of the centrifugal fan at design points, in which the total pressure and efficiency were obtained under five different numbers of grids. When the number of grids increased from 3,284,561 to 495,126, the total pressure and efficiency tended to be stable. Based on the accuracy of the simulation results and the cost of the computing time, the scheme of No. III was finally adopted.

Table 3. Scheme for grid independence check.

No.	Number of Grids	Total Pressure (Pa)	Efficiency
I	1,325,601	2820.9	0.849
II	2,578,452	2686.6	0.838
III	3,284,561	2608.4	0.831
IV	4,002,563	2606.5	0.828
V	4,951,236	2606.9	0.830

2.3. Simulation Settings

At present, the standard $k-\varepsilon$ turbulence model is the most widely used turbulence model, which has good stability and fast calculation speed compared with the zero equation model and the single equation model, and it is very suitable as the research object of this paper.

The numerical simulation was carried out in ANSYS CFX14.5, and the simulation process was based on the following settings:

- The inlet and volute were set in the static domain, and the impeller was set in the rotating domain.
- The default fluid was 25°C air, the reference pressure was 1 atm, and the flow of air was steady.
- The rotation axis was set to be the z axis, and the rotational speed was set as 1490 r/min.

- The inlet boundary condition was set to the normal speed, and the outlet boundary condition was set to the average static pressure.
- Interface models were set to general connection, and the frozen rotor method was used for interface connection.
- The SIMPLE (Semi-Implicit Method for Pressure Linked Equations) algorithm was used for pressure-velocity coupling. The continuity equation, momentum equation, and dissipation rate equation were discretized using the second-order upwind method. The solution step was 1000, and the convergence precision of all residuals was less than 10^{-5} .
- The steady simulation served as the initial condition for the unsteady simulation. The time step was set at 0.00011186 s, which corresponded to a rotating angle of 1° for each time step at a rotating speed of 1490 r/min. The time for one cycle was 0.04027 s, and five rounds were simulated. The final round was selected for analysis due to the relatively more stable flow field.

To study the possible influence of different blade outlet angles on the pressure fluctuation characteristics of the impeller outlet and volute of fan, monitoring points were set on the outlet of the impeller with mid-section ($z = 79$ mm) to monitor the unsteady flow. The layout of the monitoring points is shown in Figure 3, and the impellers with different blade outlet angles had the same monitoring position. In Figure 3b, P1 to P4 are distributed clockwise along the circumference, and P5 and P6 are arranged in the volute tongue and volute outlet section, respectively.

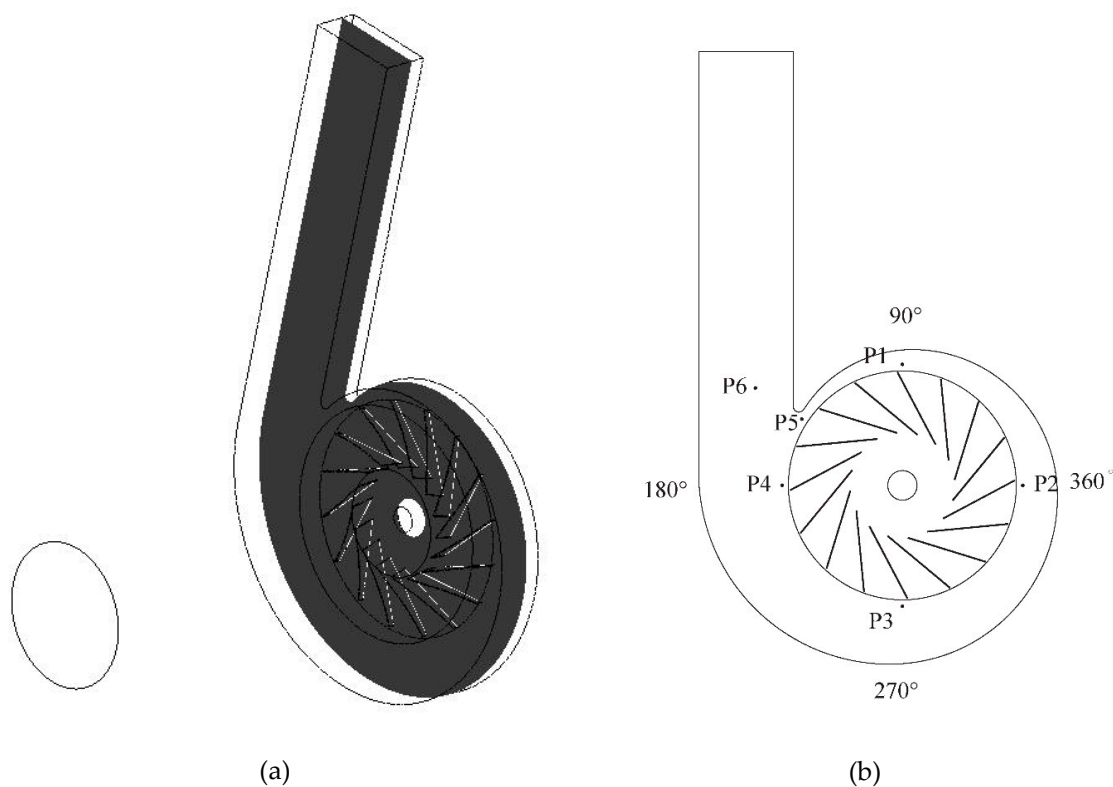


Figure 3. Schematic: (a) mid-section ($z = 79$ mm); (b) location of the monitoring point.

3. Experimental Verification

3.1. Experimental Equipment

To verify the feasibility of the established three-dimensional model of a centrifugal fan in numerical simulation, the external characteristics experiment of the fan model was carried out. The fan test was conducted according to the GB / T1236–2000 standard, the air intake test system was adopted, and the

test device was type C (pipe inlet and free outlet) specified by the national standard. The schematic diagram of the experimental device is shown in Figure 4.

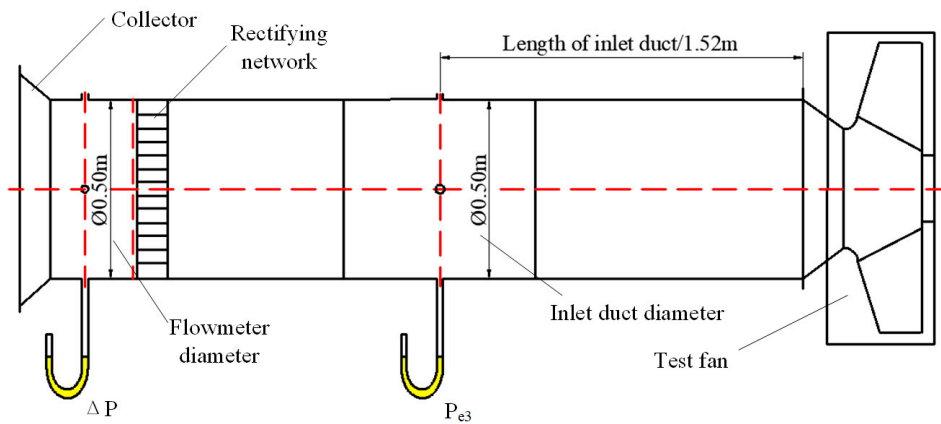


Figure 4. Schematic diagram of centrifugal fan experimental device.

The centrifugal fan test platform was primarily composed of the fan inlet pipe, main body of the centrifugal fan, and motor. Among them, the inlet pipe part mainly included the current collector, compensation micromanometer, rectifier network, and U-tube liquid pressure gauge. Table 4 shows the instrument used in the test and its specific parameters. The actual drawing of the fan is shown in Figure 5, and Figure 1 shows the geometric model of Figure 5.

Table 4. Instruments for the experiment.

Test Parameter Name	Instrument Name	Model/Specification	Minimum Scale	Accuracy
Atmospheric pressure	Aneroid barometer	YM3	100 Pa	≤ 200 Pa
Atmospheric temperature	hygrothermograph	TA298	0.1 °C	± 1 °C
Atmospheric humidity	hygrothermograph	TA298	0.10%	$\pm 5.0\%$
Flowmeter differential pressure/ ΔP	Compensation micromanometer	YJB-2500	0.01 mm	± 8 Pa
Gauge pressure/ P_{e3}	U-tube liquid pressure gauge		1 mm	$\pm 0.5\%$
Test speed			0.1 r/min	
Shaft power	Torque meter	100 N·m	0.1 kW	$\pm 0.1\%$
Torque			0.1 N·m	



Figure 5. The actual drawing of the fan.

3.2. Experimental Results

Figure 6 shows the results comparison between the numerical simulation and experiment. The longitudinal coordinate is the total pressure coefficient \bar{P} and total pressure efficiency η , and the calculation equation is expressed as:

$$\bar{P} = \frac{P}{\rho u^2}, \quad (1)$$

$$u = \frac{\pi D_2 n}{60}, \quad (2)$$

$$\eta = \frac{QP}{M\omega}, \quad (3)$$

where P , ρ , u , n , Q , M and ω respectively represent the total pressure, Pa; air density, kg/m^3 ; impeller outlet diameter, mm; rotational speed, r/min; experimental flow rate m^3/s ; torque, N·m; angular velocity, rad/s.

From Figure 6, the experiment results are close to the numerical results. Q/Q_{des} is the ratio of the experimental flow rate to the design flow rate. As the numerical simulation simplifies the model and neglects the loss, the simulation value was higher than the experimental value. The error between the tested and calculated total pressure was the smallest near the work point but gradually increased with the flow away from the design point, and the maximum deviation value did not exceed 8%.

There were two main influencing factors: One was the complex internal flow rule of fans under a small flow rate; the turbulence model selected in this paper could not effectively simulate the flow separation in the flow channel due to time and condition limitations. The other factor was that the actual flow rate of the fan was transient, which is ignored by the frozen rotor method. Although there were some errors between the experimental and the numerical results, the general changing trend of the total pressure and efficiency curves was the same, and the reliability of the numerical simulation can be confirmed according to the experimental results.

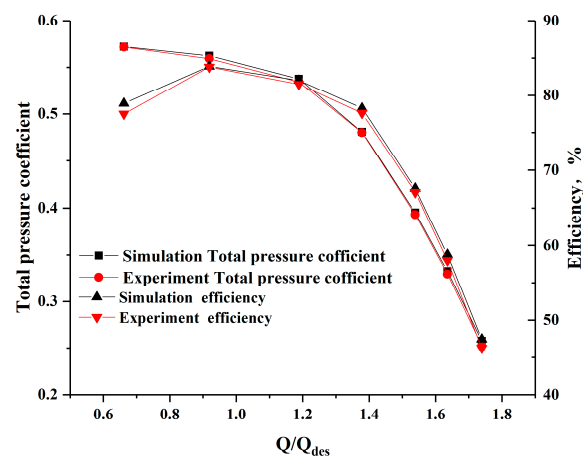


Figure 6. Curve of the total pressure coefficient and efficiency of the centrifugal fan model.

4. Results and Discussion

4.1. Contrast of External Characteristics

From Figure 7, the total pressure of the fan decreased with the increase of the flow rate. The efficiency of the fan increased first and then decreased, and it reached the highest value near the rated operating point. At $Q/Q_{\text{des}} < 1.4$, the total pressure of the fan increased first and then decreased with the rise of the blade outlet angle at the same flow rate. When $\beta_2 = 29.5^\circ$, the total pressure was the highest. In addition, the change trend of efficiency was different from the total pressure change. The outlet angle of the blade with the highest efficiency was different under different flow rates. At a

high flow rate, the efficiency increased with the increase of the outlet angle. At the design or a low flow rate, the efficiency was the highest when the blade outlet angle was 26.5° and reached the maximum of 84.85% at the designed flow rate.

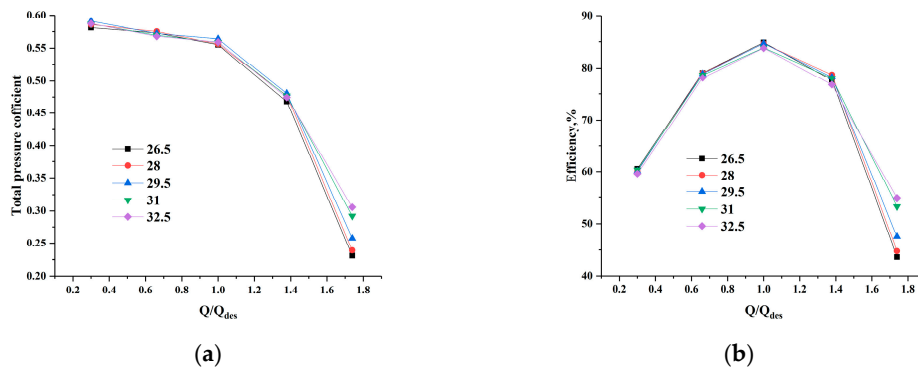


Figure 7. External characteristic curve of fan with different blade outlet angles: (a) Comparison of the total pressure coefficient. (b) Efficiency comparison.

4.2. Velocity Vector Distribution

To further describe the internal flow of the fan, the relative velocity distributions in the middle section of the flow passage were obtained, as shown in Figure 8. There were vortices of different degrees in the impeller channel between 90° and 270° (see Figure 3) at different flow rates, and the number of vortices gradually decreased with the increase of the flow rate. At a low flow rate, the outlet angle had little effect on the relative velocity distribution; however, the velocity near the volute tongue increased significantly with the increase of the outlet angle.

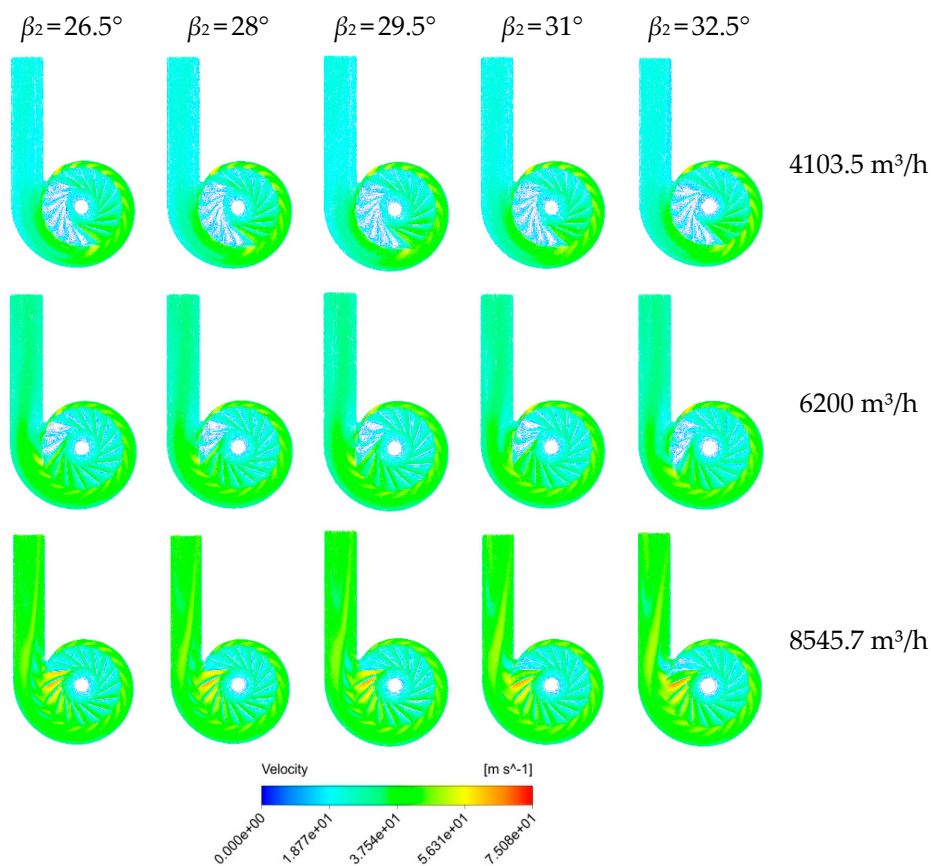


Figure 8. Velocity vector distributions at the middle span plane of the fan.

At the design flow rate, when the blade outlet angle was 31° , the number of impeller channels with a vortex was the least, and the low-speed area of the impeller outlet was the least. Under the condition of a large flow rate, there were low-speed regions of varying degrees near the impeller outlet between 90° and 270° , and the area of the low-speed area decreased with the increase of the blade outlet angle. However, the flow state of the impeller channel near the volute tongue became increasingly unstable. When $\beta_2 = 32.5^\circ$, the low velocity region and flow separation appeared on the suction surface of the trailing edge of the blade, resulting in flow blockage. It may be that the outlet angle was too large to match the volute and that the fluid impact on the volute tongue caused this phenomenon.

4.3. Pressure Distribution

Figure 9 shows the static pressure distribution of the middle span plane of impellers with different blade outlet angles and different flow rates. Under the condition of a low flow rate, the low-pressure region of the impeller inlet increased first and then decreased with the increase of the outlet angle. At the design flow rate, the area of the low-pressure zone increased first and then decreased with the increase of the impeller outlet angle between 90° and 270° . Under a large flow rate, there was a reverse pressure gradient in the impeller channel between 90° and 270° , and this phenomenon was alleviated with the increase of the blade outlet angle.

The static pressure increased with the increase of the flow rate. The maximum static pressure occurred at the impeller outlet near the volute tongue, which increased with the increase of the blade outlet angle, and the area of high pressure area became larger. In the static pressure distribution diagram of the impeller, we observed that the static pressure value of the fan gradually increased due to the continuous work of the impeller blade rotation on the air flow. At the impeller inlet, there was a clear low pressure area on the suction surface of the blade, and reverse flow occurred near the wall, resulting in separation loss. At high flow rates, this phenomenon was alleviated with the increase of the outlet angle.

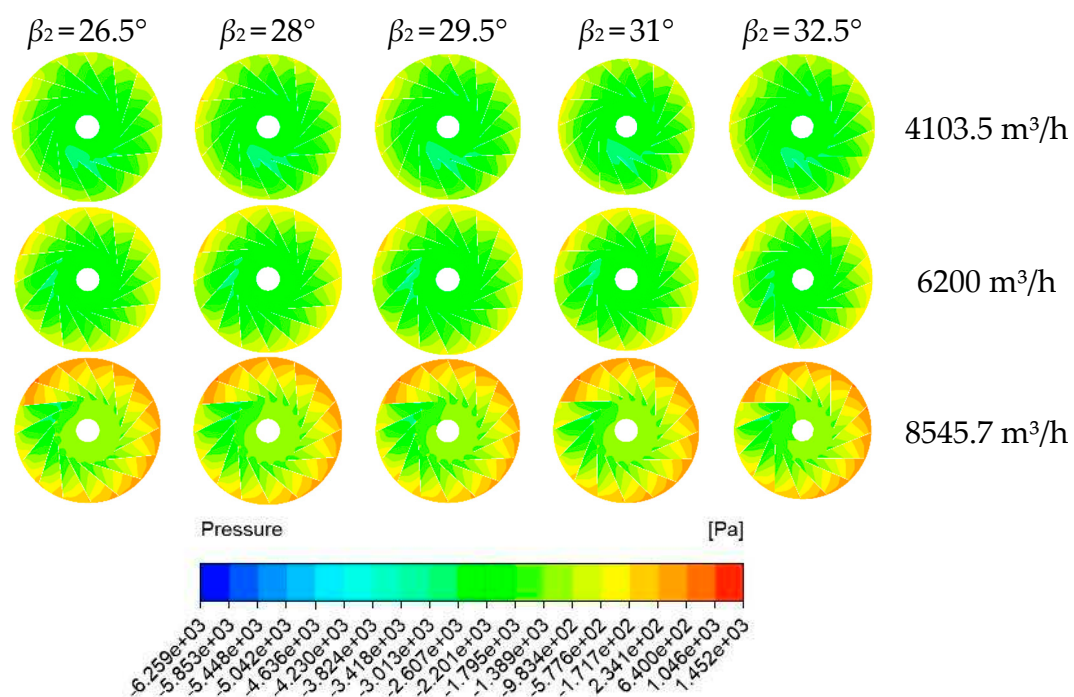


Figure 9. Static pressure distributions at the middle span plane of the impeller.

As can be seen from Figure 10, the total pressure distribution of the fan gradually increased from the impeller inlet to the outlet. As the flow rate increased, the total pressure increased. Under different outlet angles, the pressure changes in the impeller passage mainly occurred between 90° and 270° .

At a low flow rate, the total pressure did not change greatly with the increase of the blade outlet angle. At the design flow rate, the low-pressure region appeared at the outlet of the single impeller, which increased first and then decreased with the increase of the outlet angle.

Combined with the velocity vector diagram, the low-pressure area appeared in the low speed region. At high flow rates, the total pressure increased with the increasing of the outlet angle. With the increase of the blade outlet angle, the effective working area of the impeller increased, the total impeller pressure increased overall, especially in the circumferential area of the outlet of the blade. In addition, the pressure distribution of different flow paths between blades was different in the range of 90° – 270° , which indicates that the flow characteristics inside the fan were asymmetric.

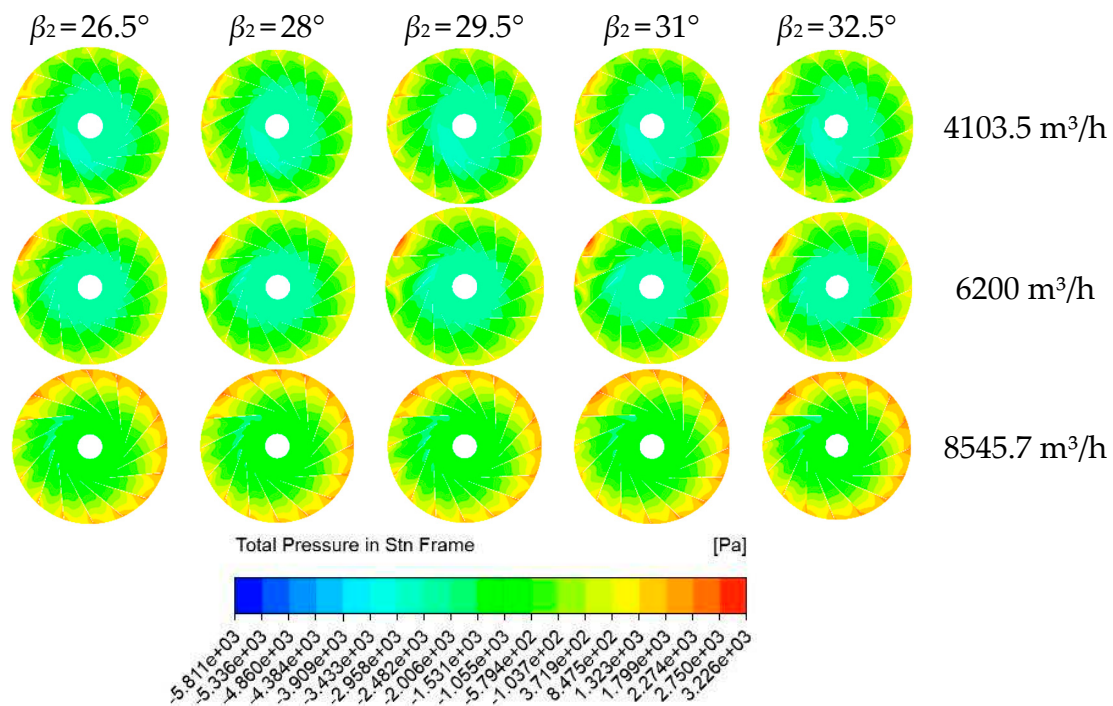


Figure 10. Total pressure distributions at the middle span plane of the impeller.

4.4. Turbulence Kinetic Energy Distribution

It can be seen from Figure 11 that the high turbulent kinetic energy region was mainly distributed near the volute tongue at the impeller outlet and gradually diffused toward the surrounding area. When the gas flowed through this area, boundary layer separation easily occurred. In general, the turbulent energy was the smallest when the blade outlet angle was 29.5° . With the increase of the blade outlet angle, the turbulent energy of the volute section first decreased and then increased. The outlet angle of the blade had a suitable value, which can reduce the flow loss of the volute section and improve the efficiency of the fan.

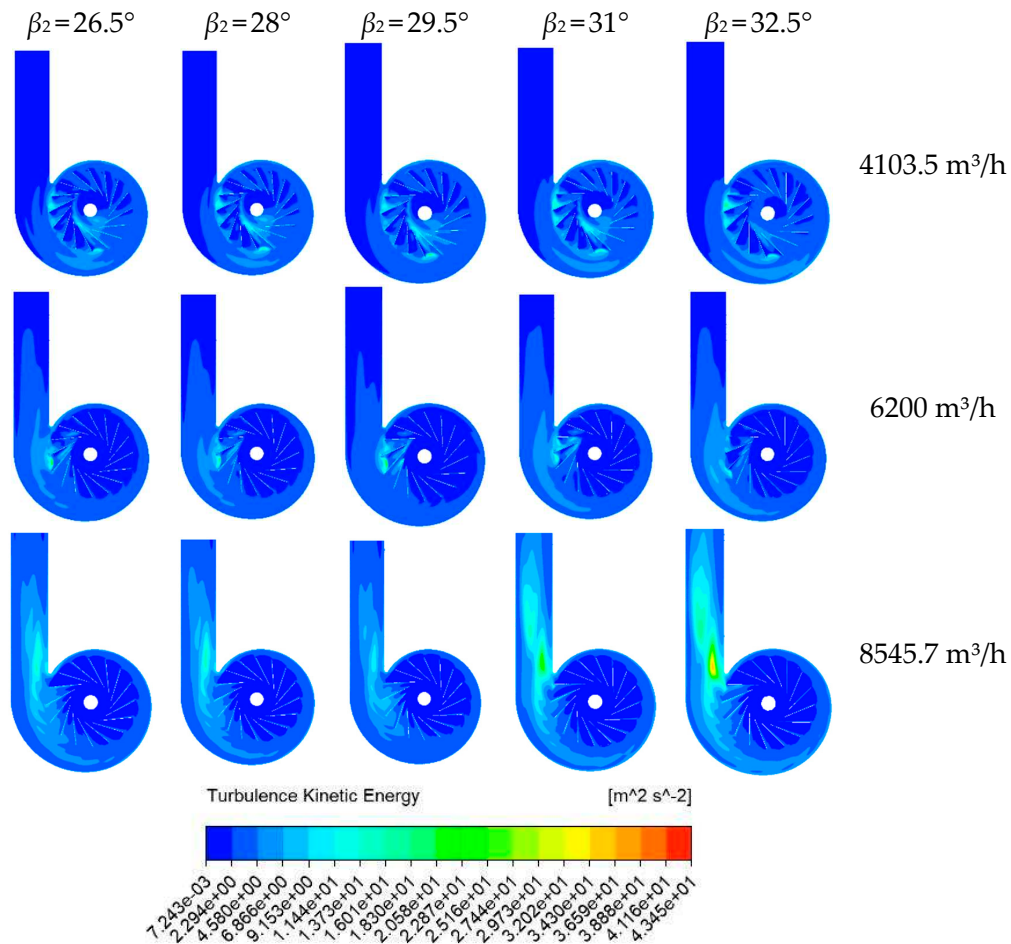


Figure 11. Turbulence kinetic energy distributions at the middle span plane of a fan.

4.5. Pressure Pulsation Analysis

To better analyze the influence of the blade outlet angle on the pressure pulsation in the impeller outlet area, the time-domain characteristics of pressure pulsation at each monitoring point of the impeller were transformed by fast Fourier transform, and the frequency domain of pressure pulsation was obtained, as shown in Figure 12. It can be seen from the diagram that the main frequency of pulsation at the monitoring point of the impeller outlet of the centrifugal fan was the blade passing frequency (f_{BPF}) and its frequency multiplication, and the amplitude of pulsation reached the maximum at the blade passing frequency. Due to rotor–stator interactions, pressure fluctuations near the volute tongue (P1, P5) were large. However, from the view of the frequency domain map of the monitoring points, the change rules of each monitoring point were different at different outlet angles, so further analysis is required. The blade passing frequency was calculated by Equation (4).

$$f_{BPF} = \frac{NZ}{60}, \tag{4}$$

where N is the speed, r/min; Z is the number of blades.

For further analysis, we use mean pressure amplitude \bar{c}_p to calculate pressure pulsation energy of all the six measuring points for different outlet angles.

$$\bar{c}_p = \frac{\sum_1^n c_{p-i}}{6} (n = 6), \tag{5}$$

where c_{p-i} represents the pressure amplitudes at f_{BEF} for different measuring positions.

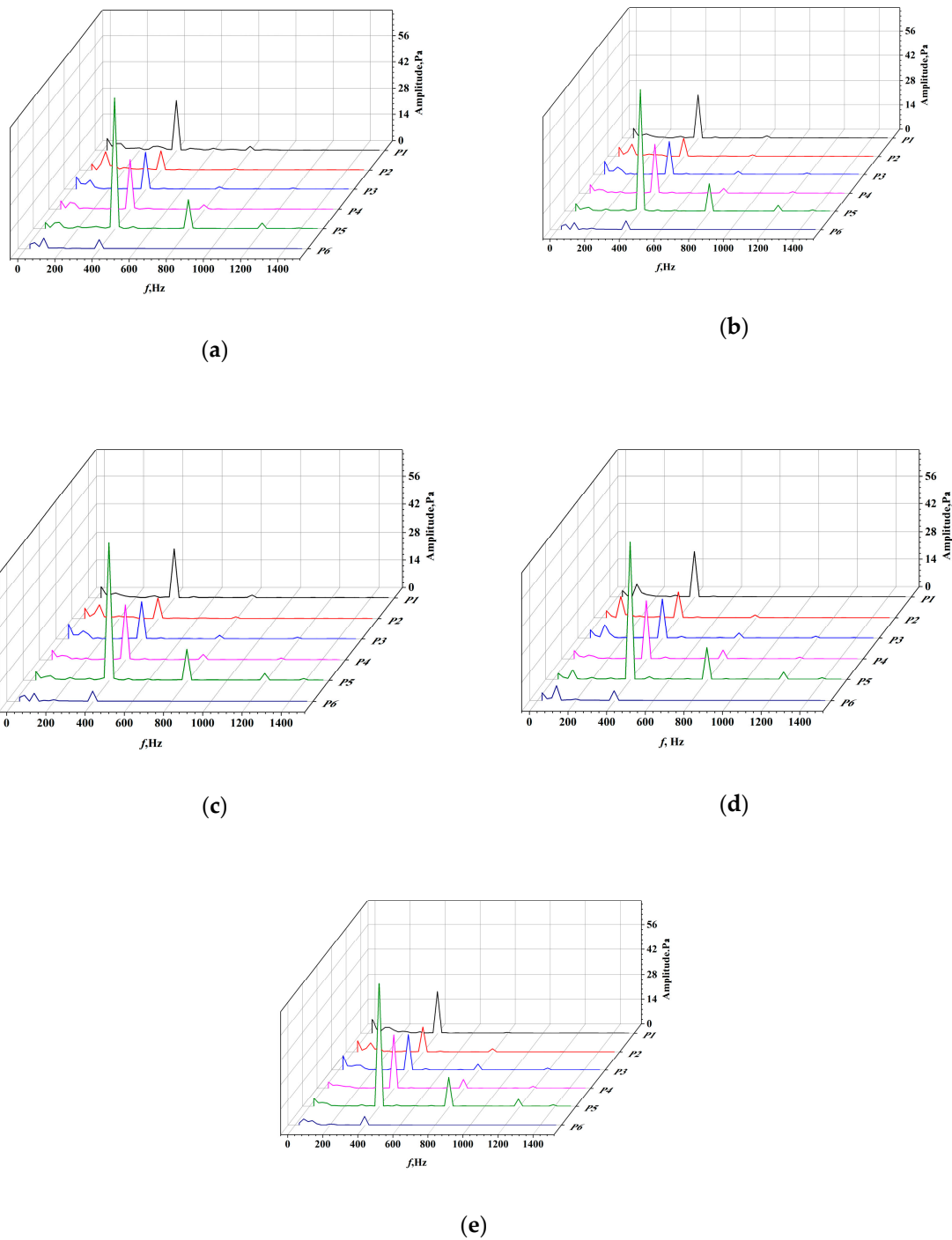


Figure 12. Frequency domain of the pressure pulsation for different blade outlet angles: (a) 26.5° ; (b) 28° ; (c) 29.5° ; (d) 31° ; and (e) 32.5° .

Figure 13 shows the average pressure amplitude at different outlet angles. In general, with the increase of the blade outlet angle, the pressure fluctuation amplitude of the fan increased. However, the amplitude of pressure fluctuation decreased with the increase of the blade outlet angle at 26.5° – 28° and 29.5° – 31° . Therefore, overall, the outlet angle of the blade increasing in a certain range reduced the pressure pulsation on the impeller, which is beneficial to reduce the noise of the impeller.

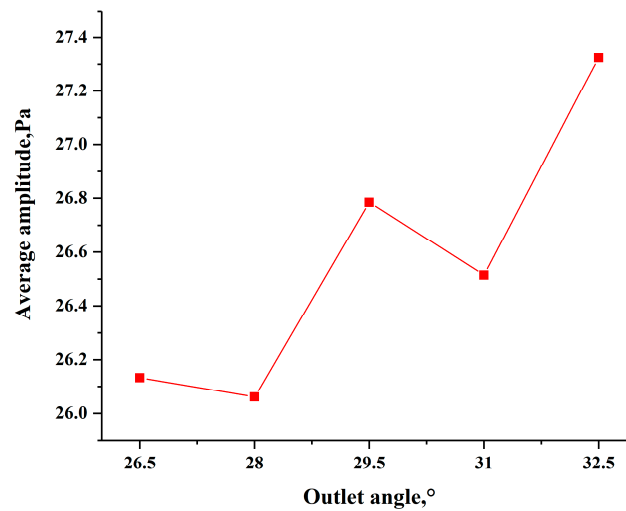


Figure 13. Average pressure amplitude at different angles.

5. Conclusions

In this paper, five models of centrifugal fan impellers with different blade outlet angles were established, and the influence of the blade outlet angle on centrifugal fan performance was studied using CFD software. The conclusions can be drawn as follows:

1. The blade outlet angle had different effects on the total pressure and efficiency. At $Q/Q_{des} < 1.4$, the total pressure coefficient of the fan first increased and then decreased with the rise of the blade outlet angle at the same flow rate. The outlet angle of the blade with the highest efficiency was different under different flow rates. At a high flow rate, the efficiency increased with the increase of the outlet angle. At the design or a low flow rate, the efficiency was the highest when the blade outlet angle was 26.5° and reached the maximum of 84.85% at the designed flow rate.
2. Through the simulation and analysis of the flow field inside a centrifugal fan, with the increase of the outlet angle, the flow speed near the volute tongue increased and the low pressure area at the impeller inlet first increased and then decreased at a low flow rate. With a blade outlet angle of 29.5° at the design flow rate, the swirl in the blade passage was minimal. In the case of a large flow rate, the increase of the blade outlet angle decreased the low speed area at the impeller outlet, decreased the reverse pressure gradient area at the blade leading edge, and increased the total pressure. The turbulent kinetic energy decreased first and then increased with the increase of the blade outlet angle.
3. Through the analysis of the frequency domain diagram, we found that the pressure fluctuation of a centrifugal fan was the smallest when the outlet angle of the blade was 28, and we found that properly increasing the outlet angle of the blade reduced the fluctuation amplitude of the fan at the blade frequency and its frequency multiplication, which is conducive to reducing impeller noise.

Author Contributions: Conceptualization, H.D.; Data curation, T.C.; Methodology, H.D. and T.C.; Software, F.L.; Supervision, H.D.; Validation, F.L.; Writing—original draft, T.C.; Writing—review and editing, H.D. All authors have read and agreed to the published version of the manuscript.

Funding: This research has been supported by key research and development project of Shandong province (2017GGX203005), Natural Science Foundation Project of Shandong province (ZR2019MEE068) and Design and performance optimization of magnetic levitation high speed centrifugal pump(201810424020). The supports are gratefully acknowledged.

Conflicts of Interest: The authors declare no conflict of interest.

References

1. Chen, Y. Optimization of Aerodynamic Performance and Noise Control on a Forward Curved Centrifugal Fan. Master's Thesis, Huazhong University of Science and Technology, Wuhan, China, 16 May 2016.
2. Zhang, X.L.; Zhang, Y.L.; Lu, C.G. Flow and noise characteristics of centrifugal fan in low pressure environment. *Processes* **2020**, *8*, 985. [[CrossRef](#)]
3. Zhou, B.; He, X.M.; Yang, H.; Zhu, Z.C.; Wei, Y.K.; Zhang, Y. Unsteady flow characteristics of rotating stall and surging in a backward centrifugal fan at low flow-rate conditions. *Processes* **2020**, *8*, 872. [[CrossRef](#)]
4. Lin, S.C.; Tsai, M.L. An integrated performance analysis for a backward-inclined centrifugal fan. *Comput. Fluids* **2012**, *56*, 24–38. [[CrossRef](#)]
5. Yu, S.B.; Li, J. Design of low-noise centrifugal fan for motorized spindle cooling system. *Procedia Eng.* **2011**, *23*, 380–386. [[CrossRef](#)]
6. Kishokanna, P.; Srithar, R.; Alessandro, R.; Wira, J. Tonal noise prediction in a small high speed centrifugal fan and experimental validation. *Appl. Acoust.* **2017**, *125*, 29–70. [[CrossRef](#)]
7. Li, X.; Wang, W.; Li, J.L.; Luo, X.Q.; Huang, Y.J. Analysis of the influence of different blade types on the performance of high specific speed centrifugal fan. In Proceedings of the Symposium on the development strategy of hydraulic machinery discipline and the 11th National Annual Conference on hydraulic machinery and its systems, Beijing, China, 19–21 October 2018.
8. Wu, R.L.; Wu, P.J.; Qin, G.L. Numerical research on the effect of blade profile on performance of centrifugal fan. *Compress. Blower Fan Technol.* **2014**, *0*, 31–36. [[CrossRef](#)]
9. Jian, X.S.; Chen, Q.; Sai, Q.Y.; Wu, H.Y.; Zhu, Z.N. Effect of the blade outlet width on the performance of small high speed backward curved centrifugal fans. *Compress. Blower Fan Technol.* **2017**, *59*, 71–76. [[CrossRef](#)]
10. Liu, D.; Li, J.; Ling, X. Performance improvement of MVR high pressure centrifugal fan with designed number and outlet diameter of blades. *fluid machinery.* **2018**, *046*, 44–48. [[CrossRef](#)]
11. Esra, S.; Yilmaz, D. Acoustic optimization for centrifugal fans. *Noise Control Eng. J.* **2012**, *60*, 379–390. [[CrossRef](#)]
12. Meng, F.N.; Dong, Q.L.; Wang, Y.; Wang, P.F.; Zhang, C.X. Numerical optimization of impeller for backward-curved centrifugal fan by response surface methodology (RSM). *Res. J. Appl. Sci. Eng. Technol.* **2013**, *6*, 2436–2442. [[CrossRef](#)]
13. Shi, Y.J.; Ge, A.X.; Fu, Y.X.; Wang, X. Retrofit analysis of the impeller and guide vanes of a centrifugal fan based on CFD. *Compress. Blower Fan Technol.* **2017**, *59*, 27–31. [[CrossRef](#)]
14. Heo, M.W.; Kim, J.H.; Kim, K.Y. Design optimization of a centrifugal fan with splitter blades. *Int. J. Turbo Jet Engines* **2015**, *32*, 143–154. [[CrossRef](#)]
15. Wang, X.; Sai, Q.Y. Multi-factor optimization and design of centrifugal fan based on orthogonal experiment method. *Energy Eng.* **2020**, *4*, 13–18. [[CrossRef](#)]
16. Swe, W.W.M.; Morimatsu, H.; Hayashi, H.; Okumura, T.; Oda, I. Study of unsteady flow simulation of backward impeller with non-uniform casing. *J. Therm. Sci.* **2017**, *26*, 208–213. [[CrossRef](#)]
17. Yu, S.Q.; Wu, D.Z.; Yang, S. Numerical study on the influence of blade outlet angle on the performance of multi-blade centrifugal fan. *Fluid Mach.* **2019**, *47*, 1–7. [[CrossRef](#)]

Publisher's Note: MDPI stays neutral with regard to jurisdictional claims in published maps and institutional affiliations.



© 2020 by the authors. Licensee MDPI, Basel, Switzerland. This article is an open access article distributed under the terms and conditions of the Creative Commons Attribution (CC BY) license (<http://creativecommons.org/licenses/by/4.0/>).

Article

A CFD-Based Shape Design Optimization Process of Fixed Flow Passages in a Francis Hydro Turbine

Ujjwal Shrestha ¹ and Young-Do Choi ^{2,*}

¹ Graduate School of Mechanical Engineering, Mokpo National University, Muan 58554, Korea; 17413283@mokpo.ac.kr

² Department of Mechanical Engineering, Institute of New and Renewable Energy Technology Research, Mokpo National University, Muan 58554, Korea

* Correspondence: ydchoi@mokpo.ac.kr

Received: 4 October 2020; Accepted: 27 October 2020; Published: 31 October 2020



Abstract: In recent times, optimization began to be popular in the turbomachinery field. The development of computational fluid dynamics (CFD) analysis and optimization technology provides the opportunity to maximize the performance of hydro turbines. The optimization techniques are focused mainly on the rotating components (runner and guide vane) of the hydro turbines. Meanwhile, fixed flow passages (stay vane, casing, and draft tube) are essential parts for the proper flow uniformity in the hydro turbines. The suppression of flow instabilities in the fixed flow passages is an inevitable process to ensure the power plant safety by the reduction of vortex-induced vibration and pressure pulsation in the hydro turbines. In this study, a CFD-based shape design optimization process is proposed with response surface methodology (RSM) to improve the flow uniformity in the fixed flow passages of a Francis hydro turbine model. The internal flow behaviors were compared between the initial and optimal shapes of the stay vane, casing, and the draft tube with J-Groove. The optimal shape design process for the fixed flow passages proved its remarkable effects on the improvement of flow uniformity in the Francis hydro turbine.

Keywords: CFD; shape optimization; Francis turbine; fixed flow passage; flow uniformity

1. Introduction

Hydropower is considered a reliable renewable source for electricity production. The hydraulic turbine is an essential component of the hydropower plant. Among various types of hydraulic turbines, Francis turbines are widely used over a wide range of flow rates and heads [1]. The main hydro passage parts of the Francis turbine are composed of a spiral casing, stay vane, guide vane, runner and draft tube. The flow instabilities in the fixed flow passages can cause failure in the whole hydro turbine system. The design of the fixed flow passages is dependent on the moving components of the runner and guide vane in the Francis turbine.

The fixed flow passages are designed to keep the proper flow uniformity by suppressing the pressure pulsation, vortex-induced vibration and swirl flow. The main objective of the stay vane is to maintain the uniform flow from the casing to guide vane and runner flow passages [2]. The non-uniform flow distribution from the stay vane causes the vortex-induced vibration, which initiates the failure in the stay vane [3]. The purpose of the spiral casing is to direct the fluid from the penstock pipe to the stay vane and guide vane. Kurokawa and Nagahara [4] explained the free-vortex, accelerating and decelerating types of the spiral casing. The flow behavior is dependent on the casing shape. The improper flow distribution causes pressure pulsation and secondary vortex, which induces the cracking in the casing wall. Price indicated that the severe pressure fluctuation in the spiral casing causes the brittle crack in the casing wall [5]. The draft tube is designed to improve the dynamic

energy in the runner outlet and recover the suction head [6]. The existence of swirl flow in the draft tube causes the flow instabilities [7–9]. J-Groove installation suppresses the flow instabilities in the draft tube of the Francis hydro turbine [10]. J-Groove is the groove engraved on the wall of the draft tube that induces reverse jet flow through the shallow groove channels to suppress the swirl flow [11].

The computational fluid dynamics (CFD) analysis has become one of the main tools for turbomachinery flow analysis. The application of CFD analysis makes it easier to evaluate a large number of design cases with precise and accurate results. It is used to predict the internal flow behavior of the turbomachinery, flow separation, and loss distribution in Francis turbine components. Many researchers have conducted CFD analysis on the Francis hydro turbine for the prediction of performance [12], part-load performance [13], suction performance [14], unsteady flow behavior [15]. The CFD analysis and optimization techniques were integrated for the optimization of the runner blade [1]. The maximum improvement in the moving components (runner and guide vane) was achieved via CFD-based optimization [16–19]. However, few studies related to the fixed flow passages (spiral casing, stay vane and draft tube) of Francis hydro turbines are available [20,21].

Nowadays, design optimization using numerical analysis is widely used for turbomachinery. Wu et al. performed the CFD-based design optimization for a Francis hydro turbine. They showed a comparison between the initial and optimal design of turbines at the design point [19]. They mainly focused on the optimization of the runner blade of the Francis hydro turbine. The conventional blade design approaches integrated with the advanced CFD analysis are powerful and effective tools for the design optimization of turbomachinery. A CFD-based design optimization system that integrates internally developed parametrized mathematical geometry models, automatic mesh generators and commercial 3D Navier–Stokes code like ANSYS CFX 19.2 permits designers to interactively generate, modify and visualize the geometric model of turbine components. The design process can be repeated until a fully optimized model with satisfactory performance is obtained. Nakamura and Kurosawa [22] conducted the design optimization of a high specific speed Francis turbine using a multi-objective genetic algorithm (MOGA). The design optimization of hydraulic machinery can be performed by multilevel CFD techniques [23]. The multilevel CFD technique reduced the computation time. Sosa et al. [6] performed the design optimization of the draft tube by using CFD analysis. Si et al. [24] proposed a multi-point design process based on CFD and an intelligent optimization method for the automotive electronic pump. Ayancik et al. [1] conducted a simulation-based design of a Francis hydro turbine runner that was performed by following a surrogate model-based optimization. The conventional CFD-based design process is executed through trial and error; hence, designing a runner for a Francis hydro turbine can take several months. Due to these drawbacks of conventional CFD-based design, CFD-based optimization design approaches can be followed for the reduction of calculation time and better shape design.

It is essential to integrate a robust and flexible design tool in a CFD-based design optimization system to allow automatic generation and modification of the design geometry. The objective of this study is to propose a CFD-based shape design optimization process for fixed flow passages in the Francis hydro turbine. For the CFD-based shape design optimization, the surrogate model was prepared by using response surface methodology (RSM). The various RSMs were evaluated by the goodness of fit test for the precise and accurate response surface. The multi-objective genetic algorithm (MOGA) was applied for the optimization of the fixed flow passages. The hydraulic design and optimization framework for stay vane, casing, and a draft tube with J-Groove can be generalized for reaction hydro turbines (Francis turbine and Pump turbine). The CFD-based optimization process included the parametric design of stay vane, casing, and the draft tube with J-Groove, fluid domain modeling, meshing, ANSYS CFX solver, post-processing, design of experiment (DOE), response surface preparation and multi-objective optimization.

2. Hydro Turbine Design and Optimization Methodology

2.1. Hydro Turbine Design

2.1.1. Process of Hydraulic Design

Figure 1 illustrates the hydraulic design process of the Francis hydro turbine proposed in this study. The conceptual design of the turbine components is based on the turbomachinery theory. The conceptual design for the Francis hydro turbine was prepared according to the turbine specification. Generally, the hydro turbine design is commenced with the runner design. The guide vane is designed according to the flow angle at the runner inlet. The stay vane design should match the inlet flow angle of the guide vane. The proper flow distribution at the stay vane inlet should be maintained by casing design. The runner outlet flow angle is a constraint for the draft tube design. A fixed flow passage design is linked with each other. Therefore, the initial shape design was completed in serial order as in the conceptual design by theory and detail design by 3D shape modeling. It was challenging to obtain the whole turbine passages optimization at once because it consisted of numerous design variables and overlapping constraints. Hence, the fixed flow passages shape was optimized for each passage separately to reduce the computational cost and make an effective optimization process. In this study, runner and guide vane design conditions were fixed, which created the constraints for the optimization process followed.

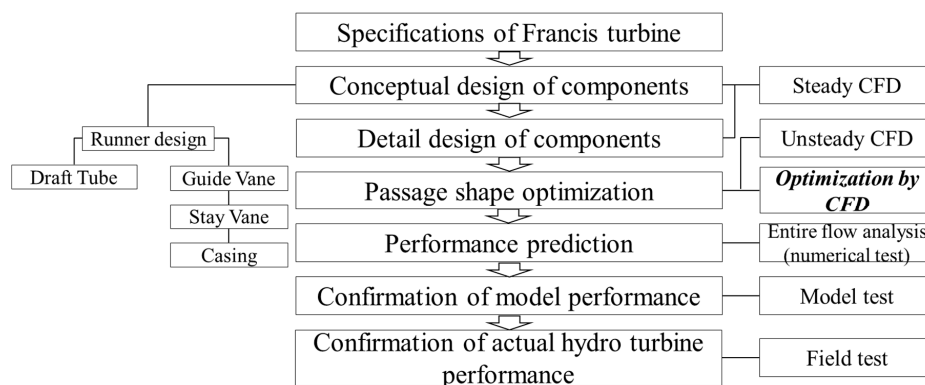


Figure 1. Hydraulic design process of the Francis hydro turbine with computational fluid dynamics (CFD)-based optimization.

2.1.2. Francis Turbine Specification and Performance

The design specification of the 100 MW class Francis hydro turbine model is shown in Table 1. The minimum and maximum heads of the Francis hydro turbine are 66.5 m and 110 m, respectively. The design flow rate of the prototype turbine is 125.4 m³/s. The turbine maximum output power is 113 MW, and the minimum output power is 62.3 MW. The specific speed N_s , unit discharge Q_{11} and unit speed N_{11} are evaluated by using Equations (1)–(3), respectively.

$$N_s = \frac{n \sqrt{P}}{H^{\frac{5}{4}}} \quad (1)$$

$$Q_{11} = \frac{Q}{D_e^2 \sqrt{H}} \quad (2)$$

$$N_{11} = \frac{n D_e}{\sqrt{H}} \quad (3)$$

where n is the rotational speed in min⁻¹, P is the output power in kW, H is effective head in m, Q is flow rate in m³/s, D_e is the runner outlet diameter.

Table 1. Design specification of the 100 MW class Francis turbine.

Nomenclature	Unit	Values
Effective head, H	m	90
Flow rate, Q	m^3/s	125.4
Power, P	MW	100
Rotational speed, n	min^{-1}	180
Inlet diameter, D_i	mm	4863
Outlet diameter, D_e	mm	3995
Specific speed, N_s	$\text{kW}\cdot\text{min}^{-1}\cdot\text{m}$	205

Francis turbine fluid domain by initial design is shown in Figure 2a, which consists of a spiral casing, 20 stay vanes, and 20 guide vanes with 13 runner blades, and the elbow-type draft tube. The runner inlet and outlet diameters are $D_i = 4863$ mm and $D_e = 3995$ mm, respectively. The installed capacity of the Francis turbine is 100 MW. The efficiency hill chart of the Francis hydro turbine by initial design and CFD analysis is shown in Figure 2b. The various guide vane openings are used to regulate the flow rate for the Francis hydro turbine. The guide vane opening from 8° to 41° is used to change the flow rate. The design point for the Francis hydro turbine is determined at $N_{11} = 76.12$ and $Q_{11} = 0.87$. The best efficiency of the Francis hydro turbine is located in the range of guide vane angles of 23° to 26° and unit speeds of $N_{11} = 70$ to $N_{11} = 80$.

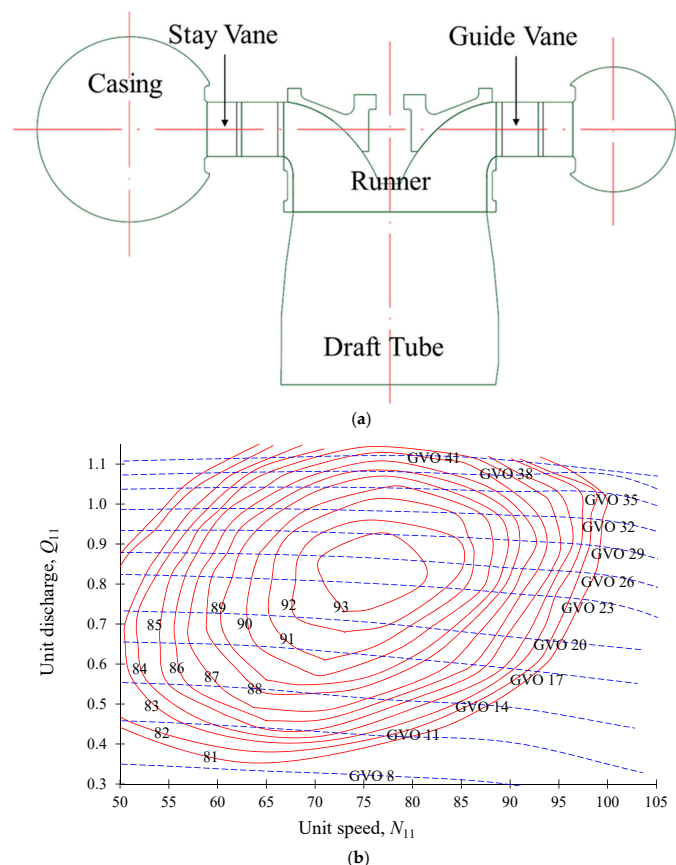


Figure 2. (a) Schematic view and (b) efficiency hill chart of the 100 MW class Francis hydro turbine by initial design.

2.1.3. Stay Vane Design

The purpose of the stay vane (SV) is to guide the water flow from the casing to guide vane and runner, and for structural purpose. The main design parameters for the stay vane are vane angles,

thickness, ellipse ratio at the leading edge, and trailing edge. The design parameters for the stay vane are shown in Figure 3a. The design parameters for the stay vane are defined as in Equation (4).

$$d_{SV} = [\alpha_1, \dots, \alpha_5, \delta_1, \dots, \delta_5, a_{le}, a_{te}]^T \tag{4}$$

where d_{SV} is the design variables matrix of the stay vane, α_i is the vane angle at i th section of the stay vane, δ_i is the thickness at i th section of the stay vane, a_{le} is the ellipse ratio at the leading edge (LE), a_{te} is the ellipse ratio at the trailing edge (TE) and superscript T indicates the transpose of the design variables matrix.

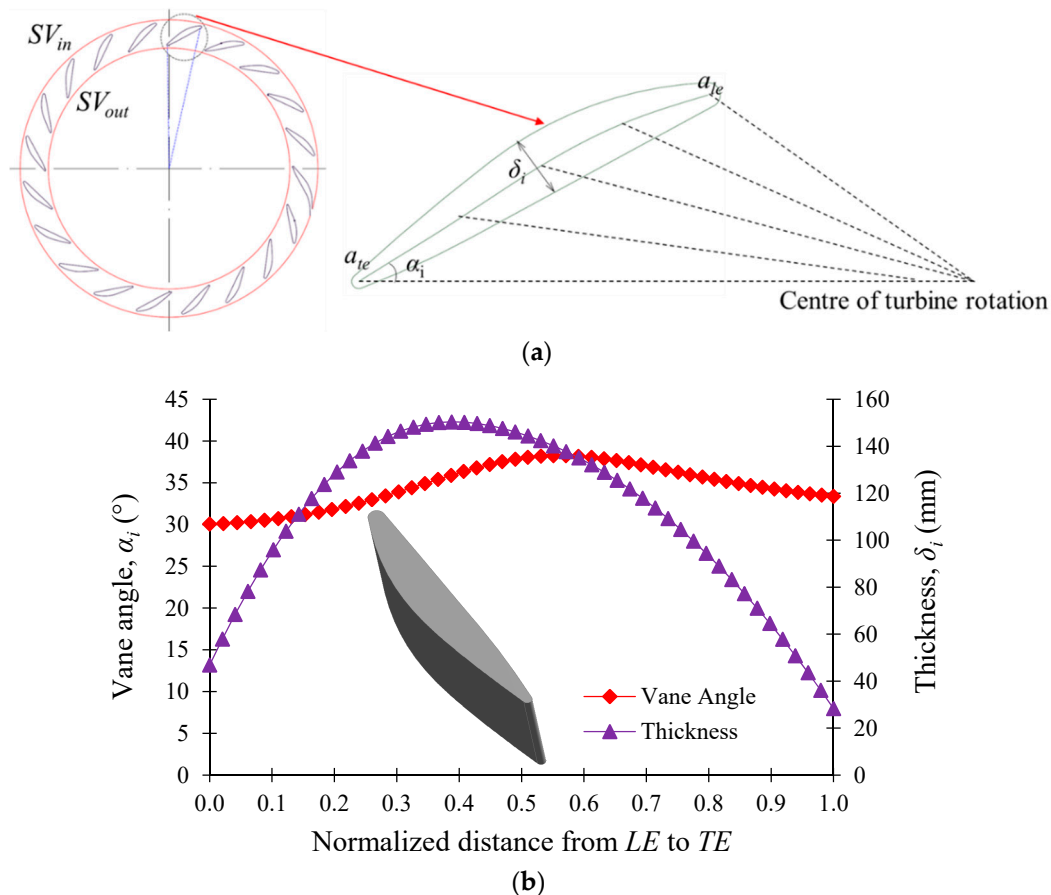


Figure 3. (a) Parametric design schematic view and (b) initial stay vane shape.

Figure 3b shows the initial stay vane shape using the vane angle and thickness distributions. The inlet vane angle is 30°, and the outlet vane angle is 33°. The thickness of the stay vane is 46 mm at the LE and 28 mm at the TE. The maximum thickness of the stay vane is 150 mm at 0.4 normalized distance from the LE. The vane angle and thickness distribution are the same throughout the stay vane.

2.1.4. Casing Design

The spiral casing shape is dependent on the cross-section radii [20]. Figure 4a,b indicates the parametric design parameters and initial shape design of the casing, respectively. The parametric design of the casing shape is defined as in Equation (5).

$$d_{CA} = [r_0, r_2, \dots, r_{11}]^T \tag{5}$$

where d_{CA} is the design variables matrix of the casing, r_i is the cross-section radius at i th section of the spiral casing.

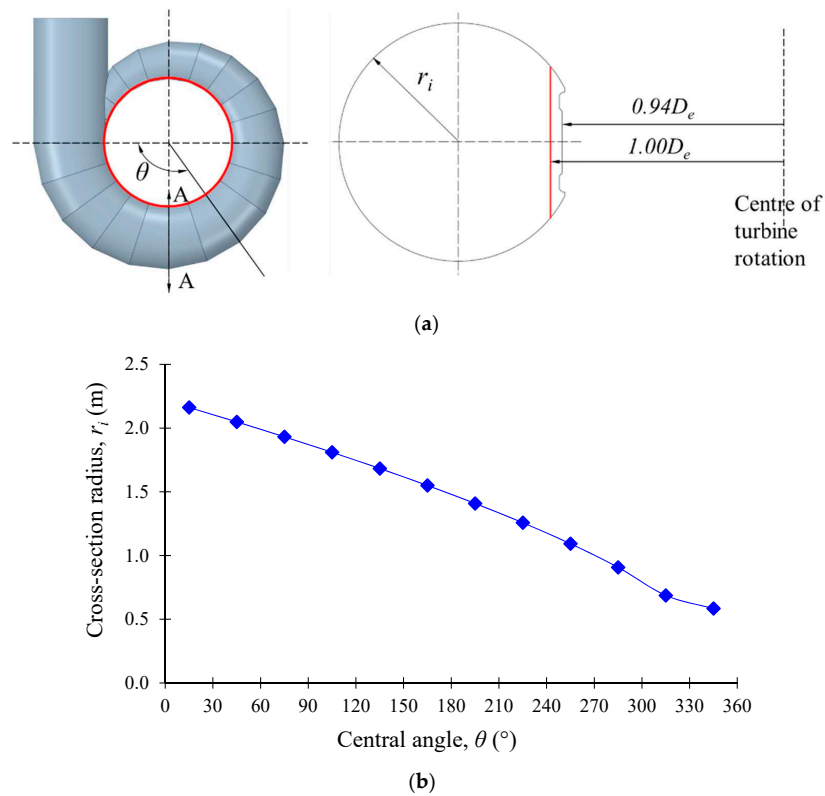


Figure 4. (a) Parametric design and (b) initial cross-section radius of casing (red line indicates measuring location).

2.1.5. Draft Tube Design with J-Groove Installation

The diffuser angle of the draft tube is generally determined in the range of 3° to 10° for minimum energy loss, which is an important design parameter for the discharge pressure recovery and flow uniformity in the draft tube [25]. The conceptual design of the draft tube shows that the diffuser angle of 3.5° provides maximum pressure recovery. Figure 5 shows the technical design of the draft tube. Moreover, in the case of the off-design condition, there exists swirl flow in the draft tube of the Francis hydro turbine, and J-Grooves can be an effective countermeasure of the flow instability in the draft tube [10]. J-Grooves are the grooves that are installed on the draft tube inner wall of the Francis turbine. The design parameters of the J-Groove are defined as angle (θ_{JG}), length (l_{JG}), depth (d_{JG}) and number (n_{JG}), which are shown in Figure 6. The J-Groove is used to suppress the swirl flow in the draft tube by the reverse flow mechanism through the J-Groove passage [11].

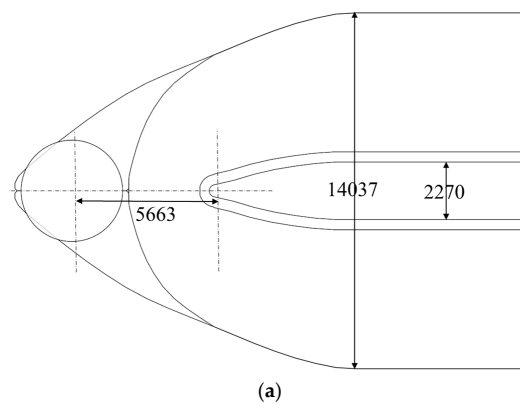


Figure 5. Cont.

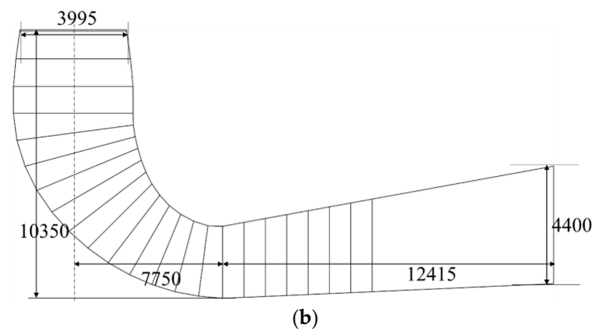


Figure 5. (a) Top view and (b) side view of draft tube (all dimensions are in mm).

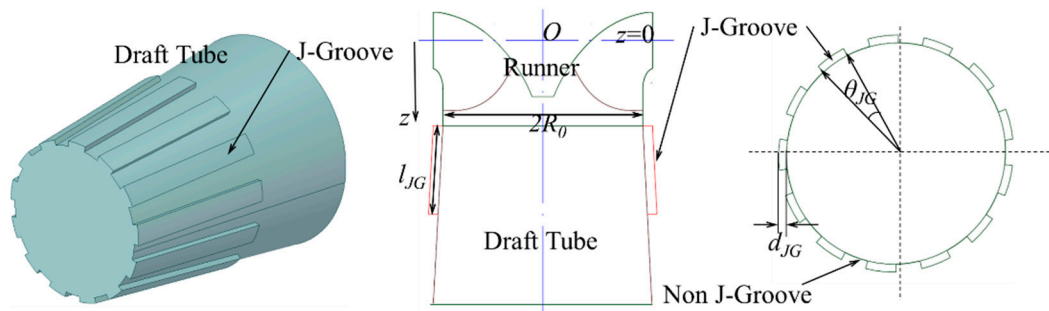


Figure 6. J-Groove shape install on the draft tube inner wall and design parameters.

The parametric design for the J-Groove is represented in Equation (6).

$$d_{DT} = [d_{JG}, \theta_{JG}, l_{JG}, n_{JG}]^T, \tag{6}$$

where d_{DT} is the design variable matrix of the J-Groove, d_{JG} is the J-Groove depth, θ_{JG} is the J-Groove angle, l_{JG} is the J-Groove length and n_{JG} is the number of J-Grooves.

The grooves are evenly distributed in the circumference of the draft tube. Therefore, the number of J-Grooves can be calculated as in Equation (7). The initial shape of the J-Groove is defined as $d_{JG} = 106$ mm, $l_{JG} = 2000$ mm, $\theta_{JG} = 12^\circ$ and $n_{JG} = 15$.

$$n_{JG} = \frac{180^\circ}{\theta_{JG}} \tag{7}$$

2.2. Optimization Methodology

2.2.1. Process of Shape Optimization

The optimization process for the shape optimization of Francis hydro turbine fixed flow passages is illustrated in Figure 7. The design of experiments (DOE) was generated by using the optimal-space filling (OSF) method. The optimization for the fixed flow passages was carried out by using response surface methodology (RSM) and multi-objective genetic algorithm (MOGA). RSM is considered a sensitivity analysis tool, which is used to improve the sensitivity between the objective functions and input parameters [26]. RSM can be expressed as in Equation (8). The RSM uses a first-order and second-order polynomial form to develop the precise and concise correlation model, and the mathematical expressions of RSM are shown in Equations (9) and (10):

$$y = f(x_1, x_2, \dots, x_n) + e \tag{8}$$

$$y = \alpha + \sum_{i=1}^n \alpha_i x_i + e_1 \tag{9}$$

$$y = \alpha + \sum_{i=1}^n \alpha_i x_i + \sum_{i=1}^n \alpha_{ii} x_i^2 + \sum_{i=1}^{n-1} \sum_{j=i+1}^n \alpha_{ij} x_i x_j + e_2 \quad (10)$$

where y is the response of the system, x_1, x_2, \dots, x_n are the independent variables and e is the error, x_i is the i th input parameter, α is the coefficient of the response surface.

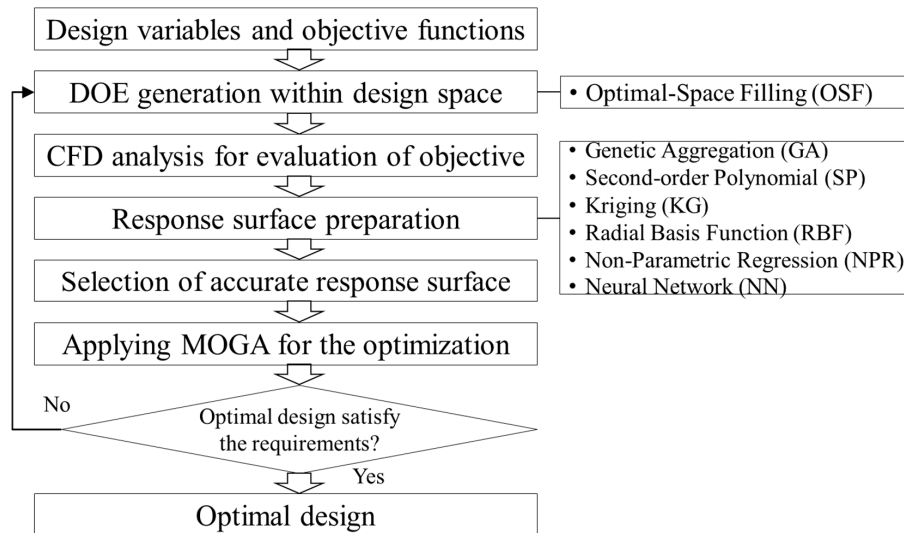


Figure 7. Optimization workflow for the 100 MW class Francis hydro turbine fixed flow passages. (DOE is Design of experiment and MOGA is Multi-Objective Genetic Algorithm).

RSM was used to decrease the computational cost in the optimization process. The response surface for the objective functions can be generated by using various RSMs such as genetic aggregation (GA) [27], radial basis function (RBF) [28], polynomial response surface (PRS) [29], Kriging (KG) [30], non-parametric regression (NPR) [31], neural network (NN) [32]. All these methodologies have their pros and cons. The selection of the RSM is based on the accuracy and consistency of the methodology. Among different RSMs, the accuracy is measured by using the goodness of fit test. The goodness of fit test can be calculated by using the coefficient of determination (CoD), maximum relative residual (MRR) and root mean square error (RMSE), which are expressed in Equations (11)–(13).

$$CoD = 1 - \frac{\sum_{i=1}^{n_s} (y_i - \hat{y}_i)^2}{\sum_{i=1}^{n_s} (y_i - \bar{y})^2} \quad (11)$$

$$MRR = \max_i \left[Abs \left(\frac{y_i - \hat{y}_i}{\bar{y}} \right) \right] \quad (12)$$

$$RMSE = \sqrt{\frac{1}{n_s} \sum_{i=1}^{n_s} (y_i - \hat{y}_i)^2} \quad (13)$$

where n_s is the number of verification points, y_i is the response from CFD analyses, \hat{y}_i is the corresponding response from the surrogate model and \bar{y} is the arithmetic mean of y_i . The verification points are used to evaluate Equations (11)–(13). If the result of the goodness measure shows $CoD = 100\%$, $MRR = 0\%$ and $RSME = 0\%$, it means that the response surface is highly precise and accurate.

The goodness measures concluded that the genetic aggregation was most suitable for the approximation of response surface, compared to other RSMs. The results of the goodness of fit test are shown in Table 2. Therefore, in this study, the genetic aggregation method was implied for the preparation of the response surface. The optimization was carried out using MOGA. Table 3 indicates the setting criteria for the optimization process.

Table 2. Results of goodness of fit test. (CoD is Coefficient of Determination, MRR is Maximum Relative Residual, RMSE is Root Mean Square Error).

Goodness Measure	RSM	Stay Vane			Casing		Draft Tube		
		$\eta(d_{SV})$	$\gamma(d_{SV})$	$H_I(d_{SV})$	$\gamma(d_{CA})$	$H_I(d_{CA})$	$\eta(d_{JC})$	$S(d_{JC})$	$H_I(d_{DT})$
CoD	GA	98%	97%	90%	98%	98%	100%	97%	99%
	SP	98%	96%	89%	100%	99%	77%	95%	77%
	KG	100%	100%	100%	100%	100%	100%	100%	100%
	RBF	100%	100%	100%	100%	100%	100%	100%	100%
	NPR	99%	99%	100%	100%	100%	100%	100%	100%
	NN	99%	98%	92%	88%	89%	28%	77%	34%
MRR	GA	0.19%	2.28%	3.57%	0.16%	8.50%	0.13%	0.19%	9.56%
	SP	0.10%	3.04%	35.74%	0.13%	31.20%	0.11%	0.69%	16.65%
	KG	0.09%	1.86%	42.96%	0.42%	20.06%	0.23%	2.94%	18.08%
	RBF	0.09%	0.09%	57.45%	0.10%	17.83%	0.13%	0.94%	14.05%
	NPR	0.19%	1.97%	38.10%	0.52%	9.78%	0.08%	0.88%	10.11%
	NN	0.15%	1.47%	28.3%	0.54%	20.13%	0.05%	0.65%	6.17%
RMSE	GA	0.01%	0.51%	0.02%	0.03%	1.46%	0.01%	0.02%	0.01%
	SP	0.01%	1.36%	0.04%	0.13%	31.20%	0.01%	0.06%	0.02%
	KG	0.01%	0.89%	0.05%	0.42%	20.06%	0.06%	0.09%	0.07%
	RBF	0.01%	0.06%	0.04%	0.10%	17.83%	0.01%	0.06%	0.01%
	NPR	0.02%	1.37%	0.04%	0.38%	7.54%	0.01%	0.06%	0.01%
	NN	0.01%	0.82%	0.03%	0.35%	16.51%	0.03%	0.04%	0.01%

Table 3. Information of setting criteria for MOGA.

Parameter	Value
Number of initial samples	300
Maximum number of cycles	30
Number of samples per cycle	100
Crossover probability	0.95
Mutation probability	0.05
Maximum allowable Pareto percentage	97
Convergence stability percentage	2

2.2.2. Process of Stay Vane Shape Optimization

In this study, the turbine efficiency $\eta(d_{SV})$, flow uniformity $\gamma(d_{SV})$, head loss $H_I(d_{SV})$, effective head $H(d_{SV})$, and flow rate $Q(d_{SV})$ were considered for the evaluation of stay vane design as in Equations (14)–(18). The measurement locations of the flow uniformity at SV_{out} and head loss are calculated by the difference between the total pressure at SV_{in} and SV_{out} , as shown in Figure 3.

$$\eta(d_{SV}) = \left[\frac{\tau\omega}{\rho g Q H} \right] \times 100\% \quad (14)$$

$$\gamma(d_{SV}) = \left[1 - \oint \frac{\sqrt{(\bar{u} - u)^2}}{2A\bar{u}} dA \right] \times 100\% \quad (15)$$

$$H_I(d_{SV}) = \frac{\Delta p_{total@SV}}{\rho g} \quad (16)$$

$$H(d_{SV}) = \frac{p_{inlet}^t - p_{outlet}^t}{\rho g} \quad (17)$$

$$Q(d_{SV}) = \frac{m_{outlet}}{\rho} \quad (18)$$

where τ is torque generated by runner (Nm) and ω is rotational speed of runner (rad/s). \bar{u} is the average velocity in stay vane passage (m/s), u is the local velocity in stay vane passage (m/s) and A is the

cross-section area of stay vane passage (m²). $\Delta p_{total@SV}$ is the change in total pressure in stay vane passage (Pa), p_{inlet}^t and p_{outlet}^t are total pressures at inlet and outlet of the turbine (Pa). m_{outlet} is mass flow rate of water at the turbine outlet (kg/s).

The optimization formulation for the stay vane is elaborated as in Equation (19).

$$\begin{aligned}
 & \text{maximize } \eta(d_{SV}), \gamma(d_{SV}) \\
 & \text{minimize } H_l(d_{SV}) \\
 & \text{subject to } 80 \text{ m} \leq H(d_{SV}) \leq 95 \text{ m} \\
 & 120 \text{ m}^3/\text{s} \leq Q(d_{SV}) \leq 135 \text{ m}^3/\text{s} \\
 & d_{SV}^L \leq d_{SV} \leq d_{SV}^U
 \end{aligned} \tag{19}$$

where d_{SV}^L and d_{SV}^U are lower and upper bounds for the design variable d_{SV} , respectively, and their values are summarized in Table 4. The turbine efficiency $\eta(d_{SV})$ and flow uniformity $\gamma(d_{SV})$ were maximized to obtain more output power, while vortex-induced vibration was suppressed. At the same time, the head loss $H_l(d_{SV})$ was minimized to prevent loss of power in the stay vane. The effective head $H(d_{SV})$ and flow rate $Q(d_{SV})$ of the turbine were used as constraints for the stay vane design.

Table 4. Bounds for design variables of stay vane.

Design Variable	Lower Bound (d_{SV}^L)	Upper Bound (d_{SV}^U)
α_1	26°	32°
α_2	29°	36°
α_3	34°	42°
α_4	32°	39°
α_5	30°	36°
δ_1	40 mm	52 mm
δ_2	120 mm	155 mm
δ_3	135 mm	155 mm
δ_4	95 mm	120 mm
δ_5	25 mm	35 mm
a_{le}, a_{te}	0.7	1.25

The optimal Pareto front for the stay vane design is shown in Figure 8. The Pareto front is plotted between turbine efficiency and flow uniformity. The trade-off between turbine efficiency and flow uniformity is required to obtain the optimal design of stay vane. Flow uniformity is measured at the outlet of the stay vane. The measuring location plays a vital role in the calculation of flow uniformity. If the measuring location changes, the nature of the Pareto front will change. The main objective of the design optimization is to have smooth flow distribution in the stay vane flow passage. The flow uniformity of the optimal stay vane should be above 90%. Based on the above assumptions, the optimal stay vane (OSV) was selected with flow uniformity 91.97% and turbine efficiency 96.37%.

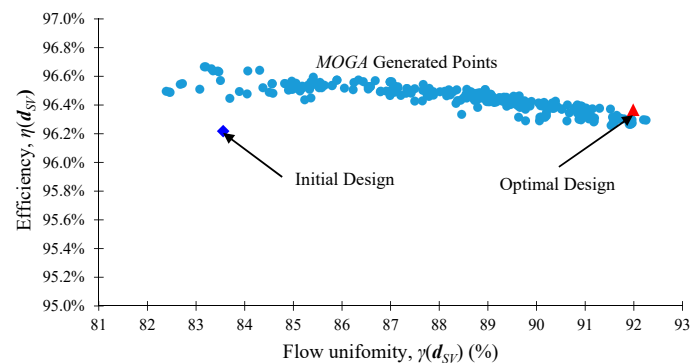


Figure 8. Pareto front for the optimization of stay vane design.

2.2.3. Process of Casing Shape Optimization

In order to evaluate the flow condition in the casing, the flow uniformity $\gamma(\mathbf{d}_{CA})$ and head loss $H_l(\mathbf{d}_{CA})$ were examined. The flow uniformity, which determines the deviation of flow velocity in the casing shape, is calculated as in Equation (20). The flow uniformity was measured as an averaged value at the location of the whole casing outlet of $1.00 D_e$ from the runner axis center, which is shown in Figure 4a by a red circle. The head loss was defined by the losses in the spiral casing passage due to flow mixing and wall friction, as in Equation (21), and the head loss was calculated by the difference between inlet and outlet of casing.

$$\gamma(\mathbf{d}_{CA}) = \left[1 - \oint \frac{\sqrt{(\bar{u} - u)^2}}{2A\bar{u}} dA \right] \times 100\% \quad (20)$$

$$H_l(\mathbf{d}_{CA}) = \frac{\Delta p_{total@casing}}{\rho g} \quad (21)$$

where \bar{u} is the average velocity in casing passage (m/s), u is the local velocity in casing passage (m/s), and A is the cross-section area of casing passage (m^2), $\Delta p_{total@casing}$ is change in total pressure in casing passage (Pa).

The design optimization problem of the casing is formulated as in Equation (22).

$$\begin{aligned} & \text{maximize } \gamma(\mathbf{d}_{CA}) \\ & \text{minimize } H_l(\mathbf{d}_{CA}) \\ & \text{subject to } \gamma(\mathbf{d}_{CA}) \geq 97\% \\ & \mathbf{d}_{CA}^L \leq \mathbf{d}_{CA} \leq \mathbf{d}_{CA}^U \end{aligned} \quad (22)$$

where \mathbf{d}_{CA}^L and \mathbf{d}_{CA}^U are lower and upper bounds for the design variable \mathbf{d}_{CA} , respectively.

The bounds for design variables of the casing are shown in Table 5. The Pareto front for the casing shape optimization was prepared by using head loss and flow uniformity. Figure 9 shows the Pareto front for the optimization of the casing. The Pareto front shows the trade-off between flow uniformity and head loss. Thus, the selection of the optimal design is based on the requirement of the user. In this study, the main objective was to increase the flow uniformity above 97%. Therefore, the optimal design was selected considering flow uniformity above 97% with minimum head loss.

Table 5. Bounds for design variables of casing.

Design Variable	Lower Bound (\mathbf{d}_{CA}^L)	Upper Bound (\mathbf{d}_{CA}^U)
r_0	1900 mm	2400 mm
r_1	1800 mm	2300 mm
r_2	1700 mm	2200 mm
r_3	1600 mm	2000 mm
r_4	1500 mm	1900 mm
r_5	1350 mm	1750 mm
r_6	1250 mm	1600 mm
r_7	1100 mm	1400 mm
r_8	950 mm	1250 mm
r_9	800 mm	1000 mm
r_{10}	600 mm	800 mm
r_{11}	500 mm	700 mm

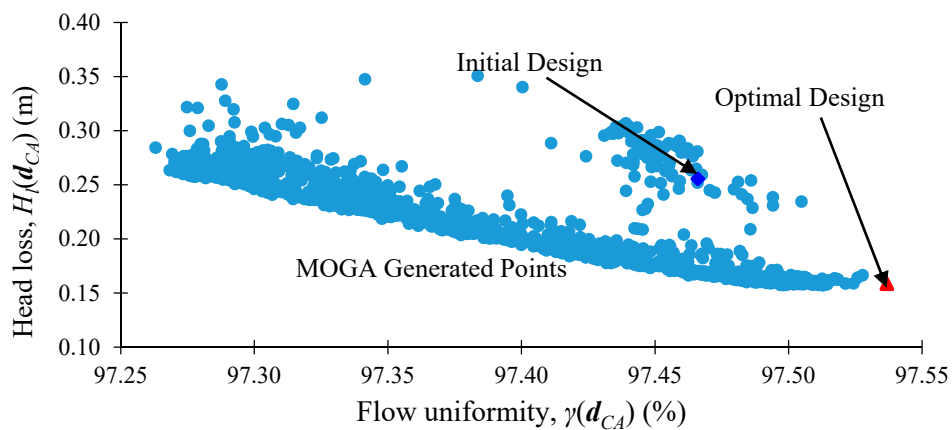


Figure 9. Pareto front for the optimization results of casing design.

2.2.4. Process of Draft Tube Shape Optimization

The optimization was carried out to obtain the optimal solution for the draft tube shape with the J-Groove installation. The turbine efficiency $\eta(d_{DT})$, swirl intensity $S(d_{DT})$, head loss $H_I(d_{DT})$, effective head $H(d_{DT})$, and flow rate $Q(d_{DT})$ were considered for the evaluation of draft tube shape design, as in Equations (23)–(25). The measurement locations of the swirl intensity were set in the range of $z/R_0 = 1.15$ to 3.60 , as shown in Figure 6.

$$\eta(d_{DT}) = \left[\frac{\tau\omega}{\rho g Q H} \right] \times 100\% \tag{23}$$

$$S(d_{DT}) = \frac{\int v_\theta v_a r^2 dr}{R \int v_a^2 r dr} \tag{24}$$

$$H_I(d_{DT}) = \frac{\Delta p_{total@JG}}{\rho g} \tag{25}$$

where τ is torque generated by runner (Nm), ω is rotational speed of runner (rad/s), $\rho = 997 \text{ kg/m}^3$ is the density of water at $25 \text{ }^\circ\text{C}$, $g = 9.81 \text{ m/s}^2$ is gravitational acceleration, Q is the flow rate (m^3/s), and H is the effective head (m), v_θ is the local tangential velocity in the draft tube (m/s), v_a is the local axial velocity in the draft tube, r is the radial position, R is the cross-section radius, $\Delta p_{total@JG}$ is the change in total pressure in draft tube passage (Pa), z is the vertical distance from the axis of turbine, R_0 is the runner outlet radius.

In order to investigate the flow instability and to express the complicated and unique internal flow behavior in the draft tube effectively, swirl intensity $S(d_{DT})$ was adopted to determine the strength of swirl flow in the draft tube. The swirl intensity represents the ratio of the axial flux of angular momentum to axial momentum, as shown in Equation (24).

The optimization formulation for the draft tube is elaborated as in Equation (26).

$$\begin{aligned} & \text{maximize } \eta(d_{DT}) \\ & \text{minimize } S(d_{DT}), H_I(d_{DT}) \\ & \text{subject to } 80 \text{ m} \leq H(d_{DT}) \leq 95 \text{ m} \\ & 120 \text{ m}^3/\text{s} \leq Q(d_{DT}) \leq 135 \text{ m}^3/\text{s} \\ & d_{DT}^L \leq d_{DT} \leq d_{DT}^U, \end{aligned} \tag{26}$$

where d_{DT}^L and d_{DT}^U are lower and upper bounds for the design variable d_{DT} , respectively, and their values are summarized in Table 6. The turbine efficiency $\eta(d_{DT})$ was maximized to obtain more output power. At the same time, the swirl intensity $S(d_{DT})$ and head loss $H_I(d_{DT})$ were minimized to suppress

the swirl flow and prevent energy loss in the draft tube flow passage. The effective head $H(d_{DT})$ and flow rate $Q(d_{DT})$ of the turbine were used as constraints for the draft tube design, which are expressed as in Equations (17) and (18), respectively.

Table 6. Bounds for design variables of draft tube shape.

Design Variable	Lower Bound (d_{DT}^L)	Upper Bound (d_{DT}^U)
d_{JG}	50 mm	200 mm
θ_{JG}	8°	20°
l_{JG}	1500 mm	3000 mm
n_{JG}	9	21

The lower and upper limits of draft tube design variables are indicated in Table 6.

The optimization of the draft tube design was carried out at the design point. The Pareto front was prepared by the trade-off between turbine efficiency and swirl intensity, which is shown in Figure 10.

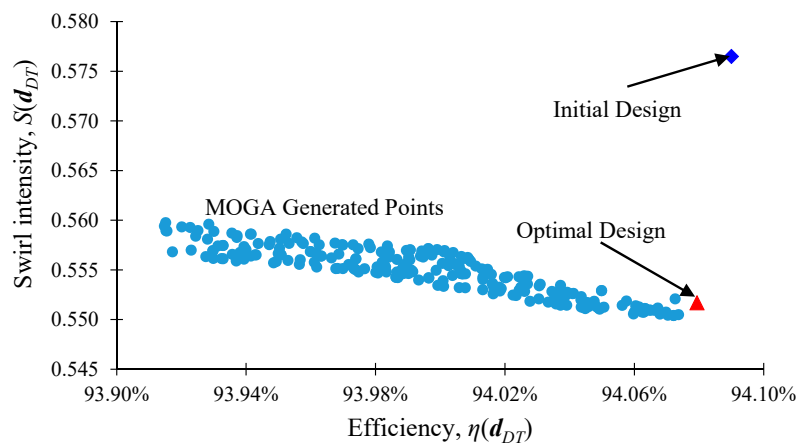


Figure 10. Pareto front for optimization of draft tube design at the design point.

3. CFD Methodology

The CFD analysis for the turbomachinery requires a highly reliable computational system for the calculation of complex internal flow phenomena. Moreover, while conducting the optimization, numerous samples are needed, which demand extensive computational cost and time for CFD analysis. Figure 11 shows the numerical scheme of CFD analysis adopted in this study, in combination with the optimal design process. The CFD analysis process is directly connected to the optimum design process. The CFD analysis method was adopted from previous studies [33–35].

The CFD analysis for the casing DOE samples was performed without stay vanes because the flow field in the spiral casing is independent of the flow field of the stay vane [36]. Furthermore, the single flow passage analysis for the stay vane was used for the calculation of DOE. It provides precise CFD analysis results and reduces the computation time. However, the full domain analysis was required for the DOE of the draft tube with the J-Groove installation because the flow field in the J-Groove is dependent on other components of the Francis hydro turbine.

The CFD analysis was conducted using a commercial code of ANSYS CFX 19.2 [37]. The numerical analysis was performed by solving the governing equations and Reynolds-averaged Navier–Stokes (RANS) with the turbulence model. In this study, the Shear Stress Transport (SST) turbulence model was selected because the SST model combines the capabilities of the $\kappa\text{-}\omega$ model away from the walls and the robustness of the $\kappa\text{-}\epsilon$ turbulence near the walls by using blending functions of the automatic near-wall treatment. The Rhie–Chow algorithm was used to interpolate the pressure–velocity coupling mechanism. The high-resolution order was used to solve the advection term, and the first-order upwind difference was used to solve the turbulence numeric [37].

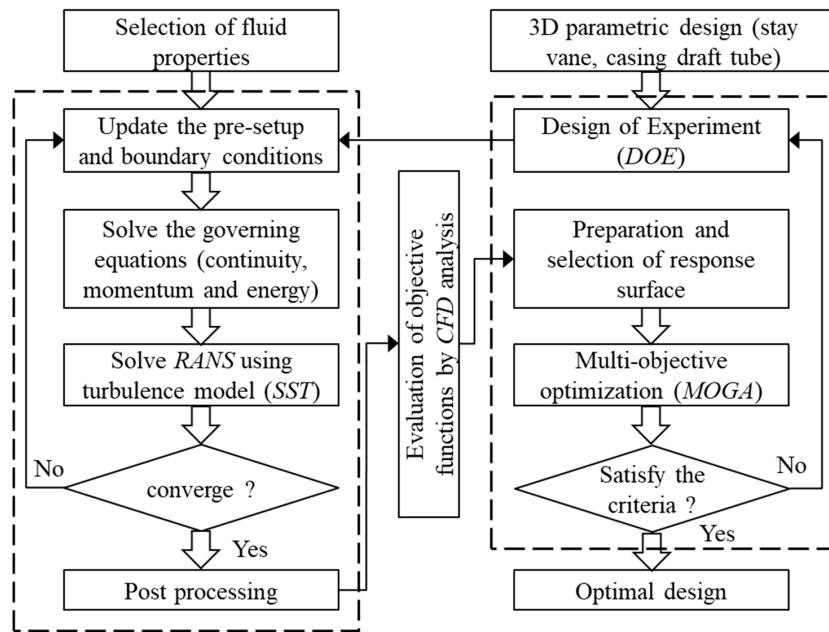


Figure 11. Numerical scheme of CFD analysis in combination with optimal design process (RANS is Reynolds-averaged Navier-Stokes).

The proper numerical grids are required for precise and accurate computational analysis. The structured mesh for the numerical analysis was generated using ANSYS ICEM 19.2 [37]. The numerical grids for the 100 MW class Francis hydro turbine are shown in Figure 12. The mesh dependence test was carried out to determine the optimum number of nodes. The results of the mesh dependence were compared with efficiency and output power. Figure 13 shows the mesh dependence test results, and we concluded that 8.2 million nodes was the optimum number for computational analysis. Table 7 presents the information on the numerical grids used for CFD analysis. The non-dimensional wall distance y^+ values for the several components of the Francis hydro turbine were less than 100, which was suitable for the SST turbulence model with automatic near-wall treatment within the reliable resolution range of $1 < y^+ < 100$. Table 8 shows the summary of boundary conditions for CFD analysis. The performance curves of the 100 MW Francis hydro turbine are shown in Figure 14. The performance curves indicated that the design point and best efficiency point were matched well. They verified that the conceptual design of the 100 MW Francis hydro turbine was acceptable.

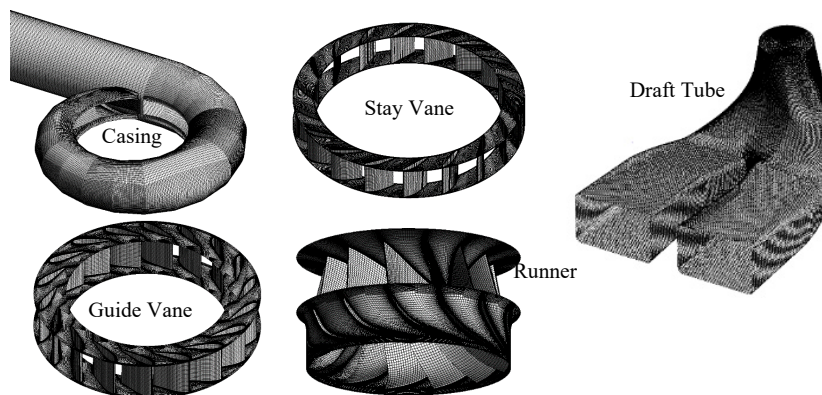


Figure 12. Numerical grids of the 100 MW class Francis turbine.

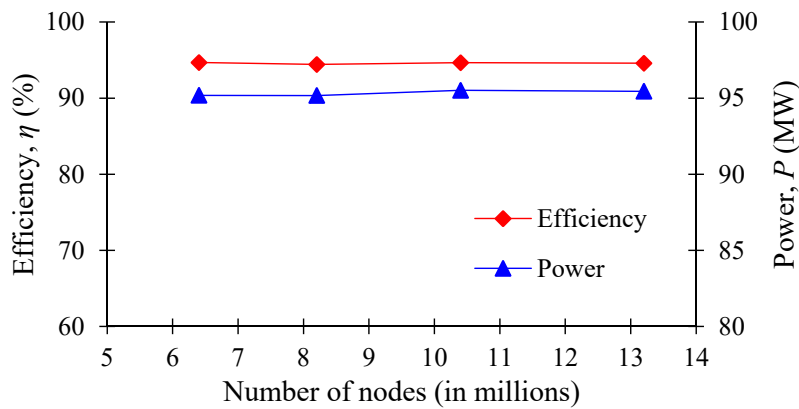


Figure 13. Mesh dependency test results for CFD analysis.

Table 7. Numerical grids information.

Components	Node Number	Mesh Size (mm)	Y + Value
Casing	435,922	7.5	29.5
Stay Vane	1,561,220	2.5	22.9
Guide Vane	2,520,000	3.0	34.3
Runner	2,294,595	5.0	84.2
Draft Tube	1,428,835	9.0	14.4
Total	8,240,572		

Table 8. Summary of boundary conditions for CFD analysis.

Parameter/Boundary	Condition/Value
Inlet	Total Pressure
Outlet	Static Pressure
Rotational speed	180 min ⁻¹
Turbulence model	Shear Stress Transport (SST)
Grid interface connection	General Grid Interface (GGI)
Physical time scale	Steady State/0.0531 s
Time step	Unsteady State/0.00185 s (2° per time step for 1 revolutions)
Interface model	Steady State/Frozen rotor Unsteady State/Transient rotor stator
Walls	No slip wall (roughness: smooth)

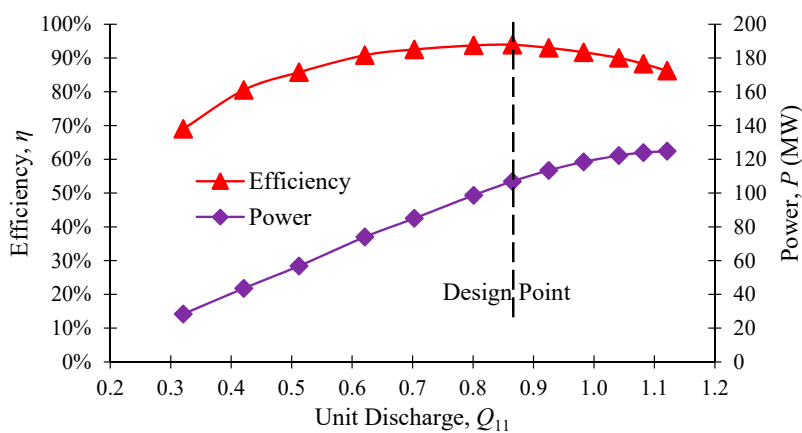


Figure 14. Validation of conceptual design of the 100 MW Francis hydro turbine by CFD analysis.

4. Results and Discussion

4.1. Stay Vane Shape Optimization

Figure 15 shows the comparison of the vane angle and thickness between the initial stay vane (ISV) and optimal stay vane (OSV) shapes. The inlet vane angle was changed from 30° to 32°. The position for the maximum thickness was modified from the normalized distance of 0.4 to 0.3. The maximum thickness was increased from 150 mm to 158 mm. The 3D view of the initial and optimal stay vane shapes are shown in Figure 15. Table 9 shows the results of stay vane optimization for the 100 MW class Francis turbine. The targeted objectives of turbine efficiency, flow uniformity and head loss were all improved remarkably.

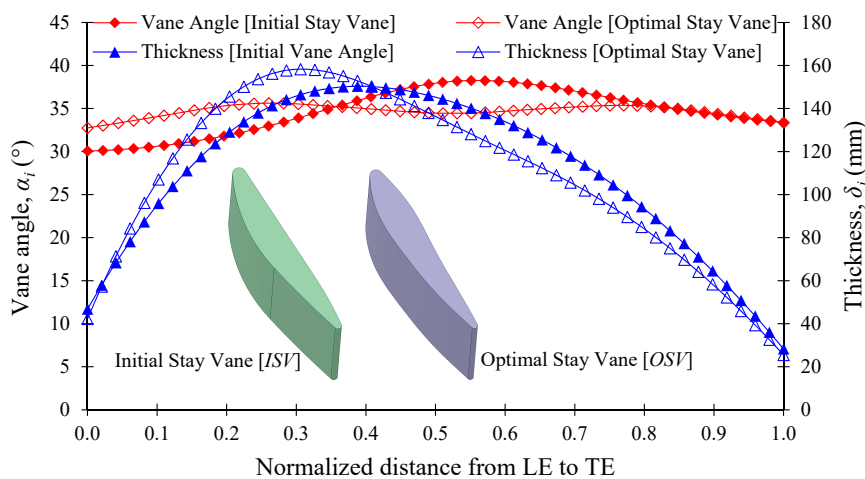


Figure 15. Comparison of initial and optimal stay vane designs for the 100 MW class Francis turbine.

Table 9. Results of stay vane optimization for the 100 MW class Francis turbine.

Parameter	Initial Stay Vane (ISV)	Optimal Stay Vane (OSV)
Head (m)	89.23	89.23
Flow Rate (m ³ /s)	130.36	130.64
Power (MW)	106.95	107.23
Efficiency (%)	93.91	93.96
Flow Uniformity (%)	91.73	95.04
Head Loss (m)	0.438	0.403

The flow uniformity was measured at the outlet of the stay vane. The flow uniformity encountered the average deviation of local velocity in the reference area. The flow deviation in the small section did not show a significant effect on flow uniformity. Therefore, flow angle distribution and vorticity were evaluated for internal flow patterns in stay vane passage. The comparison of the flow angle between the ISV and OSV is shown in Figure 16. The flow angle (θ_u) is defined by Equation (27).

$$\theta_u = \tan^{-1}\left(\frac{v_\theta}{v_r}\right) \quad (27)$$

where v_θ and v_r are tangential and radial velocity components.

Figure 16 shows the comparison of flow angle in the ISV and OSV at the design point. The peak value of the flow angle at the hub and shroud indicated the occurrence of the secondary flow near the hub and shroud walls. The flow angle difference in the passage between the outlet of stay vane and inlet of guide vane in the OSV became remarkably smaller than that of the ISV. It meant that the OSV had a relatively larger ability to maintain a proper flow angle. The smaller difference caused the lower vorticity in the passage between the stay vane and guide vane in the OSV.

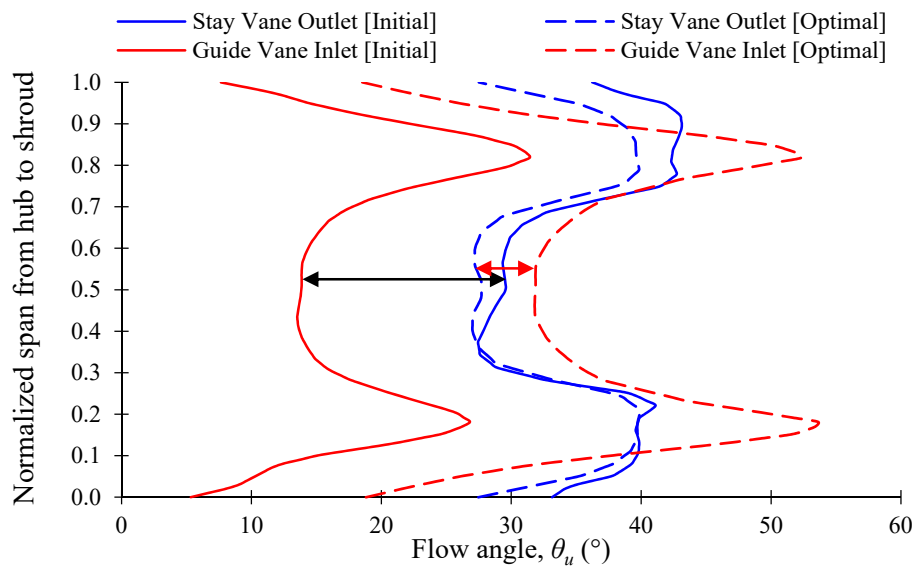


Figure 16. Comparison of flow angle in the ISV and OSV at the design point.

Figure 17 shows the strength of vorticity in between the cascade passages of the stay vane and guide vane. The decrease in the vorticity at the OSV flow passage made the flow smoother. Thus, the possibility of occurrence of secondary flow and vortices at the OSV flow passage decreased significantly in the OSV. Therefore, the OSV made a more uniform flow distribution in the vane’s passage.

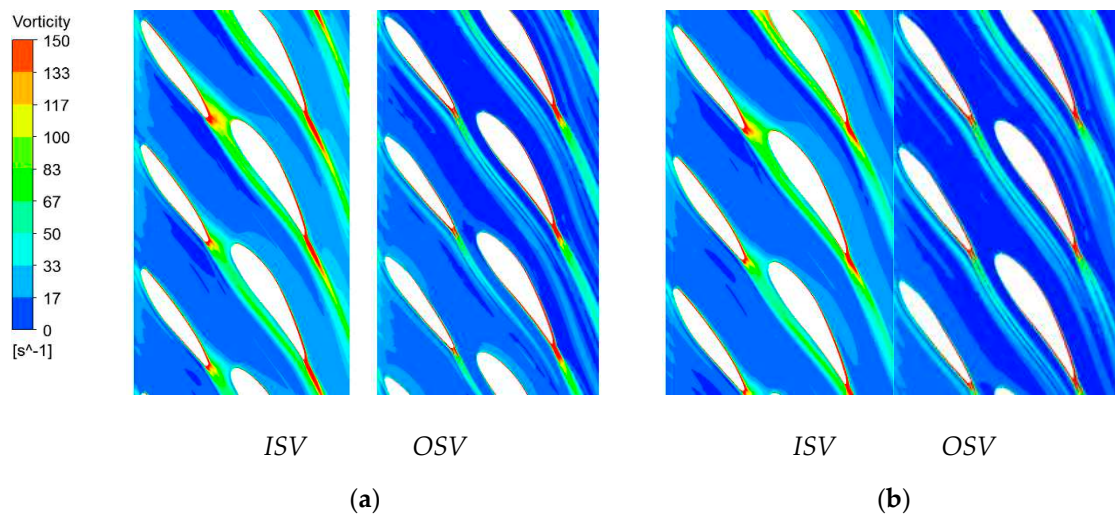


Figure 17. Comparison of vorticity in ISV and OSV flow passages (a) 0.25 span and (b) 0.75 span at design point.

4.2. Casing Shape Optimization

Figure 18 indicates the cross-section radius comparison between the initial and optimal shape of the casing. The cross-section radius of the optimal casing shape was greater than the initial casing shape at the central angles below $\theta = 180^\circ$, but the cross-section radius near the casing tongue of $\theta = 345^\circ$ was almost the same.

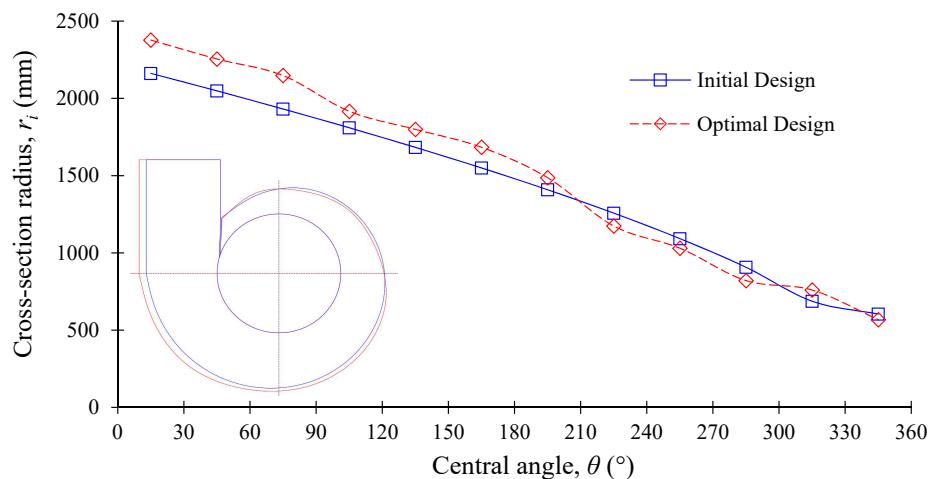


Figure 18. Comparison of initial and optimal casing design for the 100 MW class Francis turbine.

Table 10 shows the flow uniformity and head loss by the initial and optimal casing shapes, which was compared to the design point. The flow uniformity increased slightly in the optimal casing in comparison with that of the initial casing shape; furthermore, the optimal casing design showed a significant decrease in the head loss in comparison with that of the initial casing design.

Table 10. Results of casing optimization for the 100 MW class Francis turbine.

Parameter	Initial Design	Optimal Design
Flow Uniformity (%)	97.46	97.51
Head Loss (m)	0.256	0.145

The secondary vortex intensity J_{ABS}^n was used to evaluate the internal flow behavior in the casing quantitatively. The area integral of vorticity around the casing was calculated as defined in Equation (28).

$$J_{ABS}^n = \frac{1}{A} \iint_0^A |\nabla \times \vec{u}^n| dA \quad (28)$$

where \vec{u}^n is the velocity at normal direction to the cross section, A is the cross section area.

Figure 19 shows the comparison of secondary vortex intensity between the initial and optimal casing designs. The secondary vortex intensity is in increasing order from the inlet to the casing tongue. The vortex intensity was suppressed significantly by optimal design in comparison to the initial casing shape. Therefore, it was clear that the flow uniformity and head loss could be improved effectively by the current optimum design process.

4.3. Draft Tube Shape Optimization

Table 11 shows the comparison of the design parameter sizes of the J-Grooves for draft tube shape optimization. The 3D model of the J-Grooves installed on the draft tube wall is shown in Figure 20.

Table 11. Comparison of design parameter size of J-Grooves for draft tube shape optimization.

Design Parameter of J-Groove	Initial Size	Optimal Size
Length, l_{JG} (mm)	2000	2455.5
Depth, d_{JG} (mm)	106	169
Angle, θ_{JG} (°)	12	8.7
Number, n_{JG}	15	21

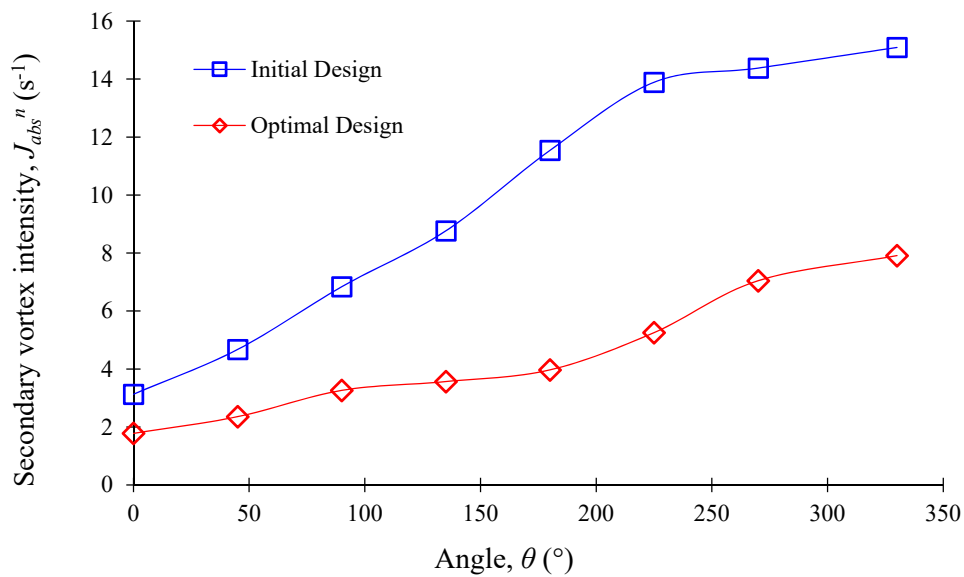


Figure 19. Comparison of secondary vortex intensity between initial and optimal casing designs.

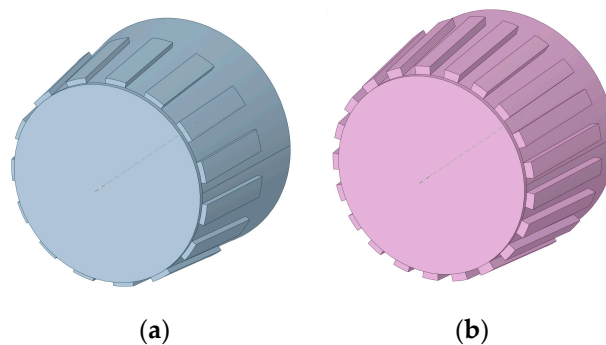


Figure 20. Comparison between (a) initial (b) optimal J-Groove models installed on the draft tube walls.

Figure 21 shows the comparison of the swirl intensity in the draft tube by J-Groove shapes at the design point. The swirl intensity was suppressed significantly with the installation of J-Groove. There was a 12.12% swirl intensity reduction with initial J-Groove installation from the case without J-Groove installation. Moreover, the additional 6.64% swirl intensity reduction was achieved by the optimized J-Groove shape from the initial J-Groove shape. Therefore, it was clear that the installation of an optimal J-Groove in the draft tube had a significant effect on the suppression of the flow instability caused by the swirl flow. Table 12 reveals the results summary of the draft tube shape optimization. The study results indicated that the installation of the J-Groove on the wall of the draft tube had almost no influence on the turbine performance but suppressed the flow instability of the swirl flow remarkably.

Table 12. Summary of draft tube shape optimization results for the 100 MW class Francis turbine.

Parameters	Without J-Groove	Initial J-Groove	Optimal J-Groove
Head (m)	88.41	88.40	88.42
Flow Rate (m^3/s)	125.4	125.53	125.50
Power (MW)	102.16	101.79	102.1
Efficiency (%)	94.12	94.09	94.08
Swirl Intensity Reduction (%) at $z/R_0 = 2.25$		12.12	18.79

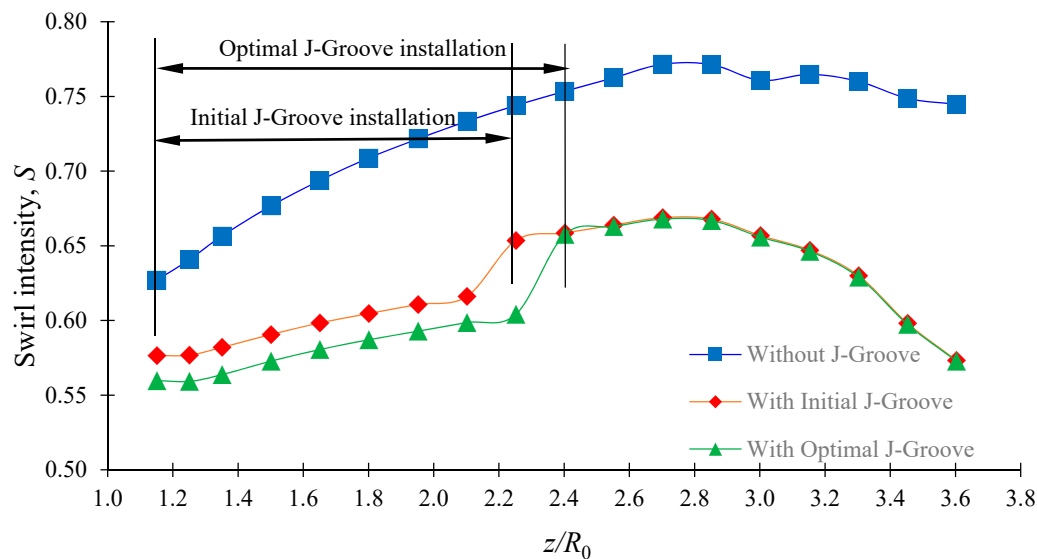


Figure 21. Comparison of swirl intensity in the draft tube by J-Groove shapes at the design point.

5. Conclusions

In the present study, the fixed flow passage shapes of a 100 MW class Francis hydro turbine were optimized for the internal flow uniformity by a CFD-based shape design optimization process. The stay vane, casing, and draft tube were optimized separately to understand the flow characteristics in each flow passage. The objective of the optimization was to maximize the flow uniformity and minimize the head loss in each flow passage.

A CFD-based shape design optimization process of the parametric conceptual design, detailed design, and optimal design of the fixed flow passage of the Francis hydro turbine was accomplished. The design and optimization process can be generalized for the reaction hydro turbine stay vane, casing, and draft tube with J-Grooves. Moreover, better flow uniformity was achieved in the Francis hydro turbine by the fixed flow passages optimization process. For the optimization process, response surface methodology was used to generate the response surface, and a multi-objective genetic aggregation method was used to determine the global optimum solution via the optimal Pareto front.

The optimum stay vane shape was achieved with the remarkably decreased vorticity around the stay vane flow passage, which resulted in the highly improved flow uniformity in the vane passage. The optimal casing passage shape was achieved with the increased flow uniformity and the significantly decreased head loss in comparison with that of the initial casing shape. The secondary vortex intensity was suppressed effectively by casing shape optimization. The installation of a J-Groove on the wall of the draft tube had almost no influence on the turbine performance but suppressed the flow instability of swirl flow remarkably in the draft tube passage.

Author Contributions: Conceptualization, U.S., and Y.-D.C.; methodology, U.S.; software, Y.-D.C.; validation, U.S. and Y.-D.C.; formal analysis, U.S.; investigation, U.S.; resources, Y.-D.C.; data curation, U.S.; writing—original draft preparation, U.S.; writing—review and editing, U.S. and Y.-D.C.; visualization, U.S.; supervision, Y.-D.C.; project administration, Y.-D.C.; funding acquisition, Y.-D.C. All authors have read and agreed to the published version of the manuscript.

Funding: This work was supported by the New and Renewable Energy of the Korea Institute of Energy Technology Evaluation and Planning (KETEP), which was funded by the Korean Government Ministry of Trade, Industry and Energy (no. 20163010060350).

Conflicts of Interest: The authors declare no conflict of interest.

References

1. Ayancik, F.; Acar, E.; Çelebioğlu, K.; Aradag, S. Simulation-based design and optimization of Francis turbine runners by using multiple types of metamodels. *Proc. Inst. Mech. Eng. Part C J. Mech. Eng. Sci.* **2016**, *231*, 1427–1444. [[CrossRef](#)]
2. Goldwag, E.; Berry, D.G. Von Karman Hydraulic Vortexes Cause Stay Vane Cracking on Propeller Turbines at the Little Long Generating Station of Ontario Hydro. *J. Eng. Power* **1968**, *90*, 213–217. [[CrossRef](#)]
3. Fischer, R.; Gummer, J.; Liess, C. Stay vane vibrations in the Nkula Falls turbines. *Hydropower Dams* **1994**, *1*, 15–20.
4. Kurokawa, J.; Nagahara, H. Flow characteristics in spiral casing of water turbines. In Proceedings of the 13th International Association for Hydraulic Research Symposium on Hydraulic Machinery and Cavitation, Montreal, QC, Canada, 2–5 September 1986.
5. Price, J.W.H. The failure of the Dartmouth turbine casing. *Int. J. Press. Vessel. Pip.* **1998**, *75*, 559–566. [[CrossRef](#)]
6. Sosa, J.B.; Urquiza, G.; García, J.C.; Castro, L.L. Computational fluid dynamics simulation and geometric design of hydraulic turbine draft tube. *Adv. Mech. Eng.* **2015**, *7*, 1–11. [[CrossRef](#)]
7. Favrel, A.; Müller, A.; Landry, C.; Yamamoto, K.; Avellan, F. Study of the vortex-induced pressure excitation source in a Francis turbine draft tube by particle image velocimetry. *Exp. Fluids* **2015**, *56*, 1–15. [[CrossRef](#)]
8. Susan-Resiga, R.; Ciocan, G.D.; Anton, I.; Avellan, F. Analysis of the Swirling Flow Downstream a Francis Turbine Runner. *J. Fluids Eng.* **2006**, *128*, 177–189. [[CrossRef](#)]
9. Susan-Resiga, R.; Muntean, S.; Avellan, F.; Anton, I. Mathematical modelling of swirling flow in hydraulic turbines for the full operating range. *Appl. Math. Model.* **2011**, *35*, 4759–4773. [[CrossRef](#)]
10. Chen, Z.; Singh, P.M.; Choi, Y.-D. Suppression of unsteady swirl flow in the draft tube of a Francis hydro turbine model using J-Groove. *J. Mech. Sci. Technol.* **2017**, *31*, 5813–5820. [[CrossRef](#)]
11. Choi, Y.-D.; Shrestha, U. Cavitation Performance Improvement of an Annular Jet Pump by J-Groove. *KSFM J. Fluid Mach.* **2020**, *23*, 25–35. [[CrossRef](#)]
12. Oh, H.W.; Yoon, E.S. Application of computational fluid dynamics to performance analysis of a Francis hydraulic turbine. *Proc. Inst. Mech. Eng. Part A J. Power Energy* **2007**, *221*, 583–590. [[CrossRef](#)]
13. Goyal, R.; Trivedi, C.; Gandhi, B.K.; Cervantes, M.J. Numerical simulation and validation of a high head model francis turbine at prat load operating condition. *J. Inst. Eng. India Series C* **2018**, *99*, 557–570. [[CrossRef](#)]
14. Escaler, X.; Roig, R.; Hidalgo, V. Sensitivity Analysis of Zwart-Gerber-Belamri Model Parameters on the Numerical Simulation of Francis Runner Cavitation. In Proceedings of the 10th International Symposium on Cavitation (CAV2018), Baltimore, MD, USA, 14–16 May 2018; pp. 911–914.
15. Agnalt, E.; Iliev, I.; Solemslie, B.W.; Dahlhaug, O.G. On the Rotor Stator Interaction Effects of Low Specific Speed Francis Turbines. *Int. J. Rotating Mach.* **2019**, *2019*, 1–11. [[CrossRef](#)]
16. Leguizamón, S.; Avellan, F. Open-Source Implementation and Validation of a 3D Inverse Design Method for Francis Turbine Runners. *Energies* **2020**, *13*, 2020. [[CrossRef](#)]
17. Kaewnai, S.; Wongwiset, S. Improvement of the Runner Design of Francis Turbine using Computational Fluid Dynamics. *Am. J. Eng. Appl. Sci.* **2011**, *4*, 540–547. [[CrossRef](#)]
18. Obrovsky, J.; Krausova, H.; Spidla, J.; Zouhar, J. Development of high specific speed Francis turbine for low head HPP. *Eng. Mech.* **2013**, *20*, 139–148.
19. Wu, J.; Shimmei, K.; Tani, K.; Niikura, K.; Sato, J. CFD-Based Design Optimization for Hydro Turbines. *J. Fluids Eng.* **2007**, *129*, 159–168. [[CrossRef](#)]
20. Shrestha, U.; Choi, Y.-D. Improvement of flow behavior in the spiral casing of Francis hydro turbine model by shape optimization. *J. Mech. Sci. Technol.* **2020**, *34*, 1–10. [[CrossRef](#)]
21. McNabb, J.; Devals, C.; Kyriacou, S.A.; Murry, N.; Mullins, B.F. CFD based draft tube hydraulic design optimization. *IOP Conf. Series Earth Environ. Sci.* **2014**, *22*, 12023. [[CrossRef](#)]
22. Nakamura, K.; Kurosawa, S. Design Optimization of a High Specific Speed Francis Turbine Using Multi-Objective Genetic Algorithm. *Int. J. Fluid Mach. Syst.* **2009**, *2*, 102–109. [[CrossRef](#)]
23. Thum, S.; Schilling, R. Optimization of Hydraulic Machinery Bladings by Multilevel CFD Techniques. *Int. J. Rotating Mach.* **2005**, *2005*, 161–167. [[CrossRef](#)]
24. Si, Q.; Lu, R.; Shen, C.; Xia, S.; Sheng, G.; Yuan, J. An Intelligent CFD-Based Optimization System for Fluid Machinery: Automotive Electronic Pump Case Application. *Appl. Sci.* **2020**, *10*, 366. [[CrossRef](#)]

25. Balje, O.E.; Japikse, D. *Turbomachines—A Guide to Design Selection and Theory*; John Wiley & Sons: Hoboken, NJ, USA, 1981; p. 163.
26. Bauer, K., Jr.; Parnell, G.S.; Meyers, D.A. Response surf Formatting. ace methodology as a sensitivity analysis tool in decision analysis. *J. Multi Criteria Decision Anal.* **1999**, *8*, 162–180. [[CrossRef](#)]
27. Wang, S.; Jian, G.; Xiao, J.; Wen, J.; Zhang, Z. Optimization investigation on configuration parameters of spiral-wound heat exchanger using Genetic Aggregation response surface and Multi-Objective Genetic Algorithm. *Appl. Therm. Eng.* **2017**, *119*, 603–609. [[CrossRef](#)]
28. Amouzgar, K.; Strömberg, N. Radial basis functions as surrogate models with a priori bias in comparison with a posteriori bias. *Struct. Multidiscip. Optim.* **2016**, *55*, 1453–1469. [[CrossRef](#)]
29. Acar, E.; Raisrohani, M. Ensemble of metamodels with optimized weight factors. *Struct. Multidiscip. Optim.* **2008**, *37*, 279–294. [[CrossRef](#)]
30. Liu, H.; Maghsoodloo, S. Simulation optimization based on Taylor Kriging and evolutionary algorithm. *Appl. Soft Comput.* **2011**, *11*, 3451–3462. [[CrossRef](#)]
31. Wang, Q. Nonparametric regression function estimation with surrogate data and validation sampling. *J. Multivar. Anal.* **2006**, *97*, 1142–1161. [[CrossRef](#)]
32. Melo, A.P.; Cóstola, D.; Lamberts, R.; Hensen, J.L.M. Development of surrogate models using artificial neural network for building shell energy labelling. *Energy Policy* **2014**, *69*, 457–466. [[CrossRef](#)]
33. Chen, Z.; Singh, P.M.; Choi, Y.-D. Francis Turbine Blade Design on the Basis of Port Area and Loss Analysis. *Energies* **2016**, *9*, 164. [[CrossRef](#)]
34. Chen, Z.; Choi, Y.-D. Suppression of cavitation in the draft tube of Francis turbine model by J-Groove. *Proc. Inst. Mech. Eng. Part C J. Mech. Sci.* **2018**, *233*, 3100–3110. [[CrossRef](#)]
35. Singh, P.M.; Chen, Z.; Choi, Y.-D. Hydraulic design and performance analysis on a small pump-turbine system for ocean renewable energy storage system. *J. Mech. Sci. Technol.* **2017**, *31*, 5089–5097. [[CrossRef](#)]
36. Maji, P.K.; Biswas, G. Three-dimensional analysis of flow in the spiral casing of a reaction turbine using a differently weighted Petrov Galerkin method. *Comput. Methods Appl. Mech. Eng.* **1998**, *167*, 167–190. [[CrossRef](#)]
37. ANSYS. *ANSYS CFX Documentation*; ANSYS Inc.: Canonsburg, PA, USA, 2017.


Publisher’s Note: MDPI stays neutral with regard to jurisdictional claims in published maps and institutional affiliations.



© 2020 by the authors. Licensee MDPI, Basel, Switzerland. This article is an open access article distributed under the terms and conditions of the Creative Commons Attribution (CC BY) license (<http://creativecommons.org/licenses/by/4.0/>).

Article

Aerodynamic Performance of an Octorotor SUAV with Different Rotor Spacing in Hover

Yao Lei ^{1,2,*} , Yuhui Huang ¹ and Hengda Wang ¹

¹ School of Mechanical Engineering and Automation, Fuzhou University, Fuzhou 350116, China; yuhuihuang2020@126.com (Y.H.); hengda_wang@163.com (H.W.)

² Key Laboratory of Fluid Power and Intelligent Electro-Hydraulic Control (Fuzhou University), Fujian Province University, Fuzhou 350116, China

* Correspondence: yaolei@fzu.edu.cn

Received: 3 October 2020; Accepted: 26 October 2020; Published: 28 October 2020



Abstract: To study the aerodynamic performance of hovering octorotor small unmanned aerial vehicles (SUAV) with different rotor spacing, the computational fluid dynamics (CFD) method is applied to analyze the flow field of an octorotor SUAV in detail. In addition, an experimental platform is built to measure the thrust and power of the rotors with rotor spacing ratios L/D of 1.0, 1.2, 1.4, 1.6, and 1.8, sequentially. According to the theory of momentum, rotor aerodynamic performance is obtained with qualitative analysis. Further analysis with numerical simulation is presented with the flow field of the octorotor SUAV, the vorticity distribution, velocity distribution, pressure distribution, and streamline. The results show that the aerodynamic performance varies with the rotor spacing. Specifically, the aerodynamic performance is poor at $L/D = 1.0$, which is accompanied with strong interaction of wake and tip vortexes and interaction with each other. However, the aerodynamic efficiency is much improved with a larger rotor spacing, especially achieving the highest at $L/D = 1.8$, which is considered to be the best rotor spacing ratio for this kind of octorotor SUAV.

Keywords: octorotor SUAV; aerodynamic performance; rotor spacing; hover; CFD; vortices distribution

1. Introduction

Small unmanned aerial vehicles (SUAVs) are normally less than 25 kg and easy to pack. Especially, the octorotor SUAVs with evenly distributed rotors have been widely used in agricultural, surveillance, and military, due to its advantages of simple operation and convenient portability. In addition, octorotor SUAVs have higher load and more damaged redundancy as compared with a quadrotor or hex-rotor SUAVs.

Considering that octorotor SUAVs often operate in environments where the Reynolds numbers are less than 10^5 , viscosity, laminar separation bubbles, thickened boundary layer, and flow separation influence the rotor tip, which can lead to increased drag on the vehicle, thus, resulting in poor aerodynamic performance. Especially, there is a strong vibration at higher rotor speed which can affect the dynamic stability of a rotorcraft [1–3]. There are two main ways to improve the aerodynamic performance of small rotary-wing UAVs. One way is to change the parameters of the blade [4], such as changing the shape of the blade platform, adding a twist, taper, and so on. The second way is to change the layout and configuration of the rotors, such as changing the distance between adjacent rotors, the number of rotors, the tilt angle of the rotors, and so on. At the same time, with the help of constantly developing computer simulation technology, we can intuitively explore the reasons that lead to a decrease or increase in aerodynamic performance of the rotor, and help to optimize the layout of the SUAVs.

Early studies have focused on hover performance analysis of a small single rotor and a small coaxial rotor. Bohorquez [5–7] experimentally measured the aerodynamic performance of the rotor and used fluorescent oil to visualize surface flow, which showed consistently poor performance for a variety of rotors with low Reynolds numbers (less than $Re_{tip} = 0.5 \times 10^5$). Ramasamy [8] used the digital particle image velocimetry (DPIV) to study the aerodynamic efficiency of the hovering micro rotor with different blade shapes and found that changing the shape of the blade, such as adding a linear twist and changing the planform of the airfoil, could effectively improve the aerodynamic performance of the blade. A series of parametric studies of hovering coaxial rotor were conducted by Lakshminarayanan [9] and Syal [10]. Changing the inter-rotor spacing proved to influence the aerodynamic of the coaxial rotor in hover.

In recent years, research on aerodynamic performance of small rotorcrafts has deepened. Yoons [11] studied the influence of the turbulence model on the flow solution accuracy of hovering rotor. High-fidelity computational fluid dynamics (CFD) simulations have been implemented for multi rotor [12,13], and adding components under the airframe was found to weaken the interactions between rotors. Henricks [14,15] investigated the effect of rotor variables on the aeroacoustics performance of a hovering rotor. Greater twist and taper were proven to improve both the aerodynamic and acoustic performance. A high-speed stereo particle-image velocimetry (SPIV) study on multi rotor was conducted by Shukla [16,17], and vortex–vortex, blade–vortex, and vortex–duct interactions were visualized. The effect of a tilting rotor on the aerodynamic performance was studied by Zhang [18]. Tilting has been shown to help keep the vehicle stable. The simulation of the downwash flow of octorotor was done by Yang [19].

The current study of rotor aerodynamic performance concentrated on the coaxial rotor and quadrotor since the rotor interference of an octorotor SUAV is relatively complicated, especially the different vortex–vortex and blade–vortex interactions with different rotor spacing. Therefore, analysis of the aerodynamic performance of octorotor is challenging work, which can also provide significant guidance for designing octorotor SUAVs.

The main research objective of this paper is to explore how the aerodynamic performance of a small octorotor SUAV changes with a change of rotor spacing, why it changes, and whether there is an optimal rotor spacing. In comparison with previous studies on small quadrotor and small hex-rotor SUAVs [20–22], the improvement of this study lies in the addition of preliminary studies on wake vortices.

2. Theoretical Analysis

Momentum theory is assumed to be an effective method for flow-field analysis of rotorcrafts. It regards the rotating rotor as an actuator disk and relates the induced airflow velocity through the actuator disk to the thrust and power of the rotor. According to the momentum theory [23], the induced flow velocity can be expressed as:

$$V_h = \sqrt{T/2\rho A} \quad (1)$$

where T is the thrust generated by the rotor, ρ is the air density, with a value of $1.225 \text{ kg} \cdot \text{m}^{-3}$, and A is the area of the rotor disk.

The induced power consumption can be expressed as:

$$P_i = TV_h = T^{3/2} / \sqrt{2\rho A} \quad (2)$$

To measure the aerodynamic efficiency of a rotor in hover, FM is defined as the ratio of induced power consumption to actual power consumption:

$$FM = \frac{P_i}{P} = \frac{T^{3/2} / \sqrt{2\rho A}}{P} = \frac{C_T^{3/2} / \sqrt{2}}{C_P} \quad (3)$$

where

$$C_T = \frac{T}{\rho A \Omega^2 R^2} \quad (4)$$

is the thrust coefficient,

$$C_P = \frac{P}{\rho A \Omega^3 R^3} \quad (5)$$

is the power coefficient. Ω is the angular velocity of the rotor and R is the radius of the rotor.

FM of a given rotor is often expressed as a function of C_T/σ . Here, σ is the solidity of the rotor, and can be defined as:

$$\sigma = Nc/\pi R \quad (6)$$

where N is the number of blades and c is the chord.

Since the tapered blade is adopted in this paper, the influence of varying chord length on the solidity must be considered, and Equation (7) is adopted to calculate the equivalent solidity:

$$\sigma_e = 3 \int_0^1 \sigma r^2 dr \quad (7)$$

The total efficiency of the aircraft is determined by the power loading:

$$PL = \frac{T}{P} = \frac{C_T}{C_P \Omega R} \quad (8)$$

Combined with momentum theory, PL can also be expressed in the following form:

$$PL = \frac{\sqrt{2\rho} FM}{\sqrt{DL}} \quad (9)$$

where DL is the disk loading and can be defined as:

$$DL = T/A \quad (10)$$

In addition, the tip chord Reynolds number in this paper is defined by the chord length at 0.75R:

$$Re_{tip} = \rho V c_{0.75} / \mu \quad (11)$$

where μ is kinematic viscosity coefficient of air, with a value of 1.79×10^{-5} Pa · s with a temperature of 293.15 K, and a pressure of 101.325 kPa.

Figure 1 shows the arrangement of octorotor and interference between adjacent rotors.

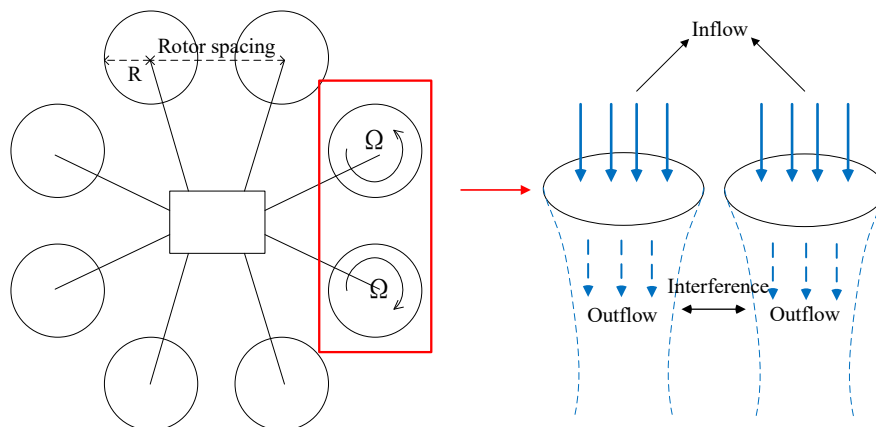


Figure 1. Sketch of the octorotor arrangement.

3. Hover Experiment

3.1. Experimental Setup

The rotor used in this paper is made of carbon fiber, and unidirectional carbon fiber cloth is used as reinforcement. The weight of one rotor is 15 g. The rotor is operating at $Re_{tip} = 0.59 \times 10^5 \sim 0.99 \times 10^5$. The specific rotor parameters are shown in Table 1.

Table 1. Rotor parameters.

Chord (mm)	Radius (m)	Solidity	Pitch (m)	Twist
28	0.2	0.09	0.157	0

The schematic diagram of the test bench is shown in Figure 2. Each rotor is fitted with a separate motor and thrust sensors (model CZL601, accuracy $\pm 0.02\%$ F.S., range 0~3 kg). Adjacent rotors rotate in opposite directions, and the rotor speed is measured with an optical tachometer (model DT2234C, accuracy $\pm 0.05 \text{ n}\% + 1 \text{ d}$). To reduce the impact brought by the ground effect, the rotor is installed at a height of 1.5 m above the ground. Rotor spacing L is defined as the distance between the rotor centers of two adjacent rotors. In this experiment, $L = 400, 480, 560, 640,$ and 720 mm , respectively. Thus, the corresponding dimensionless spacing ratios $L/D = 1.0, 1.2, 1.4, 1.6,$ and 1.8 (D is the diameter of the rotor). By changing the tip chord Reynolds number, the thrust and power consumption generated by the octorotor at five spacing are collected, and the aerodynamic performance of the octorotor is analyzed accordingly.

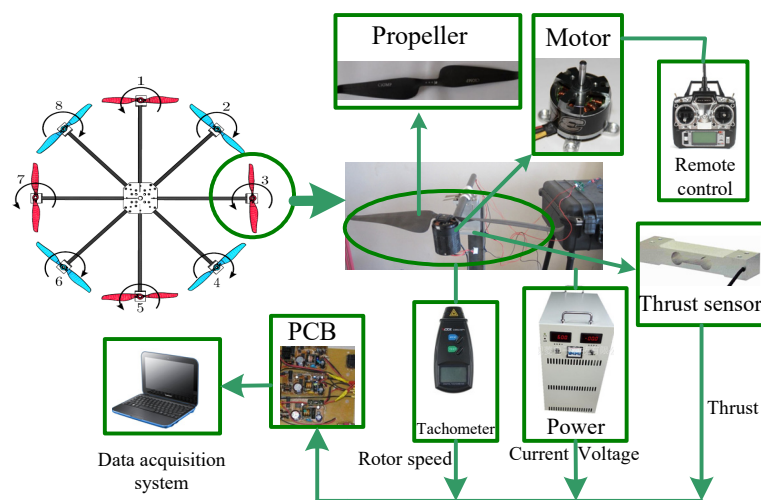


Figure 2. Schematic diagram of test bench.

3.2. Error Analysis

The main sources of error in the experiments are the standard deviations of the rotational speed and the mean voltages from the force sensors. Typical values of the standard deviations of thrust are about 1% of the mean values. Rotational speed error is related to the finite number of magnets that excite the tachometer, which causes an error of $1/24 \times 60 = 2.5 \text{ RPM}$. The statistical (random) error in the coefficient values for each run was estimated by the standard deviation of repeated samples. This experiment mainly measured variable as thrust T , torque Q , and rotational speed Ω . To determine the accuracy of the test measurements, a normalized criterion is needed in this case [24–26]. Consider a

variable X_i , the uncertainty of the calculated results can be expressed by using the “Kline–McClintock” equation [27]:

$$\Delta R = \left\{ \sum_{i=1}^N \left(\frac{\partial R}{\partial X_i} \Delta X_i \right)^2 \right\}^{1/2} \quad (12)$$

where ΔX_i is the uncertainty of X_i .

The expression of uncertainty of power can be obtained as follows:

$$\Delta P = \sqrt{\left(\frac{\partial P}{\partial Q} \Delta Q \right)^2 + \left(\frac{\partial P}{\partial \Omega} \Delta \Omega \right)^2} \quad (13)$$

The uncertainty of P as a percentage is:

$$\frac{\Delta P}{P} = \sqrt{\left(\frac{\Delta Q}{Q} \right)^2 + \left(\frac{\Delta \Omega}{\Omega} \right)^2} \quad (14)$$

Similarly:

$$\frac{\Delta PL}{PL} = \sqrt{\left(\frac{\Delta T}{T} \right)^2 + \left(-\frac{\Delta Q}{Q} \right)^2 + \left(-\frac{\Delta \Omega}{\Omega} \right)^2} \quad (15)$$

$$\frac{\Delta FM}{FM} = \sqrt{\left(\frac{3}{2} \frac{\Delta T}{T} \right)^2 + \left(-\frac{\Delta Q}{Q} \right)^2 + \left(-\frac{\Delta \Omega}{\Omega} \right)^2} \quad (16)$$

By calculation, the uncertainty of P , PL , and FM is 1.41%, 1.44%, and 1.51%, respectively. The values of uncertainty that are presented in this study are all calculated for 95% confidence levels.

3.3. Results

The thrust and power consumption of the octorotor with different spacing ratios is shown in Figure 3.

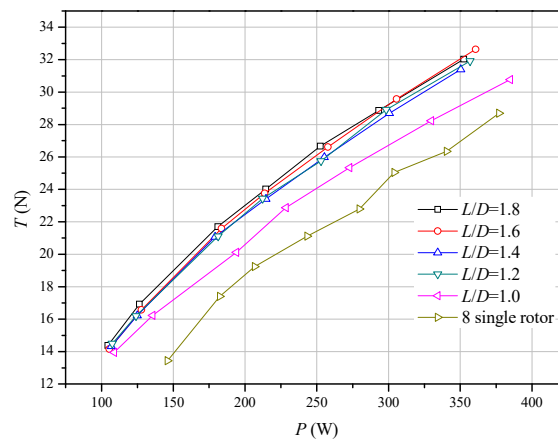


Figure 3. Thrust and power consumption variation.

It can be seen from Figure 3 that at the same power consumption, the thrust is significantly greater than the simple superposition of the thrust generated by the eight small single rotors. In addition, the thrust generated by the octorotor at $L/D = 1.0$ is significantly lower than that generated by the octorotor at the other four spacing ratios. It indicates that the rotor interference with proper rotor spacing is beneficial to improve the hover efficiency of the octorotor.

The variation of FM with different rotor spacing ratios is shown in Figure 4.

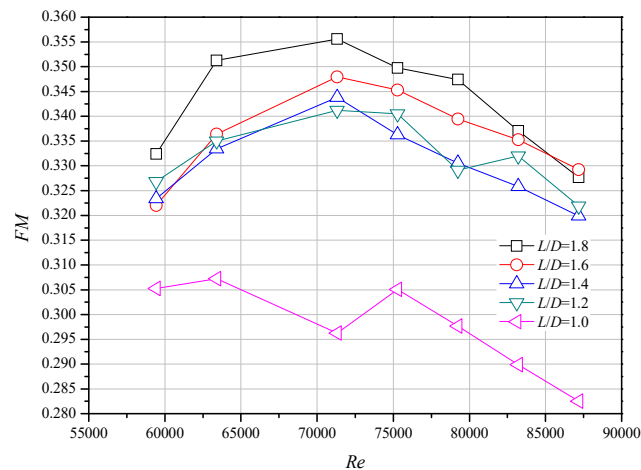


Figure 4. Variation of the figure of merit.

It can be found from Figure 4 that the FM of the octorotor shares a similar tendency, and it is very interesting to note that there is a sudden drop at $Re = 79246$ for $L/D = 1.2$ and at $Re = 71,321$ for $L/D = 1.0$. The likeliest explanation for this phenomenon is the collapse of the suction forces on the tip and the increase in vibration caused by the flow separation, which are relatively unsteady for smaller rotor spacing, where the rotor is apt to have somewhat greater interaction with its own wake. This heightened interaction is reflected in the greater variability to a decrease in FM . Furthermore, because of the unpredictable inflow and outflow of smaller rotor spacing where the rotor is apt to have interaction with its own wake, it is, therefore, not entirely surprising that some data do not follow the same trends. Additionally, the aerodynamic performance at $L/D = 1.8$ is much better than other spacing ratios with a much higher FM .

The variation of power loading versus disk loading is shown in Figure 5.

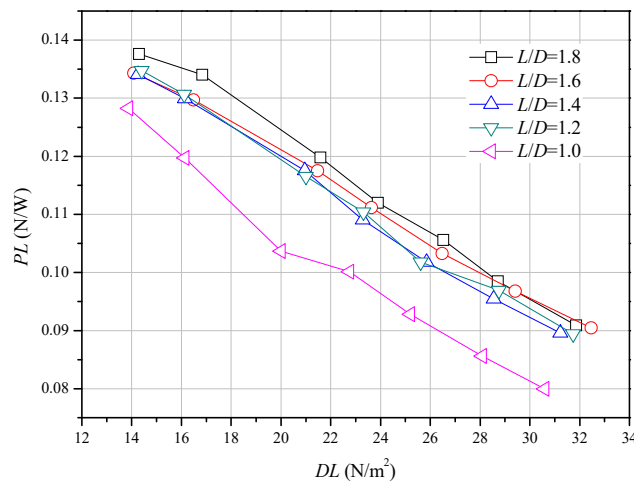


Figure 5. Variation of power loading and disk loading.

As can be seen from Figure 5, PL value at $L/D = 1.8$ always is higher than the other rotor spacings. The PL for 1.4 and 1.2 are approximately the same with a lower value. Especially, the PL for $L/D = 1.0$ was presented with lowest value which suffered from strong rotor interference.

To sum up, when the spacing ratio is 1.8, the small octorotor has better aerodynamic efficiency and total efficiency, and therefore it can be regarded as the best rotor spacing in the current working condition.

The FM comparison of the small octorotor, the small quadrotor [21], and the small hex-rotor [20] at the optimum rotor spacing is shown in Figure 6.

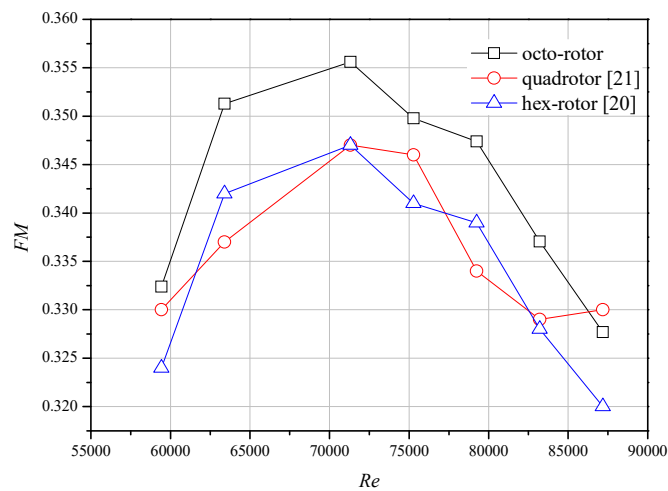


Figure 6. The FM comparison with quadrotor and hex-rotor.

It can be seen from Figure 6 that the aerodynamic performance of a small octorotor is much better than that of a small quadrotor and a small hex-rotor composed of the same rotor.

4. Numerical Simulation

4.1. Simulation Setting and Mesh Analysis

To further analyze the aerodynamic performance of the small octorotor, the flow field of the small octorotor with different spacing ratios was numerically simulated with ANSYS when $Re_{tip} = 0.79 \times 10^5$. The detailed mesh distribution is shown in Figure 7.

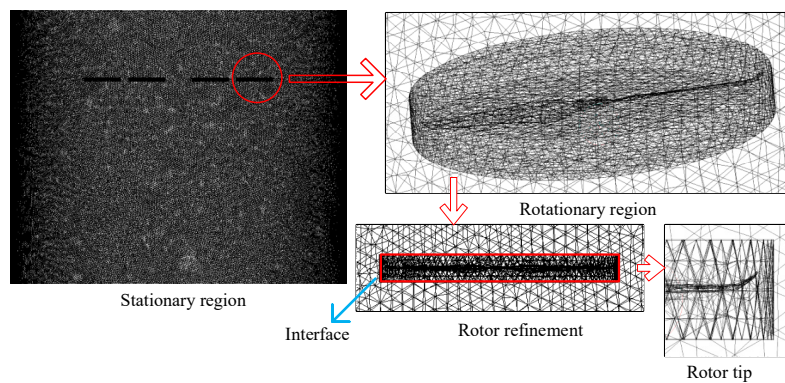


Figure 7. Mesh distribution.

The whole computational domain is divided into nine regions including one cylinder stationary region and eight cylinder rotating regions (to capture the flow detail of four rotors with refined mesh), which has a total size of 70 million cells. In addition, the UAV is located in the upper region of the domain to obtain the detail of the downwash flow of the UAV. To handle the low Reynolds number flows, multiple viscous boundary layers are used in the simulations, and the max element metrics is below 0.8 to capture the flow detail of the rotor tip and the interfaces between stationary and rotating regions. The grid is considered to be sufficient to handle these simulations and the mesh on the rotor tip is refined to reach the independence state. For the boundary conditions, all three surfaces of the cylinder domain are set as no slip wall where the rotating region and stationary overlap is set as interface. The sliding mesh is used for the transient solver. The Spalart–Allmaras turbulence model was chosen for the RANS closure which was proven to be capable of handling the aerodynamic performance of the

multi-rotors, especially at low Re . The physical time step corresponds to a rotor rotation of 30 degrees, and 12 steps correspond to a rotor revolution. The rotor made a total of 40 revolutions. Furthermore, the mesh independence study is conducted to show that the results are already reaching the grid independence state.

For the numerical simulation, the accuracy of the model used, the quality of the mesh, the selected boundary conditions, the turbulence model, and the discrete format all produce some errors. For the experiment, the sensor error is the main error source. The comparison between the experimental and simulation results of FM of octorotor is shown in Figure 8.

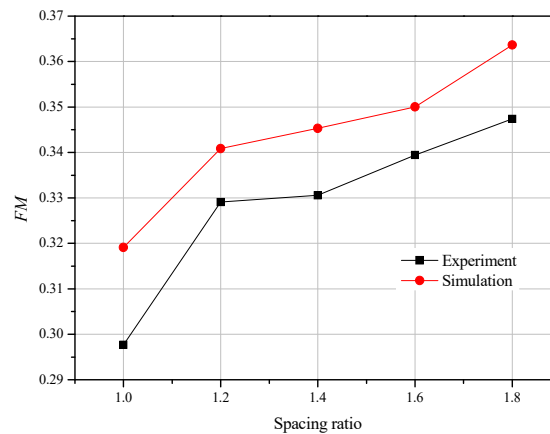


Figure 8. Comparison between experimental and simulation results.

It can be seen that the simulation results are slightly higher than the experiment, with an error of about 6%, which may be the result of the introduced C_p in experiments and the extra validation of C_p for each simulation to reach the convergence.

4.2. Simulation Results

The velocity distribution between adjacent rotors with different rotor spacing is shown in Figure 9.

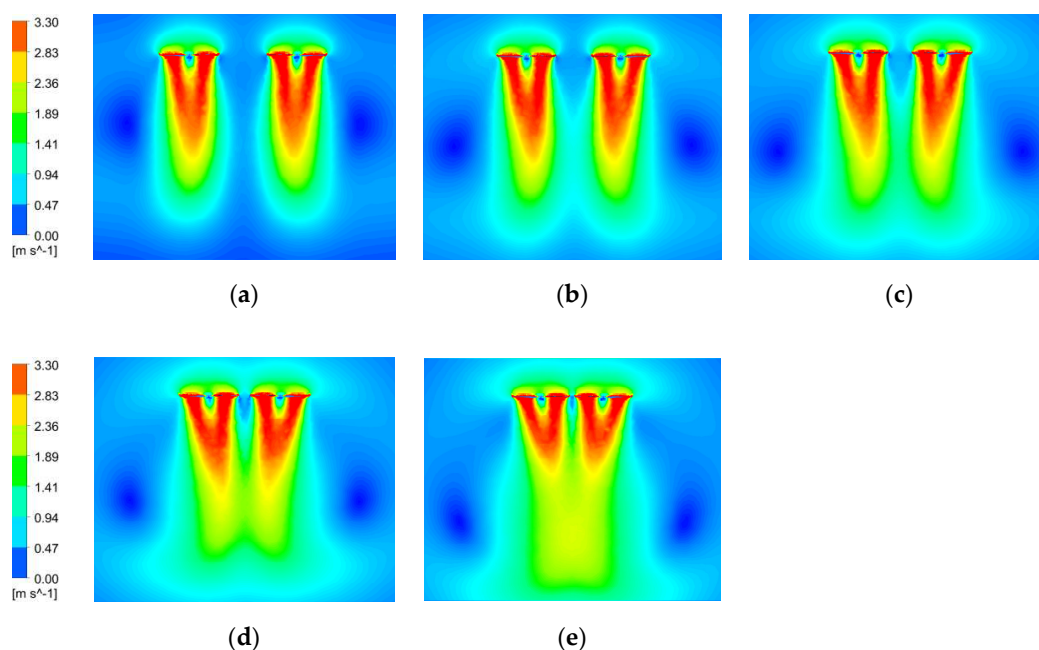


Figure 9. Velocity distribution. (a) $L/D = 1.8$; (b) $L/D = 1.6$; (c) $L/D = 1.4$; (d) $L/D = 1.2$; (e) $L/D = 1.0$.

According to Figure 9, it is not difficult to find that rotor wake began to attract each other as the rotor spacing was reduced. Since the wake of each rotor is affected by the wake of the two adjacent rotors, the wake of the rotor shows the phenomenon of inward contraction which may make the rotor unstable and affect the power consumption of the rotor. It also can be found that the vertical vortex below the side of the rotor slowly moves down as the rotor spacing decreases. In addition, the wake of 1.2 and 1.0 appears to be deeper than other spacing ratios, which may make the rotors more susceptible to ground effects.

The vortices distribution between adjacent rotors with different rotor spacing is shown in Figure 10.

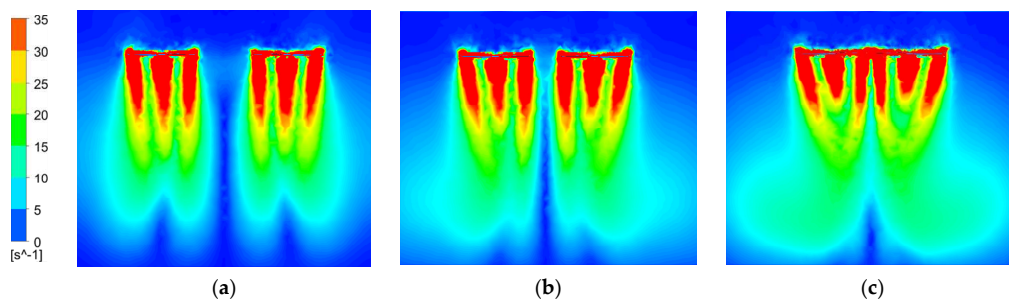


Figure 10. Vortices distribution. (a) $L/D = 1.8$; (b) $L/D = 1.4$; (c) $L/D = 1.0$.

Figure 10 shows that the tip vortices and root vortices also attract each other and with a decrease in rotor spacing, the attraction between the vortices becomes more and more intense.

The pressure distribution around the rotor tips with different rotor spacing is shown in Figure 11.

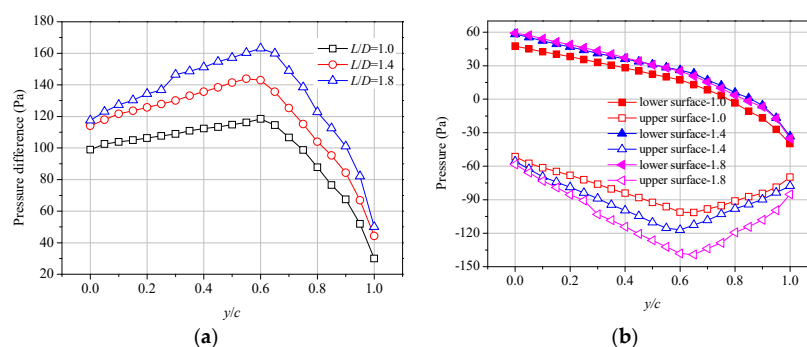


Figure 11. Pressure distribution. (a) Pressure difference between upper and lower surface; (b) Pressure distribution of upper and lower surface.

As can be seen from Figure 11a, the pressure difference between the upper and lower surface at the blade tip is intended to decrease with a decrease in rotor spacing. It means a smaller thrust is obtained at smaller spacing. Figure 11b shows that the rotor spacing has a significant effect on the pressure on the upper surface of the rotor tip, but when the spacing is too small (such as $L/D = 1.0$), the pressure on the lower surface is also affected in this case.

The streamline distribution is shown in Figure 12.

The inward contraction of the rotor wake at 1.2 and 1.0 can be clearly observed from Figure 12d,e which indicates that the thrust and power variations are related to the location and the shape of the vortex.

The Q -criterion for the octorotor with different rotor spacing is shown in Figure 13.

As can be seen in Figure 13, the wake of the rotor shows the phenomenon of inward contraction at $L/D = 1.0$.

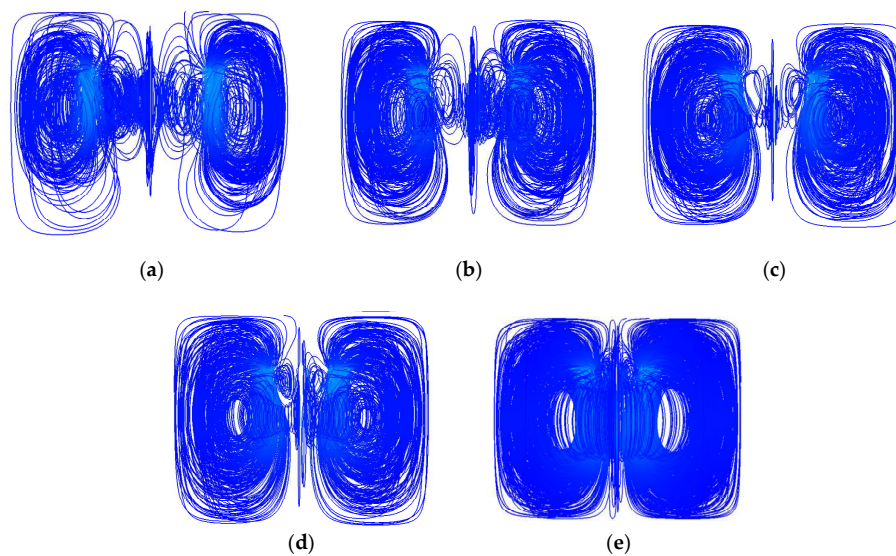


Figure 12. Streamline for octorotor in hover. (a) $L/D = 1.8$; (b) $L/D = 1.6$; (c) $L/D = 1.4$; (d) $L/D = 1.2$; (e) $L/D = 1.0$.

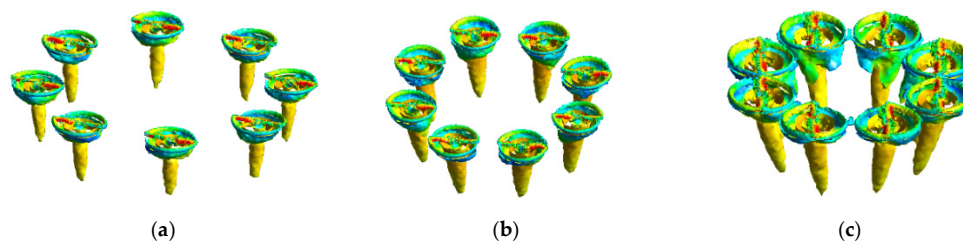


Figure 13. Q-criterion for octorotor in hover. (a) $L/D = 1.8$; (b) $L/D = 1.4$; (c) $L/D = 1.0$.

5. Conclusions

To obtain the aerodynamic performance of a small octorotor with different rotor spacing, the small rotor test bench measurements were carried out with CFD simulations. The conclusions are as follows:

1. The aerodynamic performance of the rotors change with a change of rotor spacing, but this change is not linear, and therefore it cannot be simply judged that an increase or decrease in the spacing will have a consistent impact on the aerodynamic performance of the rotors. Further analysis is needed to explore the reasons for the influence of rotor spacing on aerodynamic performance and whether or not there is a law that can be expressed mathematically. Nevertheless, through experiments, we found that FM and PL at $L/D = 1.8$ have obvious advantages as compared with other spacing ratio, which can be regarded as the best spacing ratio under the current working condition, while $L/D = 1.0$ obviously has a great negative impact on the overall aerodynamic performance due to its too small spacing.
2. As compared with eight single rotors, for a quadrotor and hex-rotor with the same rotor size, the FM of octorotor shows a higher value. Especially, $L/D = 1.8$ was proven to be the optimal rotor spacing with better aerodynamic performance. The configuration of the octorotor helps to increase the aerodynamic performance of the rotors, but at the same time increases the total area of the aircraft, resulting in a higher cost. Therefore, it is necessary to make a tradeoff on rotor arrangement and oversize of the vehicle.
3. The numerical simulation results at $Re_{tip} = 0.79 \times 10^5$ show that the wake of an octorotor and the vortices of wake attract each other. Moreover, the attraction becomes more obvious as the rotor spacing decreases, which may adversely affect the aerodynamic performance of the

rotor. A decrease in rotor spacing will also affect the pressure difference between the upper and lower surfaces of the rotor tips. When the rotor spacing is too small, the pressure difference is sharply reduced, thus affecting the thrust generated. Future work should attempt to obtain an aerodynamic model that considers rotor interference to amend the conventional control theory with application in an octorotor with tilted rotors or wind disturbance.

Author Contributions: Y.L. carried out experiments, acquired the funding, and analyzed the results; Y.H. wrote the manuscript with assistance of Y.L.; H.W. performed a new set of simulations. All authors have read and agreed to the published version of the manuscript.

Funding: This research was supported by the National Nature Science Foundation of China (grant no. 51505087), the Fuzhou University Jinjiang Science and Education Park (no. 2019-JJFDKY-59) and the Fujian Provincial Industrial Robot Basic Component Technology Research and Development Center (2014H21010011).

Acknowledgments: The author thanks the Key Laboratory of Fluid Power and Intelligent Electro-Hydraulic Control (Fuzhou University), the Fujian Province University, and the Fuzhou University Jinjiang Science and Education Park for applying the experimental field.

Conflicts of Interest: The authors declare no conflict of interest.

References

1. Lichota, P.; Szulczyk, J. Output Error Method for Tiltrotor Unstable in Hover. *Arch. Mech. Eng.* **2017**, *64*. [[CrossRef](#)]
2. Mettler, B.; Tischler, M.; Kanade, T.M.; Kanade, T. System Identification of Small-Size Unmanned Helicopter Dynamics. In Proceedings of the 55th Annual Forum of the American Helicopter Society, Montreal, QC, Canada, 25–27 May 1999; pp. 1706–1717.
3. Hrishikeshavan, V.; Benedict, M.; Chopra, I.H.; Chopra, I. Identification of Flight Dynamics of a Cylcopter Micro Air Vehicle in Hover. *J. Aircr.* **2015**, *52*, 116–129. [[CrossRef](#)]
4. Zhang, S.; Yang, B.; Xie, H.; Song, M. Applications of an Improved Aerodynamic Optimization Method on a Low Reynolds Number Cascade. *Processes* **2020**, *8*, 1150. [[CrossRef](#)]
5. Bohorquez, F.; Pines, D. Hover Performance of Rotor Blades at Low Reynolds Numbers for Rotary Wing Micro Air Vehicles. In Proceedings of the 21st AIAA Applied Aerodynamics Conference, Orlando, FL, USA, 23–26 June 2003.
6. Bohorquez, F.; Samuel, P.; Sirohi, J.; Pines, D.; Rudd, L.; Perel, R. Design, Analysis and Hover Performance of a Rotary Wing Micro Air Vehicle. *J. Am. Helicopter Soc.* **2003**, *48*, 80–90. [[CrossRef](#)]
7. Bohorquez, F.; Pines, D.; Samuel, P.D. Small Rotor Design Optimization Using Blade Element Momentum Theory and Hover Tests. *J. Aircr.* **2010**, *47*, 268–283. [[CrossRef](#)]
8. Ramasamy, M.; Johnson, B.; Leishman, J.G. Understanding the Aerodynamic Efficiency of a Hovering Micro-Rotor. *J. Am. Helicopter Soc.* **2008**, *53*, 412–428. [[CrossRef](#)]
9. Lakshminarayan, K.V.; Baeder, J.D. High-Resolution Computational Investigation of Trimmed Coaxial Rotor Aerodynamics in Hover. *J. Am. Helicopter Soc.* **2009**, *54*, 42008. [[CrossRef](#)]
10. Syal, M.; Leishman, G.J. Aerodynamic Optimization Study of a Coaxial Rotor in Hovering Flight. *J. Am. Helicopter Soc.* **2012**, *57*, 1–15. [[CrossRef](#)]
11. Yoon, S.; Chaderjian, N.; Pulliam, H.T.; Holst, T. Effect of Turbulence Modeling on Hovering Rotor Flows. In Proceedings of the 45th AIAA Fluid Dynamics Conference, Dallas, TX, USA, 22–26 June 2015.
12. Diaz, V.P.; Yoon, S. High-Fidelity Computational Aerodynamics of Multi-Rotor Unmanned Aerial Vehicles. In Proceedings of the 2018 AIAA Aerospace Sciences Meeting, Kissimmee, FL, USA, 8–12 January 2018.
13. Yoon, S.; Lee, C.H.; Pulliam, H.T. Computational Analysis of Multi-Rotor Flows. In Proceedings of the 54th AIAA Aerospace Sciences Meeting, San Diego, CL, USA, 4–8 January 2016.
14. Henricks, Q.; Wang, Z.; Zhuang, M.H.; Zhuang, M. Small-Scale Rotor Design Variables and Their Effects On Aerodynamic and Aeroacoustic Performance of a Hovering Rotor. *J. Fluids Eng.* **2020**, *142*. [[CrossRef](#)]
15. Wang, Z.; Henricks, Q.; Zhuang, M.; Pandey, A.; Sutkowsy, M.; Harter, B.; McCrink, M.; Gregory, J. Impact of Rotor–Airframe Orientation on the Aerodynamic and Aeroacoustic Characteristics of Small Unmanned Aerial Systems. *Drones* **2019**, *3*, 56. [[CrossRef](#)]

16. Shukla, D.; Hiremath, N.; Patel, S.; Komerath, N. Aerodynamic Interactions Study on Low-Re Coaxial and Quad-Rotor Configurations. In Proceedings of the ASME 2017 International Mechanical Engineering Congress and Exposition, Tampa, FL, USA, 3–9 November 2017.
17. Shukla, D.; Komerath, N. Low Reynolds number multirotor aerodynamic wake interactions. *Exp. Fluids* **2019**, *60*. [[CrossRef](#)]
18. Zhang, X.; Xu, W.; Shi, Y.; Cai, M.; Li, F. Study on the effect of tilting-rotor structure on the lift of small tilt rotor aircraft. In Proceedings of the 2017 2nd International Conference on Advanced Robotics and Mechatronics, Hefei, China, 27–31 August 2017; pp. 380–385.
19. Yang, S.; Liu, X.; Bingtai, C.; Li, S.; Zheng, Y. CFD Models and Verification of the Downwash Airflow of an Eight-rotor UAV. In Proceedings of the 2019 ASABE Annual International Meeting, Boston, MA, USA, 7–10 July 2019.
20. Lei, Y.; Wang, H. Aerodynamic Optimization of a Micro Quadrotor Aircraft with Different Rotor Spacings in Hover. *Appl. Sci.* **2020**, *10*, 1272. [[CrossRef](#)]
21. Lei, Y.; Wang, J. Aerodynamic Performance of Quadrotor UAV with Non-Planar Rotors. *Appl. Sci.* **2019**, *9*, 2779. [[CrossRef](#)]
22. Lei, Y.; Cheng, M. Aerodynamic performance of a Hex-rotor unmanned aerial vehicle with different rotor spacing. *Meas. Control* **2020**, *53*, 002029401990131. [[CrossRef](#)]
23. Johnson, W. *Helicopter Theory*; Courier Dover Publications: New York, NY, USA, 1994.
24. Lichota, P. Inclusion of the D-optimality in multisine manoeuvre design for aircraft parameter estimation. *J. Theor. Appl. Mech.* **2016**, *54*, 87–98. [[CrossRef](#)]
25. Tischler, M.B.; Remple, R.K. *Aircraft and Rotorcraft System Identification*, 2nd ed.; American Institute of Aeronautics and Astronautics: Reston, VA, USA, 2012.
26. Jategaonkar, R.V. *Flight Vehicle System Identification: A Time Domain Methodology*, 2nd ed.; American Institute of Aeronautics and Astronautics: Reston, VA, USA, 2015.
27. Kline, S.; McClintock, F. Describing Uncertainties in Single-Sample Experiments. *J. Mech. Eng.* **1953**, *75*, 3–8.

Publisher’s Note: MDPI stays neutral with regard to jurisdictional claims in published maps and institutional affiliations.



© 2020 by the authors. Licensee MDPI, Basel, Switzerland. This article is an open access article distributed under the terms and conditions of the Creative Commons Attribution (CC BY) license (<http://creativecommons.org/licenses/by/4.0/>).

Article

Effect of Rotor Spacing and Duct Diffusion Angle on the Aerodynamic Performances of a Counter-Rotating Ducted Fan in Hover Mode

Woo-Yul Kim, Santhosh Senguttuvan  and Sung-Min Kim *

School of Mechanical Engineering, Sungkyunkwan University, 300 Cheoncheon-dong, Suwon 16419, Korea; samsun215@skku.edu (W.-Y.K.); santhosh@skku.edu (S.S.)

* Correspondence: smkim@skku.edu; Tel.: +82-31-290-7433

Received: 21 August 2020; Accepted: 20 October 2020; Published: 23 October 2020



Abstract: The aerodynamic performance of a counter-rotating ducted fan in hover mode is numerically analyzed for different rotor spacings and duct diffusion angles. The design of the counter-rotating fan is inspired by a custom-designed single rotor ducted fan used in a previous study. The numerical model to predict the aerodynamic performance of the counter-rotating ducted fan is developed by adopting the frozen rotor approach for steady-state incompressible flow conditions. The relative angle between the front and the rear rotor is examined due to the usage of the frozen rotor model. The results show that the variation of thrust for the different relative angles is extremely low. The aerodynamic performances are evaluated by comparing the thrust, thrust coefficient, power coefficient, and figure of merit (FOM). The thrust, thrust coefficient, and FOM slightly increase with increasing rotor spacing up to 200 mm, regardless of the duct diffusion angle, and reduce on further increase in the rotor spacing. The duct diffusion angle of 0° generates about 9% higher thrust and increases the FOM by 6.7%, compared with the 6° duct diffusion angle. The duct diffusion angle is highly effective in improving the thrust and FOM of the counter-rotating ducted fan, rather than the rotor spacing.

Keywords: thrust coefficient; power coefficient; figure of merit; frozen rotor; UAV

1. Introduction

Unmanned aerial vehicles (UAV) are of global interest, since they can perform versatile tasks in the military, search and rescue, agriculture, and transportation fields. Particularly, rotary wing UAVs with vertical take-off and landing (VTOL) propulsion systems are highly desired due to high maneuverability and the ability to take-off and land vertically. In rotary wing UAVs, a ducted fan where a duct surrounds the rotors is more efficient in producing thrust than an open rotor [1]. According to actuator disk theory, the duct reduces the blade tip loss, enabling the ducted fan to double the thrust [2]. The duct also reduces the rotor noise and protects the high-speed rotors from the external environment.

The design of the duct plays a vital role in improving the aerodynamic performance of the ducted fan. One of the key considerations in the design of the ducted fan is the duct profile. The duct profile is usually based on airfoil shapes, due to aerodynamical advantage. Yilmaz et al. [3] experimentally studied the aerodynamic performance of a ducted fan in hover mode for five different duct profiles, based on National Advisory Committee for Aeronautics (NACA) airfoils. Pressure distributions on the inner surface of the duct and velocity profiles at both the duct inlet and outlet planes were investigated for the five different duct profiles. It was found that the propulsive efficiency was significantly affected by the duct profile. Bontempo and Manna [4] numerically investigated the effect of the camber and thickness of the duct profile on the aerodynamic performance of ducted fans. They found that the propulsive efficiency of the duct increased with the increase in the camber and thickness of the

duct profile. Xu et al. [5] developed an asymmetrical duct with a rounded and enlarged leading edge. The leading edge is designed as inflatable so that it can inflate and retract when needed [6,7]. The inflated leading edge is designed to encounter the flow separation that typically occurs around the inner surface of the duct when the ducted fan transits from forward flight (crosswind) to hovering, or from hovering to forward flight. The developed duct model eliminates the flow separation at the crosswind conditions of a 30 m/s velocity at a 50° angle of attack. Although the proposed duct model was suitable to deal with the flow separation, it involved certain complications concerned with the practical implementation of the inflatable material in ducted-fan UAVs. Graf et al. [8] conducted experiments to examine the aerodynamic characteristics of a ducted fan for five duct profiles with different leading edge radius of curvatures and duct wall thicknesses, both in hover and forward flight conditions. As a result, the characteristics of the flow separation on the leading edge of the duct in hover and forward flight modes were found to be different. The duct profile that produced the best performance was different for the hover and forward flight modes.

Apart from duct design, a counter-rotating system, where two rotors rotate in the opposite direction on the same axis, can increase the thrust and aerodynamic performance of a ducted fan. The counter-rotating system has been successfully applied to wind turbines [9,10], axial flow pumps [11,12], axial fans [13,14], and propellers [15,16]. A key advantage of this system is that it can produce a higher thrust than a single rotor, and the torque produced by the two rotors is canceled by each other. The essential parameters affecting the aerodynamic performance in the counter-rotating fan are tip clearance and rotor spacing. Ryu et al. [17] examined the effect of the tip clearance of the front and rear rotors on the aerodynamic performances of the counter-rotating ducted fan in hover mode. In the counter-rotating ducted system, the thrust is affected by relative tip clearances of the front and rear rotors. It was found that, in order to improve the aerodynamic performance of the counter-rotating ducted fan, the tip clearance need not be a minimum for both the front and rear rotors. Among various tip clearance configurations in the study, the configuration with a small tip clearance in the front rotor and a large tip clearance in the rear rotor produced the highest thrust coefficient. Moreover, the total thrust of the counter-rotating ducted fan was significantly affected by the tip clearance of the rear rotor. Han et al. [18] conducted experiments and simulations to investigate the aerodynamic performances of a counter-rotating fan with and without ducts for different blade pitch angles, rotor spacings, and tip clearances in hover mode. The results showed that the counter-rotating fan with a duct generated more thrust than the open counter-rotating fan because of the negative pressure region around the duct's leading edge created by the duct. They also found that as the rotor spacing increased, the thrust coefficient and figure of merit of the counter-rotating fan, both with and without the duct, increased. However, when the rotor spacing became higher than the rotor radius, both the thrust coefficient and figure of merit became constant.

Numerical modeling of the counter-rotating fan necessitates the consideration of the relative motion between the two rotors. This relative motion can be modeled by either a mixing plane, a frozen rotor, or a moving mesh approach. Of the three methods, the moving mesh method produces accurate, realistic flow physics by employing the unsteady coupling of the rotors. However, the moving mesh approach requires high computational effort, resulting in researchers and industrial fan designers opting for either the mixing plane or the frozen rotor approach. Besides that, for steady-state simulations, the mixing plane and frozen rotor methods produce reasonably accurate results. A major disadvantage of the mixing plane approach is that it is not capable of predicting the effect of wakes from the top rotor on the downstream rotor of the counter-rotating fan system. Compared to the mixing plane approach, the frozen rotor approach calculates the non-uniform circumferential velocity and pressure distributions to accurately predict the wake mixing in the downstream rotor and rotor-to-rotor flow physics [19].

Despite several studies conducted to enhance the aerodynamic performance of UAVs, there is still scope for improvement. It is highly important to further study and improve the aerodynamic performance of UAVs. In the present study, the effects of rotor spacing and the duct diffusion angle on the aerodynamic performances of a counter-rotating ducted fan in hover mode are investigated

numerically using the frozen rotor approach. A ducted fan model, designed by Akturk and Camci [20], is used for the present numerical study due to readily available detailed experimental data. Three essential aerodynamic performance parameters—thrust coefficient, power coefficient, and figure of merit—are examined for different rotor spacings and duct diffusion angles.

2. Numerical Model

2.1. Model Description

Figure 1 shows the schematic of the three-dimensional counter-rotating ducted fan based on the fan and duct models of Akturk and Camci [20], where they studied a single ducted fan. The design of both of the fans in the present study was identical to the single fan used by Akturk and Camci [20]. The duct diameter was 559 mm, and the fan had eight blades. The two rotors (fans) had the same tip clearance of 1.71% and rotated in opposite directions. Table 1 summarizes the detailed dimensions of the counter-rotating ducted fan. The rotor spacing (s) was changed from 120 mm to 240 mm in increments of 40 mm. While changing the rotor spacing, the length of duct was also equally changed to maintain the length of the duct diffuser at 117.85 mm. Two duct diffusion angles (θ) of 0° and 6° were considered.

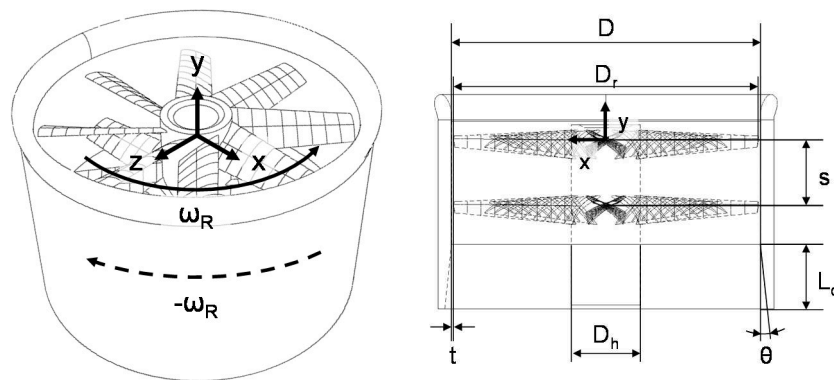


Figure 1. Schematic of counter-rotating ducted fan.

Table 1. Counter-rotating ducted fan dimensions.

Parameter	Value
Duct diameter, D	559.0 mm
Rotor diameter, D_r	558.8 mm
Tip clearance, t	1.71%
Hub diameter, D_h	127 mm
Length of the duct diffuser, L_d	117.85 mm

2.2. Governing Equation

The three-dimensional numerical model to predict the aerodynamic performances of the counter-rotating ducted fan in hover mode was developed using the commercial Computational Fluid Dynamics (CFD) software Ansys CFX 19.1 [21]. The Reynolds-averaged Navier–Stokes (RANS) equations for steady-state, turbulent, and incompressible flow conditions with constant properties were used as the governing equations. The time-averaged continuity and momentum [21] are expressed as follows:

Continuity equation:

$$\frac{\partial(\rho u_j)}{\partial x_i} = 0 \quad (1)$$

Momentum equation for the stationary domain:

$$\frac{\partial(\rho u_j)}{\partial x_i} = -\frac{\partial P}{\partial x_i} + \mu \frac{\partial^2 u_i}{\partial x_j^2} + \rho g_i \quad (2)$$

Momentum equation for the rotating domain:

$$\frac{\partial(\rho u_j)}{\partial x_i} = -\frac{\partial P}{\partial x_i} + \mu \frac{\partial^2 u_i}{\partial x_j^2} + \rho g_i + S_M \quad (3)$$

where the source term, S_M , includes the centrifugal force and Coriolis force for the rotating reference frame, which is expressed as

$$S_M = -\rho[2\vec{\omega}_R \times \vec{u} + \vec{\omega}_R \times (\vec{\omega}_R \times \vec{r})] \quad (4)$$

In the present study, the shear stress transport (SST) k - ω turbulent model developed by Menter [22,23] was used to solve the turbulent flow field. As per the SST k - ω turbulence model, the boundary layer was calculated by the standard k - ω turbulence model, and the freestream region was calculated by the k - ϵ turbulence model, which was incorporated by applying a blending function. The SST k - ω turbulence model accurately predicts the adverse pressure gradient and flow separation at the wall [22,23]. The turbulent kinetic energy and dissipation rate are expressed as follows:

Turbulent kinetic energy equation:

$$\frac{\partial(\rho u_j k)}{\partial x_k} = P - \beta^* \rho \omega k + \frac{\partial}{\partial x_j} \left[(\mu + \sigma_k \mu_t) \frac{\partial k}{\partial x_j} \right] \quad (5)$$

Dissipation rate equation:

$$\frac{\partial(\rho u_j \omega)}{\partial x_j} = \frac{\gamma}{v_t} P - \beta \rho \omega^2 + \frac{\partial}{\partial x_j} \left[(\mu + \omega \mu_t) \frac{\partial k}{\partial x_j} \right] + 2(1 - F_1) \frac{\rho \sigma_{\omega 2}}{\omega} \frac{\partial k}{\partial x_j} \frac{\partial \omega}{\partial x_j} \quad (6)$$

The production limiter (P) in Equation (5) is expressed as

$$P = \tau_{ij} \frac{\partial u_i}{\partial x_j} \quad (7)$$

where

$$\tau_{ij} = \mu_t \left(2S_{ij} - \frac{2}{3} \frac{\partial u_k}{\partial x_k} \delta_{ij} \right) - \frac{2}{3} \rho k \delta_{ij} \quad (8)$$

$$S_{ij} = \frac{1}{2} \left(\frac{\partial u_i}{\partial x_j} + \frac{\partial u_j}{\partial x_i} \right) \quad (9)$$

and the turbulent eddy viscosity is expressed as

$$\mu_t = \frac{\rho a_1 k}{\max(a_1 \omega, \Omega F_2)} \quad (10)$$

Let ϕ_1 represent the constants σ_{k1} , $\sigma_{\omega 1}$, and β_1 in the k - ω turbulence model, ϕ_2 represent the constants σ_{k2} , $\sigma_{\omega 2}$, and β_2 in k - ϵ turbulence model, and ϕ represent the constants σ_k , σ_{ω} , and β in the k - ω SST turbulence model, respectively. The relationship between ϕ , ϕ_1 , and ϕ_2 is expressed as

$$\phi = F_1 \phi_1 + (1 - F_1) \phi_2 \quad (11)$$

The additional functions in the SST k- ω turbulence model are as follows:

$$F_1 = \tanh(\text{arg}g_1^4) \quad (12)$$

$$\text{arg}g_1 = \min \left[\max \left(\frac{\sqrt{k}}{\beta^* \omega d'}, \frac{500v}{d^2 \omega} \right), \frac{4\rho\sigma_{\omega 2} k}{CD_{k\omega} d^2} \right] \quad (13)$$

$$CD_{k\omega} = \max \left(2\rho\sigma_{\omega 2} \frac{1}{\omega} \frac{\partial k}{\partial x_j} \frac{\partial \omega}{\partial x_j}, 10^{-20} \right) \quad (14)$$

$$F_2 = \tanh(\text{arg}g_2^2) \quad (15)$$

$$\text{arg}g_2 = \max \left(2 \frac{\sqrt{k}}{\beta^* \omega d'}, \frac{500v}{d^2 \omega} \right) \quad (16)$$

where d is the distance from the field point to the nearest wall and $\Omega = \sqrt{2W_{ij}W_{ij}}$, with

$$W_{ij} = \frac{1}{2} \left(\frac{\partial u_i}{\partial x_j} - \frac{\partial u_j}{\partial x_i} \right) \quad (17)$$

All the constants are as follows:

$$\begin{aligned} \gamma_1 = \frac{\beta_1}{\beta^*} - \frac{\sigma_{\omega 1} \kappa^2}{\sqrt{\beta^*}}, \quad \gamma_2 = \frac{\beta_2}{\beta^*} - \frac{\sigma_{\omega 2} \kappa^2}{\sqrt{\beta^*}}, \quad \sigma_{k1} = 0.85, \quad \sigma_{\omega 1} = 0.5, \quad \beta_1 = 0.075, \quad \sigma_{k2} = 1.0, \\ \sigma_{\omega 2} = 0.856, \quad \beta_2 = 0.0828, \quad \beta^* = 0.09, \quad \kappa = 0.41, \quad a_1 = 0.31. \end{aligned} \quad (18)$$

2.3. Numerical Method

The numerical simulations were performed as three-dimensional with steady-state and incompressible flow assumptions. Figure 2 shows the grid system, boundary, and interface conditions of the counter-rotating ducted fan. The computational domain consisted of a stationary domain, surrounding the duct and part of the hub, and two rotating domains surrounding each rotor and the remaining part of the hub. The unstructured grid was used for both the stationary and the rotating domain, and the structured hexahedral grid was used for the external fluid domain. The dimensionless distance from the wall to the first node of the mesh, defined as y^+ , is crucial in the SST k- ω turbulence model. The inflation layers were used to achieve a y^+ value less than 2.5 along all the walls to capture fluid interactions in the viscous sublayer. The axial length of the computational domain was 3.0 D and 6.0 D from the origin, located at the center of the front rotor, and the radial length was 2.5 D from the y -axis. The multiple reference frame (MRF) method was used to simulate the rotation of the rotors. The rotating domain was considered to rotate relative to the stationary domain by adding the centrifugal force and Coriolis force (see Equations (2) and (3)). The frozen rotor, mixing plane (stage), and sliding mesh methods were the available methods to model the interface between rotating and stationary domains in the MRF method. In the present study, the frozen rotor method was used for the interface between the rotating and stationary domains, as well as the interface between the two rotating domains. When using the frozen rotor, the rotor in the rotating domain is considered to be in a frozen state; this means the rotor position is fixed relative to the stationary domain. In the frozen rotor method, the results may vary depending on the rotor position. Hence, in the present study, the positions of the front and rear rotors were tested for four relative angles: 0° , 11.25° , 22.5° , and 33.75° . The opening boundary condition with zero-gauge pressure was applied to the external surfaces of the fluid domain to allow inward or outward airflow in hover mode. The no-slip condition was applied to the walls of the duct, hub, and rotors, except for the inner wall, the duct adjacent to the rotating domains. The counter-rotating wall boundary condition with an equal velocity in the opposite direction corresponding to the rotating domain was applied to the inner wall of the duct.

To reduce the computational cost, only one-eighth of the counter-rotating ducted fan was modeled in the computational domain by applying the periodic boundary conditions to the side surfaces.

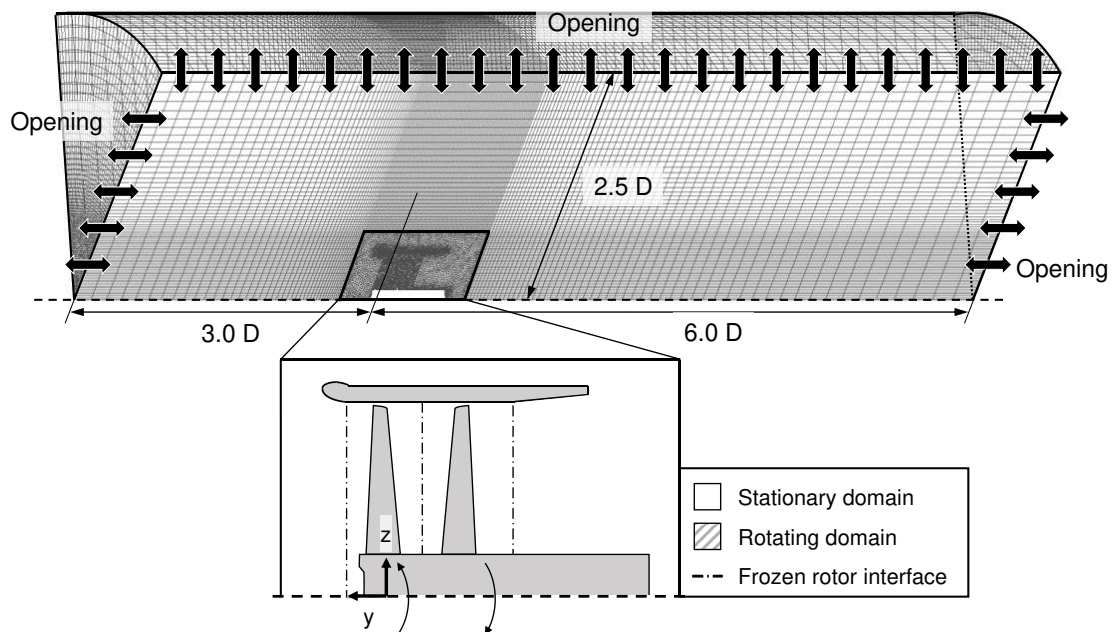


Figure 2. The grid system, boundary, and interface conditions of the counter-rotating ducted fan.

2.4. Grid Independence Test and Validation

The aerodynamic performance parameters, thrust coefficient, power coefficient, and figure of merit are expressed as follows:

Thrust coefficient:

$$C_T = \frac{\text{Thrust}}{\rho N^2 D^4} \quad (19)$$

Power coefficient:

$$C_P = \frac{\text{Power}}{\rho N^3 D^5} \quad (20)$$

Figure of merit (FOM):

$$FOM = \frac{C_T^{3/2}}{\sqrt{2} C_P} \quad (21)$$

The single ducted fan model of Akturk and Camci [20] was simulated to conduct grid independence testing and validation. The grid independence test was conducted using four different grid systems comprising 3.98, 4.79, 5.87, and 7.02 million cells at 1500 rpm. The thrust coefficient of the different grid systems is compared in Figure 3a. The discrepancy in the thrust coefficient among the 4.79, 5.87, and 7.02 million cell grids was less than 1.0%, and, thus, the grid system with 4.79 million cells was selected. The total simulation time for the selected mesh size was about 10 h in a machine with an Intel Core i7 6700 (4 physical cores and 8 threads). For validation, the single ducted fan was simulated under six different rotational speeds, corresponding to the experiments of Akturk and Camci [20]. Figure 3b compares the thrust generated for the six different rotational speeds in the present numerical study with the experiment and numerical results of Akturk and Camci [20]. The present numerical results show good agreement with the results of Akturk and Camci [20].

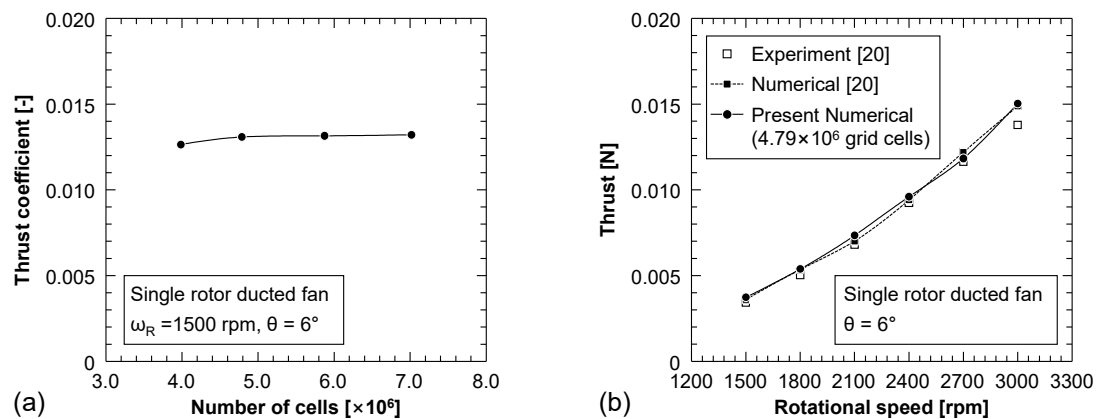


Figure 3. (a) The thrust coefficient for different grid systems, and (b) comparison of thrust on single rotor ducted fan of the present numerical study with the experiment and numerical results of Akturk and Camci [20].

3. Results and Discussion

3.1. Effect of Relative Angle between Front and Rear Rotor

Initially, the effect of the relative angle between the front and rear rotor was tested for four relative angles: 0° , 11.25° , 22.5° , and 33.75° . Each relative angle configuration was simulated for three rotational speeds—1500 rpm, 2100 rpm, and 2700 rpm—and two rotor spacings of 120 mm, and 200 mm. The diffusion angle of the duct for all of the relative angle configurations was 6° . Figure 4 shows the thrust generated at each relative angle configuration for the different rotational speeds and rotor spacings. The thrust was not significantly affected by the relative angle at 1500 rpm for both rotor spacings. However, minor variations in the thrust were observed as the rotational speed increased for both rotor spacings.

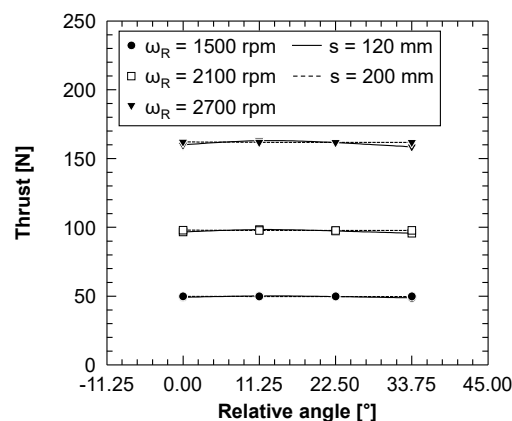


Figure 4. Thrust generated at four relative angles between the front and rear rotors for different rotational speeds and rotor spacings.

Figure 5a–d shows the total pressure contours at Plane 3 for the different relative angles under the conditions of a 2700 rpm rotational speed and 200 mm rotor spacing. Refer to Figure 6 for the location of Plane 3 in the domain. The pressure contours of the 2700 rpm rotational speed and 200 mm rotor spacing cases were compared since the thrust was slightly affected by the relative angles as the rotational speed increased. The high-pressure region, widely distributed across the center of the interface, shifted periodically with the change in relative angle. The difference in the pressure distribution for the different relative angles was negligible. Hence, the effect of the relative

angle between the front and rear rotor was negligible, and the 0° relative angle was considered for further simulations to evaluate the aerodynamic performance of the counter-rotating ducted fan. Similar relative angle studies conducted in a gas turbine pre-swirl system [24], an axial turbine [25], and a centrifugal pump [26] also concluded that the effect of the relative angle is negligible.

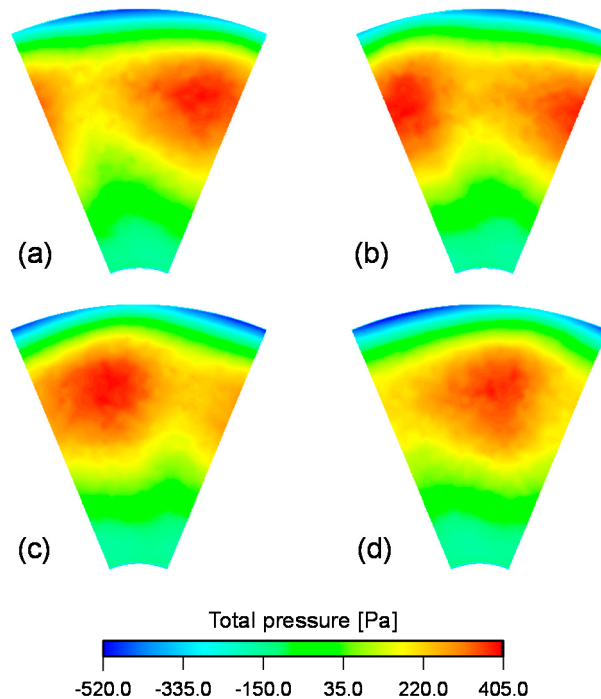
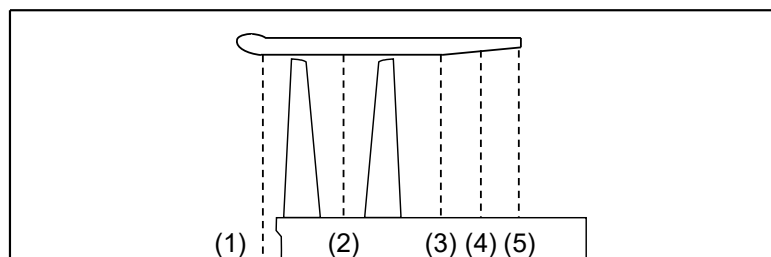


Figure 5. Total pressure contour and four relative angles between the front and rear rotors of (a) 0° ; (b) 11.25° ; (c) 22.5° ; and (d) 33.75° at Plane 3, when $s = 200$ mm, $\theta = 6^\circ$, and $\omega R = 2700$ rpm. Refer to Figure 6 for the location of Plane 3.



- (1) Plane 1 - Interface plane between front rotating domain and stationary domain
- (2) Plane 2 - Interface plane between front rotating domain and rear rotating domain
- (3) Plane 3 - Interface plane between rear rotating domain and stationary domain
- (4) Plane 4 - Middle plane of duct diffuser
- (5) Plane 5 - End plane of the duct

Figure 6. Plane locations used for plotting.

3.2. Aerodynamic Performance Analysis of Counter-Rotating Ducted Fan

Numerical simulations were done for different rotor spacings and duct diffusion angles (see Section 2.1) under five rotating speeds of 1500 rpm, 1800 rpm, 2100 rpm, 2400 rpm, and 2700 rpm in hover mode. Figure 7 shows the thrust for the different rotor spacings and duct diffusion angles. The cases with a 0° duct diffusion angle generated about 9% higher thrust than the cases with a 6° duct diffusion angle. The rotor spacing variation had a minimal effect on improving the thrust.

The maximum thrust for both duct diffusion angles was observed for the rotor spacing of 200 mm, which can also be verified quantitatively from Table 2, where the thrust, thrust coefficient, and the power coefficient are shown for all cases. The thrust increased with increasing rotor spacing up to 200 mm, and then it started to reduce upon further increase of the rotor spacing. The most substantial thrust increment occurred when the rotor spacing increased from 120 mm to 160 mm. The thrust of the 200 mm rotor spacing increased by about 1.3–1.5% compared with that of the 120 mm rotor spacing. Like the tendency of the thrust results, the maximum thrust coefficient was observed when the rotor spacing was 200 mm. Moreover, the thrust coefficient was higher when the duct diffusion angle was 0° rather than 6°. However, the power coefficient was at a minimum when the rotor spacing was 120 mm and, in terms of the diffusion angle, the minimum power coefficient was attained for a 6° diffusion angle. In summary, from Table 2, it can be observed that the thrust, thrust coefficient, and power coefficient became higher either when the duct diffusion angle decreased from 6° to 0° or when the rotor spacing increased to 200 mm. Figure 8 shows the figure of merit for different rotor spacings and duct diffusion angles. The trend of FOM is similar to the thrust results. The FOM increased by about 1% with increasing rotor spacing up to 200 mm from 120 mm, and it reduced gradually upon a further increase of rotor spacing. The duct diffusion angle was more effective than the rotor spacing for improving the FOM. The FOM increased by about 6.7% when the duct diffusion angle decreased from 6° to 0°.

Table 2. Thrust, thrust coefficient, and power coefficient of all the counter-rotating ducted fan cases.

Duct Diffusion Angle [°]	Rotor Spacing [mm]	Thrust [N]				
		Rotating Speed [rpm]				
		120	160	200	240	300
6	120	49.49	71.30	97.09	126.86	160.62
	160	50.18	72.27	98.40	128.58	162.72
	200	50.38	72.56	98.84	129.15	163.52
	240	50.22	72.34	98.54	128.75	162.99
0	120	53.96	77.76	105.90	138.38	175.21
	160	54.78	78.93	107.49	140.46	177.80
	200	54.95	79.17	107.84	140.89	178.36
	240	54.81	78.98	107.58	140.55	177.91

Duct Diffusion Angle [°]	Rotor Spacing [mm]	Thrust Coefficient				
		Rotating Speed [rpm]				
		120	160	200	240	300
6	120	0.017335	0.017343	0.017350	0.017357	0.017364
	160	0.017576	0.017579	0.017584	0.017592	0.017591
	200	0.017646	0.017650	0.017664	0.017671	0.017678
	240	0.017589	0.017595	0.017609	0.017616	0.017620
0	120	0.018902	0.018914	0.018924	0.018933	0.018942
	160	0.019193	0.019199	0.019208	0.019218	0.019221
	200	0.019247	0.019256	0.019272	0.019277	0.019281
	240	0.019199	0.019212	0.019226	0.019231	0.019234

Duct Diffusion Angle [°]	Rotor Spacing [mm]	Power Coefficient				
		Rotating Speed [rpm]				
		120	160	200	240	300
6	120	0.003112	0.003103	0.003096	0.003090	0.003085
	160	0.003152	0.003143	0.003135	0.003130	0.003125
	200	0.003160	0.003151	0.003143	0.003138	0.003133
	240	0.003148	0.003139	0.003132	0.003126	0.003122
0	120	0.003327	0.003318	0.003311	0.003305	0.003301
	160	0.003371	0.003361	0.003354	0.003349	0.003344
	200	0.003372	0.003363	0.003356	0.003351	0.003347
	240	0.003362	0.003353	0.003347	0.003341	0.003337

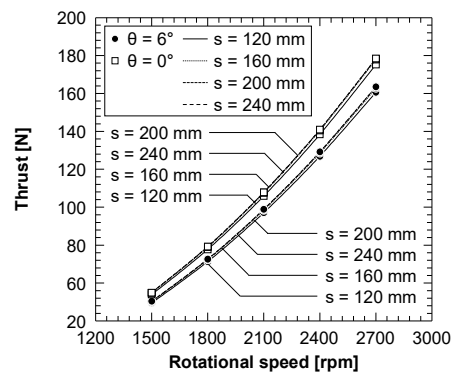


Figure 7. Thrust for different rotor spacings and duct diffusion angles.

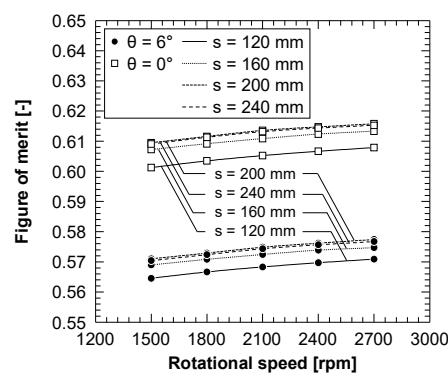


Figure 8. Figure of merit for different rotor spacings and duct diffusion angles.

Since the rotor spacing had a minimal effect on improving the aerodynamic performance of the counter-rotating ducted fan, henceforth, only the results of the cases with rotor spacings of 120 mm and 200 mm for $\theta = 0^\circ, 6^\circ$ simulated at the maximum rotational speed of 2700 rpm are discussed. Figure 9a–d displays the total pressure contour in Plane 3. See Figure 6 for the location of Plane 3.

The negative pressure region close to the duct shows rotor tip leakage loss. As the rotor spacing increases, the thrust increases by about 1%, and, hence, the positive pressure area is extended marginally. The change in the positive pressure area as the rotor spacing increases is not significant. However, when the duct diffusion angle reduces from 6° to 0° , the magnitude of the positive pressure increases significantly.

Figure 10a–d shows the axial velocity contours in Plane 4. See Figure 6 for the location of Plane 4. The axial velocity near the hub increases in the radial direction due to the 9% thrust increase as the duct diffusion angle reduces from 6° to 0° . As the duct diffusion angle is increased to 6° , the cross-sectional area of the duct is also increased, resulting in a lower axial velocity. The high axial velocity region is widened for an increase in the rotor spacing and a decrease in the duct diffusion angle.

Figure 11a–d shows the axial velocity profiles in the radial direction at different planes. See Figure 6 for the location of the planes. The radial length is normalized with the duct radius. In Figure 11a, the magnitude and profile of the axial velocities located at Plane 1 for all cases are fairly similar. Figure 11b indicates that the axial velocity increases at Plane 2 when the rotor spacing is narrow, which is caused by the influence of the rear rotor. The axial velocities in Plane 3 show variation only after the normalized radial length of about 0.7 (see Figure 11c). Moreover, at Plane 3, the magnitude of the axial velocity is higher when $s = 200$ mm, due to high thrust. In Figure 11d, the magnitude of the axial velocity at Plane 5 for $\theta = 6^\circ$ is reduced, resulting from the increased cross-sectional area of the duct.

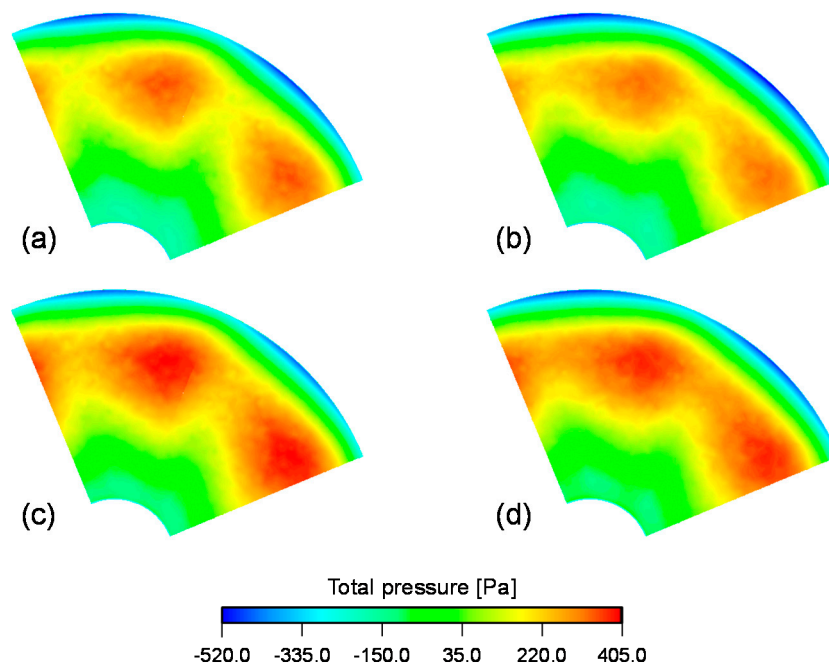


Figure 9. Total pressure contour in Plane 3 at 2700 rpm for: (a) $\theta = 6^\circ$, $s = 120$ mm; (b) $\theta = 6^\circ$, $s = 200$ mm; (c) $\theta = 0^\circ$, $s = 120$ mm; and (d) $\theta = 0^\circ$, $s = 200$ mm. See Figure 6 for the location of Plane 3.

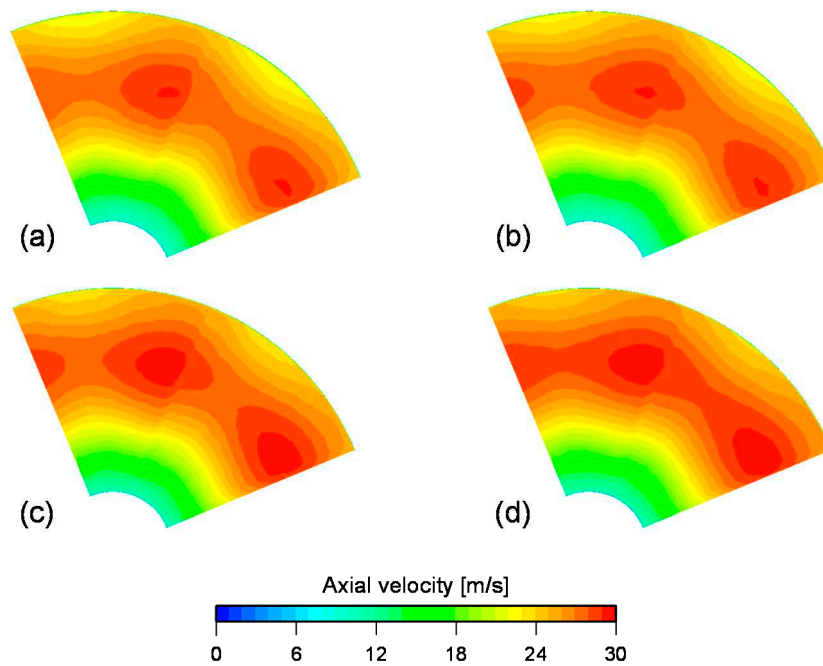


Figure 10. Axial velocity contour in Plane 4 at 2700 rpm for (a) $\theta = 6^\circ$, $s = 120$ mm; (b) $\theta = 6^\circ$, $s = 200$ mm; (c) $\theta = 0^\circ$, $s = 120$ mm; and (d) $\theta = 0^\circ$, $s = 200$ mm. See Figure 6 for the location of Plane 4.

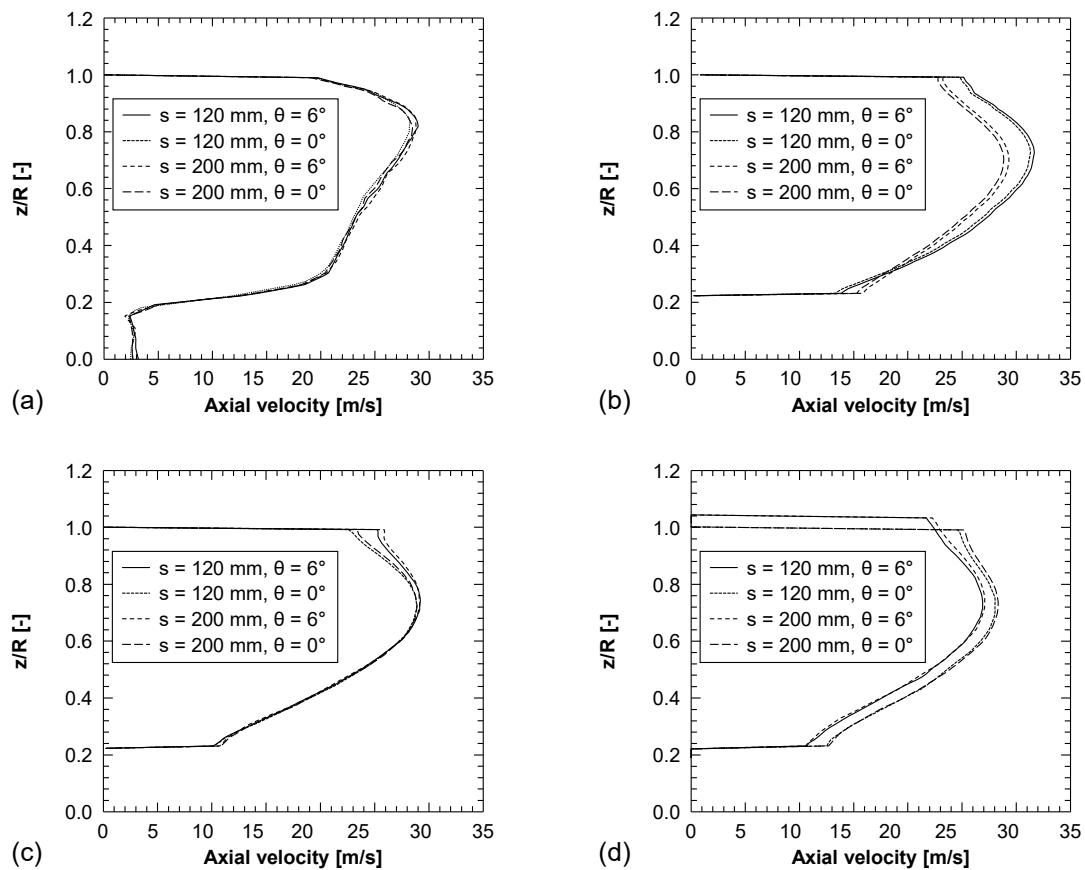


Figure 11. Axial velocity profile along the radial direction at 2700 rpm in (a) Plane 1; (b) Plane 2; (c) Plane 3; and (d) Plane 5. See Figure 6 for the location of the planes.

4. Conclusions

The present study explores the aerodynamic performances of a counter-rotating ducted fan in hover mode numerically. The effect of different rotor spacings and duct diffusion angles on the aerodynamic performances is examined. Key findings from this study are as follows:

1. The effect of the relative angle between the front and the rear rotor, due to the usage of the frozen rotor model, is negligible since the variation of thrust for the different relative angles is extremely low.
2. Comparison of the aerodynamic performance parameters for different rotor spacings revealed that the thrust, thrust coefficient, and FOM slightly increases with an increasing rotor spacing up to 200 mm, regardless of the duct diffusion angle. However, the thrust, thrust coefficient, and FOM start to reduce on further increases in the rotor spacing. Conversely, the power coefficient is at a minimum when the rotor spacing is 120 mm.
3. The maximum thrust coefficient is observed when the rotor spacing is 200 mm, and the thrust of the 200 mm rotor spacing increases by about 1.3–1.5% compared with the 120 mm rotor spacing.
4. The duct diffusion angle of 0° generates about 9% higher thrust and increases the FOM by 6.7%, compared with the 6° duct diffusion angle.
5. However, the increase in thrust also increases the power coefficient, which results in increased power consumption. The minimum power coefficient is attained for a 6° diffusion angle.
6. The duct diffusion angle is highly effective in improving the thrust and FOM of the counter-rotating ducted fan, rather than the rotor spacing.

5. Future Work

The present study discussed the effects of rotor spacing and the duct diffusion angle on the aerodynamic performances of a counter-rotating ducted fan in hover mode. However, to enhance the aerodynamic performance of the UAV, there are still several other design parameters to be considered. Different duct lip shapes and tip clearances could be considered to optimize the counter-rotating ducted fan toward the development of high-performance, efficient UAVs. Moreover, apart from the frozen rotor approach, it is critical to explore various other numerical approaches, such as harmonic analysis techniques, to numerically model the counter-rotating ducted fan.

Author Contributions: Validation, methodology, software, writing—original draft preparation, W.-Y.K.; validation, writing—original draft preparation, S.S.; conceptualization, methodology, supervision, writing—review and editing, S.-M.K. All authors have read and agreed to the published version of the manuscript.

Funding: This research received no external funding.

Conflicts of Interest: The authors declare no conflict of interest.

References

- Newman, S. *Foundations of Helicopter Flight*, 1st ed.; Elsevier: Amsterdam, The Netherlands, 1994.
- Thwaites, B. *Incompressible Aerodynamics*, 1st ed.; Oxford University Press: Oxford, UK, 1960.
- Yilmaz, S.; Erdem, D.; Kavsoglu, M.S. Performance of a ducted propeller designed for UAV applications at zero angle of attack flight: An experimental study. *Aerosp. Sci. Technol.* **2015**, *45*, 376–386. [[CrossRef](#)]
- Bontempo, R.; Manna, M. Effects of Duct Cross Section Camber and Thickness on the Performance of Ducted Propulsion Systems for Aeronautical Applications. *Int. J. Aerosp. Eng.* **2016**, *2016*, 9. [[CrossRef](#)]
- Xu, H.Y.; Xing, S.L.; Ye, Z.Y. Numerical Study of Ducted-fan Lip Stall Suppression Based on Inflatable Leading Lip Cell. In Proceedings of the 7th International Conference on Fluid Mechanics, Shandong, China, 24–27 March 2015.
- Wernicke, K.G.; Wernicke, R.K.; Weisend, N.A., Jr. Inflatable wing leading edge for high lift and deicing. In *NASA Tech Briefs*; NASA: Washington, DC, USA, 2000; Volume 1.
- Jiang, Y.; Ye, Z.; Zhan, Z. A method of inflatable leading edge for high lift, deicing and noise reduction. In Proceedings of the 47th AIAA Aerospace Sciences Meeting including The New Horizons Forum and Aerospace Exposition, Orlando, FL, USA, 5–8 January 2009.
- Graf, W.; Fleming, J.; Ng, W. Improving ducted fan UAV aerodynamics in forward flight. In Proceedings of the 46th AIAA Aerospace Sciences Meeting and Exhibit, Reno, NE, USA, 7–10 January 2008.
- Jung, S.N.; No, T.S.; Ryu, K.W. Aerodynamic performance prediction of a 30 kW counter-rotating wind turbine system. *Renew. Energy* **2005**, *30*, 631–644. [[CrossRef](#)]
- Vasel-Be-Hagh, A.; Archer, C.L. Wind farms with counter-rotating wind turbines. *Sustain. Energy Technol. Assess.* **2017**, *24*, 19–30. [[CrossRef](#)]
- Furukawa, A.; Shigemitsu, T.; Watanabe, S. Performance test and flow measurement of contra-rotating axial flow pump. *J. Therm. Sci.* **2007**, *16*, 7–13. [[CrossRef](#)]
- Kim, J.H.; Cho, B.M.; Kim, S.; Kim, J.W.; Suh, J.W.; Choi, Y.S.; Kanemoto, T.; Kim, J.H. Design technique to improve the energy efficiency of a counter-rotating type pump-turbine. *Renew. Energy* **2017**, *101*, 647–659. [[CrossRef](#)]
- Shigemitsu, T.; Fukutomi, J.; Okabe, Y. Performance and flow condition of small-sized axial fan and adoption of contra-rotating rotors. *J. Therm. Sci.* **2010**, *19*, 1–6. [[CrossRef](#)]
- Toge, T.D.; Pradeep, A.M. Experimental investigation of stall inception of a low speed contra rotating axial flow fan under circumferential distorted flow condition. *Aerosp. Sci. Technol.* **2017**, *70*, 534–548. [[CrossRef](#)]
- Srivastava, R.; Sankar, L.N. Efficient hybrid scheme for the analysis of counter-rotating propellers. *J. Propuls. Power* **1993**, *9*, 382–388. [[CrossRef](#)]
- Brizzolara, S.; Tincani, E.P.A.; Grassi, D. Design of contra-rotating propellers for high-speed stern thrusters. *Ships Offshore Struct.* **2007**, *2*, 169–182. [[CrossRef](#)]
- Ryu, M.; Cho, L.; Cho, J. The effect of tip clearance on performance of a counter-rotating ducted fan in a VTOL UAV. *Trans. Jpn. Soc. Aeronaut. Space Sci.* **2017**, *60*, 1–9. [[CrossRef](#)]

18. Han, H.; Xiang, C.; Xu, B.; Yu, Y. Experimental and computational analysis of microscale shrouded coaxial rotor in hover. In Proceedings of the 2017 International Conference on Unmanned Aircraft Systems, Miami, FL, USA, 13–16 June 2017.
19. Corsini, A.; Delibra, G.; Sheard, A.G. A critical review of computational methods and their application in industrial fan design. *ISRN Mech. Eng.* **2013**, *2013*, 20. [[CrossRef](#)]
20. Akturk, A.; Camci, C. Tip Clearance Investigation of a Ducted Fan Used in VTOL Unmanned Aerial Vehicles—Part I: Baseline Experiments and Computational Validation. *J. Turbomach.* **2014**, *136*, 021004. [[CrossRef](#)]
21. Ansys CFX 19.1. *Theory Guide 2018*; ANSYS, Inc.: Canonsburg, PA, USA, 2018.
22. Menter, F.R. Zonal two equation k-w turbulence models for aerodynamic flows. In Proceedings of the 24th Fluid Dynamics Conference, Orlando, FL, USA, 6–9 July 1993.
23. Menter, F.R. Two-equation eddy-viscosity turbulence models for engineering applications. *AIAA J.* **1994**, *32*, 1598–1605. [[CrossRef](#)]
24. Benim, A.C.; Brillert, D.; Cagan, M. Investigation Into the Computational Analysis of Direct-Transfer Pre-Swirl Systems for Gas Turbine Cooling. In Proceedings of the ASME Turbo Expo 2004: Power for Land, Sea, and Air, Vienna, Austria, 14–17 June 2004.
25. Bohn, D.; Ausmeier, S.; Ren, J. Investigation of the Optimum Clocking Position in a Two-Stage Axial Turbine. *Int. J. Rotating Mach.* **2005**, *3*, 202–210. [[CrossRef](#)]
26. Chalghoum, I.; Kanfoudi, H.; Elaoud, S.; Akrouf, M.; Zgolli, R. Numerical Modeling of the Flow Inside a Centrifugal Pump: Influence of Impeller–Volute Interaction on Velocity and Pressure Fields. *Arab. J. Sci. Eng.* **2016**, *41*, 4463–4476. [[CrossRef](#)]

Publisher’s Note: MDPI stays neutral with regard to jurisdictional claims in published maps and institutional affiliations.



© 2020 by the authors. Licensee MDPI, Basel, Switzerland. This article is an open access article distributed under the terms and conditions of the Creative Commons Attribution (CC BY) license (<http://creativecommons.org/licenses/by/4.0/>).

Article

Thermal Performance of T-shaped Obstacles in a Solar Air Heater

Seung-Yong Ahn ¹ and Kwang-Yong Kim ^{2,*} 

¹ Department of Mechanical Engineering, Graduate School, Inha University, Incheon 22212, Korea; ahnsy9028@inha.edu

² Department of Mechanical Engineering, Inha University, Incheon 22212, Korea

* Correspondence: kykim@inha.ac.kr; Tel.: +82-(32)-860-7317

Received: 18 September 2020; Accepted: 13 October 2020; Published: 17 October 2020



Abstract: This paper proposes T-shaped ribs as obstacles attached to the heat absorber plate in a rectangular solar air heater to promote heat transfer. The thermal and aerodynamic performance of the solar heater was numerically evaluated using three-dimensional Reynolds-averaged Navier–Stokes equations with the shear stress transport turbulence model. A parameter study was performed using the ratios of rib height to channel height, rib width to channel width, and rib width to rib height. The area-averaged Nusselt number and friction factor were selected as the performance parameters of the solar air heater to evaluate the heat transfer and friction loss, respectively. In addition, the performance factor was defined as the ratio of the area-averaged Nusselt number to the friction factor. The maximum area-averaged Nusselt number was found at $h/e = 0.83$ for a fixed rib area. Compared with triangular ribs, the T-shaped ribs showed up to a 65 % higher area-averaged Nusselt number and up to a 49.7% higher performance factor.

Keywords: solar air heater; ribs; Nusselt number; friction factor; Reynolds-averaged Navier–Stokes equations

1. Introduction

Recently, as the problem of environmental pollution due to the use of fossil fuels has emerged, interest in solar heat systems as a renewable energy source is increasing. A solar air heater (SAH) is a device that heats air flowing over an absorber plate by using solar energy. It is used for space heating, drying of agricultural products, and dehydration of industrial products [1].

Compared to liquid solar heaters, SAHs have a disadvantage of low heat transfer rate, because the density of air is lower than that of a liquid. The heat transfer performance of an SAH is determined by various factors such as the velocity of the flow, the length and depth of the heater, and the shape of the heat absorber plate. The ratio between the area of the actual heat absorber and the absorber area normal to the solar radiation, which is called the absorber shape factor, is an important parameter in the design of SAHs.

Obstacles attached to the heat absorber plate are generally known to increase the heat transfer by enlarging the heat transfer area and enhancing turbulence intensity. However, as the area of the obstacles attached to the heat absorber plate increases, the pressure drop through the SAH also increases. Therefore, many studies have been conducted on the shape of the obstacles to enhance the overall heat transfer performance by increasing the heat transfer while minimizing the pressure drop [2–14].

Kabeel and Mecarik [2] studied the effect of the shape of the heat absorber plate on the performance of an SAH. It was confirmed that the heat transfer performance of the SAH with triangular obstacles was higher than that with longitudinal pins. Moumni et al. [3] performed an energy analysis of an

SAH with rectangular plate fins. The results for the heat transfer coefficient were compared with the results obtained for the SAH without obstacles. The collector efficiency factor of the SAH with plate pins increased by 30% compared to the case without obstacles. Essen [4] performed energy and exergy analysis through experiments on obstacles of various shapes attached to an SAH. He concluded that the heat and exergy efficiencies of the SAH with obstacles increased as compared to the SAH without obstacles and the collector efficiency factor depended on the shape, area, orientation, and arrangements of the obstacles. Saini and Saini [5] conducted an experimental study on the effect of the rib shape on the heat transfer performance of an SAH with arc-shaped ribs. They developed correlations for the Nusselt number and friction factor in terms of Reynolds number (Re), relative roughness height, and arc angle of ribs.

Ozgen et al. [6] conducted an efficiency evaluation of an SAH with the flows flowing over the upper and lower surfaces of a heat absorber plate where aluminum cans were attached. Depaiwa et al. [7] experimentally studied the forced convective heat transfer and friction loss for the turbulent flow in an SAH with rectangular winglet vortex generators. They tested an SAH with 20 winglet vortex generators at Reynolds numbers ranging from 5000 to 23,000. The heat transfer rates in this SAH were 174% to 182% higher than that of the SAH with a smooth absorber plate. Bekele et al. [8] performed an experimental and numerical analysis on the effects of the height and longitudinal pitch of triangular obstacles on the heat transfer in an SAH. Through the analysis of the internal flow of the SAH, it was reported that recirculating flows occurring around the triangular obstacles effectively increased the turbulence intensity, thereby increasing the heat transfer rate by 3.6 times compared to the SAH without obstacles. Yadav et al. [9] conducted an experimental study on the heat transfer performance and friction factor of the turbulent flow over a heat absorber plate with circular protrusions arranged in angular arc. The Nusselt number and friction factor were found to be 2.89 times and 2.93 times higher than those of the unobstructed SAH, respectively.

Kulkarni and Kim [10] performed a numerical analysis to find the optimal shape of obstacles attached to an SAH. Numerical analysis was performed for four different shapes and three different arrangements of the obstacles. The Nusselt number and friction coefficient were greatly influenced by the shape and arrangement of the obstacles, and pentagonal obstacles showed the highest performance factor among the tested shapes. Alam and Kim [11] performed a numerical analysis to predict the heat transfer performance of an SAH with conical protrusion ribs. The maximum thermal efficiency of the collector was reported to be 69.8%. They developed correlations for the Nusselt number and friction factor in terms of Reynolds number, relative roughness height, and relative rib pitch. Compared with the results of numerical analysis, the correlations for the Nusselt numbers and friction factor showed average absolute standard deviations of 2.78% and 5.25%, respectively. In addition, studies on SAHs with various types of obstacles such as V-shaped ribs, diamond-shaped ribs, and arc-shaped ribs have been also conducted to date [12–14].

In this study, T-shaped ribs are newly proposed to further improve the performance of an SAH by considering both the heat transfer and pressure drop. The heat transfer and pressure drop characteristics of the SAH with ribs were analyzed using three-dimensional Reynolds-averaged Navier–Stokes (RANS) equations. A parametric study was conducted to confirm the effects of geometric parameters of the T-shaped ribs on the heat transfer and pressure drop in the SAH. The performance of the SAH with the proposed ribs was compared to SAHs with previously developed obstacles.

2. Solar Air Heater Model

Figure 1 shows the computational domain of the SAH and geometric parameters of the T-shaped rib. Only a half of the entire SAH domain is included in the computational domain using symmetric conditions. The computational domain consists of three sections; inlet Section ($800 \text{ mm} \times 150 \text{ mm} \times 50 \text{ mm}$ ($L_1 \times W/2 \times H$)), test Section ($1200 \text{ mm} \times 150 \text{ mm} \times 50 \text{ mm}$ ($L_2 \times W/2 \times H$)), and outlet Section ($500 \text{ mm} \times 150 \text{ mm} \times 50 \text{ mm}$ ($L_3 \times W/2 \times H$)). This computational domain for evaluating

the performance of the SAH was set according to the guidelines of the ASHRAE standard 93–97 [15], and the lengths of the inlet and outlet sections of the domain are $5(WH)^{0.5}$ and $2.5(WH)^{0.5}$, respectively.

The upper wall (i.e., heat absorber plate) of the test section absorbs solar energy, and air is heated as it flows from the inlet to the outlet of the channel. The obstacles, T-shaped ribs, are attached to the heat absorber plate. Thirteen rows of ribs are arranged in a zigzag, as shown in Figure 1a. The thickness of the rib is 0.5 mm, and t is 8 mm. Each row contains one or one and a half ribs in the computational domain. The first row of ribs is located 71.75 mm downstream of the inlet of the test section.

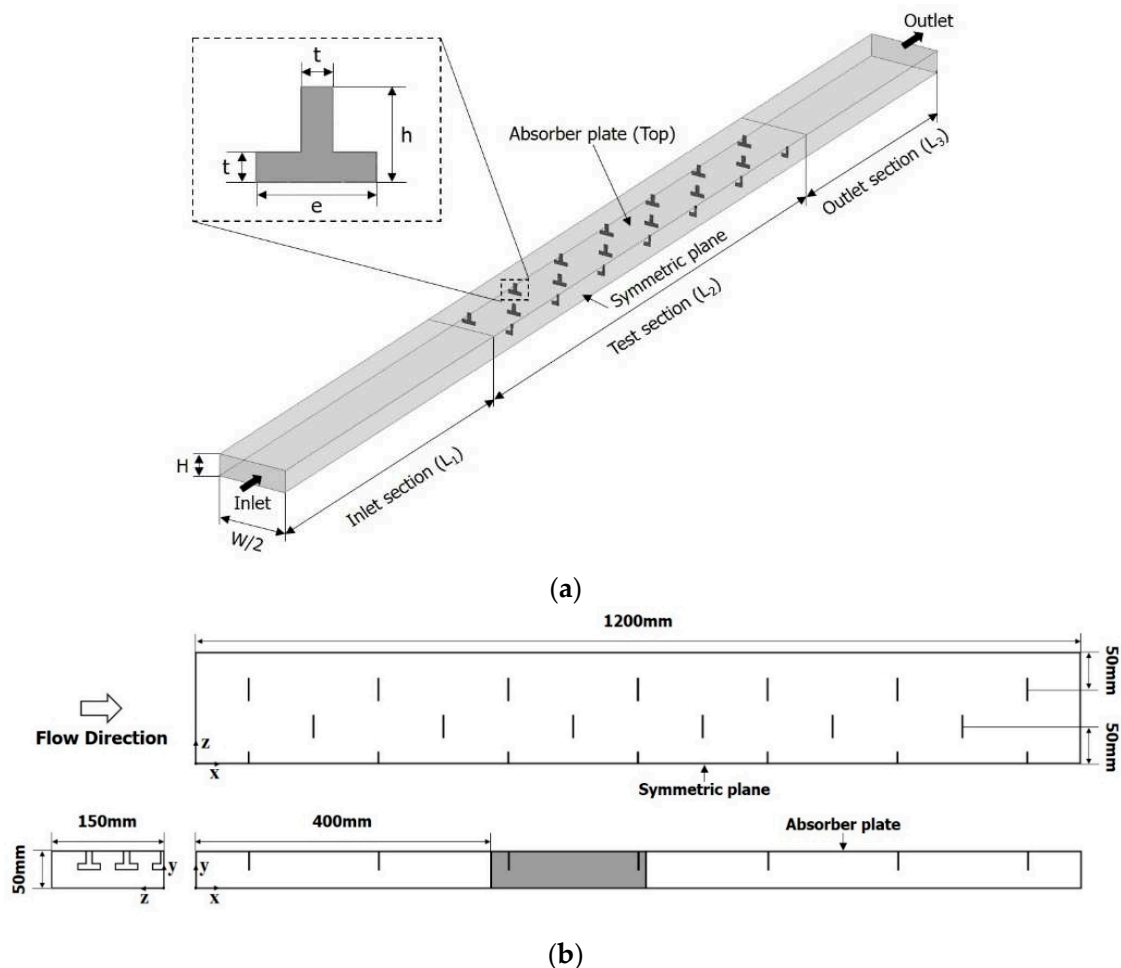


Figure 1. Computational domain of the solar air heater with T-shaped ribs. (a) Computational domain, (b) Test section.

3. Numerical Methods

In this study, ANSYS-CFX 15.0 [16], a commercial code which employs an unstructured grid, was used to analyze the flow and heat transfer using RANS equations. The shear stress transport (SST) [17] model was used for the analysis of turbulence. The SST model was designed to take advantage of the $k-\epsilon$ and $k-\omega$ models by combining these two models using a weighting function so that the $k-\omega$ model is applied near the wall and the $k-\epsilon$ model is applied in the other area. The SST model is known to be effective in predicting the flow recirculation due to separation.

Air at 25 °C was used as the working fluid, and velocity and static pressure conditions were assigned to the inlet and outlet boundaries, respectively. A constant heat flux condition of 815 W/m^2 was applied to the surface of the heat absorber plate, and the other solid surfaces were assumed to be adiabatic. The symmetric conditions were used at the symmetric plane of the computational domain, and a no-slip condition was used at the wall boundaries. An unstructured tetrahedral grid system

was constructed in most of the computational domain, but prism meshes were placed near the wall to resolve the laminar sublayer. In order to use low-Re modeling for near-wall turbulence, the y^+ values of the first grid points from the wall were kept at less than 1.0.

To find the grid dependency of the numerical solution, a test was performed according to the procedure proposed by Roache [18] and Celik and Karatekin [19]. This test analyzes the grid convergence index (GCI), which represents numerical uncertainty through the estimation of discretization error based on Richardson extrapolation. Table 1 shows the results of the GCI analysis where the grid refinement factor (r) was set to 1.3 for three different grid systems (N_1 , N_2 , and N_3). This test was performed on the SAH with the reference ribs described in Table 2. As the number of grid nodes increases, the Nusselt number tends to converge gradually. When N_2 is used, the extrapolated relative error (e_{ext}^{21}) is 0.0015% and the relative error is 0.0019%, which confirms a relatively small numerical uncertainty. Therefore, based on this result, the optimum grid system is selected as N_2 , which is shown in Figure 2.

Table 1. Results of grid convergence index (GCI) analysis using Richardson extrapolation.

Parameter		Value
Number of computational cells	$N_1/N_2/N_3$	8,071,835/3,516,156/2,336,956
Grid refinement factor	r	1.3
Computed Nusselt numbers corresponding to N_1 , N_2 , N_3	ϕ_1	178.137
	ϕ_2	178.356
	ϕ_3	180.072
Apparent order	p	5.306
Extrapolated value	ϕ_{ext}^{21}	178.134
Approximate relative error	e_a^{21}	0.123%
Extrapolated relative error	e_{ext}^{21}	0.0015%
Grid convergence index	GCI_{fine}^{21}	0.0019%

Table 2. Ranges and reference values of geometric parameters.

Parameter	Lower Limit	Upper Limit	Reference
h/H	0.3	0.7	0.50
e/W	0.067	0.133	0.10
h/e	0.38	1.75	0.83

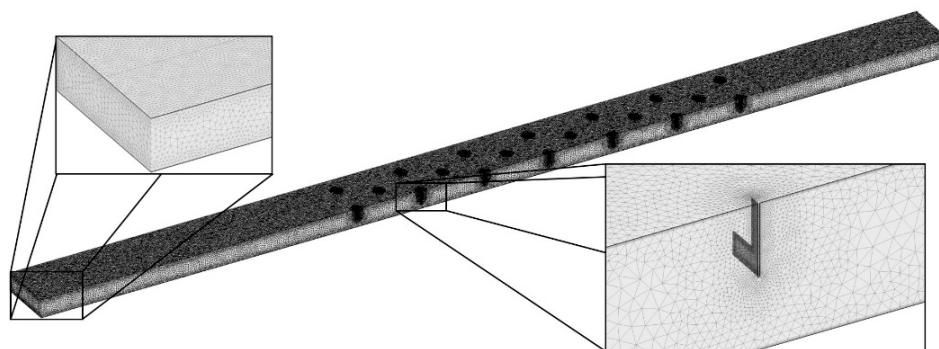


Figure 2. Example of grid system.

In order to determine the convergence of the numerical solution, the root mean square residual was reduced to 10^{-6} or less, and about 1200 iterations were performed. The computational time required for a single analysis was about 14 h when a personal computer with an Intel Core i7 3.41 GHz CPU was used for the computations.

4. Geometric and Performance Parameters

In order to examine the effects of the rib shape shown in Figure 1 on the heat transfer performance and pressure drop, three dimensionless parameters were selected; the ratios of the rib height to the channel height (h/H), the rib width to the channel width (e/W), and the rib height to the rib width (h/e). The ranges and reference values of these parameters are shown in Table 2.

Three performance parameters are defined to evaluate the heat transfer and pressure drop in the SAH. The performance parameter related to the heat transfer is defined as follows:

$$F_{Nu} = \frac{Nu_o}{Nu_s} \quad (1)$$

Nu_o is the area-averaged Nusselt number on the heat transfer surface.

$$Nu_o = \frac{q_o D_h}{k_a (T_p - T_s)} \quad (2)$$

where T_p is the average temperature at the surface of the heat absorber plate including the obstacles, T_s is the bulk temperature of the working fluid, k_a is the thermal conductivity of the fluid, q_o is the heat flux at the heat absorber plate, D_h is the hydraulic diameter of the flow channel, and Nu_s is the Nusselt number for a fully developed flow in a smooth channel without obstacles, which is calculated from the following Dittus–Boelter equation.

$$Nu_s = 0.024 Re^{0.8} Pr^{0.4} \quad (3)$$

where Reynolds number, Re , is defined using a hydraulic diameter, and Pr indicates the Prandtl number.

The definition of the performance parameter related to the pressure drop is as follows:

$$F_f = \left(\frac{f_o}{f_s} \right)^{1/3} \quad (4)$$

Here, f_o is the friction factor in the flow channel with obstacles.

$$f_o = \frac{2(\Delta P)D_h}{4\rho LU^2} \quad (5)$$

where Δp is the pressure drop in the test section, ρ is the density of the working fluid, U is the average velocity of the flow, L is the length of the flow channel (test section), and f_s is the friction factor for the fully developed flow in the smooth channel, which is calculated from the following modified Blasius equation.

$$f_s = 0.085 Re^{-0.25} \quad (6)$$

The performance factor, PF [20], for evaluating the performance of an SAH considering both the heat transfer performance and pressure drop at the same time, is defined as follows:

$$PF = \frac{F_{Nu}}{F_f} \quad (7)$$

5. Results and Discussion

To prove the validity of the numerical analysis, the numerical results for the Nusselt number, Nu_o , and friction factor, f_o , are compared with corresponding empirical formulas for different Reynolds numbers in the flow channel without obstacles, as shown in Figure 3. The numerical results show good overall agreement with the empirical formulas. As Reynolds number increases, the relative error tends to decrease in the case of Nu_o . Compared with the experimental data, the average relative error of the computed Nusselt numbers within the tested Reynolds number range is less than 3.29%, and it is less than 2.71% for the friction factor.

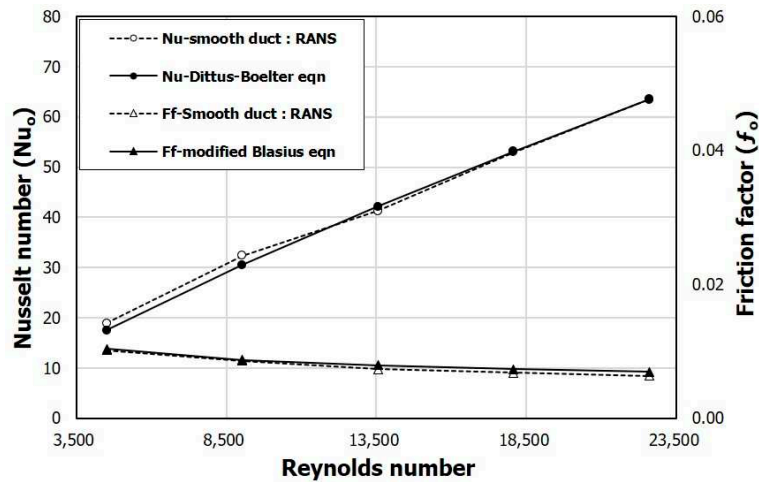


Figure 3. Validation of numerical results for smooth duct.

In addition, the validation test was also performed for the case with obstacles. The numerical results are compared with the experimental data obtained by Bekele et al. [8] for the SAH with triangular obstacles under the same boundary conditions, as shown in Figure 4. The numerical results agree well qualitatively with the experimental data. In the results for the Nusselt number, the computational and empirical slopes according to the Reynolds number are exactly the same but, quantitatively, they show a small difference unlike the case without obstacles. The average relative error for the Nusselt number compared to the experimental data within the tested Reynolds number range is less than 4.43%, and that for the friction factor is less than 1.94%, which indicates that the accuracy of the numerical analysis results is acceptable for further calculations.

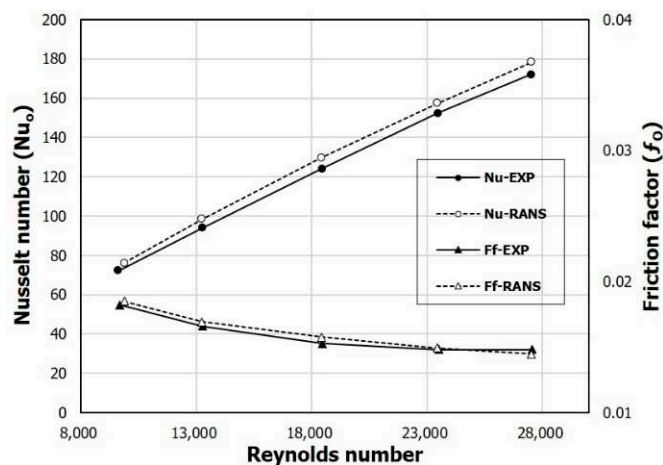


Figure 4. Validation of numerical results for a solar air heater (SAH) with triangular ribs using experimental data of Bekele et al. [8].

The three dimensionless geometric parameters of the SAH with proposed T-shaped ribs presented in Table 2 were used to find the effects of the rib shape on the performance parameters, i.e., F_{Nu} , F_f , and PF. The parametric study was performed at a Reynolds number of 22,600. In the case of two variables, h/H and e/W , the reference value in Table 2 was applied to the parameter that was not changed, and the area of the rib was changed accordingly during the parametric study. However, in the case of h/e , the test was conducted with the rib area fixed at 375 mm². Therefore, in this case, both the absolute values of h and e changed to keep the area constant according to the change of h/e . In all cases, the size of t was kept constant.

The results of the parametric study for the ratio of the rib height to the channel height (h/H) are shown in Figures 5–9. Figures 5 and 6 show the changes in the performance parameters, F_{Nu} and F_f , defined by Equations (1) and (2), respectively, in a range of $0.3 \leq h/H \leq 0.7$. The computational values are presented at five points indicated by circular symbols, and the line is a curve fit of the values at these points. It can be seen that F_{Nu} has the maximum value between $h/H = 0.5$ and 0.6 and it gradually decreases after that (Figure 5). On the other hand, F_f continues to increase as h/H increases, as shown in Figure 6. Therefore, as the rib height increases with the fixed rib width, there exists the maximum value in the heat transfer rate, but the pressure drop increases continuously. Similar heat transfer performances are found at $h/H = 0.5$ and 0.6 (Figure 5), but the pressure drop is lower at the lower rib height ($h/H = 0.5$), as shown in Figure 6. Therefore, in the PF distribution shown in Figure 7, the maximum performance factor appears at $h/H = 0.5$.

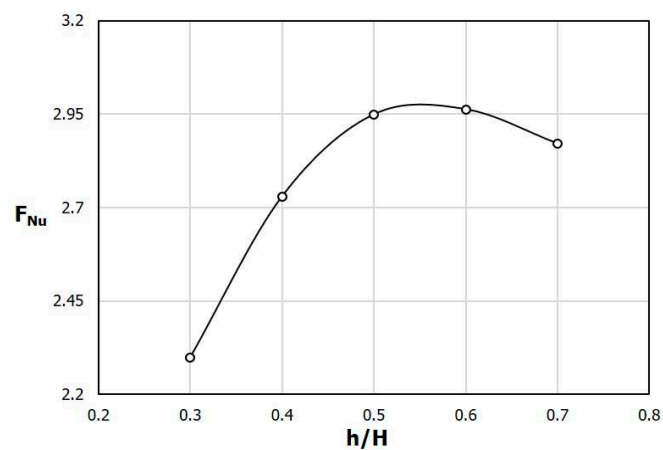


Figure 5. Variation of the performance parameter related to heat transfer (F_{Nu}) with the ratio of the rib height to the channel height (h/H) (the ratio of the rib width to the channel width (e/W) = 0.1).

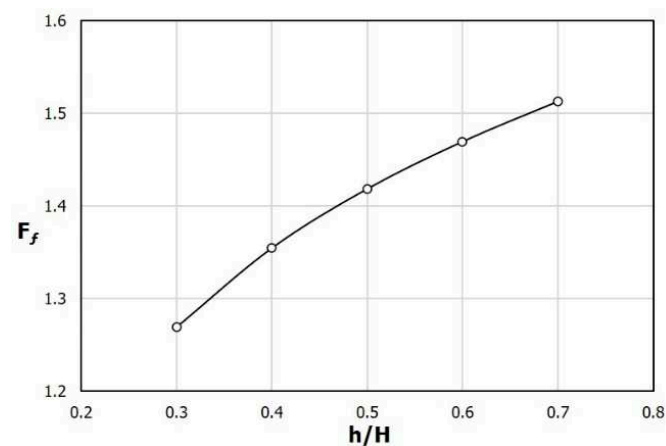


Figure 6. Variation of the performance parameter related to the pressure drop (F_f) with h/H ($e/W = 0.1$).

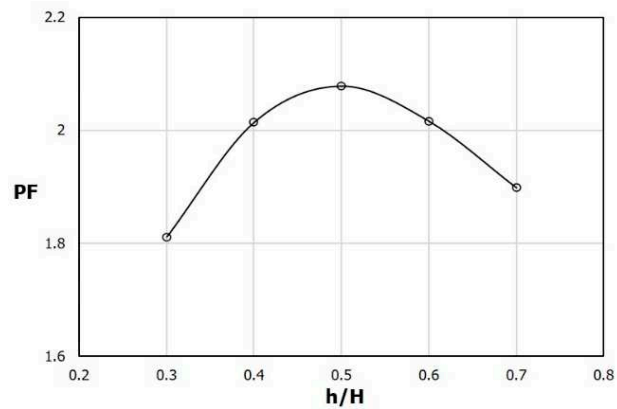


Figure 7. Variation of performance factor (PF) with h/H ($e/W = 0.1$).

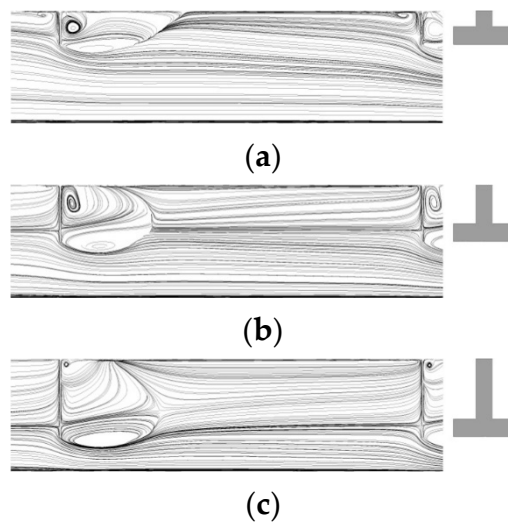


Figure 8. Streamlines on $x-y$ plane ($z = 0$) between fifth and seventh ribs (dark region in Figure 1b) for different h/H . (a) $h/H = 0.3$, (b) $h/H = 0.5$, (c) $h/H = 0.7$.

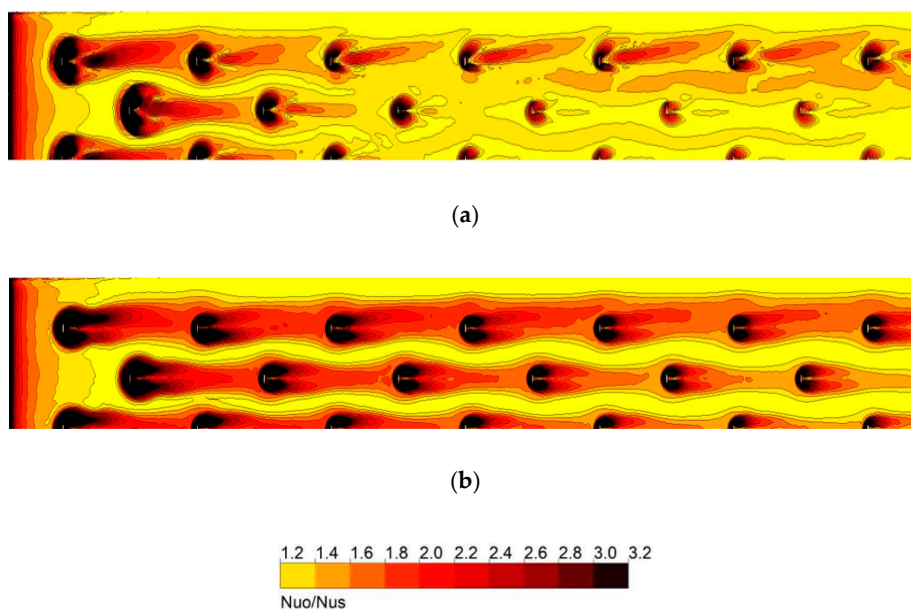


Figure 9. Nusselt number distributions on the heated surface for different h/H . (a) $h/H = 0.3$, (b) $h/H = 0.5$.

Figure 8 shows the streamlines between the 5th and 7th ribs (indicated by a dark region in Figure 1b) at the symmetric plane (i.e., x-y plane at $z = 0$) for different h/H . Due to the geometric shape of the rib, two recirculation regions are formed in the direction of the rib height. As h/H increases, the size of the recirculation region near the upper wall increases. Additionally, as h/H increases from 0.3 to 0.5, the reattachment distance rapidly decreases. This rapid reduction in the reattachment distance in this h/H range greatly enhances the heat transfer, as shown in Figure 5, due to early re-development of the thermal boundary layer. In Figure 9, the local Nusselt number distributions on the heat transfer surface for $h/H = 0.3$ and 0.5 are different. In the case of $h/H = 0.5$, the Nusselt number level appears to be higher around and downstream of each rib compared to the case of $h/H = 0.3$.

Figures 10–14 show the effects of the ratio of the rib width to the channel width (e/W) on the performance of the SAH. Figures 10 and 11 show the variations of the two performance parameters, F_{Nu} and F_f , respectively, with e/W , in a range of $0.067 \leq e/W \leq 0.133$. As e/W increases, both F_{Nu} and F_f increase almost linearly. This is presumed to be a phenomenon that occurs because both the turbulence intensity and pressure loss increase due to the increase in the area of the obstacles as e increases while the height h is kept constant. In the PF distribution shown in Figure 12, the maximum value is found around $e/W = 0.08$, but the overall variation with e/W is very small compared to that in Figure 7 for h/H .

Figure 13 shows the streamlines between the 5th and 7th ribs at the symmetric plane for different h/H . It can be seen that as e/W increases, the recirculation region located near the top of the rib increases. Since the reattachment distance does not change with e/W , the heat transfer enhancement according to the change in e/W does not seem to be related to the reattachment distance. Figure 14 shows the distributions of the Nusselt number on the heat transfer surface between the 5th and 7th ribs. As e/W increases, the increased width of the rib increases the width of the high Nusselt number area in the lateral direction, thereby increasing the overall Nusselt number.

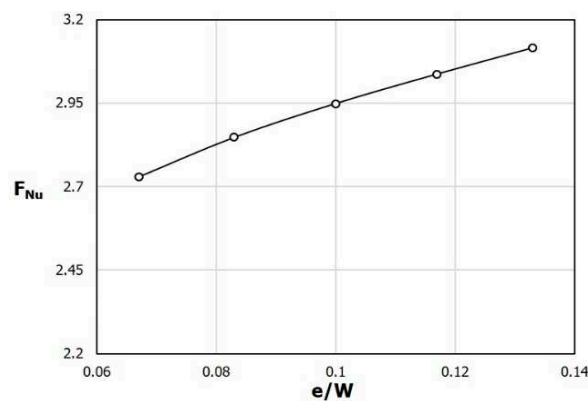


Figure 10. Variation of F_{Nu} with e/W ($h/H = 0.5$).

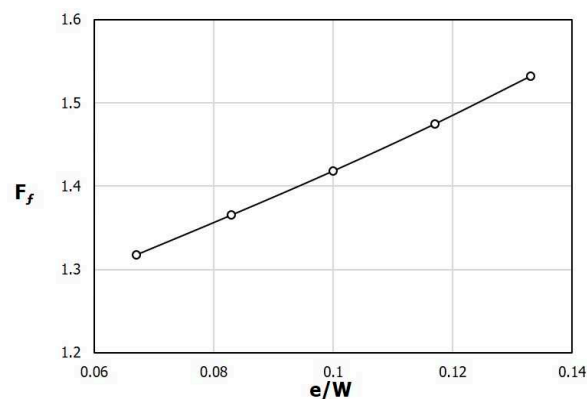


Figure 11. Variation of F_f with e/W ($h/H = 0.5$).

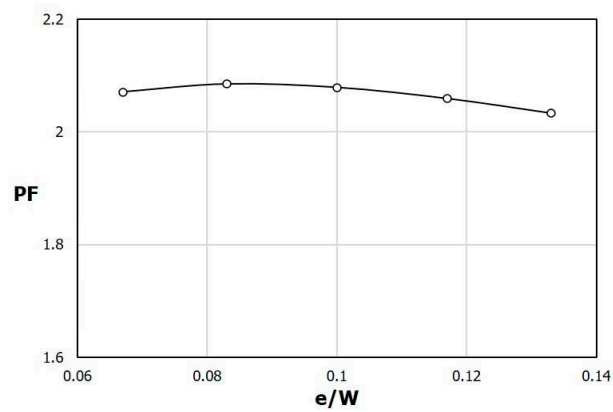


Figure 12. Variation of PF with e/W (h/H = 0.5).

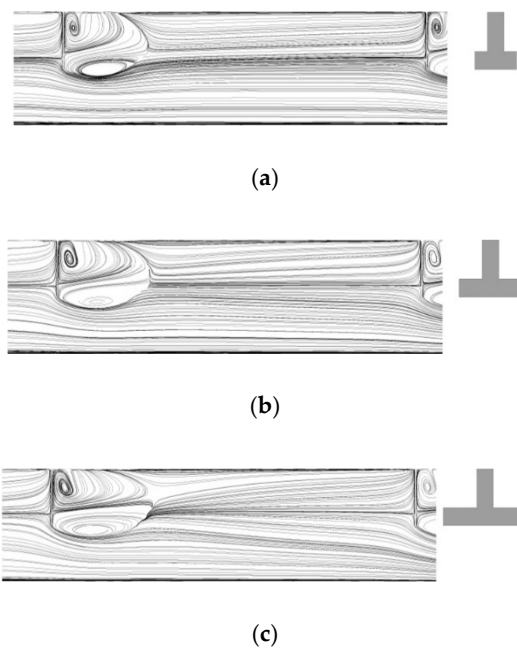


Figure 13. Streamlines on x-y plane ($z = 0$) between fifth and seventh ribs for different e/W. (a) e/W = 0.067, (b) e/W = 0.10, (c) e/W = 0.133.

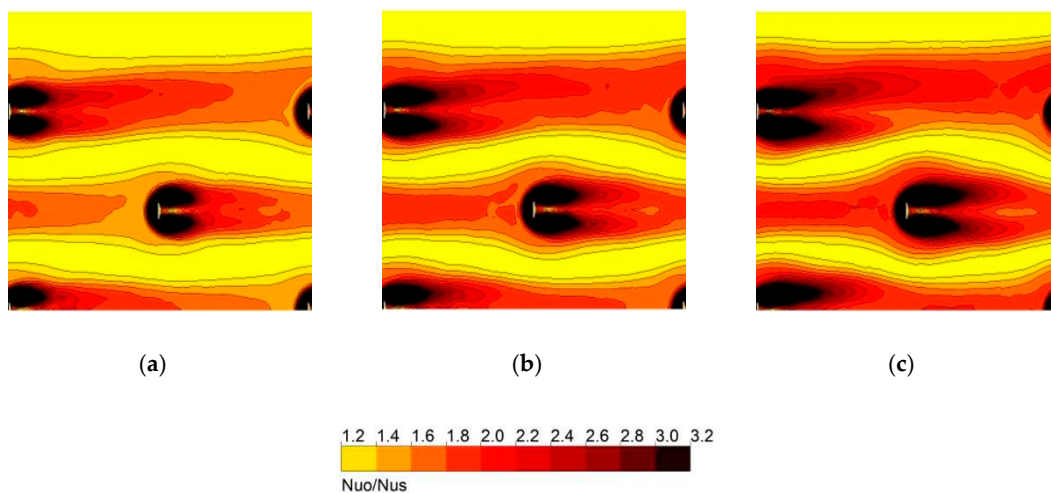


Figure 14. Nusselt distributions on the heated surface between fifth and seventh ribs for different e/W. (a) e/W = 0.067; (b) e/W = 0.10; (c) e/W = 0.133.

The variation of F_{Nu} with the ratio of the rib height to the rib width (h/e) keeping the rib area constant is shown in Figure 15. At $h/e = 0.83$, the heat transfer is maximized. This variation of F_{Nu} is similar to the variation with h/H shown in Figure 5. However, unlike Figure 5, the variation curve of F_{Nu} shown in Figure 15 is more symmetrical as the area of the rib is kept constant in this case. The variation of F_f with h/e shown in Figure 16 is very small compared to the variations with h/H and e/W shown in Figures 6 and 11, respectively. In the cases with h/H and e/W , the area of the rib changes, but in this case with h/e , the area of the rib remains constant. Accordingly, it can be seen that the pressure drop is greatly influenced by the area of the rib rather than the aspect ratio of the rib.

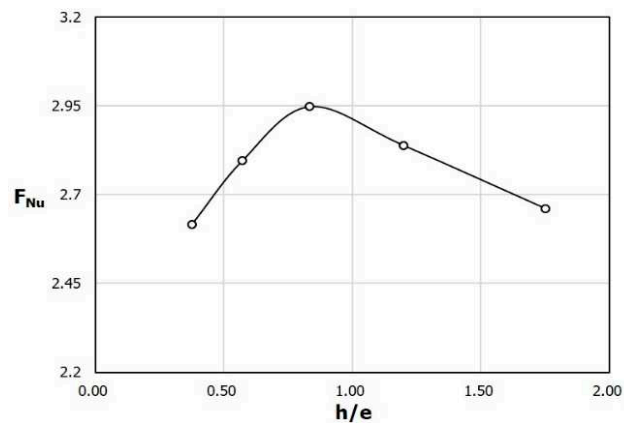


Figure 15. Variation of F_{Nu} with the ratio of the rib height to the rib width (h/e) (rib area = 375 mm^2).

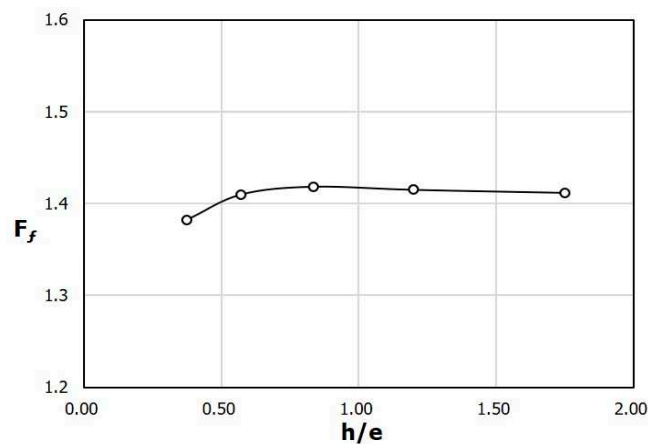


Figure 16. Variation of F_f with h/e (rib area = 375 mm^2).

Since the change in the pressure drop appears small over the entire range of h/e , the variation of the performance factor PF with h/e , shown in Figure 17, shows a qualitatively similar variation to that of F_{Nu} (Figure 15). The maximum value of PF also appears at $h/e = 0.83$.

Figure 18 shows the Nusselt number distributions on the heat transfer surface between the 5th and 7th rib rows. At $h/e = 0.83$, where the highest heat transfer occurs, the area of the high Nusselt number region is the largest. This indicates that the heat transfer enhancement due to the production of turbulent kinetic energy becomes most effective when h and e have similar sizes while keeping the rib area constant.

To demonstrate the superiority of the heat transfer performance of the SAH with T-shaped ribs proposed in this study, the performance parameters are compared with the experimental data for the SAH with triangular ribs measured by Bekele et al. [8], as shown in Figures 19 and 20. The comparison was performed for the same cross-sectional area of the ribs and the same spacing between the ribs. The T-shaped rib used for the comparison is the reference rib presented in Table 2. Figure 19 shows the

variations of the Nusselt number (Nu_o) and friction factor (f_o) with Reynolds number. In the case of the friction factor, the T-shaped ribs show a slightly larger value than that with the triangular ribs in the entire Reynolds number range. However, the Nusselt number shows a large uniform improvement at all Reynolds numbers. Compared to the triangular ribs, the T-shaped ribs show Nusselt numbers that are 65% higher at $Re = 4510$ and 21.5% higher at $Re = 22,600$. On the other hand, a 35% higher pressure drop occurs at $Re = 4510$ and a 31% higher pressure drop occurs at $Re = 22,600$ than for the triangular ribs. Figure 20 shows the comparison of the performance factor PF between the two different ribs. The PF of the T-shaped ribs is 49.7% higher at $Re = 4510$, and 11% higher at $Re = 22,600$ than for the triangular ribs.

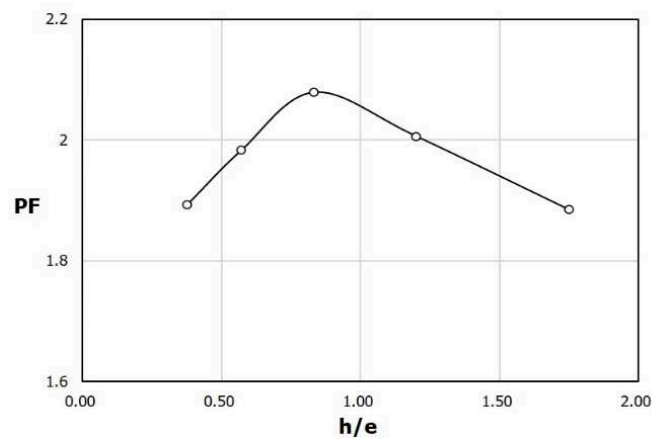


Figure 17. Variation of PF with h/e (rib area = 375 mm^2).

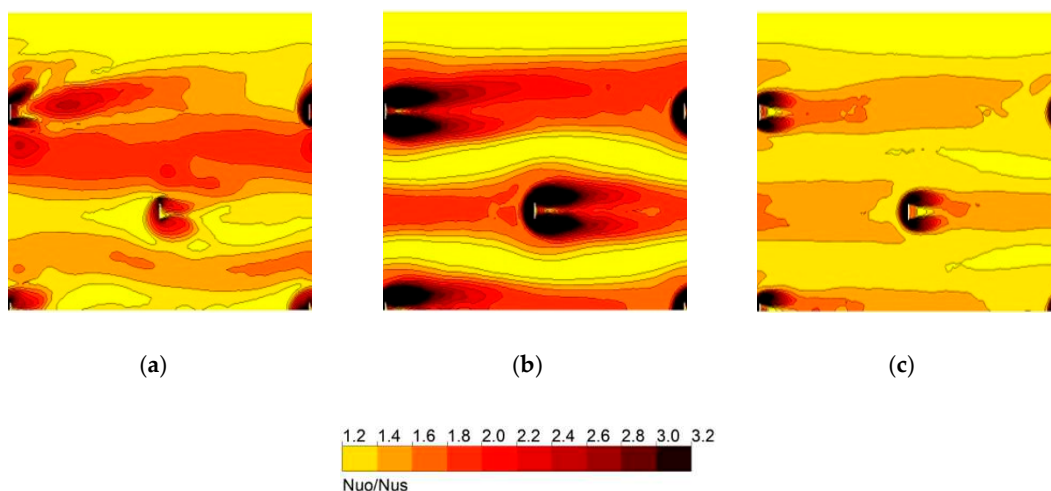


Figure 18. Nusselt number distributions on the heated surface between fifth and seventh ribs for different h/e . (a) $h/e = 0.38$; (b) $h/e = 0.83$; (c) $h/e = 1.75$.

Table 3 shows a comparison of PF ranges among various obstacle shapes developed to date. These obstacles were tested by previous experimental or numerical studies using the parameters of longitudinal pitch (P_1/e), relative obstacle height (e/H), relative roughness height (e/D), relative roughness pitch (P/e), relative longitudinal pitch between the rows of winglets (P/H), and number of waves on the delta winglet (ϕ). The T-shaped ribs proposed in this study cause two recirculation regions formed in the height direction, as shown in Figures 8 and 13, due to their unique geometric shape. These multiple recirculation zones are expected to promote the production of turbulent kinetic energy and thus further enhance the turbulent heat transfer compared to the other obstacles in Table 3.

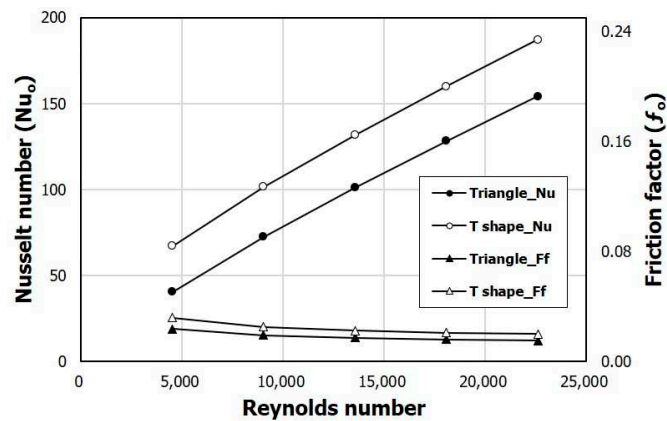


Figure 19. Comparison of performance parameters between T-shaped and triangular ribs.

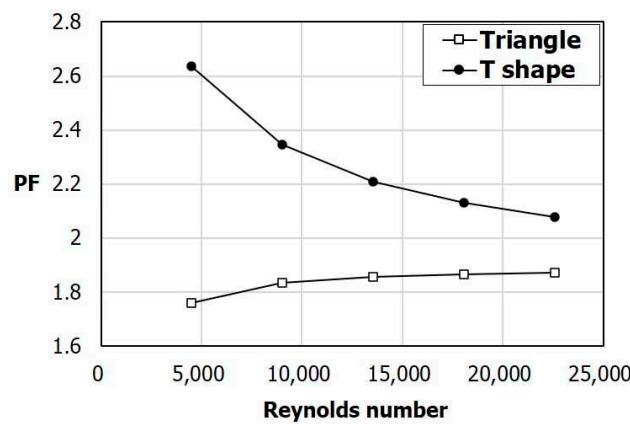


Figure 20. Comparison of PF between T-shaped and triangular ribs.

Table 3. Comparison of performance factor range obtained in the present study with those obtained in the previous experimental or numerical studies on obstacle shape.

Investigator	Geometrical Shape of Obstacles	Parameters	PF Range
Bekele et al. [8]	Delta-shaped ribs	Re = 3400–28000 P ₁ /e = 1.5–5.5 e/H = 0.5–0.75 θ = 90 °	1.10–2.14
Yadav et al. [21]	Equilateral triangular sectioned ribs	Re = 3800–18000 P ₁ /e = 7.14–35.71 e/D = 0.021–0.042	1.36–2.11
Deo et al. [22]	Multi-gap V-down ribs combined with staggered ribs	Re = 4000–12000 P/e = 4–14 e/D = 0.026–0.057 θ = 40°–80 °	2.09–2.45
Gawande et al. [23]	L-shaped ribs	Re = 3800–18000 P/e = 7.14–17.86 e/D = 0.042	1.62–1.90
Sawhney et al. [24]	Wavy delta winglets	Re = 4000–17300 P/H = 3–6 φ = 3–7 θ = 60 °	1.46–2.09
Present study	T-shaped ribs	Re = 4510–22600 h/H = 0.3–0.7 e/W = 0.067–0.133 h/e = 0.38–1.75	2.07–2.63

6. Conclusions

In this study, T-shaped ribs with a staggered arrangement are proposed to enhance the heat transfer in an SAH, and the effects of the geometric parameters of the ribs on the thermal and aerodynamic performance of the SAH were analyzed using RANS equations. The numerical results for the heat transfer rate and friction factor were validated by comparing with experimental data for the smooth duct and the SAH with triangular obstacles. In the case of the SAH with the obstacles, the average relative error of the average Nusselt number between the numerical and experimental results was less than 4.43% within the tested Reynolds number range, and that of the friction factor was less than 1.94%. In a parametric study using the ratios of the rib height to the channel height (h/H) and the rib width to the channel width (e/W), the performance factor (PF) was far more sensitive to h/H than to e/W , and the maximum PF was found at $h/H = 0.5$ for a fixed e/W . When h/e was varied by keeping the rib area constant, the variation of the friction factor with h/e was very small due to the fixed rib area, and thus the variation of the average Nusselt number was qualitatively similar to that of PF and their maximum values were commonly found at $h/e = 0.83$. The proposed T-shaped ribs showed superior performance to several other heat-transfer enhancement obstacles developed to date. For example, when compared with the triangular ribs, the T-shaped ribs showed a 49.7% higher PF at a Reynolds number of 4510, and an 11% higher PF at a Reynolds number of 22,600. To generalize the present results for staggered T-shaped obstacles, further studies are required for the SAH using different arrangements of T-shaped obstacles.

Author Contributions: S.-Y.A. presented the main idea of the T-shaped ribs; S.-Y.A. and K.-Y.K. contributed to the overall composition and writing of the manuscript; S.-Y.A. performed numerical analysis and analyzed the data; K.-Y.K. revised and finalized the manuscript. All authors have read and agreed to the published version of the manuscript.

Funding: This work was supported by a National Research Foundation of Korea (NRF) grant funded by the Korean government (MSIT) (No. 2019R1A2C1007657).

Conflicts of Interest: The authors declare there is no conflict of interest.

References

1. Varun Saini, R.P.; Singal, S.K. A review on roughness geometry used in solar air heaters. *Sol. Energy* **2007**, *81*, 1340–1350. [[CrossRef](#)]
2. Kabeel, A.E.; Mecarik, K.K. Shape optimization for absorber plates of solar air collector. *Renew. Energy* **1998**, *13*, 121–131. [[CrossRef](#)]
3. Moumami, N.; Ali, S.Y.; Moumami, A.; Desmons, J.Y. Energy analysis of a solar air collector with rows of fins. *Renew. Energy* **2004**, *29*, 2053–2064. [[CrossRef](#)]
4. Esen, H. Experimental energy and exergy analysis of a double-flow solar air heater having different obstacles on absorber plates. *Build. Environ.* **2008**, *43*, 1046–1054. [[CrossRef](#)]
5. Saini, S.K.; Saini, R.P. Development of correlations for Nusselt number and friction factor for solar air heater with roughened duct having arc-shaped wire as artificial roughness. *Sol. Energy* **2008**, *82*, 1118–1130. [[CrossRef](#)]
6. Ozgen, F.; Esen, M.; Esen, H. Experimental investigation of thermal performance of a double-flow solar air heater having aluminium cans. *Renew. Energy* **2009**, *34*, 2391–2398. [[CrossRef](#)]
7. Depaiwa, N.; Chompookham, T.; Promvong, P. Thermal enhancement in a solar air heater channel using rectangular winglet vortex generators. In Proceedings of the PEA-AIT International Conference on Energy and Sustainable Development: Issues and Strategies, Chiang Mai, Thailand, 2–4 June 2010; pp. 1–5.
8. Bekele, A.; Mishra, M.; Dutta, S. Heat transfer augmentation in solar air heater using delta shaped obstacle mounted on the absorber plate. *Int. J. Sustain. Energy* **2013**, *32*, 53–69. [[CrossRef](#)]
9. Yadav, S.; Kaushal, M.; Varun, S. Nusselt number and friction factor correlations for solar air heater duct having protrusions as roughness elements on absorber plate. *Exp. Thermal Fluid Sci.* **2013**, *44*, 34–41. [[CrossRef](#)]

10. Kulkarni, K.; Kim, K.Y. Comparative study of solar air heater performance with various shapes and configurations of obstacles. *Heat Mass Transf.* **2016**, *52*, 2795–2811. [CrossRef]
11. Alam, T.; Kim, M.H. Heat transfer enhancement in solar air heater duct with conical protrusion roughness ribs. *Appl. Therm. Eng.* **2017**, *126*, 458–469. [CrossRef]
12. Kumar, A.; Saini, R.P.; Saini, J.S. Development of correlations for Nusselt number and friction factor for solar air heater with roughened duct having multi v-shaped with gap rib as artificial roughness. *Renew. Energy* **2013**, *58*, 151–163. [CrossRef]
13. Pawar, S.S.; Hindolia, D.A.; Bhagoria, J.L. Experimental study of Nusselt number and Friction factor in solar air heater duct with diamond shaped rib roughness on absorber plate. *Am. J. Eng. Res.* **2013**, *2*, 60–68.
14. Singh, A.P.; Varun, S. Heat transfer and friction factor correlation for multiple arc shape roughness elements on the absorber plate used in solar air heaters. *Exp. Therm. Fluid. Sci.* **2014**, *54*, 117–126. [CrossRef]
15. ASHRAE. *Method of Testing to Determine the Thermal Performance of Solar Collectors*; Standard 93–97; Refrigeration and Air Conditioning Engineering: New York, NY, USA, 1997.
16. ANSYS. *ANSYS CFX-Solver Theory Guide-Release 15.0.*; ANSYS, Inc.: Canonsburg, Pennsylvania, 2013.
17. Bardina, J.E.; Huang, P.; Coakley, T. Turbulence Modeling Validation. *AIAA J. Spacecr. Rocket.* **1997**, *40*, 313–325.
18. Roache, P.J. Verification of Codes and Calculations. *AIAA J.* **1998**, *36*, 696–702. [CrossRef]
19. Celik, I.; Karatekin, O. Numerical Experiments on Application of Richardson Extrapolation with Nonuniform Grids. *ASME J. Fluids* **1997**, *119*, 584–590. [CrossRef]
20. Webb, R.I.; Eckert, E.R.G. Application of rough surface to heat exchanger design. *Int. J. Heat. Mass Transf.* **1972**, *15*, 1647–1658. [CrossRef]
21. Yadav, A.S.; Bhagoria, J.L. A CFD based thermo-hydraulic performance analysis of an artificially roughened solar air heater having equilateral triangle sectioned rib roughness on the absorber plate. *Int. J. Heat Mass Transf.* **2014**, *70*, 1016–1039. [CrossRef]
22. Saini, N.S.; Deo, S.; Chander, J.S. Performance analysis of solar air heater duct roughened with multigap V-down ribs combined with staggered ribs. *Renew. Energy* **2016**, *91*, 484–500.
23. Chamoli, V.B.; Gawande, A.S.; Dhoble, D.B.; Zodpe, S. Experimental and CFD investigation of convection heat transfer in solar air heater with reverse L-shaped ribs. *Sol. Energy* **2016**, *131*, 275–295.
24. Chamoli, J.S.; Sawhney, R.; Maithani, S. Experimental investigation of heat transfer and friction factor characteristics of solar air heater using wavy delta winglets. *Appl. Therm. Eng.* **2017**, *117*, 740–751.

Publisher's Note: MDPI stays neutral with regard to jurisdictional claims in published maps and institutional affiliations.



© 2020 by the authors. Licensee MDPI, Basel, Switzerland. This article is an open access article distributed under the terms and conditions of the Creative Commons Attribution (CC BY) license (<http://creativecommons.org/licenses/by/4.0/>).

Article

Study on the Transient Characteristics of the Centrifugal Pump during the Startup Period with Assisted Valve

Qiao Li ¹, Xiang Ma ², Peng Wu ^{1,*} , Shuai Yang ¹, Bin Huang ^{3,*} and Dazhuan Wu ^{1,4}

¹ College of Energy Engineering, Zhejiang University, Hangzhou 310027, China; 11428018@zju.edu.cn (Q.L.); 21028042@zju.edu.cn (S.Y.); wudazhuan@zju.edu.cn (D.W.)

² Xi'an Precision Machinery Research Institute Kunming Branch, Kunming 650032, China; rayrayda@163.com

³ Ocean College, Zhejiang University, Hangzhou 310027, China

⁴ The State Key Laboratory of Fluid Power Transmission and Control, Zhejiang University, Hangzhou 310027, China

* Correspondence: roc@zju.edu.cn (P.W.); binhuang@zju.edu.cn (B.H.)

Received: 19 August 2020; Accepted: 28 September 2020; Published: 2 October 2020



Abstract: The startup period, one of several transient operations in a centrifugal pump, takes note of some problems with these devices. Sometimes a transient high pressure and high flow rate over a very short period of time are required at the startup process. The pump's dynamic response is delayed because of the rotational inertia of the pump and motor. Our research focuses on how to get a large flow in a short time when the pump cannot meet the requirements alone without a large power driver. To achieve a strong response in the startup process, a ball valve is installed downstream of the pump. The pump's transient behavior during such transient operations is important and requires investigation. In this study, the external transient hydrodynamic performance and the internal flow of the pump during the transient startup period are studied by experiments and simulations. In order to find an appropriate matching method, different experiments were designed. The content and results of this paper are meaningful for performance prediction during the transient pump-valve startup period.

Keywords: transient characteristics; centrifugal pump; startup period; numerical simulation

1. Introduction

The transient operations of a pump such as the startup and shutdown periods occur in several applications of hydraulic systems. In a Navy application, the pump is used to launch weapons from submarines [1]; the pump starts up in a very short time to generate instantaneous pressure. In large pump stations, a sudden startup of the pumps will cause strong pressure fluctuations and power shocks.

The transient characteristics of pumps have been studied in recent years. Tsukamoto and Ohashi [2,3] studied the transient characteristics of a centrifugal pump, and the acceleration of the pump at the startup stage was very fast. They found that the hysteresis and transient pressure fluctuation around the vanes results in a difference between the dynamic and quasi-steady characteristics.

Lefebvre and Barker [1] conducted an experimental study on the acceleration and deceleration cycle of a mixed-flow pump. They found that the transient effect was notably on the pump performance. The quasi-steady assumptions are wrong for the performance prediction of impellers under highly transient conditions, such as at fast startup and stop periods. Saito [4] conducted an experimental study on the transient period of a pump. The results of the tests indicate that the locus of operating points on the head-capacity plane during the pump startup deviates from the system resistance curve to a great

degree as the mass of water in the pipeline becomes large. Dazin [5] and Wang [6–8] conducted startup and shutdown experiments for a pump. The transient characteristics were mainly influenced by the variation in transient velocity.

Wu [9,10] conducted simulations of the blades during startup periods. In two-dimensional simulations, he found that the sliding mesh method has a higher efficiency and stability than the dynamic mesh and dynamic reference frame methods. The startup period also influences the transient performance. Li [11,12] studied the transient characteristics of a centrifugal pump through experiments and numerical simulations during the startup period. He used the DSR (Dynamic Slip Region) method to determine the dynamic motion of the blades in the numerical simulation. The practicability of the DSR method in the dynamic impeller simulation was proved by the consistency between the experimental results and the numerical results. The instantaneous power shock is related to the joint action of a low flow rate and high acceleration in the initial stage of the startup, but the peak value is small. Due to the fluctuation in data, the observation is not very obvious.

In some applications, the pump needs to start up faster but the drive cannot provide sufficient starting acceleration, while in some applications the water hammer needs to be suppressed. A throttle valve can be installed on the pipeline, and the above-mentioned application needs can be met by adjusting the opening of the valve during startup.

The transient characteristics of valves have been studied extensively. Ming-Jyh Chern [13] used the particle tracking flow visualization (PTFV) method to conduct experimental research on the internal flow of a ball valve. He found that the valve's flow coefficient is connected with the opening degree and has nothing to do with the velocity. Yang et al. [14] showed that the main pressure drop occurred along the valve throat because the circulation area diminished when the fluid flows through the valve throat. Wang [15] used the CFX software to conduct a three-dimensional dynamic analysis during the opening period of a butterfly valve. The transformation law of the transient flow coefficient was studied during the startup period. Cho [16] carried out an experiment and simulation to study a globe valve's force balance. The pressure distribution and stress distribution were studied.

Srikanth [17] studied industrial pneumatic valves by adopting dynamic meshing technology. Experiments and numerical simulations were carried out to research the startup period of a pneumatic valve. In the numerical simulation, the unstructured tetrahedral mesh was used to discretize the flow domain, the dynamic movement of valves was defined by the dynamic mesh method, and the standard k-epsilon model was implemented. He analyzed the effects of the opening degree and speed on the flow characteristics. The simulation and experimental results showed good similarity, thereby demonstrating the effectiveness. Quang Khai Nguyen [18] has conducted experiments to research the globe valve's flow coefficient. He found that the Re and opening degree influences the flow coefficient.

The research objective of this article was to investigate a pump with an assistant valve. At present, there are few studies on the simultaneous startup of pump and valve. The key point of this paper is to study the simultaneous startup stage of a pump and assistant valve. In order to study the simultaneous startup stage of a pump and assistant valve, we designed many experiments and numerical simulations. Then, we analyzed the transient dynamic characteristics of the pump-valve system; the results of numerical simulations show the influence of the opening valve on the internal transient flow structure during the pump startup. Furthermore, we compare various startup modes and select the most suitable mode. In this paper, we focus on how to achieve a higher flow acceleration through a valve if the pump starts not fast enough.

2. Experiment

2.1. Test Equipment and Method

A schematic view of the experiment system is shown in Figures 1 and 2. The test system consists of a data acquisition system, a pump and control system, a valve, pipes, and data measurements. A ball valve is applied to change the dynamic characteristics by changing the valve close time. Two pipes are

connected to the tank, and the pipe which connects the tank and water-tap is used to hold the water level in the tank. In order to guarantee that cavitation does not happen, the level is kept about 1.2 m above the pump inlet during this series of experiments.

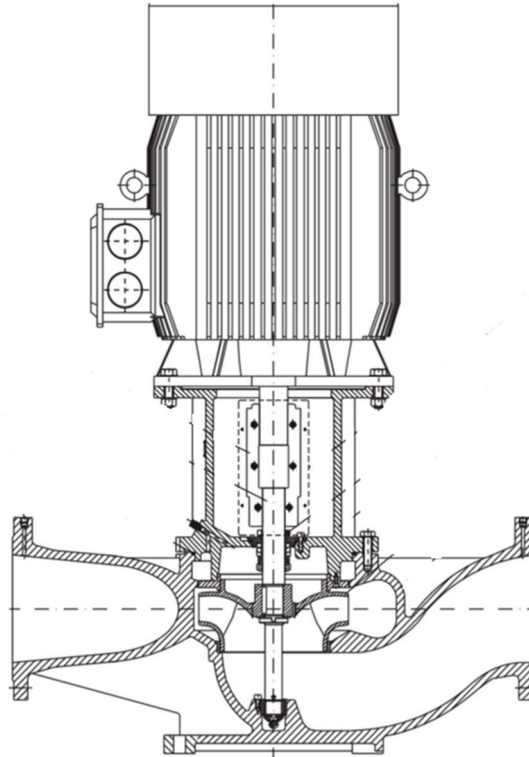


Figure 1. Illustration of the experiment pump (vertical pipe pump).

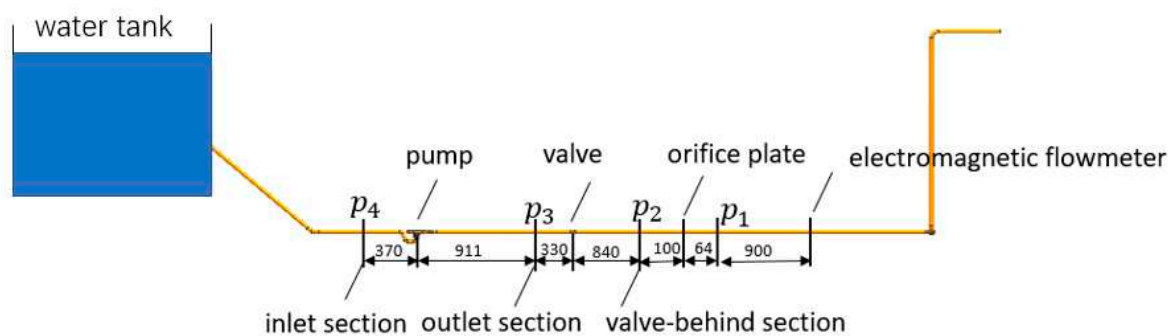


Figure 2. Diagram of the experiment (units are mm).

The data are acquired with an NI-4497. The data acquisition frequency is 5000 Hz. The pump comprises the motor, pump body, impeller, and diffuser. The parameters for the pump are listed in Table 1. The pump is controlled by a frequency conversion cabinet. The data measurements mostly contain pressure sensor, electromagnetic flowmeter, and photoelectric speed sensor. In the experiment, the pump starts up first; meanwhile, the valve remains closed for a period of time, T_c , and then the valve is rapidly full opened.

The installation locations of three pressure sensors are shown in Figure 2. The transient pressure at the inlet, outlet, and valve-behind section were measured.

The pump transported water from a tank to the atmosphere during the experiments. When the ball valve was fully opened, the flow rate was $0.0033 \text{ m}^3/\text{s}$. Then, we changed the valve opening degree to adjust the flow rate to 0.0033 , 0.00326 , 0.00309 , 0.0025 , 0.00136 , and $0 \text{ m}^3/\text{s}$, respectively. The aim of

the experiments was analyzing the steady performances at different flow rates. It took 9.1 s for the pump to reach 2900 rpm in this series of experiments.

Table 1. Specifications for the experimental pump.

Geometric Parameters	
Suction diameter	32 mm
Discharge diameter	32 mm
Impeller diameter	138 mm
Blade outer width	4 mm
Number of blades	5
Hydraulic Parameters	
Rotation speed	2900 r/min
Flow rate	11.34 m ³ /h
Total head	20 m

The transient performances of the pump-valve system were studied by many experiments during the startup process. We started the pump first and then kept the valve closed until the pump's rotational speed reached a certain value. The closed time for the valve was called T_c , and T_c was set as 0, 2.0, 3.2, 4.4, 5.9, 7.2, 8.0, 10.28, and 11.56 s, respectively. Then, at time point T_c , the valve was quickly opened in time T_o , and the data were collected until the pump reached the rated speed.

2.2. Processing the Experiment Data

A photoelectric speed sensor was used to measure the pump's transient rotation speed. The photoelectric speed sensor outputs the pulse signal. The rotational speed used the pulses gathered in the time interval. The formula is expressed as:

$$n = \frac{60N}{\Delta t} \quad (1)$$

where n is the transient speed and N is the number of pulses in Δt .

The transient head could be calculated through measuring the transient pressure of the inlet section and outlet section, and the transient head also contained a component which was used to accelerate the fluid in the startup period.

$$H = \frac{P_o - P_i}{\rho g} + \frac{Q^2}{2g} \left(\left(\frac{4}{\pi d_o^2} \right)^2 - \left(\frac{4}{\pi d_i^2} \right)^2 \right) + \left\{ L_{eq} / (gA_o) \right\} \frac{dQ}{dt} \quad (2)$$

where L_{eq} is the equivalent length, P_o is the outlet pressure, P_i is the inlet pressure, and A is the cross-sectional area of the pipeline.

The dimensionless head and flow are defined as equaling:

$$C_H = \frac{P}{\rho u_2^2 / 2} \quad (3)$$

$$C_q = \frac{Q}{\pi d_2 b_2 u_2} \quad (4)$$

where $u_2 = \pi d_2 N_r / 60$, N_r is the current rotational speed of the pump, b_2 is the outlet width of the impeller, and d_2 is the diameter of the impeller.

Transient flow is an important parameter in the startup period. The flow is mostly measured by an electromagnetic flowmeter and an orifice flowmeter. When measuring the transient flow, the electromagnetic flowmeter has a greater delay. Figure 3 is an illustration of the orifice flowmeter. Bernoulli equation and the continuity equation between the high pressure and orifice are used to obtain the flow. Formula (5) shows the flow transition equation:

$$q_V = C \cdot Q_V = \frac{C}{\sqrt{1-\beta^4}} \cdot \frac{\pi d^2}{4} \cdot \sqrt{\frac{2\Delta P}{\rho}} \quad (5)$$

where C is the outflow coefficient and β equals d/D .

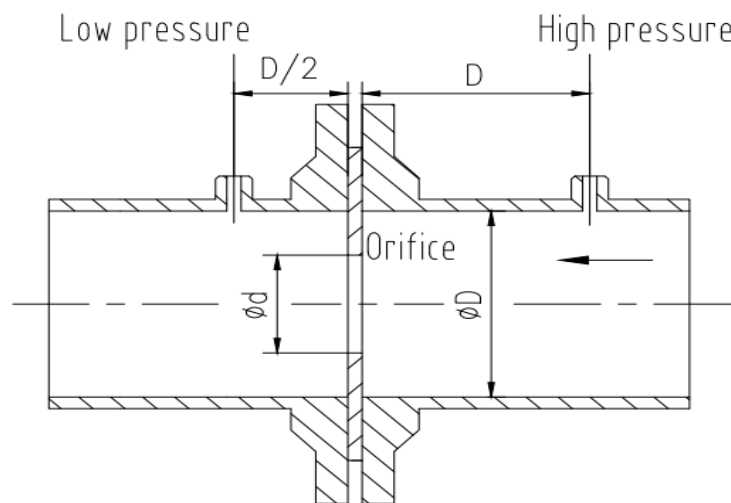


Figure 3. Illustration of the orifice flowmeter.

The outflow coefficient C is used to correct the pressure difference between the orifice and the low pressure. Yet, the orifice flowmeter does not consider the pressure loss of the orifice. In this paper, the local resistance loss is used to get the flow. Formulas (6) and (7) show the energy conservation equation and the local resistance equation. The local resistance coefficient is influenced by the orifice structure and the Reynolds number. Thus, it can be found that the pressure difference is a quadratic function of the flow:

$$\frac{P_1}{\rho g} + \frac{u_1^2}{2} = \frac{P_2}{\rho g} + \frac{u_2^2}{2} + h_{fJ} \quad (6)$$

$$h_{fJ} = \xi \frac{l_e}{d} \frac{u^2}{2} \quad (7)$$

where ξ is the resistance coefficient and l_e is the equivalent length.

Figure 4a is a schematic diagram. The distance between the low pressure and the orifice plate is $6D$, and between the high pressure and the orifice it is $3D$. The pressure measuring point for the local resistance flowmeter should be in a stable flow area, while the low pressure point in the orifice flowmeter should be in an unstable area. An electromagnetic flowmeter was installed downstream to get a precise steady flow. The orifice plates come in three sizes, and ultimately the first one was chosen because it causes the biggest pressure loss; therefore, in the small flow we can get a more definitive pressure difference. The pump is controlled by the inverter, then a series of flowrates can be found by changing the frequency. Through a series of steady state experiments, the relationship of pressure difference and flowrate can be found. Figure 5 shows the fitting curve and fitting formula.

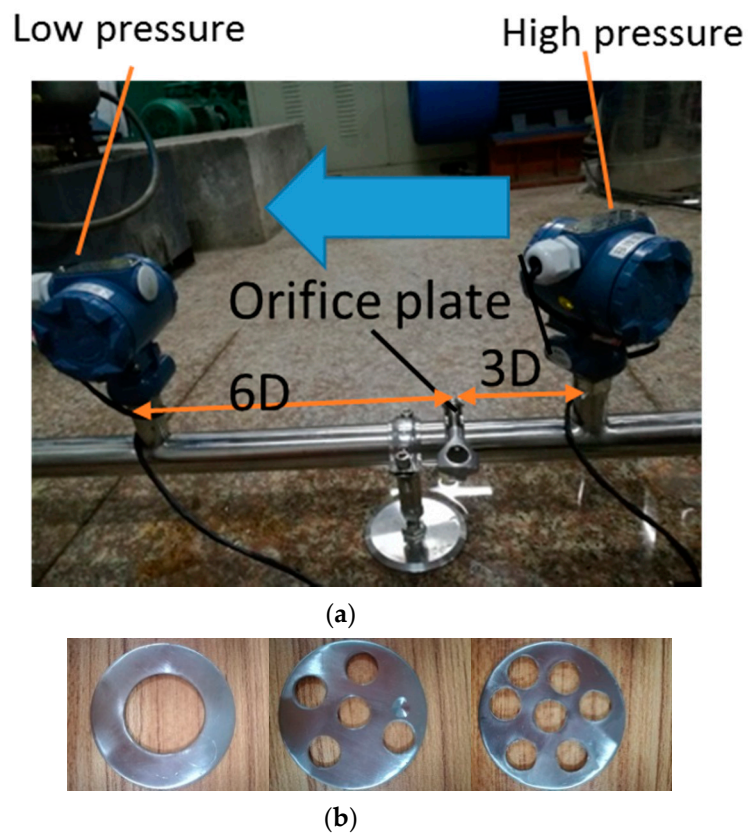


Figure 4. Illustration of the local resistance flowmeter; (a) the schematic diagram, (b) three sizes for the orifice plate.

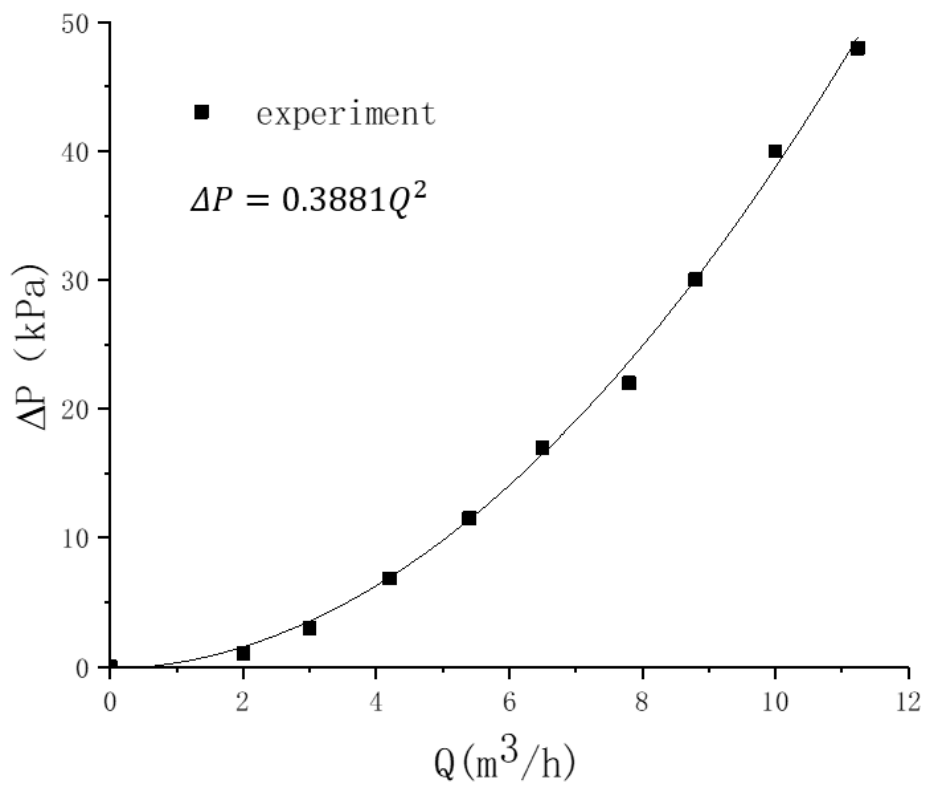


Figure 5. The fitting curve of the pressure difference and flowrate.

2.3. Results and Discussion for the Experiment

The rotational speed is shown in Figure 6. The startup time for the pump was 9.1 s. Figure 7 shows the changes in pressure during the startup period.

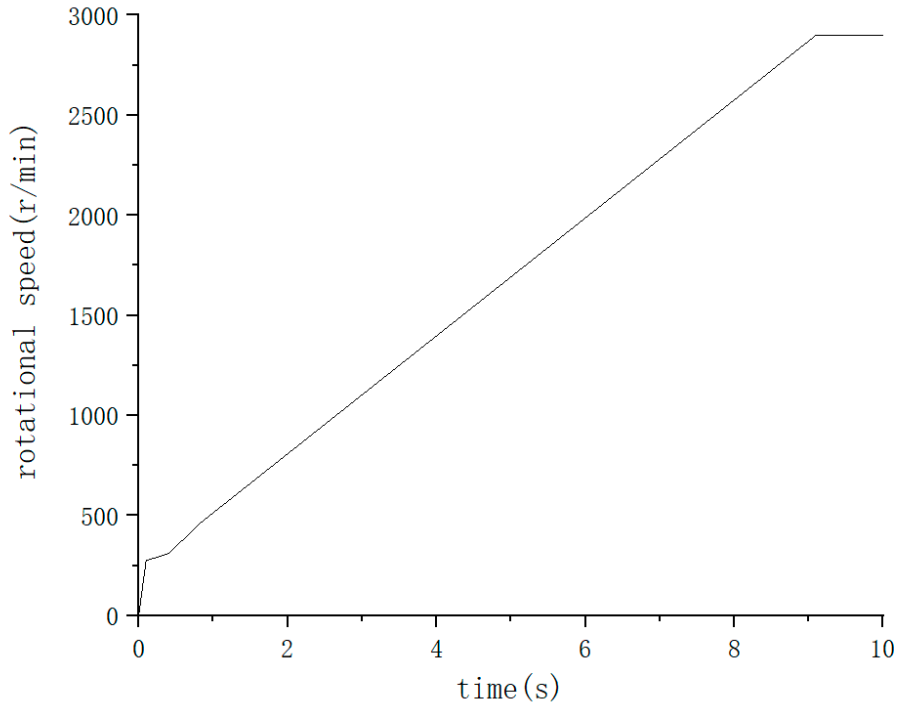


Figure 6. The rotational speed of pump measured by the photoelectric speed sensor.

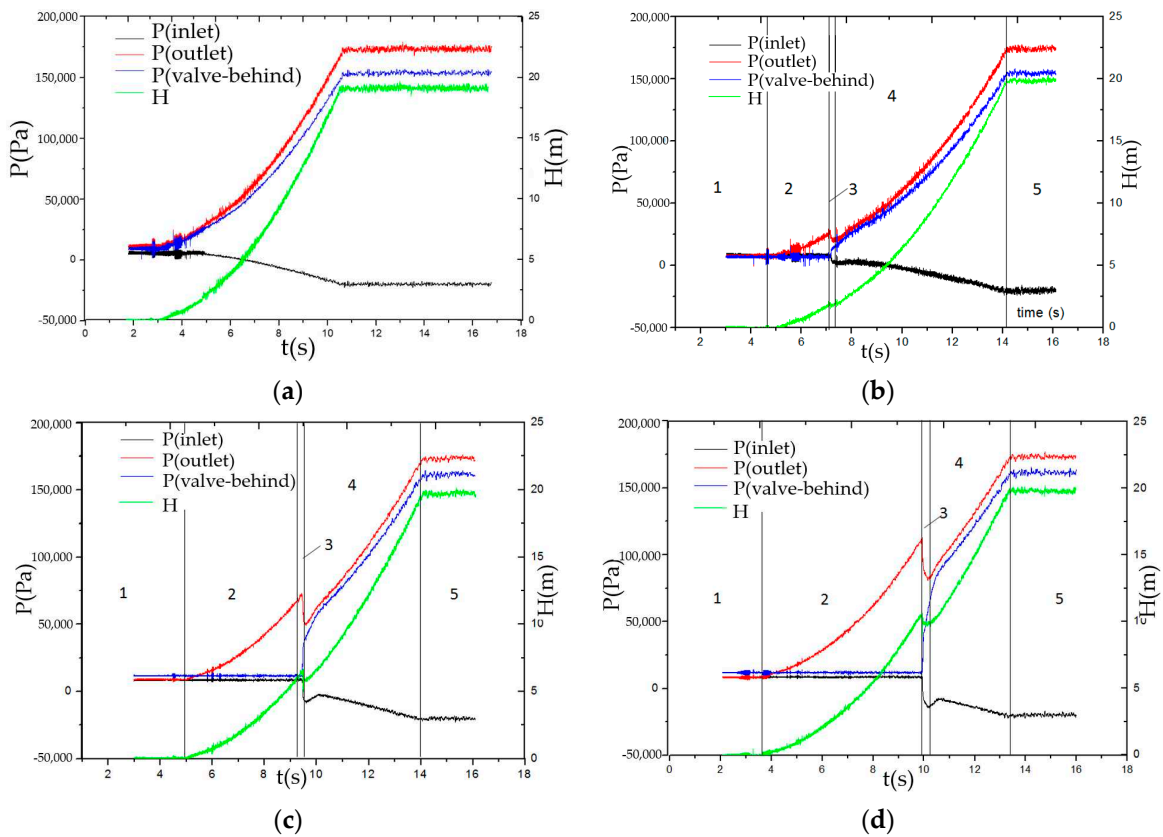


Figure 7. Cont.

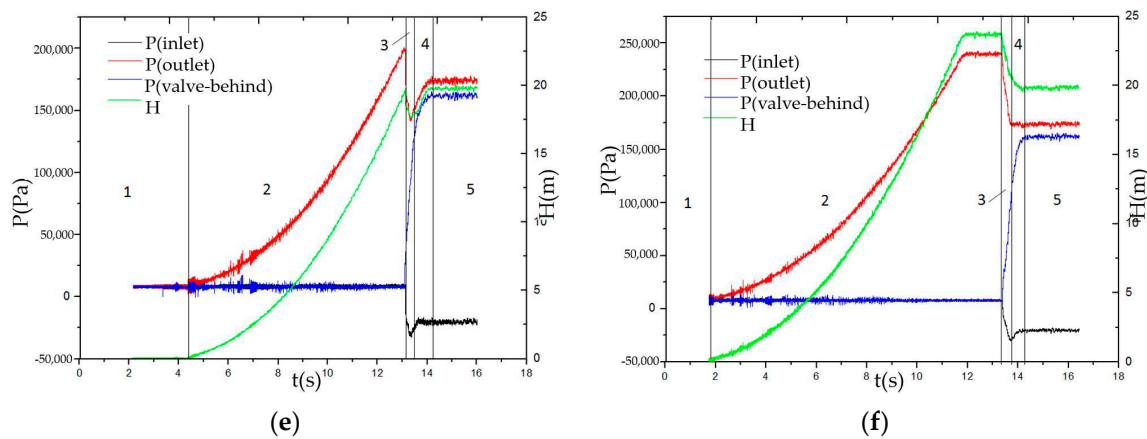


Figure 7. The inlet pressure, outlet pressure, and pressure behind the valve under different T_c during the startup process; (a) $T_c = 0$ s, (b) $T_c = 2.7$ s, (c) $T_c = 4.2$ s, (d); $T_c = 5.8$ s, (e) $T_c = 7.8$ s, (f) $T_c = 10.3$ s.

The experimental process can be divided into five parts. Zone 1 means that the pump was stopped, zone 2 means that the pump was opened while the valve was closed, zone 3 means that the valve was opening, zone 4 means that the valve was fully opened, and zone 5 means that the pump system became stable. T_c is the closing time for the valve. $T_c = 0$ means that the valve was completely open during the pump startup period. When the valve was closed, the inlet pressure and pressure behind the valve remained unchanged, while the outlet pressure increased more rapidly than the operating condition at $T_c = 0$. The outlet pressure continued to increase more rapidly. When the valve was in the process of opening, the outlet pressure had a sudden fall in 0.4 s. Meanwhile, the pressure behind the valve increased rapidly and a pressure fluctuation occurred at the inlet of the pump. When the valve was completely open, the pressure behind the valve kept growing slower. Finally, the pressures in the different working conditions reached the same value. The outlet pressure was greater than the pressure behind the valve. This deviation could be caused by the resistance between the valve and pipe. There was a jump in the rotational speed curve at the initial stage of the start that does not match with the pressure curve and head curve. In the initial stages of startup, the energy provided by the centrifugal pump was smaller than the resistance of pipe system, and therefore the response could not have been sensitive to the pressure.

In order to compare different working conditions, the dimensionless flow and head were analyzed. Figure 8 shows the changes in dimensionless flow during the startup period. T_o is the startup time of the pump. The red curve is the startup period of the pump with a completely open valve. When the valve was closed, the dimensionless flow remained around 0. When the valve was opening, C_q rapidly increased and the curve rapidly tended to the red completely open curve. When T_c was less than T_o , the C_q first increased rapidly and then had a slow increment with the same tendency compared with the completely open startup period. When T_c was bigger than T_o , the C_q quickly increased to the final value.

Figure 9 shows the changes in the non-dimensional head during the startup period. The red curve is the startup period of the pump with a completely open valve. In the pump startup period, when the valve remained closed C_h was bigger than the completely open case. In the opening period of the valve, the C_h had a sudden drop and then tended to the completely open case rapidly. Finally, C_h in all those cases reached a certain value. When T_c divided by T_o was less than or equal to 0.46, the C_h reached the maximum when the pump was fully started. When T_c divided by T_o was greater than 0.46, the C_h reached the maximum at the point where the valve was going to open. When T_c was less than T_o , the maximum of C_h increased as T_c increased. When T_c was greater than T_o , the maximum of C_h maintained a certain value. If we want to achieve a high initial C_h , then T_c should be bigger than T_o .

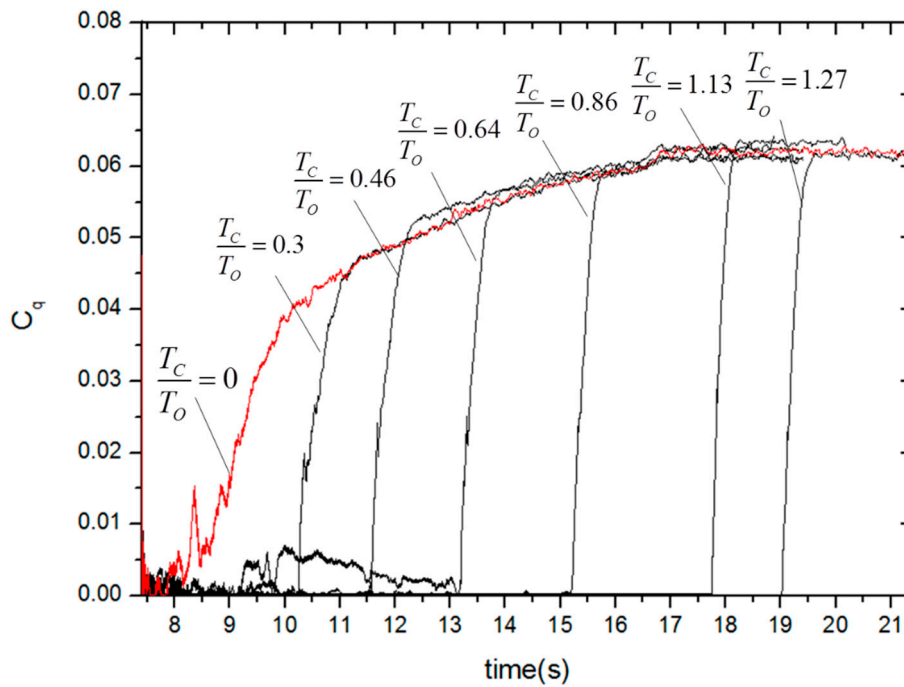


Figure 8. Dimensionless flow for different startup periods.

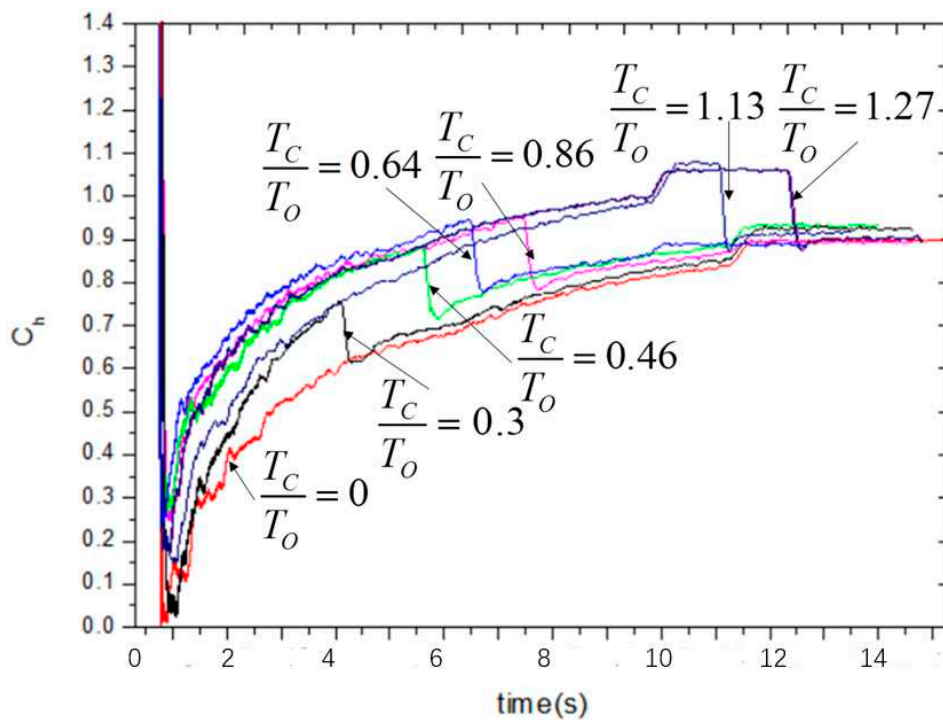


Figure 9. Dimensionless head for different startup periods.

Considering the differential of the flow, Figure 10 shows the changes for different startup periods. The red curve is the startup period of the pump with a completely open valve. Figure 10b is the enlarged image of differential Q when $T_c/T_o = 0$; when the valve was completely open during the startup period, the dQ/dT increased to the maximum of about 2.25 and then fell to 1.25 or so, and finally the dQ/dT fell to 0. From Figure 6, it can be found that the rotational speed has a higher acceleration at first and then transitions to a certain smaller acceleration. The change in speed reflects the change in dQ/dT . Figure 10a shows the dQ/dT for different startup periods. During the valve's opening period, the dQ/dT

quickly reaches the maximum and then falls to the red curve, and finally tends to 0. When T_c is less than T_o , the maximum of dQ/dT increases when T_c increases. When T_c is bigger than T_o , the maximum of dQ/dT does not increase and even decreases a little when T_c increases. Thus, in order to obtain the biggest flow during a given short period of time, the T_c should be in the vicinity of $1.13 T_o$, and there is no need to increase T_c when T_c is bigger than T_o .

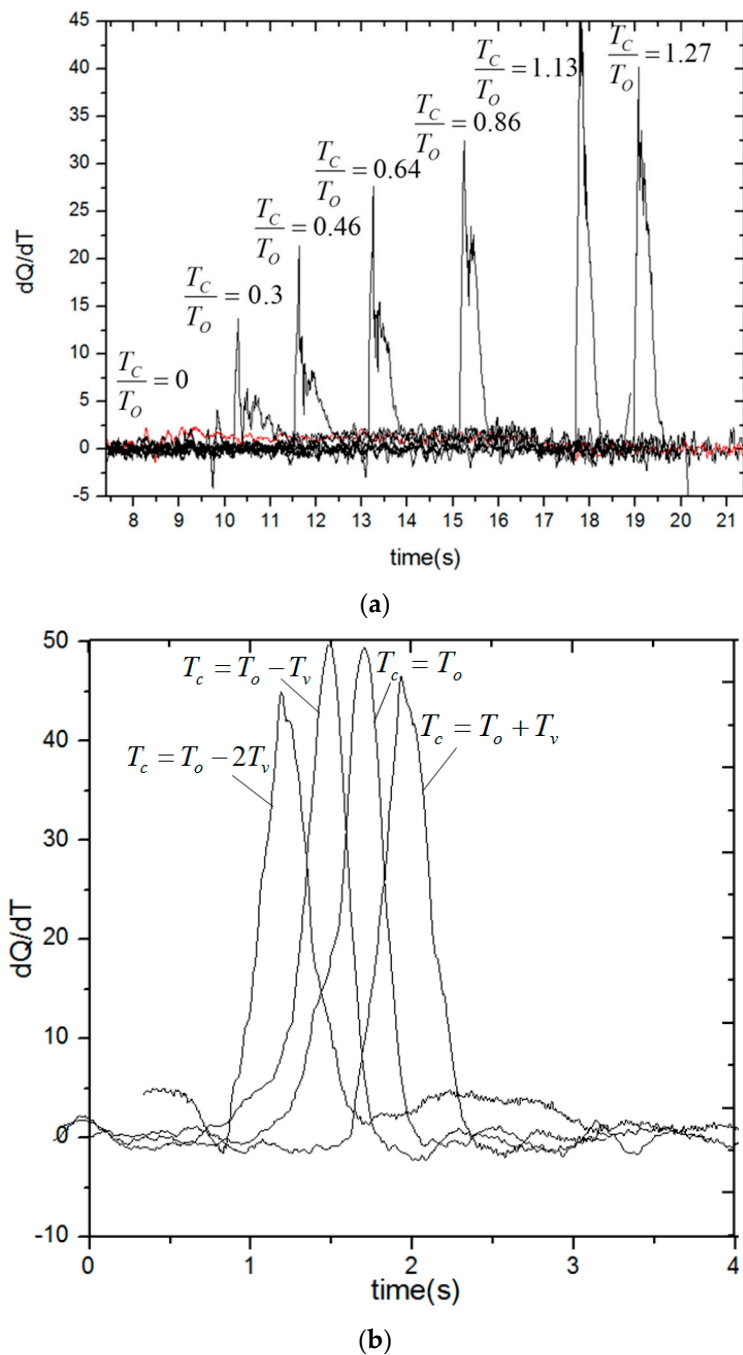


Figure 10. Differential flow for different startup periods; (a) flow change rate (dQ/dT) for different startup periods; (b) flow change rate (dQ/dT) curve when T_c is in the vicinity of $1.13 T_o$.

According to the above results, in order to find the most suitable T_c , a series of experiments when T_c is in the vicinity of $1.13 T_o$ have been performed. The results are shown in Figure 10b; it can be found that when $T_c = T_o - T_v$, the biggest flow can be found during a given short period of time.

3. Numerical Simulation

3.1. Computational Domain and Grid

The overall view of the 3D model is shown in Figures 2 and 3. The numerical 3D model's parameters were the same size as the real test system. The schematic view of numerical pump model and simplified valve model is shown in Figure 11. Table 2 shows the general view of the mesh of the pump-system model. The computational domain is discretized by an unstructured tetrahedral cell. The grid independence test is carried out, and Figure 12 shows the results. In the calculation, the scaled residuals of continuity equation and momentum equations are reduced to a magnitude below 10^{-5} , and the scaled residuals of the turbulence kinetic energy (k) and dissipation rate (ξ) are reduced to a magnitude below 10^{-4} . The $y+$ value near the critical surfaces is from 0 to 30 and the average value is within 50. The difference in head between the 1.98×10^6 grid number and the 2.71×10^6 grid number is 0.011%, and the difference in flow is 0.026%. As a result, the total number of grids is ensured to be 1.98×10^6 .

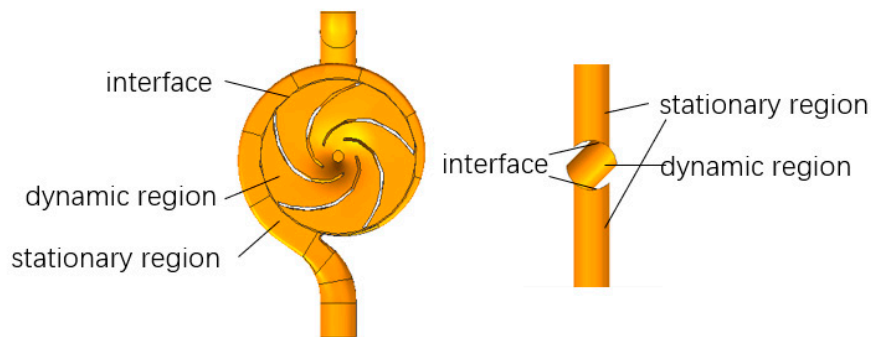


Figure 11. The numerical model for the pump and ball valve.

Table 2. Overview of the mesh in the numerical model.

Unstructured Mesh					
Regions	Impeller	Volute	Valve	Tank	Pipes
Mesh number	286,735	389,800	46,648	920,753	452,894
Mesh sizes (mm)	1	1.5	1	120	10

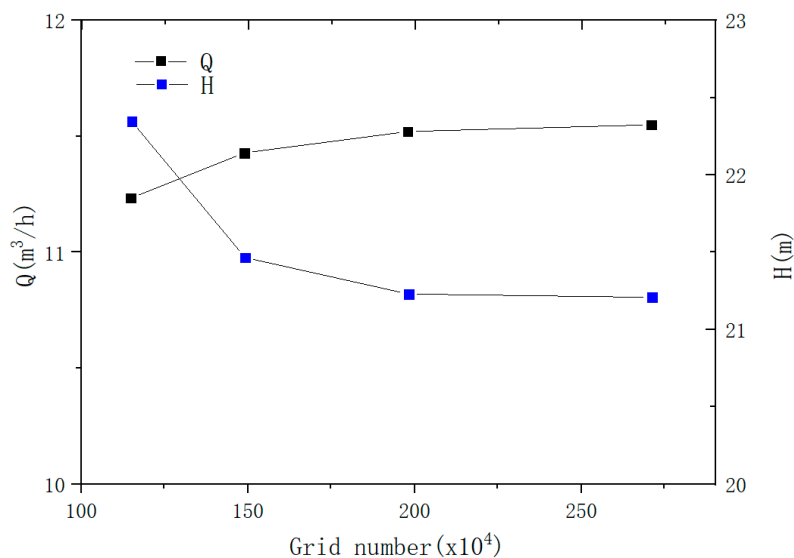


Figure 12. Results of the grid independence investigation.

Steady simulations were performed firstly. The Q - H curve between the experiment and steady simulation is shown in Figure 13. The strong similarity in the results verifies the accuracy of the 3D model and grid quality. The flow in the follow-up experiment and transient simulation was around $0.003 \text{ m}^3/\text{s}$.

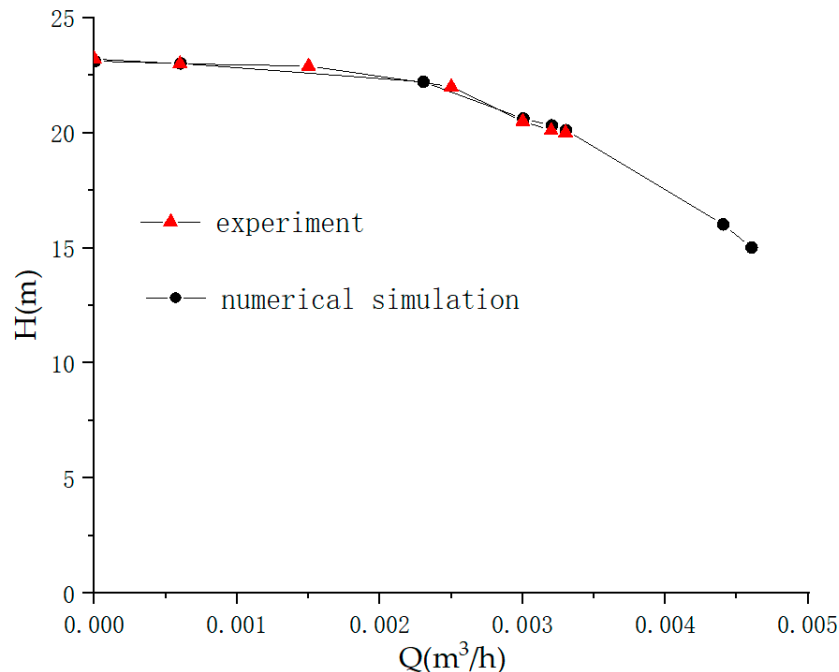


Figure 13. Comparison of the experimental and steady numerical simulation.

3.2. Boundary Conditions of the Transient Simulation

The startup period of $T_c = 8 \text{ s}$ was simulated. Li [11] demonstrated the applicability of the detached eddy simulation (DES) model and the dynamic slip region (DSR) method in a transient simulation of the pump's startup periods. For the DES (detached eddy simulation) model, in the attached boundary layer, the RANS equation is applied; the large eddy simulation (LES) model is applied in other regions. The LES is more precise and the RANS is more efficient, and the DES model integrates the advantages. Using the DES model can save computational resources and computing time to some extent.

The DSR (dynamic slip region) method segments the flow domain into dynamic and static regions. Then, the dynamic region and stationary region are discretized, respectively, and then a pair of interfaces is used to transfer and exchange data to the two individual parts. The interfaces could be set up in the fluent.

A mathematical curve is used to define the speed. It was achieved with measurements from the experiment. Figure 6 shows the rotational speed curve, and formula 8 (the unit is r/min) shows the definition of speed.

$$\text{speed} = \begin{cases} 2747.65468 \times t & t \leq 0.1 \\ 317.495 \times t^2 - 41.039 \times t + 275.315 & 0.1 < t \leq 0.85 \\ 294.566 \times t + 219.44 & 0.85 < t \leq 9.1 \\ 2900 & t > 9.1 \end{cases} \quad (8)$$

The valve's opening time is 0.4 s, and valve's rotational speed is assumed to be constant. Thus, the valve's rotational speed can be defined as follows (the unit is degree/s):

$$\omega = \begin{cases} 0 & t < 8 \\ 225 & 8 \leq t \leq 8.4 \\ 0 & t > 8.4 \end{cases} \quad (9)$$

In order to ensure both accuracy and efficiency, we set the time steps to vary with pump's rotational speed. Thus, time step is also a value that varies with time. Formula 10 (the unit is s) shows the definition of the time step. At each time step, the blade does not rotate more than one degree when $t \leq 0.85$ s, the blade does not rotate more than four degrees when $0.85 < t \leq 9.1$ s, and then the blade does not rotate more than six degrees.

$$\Delta t = \begin{cases} 0.000607 & t < 0.85 \\ \frac{\pi}{1388.1105 \times t + 1034.091} & 0.85 < t \leq 9.1 \\ 0.000345 & t > 9.1 \end{cases} \quad (10)$$

The boundary conditions of the pressure inlet and pressure outlet were chosen. Second-order implicit was applied for the time-dependent term format. The SIMPLEC algorithm was used to compute the pressure–velocity coupling. The dispersion of convective terms was calculated by the second-order upwind scheme, and the numerical under-relaxation and diffusion terms were calculated by central difference schemes.

There is an assumption that the water was incompressible in the numerical simulations at the startup period and there was no cavitation. The numerical simulation utilized Ansys Fluent.

3.3. Comparison of the Simulation and Experiment

Figures 14–16 show the comparison of the transient simulation and the experiment. The experiment was recorded at $T_c = 7.8$ s, while the simulation was made at $T_c = 8$ s. The simulated pressure is probably about 2000 Pa higher than the experiment at the initial stage; this is caused by the measurement deviation in the water level in the tank. From the head and flow pictures, we can see that before the opening of the valve the simulation and experiment show a strong agreement, and the difference between the simulation and the experiment are mainly caused by a deviation of 0.2 s. In this experiment, the ball valve is controlled manually and the deviation is inevitable. Yet, the similarity between the numerical simulation and the experiment can prove the accuracy of the simulation.

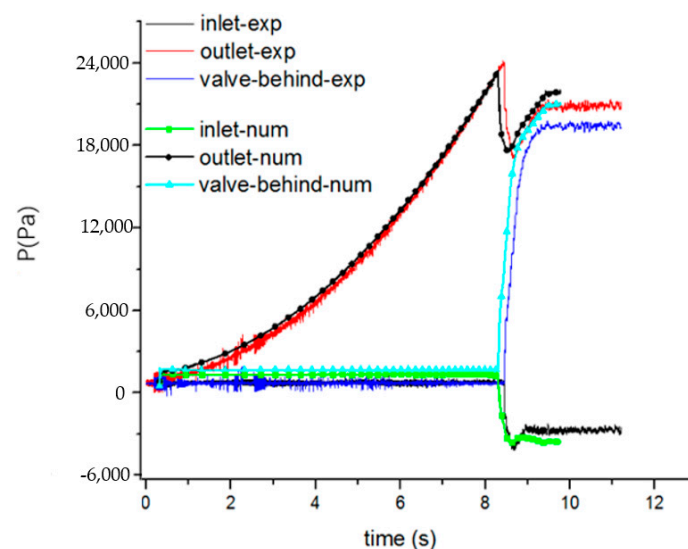


Figure 14. Comparison of the experiment and simulation pressures.

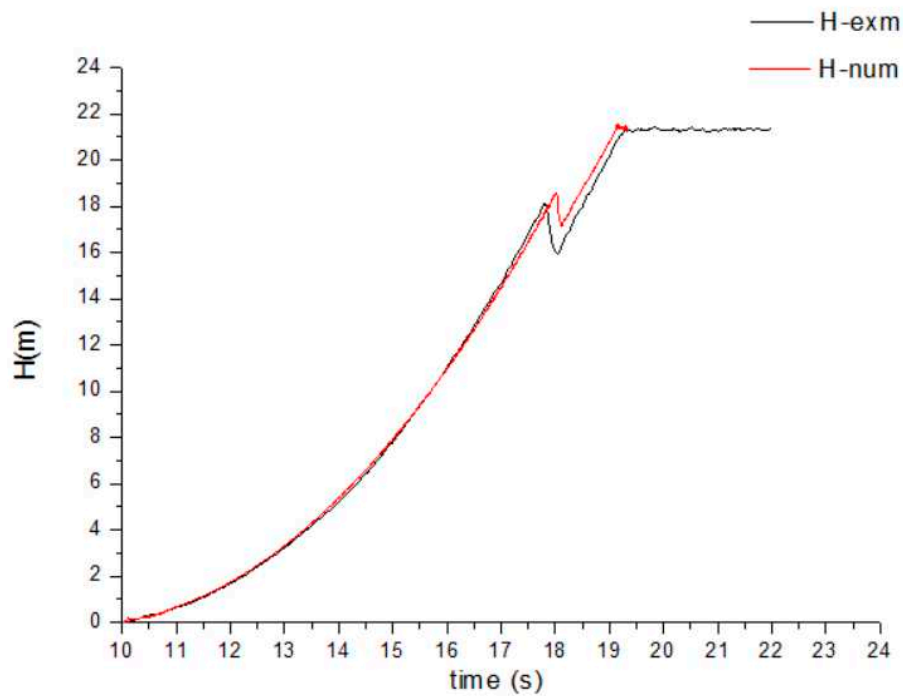


Figure 15. Comparison of the experiment and simulation heads.

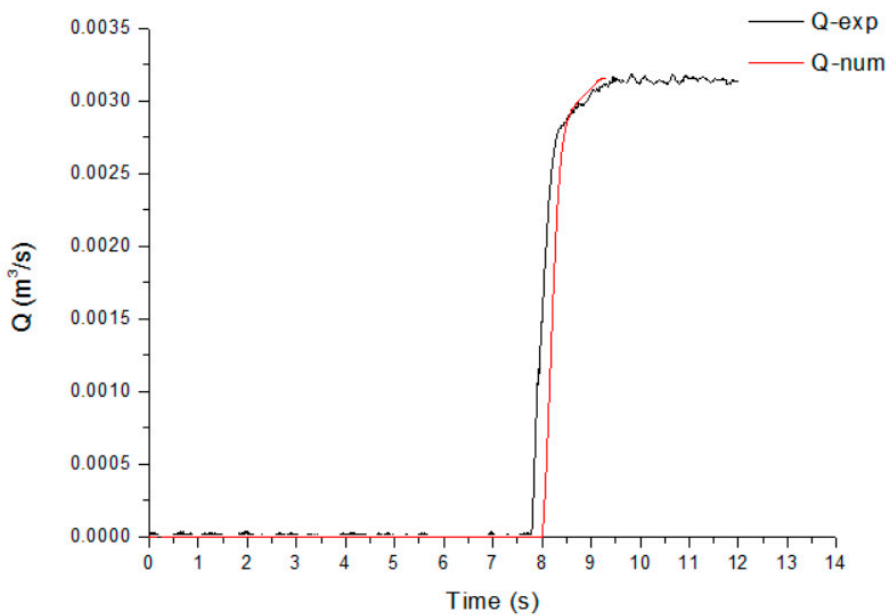


Figure 16. Comparison of the experiment and simulation flows.

3.4. Results and Discussion of the Transient Simulation

The evolution of the velocity field at the opening period of valve is shown in Figure 17. A high-velocity zone appears at nearby of interface between valve and pipe when valve is opening. With the increase of opening degree, this high-velocity region decreases. The high-velocity region results in turbulence in the vicinity region, but there is little effect on the internal flow of pump because the valve's inlet flow is generally uniform. The change in resistance has a greater impact on the transient internal flow of pump. The sudden drop in head and pressure occurred because the pump works on the domain behind the valve.

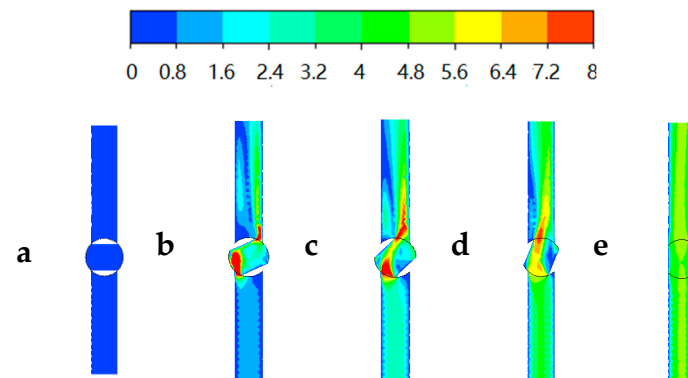


Figure 17. The velocity evolution of the valve during the valve opening process: (a) $t = 8$ s, (b) $t = 8.1$ s, (c) $t = 8.2$ s, (d) $t = 8.3$ s, (e) $t = 8.4$ s.

The internal velocity evolution of pump during the opening period of valve is shown in Figure 18. In Figure 18a, it can be found that there is a clear vortex in volute tongue and trailing edge of blades. In Figure 18b,c, it can be found that the turbulence flow occurs in the leading edge of the blades. In Figure 18e, the pump's internal flow structure changes back to a representative transient flow structure when the valve is fully open. During the valve's opening period, the vortices in the trailing edge of the blades and the volute tongue gradually disappears. In the valve's opening period, the performance of the pump has been improved. When the valve is closed, the pump's performance is weakened. This might be the reason why the maximum of flow change rate (dQ/dT) does not increase and even decreases a little, while T_c increases when T_c is bigger than T_o .

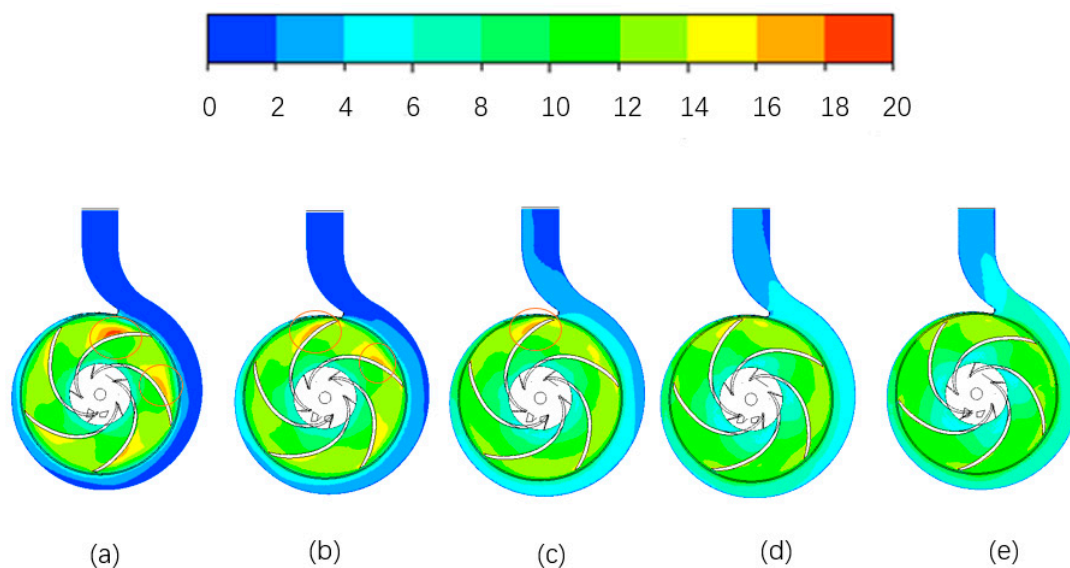


Figure 18. The internal velocity evolution of the pump during the valve opening process: (a) $t = 8$ s, (b) $t = 8.1$ s, (c) $t = 8.2$ s, (d) $t = 8.3$ s, (e) $t = 8.4$ s.

4. Conclusions

The research emphasis was a pump-valve system (centrifugal pump and ball valve). Many experiments and numerical simulations were carried out to study the transient performances of the pump-valve system. The study of transient performance mainly focused on how to get a large fluid acceleration.

In the experiments, the local resistance loss was used to measure the transient flow more accurately. The results of experiments show that a high and rapid transient response can be achieved by controlling the assistant valve during the pump's startup period. When $T_c > T_o$, the maximum of dQ and C_h

will not increase. Thus, the most suitable startup method for the pump and valve will be around $T_c = T_o$. Based on the experimental results, when $T_c = T_o - T_v$ the biggest flow can be obtained during a given short period of time. Thus, the suggested suitable startup method for the pump and valve is $T_c = T_o - T_v$, which can get the biggest flow and a lower max pressure.

The most suitable T_c is noted by considering the transient response's sensitivity and stability synthetically. When the most suitable T_c is determined by the experiments, a numerical simulation is carried out to study the internal flow. The dynamic movement of the impeller and the valve is defined by the DSR method. The transient numerical simulation uses the DES model. The simulated results and experimental results show a good agreement. The simulation predicts the pressure and head volatility because of the valve's sudden opening. During the valve's opening period, the impeller-volute interaction plays a decreasing role in the pump's performance, while the vortex's revolution plays an increasing role. During the opening period of valve, the change in the valve resistance influences the internal flow of the pump.

This paper only investigated the consequence of T_c . Others are involved in the matching method, such as the valve degree. The key point of future work will be to study these factors synthetically and find the best matching mode.

Author Contributions: Conceptualization, Q.L. and P.W.; methodology, Q.L.; software, Q.L. and S.Y.; validation, Q.L., D.W., and X.M.; formal analysis, Q.L.; investigation, Q.L.; resources, D.W. and X.M.; data curation, Q.L.; writing—original draft preparation, Q.L.; writing—review and editing, P.W. and B.H.; supervision, P.W. and B.H.; project administration, P.W. and X.M.; funding acquisition, D.W. All authors have read and agreed to the published version of the manuscript.

Funding: This study was supported by the National Natural Science Foundation of China (No. 51839010, No. 52076186).

Acknowledgments: The author sincerely thanks the support of the State Key Laboratory of Fluid Power Transmission and Control of Zhejiang University.

Conflicts of Interest: The authors declare no conflict of interest.

Nomenclature

H	Total head (m)
Q	Volume flow rate (m ³ /s)
Speed	The rotational speed of the pump (r/min)
ω	The speed of the ball valve (degree/s)
P	Pressure (Pa)
T _c	The closed time of the valve (s)
T _o	The opening time of the pump (s)
T _v	The opening time of the valve (s)
C _h	The non-dimension head
C _q	The non-dimension flow
u ₂	Outlet peripheral velocity of the impeller (m/s)
b ₂	The outlet width of impeller (mm)
d ₂	The diameter of impeller (mm)
Re	Reynolds number

References

1. Lefebvre, P.J.; Barker, W.P. Centrifugal Pump Performance during Transient Operation. *J. Fluids Eng.* **1995**, *117*, 123–128. [[CrossRef](#)]
2. Tsukamoto, H.; Ohashi, H. Transient Characteristics of a Centrifugal Pump during Starting Period. *J. Fluids Eng.* **1982**, *104*, 6–13. [[CrossRef](#)]
3. Tsukamoto, H.; Matsunaga, S.; Yoneda, H.; Hata, S. Transient Characteristics of a Centrifugal Pump during Stopping Period. *J. Fluids Eng.* **1986**, *108*, 392–399. [[CrossRef](#)]
4. Saito, S. The Transient Characteristics of a Pump during Start Up. *Bull. JSME* **1982**, *25*, 372–379. [[CrossRef](#)]

5. Wu, D. Study on Transient Characteristics of Special-Type Centrifugal Pump during Rapid Starting Period. Ph.D. Thesis, Zhejiang University, Hang Zhou, China, 2004.
6. Wu, D.Z.; Wang, L.Q.; Hu, Z.Y. Numerical simulation of centrifugal pump's transient performance during rapid starting period. *J. Zhejiang Univ. Eng. Sci.* **2005**, *39*, 1427–1430, 1454.
7. Dazin, A.; Caignaert, G.; Bois, G. Transient Behavior of Turbomachineries: Applications to Radial Flow Pump Startups. *J. Fluids Eng.* **2007**, *129*, 1436–1444. [[CrossRef](#)]
8. Wang, L.Q.; Wu, D.Z.; Zheng, S.Y.; Hu, Z.Y. Study on transient hydrodynamic performance of Mixed-Flow-Pump during starting period. *J. Zhejiang Univ. Eng. Sci.* **2004**, *38*, 751–755.
9. Wu, D.; Chen, T.; Sun, Y.; Cheng, W.; Wang, L. Study on numerical methods for transient flow induced by speed-changing impeller of fluid machinery. *J. Mech. Sci. Technol.* **2013**, *27*, 1649–1654. [[CrossRef](#)]
10. Wu, D.; Chen, T.; Sun, Y.; Li, Z.; Wang, L. A study on numerical methods for transient rotating flow induced by starting blades. *Int. J. Comput. Fluid Dyn.* **2012**, *26*, 297–312. [[CrossRef](#)]
11. Li, Z.; Wu, D.; Wang, L.; Huang, B. Numerical Simulation of the Transient Flow in a Centrifugal Pump During Starting Period. *J. Fluids Eng.* **2010**, *132*, 081102. [[CrossRef](#)]
12. Li, Z.; Wu, P.; Wu, D.; Wang, L. Experimental and numerical study of transient flow in a centrifugal pump during startup. *J. Mech. Sci. Technol.* **2011**, *25*, 749–757. [[CrossRef](#)]
13. Chern, M.-J.; Wang, C.-C.; Ma, C.-H. Performance test and flow visualization of ball valve. *Exp. Therm. Fluid Sci.* **2007**, *31*, 505–512. [[CrossRef](#)]
14. Yang, Q.; Zhang, Z.; Liu, M.; Hu, J. Numerical Simulation of Fluid Flow inside the Valve. *Procedia Eng.* **2011**, *23*, 543–550. [[CrossRef](#)]
15. Wang, L.; Song, X.G.; Park, Y.C. Dynamic analysis of three-dimensional flow in the opening process of a single-disc butterfly valve. *J. Mech. Eng. Sci.* **2010**, *224*, 329–336. [[CrossRef](#)]
16. Cho, T.-D.; Yang, S.-M.; Lee, H.-Y.; Ko, S.-H. A study on the force balance of an unbalanced globe valve. *J. Mech. Sci. Technol.* **2007**, *21*, 814–820. [[CrossRef](#)]
17. Srikanth, C.; Bhasker, C. Flow analysis in valve with moving grids through CFD techniques. *Adv. Eng. Softw.* **2009**, *40*, 193–201. [[CrossRef](#)]
18. Nguyen, Q.K.; Jung, K.H.; Lee, G.N.; Suh, S.B.; To, P. Experimental Study on Pressure Distribution and Flow Coefficient of Globe Valve. *Processes* **2020**, *8*, 875. [[CrossRef](#)]



© 2020 by the authors. Licensee MDPI, Basel, Switzerland. This article is an open access article distributed under the terms and conditions of the Creative Commons Attribution (CC BY) license (<http://creativecommons.org/licenses/by/4.0/>).

Article

Numerical Simulation of Axial Vortex in a Centrifugal Pump as Turbine with S-Blade Impeller

Xiaohui Wang *, Kailin Kuang, Zanxiu Wu and Junhu Yang

School of Energy and Power Engineering, Lanzhou University of Technology, Lanzhou 730050, China; kuangkailin@163.com (K.K.); wzx19960512@163.com (Z.W.); lzyangjh@lut.cn (J.Y.)

* Correspondence: wangxh@lut.edu.cn

Received: 18 August 2020; Accepted: 11 September 2020; Published: 20 September 2020



Abstract: Pump as turbines (PATs) are widely applied for recovering the dissipated energy of high-pressure fluids in several hydraulic energy resources. When a centrifugal pump operates as turbine, the large axial vortex occurs usually within the impeller flow passages. In view of the structure and evolution of the vortex, and its effect on pressure fluctuation and energy conversion of the machine, a PAT with specific-speed 9.1 was analyzed based on detached eddy simulation (DES), and the results showed that vortices generated at the impeller inlet region, and the size and position of detected vortices, were fixed as the impeller rotated. However, the swirling strength of vortex cores changed periodically with double rotational frequency. The influence of vortices on pressure fluctuation of PAT was relatively obvious, deteriorating the operating stability of the machine evidently. In addition, the power loss near impeller inlet region was obviously heavy as the impact of large axial vortices, which was much more serious in low flow rate conditions. The results are helpful to realize the flow field of PAT and are instructive for blade optimization design.

Keywords: energy recovery; pump as turbine; vortex; hydraulic losses; pressure fluctuation

1. Introduction

In recent decades, pump as turbine (PAT) has drawn increasing attention in energy recovery systems where a high-pressure water source exists. With a pump operating as turbine, the direction of flow and rotation are opposite. For pump, energy is supplied to the fluid via a rotating shaft, as shown in Figure 1a, it is a energy absorbing device. For PAT, energy is extracted from the fluid and output via the rotating shaft, as shown in Figure 1b, it is a energy producing device. Compared with a conventional hydraulic turbine, PAT is simple, inexpensive, easy to maintain, readily available worldwide, and has a short capital payback period. It is an attractive solution for micro-hydro power with capacity below 100 kW [1]. It would be economical to use PAT, recovering the dissipated energy of high-pressure fluids in several hydraulic energy resources, such as water distribution network (WDN) [2–5], sea water reverse osmosis (SWRO) [6], chemical processes [7], nature falls [8], etc.

Although there is a wide application of PAT, the selection of a proper pump operating as turbine is particularly challenging. Many selection techniques have been published so far, while researchers have tested their models on few pumps and recorded deviations in the order of $\pm 10\sim 20\%$ [9]. PAT may not have optimum or favorable flow behavior since pumps are usually not designed for turbine operation. The mismatch between turbine flow parameters and pump geometry may affect the stability of flow performance [10]. In addition, PATs have poor part-load performances [11,12]. Many researchers have presented the optimization of the turbine mode performance for overcoming these challenges. All mentioned issues above require a detailed understanding of the internal flow mechanism of PAT, which is important and imperative to predict the performances of PAT, as well as improve its efficiency and operating stability.

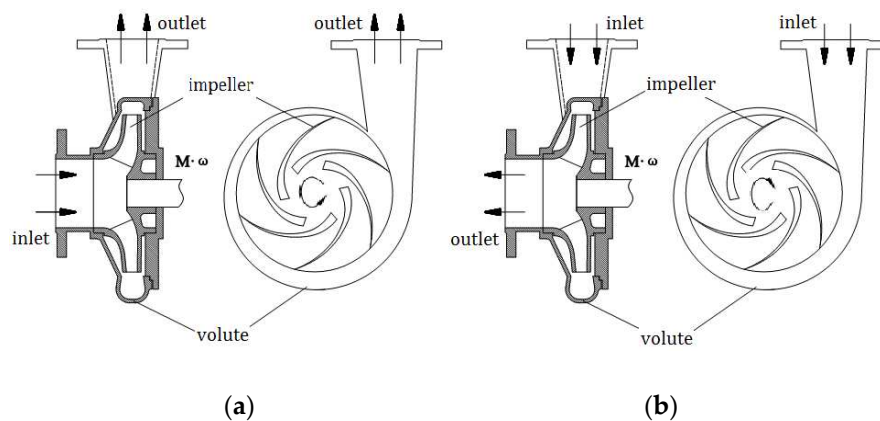


Figure 1. Directions of flow and rotation in pump and pump as turbine (PAT). (a) Pump; (b) PAT.

Computational fluid dynamics (CFDs) were adopted extensively in many earlier research studies to investigate the flow behavior of PAT. A detailed analysis of the turbulence flow structure of a pump and its reverse mode were performed by Pascoa et al. [13]. Singh and Nestmann [14] revealed the wakes and the corresponding losses (flow separation) at the inlet and exit of a PAT impeller. Yang et al. [15] discussed the velocity distribution and hydraulic losses of PAT with different blade wrap angles. Ardizzon and Pavesi [11] researched the effect of relative through-flow and eddy vortex on flow behavior in PAT impellers and established the optimum incidence angle in outward- and inward-flow impellers. Zhang et al. [16] presented a numerical simulation study that the reverse flow causes a great deal of vortex in impellers. Stanbli et al. [17] studied the instability of PAT during start-up process using numerical-based method. Zobeiri et al. [18] investigated the rotor–stator interactions in turbine mode of a pump and presented the pressure fluctuation in stator flow channels. Singh and Nestmann [9] analyzed the flow condition in different flow zones of PAT and concluded the hydraulic loss of each flow zone. Simão et al. [19,20] investigated the hydrodynamic flow behavior of centrifugal PAT to better understand the energy recovery system behavior and to reach the best efficiency operation conditions. Additionally, collaborative design of rotor and stator of PAT have been concerned to improve its efficiency recently [21,22].

The PATs have poor hydraulic performances usually as the pump manufactures do not pay attention to the performances of a pump in reverse operation. As a consequence, low efficiency and instability have been found generally due to the poor flow conditions of vortices, secondary flow, and pressure fluctuation. In this research, the flow behavior of PAT was simulated by the CFD method. The structure and evolution of the large axial vortex in impeller channels were revealed, and its impact on pressure fluctuation and power losses was observed. The results can be expected to be a support for the optimization design of PAT.

2. Theoretical Model of Vortex

For PAT, the slip phenomenon occurs inevitably in flow passages caused by finite blades. Due to the finite blades with certain thickness of PAT, the fluid in the flow passages is guided weakly, and subsequently a slip velocity Δc_u is generated, as shown in Figure 2 (where u is the peripheral velocity of impeller, w is relative velocity, c is absolute velocity, c_m and c_u are the meridian and peripheral components of absolute velocity, respectively, Δc_u is slip velocity, β is relative flow angle and β_b is the blade angle, the subscript ∞ represents infinite blades). As a consequence, the large axial vortices induced reasonably. In part-load operation, this phenomenon is much more serious on account of the non-optimum incoming flow.

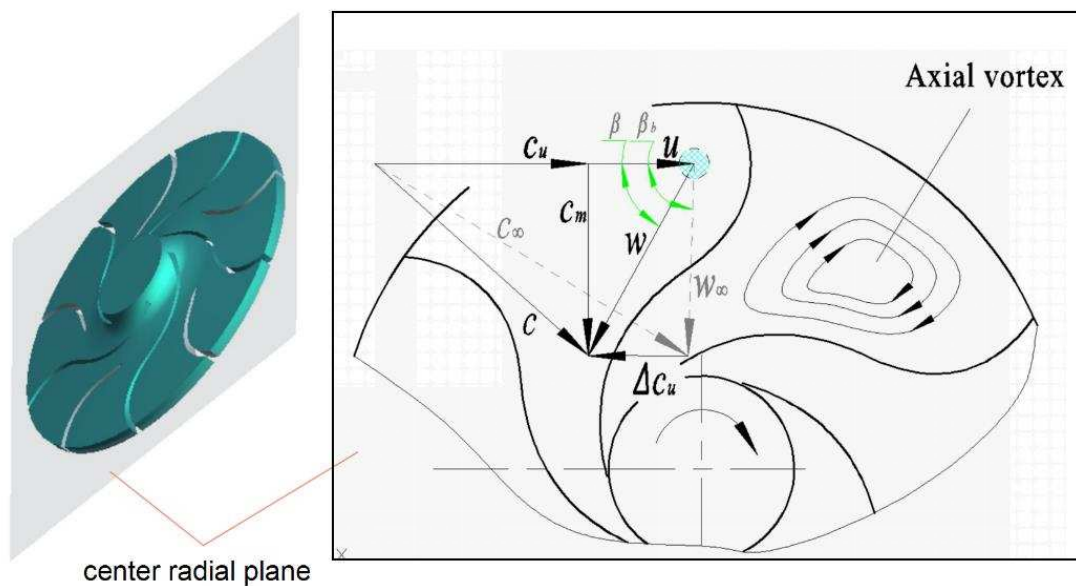


Figure 2. The model of the large axial vortex in PAT.

In recent decades, various vortex identification methods, including closed or spiral path lines, minimum local pressure, vorticity magnitude, etc., have been used to interpret vortical structures in instantaneous flow fields [23]. The vorticity magnitude is widely applied in qualifying the intensity of vortices, and the swirling strength has been adopted—usually to qualify the vorticity magnitude.

For a random element of vortex flow, the velocity gradient tensor d_{ij} can be described as

$$[d_{ij}] = [v_r v_{cr} v_{ci}] \begin{bmatrix} \lambda_r & 0 & 0 \\ 0 & \lambda_{cr} & \lambda_{ci} \\ 0 & -\lambda_{ci} & \lambda_{cr} \end{bmatrix} [v_r v_{cr} v_{ci}]^{-1} \quad (1)$$

where v_r , v_{cr} , and v_{ci} represent the axial, radial, and tangential components of the element velocity, respectively. The velocity gradient tensor d_{ij} exists one real eigenvalue λ_r and two conjugated complex eigenvalues $\lambda_{cr} \pm \lambda_{ci}$. The swirling strength is the imaginary part of the complex eigenvalues of the velocity gradient tensor, λ_{ci} ; it is positive if and only if the discriminant is positive and its value represents the strength of swirling motion around local centers. The greater the absolute value of the swirling strength, the stronger the internal circulation of fluid.

3. Numerical Simulation

3.1. Numerical Method

A modified PAT with specific speed ($nQ^{1/2}/H^{3/4}$, where n is rotational speed, Q is flow rate, and H is head) 9.1 was selected for numerical simulation, and the hydraulic parameters were 50 m for head and 50 m³/h for flow rate with the rotational speed 1500 r/min. The flow zones consisted of volute, impeller, and draft tube as shown in Figure 3. The main geometrical parameters were shown in Table 1.

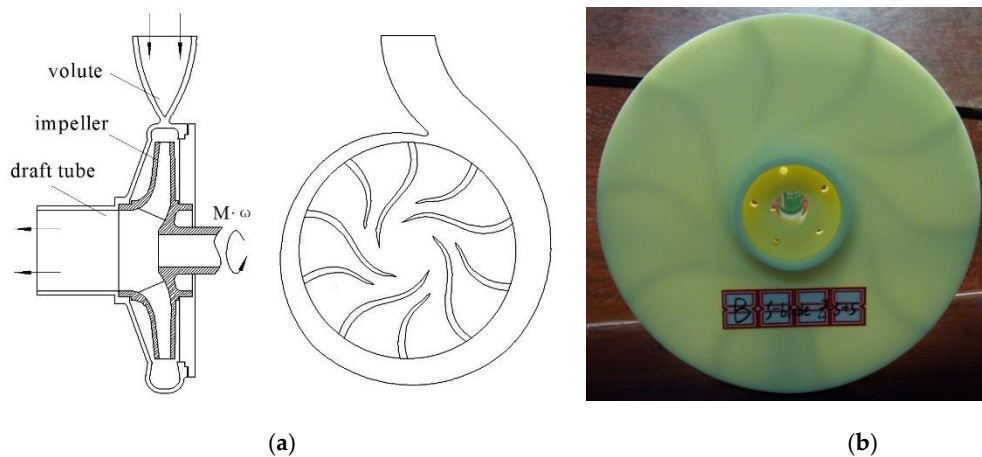


Figure 3. Structure of modified PAT. (a) Structure of selected PAT; (b) modified impeller of PAT.

Table 1. Geometrical parameters of pump as turbine (PAT).

	Categories	Parameters
Impeller	Inlet diameter D_1 (mm)	312
	Outlet diameter D_2 (mm)	80
	Hub diameter d_h (mm)	0
	Inlet width b_1 (mm)	10
	Blade inlet angle β_1 ($^\circ$)	120
	Blade number Z	10
	Blade outlet angle β_1 ($^\circ$)	30
Volute	Inlet diameter D_s (mm)	50
	Outlet width b_0 (mm)	24
	Basic circle diameter D_0 (mm)	320
Draft tube	Length L_d (mm)	120
	Exit diameter D_d (mm)	80

The numerical simulation was performed by means of the Navier–Stokes equation with an appropriate turbulence model. The Reynolds Averaged Navier–Stokes (RANS) turbulence model is not appropriate for the unsteady flow prediction, while a fully-resolved Large Eddy Simulation (LES) is almost unfeasible nowadays [24]. Recently, the Detached Eddy Simulation (DES) showed the superiority of the prediction of unsteady flow phenomenon in studies by Magnoli and Schilling [25]. DES can be described as a hybrid RANS–LES turbulence modeling approach and can be applied in a numerical simulation of rotor–stator interaction, inter-blade vortices and vortex rope successfully. It is acting as a Sub-Grid-Scale (SGS) model of LES in regions where the grid resolution is fine enough to resolve turbulent structures, while in other regions the model is used as a pure RANS model [26]. It features the advantages of a less refined grid near the wall, as well as the memory requirements of a computer. DES can be explicitly presented in the Spalart–Allmaras (SA) k – ϵ model or Shear Stress Transport (SST) model.

In the present work, the CFX (17.0, ANSYS, Pittsburgh, PA, USA, 2016) was adopted for the solution of 3D Navier–Stokes equations due to its characteristics of robust and fast convergence [15]. Steady simulations were achieved using the RNG k – ϵ model and the results were applied as the initial value of transient analysis, the SA–DES turbulence model was applied for transient simulations.

The one equation SA–DES model can be described as

$$\frac{\partial \tilde{v}}{\partial t} + u \cdot \nabla \tilde{v} = \frac{1}{\sigma Re} [\nabla \cdot ((v + \tilde{v}) \nabla \tilde{v}) + c_{b2} |\nabla \tilde{v}|^2] + c_{b1} \tilde{S} \tilde{v} - \frac{c_{w1} f_w}{Re} \left(\frac{\tilde{v}}{d_{DES}} \right)^2 \quad (2)$$

where $\tilde{\nu}$ is a destruction term for the eddy viscosity, which is proportional to $(\tilde{\nu}/d)^2$, where d is the distance to the closest wall, Re is Reynolds number. The second and last terms on the right side of the equation are the product term and destruction term, respectively. When balanced with the production term, the eddy viscosity is adjusted to scale with the local deformation rate S and d : $\tilde{\nu} \propto Sd^2$. In the Smagorinsky model, the sub-grid-scale (SGS) eddy viscosity scales with S and the grid spacing Δ : $\mu_{SGS} \propto S\Delta^2$. Thus, the SA model turns into the SGS model when d is replaced by a length proportional to Δ .

If we replace d in the SA destruction term with \tilde{d} , described as

$$\tilde{d} = \min(d, C_{DES}\Delta) \quad (3)$$

then the model is an SA turbulence model when $d \ll \Delta$, while an SGS model when $d \gg \Delta$.

Since the SA-DES model does not require any wall functions, the mesh that is close to the wall surface must be designed to accurately predict the hydrodynamic force; hence, the high-aspect-ratio cells near the wall have been generated [27]. The mesh of the fluid domain was generated using ICEM-CFD (17.0, ANSYS, Pittsburgh, PA, USA, 2016) as its advantage of a well-adapted and efficient hexahedral grid was applied for meshing, as shown in Figure 4. The length of the inlet and outlet pipes was extended to eliminate the influence of back flow. The grid convergence and grid independence tests were performed, and the results showed that the head–flow rate curve became stable as the elements of mesh over 3,612,548, as shown in Figure 5. Therefore, the final element numbers of the volute, impeller, and draft tube were 865,260, 3,007,154, and 243,200, respectively.

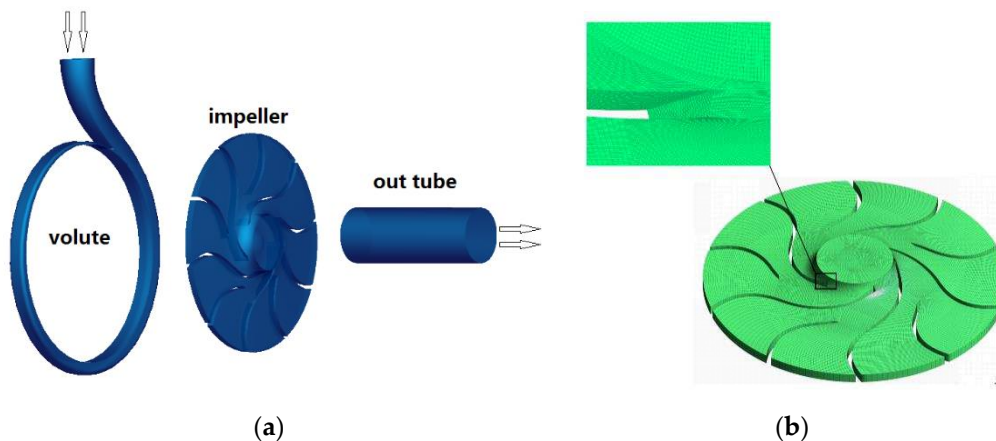


Figure 4. Computational domain and mesh. (a) Computational domain; (b) mesh.

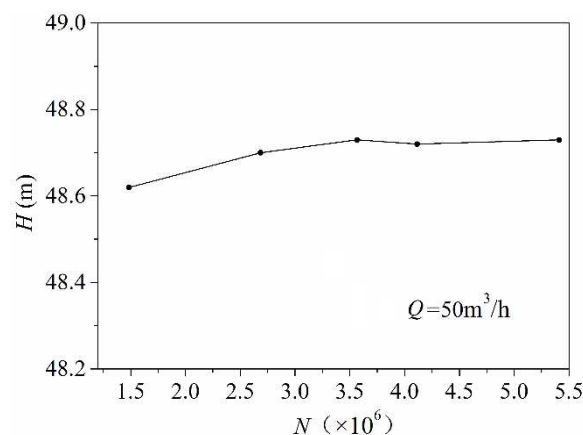


Figure 5. Grid independent test.

The boundary condition of the inlet was the total pressure with an initial value of 0.5 MPa, and the outlet was the flow rate with an initial value of 50 m³/h for design condition; the rotational speed of the impeller was fixed with 1500 r/min. The fluid was the normal water with a temperature of 20 °C, all the wall surfaces were adiabatic, and the roughness was set to 50 μm. To obtain reasonable results, the proper selection of time steps is of great importance. It is suggested that time steps for a runner rotation of 0.5–5° could provide useful information for the flow field under transients [28]. Hence, the time steps in this study were 3.3×10^{-4} s, corresponding to 3° of the impeller rotational angle. The max coefficient loop of convergence control was 40, and the residual target of the convergence criteria was 10^{-5} . The total time of the duration data was 0.4 s corresponding to 10 rotor revolutions and the last four revolution data were analyzed.

For revealing the vortex structure and pressure fluctuation in PAT flow channels, 17 monitoring points were set in the middle plane of PAT, as shown in Figure 6. Point 1 was set in the gap between volute and impeller, point 2 and 3 next to the inlet and outlet of impeller, respectively, point 4 was in center of impeller outlet, points 5, 7, 9 were on the suction profile of the short blade, while 6, 8, 10 were on the pressure side, points 11, 13, 15 were on the suction profile of the long blade, while 12, 14, 16 were on the pressure profile, point 17 was set in the flow channel.

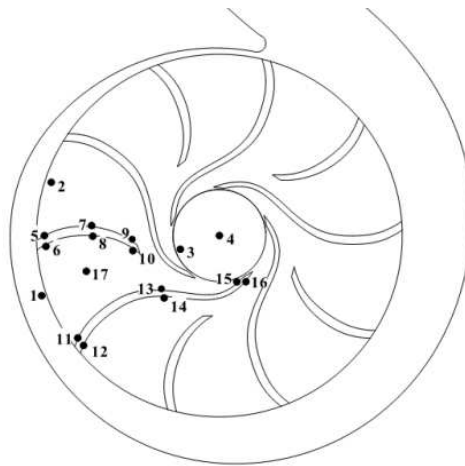


Figure 6. Monitoring sites of PAT.

3.2. Verification of Numerical Method

In this section, the numerical method was validated by the experimental results. A test rig was established for the hydraulic performance experiment of PAT. The test rig was composed by water supply, PAT, and energy dissipation sections as shown in Figure 7. A feed pump was installed to provide the head and flow rate for PAT. A magnetic power brake was equipped to balance the output power, and a loop control system was used to adjust the torque of output shaft. A flow meter was equipped at the inlet pipe of PAT for measuring the flow rate, and two pressure transducers were installed at the PAT inlet and outlet for measuring pressure. For measuring the torque and rotational speed of PAT, a torque meter was set at shaft. The head, flow rate, power and efficiency of PAT could be obtained after all parameters were measured.

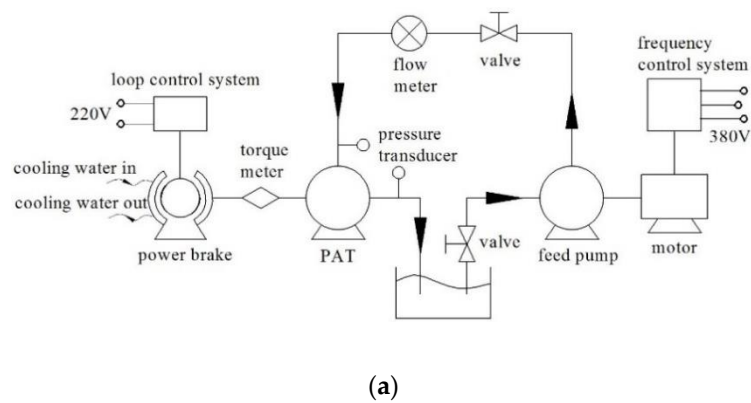


Figure 7. Experimental equipment of PAT. (a) Schematic diagram of experiment; (b) test rig.

The selected PAT was tested and the hydraulic performance curves by experimental and numerical methods were illustrated in Figure 8. It can be found that the numerical head is in good coincidence with the experimental results. In consequence, it is reasonable to believe that the employed numerical method is accurate, and it can be applied in performance predictions of PAT.

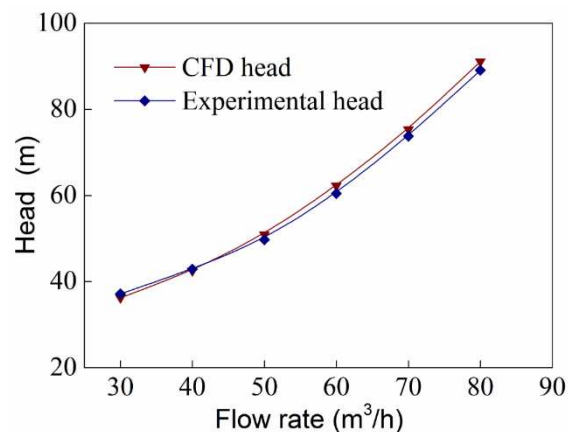


Figure 8. Comparison between experimental and numerical results.

4. Results and Discussion

4.1. Vortex Information in Flow Channels

For PAT, large axial vortices were derived in impeller flow channels even at the best efficiency point (BEP), as shown in Figure 9. It can be seen that the streamline was disordered near the suction surfaces of the impeller inlet where the large axial vortices were induced. It can be clearly observed

that the vortices were more legible on short blade surfaces. Furthermore, the size and position of detected vortices were invariant with rotor rotating, and apparently, these were stable.

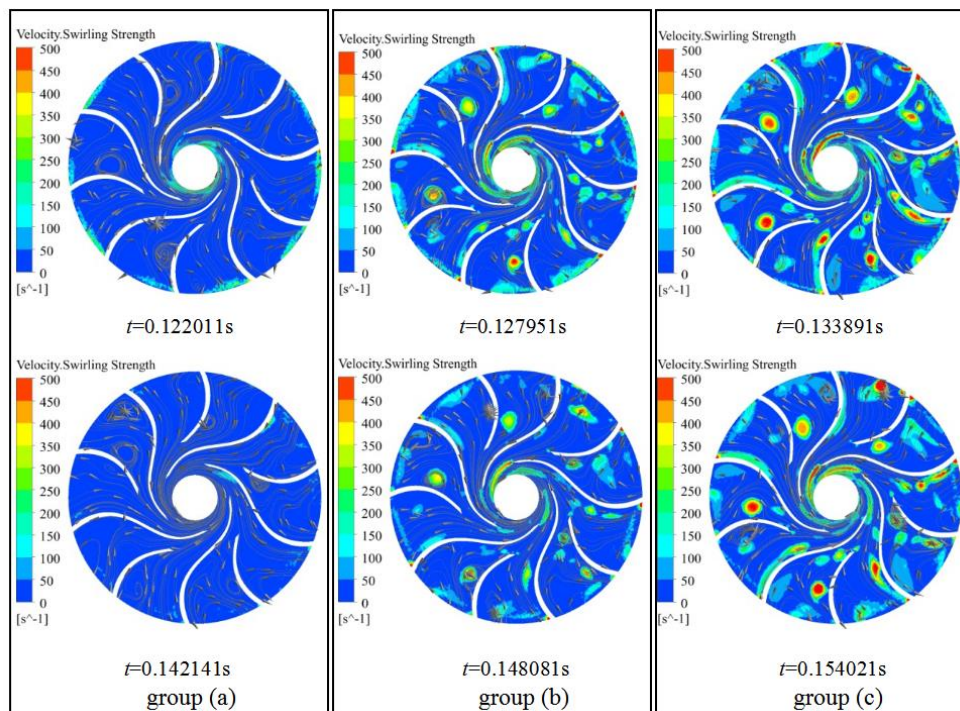


Figure 9. Streamline and swirling strength contour of impeller.

The swirling strength contour of detected vortices during one rotating cycle was displayed in Figure 9. It can be seen that although the vortex size and position were stable, the swirling strength changed with rotation of the impeller. In the first half of the rotating cycle, the swirling strength was minimum ($0\sim 50\text{ s}^{-1}$) at 0.122011 s, intensified to maximum ($450\sim 500\text{ s}^{-1}$) at 0.133891 s, and weakened to minimum ($0\sim 50\text{ s}^{-1}$) again at 0.142141 s. The revolution of the vortex swirling strength in the second half of the cycle was the same as the first half. The vortices information was extremely similar at 0.122011 s and 0.142141 s, 0.127951 s and 0.148081 s, as well as 0.133891 s and 0.154021 s. It can be found that the time steps of each working point are 0.2 s approximately for the three groups (group a, b, and c, as shown in Figure 9), that is half the time of per rotating cycle (0.4 s) for PAT. In other words, the swirling strength of the vortex develops periodically with two times the rotating frequency.

4.2. Pressure Fluctuation of Vortex

The pressure fluctuation could be produced due to the vortices with twofold rotating frequency. In order to reveal the pressure fluctuation characteristics of PAT, transient numerical simulation was performed, and results of the 17 monitoring points are given in Figure 10. Where the vertical coordinates C_p is pressure coefficient, it can be described as

$$C_p = \frac{p_i - \bar{p}}{0.5\rho u_1^2} \quad (4)$$

where p_i denotes the transient pressure of monitoring point (Pa), \bar{p} is the average pressure (Pa), ρ is the density of fluid (kg/m^3), and u_1 is the peripheral velocity of impeller inlet (m/s).

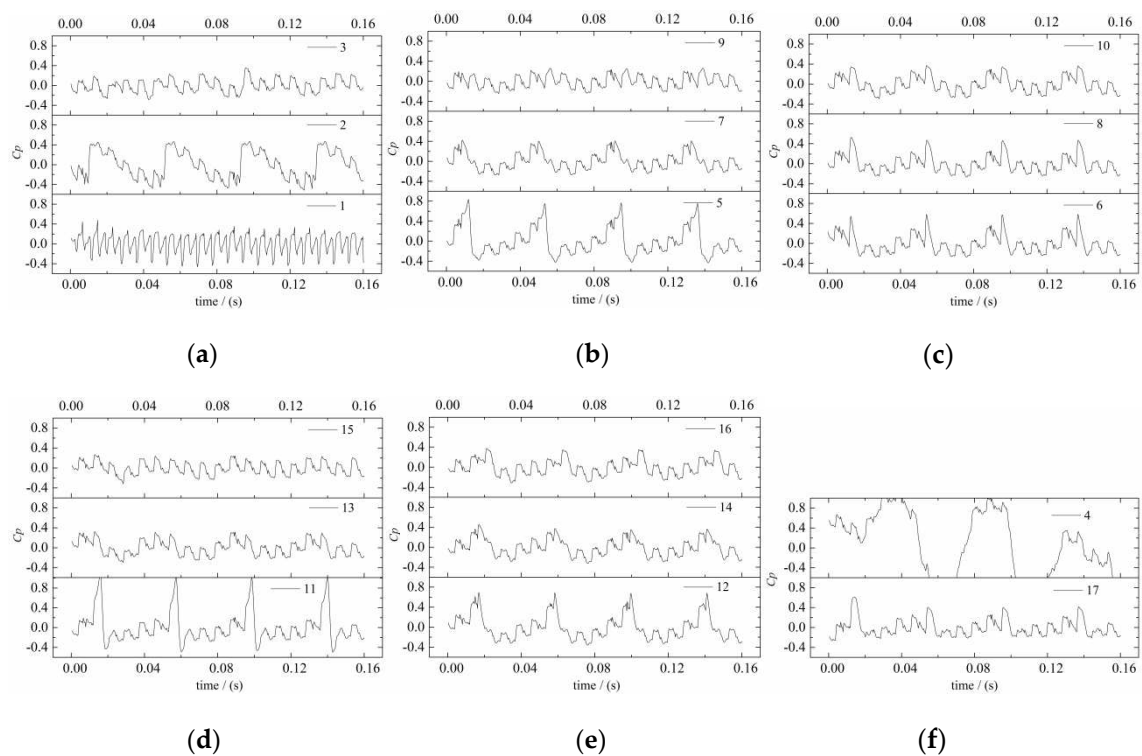


Figure 10. Pressure fluctuation coefficient with time. (a) Points 1, 2, 3; (b) Points 5, 7, 9; (c) Points 4, 6, 8; (d) Points 11, 13, 15; (e) Points 12, 14, 16; (f) Points 4, 17.

The pressure of point 1 fluctuated 10 times in a rotating cycle visibly, which was caused by the blade–volute interaction; as the point was set in the gap between the rotor and volute, it was not related to the axial vortex obviously. Point 4 could not be related to the axial vortex as well because it was set in the draft tube that was far away from the vortex regions. The pressure fluctuation at other points showed that the leading periodical impulse was related to the rotor–stator interaction. However, it was no reason to neglect the correlation between the subordinate periodical impulse and axial vortex.

Figure 11 showed the pressure fluctuation images with frequency range, which was received by fast Fourier transform (FFT) from Figure 9. For easily understanding, the horizontal axis was the ratio of frequency (ffn), where fn denoted the rotating frequency of the rotor.

It can be seen that the leading pressure fluctuation of the monitoring points occurred at $1 ffn$, $5 ffn$, $10 ffn$, and $20 ffn$. Obviously, this related to the rotor–stator interaction. Pressure fluctuation at $1 ffn$ caused by the rotor–tongue interaction, at $5 ffn$, $10 ffn$, $20 ffn$ caused by blade–tongue interaction (the impeller equipped with 5 long blades and 5 short blades). Therefore, the main factor of pressure fluctuation was the rotor–stator interaction.

However, the subordinate pressure fluctuation at $2 ffn$ was found in points 2, 5, 6, 11, 12, and 17. It was obvious, especially in points 5 and 11 as marked with dashed circle in Figure 10, as mentioned earlier, that the large axial vortices were derived in these regions usually. Consequently, it was reasonable to declare that the subordinate pressure fluctuation was related to axial vortices in impeller channels, which deteriorated the operating stability of the machine evidently.

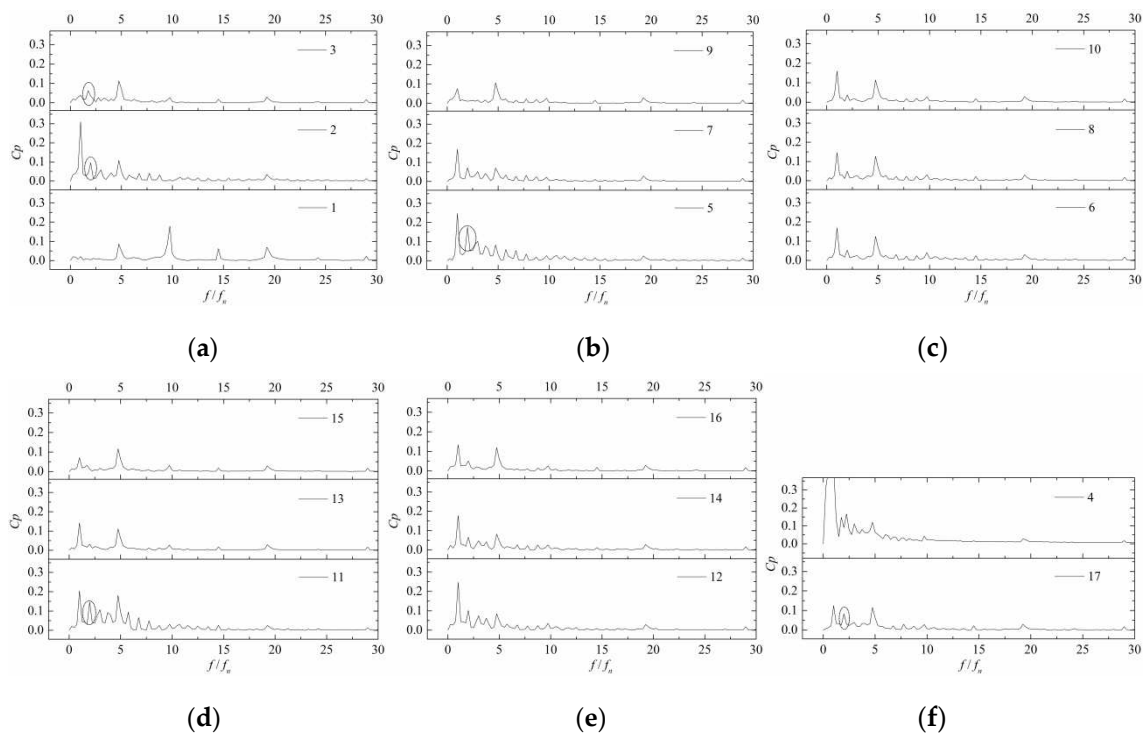


Figure 11. Pressure fluctuation coefficient with frequency. (a) Points 1, 2, 3; (b) Points 5, 7, 9; (c) Points 4, 6, 8; (d) Points 11, 13, 15; (e) Points 12, 14, 16; (f) Points 4, 17.

4.3. Power Losses Caused by Vortex

The large axial vortices provide subordinate contribution to the pressure fluctuation of PAT. More importantly, this might cause entropy generation in the flow field, and therefore, the power loss produced inevitably. In this section, the power losses caused by axial vortices were analyzed.

Flow distortion have been detected in the impeller that was caused by axial vortices, where a wake region has been found near the impeller inlet, it was significant especially for $0.6 Q_d$ and $1.0 Q_d$ (Q_d is design flow rate), as shown in Figure 12. As a consequence, a low-pressure zone appeared near the impeller inlet, and the relative velocity no longer distributed alongside the blade surfaces. In order to reveal the effect of axial vortices on performance characteristics of PAT, six monitoring cylindrical surfaces in the impeller were created as shown in Figure 13. Figure 14 was the distribution of the average relative velocity (radial component) in the impeller, and Figure 15 was the average pressure at each cylindrical surface. It can be seen that the average relative velocity (radial component) and pressure curves decreased gradually along the flow direction in the impeller channels for $1.6 Q_d$; however, a local decline of the curves appeared at surface 1 and 2 for $0.6 Q_d$ and $1.0 Q_d$. As shown in Figure 12, the streamline of $1.6 Q_d$ was uniform, and very tiny axial vortices were detected in the flow channels. However, large axial vortices can be found near the impeller inlet at $0.6 Q_d$ and $1.0 Q_d$; this was much more serious for low flow rates. It can be seen from Figure 12 that the region from surface 1 to surface 3 was worse affected by axial vortices for the low flow rates that reasonably responded to the local decline of the average relative velocity and pressure.

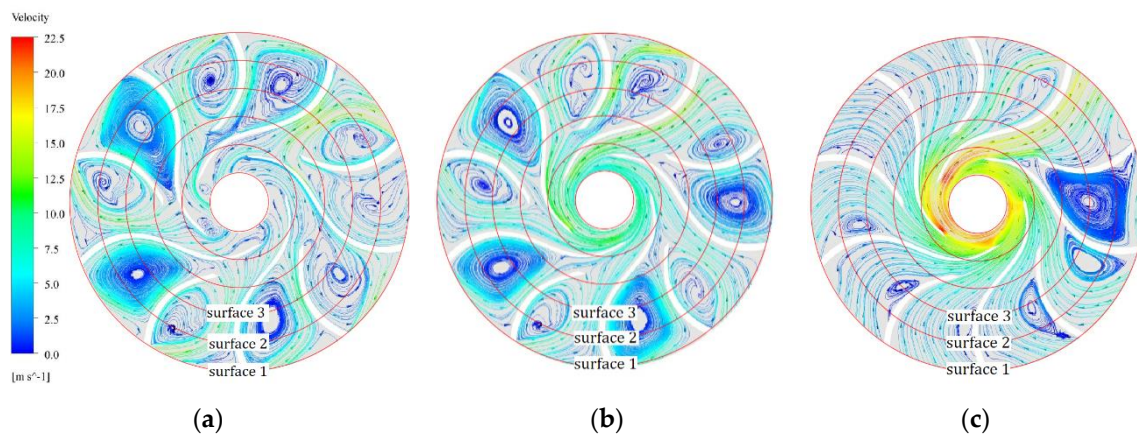


Figure 12. Streamline at radial plane of impeller. (a) $0.6 Q_d$; (b) $1.0 Q_d$; (c) $1.6 Q_d$.

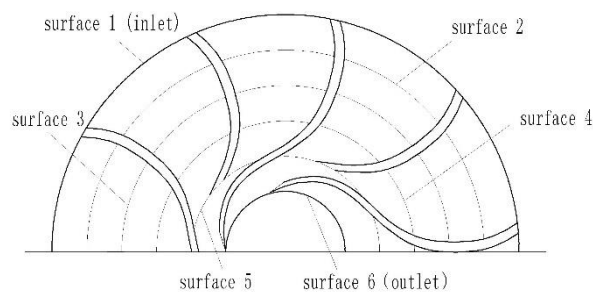


Figure 13. Monitoring surfaces of the impeller.

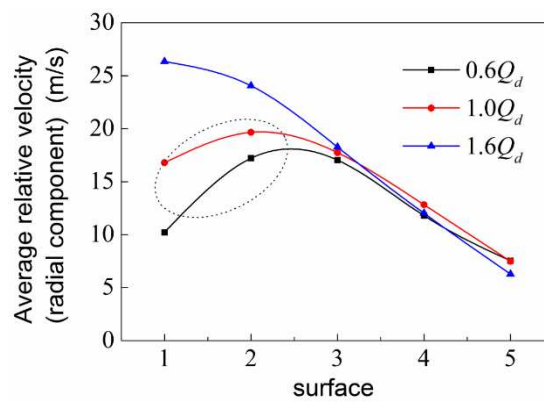


Figure 14. Average relative velocity of monitoring surfaces.

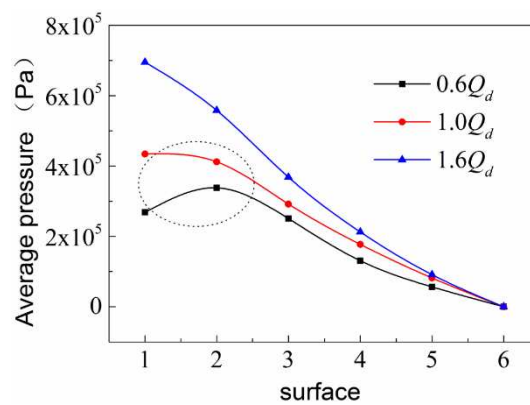


Figure 15. Average pressure of monitoring surfaces.

As the axial vortices were generated, power losses were raised inevitably. To study the power losses caused by vortices, the flow domain in the impeller was divided into six zones (Figure 16), and power losses of each zone were calculated.

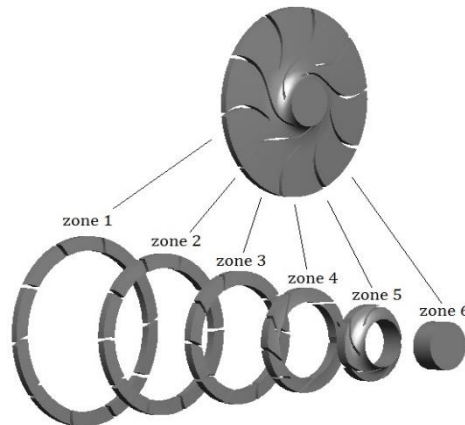


Figure 16. Zones of the impeller.

For any zone i , when the boundary condition with a pressure inlet and flow rate outlet are given, while rotating speed is fixed, the theoretical power (fluid power) and actual power (shaft power of PAT) can be obtained by numerical simulation. The theoretical power can be described as

$$p'_{(i,i+1)} = \rho g Q H_{(i,i+1)} \quad (5)$$

where ρ is the fluid density, g is the gravitational acceleration, $H_{(i,i+1)}$ is the fluid head of zone i , and Q is the flow rate. The shaft power of PAT is

$$p_{(i,i+1)} = M_{(i,i+1)} \cdot \omega \quad (6)$$

where $M_{(i,i+1)}$ is the torque of zone i , while ω is the angular speed of the impeller. Then, the relative power losses of zone i are

$$f_{(i,i+1)} = 1 - \frac{p_{(i,i+1)}}{p'_{(i,i+1)}} \quad (7)$$

As the numerical simulation did not consider the leakage and frictional losses of PAT, Equation (7) can be considered as relative power losses of zone i .

Figure 17 presented the power losses of each zone for $0.6 Q_d$, $1.0 Q_d$, $1.6 Q_d$, respectively. It can be seen that the power losses of zone 1 and 2 (the inlet region of the impeller) were higher distinctly than zone 3 and 4. As mentioned earlier, the large axial vortices occurred in this region usually, and caused the reduction in energy conversion of PAT. What calls for special attention was that the power losses of zone 5 and 6 were higher than zone 3 and 4 as well, which was related to the vortices in the draft tube to a great extent, and it deserved further research in the future.

It can be concluded also that the power losses were heaved significantly in low flow rates, which was related to the large axial vortices. As mentioned above, large axial vortices can be found near impeller inlets usually and are much more serious for low flow rates. Thus, it was believed that power losses would be induced by the large axial vortices within flow passages, and it should be considered in the design and optimization process, especially in low flow rates.

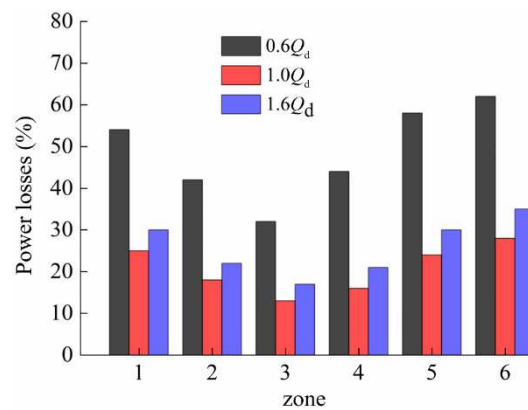


Figure 17. Hydraulic losses of different zones.

5. Conclusions

In this study, the flow behavior of a centrifugal PAT with specific speed 9.1 was researched by a verified CFD method. The large axial vortices were derived in impeller flow channels due to the slip and poor match between flow and blades. The size and position of the vortices were stable apparently. However, the swirling strength developed periodically with $2fn$ (fn is the rotating frequency of PAT).

The pressure fluctuation can be found in PAT. The leading pressure fluctuation was caused by the rotor–stator interaction, while the subordinate fluctuation was related to axial vortices in impeller channels, which deteriorated the operating stability of the machine evidently.

The power losses were induced by the large axial vortices in the impeller flow channels, and this phenomenon was much more serious in the low flow rate operation. This should be considered in the design and optimization process, especially in low flow rates.

Nevertheless, the feature of large axial vortices within PAT impeller channels deserved further research in detail based on more PATs. The influence of the rotation, geometry of the blades, entropy variation of the large axial vortex and efficiency of the PAT should be discussed deeply, especially in the pump–turbine transition processes.

Author Contributions: X.W.: Conceptualization, Methodology, Formal Analysis, Investigation, Writing. K.K.: Software, Data Curation. Z.W.: Resources, Data Curation. J.Y.: Validation. All authors have read and agreed to the published version of the manuscript.

Funding: This research was funded by the Nature Science Foundation of China (51569013), Industry Support and Guidance Plan of Colleges in Gansu (2020C-20), and the Article Processing Charge (APC) was funded by Outstanding Young Scientists Support Program of Lanzhou University of Technology (LUT).

Conflicts of Interest: The authors declare no potential conflicts of interests with respect to the research, authorship, and/or publication of this article.

References

- Giosio, D.R.; Henderson, A.D.; Waiker, J.M.; Brandner, P.A.; Sargison, J.E.; Gautam, P. Design and performance evaluation of pump-as-turbine micro-hydro test facility with incorporated inlet flow control. *Renew. Energy* **2015**, *78*, 1–6. [[CrossRef](#)]
- Lydon, T.; Coughlan, P.; McNabola, A. Pump-as-turbine: Characterization as an energy recovery device for the water distribution network. *J. Hydraul. Eng.* **2017**, *143*, 04017020.1–04017020.10. [[CrossRef](#)]
- Ramos, H.; Borga, A. Pumps as turbines: An unconventional solution to energy production. *Urban Water* **1999**, *1*, 261–263. [[CrossRef](#)]
- Rossi, M.; Nigro, A.; Pisaturo, G.R.; Renzi, M. Technical and economic analysis of Pumps-as-Turbines (PaTs) used in an Italian Water Distribution Network (WDN) for electrical energy production. *Energy Procedia* **2019**, *158*, 117–122. [[CrossRef](#)]

5. Alberizzi, J.C.; Renzi, M.; Righetti, M.; Pisaturo, G.R.; Rossi, M. Speed and pressure controls of pumps-as-turbines installed in branch of water-distribution network subjected to highly variable flow rates. *Energies* **2019**, *12*, 4738. [CrossRef]
6. Mohameda, E.S.; Papakakisa, G.; Mathioulakis, E. The effect of hydraulic energy recovery in a small sea water reverse osmosis desalination system; experimental and economical evaluation. *Desalination* **2005**, *184*, 241–246. [CrossRef]
7. Van Antwerpen, H.J.; Greyvenstein, G.P. Use of turbines for simultaneous pressure regulation and recovery in secondary cooling water systems in deep mines. *Energy Convers. Manag.* **2005**, *46*, 563–575. [CrossRef]
8. Wang, X.H.; Yang, J.H.; Xia, Z.T.; Hao, Y.; Cheng, X.R. Effect of Velocity Slip on Head Prediction for Centrifugal Pumps as Turbines. *Math. Probl. Eng.* **2019**, *2019*, 5431047. [CrossRef]
9. Singh, P.; Nestmann, F. An optimization routine on a prediction and selection model for the turbine. *Exp. Therm. Fluid Sci.* **2010**, *34*, 152–164. [CrossRef]
10. Su, X.H.; Huang, S.; Zhang, X.J.; Yang, S.S. Numerical research on unsteady flow rate characteristics of pump as turbine. *Renew. Energy* **2016**, *94*, 488–495. [CrossRef]
11. Ardizzon, G.; Pavesi, G. Optimum incidence angle in centrifugal pumps and radial inflow turbines. *Proc. Inst. Mech. Eng. Part A J. Power Energy* **1998**, *212*, 97–107. [CrossRef]
12. Singh, P. Optimization of Internal Hydraulics and of System Design for Pumps as Turbines with Field Implementation and Evaluation. Ph.D. Thesis, University of Karlsruhe, Karlsruhe, Germany, 2005.
13. Pascoa, J.C.; Silva, F.J.; Pinheiro, J.S.; Martins, D.J. Accuracy details in realistic CFD modeling of an industrial centrifugal pump in direct and reverse modes. *J. Therm. Sci.* **2010**, *19*, 491–499. [CrossRef]
14. Singh, P.; Nestmann, F. Internal hydraulic analysis of impeller rounding in centrifugal pumps as turbines. *Exp. Therm. Fluid Sci.* **2011**, *35*, 121–134. [CrossRef]
15. Yang, S.S.; Kong, F.Y.; Chen, H.; Su, X.H. Effects of blade wrap angle influencing a pump as turbine. *J. Fluids Eng.* **2012**, *134*, 061102–061109. [CrossRef]
16. Zhang, S.; Shi, Q.; Zhang, K. Flow behavior analysis of reversible pump-turbine in “S” characteristic operating zone. In Proceedings of the IOP Conferences Series: Earth and Environmental Science, Beijing, China, 19–23 August 2012; Volume 15, p. 032045.
17. Staubli, T.; Senn, F.; Sallaberger, M. Instability of Pump-Turbines during Start-up in Turbine Mode. 2008. Available online: http://xueshu.baidu.com/usercenter/paper/show?paperid=97f4d4701a82fd4c1510fe74f46d3c6c&site=xueshu_se (accessed on 13 February 2020).
18. Zobeiri, A.; Kueny, J.L.; Farhat, M.; Avellan, F. Pump-turbine rotor-stator interactions in generating mode: Pressure fluctuation in distributor channel. In Proceedings of the 23rd IAHR Symposium on Hydraulic Machinery and Systems, Yokohama, Japan, 17–21 October 2006.
19. Simão, M.; Pérez-Sanchez, M.; Carravetta, A.; Ramos, H.M. Flow Conditions for PATs Operating in Parallel: Experimental and Numerical Analyses. *Energies* **2019**, *12*, 901. [CrossRef]
20. Simão, M.; Pérez-Sanchez, M.; Carravetta, A.; Lopez-Jimenez, P.; Ramos, H.M. Velocities in a Centrifugal PAT Operation: Experiments and CFD Analyses. *Fluids* **2018**, *3*, 3. [CrossRef]
21. Barrio, R.; Fernandez, J.; Blanco, E. Performance characteristics and internal flow patterns in a reverse-running pump-turbine. *Proc. Inst. Mech. Eng. Part C J. Mech. Eng. Sci.* **2012**, *226*, 695–708. [CrossRef]
22. Shi, F.; Tsukamoto, H. Numerical study of pressure fluctuations caused by impeller-diffuser interaction in a diffuser pump stage. *J. Fluids Eng.* **2001**, *123*, 466–474. [CrossRef]
23. Zang, Z.P.; Gao, F.P.; Cui, J.S. Physical modeling and swirling strength analysis of vortex shedding from near-bed piggyback pipelines. *Appl. Ocean Res.* **2013**, *40*, 50–59. [CrossRef]
24. Krappel, T.; Kuhlmann, H.; Kirschner, O. Validation of an IDDES-type turbulence model and application to a Francis pump turbine flow simulation in comparison with experimental results. *Int. J. Heat Fluid Flow* **2015**, *55*, 167–179. [CrossRef]
25. Magnoli, M.V.; Schilling, R. Numerical simulation of pressure pulsations in Francis turbines. In *Advances in Hydroinformatics. Springer Hydrogeology*; Gourbesville, P., Cunge, J., Caignaert, G., Eds.; Springer: Singapore, 2013; pp. 389–403.
26. Masterov, M.V.; Baltussen, W.M.; Kuipers, J. Numerical simulation of a square bubble column using Detached Eddy Simulation and Euler–Lagrange approach. *Int. J. Multiph. Flow* **2018**, *107*, 275–288. [CrossRef]

27. Tu, S.Z.; Aliabadi, S.; Patel, R.; Watts, M. An implementation of the Spalart-Allmaras DESmodel in an implicit unstructured hybrid finite volume/element solver for incompressible turbulent flow. *Int. J. Numer. Methods Fluids* **2009**, *59*, 1051–1062. [[CrossRef](#)]
28. Trivedi, C.; Gandhi, B.; Michel, C.J. Effect of transients on Francis turbine runner life: A review. *J. Hydraul. Res.* **2013**, *51*, 121–132. [[CrossRef](#)]



© 2020 by the authors. Licensee MDPI, Basel, Switzerland. This article is an open access article distributed under the terms and conditions of the Creative Commons Attribution (CC BY) license (<http://creativecommons.org/licenses/by/4.0/>).

Article

Optimization Design of a Two-Vane Pump for Wastewater Treatment Using Machine-Learning-Based Surrogate Modeling

Sang-Bum Ma ¹, Sung Kim ¹ and Jin-Hyuk Kim ^{1,2,*}

¹ Clean Energy R&D Department, Korea Institute of Industrial Technology 89 Yangdaegiro-gil, Ipjang-myeon, Seobuk-gu, Cheonan, Chungcheongnam-do 31056, Korea; sbma@kitech.re.kr (S.-B.M.); ks2928@kitech.re.kr (S.K.)

² Industrial Technology, Korea University of Science & Technology, 217 Gajeong-ro, Yuseong-gu, Daejeon 34113, Korea

* Correspondence: jinhyuk@kitech.re.kr

Received: 28 July 2020; Accepted: 15 September 2020; Published: 17 September 2020



Abstract: This paper deals with three-objective optimization, using machine-learning-based surrogate modeling to improve the hydraulic performances of a two-vane pump for wastewater treatment. For analyzing the internal flow field in the pump, steady Reynolds-averaged Navier-Stokes equations were solved with the shear stress transport turbulence model as a turbulence closure model. The radial basis neural network model, which is an artificial neural network, was used as the surrogate model and trained to improve prediction accuracy. Three design variables related to the geometry of blade and volute were selected to optimize concurrently the objective functions with the total head and efficiency of the pump and size of the waste solids. The optimization results obtained by using the model showed highly accurate prediction values, and compared with the reference design, the optimum design provided improved hydraulic performances.

Keywords: two-vane pump; Computational Fluid Dynamics (CFD); Reynolds-averaged Navier-Stokes (RANS); optimization; machine learning

1. Introduction

Recently, with the increase in the usage of disposable masks because of the COVID (Corona virus disease)-19 pandemic, used masks are being commonly discarded in toilets. If the cloth wastes such as a disposable mask or large waste such as a baby diaper is disposed into a toilet, the flow path of the pump that transports wastewater is blocked, and as a result, the function of the wastewater transport system is lost. Therefore, the demand for special pumps for wastewater transportation is increasing, and it has gained attention as an industry with the potential for future growth.

As an example of the special pumps, grinder and vortex pumps are widely used for transporting wastewater. However, these special pumps have low efficiency and high maintenance costs, contributing to large operating costs. Several studies explored the treatment of sewage containing solid waste to solve these problems [1–4]. Lu et al. [1] studied the hydraulic performance and pressure fluctuation characteristics of a grinder pump. Through a numerical analysis, the hydraulic performances of the pump when the flow path is in a clogging state and in a normal operating state were compared, and steady and unsteady Reynolds-averaged Navier-Stokes (RANS) analyses was performed. It was found that, as the degree of clogging of the grinder cutter increases, the total head of the pump declines parabolically, with the best efficiency point shifting to the low flow rate region and the high efficiency area narrowing. Schivley and Dussourd analyzed and designed a vortex pump, using a one-dimensional analytical model [2]. They compared the calculated performance parameters with

those measured by using the laboratory model, and they computed the overall hydraulic characteristics of the pump and compared these characteristics with those of many test pumps. They improved the theoretical formula used in the preliminary design of a vortex pump. Ohba et al. [3] theoretically analyzed the flow characteristics inside a vortex pump and secured the theoretical reliability by comparing the predicted values with experimental results. Their theoretical formula could predict not only the hydraulic performance of the vortex pump, but also the velocity component inside the pump. The obtained results were in good agreement with the experimentally measured values. Steinmann et al. [4] analyzed the internal flow of a vortex pump through numerical analysis and experiments to investigate the unsteady cavitating flow of a vortex pump. The Rayleigh–Plesset cavitation model was used to simulate cavitation under the overload condition of the vortex pump, and an acrylic glass window was installed in the experimental apparatus, to observe this phenomenon. Under the best efficiency point condition, the numerically derived head and shaft power of the pump were about 6% higher than the experimentally measured values. Conversely, cavitation under overload was observed more in experimental results than in numerical analysis.

In addition to the grinder and vortex pumps mentioned above, single-channel pumps designed to transport relatively larger solid wastes were actively studied [5–7]. The single-channel impeller with a single free annulus passage can smoothly transfer sewage-containing solid wastes. However, this impeller has an unsymmetrical annulus flow passage, and it is difficult to stabilize the unsteady flow-induced vibration, due to the interaction between the rotating impeller and stationary volute [5]. Shi and Tsukamoto [6] numerically analyzed the pressure fluctuation due to the impeller–diffuser interaction in a diffuser pump. They confirmed that the flow characteristics due to this interaction can be analyzed through an unsteady flow analysis. Feng et al. [7] analyzed the unsteady flow characteristics between the impeller and diffuser of a radial pump by unsteady RANS (URANS) analysis and laser Doppler velocimetry (LDV); they identified two types of rotor–stator interaction effects. One is the downstream effect induced by the impeller, which has an unsteady flow characteristic because of the highly distorted flow field and the wake of the impeller. The other is the upstream effect induced by the stator, which causes unsteady pressure and velocity fluctuations. Such a single-channel pump has the advantage of being able to transport relatively large waste solids, but it has the disadvantage that the fluid-induced vibration is greater than that in the existing special pumps (e.g., grinder and vortex pumps) because of its asymmetric structural characteristics.

The special pumps for wastewater treatment introduced so far clearly have advantages and disadvantages, depending on their type. Grinder and vortex pumps have low vibration during operation, but the size of transportable solid matters is relatively small, and the maintenance costs are relatively high. On the other hand, a single-channel pump can easily transport large solid matters, but in some cases, relatively severe vibration occurs. To solve these problems, the authors intended to design a two-vane pump in this study. The impeller of the two-vane pump is composed of two blades that are symmetrical in the rotational axis. Therefore, it is structurally simple compared to the grinder and vortex pumps, and the relatively large flow path of the impeller has a small number of blades, so waste solids can be transferred smoothly. In addition, due to the symmetrical impeller geometry, the fluid-induced vibration is relatively less than that of a single-channel pump.

In the past, design optimization using numerical analysis has been widely used for fluid-based machinery [8–11]. For example, Lee et al. [10] performed an optimization to improve the efficiency of a low-speed axial flow fan, using a gradient-based search algorithm. Lee and Kim [11] optimized axial compressor blades to improve the efficiency, using numerical optimization techniques such as conjugate direction methods and the golden section method, combined with a three-dimensional (3D) thin-layer Navier–Stokes solver. Recently, with the rapid advances in computing resources, optimal design is being actively researched based on machine-learning techniques [12,13].

In this study, a two-vane pump was designed to develop a series of special pumps for transporting wastewater. Compared to a single-channel pump, this pump can transport relatively smaller waste solids but experiences less vibration during operation because of the axial symmetry of

the impeller. Considering the characteristics of this pump, a three-objective optimization design based on machine learning was performed to maximize the size of the waste solids that can be transported while simultaneously improving the hydraulic performances of the pump. For the three-objective optimization, the geometric design variables, i.e., inlet and outlet blade angles and cross-sectional area of the volute, were chosen, and the volume of the waste solids and the head and efficiency of the pump were considered as objective functions. Their relationship was predicted by using an artificial neural network (ANN) [14] based on machine learning. Then, the genetic algorithm (GA) [15] was used to find the optimal solutions, and the Pareto-optimal front surface [16] was derived as the final optimization result.

2. Numerical Methods

2.1. Two-Vane Pump Model

The preliminary two-vane pump model used in this work was designed by using CFTurbo [17], under the following design conditions: a flow rate of 0.5 m³/min, a total head of 10 m, and a rotational speed of 1760 rpm (revolution per minute).

The two-vane pump used in this study was designed for commercialization, and the preliminary design was carried out to satisfy the “KS B 6301 Standard” that requires the performance certification on fresh water under 35 °C, as the national certification system for the centrifugal pumps, including sewage types in the Republic of Korea. Therefore, the preliminary design and optimization of the pump were conducted to satisfy the design specifications when the working fluid is fresh water.

In this study, the initial impeller of the two-vane pump had two blades, as shown in Figure 1, and a diameter of 207 mm. The blades are shrouded impeller blades, and there is no tip clearance. The inlet and outlet blade angles are 6.50° and 8.00°, respectively, and have identical values from the hub to the shroud. To prevent the special case that the textile or cloth material caught on the blade, the ellipse ratio of the leading and trailing edge of the blade is designed to 1.0. Figure 1b shows the volute geometry and design constraints. Since the pump used in this study was installed through a manhole of the city water and sewage system, there are some constraints on the overall size of the pump and outlet diameter, as shown in Figure 1b.

The preliminary model has a specific speed (N_s) of 221.3 in SI (International system of units) units (rpm, m³/min, m) under the design conditions. The specific speed formula used in this study is as follows:

$$N_s = \frac{N \times \sqrt{Q}}{[H_t]^{3/4}} \quad (1)$$

where N , Q , and H_t denote the rotational speed, flow rate, and total head of the pump, respectively. Figure 2 is a diagram for helping designer to roughly judge the theoretical efficiency according to the specific speed of the pump in SI unit. Now, the type of the pump can be determined by the specific speed, as shown in Figure 2, and the efficiency can be estimated by using the following approximation formula [18]:

$$\eta = \left[0.94 - 0.294264 \times \left[\frac{Q}{N} \times X \right]^{-0.21333} - 12.893 \times \left[\log_{10} \left(\frac{2286}{N_s} \right) \right]^2 \right] \times 100 \quad (\%) \quad (2)$$

$$X = \left[\frac{3.56}{\varepsilon} \right]^2 \quad (3)$$

where ε is the absolute roughness height of the pump surfaces. It depends on the production processes and materials. In this study, the milling and die-casting methods that are commonly used in pump processing were assumed, and, accordingly, ε was calculated as 7.84 μm [18]. That is, according to Equations (2) and (3), the efficiency under design condition of the preliminary model is predicted to be about 71%.

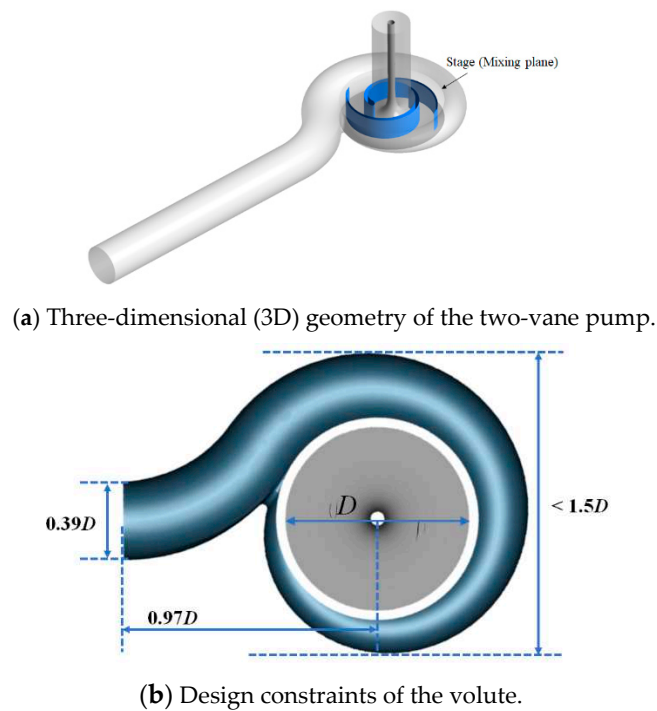


Figure 1. Geometry of the two-vane pump.

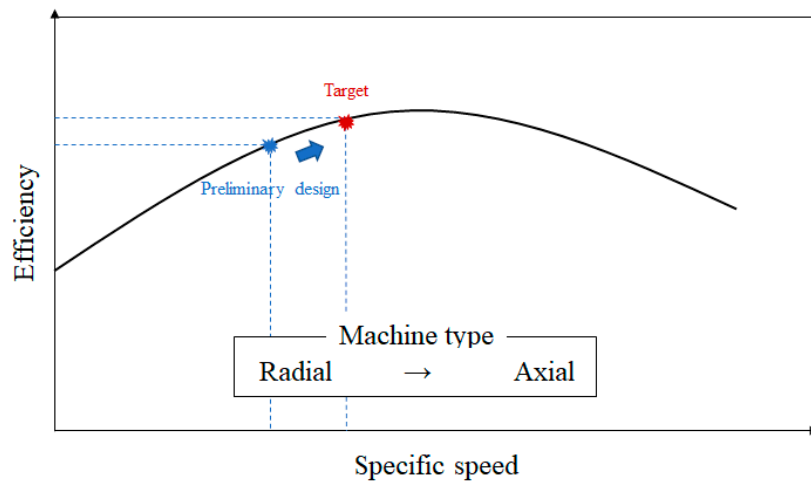


Figure 2. Efficiency according to the specific speed for the pump.

However, based on the numerical analysis of the preliminary model, the total head was predicted as about 18 m at the design flow rate, and the specific speed was calculated as 142; these values do not satisfy the design specifications. In addition, for a specific speed of 142, the efficiency will be about 65%, as shown in Figure 2. To solve this problem, by applying the similarity law, the impeller diameter was reduced by about 13%, compared to the preliminary model, and optimization was performed to improve the hydraulic performances.

2.2. Numerical Analysis

The 3D RANS equations were solved by using a $k-\omega$ -based shear stress transport (SST) turbulence model [19] for the hydraulic analysis of the two-vane pump. The SST turbulence model is known to be suitable for predicting flow separation due to an adverse pressure gradient near the wall, and the $k-\omega$ turbulence model [20] and the $k-\epsilon$ turbulence model [21] are applied near the wall and to the bulk

flow region, respectively. These two turbulence models are connected by the blending function that is influenced by the y^+ value—the dimensionless number representing the distance between the wall and the first node of the grid system [19].

Commercial code ANSYS CFX 19.1 [22] was used for the RANS analysis. The computational domain is shown in Figure 1a. The 3D geometry of the impeller was created by using ANSYS Blade-Gen [22], and the volute was created by using Solidworks 2016 [23]. ANSYS TurboGrid and ICEM [22] were used to generate the computational grids for the rotating and stationary domains, respectively. The stage (or mixing plane) method was applied at the interface between the rotating and stationary domains to calculate a steady-state solution for the problems of multiple reference frames [22].

The working fluid was water at 25 °C. The total pressure was set to 1 atm as the atmosphere condition at the inlet boundary. The numerical analysis was performed by assigning the mass flow rate to the outlet boundary. The blade and volute surfaces in the computational domain were considered to be hydraulically smooth under an adiabatic and no-slip condition.

The grid system used in the present study consists of hexahedral grids in the rotating domain and tetrahedral grids in the stationary domain, as shown in Figure 3. In the rotating domain, O-type grids were constructed around the blades. To determine the convergence of the numerical calculations, the root-mean-square values of the residuals of the governing equations were set to be less than 10^{-5} . The physical time scale was set to $1/\omega$, where ω is the angular velocity of the impeller. The computation for the steady RANS analysis was performed, using an Intel Xeon CPU with a clock speed of 2.70 GHz, and converged solutions were obtained after 1000 iterations with a computational time of approximately 8 h.

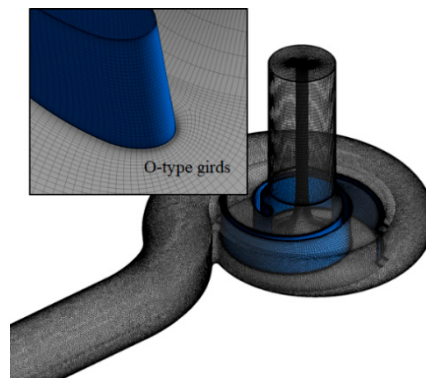


Figure 3. Grid systems of the two-vane pump.

3. Optimization Techniques

The three-objective optimization problem was defined as follows:

$$\text{Maximize: } \mathbf{F}(\mathbf{x}) = [F_1(\mathbf{x}), F_2(\mathbf{x}), F_3(\mathbf{x})]$$

$$\text{Design variable bound: } \mathbf{LB} \leq \mathbf{x} \leq \mathbf{UB}, \mathbf{x} \in \mathbf{R},$$

where $\mathbf{F}(\mathbf{x})$ is the vector of real-valued objective functions; \mathbf{x} is the vector of the design variables; \mathbf{LB} and \mathbf{UB} denote the vectors of the lower and upper bounds, respectively; and \mathbf{R} is a real number [24].

Figure 4 shows the procedure of a typical optimization design. Once the operating conditions of the design target are determined, the type of turbomachinery and airfoil (or hydrofoil) are selected. Then a preliminary design is performed through one-dimensional mean-line analysis, and the initial blade topology is derived. Subsequently, the optimization design is performed for improving the performance of the turbomachinery.

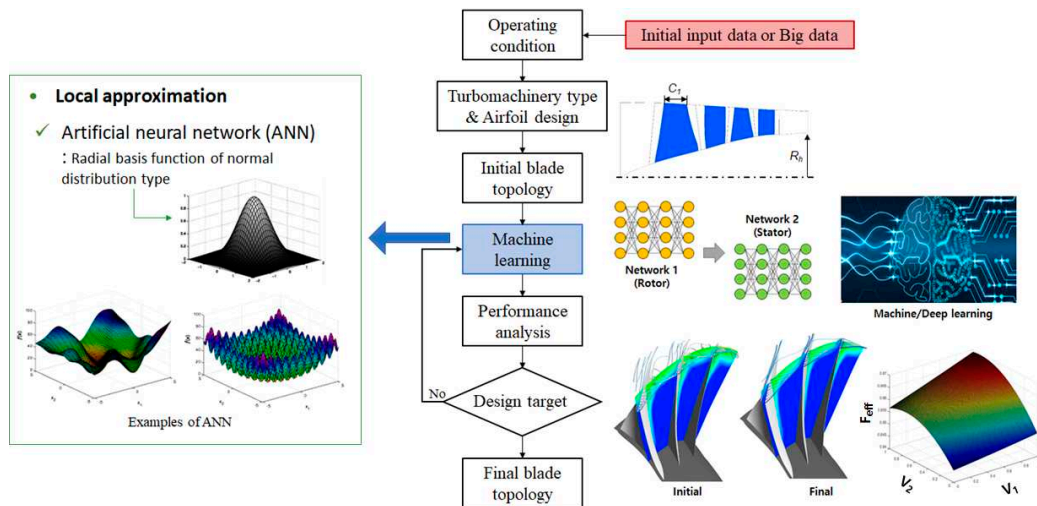


Figure 4. Procedure of the optimization design based on machine learning.

In this study, the optimization design was based on machine learning. First, the objective functions and constraints were defined according to the design goal. Subsequently, the design variables and their ranges were chosen. Thereafter, a database of the correlation between the design variables and the objective functions was established within the design space, using the design of experiment (DOE). In the next step, a predictive model was constructed by using ANN [14] to correlate the design variables and objective functions of the two-vane pump. In this step, the predictive model was trained by using machine learning. This process is described in detail in Section 3.2. The GA [15] was used to find the optimal design solution, considering the correlation of each objective function in the constructed prediction model. The GA is a well-known stochastic searching algorithm based on the mechanism of natural selection, genetics, and evolution. It evaluates various points in the design space and can be applied to find a global solution to any given problem. This algorithm proceeds as shown in Figure 5. Finally, the Pareto-optimal front surface was derived by using MATLAB R2018b [25], and the optimization procedure was terminated.

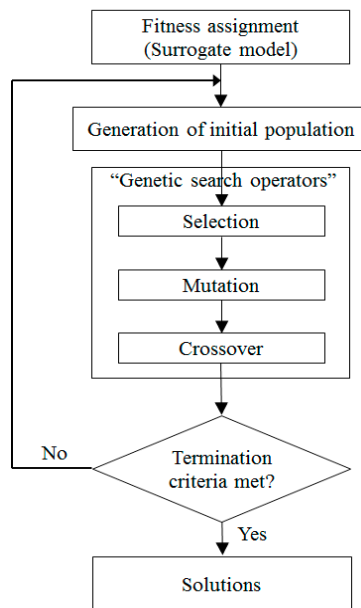


Figure 5. Genetic algorithm.

3.1. Design Variables and Objective Functions

In order to maximize the hydraulic performances and size of waste solids, the efficiency (η) and total head (H_t) of the pump and the volume of waste solids (V_s) were selected as the objective functions:

$$H_t = \frac{P_{outlet} - P_{inlet}}{\rho g} \tag{4}$$

$$\eta = \frac{(P_{outlet} - P_{inlet})Q}{\tau\omega} \times 100\% \tag{5}$$

$$V_s = \frac{1}{6}\pi D_s^3 \tag{6}$$

where P , ρ , g , Q , τ , and ω are the total pressure, density of the working fluid, acceleration due to gravity, flow rate, torque, and angular velocity, respectively. Further, D_s in Equation (6) is defined as the distance between the leading edge of the blade and the other blade at the impeller inlet, as shown in Figure 6.

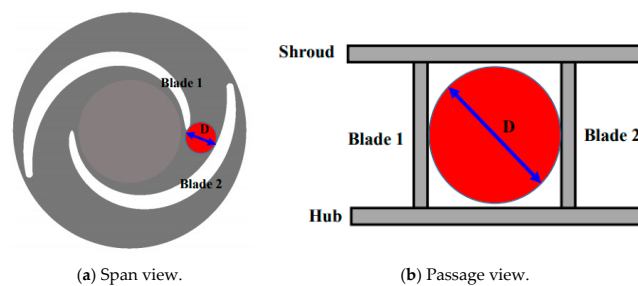


Figure 6. Definition of the waste solid volume.

Figure 7 shows the design variables considered in this work. Their ranges are listed in Table 1. The inlet and outlet blade angles and the cross-sectional area of the volute were chosen for the optimization. They are defined as shown in Figure 7. As mentioned earlier, the blade angle distribution is the same in the span direction from the hub to the shroud and is defined by using the fourth-order Bézier curve [26] in the streamwise direction, as shown in Figure 7a. In order to adjust the inlet (β_1) and outlet (β_2) blade angles, two control points (CP₁ and CP₂) were fixed. The distribution of the cross-sectional area of the volute was changed linearly in the circumferential direction, as shown in Figure 7b.

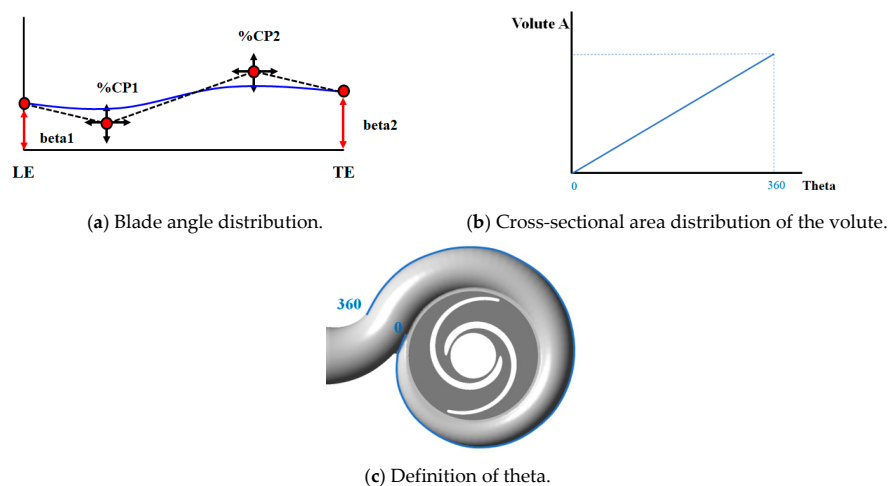


Figure 7. Definition of the design variables.

Table 1. Ranges of design variables.

	LB	Ref.	UB
$\beta_1/\beta_{1,ref}$	0.483	1.00	1.517
$\beta_2/\beta_{2,ref}$	0.119	1.00	1.381
<i>Volute A/A_{ref}</i>	0.813	1.00	1.187

LB = lower bound; UB, upper bound.

3.2. Surrogate Modeling Based on Machine Learning

In the present optimization design, supervised machine learning was adopted, considering the reasonable computation costs. This optimization technique is a very efficient approach for optimizing a system without analytical representation, fitting a surrogate model.

In order to construct the input data, the central composite design was used as the DOE. In all, 15 experimental points were arranged for three design variables, and the objective function values were derived through RANS analysis at each design point. These values are listed in Table 2. In this table, the values of the design variables and objective functions are normalized by dividing them by the corresponding reference value.

Table 2. Initial input data for the supervised machine learning.

	$\beta_1/\beta_{1,ref}$	$\beta_2/\beta_{2,ref}$	<i>Volute A/A_{ref}</i>	$H_t/H_{t,ref}$	η/η_{ref}	$V_s/V_{s,ref}$
1	0.692	0.375	0.889	0.669	1.075	0.111
2	1.308	0.375	0.889	0.666	1.059	1.125
3	0.692	1.125	0.889	0.684	1.037	0.111
4	1.308	1.125	0.889	0.683	1.030	1.260
5	0.692	0.375	1.111	0.643	1.008	0.111
6	1.308	0.375	1.111	0.650	1.009	1.125
7	0.692	1.125	1.111	0.663	0.959	0.111
8	1.308	1.125	1.111	0.659	0.979	1.260
9	0.483	0.750	1.000	0.669	0.914	1.004
10	1.517	0.750	1.000	0.649	0.941	1.728
11	1.000	0.119	1.000	0.645	1.089	0.512
12	1.000	1.381	1.000	0.693	0.997	0.593
13	1.000	0.750	0.813	0.690	1.103	0.512
14	1.000	0.750	1.187	0.646	1.017	0.512
15	1.000	0.750	1.000	0.666	1.008	0.512

A radial basis neural network (RBNN) model [27], which is a type of ANN, was used in this optimization study. The RBNN model has a hidden layer of radial neurons and an output layer of linear neurons, as shown in Figure 8. The hidden layer uses a series of radial primitives to nonlinearly modify the input space to the intermediate space. The output of the hidden layers then executes a linear combiner to produce the desired targets [27]:

$$f(x) = \sum_{j=1}^N w_j \phi_j \quad (7)$$

where w_j is the weight, and ϕ_j is radial basis function, which uses the Gaussian function. Several parameters are needed to construct a surrogate model: the input weight and the center and width of a unit for the Gaussian function. In the present RBNN model, the input weights were chosen by machine learning. The input vector with the worst performance was chosen as the center of a new hidden-layer Gaussian function [25]. Then the RBNN only needed to determine the width of the Gaussian function (spread constant). The network training was performed by adjusting the cross-validation error (CV) by changing the spread constant (SC), as shown in Figure 9. SC_1 , SC_2 ,

and SC_3 correspond to the total head, efficiency, and size of waste solids, respectively. The SC values for each objective function were chosen by a K-fold CV test [28].

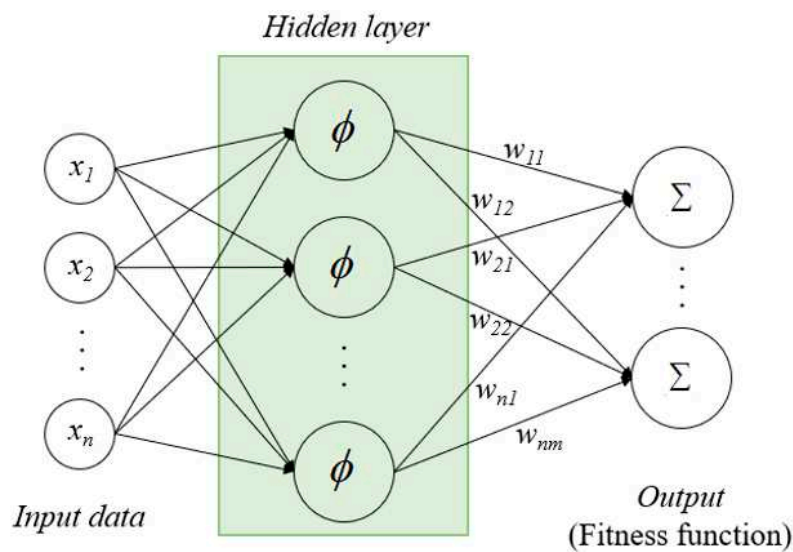


Figure 8. Schematic of the radial basis neural network.

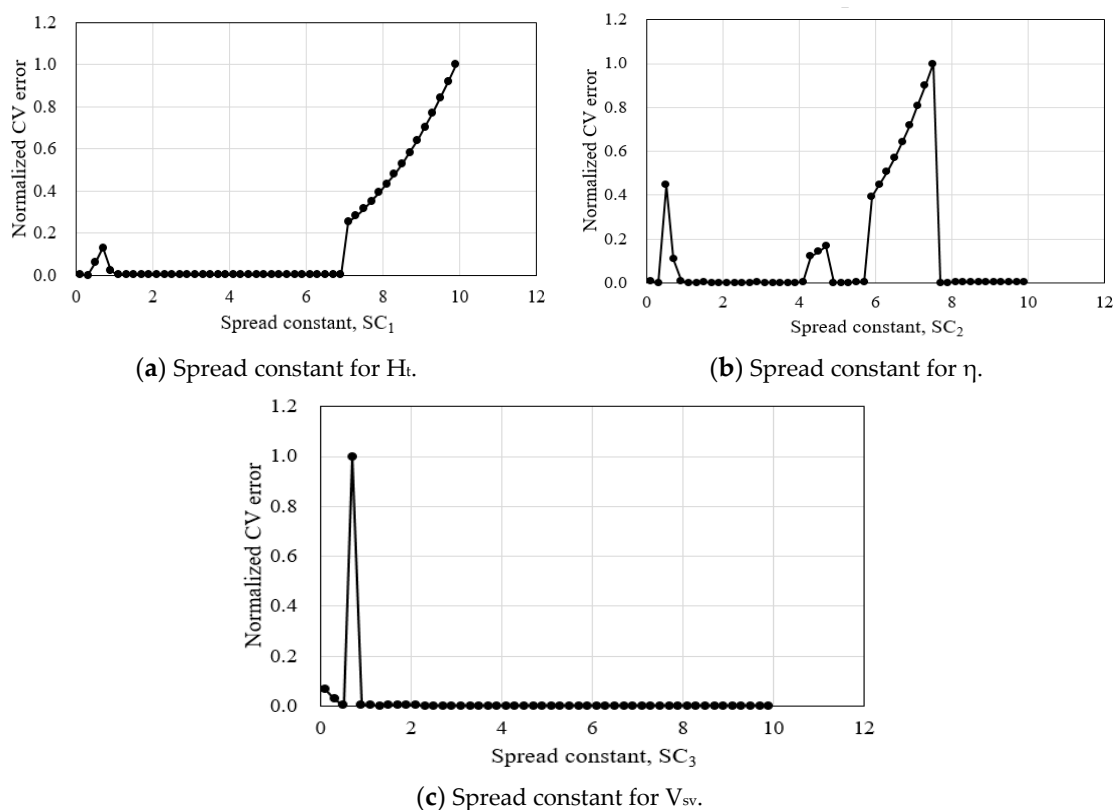


Figure 9. Cross-validation errors vs. spread constant (SC) values.

The data sample $((x_j, y_j); j = 1, \dots, N)$ was partitioned into K disjoint subsets (K -fold CV), as shown in Figure 10. Of these, $(K-1)$ folds were used to train the RBNN network, and the last fold (the K th set) was used for evaluation. This process was repeated K times, using a different fold for evaluation each time. The network training was performed by adjusting the CV error by changing SC . The CV error at a particular SC value was calculated as follows:

$$CV(SC) = \frac{1}{K} \sum_{i=1}^k \epsilon_k, \epsilon_k = \sum_{j=kth\ set} (y_j - \hat{y}_j)^2, \tag{8}$$

where ϵ_k is the prediction error for the Kth set. The predicted values \hat{y}_j were determined by using the constructed RBNN model from the sample points in the (K-1) subsets. In the present study, K was set as 15. According to the results of the K-fold CV test, the final SC values SC_1 , SC_2 , and SC_3 were set as 0.3, 1.9, and 9.9, respectively.

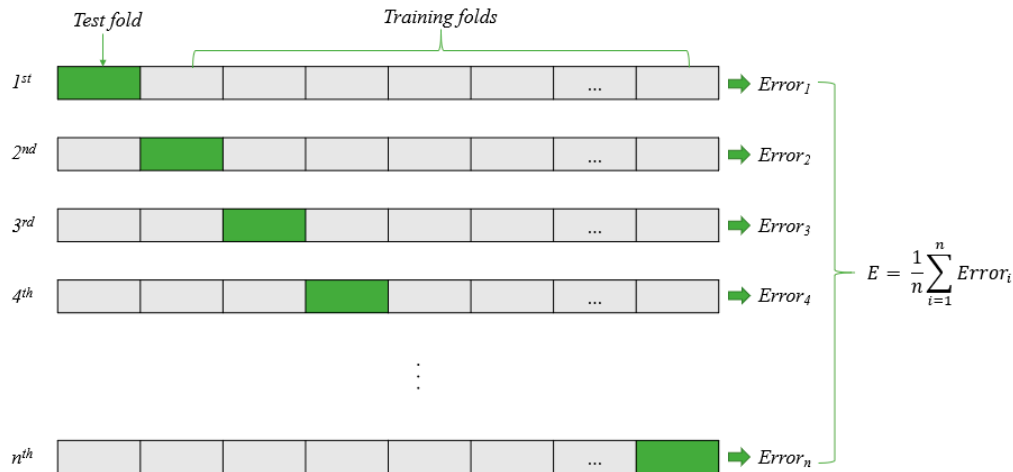


Figure 10. K-fold cross-validation.

4. Results

4.1. Grid Dependency Test and Validation of Numerical Results

To eliminate the grid dependency of the numerical solutions, grid dependency tests were performed in the computational domain, as shown in Figure 11. In these tests, the efficiency and total head under the design condition were compared, and their values were normalized by dividing by the corresponding convergence values. As shown in Figure 11, the grid system with 3.4×10^6 nodes undergoes only 0.002% and 0.083% changes in the efficiency and total head, respectively, compared with the grid system with 3.0×10^6 nodes. Hence, the latter grid system was selected as the optimal grid system for the computational domain.

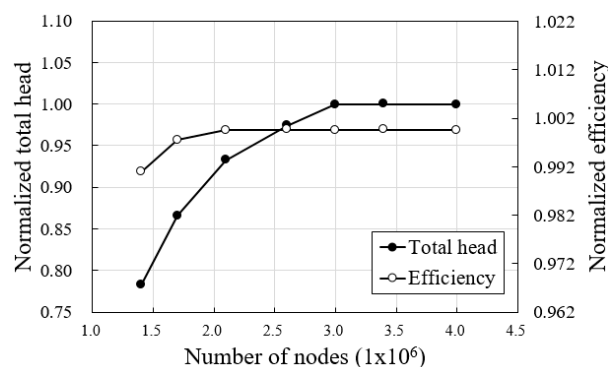


Figure 11. Grid dependency test.

In earlier research, the authors analyzed the internal flow characteristics of hydraulic machines, such as pumps and water turbines, through numerical analysis and compared and verified the numerical results through experiments [29–32]. In a previous study, a single-channel pump with design specifications similar to those of the two-vane pump considered in this study was developed,

and Figure 12 shows the results of the experiments conducted in the previous study [29]. The hydraulic performances, i.e., the head coefficient and efficiency, were compared with the corresponding experimental data in the operating ranges. The total head values derived from the numerical analysis were almost identical to the experimental data. Meanwhile, the efficiency values were relatively higher than those of the experimental data because the numerical analysis did not include the mechanical losses. However, the general trend of the efficiency curve matched well. In this study, the numerical scheme used in the previous studies of the authors [29–32] was adopted, and the numerical analysis technique was verified through several peer reviews. The results derived of this study will be verified through experiments in future work.

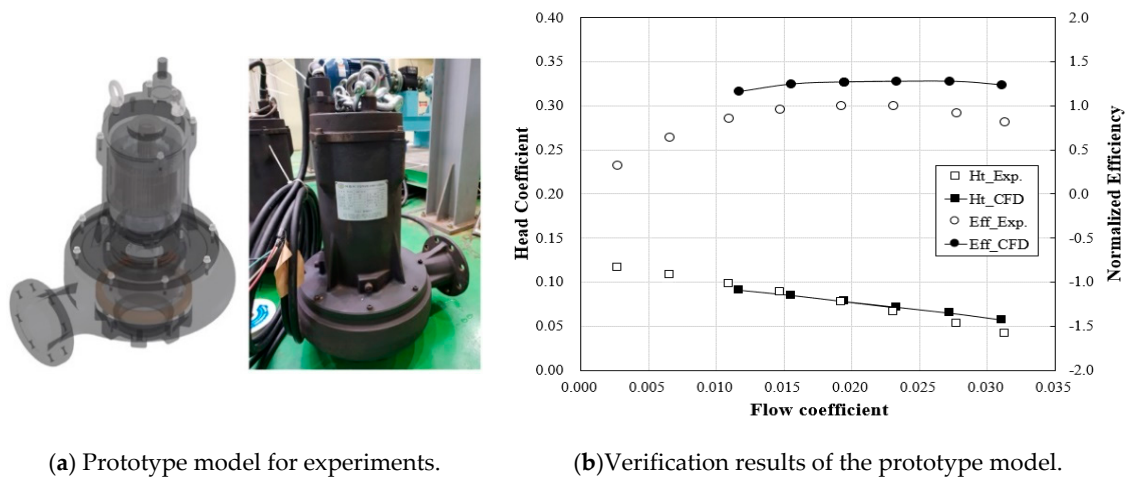


Figure 12. Validation data of previous study [29].

4.2. Optimization Results

Figure 13 shows the Pareto-optimal front surface for the three-objective optimization. This surface was obtained by using the GA based on the RBNN predictive model. To investigate the accuracy of the optimization results, five arbitrary optimal designs (AODs) were selected. They are listed in Table 3 and shown in Figure 13.

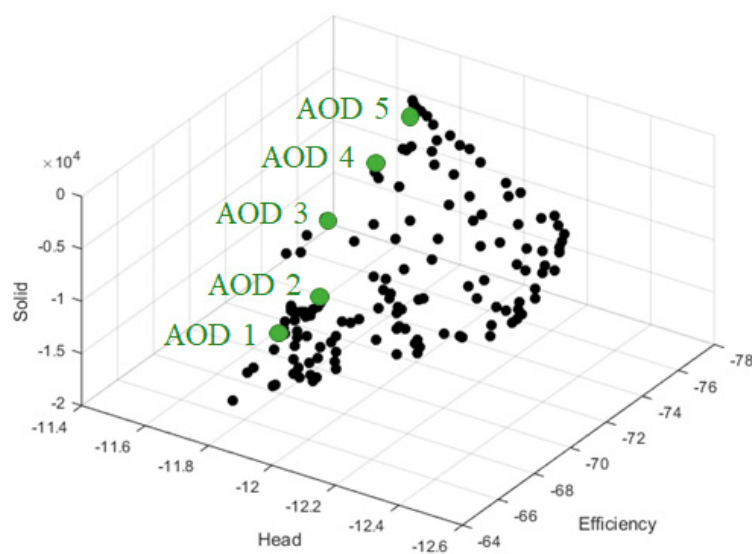


Figure 13. Pareto-optimal front surface with arbitrary optimal designs (AODs).

Table 3. Optimization results.

	Design Variables		Predicted Values				RANS		
	$\beta_1/\beta_{1,ref}$	$\beta_2/\beta_{2,ref}$	$Volute A/A_{ref}$	$H_i/H_{i,ref}$	η/η_{ref}	$V_s/V_{s,ref}$	$H_i/H_{i,ref}$	η/η_{ref}	$V_s/V_{s,ref}$
AOD 1	1.514	1.357	0.818	0.647	1.082	2.171	0.676	1.048	2.097
AOD 2	1.432	0.122	0.814	0.643	1.126	1.603	0.654	1.135	1.260
AOD 3	1.289	0.128	0.815	0.648	1.148	1.185	0.654	1.151	1.000
AOD 4	1.046	0.137	0.820	0.651	1.163	0.636	0.650	1.164	0.593
AOD 5	0.943	0.165	0.820	0.654	1.159	0.457	0.652	1.147	0.439

RANS = Reynolds-averaged Navier-Stokes.

The objective functions of the predicted AODs were calculated by RANS analysis and compared with the predicted objective function values listed in Table 3. The RANS results indicate that the maximum relative errors were less than 1.90% for the total head, 1.80% for the efficiency, and 4.00% for the size of waste solids. Thus, the surrogate model is regarded as being constructed based on reliable data, and the results of optimization indicate the excellent accuracy of surrogate prediction.

All the AODs are predicted to have a normalized total head of more than 0.611, which satisfies the design target, and the efficiency and the size of waste solids are inversely related. In addition, all the AODs have less cross-sectional area of the volute, compared to the reference design, and the efficiencies of the AODs are improved. The design focused on the size of waste solids (AOD 1) doubles the solid size compared with that in the reference design, whereas the design focused on efficiency (AOD 5) shows an increment of 14.14% in the efficiency.

5. Discussion

The size of waste solids is directly related to the blade inlet angle. As the blade inlet angle increases, the size of waste solids increases. The flow passage areas of the AODs in the meridional direction are compared in Figure 14. Their values are normalized by using the maximum area of AOD 1 in the meridional direction. It was confirmed that the inlet passage area of AOD 1 with the greatest increase in the blade inlet angle was the largest, and the inlet passage area of AOD 5 with the reduced inlet blade angle was the smallest among AODs.

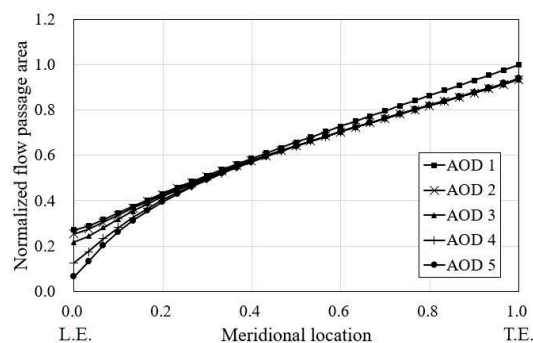
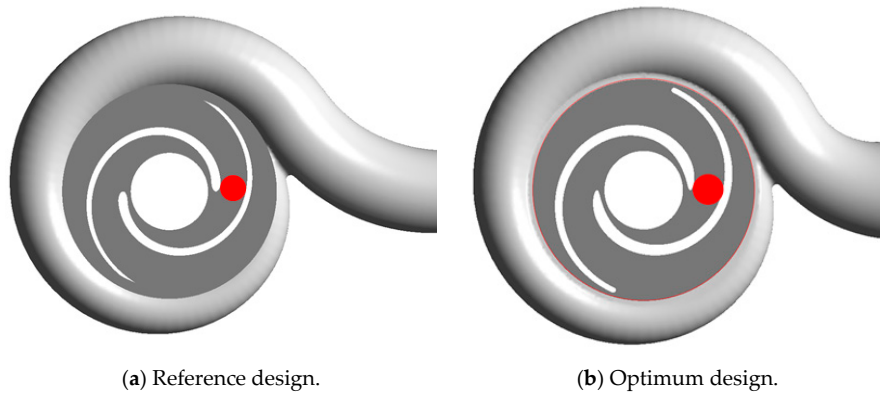


Figure 14. Flow passage area distribution in the meridional direction.

AOD 3, which satisfies the design target, was selected for further analysis of the optimum design. The 3D geometry for AOD 3 is shown in Figure 15. Through optimization, an inlet blade angle of about 1.289 times the reference design and an outlet blade angle of about 0.128 times the reference design were realized. That is, considering the change in the flow path inside the impeller, the blade wrap angle was reduced compared to the reference design. Reduction in the blade wrap angle led to a shorter flow path, thus reducing the friction loss. In the case of the volute, the cross-sectional area of the optimum design was less than that in the reference design. Furthermore, the cross-sectional area continuously decreased from the tongue to the outlet, and then it decreased by approximately 18.9% at the outlet, as shown in Figure 16.



(a) Reference design.

(b) Optimum design.

Figure 15. Comparison of three-dimensional (3D) geometries.

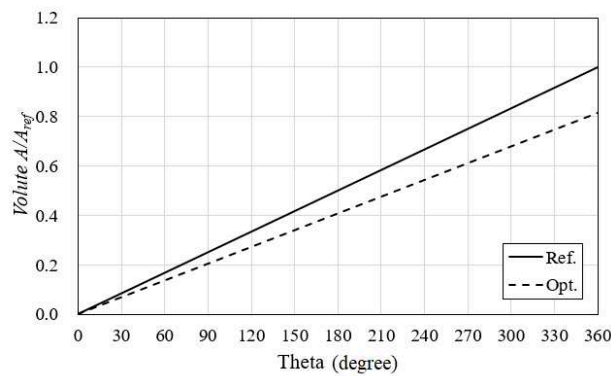
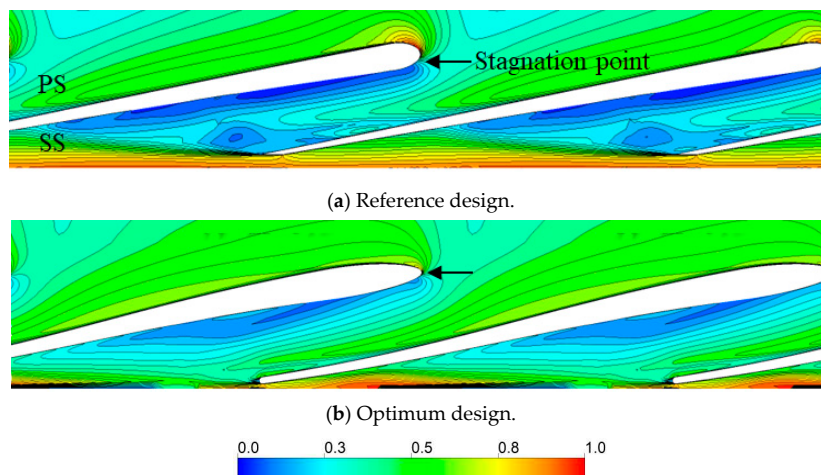


Figure 16. Cross-sectional area distribution of the volute.

Figure 17 shows the velocity distribution at 50% span of the blade. In the optimum design, the stagnation point is formed at the leading edge of the blade, whereas in the reference design, it is located relatively downstream. This phenomenon occurs because the inlet angle of the blade is not designed to fit the operating condition, and it can increase the incidence angle to cause flow separation and reduce the hydraulic performance of the pump. In addition, the stagnation point is formed on the suction side (SS) of the blade, and the flow proceeds non-uniformly. In particular, a very high-velocity region is distributed at the leading edge (LE) of the pressure side (PS), and severe flow separation occurs at the SS, resulting in a blockage inside the passage.



(a) Reference design.

(b) Optimum design.

Figure 17. Velocity distributions at 50% span.

The distribution of the streamlines and the inlet velocity component at 50% span are analyzed and shown in Figure 18. As described in Figure 17, the inlet flow collides at the SS of the blade in the case of the reference design; conversely, in the optimum design, the inlet flow collides precisely with the LE of the blade. Through the optimization, the blade inlet angle (β_b) of the optimum design is greater than that in the reference design, and, therefore, the inlet flow proceeds smoothly, as shown in Figure 17b.

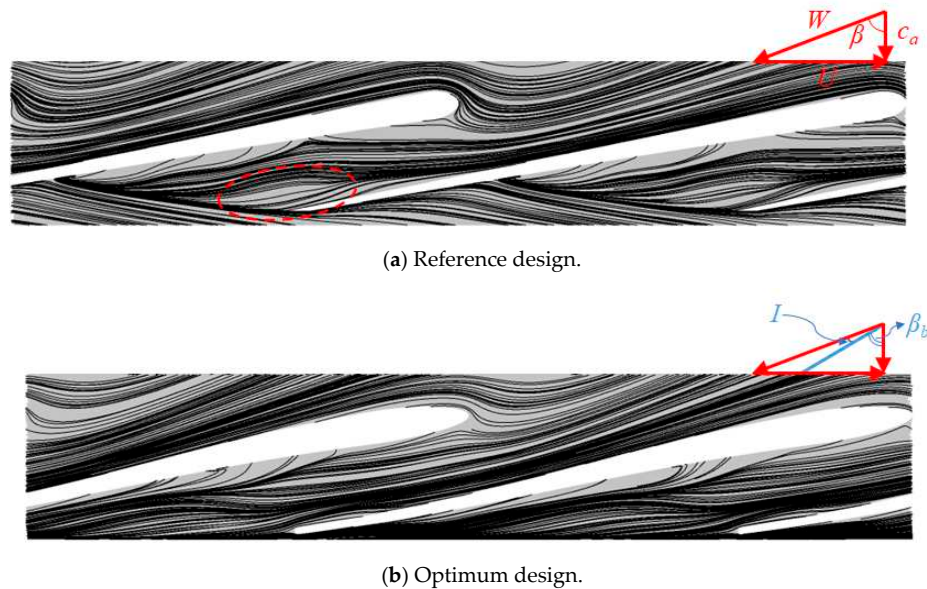


Figure 18. Streamlines at 50% span.

The rotational velocity (U) of the blade, the axial velocity (C_a), and the relative velocity (W) of the flow at the inlet of the impeller can be represented in the velocity triangle diagram. When the three velocity components are known, the flow angle (β) can be derived, and the incidence angle (I) can be calculated by comparison with the blade angle (β_b). The incidence angle distribution from the hub to the tip is shown in Figure 19. The incidence angle of the reference design gradually decreases from the hub to about 80% span and then increases again to the tip span. The tendency of the optimum model is similar to that of the reference design, but the incidence angle is small overall in all spans, compared with the reference design. The largest incidence angle in the reference design is 24° at the tip region, whereas that in the optimum design is 18° at 15% span.

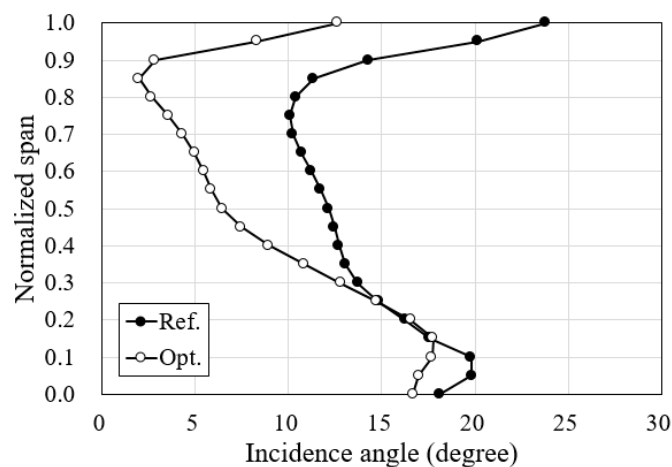


Figure 19. Incidence angle distribution at the leading edge (LE) along the span.

In rotating-fluid machines, the flow is driven by the centrifugal force. Hence, the incidence angle at the tip region is smaller than that at the hub; this improves the hydraulic performance. In particular, since the pump used in this study is a special pump for transporting wastewater, the blade angle distribution from the hub to the tip should be maintained. From this point of view, it is judged that the incidence angle distribution of the optimum design shown in Figure 19 is ideal.

Figure 20 shows the distribution of streamlines and vortices on the iso-surface of the velocity invariant ($>5 \times 10^5 \text{ s}^{-2}$), to visualize the flow characteristics inside the impeller. As shown in Figures 17 and 18, in the case of the reference design, the inlet flow angle is significantly different from the blade inlet angle, and an apparent inter-blade vortex is observed inside the passage, as shown in Figure 20a. On the other hand, the inlet flow angle of the optimum design agrees well with the blade inlet angle, and the flow proceeds smoothly into the passage, as shown in Figure 20b.

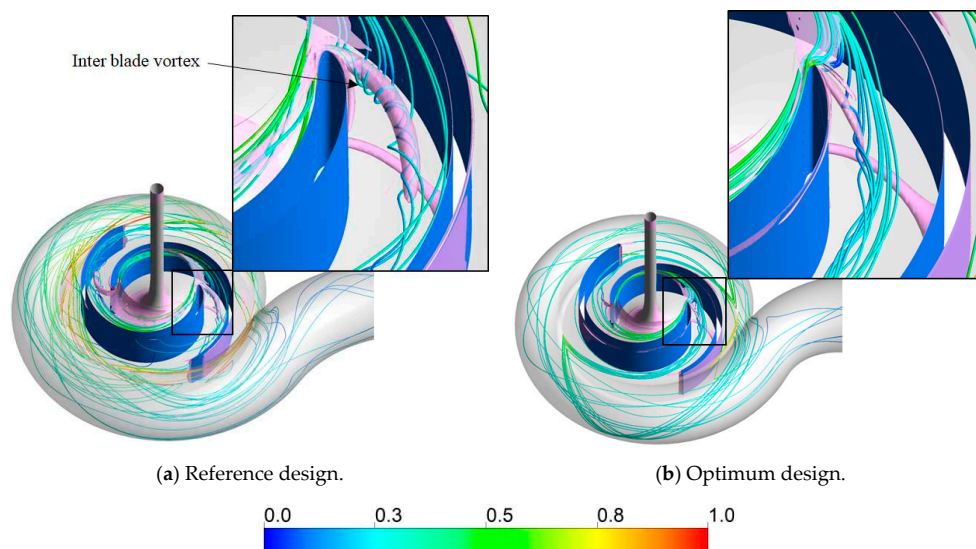


Figure 20. Three-dimensional (3D) streamlines with vortices distribution on the iso-surface of the velocity invariant ($>5 \times 10^5 \text{ s}^{-2}$).

In order to analyze the blade loading, the pressure distribution on the blade in the optimum and reference design are compared, as shown in Figure 21. The pressure values are normalized by using the maximum pressure value of the reference design. Similar to Figures 17 and 18, Figure 21 shows that the static pressure of the reference design at LE is relatively less than that in the optimal design, owing to the rapid increase in the velocity in the PS of the blade LE. In addition, the pressure on the PS and SS of the reference design shows a larger overall region than in the optimum design; in other words, the blade loading of the reference design is larger.

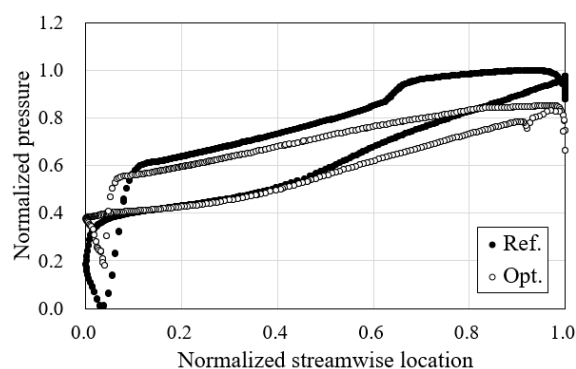


Figure 21. Pressure distributions at 50% span.

Figure 22 shows the internal velocity distribution from the volute tongue to the outlet. In the reference design, a relatively high-velocity region is distributed near the tongue, but the velocity decreases toward the outlet. On the other hand, the optimum design shows a relatively uniform velocity distribution over the entire area of the volute. In the reference design, the cross-sectional area of the volute is designed to be larger than necessary, and as the flow diffuses near the outlet, it is judged that the static pressure recovery occurs more than in the optimum design.

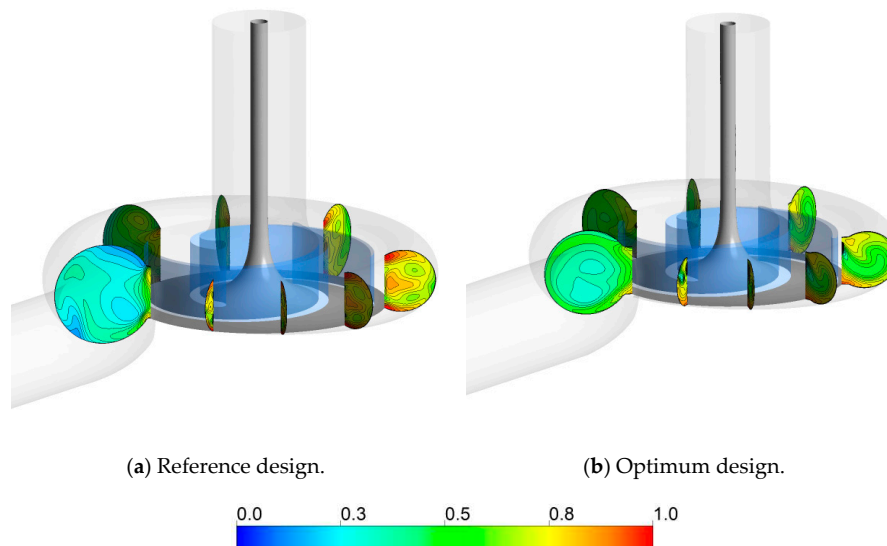


Figure 22. Velocity distributions inside the volute.

Figure 23 shows the iso-surface contours for a low velocity of 1.0 m/s, to identify the low-velocity region inside the pump. As shown in Figure 22, a relatively wide low-velocity area is formed at the outlet of the reference design. Since the two-vane pump considered in this work is used for transporting wastewater, the solids move inside the impeller and volute. Now, the presence of low-velocity region can cause solids to stagnate. Therefore, the pump should be designed so that no such low-velocity region is created. From this point of view, the optimum design is an ideal design with a significant reduction in the area of the low-velocity region.

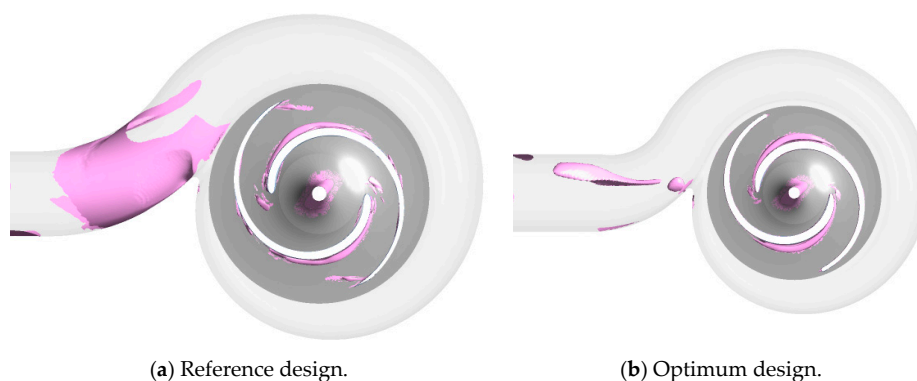


Figure 23. Iso-surface for the low-velocity region (<1 m/s).

6. Conclusions

In the present study, the shapes of a blade and volute were optimized to improve the hydraulic performance of a two-vane pump for transporting wastewater via 3D RANS analysis based on supervised machine-learning optimization. Considering the waste solids, the blade inlet and outlet

angles and the cross-sectional area of the volute were selected as the design variables. Three objective functions were considered to maximize the hydraulic performances, i.e., the total head and efficiency of the pump, while maximizing the size of the waste solids.

In this analysis, the RBNN predictive model was trained by using machine learning, and the GA was used to find global optimal solutions. The network training was performed by adjusting the CV error by changing the SC. Through training, an accurate and reliable RBNN surrogate model was constructed, and five arbitrary optimum design points were derived. They were compared with the numerical results to verify the predicted accuracy. The machine-learned surrogate model showed very accurate predictions compared with the numerical results and had relative errors less than 5%.

Through the optimization, the pump was made compact, and the efficiency was improved by about 14% compared to the reference design, while satisfying the design goal of the total head (>10 m). As the cross-sectional area of the optimum volute was reduced, excessive diffusion at the outlet was reduced, and, therefore, the velocity distribution inside the volute was more uniform compared with the reference design. In addition, as the inlet angle of the optimum blade increased, the water flowing from the impeller inlet proceeded smoothly into the flow path, and the flow separation and formation of the inter-blade vortex were significantly reduced.

In future work, the hydraulic performances of the optimum design will be investigated in more detail experimentally, and the characteristics of the flow, containing solid wastes, will be also analyzed.

Author Contributions: J.-H.K. and S.K. designed the two-vane pump; S.-B.M. and S.K. analyzed the numerical data; S.-B.M. contributed the optimization techniques and analyzed optimization results and organized draft paper. All authors have read and agreed to the published version of the manuscript.

Funding: This work was supported by the Demand-Based-Manufacturing Technique Commercialization R&D Project of the Korea Institute of Industrial Technology (KITECH) (No. JB200007), which was funded by the Ministry of Science and ICT (MSIT). The authors gratefully acknowledge this support.

Conflicts of Interest: The authors declare no potential conflicts of interest with respect to the research, authorship, and/or publication of this article.

References

1. Wang, X.; Lu, Y.; Zhu, R.; Fu, Q.; Zong, W. Study of hydraulic performance and pressure pulsation characteristics of the grid pump in case of clogging. *Bulg. Chem. Commun.* **2016**, *48*, 87–95.
2. Schivley, G.P.; Dussourd, J.L. An Analytical and Experimental Study of a Vortex Pump. *J. Basic Eng.* **1970**, *92*, 889–900. [[CrossRef](#)]
3. Ohba, H.; Nakashima, Y.; Shiramoto, K.; Shiramoto, K.; Kozima, T. A Study on Performance and Internal Flow Pattern of A Vortex Pump. *Bull. JSME* **1978**, *21*, 1741–1749. [[CrossRef](#)]
4. Steinmann, A.; Wurm, H.; Otto, A. Numerical and experimental investigations of the unsteady cavitating flow in a vortex pump. *J. Hydrodyn.* **2010**, *22*, 319–324. [[CrossRef](#)]
5. Hansen, B.F.; Henning, P.J. Waste Water Pump. U.S. Patent 9,500,204, 22 November 2016.
6. Shi, F.; Tsukamoto, H. Numerical Study of Pressure Fluctuations Caused by Impeller-Diffuser Interaction in a Diffuser Pump Stage. *J. Fluids Eng.* **2001**, *123*, 466–474. [[CrossRef](#)]
7. Feng, J.; Benra, F.-K.; Dohmen, H.-J. Investigation of Periodically Unsteady Flow in a Radial Pump by CFD Simulations and LDV Measurements. *J. Turbomach.* **2010**, *133*, 011004. [[CrossRef](#)]
8. Ma, S.-B.; Kim, K.-Y. Optimization of discrete cavities in a centrifugal compressor to enhance operating stability. *Aerosp. Sci. Technol.* **2017**, *68*, 308–319. [[CrossRef](#)]
9. Ma, S.-B.; Afzal, A.; Kim, K.-Y. Optimization of ring cavity in a centrifugal compressor based on comparative analysis of optimization algorithms. *Appl. Therm. Eng.* **2018**, *138*, 633–647. [[CrossRef](#)]
10. Lee, K.-S.; Kim, K.-Y.; Samad, A. Design optimization of low-speed axial flow fan blade with three-dimensional RANS analysis. *J. Mech. Sci. Technol.* **2008**, *22*, 1864–1869. [[CrossRef](#)]
11. Lee, S.-Y.; Kim, K.-Y. Design optimization of axial flow compressor blades with three-dimensional Navier-Stokes solver. *KSME Int. J.* **2000**, *14*, 1005–1012. [[CrossRef](#)]
12. Kim, S.H.; Boukouvala, F. Machine learning-based surrogate modeling for data-driven optimization: A comparison of subset selection for regression techniques. *Optim. Lett.* **2020**, *14*, 989–1010. [[CrossRef](#)]

13. Liu, B.; Aliakbarian, H.; Ma, Z.; VandenBosch, G.A.E.; Gielen, G.G.; Excell, P. An Efficient Method for Antenna Design Optimization Based on Evolutionary Computation and Machine Learning Techniques. *IEEE Trans. Antennas Propag.* **2014**, *62*, 7–18. [CrossRef]
14. Tripathy, R.; Bilonis, I. Deep UQ: Learning deep neural network surrogate models for high dimensional uncertainty quantification. *J. Comput. Phys.* **2018**, *375*, 565–588. [CrossRef]
15. Deb, K.; Agrawal, S.; Pratap, A.; Meyarivan, T. A fast elitist non-dominated sorting genetic algorithm for multi-objective optimization: NSGA-II. *Lecture Notes in Computer Science*. In Proceedings of the International Conference on Parallel Problem Solving from Nature, Paris, France, 18–20 September 2000; pp. 849–858.
16. Deb, K.; Gupta, H. Searching for robust Pareto-optimal solutions in multi-objective optimization. *Lecture Notes in Computer Science*. In Proceedings of the International Conference on Evolutionary Multi-Criterion Optimization, Guanajuato, Mexico, 9–11 March 2005; pp. 150–164.
17. CF Turbo. *Software Manual*; Cfturbo, Inc., 2018. Available online: <https://manual.cfturbo.com/en/index.html> (accessed on 10 May 2020).
18. Karassik, I.J.; Messina, J.P.; Cooper, P.; Heald, C.C. *Pump Handbook*, 4th ed.; McGrawHill: New York, NY, USA, 2008.
19. Menter, F.R. Two-equation eddy-viscosity turbulence models for engineering applications. *AIAA J.* **1994**, *32*, 1598–1605. [CrossRef]
20. Menter, F.R. *Improved Two-Equation k-Omega Turbulence Models for Aerodynamic Flows*; NASA Technical Memorandum; National Aeronautics and Space Administration: Washington, DC, USA, 1992; pp. 1–31. Available online: <https://ntrs.nasa.gov/search.jsp?R=19930013620> (accessed on 15 July 2020).
21. Yang, Z.; Shih, T.H. New Time Scale Based k-e Model for near-Wall Turbulence. *AIAA J.* **1993**, *31*, 1191–1198. [CrossRef]
22. ANSYS Inc. *ANSYS CFX-Solver Theory Guide*; ANSYS CFX-19.0; ANSYS Inc.: Canonsburg, PA, USA, 2018.
23. Solidworks 2016, *Tutorials*, Dassault Systems Solidworks Corporation. 2016. Available online: <https://www.solidworks.com/ko/support/resource-center> (accessed on 9 April 2020).
24. Afzal, A.; Kim, K.-Y. Optimization of pulsatile flow and geometry of a convergent-divergent micromixer. *Chem. Eng. J.* **2015**, *281*, 134–143. [CrossRef]
25. Math Work, Inc. *MATLAB 2014, The Language of Technical Computing*; Release 14; Math Work, Inc.: Natic, MA, USA, 2004.
26. Karpowitz, D. Bezier curve fitting method for existing turbine blade design. *J. Appl. Eng. Math.* **2005**, *3*, 1–4.
27. Goel, T.; Haftka, R.T.; Shyy, W.; Queipo, N.V. Ensemble of surrogates. *Struct. Multidiscip. Optim.* **2007**, *33*, 199–216. [CrossRef]
28. Stone, M. Cross-Validatory Choice and Assessment of Statistical Predictions. *J. R. Stat. Soc. Ser. B Methodol.* **1974**, *36*, 111–133. [CrossRef]
29. Kim, J.H.; Ma, S.B.; Kim, S.; Choi, Y.S.; Kim, K.Y. Design and verification of a single-channel pump for wastewater treatment based on a hybrid multi-objective optimization technique. *Processes* **2019**, *7*, 747. [CrossRef]
30. Kim, S.J.; Choi, Y.S.; Cho, Y.; Choi, J.W.; Hyun, J.J.; Joo, W.G.; Kim, J.H. Effect of fins on the internal flow characteristics in the draft tube of a Francis turbine Mode. *Energies* **2020**, *13*, 2806. [CrossRef]
31. Sonawat, A.; Choi, Y.-S.; Kim, K.M.; Kim, J.-H. Parametric study on the sensitivity and influence of axial and radial clearance on the performance of a positive displacement hydraulic turbine. *Energy* **2020**, *201*, 117587. [CrossRef]
32. Kim, S.; Kim, Y.-I.; Kim, J.-H.; Choi, Y.-S. Design optimization for mixed-flow pump impeller by improved suction performance and efficiency with variables of specific speeds. *J. Mech. Sci. Technol.* **2020**, *34*, 1–13. [CrossRef]



Article

Applications of an Improved Aerodynamic Optimization Method on a Low Reynolds Number Cascade

Shuyi Zhang, Bo Yang *, Hong Xie and Moru Song 

School of Mechanical Engineering, Shanghai Jiao Tong University, Shanghai 200240, China; shuyizhang@sjtu.edu.cn (S.Z.); xiehong1211@sjtu.edu.cn (H.X.); samuel0624@sjtu.edu.cn (M.S.)

* Correspondence: byang0626@sjtu.edu.cn

Received: 18 August 2020; Accepted: 9 September 2020; Published: 14 September 2020



Abstract: The effect of cascade aerodynamic optimization on turbomachinery design is very significant. However, for most traditional cascade optimization methods, aerodynamic parameters are considered as boundary conditions and rarely directly used as the optimization variables to realize optimization. Given this problem, this paper proposes an improved cascade aerodynamic optimization method in which an incidence angle and nine geometric parameters are used to parameterize the cascade and one modified optimization algorithm is adopted to find the cascade with the optimal aerodynamic performance. The improved parameterization approach is based on the Non-Uniform Rational B-Splines (NURBS) method, the camber line superposing thickness distribution molding (CLSTDM) method, and the plane cascade design method. To rapidly and effectively find the cascade with the largest average lift-drag ratio within a certain range of incidence angles, modified particle swarm optimization combined with the modified very fast simulated annealing algorithm (PSO-MVFSA) is adopted. To verify the feasibility of the method, a cascade with NACA4412 and a practical cascade are optimized. It is found that the average lift-drag ratios of two optimal performance cascades are respectively increased by 13.38% and 15.21% in comparison to those of two original cascades. Meanwhile, through optimizing the practical cascade of the Blade D500, under different volume flow rates, the pressure coefficient of the optimized cascade is increased by an average of more than 6.12% compared to that of the prototype, and the average efficiency is increased by 11.15%. Therefore, this improved aerodynamic optimization method is reliable and feasible for the performance improvement of cascades with a low Reynolds number.

Keywords: cascade; aerodynamic; parameterization; plane cascade design; incidence angle; PSO-MVFSA; optimization

1. Introduction

Blade design is of great importance to the efficiency and properties of turbomachinery. Achieving the aerodynamic design of a blade is a very complex and arduous task due to complicated flow phenomena and the interactions among various parameters [1]. A small geometric change of one blade can lead to a deterioration of the aerodynamic performance of the whole machine [2]. In general, the cascade design method is one of the most popular design methods employed for turbomachinery [3,4]. In this method, the blade is stacked by the sections on the different radiuses and shown in Figure 1a. Additionally, the section is projected onto the plane to form the cascade, as shown in Figure 1b. Therefore, the blade performance is affected by the cascade design. With the rapid development of the computer technique, more and more parameterization methods and optimization algorithms have been proposed and used in the design process of a cascade. This means that the time required to design a new cascade is becoming shorter and the aerodynamic performance of the new cascade is becoming better.

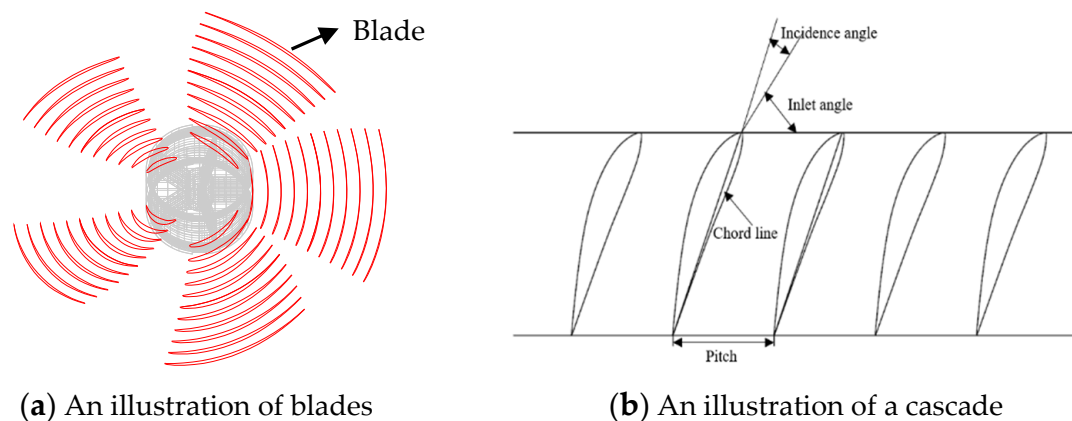


Figure 1. An explanation of blades and a cascade.

A good parameterization method can not only use fewer design variables to describe an airfoil accurately, but also rapidly re-construct one airfoil in the optimization process [5,6]. The parameterization methods are usually divided into two categories: The constructive method and the deformative method. Each method has been continuously improved by many researchers [7]. The deformative parameterization method is the simpler of the two methods. In this method, a standard airfoil is deformed to generate one new airfoil, in order to satisfy a certain condition. The Hicks-Henne function [8], radial basis function [9], Bezier function [10], B-Spline function [11], and Non-Uniform Rational B-Splines (NURBS) function [12–14] are usually used as deformative functions to generate a new airfoil based on the original airfoil. In particular, NURBS [12] is the most popular function due to its ability of local control and its conics description over the curve. However, these deformative functions are used to generate one new airfoil based on the point coordinates of an airfoil. To relate the airfoil shape to the airfoil geometric feature parameters, the camber line superposing thickness distribution molding (CLSTDM) method [15] was proposed. In this method, several airfoil geometric parameters are used to parameterize the half-thickness distribution curve and the mean camber curve through two polynomials. Then, these two curves are coupled to form a whole airfoil. The feasibility of this method has been proved by several works [15–17]. In the CLSTDM method [15,16], the blade contours described by many coordinate points can be transformed into functions controlled by several parameterized variables. Moreover, it is convenient for designers to use this method to parameterize one blade based on their experience. Nowadays, it is widely used in the optimization of turbomachinery. However, the aerodynamic parameters are not considered in the parameterization and still act as the boundary condition of flow field computing.

To rapidly find the airfoil with the optimal aerodynamic property, many intelligent optimization technologies have been used in the process. Among all of the published optimization algorithms, the genetic algorithm (GA) [18–21] and the simulated annealing (SA) algorithm [10,11,22], as two traditional intelligent optimization algorithms, have been widely used in airfoil optimization. They aim to find the airfoil with the optimal performance precisely. However, much time is required to complete the search, which leads to a poor computational efficiency [23,24]. A new intelligent algorithm, known as particle swarm optimization (PSO) and proposed by Kenney and Eberhart [25], can be used to solve this problem. PSO is a population-based, self-adaptive searching optimization method. The principle of this method is based on animal social behaviors, such as birds' migration. However, it is easy to become trapped into a local extreme value or converged to precocity by the standard PSO. Therefore, researchers began looking for improved methods to solve this problem. Shi [26] used a linearly decreasing inertia weight to balance the global and local searching character. However, the local searching capability of this method was weak. Simultaneously, it is hard to predict the maximum iteration number. Clerc [27] set a constriction factor determined by two learning factors to cancel the boundary limits of velocity, and to balance the global and local searching capability. Hu [28] adopted a stochastic inertia weight to replace the linearly decreasing inertia weight. This method could accelerate the convergence velocity

and avoid being trapped into a local best solution. However, these methods still have the risk of local convergence.

Most approaches to parameterization of the cascade have been used with only the help of geometric feature parameters, and the aerodynamic parameters were not referred to. The efficiency of optimization was thus negatively affected. Therefore, in this paper, considering the cascade aerodynamic characters, one aerodynamic parameterization approach for a low Reynolds number cascade is proposed. To find the airfoil with the optimal performance during a certain range of incidence angles, a modified PSO-MVFSA algorithm is studied. Furthermore, two cases, such as the cascade with NACA4412 and the blade of FAN D500, are selected to verify the feasibility of the improved parameterization and optimization method.

2. Aerodynamic Parameterization Method

2.1. CLSTDM-NURBS Method

In this paper, for the CLSTDM method, the pressure side and suction side are obtained through the camber curve superposing the half-thickness distribution curve. This method is used to describe an airfoil and is shown in Figure 2. Due to its good ability to design a complex geometry, the two-order NURBS function defined by Equation (1) is used to describe the camber curve and the half-thickness distribution curve.

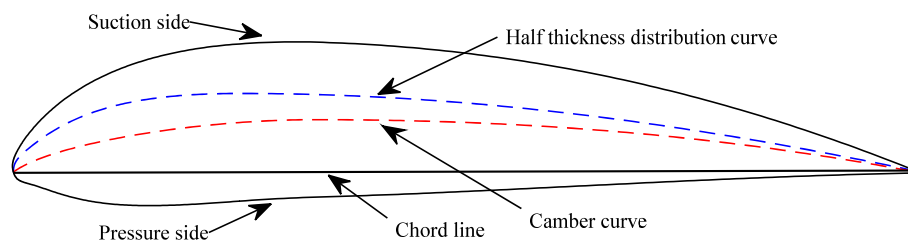


Figure 2. Airfoil parameterization.

$$\begin{cases} C(u) = \sum_{i=0}^n \frac{B_{2,i}(u)\omega_i Q_i}{B_{2,i}\omega_i(u)} \\ B_{2,i}(u) = \frac{2!}{i!(2-i)!} u^i (1-u)^{2-i} \end{cases} \quad (1)$$

where u is the knot vector, n is the order of NURBS ($n = 2$), i is the mark of the control points ($i = 0, 1, 2$), $C(u)$ is the coordinate of the point of the fitting curve parameterized by the NURBS function, $B_{2,i}(u)$ is the Bernstein function, ω_i represents the weight coefficients ($\omega_0 = 1$, $\omega_2 = 1$, $\omega_1 = \omega$), and Q_i is the control point. To solve the two-order NURBS function, the De Boor algorithm [29], which provides a fast and numerically stable way of finding a point on a B-spline curve with the given u in the domain, is adopted and programmed.

For camber parameterization, the camber curve is divided into two two-order NURBS curves (solid line), and these two NURBS curves are respectively controlled by several geometric control points (Q_0, Q_1, Q_2, Q_3, Q_4) shown in Figure 3. Five geometric feature parameters of an airfoil, such as the chord line $L = 1.0$, the leading edge angle χ_1 , the trailing edge angle χ_2 , and the coordinate of the maximum camber point (B_x, B_y), are adopted to derive the coordinates of the geometric control points of NURBS. To ensure the continuous property of two NURBS curves at the location of the maximum camber point Q_2 , two lines Q_1Q_2 and Q_2Q_3 need to be collinear. Moreover, all of the geometric control points of NURBS are derived as follows in Equation (2).

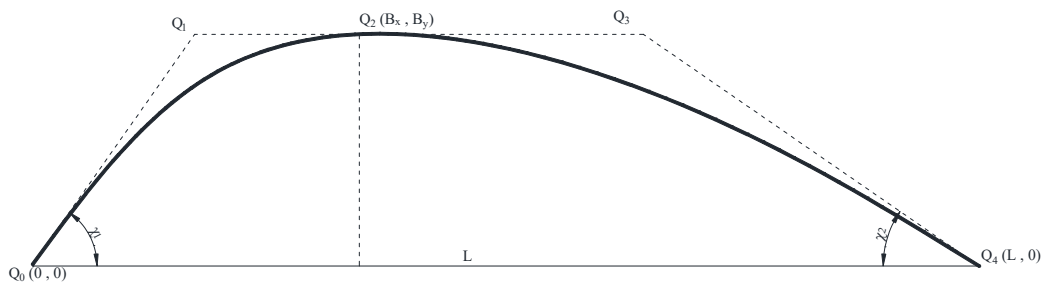


Figure 3. Camber curve parameterization.

$$\begin{bmatrix} Q_0 \\ Q_1 \\ Q_2 \\ Q_3 \\ Q_4 \end{bmatrix} = \begin{bmatrix} (0,0) \\ (B_y/\tan(\chi_1), B_x) \\ (B_x, B_y) \\ (L - B_y/\tan(\chi_2), B_y) \\ (L,0) \end{bmatrix} \tag{2}$$

For parameterization of the half-thickness distribution curve, the curve is divided into three parts, including the leading edge half-thickness, the middle half-thickness, and the trailing edge half-thickness, as shown in Figure 4. The leading edge (LE) part is described by one two-order NURBS curve, the middle part by two two-order curves, and the trailing edge (TE) part by one two-order NURBS curve. Four NURBS curves are controlled by nine geometric control points ($P_0, P_1, P_2, P_3, P_4, P_5, P_6, P_7, P_8$), which are derived by seven geometric feature parameters of the airfoil, such as the leading edge radius R_1 , the trailing edge radius R_2 , the chord line $L = 1.0$, the thickness gradient angles α_1, α_2 , and the coordinate of the maximum half-thickness point (T_x, T_y) . As is the case for the camber curve, the half-thickness distribution curve also requires continuity. Therefore, at the three geometric control points P_2, P_4, P_6 , it is necessary to maintain collinearity for the relative lines. Utilizing geometric principles, these control point coordinates are shown in Equation (3).

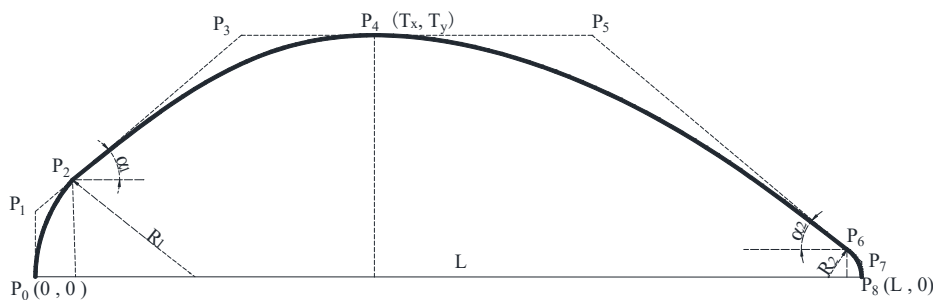


Figure 4. Half-thickness distribution curve parameterization.

$$\begin{bmatrix} P_0 \\ P_1 \\ P_2 \\ P_3 \\ P_4 \\ P_5 \\ P_6 \\ P_7 \\ P_8 \\ P_9 \end{bmatrix} = \begin{bmatrix} (0,0) \\ (0, R_1 * \cos(\alpha_1) - R_1 * \tan(\alpha_1) * (1 - \sin(\alpha_1))) \tan(\alpha_1) \\ (R_1 * (1 - \sin(\alpha_1)), R_1 * \cos(\alpha_1)) \\ ((T_y - R_1 * \cos(\alpha_1))/\tan(\alpha_1) + R_1 * (1 - \sin(\alpha_1)), T_y) \\ (T_x, T_y) \\ (-(T_y - R_2 * \cos(\alpha_2))/\tan(\alpha_2) + L - R_2 * (1 - \sin(\alpha_2)), T_y) \\ (L - R_2 * (1 - \sin(\alpha_2)), R_2 * \cos(\alpha_2)) \\ (L, R_2 * \cos(\alpha_2) - R_2 * \tan(\alpha_2) * (1 - \sin(\alpha_2))) \\ (L,0) \end{bmatrix} \tag{3}$$

2.2. Improved Aerodynamic Parameterization

Unlike conventional parameterization approaches in which the airfoil is only parameterized with the geometric feature parameters [30–32], an improved aerodynamic parameterization approach combining the plane cascade design method and the CLSTDM-NURBS is proposed, in which the incidence angle, i , and nine geometric parameters are used as control variables.

For one specific cascade, it can be assumed for the airflow condition that the inlet flow angle β_1 is constant and along the tangential line. In this case, a change of the incidence angle can cause a change of the geometric inlet angle of the cascade, and the variation of the incidence angle Δi is equal to that of the geometric inlet angle $\Delta\beta_{1A}$. From the definition of the geometric inlet angle, it is clear that the slope of the mean camber curve at the leading point is changed with the changing of the geometric inlet angle. This means that the variation of the incidence angle Δi has an indirect influence on the modified value of the leading edge angle χ'_1 . The relationship is shown in Equation (4).

$$\chi'_1 = \chi_1 - \Delta i \quad (4)$$

Simultaneously, the deviation angle δ can also be affected by a change of the incidence angle. In order to determine the deviation angle, one semi-rational formula of the deviation angle was used, based on the plane cascade experiments by Howell [33,34], which was suitable for a low Reynolds number cascade and only applicable in the application conditions ($\tau = 0.7 \sim 2.0$, $T_y = 0.05 \sim 0.12$, and $B_x = 0.4 \sim 0.5$). The definition formulas of the incidence angle i and the deviation angle δ have been proposed in the cascade design process [3,35].

$$\tau = \frac{t}{L} \quad (5)$$

$$\delta = \beta_{2A} - \beta_2 \quad (6)$$

In this paper, one special equation combining a semi-empirical formula [33,34] is shown in Equation (7), where φ is equal to 0.5 for the rotor blade. Therefore, if the aerodynamic and geometric parameters i , τ , β_1 , β_2 , and B_x are given, the geometric outlet angle β_{2A} can be calculated by Equation (7). Additionally, the revised trailing edge angle χ'_2 can be obtained by Equation (8). However, in Equation (7), it is found that the cascade solidity τ and the outlet flow angle β_2 cannot be determined.

$$(\beta_{2A} - \beta_2) = [0.23(2B_x)^2 - 0.002\beta_2 + 0.18](\beta_{2A} - i - \beta_1)\left(\frac{1}{\tau}\right)^\varphi \quad (7)$$

$$\chi'_2 = \chi_2 - \Delta\beta_{2A} \quad (8)$$

In order to obtain the abovementioned two parameters, the diffusion factor D related to the cascade solidity τ , the inlet flow angle β_1 , and the outlet flow angle β_2 , is introduced as a constraint. This coefficient can be used to control the aerodynamic load of the cascade. The definition of the diffusion factor is shown in Equation (9).

$$D = \left(1 - \frac{\sin\beta_1}{\sin\beta_2}\right) + \frac{\sin\beta_1}{2\tau}(ctg\beta_1 - ctg\beta_2) \quad (9)$$

Therefore, during the process of parameterization, the leading edge angle and trailing edge angle shown in Figure 3 are independent variables and no longer depend on the incidence angle. In this way, the control variables of cascade parameterization are determined, such as B_x , B_y , T_x , T_y , R_1 , R_2 , α_1 , α_2 , and i .

3. The Improved Airfoil Aerodynamic Optimization Method

3.1. Modified PSO-MVFSA

With the extensive use of standard particle swarm optimization (PSO), some drawbacks have been found, such as the local extreme minimum and the precocity. To solve these problems, many works have been published [26–28]. Some only adjusted the change of inertia weight to avoid being trapped into a local optimal solution. Moreover, some used two learning factors to balance the local searching and global searching. In this paper, the control variables of cascade parameterization are grouped as a particle. Additionally, the best particle position $X_{i,j}$ corresponding to the optimal cascade is obtained by the modified PSO, as shown in Equation (10) [27].

$$\begin{cases} V_{i,j}^1 &= \phi \cdot \left[\omega V_{i,j}^0 + c_1 \gamma_1 (P_{i,j} - X_{i,j}^0) + c_2 \gamma_2 (P_{g,j} - X_{i,j}^0) \right] \\ \phi &= \frac{2}{2 - (c_1 + c_2) - \sqrt{(c_1 + c_2)^2 - 4(c_1 + c_2)}} \\ \omega &= \mu_{\min} + (\mu_{\max} - \mu_{\min}) * \gamma_4 + \sigma \cdot \gamma_3 \\ X_{i,j}^1 &= X_{i,j}^0 + V_{i,j}^1 \end{cases}, \quad (10)$$

where V is the particle velocity, subscript i, j is the particle sequence, ω is the stochastic inertia weight [28], ϕ is the constriction factor [27], c_1, c_2 represents two learning factors, γ_1, γ_2 represents the random number uniformly distributed in $(0, 1)$, $P_{i,j}$ is the best position in its flight history, $P_{g,j}$ is the best position in the particle swarms, μ_{\max} is the maximum stochastic inertia weight, μ_{\min} is the minimum stochastic inertia weight, σ is the variance of the stochastic inertia weight, and γ_3, γ_4 is the random number of the standard normal distribution.

However, it is very difficult to judge whether the results are the local optimal solutions or the global solutions when only using the modified PSO. Due to the probability of the simulated annealing (SA) algorithm jumping out of the local value, it can be used to solve the problem. Furthermore, considering that the low searching velocity of the standard SA algorithm can lead to a greater time consumption, modified very fast simulated annealing (MVFSa) [36] is adopted to search for the global optimal minimum. Since the Cauchy distribution depending on temperature was better than the Gaussian distribution, the coefficient of variable perturbation y_{ij} based on the Cauchy distribution has been redefined by Equation (11). In order to improve the efficiency further, the random probability of the acceptance, P_r , has been redefined based on the Boltzmann–Gibbs distribution, as shown in Equation (12).

$$y_{ij} = T_{\max} \exp(-ck^{1/N_1}) \cdot \text{sgn}(u - 0.5) \left[\left(1 + \frac{1}{T}\right)^{|2u-1|} - 1 \right], \quad (11)$$

$$P_r = \left[1 - (1 - h) \left(E(M'_{ij}) - E(M_{ij}) \right) / T \right]^{1/(1-h)}, \quad (12)$$

where u is a random number ranging from 0 to 1, T_{\max} is the initial simulated high temperature, N_1 is the syllogism coefficient, k is the number of the marked annealing stage, c is a given constant value, M'_{ij} is the disturbed variable, M_{ij} is the undisturbed variable, and h is a real number (set $h = 0.5$). Furthermore, $E(M_{ij})$ is adopted to evaluate the current energy of the particle.

3.2. Verification of Modified PSO-MVFSA

Due to its local optimums and premature results, the Rastrigin function is usually used as a test function. The definition of the function is shown in Equation (13).

$$f(x) = \sum_{j=0}^D x_j^2 - 10 \cdot \cos(2\pi x_j) + 10 \quad x_j \in [-20, 20] \quad (13)$$

In theory, when the independent variable x_j is equal to 0, the global minimum optimum of the function is $f(x_j) = 0$. In Figure 5, three different solutions of the function are respectively shown. When the independent variable range is $[-20, 20]$, the function looks smooth and monotonic, as shown in Figure 5a. With the increase of the resolution, many small peaks and valleys are observed in Figure 5b,c. This means that the function has many widespread local minima.

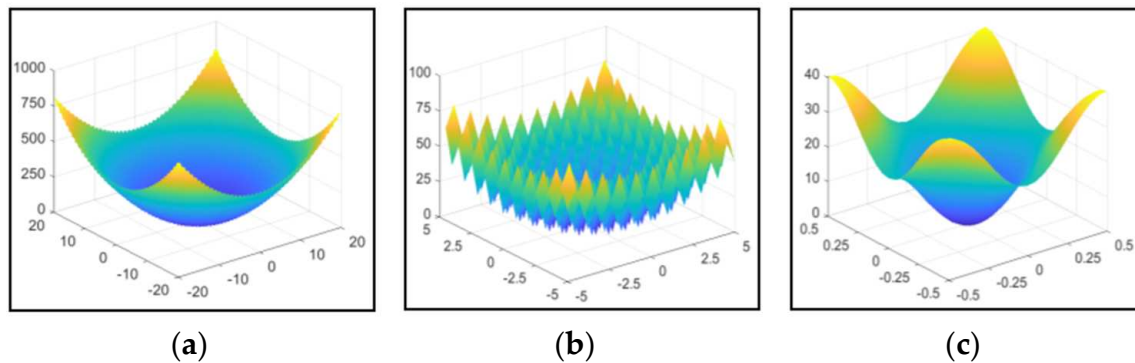


Figure 5. Rastrigin function: (a) $x_i \in [-20, 20]$; (b) $x_i \in [-5, 5]$; and (c) $x_i \in [-0.5, 0.5]$.

To prove the feasibility and accuracy of the modified PSO-MVFSA, two other PSO-based optimization algorithms, as two comparison algorithms, are adopted to search for the optimal minimum of the Rastrigin function. As the function is two-dimensional, each particle consists of two variables for three kinds of PSO algorithms. The initial particle number, the total iteration number of PSO, and the total iteration number of MVFSA are set to 30, 80, and 40, respectively. Some other coefficients are listed in Table 1, such as the positive value α , the Markov chain length J , and so on. By means of these searching optimization methods, the optimal results are obtained and shown in Table 2. It can be seen that the optimal function value obtained by PG-PSO is smaller than that of the standard PSO. However, the computing time is longer than that of the standard PSO. For the modified PSO-MVFSA, not only its time consumption, but also its ability for minimum searching, are optimal in comparison with the other two algorithms.

Table 1. Coefficients of three algorithms based on particle swarm optimization (PSO).

Maximum Stochastic Inertia Weight, μ_{\max}	Minimum Stochastic Inertia Weight, μ_{\min}	Variance Stochastic Inertia Weight, σ	Learning Factor, c_1	Learning Factor, c_2
0.8	0.4	0.2	2.25	1.85
The Initial Simulated High Temperature, T_{\max}	The Final Cooling Simulated Temperature, T_{\min}	The Syllogism Coefficient, N_1	The Positive Value, α	Markov Chain Length, J
30	0.0001	9	0.8	15

Table 2. Results of three algorithms based on PSO.

Algorithms	Computing Time T (Seconds)	Optimal Particle x_{opt}	Optimal Function Value $f(x_{opt})$
Standard PSO [22]	1.08942	(0.001225, -0.000958)	0.000481
PG-PSO [21]	1.14177	(-0.001495, 0.0000077)	0.000443
PSO -MVFSA	0.898254	(0.000177, -0.000476)	0.000051

3.3. The Improved Airfoil Aerodynamic Optimization

3.3.1. Fitness Function

For improved cascade aerodynamic optimization, nine control variables are used to parameterize the cascade and grouped as a particle. In all flights, the selection of the particle with the best position through the optimum target is very important. The lift-drag ratio of the airfoil is related to its capability regarding the power output and aerodynamic loss [16]. Therefore, the optimization proposition is set up as shown in Equation (14).

$$\begin{cases} f(S_1, S_2 \cdots S_{10}) = \sum_{i=1}^n (C_L/C_D)_i/n \\ \text{s.t.} \\ \chi_1 > \arctan(B_y/B_x) & -\chi_2 > \arctan(B_y/(1-B_x)) \\ \alpha_1 > \arctan(T_y/T_x) & -\alpha_2 > \arctan(T_y/(1-T_x)) \\ 0.4 \leq D \leq 0.6 \end{cases}, \quad (14)$$

where S_i is the control variable, C_L/C_D is the lift-drag ratio, (B_x, B_y) is the coordinate of the maximum camber point, (T_x, T_y) is the coordinate of the maximum half-thickness point, α_1, α_2 represent the LE and TE thickness gradient angles, χ_1, χ_2 represent the LE and TE angles, and n is the number of incidence angles. In this paper, the average lift-drag ratio of the airfoil is evaluated under all airflow incidence angles. Additionally, the fitness function can be obtained as shown in Equation (15).

$$\begin{aligned} -F = c_1 \frac{f(S_1, S_2 \cdots S_{10}) - \sum (C_L/C_D)_{ref}}{\sum (C_L/C_D)_{ref}} + c_2 \frac{\alpha_1 - \arctan(B_y/B_x)}{\arctan(B_y/B_x)} - c_3 \frac{\alpha_2 + \arctan(B_y/(1-B_x))}{\arctan(B_y/(1-B_x))} \\ + c_4 \frac{X_1 - \arctan(T_y/T_x)}{\arctan(T_y/T_x)} + c_5 \frac{-X_2 - \arctan(T_y/(1-T_x))}{\arctan(T_y/(1-T_x))} + c_6 (D_i - D) \end{aligned} \quad (15)$$

where c_i is the weighting factor and subscript *ref* presents the original airfoil.

3.3.2. Aerodynamic Optimization Process

During the evaluation of airfoil aerodynamic performance two-dimensional computational fluid dynamics (2D CFD) code which utilized the standard $k - \omega$ turbulence model [37,38] to solve the Reynolds Average Navier-Stokes (RANS) equations was used, and it was only used to simulate the low Reynolds number airfoils [23,39]. Due to the fact that the lift-drag ratio of one airfoil could be obtained quickly by this code, this 2D CFD code was integrated into MATLAB as a fast solver to evaluate the fitness value of each particle. The whole aerodynamic optimization flowchart is shown in Figure 6. Moreover, the detailed process is introduced in the following steps:

- Inputting coordinate points of one airfoil, and setting coefficients of the modified PSO-MVFSA;
- Selecting one angle from the sets of incidence angles and nine geometric variables as an initial particle;
- Conducting perturbation of nine geometric variables of the initial particle to generate the initial particle swarm with one incidence angle, based on the super Latin square method; constructing airfoil swarm by the improved parameterization method; and evaluating the airfoil fitness value by Equation (15);
- Finding the best previous position of the particle and the best position of the swarm, re-calculating the velocity and the position of each particle by adopting Equation (10), and re-calculating the fitness values of the new swarms;
- If $\Delta E > 0$ ($\Delta E = E(M'_{ij}) - E(M_{ij})$ is the error function), the data related to the particle are unchanged; if not, replace the data and particles with new data and particles;
- Repeating steps (d) and (e) until the total iteration of the modified PSO is reached;

- (g) Obtaining the swarm particles $(S)_i$ that satisfy $[F_{opt} - F((S)_i)]/F_{opt} < 10\%$;
- (h) Putting the swarm particles $(S)_i$ into the optimization process of MVFSA, conducting perturbation, and re-evaluating the fitness by Equation (10);
- (i) If $\Delta E > 0$, the corresponding particle is preserved; if not, the corresponding particle as a basic particle is re-disturbed and re-evaluated;
- (j) If $\Delta E > 0$, the re-disturbed particle is retained; if not, the particle is accepted with the acceptance probability equation;
- (k) Repeating steps (g) (h) (i) until the total iteration of MVFSA is reached;
- (l) Outputting the particle with the largest function F from the preserved particle swarm at different incidence angles respectively;
- (m) Selecting the best of the optimal particles by MVFSA as the final optimal particle.

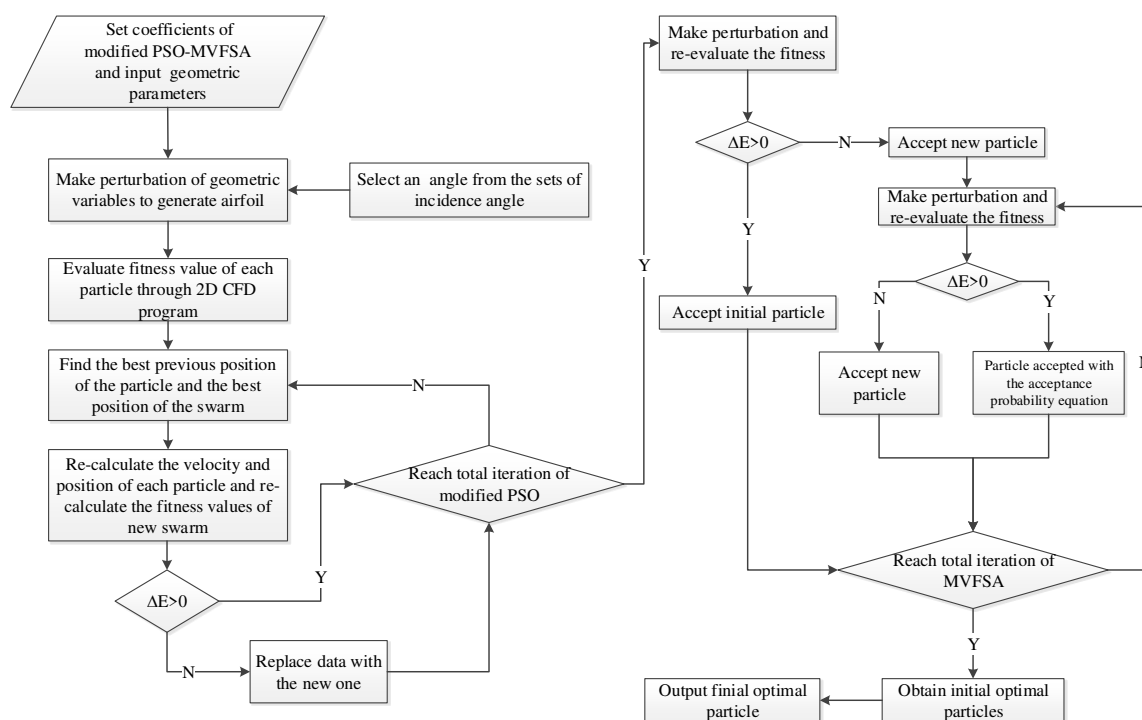


Figure 6. Flow chart of the whole aerodynamic optimization process.

4. Applications in Cascade Optimization

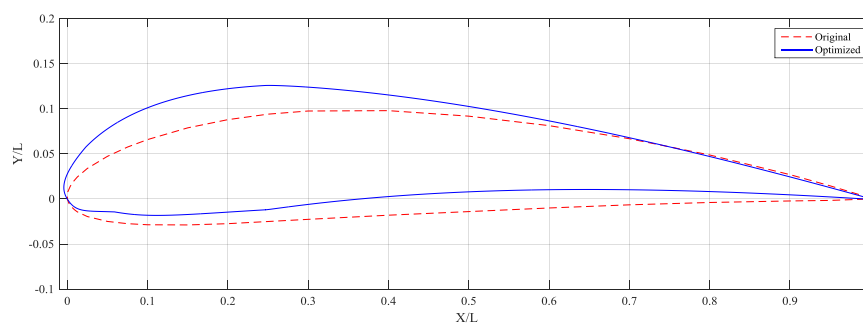
4.1. Optimization of a Cascade with an NACA4412 Profile

NACA4412 is adopted as the original basic profile of the cascade and evolved into an advanced airfoil by this improved method. The initial particle number, the total iteration number of the modified PSO, and the total iteration number of MVFSA are set to 30, 100, and 50, respectively. Each cascade is described by the improved aerodynamic parameterization method. The average lift-drag ratio of the airfoil of the cascade is calculated by the flow solver. Moreover, the constant airflow boundary condition is set so that the Reynolds number is as high as 1×10^5 , the Mach number is 0.1, and the solidity of the cascade is 1.5. Moreover, some other coefficients of the modified PSO-MVFSA are shown in Table 3.

Table 3. Coefficients of modified PSO-modified very fast simulated annealing (MVFSA).

Maximum Stochastic Inertia Weight, μ_{\max}	Minimum Stochastic Inertia Weight, μ_{\min}	Variance Stochastic Inertia Weight, σ	Learning Factor, c_1	Learning Factor, c_2
0.8	0.4	0.2	2.25	1.85
The Initial Simulated High Temperature, T_{\max}	The Final Simulated Cooling Temperature, T_{\min}	The Syllogism Coefficient, N_1	The Positive Value, α	Markov Chain Length, J
40	0.0001	9	0.8	20

In actual airflow conditions, the incidence angle of the cascade is not constant and limited to a certain range. Therefore, the aim of multi-point optimization is not to obtain the best aerodynamic performance under one constant incidence angle, but to reach the best whole aerodynamic performance in the whole working range, referred to in Equation (12). In this paper, the incidence angle is uniformly distributed from 0° to 15° by a step of 1.0° . The aerodynamic performance of each cascade parameterized by one incidence angle and eight geometric variables is calculated by the CFD simulation. Based on Equation (13), the fitness value corresponded to each cascade is figured out. Then, the global minimum value is found by the user of the improved PSO-MVFSA method. NACA4412 airfoil and the optimal airfoil are shown in Figure 7, in which the blue curve is the optimal airfoil and the red curve denotes the original airfoil. From this figure, it can be observed that the suction side and pressure side of the optimized airfoil are changed in terms of geometry in comparison with that of NACA4412.

**Figure 7.** Geometry comparison: NACA4412 airfoil and optimal airfoil.

To evaluate the aerodynamic performance of the cascade, the pressure coefficient C_p is adopted, which is defined by Equation (16).

$$C_p = -\left(\frac{p - p_\infty}{\frac{1}{2}\rho u_\infty^2}\right) = \frac{p_\infty - p}{p_0 - p_\infty}, \quad (16)$$

where p , p_0 , p_∞ are the current pressure, the stagnation pressure, and the inlet airflow pressure, respectively; ρ is the density; and u_∞ is the inlet airflow velocity.

The increasing curvature of the suction side close to LE can lead to the intensifying of the velocity increasing and the pressure decreasing. Then, the pressure coefficient of the suction side of the optimized C_p near LE is larger than that of the original cascade. However, it is due to the geometric change of the pressure side close to LE that the decreasing of the velocity and the increasing of the pressure are alleviated. These phenomena can be observed in Figure 8. In the figure, the detailed pressure distributions on the suction and pressure side are shown, which respectively correspond to four incidence angle conditions of $i = 0^\circ$, $i = 3^\circ$, $i = 6^\circ$, and $i = 12^\circ$. It is also clear that the optimized airfoil surface pressure distribution presented by the blue curve is better than that of the original airfoil described by the red curve under each condition. Therefore, the pressure differences between the pressure side and suction side of the optimized airfoil are larger than those of the original airfoil. The cascade performances under the incidence angles ranging from 0° to 15° are shown in

Figure 9. The average lift-drag ratio of the optimized cascade is increased by 13.38% in comparison with that of the cascade with NACA4412.

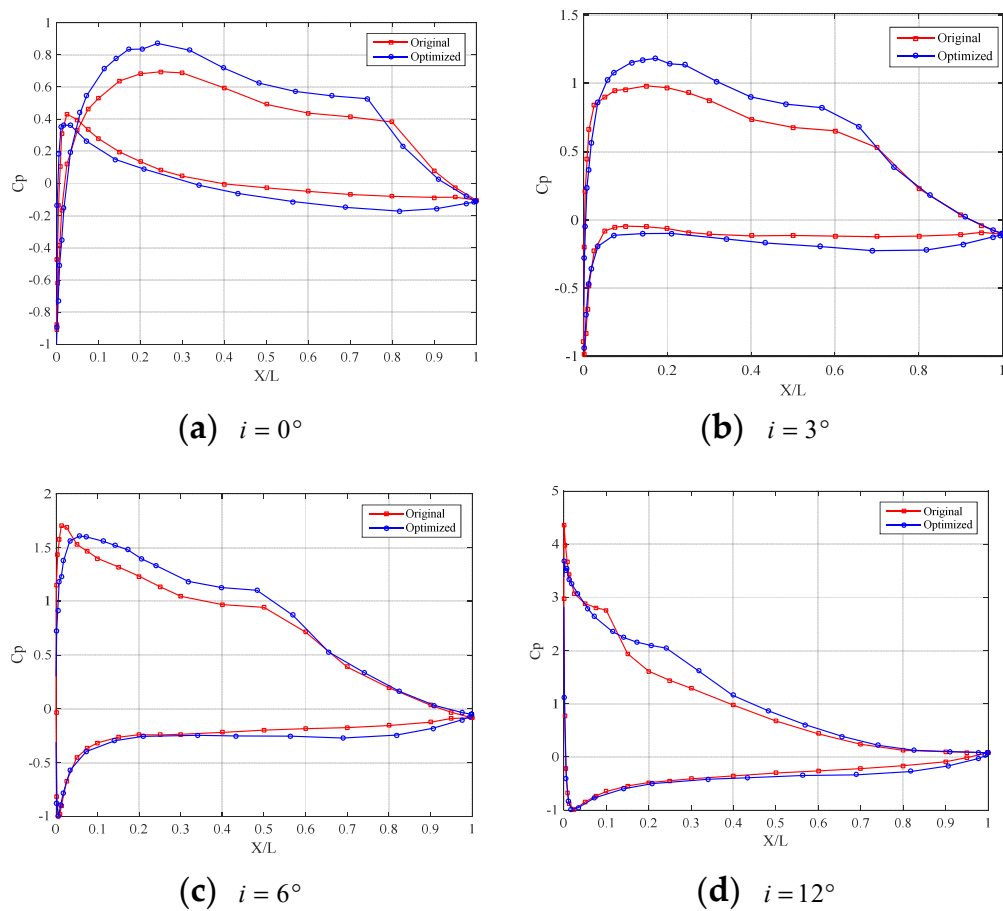


Figure 8. Surface pressure distribution comparison in multi-point optimization.

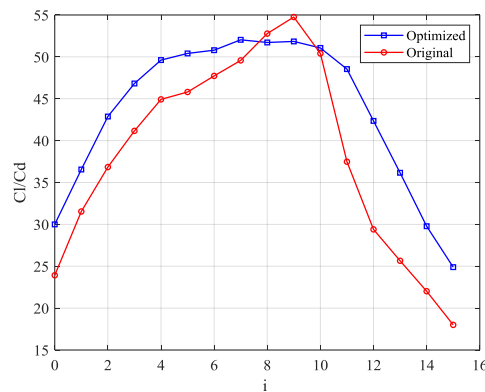


Figure 9. Airfoil performance of the average lift-drag ratio (cal., $Re = 1.0 \times 10^5$, $Ma = 0.1$).

For further analysis, CFD simulation software CFX was used to calculate the cascade performance. The velocity contours of the original and optimized cascades at incidence angles of $i = 0^\circ$ and $i = 12^\circ$ are shown in Figure 10. It is clear that the velocity difference between the suction side and pressure side of the optimized cascade is bigger than that of NACA4412. Therefore, the diffusion factor D of the optimized cascade can be increased. It can also be observed that the airflow separation point on the suction side of the optimized cascade moves backward along the airfoil in comparison with that of NACA4412 and the area of the wake becomes smaller than that of NACA4412. Therefore, it can be

considered that the aerodynamic load of the cascade is increased and the aerodynamic loss is controlled with the help of the improved aerodynamic optimization algorithm.

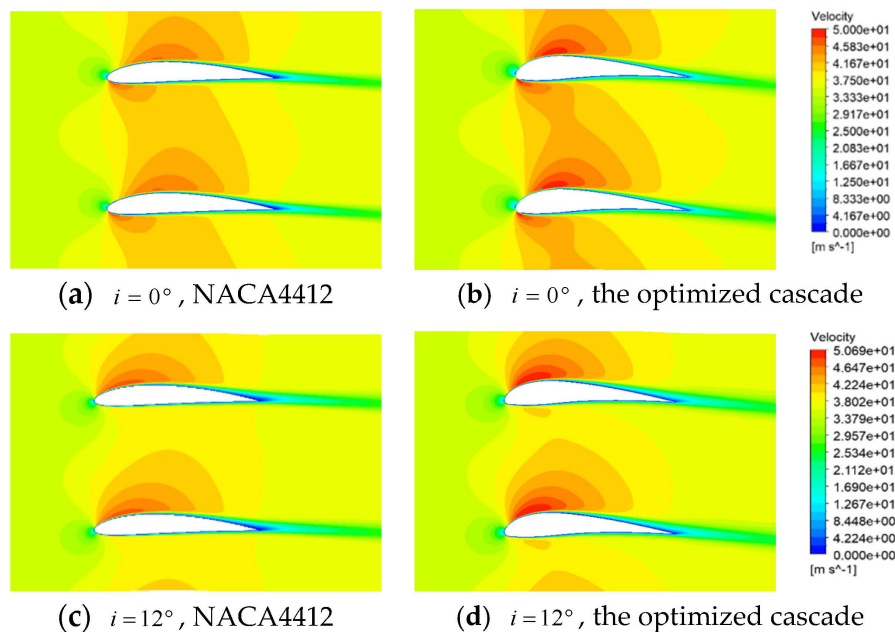


Figure 10. Velocity contours.

4.2. Blade D500 Optimization

Blade D500 is used in an axial-flow fan for an evaporator system. It is a kind of low Reynolds number 3D blade. In this work, in order to verify the feasibility of the improved method applied to the practical blade design, the cascade at the 50% radius of Blades D500 was selected and optimized. Two performance parameters, including the pressure coefficient C_p defined by Equation (16) and the efficiency η defined by Equation (17), were used to evaluate the aerodynamic performance of Blade D500. In order to obtain the aerodynamic performance parameters, CFX was used to calculate the airflow field of Blade D500.

$$\eta = \frac{Q_v \cdot P}{N}, \quad (17)$$

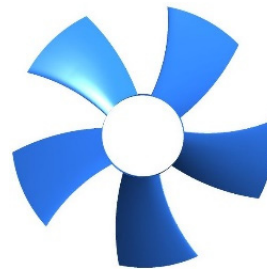
where Q_v is the volume flow rate, P is the static pressure increase, and N the aerodynamic power.

4.2.1. Validation of the CFD Simulation Based on Experiments

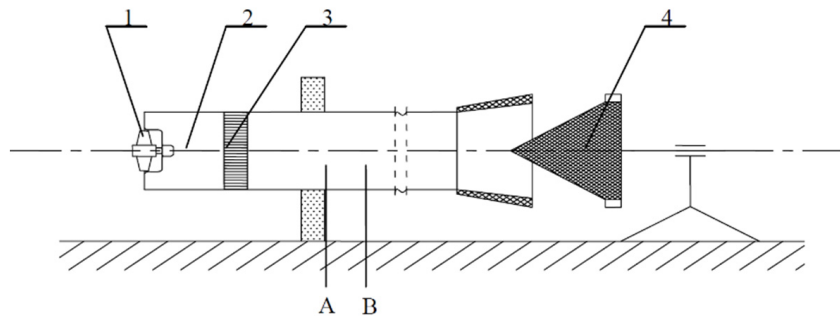
The experiments of the axial fan with Blade D500 shown in Figure 11 were conducted in the Key Lab for Power Machinery and Engineering of SJTU. In order to match the practical situation, the rotor was mounted on the guard grill, which was connected with a short bell mouth at the inlet of the tube. The diameter of the tube was increased to 600 mm to avoid destroying the flow field at the rotor outlet and simulate the real situation in the evaporator system as much as possible. The pressure probes were mounted at points A and B, by which the flow rate and the pressure increase could be calculated. Under eight volume flow rates, the pressure increases were calculated.



(a) Practical axial fan



(b) Geometric model of the axial fan

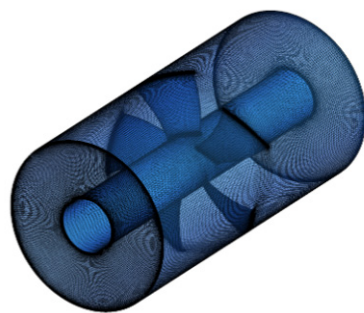


1-Test Rotor 2-Cylindrical Tube(600mm) 3-Grill 4-Conical Throttle

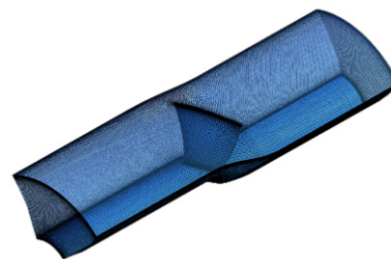
(c) A sketch of the experiment

Figure 11. The experiment of Blade D500.

Under the same conditions as those used in the experiments, CFX was adopted to simulate the aerodynamic performance of the axial fan. The grids consisted of the structured hexahedral meshes shown in Figure 12 that were generated by TurboGrid. The total number of nodes was 1,260,626 for the full channel after studying the grid independence, and the minimum value of the mesh quality was 0.3. Due to the excellent ability to simulate the flow with a fiercely adverse pressure gradient of the standard $k - \omega$ model, it was selected as the turbulent model to simulate the flow field. The mass flow and static pressure were set at the inlet and outlet, respectively.



(a) Full channel grid



(b) Single channel grid

Figure 12. Grid of the axial fan.

After a series of experiments and CFD simulations of the axial fan with Blade D500, the pressure coefficients were obtained and are shown in Figure 13. Based on Figure 13, it could be found that the pressure coefficients C_{sp} calculated by CFD are slightly higher than those calculated by experiments. However, the trends of the two curves are very similar. In Figure 14, the efficiency is compared for values obtained by calculations and experiments. It can be observed that the relative error between the

two series of average efficiencies is under 8.35%. Considering the abovementioned results, the CFD simulation can be used to feasibly estimate the aerodynamic performance of an axial fan.

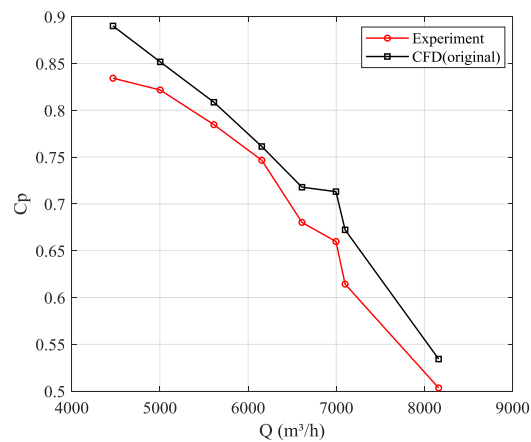


Figure 13. Static pressure coefficients calculated by CFD and the experiment.

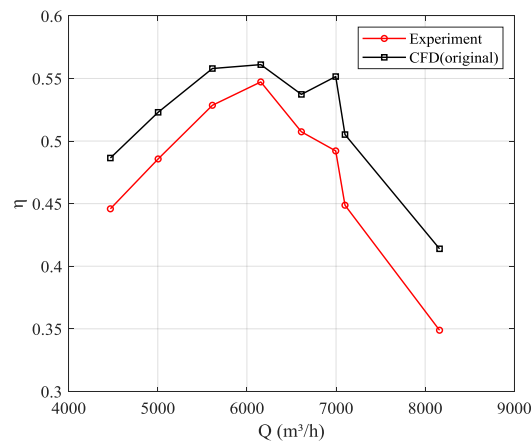


Figure 14. Average efficiencies calculated by CFD and the experiment.

4.2.2. Optimization of Blade D500

For aerodynamic optimization of the cascade at the 50% radius of Blade D500, the airflow condition was set as $Re = 1 \times 10^5$, $Ma = 0.1$, $i = 2^\circ \sim 10^\circ$, $D = 0.4 \sim 0.6$. After a series of optimization iterations, the airfoil of the optimal cascade was obtained and is shown in Figure 15, as well as the airfoil of the original cascade. It can be observed that the airfoil of the optimized cascade is different from that of the original cascade. These geometric changes of the optimal cascade can lead to an increase of the curvature of the suction side, while the pressure side is changed a little. Additionally, aerodynamic performance comparisons are shown in Figure 16. It could be found that the pressure differences of the optimized cascade are larger than those of the original airfoil along the chord line within the range of the incidence angle. After a series of simulation calculations, it could be found that the average lift-drag ratio of the optimized cascade is increased by 15.21% in comparison with that of the original cascade. Therefore, it can be considered that the aerodynamic performance of the optimized cascade is better than that of the original one.

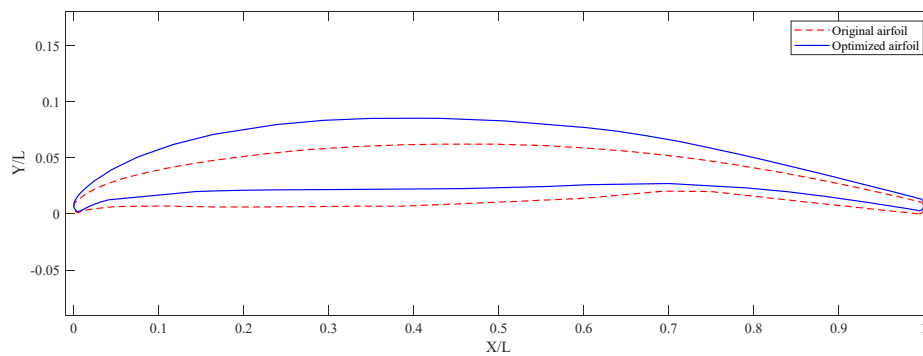


Figure 15. Geometric comparisons of the optimized and original cascades.

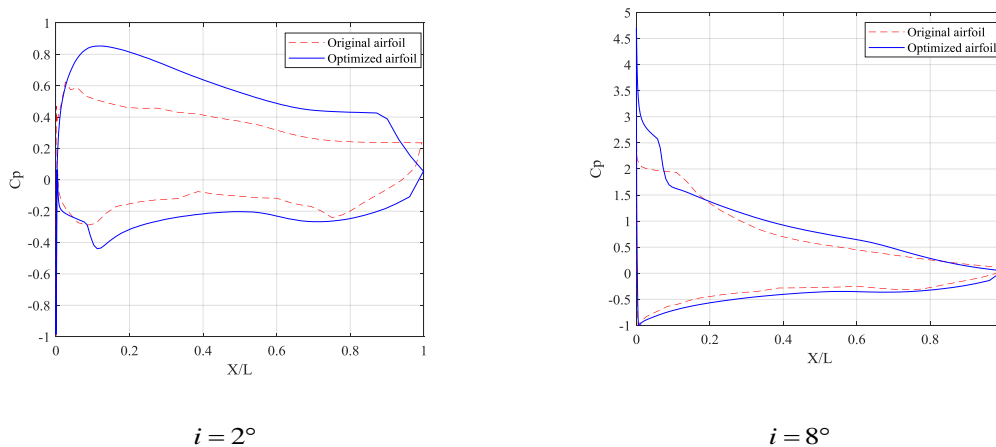
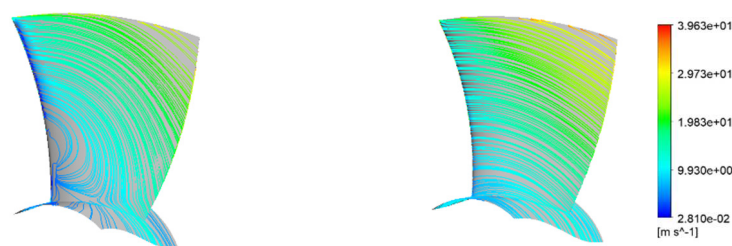


Figure 16. Surface pressure distributions.

To evaluate the feasibility of the improved aerodynamic optimization method, the optimized 3D Blade D500 and the original 3D Blade D500 were simulated by CFD under the same airflow condition. Moreover, the simulation results of two blades were compared. The streamlines of the suction surfaces of the two blades are shown in Figure 17. From the figure, it is clear that the streamline between the middle section and the hub of the original blade is not very good, and a large turbulence loss must have occurred in this region. In contrast, the streamline in the same region of the optimized blade becomes very smooth. The pressure coefficients C_{sp} of the two fans are shown in Figure 18. In this figure, it can be seen that the pressure coefficient of the optimized fan is better than that of the original fan, and the average pressure coefficient is increased by 6.12%. Meanwhile, from Figure 19, it can be observed that the efficiency of the optimized fan is higher than that of the original one, and averagely increased by 11.15%. Therefore, from the above analysis, it can be considered that the aerodynamic performance of optimized Blade D500 is improved and the improved aerodynamic optimization method is feasible.



(a) Suction surface of the original cascade (b) Suction surface of the optimized cascade

Figure 17. Surface streamline comparisons of Blade D500.

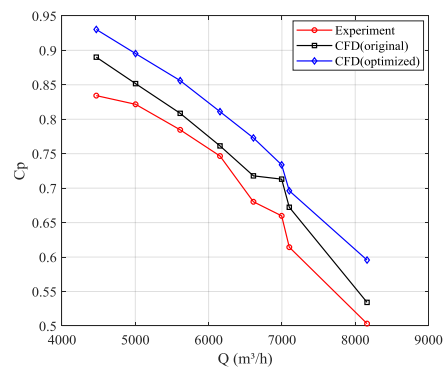


Figure 18. Pressure coefficient comparisons of Blade D500.

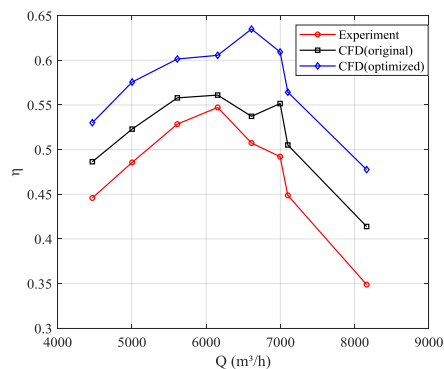


Figure 19. Efficiency comparisons of D500.

5. Conclusions

In this paper, an improved optimization method especially applied to a cascade with a low Reynolds number is proposed. In this method, the incidence angle and eight geometric parameters are used as the control variables altogether. Meanwhile, the modified PSO-MVFSA algorithm is adopted to optimize the objective cascades, and two cascade cases, such as NACA4412 and Blade D500, are selected to testify the method. Some valuable results are as follows:

- Since the aerodynamic parameter, such as the incidence angle, is considered as one of the control variables, the relationship between the geometry of the airfoil and the aerodynamic performance of the cascade is learnt. Therefore, during the whole optimization process, an improvement of the aerodynamic performance can give rise to a direct modification of the geometry so that the optimization becomes more targeted and more efficient;
- In this study, particular effort was devoted to designing a fitness function which is suitable for optimizing a cascade with a low Reynolds number. Furthermore, the combination of PSO and MVFSA succeeded in increasing the optimization efficiency and avoided the local optimal to reach a global solution, which was verified by the Rastrigin function and two cascade cases;
- Based on the analysis of the results from the two cascade cases, such as NACA4412 and Blade D500, it was demonstrated that the average lift-drag coefficient of the optimized cascade was improved, whilst the drag coefficient was kept at a low level. Therefore, it can be considered that the modified PSO-MVFSA can be adopted as an efficient and robust optimizer to solve the problems of multi-variable optimization confronted in cascade design.

Author Contributions: S.Z. and B.Y., investigation, methodology, software, and writing—original draft preparation. H.X. and M.S., validation. All authors have read and agreed to the published version of the manuscript.

Funding: This research received no external funding.

Acknowledgments: This research was supported by the National Science and Technology Major Project of China (2017-II-0006-0019).

Conflicts of Interest: The authors declare that they have no conflict of interest with regards to this work. They declare that they do not have any commercial or associative interests that represent a conflict of interest in connection with the work submitted.

Abbreviations

NURBS	Non-Uniform Rational B-Splines
CLSTDM	Camber Line Superposing Thickness Distribution Molding
PSO	Particle Swarm Optimization
PSO-MVFSA	Particle Swarm Optimization-Modified Very Fast Simulated Annealing

Nomenclature

B_x	Vertical coordinate of the maximum camber point
B_y	Horizontal coordinate of the maximum camber point
C_p	Pressure coefficient
C_L	Lift coefficient
C_D	Drag coefficient
D	Diffusion factor
L	Aerodynamic chord length
M	Variable
N_1	Syllogism coefficient
N	Shaft power
R_1	LE radius
R_2	TE radius
P	Control points of the thickness distribution curve
Q	Control points of the camber curve
Q_v	Volume flow rate
T	Temperature
χ_1	LE angle
χ_2	TE angle
T_x	Vertical coordinate of the maximum half thickness
T_y	Horizontal coordinate of the maximum half thickness
P_r	Acceptance probability
α_1	Thickness gradient angle of LE
α_2	Thickness gradient angle of TE
β_{1A}	Geometric inlet angle
β_{2A}	Geometric outlet angle
β_1	Inlet flow angle
β_2	Outlet flow angle
y_{ij}	Coefficient of variable perturbation
ω	Weight
i	Incidence angle
μ	Stochastic inertia weight
λ	Constriction factor
τ	Cascade solidity
γ	Random number in (0, 1)
η	Pressure efficiency
c	Learning factor
(x, y)	Cartesian coordinates

References

1. Li, Z.; Zheng, X. Review of design optimization methods for turbomachinery aerodynamics. *Prog. Aerosp. Sci.* **2017**, *93*, 1–23. [[CrossRef](#)]
2. Garzon, V.E.; Darmofal, D.L. Impact of geometric variability on axial compressor performance. *J. Turbomach.* **2003**, *125*, 692–703. [[CrossRef](#)]
3. Eck, B. *Ventilatoren*; Springer: Berlin/Heidelberg, Germany, 1991.
4. Batyaev, E.A.; Kurzin, V.B. Method of optimization of blade shapes in aerodynamic design of the fan cascade. *J. Appl. Mech. Tech. Phys.* **2002**, *43*, 701–705. [[CrossRef](#)]
5. Wu, H.-Y.; Yang, S.; Liu, F.; Tsai, H.-M. Comparisons of three geometric representations of airfoils for aerodynamic optimization. In Proceedings of the 16th AIAA Computational Fluid Dynamics Conference, Orlando, FL, USA, 23–26 June 2003.
6. Samareh, J.A. Survey of shape parameterization techniques for high-fidelity multidisciplinary shape optimization. *AIAA J.* **2001**, *39*, 877–884. [[CrossRef](#)]
7. Mahmood, S.M.H.; Turner, G.M.; Siddappaji, K. Flow characteristics of an optimized axial compressor rotor using smooth design parameters. In Proceedings of the ASME Turbo Expo 2016, GT2016, Seoul, Korea, 13–17 June 2016. [[CrossRef](#)]
8. Hicks, R.M.; Henne, P.A. Wing design by numerical optimization. *J. Aircr.* **1978**, *15*, 407–412. [[CrossRef](#)]
9. Buhmann, M.D. Radial basis functions. *New Algorithms Macromol. Simul.* **2004**, *37*, 31–65. [[CrossRef](#)]
10. Liu, J.-L. A novel Taguchi-simulated annealing method and its application to airfoil design optimization. In Proceedings of the 17th AIAA Computational Fluid Dynamics Conference, Toronto, ON, Canada, 6–9 June 2005. [[CrossRef](#)]
11. Chao, S.-M.; Whang, A.J.-W.; Chou, C.-H.; Su, W.-S.; Hsieh, T.-H. Optimization of a total internal reflection lens by using a hybrid Taguchi-simulated annealing algorithm. *Opt. Rev.* **2014**, *21*, 153–161. [[CrossRef](#)]
12. Ghaly, W.S.; Mengistu, T.T. Optimal geometric representation of turbomachinery cascades using NURBS. *Inverse Probl. Eng.* **2003**, *11*, 359–373. [[CrossRef](#)]
13. Sonoda, T.; Yamaguchi, Y.; Arima, T.; Olhofer, M.; Sendhoff, B.; Schreiber, H.-A. Advanced high turning compressor airfoils for low reynolds number condition: Part 1—Design and optimization. In Proceedings of the ASME Turbo Expo 2003, Collocated with the 2003 International Joint Power Generation Conference, Atlanta, GA, USA, 16–19 June 2003; Volume 6, pp. 437–450. [[CrossRef](#)]
14. Schreiber, H.-A.; Steinert, W.; Sonoda, T.; Arima, T. Erratum: “Advanced High-Turning Compressor Airfoils for Low Reynolds Number Condition—Part II: Experimental and Numerical Analysis” [Journal of Turbomachinery, 2004, 126(4), pp. 482–492]. *J. Turbomach.* **2005**, *127*, 646. [[CrossRef](#)]
15. Chen, N.; Zhang, H.; Ning, F.; Xu, Y.; Huang, W. An effective turbine blade parameterization and aerodynamic optimization procedure using an improved response surface method. In Proceedings of the ASME Turbo Expo 2006: Power for Land, Sea, and Air, Barcelona, Spain, 8–11 May 2006; Volume 6, pp. 1169–1180. [[CrossRef](#)]
16. Chen, N.; Zhang, H.; Xu, Y.; Huang, W. Blade parameterization and aerodynamic design optimization for a 3D transonic compressor rotor. *J. Therm. Sci.* **2007**, *16*, 105–114. [[CrossRef](#)]
17. Mazaheri, K.; Khayatzaheh, P.; Nezhad, S.T. Airfoil Shape Optimization Using Improved Simple Genetic Algorithm (ISGA). In Proceedings of the 5th International Conference on Heat Transfer, Fluid Mechanics and Thermodynamics, Sun City, South Africa, 1–4 July 2007.
18. Deb, K.; Pratap, A.; Agarwal, S.; Meyarivan, T. A fast and elitist multiobjective genetic algorithm: NSGA-II. *IEEE Trans. Evol. Comput.* **2002**, *6*, 182–197. [[CrossRef](#)]
19. Goldberg, D.E.; Korb, B.; Deb, K. Messy genetic algorithms: Motivation, analysis, and first results. *Complex Syst.* **1989**, *3*, 493–530.
20. Goldberg, D.E. *Genetic Algorithms in Search Optimization and Machine Learning*; Addison-Wesley: Boston, MA, USA, 1989.
21. De Oliveira, A.; Lorena, L. A constructive genetic algorithm for gate matrix layout problems. *IEEE Trans. Comput. Des. Integr. Circuits Syst.* **2002**, *21*, 969–974. [[CrossRef](#)]
22. Gopalaramasubramanian, G.; Kumar, V.S. Parameter optimization of the sheet metal shearing process in the manufacturing of leaf spring assembly using the grey Taguchi method and simulated annealing algorithm. *Adv. Mater. Res.* **2011**, *314*, 2458–2463. [[CrossRef](#)]

23. Yang, B.; Xu, Q.; He, L.; Zhao, L.H.; Gu, C.G.; Ren, P. A novel global optimization algorithm and its application to airfoil optimization. *J. Turbomach.* **2015**, *137*, 041011. [[CrossRef](#)]
24. Chandrasekar, K.; Ramana, N. Performance comparison of GA, DE, PSO and SA approaches in enhancement of total transfer capability using FACTS devices. *J. Electr. Eng. Technol.* **2012**, *7*, 493–500. [[CrossRef](#)]
25. Kennedy, J.; Eberhart, R. Particle swarm optimization. In Proceedings of the ICNN'95—International Conference on Neural Networks, Perth, Australia, 27 November–1 December 2002; Institute of Electrical and Electronics Engineers (IEEE): Cracow, Poland, 2002; Volume 4, pp. 1942–1948.
26. Shi, Y.; Eberhart, R.C. Empirical study of particle swarm optimization. In Proceedings of the 1999 Congress on Evolutionary Computation-CEC99 (Cat. No. 99TH8406), Washington, DC, USA, 6–9 July 1999; Institute of Electrical and Electronics Engineers (IEEE): Cracow, Poland, 2003; pp. 1945–1950.
27. Clerc, M.; Kennedy, J. The particle swarm—Explosion, stability, and convergence in a multidimensional complex space. *IEEE Trans. Evol. Comput.* **2002**, *6*, 58–73. [[CrossRef](#)]
28. Zhang, J.; Fu, F.-W.; Chang, Z.-L. An upper bound on the size of m-ary t-SEC/AUED codes. *J. China Univ. Posts Telecommun.* **2006**, *13*, 95–97. [[CrossRef](#)]
29. Smith, P.W. A practical guide to splines (Carl de Boor). *SIAM Rev.* **1980**, *22*, 520–521. [[CrossRef](#)]
30. Lee, S.W.; Kwon, O.J. Robust airfoil shape optimization using design for six sigma. *J. Aircr.* **2006**, *43*, 843–846. [[CrossRef](#)]
31. Vavalle, A.; Qin, N. Iterative response surface based optimization scheme for transonic airfoil design. *J. Aircr.* **2007**, *44*, 365–376. [[CrossRef](#)]
32. Grasso, F. Usage of numerical optimization in wind turbine airfoil design. *J. Aircr.* **2011**, *48*, 248–255. [[CrossRef](#)]
33. Howell, A.R. Fluid dynamics of axial compressors. *Proc. Inst. Mech. Eng.* **1945**, *153*, 441–452. [[CrossRef](#)]
34. Howell, A.R. Flow in Cascades. In *Aerodynamics of Turbines and Compressors (HAS-1)*; Princeton University Press: London, UK, 1964.
35. Üçer, A.S.; Stow, P.; Hirsch, C. *Fluid Mechanics, Thermodynamics of Turbomachinery*; Pergamon Press: Oxford, UK, 1978.
36. Ingber, L.; Rosen, B. Genetic algorithms and very fast simulated reannealing: A comparison. *Math. Comput. Model.* **1992**, *16*, 87–100. [[CrossRef](#)]
37. Wilcox, D.C. Comparison of two-equation turbulence models for boundary layers with pressure gradient. *AIAA J.* **1993**, *31*, 1414–1421. [[CrossRef](#)]
38. Menter, F.R. Performance of popular turbulence model for attached and separated adverse pressure gradient flows. *AIAA J.* **1992**, *30*, 2066–2072. [[CrossRef](#)]
39. Yang, B. A New Blade Design Scheme for Reversible Axial Flow Fan & Research on the Combined Cascades. Ph.D. Thesis, Shanghai Jiao Tong University, Shanghai, China, 2001.



© 2020 by the authors. Licensee MDPI, Basel, Switzerland. This article is an open access article distributed under the terms and conditions of the Creative Commons Attribution (CC BY) license (<http://creativecommons.org/licenses/by/4.0/>).

Article

Multi-Condition Optimization of Cavitation Performance on a Double-Suction Centrifugal Pump Based on ANN and NSGA-II

Wenjie Wang ¹, Yanpin Li ², Majeed Koranteng Osman ^{1,3,*}, Shouqi Yuan ¹, Benying Zhang ¹ and Jun Liu ⁴

¹ National Research Center of Pumps, Jiangsu University, Zhenjiang 212013, China; wenjiewang@ujs.edu.cn (W.W.); shouqiy@ujs.edu.cn (S.Y.); ujs_zby@163.com (B.Z.)

² School of Water Conservancy, North China University of Water Resources and Electric Power, Zhengzhou 450045, China; liyanpin@ncwu.edu.cn

³ Department of Mechanical Engineering, Wa Technical University, Wa XW-0547-6186, Ghana

⁴ Shandong Shuanglun Co. Ltd., 6 Dongxin Road, Weihai 264203, China; liujun@shuanglun.cn

* Correspondence: mjk@ujs.edu.cn

Received: 25 July 2020; Accepted: 4 September 2020; Published: 10 September 2020



Abstract: Double-suction centrifugal pumps form an integral part of power plant systems in maintaining operational stability. However, there has been a common problem of achieving a better cavitation performance over a wider operating range because the traditional approach for impeller design often leads to the design effect not meeting the operational needs at off-design conditions. In addressing the problem, an optimization scheme was designed with the hub and shroud inlet angles of the double-suction impeller to minimize the suction performance at non-design flow conditions. A practical approach that speeds up the cavitation simulation process was applied to solve the experimental design, and a multi-layer feed forward artificial neural network (ANN) was combined with the non-dominated sorting genetic algorithm II to solve the multi-objective problem into three-dimensional (3D) Pareto optimal solutions that meet the optimization objective. At the design point, the suction performance was improved by 6.9%. At non-design flow conditions, the cavitation performance was improved by 3.5% at $1.2Q_d$ overload condition, 4% at $0.8Q_d$, and 5% at $0.6Q_d$. Additionally, there was significant reduction in the attached cavity distribution in the impeller and suction domains when the optimized model was compared to the original model at off-design points. Finally, the optimization established a faster method for a three-objective optimization of cavitation performance using ANN and 3D Pareto solutions.

Keywords: multi-condition optimization; cavitation performance; artificial neural networks (ANN); net positive suction head (NPSH); double suction

1. Introduction

In power plants, cooling water circulation pumps play an important role of distributing water to various parts of the plant to maintain operational stability. These pumps, mostly centrifugal pumps with double-suction impellers are usually operated continuously for long running hours for systems with large capacity demands due to their ability to deliver large flow rates at a constant head [1,2]. There is however a common problem of achieving a better cavitation performance over a wide operating range because traditional approach for impeller design often leads to the design effect not meeting the requirements at off-design conditions. This puts the downstream components at risk of being damaged since in most cases the flow passage gets blocked by the attached cavities [3,4]. In view of

this, the cooling water pumps are usually operated at rated design conditions to minimize the risk of cavitation which can lead to costly damage.

There has been an extensive literature on cavitation in centrifugal pump impellers over the past years, and these are readily available in open literature. Quite a number of these investigations predicted that there is some correlation between cavitation instabilities and changes in flow angle, the pressure gradient at cavity closure, as well as the flow rate and cavitation number [5,6]. More so, the unsteadiness in the pressure field vis-à-vis the rapid head-drop phenomenon that occurs during cavitation has been periodically analyzed in a centrifugal pump, and the reason for the head drop was attributed to the vortex generation in the cavitating region [7,8].

Pei [9] applied the L_9 (3^3) orthogonal design of experiments (DOE) and computational methods to improve the required net positive suction head (NPSHr) by 0.63 m. The relationship between the hub and shroud inlet angles have also been studied and established that a shroud blade angle of 30° improved cavitation performance [10]. The inverse design methodology has also been applied to parameterize the blade profile to improve suction performance and efficiency on a mixed flow pump impeller and diffuser [11]. Xu [12] performed a multi-objective optimization study using the Taguchi method. In his study, five design parameters of a centrifugal pump were sampled into 16 different impeller designs and optimized to improve design efficiency and cavitation performance.

Recently, there has been a shift from the single objective optimization methods to the application of genetic algorithms (GA) and surrogate models to find optimum global geometrical parameter combinations that can solve multi-objective optimization problems [13,14]. Jin [15] extensively reviewed the various surrogate models using their prediction accuracy, efficiency, and robustness, and concluded that for higher-order nonlinear problems, neural networks should be used. The application of artificial neural networks has gained much recognition in turbomachinery optimization. In centrifugal pumps, the radial bias neural network (RBNN) had the best prediction accuracy when compared with kriging and the response surface approximation model [16]. Moreover, Pei [13] carried out a multi-objective optimization on the inlet pipe shape of a vertical inline pump using artificial neural network (ANN) and multi-objective genetic algorithm (MOGA) to increase the efficiency over a wider range. Furthermore, the multi-layer neural network has been established to have a better prediction accuracy compared to the single-layer neural network [17].

Despite several optimization works on cavitation performance in centrifugal pumps, most of the studies have been focused on optimizing the inlet blade angle without focusing much on other impeller parameters such as the hub and shroud angles whose effect on cavitation performance has not been well researched. In addition, there is a common problem of achieving a better cavitation performance over a wider operating range in centrifugal pumps [18] since cavitation optimization studies have usually been centered on design and near-design flow conditions.

Therefore, in order to adapt to its multi-operating condition and broaden its non-cavitation operating range, an orthogonal scheme was designed to execute a multi-flow condition optimization for cavitation performance using a multi-layer feedforward neural network and the non-dominated sorting genetic algorithm II (NSGA-II). Since the traditional approach to predicting NPSHr is time consuming, a faster approach [19,20] was applied to reduce the simulation time during the optimization process. For this paper, a numerical anti-cavitation optimization design of the double-suction impeller was carried out at part load, the design point and at an overload condition to establish a set of optimum parameters that would best improve the suction performance at off-design flow conditions.

2. Optimization Procedure

Figure 1 shows the optimization procedure. The initial process was to sample the input bound variables based on an orthogonal design of experiment. Secondly, series of 3D model double-suction impellers were designed by bladegen in ANSYS 2019 R3 and CREO 5.0. ANSYS was adopted for the numerical simulations to obtain the objective function values, which was used to train the surrogate

models. The multi-objective problem was then solved to obtain 3D Pareto solutions, which were then verified by numerical simulation to determine the reliability of the optimization.

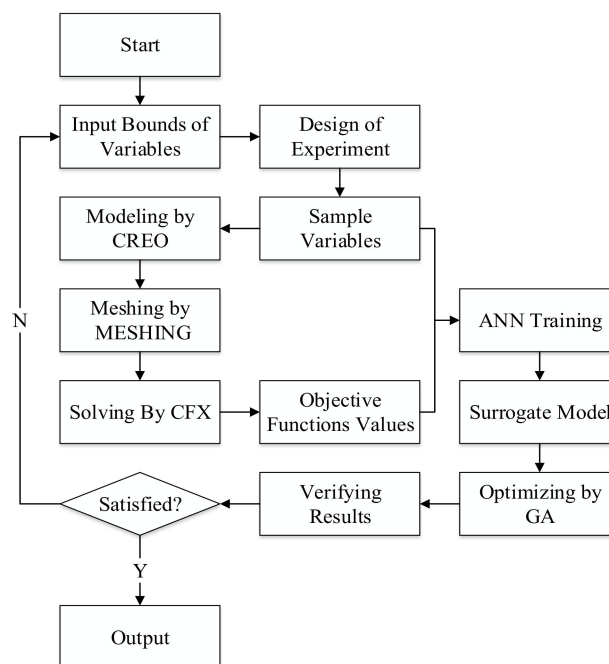


Figure 1. Flowchart of optimization process.

2.1. Objective Functions

During the optimization process of centrifugal pumps, the goals and targets are considered as significant indexes for performance evaluation. For this study, the NPSHr at three flow conditions were selected as the optimization targets. The objective function is to minimize the NPSHr at part loads ($0.8Q_d$), the nominal flow condition ($1.0Q_d$), and overload ($1.2Q_d$) flow conditions. These conditions are obtained by numerical calculations. The mathematical relation for NPSH is

$$NPSH = \frac{p - p_v}{\rho g} + \frac{V_{in}^2}{2g} \quad (1)$$

p and V_{in} represents static pressure and velocity at the pump inlet respectively, p_v is the vapor pressure, ρ is density, and g is the gravitational acceleration [21].

2.2. Design of Experiment

In deciding the optimization variables, the inlet diameter of the impeller, D_1 , the impeller diameter at the outlet, D_2 , the diameter of the hub D_h , and the blade width at outlet b_2 were held constant. This was to maintain the shape of the impeller due to space constrains of the suction and volute casing of the double-suction centrifugal pump. The choice of decision variables was limited to the blade inlet profile at hub and shroud. Three geometrical parameters, namely, hub inlet angle β_1 hub, middle inlet angle β_2 middle, and the shroud inlet angle β_3 shroud were selected as optimization variables. Each parameter was given a set of five values. Table 1 shows the decision variables and their set of values used for the parameterization. Orthogonal design of experiment was applied here to design the experimental scheme. From Table 1, there were 3 factors and 5 levels for the design. An orthogonal scheme of $L_{25} (3^5)$ was designed according to Equation (2). Twenty-five impeller models were generated based on the sampling results from the DOE using ANSYS bladegen. Table 2 is the

orthogonal scheme and the meridional shape of the impeller is shown in Figure 2. The position of the inlet profile was adjusted by a Bézier curve with three points.

$$L_m(n^p) \tag{2}$$

Table 1. Range of design variables.

	A	B	C
No	$\beta_{1hub}/^\circ$	$\beta_{2middle}/^\circ$	$\beta_{3shroud}/^\circ$
1	17	13	11
2	19	16	14
3	21	18	17
4	23	21	19
5	25	23	21

Table 2. Orthogonal scheme.

	A	B	C		A	B	C
No	$\beta_{1hub}/^\circ$	$\beta_{2middle}/^\circ$	$\beta_{3shroud}/^\circ$	No	$\beta_{1hub}/^\circ$	$\beta_{2middle}/^\circ$	$\beta_{3shroud}/^\circ$
1	17	18	17	14	25	23	17
2	17	16	14	15	19	18	21
3	19	13	17	16	25	16	21
4	21	16	11	17	17	21	19
5	23	16	17	18	17	23	21
6	21	13	21	19	17	13	11
7	21	21	17	20	23	21	21
8	23	18	19	21	25	18	11
9	25	13	19	22	19	23	14
10	19	16	19	23	21	18	14
11	21	23	19	24	23	13	14
12	23	23	11	25	19	21	11
13	25	21	14				

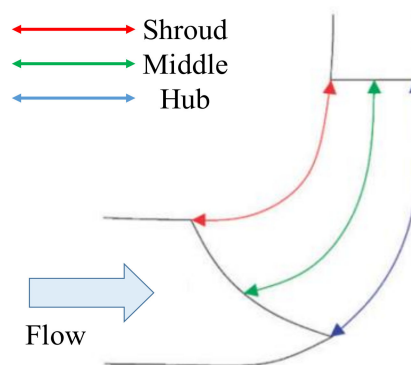


Figure 2. Meridional shape.

2.3. Surrogate Training and Optimum Solution Solving

Artificial neural network (ANN) was used for the surrogate modeling. The concept of ANN and MOGA has been explained in the previous works [13,14]. The Levenberg–Marquardt algorithm was adopted as the training algorithm since it has the fastest convergence rate. Tangent hyperbolic activation function (*tanh*) was applied because it has a much better recognition accuracy for multi-layer neural networks. For this study, a dual-layer feed-forward ANN with 10 hidden neurons was adopted. Figure 3 is the multi-layer feedforward ANN structures used for training the NPSHr objectives.

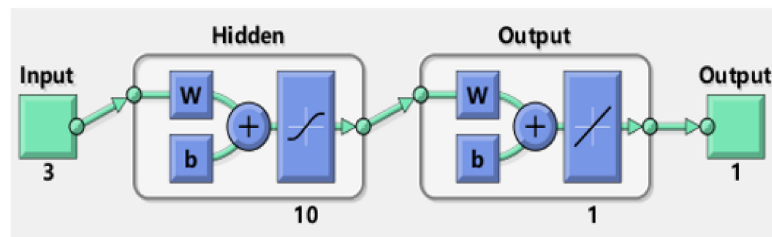


Figure 3. Artificial neural network (ANN) structure for the required net positive suction head (NPSHr) objective.

The mathematical relation for the ANN function is written as Equation (3), the activation function, \tanh is written as Equation (4) and the linear function as Equation (5).

$$y = g\left(\sum_{j=1}^n w_j^2 \times f\left(\sum_{k=1}^m w_{k,j}^1 x_k + b_n^1\right)\right) + b^2 \quad (3)$$

$$f(x) = \left[\frac{2}{(1 + e^{-2x})}\right] - 1 \quad (4)$$

$$g(x) = ax + b \quad (5)$$

To obtain the global Pareto frontier for the three-objective functions, the multi-objective genetic algorithm was applied to solve the problem. The problem for the three-objective optimization can be described as follows.

$$\left\{ \begin{array}{l} \text{find} \left\{ \begin{array}{l} \text{minimize } NPSHr \ 0.8Q_d = f_1 \\ \quad \quad \quad NPSHr \ 1.0Q_d = f_2 \\ \quad \quad \quad NPSHr \ 1.2Q_d = f_3 \end{array} \right. \\ \text{subject to} \\ \quad \quad \quad 17^\circ \leq A \leq 25^\circ \\ \quad \quad \quad 13^\circ \leq B \leq 23^\circ \\ \quad \quad \quad 11^\circ \leq C \leq 21^\circ \end{array} \right. \quad (6)$$

Since the problem was a three-objective problem, a 3D Pareto optimal solution was required. In construction of the Pareto solutions, the following input parameters were used. Population size was 200. A 0.8 Pareto-front population and 0.85 crossover fraction were applied with 1000 generations at a function tolerance of 10.

3. Tested Pump and Computational Domain

3.1. Description of Test Pump

The test object is a 250GS40 double-suction centrifugal pump that has a specific speed of 89.5. The flow domain has been divided into the semi-spiral suction domain, a shrouded impeller which has six twisted blades and a volute which also serves as the outlet domain. The test object is shown in Figure 4. Figure 4a shows the computational domain of the volute and suction unit and Figure 4b shows that of the impeller. The design parameters of the pump are presented in Table 3. The specific speed was derived as follows:

$$n_s = 3.65 \times \frac{N \times \sqrt{Q_d}}{60 \times H^{\frac{3}{4}}} \quad (7)$$

where n_s is specific speed, N (rpm) represents rotating speed, Q_d (m³/h) is the nominal flow rate, and H (m), is the design point head.

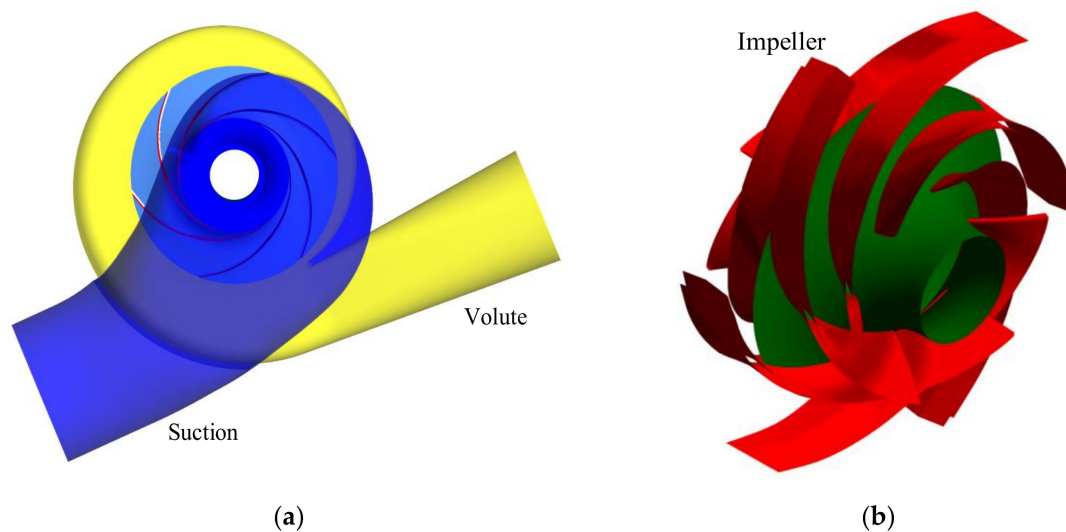


Figure 4. Computational domain of impeller, suction and volute.

Table 3. Design specifications of model pump.

Design Parameters	Value
Nominal flow rate, Q_d (m ³ /h)	500
Head, H (m)	40
Rotating speed, N (rpm)	1480
Blade number, z	6
Diameter of suction, D_s (mm)	250
Diameter at impeller inlet, D_1 (mm)	192
Diameter at impeller outlet, D_2 (mm)	365
Diameter of discharge, D_d (mm)	200
Efficiency, η (%)	84
NPSHr (m)	3.5

3.2. NPSHr Prediction Procedure

A novel NPSHr prediction method originally introduced by Ding et al. [19] was applied to speed up the calculation process due to the large sample size of the optimization cases. This new method has been compared with the traditional method of NPSHr prediction using the multi reference frame (MRF) model [20], and further applied to cavitation studies in the double-suction centrifugal pump by Pei [22] and Wang [14]. There are three main prediction steps, and a convergence method, which speeds up to the desired accuracy where convergence is not reached after the third step.

Step 1: The pump head is calculated by introducing a new boundary pair, which is flow rate at the inlet and static pressure at the outlet. The static pressure at the outlet p_{out} is estimated as follows.

$$P_{out}(1) = H(0) + P_{tot-in}(0) - H_D(0) = P_{out-in}(0) \quad (8)$$

p_{tot-in} here is the total pressure at the inlet.

Step 2: In step 2 the static pressure at the outlet is calculated to correspond to a 3% drop in the pump head. Here the static pressure is estimate as

$$P_{out}(2) = 0.97H_{100} - H_D(1) \quad (9)$$

Here, H_{100} , the head at 0% drop in head and H_D is the dynamic head.

Step 3: The third step is to adjust the errors to converge at the 3% head drop. The outlet static pressure for this step is calculated as

$$P_{out}(3) = 0.97H_{100} + P_{tot-in}(2) - H_D(2) \quad (10)$$

Step ($n + 1$): This step is applied when convergence is not achieved after the third step. This step has been explained in detail by Ding [19] and Pei [20]. Outlet static pressure is calculated as

$$P_{out}(n + 1) = 0.97H_{100} + n_3 - H_D(n) \quad (11)$$

3.3. Governing Equations

The time dependent Navier–Stokes equation is derived from the continuity equation [23] is given as

$$\frac{\partial \rho_m}{\partial t} + \frac{\partial}{\partial x_j}(\rho_m u_j) = 0 \quad (12)$$

$$\frac{\partial(\rho_m u_i u_j)}{\partial x_j} + \frac{\partial}{\partial t}(\rho_m u_i) = \frac{\partial P}{\partial x_i} + \frac{\partial}{\partial x_j} \left[(\mu + \mu_t) \left(\frac{\partial u_i}{\partial x_j} + \frac{\partial u_j}{\partial x_i} + \frac{2}{3} \frac{\partial u_k}{\partial x_k} \delta_{ij} \right) \right] \quad (13)$$

Shear stress transport (SST $k-\omega$) was applied since it has the advantages of both the $k-\omega$ and $k-\epsilon$ turbulence models [24,25]. To simulate cavitating flows, the equation of mass transport is built from the Rayleigh–Plesset equation, and is expressed as

$$\frac{\partial(\rho_v \alpha_v)}{\partial t} + \frac{\partial}{\partial x_j}(\rho_v \alpha_v u_j) = \dot{m} = \dot{m}^+ - \dot{m}^- \quad (14)$$

$$\dot{m}^+ = C_{vap} \frac{3r_g(1 - \alpha_v)\rho_v}{R_b} \sqrt{\frac{2}{3} \frac{\max(P_v - P, 0)}{\rho_l}} \quad (15)$$

$$\dot{m}^- = C_{cond} \frac{3\alpha_v \rho_v}{R_b} \sqrt{\frac{2}{3} \frac{\max(P - P_v, 0)}{\rho_l}} \quad (16)$$

From literature, the standardized values are $C_{vap} = 50$, $C_{cond} = 0.01$, $r_g = 5 \times 10^{-4}$, $R_b = 10^{-6}$ m, $\rho_v = 0.554$ kg/m³, $\rho_l = 1000$ kg/m³, and $p_v = 3169$ Pa [26,27].

3.4. Test of Grid Independence

For maximum simulation accuracy, the test object was meshed using high quality structural hexahedral mesh with ANSYS ICEM. To attain higher precision and boundary motion features, the grids were refined with large numbers and concentrated near the walls. Figure 5 presents an overview of the mesh topology. The volute tongue can be seen in Figure 5a, the impeller in Figure 5b, and suction tongue in Figure 5c. After building the mesh, a test of grid independence was carried out by building 5 independent grids to speed up the calculation time and still maintain accuracy. This was done at the nominal flow condition. It has been established that performance parameters such as head and efficiency are not sufficient enough during the test for grid independence [22,28]; hence, in this research, the influence of the different grid numbers on the volute wall pressure was considered. Monitor points were set in the volute for investigation as shown in Figure 6 and presented in Table 4. The effect of the mesh density on the pump head, efficiency and pressure was least felt at monitor points V1 and V7 as the total mesh number reached 4,266,423. Mesh III was therefore adapted for the numerical simulations to reduce computation load and time. The final mesh has an average Y-plus less than 50, and the distribution can be seen in Figure 7.

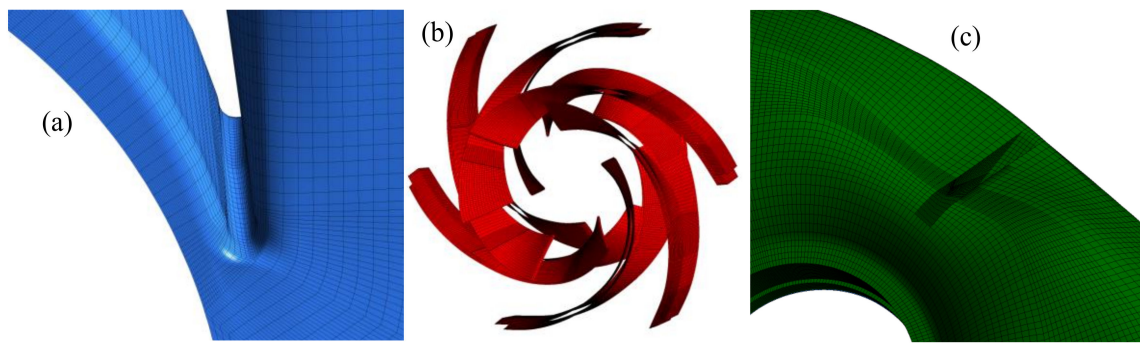


Figure 5. Mesh of calculation domain: (a) volute tongue, (b) impeller, and (c) suction tongue.

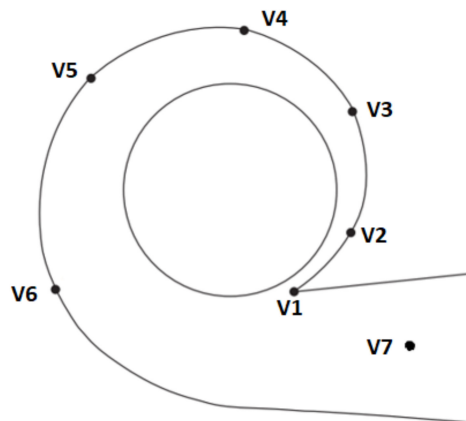


Figure 6. Monitors points in the volute.

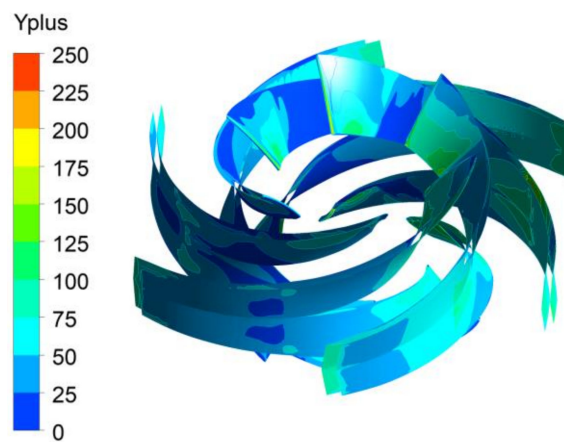


Figure 7. Yplus distribution on blade surface.

Table 4. Grid cells of the selected mesh.

Item	Mesh I	Mesh II	Mesh III	Mesh IV	Mesh V
Total Mesh	2,878,243	3,679,342	4,266,423	4,958,168	5,847,757
H/H_1	1.0000	1.1563	1.2211	1.2201	1.2213
η/η_1	1.0000	1.1324	1.3043	1.3044	1.3043
$p_{v1}/p_{v1,1}$	1.0000	1.1520	1.3112	1.3114	1.3111
$p_{v7}/p_{v7,1}$	1.0000	1.1562	1.2819	1.2822	1.2820

3.5. Numerical Calculation Setup

The computational domain was calculated using ANSYS 2019 R3 to solve the Reynolds-averaged Navier–Stokes equations. Water was used as the working fluid while assuming an isothermal heat

transfer of 25 °C. The SST ($k-\omega$) turbulence model was applied since its combined advantages can be extended by the automatic wall treatment to ensure the accuracy of the pressure gradient regardless of the distance to the nearest wall [24,25]. The direction of the flow was set normal to the boundary condition, and a smooth non-slip wall was applied. The default turbulence intensity level of 5% was applied at inlet based on similar works on centrifugal pumps with similar characteristics [14,29]. A high-resolution upwind scheme was applied to ensure accuracy and convergence consistency. At the domain interfaces, a frozen rotor with pitch angle of 360° was set between the rotor and the stator. The boundary conditions were specified as flow rate at inlet and static pressure at the outlet. The Zwart–Gerber–Belamri (ZGB) model was used for cavitation simulations. To determine the convergence criteria, maximum residual values of 10^{-5} were maintained, and iterations had to be periodic stable. Performance indicators were calculated as follows [21].

The Head:

$$H = \frac{P_{tot-out} - P_{tot-in}}{\rho g} \quad (17)$$

$p_{tot-out}$ and p_{tot-in} are the total pressures at outlet and inlet.

Shaft power:

$$P_s = T\omega \quad (18)$$

T denotes shaft torque while ω , is the angular speed.

Efficiency:

$$\eta = \frac{\rho g H Q}{P_s} \quad (19)$$

3.6. Description of Test System

The experimental test was performed in an open test rig system. Test schematics can be found in Figures 8 and 9 is the experimental setup system. The suction pipe has a diameter of 250 mm while the delivery pipe has a diameter of 200 mm. High precision WT200 pressure transmitters were installed directly in the pipes at the suction and discharge points. The pressure transmitter at the suction end had a measuring range of -0.1 to 0.1 MPa, whereas the outlet transmitter had a measuring range of 0 – 1.6 MPa. Their measurement uncertainty was 0.5%. The flow rate was measured with LWGY-200A electromagnetic flowmeter with an uncertainty of 0.07%. Hydraulic and cavitation tests were performed at design and non-design flow conditions. To determine the experimental uncertainty, the Type B evaluation was used, and the systematic uncertainty of the experiment was $\pm 0.411\%$. Further details of the experiments have been provided in our previous studies [20].

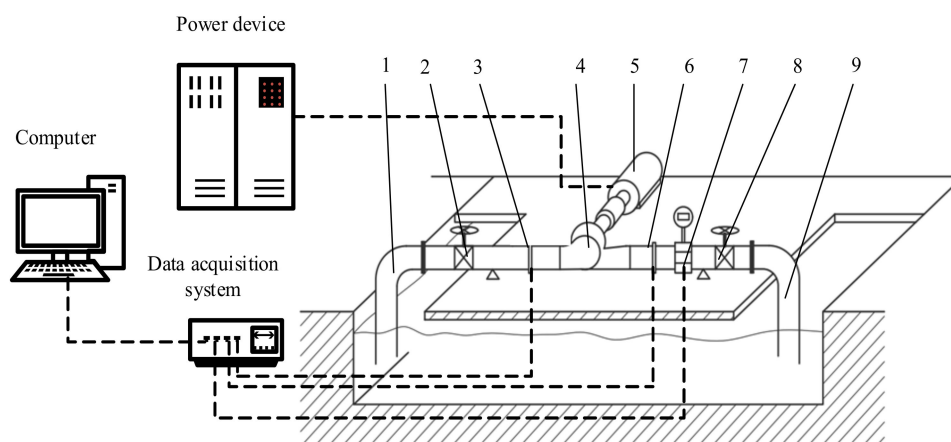


Figure 8. Schematics of the test setup. 1: Inlet pipe, 2(8): Valve, 3(6): Pressure transducer, 4: Tested pump, 5: Driven motor, 7: Magnetic flow meter, and 9: Outlet pipe.

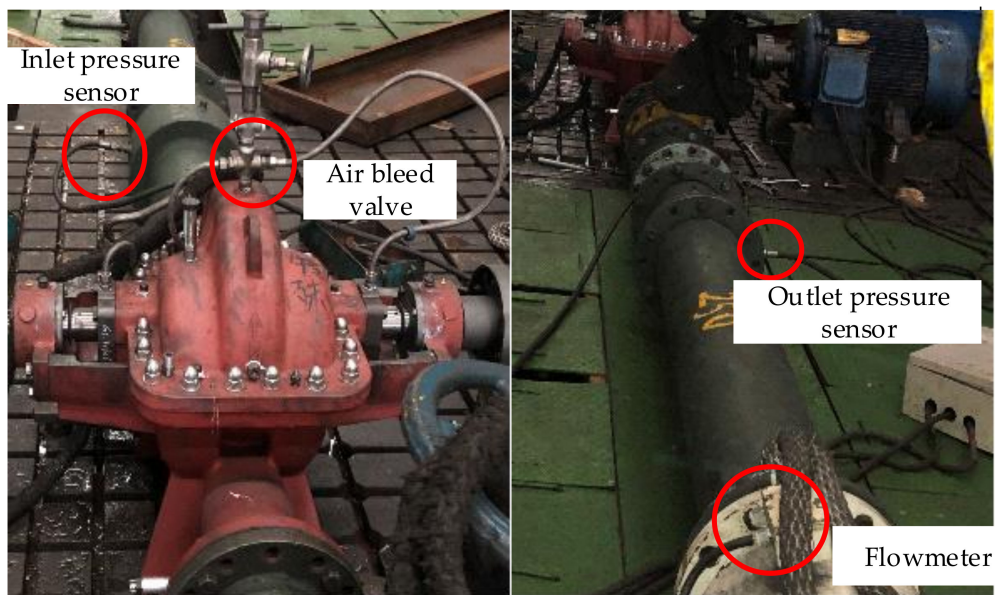


Figure 9. Experimental setup.

4. Discussion of Results

4.1. Validation of Numerical Method

To prove the reliability of the numerical approach, the test results were compared with the computation results and presented in Figure 10. The efficiency curve rose gently from deep part loads to the maximum point of 86.63% at 41.49 m head, and started a steeper decline. The trend was same for both the experiments and numerical results with deviations of 3.01% and 2.03% between the efficiency and head respectively. In the numerical simulations, a smooth wall was assumed. Practically, it is very expensive and difficult to achieve a very smooth surface, and this could account for the minimal deviations between the tests and simulation results. The numerical approach was therefore said to be reliable and suitable for the optimization studies since it agreed with the experiments.

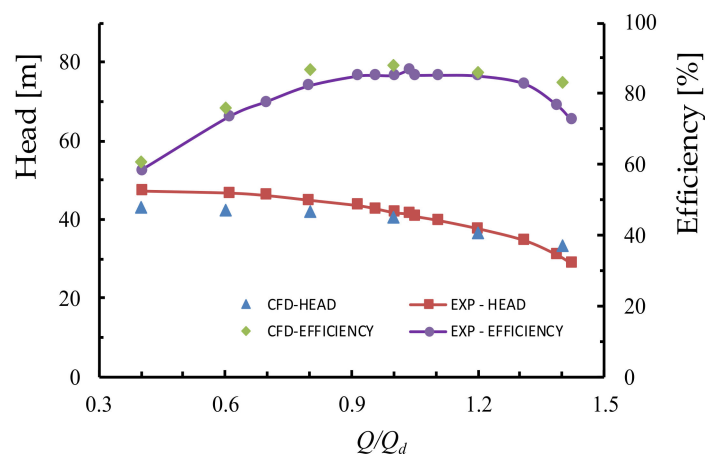
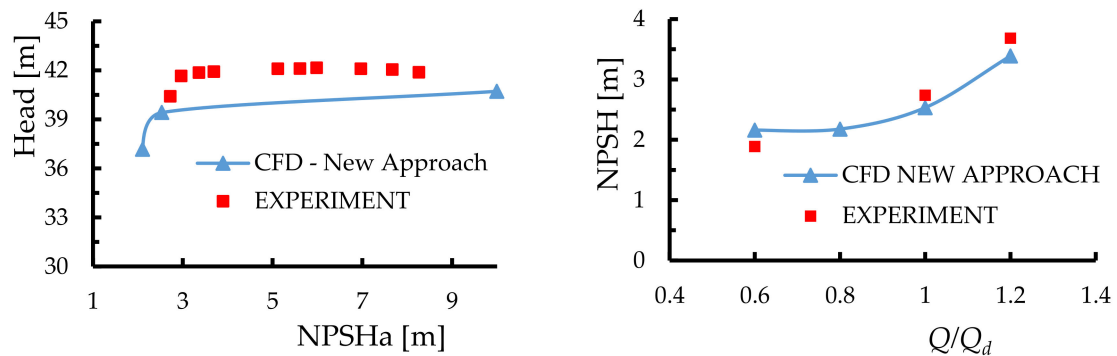


Figure 10. Validation with test results.

4.2. Cavitation Model Validation

The cavitation model was also validated with the test results to further confirm the reliability of the numerical method for cavitation flow simulations. At the nominal flow condition, (Figure 11a), the NPSHr was calculated in only three simulation attempts, which resulted in 3.12% drop in head at NPSHr = 2.628 m. At non-design flow conditions (Figure 11b), the suction performance for the

experimental test was well predicted by the numerical results and the maximum deviation was 4.05%. For all flow conditions, the NPSHr did not exceed the design NPSHr of the pump. At $0.6Q_d$ the computational results were higher than the test values but lower at design and overload conditions. This could also be attributed to the assumption of a smooth non-slip wall during the calculations. The minimum deviations confirm that the cavitation model can be reliable for NPSHr prediction for the optimization studies.



(a) Suction performance at design point

(b) Suction performance at off design points

Figure 11. Comparison of suction performance with test results at design and off design points.

4.3. Results from Optimization Studies

4.3.1. Orthogonal Test Results

The 25 impellers designed from Table 2 were simulated for the three flow conditions. Three of the parameter combinations were invalid. Table 5 gives the upper and lower bounds for the decision variables used for surrogate training, and the results from the orthogonal test is presented in Table 6. From direct analysis, it is observed that, majority of the schemes can satisfy the individual objectives; however, deciding the best scheme from the orthogonal results is difficult. It becomes necessary to apply surrogate models to search for the optimum parameters that would meet the objectives.

Table 5. Boundaries and variables for ANN.

Variables	A	B	C
Upper Bounds	17	13	11
Lower Bounds	25	23	21

4.3.2. Training of Surrogate Model

Artificial neural networks were adopted as the metamodel to build the relationship between the objective functions and decision variables. ANN was then trained to study the relationship between the input and output parameters. The strength of the relationship between the linear model and the dependent variable was determined through R^2 analysis. This determines the suitability of the surrogates for further optimization. Figure 12 shows the R^2 of the ANN models of the objective functions calculated as 0.9877 for $0.8Q_d$ (Figure 12a), 0.9805 for $1.0Q_d$ (Figure 12b), and 0.9759 for $1.2Q_d$ (Figure 12c), indicating that the ANN models for could be applied to the three-objective optimization since the prediction accuracy is high enough. Validation of a surrogate is a requirement hence a comparison of the ANN prediction and the CFD simulation results from Table 6 is drawn in Figures 13–15. From the graphs, the predicted ANN model values are in agreement with the CFD simulation values. The three conditions can all be used as objective functions in the three-objective optimization.

Table 6. Orthogonal scheme results.

Trial No.	$\beta_1/^\circ$			NPSHr (m)		
	Hub	Middle	Shroud	$0.8Q_d$	$1.0Q_d$	$1.2Q_d$
1	17	18	17	2.20493	2.47272	3.34366
2	17	16	14	2.242	2.4631	3.5327
3	19	13	17	2.239	2.60439	3.41053
4	21	16	11	2.13633	2.5389	3.49375
5	23	16	17	2.19513	2.49717	3.34304
6	21	13	21	2.32698	2.55007	3.25851
7	21	21	17	2.15205	2.37423	3.20435
9	25	13	19	2.11472	2.44115	3.34089
10	19	16	19	2.15242	2.48385	3.36682
11	21	23	19	2.1968	2.34822	3.12789
12	23	23	11	2.11707	2.46779	3.29704
13	25	21	14	2.19055	2.40843	3.20562
14	25	23	17	2.22882	2.49238	3.19525
15	19	18	21	2.27685	2.37688	3.32605
16	25	16	21	2.16954	2.46852	3.31924
17	17	21	19	2.19175	2.41485	3.21403
18	17	23	21	2.13016	2.49771	3.11064
19	17	13	11	2.11841	2.55672	3.32263
21	25	18	11	2.15538	2.52129	3.41646
22	19	23	14	2.21103	2.41971	3.2512
23	21	18	14	2.18358	2.47889	3.42864
25	19	21	11	2.19366	2.50587	3.49847

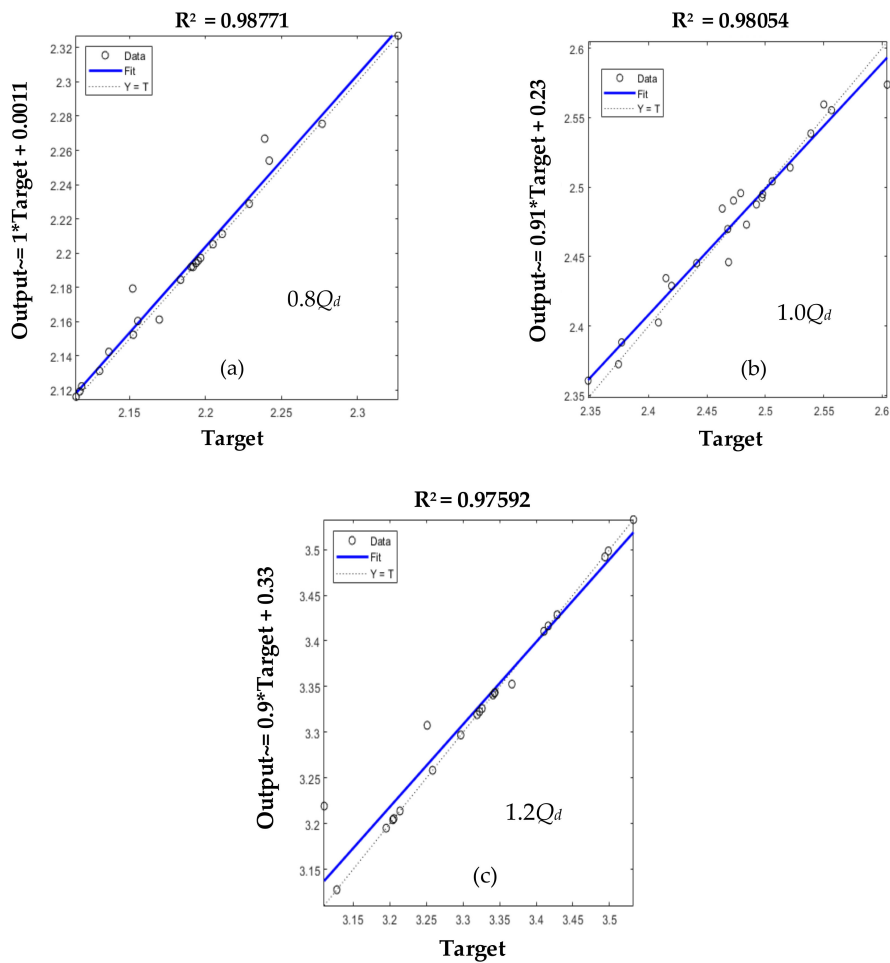


Figure 12. R^2 analysis of NPSHr at $0.8Q_d$, $1.0Q_d$ and $1.2Q_d$.

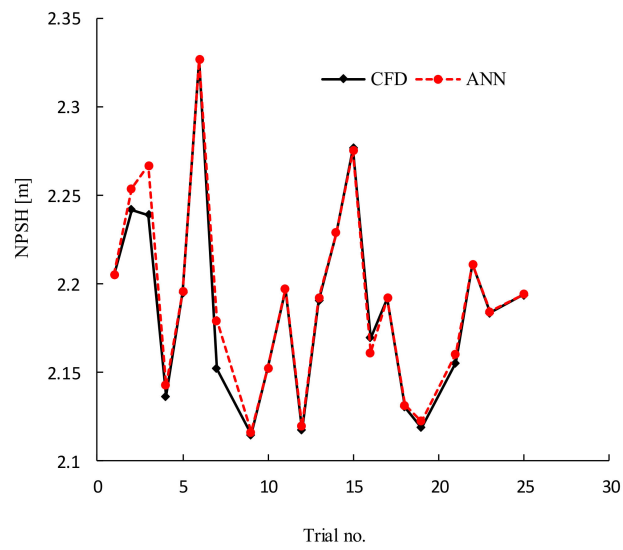


Figure 13. Validation of ANN NPSHr prediction with CFD at $0.8Q_d$.

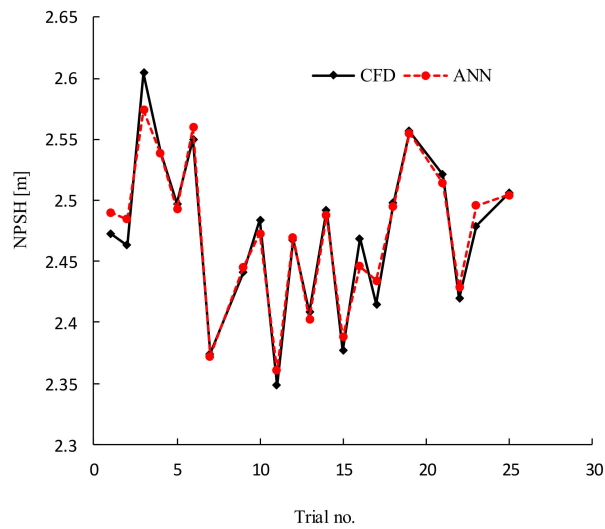


Figure 14. Validation of ANN prediction with CFD at $1.0 Q_d$.

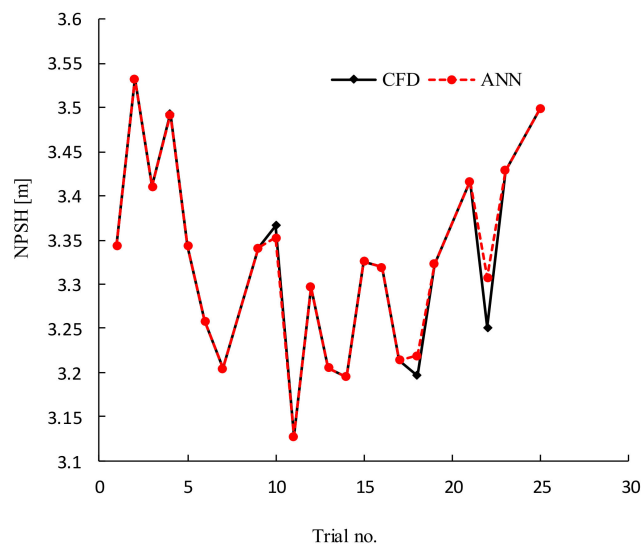


Figure 15. Validation of ANN prediction with CFD at $1.2 Q_d$.

4.3.3. Solutions to the Three-Objective Problem

The Pareto frontiers from ANN for the three objective functions have been presented in Figure 16. The optimum solutions were presented as blue points in the Pareto optimum front, and each point represents a model impeller. The Pareto solutions presented a set of 200 optimized impellers schemes that satisfied the optimization objective. Three best impeller schemes were selected and built according to the optimum decision variables in Table 7 and calculated by CFD.

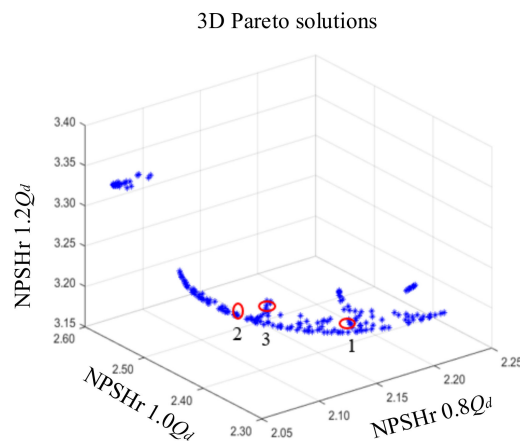


Figure 16. Pareto-frontiers from ANN.

Table 7. Variables for optimum cases.

No	A	B	C	Results		
	β_{1hub}°	$\beta_{2middle}^{\circ}$	$\beta_{3shroud}^{\circ}$	$0.8Q_d$	$1.0Q_d$	$1.2Q_d$
1	19.4863	21	16.767	2.108	2.353	3.215
2	19.3992	21	17.262	2.124	2.340	3.210
3	19.3079	21	17.566	2.134	2.334	3.208

Table 8 presents the CFD results from the optimized cases. The CFD predictions were very close to the 3D Pareto predictions rendering the results valid. At part load and design conditions, optimized case 1 performed better than the other cases. At overload condition, optimized case 2 performed better than optimized case 1. For all three cases, optimized case 3 had the worst cavitation performance although the optimization objective was achieved in all cases. Moreover, the head at the design condition was compared for the three flow conditions. Case 3 had the worst head of 38.73 m. Comparing the three cases, the best single case for the optimization objective is case 1. The head comparison at design point is in Table 9.

Table 8. Comparison of original case and best optimal cases.

Name	NPSHr 0.8Q	NPSHr 1.0Q	NPSHr 1.2Q
Original	2.176 m	2.532 m	3.39 m
Case 1	2.089 m	2.358 m	3.271 m
Case 2	2.132 m	2.419 m	3.254 m
Case 3	2.132 m	2.44 m	3.288 m

Table 9. Head comparison at $1.0Q_d$.

Name	Head (m)
Original	40.52
Case 1	40.05
Case 2	39.98
Case 3	38.73

4.3.4. Comparison of Suction Performance—Optimized and Original Design

The suction performance of the three optimum cases were compared in Figure 17. In each optimized condition, the results were good. All the three optimum cases performed better, however optimized case 1 performed best at all the flow conditions. At $0.8Q_d$, the effect of the optimization was less for all flow conditions. The selected optimum case was compared with the original model in Figure 18. It was seen that for the original pump, reducing the hub inlet angle from 17° to 16.77° and increasing the hub inlet angle from 15° to 19.49° gave a remarkable improvement of 6.9% in suction performance at $1.0Q_d$. Cavitation performance was improved by 3.5% at overload condition, 4% $0.8Q_d$ and 5% $0.6Q_d$ at non-design conditions. Comparing with the test results the optimization achieved its objective of improving the cavitation performance at non-design points.

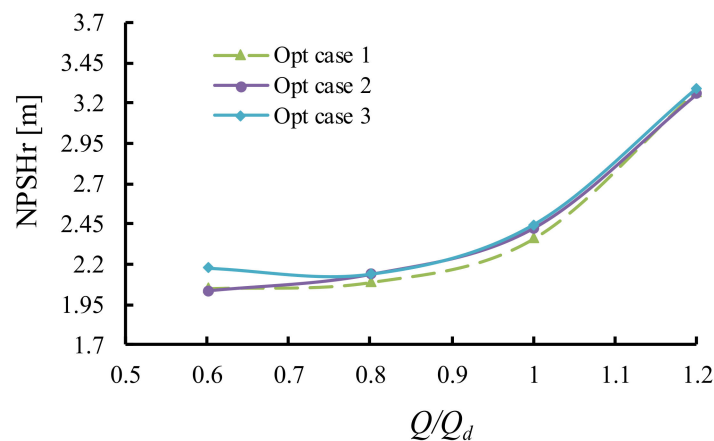


Figure 17. Suction performance of optimized cases and experiments.

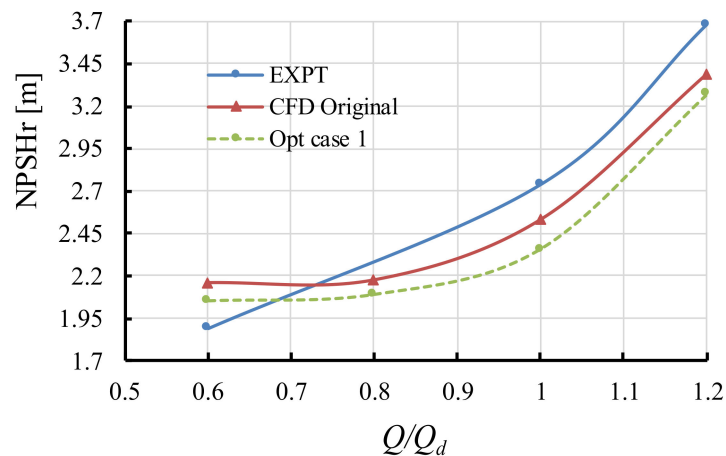


Figure 18. Verification of optimized case 1 with original model.

4.3.5. Internal Flow Analysis

The internal flow of the optimized impeller (case 1) was compared with the original model to reveal the optimization effect on the flow structure. Figure 19 compares the variation of pressure on the blade surface for the three flow conditions that were optimized. At $0.8Q_d$ flow rate, the pressure contour for the original and optimized blades were almost uniform. Looking at the pressure variation the difference was very minimal. At the design condition, the very low pressure areas at the blade leading regions had reduced after optimization. Compared to the original model the low pressure regions covered a wider area than in the optimized model which is an indication that cavitation performance could improve. At overload condition, the low pressure regions within the optimized blade had narrowed as well. The difference was quite clear as compared to the design condition

and part load. The extremely low pressure contours at the leading regions had reduced too. For the three flow conditions, the low pressure distribution on the blade leading regions were reduced after optimization and this can translate to an improvement in suction performance.

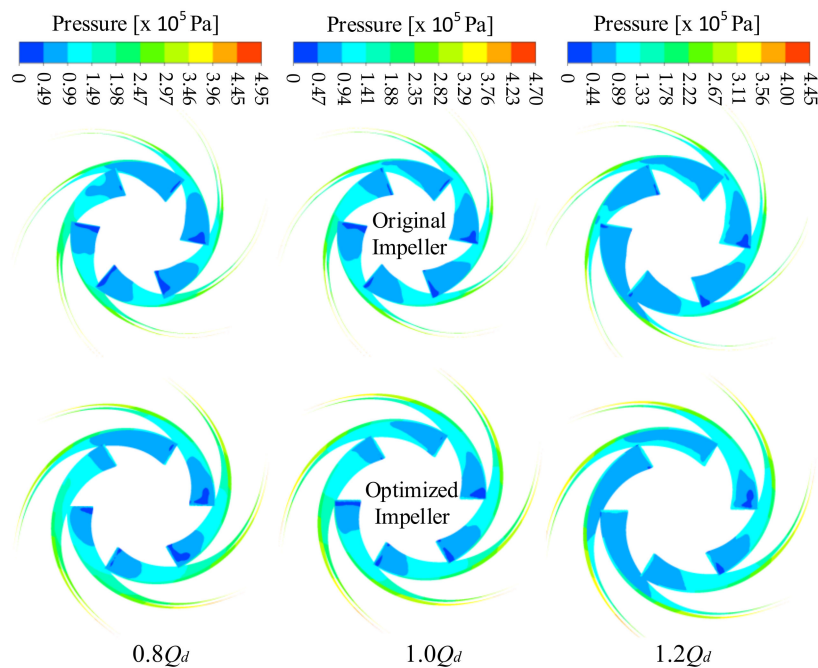


Figure 19. Pressure distribution on blade surface at 0% head drop.

In Figure 20, the pressure fluctuation on the blade surface at critical cavitation conditions were compared. The comparison was done at the critical cavitation point of the original impeller (at NPSH = 2.16 m, NPSH = 2.35 m, and NPSH = 3.16 m), for $0.8Q_d$, $1.0Q_d$, and $1.2Q_d$, respectively. For all the flow conditions, the variation of pressure along the blade surface was improved as compared to the original model. The original model had lower blade surface pressures than the optimized case, indication that suction performance would improve for all the three conditions investigated. The streamline distribution in the impeller flow channel was also analyzed for the various flow conditions in Figure 21 at no cavitation condition. At $0.8Q_d$ part load condition, the flow was distorted in two impeller channels of the original impeller. In one of the channels, some vortex was observed between the leading region and the middle of the impeller. Towards the trailing region the flow separated before normalizing. For the optimized impeller, the flow was uniform, and there was no vortex or separation. The streamline in the channels were uniform in both the original and optimized models at $1.0Q_d$ and $1.2Q_d$, respectively.

4.3.6. Attached Cavity Distribution in the Flow Domain

To clearly see the difference in attached cavity distribution, the critical cavitation point in the original model for each flow rate was used as the reference condition. The cavity distribution in the impeller, suction, and volute of the optimized impeller was compared to the original impeller for that point. Figure 22 is a comparison of the attached cavity distribution in the impeller for different flow conditions. At $0.8Q_d$, the attached cavities in the impeller reduced slightly at NPSH = 2.176, which is the critical cavitation point of the original model. At the design condition, a clear difference was observed. The bubbles covered the entire leading regions in the original impeller. In the optimized model, however, the cavity distribution had reduced, and portions of the leading edge were free from cavitation bubbles at NPSH = 2.53 m. The overload condition was similar to the design condition. Some parts of the leading edge were free from attached cavities; however, the difference in cavity distribution between the two impellers at overload condition was less.

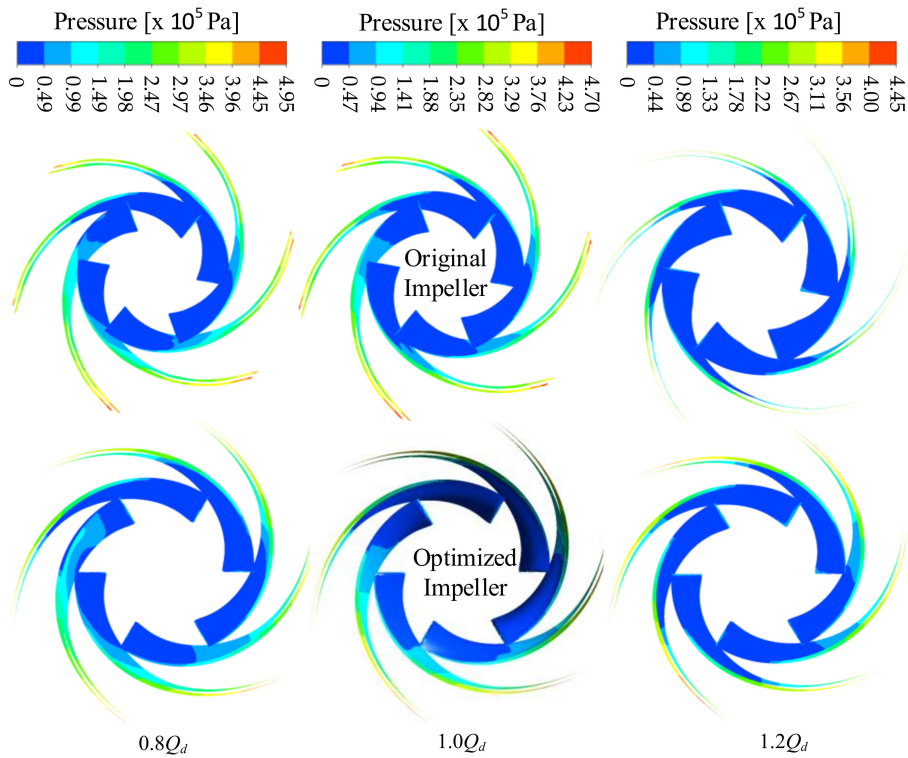


Figure 20. Pressure distribution on blade surface at 3% head drop.

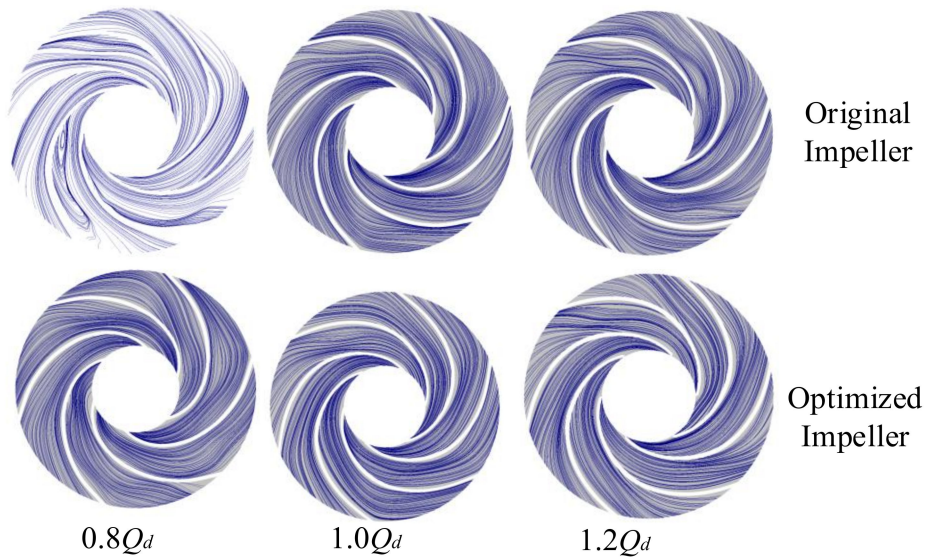


Figure 21. Streamline pattern in impeller channel.

In the suction domain, cavitation occurred around the suction rings. At part load, the attached cavity distribution was not symmetric in both designs. The suction ring at impeller inlet 1 (Figure 4) had cavities made up of bubbles forming around it. It was, however, observed after the optimization that the attached cavities in the suction unit with the optimized impeller had reduced at the critical cavitation point (NPSH = 2.176 m) of the original model. Cavity distribution in the suction at the design point was compared at NPSH = 2.532 m. This was similar to part load condition. Bubbles appeared on suction ring at impeller inlet 1, and there was a reduction in the attached cavities around the suction ring. For $1.2Q_d$, the original impeller had bubbles on both rings. In the optimized model, the cavities had reduced to a single suction ring when the comparison was done at NPSH = 3.39 m. Only the suction ring at impeller inlet 2 had attached cavity distributions. Generally, there was reduction in

cavitation bubbles for all flow conditions. This meant that the suction performance had improved for all three conditions and the optimization target has been achieved. Figure 23 shows the bubble distribution in the suction domain.

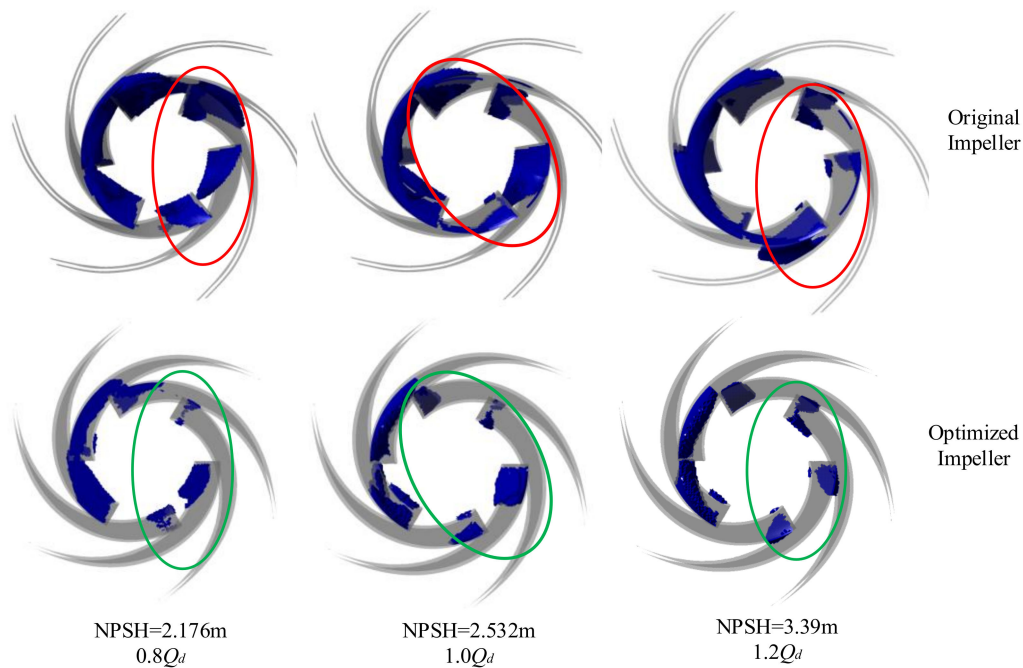


Figure 22. Bubble distribution in the impeller.

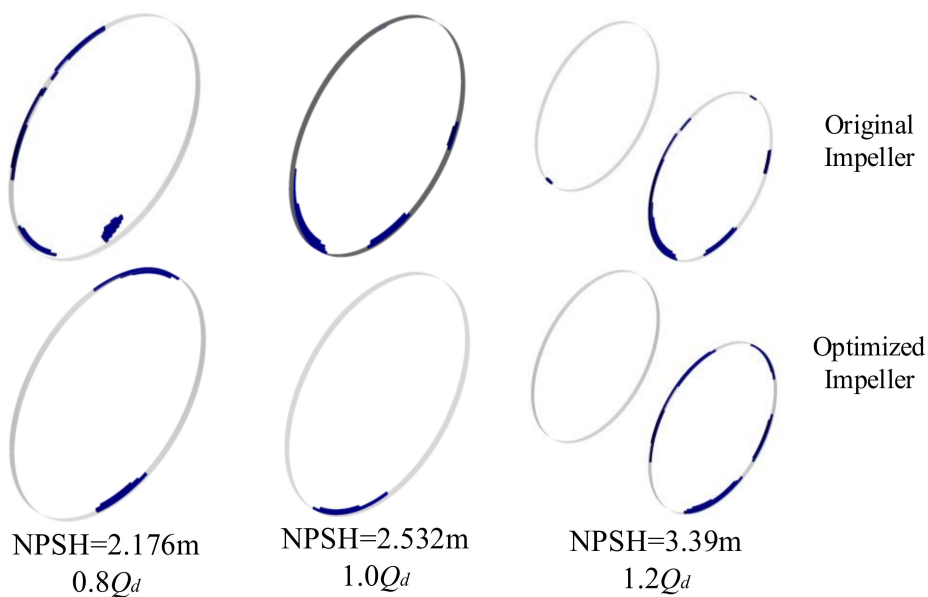


Figure 23. Attached cavity distribution in the suction.

5. Conclusions

Cavitation has been a treat to cooling water circulation pumps leading to reduced efficiency and damage of pump impellers. Hence, to improve the anti-cavitation performance and ensure longer life and reliability of cooling water circulation pumps, a multi-parameter and a multi-condition optimization approach was designed. In the optimization design, a dual-layer feedforward artificial neural network and genetic algorithm was then applied to improve the cavitation performance of the double-suction impeller over a wider range of operating conditions. The results from the study are as follows:

1. For the best case, there was a 6.9% improvement of suction performance at the design point. At non-design flow conditions, the cavitation performance was improved by 3.5% at $1.2Q_d$ overload condition, 4% at $0.8Q_d$, and 5% at $0.6Q_d$.
2. The pressure distribution on the blade was improved compared to the original model, and the streamline at $0.8Q_d$ was improved also.
3. The attached cavity distribution in the impeller and suction were lower than the original model when they were compared at NPSH = 2.176 m for $0.8Q_d$, at NPSH = 2.532 m for the nominal flow condition, and at NPSH = 3.36 m overload condition of $1.2Q_d$.
4. Finally, in this optimization, the suction performance of the double-suction centrifugal pump was improved at non-design flow conditions using a faster method for cavitation flow simulations. This can serve as a theoretical reference for pump optimization design against cavitation.

Author Contributions: Conceptualization, W.W. and Y.L.; methodology, M.K.O. and S.Y.; software, M.K.O.; validation, J.L. and B.Z.; formal analysis, W.W., Y.L., M.K.O., and B.Z.; writing—original draft preparation, M.K.O.; writing—review and editing, M.K.O. and W.W.; and project administration, S.Y. All authors have read and agreed to the published version of the manuscript.

Funding: This work is supported by the Natural Science Foundation of Jiangsu Province (Grant No. BK20190851), Primary Research & Development Plan of Shandong Province (Grant No. 2019TSLH0304), Natural Science Foundation of China (Grant No. 51879121, 51579104) and Primary Research & Development Plan of Jiangsu Province (Grant No. BE2019009-1).

Conflicts of Interest: The authors declare no conflict of interest.

References

1. Osman, M.K.; Wang, W.; Yuan, J.; Zhao, J.; Wang, Y.; Liu, J. Flow loss analysis of a two-stage axially split centrifugal pump with double inlet under different channel designs. *Proc. Inst. Mech. Eng. Part C J. Mech. Eng. Sci.* **2019**, *233*, 5316–5328. [[CrossRef](#)]
2. Pei, J.; Wang, W.; Pavesi, G.; Osman, M.K.; Meng, F. Experimental investigation of the nonlinear pressure fluctuations in a residual heat removal pump. *Ann. Nucl. Energy* **2019**, *131*, 63–79. [[CrossRef](#)]
3. Kang, C.; Mao, N.; Zhang, W.; Gu, Y. The influence of blade configuration on cavitation performance of a condensate pump. *Ann. Nucl. Energy* **2017**, *110*, 789–797. [[CrossRef](#)]
4. Wei, Z.; Yang, W.; Xiao, R. Pressure Fluctuation and Flow Characteristics in a Two-Stage Double-Suction Centrifugal Pump. *Symmetry* **2019**, *11*, 65. [[CrossRef](#)]
5. Tani, N.; Yamanishi, N.; Tsujimoto, Y. Influence of flow coefficient and flow structure on rotational cavitation in inducer. *J. Fluids Eng.* **2012**, *134*, 021302. [[CrossRef](#)]
6. Kobayashi, K.; Chiba, Y. Numerical simulation of cavitating flow in mixed flow pump with closed type impeller. In Proceedings of the ASME 2009 Fluids Engineering Division Summer Meeting, Vail, CO, USA, 2–6 August 2009; pp. 339–347.
7. Li, X.; Yuan, S.; Pan, Z.; Yuan, J.; Fu, Y. Numerical simulation of leading edge cavitation within the whole flow passage of a centrifugal pump. *Sci. China Technol. Sci.* **2013**, *56*, 2156–2162. [[CrossRef](#)]
8. Fu, Q.; Zhang, F.; Zhu, R.; He, B. A systematic investigation on flow characteristics of impeller passage in a nuclear centrifugal pump under cavitation state. *Ann. Nucl. Energy* **2016**, *97*, 190–197. [[CrossRef](#)]
9. Pei, J.; Yin, T.; Yuan, S.; Wang, W.; Wang, J. Cavitation optimization for a centrifugal pump impeller by using orthogonal design of experiment. *Chin. J. Mech. Eng.* **2017**, *30*, 103–109. [[CrossRef](#)]
10. Dönmez, A.H.; Yumurtacı, Z.; Kavurmacioğlu, L. The Effect of Inlet Blade Angle Variation on Cavitation Performance of a Centrifugal Pump: A Parametric Study. *J. Fluids Eng.* **2018**, *141*, 021101. [[CrossRef](#)]
11. Bonaiuti, D.; Zangeneh, M.; Aartojarvi, R.; Eriksson, J. Parametric Design of a Waterjet Pump by Means of Inverse Design, CFD Calculations and Experimental Analyses. *J. Fluids Eng.* **2010**, *132*, 031104. [[CrossRef](#)]
12. Xu, Y.; Tan, L.; Cao, S.; Qu, W. Multiparameter and multiobjective optimization design of centrifugal pump based on orthogonal method. *Proc. Inst. Mech. Eng. Part C J. Mech. Eng. Sci.* **2017**, *231*, 2569–2579. [[CrossRef](#)]
13. Pei, J.; Gan, X.; Wang, W.; Yuan, S.; Tang, Y. Multi-objective Shape Optimization on the Inlet Pipe of a Vertical Inline Pump. *J. Fluids Eng.* **2019**. [[CrossRef](#)]


14. Wang, W.; Osman, M.K.; Pei, J.; Gan, X.; Yin, T. Artificial Neural Networks Approach for a Multi-Objective Cavitation Optimization Design in a Double-Suction Centrifugal Pump. *Processes* **2019**, *7*, 246. [[CrossRef](#)]
15. Jin, R.; Wei, C.; Simpson, T.W. Comparative studies of metamodelling techniques under multiple modelling criteria. *Struct. Multidiscip. Optim.* **2001**, *23*, 1–13. [[CrossRef](#)]
16. Wang, W.; Pei, J.; Yuan, S.; Zhang, J.; Yuan, J.; Xu, C. Application of different surrogate models on the optimization of centrifugal pump. *J. Mech. Sci. Technol.* **2016**, *30*, 567–574. [[CrossRef](#)]
17. Pei, J.; Wang, W.; Osman, M.K.; Gan, X. Multiparameter optimization for the nonlinear performance improvement of centrifugal pumps using a multilayer neural network. *J. Mech. Sci. Technol.* **2019**, *33*, 2681–2691. [[CrossRef](#)]
18. Tao, R.; Xiao, R.; Zhu, D.; Wang, F. Multi-objective optimization of double suction centrifugal pump. *Proc. Inst. Mech. Eng. Part C J. Mech. Eng. Sci.* **2018**, *232*, 1108–1117. [[CrossRef](#)]
19. Ding, H.; Visser, F.; Jiang, Y. A practical approach to speed up NPSHR prediction of centrifugal pumps using CFD cavitation model. In Proceedings of the ASME 2012 Fluids Engineering Division Summer Meeting collocated with the ASME 2012 Heat Transfer Summer Conference and the ASME 2012 10th International Conference on Nanochannels, Microchannels, and Minichannels, Rio Grande, PR, USA, 8–12 July 2012; pp. 505–514.
20. Pei, J.; Osman, M.K.; Wang, W.; Appiah, D.; Yin, T.; Deng, Q. A Practical Method for Speeding up the Cavitation Prediction in an Industrial Double-Suction Centrifugal Pump. *Energies* **2019**, *12*, 2088. [[CrossRef](#)]
21. Güllich, J.F. *Centrifugal Pumps*; Springer: Berlin/Heidelberg, Germany, 2010.
22. Pei, J.; Osman, M.K.; Wang, W.; Yuan, J.; Yin, T.; Appiah, D. Unsteady flow characteristics and cavitation prediction in the double-suction centrifugal pump using a novel approach. *Proc. Inst. Mech. Eng. Part A J. Power Energy* **2020**, *234*, 283–299. [[CrossRef](#)]
23. Medvitz, R.B.; Kunz, R.F.; Boger, D.A.; Lindau, J.W.; Yocum, A.M.; Pauley, L.L. Performance analysis of cavitating flow in centrifugal pumps using multiphase CFD. *J. Fluids Eng.* **2002**, *124*, 377–383. [[CrossRef](#)]
24. Menter, F.R. Two-equation eddy-viscosity turbulence models for engineering applications. *AIAA J.* **1994**, *32*, 1598–1605. [[CrossRef](#)]
25. Bardina, J.; Huang, P.; Coakley, T.; Bardina, J.; Huang, P.; Coakley, T. Turbulence modeling validation. In Proceedings of the 28th Fluid Dynamics Conference, Snowmass Village, CO, USA, 29 June–2 July 1997; p. 2121.
26. Zwart, P.J.; Gerber, A.G.; Belamri, T. A two-phase flow model for predicting cavitation dynamics. In Proceedings of the Fifth International Conference on Multiphase Flow, Yokohama, Japan, 30 May–3 June 2004.
27. Mejri, I.; Bakir, F.; Rey, R.; Belamri, T. Comparison of computational results obtained from a homogeneous cavitation model with experimental investigations of three inducers. *J. Fluids Eng.* **2006**, *128*, 1308–1323. [[CrossRef](#)]
28. Pei, J.; Zhang, F.; Appiah, D.; Hu, B.; Yuan, S.; Chen, K.; Asomani, S. Performance Prediction Based on Effects of Wrapping Angle of a Side Channel Pump. *Energies* **2019**, *12*, 139. [[CrossRef](#)]
29. Tang, X.; Zou, M.; Wang, F.; Li, X.; Shi, X. Comprehensive Numerical Investigations of Unsteady Internal Flows and Cavitation Characteristics in Double-Suction Centrifugal Pump. *Math. Probl. Eng.* **2017**, *2017*, 1–13. [[CrossRef](#)]



© 2020 by the authors. Licensee MDPI, Basel, Switzerland. This article is an open access article distributed under the terms and conditions of the Creative Commons Attribution (CC BY) license (<http://creativecommons.org/licenses/by/4.0/>).

Article

Research on the Application of Partial Similarity for a 1-1/2 Axial Compressor

Hong Xie , Moru Song  and Bo Yang *

School of Mechanical Engineering, Shanghai Jiaotong University, Shanghai 200240, China; xiehong1211@sjtu.edu.cn (H.X.); samuel0624@sjtu.edu.cn (M.S.)

* Correspondence: byang0626@sjtu.edu.cn; Tel.: +86-21-3420-6871

Received: 18 August 2020; Accepted: 7 September 2020; Published: 9 September 2020



Abstract: In this paper, a method based on the partial similarity principle is presented to improve the aerodynamic design with low cost and high accuracy for a 1-1/2 axial compressor. By means of this method, during the process of a similar design, the machine Mach number and flowrate coefficient are maintained. The flow similarity between the prototype and its large-scaled alternative was observed, according to a detailed analysis of flow fields of rotor and stator. As well, the relative discrepancies of isentropic efficiency and pressure ratio between two models are 1.25% and 0.4% at design point, respectively. Besides, their performance curves agreed very well in the whole operating range. Moreover, it was also found that the flow similarity between the two models can be maintained under unsteady working conditions. Thereafter, in order to investigate the impact of stability optimization method on the similarity principle, casing treatment with single circumferential groove was applied to these two models. The flow similarity was still maintained and the flowrate near the stall was reduced about 1.1% with negligible deterioration of the overall performance.

Keywords: partial similarity principle; flow similarity; stability improvement

1. Introduction

A high-pressure axial compressor is one of the three major parts in the state-of-the-art aero-engine, and this kind of compressor is one of the most complicated products among all compressor technology [1]. With the increasing performance and stability demands, it is vital to obtain the in-depth understanding of its internal intricate flow regimes [2]. Under the current experimental conditions, it is too difficult and hazardous to conduct experiments on the high-pressure and high-speed compressors. Consequently, low-speed and large-scale model testing developed into an achievable and reliable method, due to the benefits of low cost, better accuracy and relatively low risk [3]. The prototype can be scaled-up and its rotation speed is reduced accordingly; then thorough measurements can be realized by easily to investigate flow interactions.

The concept of low-speed model testing was first presented by Wisler in the study of exit stages in the core compressor [4]. Then, this method was applied for loss reduction and performance improvement with structural optimization [5]. Robinson improved the end-wall flow pattern in a four-stage, low-speed axial compressor with end-bent blading technology [6]. Lyes optimized the high-pressure compressor through research on blade bending and sweeping based on a low-speed model [7], which was also used for sweep and dihedral blading studies by RR Company and Cambridge University [8,9]. Besides, Boos and Lange also carried out a high loaded blading investigation on this large-scale, low-speed compressor [10,11]. Zhang to reached performance optimization of a low-speed axial rotor by three-dimensional (3D) optimization with numerical computation, and then the experiments were carried out for validation of the numerical results [12,13]. Zhang summarized four procedures with which to achieve the whole process of compressor scaling and performance

optimization. The procedures included establishing a low-speed model that behaves similarly in a flow field to the high-speed compressor; detailed and accurate flow field measurement in the low-speed model; revising the design for the performance improvement; and the verification of new design methodology for the high-speed compressor at last [14]. The research above all employed the same modeling principles as that of Wisler [3]. These principles focused on some geometric parameters and aerodynamic parameters, such as the blade surface pressure and velocity distribution, and ignored the Mach number and Reynolds number.

However, the model principles mentioned above brought about some shortages. At first, the flow field is complex in 3D space, so it is not adequate to just keep the surface aerodynamic parameters the same. Then, the low-speed four-repeating-stage, studied by Wisler [3] and Zhang [14], required achieving a repeating condition for the similar inlet and outlet aerodynamic parameters. However, only the third stage can be used for the investigation, leading to wasted time and money. Additionally, this low-speed model can only be used for the investigation of a single stage, and cannot be used for multi-stage investigations. In addition, this model can be only used for the investigation at design point, but investigations at off-design points need to be similar. Besides, this kind of scaling process, based on the inverse method, is time-consuming and complicated. Finally, there is an unavoidable shortcoming of this model principle. The principle cannot be used for the transonic compressor or stage, because the shock waves' effects cannot be evaluated. Consequently, it is necessary to propose a simple, convenient, wider-in-applicability and relatively less disadvantages methodology for high-to-low-speed compressor transformation.

In recent decades, the scaling method for the low-speed model had been adopted by many researchers. The effects of Re on performance similarity were theoretically studied by Ma [15], and it has been proven that it is very important to maintain Ma in some cases [16,17]. In order to fulfill complete flow similarity, Ma and Re need to be identical for a high-speed compressor and low-speed model [18,19]. Nevertheless, it is almost impossible to maintain Re and Ma simultaneously, resulting in a performance difference between the prototype and the low-speed model. In practical applications, effects caused by changed Re can be compensated by some modifications of structural parameters [20,21]. Then, the Re could be ignored and the scaling process could be simplified accordingly, and this scaling laws can be summarized as a partial similarity principle. In this study, the partial similarity principle is innovatively used for the high-to-low transformation in the axial compressor.

The optimization of the compressor is the ultimate objective after successful establishment of the low-speed model. The stable operating range is one of the most vital objectives, and the delay of stall is an efficient method. Spike disturbance is often occurred in a low-speed compressor [22], and there are two criteria necessary for the emergence of spike disturbances, both of which are related to the tip clearance flow. One of the criteria is that the interface between the tip leakage flow and main flow aligns with the leading-edge plane [23]. Casing treatment technology has been proven to be a successful method for enhancing the stability margin of an axial compressor [24]. The interface can be delayed downstream under the impact of the casing treatment, resulting in better stall margin.

Two kinds of casing treatment are most commonly investigated. The first employs a lot of slots which are cut into the end-wall [25]. The stall margin of a compressor with slots can be improved largely, but with a large efficiency penalty [26]. The other one employs a single or several grooves which are cut into the end-wall circumferentially [27]. The stall margin improvements of a compressor with grooves are smaller than those of the first one, but the efficiency penalty is decreased [28]. Zhao concluded that the axial location had the most important effect on the stall margin improvement [29]. Houghton and Day obtained two optimum axial locations by applying a sequence of single-groove casings in two low-speed compressors—one was near the leading edge and the other near the mid-chord [30]. Du depicted that the optimal groove location in the low-speed compressor is 57% along the axial chord nearing the mid-chord [31], which coincided with the experiment results of Bailey [32].

In this study, a low-speed and large-scale axial compressor was fabricated from a high-pressure and high-speed prototype based on the partial similarity principle, the similar flow fields of which

were validated by numerical computation. Then, in order to investigate whether the flow similarity can be contained when using the similarity principle, casing treatment with single circumferential groove was applied to these two models. Meanwhile, in this study, performance experiments were carried out to validate the reliability of the numerical method. The aim of this paper is to propose a method which can be used conveniently and quickly for a type of compressor with small dimensions and high rotation speed, rather than a certain compressor.

2. Scaling Laws

The design of low-speed model is different from general compressor design. The low-speed model is modeled from a high-speed prototype based on the similarity scaling laws. In general, the scaling method can be divided into exact similarity method and partial similarity method. The key difference between the two methods is whether Re remains constant or not. In this study, the Re of the prototype is calculated as Equation (1).

$$Re = \frac{Ub_2}{\nu} \quad (1)$$

where ν is the inlet kinematic viscosity.

In the practical application of the partial similarity principle, there are two dimensionless parameters that need to be kept constant [33]: the mass flow coefficient ϕ and the machine Mach number Ma_U . The two parameters can be expressed as follows.

$$\phi = \frac{Q}{\pi/4 \cdot U \cdot D_2^2} \quad (2)$$

$$Ma_U = \frac{U}{\sqrt{\kappa RT_0}} \quad (3)$$

The complete dimensional analysis process, based on the Buckingham–PI theorem, is described as follows. Generally, there are 7 variables overall when applying the partial similarity principle in this case, which are $\rho, u_2, D_2, P, T, t, \mu$. The length dimension L , mass dimension M and time dimension t are chosen to be the base dimensions. Simultaneously, ρ, u_2, D_2 are selected to be the base variables. Then, the flow characteristics and the dimensional analysis can be depicted as follows.

$$f(\rho, u_2, D_2, P, T, t, \mu) = 0, \quad (4)$$

where μ is the dynamic viscosity. The deduction of similarity criterion can be described as follows.

$$\begin{cases} \pi_1 = \rho^{a_1} u_2^{b_1} D_2^{c_1} P \\ \pi_2 = \rho^{a_2} u_2^{b_2} D_2^{c_2} T \\ \pi_3 = \rho^{a_3} u_2^{b_3} D_2^{c_3} t \\ \pi_4 = \rho^{a_4} u_2^{b_4} D_2^{c_4} \mu \end{cases} \quad (5)$$

$$\begin{cases} [\pi_1] = M^0 L^0 t^0 = (ML^{-3})^{a_1} (Lt^{-1})^{b_1} (L)^{c_1} (ML^{-1}t^{-2}) \\ [\pi_2] = M^0 L^0 t^0 = (ML^{-3})^{a_2} (Lt^{-1})^{b_2} (L)^{c_2} (L^2t^{-2}) \\ [\pi_3] = M^0 L^0 t^0 = (ML^{-3})^{a_3} (Lt^{-1})^{b_3} (L)^{c_3} t \\ [\pi_4] = M^0 L^0 t^0 = (ML^{-3})^{a_4} (Lt^{-1})^{b_4} (L)^{c_4} (ML^{-1}t^{-1}) \end{cases} \quad (6)$$

$$\begin{cases} a_1 = -1, b_1 = -2, c_1 = 0 \\ a_2 = 0, b_2 = -2, c_2 = 0 \\ a_3 = 0, b_3 = 1, c_3 = -1 \\ a_4 = -1, b_4 = -1, c_4 = -1 \end{cases} \quad (7)$$

$$\begin{cases} \pi_1 = \rho^{-1} u_2^{-2} D_2^0 P = \frac{P}{\rho u_2^2} = \frac{\rho R T}{\rho u_2^2} = \frac{R T}{u_2^2} = \frac{1}{\kappa} \frac{\kappa R T}{u_2^2} = \frac{1}{\kappa} \left(\frac{1}{Ma} \right)^2 \\ \pi_2 = \rho^0 u_2^{-2} D_2^0 T = \frac{T}{u_2^2} = \frac{1}{\kappa R} \frac{\kappa R T}{u_2^2} = \frac{1}{\kappa R} \left(\frac{1}{Ma} \right)^2 \\ \pi_3 = \rho^0 u_2^1 D_2^{-1} t = \frac{u_2 t}{D_2} = \frac{\frac{\pi}{4} D_2^2 u_2}{\frac{\pi}{4} D_2^2 \frac{D_2}{r}} = \frac{\frac{\pi}{4} D_2^2 u_2}{Q} = \frac{1}{\phi} \\ \pi_4 = \rho^{-1} u_2^{-1} D_2^{-1} \mu = \frac{\mu}{\rho u_2 D_2} = \frac{1}{Re} \end{cases}, \quad (8)$$

Finally, the flow characteristics are summarized as Equation (8).

$$F\left(\frac{1}{\kappa} \left(\frac{1}{Ma}\right)^2, \frac{1}{\kappa R} \left(\frac{1}{Ma}\right)^2, \frac{1}{\phi}, \frac{1}{Re}\right) = 0, \quad (9)$$

Consequently, in this case, if the mass flow coefficient ϕ and machine Mach number Ma_{u_2} are constant and the Re is ignored, the flow similarity can be achieved in partial similarity principle.

The aerodynamic parameters at the design point of the prototype were chosen as the modeled conditions. In this study, the scaling factor is 10, so the speed of scaled-up model is low enough according to the scaling laws. The scaled-up compressor possesses completely the same relative geometric parameters as the prototype, including solidity, aspect ratio, hub-to-tip ratio, axial-space-chord ratio, airfoil stacking, relative radial clearance, etc. In the following study, the scaling process is qualified by not only the performance curve, but also the detailed flow field characteristics of the prototype and scaled-up model. The procedure, including scaling-up and operating range optimization, is shown in Figure 1. The whole process can be divided into the scaling-up process and the improving process. Firstly, the prototype is scaled-up to be a large-scale and low-speed model, which achieves enough flow similarity with the prototype. Then, the same casing treatment is used in the prototype and large model for the performance optimization. The following sections introduce those steps one by one.

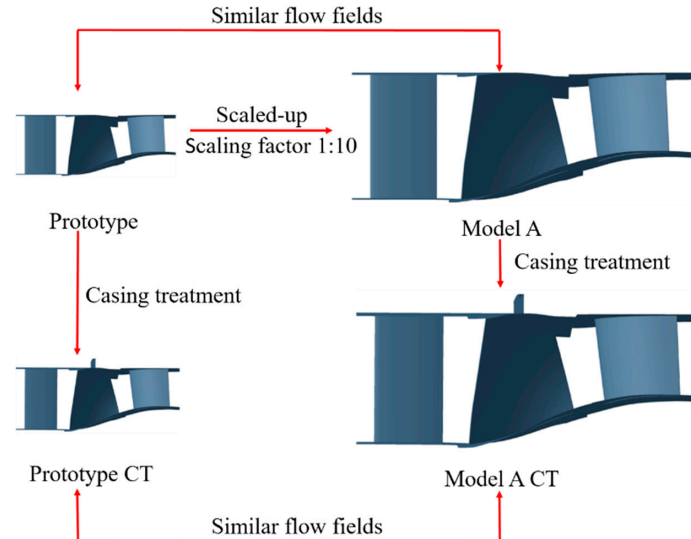


Figure 1. Scheme of performance analysis and improvement.

3. Numerical Method

Numerical simulations were accomplished with commercial code EURANUS, which contains steady and unsteady solvers by calculating the conservative Reynolds-averaged N-S (Navier-Stokes) equations. It discretized the N-S equations using a cell-centered finite volume formulation in space, and applied Gauss's theorem and central difference method to determine viscous flux. In order to obtain the flow regimes accurately in the flow passage and the detailed flow pattern near the casing, a second-order central spatial discretization scheme was selected to estimate the inviscid fluxes. Frozen rotor technique was employed to deal with the interface between the inlet guide vane (IGV)

and rotor and between the rotor and stator. According to published research [34], Spalart-Allmaras's model can give fairly good results in the numerical simulation of turbomachinery. Thus, in this case, Spalart-Allmaras's model was used for turbulence simulation to evaluate the eddy viscosity [35].

Upstream and downstream, the numerical computational domain was extended, among which mesh was generated with NUMECA Auto Grid 5. The minimum grid spacing of the first layer was set to be 0.001 mm. According to Numeca FineTurbo user guide [36], the y^+ is recommended to be below 10 when the Spalart-Allmaras model is used. Besides, the value of y^+ is recommended to be below 5 in some published research [35,37]. In this paper, the y^+ is about 1, which satisfies the need of the Spalart-Allmaras model. In order to analyze flow field in the tip gap, the number of total layers within tip clearance was set to be 17. A single-passage model was used in the steady computation to validate the consistency between numerical simulations and experiments. However, a single-passage model is not adequate to capture some flow characteristics of the stall inception process, such as the precursors, occurrence, evolution and initiation of the stall and the cross-passage flow. Moreover, the disturbances would propagate circumferentially when approaching the stall point, which plays a significant role in the simulation near the stall. Thus, after validating the reliability of numerical simulations, all the following numerical simulations employed the multi-passage model. As the sliding grid scheme requires two connected regions to have the same circumferential length, the same circumferential length is required for unsteady calculations. The quantities of blades can be changed based on the research of Rai [38], and the numbers of IGVs, rotors and stators were changed to 30, 30 and 30, respectively, so there were 30 passages in the full-annulus. Considering the limitations of the computing resources, a five-passage model was selected. Naturally, the performance of a five-passage model was different from that of the prototype because of the revised blade numbers, but it was considered to be enough to predict the general flow structure for the comparison among and optimization of prototype and low-speed models. The mesh numbers of single-passage and five-passage are about 3 million and 15 million, respectively, which can be seen in Figure 2. The mesh density is appropriate from the validation result of the grid independence. A three level multi-grid was adopted to accelerate the calculation.

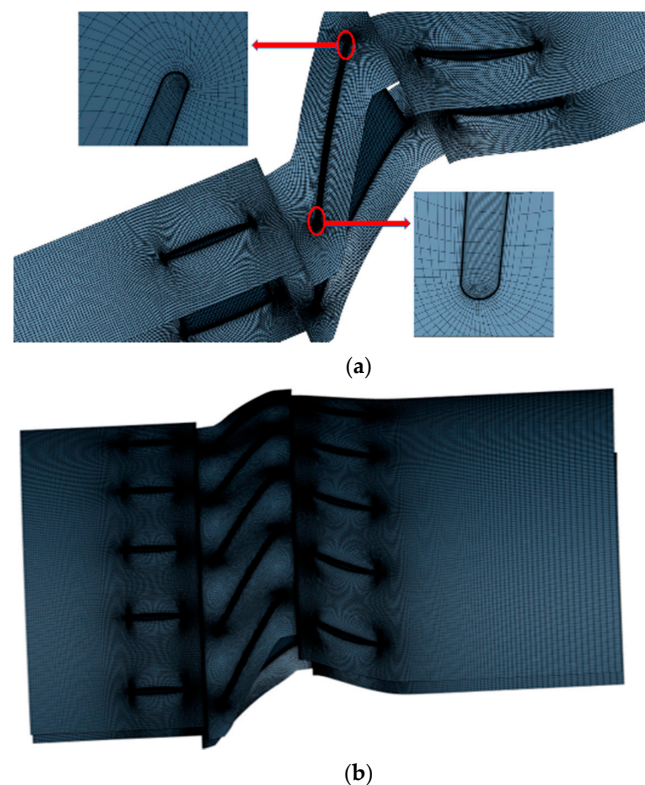


Figure 2. Mesh of computation domain: (a) single-passage model; (b) five-passage model.

No-slip and adiabatic conditions were set at all the solid boundaries. Velocity direction, total pressure and total temperature were imposed at the inlet and average static pressure at the outlet as the boundary conditions. The back pressure was increased gradually to obtain the global stable performance maps. The last converged point was inferred to the near-stall point in this study. The steady computation results were used for the performance comparison and analysis, and the unsteady computation was also conducted to capture the unstable characteristics of the flow field. The dual-time step (DTS) method was employed to improve the time marching in the unsteady simulation. The number of angular positions was 10 in one single passage and 20 inner iterations were set for two successive computations, which is enough to get detailed unsteady information.

4. Results and Analysis

4.1. Evaluation of the Numerical Method

For the validation of the numerical method, the test was carried out in the 1-1/2 stage axial subsonic compressor in Shanghai Jiao Tong University, as shown in Figure 3 [39]. The blade numbers were 32, and 29 and 37 for the inlet guide vane (IGV), rotor and stator respectively. The section profile of all blades is NACA0012. Hub/tip ratio (ratio of the diameter of blade hub to the diameter of blade tip) was 0.76. The rotational speed was 12,000 rpm, with which the tip Mach number was less than 0.9 at design point. The height of tip clearance was 1% chord length at the blade tip. To acquire the aerodynamic parameters of inlet and outlet, temperature sensors and pressure sensors were arranged at the upstream (plane A) and downstream (plane D) areas, as shown in Figure 3a. On plane A, two static pressure probes and two five-hole total pressure probes (accuracy 0.02%) were installed to obtain inlet static pressure and total pressure, respectively. One five-point temperature probe (accuracy 0.2%) was set to measure the inlet total temperature. The same types sensors were equipped on the plane D to obtain outlet pressure and temperature. In this case, the absolute measurement errors of total pressure and temperature were about 0.02 Kpa and 0.5 K, respectively. The measurement error of prototype-stage isentropic efficiency was about 1.5%. The overall performance of the prototype was acquired with the adjustment of throttle area at outlet. A flowmeter was placed upstream of IGV to measure the flow rate. The geometric parameters of prototype are listed in Table 1.

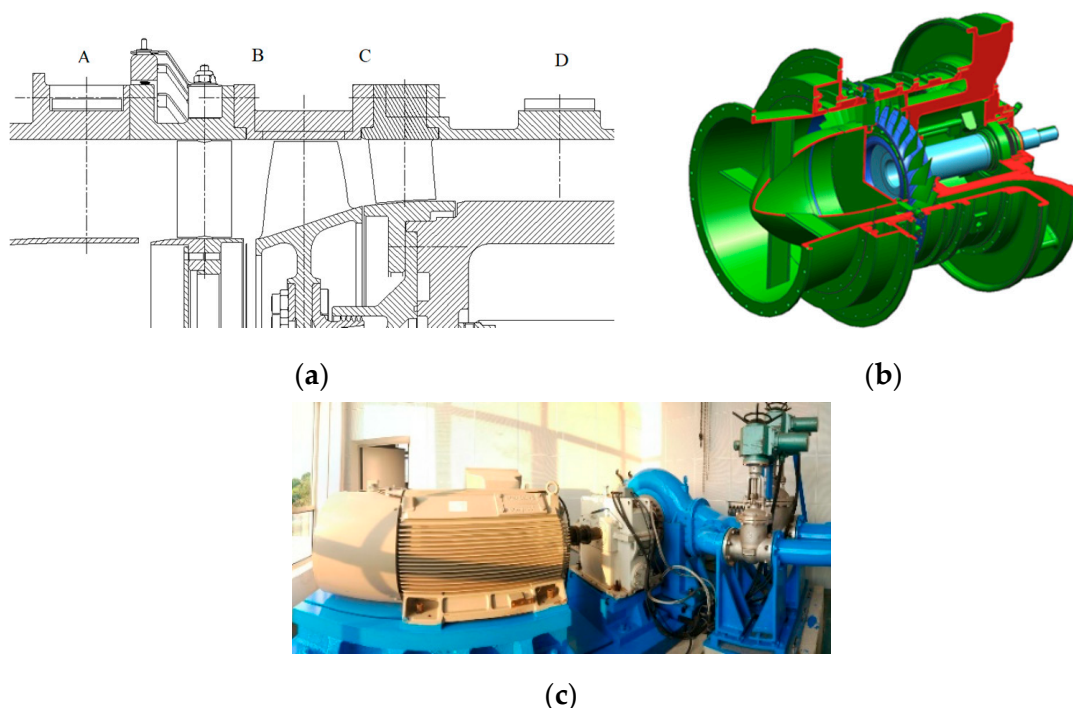


Figure 3. Test facility: (a) meridional plane of prototype; (b) 3D model of prototype; (c) test rig.

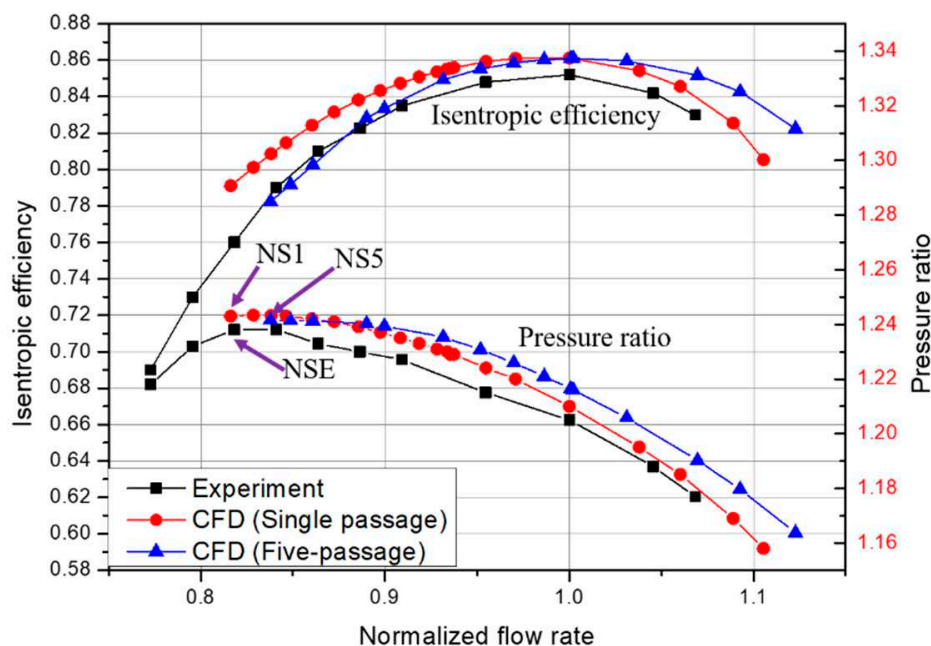
Table 1. Design parameters of the prototype.

Parameters	Unit	Value (Prototype)
Diameter, D2	mm	370
Hub/tip ratio	-	0.76
Blade height	mm	56
Tip clearance, ε	mm	0.65
Rotor blade chord length, b2	mm	65
ε/b_2	-	1%
Rotation speed, N	rpm	12,000

The experiment and numerical performance versus normalized flow rate are shown in Figure 4. Squares, triangles and circles were applied to make a distinction among the performance curves of experiment results and numerical results of single-passage and five-passage, respectively. The upper lines depict the isentropic efficiency characteristic and the lines below depict the pressure ratio characteristic. In this case, the isentropic efficiency η_s is calculated as Equation (10).

$$\eta_s = \frac{(P_1/P_0)^{\frac{\kappa-1}{\kappa}} - 1}{T_1/T_0 - 1} \quad (10)$$

where κ is the Adiabatic exponent, P_0 the inlet total pressure, P_1 the outlet total pressure, T_0 the inlet total temperature and T_1 the outlet total temperature.

**Figure 4.** Overall performances of prototype stages.

Three points are labeled in Figure 4 for depicting the near-stall points conveniently. NSE represents the last point of the characteristic at minimum normalized flow rate $Q/Q_{ref} = 0.77$ in experiment, NS1 and NS5 represent the solution limit under the steady computation of single-passage and five-passage, respectively. The computation results of single-passage and experiment results correspond well with each other. The discrepancy at design point is less than 1.5%, and the tendencies of the curves agree well. The major difference at the off-design points is that the computation results overestimate the limit flow rate about 4.2%; that is because of the limitation of the steady simulation. However, the NS1 is very close to the NSE, which means that the steady simulation can exactly capture the point near the stall. The errors exist between the curves of single-passage and five-passage because of the changed

blade number. The five-passage model shows better performance in a relatively large flow rate, and the single-passage model shows a better stall margin. In generally, the steady simulation was adequately accurate to obtain the performance and the point near the stall. The five-passage model was used for the follow-up study to capture the circumferential flow characteristics, and the five-passage high-speed model was set to be the prototype accordingly.

4.2. Performance Analysis of the Scaled-Up Compressors

4.2.1. Comparison of the Prototype and Scaled-Up, Low-Speed Model A at Design Point

The low-speed model A was scaled-up with the scaling factor 1:10 from the prototype geometrically, and the five-passage model was too. Model A maintained the machine Mach number and mass flow coefficient and kept the inlet and outlet parameters. The geometric and aerodynamic parameters of the prototype and model A are listed in Table 2.

Table 2. Design parameters of prototype and compressor A.

Parameters	Unit	Value (Prototype)	Value (Model A)
Inlet total pressure, P_0	kPa	101.025	101.025
Inlet total temperature, T_0	K	284	284
Design Mass flow rate, Q_d	Kg/s	6.1	610
Diameter, D_2	mm	370	3700
Tip clearance, ε	Mm	0.65	6.5
Rotor blade chord length, b_2	mm	65	650
ε/b_2	-	1%	1%
Design rotational speed, N	rpm	12,000	1200
Peripheral velocity of impeller, U	m/s	232	232
Reynolds number, Re		1.05×10^6	1.05×10^6
Mass flow coefficient	-	0.2446	0.2446
Working fluid	-	Air	Air
Adiabatic index, κ	-	1.4	1.4

The distributions of averaged circumferential static pressure coefficient, C_p , at five spanwise points of the rotor and stator for the prototype and model A at design point are shown in Figures 5 and 6. C_p is defined as

$$C_p = \frac{P}{P_{total,in}} \quad (11)$$

where P and $P_{total,in}$ denote the surface static pressure and the total pressure at inlet. The static pressure distributions of numerical results of prototype and model A are shown in Figure 5. Overall, the distributions of static pressure of rotor between prototype and model A are almost exactly the same in the whole flow passage. However, there is still small a difference at mid-span, which will be analyzed next. The flow field near the hub and the casing reached good flow similarity, which was not realized by the former studies. The distributions of static pressure of stators also agree well, as shown in Figure 6. Nevertheless, the flow similarity of the stator is not as good as that of the rotors. Moreover, the similarity of the stator over 50% spanwise was worse than that of rotor. Besides, it can be seen that the static pressure rise of stator of model A was larger than that of prototype at all spanwise values.

The comparisons of averaged circumferential values of aerodynamic parameters along the blade height of rotor and stator are shown in Figures 7 and 8. In general, the tendencies of inlet and outlet relative flow angles of the rotor match well. The distributions of flow turning angle near the end-wall are nearly the same. However, the discrepancy of occurs from 5% to 95% blade height, for which the maximum is about 1.5 degrees. The good agreement also appears at the axial velocity distributions at inlet and outlet of rotor. However, the outlet axial velocity of model A is a little smaller than that of the prototype at the same region as the flow turning angle distribution. It can be inferred that the

decreased axial velocity attributed the decreasing turning angle, which may be related to the variation of Re. The flow angle and axial velocity distributions of stators still agree well for the prototype and model A, though the error of outlet flow angle is bigger than that of rotor, which may not only be affected by the enlarged Re but the upstream effects of the rotor.

Averaged circumferential isentropic efficiency of the rotor and loss coefficient distributions of rotor and stator along blade height are shown in Figures 9 and 10, respectively. The total pressure loss coefficients of rotor ω_R and stator ω_S are expressed as:

$$\omega_R = (P_{0w} - P_{1w}) / (P_{0w} - P_0) \quad (12)$$

$$\omega_S = (P_{1t} - P_{2t}) / (P_{1t} - P_1) \quad (13)$$

where P_0 is the inlet static pressure of the rotor, P_{0w} is the average inlet relative total pressure of the rotor, P_{1w} is the average outlet relative total pressure of the rotor, P_1 is the inlet static pressure of the stator, P_{2t} is the average outlet absolute total pressure of the stator and P_{1t} is the average inlet absolute total pressure of the stator. The efficiency of model A is improved from 10% to 85% blade height, and the loss is reduced slightly accordingly. The efficiency and loss curves are approaching. There are two regions with obvious error that can be observed in the loss curves of stators; one is near the hub end-wall and one is from 70% to 100% blade height. The discrepancy may have resulted from the different impact on the downstream stator, caused by the wake flow, leakage flow and main flow. This impact varied with the varied wake flow, leakage flow and main flow along the radial direction, because of the different absolute values of blade height and axial gap between the rotor and stator. Thus, the difference in the upper parts of the downstream stators was brought about. Besides, the difference near the hub end-wall may be relative to the different friction loss, caused by the different boundary effects because of different Re and blade height.

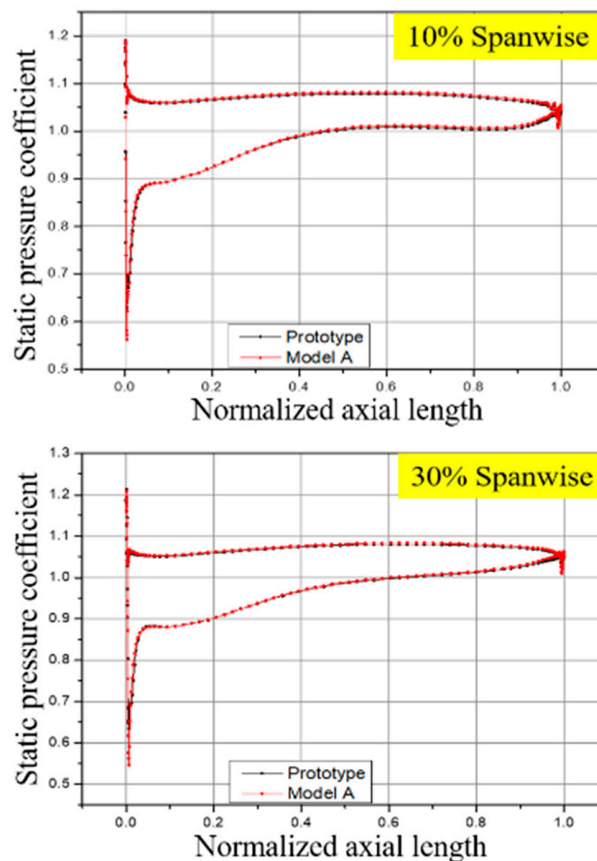


Figure 5. Cont.

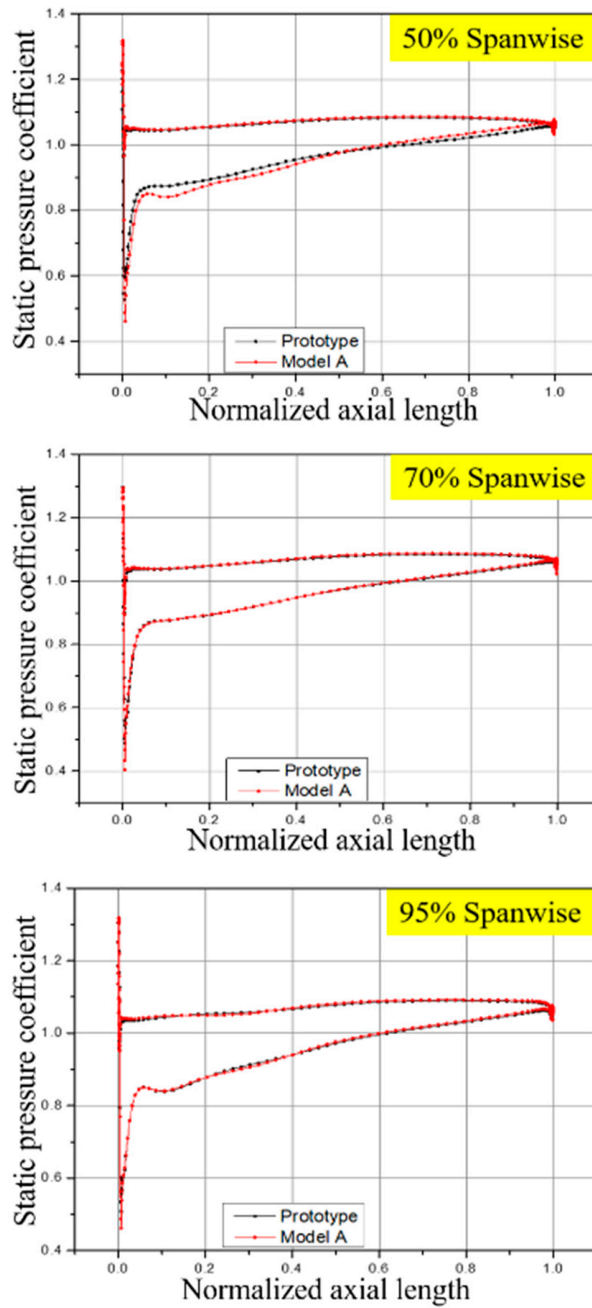


Figure 5. Static pressure distributions of the rotor.

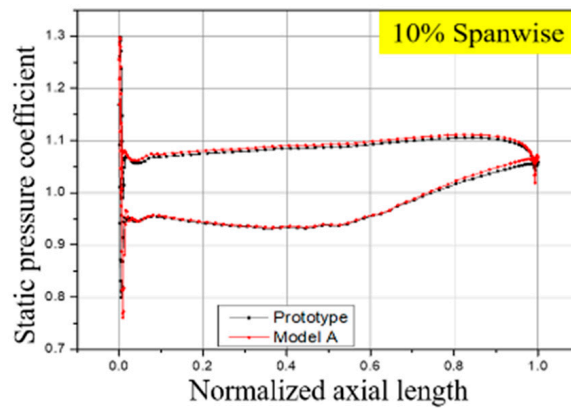


Figure 6. Cont.

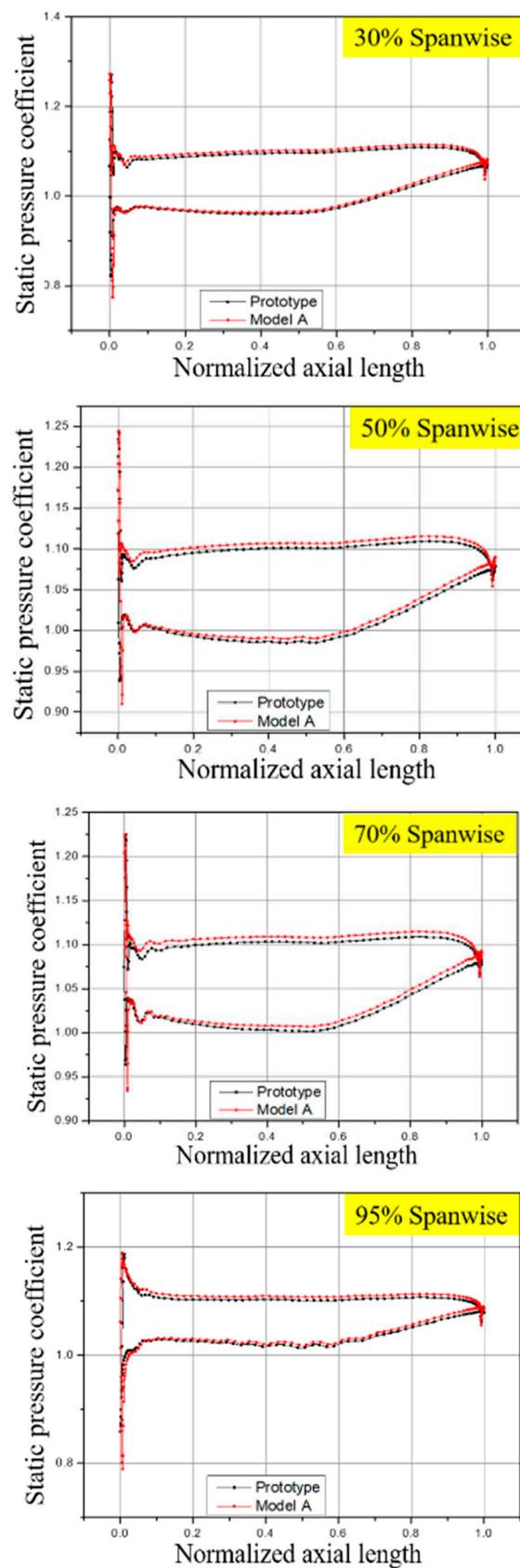


Figure 6. Static pressure distributions of the stator.

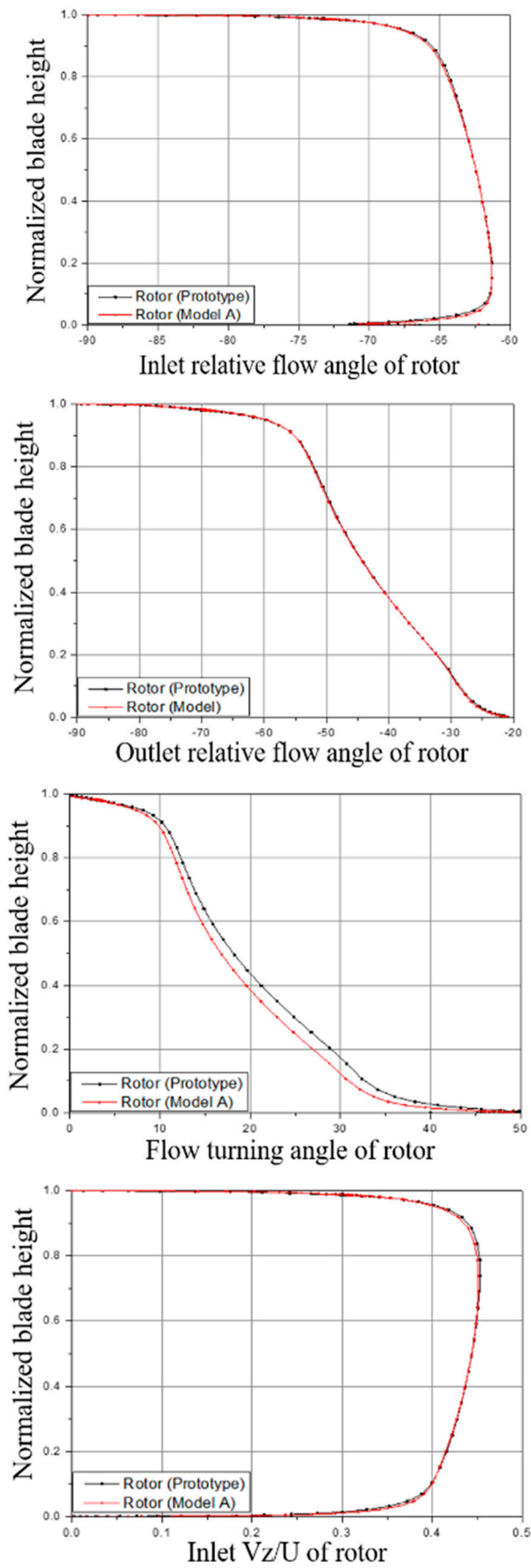


Figure 7. Cont.

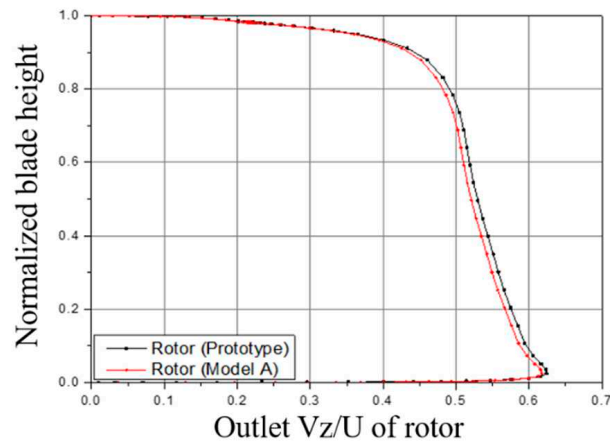


Figure 7. Averaged circumferential values of aerodynamic parameters of the rotor.

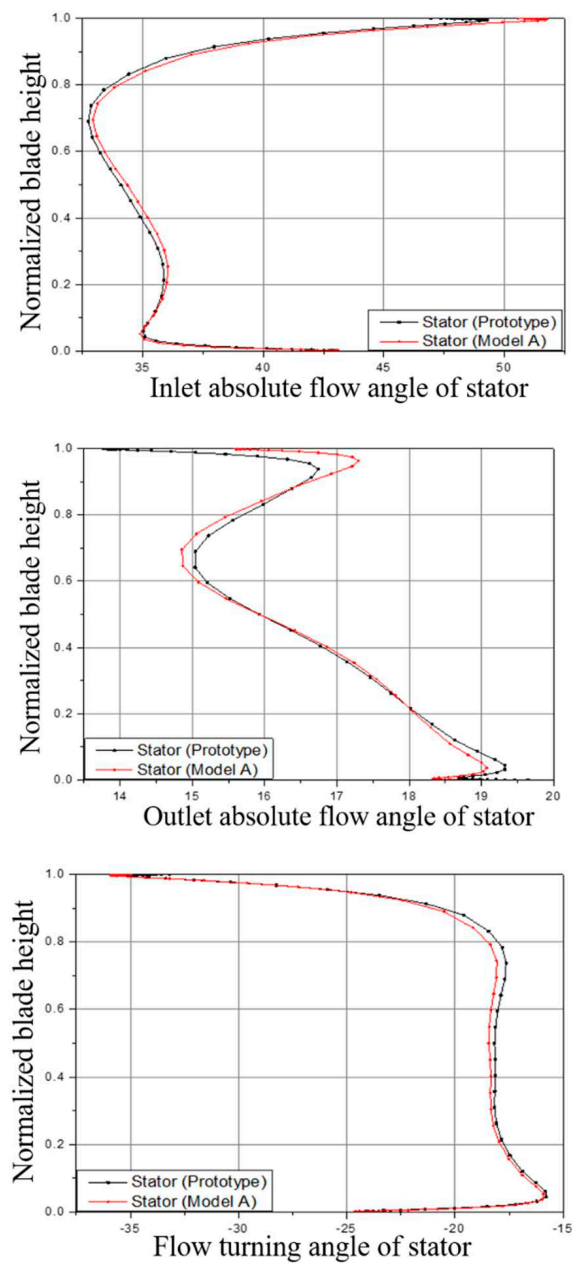


Figure 8. Cont.

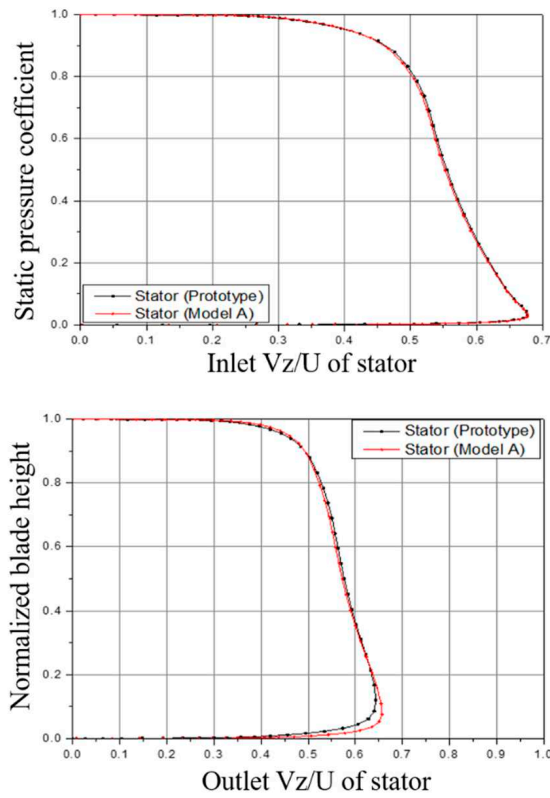


Figure 8. Averaged circumferential values of aerodynamic parameters of the stator.

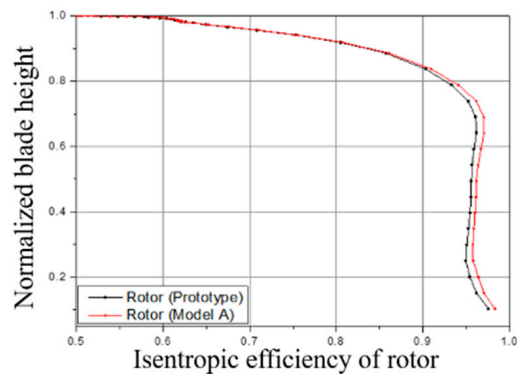


Figure 9. Isentropic efficiency of the rotor.

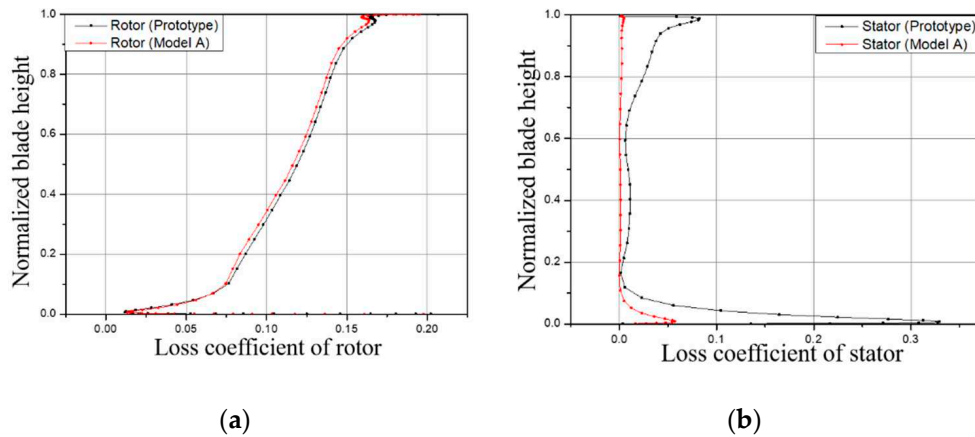


Figure 10. Loss coefficient distributions of the rotor and stator: (a) loss coefficient of rotor; (b) loss coefficient of stator.

According to the comparison and analysis of this section, the low-speed model was successfully fabricated based on the scaling laws. Exact flow similarity was achieved in the rotor and stator, although there was a little error. It is very convenient to realize the scaling process without a complicated iterative process based on the complex inverse method, and the flow similarity of the rotor and stator is reached at the same time. After the successful process at design point, the study on the off-design followed, which was for discussing the flow similarity in the whole operating range.

4.2.2. Comparison of the Prototype and Scaled-Up, Low-Speed Model A in Operating Conditions

The performance comparison between the prototype and model A is shown as a function of normalized mass flow rate in Figure 11. The tendency of performance curves agrees well for the prototype and model A under the operating flow rate. The discrepancies of efficiency and pressure were less than 1.5% and 0.5%, and they were only 1.25% and 0.4% at design point, respectively. It was proven that the flow similarity is not only achieved at design point but for the whole operating flow rate based on the partial similarity principle. However, the flow rate near the stall of model A (the normalized flowrate at this point is namely, NSA) was about 4.2% less than that of prototype (the normalized flowrate at this point is namely, NSP), meaning that the stability is worsened when conducting the scaling-up process.

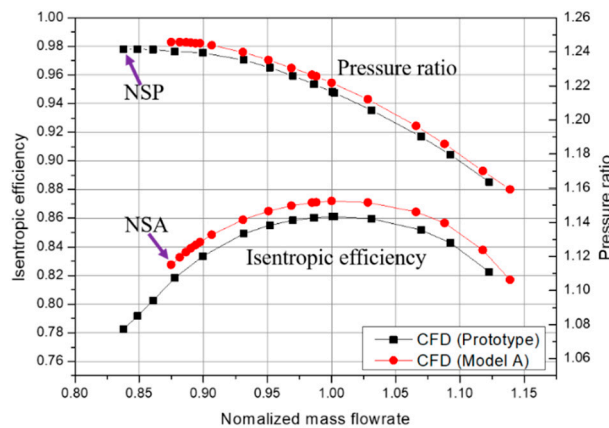


Figure 11. Performance in the whole operating range.

The static pressure and entropy distributions near the casing (99.5% spanwise) of model A at NSA, for prototype at NSP, and for the prototype at NSA, are compared in Figure 12. The red dotted line is static pressure and it is used to detect the trajectory of tip clearance vortex [40]. One of the characteristics for spike disturbance initiating rotating stall is that the interface, where the oncoming and tip leakage flows meet, is aligned to the leading-edge plane. In other words, the tip leakage flow spilled below the blade tip [32]. As shown in Figure 12a, the tip leakage flow of model A at NSA nearly spills below the blade tip, and this flow phenomenon can be also observed in the prototype at NSP. Furthermore, the flow field between model and prototype is similar, so it can be inferred that the flow similarity is maintained near the stall point, and the type of stall inception is also the same. The tip leakage vortex of prototype migrates downstream at NSA, near the stall point of model A. It illustrates that the scaling-up model promotes the tip leakage vortex moving upstream, which results in rotating stalling before the prototype. The entropy distribution can be applied for distinguishing the interface between main flow and tip leakage flow [31]. The black dashed line, where the entropy increases severely, describes the location of the interface. The black line is successive and parallel to the leading-edge plane at NSA in model A and at NSP in the prototype, meaning the inception of stalling. The interface of prototype at NSA is still in the passage, corresponding with the analysis on the static pressure distribution.

Based on the above sections, the high-speed compressor is successfully transformed to the low-speed, large-scale compressor in the whole operating range, although there are some tiny errors.

These tiny errors may be caused for several reasons, such as the changed Re , the variations of absolute values of geometric parameters and so on. The further research about diminishing the errors was the content of the next study to achieve further flow similarity. It is worth noting that almost complete flow similarity was achieved under steady conditions, as shown in Figures 5, 7, 9 and 10. Then, it was necessary to study whether the flow similarity was contained in the unsteady state when using the scaling laws, because some important flow characteristics are closely related to the unsteady condition.

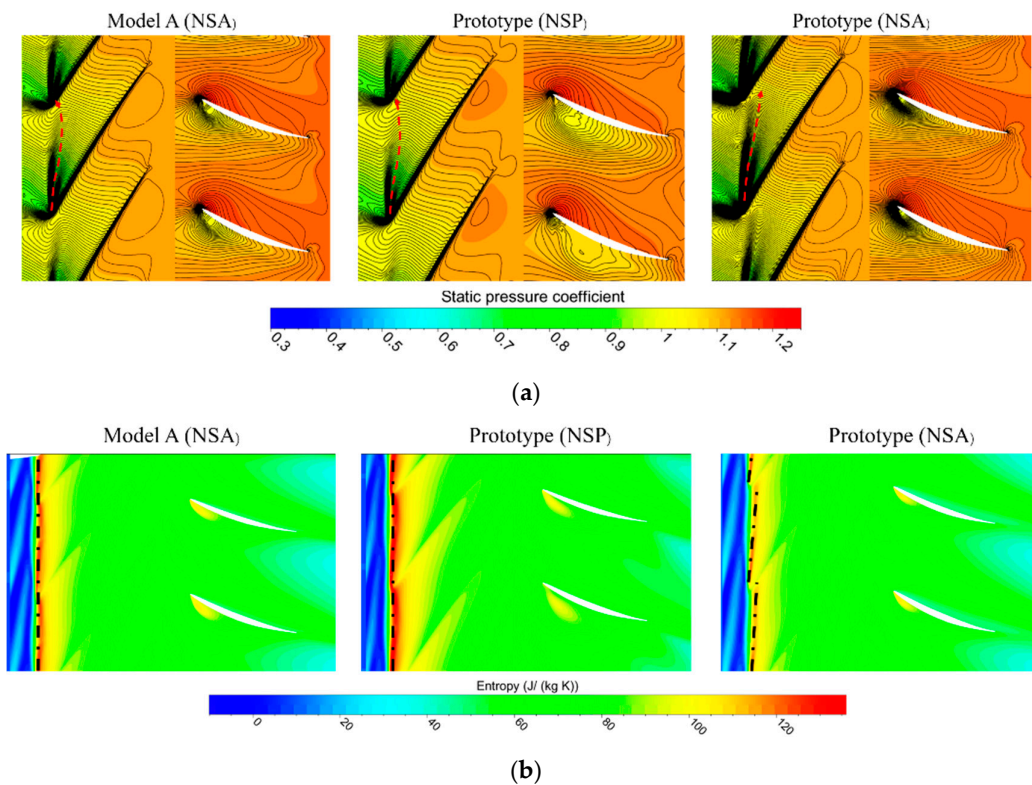


Figure 12. Comparisons of static pressure and entropy distributions at 99.5% spanwise: (a) static pressure distribution; (b) entropy distribution.

4.2.3. Comparison of the Prototype and Scaled-Up, Low-Speed Model A under Unsteady Condition

The flow similarity between the high-speed prototype and low-speed large-scale model A is realized under steady condition. The transient normalized relative axial velocity contours at 99.5% and 97% spanwise of prototype and model A at design point are shown in Figure 13. It can be observed that the flow field within the tip clearance and near the casing is stable, and there is not migration of tip leakage vortex. The velocity at 99.5% spanwise of model A is a little larger than that of prototype along the trajectory of leakage vortex, while it is opposite at 97% spanwise. Yet, on the whole, the evolution of the flow field for prototype is similar to that of and model, implying that the flow similarity is preserved under the unsteady condition at design point. The transient characteristics of velocity at 99.5% and 97% spanwise between prototype and model A at the near-stall point are compared in Figure 13.

The instantaneous velocity contours near the stall are shown in Figure 14. The fluctuation of the red dotted curve, detecting the trajectory of tip leakage vortex, indicates that the tip leakage vortex is unstable. The vortex is generated at the leading edge of the blade, and then migrates circumferentially, which can be deduced from the region depicted with A and B. When the vortex impinges the adjacent blades, its intensity is decreased, and the secondary leakage even multi-leakage appears. The red ellipse also presents the movement of the vortex. Again, the unstable characteristics of the prototype and model near the stall are similar, demonstrating that the unsteady flow features are maintained in the design and off-design operating conditions.

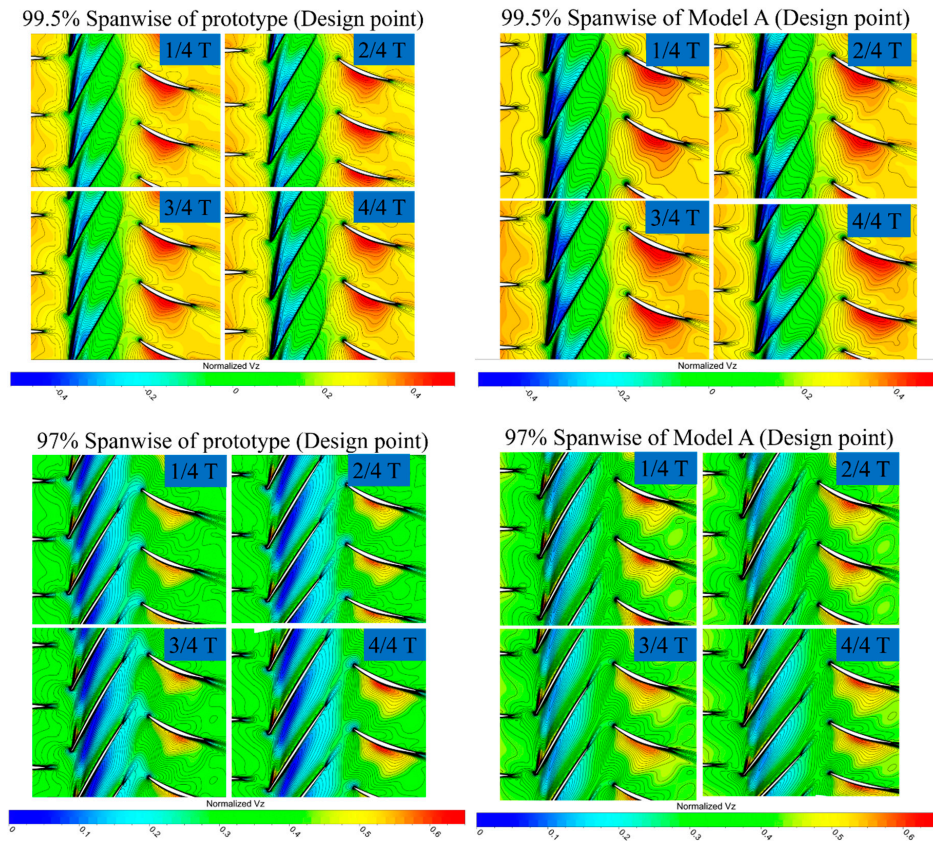


Figure 13. Transient axial relative velocity of the prototype and model A at 99.5% and 97% spanwise at design point.

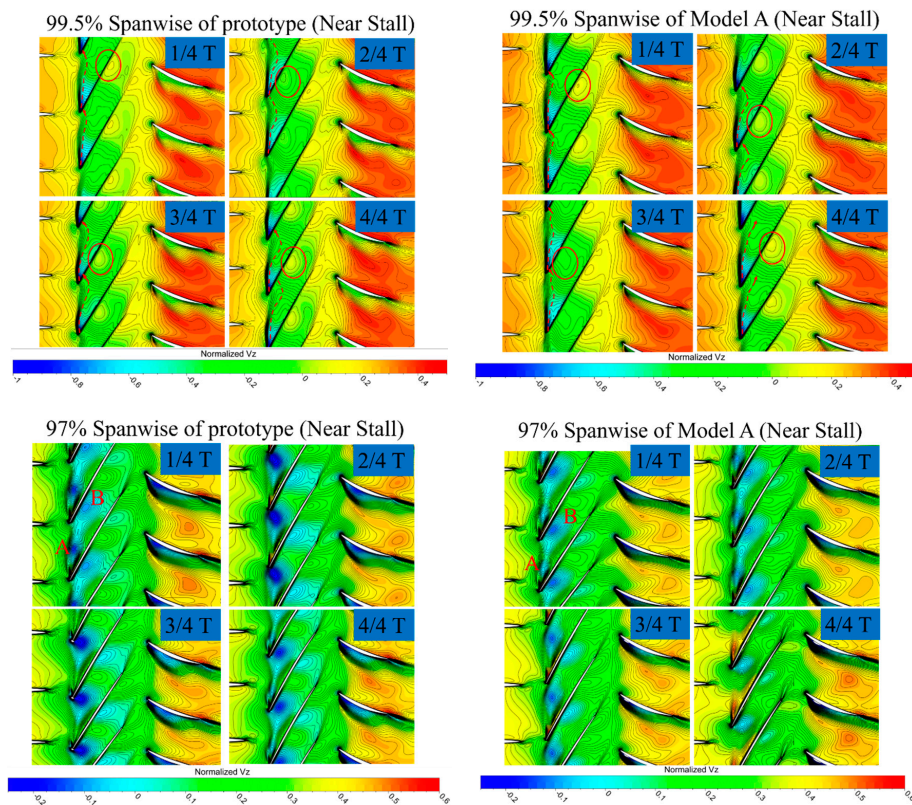


Figure 14. Transient axial relative velocity of the prototype and model A at 99.5% and 97% spanwise near the stall.

4.3. Stability Improvement through Casing Treatment

In this study, the single circumferential groove was applied as the casing treatment technology. The location and geometric parameters, and the mesh of the flow passage with groove of model A are shown in Figure 15, and the mesh number of the groove was about 5 million, which is fine enough to provide grid independence.

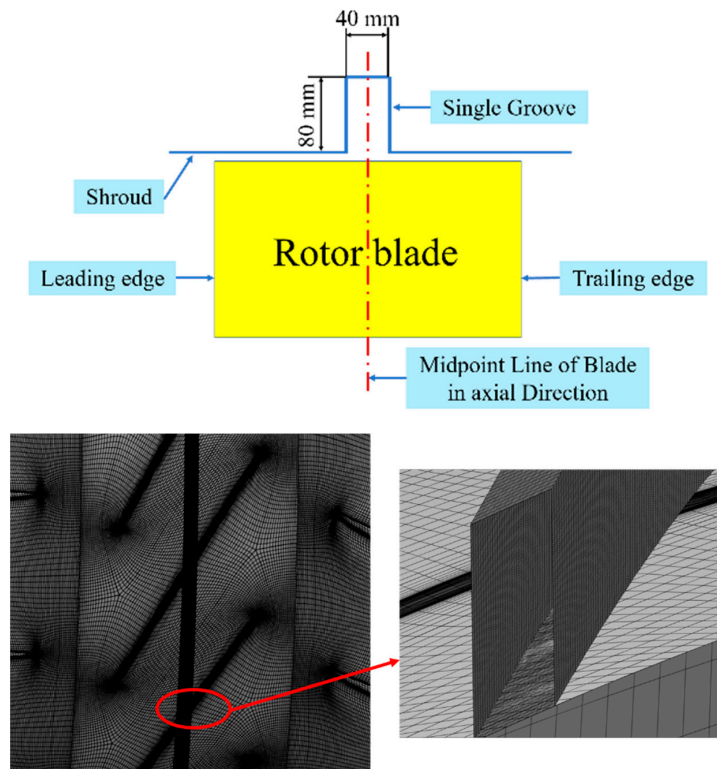


Figure 15. Sketch map of groove geometry and mesh.

The characteristics of the smooth solid wall and the grooved casing treatment are shown in Figure 16. The model A with a groove is named model A CT, and NSACT means the near-stall point of model A CT. The efficiency and pressure ratio of model A were decreased about 0.4% and 0.3% at design point. The reduction of performance decreased along the direction of small flowrate and increased towards the large flowrate.

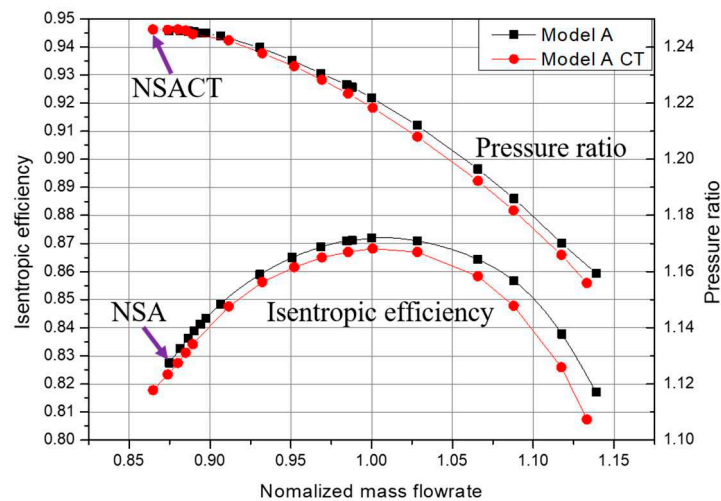


Figure 16. Pressure ratio and isentropic efficiency of a smooth solid wall and grooved casing treatment.

The reason for the decrease can be explained in Figure 17, which shows the apparent increasing entropy around and downstream the region existing groove. The two black lines added in this figure represent the upstream and downstream edges of groove. Besides, it can be observed that the impact of groove not only exists in the tip clearance but in the region near the casing. However, the solution limit near the stall is obviously moved toward the small flowrate, elucidating that the stability improvement of model A was achieved. The reduction of the flowrate near the stall of the prototype was about 1.2%.

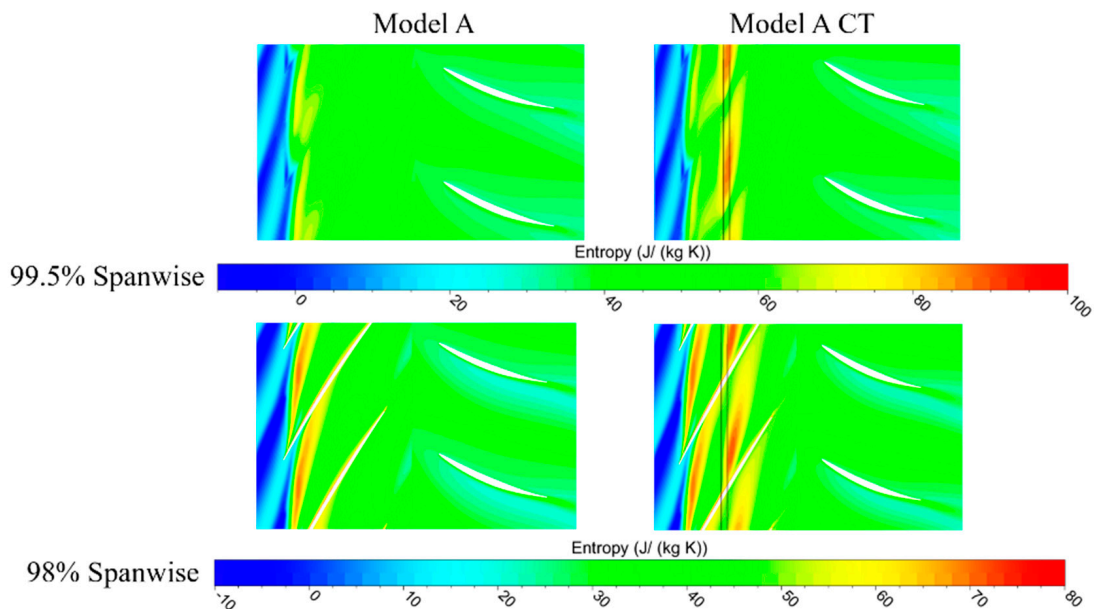


Figure 17. Entropy distributions at 99.5% and 98% spanwise.

The stability improvement of the prototype was the ultimate object of this research, so the single circumferential groove was also applied to the prototype. The location of the groove was the same as for model A CT, and the geometric parameters were scaled down by the scaling factor 1:10 accordingly. The prototype applying the groove was named prototype CT, and NSPCT means the near-stall point of model A CT. The simulation results for the prototype and prototype CT are shown in Figure 18. The efficiency and pressure ratio of prototype decreased about 0.54% and 0.35% at design point—a little more than for model A, and the tendencies of the curves are similar to those of model A. The reduction of the flowrate of the prototype was 1.1%, which is very close to that of model A.

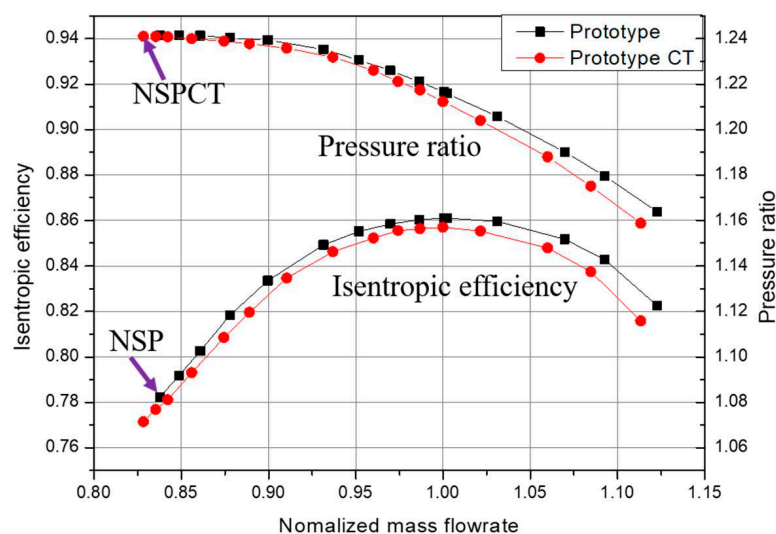


Figure 18. Pressure ratio and isentropic efficiency of the smooth solid wall and grooved casing treatment.

As shown in Figure 19, the entropy also increased apparently around and downstream the region existing groove. The higher entropy distribution around groove of prototype explain the larger performance decrease of prototype. Furthermore, the entropy distribution of prototype CT is similar to that of model A CT, indicating that the effect of groove on the two models is similar and the flow similarity is maintained. The mechanism of stability improvement applying the circumferential groove has been elucidated clearly in many publications [27–29], which is outside the scope of this study, so it will not be covered in this paper. The flow similarity between prototype and model A prove that the research of the casing treatment on the model A can be used for the prototype.

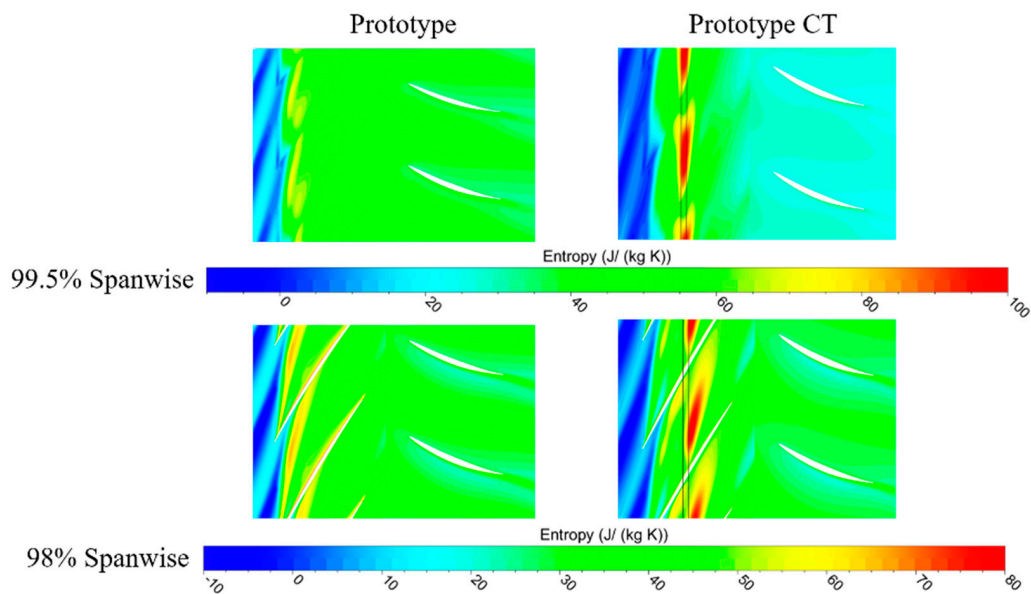


Figure 19. Entropy distributions at 99.5% and 98% spanwise.

5. Discussion

In this study, the flow similarity at the design and off-design points has been achieved well, except that there is a little distinction in the solution limit flowrate near the stall. Thus, further flow similarities will be focused on in the following research, such as the geometric corrections, including the value of tip clearance, the axial gap between rotor and stator, etc. Besides, the casing treatment is one of the effective technologies for stability and performance improvement; there are many other technologies can be used. Furthermore, the detailed measurement of aerodynamic parameters through establishing low-speed large-scale test facility will be carried out after the adequate flow similarity is achieved.

Some comments on the effect of Reynolds number on aerodynamic performance are significant. When scaling-up the prototype, the Re increases as the absolute dimensions of the prototype are enlarged, and the relationship of Re between the prototype and scaled model has been presented in the research of Perter [41]. The friction coefficient value of scaled-up model is decreased with increasing Re , which leads to better efficiency. Nevertheless, the decrease of friction coefficient is finite. The friction coefficient is determined not only by Re but also by the relative height of the roughness of the surface, which is limited. However, CFD computations in this paper were carried out for the cases of smooth surfaces and the roughness of the surface was neglected in this paper. Besides, the displacement thickness of the boundary layer is also effected by the changed Re [42]. Therefore, further investigation is necessary and will be discussed in future research.

6. Conclusions

In this paper, a method based on the partial similarity principle is proposed. In practical applications, this method can be used conveniently and quickly for the transformation of a high-speed,

small compressor. In our case, a 1-1/2 axial compressor has been scaled up to be a low-speed, large-scale model, based on the high-to-low-speed transforming methodology—the partial similarity principle. Thereafter, casing treatment was used for the stability improvement and the flow similarity still remained. Numerical simulations were used for the analysis of the scaled-up process and the stability optimization process. In addition, experimental tests were carried out for the validation of simulation results. On the basis of studies, the following conclusions were drawn.

- The high-speed compressor was successfully transformed to be a low-speed, large-scale model based on the partial similarity principle, which keeps the Ma and flowrate coefficient constant and neglects the effects of Re. This principle is simple and convenient compared to the conventional low-speed model methodology based on the inverse method.
- The surface aerodynamic parameters of the rotor and stator are maintained well. The maximum deviations of isentropic efficiency and pressure between prototype and model A were 1.5% and 0.5%, respectively. The deviations were only 1.25% and 0.4% at design point. The flow fields were similar in the whole operating range. The flow similarity and the type of stall inception were retained at the near-stall point. The error of the solution limit flowrate near the stall was about 4.2%, which may have been caused by the changed Re and absolute value of geometric value. Additionally, further flow similarity, through geometric corrections to compensate for the effects of changed Re and dimensions, will be researched in next study.
- A single circumferential groove was used as the casing treatment technology. The stability was improved with a negligible performance penalty. The reductions of the near-stall flowrate of the prototype and model were 1.1% and 1.2%, respectively. The similar flow fields and performance indicated that the flow similarity was kept when casing treatment was employed. The flow similarity was maintained not only under steady condition but unsteady condition, according to the unsteady simulation results.

Author Contributions: Conceptualization, H.X. and B.Y.; methodology, H.X.; software, M.S.; validation, H.X., M.S.; formal analysis, H.X.; investigation, H.X.; resources, H.X., M.S.; data curation, H.X.; writing—original draft preparation, H.X.; writing—review and editing, B.Y.; visualization, H.X.; supervision, B.Y.; project administration, H.X.; funding acquisition, B.Y. All authors have read and agreed to the published version of the manuscript.

Funding: This research was funded by the National Science and Technology Major Project (2017-V-0012-0064).

Conflicts of Interest: The authors declare no conflict of interest.

References

1. Koff, B.L. Gas Turbine Technology Evolution: A Designers Perspective. *J. Propuls. Power* **2004**, *20*, 577–595. [[CrossRef](#)]
2. Massardo, A.; Satta, A.; Marini, M. Axial Flow Compressor Design Optimization: Part II—Throughflow Analysis. *ASME J. Turbomach.* **1990**, *112*, 405. [[CrossRef](#)]
3. Wisler, D.C. Loss Reduction in Axial-Flow Compressor Through Low-Speed Model Testing. *ASME J. Eng. Power* **1985**, *107*, 90. [[CrossRef](#)]
4. Wisler, D.C. *Core Compressor Exit Stage Study*; NASA CR No. 135391; NASA Lewis Research Center: Cleveland, OH, USA, 1977; Volume 1.
5. Wisler, D.C. Improving Compressor and Turbine Performance through Cost-Effective Low-Speed Testing. In Proceedings of the ISABE 14th International Symposium on Air-Breathing Engines, Florence, Italy, 5–10 September 1999. ISABE 99-7073.
6. Robinson, C.J. Endwall Flows and Blading Design for Axial Flow Compressors. Ph.D. Thesis, Cranfield University, Cranfield, UK, 1991.
7. Lyes, P.A. Low Speed Axial Compressor Design and Evaluation; High Speed Representation and Endwall Flow Control Studies. Ph.D. Thesis, Cranfield University, Cranfield, UK, 1999.
8. Gallimore, S.J.; Bolger, J.J.; Cumpsty, N.A.; Taylor, M.J.; Wright, P.I.; Place, J.M. The Use of Sweep and Dihedral in Multistage Axial Flow Compressor Blading—Part I: University Research and Methods Development. *ASME J. Turbomach.* **2002**, *124*, 521–532. [[CrossRef](#)]

9. Gallimore, S.J.; Bolger, J.J.; Cumpsty, N.A.; Taylor, M.J.; Wright, P.I.; Place, J.M. The Use of Sweep and Dihedral in Multistage Axial Flow Compressor Blading—Part II: Low and high-speed designs and test verification. *ASME J. Turbomach.* **2002**, *124*, 533–541. [[CrossRef](#)]
10. Boos, P.; Mockel, H.; Henne, J.M.; Seimeler, R. Flow Measurement in a Multistage Large Scale Low Speed Axial Flow Research Compressor. In Proceedings of the ASME, Turbo Expo: Power for Land, Sea, and Air, Stockholm, Sweden, 2–5 June 1998; ASME Paper No. 98-GT-432. p. V001T01A104. [[CrossRef](#)]
11. Lange, M.; Vogeler, M.K.; Mailach, R.; Elorza-Gomez, S. An experimental Verification of a New Design for Cantilevered Stators with Large Hub Clearance. *ASME J. Turbomach.* **2013**, *135*, 041022. [[CrossRef](#)]
12. Zhang, C.K.; Hu, J.; Wang, Z.Q.; Yin, C.; Yan, W. Numerical Study on Three-Dimensional Optimization of a Low-Speed Axial Compressor Rotor. In Proceedings of the ASME, Turbo Expo: Power for Land, Sea, and Air, Dusseldorf, Germany, 16–20 June 2014; ASME Paper No. GT2014-26431. p. V02BT45A016. [[CrossRef](#)]
13. Zhang, C.K.; Hu, J.; Wang, Z.Q.; Li, J. Experimental Investigations on Three-Dimensional Blading Optimization for Low-Speed Model Testing. *ASME J. Gas. Turbines Power* **2016**, *138*, GTP-15–1570. [[CrossRef](#)]
14. Zhang, C.K.; Hu, J.; Wang, Z.Q.; Gao, X. Design Work of a Compressor Stage Through High-To-Low Speed Compressor Transformation. *ASME J. Gas. Turbines Power* **2014**, *136*, 064501. [[CrossRef](#)]
15. Ma, Y.; Xi, G. Effects of Reynolds Number and Heat Transfer on Scaling of a Centrifugal Compressor Impeller. In Proceedings of the ASME, Turbo Expo: Power for Land, Sea, and Air, Glasgow, UK, 14–18 June 2010; ASME Paper No. GT2010-23372. pp. 565–572. [[CrossRef](#)]
16. Zhu, C.; Qin, G. Performance Prediction of Centrifugal Compressor Based on Performance Test, Similarity Conversion and CFD Simulation. *Int. J. Fluid Mach. Syst.* **2012**, *5*, 38–48. [[CrossRef](#)]
17. Florian, F.; Peter, J.; Hoiger, F. On the Scaling of Aeroelastic parameters for High Pressure Applications in Centrifugal Compressors. In Proceedings of the ASME, Turbo Expo: Power for Land, Sea, and Air, Seoul, Korea, 13–17 June 2016; ASME Paper No. GT2016-57409. p. V07BT34A019. [[CrossRef](#)]
18. Asad, M.S.; William, K.; George, W.K., Jr. Reconsideration of the Fan Scaling Laws: Part I—Theory. In Proceedings of the ASME/JSME 2003 4th Joint Fluids Summer Engineering Conference, Honolulu, HI, USA, 6–10 July 2003; ASME Paper No. FEDSM2003-45414. pp. 1307–1315. [[CrossRef](#)]
19. Asad, M.S.; William, K.; George, W.K., Jr. Reconsideration of the Fan Scaling Laws: Part II—Applications. In Proceedings of the ASME/JSME 2003 4th Joint Fluids Summer Engineering Conference, Honolulu, HI, USA, 6–10 July 2003; ASME Paper No. FEDSM2003-45418. pp. 1329–1336. [[CrossRef](#)]
20. Zhu, N.G.; Xu, L.; Chen, M.Z. Similarity transformation for compressor blading. *ASME J. Turbomach.* **1991**, *114*, 561–568. [[CrossRef](#)]
21. Xie, H.; Yang, B.; Zhang, S.; Song, M. Performance Analysis and Improvement of a Centrifugal Compressor Based on Partial Similarity Principle. *ASME J. Eng. Gas. Turbines Power* **2020**, *142*, 05012. [[CrossRef](#)]
22. Tan, C.S.; Day, I.; Morris, S.; Wadia, A. Spike-Type Compressor Stall Inception, Detection, and Control. *Annu. Rev. Fluids Mech.* **2010**, *42*, 275–300. [[CrossRef](#)]
23. Vo, H.D.; Tan, C.S.; Greitzer, E.M. Criteria for Spike Initiated Rotaing Stall. *ASME J. Turbomach.* **2008**, *130*, 011023. [[CrossRef](#)]
24. Du, J.; Gao, L.P.; Li, J.C.; Lin, F.; Chen, J.Y. Initial selection of groove location combination for multi-groove casing treatment. *J. Mech. Sci. Technol.* **2015**, *30*, 697–704. [[CrossRef](#)]
25. Seitz, P.A. Casing Treatment for Axial Flow Compressors. Ph.D. Thesis, Cambridge University, Cambridge, UK, 1999.
26. Wilke, I.; Kau, H.-P.A. Numerical Investigation of the Flow Mechanisms in a High Pressure Compressor Front Stage with Axial Slots. *ASME J. Turbomach.* **2004**, *126*, 339–349. [[CrossRef](#)]
27. Osborn, W.M.; Lewis, G.W.; Heidelberg, L.J. *Effects of Several Porous Casing Treatments on Stall Limit and Overall Performance of an Axial Compressor Rotor*; NASA Report TN 6537; National Aeronautics and Space Administration: Washington, DC, USA, 1971.
28. Fujita, H.; Takatta, H. A study on configurations of casing treatment for axial flow compressors. *JSME Bull.* **1983**, *27*, 1675–1681. [[CrossRef](#)]
29. Zhao, S.F.; Lu, X.G.; Zhu, J.Q.; Zhang, H.W. Investigation for the Effects of Circumferential Grooves on the Unsteadiness of Tip Clearance Flow to Enhance Compressor Flow Instability. In Proceedings of the ASME, Turbo Expo: Power for Land, Sea, and Air, Glasgow, UK, 14–18 June 2010; ASME Paper No. GT2010-22652. pp. 269–277. [[CrossRef](#)]

30. Houghton, T.; Day, I. Enhancing the Stability of Subsonic Compressors Using Grooves. *ASME J. Turbomach.* **2011**, *133*, 021007. [[CrossRef](#)]
31. Du, J.; Gao, L.P.; Li, J.C.; Lin, F.; Chen, J.Y. The Impact of Casing Groove Location on Stall Margin and Tip clearance Flow in a Low-Speed Axial Compressor. *ASME J. Turbomach.* **2016**, *138*, 121007. [[CrossRef](#)]
32. Bailey, E.E. *Effect of Grooved Casing Treatment on the Flow Range Capability of a Single-stage Axial-flow Compressor*; NASA Report TM 2459; National Aeronautics and Space Administration: Washington, DC, USA, 1972.
33. Dufour, G.; Carbonneau, X.; Cazalbou, J.; Chassaing, P. Practical Use of Similarity and Scaling Laws for Centrifugal Compressor Design. In Proceedings of the ASME, Turbo Expo: Power for Land, Sea, and Air, Barcelona, Spain, 8–11 May 2006; ASME paper No. GT2006-91227. pp. 1131–1140. [[CrossRef](#)]
34. Ning, F.; Xu, L. Numerical investigation of transonic compressor rotor flow using an implicit 3D flow solver with one-equation Spalart-Allmaras turbulence model. In Proceedings of the ASME, Turbo Expo: Power for Land, Sea, and Air, New Orleans, LA, USA, 4–7 June 2001; ASME paper No. 2001-GT-0.59. p. V001T03A054. [[CrossRef](#)]
35. Spalart, P.R.; Allmaras, S.R. A one equation turbulence model for aerodynamic flows. In Proceedings of the 30th Aerospace Sciences Meeting and Exhibit, Reno, NV, USA, 6–9 January 1992. AIAA paper. [[CrossRef](#)]
36. Numeca. *Numeca FINETurbo User Guide, Version 11.1*; NUMECA: Beijing, China, 2017.
37. Assam, A.; Narayan Kalkote, N.; Sharma, V.; Eswaran, V. An Automatic Wall Treatment for Spalart-Allmaras Turbulence Model. *ASME J. Fluids Eng.* **2018**, *140*, 061403. [[CrossRef](#)]
38. Rai, M.M. Three-Dimensional Navier-Stokes Simulations of Turbine Rotor-Stator Interaction. *ASME J. Turbomach.* **1987**, *112*, 377–384. [[CrossRef](#)]
39. Song, M.R.; Yang, B.; Dong, G.M.; Liu, X.L.; Wang, J.Q.; Xie, H.; Lu, Z.H. Research on Accuracy of Flowing Field Based on Numerical Simulation for Tonal Noise Prediction in Axial Compressor. In Proceedings of the ASME, Turbo Expo: Power for Land, Sea, and Air, Oslo, Norway, 11–15 June 2018. ASME Paper No. GT2018-76382. [[CrossRef](#)]
40. Yoon, Y.S.; Song, S.J.; Shin, H.W. Influence of Flow Coefficient, Stagger Angle, and Tip Clearance on Tip Vortex in Axial Compressor. *ASME J. Fluids Eng.* **2006**, *128*, 1274–1280. [[CrossRef](#)]
41. Pelz, P.F.; Stonjek, S. Introduction of an universal scale-up method for the efficiency of axial and centrifugal fans. In Proceedings of the ASME Turbo Expo 2014: Turbine Conference and Exposition, Dusseldorf, Germany, 16–20 June 2014; ASME Paper No. GT2014-25403. p. V01AT10A007. [[CrossRef](#)]
42. Koch, C.C.; Smith, L.H. Loss sources and magnitudes in axial-flow compressor. *ASME J. Gas. Turbines Power* **1976**, *98*, 411–424. [[CrossRef](#)]



© 2020 by the authors. Licensee MDPI, Basel, Switzerland. This article is an open access article distributed under the terms and conditions of the Creative Commons Attribution (CC BY) license (<http://creativecommons.org/licenses/by/4.0/>).

Article

Numerical Study on the Influence of Step Casing on Cavitating Flows and Instabilities in Inducers with Equal and Varying Pitches

Lu Yu ¹, Haochen Zhang ¹, Hui Chen ², Zhigang Zuo ^{1,3,*} and Shuhong Liu ^{1,*}

¹ Department of Energy and Power Engineering, State Key Laboratory of Hydrosience and Engineering Laboratory, Tsinghua University, Beijing 100084, China; l-yu16@mails.tsinghua.edu.cn (L.Y.); zhanghaochen1992@163.com (H.Z.)

² Science and Technology on Liquid Rocket Engine Laboratory, Xi'an Aerospace Propulsion Institute, Xi'an 710100, China; chenhui2013abc@163.com

³ Yantai Research Institute and Graduate School, Harbin Engineering University, Yantai 264010, China

* Correspondence: zhigang200@mail.tsinghua.edu.cn (Z.Z.); liushuhong@mail.tsinghua.edu.cn (S.L.)

Received: 17 August 2020; Accepted: 1 September 2020; Published: 4 September 2020



Abstract: It is known that cavitating flow characteristics and instabilities in inducers can greatly impact the safety and stability of a liquid rocket. In this paper, step casing optimization design (Model OE and Model AE) was carried out for two three-bladed inducers with an equal (Model O) and a varying pitch (Model A), respectively. The unsteady cavitation flow field and accompanied instabilities were studied via numerical simulations. Reductions of the cavity size and fluctuation were observed in cases with a step casing. A significant difference in cavity structures was seen as well. Referring to the pressure distributions on the blades and details of the flow field, the mechanism of cavitation suppression was revealed. This work provides a feasible and convenient method in engineering practice for optimizing the characteristic of the cavitating flow field and instabilities for the inducer.

Keywords: inducer; step casing; varying pitch; cavitating flow and instabilities

1. Introduction

In hydraulic systems of liquid rocket engines, turbopumps are the main hydraulic components that convey fuel and oxidizers. Due to the demand for a maximum power/weight ratio of the main pump, cavitation may develop on the suction sides of the blades at the inlet of the main impeller [1,2], leading to performance degradation (i.e., sharp decrease in head and efficiency) and hydraulic instabilities (i.e., significant pressure fluctuations). Installing an inducer at the upstream of the main pump is a common solution to mitigate the aforementioned effects. Therefore, the inducer often operates under cavitation conditions accompanied by complex cavitation instabilities [3–7]. Among them, rotating cavitation (RC) is widely considered as a major cause for the premature cutoff of engines [8,9].

Great efforts including inducer impeller optimization and casing modifications were made to alleviate the influences of cavitation and its associated instabilities. Considering the manufacturing convenience and the degree of overall structural change, casing modification, especially step casing design, has been widely studied [10–14]. With a local clearance enlargement, it tends to be an effective and realizable way for performance improvement. Kamijo et al. [4] designed five casings with upstream/trailing edge enlargements and proposed a criterion for RC suppression in a LE-7 LOX (Liquid Oxygen) turbopump inducer. Hashimoto et al. [10] experimentally illustrated the influence of step casing with an upstream enlargement. It was observed that the onset and occurrence region of RC were modified effectively. Furthermore, Shimagaki et al. [15] described the mechanism for

RC suppression with step casing (i.e., a decrement of incidence angel by a thickened backflow vortex with a wider tip clearance) by combining particle imaging velocimetry (PIV) and high-speed photography. Moreover, Fujii et al. [16] carried out experiments of 8 step casings to study the effects of geometries (depth, location, etc.). Therefore, it can be concluded that step casing with an upstream enlargement may be a possible method for RC suppression. However, concrete analysis is still needed for specific inducers.

In this paper, step casing optimization design was carried out for two three-bladed inducers with equal and varying pitch, respectively. Emphasis was exerted on the unsteady cavitation flow field and the accompanied instabilities by numerical simulations. The characteristic of the cavitation area on the blades and three-dimensional cavity structures was analyzed. The reductions of the cavity size and RC fluctuation were observed in cases with step casing. Referring to the pressure distributions on the blades and the details of the flow field, the mechanism of cavitation suppression was revealed.

2. Numerical Studies

2.1. Numerical Methods

The computational domain is shown in Figure 1, which consisted of an inlet pipe, an annulus inlet casing, an inducer impeller, and an outlet pipe. An annulus casing with deflectors was placed upstream of the inducer and aimed at forming a uniform inlet flow [17]. The inlet and outlet pipes were extended for a fully developed flow simulation (5 times the diameter of the annulus inlet casing and 7 times the diameter of the inducer blade tip, respectively).

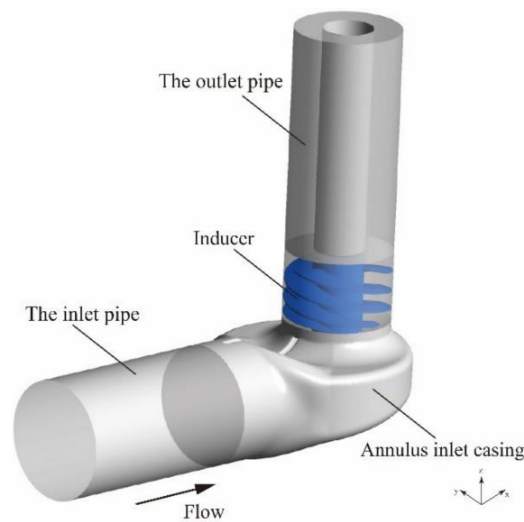


Figure 1. Computational domain.

Reynolds averaged Navier–Stokes (RANS) equations were solved in ANSYS CFX 19.2 code. A SST (Shear Stress Transfer) $k - \omega$ turbulence model [18] and Zwart-Gerber-Belamri (ZGB) cavitation model [19] were utilized for turbulence and cavitation modeling with the boundary conditions of mass flow rate and pressure at the inlet and outlet, respectively.

The entire mesh system was developed in a commercial software package ICEM-CFD (Integrated Computer Engineering and Manufacturing code for Computational Fluid Dynamics). Unstructured hybrid grids were utilized for the annulus inlet casing and inducer. As for the inlet and outlet pipes, hexahedral grids were developed. A 10-layer boundary layer grid was utilized with a height of 0.01 mm at the first layer. More than 20 layers of mesh were set on the tip to accurately capture the clearance flow characteristic.

Unsteady simulations were applied to evaluate the characteristics of cavitation instabilities. The grid and time independence studies were carried out to find the best compromise between

accuracy and efficiency. The mesh system with 2.1×10^7 elements (Figure 2 shows the mesh of the inducer) and the time step corresponding to 2° of the inducer impeller rotations were chosen for the following simulations. The verification of the above numerical setup can be referred to in our previous research [20].

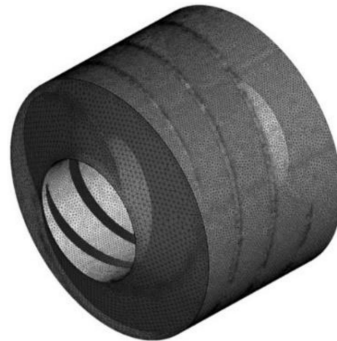


Figure 2. Mesh of the inducer.

2.2. The Inducers and Step Casing Design

Two inducers with an equal (Model O) and varying pitch (Model A) were selected to compare the influence of step casing design (Model O and Model OE, Model A and Model AE). Tables 1 and 2 summarize the geometries of the studied inducers. For the equal pitch inducer, the blade profile was a straight line (shown on the left of Figure 3) leading to an equal inlet and outlet blade angle. As for the varying pitch inducer, the inlet and outlet blade angle was reduced and increased, respectively. Therefore, the blade profile of the varying pitch inducer on the right side of Figure 3 was curved. It should be pointed out that both the inlet and outlet blade angles of the two inducers were different and thus results between the equal and varying pitch were not comparable. The study in this paper mainly focused on the influence of step casing on the equal and varying pitch inducers, respectively, and the cross-comparison was not involved.

Table 1. Geometrical parameters of the cases with the equal pitch inducer.

Model	Inlet Blade Angle β_1	Outlet Blade Angle β_2	Pitch Variation	Casing Geometry
O	β	β	Constant	Straight
OE	β	β	Constant	Step

Table 2. Geometrical parameters of the cases with the varying pitch inducer.

Model	Inlet Blade Angle β_1	Outlet Blade Angle β_2	Pitch Variation	Casing Geometry
A	$\beta - 1.8^\circ$	$\beta + 0.6^\circ$	Linear	Straight
AE	$\beta - 1.8^\circ$	$\beta + 0.6^\circ$	Linear	Step

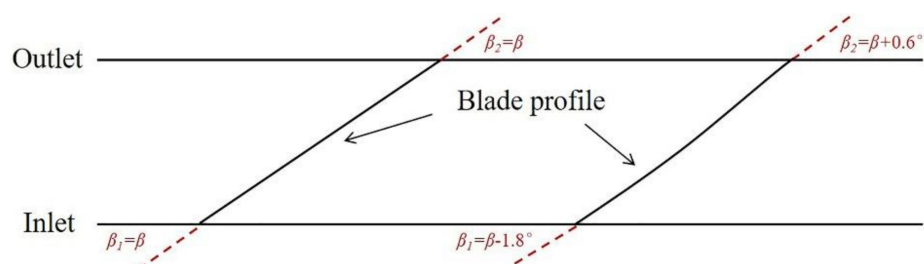


Figure 3. Schematic of the blade profile. (Left one for the equal pitch inducer and the right one for the varying pitch inducer).

Figure 4 shows the schematics of the two casings used in this study. Figure 4a terms a step casing, with enlargement near the leading edge of the inducer. While the other (shown in Figure 4b) is a straight one, owning a constant diameter from the inlet to the outlet.

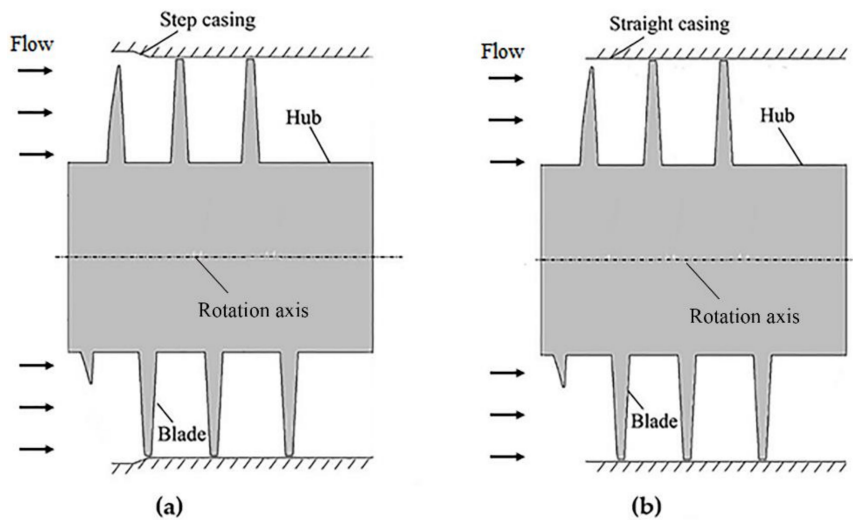


Figure 4. Schematics of the studied casings: (a) Step casing; (b) straight casing.

3. Results

3.1. Characteristics of Cavity Oscillation on the Blades

The oscillation of the cavity on the blades was monitored to understand cavitating instabilities. Figure 5 shows the variation of a nondimensional cavity area S_{cav}' over time on three blades of Model O. The ratio of the cavity area on the blade to the area of the inlet, $=S_{cav}'/S_f$; from the perspective of cavitation suppression, was expected to be as small as possible. It can be seen that the cavity variation on each blade was similar. They changed in an approximate sinusoidal pattern with a frequency of 152 Hz ($\sim f_0$) and a certain phase difference between neighboring blades. It can be inferred that there was rotating cavitation in the studied inducer. Such asymmetric distribution of cavities might influence the operation's safety and stability.

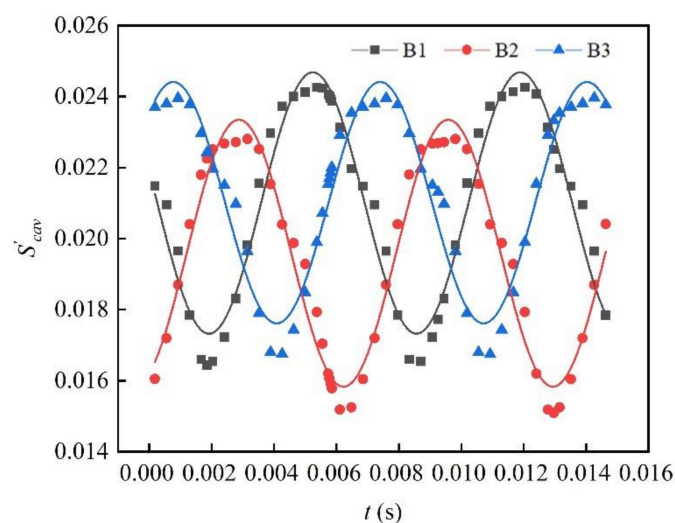


Figure 5. The variation of the nondimensional cavity area over time on three blades of Model O.

Taking the result of a certain blade as an example, the impact of the step casing design on the cavity oscillation is discussed below. Figures 6 and 7 show the comparison of cavity oscillation in

Model O and OE (cases with the equal pitch inducer), as well as Model A and AE (cases with the varying pitch inducer). The influence of step casing tended to be similar both in equal and varying pitch inducers. Significant reduction of cavities was seen when step casing was applied, showing that the step casing design had a positive effect on cavitation suppression both in equal pitch and varying pitch inducers.

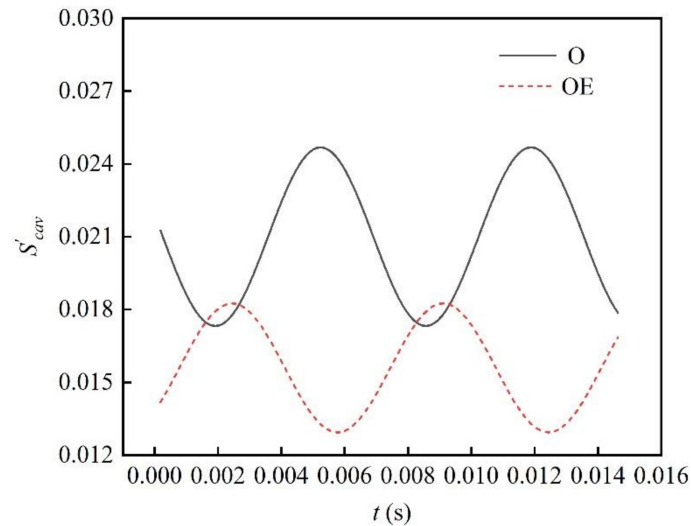


Figure 6. The variation of the nondimensional cavity area over time on Blade 1 of Model O and OE (cases with the equal pitch inducer).

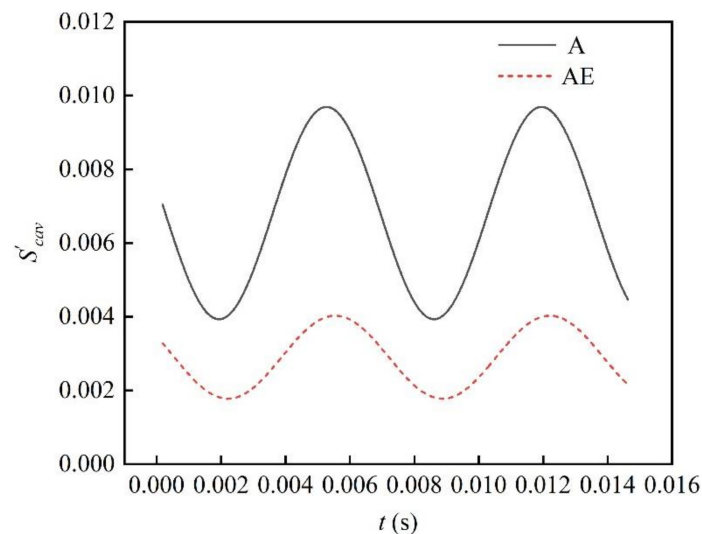


Figure 7. The variation of the nondimensional cavity area over time on Blade 1 of Model A and AE (cases with the varying pitch inducer).

3.2. Characteristics of Three-Dimensional Cavity Structures

3.2.1. The Results of Cases with the Equal Pitch Inducer

Three-dimensional cavity structures were analyzed with the help of the isosurface of the vapor volume fraction $\alpha_v = 0.3$. As shown in Figure 8a,b, the cavity mainly appeared near the leading edge in both Model O and OE. The cavity structures were similar. Cavities in both Model O and OE had two subregions with different characteristics: Type I resembled the attached cavitation region and Type II resembled cloud cavitation. With the step casing, substantial suppression of the cavity in both streamwise and axial directions was figured out. Next, we show details regarding the cavity on three

typical sections along the streamwise direction within 1 revolution, thus demonstrating the varying features of cavity structure over time.

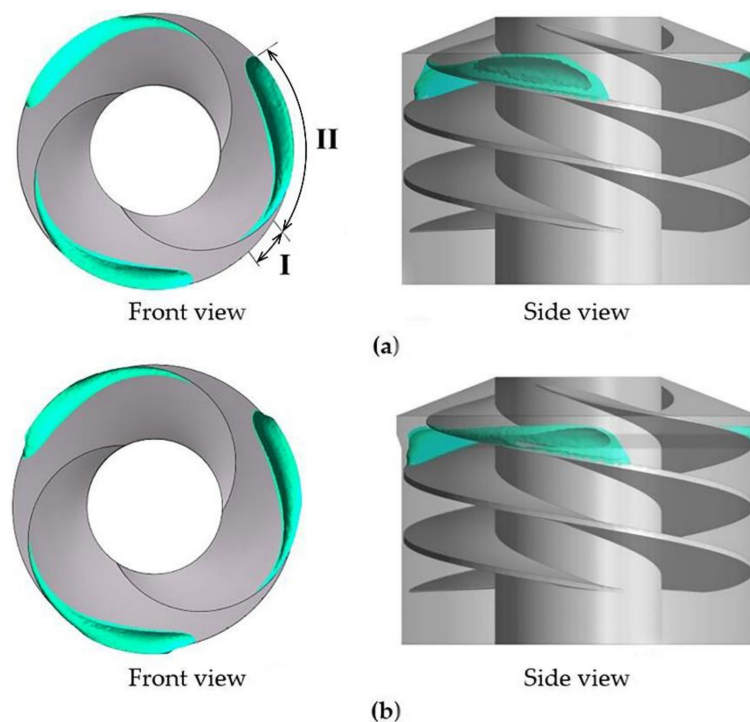


Figure 8. The 3D cavity structures of (a) Model O and (b) Model OE.

As shown in Figure 9a, the first section (S_1) was in the middle of Type I. $\theta_1 = \theta_0 + \frac{1}{2}\Delta\theta_I$, θ_0 indicates the inception position of Type I; $\Delta\theta_I$ indicates the region Type I occupies streamwise, indicating the characteristic of Type I cavitation. Figure 9b,c show the variation of cavities within 1 revolution (T) at S_1 for Model O and OE. Here, PS stands for the pressure side, whereas SS denotes the suction side. Furthermore, r' indicates the ratio of radial position and tip radius ($=r/r_T$), while Z' indicates the ratio of axial position and the axial length of the blade ($=Z/L_B$). With a weak radial fluctuation and almost no axial fluctuation, the variation pattern of Type I in each case tends to be similar. We found the cavity area as $O \approx OE$. $\theta_{1OE} > \theta_{1O}$ indicated that the application of step casing may result in downstream cavitation inception.

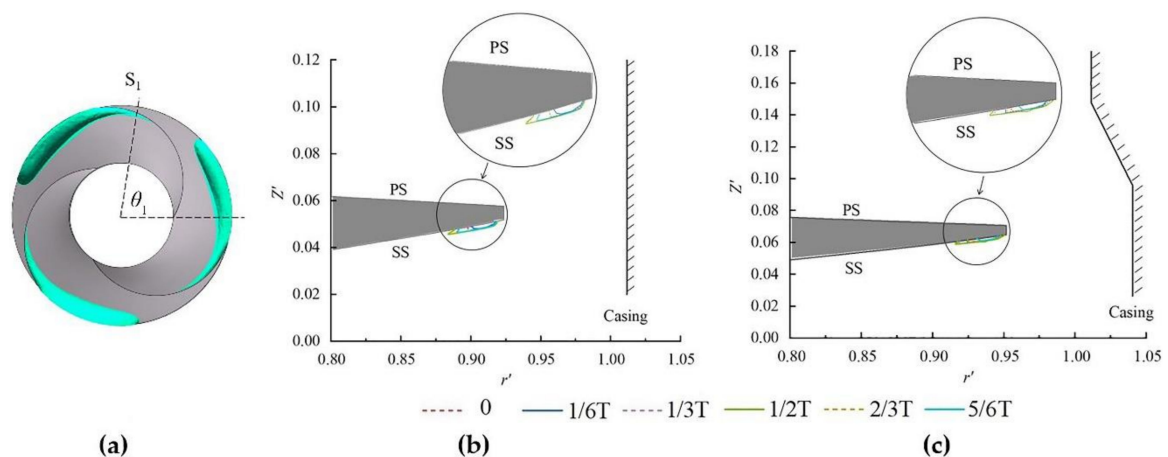


Figure 9. The variation of cavities over time at S_1 . (a) Schematic of S_1 , (b) Model O, and (c) Model OE.

The section at the end of the sweep was chosen as S_2 , thus finding that $\theta_{2O} = \theta_{2OE} = 110^\circ$. For Model O and OE, S_2 located the region of Type II with significant radial and axial variations

(Figure 10a). Obvious morphological differences of cavities were observed. Cavities in Model O (Figure 10b) developed in a much wider range along the radial and axial direction and were limited by the casing. However, in Model OE (Figure 10c), with a local increment of clearance, the cavities were far away from the casing and presented a semi-elliptical shape.

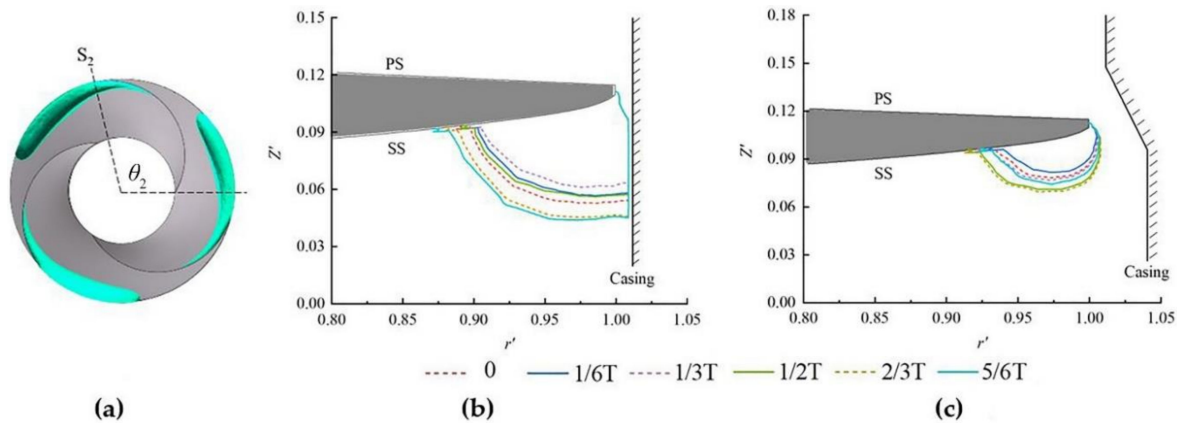


Figure 10. The variation of cavities over time at S_2 . (a) Schematic of S_2 , (b) Model O, and (c) Model OE.

The section of average cavitation oscillation along streamwise was taken as S_3 (Figure 11a), which led to the lack of results. In Model O and OE (Figure 11b,c), the radial and axial fluctuations of the cavities were captured, and there was little difference in morphology as the blade was away from the step in Model OE.

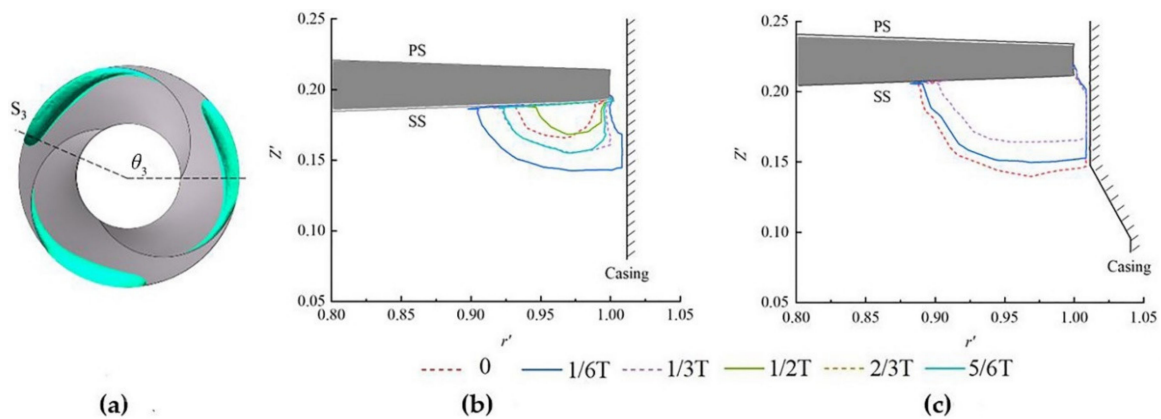


Figure 11. The variation of cavities over time at S_3 . (a) Schematic of S_3 , (b) Model O, and (c) Model OE.

Table 3 summarizes the detailed characteristics of the cavity of cases with an equal pitch inducer along the streamwise, radial, and axial directions. It can be seen that the cavities in Model O and OE consisted of two regimes—Type I and II—and there were slight differences in the inception location and occupied range along the streamwise direction. However, there was an increase in the maximum range along the radial direction while the maximum range along the axial direction decreased.

Table 3. Geometrical parameters of the studied inducers.

Model	Region	θ	$\Delta\theta$	$(\Delta r)_{\max}$	$(\Delta z)_{\max}$
O	I	$75^\circ \sim 85^\circ$	10°	11.9%	13.5%
	II	$85^\circ \sim 160^\circ$	75°		
OE	I	$80^\circ \sim 90^\circ$	10°	19.8%	11.1%
	II	$90^\circ \sim 170^\circ$	80°		

3.2.2. The Results of Cases with the Varying Pitch Inducer

Three-dimensional cavity structures for the varying pitch inducer are shown in Figure 12a,b. Unlike the equal pitch inducer, a significant difference in cavity structures were seen in the varying pitch inducer when the step casing was applied. Cavities in Model A owned two subregions. In Model AE, only clearance cavitation was observed and nearly no leakage cavitation occurred in other cases. Thus, there was only the Type I cavity.

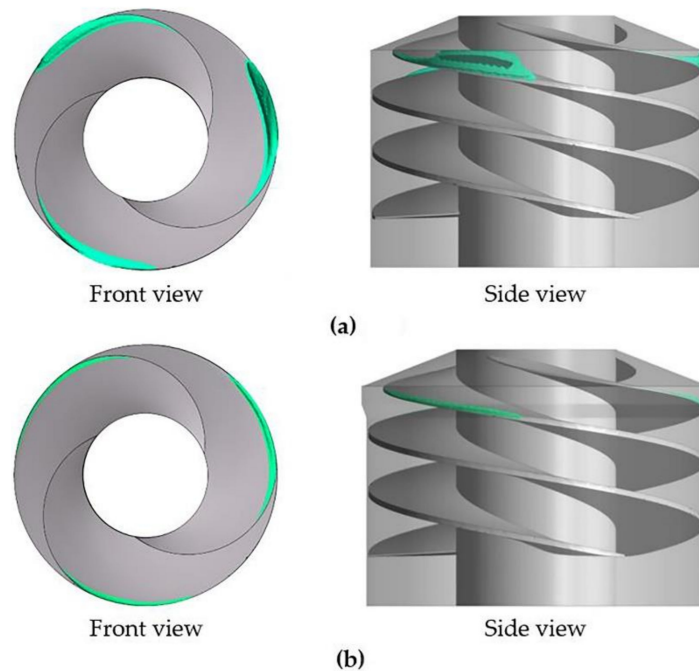


Figure 12. The 3D cavity structures of (a) Model A and (b) Model AE.

Cavity details varying pitch cases were analyzed. Figure 13b,c shows the characteristics at S_1 (Figure 13a). For Model A, the midsection of Type I ($\theta_1 = \theta_0 + \frac{1}{2}\Delta\theta_I$) was taken. As for AE, $\theta_{1AE} = \theta_{0AE} + \frac{1}{2}\Delta\theta_{IA}$. A weak radial fluctuation and almost no axial fluctuation of cavity variation was observed in both cases. In terms of the cavity area, we found that $A \approx AE$. $\theta_{1AE} > \theta_{1A}$ indicates that the application of step casing could result in downstream cavitation inception.

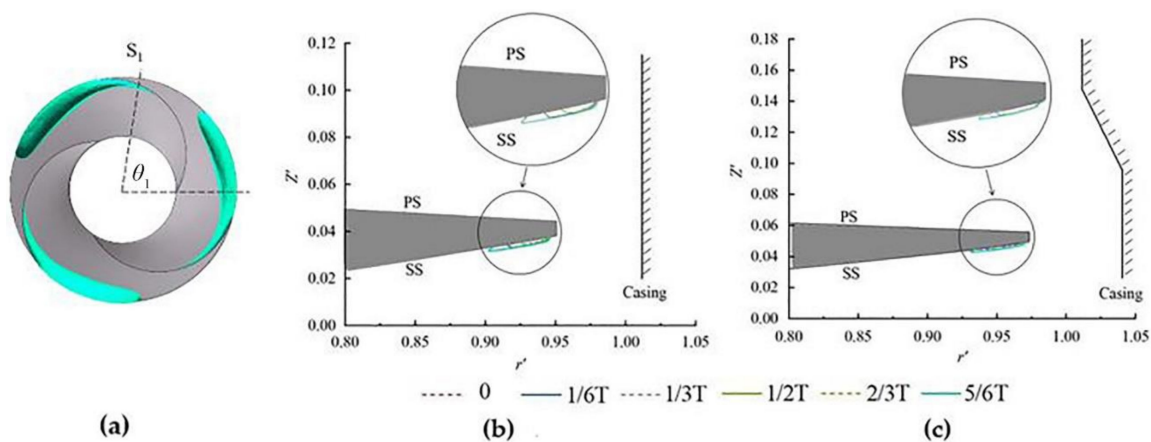


Figure 13. The variation of cavities over time at S_1 . (a) Schematic of S_1 , (b) Model A, and (c) Model AE.

The results at S_2 (Figure 14a, $\theta_{2A} = \theta_{2AE} = 110^\circ$) are shown in Figure 14b,c. A striking influence of step casing was observed. In Model A, the cavity variations were similar to Model O and OE,

indicating a Type II cavitation. While in Model AE, the fluctuation in the axial direction greatly reduced and tended toward Type I.

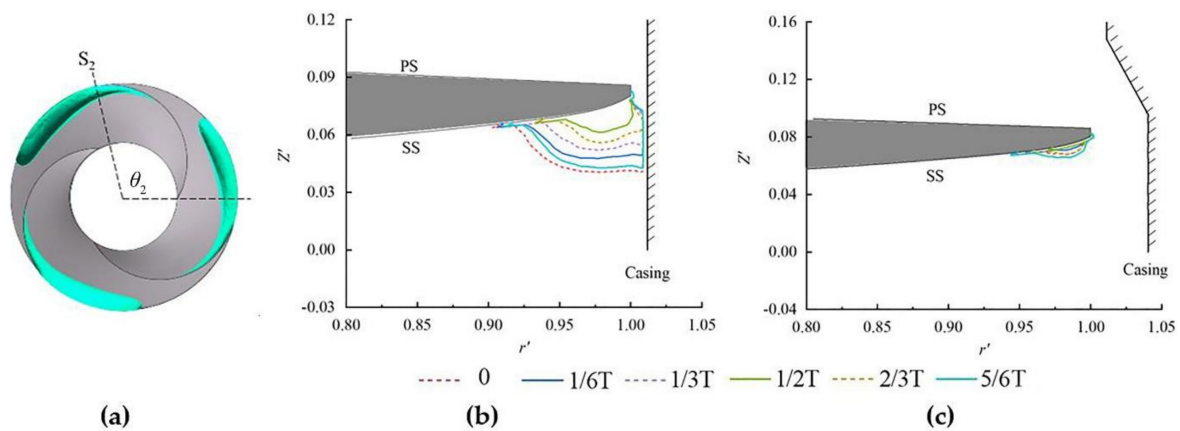


Figure 14. The variation of cavities over time at S_2 . (a) Schematic of S_2 , (b) Model A, and (c) Model AE.

At S_3 (Figure 15a), significant differences of morphology and fluctuation characteristics were observed (Figure 15b,c). Apparent radial and axial fluctuations of the cavities were captured in Model A, indicating a Type II cavitation. In Model AE, the cavities tended to be Type I

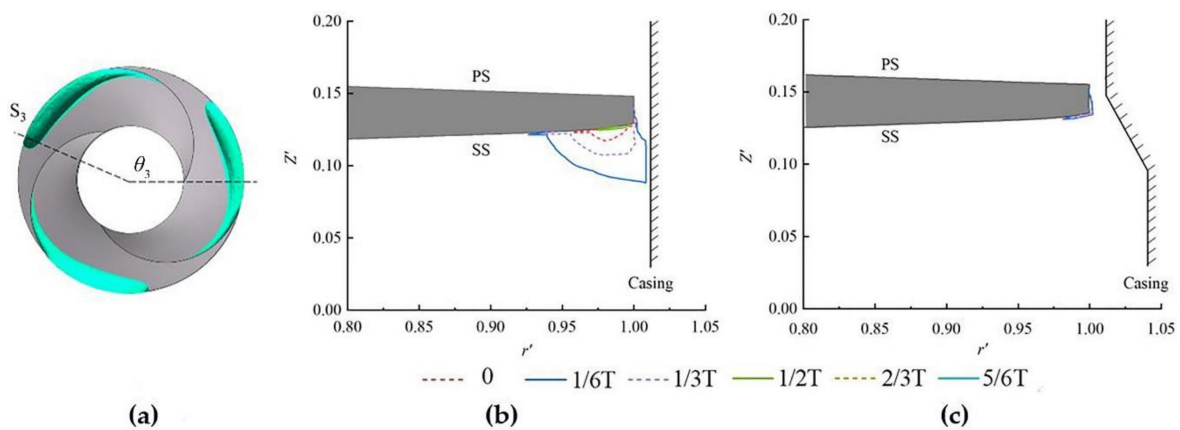


Figure 15. The variation of cavities over time at S_3 . (a) Schematic of S_3 , (b) Model A, and (c) Model AE.

Table 4 summarizes the detailed characteristics of the cavity along the streamwise, radial, and axial directions. For varying inducer cases (Model A and AE), close inception location and total occupied range along the streamwise were observed, whereas in Model AE, the maximum range along the radial and axial direction decreased significantly. As mentioned above, cavities in Model AE mainly manifested as Type. Model A, however, owned Type I and II.

Table 4. Geometrical parameters of the studied inducers.

Model	Region	θ	$\Delta\theta$	$(\Delta r)_{\max}$	$(\Delta z)_{\max}$
A	I	$75^\circ \sim 93^\circ$	18°	11.9%	9.0%
	II	$93^\circ \sim 146^\circ$	53°		
AE	I	$80^\circ \sim 150^\circ$	70°	4.1%	6.8%

3.3. Characteristics of Blade Loading and Flow Field

To further analyze the influence of the step casing on the flow field, Figures 16 and 17 show the blade loading C_p (equals to the difference between the static pressure and the inlet pressure at each

position divided by the dynamic pressure) along the streamwise direction at a 95% span on certain blades. The distribution on the other two blades was similar. In both the equal and varying pitch inducers, with a local increment in the clearance in the vicinity of the leading edge (LE), the impact of the step casing was shown near the leading edge (0~0.25). The reduction of the maximum pressure and pressure difference between SS and PS was observed. In the subsequent area (>0.25, till the trailing edge (TE)), the step casing design showed little influence on blade loading.

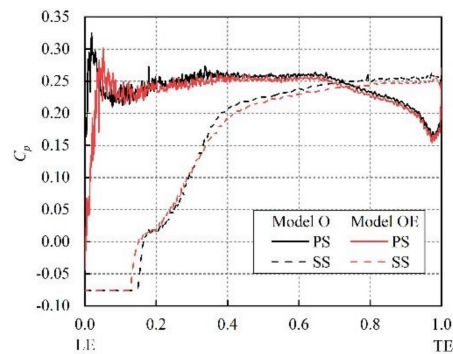


Figure 16. Blade loading along the streamwise direction at a 95% span for a certain blade in Models O and OE.

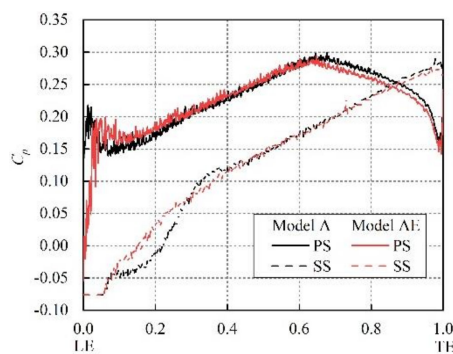


Figure 17. Blade loading along the streamwise direction at a 95% span for a certain blade in Models A and AE.

Tables 5 and 6 demonstrate the characteristics of the clearance flow at S_2 . With the reduction of Δp (pressure difference between SS and PS) and the increment of local tip clearance when step casing was applied, the average velocity at the clearance significantly reduced, while the leakage flow rate increased (145% in Model OE and 56% in Model AE).

Table 5. Characteristic parameters of clearance flow in the cases with the equal pitch inducer.

Model	Δp (Pa)	Average Velocity at the Clearance (m/s)	Leakage Flow Rate (kg/s)
O	1.11×10^6	-16.18	0.094
OE	1.04×10^6	-10.69	0.230

Table 6. Characteristic parameters of clearance flow in the cases with the varying pitch inducer.

Model	Δp (Pa)	Average Velocity at the Clearance (m/s)	Leakage Flow Rate (kg/s)
A	8.40×10^5	-7.45	0.045
AE	6.70×10^5	-1.33	0.070

Furthermore, the distribution of the vapor volume fraction α_v and velocity vectors are shown in Figures 18 and 19 (Figure 18a for Model O, Figure 18b for Model OE. And Figure 19a for Model A,

Figure 19b for Model AE). Clearance flow in cases without step casing (Model O and Model A) tended to penetrate upstream and interact with the main flow, leading to a more apparent axial extension of cavities. As for Model OE and AE, with lower velocity and higher leakage flow rates, the clearance flow tended to interact with the main flow in a closer region.

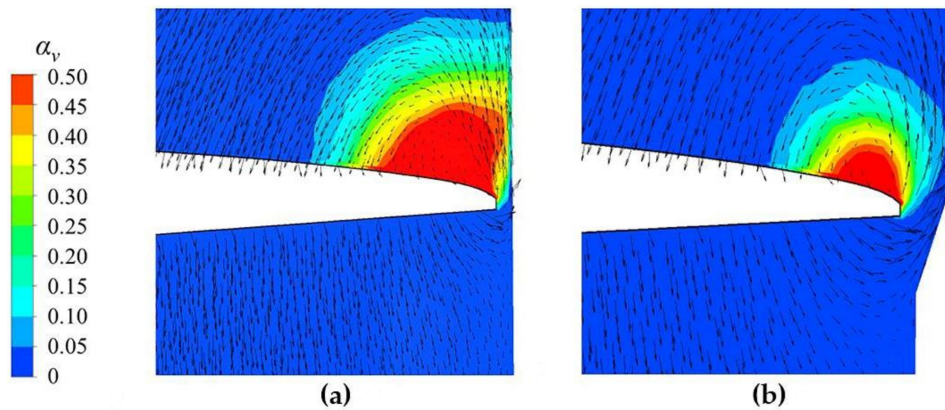


Figure 18. Flow fields at S_2 . (a) Model O and (b) Model OE.

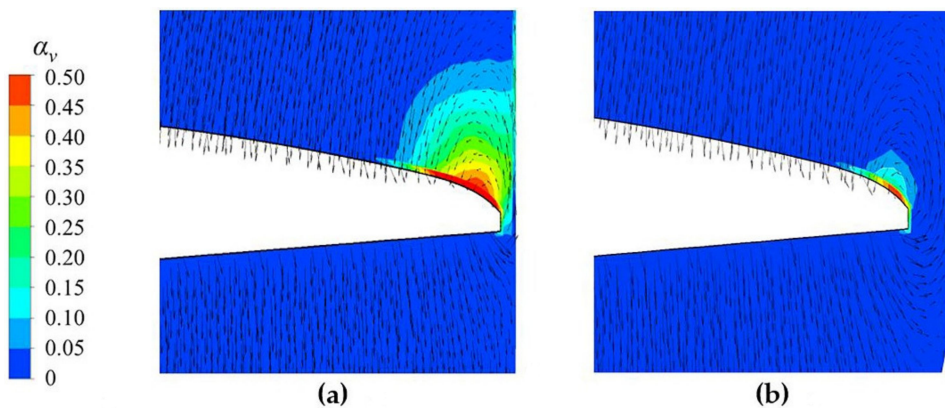


Figure 19. Flow fields at S_2 . (a) Model A and (b) Model AE.

4. Conclusions

To evaluate the influences of step casing design on cavitating flows and instabilities in inducers with equal and varying pitches, a numerical simulation was employed in four cases. We analyzed cavitation area characteristics on blades and three-dimensional cavity structures. The step casing design showed a positive effect on cavitation suppression in both equal and varying inducers with a significant reduction of cavity size and fluctuation. Its impact on cavity structures, however, was quite different. In Models O and OE (cases with the equal pitch inducer), there were two regimes: Type I (resembled attached cavitation) and Type II (resembled cloud cavitation). While in cases with the varying pitch inducer, a significant difference was observed. Model A owned two regimes (Type I and II), while in Model AE there was only the Type I cavity. Referring to the pressure distributions on the blades and the details of the flow field, it seemed that with the alteration of clearance flow characteristics, the cavity feature varied. Clearance flow in the straight casing tended to penetrate far more upstream, resulting in a more apparent axial extension of cavities. As for step casing, the clearance flow tended to interact with the main flow in a closer region with lower clearance velocity and higher leakage flow rate.

Author Contributions: Investigation, L.Y.; data curation, L.Y.; methodology, L.Y. and H.Z.; validation, L.Y. and H.Z.; writing—original draft preparation, L.Y.; writing—review and editing, H.C., Z.Z., and S.L.; supervision, H.C., Z.Z., and S.L.; funding acquisition, H.C., Z.Z., and S.L. All authors have read and agreed to the published version of the manuscript.

Funding: This research was funded by the National Key RD Program of China, grant No. 2018YFB0606103 and the National Basic Research Program of China (“973” Project), grant No. 613321.

Conflicts of Interest: The authors declare no conflict of interest.

References

1. D’Agostino, L. Turbomachinery Developments and Cavitation. In Proceedings of the VKI Lecture Series on Fluid Dynamics Associated to Launcher Developments, Rhode-Saint-Genese, Belgium, 15–17 April 2013; von Karman Institute of Fluid Dynamics: Rhode-Saint-Genese, Belgium, 2013.
2. D’Agostino, L.; Cervone, A.; Torre, L.; Pace, G.; Valentini, D.; Pasini, A. An Introduction to Flow-Induced Instabilities in Rocket Engine Inducers and Turbopumps. In *Cavitation Instabilities and Rotordynamic Effects in Turbopumps and Hydroturbines: Turbopump and Inducer Cavitation, Experiments and Design*; d’Agostino, L., Salvetti, M.V., Eds.; Springer International Publishing: Cham, Switzerland, 2017; pp. 65–86.
3. Sack, L.E.; Nottage, H. System oscillations associated with cavitating inducers. *J. Fluids Eng.* **1965**, *87*, 917–924. [[CrossRef](#)]
4. Kamijo, K.; Yoshida, M.; Tsujimoto, Y. Hydraulic and mechanical performance of LE-7 LOX pump inducer. *J. Propuls. Power* **1993**, *9*, 819–826. [[CrossRef](#)]
5. Braisted, D.; Brennen, C. Auto-oscillation of cavitating inducers. In Proceedings of the symposium on Polyphase Flow and Transport Technology, San Francisco, CA, USA, 13–15 August 1980; American Society of Mechanical Engineers (ASME): San Francisco, CA, USA; pp. 157–166.
6. Tsujimoto, Y. Cavitation instabilities in turbopump inducers. In *Fluid Dynamics of Cavitation and Cavitating Turbopumps*; d’Agostino, L., Maria Vittoria, S., Eds.; Springer: Pisa, Italy, 2007; pp. 169–190.
7. Brennen, C.E. *Hydrodynamics of Pumps*; Cambridge University Press: New York, NY, USA, 2011.
8. Ryan, R.; Gross, L.; Mills, D.; Mitchell, P. The Space Shuttle Main Engine liquid oxygen pump high-synchronous vibration issue, the problem, the resolution approach, the solution. In Proceedings of the 30th Joint Propulsion Conference and Exhibit, Indianapolis, IN, USA, 27–29 June 1994; American Institute of Aeronautics and Astronautics (AIAA): Indianapolis, IN, USA, 1994.
9. Sekita, R.; Watanabe, A.; Hirata, K.; Imoto, T. Lessons learned from H-2 failure and enhancement of H-2A project. *Acta Astronaut.* **2001**, *48*, 431–438. [[CrossRef](#)]
10. Hashimoto, T.; Yamada, H.; Funatsu, S.; Ishimoto, J.; Kamijo, K.; Tsujimoto, Y.; Hashimoto, T.; Yamada, H.; Funatsu, S.; Ishimoto, J.; et al. Rotating cavitation in three and four-bladed inducers. In Proceedings of the 33rd Joint Propulsion Conference and Exhibit, Seattle, WA, USA, 6–9 July 1997; American Institute of Aeronautics and Astronautics (AIAA): Reston, VA, USA, 1997.
11. Kang, D.; Arimoto, Y.; Yonezawa, K.; Horiguchi, H.; Kawata, Y.; Hah, C.; Tsujimoto, Y. Suppression of Cavitation Instabilities in an Inducer by Circumferential Groove and Explanation of Higher Frequency Components. *Int. J. Fluid Mach. Syst.* **2010**, *3*, 137–149. [[CrossRef](#)]
12. Torre, L.; Pasini, A.; Cervone, A.; Pace, G.; Miloro, P.; D’Agostino, L. Effect of Tip Clearance on the Performance of a Three-Bladed Axial Inducer. *J. Propuls. Power* **2011**, *27*, 890–898. [[CrossRef](#)]
13. Shimiya, N.; Fujii, A.; Horiguchi, H.; Uchiumi, M.; Kurokawa, J.; Tsujimoto, Y. Suppression of Cavitation Instabilities in an Inducer by J Groove. *J. Fluids Eng.* **2008**, *130*, 021302. [[CrossRef](#)]
14. Xu, B.; Shen, X.; Zhang, D.; Zhang, W. Experimental and Numerical Investigation on the Tip Leakage Vortex Cavitation in an Axial Flow Pump with Different Tip Clearances. *Processes* **2019**, *7*, 935. [[CrossRef](#)]
15. Shimagaki, M.; Watanabe, M.; Hashimoto, T.; Hasegawa, S.; Yoshida, Y.; Nakamura, N. Effect of the casing configurations on the internal flow in rocket pump inducer. In Proceedings of the 42nd AIAA/ASME/SAE/ASEE Joint Propulsion Conference & Exhibit, Sacramento, CA, USA, 9–12 July 2006; American Institute of Aeronautics and Astronautics (AIAA): Sacramento, CA, USA, 2006.
16. Fujii, A.; Azuma, S.; Yoshida, Y.; Tsujimoto, Y.; Uchiumi, M.; Warashina, S. Effects of Inlet Casing Geometries on Unsteady Cavitation in an Inducer. *Trans. Jpn. Soc. Mech. Eng. B* **2004**, *16*, 1450–1458.
17. Tang, F.; Li, J.; Chen, H.; Li, X.; Xuan, T. Study on Cavitation Performance of Inducer with Annulus Inlet Casing. *J. Mech. Eng.* **2011**, *47*, 171–176. [[CrossRef](#)]
18. Menter, F.R. Two-equation eddy-viscosity turbulence models for engineering applications. *AIAA J.* **1994**, *32*, 1598–1605. [[CrossRef](#)]

19. Zwart, P.J.; Gerber, A.G.; Belamri, T. A two-phase flow model for predicting cavitation dynamics. In Proceedings of the Fifth international conference on multiphase flow, Yokohama, Japan, 30 May–3 June 2004; International Conference on Multiphase Flow (ICMF): Yokohama, Japan, 2004.
20. Yu, L.; Zhang, H.; Chen, H.; Li, Y.; Zuo, Z.; Liu, S. Geometrical optimization of an inducer with respect to rotating cavitation generated radial forces by using an orthogonal experiment. *J. Appl. Fluid Mech.* **2018**, *11*, 1591–1598. [[CrossRef](#)]



© 2020 by the authors. Licensee MDPI, Basel, Switzerland. This article is an open access article distributed under the terms and conditions of the Creative Commons Attribution (CC BY) license (<http://creativecommons.org/licenses/by/4.0/>).

Article

Research on the Dynamic Characteristics of Mechanical Seal under Different Extrusion Fault Degrees

Yin Luo *, Yakun Fan, Yuejiang Han, Weqi Zhang and Emmanuel Acheaw

Research Center of Fluid Machinery Engineering and Technology, Jiangsu University, Zhenjiang 212013, China; 2221811033@stmail.ujs.edu.cn (Y.F.); 2221711011@stmail.ujs.edu.cn (Y.H.); 2221811018@stmail.ujs.edu.cn (W.Z.); 5103190336@stmail.ujs.edu.cn (E.A.)

* Correspondence: luoyin@ujs.edu.cn; Tel.: +86-132-2262-6939

Received: 24 July 2020; Accepted: 27 August 2020; Published: 30 August 2020



Abstract: In order to explore the dynamic characteristics of the mechanical seal under different fault degrees, this paper selected the upstream pumping mechanical seal as the object of study. The research established the rotating ring-fluid film-stationary ring 3D model, which was built to analyze the fault mechanism. To study extrusion fault mechanism and characteristics, different dynamic parameters were used in the analysis process. Theoretical analysis, numerical simulation, and comparison were conducted to study the relationship between the fault degree and dynamic characteristics. It is the first time to research the dynamic characteristics of mechanical seals in the specific extrusion fault. This paper proved feasibility and effectiveness of the new analysis method. The fluid film thickness and dynamic characteristics could reflect the degree of the extrusion fault. Results show that the fluid film pressure fluctuation tends to be more intensive under the serious extrusion fault condition. The extrusion fault is more likely to occur when the fluid film thickness is too large or too small. Results illustrate the opening force is affected with the fluid film lubrication status and seal extrusion fault degrees. The fluid film stiffness would not always increase with the rotating speed growth. The seal fault would occur with the increasing of rotating speeds, and the leakage growth fluctuations could reflect the fault degree.

Keywords: mechanical seal; dynamic characteristics; extrusion fault; numerical simulation; sealing performance; fluent

1. Introduction

As a widely used fluid transmission device, centrifugal pump plays a crucial role in the national economy. The proportion of pumps equipped with mechanical seals in industry has risen to 80%. The ratio is even greater among petrochemical industry, affecting up to 90%. Besides, statistics reveal that the fault caused by mechanical seals accounts for more than 40% in all machine faults. According to the statistics of centrifugal pump faults from the German Engineering Association [1], the sealing fault ratio is 31%, the rolling bearing fault ratio is 20%, the leakage fault ratio is 10%, the motor fault ratio is 10%, the rotor fault ratio is 9%, and the sliding bearing fault ratio is 8%. The sealing fault can cause an unpredictable waste of resources [2–4]. Mechanical seal faults can affect the internal flow of the centrifugal pump [5–7]. A serious situation would cause casualties and property losses. Thus, the research on mechanical seal fault diagnosis is necessary to ensure reliability and safety [8–10]. Moreover, it is necessary to research the dynamic characteristics detection of each stage when the mechanical seal fault occurs.

Great efforts have been made to do research on the dynamic characteristics of mechanical seals [11–14]. He et al. [15] studied that the viscous shear heat and frictional heat due to asperity

contact decrease with an increase in the thickness of the tapered film. As the shaft decelerates, the wear distance rate increases with an increase in the axial stiffness. The axial damping only affects the duration of the oscillations. Zhang et al. [16] researched that lubrication reduces friction and wear and generates heat, but leakage has to be considered. The effects of the sealing surface characteristics on the leakage, and the effects of the external factors of the sealing device on the leak rate. Towsyfyhan et al. [17] mainly introduces the fault detection of mechanical seal friction by acoustic emission technology. Zhang et al. [18] investigated the fluidic leak rate through metal sealing surfaces by developing fractal models for the contact process and leakage process. Gropper et al. [19] provides a comparative summary of different modeling techniques for fluid flow, cavitation, and micro-hydrodynamic effects. Migout et al. [20] studied the relationship between the temperature change of the sealing medium and the vaporization of the medium under the seal rings face deformation condition, and pointed out that the stability of the fluid film would be seriously affected when the temperature change gradient of the medium is large. Varney et al. [21] researched the influence of the installation misalignment of the seal rings, established a three-degree-freedom dynamic model of the stationary ring, analyzed the response characteristics formed by the force excitation in all directions, and pointed out that the increase of the excitation intensity would lead to the occurrence of the collision phenomenon of the seal rings. Zhu et al. [22] studied that the sealing performance is enhanced by increasing the spacing of adjacent sealing sheets. The sealing sheets with positive bending angle have less air resistance in the flow path, which would lead to larger leakage. The increase in the number of sealing sheets gives rise to an increase in the generation probability of recirculation zone and vortex, which aggravates the mainstream energy loss. Mosavat et al. [23] researched that the influences of the thermal radiation on the temperature distribution of the mechanical face seal are investigated. Also, the effect of the stretching and shrinking on the thermal performance of the fin with different profiles are comprehensively studied.

Three-dimensional models of single-cone and double-cone were established [24]. A comparison made between the flow velocity, a shear rate and shear stress in single-cone and double-cone zones. This paper revealed the CFD analysis of the flow of a polymeric material inside the double-cone plasticization-homogenization zone of the screw-disc extruder.

Plenty of investigation and discussion have been undertaken on the development of sealing performance, temperature change, and distribution of mechanical seal. At present, there is a lack of monitoring research on mechanical seal failure state. The difference of this paper is to judge the fault degree of mechanical seal according to the dynamic characteristics.

Current research about the dynamic characteristics of mechanical seals mainly focuses on the seal rings modality variation and internal flow field analysis of mechanical seals. However, there is deficiency existing in mechanical seal fault though pressure, opening force, and the leakage. Therefore, the dynamic characteristics and fault mechanism of mechanical seal in different stages need to be studied urgently.

2. Analysis of Sealing Fault Mechanism

2.1. Normal State

As shown in Figure 1, mechanical seal is an important part to prevent leakage in centrifugal pumps. Mechanical seal model in normal state is shown in Figure 1. The rotating and stationary rings stick to each other. The function principle of mechanical seal is that a thin fluid film is formed between the rotating ring and the stationary ring. Hydrodynamic effects would be formed because of the thin fluid film. The fluid film with proper thickness can improve the lubrication performance and seal performance. A certain distance between the rotating ring and the stationary ring would be formed because of the hydrodynamic effects. The normal state is that the thickness between rotating ring and stationary ring is proper. At this time, the fluid film could provide enough open force to prevent the direct contact between the rotating ring and stationary ring. The fluid film would form a certain

resistance to prevent the medium from leaking out, and make the seal surface lubricated, so as to achieve the better sealing effect.

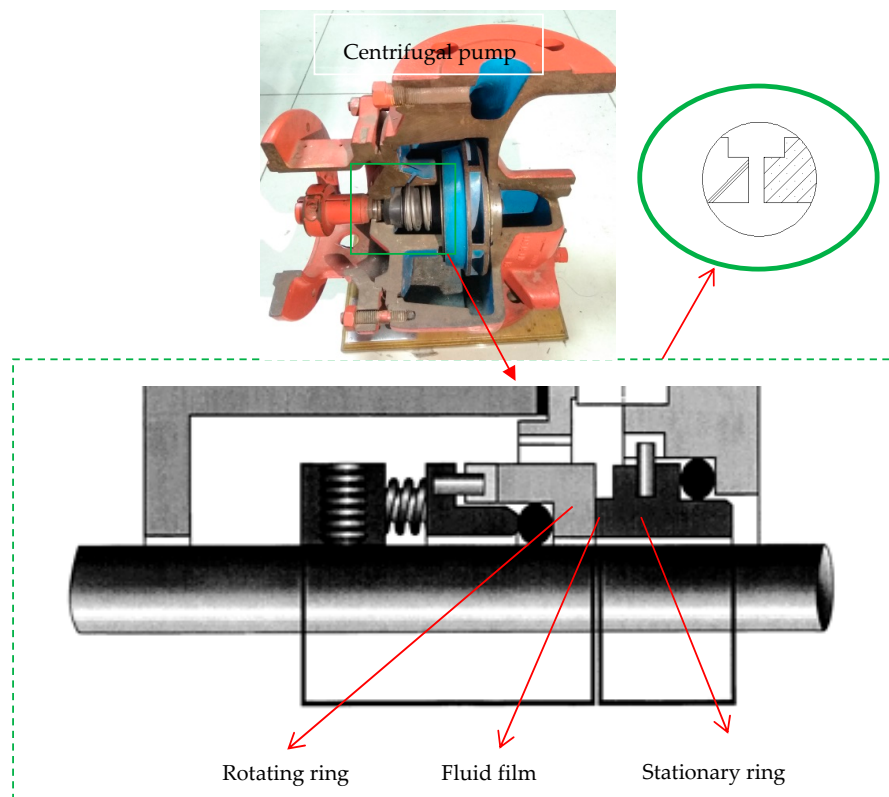


Figure 1. Schemes of mechanical seal model.

2.2. Fault State

The mechanical seal would often be in fault due to that the friction and wear behavior are universal phenomena in the rotating parts. Seal fault could be divided into many kinds, including seal surface extrusion fault, face temperature resistance fault, lateral load increasing. Many faults are caused by the squeezing of rotating and stationary rings. Figure 2 depicts the fault schematic diagrams, which show the extrusion fault in different degrees. The cause of the extrusion fault on the mechanical seal face might result from the relative deviation of the two seal ring surfaces during operation, the misaligned installation of the mechanical seal, or the mechanical seal external pressure.

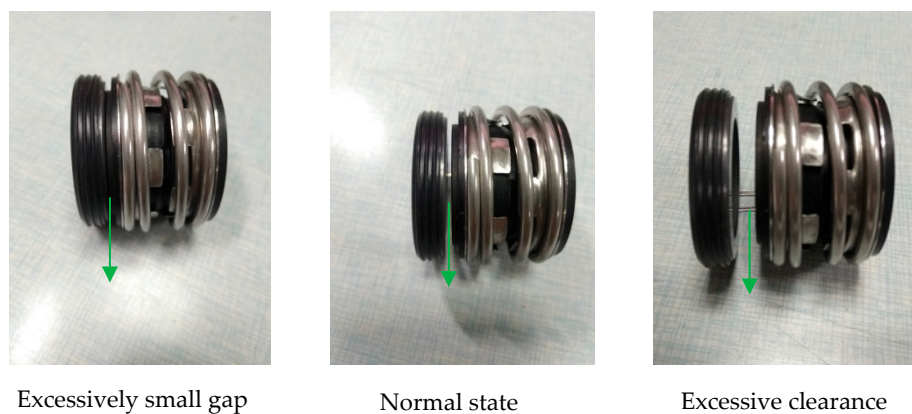


Figure 2. Physical pictures of different fault degrees.

2.3. Extrusion Faults

This paper mainly studied the fault caused by the rotating and stationary ring extrusion of the mechanical seal. The mechanical seal would form a stable fluid film during normal operation. However, the stable fluid film would be destroyed, when the mechanical seal is in fault state. From normal to fault operation state, the internal hydrodynamic pressure and the force of seal rings would change. When the relative movement of the rotating and stationary rings results in extrusion fault, the slight faults would affect the sealing performance and the serious faults would result in extrusion deformation, wear damage, and fault of the rotating and stationary rings.

Figure 3 showed that the characteristics and change of the rotating ring surface under different fault degrees. Figure 3a indicated that the seal surface would be smooth and intact in normal state. Abrasion and damage would be found in the rotating ring surface when the seal is in slight faults, which is showed in Figure 3b. The crack caused by light extrusion could be seen in the red circle of Figure 3c. Significant damage and obvious behaviors would occur when the seal was in severe faults, which are illustrated in Figure 3c. The end face damage caused by severe extrusion fault could be seen in the red circle in Figure 3c.



Figure 3. Rotating ring in different extrusion fault.

Change in mechanical seal rings was too complicated to be expressed by mathematical equations. Fault physical models were necessary to be carried out to describe the corresponding relationship between the extrusion fault and mechanical seal characteristics.

3. Establishment of Calculation Model

3.1. Fault Physical Models

In order to study the causes of mechanical seal fault and the internal sealing mechanism, it was necessary to establish a reasonable method and a proper fault physical model for analysis. The actual mechanical seal fault problem was affected by various factors. Therefore, the physical model of mechanical seal fault should be simplified. The fault of mechanical seal was mostly caused by extrusion wear of rotating and stationary rings, which resulted from the long-term uneven stress and the change of relative position of rotating and stationary rings during the long-term operation. In this paper, a simplified physical model of mechanical seal fault was established to analyze the extrusion fault of rotating and stationary rings. To establish the fault physical model, two aspects need to be considered. One is to assume that the relative movement of the rotating and stationary rings only occurs along the axial direction, and the movement along the radial direction was assumed to be zero. The second is to assume that the material texture of the rotating and stationary ring is uniform. In this paper, the thickness of the fluid film between the rotating and stationary rings was used to represent the distance between the rotating and stationary rings when different extrusion faults occur in the axial direction of the mechanical seal. The dynamic characteristics of fluid film with different thickness could reflect the different fault degrees of mechanical seal when extrusion fault occurs. Finally, the fault model of mechanical seal under this fault was formed.

In this paper, the upstream pumping mechanical seal was selected as the research object. The physical model was composed of three main parts: rotating ring, fluid film, and stationary ring. Figure 4 showed the axial section diagram of the rotating ring modeling and the geometric parameters of the section. The main geometrical parameters of the fluid film were selected: the inner radius of the rotating rings $r_i = 25$ mm, the outer radius of the rotating ring $r_o = 32$ mm. Figure 5 indicated the axial section diagram of the stationary ring modeling and the geometric parameters of the section. The inner radius of the stationary ring $r_i = 24.5$ mm, the outer radius of the rotating ring $r_o = 31$ mm. Figure 6 showed the three-dimensional diagram of fluid film modeling. Besides, the dimensions of the inner and outer rings of the fluid film were shown in detail. Because the order of magnitude in the direction of film thickness was micrometer, Figure 6 showed the enlarged fluid film thickness. The thickness of the fluid film was set to 1, 2, 3, 4, 5, 6, 7, 8, 9 μm , respectively. Figure 7 illustrated the computational domains of the mechanical seals.

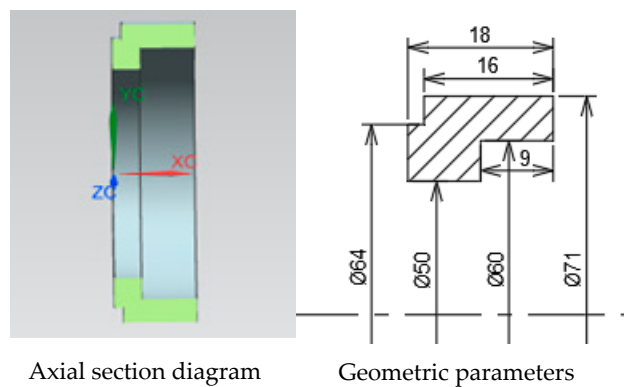


Figure 4. Rotating ring modeling diagram.

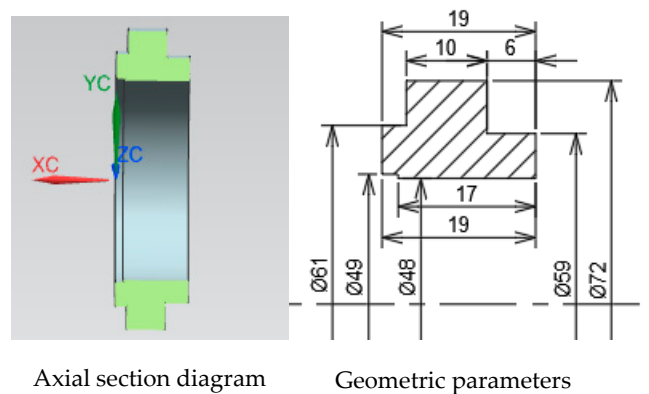


Figure 5. Stationary ring modeling diagram.

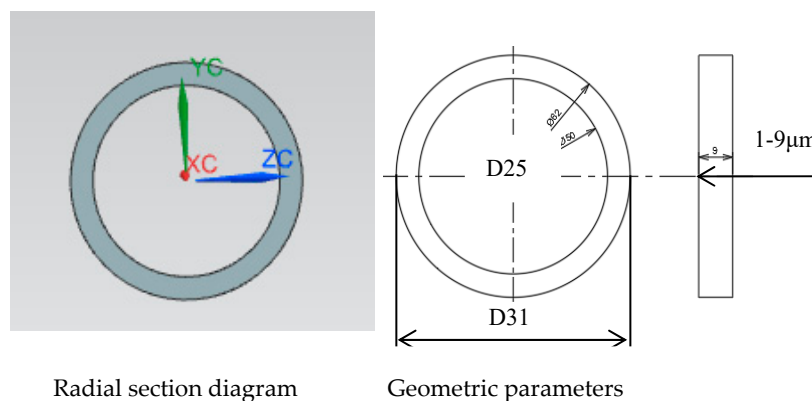


Figure 6. 3D diagrams of fluid film modeling.

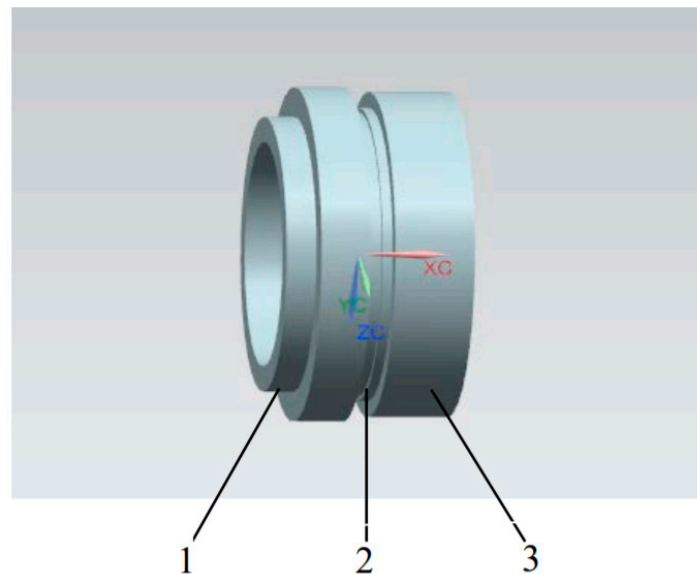


Figure 7. Computational domains of the mechanical seal (1-stationary ring, 2-fluid film, 3-rotating ring).

This section may be divided by subheadings. It should provide a concise and precise description of the experimental results, their interpretation as well as the experimental conclusions that can be drawn.

3.2. Dynamic Calculation Model

The fault of the mechanical seal was mostly manifested in the squeeze and wear fault of the rotating and stationary rings. The dynamic calculation model was selected according to the simplified fault physical model given above when the rotating and stationary rings fail due to extrusion fault. With the deepening of theoretical research on mechanical seals, the mechanical seal faults include various sciences such as mechanics, power, fluids, materials, chemistry, heat transfer, and tribology. In order to study the law between the mechanism and structural characteristics of mechanical seal when extrusion fault occurs, a dynamic calculation model suitable for fault physical model was adopted in this paper.

In order to make the simulation simple and clear, the following assumptions were made in this paper, considering the existence of fluid pressure, elastic force, solid deformation and the interaction force and heat transfer between fluid and solid in the mechanical seal.

- Mechanical seal consists of rotating ring, fluid film, stationary ring, and auxiliary system, the rotating ring part was provided with elastic force by the elastic element. The fluid film was formed by the liquid between the rotating and stationary ring. The stationary ring is a static part of the mechanical seal. The mechanical seal is simplified to simulate the process of faults conveniently. Thus, it is simplified into three parts: rotating ring, stationary ring, and fluid film.
- Because the distance between the rotating ring and the stationary ring is quite close and the thickness of the fluid film is tiny in the actual work of mechanical seal, the fluid film conforms to the Newton's law of viscosity and the effect of volume force and inertia force is ignored.
- The sealing medium is generally an incompressible fluid, but the density would change with pressure in this paper.
- It is assumed that the heat generated by friction is only transferred between the rotating and stationary rings of the mechanical seal, and the heat loss caused by stirring, thermal radiation, and leakage is ignored.
- It is assumed that the fluid has no velocity slip on the solid boundary.

3.2.1. Control Equations

The flow and diffusion of the liquid film fluid inside the mechanical seal satisfies the momentum equation, energy equation, and continuity equation [25].

1. Fluid Domain Equation

The mass conservation equation

$$\frac{\partial \rho_f}{\partial t} + \frac{\partial}{\partial x_j}(\rho_f v_i) = 0 \quad (1)$$

In the above formula: ρ_f is the fluid density; v is the fluid velocity, subscript $i, j = 1, 2, 3$, representing the components in three directions, t is the time.

The momentum equation

$$\frac{\partial(\rho_f v_i)}{\partial t} + \frac{\partial}{\partial x_j}(\rho_f v_i v_j) = -\frac{\partial p}{\partial x_i} + \frac{\partial}{\partial x_j}(\mu \bullet \frac{\partial v_i}{\partial x_j}) \quad (2)$$

In the above formula: p is the pressure of fluid film, μ is the dynamic viscosity of the fluid.

The energy equation

$$\frac{\partial \rho E}{\partial t} + \nabla \bullet [v(\rho E + p)] = \nabla \bullet \left[k_{eff} \nabla T - \sum_j h_j J_j + (\Gamma_{eff} \bullet v) \right] + S_h \quad (3)$$

In the above formula: E is the total energy of the fluid micelle, ρ is the density of the fluid micelle, and p is the pressure of fluid film. Γ_{eff} is the effective stress of fluid domain, h_j is the enthalpy of the component, K_{eff} is the effective thermal conductivity of fluid film, J_j is the diffusion flux of the component j , S_h is the source term including other volumetric heat.

2. Solid Domain Equation

$$M_s \ddot{d} + C_s \dot{d} + K_s d + \tau_s = 0 \quad (4)$$

In the equation, M_s represents for the mass matrix of the solid element, C_s represents for the damping matrix of the solid element, K_s represents for the rigidity matrix of the solid element, d represents for the displacement vector of the solid element, τ_s represents for the stress on the rotating ring and stationary ring.

At the same time, the thermal deformation term caused by the temperature difference in the solid area as followed.

$$f_T = \alpha_T \bullet \nabla T \quad (5)$$

In the formula: α_T is the coefficient of thermal expansion related to temperature. T is the temperature of the seal rings.

3. Dynamic Model of Axial Movement

Based on the analysis of the kinematic relationship, the dynamical model of mechanical seal system was derived by using the D'Alembert principle. The force and axial movement of the mechanical seal are shown in Figure 8.

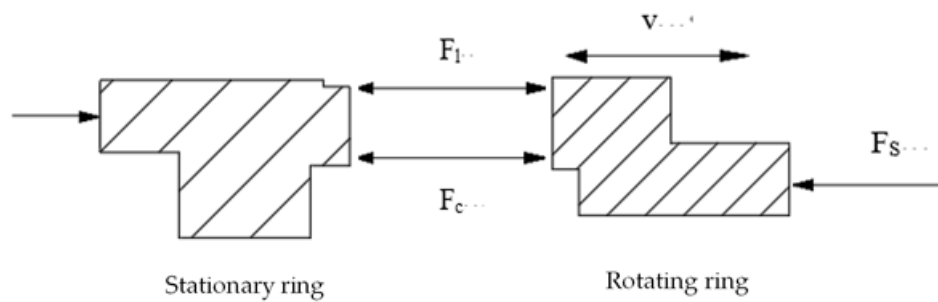


Figure 8. Axial dynamic model of mechanical seal.

From the dynamic point of view, the dynamic equation of mechanical seal axial movement was established as follows [26].

$$m\ddot{Z}_s + c\dot{Z}_s + F_s = F_l + F_c \quad (6)$$

In the formula: m is the equivalent mass of the rotating ring and the spring. Z_s is the axial relative displacement between the rotating ring and the stationary ring. c is the axial damping coefficient of spring and auxiliary seal rings. F_s is the force of the spring on the rotating ring. F_l is the axial force of the fluid film between the end faces of the rotating ring and stationary ring, and F_c is the axial contact force between the rotating ring and stationary ring.

3.2.2. Sealing Performance Parameters

1. Seal Opening Force

The opening force of mechanical seal surface is the sum of the pressure exerted on the seal surface by the liquid film fluid. The opening force could be obtained by integrating the pressure field of the liquid film on the seal surface.

$$F_0^\Omega = \int \int p dA = \int \int p r dr d\theta \quad (7)$$

In the formula: p is the pressure of fluid film, r is the radial coordinate, and Ω is the whole calculation area.

2. Leakage of Mechanical Seal

Leakage is an important indicator for measuring the performance of mechanical seal. Leakage Q could be synthesized by this formula [27].

$$Q = \frac{\pi d_m h_o^3 \Delta p}{12 \mu b} \quad (8)$$

Q -leakage, d_m -average diameter of the sealing surface, h_o -the thickness of fluid film, Δp -pressure difference, μ -dynamic viscosity of the medium, b -effective width of the seal.

4. Dynamic Simulations and Analysis

In this paper, the computational domains were meshed using the structured blocking hexahedral method. Due to the large difference between the radial and axial length of the fluid film parameters, the diameter of the fluid film is millimeter, but the thickness of the fluid film is micron, thus it is difficult to directly divide the three-dimensional mesh of the liquid film. Therefore, the fluid film corresponding to the center angle of 8.5 degrees was first meshed in this paper, and then the entire fluid film is formed based on this array. Figure 9 revealed coupling relationship among multiple fields in the dynamic simulations. To ensure the computational accuracy, mesh independence analysis was

conducted. Calculation of fluid film parameters with different number of grids was shown in the Table 1. The velocity was not growing when the number of grids increased to 3.6 million. As shown in Figure 10, the pressure became relatively stable after increasing the grid number to 3.6 million elements. After the grid independence test, the final grid number unit was 362,943. The fluid membrane grids were shown in Figure 11. In order to remove the influence of the order of magnitude of radial and axial fluid film grids on the simulation results, a grid-independent assessment was conducted. The numerical results were obtained by dividing the fluid film into different mesh numbers and repeating the simulation. The error of the final results is less than 1%, which shows that the mesh division has no effect on the simulation results.

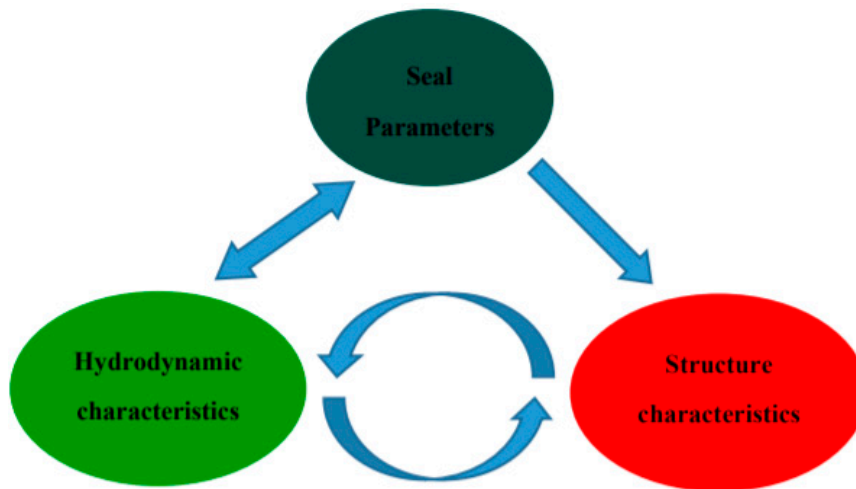


Figure 9. Multi-field coupling.

Table 1. Calculation of fluid film parameters with different number of grids.

Grid Number ($\times 10^5$)	Pressure (Mpa)	Velocity (m/s)
3.43	0.1615	6.74
3.51	0.1782	6.81
3.62	0.1825	6.85
3.67	0.1834	6.85
3.74	0.1852	6.85
3.85	0.1873	6.85
3.87	0.1869	6.85

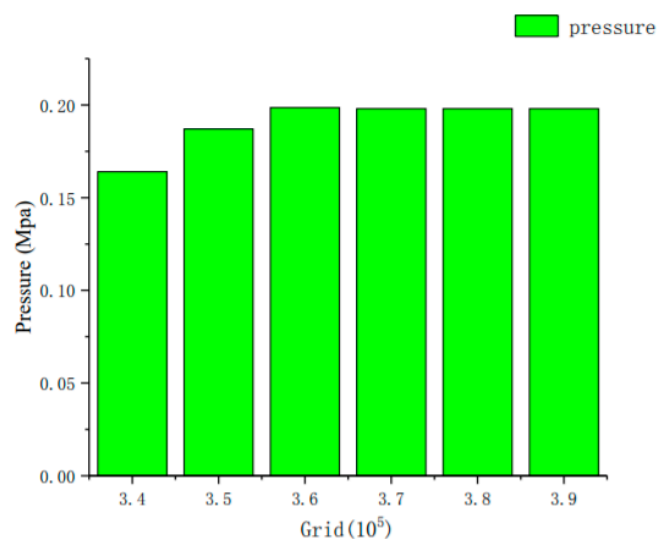
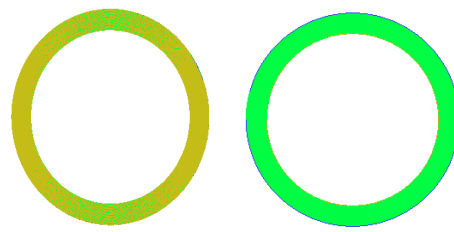
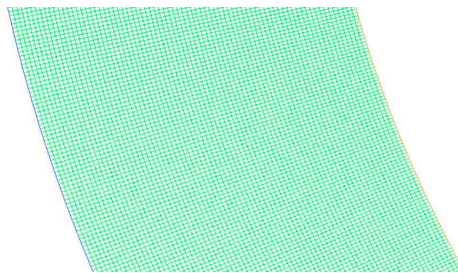


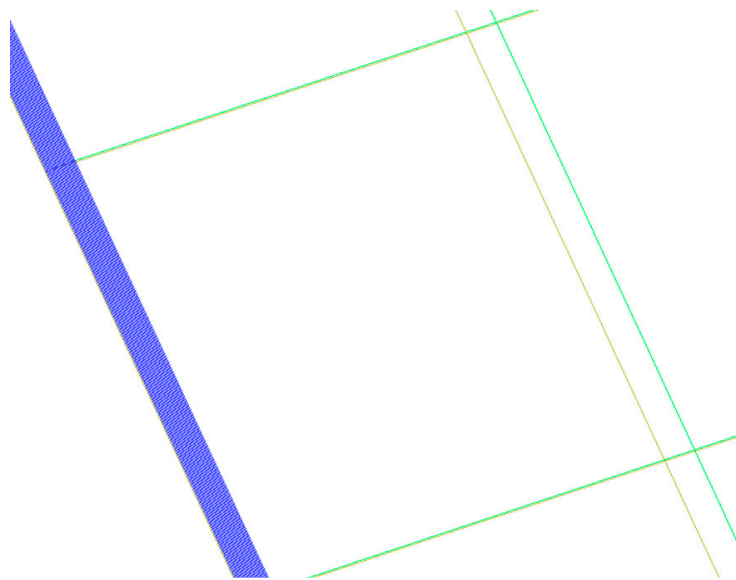
Figure 10. Mesh independence.



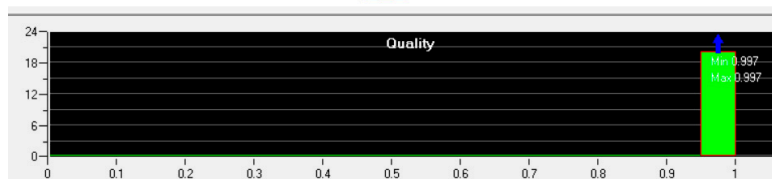
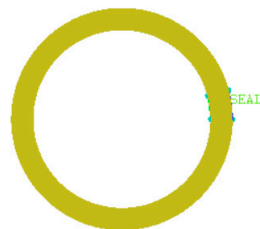
(a) Global mesh of fluid film



(b) Local enlarged graphs of mesh



(c) Mesh in the thickness direction of fluid film



(d) Mesh quality

Figure 11. Mesh of fluid film and mesh quality.

Mechanical seal material and boundary condition were set as followed:

The rotating ring material used in this paper is silicon carbide, and the stationary ring material is carbon graphite. The main properties of the materials used in the rotating and stationary rings are shown in Table 2.

Table 2. The material properties of mechanical seal.

Properties	Rotating Ring	Stationary Ring
Material	Silicon Carbide	Carbon Graphite
Density ρ (kg/m ³)	3150	1810
Specific heat capacity c (J/kg·K)	710	880
Thermal conductivity k (W/m·K)	150	45
Thermal expansion coefficient α (1/K)	4.3×10^{-6}	6.2×10^{-6}
Poisson ratio	0.27	0.26
Elastic modulus E (GPa)	380	25

The details about boundary, mesh, and calculation are listed in Table 3.

Table 3. Details about boundary, mesh and calculation.

Type	Details
Entrance boundary	pressure inlet
Exit boundary	pressure outlet
Wall boundary	standard wall functions
Mesh quality	0.9
Grid number	362,943
Flow state	laminar flow
Algorithm	Simple C
Solver	Steady-state solver

When the residual values of all variables are reduced to 10^{-3} , the calculation converged.

Entrance boundary conditions in numerical simulation: the pressure inlet boundary condition was adopted, and the inlet boundary position was set outside the fluid film.

Exit boundary conditions in numerical simulation: the pressure outlet boundary condition was adopted, and the outlet boundary position was set inside the fluid film.

Wall boundary conditions in numerical simulation: Standard wall functions were used.

It had been a hot issue that the fluid film flow is laminar flow or turbulent flow in the mechanical seal field. The fluid coefficient α method was adopted to determine whether it is laminar or turbulent [28] in this paper.

$$\alpha = \sqrt{\left(\frac{Re_c}{1600}\right)^2 + \left(\frac{Re_p}{1600}\right)^2} \quad (9)$$

$\alpha < 0.58$, is laminar flow. $\alpha > 1$, is turbulent flow.

$$Re_c = \frac{2\pi\rho nrh}{60\mu} \quad (10)$$

$$Re_p = \frac{\rho Q}{2\pi\mu r} \quad (11)$$

$Q = 1.12 \times 10^{-5}$ kg/s, $n = 1500\sim 6000$ rpm, $r = 0.031$ m, $h = 1\sim 9$ μ m, $\rho = 998$ kg/m³.

Through calculation could get, $\alpha = 0.29 < 0.58$, the fluid film is laminar flow. Therefore, the laminar model was adopted for the relevant flow dynamic calculation.

The simulation part was set according to the theoretical physical fault model and the dynamic model set up in the Section 3.2.1., and the flow chart of simulation and the analysis details are shown

in Figure 12. Simple C algorithm and steady-state solver were used during the calculation of the fluid domain. Firstly, the fluid domain results were calculated by CFD. Then, the fluid domain results were loaded to the solid domain through the Workbench platform. The dynamic equation of mechanical seal axial movement was used during the calculation of the deformation and forces in solid domain. Thus, the solid domain dynamic results, deformation, and forces were obtained. Finally, the fluid film dynamic characteristics, the force, and deformation of the seal rings could be analyzed from the results.

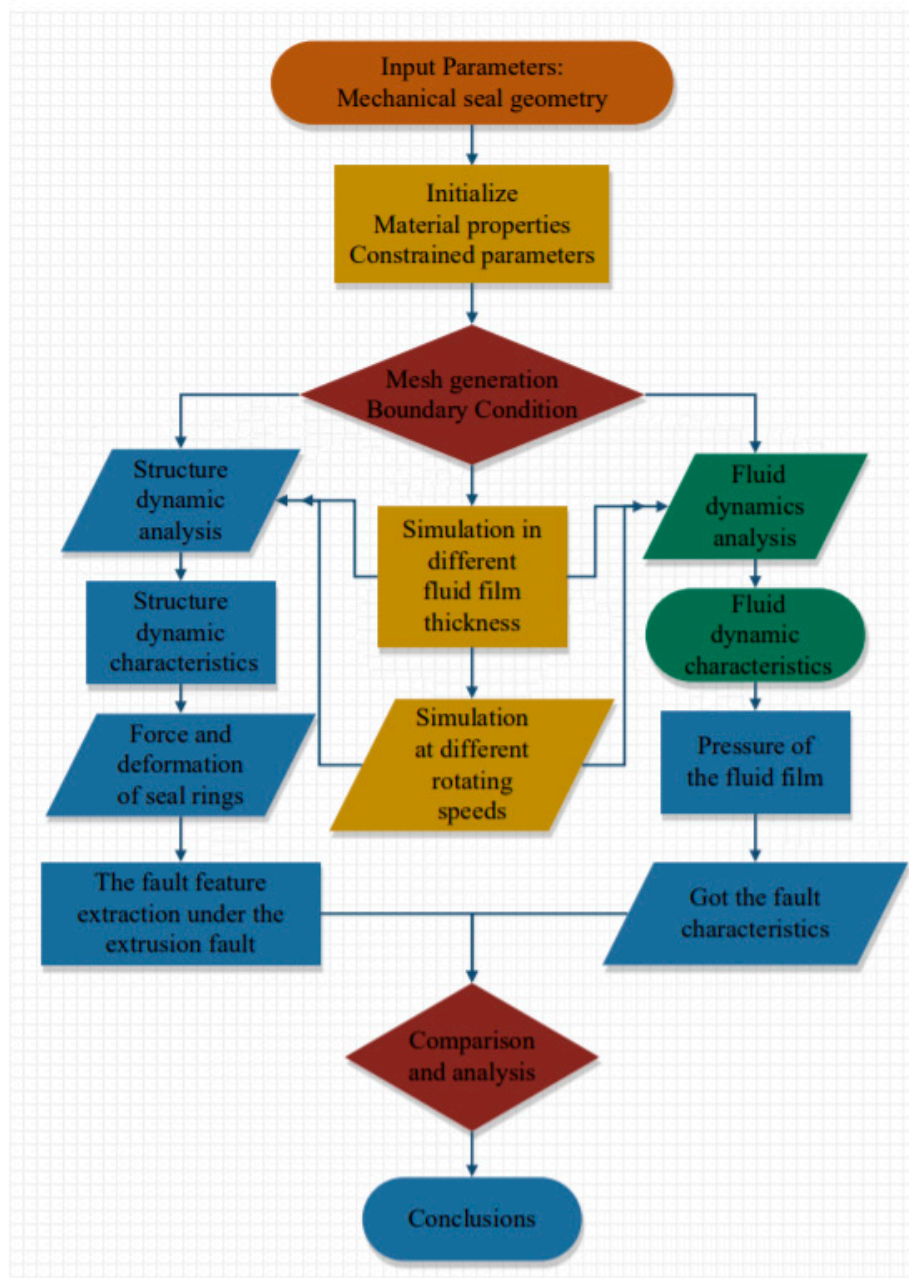


Figure 12. Flow chart of calculation.

The first group of simulation process is for different film thickness. The force and deformation simulation data of rotating ring and stationary ring were obtained, and the pressure of fluid film could be got at the same time.

The second group in the simulation process was carried out under different speeds. The hydrodynamic and structural dynamic characteristics were obtained.

Repeat each simulation process. Find the characteristics under different conditions through data analysis.

5. Results and Discussion

5.1. Fluid Film Pressure Analysis

The pressure distributions under different extrusion degrees are shown in Figure 13. The fluid film pressure would grow as the fluid film thickness increases when the rotating speed $n = 2950$ r/min, pressure inlet was 0.2 MPa. The fluid film thickness represents the extrusion fault degree. The dynamic characteristic parameters could be reflected by three typical cases. Two- μm fluid film could reflect the serious extrusion fault, 3- μm fluid film was a sign of slight extrusion fault, 4- μm -fluid film was on behalf of the normal state. Such large pressure change between 2- μm fluid film and 3- μm fluid film means that the fluid film thickness has strong recognition capability for the changes of the mechanical seal operation. When the extrusion fault of mechanical seal becomes severer, the fluid film pressure fluctuation would tend to be more intensive. Such tendency indicated that the thickness and the pressure could be treated as the indicator of extrusion fault.

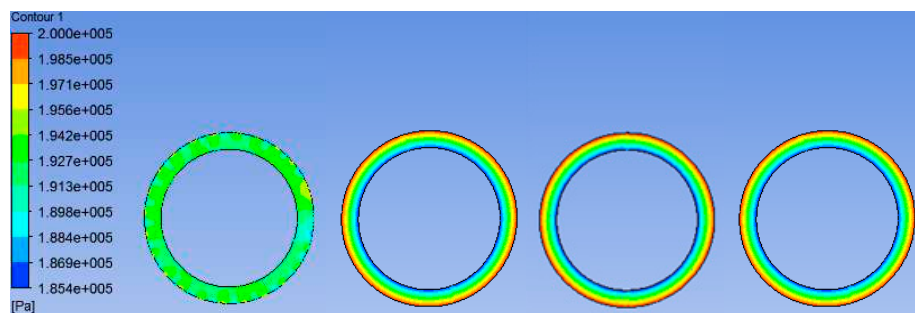


Figure 13. The pressure of 2, 3, 4 and 5 μm fluid film.

No significant fluctuation could be found in the 4- μm fluid film pressure contours. This was mainly due to that the 4- μm fluid film was the relatively proper thickness for this mechanical seal. From Figure 13, it could be seen that the pressure was relatively evenly distributed at this time. The thicker fluid film led to the bigger viscous shear flow. In addition, pressure bearing capacity could also become stronger with the rapidly increasing thickness. The results indicated that the thicker fluid film could efficiently be used to maintain the hydrodynamic effects and improve the lubrication performance. However, there was deficiency existing in this parameter, which was not sensitive to the light extrusion fault.

The pressure fluctuation under different fluid film is shown in Figure 14. The pressure mainly fluctuates at 0.189 MPa when the thickness of the fluid film is 2 μm . The pressure mainly fluctuates at 0.192 MPa when the thickness of the fluid film is 3 μm . The pressure mainly fluctuates at 0.195 MPa when the thickness of the fluid film is 4 μm . The pressure mainly fluctuates at 0.198 MPa when the thickness of the fluid film is 5 μm . The pressure fluctuation is largely affected by the operation of the rotating ring and stationary ring. When there is extrusion fault, the operation of the rotating ring and stationary ring will change. The pressure distribution and pressure fluctuation of the fluid film will change with the fault. To a certain extent, the pressure fluctuation could reflect the occurrence of extrusion fault. Besides, the fault degree could be preliminarily judged according to the pressure distribution and pressure fluctuation within a certain range.

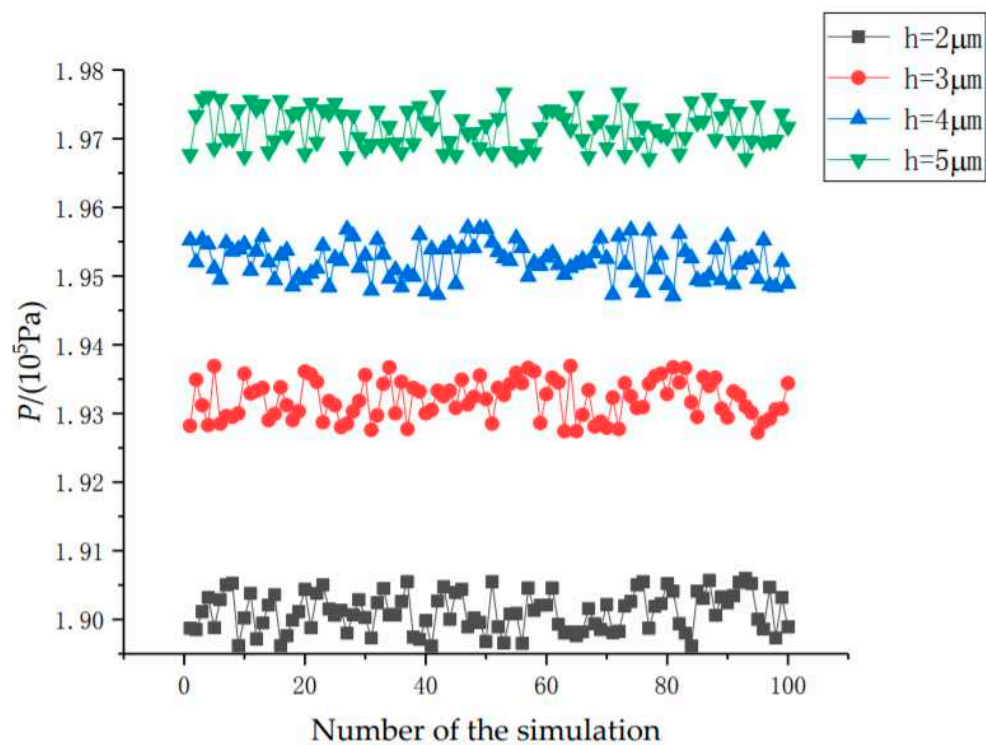


Figure 14. Pressure fluctuation diagram under different fluid films.

5.2. Seal Performance Analysis

Compared with pressure, leakage Q showed a stronger ability in reflecting the slight extrusion fault. That was mainly due to the leakage as the main indicator that could measure seal fault. Figure 15 showed that the leakage increases with fluctuations when the fluid film becomes thicker. Besides, the minimum value of the leakage, shown in Figure 15, under different fluid film thickness. As shown in the red circle in Figure 15a, too thin fluid film could lead to the severe wear. The leakage curve reflected that the leakage increasing rate is the slowest when the fluid film thickness is between 5 and 6 μm . It depicted that this fluid film thickness was the most beneficial to mechanical seal. So, the best thickness area for this mechanical seal was from 5 to 6 μm . However, the increasing tendency is obvious when the fluid film thickness was more than 6 μm in the red circle in Figure 15b. It could be concluded that faults have occurred on the mechanical seal. With the development of faults, the leakage curve would still increase. According to Figure 15, a large amount of leakage resulted from too thick fluid film, which was directly related with the extrusion fault. During the simulation operation of this mechanical seal, the extrusion fault was more likely to occur when the fluid film thickness was too large or too small. Dynamic characteristics of fluid film would change when the extrusion fault occurs. Hydrodynamic effects were the typical parameters to measure the sealing performance. As the fluid film thickness beyond the best thickness area marked with red circle in Figure 15c, the hydrodynamic effects of fundamental frequency became weaker, while volume force and inertia force got larger.

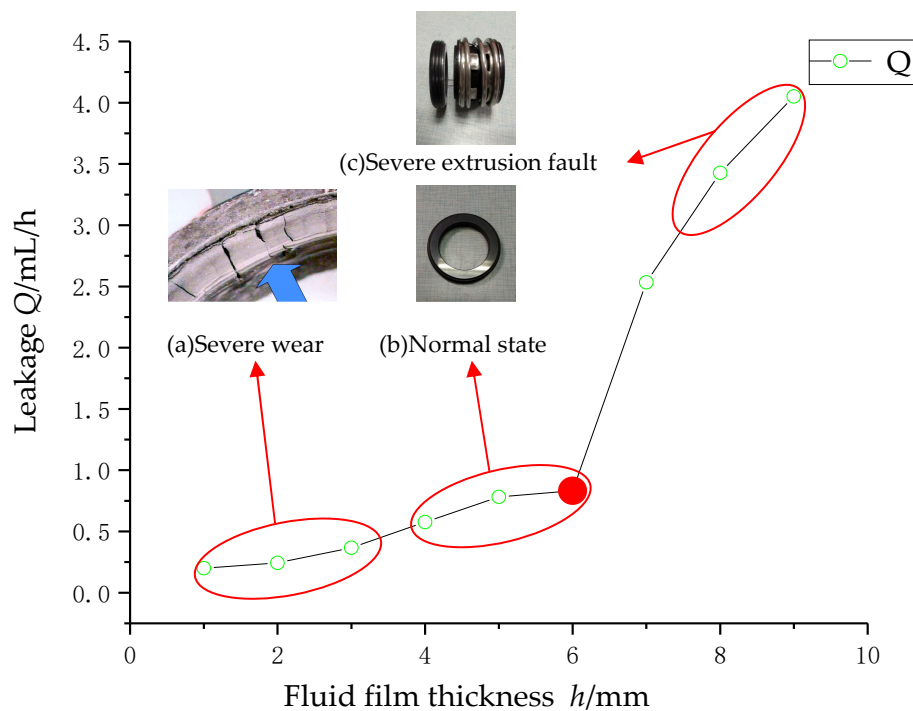


Figure 15. Leakage under different fluid film.

The thickness of fluid film was set from 1 to 9 μm . The opening force changed from 60 N to 87 N. The rotating speed was set as 2950 r/min. Figure 16 illustrated that with the increasing of fluid film thickness, opening force became larger rapidly. Moreover, the opening force would have a fluctuating downward trend as the fluid film thickness increases. The opening force could be regarded as the important parameter for the seal dynamic characteristics. As shown in the Figure 16, the opening force was small when the fluid film thickness was less than 3 μm . It was because that severe extrusion fault occurs when the thickness was too thin. The mechanical seal surface friction would happen directly when the thickness was too small. Thus, there would be less or no hydrodynamic effect in this situation. A downward trend of opening force was shown in curve when the fluid film thickness was more than 4 μm . Moreover, the opening force was smaller while the thickness is larger. It indicates that serious damage has occurred on the surface of the rotating ring and stationary ring with the increasing of the thickness. The opening force could have relationship with the fluid film lubrication status and seal extrusion fault degree.

Besides, cavitation could be found in Figure 16b,c. With the increase of fluid film thickness, cavitation phenomenon is further strengthened. It is also due to the cavitation phenomenon that the opening force increases firstly and then decreases with the increase of film thickness. The pressure reduction of mechanical seal is mainly due to the local separation caused by narrow gap, micro groove machined on the surface and surface roughness, and vortex caused by micro modeling. In the conventional scale flow, the surface roughness of micro channel, which is often neglected due to its small influence, has a significant influence in the micro channel flow. The micro disturbance caused by the surface roughness often affects the flow at the edge of the fluid film, which is also one of the main reasons for the cavitation of the micro gap fluid film in the mechanical seal.

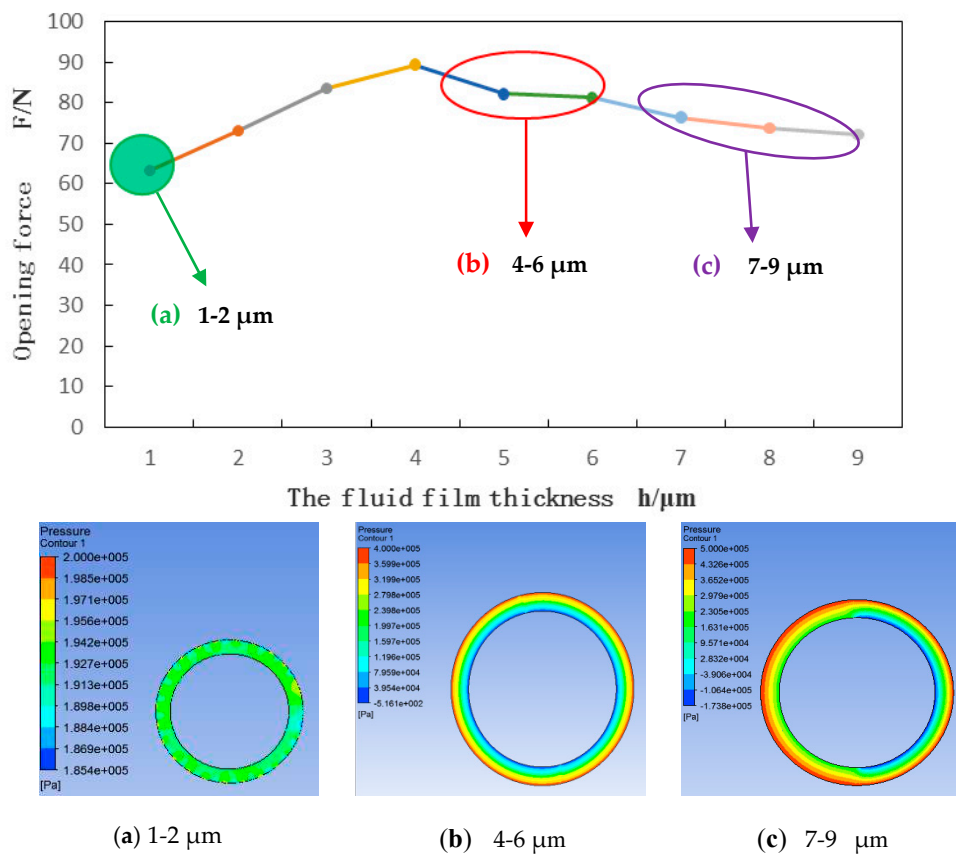
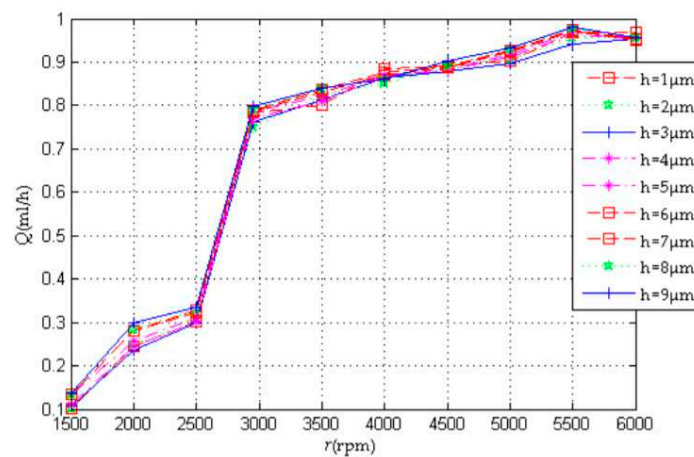
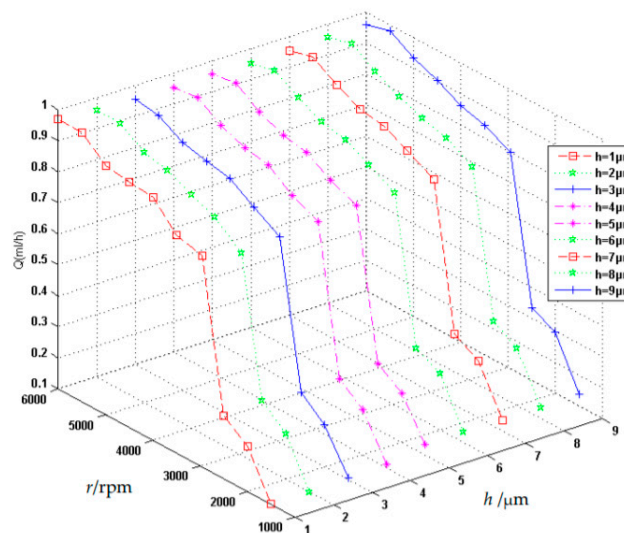


Figure 16. Opening force under different fluid film.

As shown in Figure 17, with the increasing of rotating speed, the leakage grew with many fluctuations. The Figure 17a could reflect the same trend of leakage under different film thickness, and Figure 17b could reflect the difference under each speed. It could be seen that the most obvious growth occurs when the rotating speed n from 2500 r/min to 3500 r/min. This was mainly due to that the mechanical seal was from normal operation state to the fault status. The inherent factors could be the opening force and friction torque, which resulted in the rapid growth of leakage. Thus, the leakage could be related to the rotating speed. The fluid film stiffness would not always increase with the rotating speed growth, because the growth of the friction torque was suppressed to a certain extent. Based on the combined action of the hydrodynamic and fluid film stiffness, the seal leakage could reflect the sealing performance and the seal faults.



(a) Leakage under different film thickness



(b) Leakage at different speeds

Figure 17. Leakage under different rotating speeds and fluid film thickness.

6. Conclusions

The dynamic characteristics of mechanical seal under different fault conditions were processed and analyzed in this research. Several conclusions could be drawn from the results described above.

1. It was the first time to do research on the dynamic characteristics of mechanical seal in the different fault degrees, and proved feasibility of this method. Meanwhile, the leakage Q , opening force F , rotating speed n were combined for the research on seal performance, fault mechanism, and fault degrees analysis.
2. The leakage analysis of mechanical seal in the different degrees of extrusion fault was conducted with the increasing of fluid film thickness. The extrusion fault is more likely to occur when the fluid film thickness is too large or too small. As the fluid film thickness beyond the best thickness area, the hydrodynamic effects of fluid film turn weaker, while volume force and inertia force get larger. Such tendency has the reference value of mechanical seal fault detection.
3. The leakage and opening force present obvious change of fluid film thickness. With the increasing of rotating speeds, the leakage grows with many fluctuations. Based on the combined action of

the hydrodynamic and fluid film stiffness, the seal leakage could reflect the sealing performance and the seal fault. There must be a law between the extrusion degrees and fluid film thickness. This paper researched the law that too thin or too thick fluid film would result in the heavy extrusion fault. The fluid film stiffness, leakage, and opening force are the important parameters, which have recognition capability for the extrusion degrees of the mechanical.

This research work has proved the feasibility that the dynamic characteristics of mechanical seal could be found to reflect the degree of extrusion fault. Besides, the research conclusions could have the reference value of mechanical seal fault detection. Further research should focus on the different type of the mechanical seal and find the accurate correspondence relationship.

Author Contributions: Conceptualization, Y.L.; methodology and software, Y.L. and Y.F.; validation, Y.L. and Y.F.; formal analysis, Y.L. and Y.F.; investigation, Y.F. and W.Z.; data curation, Y.L. and Y.F.; writing—original draft preparation, Y.L. and Y.F.; writing—review & editing, Y.L., Y.H. and E.A.; project administration, Y.L. All authors have read and agreed to the published version of the manuscript.

Funding: This research was funded by the National Natural Science Foundation of China, grant number 51979127, the Nature Science Foundation of Jiangsu Providence, grant number BK20171403, and German KSB Global Headquarters Research Fund, project number: 1.2018.07.1

Conflicts of Interest: The authors declare no conflict of interest.

References

1. Beckerle, P.; Schaede, H.; Rinderknecht, S. Fault diagnosis and state detection in centrifugal pumps—A review of applications. In *Proceedings of the 9th IFToMM International Conference on Rotor Dynamics*; Springer: Cham, Switzerland, 2015; pp. 387–398. [[CrossRef](#)]
2. Ma, X.; Meng, X.; Wang, Y.; Peng, X. Suction effect of cavitation in the reverse-spiral-grooved mechanical face seals. *Tribol. Int.* **2019**, *132*, 142–153. [[CrossRef](#)]
3. Chen, Z.; Liu, T.; Li, J. The effect of the O-ring on the end face deformation of mechanical seals based on numerical simulation. *Tribol. Int.* **2016**, *97*, 278–287. [[CrossRef](#)]
4. Li, K.; Jia, X.; Guo, F. A model for breakaway distance and maximum static friction to study the static frictional behavior of the secondary seal in non-contacting mechanical seals. *Tribol. Int.* **2019**, *135*, 219–229. [[CrossRef](#)]
5. Cao, W.; Mao, J. Study of the affinity law of energy and cavitation characteristics in emergency drainage pumps at different rotating speeds. *Processes* **2019**, *7*, 932. [[CrossRef](#)]
6. Li, F.; Cui, B.; Zhai, L. Research on rotor dynamic characteristics of pump annular seals based on a new transient CFD method. *Processes* **2020**, *8*, 227. [[CrossRef](#)]
7. Wang, C.; He, X.; Cheng, L.; Luo, C.; Xu, J.; Chen, K.; Jiao, W. Numerical simulation on hydraulic characteristics of nozzle in waterjet propulsion system. *Processes* **2019**, *7*, 915. [[CrossRef](#)]
8. Luo, Y.; Yuan, S.Q.; Yuan, J.P.; Lu, J.X. Research on characteristics of the vibration spectral entropy for centrifugal pump. *Adv. Mech. Eng.* **2015**, *6*, 698938. [[CrossRef](#)]
9. Black, H.F. Effects of hydraulic forces in annular pressure seals on the vibration of centrifugal pump rotors. *Arch. J. Mech. Eng.* **1969**, *11*, 206–213. [[CrossRef](#)]
10. Brunetière, N.; Tournier, B. Numerical analysis of a surface-textured mechanical seal operating in mixed lubrication regime. *Tribol. Int.* **2012**, *49*, 80–89. [[CrossRef](#)]
11. Sun, J.; Ma, C.; Yu, Q.; Lu, J.; Zhou, M.; Zhou, P. Numerical analysis on a new pump-out hydrodynamic mechanical seal. *Tribol. Int.* **2017**, *106*, 62–70. [[CrossRef](#)]
12. Xie, F.; Li, Y.; Ma, Y.; Xia, S.; Ren, J. Cooling behaviors of a novel flow channel in mechanical seals of extreme high-speed rotation for cryogenic rockets. *Cryogenics* **2020**, *107*, 103055. [[CrossRef](#)]
13. Jana, T.; Mitra, A.; Sahoo, P. Dynamic contact interactions of fractal surfaces. *Appl. Surf. Sci.* **2016**, *392*, 872–882. [[CrossRef](#)]
14. Wang, X.; Liu, M.; Kao-Walter, S.; Hu, X. Numerical Evaluation of rotordynamic coefficients for compliant foil gas seal. *Appl. Sci.* **2020**, *10*, 3828. [[CrossRef](#)]
15. He, W.; Wang, S.; Zhang, C.; Wang, X.; Liu, D. A wear simulation method for mechanical face seals under friction instability conditions. *Appl. Sci.* **2020**, *10*, 2875. [[CrossRef](#)]

16. Zhang, Q.; Chen, X.; Huang, Y.; Zhang, X. An Experimental study of the leakage mechanism in static seals. *Appl. Sci.* **2018**, *8*, 1404. [[CrossRef](#)]
17. Towsyfy, H.; Gu, F.; Ball, A.D.; Liang, B. Modelling acoustic emissions generated by tribological behaviour of mechanical seals for condition monitoring and fault detection. *Tribol. Int.* **2018**, *125*, 46–58. [[CrossRef](#)]
18. Zhang, Q.; Chen, X.; Huang, Y.; Chen, Y. Fractal modeling of fluidic leakage through metal sealing surfaces. *AIP Adv.* **2018**, *8*, 045310. [[CrossRef](#)]
19. Gropper, D.; Wang, L.; Harvey, T.J. Hydrodynamic lubrication of textured surfaces: A review of modeling techniques and key findings. *Tribol. Int.* **2016**, *94*, 509–529. [[CrossRef](#)]
20. Migout, F.; Brunetière, N.; Tournerie, B. Study of the fluid film vaporization in the interface of a mechanical face seal. *Tribol. Int.* **2015**, *92*, 84–95. [[CrossRef](#)]
21. Varney, P.; Green, I. Impact phenomena in a noncontacting mechanical face seal. *J. Tribol.* **2017**, *139*, 022201. [[CrossRef](#)]
22. Zhu, H.; Li, D.; Pu, H.; Wang, L.; He, Y.; Bu, Y.; Che, D.F. Experimental and numerical investigations on the local direct leakage process of rotary regenerative air preheater. *Appl. Sci.* **2020**, *10*, 1523. [[CrossRef](#)]
23. Mosavat, M.; Moradi, R.; Rahimi Takami, M.; Barzegar Gerdoodbary, M.; Ganji, D.D. Heat transfer study of mechanical face seal and fin by analytical method. *Eng. Sci. Technol. Int. J.* **2018**, *21*, 380–388. [[CrossRef](#)]
24. Michalska-Pozoga, I.; Jakubowski, M. CFD analysis of the flow of a polymeric material inside the double-cone plasticization-homogenization zone of the screw-disc extruder. *Przem. Chem.* **2015**, *94*, 2105–2111.
25. Pascovici, M.D.; Etsion, I. A thermo-hydrodynamic analysis of a mechanical face seal. *J. Tribol.* **1992**, *114*, 639–645. [[CrossRef](#)]
26. Harp, S.R.; Salant, R.F. Inter-asperity cavitation and global cavitation in seals: An average flow analysis. *Tribol. Int.* **2002**, *35*, 113–121. [[CrossRef](#)]
27. Lebeck, A.O. A study of a mixed lubrication in contacting mechanical face seals. In Proceedings of the 4th Leeds-Lyon Symposium on Lubrication, Lyon, France, 13–16 September 1977; pp. 46–57.
28. Brunetière, N.; Tournerie, B.; Frêne, J. Influence of fluid flow regimes on performances of non-contacting liquid face seals. *Tribology* **2002**, *124*, 515–523. [[CrossRef](#)]



© 2020 by the authors. Licensee MDPI, Basel, Switzerland. This article is an open access article distributed under the terms and conditions of the Creative Commons Attribution (CC BY) license (<http://creativecommons.org/licenses/by/4.0/>).

Article

Flow and Noise Characteristics of Centrifugal Fan in Low Pressure Environment

Xilong Zhang, Yongliang Zhang * and Chenggang Lu

School of Mechanical and Automotive Engineering, Qingdao University of Technology, Qingdao 266520, China; zhangxilong@qut.edu.cn (X.Z.); papqut@yeah.net (C.L.)

* Correspondence: zhangyongliang@qut.edu.cn

Received: 16 July 2020; Accepted: 12 August 2020; Published: 13 August 2020



Abstract: The influence of low-pressure environment on centrifugal fan's flow and noise characteristics was studied experimentally and numerically. A testbed was established to conduct the experimental test on the performance of a centrifugal fan, and the characteristic curve and power consumption curve of the fan under different pressure were obtained. Then the simulation model of the centrifugal fan was established, which was used to simulate the working process of centrifugal fan under different negative pressures. The results showed that the total pressure and static pressure of the fan decrease with the decrease of the ambient pressure. The total and static pressures of the fan under 60 kPa pressure condition decreased by 42.3% and 38.3%, respectively, compared with those of fan under the normal pressure. The main reason for this phenomenon is that the decrease of the environmental pressure leads to the decrease of air density. Besides, with the drop of environmental pressure, the sound pressure and sound power of the fan noise decreases.

Keywords: centrifugal fan; noise characteristics; power consumption; negative pressure; sound pressure

1. Introduction

Under the plateau environment, the air is thin and the air pressure is low, which changes the physical properties and flow characteristics of the air. For every 1000 m increment in altitude, the atmospheric pressure drops by about 10 kPa, and the air density also gradually decreases. When the altitude is 5000 m, the air density is 0.7263 kg/m^3 , which is only about half of that in the plain area [1,2]. However, from the sea level to the elevation below 85,000 m, the volume ratio of the main gases such as nitrogen and oxygen is basically the same at each altitude. So, the relative molecular mass of air remains basically unchanged. Density is proportional to atmospheric pressure at a given temperature [3,4]. When the temperature is constant, molecular concentration and air density increase with an increase of pressure [5]. The characteristics of air flow and noise change correspondingly in the application of vehicle fan and air conditioning fan. The flow rate, static pressure, axial power, efficiency, rotational speed, noise, and other performance parameters of the fan are all related to the physical properties of the air, so the flow and noise characteristics of the fan will inevitably be affected by the change of environmental pressure.

At present, many scholars conducted deep research on the flow and noise characteristics of the fan. Lee et al. [6] studied the effect of blade inclination angle, blade thickness, and maximum blade thickness location of the low-speed axial fan on fan efficiency by response surface method. It was concluded that the blade inclination angle had the greatest influence on the fan efficiency. Gholamian et al. [7] used the method of CFD to study the effect of inlet diameter on fan efficiency and flow field. It was found that the size of the inlet diameter had a great influence on the fan performance and efficiency. When the inlet diameter differs by 2 cm, the fan performance and fan efficiency change by more than 14%. In order to improve the performance of the fan, a variety of advanced technologies have been

put forward and a great deal of research has been carried out. For example, fan blade bending sweep technology [8] and blade twisting technology [9] are the most commonly used techniques.

However, the studies on the performance of fans under low pressure environment are still relatively few. The existing studies do not take the impact of environmental pressure on fan efficiency into consideration, which lacks experimental verification. So, it is insufficient to provide theoretical support for the application of fans in low-pressure environment at plateau, and further research is urgently needed.

In the noise characteristics of fans, through theoretical analysis, it was found by Sharland [10] that the aerodynamic noise source of axial fan belonged to dipole source, which was closely related to the pressure pulsation of blade acting on the air passing through the fan. Li [11] regarded the air as an incompressible fluid to calculate the fan performance, which saved the calculation time, and the error was within the allowable scope of the project. By analyzing the influence of metal stamping fan blade thickness on fan performance, it can be known that the greater the blade thickness is, the greater the noise will be generated. Hodgson et al. [12] concluded that the magnitude of fan noise was positively correlated with driving voltage and negatively correlated with outlet flow through the computer cooling fan noise test.

From the existing literature, the studies on the fan were mainly based on one atmosphere. However, the articles that studied the noise characteristics of the fan in the low-pressure environment were not retrieved. So far, it is difficult to reveal the mechanism of low-pressure environment on the flow and noise characteristics of fans. Furthermore, it is difficult to meet the design and calculation requirements of fans in low pressure environment.

2. Analysis of the Influence of Low-Pressure Environment on Noise Characteristics of Centrifugal Fan

2.1. Simplification of Air Flow in Centrifugal Fan

In order to study air flow in a centrifugal fan, the flow in the fan is properly simplified as follows:

1. The blades are infinitely thinner than axial thickness of fan, and the trajectory of fluid completely coincides with the blade profile;
2. The fluid is ideal, that is, the flow loss in the fan caused by uneven velocity field due to viscosity is not considered;
3. The flow is considered to be incompressible, axisymmetric, and steady;
4. The gravitational potential energy of the air inside the fan is neglected.

2.2. Noise Analysis of Centrifugal Fan in Low Pressure Environment

The noise of the fan blade is mainly determined by the Lighthill fundamental equation [13]. Namely, the sound power (W) dominates, which has the following relationship with air flow rate (u_f):

$$W \sim \rho L^2 \frac{u_f^6}{c^3}, \quad (1)$$

where ρ is air density, L is the length along the direction of the flow, and u_f is average flow rate (u_f).

The formula for calculating the propagation velocity (c) of sound in air in the above formula is $c = (k/\rho)^{0.5}$ [14], in which k is the volumetric modulus of elasticity of the medium.

According to the theory of fluid molecules, the specific heat of air can be regarded as a constant value in the pressure change range of 0~1 atm, so the k value does not change with the ambient pressure. According to Equation (1), when the air temperature is the same, the sound propagation velocity c at different pressures can be approximately considered to remain unchanged. Therefore, according to Equation (1), the sound power W generated by the fan has a linear relationship with the air density ρ , namely $W \sim \rho$.

The relationship between sound pressure (P) and sound power (W) [15] is $P = \sqrt{W\rho c/A}$, in which A means effective flow area. So, the sound pressure ratio at different ambient pressures is

$$\frac{P_H}{P_0} = \sqrt{\frac{W_H \rho_H}{W_0 \rho_0}}, \quad (2)$$

where the subscript H and 0 mean that the height above sea level are H m and 0 m, respectively.

The above equation can be further simplified as $P_H/P_0 = \rho_H/\rho_0$, in which it can be seen that the sound pressure P is also in a linear relationship with the air density.

From the above analysis, it can be seen that the sound power (W) and sound pressure (P) of the fan are in a linear relationship with the air density (ρ). While the air density is greatly affected by the environmental pressure, so the noise of the fan is closely related to the environmental pressure.

3. Experimental Study

3.1. Fan Testbed

The performance test of centrifugal fan is conducted on a fan testbed, which is composed of air loop, fan, and control unit and auxiliary equipment. The fan testbed is shown in Figure 1. The real experimental device is shown in Figure 2.

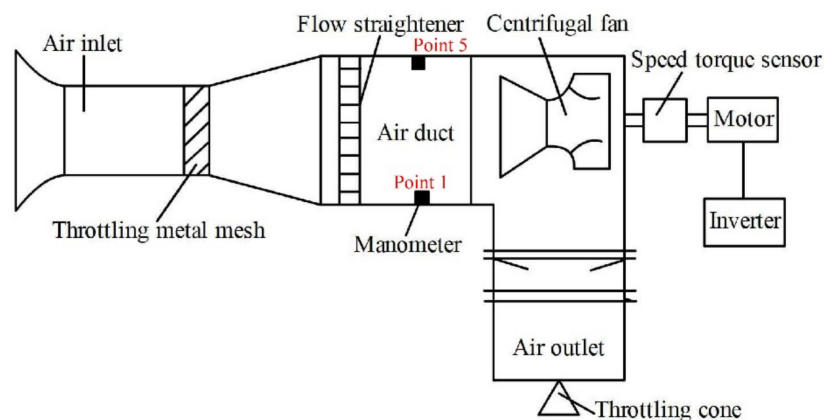


Figure 1. Centrifugal fan testbed.



Figure 2. The real experimental device.

During the experiment, the method of gradually loading a uniform circular plug at the throttling metal mesh is used to simulate the resistance and to form a vacuum in the wind tunnel. The motor's electric parameters of centrifugal fan are measured by using a motor economic operation

instrument. The pressures in Point 1 and Point 5 in Figure 1 are measured with a high-precision manometer, which are converted to obtain the flow rate of air [16]. The ambient temperature, humidity, and atmospheric pressure are measured with a thermometer, hygrometer, and atmospheric pressure gauge, respectively.

3.2. Uncertainty in Experiments

The experimental sample is a centrifugal fan, which is shown in Figure 3. The thickness of the blade is 3 mm, the outlet mounting angle is 60° , the outer diameter is 600 mm, and the number of blades is 13.



Figure 3. Experimental sample of centrifugal fan.

The rated rotational speed and maximum rotational speed of this centrifugal fan are 5000 r/min and 5994 r/min, respectively. The rated power and maximum power are 78.4 kW and 92 kW, respectively. The rated air volume and rated static pressure are $7.6 \text{ m}^3/\text{s}$ and 5427 Pa, respectively.

The uncertainty of the fan testbed is calculated using the method in the literature [17], which is described as:

$$\frac{\delta R}{R} = \sqrt{\left(\frac{\partial R}{\partial v_1}\right)^2 \left(\frac{\delta v_1}{v_1}\right)^2 + \left(\frac{\partial R}{\partial v_2}\right)^2 \left(\frac{\delta v_2}{v_2}\right)^2 + \dots + \left(\frac{\partial R}{\partial v_n}\right)^2 \left(\frac{\delta v_n}{v_n}\right)^2}, \quad (3)$$

where R is a function of the variables v_i ($i = 1, 2, \dots, n$), and δv_i ($i = 1, 2, \dots, n$) represents the uncertainties of variables v_i . After calculation, the uncertainties of mass flow rate is 0.212%, the fan pressure head is 0.257%, the fan efficiency is 0.97%, and the average uncertainties of the main parameters are less than 1%. The relationship between R and v_i is shown in Table 1. In the table, ε is blade displacement coefficient; D is blade diameter; b is width of blade; v_r is the radial component of the absolute velocity; ρ is air density; D_o is diameter of outlet; D_i is diameter of inlet; S_r is radial blade clearance; g is gravitational acceleration; u is peripheral speed; v_u is the axial component of the absolute velocity. Therefore, it can be considered that the testbed can meet the requirements of fan test accuracy.

Table 1. The relationship between R and v_i .

R	v_1	v_2	v_3	v_4
q_m	D	b	v_r	ρ
η	D_o	D_i	S_r	
H	g	u	v_u	

3.3. Experimental Results and Analysis

As the fan rotates, the air can be considered as an incompressible flow medium; that is, the density of air can be considered as constant. So, the flow characteristics of the fan can be characterized by the volume of medium passing through the fan per unit time and is denoted by q_v .

As the air passes through the fan, the increase of pressure is the total pressure of the fan and is denoted as P_{tF} , i.e.:

$$P_{tF} = P_2 - P_1 + \rho \frac{u_{f2}^2 - u_{f1}^2}{2}, \quad (4)$$

where P_1 and P_2 are the static pressure at the inlet and outlet; u_{f1} and u_{f2} are the average flow rate at the inlet and outlet, and r is the rotating radius of the blade.

The increased total power P_f of the medium of the fan in unit time can be expressed as

$$P_f = q_v P_{tF} \quad (5)$$

During the experiment, the power consumption curve of the fan is measured by adjusting the speed and volume flow rate of the fan, which is shown in Figure 4.

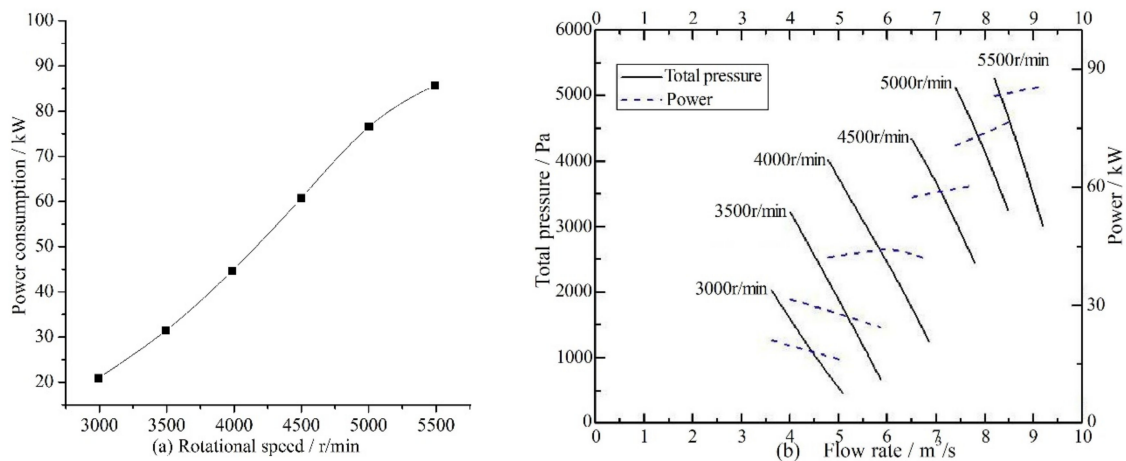


Figure 4. (a) Power consumption curve of centrifugal fan; (b) Performance characteristic curve of centrifugal fan.

In Figure 4, a total of 6 speed test points are selected in the experiment around the rated speed of 5000 r/min, which are 3000 r/min, 3500 r/min, 4000 r/min, 4500 r/min, 5000 r/min and 5500 r/min, respectively. The relationship of volume flow rate, rotational speed, power, and total pressure of the fan is shown in Figure 4b. During the whole test process, the volume flow rate of the fan varies from 3.5 m³/s to 9.4 m³/s, and the fan average power varies from 16 kW to 92.8 kW. It can be found that with the same speed of fan and with the decrease of volume flow rate, the total pressure of the fan and the power consumed by the fan increase gradually.

4. Simulation Study

4.1. Grid Division and Definition of the Boundary

The finite volume analysis software Ansys Fluent [18] is used to simulate the centrifugal fan, and the flow field model of the fan is shown in Figure 5. The flow field model of fan is divided into three parts, which include inlet extension area, rotating fluid area, and outlet extension area. Besides, a multi-reference frame (MRF) approach is adopted for the rotating fluid area. The medium flowing in the fan channel is air, and the fluid in the fan moving area belongs to turbulence flow. The effect of gravity on the flow field is ignored. The standard $k-\varepsilon$ model is used. In the simulation process, only the ambient pressure and its corresponding air physical properties are changed, while other boundary conditions are not changed. Given the complexity of the fan simulation model, a mixture of structured and unstructured grids is used to partition the fluid region. In the inlet extension and outlet extension areas, structured grid is adopted [19].

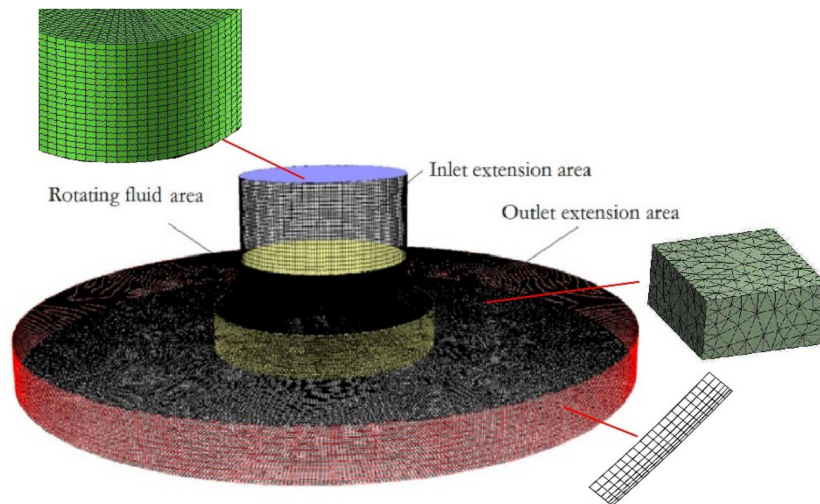


Figure 5. Flow field model and grid division of centrifugal fan.

In the rotating fluid areas, the tetrahedral grid is used. The near-wall grids are locally encrypted. To assess the influence of the number of grids on the accuracy of the calculation, the grid independence is calculated. Five grid systems, 0.44 million, 0.72 million, 1 million, 1.28 million, and 1.56 million, are tested. It is found that the relative errors of total pressure of fan between the solutions of 1.28 million and 1.56 million are less than 0.07%. It can be considered that the simulation calculation result is independent of the number of grids when the number of grids is encrypted to 1.28 million [20]. The inlet is set as “Velocity inlet”, the outlet is set as free “Outflow”, and the rotating fluid area is set as “no-slip boundary condition”.

4.2. Governing Equations

The governing equations mainly include mass conservation, momentum conservation, and energy conservation equations, which are

1. Mass conservation equation

$$\frac{\partial \rho}{\partial \tau} + \nabla \cdot (\rho U) = 0, \quad (6)$$

where U is the velocity vector, ρ is the density, and τ is time.

2. Momentum conservation equation

$$\left. \begin{aligned} \frac{\partial(\rho u_1)}{\partial \tau} + \text{div}(\rho u_1 \cdot U) &= \text{div}(\mu \text{grad} u_1) - \frac{\partial p}{\partial x} + S_u \\ \frac{\partial(\rho u_2)}{\partial \tau} + \text{div}(\rho u_2 \cdot U) &= \text{div}(\mu \text{grad} u_2) - \frac{\partial p}{\partial y} + S_v \\ \frac{\partial(\rho u_3)}{\partial \tau} + \text{div}(\rho u_3 \cdot U) &= \text{div}(\mu \text{grad} u_3) - \frac{\partial p}{\partial z} + S_w \end{aligned} \right\}, \quad (7)$$

where μ is kinetic viscosity, p is pressure, u_1 , u_2 , and u_3 are the components of the velocity vector in the X, Y, and Z directions, and S_u , S_v , S_w are the generalized source terms.

3. Energy conservation equation

$$\frac{\partial(\rho t)}{\partial t} + \text{div}(\rho U t) = \text{div}\left(\frac{\lambda}{c_p} \text{grad} T\right) - \frac{\partial p}{\partial x} + S_T, \quad (8)$$

where T is the temperature, λ is the heat transfer coefficient of the fluid, c_p is the specific heat capacity, and S_T is the viscous dissipation term.

The solver uses the SEGREGATED separate implicit solver. The turbulence energy, turbulence dissipation term, and momentum conservation equations are all discretized using the second-order upwind scheme. The governing equations are solved using the transient-SIMPLE method. Second order upwind scheme is chosen to discretize these governing equations. Due to the strong nonlinear relationship between the variables, the iterative solution uses subrelaxation factors. The inlet and outlet turbulence are all set to 0.5%, and the detection surface of mass flow rate is set at the fan outlet section. For the mass conservation equation, when the results of two adjacent calculations are less than 10^{-6} , the numerical simulation results can be considered to converge.

4.3. Simulation Model Verification

The diagram of the comparison between the simulation calculation results and the experimental results at the rotational speed of 5500 r/min under normal pressure is shown in Figure 6.

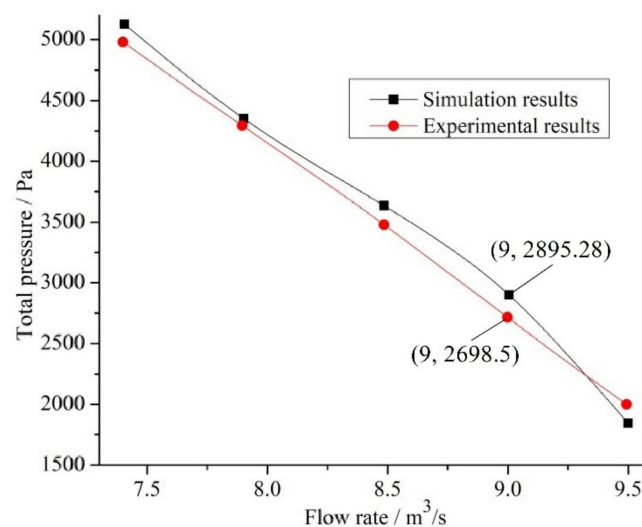


Figure 6. Comparison between the experimental and the simulation results of total pressure of the fan.

It can be seen from the figure that the error between the experimental value and the calculated value is within 6.8% in the whole experiment process, which indicates that the simulation model is reliable. The deviation between the simulation and the experimental results may be caused to some extent by the simplification of the fan model, measurement errors in the experimental process, and errors inherent in the simulation calculation method. At the same time, the simulation model is mainly used for comparative study. Therefore, the simulation model can be used to simulate the fan performance under different environmental pressures.

4.4. Numerical Calculation Results and Analysis

4.4.1. Pressure Analysis of the Fan under Different Ambient Pressures

Using this model, the performance of the fan under the same rotational speed (5500 r/min) and different ambient pressure is simulated, and the calculation results are shown in Figure 7.

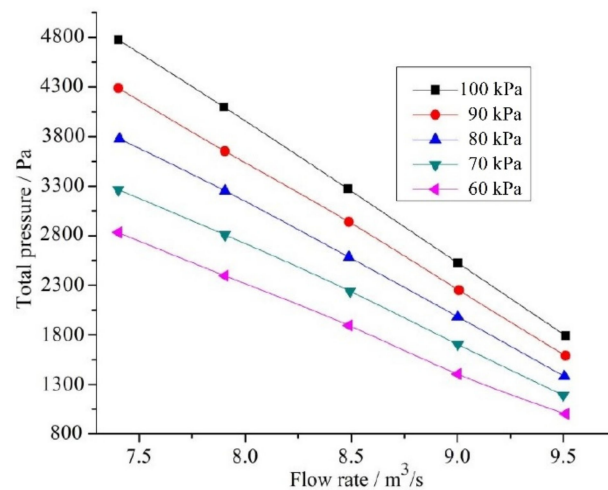


Figure 7. Total pressure of the fan under different ambient pressures.

It can be seen from Figure 7 that the total pressure of the fan decreases with the decrease of flow rate, and the lower ambient pressure indicates that the total pressure of the fan is lower under the same condition. The quantitative analysis shows that compared with the normal pressure condition, the total pressure drop amplitude of the fan is basically the same at each working point under low pressure condition. Taking 60 kPa pressure operating point as an example, the average decrease range of total pressure of the fan is 42.3% compared with the normal pressure condition.

Figure 8 shows the changing curve of the static pressure versus flow rate of the fan under different ambient pressures. It can be seen from the figure that the variation trend of the fan static pressure and the total pressure is similar. The lower the ambient pressure, the lower the fan static pressure. Compared with the normal pressure condition, the static pressure drop extent of the fan is basically the same at each working point under the low-pressure condition. Taking 60 kPa pressure operating point as an example, the average decrease extent of fan static pressure is 38.3% compared with normal pressure operating point. At the same time, the air density at 60 kPa is about 39.5% lower than that at atmospheric pressure. Thus, the decline in the total pressure and static pressure performance of the fan is mainly due to the drop in the air density caused by the reduction of the environmental pressure.

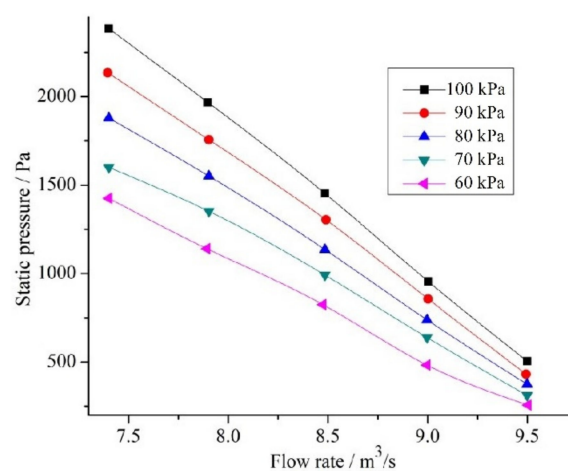


Figure 8. Static pressure of the fan under different ambient pressure.

Figure 9 shows the change curve of fan outlet pressure head along with flow rate (u_f) under different ambient pressure. The figure shows that the outlet pressure head of the fan increases with the increase of flow rate (u_f) but changes little under different ambient pressure. It can be seen that the

environmental pressure has little effect on the outlet pressure head of the fan. Although this change is not obvious, it can be found that the outlet pressure head decreases gradually with the increase of ambient pressure.

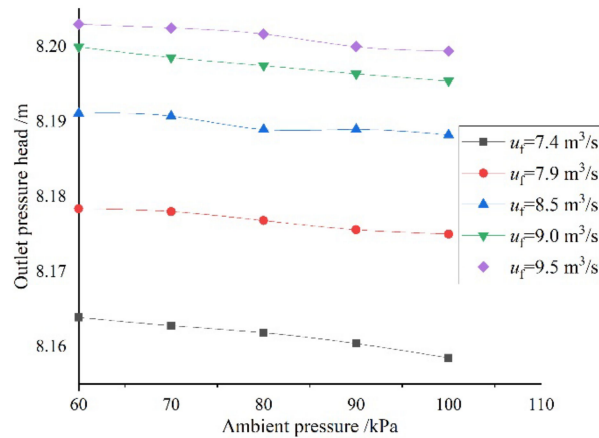


Figure 9. Fan outlet pressure head under different ambient pressure.

4.4.2. Noise Analysis under Different Ambient Pressure

Fan noise propagation is an unsteady process. Large Eddy Simulation (LES) model is used to simulate the sound field, in which the time step is 0.01 ms and each time step is iterated 20 times. At the same time, two noise monitoring points (as shown in Figure 10) are set along the fan radial direction and axis central direction respectively for real-time monitoring of the sound pressure change of the fan. The location of Point 1 and Point 2 are shown in Figure 10, and all dimensions are in millimetres [21,22]. The noise spectrogram of the prototype fan is shown in Figure 11 when the rotational speed of the fan is 5500 r/min and the flow rate is 8.5 m³/s at atmospheric pressure. It can also be seen from Figure 11 that although Point 1 is more than twice as far away from Point 2, the sound pressure level differs little at different frequencies. At the same time, for Point 2 in the axial direction, with the continuous increase of frequency (0–50,000 Hz), the sound pressure level gradually decreases and the trend eases. In the radial direction, with the increase of frequency, the variation of sound pressure level fluctuates greatly, which is the smallest when the frequency reaches 5000 Hz. This is because the change in axial pressure is much smaller than the change in radial pressure.

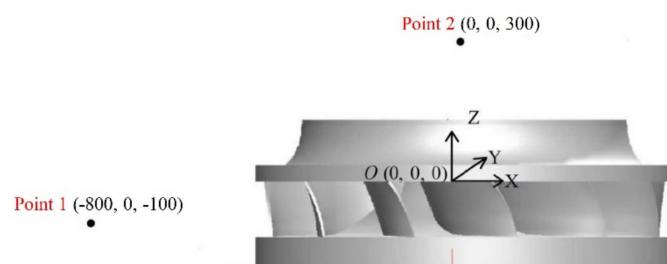


Figure 10. The location of noise measurement Points 1 and 2.

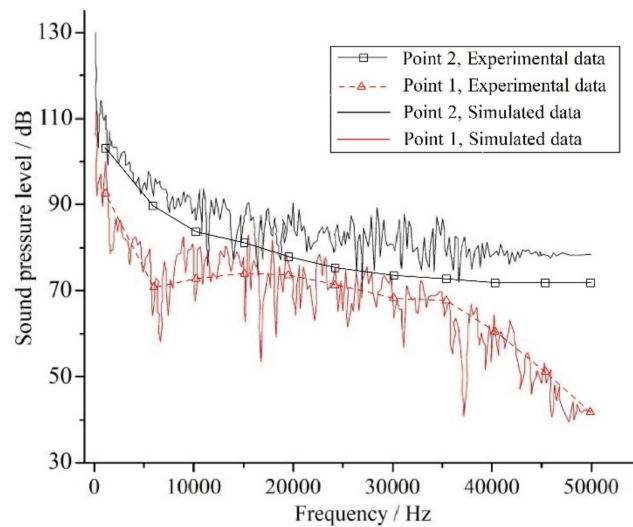


Figure 11. The spectrogram of two monitoring points of centrifugal fan under normal pressure.

Changing the ambient pressure and fluid physical properties, the total sound pressure level of the prototype fan under different ambient pressures is obtained as shown in Figure 12. It can be seen from Figure 12 that as the ambient pressure decreases from 100 kPa to 50 kPa, the noise of the fan gradually becomes lower. In measurement Point 1, noise decreases from 103.85 dB to 98.2 dB. In measurement Point 2, it decreases from 121.45 dB to 118.1 dB. So, the sound pressure levels at the two measurement points decrease by about 5.8% and 2.8%, respectively. This means that the sound pressure level at negative pressure is smaller than that at one atmosphere. This also means that the noise produced by the centrifugal fan is less than that produced by one standard atmospheric pressure under the low-pressure environment such as the plateau environment. The general reason mainly lies in that the air density decreases when the air pressure is low, and the pressure variation range in the air during the operation of the centrifugal fan is small.

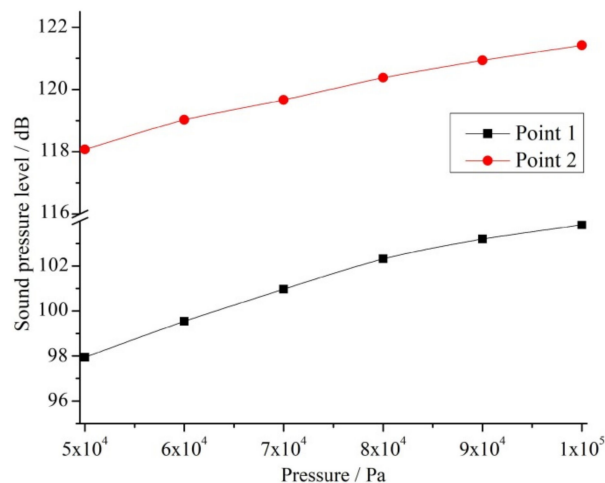


Figure 12. Fan noise under negative pressure.

At the same time, with the decrease of ambient pressure, the sound pressure level of fan noise presents an approximate logarithmic reduction trend. The relationship between sound pressure level and sound power can be transformed into

$$L_P = 10 \lg \frac{W}{W_0} - 20 \lg r - 11, \quad (9)$$

where W_0 is the reference sound power, and it is generally taken as 10^{-2} W. As can be seen from Equation (9), we can obtain that $L_p \sim \lg W$. Since the sound power W and the air density ρ are in a linear relationship, namely $W \sim \rho$, so $L_p \sim \lg \rho$, it can be seen that the logarithmic relationship of the sound pressure level and the air density is linear.

5. Conclusions

In this paper, the flow and noise characteristics of centrifugal fan in low-pressure environment (50 kPa–100 kPa) are studied; the following conclusions can be obtained:

1. The sound power and sound pressure of the fan are proportional to the air density, while the sound pressure level of the fan is proportional to the logarithm of the air density.
2. The total pressure and static pressure of the fan decrease with the decrease of environmental pressure. The total pressure and static pressure of the fan at 60 kPa pressure operating mode decrease by 42.3% and 38.3%, respectively, compared with the normal pressure. The main reason for this phenomenon is the decrease of air density due to the decrease of environmental pressure.
3. Under the same working condition (fan rotational speed of 5500 r/min, flow rate of 8.5 m³/s), the sound pressure level at the two measuring points of the centrifugal fan increases by about 5.8% and 2.8%, respectively, as the ambient pressure increases from 50 kPa to 100 kPa. With the increase of ambient pressure, the sound pressure level of fan noise shows an approximate logarithmic growth trend.

Author Contributions: Conceptualization, X.Z.; methodology, X.Z.; software, Y.Z.; validation, Y.Z.; formal analysis, C.L.; writing—original draft preparation, C.L. All authors have read and agreed to the published version of the manuscript.

Funding: This research was funded by National Natural Science Foundation of China, grant number 51806114 and 51874187.

Conflicts of Interest: The authors declare no conflict of interest.

References

1. Liu, J.; Ge, Y.; Wang, X. On-board measurement of particle numbers and their size distribution from a light-duty diesel vehicle: Influences of VSP and altitude. *J. Environ. Sci.* **2017**, *57*, 238–248. [[CrossRef](#)] [[PubMed](#)]
2. Xi, Y.; Yan, D.; Zhang, X.; Zhanng, X. Prediction of particle-collection efficiency for vacuum-blowing cleaning system based on operational conditions. *Processes* **2020**, *8*, 809. [[CrossRef](#)]
3. Lun, Y.X.; Ye, X.X.; Lin, L.M.; Ying, C.L.; Wei, Y.K. Unsteady characteristics of forward multi-wing centrifugal fan at low flow rate. *Processes* **2019**, *7*, 691. [[CrossRef](#)]
4. Genglin, C.; Wei, X.; Jinyun, Z.; Haipeng, Z. Energy-Saving performance of flap-adjustment-based centrifugal fan. *Energies* **2018**, *11*, 162.
5. Huang, P.; Zhang, Y.L. Analysis of seepage characteristics of mine fractures based on geothermal utilization. *Bulg. Chem. Commun.* **2017**, *11*, 44–48.
6. Lee, K.S.; Kim, K.Y.; Samad, A. Design optimization of low-speed axial flow fan blade with three-dimensional RANS analysis. *J. Mech. Sci. Technol.* **2008**, *22*, 1864–1869. [[CrossRef](#)]
7. Gholamian, M.; Rao, G.K.M.; Bhramara, P. Effect of Inlet Diffuser Diameter on Flow Pattern and Efficiency of Squirrel Cage Fans with CFD Method. *Int. J. Fluid Mech. Res.* **2014**, *41*, 106–119. [[CrossRef](#)]
8. Hurault, J.; Kouidri, S.; Bakir, F. Experimental investigations on the wall pressure measurement on the blade of axial flow fans. *Exp. Fluid Sci.* **2012**, *40*, 29–37. [[CrossRef](#)]
9. Zhang, J. Research on twist Pattern of Single Impeller Axial Blade and Design of Thin Blade. *Mach. China* **2015**, *3*, 189–190.
10. Sharland, I.J. Sources of noise in axial flow fans. *J. Sound Vib.* **1964**, *1*, 302–322. [[CrossRef](#)]
11. Li, H. Flow driven by a stamped metal cooling fan—Numerical model and validation. *Exp. Fluid Sci.* **2009**, *33*, 683–694. [[CrossRef](#)]

12. Hodgson, M.; Li, I. Experimental study of the noise emission of personal computer cooling fans. *Appl. Acoust.* **2006**, *67*, 849–863. [[CrossRef](#)]
13. Bredell, J.R.; Kröger, D.G.; Thiart, G.D. Numerical investigation of fan performance in a forced draft air-cooled steam condenser. *Appl. Eng.* **2006**, *26*, 846–852. [[CrossRef](#)]
14. Ommi, F.; Azimi, M. Main fan noise mitigation technologies in turbofan engines. *Aviation* **2014**, *18*, 141–146. [[CrossRef](#)]
15. Wei, R.J. Accurate calculation of sound speed in air. *J. Nanjing Univ.* **1995**, *1*, 10–16.
16. Zhang, X.L.; Wang, Y.C.; Cang, P. Experimental investigation of thermal hydraulic performance of heat exchangers with different Reynolds numbers on both air-side and water-side. *Appl. Eng.* **2016**, *99*, 1331–1339. [[CrossRef](#)]
17. Zhang, X.L.; Wang, Y.C.; Li, M. Improved flow and heat transfer characteristics for heat exchanger by using a new humped wavy fin. *Appl. Eng.* **2017**, *124*, 510–520. [[CrossRef](#)]
18. Zhang, X.; Zhang, Y.; Liu, Z.; Liu, J. Analysis of heat transfer and flow characteristics in typical cambered ducts. *Int. J. Therm. Sci.* **2020**, *150*, 106226. [[CrossRef](#)]
19. Zhang, Y.L.; Zhang, X.L.; Li, M. Research on heat transfer enhancement and flow characteristic of heat exchange surface in cosine style runner. *Heat Mass Transf.* **2019**, *55*, 3117–3131. [[CrossRef](#)]
20. Xu, C.W.; Nie, W.; Liu, Z.Q. Multi-factor numerical simulation study on spray dust suppression device in coal mining process. *Energy* **2019**, *182*, 544–558. [[CrossRef](#)]
21. Wei, Y.; Ying, C.; Xu, J.; Cao, W.; Wang, Z.; Zhu, Z. Effects of single-arc blade profile length on the performance of a forward multiblade fan. *Processes* **2019**, *7*, 629. [[CrossRef](#)]
22. Zhang, J.; Chu, W.; Zhang, J.; Lv, Y. Vibroacoustic Optimization Study for the Volute Casing of a Centrifugal Fan. *Appl. Sci.* **2019**, *9*, 859. [[CrossRef](#)]



© 2020 by the authors. Licensee MDPI, Basel, Switzerland. This article is an open access article distributed under the terms and conditions of the Creative Commons Attribution (CC BY) license (<http://creativecommons.org/licenses/by/4.0/>).

MDPI
St. Alban-Anlage 66
4052 Basel
Switzerland
Tel. +41 61 683 77 34
Fax +41 61 302 89 18
www.mdpi.com

Processes Editorial Office
E-mail: processes@mdpi.com
www.mdpi.com/journal/processes



MDPI
St. Alban-Anlage 66
4052 Basel
Switzerland

Tel: +41 61 683 77 34
Fax: +41 61 302 89 18

www.mdpi.com



ISBN 978-3-0365-1815-2